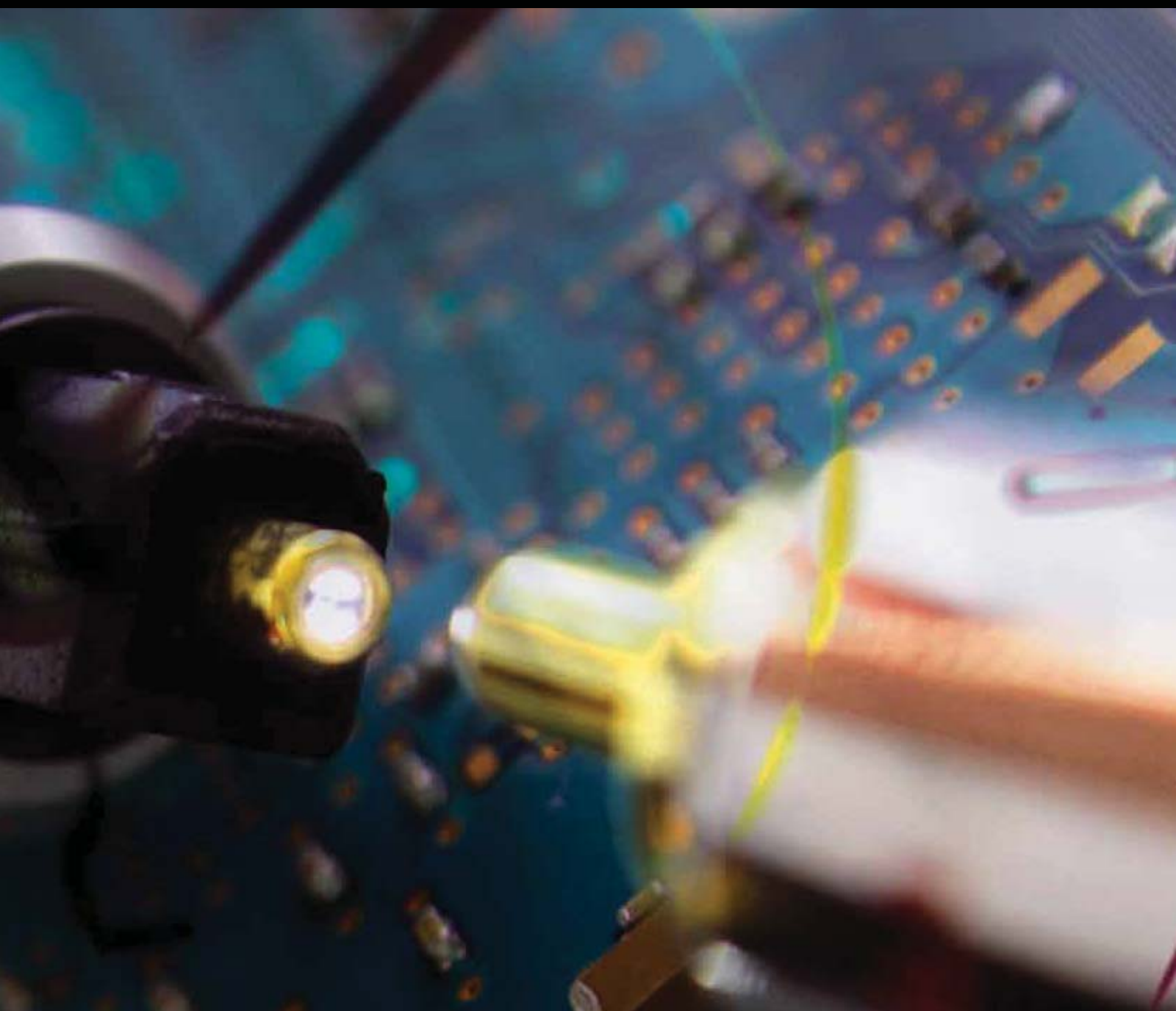


Nanomaterials for Chemical Sensing Technologies

Guest Editors: Michele Penza, Giorgio Sberveglieri,
Wojtek Wlodarski, and Yongxiang Li





Nanomaterials for Chemical Sensing Technologies

Nanomaterials for Chemical Sensing Technologies

Guest Editors: Michele Penza, Giorgio Sberveglieri, Wojtek Wlodarski, and Yongxiang Li



Copyright © 2009 Hindawi Publishing Corporation. All rights reserved.

This is a special issue published in volume 2009 of "Journal of Sensors." All articles are open access articles distributed under the Creative Commons Attribution License, which permits unrestricted use, distribution, and reproduction in any medium, provided the original work is properly cited.

Editor-in-Chief

Francisco J. Arregui, Public University of Navarre, Spain

Associate Editors

Francesco Baldini, Italy

Amine Bermak, Hong Kong

Mehmet Can Vuran, USA

Andrea Cusano, Italy

Cristina E. Davis, USA

Utkan Demirci, USA

Jiri Homola, Czech Republic

Bernhard Jakoby, Austria

K. Kalantar-Zadeh, Australia

Challa S S R Kumar, USA

Hiroki Kuwano, Japan

Yongxiang Li, China

Franco Maloberti, Italy

Ignacio R. Matias, Spain

Mike McShane, USA

Igor L. Medintz, USA

Tommaso Melodia, USA

Joan Ramon Morante, Spain

S. C. Mukhopadhyay, New Zealand

K. S. Narayan, India

Michele Penza, Italy

Pavel Ripka, Czech Republic

Giorgio Sberveglieri, Italy

Pietro Siciliano, Italy

Weilian Su, USA

Isao Takayanagi, Japan

Maria Tenje, Denmark

Athanasios T. Vasilakos, Greece

Wojtek Wlodarski, Australia

Stanley E. Woodard, USA

Hai Xiao, USA

Contents

Nanomaterials for Chemical Sensing Technologies, Michele Penza, Giorgio Sberveglieri, Wojtek Wlodarski, and Yongxiang Li
Volume 2009, Article ID 924941, 2 pages

Carbon Nanotube-Based Electrochemical Sensors: Principles and Applications in Biomedical Systems, Chengguo Hu and Shengshui Hu
Volume 2009, Article ID 187615, 40 pages

Carbon Nanotubes as Active Components for Gas Sensors, Wei-De Zhang and Wen-Hui Zhang
Volume 2009, Article ID 160698, 16 pages

A Review of Carbon Nanotubes-Based Gas Sensors, Yun Wang and John T. W. Yeow
Volume 2009, Article ID 493904, 24 pages

Conductometric Gas Nanosensors, Girolamo Di Francia, Brigida Alfano, and Vera La Ferrara
Volume 2009, Article ID 659275, 18 pages

Fabrication of TiO_2 Nanotube Thin Films and Their Gas Sensing Properties, Yongxiang Li, Xiaofeng Yu, and Qunbao Yang
Volume 2009, Article ID 402174, 19 pages

Porphyrin-Based Nanostructures for Sensing Applications, Donato Monti, Sara Nardis, Manuela Stefanelli, Roberto Paolesse, Corrado Di Natale, and Arnaldo D'Amico
Volume 2009, Article ID 856053, 10 pages

Nanocrystalline Metal Oxides for Methane Sensors: Role of Noble Metals, S. Basu and P. K. Basu
Volume 2009, Article ID 861968, 20 pages

Shrinkage Effects of the Conduction Zone in the Electrical Properties of Metal Oxide Nanocrystals: The Basis for Room Temperature Conductometric Gas Sensor, M. Manzanares, T. Andreu, J. D. Prades, J. Arbiol, F. Hernandez-Ramírez, A. Cirera, and J. R. Morante
Volume 2009, Article ID 783675, 6 pages

Sb- SnO_2 -Nanosized-Based Resistive Sensors for NO_2 Detection, T. Krishnakumar, R. Jayaprakash, N. Pinna, A. Donato, N. Donato, G. Micali, and G. Neri
Volume 2009, Article ID 980965, 7 pages

Highly Sensitive InO_x Ozone Sensing Films on Flexible Substrates, G. Kiriakidis, K. Moschovis, I. Kortidis, and R. Skarvelakis
Volume 2009, Article ID 727893, 5 pages

Designing Zirconium Coated Polystyrene Colloids and Application, Diana Chira and Seong S. Seo
Volume 2009, Article ID 514947, 6 pages

A Simple Optical Model for the Swelling Evaluation in Polymer Nanocomposites,
Anna De Girolamo Del Mauro, Angelica Immacolata Grimaldi, Vera La Ferrara, Ettore Massera, Maria Lucia
Miglietta, Tiziana Polichetti, and Girolamo Di Francia
Volume 2009, Article ID 703206, 6 pages

**Schottky Junction Methane Sensors Using Electrochemically Grown Nanocrystalline-Nanoporous ZnO
Thin Films**, P. K. Basu, N. Saha, S. K. Jana, H. Saha, A. Lloyd Spetz, and S. Basu
Volume 2009, Article ID 790476, 9 pages

On the Low-Temperature Response of Semiconductor Gas Sensors, A. Helwig, G. Müller, G. Sberveglieri,
and M. Eickhoff
Volume 2009, Article ID 620720, 17 pages

Quartz Crystal Microbalance as a Sensor to Characterize Macromolecular Assembly Dynamics,
K. Kanazawa and Nam-Joon Cho
Volume 2009, Article ID 824947, 17 pages

Integrated MEMS/NEMS Resonant Cantilevers for Ultrasensitive Biological Detection, Xinxin Li,
Haitao Yu, Xiaohua Gan, Xiaoyuan Xia, Pengcheng Xu, Jungang Li, Min Liu, and Yongxiang Li
Volume 2009, Article ID 637874, 10 pages

On Mass Loading and Dissipation Measured with Acoustic Wave Sensors: A Review, Marina V. Voinova
Volume 2009, Article ID 943125, 13 pages

Analyzing Spur-Distorted Impedance Spectra for the QCM, Sae Moon Yoon, Nam Joon Cho,
and Kay Kanazawa
Volume 2009, Article ID 259746, 8 pages

Nanostructure-Enhanced Surface Acoustic Waves Biosensor and Its Computational Modeling,
Guigen Zhang
Volume 2009, Article ID 215085, 11 pages

Receptor Function and Response of Semiconductor Gas Sensor, Noboru Yamazoe and Kengo Shimanoe
Volume 2009, Article ID 875704, 21 pages

Optimized Feature Extraction for Temperature-Modulated Gas Sensors, Alexander Vergara,
Eugenio Martinelli, Eduard Llobet, Arnaldo D'Amico, and Corrado Di Natale
Volume 2009, Article ID 716316, 10 pages

**YSZ-Based Oxygen Sensors and the Use of Nanomaterials: A Review from Classical Models to Current
Trends**, Carlos López-Gándara, Francisco M. Ramos, and Albert Cirera
Volume 2009, Article ID 258489, 15 pages

Field-Assisted and Thermionic Contributions to Conductance in SrO_2 Thick-Films, C. Malagù, M. C. Carotta, G. Martinelli, M. A. Ponce, M. S. Castro, and C. M. Aldao
Volume 2009, Article ID 402527, 5 pages

Nanotechnology: A Tool for Improved Performance on Electrochemical Screen-Printed (Bio)Sensors, Elena Jubete, Oscar A. Loaiza, Estibalitz Ochoteco, Jose A. Pomposo, Hans Grande, and Javier Rodríguez
Volume 2009, Article ID 842575, 13 pages

Sensitivity Improvement of an Impedimetric Immunosensor Using Functionalized Iron Oxide Nanoparticles, Imen Hafaïd, Asma Gallouz, Walid Mohamed Hassen, Adnane Abdelghani, Zina Sassi, Francois Bessueille, and Nicole Jaffrezic-Renault
Volume 2009, Article ID 746548, 12 pages

YSZ-Based Oxygen Sensors and the Use of Nanomaterials: A Review from Classical Models to Current Trends, Carlos López-Gándara, Francisco M. Ramos, and Albert Cirera
Volume 2009, Article ID 258489, 15 pages

The Adsorption Properties of *Bacillus atrophaeus* Spores on Single-Wall Carbon Nanotubes, P. Cortes, S. Deng, and G. B. Smith
Volume 2009, Article ID 131628, 6 pages

Electrochemical Sensing System Utilizing Simazine-Imprinted Polymer Receptor for the Detection of Simazine in Tap Water, Yusuke Fuchiwaki, Naoki Sasaki, and Izumi Kubo
Volume 2009, Article ID 503464, 6 pages

A Novel Biosensor to Detect MicroRNAs Rapidly, Jie-Ying Liao, James Q. Yin, and Jia-Chang Yue
Volume 2009, Article ID 671896, 6 pages

Ozone Sensor for Application in Medium Voltage Switchboard, Letizia De Maria and Giuseppe Rizzi
Volume 2009, Article ID 608714, 5 pages

Editorial

Nanomaterials for Chemical Sensing Technologies

Michele Penza,¹ Giorgio Sberveglieri,² Wojtek Wlodarski,³ and Yongxiang Li⁴

¹ Department of Physical Technologies and New Materials, ENEA, Italian National Agency for New Technologies, Energy, and Sustainable Economic Development, Brindisi Research Center, 72100 Brindisi, Italy

² Department of Chemistry and Physics for Engineering and Materials, University of Brescia, 25133 Brescia, Italy

³ School of Electrical and Computer Systems Engineering, RMIT University, Melbourne 3001, Australia

⁴ State Key Laboratory of High Performance Ceramics and Superfine Microstructures, Shanghai Institute of Ceramics, Chinese Academy of Sciences, Shanghai 200050, China

Correspondence should be addressed to Michele Penza, michele.penza@enea.it

Received 16 November 2009; Accepted 16 November 2009

Copyright © 2009 Michele Penza et al. This is an open access article distributed under the Creative Commons Attribution License, which permits unrestricted use, distribution, and reproduction in any medium, provided the original work is properly cited.

Current trend in the solid-state sensing technology is the development of nanomaterials and nanostructures with novel functionalities and innovative properties at the nanoscale for high-performance chemical sensing.

The actual state of the nanotechnology has reached mature advancements for nanomaterials processing including functionalizations, nanocomposites, hybridization of materials, nanoparticles, nanowires, nanotubes, nanofibers, nanobelts, nanowalls, and sensing nanodevices to fabricate chemical sensors and sensor arrays with tailored characteristics and tuned properties at the nanoscale level.

In this direction, great efforts in the ongoing research have been doing to fabricate sensors with advanced sensing nanostructures and innovative transducers coupled to proper electronic interfaces and new algorithms of pattern recognition and signal processing.

The key role for high-performance sensors is the engineering of nanomaterials with novel sensing properties for sensing nanodevices and emerging transducers to develop sensor systems at high-sensitivity, high-resolution and high-specificity.

This special issue, NCST, for open-access Journal of Sensors (<http://www.hindawi.com/journals/js/>) has been completely devoted to nanomaterials for sensors and sensing Technologies. This issue has openly called for perspective and original contributions in the field of sensor nanomaterials and sensor technology from outstanding scientists and nanotechnologists. The issue has accepted contributions to cover the full range of sensors from the theory, basic properties, modelling, design, fabrication, processing, integration,

characterization, to the applications of the sensors. The submission of the manuscripts related to the fundamental and applied aspects for the sensory nanomaterials and their novel functionalities and applications included, but not limited to:

- (i) Sensor nanomaterials
- (ii) Nanostructures and thin films for gas sensors
- (iii) Carbon nanotubes chemical sensors
- (iv) Metal oxides nanowires for gas sensors
- (v) Hybrid materials for sensors
- (vi) Nanocomposites and functionalizations for sensing devices
- (vii) Nanostructured materials for gas sensors
- (viii) Mass-sensitive sensors: SAW, TFBAR, QCM
- (ix) Gas sensors and chemiresistors
- (x) Nanosensors
- (xi) Gas sensor arrays
- (xii) Pattern recognition and signal processing
- (xiii) Modelling for chemical sensors
- (xiv) Applications of sensor systems.

The special issue NCST, launched at April 2008, has been officially closed at February 2009, receiving 39 submitted manuscripts, 19 Review Articles and 20 Research

Articles, from worldwide outstanding scientists and top-leading researchers of 17 different Countries according to the geographic-area sharing 52% of the total submitted papers from Europe/Africa, 29% from Asia, and 19% from Americas. The submission full process of the papers was electronically made through the Journal of Sensors Manuscript Tracking System (<http://mts.hindawi.com/>). The four Guest Editors have managed a balanced number of papers according to own expertise by inviting qualified reviewers and by assigning at least 2 referees per paper, excluding some cases. The total number of the reviewers involved in the peer-review process has been about 80.

Review on Special Issue NCST for Journal of Sensors

Gas sensor technologies were first developed in the 1970s and 1980s and have been commercialised by companies that exploit the different sensing principles, namely, optical, electrochemical, resistive and gravimetric. The first two technologies are arguably the most successful but the latter two offer lower cost and higher sensitivity. Recently, new chemical sensing materials and technologies have been invented that exploit the emerging fields of nanoscience and nanotechnology. This special issue contains a valuable collection of articles that relate to nanomaterials, nanotransducers, and signal processing methods. In particular, it covers the emergence of functionalised carbon nanotubes and new metal oxide materials as well as MEMS transducers for the detection of chemicals. The issue is very welcome at a time when many different technologies are being reported, such as carbon nanotubes, but have yet to prove themselves *commercially* when compared to existing electrochemical cells and optical spectrometers. Nevertheless, it is likely that we will see some of these new technologies exploited at a scale unseen before because of the ultralow power and cost that they potentially offer perhaps leading to a new generation of the so-called ubiquitous chemical sensors.

Julian Gardner
Warwick University, School of Engineering
Professor of Electronic Engineering
School of Engineering, University of Warwick,
Coventry CV4 7AL, UK
Email: j.w.gardner@warwick.ac.uk
URL: www.eng.warwick.ac.uk/SRL

Acknowledgment

The authors are very thankful both to the Editor-in-Chief of Journal Sensors (Prof. Francisco J. Arregui) and the Editorial Board for approving and supporting the special issue NCST.

Michele Penza
Giorgio Sberveglieri
Wojtek Wlodarski
Yongxiang Li

Review Article

Carbon Nanotube-Based Electrochemical Sensors: Principles and Applications in Biomedical Systems

Chengguo Hu^{1,2} and Shengshui Hu^{1,2}

¹Key Laboratory of Analytical Chemistry for Biology and Medicine (Ministry of Education),
College of Chemistry and Molecular Sciences, Wuhan University, Wuhan 430072, China

²State Key Laboratory of Transducer Technology, Chinese Academy of Sciences, Beijing 100080, China

Correspondence should be addressed to Shengshui Hu, sshu@whu.edu.cn

Received 20 December 2008; Accepted 18 March 2009

Recommended by Michele Penza

Carbon nanotubes (CNTs) have received considerable attention in the field of electrochemical sensing, due to their unique structural, electronic and chemical properties, for instance, unique tubular nanostructure, large specific surface, excellent conductivity, modifiable sidewall, high conductivity, good biocompatibility, and so on. Here, we tried to give a comprehensive review on some important aspects of the applications of CNT-based electrochemical sensors in biomedical systems, including the electrochemical nature of CNTs, the methods for dispersing CNTs in solution, the approaches to the immobilization of functional CNT sensing films on electrodes, and the extensive biomedical applications of the CNT-based electrochemical sensors. In the last section, we mainly focused on the applications of CNT-based electrochemical sensors in the analysis of various biological substances and drugs, the methods for constructing enzyme-based electrochemical biosensors and the direct electron transfer of redox proteins on CNTs. Because several crucial factors (e.g., the surface properties of carbon nanotubes, the methods for constructing carbon nanotube electrodes and the manners for electrochemical sensing applications) predominated the analytical performances of carbon nanotube electrodes, a systematical comprehension of the related knowledge was essential to the acquaintance, mastery and development of carbon nanotube-based electrochemical sensors.

Copyright © 2009 C. Hu and S. Hu. This is an open access article distributed under the Creative Commons Attribution License, which permits unrestricted use, distribution, and reproduction in any medium, provided the original work is properly cited.

1. Introduction

Carbon nanotubes (CNTs) have become the subject of intense researches in the last decades because of their unique properties and the promising applications in any aspect of nanotechnology. Because of their unique one-dimensional nanostructures, CNTs display fascinating electronic and optical properties that are distinct from other carbonaceous materials and nanoparticles of other types. CNTs are widely used in electronic and optoelectronic, biomedical, pharmaceutical, energy, catalytic, analytical, and material fields. Particularly, the properties of small dimensions, functional surfaces, good conductivity, excellent biocompatibility, modifiable sidewall, and high reactivity make CNTs ideal candidates for constructing sensors with high performances. As an example, CNTs have been extensively employed in constructing various electrochemical sensors. Compared with the conventional scale materials and other types of nanomaterials, the special nanostructural properties make

CNTs have some overwhelming advantages in fabricating electrochemical sensors, including

- (i) the large specific area producing high sensitivity;
- (ii) the tubular nanostructure and the chemical stability allowing the fabrication of ultrasensitive sensors consisting of only one nanotube;
- (iii) the good biocompatibility that is suitable for constructing electrochemical biosensors, especially for facilitating the electron transfer of redox proteins and enzymes;
- (iv) the modifiable ends and sidewalls providing a chance for fabricating multifunctioned electrochemical sensors via the construction of functional nanostructures;
- (v) the possibility of achieving miniaturization;
- (vi) the possibility of constructing ultrasensitive nanoarrays.

In fact, since the first application of CNTs in electrochemistry by Britto et al. [1], numerous works have dealt with the construction of electrochemical sensors by CNTs and the subsequent applications. Generally, the replacement of ordinary materials by CNTs can effectively improve the redox currents of inorganic molecules, organic compounds, macromolecules or even biological cells and reduce the redox overpotentials. The electron transfer and the direct electrochemistry of redox proteins at CNT-based electrochemical sensors were also widely reported. Due to the well-defined structure, the chemistry stability and the electrocatalytic activity toward many substances, CNTs are also extensively used as the carrier platforms for constructing various electrochemical sensors. The promising applications of CNTs have been reviewed by several authors [2–6]. Instead of covering all aspects of CNT applications in electrochemistry, this review is restricted to electrochemical sensors based on traditional electrochemical methods (e.g., voltammetry and amperometry), and does not cover other methods like potentiometry, impedance spectroscopy and piezoelectricity. It not only pays attention to the principle, the fabrication and the biomedical applications of various CNT-based electrochemical sensors but also attempts to focus on the fundamental electrochemical knowledge of CNTs.

2. Electrochemical Properties of Carbon Nanotubes

The electrochemical qualities of carbon material-based electrodes are significantly dependent on the surface properties as the creation of specific surface functional groups (especially oxygen-containing groups) can considerably increase the rate of electron transfer (ET) [7]. Based on their specific structures, two distinct surface regions exist in carbon nanotubes (CNTs): the sidewalls and the ends. Since carbon nanotubes can be seen as the graphene sheets rolled into tubes, the electrochemical properties of carbon nanotubes are comparable to the basal planes of pyrolytic graphite (bpgg). For intact carbon nanotubes, the defect-free structure makes the whole tubes possess almost the same properties to that of bpgg except that the cap regions may be more reactive due to the much higher curve strain than the sidewall. The opening of the ends by physical/chemical treatments on carbon nanotubes produces a variety of oxygen-containing groups, which possess the properties similar to the edge places of bpgg [8].

Due to the simple and well-defined responses at carbon materials, the $\text{Fe}(\text{CN})_6^{3-}/\text{Fe}(\text{CN})_6^{4-}$ couple has been widely used to characterize the surface properties of all kinds of carbon electrodes. Similarly, the electrochemical properties of carbon nanotube-based electrodes are generally investigated by $\text{Fe}(\text{CN})_6^{3-}/\text{Fe}(\text{CN})_6^{4-}$ as the probe. Nugent et al. [9] compared the electrochemical behaviors of aligned bundles of carbon nanotubes with other carbon electrodes of similar structures. The results indicated that $\text{Fe}(\text{CN})_6^{3-}/\text{Fe}(\text{CN})_6^{4-}$ showed an ideal redox peak separation (ΔE_p) of 59 mV at the aligned multiwalled carbon nanotubes (MWNTs). In

comparison, they reported ΔE_p of more than 100 mV and 700 mV for the basal planes of highly oriented pyrolytic graphite (HOPG) with and without electrochemical pretreatments, respectively. Whereas, ΔE_p of about 70 mV was observed at the edge planes of HOPG. In contrast to the ideal response reported by Nugent et al. [9], Li et al. [8] observed much larger ΔE_p at single-walled carbon nanotube (SWNT) papers ($\Delta E_p = 96$ mV) and at aligned MWNTs with heat pretreatment to remove impurities like amorphous carbon and catalyst ($\Delta E_p = 230$ mV). Particularly, for aligned MWNTs, the apparent electron transfer rate (as indicated by ΔE_p) was found to correlate with both the area of the exposed sidewalls (with graphite basal-plane-like properties) and the density of graphite edge-plane-like defects, that is, the electrochemistry of the probe was also influenced by the sidewalls of the nanotubes. They attributed the small ΔE_p at the SWNT paper to the promoted electron transfer by the oxygen-containing defects produced during the acid purification step for preparing the papers. Recently, the fundamental electrochemical properties of inherently hydrophobic MWNT electrodes and acid-treated MWNTs were reported by Papakonstantinou et al. using AC impedance spectroscopy and cyclic voltammetry (CV) [10]. Slow electron transfer kinetics with ΔE_p larger than 200 mV and an electron transfer resistance of about 370 Ω were observed on pristine MWNTs, close to the results reported by Li et al. at aligned MWNTs [8]. However, acid treatment was found to significantly improve the electron transfer kinetics of $\text{Fe}(\text{CN})_6^{3-}/\text{Fe}(\text{CN})_6^{4-}$ redox couple, approaching almost reversible ET kinetics. They believed that the acid treatment modified the charge carrier density at the surface by introducing surface states and served to facilitate electron transfer. The better wetting properties of functionalized CNTs and the higher local density of states as compared with untreated MWNTs were regarded responsible for favoring faster ET kinetics. In a word, the intact CNT sidewalls resemble the basal planes of pyrolytic graphite and can be regarded electrochemically inert to electroactive species. The apparent improved electron transfer at the intact nanotube sidewalls is attributed to the higher stains than the basal planes. As for the opened caps, the presence of defects and oxygen-containing functional groups makes them possess similar electrochemical properties to those of edge planes of pyrolytic graphite. The introduction of edge-like defect sites and oxygen-containing functional groups at both the caps and the sidewalls by chemical or physical treatments can significantly improve the electrochemical properties of CNTs by changing the electronic structures, the surface states and the wettability of the sidewall, reflected by the apparently facilitated electron transfer kinetics.

The critical roles of defect sites and oxygen-containing groups on the electrochemical performances of CNT-based electrodes have been proved by several fundamental research works [11–14]. Compton et al. [12] compared the oxidative behaviors of reduced β -nicotinamide adenine dinucleotide (NADH), epinephrine (EP) and norepinephrine (NE) that were widely used to verify the so-called “electrocatalytic properties” of CNTs at CNT- and graphite powder-modified basal plane pyrolytic graphite electrodes. They

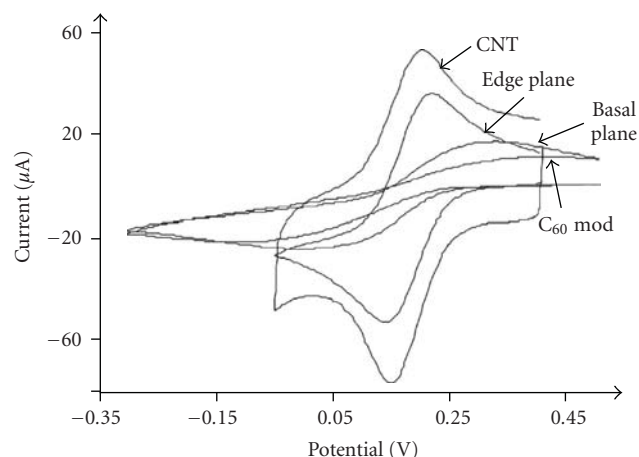


FIGURE 1: Cyclic voltammograms for the reduction of 1 mM ferricyanide for CNT- and C_{60} film-modified bppg electrodes. Also shown is the response of a bare bppg electrode and an edge plane pyrolytic graphite electrode. All scans at a rate of 100 mV/s. [Reprinted with permission from Banks et al. [11], *Chem. Commun.*, **16**, 1804 (2004). Copyright 2004, Royal Society of Chemistry.]

found both the nanotube- and graphite powder-modified electrodes show that electrocatalytic activities toward these species, with enhanced currents and reduced peak-to-peak separations in comparison with the naked basal plane pyrolytic graphite. Moreover, the electrocatalytic activity of CNTs toward hydrogen peroxide was approved to arise from the residual catalyst of iron instead of CNTs themselves [15]. Based on this, they recommended that the catalytic properties should be cautiously assigned to carbon nanotubes. Further, they explored the origin of catalytic properties of CNTs by comparing the voltammetric behaviors of ferricyanide and epinephrine at different chemically modified pyrolytic graphite electrodes [11, 13]. The results indicated that these species exhibited similar behaviors at the C_{60} film-modified bppg electrode and at the naked bppg electrode [13]. Whereas, the response at the CNT film-modified electrode was close to that at the edge plane pyrolytic graphite electrode [11, 13] (Figure 1). They concluded that the basis of the electrocatalytic nature of MWNTs was suggested to reside in electron transfer from the edge-plane-like defect sites at the open ends of nanotubes, which structurally resembled the behavior of edge plane (as opposed to basal plane) graphite. Latter, Gooding et al. [14] demonstrated the critical role of oxygen-containing groups on the electrochemical properties of CNT-based electrodes using randomly orientated nanotube films by a simple casting method and vertically aligned nanotubes by a self-assembled method. In fact, a pair of redox couple located at around 0.0 V in neutral media was usually observed at acid-treated CNT-based electrodes, which was attributed to the redox of the carboxyl groups by Li. et al. using XPS and infrared spectra (IR) [16]. In addition, the electrode process involved four electrons while the rate-determining step was a one-electron reduction. Our

recent work indicated that both the hydrophobic structural defect sites and the hydrophilic oxygen-containing groups were the electroactive sites of CNTs [17]. That is to say, the surface property of CNTs could be conveniently designed by simple pretreatments for optimizing the adsorption and the electrochemical response of analytes. For instance, the hydrophobic defect sites created during the growth or the workup of CNTs were favorable to the adsorption and the electrochemical response of hydrophobic analytes, while the hydrophilic oxygen-containing groups produced by acid treatments facilitated the stable adsorption and the direct electrochemistry of redox proteins.

As a result of the strong intertube interactions, CNTs generally existed as highly tangled ropes and were insoluble in almost all solvents, which greatly hindered their practical applications. In addition, as-produced SWNTs, regardless of the production procedure, usually contain amorphous carbon, carbon nanoparticles and residues from the metal catalysts. To overcome these limitations and to create defect-like sites and oxygen-containing groups on CNTs that favored the electrochemical properties of CNTs, as-received CNTs were usually treated by chemical methods using oxidative, such as refluxing in dilute nitric acid or refluxing/sonication in a concentrated H_2SO_4/HNO_3 mixture [19]. These treatments, by generating surface defects and sometimes resulting in tube shortening, can provide abundant carboxylated sites along the nanotube surface and the shortened tube ends [19–21]. During these processes, nitric acid molecules or NO_x residues can intercalate SWNTs [22] and lead to changes in the Raman spectra of SWNTs by doping [23], which can be deintercalated by thermal annealing treatments in vacuum or argon along with the removal of most defect-like sites on CNTs [24]. A typical example of the annealing treatment effect on the defect sites of CNTs was reported by Kuznetsova et al. using transmission IR spectra (Figure 2) [18]. It is clear that the oxygen-containing groups on the defect sites can be effectively eliminated with annealing treatment. Whereas, the defect sites are not removed by this method, that is, the annealing treatment cannot restore the perfect structure of CNTs. The annealing effects on the electrochemical properties of CNT-based electrodes were investigated by Barisci et al. [25, 26]. They found that thermal annealing produced significant changes in a range of properties of the material including increased hydrophobicity and elimination of electroactive surface functional groups. The activation of CNTs was also achieved by electrochemical methods. Wang et al. [27] explored the electrochemical activation of MWNTs from different sources by anodization treatment. They found that while the anodic pretreatment resulted in a dramatic improvement in the electrochemical reactivity of the ARC-produced CNTs, CNTs produced by chemical vapour deposition (CVD) appeared to be resistant to the anodic activation. These differences in the effect of the electrochemical pretreatment were attributed to the anodic preanodization effectively “breaking” the basal-plane end caps of ARC-CNTs thereby exposing edge plane defects, similar to those already present in the open-end caps of CVD-CNTs. The electrochemical activation of as-grown CNTs ensembles in 1.0 M NaOH was also achieved by Lin et al. [28] by applying a bias at

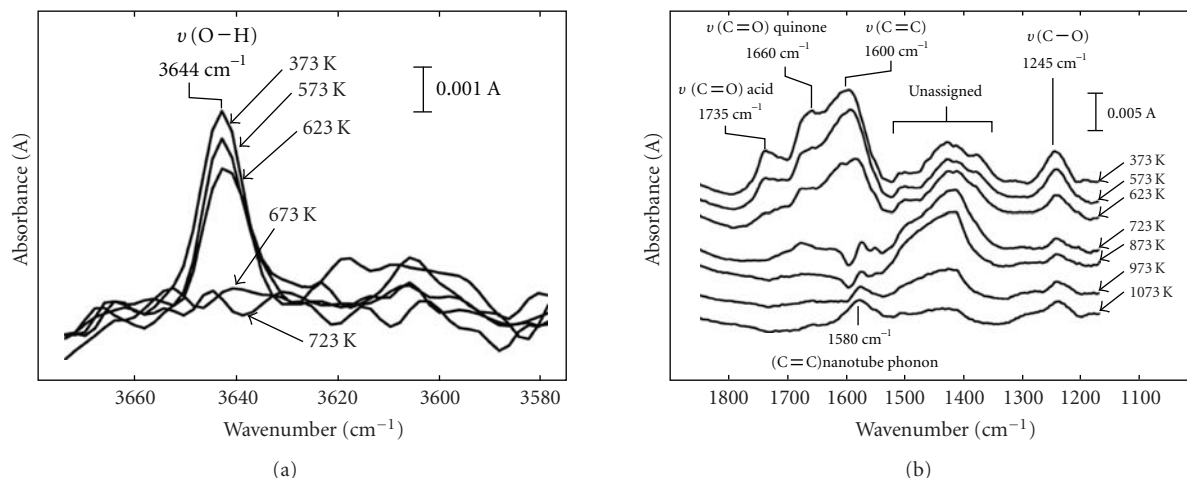


FIGURE 2: Decomposition of oxygen related functionalities on o-SWNTs. Transmission IR spectra of o-SWNTs following heating in vacuum to the indicated temperatures. The spectra indicate that carboxylic acid and quinone groups are thermally destroyed in vacuum above about 600 K. Other unassigned surface functionalities are also observed to disappear upon heating. Removal of these functionalities reveals the IR transition associated with a 1580 cm^{-1} phonon mode of nanotubes. [Adapted with permission from Kuznetsova et al. [18], *Chem. Phys. Lett.*, **321**, 292 (2000). Copyright 2000, Elsevier Science.]

1.5 V for 90 seconds. After electrochemical treatment, some functional groups (e.g., carboxylic acid) were created at the CNTs ends, which were further utilized to immobilize proteins using standard water-soluble coupling agents 1-ethyl-3-(3-dimethylaminopropyl)carbodiimide (EDC) and N-hydroxysulfo-succinimide (sulfo-NHS) by forming amide linkages between their amine residues and the carboxylic acid groups on the CNTs ends.

3. Fabrication of Carbon Nanotube-Based Electrochemical Sensors

Since their first application in electrochemistry by Britto et al. [1], numerous papers dealing with the use of CNTs as electrodes have been reported. The major problem on the promising applications of CNTs in electrochemical sensors is the immobilization of activated CNTs on the electrode surface because CNTs generally exist as highly tangled ropes and are insoluble in almost all solvents, which greatly hinder their capacity of forming uniform and stable films. To overcome this deficiency, CNTs are firstly dispersed or dissolved in various solutions or suspensions and immobilized on the surfaces of various substrates by physical or chemical methods. This section focuses on the introduction of some typical immobilization methods of CNTs on electrode surfaces that are widely used in constructing CNT-based electrochemical sensors.

3.1. Solvent Dispersion and Casting Immobilization. The most widely used methods for fabricating CNT-based electrochemical sensors are the approaches that involve the dispersing of CNTs in a certain solvent with sonication after their purification and activation pretreatments, followed by dropping the resultant suspensions on the electrode surfaces and allowing to dry (i.e., the casting methods). Among the

reported solvents, N,N-dimethylformamide (DMF) is the most extensively used polar solvent and more than half of the papers deal with CNT-based electrochemical sensors using DMF as the dispersing solvent [16, 29–42]. There are also some other solvents used to prepare CNT suspensions, including water [43–48], acetone [49–53], ethanol [54–56] and even toluene [57, 58]. However, compared with these solvents, DMF has some overwhelming advantages for dispersing CNTs, for example, much higher solubility, stability and exfoliation efficiency. The debundling and dissolution of SWNTs in DMF and N-methyl-2-pyrrolidone (NMP) have been systematically investigated by Furtado et al. [59]. Compared with other approaches, the solvent-dispersing methods of CNTs inevitably suffer from some disadvantages, such as low solubility, low stability and low exfoliation efficiency, due to the rather weak interactions between these solvents and CNTs. The predominance of these methods is their simplicity, convenience and no need of other additives, which makes them suitable for using as the foregoing step in multistep fabrications of complex CNT-based electrochemical sensors.

3.2. Additive-Assisted Dispersion and Immobilization. To improve the solubility and stability of CNTs in their suspensions, various additives are added into solvents to assist the dispersion of CNTs, such as surfactants and polymers. The structures of these species are shown in Figure 3.

3.2.1. Nafion. As a typical cationic ion exchange resin, Nafion has been used extensively for the modification of electrode surfaces and for the construction of amperometric biosensors, due to the unique ion-exchange, discriminative, and biocompatibility properties [60, 61]. It is clear from Figure 3(a) that Nafion contains two different regions: the hydrophobic polymer backbone and the ionized hydrophilic

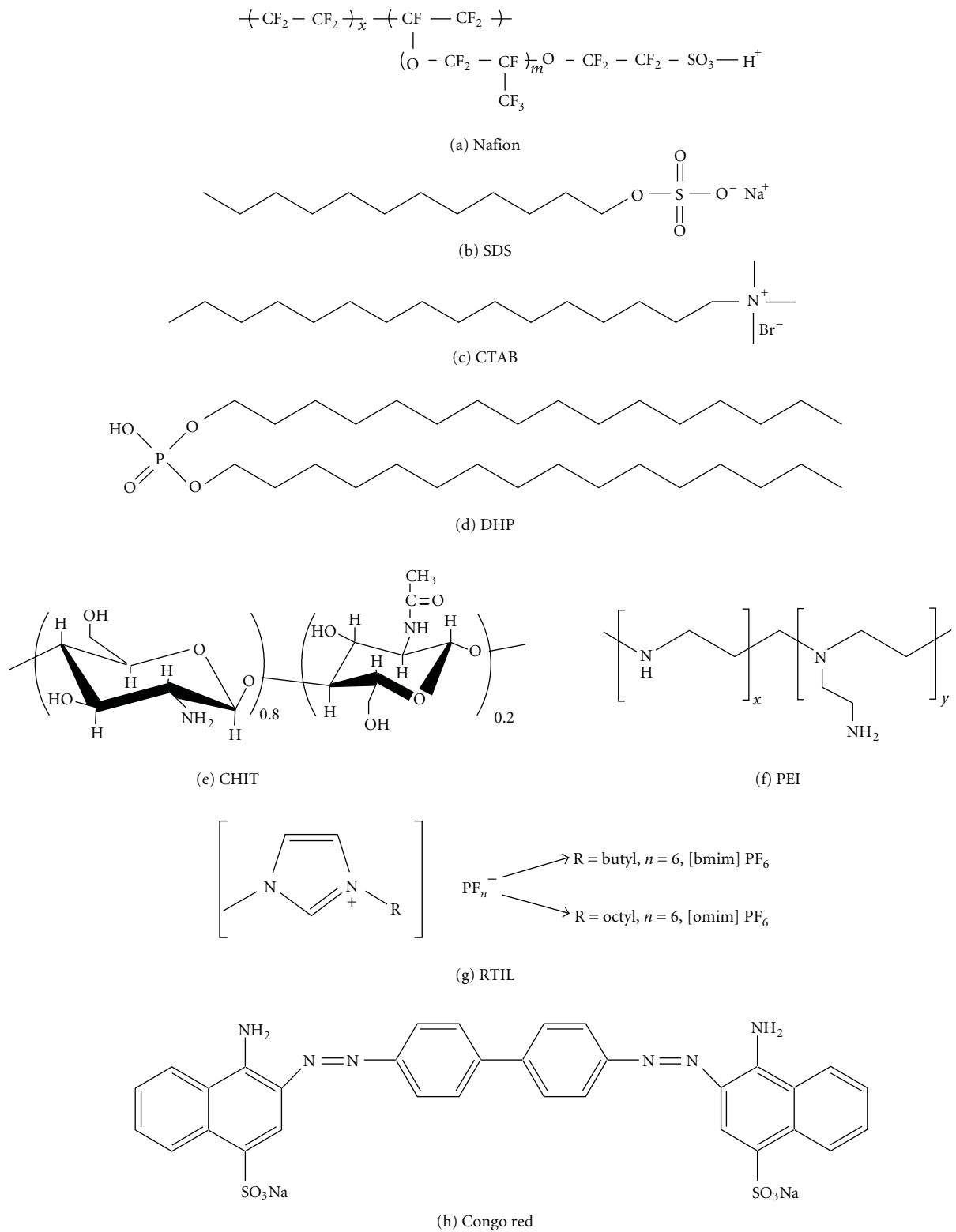


FIGURE 3: Molecular structures of various additives for dispersing CNTs in solutions.

sulfonate groups outside the hydrophobic region. This special amphiphilic structure makes Nafion bear the capacity of combining with CNTs by hydrophobic interactions between the hydrophobic backbone of Nafion and the sidewall of CNTs as well as dispersing them in solutions by the hydrophilic groups. The dispersion of CNTs in Nafion solutions with sonication was firstly reported by Wu et al. and used for the selective determination of dopamine (DA) via the elimination of potential interferences from negatively charged uric acid (UA) and ascorbic acid (AA) by the Nafion film [62]. Later, Wang et al. systematically studied the dispersion of CNTs in Nafion solutions and used this system to construct glucose electrochemical biosensors based on the electrocatalytic action toward hydrogen peroxide (H_2O_2) [63]. Since then, many works focused on the construction of CNT-based electrochemical sensors by this method, including the direct determination of DA [64, 65], nitrophenol [66, 67], cadmium ion [68], carbohydrates [69] and homocysteine (HcySH) [70], and the fixation of glucose oxidase (GOx) [71], copper (Cu) [72] and platinum (Pt) nanoparticles [73] for constructing glucose electrochemical sensors as well as the electrodeposition of nickel (Ni) for analysis of amino acids in flow injection analysis (FIA) [74].

3.2.2. Surfactants

(1) *Water-Soluble Surfactants.* Since the report by Abatemarco [75], sodium dodecyl sulphate (SDS) (Figure 3(b)) has been widely used to prepare stable suspensions of purified SWNTs in water with the aid of sonication. The mechanism for the dissolution of SWNTs in SDS aqueous solutions is well investigated. The common agreement is that the encapsulation of SWNTs in SDS micelles and the repulsive interactions between negatively charged SDS micelles account for the stable suspension of SWNTs in solution. The reports on the applications of SDS-dispersed CNTs in electrochemical sensors are rare, due to the rather weak adsorption of SDS-CNT composites on the smooth surfaces of conventional solid electrodes and the unstable films prepared from this suspension. However, Chen et al. prepared a SWNT modified carbon fiber nanoelectrode (CFNE) for the sensitive determination of DA from the suspension of SWNTs in SDS aqueous solution [76]. The achievement of this successful preparation might arise from the strong adsorption of SWNTs on the porous and hydrophilic surface of CFNE. The interaction between the oxygen-containing groups on acid treated SWNTs and on the CFNE pretreated by burning in air might also contribute to the strong attachment of SWNTs on CFNE. The suspension of CNTs in cetyltrimethylammonium bromide (CTAB) (Figure 3(c)) aqueous solution was used by Cai et al. to prepare CNT-based hemoglobin (Hb) electrochemical biosensors [77]. The suspension of CNTs was mixed with the phosphate buffer solution (PBS) containing Hb and fixed on the surface of a glassy carbon electrode (GCE) by a Nafion coating, resulting in the direct electrochemistry of Hb. Similarly, the direct electrochemistry of GOx was achieved at similar electrochemical biosensors and used for the determination of glucose [78].

(2) *Water-Insoluble Surfactants.* Besides the Nafion dispersing system of CNTs, Wu et al. also developed another CNT dispersing system on the basis of the stable dispersion of CNTs in the aqueous solution of dihexadecyl hydrogen phosphate (DHP) (Figure 3(d)) [79]. Different from SDS and CTAB, DHP consists of two hydrophobic tails and a dissociable phosphate group. This special structure enables DHP to form stable and homogeneous suspensions in water, which can be cast on the electrode surfaces to prepare stable and uniform films. Based on the hydrophobic interactions between the hydrophobic tails of DHP and the sidewall of the nanotubes as well as the possible interactions between the phosphate groups on DHP and the oxygen-containing groups on acid-treated CNTs, MWNTs were dispersed in the aqueous suspension of DHP with sonication, resulting in the formation of a stable and homogeneous aqueous suspension of DHP and CNTs. The casting of the suspension of DHP and MWNTs on the electrode surface produced CNT-based electrochemical sensors that showed excellent electrochemical activity toward many species, such as hormone [80–82], drugs [83–93], biomolecules [79, 94–99], and heavy metal ions [100, 101].

3.2.3. *Chitosan.* Chitosan (CHIT) is a polysaccharide biopolymer (Figure 3(e)), which displays excellent film-forming ability, high water permeability, good adhesion, and susceptibility to chemical modifications due to the presence of reactive amino and hydroxyl functional groups. Jiang et al. firstly reported the stable dispersion of CNTs in the acidic aqueous solutions of CHIT with sonication and used to the simultaneous determination of DA and UA [102]. The special interaction between CHIT and CNTs was characterized by Zhang et al. [103]. They demonstrated by thermogravimetric analysis (TGA) that CHIT might be adsorbed onto CNTs and form a special CHIT-CNT system, which can be precipitated from the solutions by the addition of concentrated salts or the adjustment of solution acidity. The selective interaction between CHIT and CNTs also provided a possible approach for separating CNTs from carbonaceous impurities. Based on the derivation of the reactive groups on CHIT, they developed a CNT-based glucose electrochemical biosensor, which might be applied to a large group of dehydrogenase enzymes for the designing of a variety of bioelectrochemical devices (e.g., sensors, biosensors, biofuel cells). In fact, the solubilization of CNTs in aqueous solutions by polysaccharides has been reported previously by Star et al. using starch as the dispersing agent [104]. They found that common starch, provided it is activated toward complexation by wrapping itself helically around small molecules, would transport SWNTs competitively into aqueous solutions, and that the process was sufficiently reversible at high temperatures to permit the separation of SWNTs in their supramolecular starch-wrapped form by a series of physical manipulations from amorphous carbon. Based on their previous work [102], Jiang et al. applied the CHIT-CNT system for the direct determination of nitrite [38], the simultaneous detection of UA and NE [105], and the selective determination of DA in the presence of

AA [106]. Another marvelous work on the simultaneous electrodeposition of CHIT-CNTs on gold electrodes was reported by Chen et al. [107]. The typical electrodeposition procedure was expressed as follows: a pair of polished and cleaned gold electrodes (diameter 2.0 mm, separation of about 0.5 cm) was connected to a direct current power supply (3.0 V) and dipped into the CNT-CHIT solution (pH 5.0); H^+ in the solution was reduced to H_2 at the cathode, and the pH near the cathode surface gradually increased; as the solubility of CHIT was pH-dependent, when the pH exceeded the pKa of CHIT (about pH 6.3), CHIT became insoluble and the CHIT entrapped CNTs would deposit onto the cathode surface as a result. Based on this, they developed a glucose electrochemical biosensor through the codeposition of GOx with CHIT-CNTs. This simple and controllable electrodeposition method overcomes the major obstacle for preparing CNT-based biosensor systems and expands the scope of electrochemical devices based on CNTs. However, this method might suffer from some inevitable disadvantages, for example, the using of high potential bias (3.0 V) might influence the quality of the substrate electrodes and the bubbling of H_2 produced during the electrolysis process might influence the uniformity of the deposited films.

3.2.4. Polyethyleneimine. As a positively charged polyelectrolyte, polyethyleneimine (PEI) (Figure 3(f)) was also extensively employed as an efficient additive for the dispersion of CNTs in aqueous solutions. The resulting PEI-CNT composite was proved to have good stability and biocompatibility [108]. Based on the reactivity of amino groups on PEI, the noncovalent or covalent modification of CNTs by PEI provides a simple approach to the further surface functionalization of CNTs by quantum dots [109], metal nanoparticles [110, 111]. PEI-functionalized CNTs are a useful nanocomposite in electrometry and electroanalytical chemistry. For instance, based on the interactions between PEI and GOx as well as the strong adsorption of PEI on MWNTs, Ivnitski et al. proposed a GOx anode for biofuel cell by using PEI as the binder for grafting GOx on the surface of MWNTs [112]. Similarly, Rivas et al. developed an electrochemical sensor for the sensitive determination of ascorbic acid, dopamine, 3,4-dihydroxyphenylacetic acid (dopac) and hydrogen peroxide [113], on the basis of the stable suspension of CNTs in PEI aqueous solution and the surface modification of a glassy carbon electrode (GCE) by the PEI-MWNT composite. Later, they employed this electrochemical sensor as the detector in flow systems to achieve highly sensitive detections of hydrogen peroxide, different neurotransmitters (dopamine (D) and its metabolite dopac, epinephrine (E), norepinephrine (NE)), phenolic compounds (phenol (P), 3-chlorophenol (3-CP) and 2,3-dichlorophenol (2,3CP)) and herbicides (amitrol), with sensitivities enhancements of 150 and 140 folds compared to GCE for hydrogen peroxide and amitrol, respectively [114]. One of the most remarkable properties of this sensor was the antifouling effect of the CNT/PEI layer. This unique property was further demonstrated by Chicharro et al. by examining the analytical

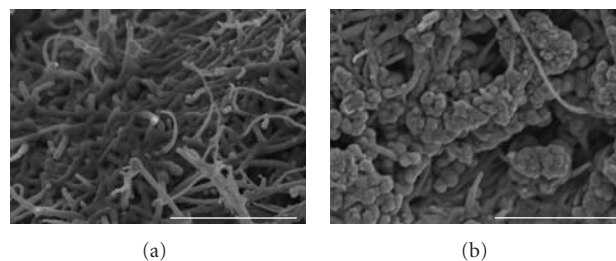


FIGURE 4: SEM pictures of the surface of the CNTs sol-gel composite (a) without and (b) with 0.25 mg colloidal silica particles per mg of MWNTs. Bar, 5 μm . [Reprinted with permission from Gavalas et al. [118], *Anal. Biochem.*, **329**, 247 (2004). Copyright 2004, Elsevier Science.]

performance of PEI-CNT composite modified electrodes as electrochemical sensors in capillary electrophoresis for the MEKC separations of phenolic pollutants (phenol, 3-chlorophenol, 2,3-dichlorophenol, and 4-nitrophenol) and herbicides (amitrol, asulam, diuron, fenuron, monuron, and chlortoluron) [115]. A recent work of Rivas revealed that the highly selective and sensitive voltammetric dopamine quantification in the presence of ascorbic acid and serotonin could be obtained at glassy carbon electrodes modified with PEI-MWNT composite [116]. On the other hand, Qiu et al. developed a sensitive electrochemical system for the selective determination of ascorbic acid by incorporating a mediator, ferrocenyl group (Fc), into the MWNT composite by using PEI as a binder [117].

3.2.5. Sol-Gels. The sol-gel and hydrogel have been widely used in recent years to immobilize biomolecules (e.g., enzymes) for constructing electrochemical biosensors because of their easy fabrication, chemical inertness, thermal stability and good biocompatibility. However, the lack of electrochemical reactivity and the poor conductivity of these materials, especially for silica sol-gel, greatly hinder their promising applications. A typical procedure for preparing CNT-based sol-gel consists of the dispersion of CNTs in solvents, the mixing of the CNT suspensions with the sols and finally the casting of the resultant mixture on the electrode surfaces. Recently, Gavalas et al. prepared CNT aqueous sol-gel composites as enzyme-friendly platforms for the development of stable biosensors [118] (Figure 4). These CNT-based sol-gel electrochemical biosensing platforms were demonstrated to possess both the electrochemical characteristics of CNTs and the role of sol-gel for eliminating by-products. Tan et al. reported a new type of amperometric cholesterol biosensor based on sol-gel CHIT/silica and MWNT organic-inorganic hybrid composite materials [119]. They found that MWNTs acted as both nanometer conducting wires and catalysts, which can effectively promote electron transfer between enzymes and the electrode surface. Gong et al. developed a new kind of ceramic-carbon nanotube nanocomposite electrodes (CCNNEs) prepared by doping MWNTs into silicate gel [120]. In contrast to the conventional sol-gel or CNT-based

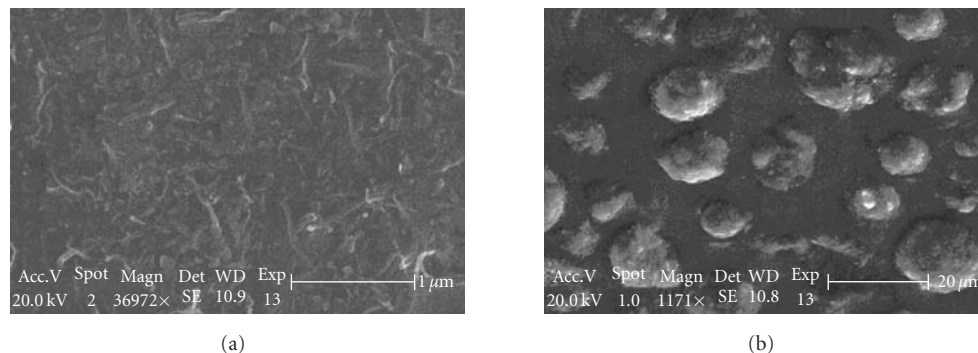


FIGURE 5: Environmental scanning electron microscopic (ESEM) images of (a) MWNT/[bmim]PF₆ and (b) MCMB/[bmim]PF₆, the scale bar is 1 μm in (a) and 20 μm in (b). The accelerating voltage is 20 kV. [Adapted with permission from Zhao et al. [122], *Anal. Chem.*, **76**, 4960 (2004). Copyright 2004, American Chemical Society.]

electrochemical sensors, the electrochemical response of these electrodes can be conveniently tuned from that of conventional scale electrodes to that of microelectrodes by just varying the content of MWNTs in the composites. Besides silica-based sol-gel, the preparation of CNT-redox polymer hydrogel composite films was also reported recently by Joshi et al. [121]. By incorporating enzyme modified SWNT into PVP-Os polymer hydrogel, the sensor's current output was increased for 2-3 times.

3.2.6. Room-Temperature Ionic Liquids. Room-temperature ionic liquids (RTILs) are thermally stable salts, liquid at room temperature, constituted by an organic cation and either an organic or an inorganic anion. Unlike traditional inorganic molten salts such as NaCl, NaAlF₆, or the eutectic mixture LiCl-KCl, room temperature ionic liquids present a high degree of asymmetry that inhibits crystallisation at room temperatures. RTILs have some marvelous properties, including nonvolatile nature or nonmeasurable vapour pressure, low melt point (even as low as -90°C), wide liquidus range (up to 200°C), strong electrostatic field, wide electrochemical potential range (i.e., RTILs remain stable at potentials even higher than 5 V), relative air and water stability, high polarity, favorable viscosity and density as solvents, high thermal stability (i.e., decomposition temperature might be higher than 400°C), and the ability of solvating a wide range of species including organic, inorganic, and organometallic compounds by varying the R group in RTILs. These special properties make them have promising applications in green chemistry (including synthesis, catalysis and biocatalysis), functional materials (e.g., photoelectrical materials and lubricate materials), energy science, environment science, and so on. Recently, Zhao et al. [122] proposed a novel strategy for investigating the electrical-ionic properties of RTILs and carbon composite materials formed by mixing a water-insoluble RTILs (1-butyl-3-methylimidazolium hexafluoro-phosphate, [bmim]PF₆) (Figure 3(g)) and carbon materials of two types: one was MWNTs with a tube shape and the other was mesocarbon microbeads (MCMBs) with a bead shape (Figure 5). The hybrid MWNT/RTIL and MCMB/RTIL materials showed a different conductivity

mechanism determined by ac impedance technology. The RTIL and carbon composite materials can also be used to act as modifiers in the direct electrochemistry of protein and to catalyze the reduction of O₂ and H₂O₂. Later, Zhang et al. [123] developed an RTILs supported three-dimensional network SWNT electrode. In that work, large quantities of SWNTs were considerably untangled in RTILs so as to greatly increase the effective area of the electrode. N-succinimidyl acrylate (NSA), as a model monomer, was dissolved in the supporting RTILs and was electrografted onto SWNTs (SWNT-poly-NSA). Then, GOx was directly covalently anchored on the SWNT-poly-NSA assembly. More recently, Zhao et al. [124] prepared an RTIL-CNT-modified GCE by grinding the mixture of an RTILs (1-octyl-3-methyl imidazolium hexafluorophosphate, OMIMPF₆) (Figure 3(f)) and MWNTs on a certain weight ratio and casting the resulting black gel on the electrode surface, which was successfully used to the selective determination of DA in the presence of UA and AA.

3.2.7. Proteins. The employment of proteins as functional biomaterials has been widely reported due to the excellent biocompatibility and the abundant derivative surface groups. As a kind of special amphiphilic biomacromolecules, proteins are proved to be capable of dispersing CNTs in water. Lin et al. firstly discovered that SWNTs are naturally protein-affinitive in an aqueous ferritin solution, resulting in significant ferritin-SWNT conjugation and the solubilization of the nanotubes [126]. The conjugation can be further enhanced and stabilized in the presence of a coupling agent for amidation to promote the formation of covalent linkages. Later, Karajanagi et al. reported that a variety of proteins differing in size and structure, for example, bovine serum albumin (BSA), peroxidases from soybean and horseradish, trypsin, ferritin, and *mucor javanicus* lipase (MJL), were able to generate individual nanotube solutions by a noncovalent functionalization procedure [127]. Our recent work also demonstrated that glucose oxidase (GOx) can be grafted on the surface of MWNTs by a simple non-covalent functionalization to achieve both the solubilization of MWNTs in water and the direct electrochemistry of GOx

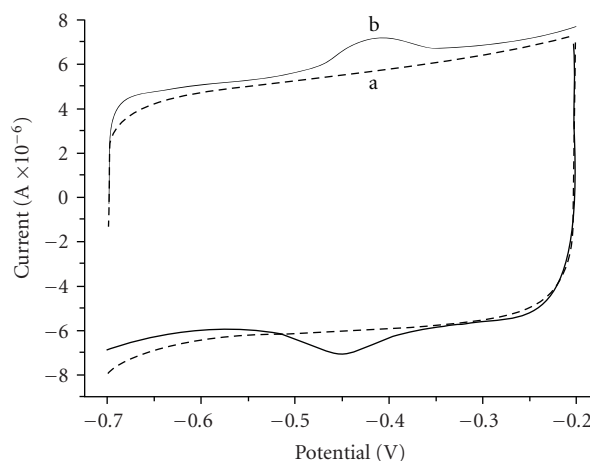


FIGURE 6: Photos of GOx-grafted MWNTs (a) and MWNTs (b) in water (left), and cyclic voltammograms of the MWNT- (a) and GOx-grafted MWNT- (b) modified glass carbon electrode in 0.1 M phosphate buffer solution (pH 6.9) (right) [125].

(Figure 6) [125]. Moreover, the oxygen-containing groups on MWNTs produced by acid treatments are crucial to the stable adsorption of GOx on MWNTs [128]. Since the protein-CNT hybrid has the properties of both proteins and CNTs, it might have promising applications in various fields like biomedical, material and analytical sciences.

3.2.8. Cyclodextrins. Cyclodextrins (CDs) are crystalline, water soluble, and cyclic oligosaccharides built up of glucopyranose units (glucose units) and contain a relatively hydrophobic central cavity and hydrophilic outer surface. The soft cutting of SWNTs by CDs was firstly reported by Chen et al. [129] and then characterized by Chambers et al. [130] using adsorption and Raman spectra as well as differential scanning calorimetry (DSC). The results confirmed conclusively that γ -CDs and SWNTs did interact with each other in a fashion similar to that originally suggested by Chen et al. [129], who proposed that CDs were adsorbed at the surface of nanotube ropes by van der Waals forces. This result foretold the use of CDs for the chemical manipulation and processing of CNTs. Based on this, Luo et al. developed CD-CNT composite film-modified electrodes by dispersing CNTs in the aqueous solutions of either α - [131–133] or β -CD [134, 135] with sonication, which was used for the determination of NE [135], UA [134] and thymine [131], the selective determination of *p*-nitrophenol [132], and the simultaneous determination of DA and EP [133].

3.2.9. Organic Dyes. Different from the above weak Van der Waals interactions between the dispersing agents and CNTs, conjugated organic compounds, especially organic dyes containing amino groups, can combine with CNTs via stronger π - π interactions to form much stabler hybrids, which leads to a much higher stability and solubility of CNTs in solution. Chen et al. firstly reported the strong adsorption of an amino-derivative pyrene on the sidewall of SWNTs via π - π interactions for the surface modification of SWNTs

[137]. They foresaw that this noncovalent method might also hold the key to forming stable suspensions of functionalized SWNTs in solutions and open up the possibility of self-assembly of nanotubes with unperturbed sp^2 structures and electronic properties. Based on the strong π - π interactions between methylene blue and SWNTs, Yan et al. developed a simple noncovalent method for the dissolution of SWNTs in water [138]. The MB-functionalized SWNTs were positively charged and utilized to construct an electroactive multilayer of MB and SWNTs through a layer-by-layer assembling method, which showed excellent electrocatalytic activity toward the reduction of oxygen. Our group also proposed a simple noncovalent method for dissolving CNTs in water by Congo red (CR) (Figure 3(h)), a negatively charged organic dye, based on the strong π - π interactions between CR and CNTs [136, 139–141]. This method had the merit of high solubility, stability and selectivity, and was able to dissolve a variety of CNTs, for example, pristine or acid-treated SWNTs or MWNTs. The resulting CR-functionalized CNTs (CNT-CR) had a unique property of forming uniform, compact but stable CNT films on various substrates when completely dried (Figure 7), which had been proven to possess excellent electrochemical performances toward various substances, such as redox proteins [128], drugs [140], small biomolecules [141], hormones [136], and so on. The reversible adsorption of surfactants on the naked surface of CNT-CR conjugate also provided a simple approach to the further enhancement of the electrochemical response of hydrophobic species and the improvement of the antifouling capacity of the CNT sensing films [136].

3.3. Self-Assembling Immobilization

3.3.1. Polyelectrolyte Assisted Self-Assembly. The applications of CNTs in electrochemical sensors by self-assembled methods were mainly achieved through the attachment of water-soluble polyelectrolytes on the sidewall of CNTs. The molecular design of strong SWNT/polyelectrolyte multilayer composites has been reported previously [143]. The typical

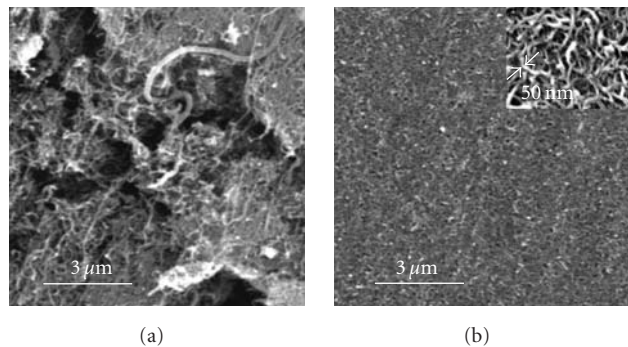


FIGURE 7: SEM images of as-received MWNTs (a) and CR-functionalized MWNTs (b) [136]. [Reprinted with permission from Hu et al. [136], *Electrochem. Commun.*, **9**, 128 (2004). Copyright 2007, Elsevier Science.]

polyelectrolyte used for preparing CNT-based electrochemical sensors by self-assembled methods was a cationic polyelectrolyte, poly(diallyl dimethyl ammonium) chloride (PDDA). The interaction between PDDA and CNTs has been systematically investigated by Yang et al. [144] using XPS and photoacoustic Fourier transform infrared (PA-FTIR) spectroscopies. They found that the mild sonication of MWNTs in aqueous PDDA resulted in a significant improvement of CNT dispersibility and greatly enhanced their adhesion to Au and Si substrates. The MWNT-PDDA interaction was due to the presence of an unsaturated contaminant in the PDDA chain, as confirmed by both XPS and PA-FTIR, which entered into a π - π interaction with the CNTs. Electrostatic group repulsions of the coated CNTs then provided the dispersibility and adhesion. Guo et al. firstly reported the electrostatic assembly of calf thymus DNA on MWNT-modified gold electrode via PDDA and used this electrode to study the interaction between chlorpromazine chloride and DNA [44]. Soon, they also prepared a CNT-based amperometric cholesterol biosensor through layer-by-layer (LBL) deposition of PDDA and cholesterol oxidase (ChOx) on MWNT-modified gold electrode, followed by electrochemical generation of a nonconducting poly(o-phenylenediamine) (PPD) film as the protective coating [145]. Zhang et al. fabricated multilayer films of shortened MWNTs that were homogeneously and stably assembled on GCE with the LBL method based on the electrostatic interaction of positively charged PDDA and negatively charged and shortened MWNTs (Figure 8), which were further applied to the electrocatalytic reduction of O_2 [142] as well as the selective determination of DA [146]. Recently, He et al. introduced a new fabrication of DNA-CNT particles using the LBL technique on SWNTs by the alternative deposition of PDDA and DNA on the water-soluble oxidized SWNTs [147]. The electrodes modified by the DNA/PDDA/SWNT particles were used as DNA sensors for the investigation of DNA damage by nitric oxide. The self-assembly of negatively charged poly(aminobenzenesulfonic acid) (PABS) on SWNTs was proposed by Liu et al. [148], which was used for the assembly of a conducting polymer, polyaniline (PANI), on the surface of SWNTs. The obtained PANI/PABS-SWNT

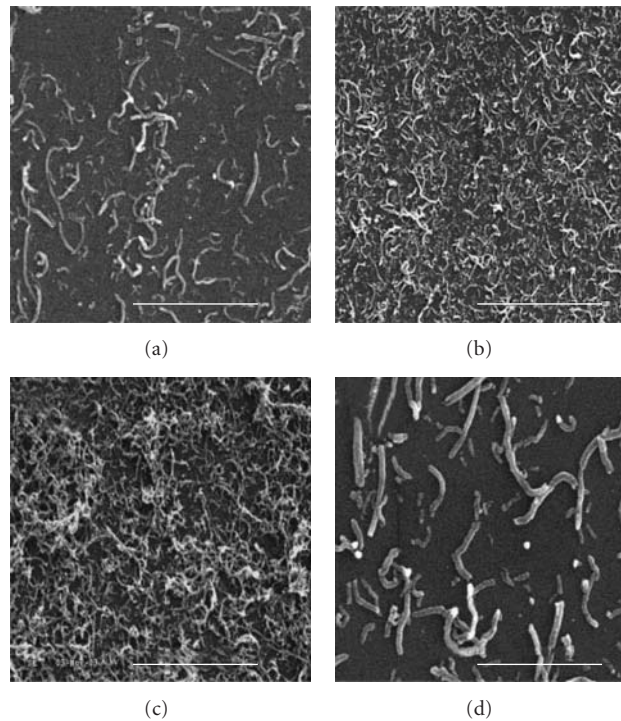


FIGURE 8: Representative SEM images of $\{PDDA/MWNTs\}_1$ (a), $\{PDDA/MWNTs\}_3$ (b), and $\{PDDA/MWNTs\}_5$ (c) assembled on a silicon wafer. The scale bar in (a)–(c) was $5\ \mu\text{m}$. (d) represents the SEM image of $\{PDDA/MWNTs\}_1$ with a high amplification with a scale bar of $1\ \mu\text{m}$. [Reprinted with permission from Zhang et al. [142], *Langmuir*, **20**, 8781 (2004). Copyright 2004, American Chemical Society.]

multilayer films were very stable and showed high electrocatalytic ability toward the oxidation of NADH at a much lower potential (about +50 mV versus Ag|AgCl). Lenihan et al. proposed a protocol for immobilizing alkaline phosphatase on the surface of MWNTs utilizing an LBL methodology. They firstly incubated CNTs with streptavidin to form a protein layer on the surface of the nanotubes and then attached biotinylated alkaline phosphatase to streptavidin, anchoring the sensing protein onto the surface of CNTs, which was used to the determination of 1-naphthyl phosphate. Besides macromolecules, small conjugated molecules were also used for the construction of CNT-based electrochemical sensors. Yan et al. described and characterized the adsorption of electroactive methylene blue (MB) dye onto SWNTs to form an electrochemically functional nanostructure [138, 149]. They found that MB essentially interacted with SWNTs through charge-transfer and hydrophobic interactions, leading to the formation of an MB-SWNT adsorptive nanostructure, which exhibited distinct electrochemical properties from those of MB adsorbed onto GCE. The stable adsorption of water-soluble and positively charged MB molecules onto SWNTs was further demonstrated to be able to solubilize the formed nanostructure in water quite well and to fabricate a functional nanocomposite by LBL assembling of the formed nanostructure on a solid substrate.

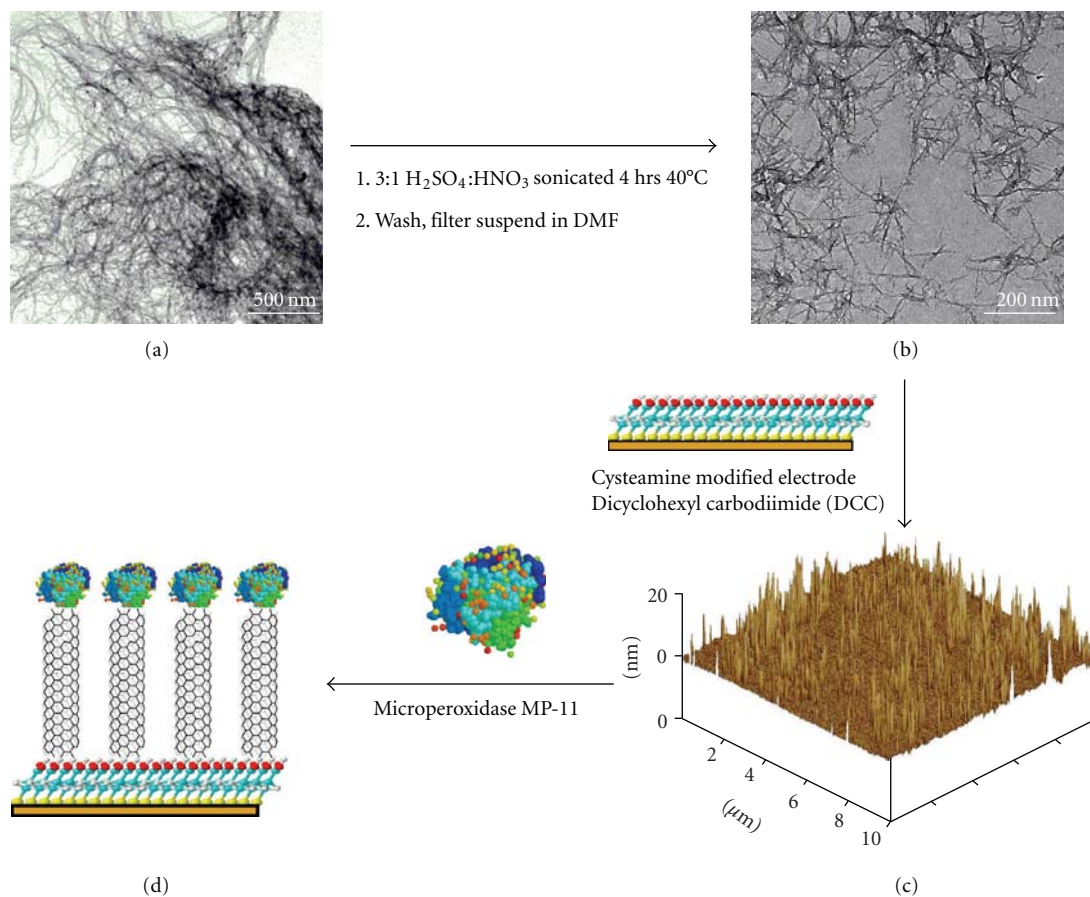


FIGURE 9: A schematic showing the steps involved in the fabrication of aligned shortened SWNTs arrays for direct electron transfer with enzymes such as microperoxidase MP-11. [Reprinted with permission from Gooding et al. [150], *J. Am. Chem. Soc.*, **125**, 9006 (2003). Copyright 2003, American Chemical Society.]

3.3.2. Direct Self-Assembly. The negatively charged carboxyl groups on CNTs produced during the acid treatments provide two approaches for the direct self-assembling immobilization of CNTs on electrode surfaces: one is the covalent bonding of CNTs to cysteamine self-assembled monolayer (SAM) modified gold electrodes via the reaction of carboxyl groups on CNTs and amino groups on cysteamine SAM in the presence of coupling reagents; the other is the attachment of CNTs to electrode surfaces via the electrostatic interactions between negatively charged carboxyl groups on CNTs and the positively charged species on the electrode surfaces. The self-assembly of CNTs on a gold electrode was reported by Liu et al. [151]. They firstly cut as-grown nanotubes into short pipes and thiol-derivatized at the open ends by chemical methods. The ordered assembly of SWNTs was then made by their spontaneous chemical adsorption to gold via Au-S bonds. They found that the nanotubes were organized on gold, forming a self-assembled monolayer structure with a perpendicular orientation, and the adsorption kinetics of the nanotubes was very slow in comparison to conventional alkanethiols. Different from the work by Liu et al. [151], Gooding et al. fabricated an aligned CNTs array for the direct electrochemistry of microperoxidase MP-11 via a three-step

procedure [150] (Figure 9). Later, they applied this method to GOx and also accomplished the direct electron transfer between the electrode and the redox active centre of GOx, flavin adenine dnuucleotide (FAD) [152]. Recently, Xu et al. fabricated an MWNT monolayer modified gold electrode by a similar method and achieved the direct electrochemistry of horseradish peroxidase (HRP) physically adsorbed on the surface of MWNTs [153]. In contrast to the covalent methods for attaching CNTs to cysteamine modified gold electrodes, Qu et al. [154] attached acid-treated SWNTs to cysteamine modified gold electrodes via electrostatic adsorption. Chattopadhyay et al. also developed another method for preparing aligned CNT arrays on the surface of ordinary pyrolytic graphite (PG) electrodes from randomly dispersed CNTs by using a Nafion solution [155]. Based on the successful fabrication of the CNT arrays on the electrode surfaces, proteins like HRP were either covalently attached [156] or physically adsorbed [157] onto the end of the CNT arrays and achieved their electroanalytical applications.

3.4. Carbon Nanotube Paste Electrodes. CNT paste electrodes (CNTPEs) refer to the paste electrodes made up

of liquid binder and CNTs. CNTPEs retain the properties of the classical carbon paste electrodes (CPEs) such as the feasibility to incorporate different substances, the low background currents, the wide potential range, the easy renewal and composite nature. CNTPEs also preserve the unique electrochemical properties of CNTs, like the ability to promote electron-transfer reactions of various species, especially for biomolecules. Compared with other methods for preparing CNT-based electrochemical sensors, CNTs in CNTPEs do not need any additional treatment (e.g., purification, modification or shortening treatment) and are suitable for all kinds of CNTs. Britto et al. [158] firstly reported a dramatic improvement in the electrochemical behavior of DA with ΔE_p of 30 mV at nonactivated carbon nanotube electrodes constructed by using bromoform as binder. Davis et al. [159] further explored the possibility of using CNTs as the electrode materials. They achieved for the first time the direct electrochemistry of proteins at a CNTPE that was prepared from protein decorated CNTs by physical adsorption. The formal appellation "CNT paste" or "CNTPE" electrode was firstly reported by Valentini et al. in 2003 [160]. In that work, they prepared CNTPEs by mixing SWNTs with mineral oil. Studies on the composition of the SWNT paste electrodes showed a different behavior, as compared to graphite paste electrodes (CPEs). In the case of CPEs, the treatment of graphite powder with HNO_3 oxidation hardly changed the electrochemical properties of CPEs. As for CNTPEs, the HNO_3 oxidation treatment significantly improved the electrochemical activity of CNTPEs toward many electroactive substances, especially for small biomolecules. Later, Valentini et al. [161] further explored the various advantages of CNTPEs over conventional carbon paste (CP), Pt, and glassy carbon electrodes, such as a very low capacitance (background current) and fast electron transfer rates toward various redox couples, especially for two-electron quinonic structure species. Since then, more and more works focus on the preparation and applications of CNTPEs in electrochemical sensors, including the determination of amitrole [162], HcySH [163] and DNA [164] at CNTPEs, the determination of carbohydrates at a copper particle incorporated CNTPE [165], the determination of lactate, phenols, catechols, alcohols or glucose at enzyme incorporated CNTPEs [166, 167], and the electrocatalytic oxidation of NADH at a 3,4-dihydroxybenzaldehyde (3,4-DHB) modified CNTPE [168, 169]. Using solid binders in preparing CNTPEs was also reported. Wang et al. prepared CNT/Teflon composite electrodes by the dispersion of CNTs within a Teflon binder [170]. The resulting CNT/Teflon material brought new capabilities for electrochemical devices by combining the advantages of CNTs and "bulk" composite electrodes, including the accelerated electron transfer, the minimization of surface fouling and surface renewability. The electrocatalytic properties of CNTs were not impaired by their association with the Teflon binder. Later, Chen et al. prepared a CNT-epoxy composite microdisc electrode by mixing CNT powder with epoxy resin/hardener and packing the resulting CNT-epoxy composite into the opening end of capillary [171].

3.5. Abrasive Immobilization

3.5.1. Carbon Nanotube Powder Microelectrodes. Powder microelectrodes (PMEs) have been proved to be an effective technology for the purpose. PMEs, originated from Liu's laboratory, are a convenient technique for both the characterization of powder materials and the subsequent electroanalytical applications [172]. In fact, the so-called PME is a combination of porous and microelectrode. Besides, PMEs have the properties of the thin layer cell to some extent. No binder is needed for preparing PMEs; this not only makes the preparation simple but also can prevent impurities and keep the powder material in its pristine state [172]. Liu et al. [173] firstly reported the immobilization of CNTs on PMEs by filling CNTs in the microcaves of PMEs through a simple rubbing operation. The resultant CNT-based PMEs (CNTPMEs) were further modified by $\text{Os}(\text{bpy})_3^{2+}$ and used for the electrocatalytic determination of nitrite. Then, CNTPMEs were used for the determination of hydrazine [174] and cysteine (CySH) [175], the direct electrochemistry of HRP [176], and the studies on the electrochemical properties and scavenge of superoxide anion in aprotic media by Hu et al. [177].

3.5.2. Carbon Nanotube Abrasively Modified Conventional Scale Electrodes. The grinding immobilization of CNTs on the surface of conventional scale electrodes was firstly reported by Luo et al. [178]. In that work, a CNT-intercalated graphite electrode (CNT-IE) was fabricated by grinding with a suitable amount of CNTs powder. A thin CNT layer was formed on the graphite surface by intercalating CNTs into the soft graphite layers with the aid of mechanical force and also the action of chemical and physical adsorption. CNT-IE can effectively separate the oxidation potential of DA and AA, which was used for the simultaneous determination of DA and AA [178] and the selective determination of DA and serotonin (5-HT) in the presence of AA [179]. CNT-IE was further employed by Shi et al. to prepare an amperometric cholesterol biosensor by immobilizing of ChOx in sol-gel on a Pt-decorated CNT-IE [180] and a Pt-decorated CNT intercalated waxed graphite electrode [181]. Salimi et al. developed a CNT intercalated bppg electrode by gently rubbing the electrode surface of bppg on fine qualitative filter paper containing CNTs for 1 minute, which was used for the determination of EP [182] (Figure 10). Based on this electrode, they also prepared a glucose electrochemical biosensor by coating the CNT intercalated bppg electrode with a sol-gel composite film containing GOx [183]. Later, Salimi et al. produced a CNT intercalated GCE by immobilizing MWNTs on GCE that was preheated for 5 minutes at 50°C through gentle rubbing of the electrode surface on a filter paper supporting CNTs, which was applied to the determination of morphine [184], and thiols like thiocytosine, L-CySH, and glutathione (GSH) [185].

3.6. Electropolymerization Immobilization. The polymerization of various monomers in the presence of dispersed CNTs in solutions by electrochemical methods has been employed for the immobilization of CNTs on the electrode surface.

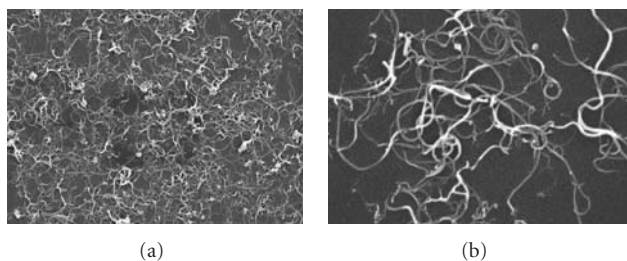


FIGURE 10: SEM images of CNTs used to fabricate the CNT-modified bppg electrode, magnification (a) 10000 and (b) 33000. [Reprinted with permission from Salimi et al. [182], *Analyst*, **129**, 225 (2004). Copyright 2004, Royal Society of Chemistry.]

In this process, CNTs were enwrapped in polymers during the electropolymerization process in the form of counter ions or dopants. Wu et al. reported a marvelous method for the dispersion and immobilization of CNTs on the electrode surface by water-soluble alizarin red S (ARS, 3,4-dihydroxy-9,10-dioxo-2-anthracenesulfonic acid, sodium salt) [186]. Pan et al. prepared a CNT-based glucose electrochemical biosensor by the simultaneous immobilization of CNTs and GOx on the gold electrode through the electropolymerization of *o*-aminophenol (*o*-AP) in 0.2 M acetate buffer solution (pH 5.0) containing GOx, *o*-AP monomer and fresh CNT dispersion [187]. Cheng et al. fabricated a MWNT/polypyrrole (PPy) modified electrode through cyclic sweeping from 0.0 to 0.7 V at GCE with the scan rate 0.1 V/s for eight circles in solution containing 0.1 M pyrrole, 0.2 mg/mL MWNTs and 0.2 M KCl in phosphate buffer (pH 2.0) [188]. It is clear that in these two works, CNTs were used as the dopants in the polymers. Wang et al. reported a one-step preparation route of amperometric enzyme electrodes by incorporating the CNT dopant and the biocatalyst (e.g., GOx) in an electropolymerized polypyrrole film [189]. They found that the entrapment of CNTs had little effect upon the electropolymerization rate and redox properties of the resulting film, and the CNT dopants retained its electrocatalytic activity to impart high sensitivity and selectivity. Recently, we established a noncovalent method for the dissolution of MWNTs in water by a conjugated organic dye, azocarmine B (ACB) [190]. The resulting ACB-MWNT mixture could be used for the immobilization of MWNTs on a glass carbon electrode by a simple electropolymerization method, which showed excellent electrochemical response toward the oxidation of nitric oxide (NO), an important radical molecule in life sciences.

3.7. Direct Growth. Despite the randomly dispersed CNTs, well-aligned CNTs were also used for constructing electrochemical sensors. These CNT-based sensors were generally constructed from CNT ensembles directly grown from CVD methods. Based on their different density, aligned CNT electrodes have the electrochemical properties resembling conventional scale electrodes at high density or microelectrode arrays at low density. This section will introduce the fabrication of aligned CNT electrochemical sensors made up of these two kinds.

3.7.1. Dense Carbon Nanotube Forests

(1) Unmodified Carbon Nanotubes. The unmodified aligned CNT electrodes were typically constructed by two steps: the CVD synthesis and the transfer of the aligned CNT ensembles to various substrates. Sometimes, the prepared aligned CNT electrodes were further activated by electrochemical methods. Ye et al. developed an aligned CNT electrode for the selective determination of UA [191]. They found that compared to GCE, the CNT electrode catalyzed the oxidation of UA and L-AA, reducing the overpotentials by about 0.028 and 0.416 V, respectively, and resolved the overlapping voltammetric response of UA and L-AA into two well-defined voltammetric peaks in both cyclic voltammetry (CV) and differential pulse voltammetry (DPV). Chen et al. developed a simple method for preparing ordered CNTs (OCNTs) in the nanopores of an alumina template membrane [192]. Ye et al. also reported a nonenzymatic glucose electrochemical sensor using aligned CNTs [193]. They firstly synthesized the aligned CNTs on a tantalum (Ta) plate and then attached the CNT ensembles to the surface of GCE using conductive silver paint. The CNT-based electrode was used without any further treatment. Compared to GCE, a substantial (+400 mV) decrease in the overpotential of the glucose oxidation reaction was observed at this electrode with oxidation starting at ca. +0.10 V (versus 3 M KCl-Ag|AgCl).

(2) Modified Carbon Nanotubes. The modified aligned CNT electrochemical sensors were usually fabricated through the immobilization of functional species (e.g., biocatalysts like enzymes) by various methods. Soundarrajan et al. developed a simple pyrolytic method for large-scale production of aligned CNTs arrays perpendicular to the substrate [194]. These aligned CNT arrays can be transferred onto various substrates of particular interest (e.g., polymer films for organic optoelectronic devices) in either a patterned or nonpatterned fashion. They further prepared aligned coaxial nanowires by electrochemically depositing a concentric layer of an appropriate conducting polymer onto the individual aligned CNTs, which were used for electrochemical sensing applications. On the basis of electropolymerization of some organic monomers, GOx was immobilized on the aligned CNTs to prepared CNT-based glucose electrochemical biosensors by Gao et al. using pyrrole [195, 196], Loh et al. using 3,3'-diaminobenzidine (DAB) [197], and Ye et al. using *o*-aminophenol [198] as the monomers. The physical adsorption of GOx on the naked [199] or the Pt decorated [200] surfaces of aligned CNTs were also employed for constructing glucose electrochemical biosensors. Recently, Ye et al. developed a novel oxygen sensor for working at a relatively low potential by the physical adsorption of hemin on an aligned CNT electrode [201]. They found that CV of the hemin-modified MWNTs electrode in pH 7.4 PBS clearly showed the dioxygen reduction peaks close to 0.0 V (versus Ag|AgCl).

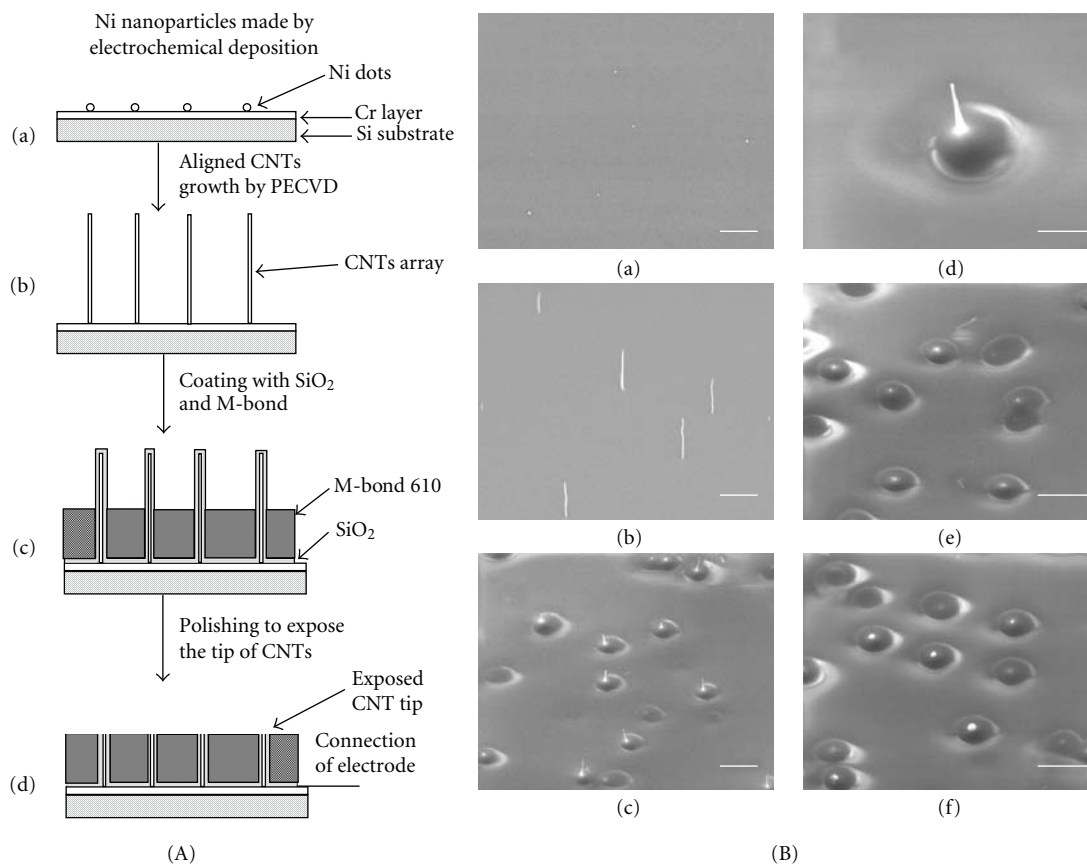


FIGURE 11: Fabrication scheme of the NEAs (A): (a) Ni nanoparticles electrodeposition; (b) aligned carbon nanotube growth; (c) coating of SiO_2 and M-Bond; and (d) polishing to expose CNTs. Scanning electron microscope images of the NEAs (B): (a) Top view; (b)–(f) from a 45° side view. All of the scale bars represent $5\ \mu\text{m}$. (a) Electrodeposited Ni nanoparticles; (b) low site density aligned CNTs array; (c) CNTs array coated with SiO_2 and an epoxy layer, (d) close-up look at a single half-embedded CNTs; (e) CNTs after polishing; and (f) second electrodeposition of Ni nanoparticles on the broken CNTs only. [Adapted with permission from Tu et al. [202], *Nano Lett.*, **3**, 107 (2003). Copyright 2003, American Chemical Society.]

3.7.2. Carbon Nanotube Nanoelectrode Arrays. At low density, the CNT ensembles possessed the electrochemical properties resembled the microelectrodes, which were denoted as CNT nanoelectrode arrays (NEAs). To make each nanotube work as an individual nanoelectrode, the spacing needs to be sufficiently larger than the diameter of the nanotubes to prevent diffusion layer overlap with the neighboring electrodes. In contrast to the conventional scale aligned CNT ensembles at high density, the size reduction of each individual electrode and the increased total number of electrodes result in improvements in both the signal-to-noise ratio and detection limits (DLs). A typical procedure for preparing CNT-based NEAs included the direct CVD growth of well-aligned CNTs with low density, the coating of the CNT layer by insulating materials (e.g., epoxy) and the removing of the protruding parts of CNTs by polishing. Sometimes, the CNT-based NEAs were further electrochemically activated by applying a potential bias $1.0\ \text{M NaOH}$ for a certain period to obtain functional groups like carboxyl groups. The major works regarding the construction of CNT-based NEAs were done by Ren [28, 202–204] and Meyyappan [205–207]. Ren et al. firstly

fabricated CNT-based NEAs from low site density aligned CNTs by plasma-enhanced CVD on Ni nanoparticles made by electrochemical deposition [202] (Figure 11). They found that each nanotube was separated from the nearest neighbor by several micrometers and NEAs of $1\ \text{cm}^2$ consisted of up to millions of individual nanoelectrodes, each with a diameter of $100\ \text{nm}$. Based on this method, they further constructed a glucose electrochemical biosensor through the covalent immobilization of GOx on the ends of CNT NEAs that were activated in $1.0\ \text{M NaOH}$ at $1.5\ \text{V}$ for 90 seconds beforehand [28]. The CNT-based NEAs were also used successfully by Ren et al. for the voltammetric detection of trace concentrations of lead (II) [203, 204] and cadmium(II) [204] at ppb level. Meyyappan et al. mainly focused on the construction of ultrasensitive DNA sensors from CNT-based NEAs. Based on the signal change of the electrochemical indicator, $\text{Ru}(\text{bpy})_3^{2+}$, before and after the hybridization of the oligonucleotide probes that were covalently attached to the open ends of CNTs with the target oligonucleotides, ultrasensitive determinations of DNA/RNA were achieved with low detection limits of nM level [205–207].

4. Carbon Nanotube-Based Electrochemical Sensors for Electroanalysis

Although possessing the electrochemical properties similar to edge plane pyrolytic graphite electrodes, CNTs still have some overwhelming advantages for fabricating carbon material-based electrochemical sensors, including the good conductivity, the good biocompatibility, the large specific area, the well-defined nanotube structure, the modifiable surface, the functional groups on the surface with pretreatments and the capacity of being solubilized or dispersed in solutions. Based on these unique properties, numerous works have been dealt with CNT-based electrochemical sensors, which can be mainly divided into two kinds: the nonenzymatic and the enzymatic CNT-based electrochemical sensors.

4.1. Carbon Nanotube-Based Nonenzymatic Electrochemical Sensors

4.1.1. Carbon Nanotube-Based Nonenzymatic Electrochemical Sensors for Biomedical Analysis

(1) *Thiols*. Amino thiols are of physiological importance as biological agents and metabolites. The levels of these compounds in biological matrices such as plasma and urine are valuable biomarkers in a number of clinical situations. Increased levels of HcySH and CySH are associated with risk of cardiovascular diseases. The ratio of GSH to glutathione disulfide (GSSG) indicates the redox status of cells. In addition, N-acetylcysteine is an important mucolytic agent used to reduce the viscosity of pulmonary secretions in respiratory diseases. A substantial challenge to the development of electrochemical methods for thiol detection was that the direct oxidation of thiols at solid electrodes is slow and usually large overpotentials are required [171]. Recently, Cao et al. reported the direct determination of L-CySH and GSH at a MWNT modified electrode [208]. They found that the CNT-modified electrode exhibited efficiently electrocatalytic oxidation for L-CySH and GSH with a relatively high sensitivity, stability and long-life. Coupled with high performance liquid chromatography (HPLC), this electrode was utilized for the amperometric detection of these thiols. The peak currents of L-CySH and GSH were linear to their concentrations ranging from 3.0×10^{-7} to 1.0×10^{-3} M with the calculated detection limits (signal-to-noise ratio (S/N) = 3) of 1.2×10^{-7} and 2.2×10^{-7} M, respectively. This method was successfully applied to the content estimate of L-CySH and GSH in rat striatal microdialysates. This work paved the way to determine thiols by CNT-based electrochemical sensors. Since then, many works regarding the determination of thiols by electrochemical methods used CNTs to construct the working electrodes. In general, these CNT-based electrochemical sensors were constructed from two types of sensing materials: CNTs and Pt-CNT composites.

(a) *Unmodified Carbon Nanotube-Based Electrochemical Sensors*. The electrochemical behavior of CySH at CNT powder

microelectrodes (CNTPMEs) was investigated by Zhao et al. [175]. In contrast to the absence of signals at a GCE and a graphite powder modified powder microelectrode, CySH exhibited a sensitive oxidation peak at around 0.58 V (versus SCE) in 0.2 M H₂SO₄ at a CNTPME, indicating the strong ability of CNTs to improve the electrochemical response of CySH. Chen et al. reported the fabrication of a CNT-based microdisc electrode by mixing MWNTs with epoxy for a specially designed miniaturized capillary electrophoresis (CE)-amperometric detection system for the separation and detection of several bioactive thiols [171]. The end-channel CNT amperometric detector offered favorable signal-to-noise characteristics at a relatively low potential (0.8 V) for detecting thiol compounds. Four thiols (HcySH, CySH, GSH, and N-acetylcysteine) were separated within 130 seconds at a separation voltage of 2000 V using a 20 mM phosphate running buffer (pH 7.8). A highly linear response was obtained for HcySH, CySH, GSH, and N-acetylcysteine over the range of 5–50 μM with detection limits of 0.75, 0.8, 2.9, and 3.3 μM, respectively. Lawrence et al. reported an effective means for the determination of HcySH at a CNT electrode [163]. HcySH showed a well-defined electrochemical signal emerging at +0.28 V and a current plateau at +0.64 V on the CNT electrode. In contrast, the HcySH response obtained at the carbon paste electrode showed only a slight increase in the oxidation current at +0.40 V. The sensitive determination of HcySH was also achieved by Gong et al. at a CNT-modified GCE [70]. Cyclic voltammetric results clearly showed that CNTs, especially those pretreated with HNO₃, possessed an excellent electrocatalytic activity toward the oxidation of HcySH at a low potential (0.0 V versus Ag/AgCl). The remarkable catalytic property of acid-pretreated CNTs was believed essentially associated with oxygen-containing moieties introduced on the tube surface. Zhang et al. also studied the electrochemical behaviors of GSH and GSSG at an acid-treated MWNT modified GCE [42]. They found that the functionalized CNTs exhibited efficiently electrocatalysis on the current responses of GSH and GSSG. Recently, Salimi et al. reported the electrochemical responses of three thiols, thiocytosine, GSH and L-CySH, at a CNT-modified GCE constructed by abrasive methods [185]. They found that the overpotentials of these species were apparently reduced along with a dramatic increase in the peak currents in comparison to bare GCE. Furthermore, the thiols amperometric responses of the coated electrodes were extremely stable, with more than 95% of the initial activity after 30 minutes stirring of 0.1 mM thiols.

(b) *Platinum-Carbon Nanotube Composite-Based Electrochemical Sensors*. Besides the unmodified CNTs, Pt decorated CNTs were also used for the sensitive determination of thiols. Xian et al. prepared a MWNT/Pt microparticle nanocomposite by electrodepositing Pt microparticles onto the MWNT matrix [209]. The GCE modified with this nanocomposite was used for the measurement of thiols, such as L-CySH and GSH. Compared with the MWNT or Pt microparticle modified electrode, the nanocomposite modified electrode exhibited high sensitivity and good stability

for detection of thiols, which was successfully applied to the HPLC-electrochemical detection (ECD) system for the determination of L-CySH and GSH in rat striatum. The electrochemical behavior of L-CySH on the Pt/CNT electrode was investigated by Fei et al. using cyclic voltammetry [210]. In that work, CNTs were grown directly on graphite disk by CVD, and Pt was electrochemically deposited on the activated CNT/graphite electrode by electroreduction of Pt(IV) complex ion on the surface of CNTs. Among graphite, CNT/graphite, and Pt/CNT electrodes, the improved electrochemical behavior of CySH oxidation was found with the Pt/CNT electrode.

(2) *Carbohydrates*. Electrocatalytic oxidation of carbohydrates is of great interest in the points of view ranging from medical applications of the blood glucose sensing to ecological approaches (e.g., waste-water treatment in food industry). Most previous studies on this subject involved the use of GOx, which catalyzes the oxidation of glucose to gluconolactone. However, due to the intrinsic nature of enzymes, such enzyme-based sensors suffer from the stability problem. Thus, great efforts are made to achieve direct determination of carbohydrates. Ye et al. recently reported the direct electrocatalytic oxidation of glucose in alkaline medium at well-aligned MWNT electrodes [193]. Compared to GCE, a substantial (+400 mV) decrease in the overpotential of the glucose oxidation reaction was observed at MWNT electrodes with oxidation starting at ca. +0.10 V (versus 3 M KCl-Ag|AgCl). The only problem of using this electrode for the direct determination of glucose was the serious interferences from some electroactive biomolecules like UA and AA, which might coexist in real biological samples. Deo et al. also reported on the electrocatalytic oxidation of carbohydrates at glassy carbon electrodes modified with SWNT coatings [69]. They found that the oxidation processes of four carbohydrates, including galactose, fructose, mannose and xylose, started around +0.25 V in 0.1 M NaOH solution. Moreover, the amperometric responses of these species at the CNT-modified electrodes were extremely stable, with no loss in sensitivity over a continuous 2-hour operation.

Besides unmodified CNTs, the composites made up of copper particles and CNTs were also used by several works to achieve the electrooxidation of carbohydrates. Male et al. reported a copper decorated CNT-based electrochemical sensor for the determination of carbohydrates [72]. In that work, copper (Cu) nanoparticles (4–8 nm in diameter), prepared by using sodium borohydride to reduce copper dodecyl sulfate ($\text{Cu}(\text{DS})_2$), were used with SWNTs to fabricate electrochemical sensors. Nafion was used to solubilize SWNTs and displayed interactions with Cu nanoparticles to form a network, connecting Cu nanoparticles to a glassy carbon (GC) or Cu electrode surface. The composite of SWNT/ Cu_{nano} gave a much enhanced current response at +0.65 V with a relatively low starting oxidation potential (+0.3 V versus Ag|AgCl (3 M NaCl)) in comparison to the GC electrode modified by either Cu nanoparticles or SWNTs alone. Similar results were observed from amperometric detection when 0.1 mM glucose was detected at +0.65 V.

The current responses for other saccharides (100 μM) were analyzed and compared to the glucose response. The monosaccharides, galactose (120%), arabinose (94%), xylose (109%), fructose (99%), and mannose (97%) gave similar responses as glucose. However, the current signal was lower for the disaccharides (i.e., maltose (50%), lactose (56%), sucrose (39%), trehalose (28%) and the trisaccharide raffinose (56%)).

(3) *Electroactive Microbiomolecules*. The determination of neurotransmitters and other important biomolecules is of considerable significance in biochemical and clinical diagnosis. Generally, these species are electroactive, providing a simple but sensitive way for their determination by electrochemical methods. However, owing to the overlapping of the oxidation potentials of these species, it is difficult to selectively determine them at bare electrodes. To overcome this obstacle, various materials have been used to modify the bare electrodes. Among these modifiers, CNTs have become the most outstanding material and most recent works on the determination of the biomolecules employ CNTs as the sensing materials.

(a) *Unmodified Carbon Nanotube-Based Electrochemical Sensors*. The work regarding the enhanced electrochemical response of some biomolecules at CNT electrodes was firstly reported by Luo et al. [16]. In contrast to the poor response at bare GCE, DA exhibited a pair of well-defined redox peaks at SWNT modified GCE. Similar enhanced signals of AA and NE were also observed at the modified electrodes. Since then, many works focused on the selective or simultaneous determination of these species at CNT-modified electrodes (Table 1).

(b) *Carbon Nanotube Composite-Based Electrochemical Sensors*. The selective determination of the electroactive biomolecules was also performed at CNT composite modified electrodes. Compared with CNTs, the combination of CNTs with other components not only provides higher stability and better uniformity of the composite films but also endows the composite films with the unique properties of both components. A typical example is that the composite films made up of CNTs and Nafion can effectively eliminate the interference of negatively charged AA on the determination of other species due to the exclusion of AA from the electrode surface by a negatively charged Nafion film. Table 2 lists the recent works on the determination of electroactive biomolecules at CNT composite films modified electrodes.

(4) *Amino Acids*. Amino acids detected by electrochemical methods are generally electroactive and usually contain phenol moieties. Xu et al. prepared a MWNT film-modified electrode and coupled this electrode to an ion chromatography system for the simultaneous determination of oxidizable amino acids, including CySH, tryptophane and tyrosine [217]. The results show that the peak currents responded linearly to the concentrations of these analytes when the

TABLE 1: Sensitive determination of electroactive microbiomolecules at CNT-based sensors.

Targets	Electrodes	Supporting electrolyte	Detection potential/V	Linear range/ μM	DL/ μM	Ref.
UA	SWNT/Au	0.1 M HAc-NaAc pH 5.0	0.451	4.0 ~ 700	1.0	[211]
Thymine	MWNT-CD/CE	NaHCO ₃ -Na ₂ CO ₃ pH 10.8	0.87	25 ~ 1800	5.0	[131]
NE	SWNT/GCE	B-R pH 5.72	0.261	10 ~ 1100	6.0	[212]
Xanthine (Xa)	MWNT/GCE	HAc-NaAc pH 5.20	0.8	0.2 ~ 20	0.004	[213]
DA	MWNT-IE	0.05 M PBS pH 7.4	0.13	0.5 ~ 10	0.1	[179]
5-HT			0.32	1 ~ 15	0.2	
Hypo-xanthine	MWNT-DHP/GCE	0.1 M PBS pH 7.3	1.06	0.5 ~ 200	0.2	[94]
DA	MWNT-IE	50 mM NaH ₂ PO ₄ pH 5.0	0.4	0.5 ~ 10	0.1	[178]
AA			0.13	80 ~ 1360	20	
DA			0.24	0.0005 ~ 10	0.00025	
NE	MWNT/GCE	0.2 M PBS pH 5.0	—	0.0005 ~ 10	0.00025	[214]*
5-HT			—	0.0007 ~ 10	0.00035	
DA				0.1 ~ 100	0.0077	
EP	SWNT/CFNE	25 mM Tris-HCl pH 7.4	—	0.3 ~ 100	0.038	[76]
NE				0.5 ~ 100	0.042	
UA	Aligned MWNTs	PBS pH 7.4	0.295	0.2 ~ 80	0.1	[191]
Dopa	SWNT/GCE	0.1 M PBS pH 5.0	0.27	0.5 ~ 20	0.3	[30]
EP	MWNT/bppg	0.1 M PBS pH 4.3	0.18	0.1 ~ 100	0.02	[182]
DA				0.0005 ~ 10	0.0002	
NE	MWNT/GCE	0.2 M PBS pH 5.0	—	0.0004 ~ 10	0.0002	[215]*
5-HT				0.0007 ~ 10	0.0003	

*The results were obtained from an electrochemical detection (ED) system for liquid chromatography (LC).

TABLE 2: Sensitive determination of electroactive microbiomolecules at CNT composite film-modified electrodes.

Targets	Electrodes	Supporting electrolyte	Detection potential/V	Linear range/ μM	DL/ μM	Ref.
UA	CNT- β -CD/PG	0.2 M HAc-NaAc pH 4.5	0.45	0.5 ~ 50	0.2	[134]
DA	MWNT-Nafion/GCE	0.1 M PBS pH 5.5	0.235	0.05 ~ 1.0	0.0025	[62]
XA			0.77	0.02 ~ 20	0.04	
UA	MWNT-DHP/GCE	0.1 M PBS pH 5.5	0.38	0.1 ~ 100	0.01	[79]
DA			0.18	0.05 ~ 5.0	0.011	
5-HT	MWNT-DHP/GCE	0.1 M PBS pH 7.0	0.36	0.02 ~ 5.0	0.005	[96]
NE	CNT- β -CD/PG	0.1 M PBS pH 6.0	0.25	1.0 ~ 300	0.5	[135]
DA			0.144	0.5 ~ 100	0.2	
AA	MWNT-CHIT/GCE	0.1 M PBS pH 7.2	-0.029	5.0 ~ 1000	2.0	[102]
DA	MWNT-Nafion/GCE	0.1 M PBS pH 6.0	0.235	0.01 ~ 10	0.0025	[64]
UA			0.484	2.0 ~ 100	0.75	
EP	MWNT-CHIT/GCE	0.1 M PBS pH 5.5	0.329	5.0 ~ 250	1.0	[105]
DA	MWNT-Nafion/CFME	0.05 M PBS pH 7.5	0.145	2.0 ~ 20	0.07	[65]
DA	MWNT-RTIL/GCE	0.1 M PBS pH 7.0	0.16	1.0 ~ 100	0.1	[124]
EP	MWNT-PBCB/GCE	0.1 M PBS pH 6.0	0.28	0.05 ~ 50	0.01	[216]

concentrations ranged from 1.5×10^{-6} to 2.5×10^{-4} M for CySH, 5.5×10^{-7} to 1.5×10^{-4} M for tryptophane and 9.0×10^{-7} to 3.5×10^{-4} M for tyrosine, respectively. The detection limits were 7.0×10^{-7} M for CySH, 2.0×10^{-7} M for tryptophane and 3.5×10^{-7} M for tyrosine (S/N = 3). Wu et al. investigated the electrochemical behavior of tryptophan at MWNT/GCE [51]. Compared with a bare electrode, the oxidation peak current of tryptophan was obviously increased, and the peak potential negatively shifted. Under the chosen conditions, the DPV peak current

was linear to the concentration of tryptophan in the range of 2.5×10^{-7} ~ 1.0×10^{-4} M, and the detection limit was 2.7×10^{-8} M. The voltammetric response of tryptophan at a SWNT modified GCE was also studied by Huang et al. [97]. In pH 2.5 Na₂HPO₄-citric acid buffer, tryptophan yielded a well-defined and very sensitive oxidation peak at about 1.08 V at the SWNT-film coated GCE. The oxidation peak current increased greatly and the peak potential shifted toward the negative direction at the SWNT-modified GCE in contrast to that at the bare GCE. Under optimized

conditions, the oxidation peak current was proportional to the concentration of tryptophan over the range from 4×10^{-8} to 1×10^{-5} M. The detection limit was 1×10^{-8} M for 3 minutes accumulation.

The electrochemical determination of traditionally “non-electroactive” amino acids was also performed by Deo et al. at a SWNT modified electrode that was coated by a nickel hydroxide film [74]. The determination process was achieved through the electrocatalytic oxidation of these amino acids at the Ni(OH)₂ layer that was electrodeposited on surface of SWNTs. In the presence of amino acid, the Ni-CNT layer underwent an electrocatalytic process in which amino acids reduce the newly formed NiO(OH) species. The results showed that under flow injection analysis conditions, a linear response was observed from 10~80 mM arginine with a detection limit of around 1 mM (based on S/N~3). This electrode was also applied to the detection of other amino acids like histidine, lysine, asparagine, methionine and phenylalanine.

4.1.2. Carbon Nanotube-Based Nonenzymatic Electrochemical Sensors for Drug Analysis. The development of sensitive analytical techniques of drugs has drawn much attention due to the promising applications in environment protection, pharmacology and biomedical studies. However, due to the chemical stability and the large bodies, the responses of these substances were generally weak at common bare electrodes. To improve the detection sensitivity, various nanomaterials are employed to fabricate modified electrodes with high performance. Among these materials, CNTs have also been widely to improve the sensitivity of some drugs. Compared with other nanomaterials, CNTs have some advantages, such as good conductivity and strong electrocatalytic activity. The enhanced adsorption of some water insoluble or conjugated drugs on the hydrophobic and π -conjugated sidewalls of CNTs contributes to the sensitive determination of these species at CNT electrodes. Table 3 lists the applications of CNT-based electrochemical sensors for drug analysis.

4.2. Carbon Nanotube-Based Enzymatic Electrochemical Sensors

4.2.1. Carbon Nanotube-Based Enzymatic Electrochemical Biosensors for Electroanalysis. The incorporation of enzymes in a transducer allows one to fabricate enzyme electrodes which exhibit high selectivity, high-sensitivity and long-term stable response to bioanalytes. Many different materials and methods have been used to immobilize enzymes on the electrode surfaces, such as sol-gels, carbon pastes, conductive polymers and recently nanostructured materials. Of particular interest is the use of CNTs as an electrochemical transducer, due to the excellent electron transfer rate, the well-defined nanostructure, the good biocompatibility, and the modifiable surface allowing biomaterial immobilization of CNTs.

(1) *Glucose Oxidase.* Among all the enzyme-based biosensors, glucose biosensors are most widely studied because the

diagnosis of diabetes mellitus requires an accurate monitoring of blood glucose levels. Most of the amperometric glucose biosensors are based on glucose oxidase (GOx), which catalyzes the oxidation of glucose to gluconolactone:



The quantification of glucose can be achieved via the electrochemical detection of the enzymatically liberated H₂O₂. However, the overpotential necessary for the oxidation or the reduction of H₂O₂ at solid electrodes is rather high. Recently, Wang et al. demonstrated that the overpotential of H₂O₂ can be greatly reduced at CNT-based electrodes [63], indicating the promising applications of CNTs in constructing glucose electrochemical biosensors. The hybrids of CNTs and some noble metal nanoparticles, such as palladium, platinum, gold, copper and iridium, have also been demonstrated to lower the H₂O₂ oxidation/reduction overpotential efficiently. Besides the materials, the immobilization methods effectively influence the activity and the quality of enzyme electrodes. Typical GOx immobilization methods include electropolymerization embedment, composite blending, covalent bonding, electrodeposition and physical adsorption.

(a) *Electropolymerization Embedment.* Electropolymerization represents an attractive and well-controlled one-step avenue for preparing amperometric enzyme electrodes. The main advantages of this immobilization avenue are the simple one-step preparation, exclusion of electroactive and surface-active interferences, control of film thickness, and localization of biocatalysts onto tiny electrode surfaces [189]. The electropolymerization of some monomers on the surface of CNTs provided a simple but effective approach for the immobilization of GOx on CNTs, including pyrrole, o-aminophenol, o-phenylenediamine, and so on. In a typical immobilization process, GOx and the monomers are placed together in the supporting electrolytes on a certain ratio. GOx is then immobilized on the electrode surface via the physical entrapment of GOx within the electropolymerized film during the electropolymerization process. Gao et al. reported a glucose electrochemical biosensor through the immobilization of GOx on well-aligned CNTs via pyrrole electropolymerization [195, 196]. They prepared the biosensor by immobilizing GOx in the electropolymerization film of pyrrole through electrochemically oxidizing pyrrole monomer (0.1 M) in a pH 7.45 buffer solution containing 2 mg/mL GOx and 0.1 M NaClO₄ at a constant potential of 1.0 V for 1 minute at 10°C. The oxidation potential of H₂O₂ at this electrode (0.45 V versus Ag|AgCl) was found to be apparently lower than that at a gold electrode (0.65 V versus Ag|AgCl), providing a selective approach for glucose determination. Callegari et al. proposed a convenient and versatile strategy for the construction of glucose amperometric biosensors [230]. They prepared the sensors by the coimmobilization of GOx and a suitable redox mediator, namely ferrocenyl-derivatised SWNTs (Fc-SWNTs) within a thin polypyrrole film adsorbed onto the GCE surface. They found that Fc-SWNTs might provide preferential routes for the electrical wiring of the enzyme to

TABLE 3: Sensitive determination of drugs at CNT-modified electrodes.

Targets	Electrodes	Supporting electrolyte	Detection potential/V	Linear range/ μM	DL/ μM	Ref.
6-Mercaptopurine	MWNT/GCE	0.1 M PBS pH 7.0	0.53	0.4 ~ 100	0.2	[218]
Daunomycin	MWNT-DHP/GCE	0.1 M PBS pH 5.0	-0.564	0.02 ~ 10	0.008	[83]
6-Benzylamino-purine	CNT/GCE	NH ₃ -NH ₄ Cl	0.65	0.08 ~ 10	0.005	[219]
Chloramphenicol	MWNT-DHP/GCE	0.1 M PBS pH 7.0	-0.65	0.3 ~ 12	0.045	[84]
Indole-3-acetic acid	MWNT-DHP/GCE	0.1 M PBS pH 2.0	0.68	0.1 ~ 50	0.02	[80]
Vitamin B6	MWNT-DHP/GCE	0.1 M PBS pH 6.0	0.8	0.5 ~ 100	0.2	[220]
Thyroxine	MWNT-DHP/GCE	0.1 M HCl	0.8	15 ~ 400 $\mu\text{g/L}$	5 $\mu\text{g/L}$	[81]
8-Azaguanine	MWNT-DHP/GCE	0.1 M PBS pH 7.0	0.86	0.025 ~ 10	0.01	[87]
Insulin	MWNT/GCE	0.1 M PBS pH 7.4+0.02% (v/v) Tween-80	0.8	0.1 ~ 1.0	0.014	[221]
Tinidazole	MWNT-DHP/GCE	0.1 M B-R pH 10.0	-0.78	0.05 ~ 40	0.01	[222]
Metronidazole	MWNT-DHP/GCE	0.1 M B-R pH 9.0	-0.71	0.025 ~ 10	0.006	[88]
Fluphenazin	MWNT-MPS/Au	0.05 M HAc-NaAc pH 3.0	0.78	0.05 ~ 15	0.01	[223]
Thyroxine	SWNT-DHP/GCE	0.1 M HCl	0.78	0.1 ~ 7.0	0.02	[82]
Reserpine	MWNT-DHP/GCE	0.1 M PBS pH 6.0	0.64	0.02 ~ 10	0.0075	[90]
Mitomycin c	MWNT-DHP/GCE	—	0.79	0.25 ~ 100	0.08	[91]
Epirubicin	SWNT-DHP/GCE	0.1 M PBS pH 7.0	-0.74	0.05 ~ 10	0.02	[92]
Brucine	MWNT/GCE	H ₂ SO ₄ pH 1.0	0.405	1.0 ~ 100	0.2	[224]
Amitrole	CNTPE	0.05 M PBS pH 7.4	0.9	0.8 ~ 7.0	0.57	[162]
Simvastatin	MWNT-DHP/GCE	0.1 M H ₂ SO ₄	1.06	0.1 ~ 7.5	0.05	[93]
Morphine	MWNT/GCE	0.1 M PBS pH 7.0	0.5	0.5 ~ 150	0.2	[184]
Prochlorperazine	MWNT/DDT/Au	0.05 M PBS pH 5.8	0.69	0.5 ~ 15	0.1	[225]
Melatonin	MWNT-DHP/GCE	0.1 M PBS pH 7.5	0.61	0.08 ~ 10	0.02	[226]
Diclofenac sodium	MWNT-DHP/GCE	0.1 M HAc-NaAc pH 5.0	0.69	0.17 ~ 75	0.08	[227]
Ofloxacin	MWNT-CR/GCE	0.1 M PBS pH 6.0	0.9	0.05 ~ 30	0.009	[140]
Acetylspiramycin	SWNT-DHP/GCE	0.1 M PBS pH 5.5	0.89	6.7 ~ 133	1.3	[228]
Lincomycin	MWNT-DHP/GCE	0.1 M PBS pH 7.0	0.85	0.45 ~ 150	0.2	[229]

the electrode, likely via the aligned ferrocenyl groups, and illustrate the potentialities of such redox-active CNTs for the elaboration of mediated biosensors. The coimmobilization of GOx on iron-phthalocyanine (FePc) functionalized well-aligned MWNTs by the electropolymerization of nonconducting polymers was performed by Ye et al. to prepare a glucose biosensor [198]. FePc on CNTs was used to electrocatalyze the oxidation of H₂O₂ that was liberated by the enzymatic reaction of glucose. Wang et al. recently proposed a one-step method for the construction of glucose biosensors by applying a fixed potential (usually 0.7 V) onto a GCE that was placed beforehand in an aqueous solution containing CNTs, GOx and pyrrole monomer [189]. They found that the CNT dopant retained their electrocatalytic activity toward hydrogen peroxide to impart high sensitivity upon entrapment within the PPy network. The simultaneous incorporation of CNTs and GOx thus endowed amperometric transducers with biocatalytic and electrocatalytic properties and represented a simple and effective route for preparing enzyme electrodes. A similar

method was used by Pan et al. to fabricate glucose biosensors except that additional supporting electrolytes were added to the electropolymerization solution [187].

(b) Blending

(i) *Composite Films.* Blending of enzymes and some polymeric materials that are capable of forming uniform and stable films on electrode surfaces provides a convenient noncovalent approach for the immobilization of enzymes while maintaining the native properties and reactivities of enzymes. This makes the composite blending technique a potential tool for the development of new electrochemical biosensors. Leaching of the entrapped enzymes does not occur or occurs very slowly because these species usually have large bodies and possible interactions (e.g., electrostatic and hydrophobic interactions) between enzymes and the film matrices might exist. Several types of film matrices have been employed for constructing glucose electrochemical biosensors, including sol-gels, Nafion, and CHIT. However,

due to their poor conductivity and film compactness, the performance of the biosensors fabricated from these species and enzymes were usually poor. This deficiency can be completely overcome by the incorporation of CNTs, which leads to the improvement of the conductivity and the diffusion process of the composite films.

On the basis of the stable dispersion of CNTs in Nafion solutions, Wang et al. firstly studied the electrochemical behavior of H_2O_2 at CNT-based electrodes [63]. In contrast to the absence of redox activity at a bare GCE over a wide potential range ($-0.4 \sim 1.0 \text{ V}$), the CNT-coated electrode was found to exhibit significant oxidation and reduction currents of H_2O_2 with a rather low starting potential (around $+0.20 \text{ V}$), providing a highly selective low-potential biosensing of glucose when GOx was immobilized in the CNT-Nafion composite. The excellent analytical performance of the CNT/Nafion/GOx electrode was further demonstrated by Tsai et al. [71]. They found that under optimal conditions, the glucose biosensor displayed a sensitivity of 330 nA/mM , a linear range of up to 2 mM , a detection limit of $4 \mu\text{M}$, and a response time of <3 seconds. Zhu et al. fabricated an amperometric glucose biosensor based on an enzyme electrode modified by CNT/Pt nanoparticles [231]. GOx in gelatin was cross-linked by the use of glutaraldehyde (GDI). Compared with normal GOx/Pt electrode, the analytical property of GOx/CNT-Pt/GCE electrode was apparently improved, reflected by the lowered detection limit, overpotential and response time. Salimi et al. developed a glucose biosensor by introducing GOx into a sol-gel composite at the surface of a bppg electrode modified with MWNTs [183]. The CNT-modified electrode was found to offer excellent electrocatalytic activity toward reduction and oxidation of hydrogen peroxide liberated in the enzymatic reaction between GOx and glucose, enabling sensitive determination of glucose. The amperometric detection of glucose carried out at 0.3 V (versus SCE) in 0.05 M PBS ($\text{pH } 7.4$) showed a good linear response range of $0.2 \sim 20 \text{ mM}$ glucose with a low detection limit of $50 \mu\text{M}$ ($\text{S/N} = 3$). In addition, the response time of the electrode was less than 5 seconds when it was stored dried at 4°C . The sensor showed almost no change in the analytical performance after operation for 3 weeks. Recently, Joshi et al. described the construction of amperometric biosensors based on the incorporation of SWNT modified with GOx into a redox polymer hydrogel [121]. The composite films were constructed by firstly incubating GOx in a SWNT solution and then cross-linking within a poly[(vinylpyridine)Os(bipyridyl) $_2\text{Cl}^{2+/3+}$] polymer film. Incorporation of GOx modified SWNTs into the redox polymer films resulted in a 2-10-fold increase in the oxidation and reduction peak currents during cyclic voltammetry.

(ii) *Carbon Pastes.* As a typical method, carbon pastes have been extensively used to prepare enzyme-based electrochemical biosensor because this method has some unique advantages, such as easy fabrication, low cost, wide potential window, high signal-to-noise ratio and retaining of enzyme activity. Recently, Rubianes et al. studied the electrochemical response of H_2O_2 at a CNTPE by the hydrodynamic

voltammetric method. Similar to that at the MWNT-Nafion/GCE [63], the signals of H_2O_2 were significantly improved at CNTPE in comparison with common carbon paste electrodes. And, decreases of 300 mV in the oxidation overpotential and 400 mV in the reduction overpotential were obtained for hydrogen peroxide, allowing the development of a highly selective and sensitive glucose biosensor without using any metal, redox mediator, or anti-interference membrane. Ricci et al. also prepared a Prussian blue (PB) modified CNTPE, which showed a high sensitivity toward hydrogen peroxide with a detection limit of $7.4 \times 10^{-6} \text{ M}$. Further, they fabricated a glucose biosensor by incorporating GOx into the paste, creating a sensitive tool for the detection of glucose in the range between 0.1 and 50 mM .

(c) *Covalent Bonding.* Although the noncovalent methods for fabricating CNT-based electrochemical biosensors have some advantages like easy fabrication and low cost, the poor stability and leaching of enzymes sometimes significantly influence the analytical performance of these biosensors. To overcome this limitation, great efforts have been made to covalently attach enzymes to the electrode surfaces via various methods and reagents. Xue et al. described a simple method for fabricating glucose biosensors by covalently attaching GOx onto a SWNT modified Pt electrode [232, 233]. The Pt/SWNT electrode was firstly activated with EDC in PBS with $\text{pH } 5.5$ for 1 hour, and then immersed in the PBS containing 5 mg/mL GOx at 4°C for 12 hours. The resulting enzyme electrode was washed thoroughly with PBS and stored at -10°C . This biosensor showed a stable amperometric response at a low applied potential (0.4 V versus SCE), a wide response range of $\text{pH } (5.5\text{--}8.0)$ and good stability (kept 90% activity after 4 months) [233]. As mentioned above, Gooding et al. also covalently immobilized MP-11 on the open end of a SWNT array that was fabricated by self-assembling methods with the aid of EDC [150]. Hrapovic et al. [73] recently developed a highly sensitive hydrogen peroxide sensor by the incorporation of CNTs and Pt nanoparticles into the Nafion films on a GCE, which exhibited a linear range from 25 nM to $10 \mu\text{M}$ ($R^2 = 0.997$, sensitivity of $3.57 \text{ A M}^{-1} \text{ cm}^{-2}$), and also from $100 \mu\text{M}$ to 2 mM ($R^2 = 0.996$, sensitivity of $1.85 \text{ A M}^{-1} \text{ cm}^{-2}$), with a rather low detection limit of 25 nM ($\text{S/N} = 3$) (Figure 12). They further prepared a glucose biosensor by cross-linking the GOx films that were dropped and dried on the CNT/Pt-modified GC electrode with 2.5% glutaraldehyde (GDI). This nanocomposite biosensor exhibited a rapid response (3 seconds), a low detection limit ($0.5 \mu\text{M}$, $\text{S/N} = 3$) and a wide linear range from $0.5 \mu\text{M}$ up to 5 mM with a sensitivity of $2.11 \mu\text{A/mM}$. There was also an interesting work performed by Zhang et al. for the covalent immobilization of GOx on CNT composites using RTILs as the CNT dispersing reagent and N-succinimidyl acrylate (NSA) as both the surface modifier of CNTs and the functional sites for GOx covalent immobilization [123].

(d) *Other Methods.* Some other methods have also been proposed by several workers for immobilizing of GOx on

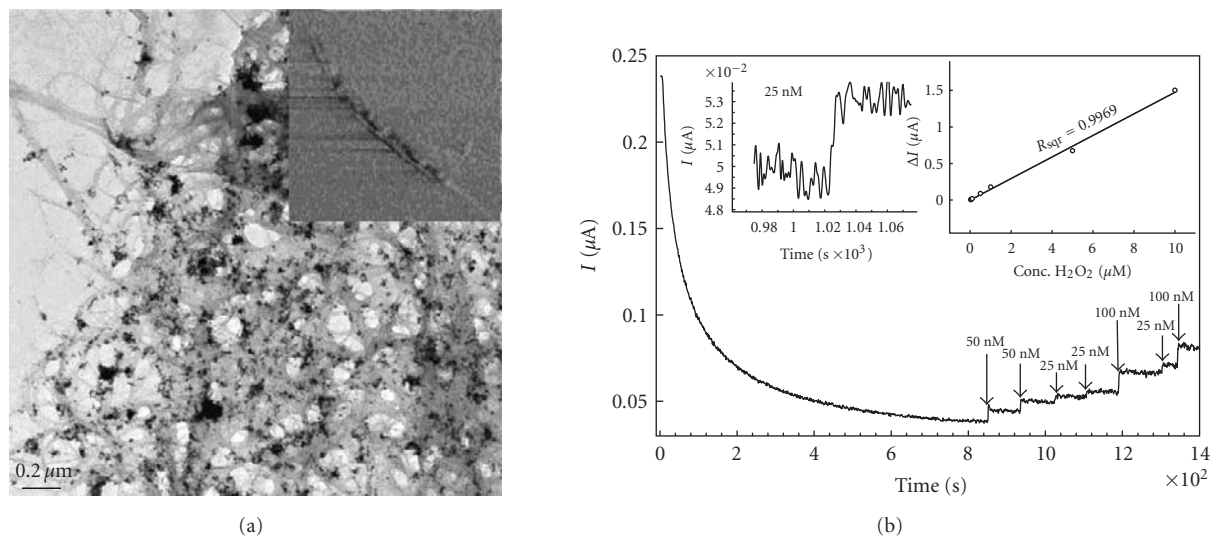


FIGURE 12: (a) TEM micrograph of SWNTs in the presence of Pt nanoparticles. Inset: AFM tapping-mode phase image (size, $1 \mu\text{m} \times 1 \mu\text{m}$; data scale, 20 nm) of one SWNTs in the presence of Pt nanoparticles. (b) Performance of GC/CNT + Pt_{nano} electrode in amperometric detection of low concentrations of hydrogen peroxide at +0.55 V versus Ag|AgCl (3 M NaCl). The inset (left) shows detection limit of 25 nM with S/N = 3. Inset (right) shows calibration curve for H₂O₂ concentrations between 25 nM and 10 μM . [Adapted with permission from Hrapovic et al. [73], *Anal. Chem.*, **76**, 1083 (2004). Copyright 2004, American Chemical Society.]

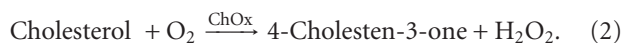
CNT-based electrodes to prepare glucose electrochemical biosensors, such as physical adsorption and coelectrodeposition. Wang et al. developed a novel biosensor, comprising of electrode of gold/MWNT-GOx (Au/MWNT-GOx) [199]. MWNTs were grown on n-type silicon substrates using an ASTeX microwave plasma system. After growth of MWNTs on silicon substrate, a thin gold film was E-beam evaporated on the top surface of MWNTs. Then, the silicon substrate was etched away using a mixture acid solution of HCl and HNO₃. Finally, the electrode modified with MWNTs (Au/MWNTs) was put into the 0.1 M PBS containing GOx, and the GOx was immobilized by MWNTs. The biosensor showed a linear response to glucose concentration within the range from 0.05 to 13 mM with a low detection limit of less than 0.01 mM for glucose, suggesting MWNTs enhanced efficiency of electron transfer between GOx and electrode greatly, resulting in high sensitivity in detecting glucose. Loh et al. prepared a glucose biosensor by the physical adsorption of GOx on the poly(3,3'-diaminobenzidine) (PDAB) film-modified electrode [197]. They firstly grew MWNTs (10-mm thick, erected) in a quartz furnace using ethylenediamine on 1-mm diameter tantalum substrates seeded with cobalt nanoparticles, which was further functionalized with DAB by the electropolymerization of DAB using a CV method and a self-limiting, very thin layer of polymer with NH₂ functional groups can be introduced onto the CNTs surface in one easy step. For immobilizing the GOx on the DAB-modified electrode surface, a second round of CV was then performed with GOx in the buffer solution to attach the GOx on the DAB-modified CNTs. They believed that the immobilization of GOx probably proceeded via entrapment within the highly porous wiring matrix of CNTs. This glucose biosensor had some overwhelming advantages, such as the low detection potential due to the lowered overpotential of H₂O₂ at

the CNT electrode and the absence of the concomitant oxidation of interferent molecules like AA and UA. Tang et al. fabricated a new amperometric biosensor, based on adsorption of GOx at the Pt nanoparticle-modified CNT electrode [200]. The CNT/graphite electrode ($0.4 \times 0.4 \text{ cm}$, geometry area 0.16 cm^2) was prepared by the CVD method and used as the working electrode. Using a standard three-electrode cell, Pt nanoparticles were electrodeposited on the CNT electrode by the potential step deposition method from N₂-saturated 7.7 mM H₂PtCl₆ plus 0.5 M HCl aqueous solution. GOx immobilization was achieved by incubation for 12 hours in a GOx solution (500 U/mL) at less than 4°C. The obtained GOx/Pt/CNT electrode was washed carefully with double-distilled water and dried at less than 4°C, and then 0.5 wt% Nafion solution was cast on the surface of the resulting GOx/Pt/CNT electrode to avoid the loss of GOx in determination and to improve the anti-interferent ability. The excellent electrocatalytic activity and special three-dimensional structure of the enzyme electrode resulted in good characteristics such as a large determination range (0.1 ~ 13.5 mM), a short response time (within 5 seconds), a large current density (1.176 mA/cm^2), and high sensitivity ($91 \text{ mA M}^{-1} \text{ cm}^{-2}$) and stability (73.5% remains after 22 days). Lim et al. employed an electrodeposition method for the codeposition of GOx and palladium nanoparticles onto a Nafion-solubilized CNTs film [58]. The codeposited Pd-GOx-Nafion CNTs bioelectrode retained its biocatalytic activity and offered an efficient oxidation and reduction of the enzymatically liberated H₂O₂, allowing for fast and sensitive glucose quantification. The combination of Pd-GOx electrodeposition with Nafion-solubilized CNTs enhanced the storage time and performance of the sensor. An extra Nafion coating was used to eliminate common interferents such as UA and AA. The fabricated Pd-GOx-Nafion CNTs

glucose biosensor exhibited a linear response up to 12 mM glucose and a detection limit of 0.15 mM (S/N = 3).

(2) Other Enzymes

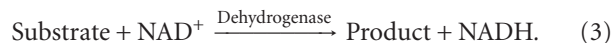
(a) *Cholesterol Oxidase*. The determination of cholesterol is of great significance in clinical diagnosis of coronary heart disease, arteriosclerosis, myocardial infarction and brain thrombosis. Among the various biosensors of cholesterol, cholesterol oxidase (ChOx)-based electrochemical biosensors are especially attractive because they offer a simple, rapid and inexpensive means of quantifying cholesterol. Similar to glucose electrochemical biosensors, most of the amperometric cholesterol biosensors are based on the ChOx enzyme, which catalyzes the oxidation of cholesterol to 4-cholesten-3-one:



The quantification of cholesterol can be achieved via electrochemical detection of the enzymatically liberated H_2O_2 . Guo et al. proposed a CNT-based amperometric cholesterol biosensor through the LBL deposition of PDDA and ChOx on an MWNT-modified gold electrode, followed by electrochemical generation of a nonconducting PPD film as the protective coating [145]. Due to the strong electrocatalytic properties of MWNTs toward H_2O_2 and the low permeability of PPD film for electroactive species, such as AA, UA and acetaminophen, this biosensor exhibited high sensitivity and good anti-interferent ability in the detection of cholesterol with a linear range up to 6.0 mM and a detection limit of 0.2 mM. Tan et al. developed an amperometric cholesterol biosensor based on sol-gel CHIT/silica and MWNT organic-inorganic hybrid composite material [119]. They firstly prepared a Prussian blue-modified GCE (PB/GCE) by electrodeposition, followed by the casting of the aqueous mixture of MWNTs, sol-gel silica, CHIT and ChOx on the surface of PB/GCE. The analytical characteristics and dynamic parameters of the biosensors with and without MWNTs in the hybrid film were compared. The results showed that the analytical performance of the biosensor can be improved greatly after introduction of MWNTs. Shi et al. recently fabricated a novel H_2O_2 sensor by intercalating Pt nanoparticle decorated CNTs (CNT-Pt) prepared using a chemical reduction method on the surface of a waxed graphite electrode [181]. The Pt nanoparticles at the waxed graphite electrode exhibited high catalytic activity for the reduction of hydrogen peroxide. Based on this, ChOx was immobilized with sol-gel on the CNT-Pt based electrode to construct a cholesterol biosensor, which was found to have excellent analytical performance for cholesterol detection with a rapid response (<20 seconds), a wide linear range of 4.0×10^{-6} – 1.0×10^{-4} M, and a low detection limit of 1.4×10^{-6} M.

(b) *Dehydrogenases*. Similar to the oxidases, some dehydrogenases are also employed to construct various electrochemical biosensors, including alcohol-dehydrogenase (ADH),

D-fructose dehydrogenase (FDH) and glucose dehydrogenase (GDH). Generally, the response of dehydrogenase-based electrochemical biosensors is a current due to the electrooxidation of NADH that is produced in the enzymatic reaction



In this process, NAD^+ behaves as an enzymatic mediator. This section will firstly focus on the development of CNT-based NADH electrochemical sensors and then on the construction of dehydrogenases-based electrochemical biosensors.

(i) Carbon Nanotube-Based NADH Electrochemical Sensors.

The direct electrochemical oxidation of NADH is becoming more and more interesting since many dehydrogenases need it as cofactors to catalyze redox reaction. However, the direct electrochemical oxidation of NADH at a bare electrode takes place at high overpotentials, for example, the reported overpotential at pH 7.0 is about 1.1 V at carbon electrodes and 1.3 V at Pt electrodes. Many efforts have been made to reduce the overpotential of NADH electrooxidation. Musameh et al. [234] firstly reported the electrocatalytic oxidation of NADH at a GC electrode modified with disordered CNT coatings with a decrease of 490 mV in overpotential. Since then, many works dealt with the electrocatalytic oxidation of NADH at various CNT-based electrodes. Chen et al. studied the electrochemical behavior of NADH at an OCNT/GC electrode [192, 235]. They found that the direct electrocatalytic oxidation of NADH occurred at a much lower potential (at about 0.0 V) with high stability at an OCNT/GC electrode than at disordered CNT-modified electrode. A reduction of the overpotential of more than 600 mV was achieved, and the anodic peak currents increased linearly with NADH concentration from 2×10^{-5} to 1×10^{-3} M with a low detection limit of about 5×10^{-7} M. Recently, Zhang et al. [236] developed a CHIT-CNT system by integrating the redox mediator Toluidine Blue O (TBO) and CNTs in CHIT for the determination of NADH. In that work, they firstly covalently attached TBO to CHIT via a two-step procedure and then solubilized CNTs in the aqueous solution of CHIT-TBO. The resulting mixture was cast on the surface of a GCE to form thin CHIT-TBO/CNT surface films. As compared to CHIT-TBO, the CHIT-TBO/CNT films displayed large amplification of a current due to the TBO-mediated oxidation of NADH at -0.10 V. This was discussed in terms of the TBO/CNT synergy that resulted in the improved charge propagation through the CHIT-TBO/CNT matrix. The electrocatalytic oxidation of NADH was also achieved by Liu et al. at PANI/PABS-SWNT multilayer films [148].

(ii) *Dehydrogenase-Based Electrochemical Biosensors*. Based on the electrocatalytic oxidation of NADH at CNT electrodes, several dehydrogenase-based electrochemical biosensors have been constructed. Wang et al. reported a MWNT-based alcohol biosensor, based on the incorporation of alcohol-dehydrogenase/NAD⁺ within a three-dimensional

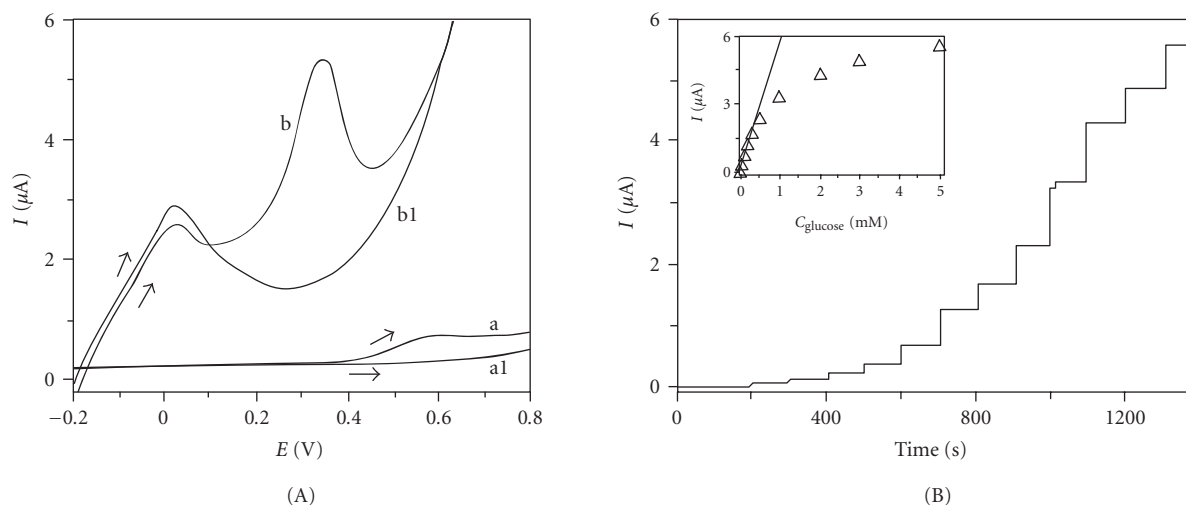


FIGURE 13: (A) Linear scan voltammograms recorded at (a) GC/CHIT and (b) GC/CNT-CHIT film electrodes in 0.10 mM NADH solution. Traces a1 and b1 were recorded in a background electrolyte solution. For the clarity of presentation, traces b and b1 were shifted downward by $6\ \mu\text{A}$ along the y -axis. Scan rate, 50 mV/s. (B) Amperometric response of the GC/CNT-CHIT-GDI-GDH film electrode to additions of glucose aliquots ($10\ \mu\text{M}$ –5.0 mM) into a stirred solution of pH 7.40 phosphate buffer that contained 0.10 mM NAD^+ . Inset: corresponding calibration plots. Potential, 0.400 V. [Adapted with permission from Zhang et al. [103], *Anal. Chem.*, 76, 5045 (2004). Copyright 2004, American Chemical Society.]

MWNT/Teflon matrix [237]. The MWNT component offered a marked decrease in the overpotential for the oxidation of liberated NADH along with minimal surface fouling effects, hence allowing convenient low-potential stable detection of ethanol. Antiochia et al. developed a new mediated CNTP amperometric biosensor of fructose [238]. The biosensor was formed by a CNTP electrode modified with an electropolymerized film of 3,4-dihydroxy benzaldehyde (3,4-DHB), based on the activity of a commercial available D-fructose dehydrogenase (FDH) immobilized on an immobilon membrane placed on the top of the electrode surface. The biosensor response current was directly proportional to D-fructose concentration from 5×10^{-6} to 2×10^{-3} M with a detection limit of 1×10^{-6} M. On the basis of the electrocatalytic oxidation of NADH at a CNT-CHIT composite film-modified GCE, Zhang et al. recently proposed a simple but useful approach for the fabrication of glucose biosensors by the incorporation of glucose dehydrogenase (GDH) into the CNT-CHIT films through the tethering of GDH to CHIT with GDI [103] (Figure 13). The stability and sensitivity of the GC/CNT-CHIT-GDI-GDH biosensor allowed for the interference-free determination of glucose in the physiological matrix (urine). In pH 7.4 PBS, linear least-square calibration plots over the range 5–300 μM glucose (10 points) had slopes $80\ \text{mA}\ \text{M}^{-1}\ \text{cm}^{-2}$ and a correlation coefficient 0.996. The detection limit was 3 μM glucose ($S/N = 3$). Another advantage of such electrode system was that oxygen did not influence its analytical performance. This was in contrast to oxidase-based electrodes that were prone to interferences from changing levels of oxygen in the samples. Rubianes et al. also studied the performance of enzymatic biosensors based on the immobilization of different dehydrogenase within a CNTPE prepared from MWNTs and mineral oil

[167]. The strong electrocatalytic activity of CNTs toward the oxidation of NADH allowed an effective low-potential amperometric determination of ethanol, in connection with the incorporation of alcohol dehydrogenase/ NAD^+ within the composite matrix. Compared to the analogous enzymatic CPEs, a great enhancement in the response was observed at the enzymatic CNTPEs.

(c) *Other Enzymes.* There were also some other enzymes used by several workers to prepare electrochemical biosensors, such as acetylcholinesterase, alkaline phosphatase, organophosphorus hydrolase, urease and tyrosinase. Based on the reversible Nernstian response of a SWNT modified electrode to analytes associated with solution pH change, Xu et al. constructed voltammetric urease and acetylcholinesterase biosensors by immobilizing the enzymes with a sol-gel hybrid material that was cast on the surface of the SWNT modified electrode [31]. These biosensors were used for the determination of urea and acetylthiocholine according the potential shift of the anodic peak of SWNTs. Moreover, the methods for preparing sensors and biosensors were simple and reproducible, and the range of analytes could be extended to substrates of other hydrolyases and esterases. Lenihan et al. proposed a new approach to the modification of CNTs with biomolecules for the development of nanoscale biosensors [239]. Alkaline phosphatase was immobilized on the surface of MWNTs utilizing an LBL methodology. CNTs were incubated with streptavidin, resulting in the formation of a protein layer on the surface of the nanotubes. Biotinylated alkaline phosphatase was then allowed to bind to streptavidin, anchoring the sensing protein onto the surface. Electrochemical biosensors were constructed by using carbon nanotubes compacted into

pellets. Electrodes constructed in this manner were observed to generate an electrochemical signal that was a function of substrate concentration. Trojanowicz et al. prepared pesticide paraoxon biosensors by the physical adsorption of organophosphorus hydrolase on the surface of MWNT modified working graphite ink electrode of the three-electrode screen-printed sensing stripe [240]. Joshi et al. reported the fabrication of a disposable biosensor based on acetylcholinesterase-CNT-modified thick film strip electrode for organophosphorus (OP) insecticides [41]. The degree of inhibition of the enzyme acetylcholinesterase (AChE) by OP compounds was determined by measuring the electrooxidation current of the thiocholine generated by the AChE catalyzed hydrolysis of acetylthiocholine (ATCh). The large surface area and electro-catalytic activity of CNTs lowered the overpotential for thiocholine oxidation to 200 mV (versus Ag|AgCl) without the use of mediating redox species and enzyme immobilization by physical adsorption. The biosensor detected as low as 0.5 nM (0.145 ppb) of the model organophosphate nerve agent paraoxon with good precision, reproducibility and stability. HRP was also employed by several workers to prepare hydrogen peroxide biosensors. Xu et al. used MWNTs as a coimmobilization matrix for the incorporation of HRP and electron transfer mediator MB onto a GCE surface [241]. Cyclic voltammetry and amperometric measurements demonstrated the feasibility of MB as an electron carrier between the immobilized peroxidase and the surface of GCE. The amperometric response of this resulting biosensor to H₂O₂ showed a linear relation in the range from 4 μM to 2 mM with a detection limit of 1 μM (S/N = 3). Yamamoto et al. reported a hydrogen peroxide biosensor based on the immobilization of HRP on the surface of a MWNT modified electrode via the cross-linking of HRP and BSA composite film by GDI [29]. The MWNT-HRP modified electrode showed excellent response of reduction current for the determination of H₂O₂ at the potential of -300 mV (versus Ag|AgCl) with a linear concentration range of $3.0 \times 10^{-7} \sim 2.0 \times 10^{-4}$ M and a low detection limit of 1.0×10^{-7} M (S/N = 3).

4.2.2. Carbon Nanotube-Promoted Direct Electron Transfer of Redox Proteins and Enzymes. The direct electron transfer of redox proteins and enzymes at electrode surface has attracted more and more attention recently. These works are of great importance for studying the biological redox process, which can help us to understand the energy transform and the material metabolism in life action. But unfortunately, it is difficult for these macromolecules to achieve direct exchange electron at electrode surfaces because they usually have big and complex structures with the redox centers deeply immersing in the bodies. Furthermore, the adsorption of these species at the electrode surface often results in the change of their native configuration and the consequent denature. Earlier, mediators were employed by some groups to improve the electron contact between enzymes and electrodes. However, using mediators generally makes the biosensors complicated and leads to a slow response. The development of mediatorless biosensors, thus, becomes the

goal of extensive researches. The first work regarding the direct electron transfer of proteins at CNT electrodes was reported by Davis et al. in 1997 by the physical adsorption of horse heart cytochrome c (Cyt c) on CNTs [159]. Since then, many works focused on the achievement of the direct electron transfer of various redox proteins and enzymes at CNT electrodes, including hemoglobin (Hb) [46, 56, 77, 242], myoglobin (Mb) [50, 52, 243, 244], Cyt c [43, 53, 154, 245–247], peroxidases (e.g., HRP [122, 176, 248, 249], catalase (Ct) [34, 250] and MP-11 [122, 150, 251]), oxidases (e.g., GOx [78, 152, 252–255], putrescine oxidase (POx) [256, 257], xanthine oxidase (XOs) [258, 259]), and so on.

(1) Direct Electron Transfer of Redox Proteins and Enzymes at Carbon Nanotube Electrodes

(a) Heme proteins

(i) Myoglobin. Myoglobin (Mb) is a small size heme protein with a molar mass of approximately 17 500, and it functions in both transport and short-term storage of oxygen. Due to its commercial availability and a well-known structure, Mb is considered to be an ideal model protein for the study of heme proteins or enzymes. Thus, the achievement of the direct electron transfer (DET) of Mb not only provides a convenient approach for fabricating Mb-based biosensors but also creates nice model systems for studying the biological functions of these proteins. Similar to other nanoscale materials, the good conductivity, the nanosized tubular structural and the functional groups make CNTs act as molecular wires to allow the electrical communication between the underlying electrodes and Mb. Recently Zhao's group developed a simple but effective method for the immobilization and the direct electron transfer of Mb at CNT-based electrodes [50, 52, 253, 254]. In a typical procedure, Mb was immobilized on the surface of a MWNT modified electrode by immersing the CNT electrode in an acetate buffer solution of Mb for a long period (e.g., 72 hours), followed by thoroughly washing with double-distilled water to remove loosely bonded enzyme molecules. The resultant electrode exhibited a pair of well-defined redox peaks with cathodic and anodic peak potentials at 0.298 and 0.198 V (versus SCE), respectively. The shapes of the cathodic and anodic peak were nearly symmetric, and the reduction and oxidation peaks have the same heights, indicating a reversible process of Mb at this electrode. This biosensor was further used for the sensitive detection of nitric oxide (NO) [50, 254], O₂ [253], and H₂O₂ [52] (Figure 14).

(ii) Hemoglobin. Hemoglobin (Hb), functioning physiologically in the storage and transport of molecular oxygen in the blood of vertebrates, has a molecular weight of 64.000 to 67.000, and comprises four polypeptide subunits (two α and two β subunits), each of which has an iron-bearing heme within molecularly accessible crevices and has a similar structure. Although Hb does not play a role as an electron carrier in biological systems, it has been shown to possess enzyme-like catalytic activity. Similar to Mb, it is also an ideal

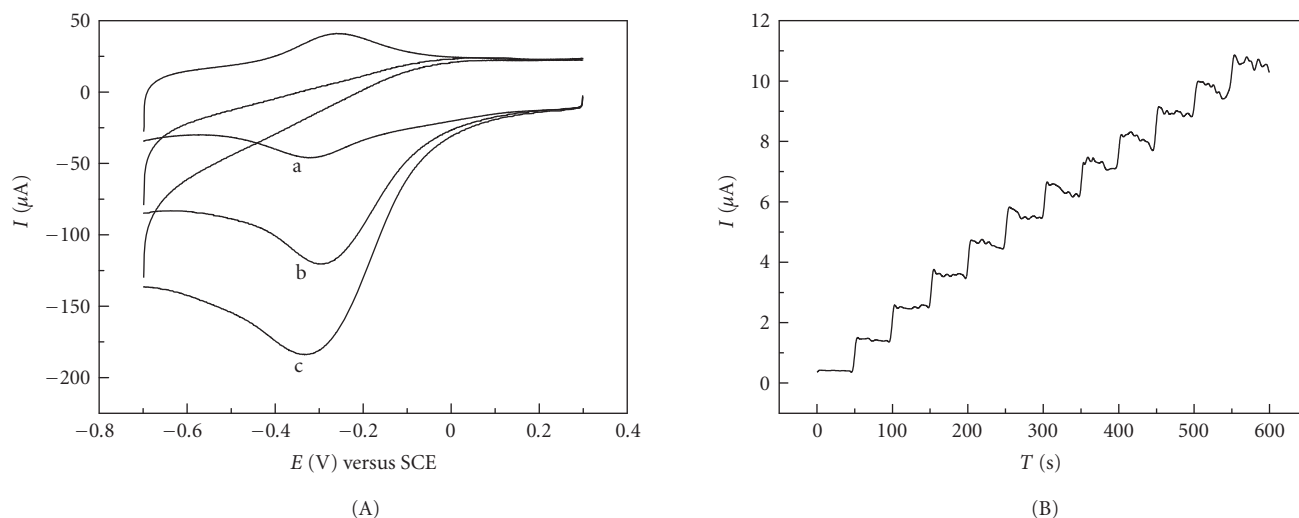


FIGURE 14: (A) CV of Mb/MWNT/GCE in the presence of H_2O_2 : (a) 0 mM, (b) 0.4 mM, and (c) 0.8 mM; scan rate: 200 mV/s. (B) Amperometric response of H_2O_2 at Mb/MWNT/GCE in 0.1 M PBS (pH 4.0); each addition was 30 $\mu\text{mol/L}$ H_2O_2 ; operation potential -0.14 V. [Adapted with permission from Zhao et al. [52], *Anal. Biochem.*, **329**, 160 (2004). Copyright 2004, Elsevier Science.]

model molecule for the study of direct electron transfer reactions of heme enzymes because of its commercial availability and a known and documented structure. The direct electron transfer of Hb at CNT electrodes has been achieved by Cai et al. through different immobilization methods [46, 77]. Based on the facilitated dispersing of CNTs in water by CTAB, Cai et al. fabricated a CNT-based Hb electrochemical biosensor by firstly casting the mixture of CNT aqueous suspension and Hb phosphate buffer solution and fixing the resultant composite film with a Nafion coating [77]. Cyclic voltammetric results showed a pair of well-defined redox peaks, corresponding to the direct electron transfer of Hb, with a formal potential ($E^{\circ'}$) at about 0.343 V (versus SCE) in the PBS (pH 6.8). Further experiments demonstrated that the immobilized Hb retained its bioelectrocatalytic activity for the reduction of H_2O_2 . The electrocatalytic current was proportional to the concentration of H_2O_2 at least up to 20 mM. Cai et al. reported an adsorption method for the immobilization of Hb on a CNT electrode by incubating the electrode into the protein solution (5 mg/mL in 0.1 M PBS, pH 5.5) for 1 hour at 4°C [46]. Jia et al. also reported the using of novel bamboo-like nitrogen-doping CNx nanotubes for the immobilization of Hb by dipping the CNT electrode into a 0.2 M acetate buffer solution (pH 6.0) containing 10 mg/mL Hb over 72 hour at 4°C [54]. The transmission electron microscopy (TEM) clearly showed that Hb could be strongly adsorbed on the surface of CNx nanotubes. The CV results of Hb/CNx nanotube modified electrode showed a pair of well-defined and quasireversible redox peaks centered at approximate 0.33 V (versus SCE) in pH 7.0 PBS.

(iii) *Cytochrome c*. Cytochrome c (Cyt c) is a basic redox heme protein with 12,384 g/mol molecular weight and approximately spherical shaper with 34 Å diameter. It plays an important role in the biological respiratory chain, whose

function is to receive electrons from Cyt c reductase and deliver them to Cyt c oxidase. As mentioned above, the direct electron transfer of Cyt at CNT electrodes was firstly reported by Davis et al. in 1997 [159]. The electrochemistry of Cyt c was later studied by Wang et al. using cyclic voltammetry at a GCE modified with SWNTs [245]. A pair of well-defined redox waves was obtained in Cyt c aqueous solution at an activated SWNT film-modified electrode. The electrode reaction of Cyt c was found to be a diffusion-controlled process. The peak current increased linearly with the concentration of Cyt c in the range from $3.0 \times 10^{-5} \sim 7.0 \times 10^{-4}$ M with a detection limit of 1.0×10^{-5} M. Chen et al. successfully immobilized MWNTs on the surface of a Pt electrode by mixing with DNA [43]. The experimental data indicated that Cyt c can strongly adsorb on the surface of the modified electrode, and forms an approximate monolayer. The immobilized MWNTs can promote the redox of Cyt c, which gave reversible redox peaks with a formal potential of 81 mV versus SCE. Recently, Qu et al. [154] characterized the SWNTs submonolayer film that was prepared by electrostatically adsorbing nanotubes onto a 2-aminoethanethiol self-assembled monolayer (SAM) on a gold bead electrode using tapping-mode atomic force microscopy (TM-AFM). The results showed that the orientation of SWNTs on the SAM was horizontal and the surface coverage was quite low. However, this electrode was demonstrated to be capable of facilitating the direct electron transfer of Cyt c in solution. Zhao et al. also studied the direct electron transfer of Cyt c on a MWNT modified electrode [53]. In contrast to the time-consuming methods by immersing the CNT electrodes in the protein or enzyme solutions for a long period [50, 52, 243, 244], they fabricated the Cyt c modified CNT electrodes by placing a MWNT modified electrode in a Cyt c solution (0.09 mmol/L, pH 7.0 PBS) and then performing a consecutive cyclic potential scans in the potential range from 0.3 to -0.8 V with a scan rate 50 mV/s up to obtain a stable

CV curve. The results from electrochemical impedance spectroscopy (EIS) and CV suggested that Cyt c could be tightly adsorbed on the surface of MWNTs and MWNTs showed an obvious promotion for the direct electron transfer between Cyt c and electrode. A couple of well-defined and quasi-reversible CV peaks of Cyt c can be observed in a PBS (pH 7.0). Cyt c adsorbed on MWNTs exhibited a remarkable electrocatalytic activity for the reduction of hydrogen peroxide (H_2O_2).

(b) Peroxidases

(i) *Horseradish Peroxidase*. Horseradish peroxidase (HRP), functioning physiologically as the biocatalysis of H_2O_2 , has been extensively investigated, due to its commercial availability and the well-known structure. HRP has been used as a typical model for studying the structural, kinetic and thermodynamic properties of peroxidases. The first work on the direct electron transfer of HRP was reported by Zhao et al. using CNT-based powder microelectrodes (CNTPME) [176]. The immobilization of HRP was achieved by mixing 1 mg CNT powder with 200 mL 0.1 M PBS solution containing 1 mg/mL HRP and packing the dry mixture into the microcaves of CNTPME. The resultant electrode exhibited a pair of reversible redox peaks -0.7 and -0.6 V in 0.1 M PBS (pH 7.0). It was found that the adsorbing HRP kept its catalytic activity to H_2O_2 upon the immobilization on the CNT electrode. Cai et al. [248] also developed a HRP biosensor based on the method used for constructing Mb biosensors [77]. It was found that HRP underwent effective and stable direct electron transfer reaction and retained its catalytic activity toward H_2O_2 . Based on the stable dispersion of CNTs in RTILs, Zhao et al. prepared a HRP biosensor by firstly dispersing HRP and MWNTs in an RTIL, then grinding the mixture to form a black gel and casting the gel on the electrode surface with spinning [122]. HRP coated by RTIL-modified gold and glassy carbon electrodes allowed efficient electron transfer between the electrode and the protein and also catalyzed the reduction of O_2 and H_2O_2 .

(ii) *Catalase*. Catalase (Ct) is a redox enzyme, present in almost all aerobic organisms. It catalyses the disproportionation of hydrogen peroxide into oxygen and water without the formation of free radicals, so it serves in part to protect cells from the toxic effects of hydrogen peroxide. Catalase contains four equal subunits, and each of them has a molecular weight of 57,000 daltons and is equipped with a Fe (III)-protoporphyrin-IX. The direct electron transfer of Ct was mainly accomplished through physical adsorption approaches. Wang et al. recently studied the direct electron transfer of Ct at a gold electrode modified with SWNTs [34]. They found that a pair of well-defined redox peaks was obtained for Ct with the reduction peak potential at -0.414 V and a peak potential separation of 32 mV in 0.05 M PBS (pH 5.9). Both reflectance FT-IR spectra and the dependence of the reduction peak current on

the scan rate revealed that Ct adsorbed onto the SWNT surfaces. Compared to other types of carbonaceous electrode materials (e.g., graphite and carbon soot), the electron transfer rate of Ct redox reaction was greatly enhanced at the SWNT-modified electrode. The peak current was found to increase linearly with the Ct concentration in the range of $8 \times 10^{-6} \sim 8 \times 10^{-5}$ M used for the electrode preparation. The catalytic activity of Ct adsorbates at the SWNT appears to be retained, as the addition of H_2O_2 produced a characteristic catalytic redox wave. Similar direct electron transfer of Ct at a SWNT modified GCE was studied by Zhao et al. [250].

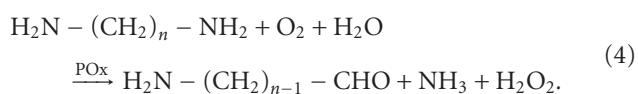
(iii) *Microperoxidase*. Microperoxidase (MP-11) is an oligopeptide consisting of eleven amino acids and a covalently linked FeIII-protoporphyrin IX heme site. The direct electron transfer between MP-11 and electrodes can be used in biosensors and biofuel cells. In biofuel cells, the MP-11 modified electrodes are used as cathode materials to catalyze the reduction of oxygen. The direct electron transfer of MP-11 has recently been studied by Dong et al. in different CNT-based electrode systems [122, 251]. Based on the immobilization of enzymes in the RTIL-MWNT composite films, Dong et al. also studied the direct electron transfer of MP-11 at this film-modified electrode [122]. In 0.1 M PBS, a pair of well-defined redox waves was obtained, corresponding to the active FeIII/II center of MP-11 at $E_{1/2}[(E_{pa} + E_{pc})/2]$ (versus Ag|AgCl) = -0.25 V with a peak separation of 61 mV at a scan rate of 100 mV/s. This result was different from the report by Willner et al. at $E_{1/2} = -0.4$ V (versus SCE), which was attributed to the fact that the redox active center in MP-11, an iron protoporphyrin IX, was not shielded by a polypeptide and was easily affected by the environments of the ionic liquids compared with other systems. They also studied the direct electron transfer of MP-11 by cyclic voltammetry at a GCE modified with MWNTs. In that work, MP-11 was immobilized by immersing the CNT electrode in 0.1 M PBS containing 1 mg/mL MP-11 at 4°C for about 10 hours. The resulting electrode showed a pair of well-defined redox peaks with a formal potential at about -0.26 V (versus Ag|AgCl) in PBS (pH 7.0). The experimental results also demonstrated that the immobilized MP-11 retained its bioelectrocatalytic activity to the reduction of H_2O_2 and O_2 .

(c) Oxidases

(i) *Glucose Oxidase*. Glucose oxidase (GOx), from *Aspergillus* or *Penicillium*, is a homodimer with a molecular weight of about 150 ~ 180 kDa containing two tightly bound flavine adenine dinucleotide (FAD) cofactors and catalyzes the electron transfer from glucose to oxygen accompanying the production of gluconic acid and hydrogen peroxide. Industrially, it has been used in the production of gluconic acid. The most important application is in biosensors for the quantitative determination of glucose in body fluids, foodstuffs, beverages, and fermentation liquor. As mentioned above, although CNTs have been widely used to

fabricate the GOx-based glucose electrochemical biosensors due to the excellent electrocatalytic activity of CNTs toward H_2O_2 , few works accomplished the direct electron transfer between GOx and the underlying electrodes. Xu et al. recently studied the electrochemical behavior of GOx at a MWNT modified electrode by cyclic voltammetry [252]. They found that the MWNT electrode exhibited two pairs of redox peaks with formal potentials of -0.45 and -0.55 V (versus SCE) when immersed into 0.1 M PBS containing 2 mg/mL GOx for 2 hours, which were attributed to the responses from GOx in the solution and adsorbed on the MWNT surface, respectively. In addition, with the increase of scan time, the currents of both redox peaks decreased except that the redox peaks at -0.45 V disappeared after about 1 hour, and the redox peaks at -0.55 V tended to be a stable value. The reservation of adsorbed GOx at MWNTs foretells the possibility of immobilization of GOx on CNTs by physical adsorption. Wang et al. proposed a simple approach for the immobilization and the direct electron transfer of GOx at CNT electrodes [254]. The GOx modified SWNT (GOx/SWNT) electrode was prepared by just dropping $5\ \mu\text{L}$ 1.0×10^{-4} M GOx solution onto the surface of the electrode surface and allowing to dry under ambient conditions. The resultant GOx/SWNT electrode was rinsed firstly with water and then the working buffer solution prior to any measurements. A pair of well-defined redox peaks was obtained for GOx with the reduction peak potential at -0.465 V and a peak potential separation of 23 mV in 0.05 M PBS. The specific enzyme activity of GOx adsorbates at SWNTs was proved to be retained by spectral methods. Based on the facilitated dispersing of CNTs in water by CTAB [77], Cai et al. fabricated a CNT-based GOx biosensor by firstly casting the mixture of CNT aqueous suspension and GOx phosphate buffer solution and fixing the resultant composite film with a Nafion coating [78]. Cyclic voltammetric results showed a pair of well-defined redox peaks, which corresponded to the direct electron transfer of GOx, with a midpoint potential of about -0.466 V (versus SCE) in the PBS (pH 6.9). The experimental results also demonstrated that the immobilized GOx retained its bioelectrocatalytic activity for the oxidation of glucose, suggesting that the electrode may find use in biosensors (e.g., it may be used as a bioanode in biofuel cells).

(ii) *Putrescine Oxidase and Xanthine Oxidase*. Besides GOx, the direct electron transfer of some other oxidases like putrescine oxidase (POx) and xanthine oxidase (XOx) was also investigated. Similar to other oxidases, POx is a rather big molecule (>200 kDa) with the redox center deeply inlaid in its structure, which reacts with biogenic amines (e.g., putrescine, cadaverine and histamine) with a certain degree of substrate specifically as follows:



Although feasible, the electrochemical measurement of H_2O_2 at positive potentials usually suffers from the serious interfer-

ences from some electroactive micromolecules like UA and AA, even for CNT electrodes. The direct electron transfer of POx at CNT electrodes was mainly accomplished by Luong et al. [256, 257]. In their earlier work, POx was immobilized on the electrode surface by the deposition of a mixture of MWNTs, PDDA, APTES, and POx on the electrode surface and the coating of the resulting electrode by a Nafion film [256]. The use of APTES permits the adsorption of GOx on CNTs. They believed that nanoscale “dendrites” of MWNTs were reasoned to form a network, projecting outward from the electrode surface acting like bundled ultramicroelectrodes, thereby permitting access to the active site and facilitating direct electron transfer to the immobilized enzyme. This was demonstrated by the appearance of a pair of redox peaks for POx with an oxidation peak near -0.45 V and a reduction peak near -0.49 V (versus Ag|AgCl, 3 M NaCl) in 0.05 M PBS (pH 7.0). The direct electron transfer permitted the detection of putrescine at negative potentials, circumventing the interference of endogenous ascorbic and uric acids. Compared with the most common interfering species, such as spermine, spermidine, cadaverine, and histamine, a detection limit of $5\ \mu\text{M}$ and a response of 20 times greater were found for putrescine. Later, Luong et al. further fabricated a POx-based biosensor through a covalent method [85]. In that work, MWNTs were dissolved in a mixture of APTES, Nafion and ethanol with sonication to get uniformly dispersed CNTs. The resulting mixture was dropped on the electrode surface and allowed to dry. Upon the enzyme preparation, a drop of the enzyme solution was dried on the CNT/APTES modified electrode and a certain volume of GDI was dropped on the resulting electrode to cross-link the enzyme with APTES. Similar to the noncovalent immobilization method [256], POx exhibited a pair of well-defined peaks at -0.52 V (versus Ag|AgCl) in 0.05 M borate buffer (pH 8.35), providing a selective and sensitive method for putrescine determination. Similar to the immobilization of GOx on CNT electrodes [254], Wang et al. reported the noncovalent immobilization of XOx on CNT electrodes by just dropping the XOx solution onto the surface of the electrode surface and allowing to dry under ambient conditions [251]. The resulting electrodes were completely rinsed with water prior to any measurements, which exhibited a pair of well-defined redox peaks at around -0.46 V with a small peak separation of 28 mV in 0.05 M phosphate buffer (pH 7.0).

(2) *Fundamentals of Direct Electron Transfer of Redox Proteins and Enzymes at Carbon Nanotube Electrodes*. Based on the above discussions, it is clear that CNT electrodes can effectively facilitate the direct electron transfer of various redox proteins and enzymes. However, few works gain insights into the fundamental information of this important process. Guiseppi-Elie et al. studied the direct electron transfer between SWNTs and the redox center of adsorbed GOx [260]. It was found that both FAD and GOx spontaneously adsorbed to annealed CNTs and displayed quasi-reversible one-electron transfer. They believed that the nanotubes become positioned within a tunneling distance of the

cofactors with little consequence to denaturation. Willner's group proposed an approach for the covalent attachment of reconstituted GOx on the end of aligned SWNTs [261]. The electrons were transported along distances higher than 150 nm and the transport rate was controlled by the nanotube length, interfacial electron transfer rate constants for 50 and 100 nm SWNTs were 42 and 19 s⁻¹, respectively. Such plugging of CNTs into enzymes was also reported by Gooding et al. by two different ways [152]. In the first method, native GOx was covalently attached to the ends of the aligned tubes, which allowed close approach to FAD and direct electron transfer to be observed with a rate constant of 0.3 s⁻¹. The second strategy was similar to the method proposed by Willner et al. [261], that is, FAD was attached to the ends of the tubes and the enzyme reconstituted around the surface immobilized FAD. This latter approach allowed more efficient electron transfer to the FAD with a rate constant of 9⁻¹. The direct electron transfer of both native and reconstituted GOx at aligned CNTs demonstrated the molecular wire role of CNTs in promoting the electron transfer of redox proteins and enzymes. Rusling et al. [156] investigated the electrochemical behaviors of HRP and Mb covalently bound to the ends of SWNT forest electrodes. Their data indicated that the "trees" in the nanotube forest behaved electrically similar to a metal, conducting electrons from the external circuit to the redox sites of the enzymes. The peroxidase activity of these enzymes was demonstrated, with detection limits for hydrogen peroxide in buffer solutions of ~100 nM. The direct electron transfer of MP-11 covalently attached to aligned SWNT arrays was also examined by Gooding et al. [150]. It was found that although the enzyme also adsorbed along the hydrophobic walls of the nanotubes, the majority of the electron transfer was dominated by proteins immobilized on the electroactive ends of the nanotubes, which further supported the excellent electrochemical properties of the ends of the nanotubes. In addition, despite different distributions of tube lengths, the rate constants for heterogeneous electron transfer to the enzyme were essentially the same, demonstrating the efficiency of the shortened nanotubes as molecular wires. Jiang et al. recently studied the electrochemical redox processes of Cyt c at a SWNT modified electrode by in situ UV-vis and circular dichroism (CD) spectroelectrochemistry [39]. It was found that SWNTs can effectively decrease the effect of electric field on the configurational changes of Cyt c and stabilize the Met80-Fe bond of adsorbed Cyt c, and that electron transfer induced a more opening configurational change at SWNT/GCE than that at the bare electrode, which might be responsible for the direct electron transfer of enzymes on CNT electrodes and the retaining of their biocatalytic activity. The CNT-induced configurational change of enzymes has been verified by Gooding et al. [262]. Rate constants for direct electron transfer to GOx at CNT-modified electrodes and graphite electrodes suggest that the enzyme was partially denatured from its native configuration, thus bringing the redox-active center of the enzyme closer to the electrode and allowing appreciable electron transfer.

4.3. Carbon Nanotube-Based DNA Electrochemical Sensors. Sequence-specific DNA detection has been a topic of significant interest due to its promising application in the diagnosis of pathogenic and genetic diseases. Electrochemical DNA biosensors are currently receiving considerable attention because of their high sensitivity, portability, low-cost and rapid response. Such devices rely on the conversion of the nucleic acid recognition processes into a useful electrical signal. Similar to other electrochemical sensors, the DNA electrochemical sensors benefit much from the use of CNTs based on the enhanced oxidation of the oxidable bases, the improved responses of the indicators or the excellent properties of CNTs as the carrier platforms.

Fang's group has reported several CNT-based DNA electrochemical sensors for the determination of sequence-specific DNA over the last few years [188, 263–265]. In an earlier work, they developed a novel and sensitive electrochemical DNA biosensor based on MWNTs functionalized with carboxylic acid groups for the covalent DNA immobilization and the enhanced hybridization detection [263]. The MWNT modified GCE was fabricated from a simple casting method and oligonucleotides with the 5'-amino group were covalently bonded to the carboxyl groups of CNTs with the aid of EDC. The hybridization process on the electrode was monitored by DPV analysis using an electroactive intercalator daunomycin (DNR) as an indicator. The sensitive response of DNR at CNT electrode led to a significant increase of the hybridization signal of DNA compared to DNA sensors with oligonucleotides directly incorporated on carbon electrodes. Similar improved hybridization responses of DNA covalently immobilized on CNT electrodes were also observed by Wang et al. [266] and Kerman et al. [267] using MB and Escherichia coli single-strand binding protein (SSB) as the indicators, respectively. Wang et al. proposed an effective method for amplifying electrical detection of DNA hybridization based on CNTs carrying a large number of CdS particle tracers [268]. Such use of CNT amplification platforms was combined with an ultrasensitive stripping voltammetric detection of the dissolved CdS tags following dual hybridization events of a sandwich assay on a streptavidin modified 96-well microplate. Fang et al. also reported a new indicator free biosensing strategy for direct electrochemical detection of DNA hybridization by AC impedance measurement [264]. They firstly immobilized the oligonucleotide probes on a MWNT modified GCE through the entrapping of DNA as the sole counter anion during the electropolymerization growth of the PPy films. Before and after hybridization reaction with the complementary DNA sequences, a decrease of impedance values was observed as a result of the reduction of the electrode resistance. Hybridization amounts of the one-base, two-base and three-base mismatched sequences were obtained only in a 51%, 18% and 8.2% response when compared to that for the complementary matched sequence. Such unique response was attributed to the concomitant conductivity changes of the PPy-polymerized CNTs, and offered great promise for reagentless DNA hybridization analysis. Later, they further improved this method by adding zinc ions (Zn²⁺) to the hybridization solution, resulting in the formation of

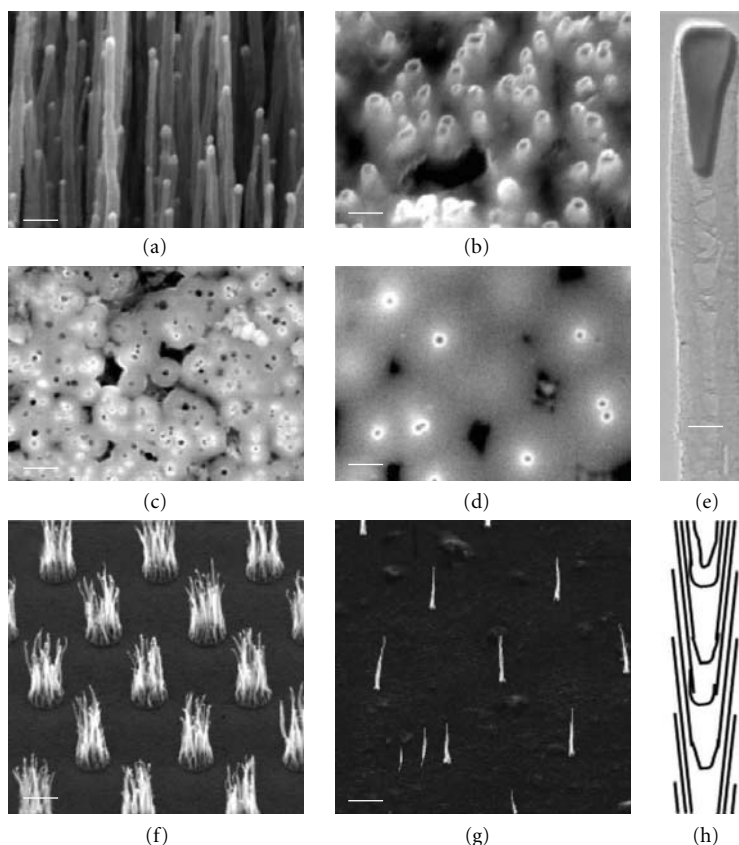


FIGURE 15: SEM images of (a) an as-grown MWCNT array, (b) the surface of a polished MWCNT array embedded in an SiO₂ matrix, (c) a high-density MWCNT nanoelectrode array (hd, $\sim 2 \times 10^9$ electrodes cm⁻²), (d) a low-density one (ld-1, $\sim 7 \times 10^7$ electrodes cm⁻²), (f) an as-grown MWCNT array on 2 nm Ni spots patterned with UV lithography, and (g) an as-grown MWCNT array on ~ 100 nm diameter Ni spots patterned with e-beam lithography, and (h) a schematic of the defective bamboo-like structure. (a), (b), (f), and (g) are 45° uperspective views while (c) and (d) are top views. (e) is the TEM view of a single MWCNT. The scale bars in (a)–(g) are 500 nm, 200 nm, 500 nm, 500 nm, 50 nm, 2 μ m, and 5 μ m, respectively. [Reprinted with permission from Koehne et al. [206], *J. Mater. Chem.*, **14**, 676 (2004). Copyright 2003, Royal Society of Chemistry.]

metallized double-stranded DNA (M-DNA) that can significantly change the electrochemical impedance response [265]. Recently, Fang et al. reported a new sensitive electrochemical biosensor based on magnetite nanoparticles for monitoring DNA hybridization by using MWNT/PPy-modified glassy carbon electrode [188]. In such detection system, mercaptoacetic acid (RSH)-coated magnetite nanoparticles, capped with 5'-(NH₂) oligonucleotide, were used as DNA probe to complex a 29-base polynucleotide target (a piece of human porphobilinogen deaminase PBGD promoter from 170 to 142). Target sequence hybridized with the probe resulted in the decrease of the reduction peak current of DNR connected with probe. As mentioned above, Meyyappan et al. reported a novel approach for the fabrication of nanoelectrode arrays using vertically aligned MWNTs embedded within a SiO₂ matrix [205, 206] (Figure 15). Based on the a low background and a small cell time constant of these nanoelectrodes, they prepared a highly sensitive DNA sensors by covalently attaching the DNA probes on the ends of the CNTs and monitoring the electrochemical response of Ru(bpy)₃²⁺ mediator amplified guanine oxidation.

Wu et al. studied the electrochemical behaviors of DNA, guanine and adenine at a MWNT-DHP composite film-modified electrode (MWNT-DHP/GCE) [95]. Compared with the undiscerned responses at the bare electrode, adenine and guanine exhibited a sensitive oxidation peak at 0.73 and 1.02 V on MWNT-DHP/GCE in 0.1 M PBS (pH 7.0), respectively. The responses were also observed for the hydrolyzed product of calf thymus DNA, providing a simple but sensitive method for DNA measurement. The enhanced oxidation of guanine and adenine residues in DNA was also observed by Wang et al. at a SWNT modified GCE [269]. On the basis of the enhanced oxidation of guanine on pretreated CNTPEs, Pedano et al. recently proposed an adsorptive stripping potentiometric method for the measurement of nucleic acids [164]. Trace (μ g/L) levels of the oligonucleotides and polynucleotides can be readily detected following short accumulation periods with detection limits of 2.0 μ g/L for a 21-base oligonucleotide and 170 μ g/L for calf thymus dsDNA. The interaction between nucleic acids and CNTPE was demonstrated to be mainly hydrophobic.

Besides the application in DNA detection, CNTs were also used as the carrier platforms of DNA by several workers. Guo et al. examined the electrochemical characteristics of the covalent immobilization of calf thymus DNA molecules on MWNTs by EDC [45]. By studying the CV and the electrochemical impedance spectroscopy (EIS) of $\text{Fe}(\text{CN})_6^{3-}/\text{Fe}(\text{CN})_6^{4-}$, they found that most of calf thymus DNA are covalently immobilized on MWNTs via diimide-activated amidation between the carboxylic acid groups on CNTs and the amino groups on DNA bases, though the direct adsorption of the DNA molecules on MWNTs can be also observed. The studies on the interaction between DNA molecules and small biomolecules ethidium bromide (EB) implied that DNA molecules immobilized at the surface of MWNTs still had the ability to interact with small biomolecules. Based on the strong adsorption of PDDA on CNTs, Guo et al. also proposed an LBL method for the immobilization of DNA on the electrode surface and monitored the electrostatic assembly of DNA on PDDA modified CNTs by the piezoelectric quartz crystal impedance (PQCI) technique [44]. It was found that PDDA played a key role in the attachment of DNA to MWNTs and acted as a bridge to connect DNA with MWNTs, though the direct adsorption of DNA on MWNTs has been observed. Recently, He et al. introduced a new fabrication of DNA-CNT particles using the LBL technique on SWNTs [147]. PDDA, a positively charged polyelectrolyte, and DNA as a negatively charged counterpart macromolecule were alternatively deposited on the water-soluble oxidized SWNTs. Pure DNA/PDDA/SWNT particles can be prepared and separated by simple ultracentrifugation. An electrode modified by the DNA/PDDA/SWNT particles shows a dramatic change of the electrochemical signal in solutions of $\text{Ru}(\text{bpy})_3^{2+}$ as a reporting redox probe. A preliminary application of the DNA-modified carbon nanotubes in the development of DNA sensors used in the investigation of DNA damage by nitric oxide was presented.

5. Conclusions and Perspectives

As a new type of carbonaceous materials, carbon nanotubes (CNTs) possess some unique properties that are much different from either the conventional scaled materials or other types of nanoparticles, such as the special and well-defined tubular structure of nanosizes, the excellent chemical stability, the modifiable surface and the strong electrocatalytic activity. These special properties foresee their promising applications in electroanalytical chemistry for constructing CNT-based sensors. The fact is that the modification of electrodes with CNTs has been observed to apparently improve the responses of substrates from small H_2O_2 molecules to huge redox proteins. Most of current works mainly focused on the fabrication of randomly dispersed CNT-based electrochemical sensors and few reports deal with the fabrications of well organized nanostructures of CNTs. As a tubular nanomaterials, the key advantages of CNTs are their small diameter and huge length to diameter ratio that allows them to be used as molecular wires for facilitating electron

transfer between proteins and electrodes or to be organized in a low density manner for using as a single nanoelectrode or nanoelectrode arrays with ultrasensitivity. Since the direct growth by CVD methods inevitably suffers from the need of rigorous conditions, development of simple physical or chemical immobilization methods that can control the orientation of CNTs on electrode surfaces has become a matter of great urgency.

Abbreviations

AA:	Ascorbic acid
AChE:	Acetylcholinesterase
ADH:	Alcohol-dehydrogenase
o-AP:	o-aminophenol
APTES:	3-aminopropyltriethoxy-silane
ARS:	3,4-dihydroxy-9,10-dioxo-2-anthracenesulfonic acid, sodium salt
ASV:	Anodic stripping voltammetry
ATCh:	Acetylthiocholine
[bmim]PF ₆ :	1-butyl-3-methylimidazolium hexafluorophosphate
Bppg:	Basal-plane pyrolytic graphite
CCNNEs:	Ceramic-carbon nanotubes nanocomposite electrodes
CDs:	Cyclodextrins
CE:	Capillary electrophoresis
CFNE:	Carbon fiber nanoelectrode
CHIT:	Chitosan
ChOx:	Cholesterol oxidase
CNTPEs:	Carbon nanotube paste electrodes
CNTPMEs:	Carbon nanotube powder microelectrodes
CNTs:	Carbon nanotubes
CNT-IE:	Carbon nanotubes-intercalated graphite electrode
CoTMPyP:	[tetrakis(N-methylpyridyl)porphyrinato] cobalt
CP:	Carbon paste
CPEs:	Carbon paste electrodes
Ct:	Catalase
CTAB:	Cetyltrimethylammonium bromide
CV:	Cyclic voltammetry
CVD:	Chemical vapour deposition
CySH:	Cysteine
Cyt c:	Cytochrome c
Da:	Dalton
DA:	Dopamine
DAB:	Diaminobenzidine
DCC:	Dicyclohexyl carbodiimide
DET:	Direct electron transfer
DHB:	Dihydroxybenzaldehyde
DHP:	Dihexadecyl hydrogen phosphate
DL:	Detection limit
DMF:	N,N-dimethylformamide
dsDNA:	Double-strand DNA
ssDNA:	Single-strand DNA
DNR:	Daunomycin
DPV:	Differential pulse voltammetry

E° :	Formal potential
EB:	Ethidium bromide
ECD:	Electrochemical detection
EDC:	1-ethyl-3-(3-dimethylaminopropyl)carbodiimide
EIS:	Electrochemical impedance spectroscopy
ΔE_p :	Redox peak separation
EP:	Epinephrine
ESEM:	Environmental scanning electron microscopy
ET:	Electron transfer
FAD:	Flavin adenine dinucleotide
Fc-SWNTs:	Ferrocenyl-derivatised SWNTs
FDH:	D-fructose dehydrogenase
FePc:	Iron-phthalocyanine
FIA:	Flow injection analysis
GCE:	Glassy carbon electrode
GDH:	Glucose dehydrogenase
GDI:	Glutaraldehyde
GOx:	Glucose oxidase
GSH:	Glutathione
GSSG:	Glutathione disulfide
Hb:	Hemoglobin
HcySH:	Homocysteine
HOPG:	Highly oriented pyrolytic graphite
HPLC:	High performance liquid chromatography
HRP:	Horseradish peroxidase
5-HT:	Serotonin
IR:	Infrared spectra
LBL:	Layer-by-layer
Mb:	Myoglobin
MB:	Methylene blue
MCMB:	Mesocarbon microbeads
M-DNA:	Metallized double-stranded DNA
MWNTs:	Multiwalled carbon nanotubes
MP-11:	Microperoxidase
NAD ⁺ :	β -nicotinamide adenine dinucleotide
NADH:	Reduced β -nicotinamide adenine dinucleotide
NE:	Norepinephrine
NEAs:	Nanoelectrode arrays
NMP:	N-methyl-2-pyrrolidone
NSA:	N-succinimidyl acrylate
OCNTs:	Ordered carbon nanotubes
OMIMPF ₆ :	1-octyl-3-methyl imidazolium hexafluorophosphate
OP:	Organophosphorus
PABS:	Poly(aminobenzenesulfonic acid)
PA-FTIR:	Photoacoustic Fourier transform infrared
PANT:	Polyaniline
PB:	Prussian blue
PBS:	Phosphate buffer solution
PDAB:	Poly(3,3'-diaminobenzidine)
PDDA:	Poly(diallyl dimethyl ammonium) chloride
PG:	Pyrolytic graphite
PMEs:	Powder microelectrodes
Pox:	Putrescine oxidase
PPD:	Poly(o-phenylenediamine)
PPy:	Polypyrrole
PQCI:	Piezoelectric quartz crystal impedance

RTILs:	Room-temperature ionic liquids
RSH:	Mercaptoacetic acid
SAMs:	Self-assembled monolayers
SCE:	Saturated calomel electrode
SDS:	Sodium dodecyl sulphate
SEM:	Scanning electron microscopy
S/N:	Signal-to-noise ratio
SSB:	Escherichia coli single-strand binding protein
sulfo-NHS:	N-hydroxysulfo-succinimide
SWNTs:	Single-walled carbon nanotubes
TBO:	Toluidine Blue O
TEM:	Transmission electron microscopy
TGA:	Thermogravimetric analysis
TM-AFM:	Tapping-mode atomic force microscopy
TPP:	Tetra-phenyl-porphyrin
UA:	Uric acid
Xa:	Xanthine
XOx:	Xanthine oxidase
XPS:	X-ray photoelectron spectroscopy

Acknowledgment

The research is supported by the National Natural Science Foundation of China (Nos. 30770549, 20805035, and 90817103).

References

- [1] P. J. Britto, K. S. V. Santhanam, and P. M. Ajayan, "Carbon nanotube electrode for oxidation of dopamine," *Bioelectrochemistry and Bioenergetics*, vol. 41, no. 1, pp. 121–125, 1996.
- [2] Q. Zhao, Z. Gan, and Q. Zhuang, "Electrochemical sensors based on carbon nanotubes," *Electroanalysis*, vol. 14, no. 23, pp. 1609–1613, 2002.
- [3] N. Li, J. Wang, and M. Li, "Electrochemistry at carbon nanotube electrodes," *Reviews in Analytical Chemistry*, vol. 22, no. 1, pp. 19–33, 2003.
- [4] J. Li, J. E. Koehne, A. M. Cassell, et al., "Inlaid multi-walled carbon nanotube nanoelectrode arrays for electroanalysis," *Electroanalysis*, vol. 17, no. 1, pp. 15–27, 2005.
- [5] J. Wang, "Carbon-nanotube based electrochemical biosensors: a review," *Electroanalysis*, vol. 17, no. 1, pp. 7–14, 2005.
- [6] J. J. Gooding, "Nanostructuring electrodes with carbon nanotubes: a review on electrochemistry and applications for sensing," *Electrochimica Acta*, vol. 50, no. 15, pp. 3049–3060, 2005.
- [7] R. L. McCreery, "Carbon electrodes: structural effects on electron transfer kinetics," in *Electroanalytical Chemistry*, vol. 17, pp. 221–374, Marcel Dekker, New York, NY, USA, 1991.
- [8] J. Li, A. Cassell, L. Delzeit, J. Han, and M. Meyyappan, "Novel three-dimensional electrodes: electrochemical properties of carbon nanotube ensembles," *The Journal of Physical Chemistry B*, vol. 106, no. 36, pp. 9299–9305, 2002.
- [9] J. M. Nugent, K. S. V. Santhanam, A. Rubio, and P. M. Ajayan, "Fast electron transfer kinetics on multiwalled carbon nanotube microbundle electrodes," *Nano Letters*, vol. 1, no. 2, pp. 87–91, 2001.
- [10] P. Papakonstantinou, R. Kern, J. Irvine, E. McAdams, J. McLaughlin, and T. McNally, "Fundamental electrochemical properties of carbon nanotube electrodes," *Fullerenes Nanotubes and Carbon Nanostructures*, vol. 13, supplement 1, pp. 275–285, 2005.

- [11] C. E. Banks, R. R. Moore, T. J. Davies, and R. G. Compton, "Investigation of modified basal plane pyrolytic graphite electrodes: definitive evidence for the electrocatalytic properties of the ends of carbon nanotubes," *Chemical Communications*, no. 6, pp. 1804–1805, 2004.
- [12] R. R. Moore, C. E. Banks, and R. G. Compton, "Basal plane pyrolytic graphite modified electrodes: comparison of carbon nanotubes and graphite powder as electrocatalysts," *Analytical Chemistry*, vol. 76, no. 10, pp. 2677–2682, 2004.
- [13] C. E. Banks, T. J. Davies, G. G. Wildgoose, and R. G. Compton, "Electrocatalysis at graphite and carbon nanotube modified electrodes: edge-plane sites and tube ends are the reactive sites," *Chemical Communications*, no. 7, pp. 829–841, 2005.
- [14] A. Chou, T. Bocking, N. K. Singh, and J. J. Gooding, "Demonstration of the importance of oxygenated species at the ends of carbon nanotubes for their favourable electrochemical properties," *Chemical Communications*, vol. 7, pp. 842–844, 2005.
- [15] B. Šljukić, C. E. Banks, and R. G. Compton, "Iron oxide particles are the active sites for hydrogen peroxide sensing at multiwalled carbon nanotube modified electrodes," *Nano Letters*, vol. 6, no. 7, pp. 1556–1558, 2006.
- [16] H. Luo, Z. Shi, N. Li, Z. Gu, and Q. Zhuang, "Investigation of the electrochemical and electrocatalytic behavior of single-wall carbon nanotube film on a glassy carbon electrode," *Analytical Chemistry*, vol. 73, no. 5, pp. 915–920, 2001.
- [17] C. Hu and S. Hu, "Surface design of carbon nanotubes for optimizing the adsorption and electrochemical response of analytes," *Langmuir*, vol. 24, no. 16, pp. 8890–8897, 2008.
- [18] A. Kuznetsova, D. B. Mawhinney, V. Naumenko, J. T. Yates Jr., J. Liu, and R. E. Smalley, "Enhancement of adsorption inside of single-walled nanotubes: opening the entry ports," *Chemical Physics Letters*, vol. 321, no. 3-4, pp. 292–296, 2000.
- [19] J. Liu, A. G. Rinzler, H. Dai, et al., "Fullerene pipes," *Science*, vol. 280, no. 5367, pp. 1253–1256, 1998.
- [20] H. Hu, P. Bhowmik, B. Zhao, M. A. Hamon, M. E. Itkis, and R. C. Haddon, "Determination of the acidic sites of purified single-walled carbon nanotubes by acid-base titration," *Chemical Physics Letters*, vol. 345, no. 1-2, pp. 25–28, 2001.
- [21] D. B. Mawhinney, V. Naumenko, A. Kuznetsova, J. T. Yates Jr., J. Liu, and R. E. Smalley, "Surface defect site density on single walled carbon nanotubes by titration," *Chemical Physics Letters*, vol. 324, no. 1–3, pp. 213–216, 2000.
- [22] C. Bower, A. Kleinhammes, Y. Wu, and O. Zhou, "Intercalation and partial exfoliation of single-walled carbon nanotubes by nitric acid," *Chemical Physics Letters*, vol. 288, no. 2–4, pp. 481–486, 1998.
- [23] A. Kukovec, Ch. Kramberger, M. Holzinger, et al., "On the stacking behavior of functionalized single-wall carbon nanotubes," *The Journal of Physical Chemistry B*, vol. 106, no. 25, pp. 6374–6380, 2002.
- [24] M. T. Martínez, M. A. Callejas, A. M. Benito, et al., "Modifications of single-wall carbon nanotubes upon oxidative purification treatments," *Nanotechnology*, vol. 14, no. 7, pp. 691–695, 2003.
- [25] J. N. Barisci, G. G. Wallace, D. Chattopadhyay, F. Papadimitrakopoulos, and R. H. Baughman, "Electrochemical properties of single-wall carbon nanotube electrodes," *Journal of the Electrochemical Society*, vol. 150, no. 9, pp. E409–E415, 2003.
- [26] J. N. Barisci, G. G. Wallace, and R. H. Baughman, "Electrochemical studies of single-wall carbon nanotubes in aqueous solutions," *Journal of Electroanalytical Chemistry*, vol. 488, no. 2, pp. 92–98, 2000.
- [27] M. Musameh, N. S. Lawrence, and J. Wang, "Electrochemical activation of carbon nanotubes," *Electrochemistry Communications*, vol. 7, no. 1, pp. 14–18, 2005.
- [28] Y. Lin, F. Lu, Y. Tu, and Z. Ren, "Glucose biosensors based on carbon nanotube nanoelectrode ensembles," *Nano Letters*, vol. 4, no. 2, pp. 191–195, 2004.
- [29] K. Yamamoto, G. Shi, T. Zhou, et al., "Study of carbon nanotubes-HRP modified electrode and its application for novel on-line biosensors," *Analyst*, vol. 128, no. 3, pp. 249–254, 2003.
- [30] X.-X. Yan, D.-W. Pang, Z.-X. Lu, J.-Q. Lü, and H. Tong, "Electrochemical behavior of L-dopa at single-wall carbon nanotube-modified glassy carbon electrodes," *Journal of Electroanalytical Chemistry*, vol. 569, no. 1, pp. 47–52, 2004.
- [31] Z. Xu, X. Chen, X. Qu, J. Jia, and S. Dong, "Single-wall carbon nanotube-based voltammetric sensor and biosensor," *Biosensors and Bioelectronics*, vol. 20, no. 3, pp. 579–584, 2004.
- [32] Q. Zhao, Z.-N. Gu, and Q.-K. Zhuang, "Electrochemical study of tetra-phenyl-porphyrin on the SWNTs film modified glassy carbon electrode," *Electrochemistry Communications*, vol. 6, no. 1, pp. 83–86, 2004.
- [33] J. Wang, S. B. Hocevar, and B. Ogorevc, "Carbon nanotube-modified glassy carbon electrode for adsorptive stripping voltammetric detection of ultratrace levels of 2,4,6-trinitrotoluene," *Electrochemistry Communications*, vol. 6, no. 2, pp. 176–179, 2004.
- [34] L. Wang, J. Wang, and F. Zhou, "Direct electrochemistry of catalase at a gold electrode modified with single-wall carbon nanotubes," *Electroanalysis*, vol. 16, no. 8, pp. 627–632, 2004.
- [35] Z.-H. Gan, Q. Zhao, Z.-N. Gu, and Q.-K. Zhuang, "Electrochemical studies of single-wall carbon nanotubes as nanometer-sized activators in enzyme-catalyzed reaction," *Analytica Chimica Acta*, vol. 511, no. 2, pp. 239–247, 2004.
- [36] N. S. Lawrence, R. P. Deo, and J. Wang, "Electrochemical determination of hydrogen sulfide at carbon nanotube modified electrodes," *Analytica Chimica Acta*, vol. 517, no. 1-2, pp. 131–137, 2004.
- [37] Y.-P. Ding, W.-L. Liu, Q.-S. Wu, and X.-G. Wang, "Direct simultaneous determination of dihydroxybenzene isomers at C-nanotube-modified electrodes by derivative voltammetry," *Journal of Electroanalytical Chemistry*, vol. 575, no. 2, pp. 275–280, 2005.
- [38] L. Jiang, R. Wang, X. Li, L. Jiang, and G. Lu, "Electrochemical oxidation behavior of nitrite on a chitosan-carboxylated multiwall carbon nanotube modified electrode," *Electrochemistry Communications*, vol. 7, no. 6, pp. 597–601, 2005.
- [39] X. Jiang, Z. Zhang, H. Bai, et al., "Effect of electrode surface microstructure on electron transfer induced conformation changes in cytochrome c monitored by in situ UV and CD spectroelectrochemistry," *Spectrochimica Acta Part A*, vol. 61, no. 5, pp. 943–951, 2005.
- [40] Q. Zhao, L. Guan, Z. Gu, and Q. Zhuang, "Determination of phenolic compounds based on the tyrosinase-single walled carbon nanotubes sensor," *Electroanalysis*, vol. 17, no. 1, pp. 85–88, 2005.
- [41] K. A. Joshi, J. Tang, R. Haddon, J. Wang, W. Chen, and A. Mulchandani, "A disposable biosensor for organophosphorus nerve agents based on carbon nanotubes modified thick

- film strip electrode," *Electroanalysis*, vol. 17, no. 1, pp. 54–58, 2005.
- [42] W. Zhang, F. Wan, W. Zhu, et al., "Determination of glutathione and glutathione disulfide in hepatocytes by liquid chromatography with an electrode modified with functionalized carbon nanotubes," *Journal of Chromatography B*, vol. 818, no. 2, pp. 227–232, 2005.
- [43] G. Wang, J.-J. Xu, and H.-Y. Chen, "Interfacing cytochrome *c* to electrodes with a DNA-carbon nanotube composite film," *Electrochemistry Communications*, vol. 4, no. 6, pp. 506–509, 2002.
- [44] M. Guo, J. Chen, L. Nie, and S. Yao, "Electrostatic assembly of calf thymus DNA on multi-walled carbon nanotube modified gold electrode and its interaction with chlorpromazine hydrochloride," *Electrochimica Acta*, vol. 49, no. 16, pp. 2637–2643, 2004.
- [45] M. Guo, J. Chen, D. Liu, L. Nie, and S. Yao, "Electrochemical characteristics of the immobilization of calf thymus DNA molecules on multi-walled carbon nanotubes," *Bioelectrochemistry*, vol. 62, no. 1, pp. 29–35, 2004.
- [46] J. Chen and C. X. Cai, "Promotion of the direct electron transfer of hemoglobin by the carbon nanotube," *Chinese Chemical Letters*, vol. 15, no. 7, pp. 813–816, 2004.
- [47] Y. Zhang, Y. Wen, Y. Liu, D. Li, and J. Li, "Functionalization of single-walled carbon nanotubes with Prussian blue," *Electrochemistry Communications*, vol. 6, no. 11, pp. 1180–1184, 2004.
- [48] M. Guo, J. Chen, J. Li, B. Tao, and S. Yao, "Fabrication of polyaniline/carbon nanotube composite modified electrode and its electrocatalytic property to the reduction of nitrite," *Analytica Chimica Acta*, vol. 532, no. 1, pp. 71–77, 2005.
- [49] F.-H. Wu, G.-C. Zhao, and X.-W. Wei, "Electrocatalytic oxidation of nitric oxide at multi-walled carbon nanotubes modified electrode," *Electrochemistry Communications*, vol. 4, no. 9, pp. 690–694, 2002.
- [50] G.-C. Zhao, L. Zhang, X.-W. Wei, and Z.-S. Yang, "Myoglobin on multi-walled carbon nanotubes modified electrode: direct electrochemistry and electrocatalysis," *Electrochemistry Communications*, vol. 5, no. 9, pp. 825–829, 2003.
- [51] F.-H. Wu, G.-C. Zhao, X.-W. Wei, and Z.-S. Yang, "Electrocatalysis of tryptophan at multi-walled carbon nanotube modified electrode," *Microchimica Acta*, vol. 144, no. 4, pp. 243–247, 2004.
- [52] G.-C. Zhao, L. Zhang, and X.-W. Wei, "An unmediated H₂O₂ biosensor based on the enzyme-like activity of myoglobin on multi-walled carbon nanotubes," *Analytical Biochemistry*, vol. 329, no. 1, pp. 160–161, 2004.
- [53] G.-C. Zhao, Z.-Z. Yin, L. Zhang, and X.-W. Wei, "Direct electrochemistry of cytochrome *c* on a multi-walled carbon nanotubes modified electrode and its electrocatalytic activity for the reduction of H₂O₂," *Electrochemistry Communications*, vol. 7, no. 3, pp. 256–260, 2005.
- [54] C. Hu, W. L. Wang, S. X. Wang, W. Zhu, and Y. Li, "Investigation on electrochemical properties of carbon nanotubes," *Diamond and Related Materials*, vol. 12, no. 8, pp. 1295–1299, 2003.
- [55] J. Qu, Y. Shen, X. Qu, and S. Dong, "Preparation of hybrid thin film modified carbon nanotubes on glassy carbon electrode and its electrocatalysis for oxygen reduction," *Chemical Communications*, no. 1, pp. 34–35, 2004.
- [56] N. Jia, L. Wang, L. Liu, Q. Zhou, and Z. Jiang, "Bamboo-like CN_x nanotubes for the immobilization of hemoglobin and its bioelectrochemistry," *Electrochemistry Communications*, vol. 7, no. 4, pp. 349–354, 2005.
- [57] S. Lefrant, M. Baibarac, I. Baltog, J. Y. Mevellec, L. Mihut, and O. Chauvet, "SERS spectroscopy studies on the electrochemical oxidation of single-walled carbon nanotubes in sulfuric acid solutions," *Synthetic Metals*, vol. 144, no. 2, pp. 133–142, 2004.
- [58] S. H. Lim, J. Wei, J. Lin, Q. Li, and J. KuaYou, "A glucose biosensor based on electrodeposition of palladium nanoparticles and glucose oxidase onto Nafion-solubilized carbon nanotube electrode," *Biosensors and Bioelectronics*, vol. 20, no. 11, pp. 2341–2346, 2005.
- [59] C. A. Furtado, U. J. Kim, H. R. Gutierrez, L. Pan, E. C. Dickey, and P. C. Eklund, "Debundling and dissolution of single-walled carbon nanotubes in amide solvents," *Journal of the American Chemical Society*, vol. 126, no. 19, pp. 6095–6105, 2004.
- [60] G. Fortier, M. Vaillancourt, and D. Bélanger, "Evaluation of nafion as media for glucose oxidase immobilization for the development of an amperometric glucose biosensor," *Electroanalysis*, vol. 4, no. 3, pp. 275–283, 1992.
- [61] Z. Fan and D. J. Harrison, "Permeability of glucose and other neutral species through recast perfluorosulfonated ionomer films," *Analytical Chemistry*, vol. 64, no. 11, pp. 1304–1310, 1992.
- [62] Y. Y. Sun, K. B. Wu, and S. Hu, "Selective determination of dopamine in the presence of high concentration ascorbic acid and uric acid using carbon nanotube modified glassy carbon electrode," *Chemical Journal of Chinese Universities*, vol. 23, no. 11, pp. 2067–2069, 2002.
- [63] J. Wang, M. Musameh, and Y. Lin, "Solubilization of carbon nanotubes by Nafion toward the preparation of amperometric biosensors," *Journal of the American Chemical Society*, vol. 125, no. 9, pp. 2408–2409, 2003.
- [64] K. Wu and S. Hu, "Electrochemical study and selective determination of dopamine at a multi-wall carbon nanotube-nafion film coated glassy carbon electrode," *Microchimica Acta*, vol. 144, no. 1–3, pp. 131–137, 2004.
- [65] S. B. Hočevar, J. Wang, R. P. Deo, M. Musameh, and B. Ogorevc, "Carbon nanotube modified microelectrode for enhanced voltammetric detection of dopamine in the presence of ascorbate," *Electroanalysis*, vol. 17, no. 5–6, pp. 417–422, 2005.
- [66] W. Huang, C. Yang, and S. Zhang, "Simultaneous determination of 2-nitrophenol and 4-nitrophenol based on the multi-wall carbon nanotubes Nafion-modified electrode," *Analytical and Bioanalytical Chemistry*, vol. 375, no. 5, pp. 703–707, 2003.
- [67] W. Huang, W. Hu, and J. Song, "Adsorptive stripping voltammetric determination of 4-aminophenol at a single-wall carbon nanotubes film coated electrode," *Talanta*, vol. 61, no. 3, pp. 411–416, 2003.
- [68] Y.-C. Tsai, J.-M. Chen, S.-C. Li, and F. Marken, "Electroanalytical thin film electrodes based on a NafionTM—multi-walled carbon nanotube composite," *Electrochemistry Communications*, vol. 6, no. 9, pp. 917–922, 2004.
- [69] R. P. Deo and J. Wang, "Electrochemical detection of carbohydrates at carbon-nanotube modified glassy-carbon electrodes," *Electrochemistry Communications*, vol. 6, no. 3, pp. 284–287, 2004.
- [70] K. Gong, Y. Dong, S. Xiong, Y. Chen, and L. Mao, "Novel electrochemical method for sensitive determination of homocysteine with carbon nanotube-based electrodes," *Biosensors and Bioelectronics*, vol. 20, no. 2, pp. 253–259, 2004.

- [71] Y.-C. Tsai, S.-C. Li, and J.-M. Chen, "Cast thin film biosensor design based on a nafion backbone, a multiwalled carbon nanotube conduit, and a glucose oxidase function," *Langmuir*, vol. 21, no. 8, pp. 3653–3658, 2005.
- [72] K. B. Male, S. Hrapovic, Y. Liu, D. Wang, and J. H. T. Luong, "Electrochemical detection of carbohydrates using copper nanoparticles and carbon nanotubes," *Analytica Chimica Acta*, vol. 516, no. 1-2, pp. 35–41, 2004.
- [73] S. Hrapovic, Y. Liu, K. B. Male, and J. H. T. Luong, "Electrochemical biosensing platforms using platinum nanoparticles and carbon nanotubes," *Analytical Chemistry*, vol. 76, no. 4, pp. 1083–1088, 2004.
- [74] R. P. Deo, N. S. Lawrence, and J. Wang, "Electrochemical detection of amino acids at carbon nanotube and nickel-carbon nanotube modified electrodes," *Analyst*, vol. 129, no. 11, pp. 1076–1081, 2004.
- [75] T. Abatemarco, J. Stickel, J. Belfort, B. P. Frank, P. M. Ajayan, and G. Belfort, "Fractionation of multiwalled carbon nanotubes by cascade membrane microfiltration," *Journal of Physical Chemistry B*, vol. 103, no. 18, pp. 3534–3538, 1999.
- [76] R.-S. Chen, W.-H. Huang, H. Tong, Z.-L. Wang, and J.-K. Cheng, "Carbon fiber nanoelectrodes modified by single-walled carbon nanotubes," *Analytical Chemistry*, vol. 75, no. 22, pp. 6341–6345, 2003.
- [77] C. Cai and J. Chen, "Direct electron transfer and biocatalysis of hemoglobin at a carbon nanotube electrode," *Analytical Biochemistry*, vol. 325, no. 2, pp. 285–292, 2004.
- [78] C. Cai and J. Chen, "Direct electron transfer of glucose oxidase promoted by carbon nanotubes," *Analytical Biochemistry*, vol. 332, no. 1, pp. 75–83, 2004.
- [79] Y. Sun, J. Fei, K. Wu, and S. Hu, "Simultaneous electrochemical determination of xanthine and uric acid at a nanoparticle film electrode," *Analytical and Bioanalytical Chemistry*, vol. 375, no. 4, pp. 544–549, 2003.
- [80] K. Wu, Y. Sun, and S. Hu, "Development of an amperometric indole-3-acetic acid sensor based on carbon nanotubes film coated glassy carbon electrode," *Sensors and Actuators B*, vol. 96, no. 3, pp. 658–662, 2003.
- [81] K. Wu, X. Ji, J. Fei, and S. Hu, "The fabrication of a carbon nanotube film on a glassy carbon electrode and its application to determining thyroxine," *Nanotechnology*, vol. 15, no. 3, pp. 287–291, 2004.
- [82] F. Wang, J. Fei, and S. Hu, "The influence of cetyltrimethyl ammonium bromide on electrochemical properties of thyroxine reduction at carbon nanotubes modified electrode," *Colloids and Surfaces B*, vol. 39, no. 1-2, pp. 95–101, 2004.
- [83] S. Lü, "Electrochemical behavior and detection of daunomycin at multi-walled carbon nanotubes modified electrode," *Analytical Letters*, vol. 36, no. 12, pp. 2597–2608, 2003.
- [84] S. Lü, X. Dang, K. Wu, and S. Hu, "Electrocatalytic reduction of chloramphenicol at multiwall carbon nanotube-modified electrodes," *Journal of Nanoscience and Nanotechnology*, vol. 3, no. 5, pp. 401–405, 2003.
- [85] Y. Wu, X. Ji, and S. Hu, "Studies on electrochemical oxidation of azithromycin and its interaction with bovine serum albumin," *Bioelectrochemistry*, vol. 64, no. 1, pp. 91–97, 2004.
- [86] S. Lü, "Voltammetric determination of Tinidazole using multi-walled carbon nanotubes modified glassy carbon electrode," *Chinese Journal of Analytical Chemistry*, vol. 32, no. 3, p. 412, 2004.
- [87] S. Lü, "Electrochemical determination of 8-azaguanine in human urine at a multi-carbon nanotubes modified electrode," *Microchemical Journal*, vol. 77, no. 1, pp. 37–42, 2004.
- [88] S. Lü, K. Wu, X. Dang, and S. Hu, "Electrochemical reduction and voltammetric determination of metronidazole at a nanomaterial thin film coated glassy carbon electrode," *Talanta*, vol. 63, no. 3, pp. 653–657, 2004.
- [89] S. Lü, "Electrochemical determination of tannins using multi-wall carbon nanotubes modified glassy carbon electrode," *Russian Journal of Electrochemistry*, vol. 40, no. 7, pp. 750–754, 2004.
- [90] H. Zhang and K. Wu, "Sensitive adsorption stripping voltammetric determination of reserpine by a glassy carbon electrode modified with multi-wall carbon nanotubes," *Microchimica Acta*, vol. 149, no. 1-2, pp. 73–78, 2005.
- [91] W. Qu, H. Wang, and K. Wu, "Voltammetric determination of mitomycin c using a chemically-modified glassy carbon electrode," *Collection of Czechoslovak Chemical Communications*, vol. 70, no. 2, pp. 178–187, 2005.
- [92] H. Zhang, "Fabrication of a single-walled carbon nanotube-modified glassy carbon electrode and its application in the electrochemical determination of epirubicin," *Journal of Nanoparticle Research*, vol. 6, no. 6, pp. 665–669, 2004.
- [93] H. Zhang, C. Hu, S. Wu, and S. Hu, "Enhanced oxidation of simvastatin at a multi-walled carbon nanotubes-dihexadecyl hydrogen phosphate composite modified glassy carbon electrode and the application in determining simvastatin in pharmaceutical dosage forms," *Electroanalysis*, vol. 17, no. 9, pp. 749–754, 2005.
- [94] S. Lü, "A multi-wall carbon nanotubes-dicetyl phosphate electrode for the determination of hypoxanthine in fish," *Analytical Sciences*, vol. 19, no. 9, pp. 1309–1312, 2003.
- [95] K. Wu, J. Fei, W. Bai, and S. Hu, "Direct electrochemistry of DNA, guanine and adenine at a nanostructured film-modified electrode," *Analytical and Bioanalytical Chemistry*, vol. 376, no. 2, pp. 205–209, 2003.
- [96] K. Wu, J. Fei, and S. Hu, "Simultaneous determination of dopamine and serotonin on a glassy carbon electrode coated with a film of carbon nanotubes," *Analytical Biochemistry*, vol. 318, no. 1, pp. 100–106, 2003.
- [97] W. S. Huang, G. Mai, Y. X. Liu, C. Yang, and W. Y. Qu, "Voltammetric determination of tryptophan at a single-wall carbon nanotubes modified electrode," *Journal of Nanoscience and Nanotechnology*, vol. 4, no. 4, pp. 423–427, 2004.
- [98] S. Zhang, W. Qu, W. Huang, and Y. Wu, "Fabrication of multi-wall carbon nanotube film on glassy carbon electrode surface and the determination of tyrosine," *Journal of Nanoscience and Nanotechnology*, vol. 4, no. 5, pp. 553–557, 2004.
- [99] Y. Wang, Q. Li, and S. Hu, "A multiwall carbon nanotubes film-modified carbon fiber ultramicroelectrode for the determination of nitric oxide radical in liver mitochondria," *Bioelectrochemistry*, vol. 65, no. 2, pp. 135–142, 2005.
- [100] K. Wu, S. Hu, J. Fei, and W. Bai, "Mercury-free simultaneous determination of cadmium and lead at a glassy carbon electrode modified with multi-wall carbon nanotubes," *Analytica Chimica Acta*, vol. 489, no. 2, pp. 215–221, 2003.
- [101] H. Yi, "Anodic stripping voltammetric determination of mercury using multi-walled carbon nanotubes film coated glassy carbon electrode," *Analytical and Bioanalytical Chemistry*, vol. 377, no. 4, pp. 770–774, 2003.
- [102] L. Jiang, C. Liu, L. Jiang, Z. Peng, and G. Lu, "A chitosan-multiwall carbon nanotube modified electrode for simultaneous detection of dopamine and ascorbic acid," *Analytical Sciences*, vol. 20, no. 7, pp. 1055–1059, 2004.

- [103] M. Zhang, A. Smith, and W. Gorski, "Carbon nanotube-chitosan system for electrochemical sensing based on dehydrogenase enzymes," *Analytical Chemistry*, vol. 76, no. 17, pp. 5045–5050, 2004.
- [104] A. Star, D. W. Steurman, J. R. Heath, and J. F. Stoddart, "Starched carbon nanotubes," *Angewandte Chemie International Edition*, vol. 41, no. 14, pp. 2508–2512, 2002.
- [105] G. Lu, L. Jiang, F. Song, C. Liu, and L. Jiang, "Determination of uric acid and norepinephrine by chitosan-multiwall carbon nanotube modified electrode," *Electroanalysis*, vol. 17, no. 10, pp. 901–905, 2005.
- [106] L. Y. Jiang, C. Y. Liu, L. P. Jiang, and G. H. Lu, "A multiwall carbon nanotube-chitosan modified electrode for selective detection of dopamine in the presence of ascorbic acid," *Chinese Chemical Letters*, vol. 16, no. 2, pp. 229–232, 2005.
- [107] X. L. Luo, J. J. Xu, J. L. Wang, and H. Y. Chen, "Electrochemically deposited nanocomposite of chitosan and carbon nanotubes for biosensor application," *Chemical Communications*, no. 16, pp. 2169–2171, 2005.
- [108] Y. Liu, D.-C. Wu, W.-D. Zhang, et al., "Polyethylenimine-grafted multiwalled carbon nanotubes for secure noncovalent immobilization and efficient delivery of DNA," *Angewandte Chemie International Edition*, vol. 44, no. 30, pp. 4782–4785, 2005.
- [109] Y. Shan and L. Gao, "In situ coating carbon nanotubes with wurtzite ZnS nanocrystals," *Journal of the American Ceramic Society*, vol. 89, no. 2, pp. 759–762, 2006.
- [110] X. Hu, T. Wang, X. Qu, and S. Dong, "In situ synthesis and characterization of multiwalled carbon nanotube/Au nanoparticle composite materials," *The Journal of Physical Chemistry B*, vol. 110, no. 2, pp. 853–857, 2006.
- [111] X. Hu, T. Wang, L. Wang, S. Guo, and S. Dong, "A general route to prepare one- and three-dimensional carbon nanotube/metal nanoparticle composite nanostructures," *Langmuir*, vol. 23, no. 11, pp. 6352–6357, 2007.
- [112] D. Ivnitski, B. Branch, P. Atanassov, and C. Apblett, "Glucose oxidase anode for biofuel cell based on direct electron transfer," *Electrochemistry Communications*, vol. 8, no. 8, pp. 1204–1210, 2006.
- [113] M. D. Rubianes and G. A. Rivas, "Dispersion of multi-wall carbon nanotubes in polyethylenimine: a new alternative for preparing electrochemical sensors," *Electrochemistry Communications*, vol. 9, no. 3, pp. 480–484, 2007.
- [114] A. S. Arribas, E. Bermejo, M. Chicharro, et al., "Analytical applications of glassy carbon electrodes modified with multi-wall carbon nanotubes dispersed in polyethylenimine as detectors in flow systems," *Analytica Chimica Acta*, vol. 596, no. 2, pp. 183–194, 2007.
- [115] M. Chicharro, A. S. Arribas, M. Moreno, E. Bermejo, and A. Zapardiel, "Comparative study of multi walled carbon nanotubes-based electrodes in micellar media and their application to micellar electrokinetic capillary chromatography," *Talanta*, vol. 74, no. 3, pp. 376–386, 2007.
- [116] M. C. Rodríguez, M. D. Rubianes, and G. A. Rivas, "Highly selective determination of dopamine in the presence of ascorbic acid and serotonin at glassy carbon electrodes modified with carbon nanotubes dispersed in polyethylenimine," *Journal of Nanoscience and Nanotechnology*, vol. 8, no. 11, pp. 6003–6009, 2008.
- [117] J.-D. Qiu, R. Wang, R.-P. Liang, and M. Xiong, "Synthesis and characterization of MWNTs/AuNPs/HS(CH₂)₆Fc nanocomposite: application to electrochemical determination of ascorbic acid," *Electroanalysis*, vol. 20, no. 16, pp. 1819–1824, 2008.
- [118] V. G. Gavalas, S. A. Law, J. C. Ball, R. Andrews, and L. G. Bachas, "Carbon nanotube aqueous sol-gel composites: enzyme-friendly platforms for the development of stable biosensors," *Analytical Biochemistry*, vol. 329, no. 2, pp. 247–252, 2004.
- [119] X. Tan, M. Li, P. Cai, L. Luo, and X. Zou, "An amperometric cholesterol biosensor based on multiwalled carbon nanotubes and organically modified sol-gel/chitosan hybrid composite film," *Analytical Biochemistry*, vol. 337, no. 1, pp. 111–120, 2005.
- [120] K. Gong, M. Zhang, Y. Yan, et al., "Sol-gel-derived ceramic-carbon nanotube nanocomposite electrodes: tunable electrode dimension and potential electrochemical applications," *Analytical Chemistry*, vol. 76, no. 21, pp. 6500–6505, 2004.
- [121] P. P. Joshi, S. A. Merchant, Y. Wang, and D. W. Schmidtke, "Amperometric biosensors based on redox polymer-carbon nanotube-enzyme composites," *Analytical Chemistry*, vol. 77, no. 10, pp. 3183–3188, 2005.
- [122] F. Zhao, X. Wu, M. Wang, Y. Liu, L. Gao, and S. Dong, "Electrochemical and bioelectrochemistry properties of room-temperature ionic liquids and carbon composite materials," *Analytical Chemistry*, vol. 76, no. 17, pp. 4960–4967, 2004.
- [123] Y. Zhang, Y. Shen, J. Li, L. Niu, S. Dong, and A. Ivaska, "Electrochemical functionalization of single-walled carbon nanotubes in large quantities at a room-temperature ionic liquid supported three-dimensional network electrode," *Langmuir*, vol. 21, no. 11, pp. 4797–4800, 2005.
- [124] Y. Zhao, Y. Gao, D. Zhan, et al., "Selective detection of dopamine in the presence of ascorbic acid and uric acid by a carbon nanotubes-ionic liquid gel modified electrode," *Talanta*, vol. 66, no. 1, pp. 51–57, 2005.
- [125] J. Zhao, "Glucose electrochemical sensors based on nanostructures: fabrication and analytical application," Ph.D. thesis, Wuhan University, Wuhan, China, 2006.
- [126] Y. Lin, L. F. Allard, and Y.-P. Sun, "Protein-affinity of single-walled carbon nanotubes in water," *The Journal of Physical Chemistry B*, vol. 108, no. 12, pp. 3760–3764, 2004.
- [127] S. S. Karajanagi, H. Yang, P. Asuri, E. Sellitto, J. S. Dordick, and R. S. Kane, "Protein-assisted solubilization of single-walled carbon nanotubes," *Langmuir*, vol. 22, no. 4, pp. 1392–1395, 2006.
- [128] C. H. Yang, C. Hu, and S. Hu, "Predominating stable adsorption and direct electrochemistry of glucose oxidase on carbon nanotubes by oxygen-containing groups," *Chinese Chemical Letters*, vol. 18, no. 3, pp. 313–315, 2007.
- [129] J. Chen, M. J. Dyer, and M.-F. Yu, "Cyclodextrin-mediated soft cutting of single-walled carbon nanotubes," *Journal of the American Chemical Society*, vol. 123, no. 25, pp. 6201–6202, 2001.
- [130] G. Chambers, C. Carroll, G. F. Farrell, et al., "Characterization of the interaction of gamma cyclodextrin with single-walled carbon nanotubes," *Nano Letters*, vol. 3, no. 6, pp. 843–846, 2003.
- [131] Z. Wang, Y. Wang, and G. Luo, "The electrocatalytic oxidation of thymine at α -cyclodextrin incorporated carbon nanotube-coated electrode," *Electroanalysis*, vol. 15, no. 13, pp. 1129–1133, 2003.
- [132] Z.-H. Wang, G.-A. Luo, S.-F. Xiao, and G.-Y. Wang, "Electrocatalytic behavior of nitrophenol isomers at α -cyclodextrin incorporated carbon nanotubes-coated electrode," *Chemical Journal of Chinese Universities*, vol. 24, part 5, pp. 811–813, 2003.

- [133] G.-Y. Wang, X.-J. Liu, G.-A. Luo, and Z.-H. Wang, " α -cyclodextrin incorporated carbon nanotube-coated electrode for the simultaneous determination of dopamine and epinephrine," *Chinese Journal of Chemistry*, vol. 23, no. 3, pp. 297–302, 2005.
- [134] Z. Wang, Y. Wang, and G. Luo, "A selective voltammetric method for uric acid detection at β -cyclodextrin modified electrode incorporating carbon nanotubes," *Analyst*, vol. 127, no. 10, pp. 1353–1358, 2002.
- [135] G. Wang, X. Liu, B. Yu, and G. Luo, "Electrocatalytic response of norepinephrine at a β -cyclodextrin incorporated carbon nanotube modified electrode," *Journal of Electroanalytical Chemistry*, vol. 567, no. 2, pp. 227–231, 2004.
- [136] C. Hu, C. Yang, and S. Hu, "Hydrophobic adsorption of surfactants on water-soluble carbon nanotubes: a simple approach to improve sensitivity and antifouling capacity of carbon nanotubes-based electrochemical sensors," *Electrochemistry Communications*, vol. 9, no. 1, pp. 128–134, 2007.
- [137] R. J. Chen, Y. Zhang, D. Wang, and H. Dai, "Noncovalent sidewall functionalization of single-walled carbon nanotubes for protein immobilization," *Journal of the American Chemical Society*, vol. 123, no. 16, pp. 3838–3839, 2001.
- [138] Y. Yan, M. Zhang, K. Gong, L. Su, Z. Guo, and L. Mao, "Adsorption of methylene blue dye onto carbon nanotubes: a route to an electrochemically functional nanostructure and its layer-by-layer assembled nanocomposite," *Chemistry of Materials*, vol. 17, no. 13, pp. 3457–3463, 2005.
- [139] C. Hu, Z. Chen, A. Shen, X. Shen, J. Li, and S. Hu, "Water-soluble single-walled carbon nanotubes via noncovalent functionalization by a rigid, planar and conjugated diazo dye," *Carbon*, vol. 44, no. 3, pp. 428–434, 2006.
- [140] C. Yang, Y. Xu, C. Hu, and S. Hu, "Voltammetric detection of ofloxacin in human urine at a Congo red functionalized water-soluble carbon nanotube film electrode," *Electroanalysis*, vol. 20, no. 2, pp. 144–149, 2008.
- [141] C. Hu, X. Chen, and S. Hu, "Water-soluble single-walled carbon nanotubes films: preparation, characterization and applications as electrochemical sensing films," *Journal of Electroanalytical Chemistry*, vol. 586, no. 1, pp. 77–85, 2006.
- [142] M. Zhang, Y. Yan, K. Gong, L. Mao, Z. Guo, and Y. Chen, "Electrostatic layer-by-layer assembled carbon nanotube multilayer film and its electrocatalytic activity for O_2 reduction," *Langmuir*, vol. 20, no. 20, pp. 8781–8785, 2004.
- [143] A. A. Mamedov, N. A. Kotov, M. Prato, D. M. Guldi, J. P. Wicksted, and A. Hirsch, "Molecular design of strong single-wall carbon nanotube/polyelectrolyte multilayer composites," *Nature Materials*, vol. 1, no. 3, pp. 190–194, 2002.
- [144] D.-Q. Yang, J.-F. Rochelste, and E. Sacher, "Spectroscopic evidence for $\pi - \pi$ interaction between poly(diallyl dimethylammonium) chloride and multiwalled carbon nanotubes," *The Journal of Physical Chemistry B*, vol. 109, no. 10, pp. 4481–4484, 2005.
- [145] M. Guo, J. Chen, J. Li, L. Nie, and S. Yao, "Carbon nanotubes-based amperometric cholesterol biosensor fabricated through layer-by-layer technique," *Electroanalysis*, vol. 16, no. 23, pp. 1992–1998, 2004.
- [146] M. Zhang, K. Gong, H. Zhang, and L. Mao, "Layer-by-layer assembled carbon nanotubes for selective determination of dopamine in the presence of ascorbic acid," *Biosensors and Bioelectronics*, vol. 20, no. 7, pp. 1270–1276, 2005.
- [147] P. He and M. Bayachou, "Layer-by-layer fabrication and characterization of DNA-wrapped single-walled carbon nanotube particles," *Langmuir*, vol. 21, no. 13, pp. 6086–6092, 2005.
- [148] J. Liu, S. Tian, and W. Knoll, "Properties of polyaniline/carbon nanotube multilayer films in neutral solution and their application for stable low-potential detection of reduced β -nicotinamide adenine dinucleotide," *Langmuir*, vol. 21, no. 12, pp. 5596–5599, 2005.
- [149] X. Li, L. Zhang, L. Su, T. Ohsaka, and L. Mao, "A miniature glucose/ O_2 biofuel cell with a high tolerance against ascorbic acid," *Fuel Cells*, vol. 9, no. 1, pp. 85–91, 2009.
- [150] J. J. Gooding, R. Wibowo, J. Liu, et al., "Protein electrochemistry using aligned carbon nanotube arrays," *Journal of the American Chemical Society*, vol. 125, no. 30, pp. 9006–9007, 2003.
- [151] Z. Liu, Z. Shen, T. Zhu, et al., "Organizing single-walled carbon nanotubes on gold using a wet chemical self-assembling technique," *Langmuir*, vol. 16, no. 8, pp. 3569–3573, 2000.
- [152] J. Liu, A. Chou, W. Rahmat, M. N. Paddon-Row, and J. J. Gooding, "Achieving direct electrical connection to glucose oxidase using aligned single walled carbon nanotube arrays," *Electroanalysis*, vol. 17, no. 1, pp. 38–46, 2005.
- [153] J. J. Xu, G. Wang, Q. Zhang, X. H. Xia, and H. Y. Chen, "Third generation horseradish peroxidase biosensor based on self-assembling carbon nanotubes to gold electrode surface," *Chinese Chemical Letters*, vol. 16, no. 4, pp. 523–526, 2005.
- [154] X. Qu, Z. Peng, Y. Wang, and S. Dong, "Atomic force microscopic and electrochemical investigations of an electrostatically fabricated single-wall carbon nanotubes modified electrode," *Electroanalysis*, vol. 17, no. 1, pp. 59–64, 2005.
- [155] D. Chattopadhyay, I. Galeska, and F. Papadimitrakopoulos, "Metal-assisted organization of shortened carbon nanotubes in monolayer and multilayer forest assemblies," *Journal of the American Chemical Society*, vol. 123, no. 38, pp. 9451–9452, 2001.
- [156] X. Yu, D. Chattopadhyay, I. Galeska, F. Papadimitrakopoulos, and J. F. Rusling, "Peroxidase activity of enzymes bound to the ends of single-wall carbon nanotube forest electrodes," *Electrochemistry Communications*, vol. 5, no. 5, pp. 408–411, 2003.
- [157] M. O'Connor, S. N. Kim, A. J. Killard, et al., "Mediated amperometric immunosensing using single walled carbon nanotube forests," *Analyst*, vol. 129, no. 12, pp. 1176–1180, 2004.
- [158] P. J. Britto, K. S. V. Santhanam, and P. M. Ajayan, "Carbon nanotube electrode for oxidation of dopamine," *Bioelectrochemistry and Bioenergetics*, vol. 41, no. 1, pp. 121–125, 1996.
- [159] J. J. Davis, R. J. Coles, and H. A. O. Hill, "Protein electrochemistry at carbon nanotube electrodes," *Journal of Electroanalytical Chemistry*, vol. 440, no. 1–2, pp. 279–282, 1997.
- [160] F. Valentini, A. Amine, S. Orlanducci, M. L. Terranova, and G. Palleschi, "Carbon nanotube purification: preparation and characterization of carbon nanotube paste electrodes," *Analytical Chemistry*, vol. 75, no. 20, pp. 5413–5421, 2003.
- [161] R. Antiochia, I. Lavagnini, F. Magno, F. Valentini, and G. Palleschi, "Single-wall carbon nanotube paste electrodes: a comparison with carbon paste, platinum and glassy carbon electrodes via cyclic voltammetric data," *Electroanalysis*, vol. 16, no. 17, pp. 1451–1458, 2004.
- [162] M. Chicharro, E. Bermejo, M. Moreno, A. Sánchez, A. Zapardiel, and G. Rivas, "Adsorptive stripping voltammetric determination of amitrole at a multi-wall carbon nanotubes paste electrode," *Electroanalysis*, vol. 17, no. 5–6, pp. 476–482, 2005.

- [163] N. S. Lawrence, R. P. Deo, and J. Wang, "Detection of homocysteine at carbon nanotube paste electrodes," *Talanta*, vol. 63, no. 2, pp. 443–449, 2004.
- [164] M. L. Pedano and G. A. Rivas, "Adsorption and electrooxidation of nucleic acids at carbon nanotubes paste electrodes," *Electrochemistry Communications*, vol. 6, no. 1, pp. 10–16, 2004.
- [165] J. Wang, G. Chen, M. Wang, and M. P. Chatrathi, "Carbon-nanotube/copper composite electrodes for capillary electrophoresis microchip detection of carbohydrates," *Analyst*, vol. 129, no. 6, pp. 512–515, 2004.
- [166] M. D. Rubianes and G. A. Rivas, "Carbon nanotubes paste electrode," *Electrochemistry Communications*, vol. 5, no. 8, pp. 689–694, 2003.
- [167] M. D. Rubianes and G. A. Rivas, "Enzymatic biosensors based on carbon nanotubes paste electrodes," *Electroanalysis*, vol. 17, no. 1, pp. 73–78, 2005.
- [168] R. Antiochia, I. Lavagnini, P. Pastore, and F. Magno, "A comparison between the use of a redox mediator in solution and of surface modified electrodes in the electrocatalytic oxidation of nicotinamide adenine dinucleotide," *Bioelectrochemistry*, vol. 64, no. 2, pp. 157–163, 2004.
- [169] R. Antiochia, I. Lavagnini, and F. Magno, "Electrocatalytic oxidation of NADH at single-wall carbon-nanotube-paste electrodes: kinetic considerations for use of a redox mediator in solution and dissolved in the paste," *Analytical and Bioanalytical Chemistry*, vol. 381, no. 7, pp. 1355–1361, 2005.
- [170] J. Wang and M. Musameh, "Carbon nanotube/teflon composite electrochemical sensors and biosensors," *Analytical Chemistry*, vol. 75, no. 9, pp. 2075–2079, 2003.
- [171] G. Chen, L. Y. Zhang, and J. Wang, "Miniaturized capillary electrophoresis system with a carbon nanotube microelectrode for rapid separation and detection of thiols," *Talanta*, vol. 64, no. 4, pp. 1018–1023, 2004.
- [172] C. S. Cha, C. M. Li, H. X. Yang, and P. F. Liu, "Powder microelectrodes," *Journal of Electroanalytical Chemistry*, vol. 368, no. 1-2, pp. 47–54, 1994.
- [173] P. Liu and J. H. Hu, "Carbon nanotube powder microelectrodes for nitrite detection," *Sensors and Actuators B*, vol. 84, no. 2-3, pp. 194–199, 2002.
- [174] Y.-D. Zhao, W.-D. Zhang, H. Chen, and Q.-M. Luo, "Anodic oxidation of hydrazine at carbon nanotube powder microelectrode and its detection," *Talanta*, vol. 58, no. 3, pp. 529–534, 2002.
- [175] Y.-D. Zhao, W.-D. Zhang, H. Chen, and Q.-M. Luo, "Electrocatalytic oxidation of cysteine at carbon nanotube powder microelectrode and its detection," *Sensors and Actuators B*, vol. 92, no. 3, pp. 279–285, 2003.
- [176] Y.-D. Zhao, W.-D. Zhang, H. Chen, Q.-M. Luo, and S. F. Y. Li, "Direct electrochemistry of horseradish peroxidase at carbon nanotube powder microelectrode," *Sensors and Actuators B*, vol. 87, no. 1, pp. 168–172, 2002.
- [177] Y. L. Wei, X. Ji, X. Dang, and S. Hu, "Studies on electrochemical properties and scavenge of superoxide anion in aprotic media by using carbon nanotubes powder microelectrode," *Bioelectrochemistry*, vol. 61, no. 1-2, pp. 51–56, 2003.
- [178] Z. Wang, J. Liu, Q. Liang, Y. Wang, and G. Luo, "Carbon nanotube-modified electrodes for the simultaneous determination of dopamine and ascorbic acid," *Analyst*, vol. 127, no. 5, pp. 653–658, 2002.
- [179] Z.-H. Wang, Q.-L. Liang, Y.-M. Wang, and G.-A. Luo, "Carbon nanotube-intercalated graphite electrodes for simultaneous determination of dopamine and serotonin in the presence of ascorbic acid," *Journal of Electroanalytical Chemistry*, vol. 540, pp. 129–134, 2003.
- [180] Q. Shi, T. Peng, and J. Cheng, "A cholesterol biosensor based on cholesterol oxidase immobilized in a sol-gel on a platinum-decorated carbon nanotubes modified electrode," *Chinese Journal of Analytical Chemistry*, vol. 33, no. 3, pp. 329–332, 2005.
- [181] Q. Shi, T. Peng, Y. Zhu, and C. F. Yang, "An electrochemical biosensor with cholesterol oxidase/sol-gel film on a nanoplatinum/carbon nanotube electrode," *Electroanalysis*, vol. 17, no. 10, pp. 857–861, 2005.
- [182] A. Salimi, C. E. Banks, and R. G. Compton, "Abrasive immobilization of carbon nanotubes on a basal plane pyrolytic graphite electrode: application to the detection of epinephrine," *Analyst*, vol. 129, no. 3, pp. 225–228, 2004.
- [183] A. Salimi, R. G. Compton, and R. Hallaj, "Glucose biosensor prepared by glucose oxidase encapsulated sol-gel and carbon-nanotube-modified basal plane pyrolytic graphite electrode," *Analytical Biochemistry*, vol. 333, no. 1, pp. 49–56, 2004.
- [184] A. Salimi, R. Hallaj, and G.-R. Khayatian, "Amperometric detection of morphine at preheated glassy carbon electrode modified with multiwall carbon nanotubes," *Electroanalysis*, vol. 17, no. 10, pp. 873–879, 2005.
- [185] A. Salimi and R. Hallaj, "Catalytic oxidation of thiols at preheated glassy carbon electrode modified with abrasive immobilization of multiwall carbon nanotubes: applications to amperometric detection of thiocytosine, L-cysteine and glutathione," *Talanta*, vol. 66, no. 4, pp. 967–975, 2005.
- [186] K. Wu and S. Hu, "Deposition of a thin film of carbon nanotubes onto a glassy carbon electrode by electropolymerization," *Carbon*, vol. 42, no. 15, pp. 3237–3242, 2004.
- [187] D. Pan, J. Chen, S. Yao, W. Tao, and L. Nie, "An amperometric glucose biosensor based on glucose oxidase immobilized in electropolymerized poly(*o*-aminophenol) and carbon nanotubes composite film on a gold electrode," *Analytical Sciences*, vol. 21, no. 4, pp. 367–371, 2005.
- [188] G. Cheng, J. Zhao, Y. Tu, P. He, and Y. Fang, "A sensitive DNA electrochemical biosensor based on magnetite with a glassy carbon electrode modified by multi-walled carbon nanotubes in polypyrrole," *Analytica Chimica Acta*, vol. 533, no. 1, pp. 11–16, 2005.
- [189] J. Wang and M. Musameh, "Carbon-nanotubes doped polypyrrole glucose biosensor," *Analytica Chimica Acta*, vol. 539, no. 1-2, pp. 209–213, 2005.
- [190] D. Zheng, C. Hu, Y. Peng, W. Yue, and S. Hu, "Noncovalently functionalized water-soluble multiwall-nanotubes through azocarmine B and their application in nitric oxide sensor," *Electrochemistry Communications*, vol. 10, no. 1, pp. 90–94, 2008.
- [191] J.-S. Ye, Y. Wen, W. De Zhang, L. M. Gan, G. Q. Xu, and F.-S. Sheu, "Selective voltammetric detection of uric acid in the presence of ascorbic acid at well-aligned carbon nanotube electrode," *Electroanalysis*, vol. 15, no. 21, pp. 1693–1698, 2003.
- [192] J. Chen, J. Bao, C. Cai, and T. Lu, "Electrocatalytic oxidation of NADH at an ordered carbon nanotubes modified glassy carbon electrode," *Analytica Chimica Acta*, vol. 516, no. 1-2, pp. 29–34, 2004.
- [193] J.-S. Ye, Y. Wen, W. De Zhang, L. M. Gan, G. Q. Xu, and F.-S. Sheu, "Nonenzymatic glucose detection using multi-walled carbon nanotube electrodes," *Electrochemistry Communications*, vol. 6, no. 1, pp. 66–70, 2004.

- [194] P. Soundarrajan, A. Patil, and L. Dai, "Surface modification of aligned carbon nanotube arrays for electrochemical sensing applications," *Journal of Vacuum Science and Technology A*, vol. 21, no. 4, pp. 1198–1201, 2003.
- [195] M. Gao, L. Dai, and G. G. Wallace, "Biosensors based on aligned carbon nanotubes coated with inherently conducting polymers," *Electroanalysis*, vol. 15, no. 13, pp. 1089–1094, 2003.
- [196] M. Gao, L. Dai, and G. G. Wallace, "Glucose sensors based on glucose-oxidase-containing polypyrrole/aligned carbon nanotube coaxial nanowire electrodes," *Synthetic Metals*, vol. 137, no. 1–3, pp. 1393–1394, 2003.
- [197] K. P. Loh, S. L. Zhao, and W. De Zhang, "Diamond and carbon nanotube glucose sensors based on electropolymerization," *Diamond and Related Materials*, vol. 13, no. 4–8, pp. 1075–1079, 2004.
- [198] J.-S. Ye, Y. Wen, W. De Zhang, H. F. Cui, G. Q. Xu, and F.-S. Sheu, "Electrochemical biosensing platforms using phthalocyanine-functionalized carbon nanotube electrode," *Electroanalysis*, vol. 17, no. 1, pp. 89–96, 2005.
- [199] S. G. Wang, Q. Zhang, R. Wang, et al., "Multi-walled carbon nanotubes for the immobilization of enzyme in glucose biosensors," *Electrochemistry Communications*, vol. 5, no. 9, pp. 800–803, 2003.
- [200] H. Tang, J. Chen, S. Yao, L. Nie, G. Deng, and Y. Kuang, "Amperometric glucose biosensor based on adsorption of glucose oxidase at platinum nanoparticle-modified carbon nanotube electrode," *Analytical Biochemistry*, vol. 331, no. 1, pp. 89–97, 2004.
- [201] J.-S. Ye, Y. Wen, W. De Zhang, et al., "Application of multi-walled carbon nanotubes functionalized with hemin for oxygen detection in neutral solution," *Journal of Electroanalytical Chemistry*, vol. 562, no. 2, pp. 241–246, 2004.
- [202] Y. Tu, Y. Lin, and Z. F. Ren, "Nanoelectrode arrays based on low site density aligned carbon nanotubes," *Nano Letters*, vol. 3, no. 1, pp. 107–109, 2003.
- [203] Y. Tu, Y. Lin, W. Yantasee, and Z. Ren, "Carbon nanotubes based nanoelectrode arrays: fabrication, evaluation, and application in voltammetric analysis," *Electroanalysis*, vol. 17, no. 1, pp. 79–84, 2005.
- [204] G. Liu, Y. Lin, Y. Tu, and Z. Ren, "Ultrasensitive voltammetric detection of trace heavy metal ions using carbon nanotube nanoelectrode array," *Analyst*, vol. 130, no. 7, pp. 1098–1101, 2005.
- [205] J. Li, H. T. Ng, A. Cassell, et al., "Carbon nanotube nanoelectrode array for ultrasensitive DNA detection," *Nano Letters*, vol. 3, no. 5, pp. 597–602, 2003.
- [206] J. Koehne, J. Li, A. M. Cassell, et al., "The fabrication and electrochemical characterization of carbon nanotube nanoelectrode arrays," *Journal of Materials Chemistry*, vol. 14, no. 4, pp. 676–684, 2004.
- [207] J. E. Koehne, H. Chen, A. M. Cassell, et al., "Miniaturized multiplex label-free electronic chip for rapid nucleic acid analysis based on carbon nanotube nanoelectrode arrays," *Clinical Chemistry*, vol. 50, no. 10, pp. 1886–1893, 2004.
- [208] X.-N. Cao, L. Lin, Y.-Z. Xian, W. Zhang, Y.-F. Xie, and L.-T. Jin, "In vivo monitoring of the thiols in rat striatum by liquid chromatography with amperometric detection at a functionalized multi-wall carbon nanotubes modified electrode," *Electroanalysis*, vol. 15, no. 10, pp. 892–897, 2003.
- [209] Y. Xian, Y. Zhou, H. Wang, L. Zhou, F. Liu, and L. Jin, "Nanostructured electrode based on multi-wall carbon nanotubes/Pt microparticles nanocomposite for electrochemical determination of thiols in rat striatum by high performance liquid chromatography separation," *Journal of Chromatography B*, vol. 817, no. 2, pp. 239–246, 2005.
- [210] S. Fei, J. Chen, S. Yao, G. Deng, D. He, and Y. Kuang, "Electrochemical behavior of L-cysteine and its detection at carbon nanotube electrode modified with platinum," *Analytical Biochemistry*, vol. 339, no. 1, pp. 29–35, 2005.
- [211] J. Wang, M. Li, Z. Shi, N. Li, and Z. Gu, "Investigation of the electrocatalytic behavior of single-wall carbon nanotube films on an Au electrode," *Microchemical Journal*, vol. 73, no. 3, pp. 325–333, 2002.
- [212] J. Wang, M. Li, Z. Shi, N. Li, and Z. Gu, "Electrocatalytic oxidation of norepinephrine at a glassy carbon electrode modified with single wall carbon nanotubes," *Electroanalysis*, vol. 14, no. 3, pp. 225–230, 2002.
- [213] G. Zhao, S. Zang, K. Liu, et al., "Determination of trace xanthine by anodic stripping voltammetry with carbon nanotube modified glassy carbon electrode," *Analytical Letters*, vol. 35, no. 14, pp. 2233–2244, 2002.
- [214] W. Zhang, Y. Xie, S. Ai, et al., "Liquid chromatography with amperometric detection using functionalized multi-wall carbon nanotube modified electrode for the determination of monoamine neurotransmitters and their metabolites," *Journal of Chromatography B*, vol. 791, no. 1–2, pp. 217–225, 2003.
- [215] W. Zhang, F. Wan, Y. Xie, et al., "Amperometric determination of (R)-salsolinol, (R)-N-methylsalsolinol and monoamine neurotransmitters with liquid chromatography using functionalized multi-wall carbon nanotube modified electrode in Parkinson's patients' cerebrospinal fluid," *Analytica Chimica Acta*, vol. 512, no. 2, pp. 207–214, 2004.
- [216] H. Yi, D. Zheng, C. Hu, and S. Hu, "Functionalized multiwalled carbon nanotubes through in situ electropolymerization of brilliant cresyl blue for determination of epinephrine," *Electroanalysis*, vol. 20, no. 10, pp. 1143–1146, 2008.
- [217] J. Xu, Y. Wang, Y. Xian, L. Jin, and K. Tanaka, "Preparation of multiwall carbon nanotubes film modified electrode and its application to simultaneous determination of oxidizable amino acids in ion chromatography," *Talanta*, vol. 60, no. 6, pp. 1123–1130, 2003.
- [218] X.-N. Cao, L. Lin, Y.-Y. Zhou, et al., "Amperometric determination of 6-mercaptopurine on functionalized multi-wall carbon nanotubes modified electrode by liquid chromatography coupled with microdialysis and its application to pharmacokinetics in rabbit," *Talanta*, vol. 60, no. 5, pp. 1063–1070, 2003.
- [219] G. Zhao, K. Liu, S. Lin, J. Liang, X. Guo, and Z. Zhang, "Application of a carbon nanotube modified electrode in anodic stripping voltammetry for determination of trace amounts of 6-benzylaminopurine," *Microchimica Acta*, vol. 143, no. 4, pp. 255–260, 2003.
- [220] W. Qu, K. Wu, and S. Hu, "Voltammetric determination of pyridoxine (Vitamin B₆) by use of a chemically-modified glassy carbon electrode," *Journal of Pharmaceutical and Biomedical Analysis*, vol. 36, no. 3, pp. 631–635, 2004.
- [221] J. Wang and M. Musameh, "Electrochemical detection of trace insulin at carbon-nanotube-modified electrodes," *Analytica Chimica Acta*, vol. 511, no. 1, pp. 33–36, 2004.
- [222] C. Yang, "Voltammetric determination of tinidazole using a glassy carbon electrode modified with single-wall carbon nanotubes," *Analytical Sciences*, vol. 20, no. 5, pp. 821–824, 2004.

- [223] B. Zeng and F. Huang, "Electrochemical behavior and determination of fluphenazine at multi-walled carbon nanotubes/(3-mercaptopropyl)trimethoxysilane bilayer modified gold electrodes," *Talanta*, vol. 64, no. 2, pp. 380–386, 2004.
- [224] S.-F. Wang and Q. Xu, "Square wave voltammetry determination of brucine at multiwall carbon nanotube-modified glassy carbon electrodes," *Analytical Letters*, vol. 38, no. 4, pp. 657–671, 2005.
- [225] F. Zhao, F. Huang, Q. Yan, and B. Zeng, "Characterization of dodecanethiol SAM and multi-walled carbon nanotube modified gold electrodes, and voltammetric determination of prochlorperazine," *Microchimica Acta*, vol. 150, no. 2, pp. 179–185, 2005.
- [226] W. Qu, F. Wang, S. Hu, and D. Cui, "Electrocatalytic properties and voltammetric determination of melatonin at a nanostructured film electrode," *Microchimica Acta*, vol. 150, no. 2, pp. 109–114, 2005.
- [227] X. Yang, F. Wang, and S. Hu, "Enhanced oxidation of diclofenac sodium at a nano-structured electrochemical sensing film constructed by multi-wall carbon nanotubes-surfactant composite," *Materials Science and Engineering C*, vol. 28, no. 1, pp. 188–194, 2008.
- [228] Y. Peng, C. Lu, B. Hu, Z. Wang, and S. Hu, "Development of an acetylspiramycin sensor based on a single-walled carbon nanotubes film electrode," *Microchimica Acta*, vol. 158, no. 1–2, pp. 79–84, 2007.
- [229] Y. Wu, S. Ye, and S. Hu, "Electrochemical study of lincomycin on a multi-wall carbon nanotubes modified glassy carbon electrode and its determination in tablets," *Journal of Pharmaceutical and Biomedical Analysis*, vol. 41, no. 3, pp. 820–824, 2006.
- [230] A. Callegari, S. Cosnier, M. Marcaccio, et al., "Functionalised single wall carbon nanotubes/polypyrrole composites for the preparation of amperometric glucose biosensors," *Journal of Materials Chemistry*, vol. 14, no. 5, pp. 807–810, 2004.
- [231] Y. Zhu, T. Peng, and J. Li, "A glucose biosensor based on the enzyme electrode with carbon nanotube/platinum nanoparticle," *Chinese Journal of Analytical Chemistry*, vol. 32, no. 10, pp. 1299–1303, 2004.
- [232] H. G. Xue, W. L. Sun, B.-J. He, and Z. Q. Shen, "A new application of carbon nanotubes constructing biosensor," *Chinese Chemical Letters*, vol. 13, no. 8, pp. 799–800, 2002.
- [233] H. G. Xue, W. L. Sun, B.-J. He, and Z. Q. Shen, "Single-wall carbon nanotubes as immobilization material for glucose biosensor," *Synthetic Metals*, vol. 135–136, pp. 831–832, 2003.
- [234] M. Musameh, J. Wang, A. Merkoci, and Y. Lin, "Low-potential stable NADH detection at carbon-nanotube-modified glassy carbon electrodes," *Electrochemistry Communications*, vol. 4, no. 10, pp. 743–746, 2002.
- [235] J. Chen, J. C. Bao, C. X. Cai, and T. H. Lu, "Direct electrochemical oxidation of dihydronicotinamide adenine dinucleotide (NADH) at an ordered carbon nanotubes electrode," *Chinese Chemical Letters*, vol. 14, no. 11, pp. 1171–1174, 2003.
- [236] M. Zhang and W. Gorski, "Electrochemical sensing platform based on the carbon nanotubes/redox mediators-biopolymer system," *Journal of the American Chemical Society*, vol. 127, no. 7, pp. 2058–2059, 2005.
- [237] J. Wang and M. Musameh, "A reagentless amperometric alcohol biosensor based on carbon-nanotube/teflon composite electrodes," *Analytical Letters*, vol. 36, no. 9, pp. 2041–2048, 2003.
- [238] R. Antiochia, I. Lavagnini, and F. Magno, "Amperometric mediated carbon nanotube paste biosensor for fructose determination," *Analytical Letters*, vol. 37, no. 8, pp. 1657–1669, 2004.
- [239] J. S. Lenihan, V. G. Gavalas, J. Wang, R. Andrews, and L. G. Bachas, "Protein immobilization on carbon nanotubes through a molecular adapter," *Journal of Nanoscience and Nanotechnology*, vol. 4, no. 6, pp. 600–604, 2004.
- [240] M. Trojanowicz, A. Mulchandani, and M. Mascini, "Carbon nanotubes-modified screen-printed electrodes for chemical sensors and biosensors," *Analytical Letters*, vol. 37, no. 15, pp. 3185–3204, 2004.
- [241] J.-Z. Xu, J.-J. Zhu, Q. Wu, Z. Hu, and H.-Y. Chen, "An amperometric biosensor based on the coimmobilization of horseradish peroxidase and methylene blue on a carbon nanotubes modified electrode," *Electroanalysis*, vol. 15, no. 3, pp. 219–224, 2003.
- [242] Y.-P. Li, H.-B. Cao, and Y. Zhang, "Direct electrochemistry of hemoglobin immobilized on carbon paste electrode modified by carbon nanotubes," *Acta Physico-Chimica Sinica*, vol. 21, no. 2, pp. 187–191, 2005.
- [243] L. Zhang, G.-C. Zhao, X.-W. Wei, and Z.-S. Yang, "Electroreduction of oxygen by myoglobin on multi-walled carbon nanotube-modified glassy carbon electrode," *Chemistry Letters*, vol. 33, no. 2, pp. 86–87, 2004.
- [244] L. Zhang, G.-C. Zhao, X.-W. Wei, and Z.-S. Yang, "A nitric oxide biosensor based on myoglobin adsorbed on multi-walled carbon nanotubes," *Electroanalysis*, vol. 17, no. 7, pp. 630–634, 2005.
- [245] J. Wang, M. Li, Z. Shi, N. Li, and Z. Gu, "Direct electrochemistry of cytochrome *c* at a glassy carbon electrode modified with single-wall carbon nanotubes," *Analytical Chemistry*, vol. 74, no. 9, pp. 1993–1997, 2002.
- [246] F.-L. Cheng, S. Du, and B.-K. Jin, "Electrochemical studies of cytochrome *c* on electrodes modified by single-wall carbon nanotubes," *Chinese Journal of Chemistry*, vol. 21, no. 4, pp. 436–441, 2003.
- [247] Y. Wu and S. Hu, "The fabrication of a colloidal gold-carbon nanotubes composite film on a gold electrode and its application for the determination of cytochrome *c*," *Colloids and Surfaces B*, vol. 41, no. 4, pp. 299–304, 2005.
- [248] C. X. Cai and J. Chen, "Direct electrochemistry of horseradish peroxidase at a carbon nanotube electrode," *Acta Chimica Sinica*, vol. 62, no. 3, pp. 335–340, 2004.
- [249] W. Zheng, Q. Li, Y. Yan, L. Su, and L. Mao, "Functionalization of carbon nanotubes for direct electrochemistry of horseradish peroxidase," *Indian Journal of Chemistry. Section A*, vol. 44, no. 5, pp. 950–955, 2005.
- [250] Q. Zhao, L. H. Guan, Z. N. Gu, and Q. K. Zhuang, "Direct electrochemistry of catalase on single wall carbon nanotubes modified glassy carbon electrode," *Chinese Chemical Letters*, vol. 16, no. 4, pp. 501–504, 2005.
- [251] M. Wang, Y. Shen, Y. Liu, et al., "Direct electrochemistry of microperoxidase 11 using carbon nanotube modified electrodes," *Journal of Electroanalytical Chemistry*, vol. 578, no. 1, pp. 121–127, 2005.
- [252] J.-Z. Xu, J.-J. Zhu, Q. Wu, Z. Hu, and H.-Y. Chen, "Direct electron transfer between glucose oxidase and multi-walled carbon nanotubes," *Chinese Journal of Chemistry*, vol. 21, no. 8, pp. 1088–1091, 2003.
- [253] C. X. Cai, J. Chen, and T. Lu, "Direct electron transfer of glucose oxidase on the carbon nanotube electrode," *Science in China, Series B*, vol. 47, no. 2, pp. 113–119, 2004.

- [254] W. Liang and Y. Zhuobin, "Direct electrochemistry of glucose oxidase at a gold electrode modified with single-wall carbon nanotubes," *Sensors*, vol. 3, no. 12, pp. 544–554, 2003.
- [255] J. H. T. Luong, S. Hrapovic, D. Wang, F. Bensebaa, and B. Simard, "Solubilization of multiwall carbon nanotubes by 3-aminopropyltriethoxysilane towards the fabrication of electrochemical biosensors with promoted electron transfer," *Electroanalysis*, vol. 16, no. 1-2, pp. 132–139, 2004.
- [256] J.-F. Rochette, E. Sacher, M. Meunier, and J. H. T. Luong, "A mediatorless biosensor for putrescine using multiwalled carbon nanotubes," *Analytical Biochemistry*, vol. 336, no. 2, pp. 305–311, 2005.
- [257] J. H. T. Luong, S. Hrapovic, and D. Wang, "Multiwall carbon nanotube (MWCNT) based electrochemical biosensors for mediatorless detection of putrescine," *Electroanalysis*, vol. 17, no. 1, pp. 47–53, 2005.
- [258] L. Wang and Z. Yuan, "Direct electrochemistry of xanthine oxidase at a gold electrode modified with single-wall carbon nanotubes," *Analytical Sciences*, vol. 20, no. 4, pp. 635–638, 2004.
- [259] Y. Wu and S. Hu, "Direct electron transfer of xanthine oxidase and its catalytic reduction to nitrate," *Analytica Chimica Acta*, vol. 602, no. 2, pp. 181–186, 2007.
- [260] A. Guiseppi-Elie, C. Lei, and R. H. Baughman, "Direct electron transfer of glucose oxidase on carbon nanotubes," *Nanotechnology*, vol. 13, no. 5, pp. 559–564, 2002.
- [261] F. Patolsky, Y. Weizmann, and I. Willner, "Long-range electrical contacting of redox enzymes by SWCNT connectors," *Angewandte Chemie International Edition*, vol. 43, no. 16, pp. 2113–2117, 2004.
- [262] J. Liu, M. N. Paddon-Row, and J. J. Gooding, "Heterogeneous electron-transfer kinetics for flavin adenine dinucleotide and ferrocene through alkanethiol mixed monolayers on gold electrodes," *Journal of Physical Chemistry B*, vol. 108, no. 24, pp. 8460–8466, 2004.
- [263] H. Cai, X. Cao, Y. Jiang, P.-G. He, and Y.-Z. Fang, "Carbon nanotube-enhanced electrochemical DNA biosensor for DNA hybridization detection," *Analytical and Bioanalytical Chemistry*, vol. 375, no. 2, pp. 287–293, 2003.
- [264] H. Cai, Y. Xu, P.-G. He, and Y.-Z. Fang, "Indicator free DNA hybridization detection by impedance measurement based on the DNA-doped conducting polymer film formed on the carbon nanotube modified electrode," *Electroanalysis*, vol. 15, no. 23-24, pp. 1864–1870, 2003.
- [265] Y. Xu, Y. Jiang, H. Cai, P.-G. He, and Y.-Z. Fang, "Electrochemical impedance detection of DNA hybridization based on the formation of M-DNA on polypyrrole/carbon nanotube modified electrode," *Analytica Chimica Acta*, vol. 516, no. 1-2, pp. 19–27, 2004.
- [266] S. G. Wang, R. Wang, P. J. Sellin, and Q. Zhang, "DNA biosensors based on self-assembled carbon nanotubes," *Biochemical and Biophysical Research Communications*, vol. 325, no. 4, pp. 1433–1437, 2004.
- [267] K. Kerman, Y. Morita, Y. Takamura, and E. Tamiya, "Escherichia coli single-strand binding protein-DNA interactions on carbon nanotube-modified electrodes from a label-free electrochemical hybridization sensor," *Analytical and Bioanalytical Chemistry*, vol. 381, no. 6, pp. 1114–1121, 2005.
- [268] J. Wang, G. Liu, M. R. Jan, and Q. Zhu, "Electrochemical detection of DNA hybridization based on carbon-nanotubes loaded with CdS tags," *Electrochemistry Communications*, vol. 5, no. 12, pp. 1000–1004, 2003.
- [269] J. Wang, M. Li, Z. Shi, N. Li, and Z. Gu, "Electrochemistry of DNA at single-wall carbon nanotubes," *Electroanalysis*, vol. 16, no. 1-2, pp. 140–144, 2004.

Review Article

Carbon Nanotubes as Active Components for Gas Sensors

Wei-De Zhang and Wen-Hui Zhang

Nano Science Research Center, School of Chemistry and Chemical Engineering, South China University of Technology, 381 Wushan Road, Guangzhou 510640, China

Correspondence should be addressed to Wei-De Zhang, zhangwd@scut.edu.cn

Received 24 December 2008; Revised 30 March 2009; Accepted 13 April 2009

Recommended by Michele Penza

The unique structure of carbon nanotubes endows them with fantastic physical and chemical characteristics. Carbon nanotubes have been widely studied due to their potential applications in many fields including conductive and high-strength composites, energy storage and energy conversion devices, sensors, field emission displays and radiation sources, hydrogen storage media, and nanometer-sized semiconductor devices, probes, and quantum wires. Some of these applications have been realized in products, while others show great potentials. The development of carbon nanotubes-based sensors has attracted intensive interest in the last several years because of their excellent sensing properties such as high selectivity and prompt response. Carbon nanotube-based gas sensors are summarized in this paper. Sensors based on single-walled, multiwalled, and well-aligned carbon nanotubes arrays are introduced. Modification of carbon nanotubes with functional groups, metals, oxides, polymers, or doping carbon nanotubes with other elements to enhance the response and selectivity of the sensors is also discussed.

Copyright © 2009 W.-D. Zhang and W.-H. Zhang. This is an open access article distributed under the Creative Commons Attribution License, which permits unrestricted use, distribution, and reproduction in any medium, provided the original work is properly cited.

1. Introduction

Carbon nanotubes (CNTs) are a group of one-dimensional nanoscale materials composed of carbon atoms with fullerene structure, in which each carbon atom is sp^2 hybrid and every carbon atom is covalently bonded to another three adjacent carbon atoms. According to the number of their wall layer, they can be single-walled carbon nanotubes (SWCNTs) and multiwalled carbon nanotubes (MWCNTs). A single-walled carbon nanotube can be considered as being formed by rolling a piece of graphene to create a seamless cylinder with diameters of 0.4–2 nm. MWCNT comprise of several layers of graphene cylinders that are concentrically nested like rings of a tree trunk, with an interlayer distance close to that of graphite (0.34 nm). Both MWCNTs and SWCNTs have diameters in the range between fractions of nanometers and tens of nanometers and length up to several centimeters with both their ends normally capped by fullerene-like structures [1]. Three main methods being developed for CNTs synthesis are arc-discharge, laser ablation, and chemical vapor deposition (CVD) [2]. Since the discovery of MWCNTs [3] in 1991 and the SWCNTs in 1993 [4], CNTs have attracted extensive research interest due

to their outstanding structural, electronic, and mechanical properties such as unique tubular structure like fullerene, high chemical and thermal stability, low weight, high electrical conductivity, stability, good heat conductance, large surface area, flexibility, high elasticity, and, high mechanical strength. CNTs play very important role in nanotechnology which greatly influences many different disciplines involving biology, chemistry, physics, medicine, engineering, electronics and material science [5].

The electronic property of SWCNTs is determined by their size and chirality. The SWCNTs can be metallic or semiconductive. The conductivity of each layer of MWCNTs behaves like an SWCNT along the axial direction, while it is very poor between the layers. As a whole, most MWCNTs display good conductivity. The unique electronic property combining with others makes carbon nanotubes ideal building block for electronic devices such as quantum wires, diodes, field-effect transistors (FETs), sensors, and cold cathode field emitters [1].

Carbon nanotubes are attractive for the task of chemical sensors, especially for nanoscale gas sensors. The development of CNTs-based gas sensors has attracted intensive interest in the last several years because of their high response,

prompt response, low power consumption, small size and low operating temperature. The fabrication, structure and gas-sensing characteristics of CNTs-based gas sensors are reviewed in this paper and the challenge and strategic consideration for future development are also discussed. Gas sensors based on pristine CNTs including SWCNTs, MWCNTs and aligned CNTs are introduced, and the modification of CNTs with functional groups, metals, metal oxides and polymers for gas sensors are also discussed.

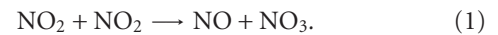
Most of the CNT sensors are based on FET devices with a semiconductive single nanotube (Figure 1(a)) or nanotube networks (Figure 1(b)) as the active sensing elements, and the conductivity of the CNTs was monitored when the sensors were exposed to various atmospheres.

2. Gas Sensors Based on Pristine Carbon Nanotubes

2.1. Gas Sensors Based on SWCNTs. It has been reported that SWCNTs are sensitive to NO₂, NH₃ and volatile organic compounds. The adsorption of gaseous molecules either donates or withdraws electron from the SWCNTs, leading to changes of electrical properties of the SWCNTs [6]. The high and fast response of the SWCNTs gas sensors has been assured. The drawback of these sensors is slow and incomplete recovery. To date, there have been a variety of attempts to overcome this limitation.

Kong et al. demonstrated the potential of CNT-based gas sensors when they reported the response of field-effect transistor (FET) devices to NO₂ and NH₃ [7]. The FET devices, utilizing a single semiconductive SWCNT (S-SWCNT) as the conduction channel, showed a unique response to NH₃ and NO₂ through chemical gating of the SWCNT. The response time of the devices to 200 ppm NO₂ was a few seconds, and the response (defined as the ratio between resistance after and before gas exposure) was approximately 100–1000. Recovery was slow at room temperature (ca. 12 hours), but decreased to approximately 1 hour upon heating. The response time to approximately 1% NH₃ was a few minutes with the response between 10 and 100. An individual nanotube sensor can be used to detect different types of molecules. The selectivity is achieved by adjusting the electrical gate to set the S-SWCNT sample in an initial conducting or insulating state. However, the mechanism causing the response of the FET based on single CNT remains unclear. Three models have been proposed to explain it. The first is charge transfer between the nanotube and the molecules adsorbed on its surface. The second is molecular gating of the CNT by the polar molecules such as NO₂, which results in shift of the gate threshold of the semiconducting SWCNT. The third is a change in the Schottky barriers between the nanotube and the electrodes [8, 9]. Peng et al. studied the adsorption, diffusion, and reaction of NO₂ on a SWCNT using *ab initio* simulations [10]. Since there are catalyst islands on SWCNT, and NO₂ molecules are known to interact with catalytic surfaces to form NO

and NO₃ molecules, a chemical reaction may occur as follows:



On the equilibrium, the desorption of NO₂ and NO molecules is very fast (less than 1 second at room temperature), while the desorption of NO₃ molecules is much slower (about 12 hours). From the fact that NO₃ is the major concentration on the SWCNT surface, and its recovery time will accordingly determine the recovery time of the overall SWCNT system, they deduced that it is NO₃ that is responsible for the slow recovery.

The different recovery rate can be interpreted in terms of the desorption energy barrier of gas molecules on the CNT. For FET devices, the desorption energy barrier for adsorbed dimethyl methylphosphonate [11], NH₃ [12], or NO_x [13] molecules on SWCNT could be reduced under positive gate voltages. A negative gate bias bends the energy band of the CNT upwards. Due to a thin barrier width, holes could tunnel through the barrier and enter the CNT channel easily. When a positive gate bias is applied, the CNT's energy band is bent downwards and hole tunneling is suppressed. A positive gate bias can promote fast recovery, which suggests that room temperature reversible CNT sensors for dimethyl methylphosphonate or NH₃ are feasible.

By simply casting of SWCNTs on an interdigitated electrode, Li et al. [14] fabricated a gas sensor for detection of gases and organic vapors at room temperature. The sensor responses are linear for concentrations of sub ppm to hundreds of ppm with detection limit of 44 ppb for NO₂ and 262 ppb for nitrotoluene. The recovery time was very long, on the order of 10 hours because of the higher bonding energy between SWNTs and NO₂. By using ultraviolet (UV) light to knock the adsorbed molecules out of the SWCNT sites, the recovery time was shortened to about 10 minutes. The UV exposure decreases the desorption-energy barrier to ease the NO₂ desorption. Under UV illumination, oxygen photodesorption causes a reduction of the hole carriers in the SWCNT, thus lowering the conductance of the sample. In air, gradual oxygen re-adsorption onto the nanotube upon turning off the light leads to the recovery of sample conductance [15].

Efforts have also been made to improve gas desorption by heating the sensors and increasing the flux rate of carrier gas. Quang et al. fabricated sensors from SWCNTs by a screen-printing method [16]. These sensors have been exposed to NH₃ gas at room temperature with nitrogen as the carrier gas. The SWCNTs are very sensitive to NH₃ and can detect NH₃ with low concentration of 5 ppm with a response time of 10 minutes. When the sensor is exposed to NH₃, electrons are transferred from NH₃ to SWCNTs. NH₃ donates electrons to the valence band of the carbon nanotubes, decreasing the number of holes, thereby increasing the separation between the Fermi level and the valence band. This forms a space charge region at the surface of the semiconducting SWCNTs, which increases

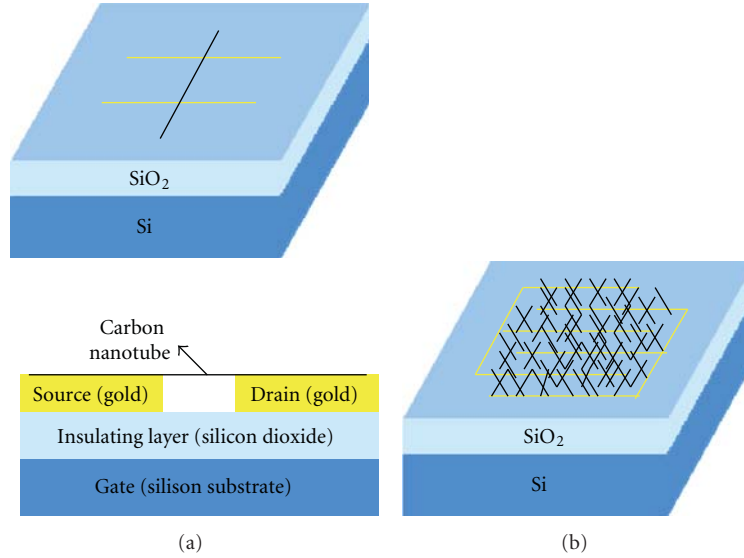


FIGURE 1: Schematic diagrams of (a) a gas sensor based on FET with a single carbon nanotube as sensing element, and (b) a resistive gas sensor with CNT bundles or thin film as sensing element.

the electrical resistance. A saturation state is established at a concentration of about 40 ppm, and the response of the sensor continues to increase in conjunction with an increase in concentration levels. The sensor completely recovers to its initial state at 80°C and under 1000 sccm N₂ flux. Nguyen et al. also constructed sensors from SWCNT powders by screen-printing, followed by annealing pretreatment in open-air for 2 hours at various temperatures to enhance the sensor characteristics [17]. The sensor annealed at 200°C was employed for detection of NH₃ with 500 sccm N₂ flowing. After being exposed to 5 ppm NH₃ for 10 minutes at room temperature, the resistance of the sensor increased up to 8% in comparison with its initial value. The strong bonding between NH₃ molecules and the SWCNTs requires a long time to degas and it causes the slow recovery of the SWCNT-based sensor. The carrier gas flux was intensified in desorption time to remove the adsorbed NH₃ molecules from the SWCNTs. The stronger carrier gas flux was conducted, the better recovery the sensor exhibited. The behavior of the SWCNT shows a transition from semiconducting at a moderate temperature (<350°C) to metallic at high temperature (>350°C), which suggested that the heating treatment might cause a structural change in the SWCNT, leading to a change in its chirality. Heating at a moderate temperature could reduce the resistance of the sensor, therefore degrading response in detection of NH₃. In order to avoid this problem, heating was not applied in sensing duration but in desorption time, for only 5 minutes at 70°C. In addition, the carrier gas flux was maximized to 1000 sccm for degassing. In summary, by increasing the carrier gas flux, combined with heating at 70°C, the sensor recovery was dramatically improved. All these methods improved partly the recovery of the SWCNTs-based sensors, but the recovery time is still not satisfactory.

According to the thermodynamics, the adsorption or desorption rate of gas molecules on solid surface could be expressed as follows:

$$\begin{aligned} r_a &= K f(\theta) \exp\left(-\frac{E_a}{RT}\right), \\ r_d &= K' f'(\theta) \exp\left(-\frac{E_d}{RT}\right), \end{aligned} \quad (2)$$

where r_a and r_d are the rate of adsorption and desorption, respectively; E_a and E_d are the activation energy of adsorption and desorption, respectively; T is the temperature; K and K' are the adsorption or desorption rate constant. θ is the fraction of the surface occupancy. $f(\theta)$ is a function related to surface vacancy ($1 - \theta$), $f'(\theta)$ is a function related to generally written to be related to surface occupancy (θ). Based on the above equations, r_a increases with the increasing of the gaseous pressure and fraction of the surface vacancy and reduces with the increasing of the adsorption activation energy. r_d increases with the increasing of the desorption temperature and fraction of the surface covered and reduces with the increasing of the desorption activation energy. As a result, heating is favorable for desorption, thus enhancing the recovery of the sensors. On the other hand, irradiation with UV light reduces the desorption activation energy, which is plausible for recovery of the gas sensors also.

2.2. Gas Sensors Based on MWCNTs. So far, it has been reported that MWCNTs are sensitive to a variety of gases such as NH₃, NO, NO₂, H₂, SF₆, and Cl₂. The main drawback of MWCNTs gas sensors is also the slow recovery. For example, Varghese et al. [18] investigated two sensor geometries, one capacitive with MWCNT-SiO₂ composite placed over a planar interdigital capacitor, the other resistive with MWCNTs

grown upon a serpentine SiO₂ pattern. Reversible behavior is demonstrated for the MWCNTs sensors in response to humidity, CO and CO₂. The response time of both sensors to NH₃ was approximately 2-3 minutes but it took the sensor several days in vacuum at 100°C to recover the original response. The impedance changes are attributed to p-type conductivity in semiconducting MWCNTs, and the formation of Schottky barriers between the metallic and semiconducting nanotubes. Of the sensors tested, the interdigital capacitor showed higher response. Nguyen et al. [19] developed a device with interdigital Pt electrodes on an Al₂O₃ substrate in order to evaluate the MWCNTs-based gas sensor capabilities. The MWCNT films were found to exhibit a fast response and a high response to NH₃ at room temperature. The response ($S = (R_0 - R)/R_0$, where R_0 represents the resistance in dry air and R is the resistance in the NH₃ gas environment), varies from 75% to 85% when the gas concentration increases from 2500 to 7500 ppm. This change is due to the electron transfer from gas molecules to the nanotubes, leading to decrease of the resistance of the CNTs film. Moon et al. [20] fabricated the sensor employing MWCNTs as an active sensing element by using screen-printing method, and the sensor returned to the initial conductance employing a bias voltage for detecting NO₂. The response ($S = G_g/G_0$, where G_0 is the initial conductance of the sensor and G_g is the conductance of nanotube films being exposed to NO₂) to 50 ppm NO₂ was approximately 22.7%. In a vacuum state, the sensor conductance was refreshed using a CNT-bias-heating method. The recovery was maintained for 10 minutes with bias voltage of 10 V, and the heating value was 28.8 cal. The recovery time decreased when the degassing energy was provided all at once, more than the divided heating. MWCNT films in the sensor could be used as a heater with a bias voltage, and the recovery time could be controlled by a bias voltage. The temperature variation was dependent on the bias voltage and the possible high electrical current. Gas desorption is affected by heating value which is controlled by time and bias voltage. The recovery time decreased upon an increase of bias voltage.

Suehiro et al. [21] demonstrated the partial discharge detection in SF₆ gas using an MWCNTs-based gas sensor. The sensor was fabricated by positive dielectrophoresis of MWCNTs on a microelectrode array. The sensor can detect main decomposition products such as SO₂ or HF at ppm level. When the partial discharge was generated, the electrical conductance of the MWCNT sensor gradually increased. The sensor response was reversible and was influenced by both the partial discharge intensity and the relative position of the sensor to the point electrode. The increase of the sensor conductance was caused by an electronic interaction between MWCNTs and nonidentified oxidative decomposition products. The sensor could realize a real-time detection of faint partial discharge activities that detection tubes could not sense.

An electrochemical gas sensor modified with MWCNTs film as electrocatalyst for the determination of Cl₂ has also been constructed [22]. Cl₂ gas was allowed through the cathode surface of the sensor, and the resulting galvanic effects were monitored. This amperometric gas sensor showed

excellent response, high stability, and fast recovery for the determination of Cl₂ in H₂SO₄. In the plateau potential region, the reduction of Cl₂ is controlled with the mass transfer of Cl₂ through the working electrode. Therefore, the limiting current produced in this region can be used to quantify the Cl₂ concentration. When using nanotube-based microelectrode, the electrode has a porous structure and is probably well wetted by the solvent/electrolyte medium [23]. The performance of the electrochemical sensor for Cl₂ with MWCNTs as electrocatalyst was stable and it was not interfered by the redox gases, such as CO, NO, O₂, CO₂, and C₃H₈. CO₂ is an inert gas, so it is difficult to react on the surface of MWCNTs-modified electrode. The response and recovery time of this sensor is about 150 seconds. The response time for MWCNTs is prolonged to about 150 seconds due to the small proportion of exposed edge plane.

As mentioned before, SWCNTs consist of single graphite sheets, while MWCNTs comprise an array of nanotubes that are concentrically nested. Depending on their chirality and diameter, an SWCNT can be either metallic or semiconducting. In practice, it is difficult to obtain only semiconducting nanotubes from grown samples, which are usually mixtures of both metallic and semiconducting SWCNTs [24]. Suehiro et al. [25] demonstrated that the normalized response of the SWCNT sensor was higher than that of the MWCNT sensor. Probably it is because SWCNTs contained more semiconducting tubes. In general, MWCNTs show a conducting (metallic) behavior at room temperature. However, MWCNTs could contain some semiconducting tubes among predominantly metallic ones. The higher normalized response of the SWCNT sensor may be attributed to higher abundance of the semiconducting tube, which is responsible for the sensor response.

2.3. Gas Sensors Based on Well-Aligned CNTs. It has been reported that aligned CNTs (ACNTs) are sensitive to NO₂, NH₃ and H₂. For example, Valentini et al. [26] prepared aligned CNT thin films by pulsed plasma chemical vapor deposition system for the detection of NO₂. The sensors exhibited fast and high response at room temperature and could detect as low as 10 ppb NO₂ at 165°C with fast recovery. The resistance of CNTs films decreased while contacting with NO₂, whereas it increased with NH₃, ethanol, humidity, and C₆H₆. The CNT film can be viewed as an aligned network of CNTs somewhere connected with CNT/CNT junctions. The crossed junctions between CNTs act as a gate for carriers to move in the film, and they may consist either in directly cross-linked defective nanotubes or in amorphous carbon impurities. Therefore the CNT film can be represented as a network of effective resistors formed by the resistance of the nanotube body, the resistance of the junctions, and the tunnelling resistance due to tube-tube electronic coupling between adjacent but not connected nanotubes. At 165°C, NO₂ is favored to decompose O₂ molecules in the air, generating atomic oxygen which preferentially attacks the defective sites of the CNT, thus produced volatile species like CO and CO₂ with the consumption of the defective sites. Moreover, amorphous carbon impurities

were also oxidized in such conditions, thus decreased the number of metallic like (Fermi) junctions. Cho et al. [27] fabricated a sensor by using selectively grown MWCNTs as the sensing element on a substrate of a stacked microheater structure with a Cr heater and a diaphragm to improve the recovery time and response of the MWCNTs films. To offer more reaction area between MWCNTs and NO₂ molecules, MWCNTs' films with mesh and serpentine shapes were fabricated. It took about 6 hours for the sensor to return to the initial resistance at room temperature. The MWCNTs thin films can be better recovered only by properly selecting the thermal treatment protocols. The change of the resistance of the mesh-shaped MWCNTs films to NO₂ was found to be larger than that of the serpentine-shaped MWCNTs films because the number of reaction areas between MWCNTs and NO₂ molecules was increased. Ueda et al. [28] prepared well-aligned CNTs on Si substrate by thermal CVD. The resistance of the sensor decreased with an increase of ambient NO and NO₂ gas concentration. The CNTs thin film can be applicable to an NO_x gas sensor. The changing rate of the resistance of the sensor was proportional to the concentration of the target gas. UV light irradiation can reset the resistance of the CNTs sensor by photodetachment of adsorbed molecules at room temperature. Hoa et al. [29] developed a vertical transport type CNTs-based NH₃ gas sensor structure. The structure features regular arrays of CNTs with uniform diameter and length, but the nanotubes also have high defect levels. The sensor shows high response, fast response time of less than 1 minute and good reproducible recovery behavior in atmospheric pressure with the forward biases of 5 V at room temperature due to the high defect density, and could detect NH₃ at the range of 0.1–6%. The CNTs with a higher defect density revealed better response. The oxygenation degrades the response to NH₃, but the crystallographic defects can enhance it in the CNT sensors. The recovery time is not sensitive to the gas concentration, which may be due to the forced desorption of the NH₃ molecules by the refreshing nitrogen flow. Figure 2 shows the schematics of sensor fabrication process and switching of the sensor measured at different NH₃ concentration. The regularity of the CNTs in diameter and length was a great help in clearly defining the sensors' specification and in realizing sensor-to-sensor uniformity.

N₂ absorption characteristics of the vertically aligned CNTs-based three-terminal gas sensor at room temperature were also studied [30]. Upon exposure to N₂ (filling pressure from 50 mTorr to 500 Torr) and without N₂ at 10 V bias voltage, the electrical resistance of the as-made devices was found to increase and to return back, respectively. Compared to a low bias, a high drain-source voltage enhanced the response for monitoring N₂ gas. N₂, owning higher adsorption energy, was easier to absorb by CNTs than Ar. The response was further improved by applying a negative gate voltage owing to the addition of conducting holes to the CNTs mat.

The response of multifinger with aligned SWCNT is double with respect to disordered SWCNT [31]. This effect is probably induced by the fact that the ordered SWCNTs are more uniformly exposed to the NH₃ molecules, than the case of placement of SWCNTs in form of a random network,

in which part of the SWCNT remains inaccessible to the gas molecules.

Gas-sensing performance of pristine CNT sensors is summarized in Table 1.

3. Gas Sensors Based on Modified Carbon Nanotubes

3.1. Gas Sensors Based on CNTs with Functional Groups.

Modification of CNTs with functional groups, metal nanoparticles, oxides, and polymers will change the electronic properties of them, and enhancing the selectivity and response to specific gases though the interaction of the target molecules with the functional groups or additives is very different. Most of the previous reports are based on utilization of carboxylic acid (–COOH) group, which provides reactive sites for interacting with different reactive compounds, at the ends and side-walls of the CNTs. Hsu et al. [32] reported that the –COOH group grafted on MWCNTs provides reactive sites via esterification or elimination, and the MWCNTs retain the graphitic structure. The HCl-treated MWCNTs were efficiently oxidized with nitric acid/hydrogen peroxide ($v/v = 2/1$) solution to generate –COOH group on the defect sites of MWCNTs. The surface acoustic wave (SAW) crystal sensor coated with MWCNT–COOH/poly(*n,n*-dimethylamino propylsilsequioxane) exhibited a high response for ethanol vapor efficiently. Mäklin et al. [33] demonstrated NO gas sensing with carboxyl functionalized SWCNTs and MWCNTs. When exposed to NO, the conductivity of the sensors changed up to about 40% for SWCNTs and 12% for MWCNTs; however, the response was found to be fairly independent on NO concentration. Sensors made of SWCNTs outperform their counterparts with MWCNTs, which is a sign of tunable Fermi level in the semiconducting nanotubes. Recently, Fu et al. [34] demonstrated experimentally that sensors made of carboxylated SWCNTs were sensitive to CO, with a lower detection limit of 1 ppm, whereas pristine SWCNTs did not respond. The authors exploited the different responses of carboxylated and pristine SWCNTs to differentiate between CO, NO, and NO₂. The COOH functionality is crucial to the CO sensing, and the CO molecules can be absorbed on carboxylic acid functionalities through weak hydrogen bonding.

Tran et al. [35] investigated the effect of –NH₂ functionalized SiO₂ surface on the gas sensing properties of SWCNTs modified with 3-aminopropyltriethoxysilane (APTES). The relative resistance change of the SWCNTs to NO₂ in the case of the APTES-treated surface was twice larger than the case without surface treatment under the same conditions. The surface treatment by the SWCNTs did not affect the recovery time of the gas sensor. A significantly fast response time of the sensor with the SWCNTs treatment was observed when exposed to 10 ppm or 50 ppm NO₂. The amine groups in the APTES monolayer, electron donating in nature, played a role of charge transfer to the semiconducting SWCNTs, and hence the amount of electrons transferred from SWCNTs to NO₂ molecules increased.

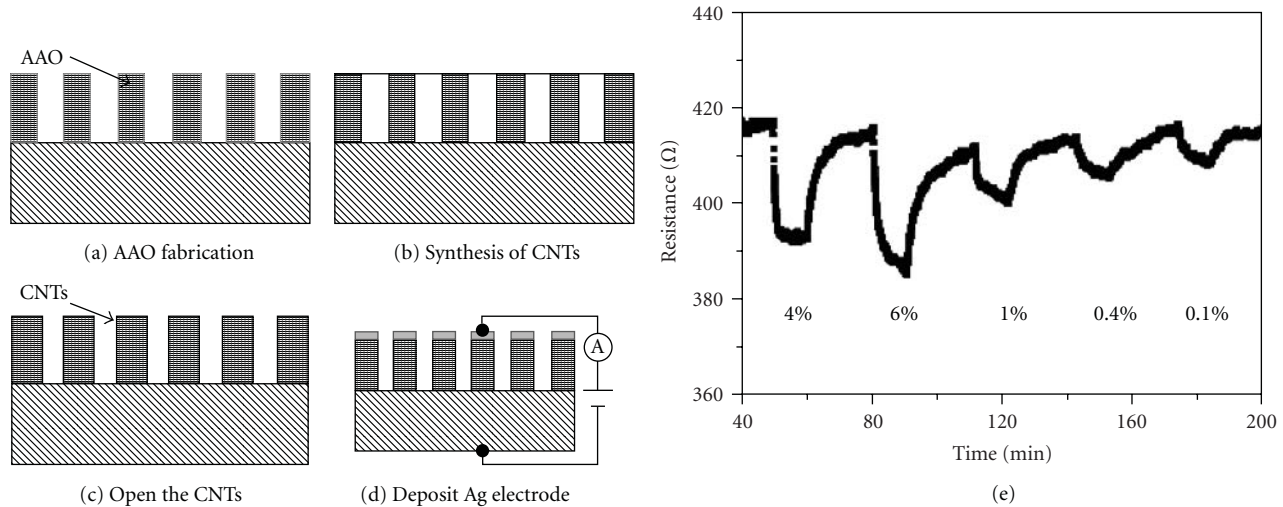


FIGURE 2: Schematics of sensor fabrication process. (a) Synthesis of anodic aluminum oxide (AAO) on p-type Si substrate, (b) synthesis of CNTs by thermal CVD, (c) removal of the top carbon layer by oxygen plasma, (d) Ag electrode deposition and (e) switching of the sensor measured at different NH_3 concentrations. Reprinted with permission [29].

TABLE 1: Summary of gas-sensing performance of pristine CNT gas sensors. (Note: N/S = Not-stated.)

CNT type	Sensor configuration	Targeted analytes	Detection limit	Response time	Recovery time	Reference
S-SWCNT	FET	NO_2 , NH_3	2 ppm NO_2 , 0.1% NH_3	<10 min	~1 h (200°C)	[7]
SWCNTs	Resistor	NO_2 , Nitrotoluene	44 ppb NO_2 , 262 ppb Nitrotoluene	10 min	10 min (UV)	[14]
SWCNTs	Resistor	NH_3	5 ppm	~10 min	~20 min (80°C)	[16]
SWCNTs	Resistor	NH_3	5 ppm	~10 min	~10 min (70°C)	[17]
MWCNTs	Capacitor and Resistor	NH_3	10 ppm	2-3 min	several days (100°C in vacuum)	[18]
MWCNTs	Resistor	NH_3	2500 ppm	N/S	N/S	[19]
MWCNTs	FET	NO_2	50 ppm	~500 s	~10 min (10 V bias potential)	[20]
MWCNTs	Resistor	SO_2 , HF	10 ppm SO_2 , 4 ppm HF	N/S	N/S	[21]
MWCNTs	Electrochemical Gas sensor	Cl_2	100 ppm	~150 s	~150 s	[22]
ACNTs	Resistor	NO_2	10 ppb	~60 min	~60 min (165°C)	[26]
ACNTs	Resistor	NO_2	10 ppm	N/S	N/S	[27]
ACNTs	Resistor	NO , NO_2	2 ppm NO , 2 ppm NO_2	N/S	~20 min (150°C and UV)	[28]
ACNTs	Resistor	NH_3	~0.1%	N/S	N/S	[29]
ACNTs	FET	N_2	50 mTorr	N/S	N/S	[30]

3.2. Gas Sensors Based on Polymer Functionalized CNTs. Among the organic polymers, conducting polymers are the most promising materials for gas sensing as they have delocalized bonds that make them semiconducting or even highly conductive. Several conducting polymers, for example, polyaniline, polypyrrole, polythiophene have been demonstrated to be good sensing materials to function

at room temperature. They have been applied as conductometric, potentiometric, amperometric and voltammetric transducers for the detection of a wide variety of gas or vapors such as NH_3 , NO_2 , CO and VOCs. However, their selectivity and the environmental stability are poor. Recently, enhanced gas sensing by combining SWCNTs with organic polymers has been demonstrated. Qi et al. showed that

noncovalently dropcoating of polyethyleneimine (PEI) and Nafion (a polymeric perfluorinated sulfonic acid ionomer) onto SWCNTs FETs resulted in gas sensors with improved response and selectivity for NO_2 and NH_3 [36]. The PEI functionalization changed the SWCNTs from p-type to n-type semiconductors, and the sensors based on PEI modified SWCNTs were able to detect less than 1 ppb NO_2 with a response time of 1-2 minutes (defined as the time for 80% conductance change to take place) while being insensitive toward NH_3 . The conductance of the n-type multiwalled tube devices decreased upon NO_2 binding due to electron transfer to NO_2 reducing the majority carriers in the nanotubes. This NH_3 insensitivity is attributed to low binding affinity and sticking coefficient of NH_3 on the electron-rich (due to high-density amines on PEI) n-type SWCNTs. PEI functionalized SWCNTs are highly selective to many other molecules including CO , CO_2 , CH_4 , H_2 , and O_2 . The sensor recovery was done by desorbing NO_2 with UV light illumination. Contrary to PEI-coated sensors, Nafion coated SWCNTs were insensitive to NO_2 but exhibiting a good sensitivity toward NH_3 . Chemical functionalization of SWCNTs with covalently attached poly-(m-aminobenzene sulfonic acid) (PABS) has been demonstrated to have better sensing performance toward NH_3 and NO_2 than simply carboxylated SWCNTs. Bekyarova et al. reported that the SWCNTs-PABS devices showed significant sensitivity to 5 ppm NH_3 owing to PABS deprotonation during NH_3 exposure [37]. This deprotonation resulted in hole depletion from the SWCNTs and a reduction in the overall conductance of the SWCNTs-PABS system. Zhang et al. used SWCNTs-PABS devices to reach detection limits of 100 ppb NH_3 and 20 ppb NO_2 with short response time and full recovery [38]. At 20–30°C, SWCNTs-PABS sensors usually take several hours to regenerate after exposure to NO_2 above 300 ppb. Sulfonic acid groups as dopants play an important role in balancing the charge distribution within the polymer, and they are especially attractive for introducing acid-base response. When PABS is exposed to NH_3 or water vapor, the adsorbed molecules cause deprotonation of the polymer, which depletes hole carriers and thus resulting in an increased electrical resistance. In contrast, exposure to NO_2 causes protonation of the polymer, which induces hole accumulation and results in a decreased resistance of the SWCNT-PABS sensors. When the sensor is purged with reference gas, the process is reversed and the original electrical resistance is restored.

CNTs have also been incorporated into polymers to form nanocomposites, which are usually casted to thin films and serve as sensing elements. For example, polypyrrole (PPy) /SWCNTs nanocomposite-based gas sensors have been fabricated by using a chemical polymerization technique followed by spin-casting onto prepatterned electrodes [39]. The response of the nanocomposites was about ten times higher than that of PPy (the resistance changed about 6% at 200 ppm NO_2). The response was recovered fully after about 2 hours in the first cycle. However, in the next cycles, not only the response was degraded, it was also not fully recovered. The SWCNT bundles could be nanodispersed, which may increase the specific surface area of the coated

PPy and thereby increase the response further. The recovery time could be shortened, particularly in the nanocomposite, by taking advantage of the Joule-heating effect. Liu et al. synthesize individual SWCNT/PPy composite nanocables based on nanotube FET [40]. A recovery in conductance was observed with nanotube/PPy nanocables upon further deposition of PPy, which results from the conduction through the conducting PPy layer. Furthermore, these composite materials enhanced conductance upon NO_2 exposure and reduced conductance upon NH_3 exposure. The observed conductance suppression in nanotube/PPy nanocables may originate from several factors. The first is the formation of scattering centers close to the nanotube when PPy was deposited. The deposited PPy might form covalent bonds with the nanotube at the defect sites and subsequently lead to enhanced scattering. The PPy coating may significantly alter the Schottky barrier at the metal-nanotube contacts and contribute to the observed conductance suppression. Santhosh et al. developed an amperometric sensor based on polydiphenylamine (PDPA) grafted MWCNTs (MWNT-g-PDPA) for determination of CO . Cyclic voltammetry is used to fabricate the modified electrode and to demonstrate the electroactivity of MWNT-g-PDPA-ME toward gaseous CO . The sensor exhibited high response for oxidation of CO in a 0.5 M HClO_4 solution [41]. The sensor showed excellent linear concentration range between 10 and 200 ppm (correlation coefficient $r = 0.9941$) with a substantially low detection limit of 0.01 ppm. The response to CO was rather quick; time for 96% response and 98% recovery to 100 ppm CO was about 2 and 3 seconds, respectively. The oxidation of CO to CO_2 occurred at the triple-phase boundary among the electrolyte, MWNT-g-PDPA-ME and CO . When the MWNT-g-PDPA-ME was coated with 0.5% Nafion, the interference from NH_3 , CH_4 , C_3H_8 , and N_2O (500 ppm) was not detected at MWNT-g-PDPA-ME. The insignificant or noninterference from these gases is attributed to the solubility and dielectric properties of the gases at a fluorinated polymer. Long-term stability of the MWNT-g-PDPA-ME was checked for 10 days, and no change in the sensing current was observed.

Modification of CNTs with polymers also improves their sensing properties toward vapors of organic compounds (VOCs). Abraham et al. developed a compact wireless gas sensor based on an MWCNTs/PMMA composite chemiresistor [42]. The composite film was made by ultrasonication of MWCNTs and PMMA (1 : 4 by weight) for 2 hours in dichloromethane, and the chemiresistors were fabricated by dip-coating. The sensor shows fast response (2–5 seconds) and 10^2 - 10^3 order increase in resistance upon exposure to dichloromethane, chloroform and acetone vapors. It returns to the initial level immediately after removing the gas. The sensing mechanism was explained by swelling of the polymer due to absorption of organic vapors into the PMMA and the charge transfer when polar organic vapors adsorb on the CNT surface. Solvents such as methanol, ethyl acetate and toluene, in which PMMA is insoluble or less soluble, also showed response. The polar nature of the solvents and the extent of interaction determine the response of the sensor. Methanol vapor which can form hydrogen

bonding with the polar groups on the CNT surface showed the maximum response among the three. However, this mechanism can induce only a weak response. Hexane is not a good solvent for PMMA. Being nonpolar, it did not show any response. The poly(3-methylthiophene)/MWCNTs nanocomposite-based sensor was used to selectively discriminate between chloromethane and methane, as the sensor showed a high response to chloromethane, while no response was observed when exposed to methane or many other VOCs [43]. The response and recovery time of the sensor was about 60 seconds and 30–45 seconds, respectively. The sensing mechanism was proposed to be based on ionization potential of the analytes. The nanocomposite sensor does not respond to vapors of acetone, acetaldehyde, benzaldehyde, tetrahydrofuran, methanol and ethanol. Zhang et al. fabricated the conductive polymer composites by in situ polymerization of styrene (PS) in the presence of MWCNTs or solution mixing of polystyrene with MWCNTs, respectively [44]. Compared with the composites prepared by solution mixing, the ones by in situ polymerization show much higher response to organic vapors over a wide range of MWCNTs (5–15 wt.%). Sorption of organic vapors into the polymeric phase of the composites leads to swelling of the matrix, expands the interparticulates' intervals and partially destroys the conductive networks. As a result, a drastic rise in resistivity of the materials is perceived. When the amount of MWCNT in the composites is low, tunneling effect contributes to conduction of the composites to a great extent besides the direct interfiller contacts. In the case of high MWCNT content, the excessive fillers inevitably resulted in aggregation of MWCNTs and broke the conducting paths. Only at certain optimized filler content, the conducting paths are mainly constructed by the bridged MWCNTs, which are easy to be broken down by the swelling of the matrix, and the vapor response reaches the maximum. The composites synthesized through polymerization-filling exhibit significant responsiveness to those organic vapors which are good solvents for the matrix, like tetrahydrofuran (THF), benzene, toluene, cyclohexane, carbon tetrachloride, chloroform, ethyl acetate and diethyl ether within short time of exposure, but low in response to those nonsolvents, such as alcohol. The resistance can be quickly and completely recovered to its original value as soon as the sample is transferred into air. Niu et al. constructed a highly selective gas sensor by chemical modification of MWCNTs containing carboxyl groups (MWCNT-COOH) with poly(ethylene glycol) (PEG) in the presence of N,N-dicyclohexylcarbodiimide (DCC) [45]. The MWCNTs grafted PEG sensor displayed high chemical selectivity, fast response and good reproducibility/high stability to chloroform vapor at room temperature. The resistance of the sensing film drastically increased over 10^7 within 1 second upon exposed to chloroform vapor. When it was transferred from the solvent vapor into dry air, the electrical resistance returned to the original value rapidly. This is attributed to the weak hydrogen bond interaction between chloroform vapor and polymers, which results in an abrupt adsorption of analyte molecules in a short time. The response of the MWNT-g-PEG system toward ethanoic acid and water is about 10^2 and 10^1 respectively, and only very

small response to any other solvent vapors was observed, and the film did not respond basically against nonpolar solvent vapors, for example, n-hexane.

Vertically aligned carbon nanotubes have also been modified with polymers for gas sensors. Valentini et al. fabricated a gas sensor by selective growth of aligned CNTs on $\text{Si}_3\text{N}_4/\text{Si}$ substrates patterned by metallic platinum [46]. The sensor was presented for inorganic vapor detection at room temperature. Poly(o-anisidine) (POAS) deposition onto the CNTs device was shown to impart higher response to the sensor. Upon exposure to HCl, the variation of the CNTs response is less than 4%, while the POAS-coated CNTs devices offer a higher response of 28%. The extended detection capability to inorganic vapors is attributed to direct charge transfer with electron hopping effects on intertube conductivity through physically adsorbed POAS between CNTs. Wei et al. developed novel multifunctional chemical sensors based on vertically aligned MWCNTs and polymer composites [47]. The sensors were fabricated by partially coating perpendicularly aligned MWCNTs with polymers, such as poly(vinyl acetate), polyisoprene, and then sputtering with gold electrodes. Rapid and reversible sensing of high concentrations of a variety of volatile organic solvents was demonstrated. The sensing mechanism was attributed to the charge transfer interaction with gas molecules and/or the intertube distance change induced by polymer swelling during gas adsorption.

Gas-sensing performance of polymer functionalized CNT gas sensors is summarized in Table 2.

3.3. Gas Sensors Based on Metal Nanoparticles Modified CNTs.

Metals exhibit a broad range of electronic, chemical and physical properties that are often highly sensitive to changes in their chemical environment [48]. They are mechanically and chemically robust and stable, hence, compared to polymer-based sensors, metal-based sensors can operate at higher temperature and in harsher environment.

Palladium is one of the most important metal catalysts for activation of small molecules such as H_2 . It is also used as active component in gas sensors, including CNTs-based gas sensors. Kong et al. demonstrated room temperature H_2 sensors based on Pd nanoparticles modified SWCNTs prepared by electron-beam evaporation deposition [49]. Pd-functionalized SWCNTs were shown to be highly sensitive toward H_2 , with 50% greater response of up to 50% relative resistance change to 400 ppm H_2 compared to bare SWCNT bundles. The response time was 5–10 seconds, and the time for recovery was about 400 seconds. It is well established that at room temperature, the adsorbed H_2 molecules on the surface of Pd nanoparticles are dissociated as hydrogen atoms, which dissolve into Pd with high solubility, leading to a decrease in the work function of Pd. This causes electron transfer from Pd to SWCNT and reduces the hole-carriers in the p-type SWCNT, and hence causes a decrease in conductance. The process is reversible as dissolved atomic hydrogen in Pd can combine with O_2 in air to form OH which will further combine with atomic hydrogen to form water and then leave the Pd-SWCNT system, thus

TABLE 2: Summary of sensing performance of polymer functionalized CNT sensors. (Note: N/S = Not-stated.)

polymer	CNT type	Sensor configuration	Targeted analytes	Detection limit	Response time	Recovery time	Reference
PEI, Nafion	SWCNTs	FET	NO ₂ , NH ₃	100 ppb NO ₂	~1-2 min	N/S	[36]
PABS	SWCNTs	Resistor	NH ₃ , NO ₂ , H ₂ O	20 ppb NO ₂ , 100 ppb NH ₃	1–10 min	Several hours	[38]
PPy	SWCNTs	FET	NO ₂	N/S	N/S	~2 h	[39]
PPy	S-SWCNT	FET	NO ₂ , NH ₃	100 ppm NO ₂ , 5 ppm NH ₃	N/S	N/S	[40]
PDPA	MWCNTs	Electrochemical gas sensor	CO	0.01 ppm	~2 s	~3 s	[41]
PMMA	MWCNTs	Resistor	dichloromethane, chloroform, acetone	N/S	2–5 s	~10 s	[42]
Poly(3-methylthiophene)	MWCNTs	Resistor	CH ₂ Cl ₂ , CHCl ₃ , CCl ₄ , CH ₄	N/S	60 s	30–45 s	[43]
polystyrene	MWCNTs	Resistor	the good solvents of PS	N/S	<4 min	~1 min	[44]
PEG	MWCNTs	Resistor	chloroform	N/S	<1 s	N/S	[45]
POAS	ACNTs	Resistor	HCl	100 ppm	N/S	N/S	[46]
poly(vinylacetate), polyisoprene, etc.	ACNTs	Resistor	Ethanol cyclohexane, tetrahydrofuran	N/S	<2 min	<2 min	[47]

recovering the sensor's initial conductance. Sayago et al. reported two different methods for the functionalization of SWCNTs with Pd for H₂ sensors [50]. The SWCNTs either being chemically functionalized with Pd or sputtered with Pd showed increased resistance when exposed to 0.1–2% H₂ at room temperature. The chemically functionalized Pd-SWCNTs sensors were superior to the sputtered ones. Both response time and response decreased with increasing temperature. However, only aged sensors provided good selectivity with minimum response to octane, toluene and ammonia in reversible and reproducible experiments performed at room temperature. This might be related to changes in the employed material, for example, introduction of carboxylic acid functionalities due to oxygen exposure, and/or to the complete removal of solvent residues, that might increase either the effective surface area or the hydrogen adsorption capabilities. Mubeen et al. developed a simple electrochemical functionalization method to fabricate a H₂ nanosensor by site-specific electrodeposition of Pd nanoparticles on SWCNTs [51]. Optimal sensing performance was obtained by varying the synthesis conditions (e.g., Pd electrodeposition charge, deposition potential and initial baseline resistance of the SWCNTs network). At room temperature, the optimized sensor showed good response toward H₂ (0.42% resistance change per ppm) with a detection limit of 100 ppm and a linear response up to 1000 ppm. The response time decreased from tens of minutes to a few minutes with increasing hydrogen concentration. The sensor's recovery time was shortened under humid air compared to dry air condition. Complete recovery was observed for the sensors at all tested concentration range and recovery time varied from 20 minutes at 100 ppm to

55 minutes at 1000 ppm. H₂ sensors based on SWCNTs decorated with Pd nanoparticles via a simple electrodeposition process on a flexible plastic substrate have also been demonstrated [52]. The Pd functionalized SWCNTs flexible sensors could readily detect 100 ppm H₂ (with 5% relative response) at room temperature. The response time for 37% of the steady state resistance change was in the range of a few seconds up to 1 minute, or close to 5 minutes to reach a value close to steady state. The typical flexible sensors exhibited response of ~75% for 0.05% hydrogen in air and response time of ~3 seconds for 1% hydrogen at room temperature. The mechanical bendability of the flexible sensors was proved to have negligible effect (<5%) on the sensing performance. Oakley et al. prepared SWCNTs films by a simple filtration process, subsequently coated with palladium [53]. The Pd-coated SWCNTs film could detect 10 ppm H₂ at room temperature and relative resistance change was about 20% for 100 ppm H₂ and 40% for 500 ppm H₂. The time for substantial recovery is less than 30 seconds when exposed to air and the power consumption is 0.25 mW. Ding et al. [54] fabricated robust CNTs-based hydrogen sensors with aligned CNTs grown in an anodic aluminum oxide (AAO) template. Without Pd modification, an Au-electrode CNTs sensor showed no response to H₂. A Pd-electrode CNTs sensor could detect H₂ (from 0.1% to 1.5% H₂) with a reversible response at room temperature. Typical response time of the Pd-electrode CNTs sensor is about 3-4 minutes. Furthermore, the CNTs grown in the AAO template were also demonstrated to be a good supporting material for nanoporous Pd film sensors. Typical response time of the CNTs-supported Pd film sensor is less than 7 minutes for dilute H₂, and less

than 4 minutes for medium concentration of H_2 . For the Pd-electrode CNT sensor, CNTs provide better contacts between the Pd-electrode and the substrate, while for the CNT-supported Pd film sensor, CNTs provide a better mechanical support and anchoring role so that the Pd film does not peel off easily after exposure to H_2 . The Pd film in the CNT-supported Pd film sensor mainly contributes to the total resistance of the sensor. Whereas, in the Pd-electrode CNT sensor, both the Pd film and the CNTs contribute to the total resistance of the sensor. Since the CNTs are less sensitive to hydrogen gas than the Pd is, less response has been found with the Pd-electrode CNT sensor than that with the CNT-supported Pd film sensor. SWCNTs coated with Pd nanoparticles by sputtering have been used to detect CH_4 ranging from 6 to 100 ppm. At room temperature, the Pd coated SWCNTs sensors give reproducible trends and consistently respond to heat and UV light for speed recovery [55]. A charge transfer sensing mechanism was proposed. Hydrogen atoms in CH_4 attract electrons from Pd, and electrons are withdrawn from the SWCNTs. This results in a weakly bound complex $Pd^{\delta+}(CH_4)^{\delta-}$, leaving more holes in the SWCNTs, thereby increasing the conductance of p-type or hole-occupied SWCNTs when exposed to CH_4 . Li et al. reported a composite of MWCNTs/Pd prepared by a facile method of chemical reduction exhibited a reversible and reproducible response magnitude of 4.5% toward 2% CH_4 at room temperature [56]. The response and recovery time was estimated to be 310 seconds and 176 seconds, respectively. The inert CH_4 does not undergo a charge transfer reaction with the MWCNTs to initiate a change in electrical properties, so MWCNTs alone are insensitive to methane. In the composite, the palladium nanoparticles undergo a weak interaction with the CH_4 molecules adsorbed on the composite to form a long range weakly bound complex $Pd^{\delta+}(CH_4)^{\delta-}$ at room temperature. The MWCNTs donate electrons to Pd^0 to promote the formation of the complex where CH_4 is electronegative. The hole density in the MWCNTs is thus increased, resulting in a higher current in the composite.

Carbon nanotubes have also been modified with other metals for gas sensors. Kumar et al. fabricated H_2 sensors based on MWCNTs functionalized with Pt or Pd by aqueous solution reduction of H_2PtCl_6 or $PdCl_2$ [57, 58]. They showed high response and reversibility at room temperature. The response time and recovery time are 10 minutes and 15 minutes for MWCNTs functionalized with Pt, respectively. Both the response time and recovery time are about 7 minutes for Pd-MWCNTs. The dissolved atomic hydrogen in Pt or Pd interstitials and the chemisorbed hydrogen on MWCNTs combine with oxygen in air, departing the Pt-MWCNTs or Pd-MWCNTs system in the form of water and thus recovering the sample electrical characteristics. Hydrogen sensing properties of Pd-decorated SWCNTs bundles and Pd-decorated exfoliated SWCNTs via Arabic gum treatment showed an improved hydrogen sensing behavior due to improved accessible surface area [59]. The response time and recovery time are 10 minutes and 14 minutes for Pd-exfoliated SWCNTs, respectively. The exfoliated SWCNTs are loosely bound and this results in an increase in accessible

surface area of SWCNTs which in turn decreases the time scale for the adsorbed hydrogen to escape from the sample surface. The resistance change in Pd-exfoliated SWCNTs is about 15%, which is more than doubled when compared with nonexfoliated Pd-SWNT (about 5%). Kamarchuk et al. demonstrated the effect of point heterocontact between SWCNTs and a gold microwire on the gas response [60]. Au-SWCNTs heterocontact sensors exhibit high response to NH_3 and NO_2 with fast response and relaxation and these two gases can be distinguished based on the direction of charge transfer between the analyte and the SWCNTs. The response time to 200 ppb NH_3 was 150 seconds, and the recovery time was 200 seconds. The mechanism of sensing is associated with formation of a thin conductive channel between Au and SWCNTs but the sign of the resistance change is controlled by the SWCNTs. Penza et al. demonstrated Au and Pt nanocluster functionalized MWCNTs chemiresistive sensors for NO_2 and NH_3 sensing at working temperature of 100–250 °C [61]. Au and Pt nanoclusters were sputtered on the surface of MWCNTs. The gas response of Pt- and Au-functionalized MWCNT gas sensors significantly improved by a factor up to an order of magnitude for NH_3 and NO_2 detection, respectively. The enhancement of the gas response of the metal-modified MWCNT sensors could be caused by a combination of two additional effects of (1) direct charge injection and (2) catalytically induced charge into functionalized MWCNTs. Espinosa et al. coated MWCNTs with Au or Ag nanoclusters deposited by electron beam evaporation [62]. The decorated MWCNTs' sensors were able to detect NO_2 at the range of 500 ppb–6.5 ppm at room temperature and significantly more selective than sensors based on MWCNTs without metal nanoclusters attached to their surface. The response of Au-MWCNTs sensors to NO_2 was higher than the one of Ag-MWCNTs. Both materials showed a reversible behavior after NO_2 exposure, provided that their operating temperature was raised to 150 °C in a flow of dry air. Upon adsorption of NO_2 gas molecules, there is a significant charge transfer between the metallic nanoclusters and the nanotubes, which results in a measurable change in the overall conductance of the active film. The decorated MWCNTs sensors were almost insensitive to CO, ethanol, or ethylene at concentrations up to 50 ppm.

Metal nanoparticle functionalized CNTs sensor arrays have also been reported. Star et al. fabricated gas sensor arrays by site-selective electroplating of Au, Pt, Pd, and Rh metals on isolated SWCNTs networks located on a single chip [63]. The difference in catalytic activities of the metal nanoparticles caused different selectivities for the detection of H_2 , CH_4 , CO, H_2S , NH_3 , and NO_2 . The output of the sensor array was analyzed using principal component analysis (PCA) and partial least squares regression (PLS) in order to identify the above-mentioned gases. Lu et al. demonstrated a gas sensor array composed of 32 sensing elements with pristine, metal-decorated (Pd, Au), and polymer-decorated SWCNTs for discriminating gases such as NO_2 , HCN, HCl, Cl_2 , acetone, and benzene at ppm levels [64]. CNTs-based technology holds the potential to excel in the design of arrays because the inherently small size of CNTs devices will allow for the integration of large numbers of functionalized

CNTs sensor elements that would show a unique response to numerous species.

Gas-sensing performance of metal functionalized CNT gas sensors is summarized in Table 3.

3.4. Gas Sensors Based on Nanostructured Oxides Modified CNTs. Metal oxide gas sensors have been investigated extensively since decades ago owing to their advantages of high response to pollutant gases, fast response and recovery, low cost, easy implementation, and small in size. However, they are usually operated at temperature range between 200 and 800°C. Sensors based on metal oxides (SnO₂, WO₃ or TiO₂) modified CNTs can detect gases such as NO₂, CO, NH₃ and ethanol vapors at low operating temperature with improved sensing properties.

Recently, sensors based on SWCNTs/SnO₂ nanocomposites with enhanced gas sensing performance have been reported. Wei et al. constructed SWCNTs/SnO₂ gas sensor by incorporating SWCNTs into a SnO₂ substrate. The fabrication involved heat treatment of the SWCNTs/SnO₂ layer, which was fabricated by spin coating using an organometallic solution dispersed with SWCNTs [65]. The prepared SWCNTs/SnO₂ nanocomposite sensors exhibit much higher response and recovery property in detecting NO₂ at room temperature than the blank SnO₂ sensor. The response time and recovery time are 9 minutes and 1.5 minute, respectively. A model is presented to relate potential barriers to electronic conduction in the hybrid material. This model suggests that the high response is associated with the stretching of the depletion layers at the grain boundaries of SnO₂ and the SWCNTs interfaces when detected gases are adsorbed. Gong et al. developed MEMS-based sensors integrated with nanocrystalline SWCNTs/SnO₂ sensing films realized by a polymeric sol-gel process [66]. The response of the SWCNTs/SnO₂ sensor is three times greater than that of the pure SnO₂ sensor with faster response and recovery in hydrogen detection. The response time and recovery time are 2–5 seconds and 3–5 seconds at the working temperature of 200 and 250°C, respectively. The working temperature has been reduced as low as 150°C. The greatly improved performance is attributed to the effective gas accessing nanopasses formed by SWCNTs. Hoa et al. fabricate an NH₃ sensor with a composite of SWCNTs and SnO₂ [67]. The sensor could detect the concentration of NH₃ down to 10 ppm at room temperature, and exhibited a fast response time of 100 seconds and recovery time of about 3.2 minutes. The SWCNTs in the matrix of SnO₂ provide the main conducting channels that effectively varies in its conductance upon adsorption of NH₃. The recovery time depends on the bonding force of NH₃ molecules to the SWCNT surface with respect to the desorption under nitrogen flowing. Thus, it can vary with the nitrogen flow rate.

MWCNTs have also been incorporated with SnO₂ for gas sensors with improved sensing properties. Liu et al. synthesized a compound material of MWCNTs coated with SnO₂ at ambient conditions [68]. The MWCNTs/SnO₂ sensor exhibited good sensing responses to liquefied petroleum gas (LPG) and ethanol (C₂H₅OH) vapor with fast response

and recovery within seconds at temperature of 335°C. Furthermore, the gas sensor response increased linearly with the increment of gas concentration of LPG and ethanol. The high response and low resistance may be attributed to the particular electrical transport mechanism. The resistance of the sensor is dominated by the barriers among the SnO₂ grains on the MWCNTs. Electrons travel through the SnO₂ grains into the MWCNTs, and then conduct in the MWCNTs with low resistance. Chen et al. synthesized MWCNTs/SnO₂ core/shell nanostructures by a simple wet-chemical method [69]. The thickness of the SnO₂ shell was about 10 nm and the diameters of the SnO₂ particles were 2–8 nm. Sensors based on the core/shell heterostructures exhibited enhanced ethanol sensing properties at working temperature of 300°C. The response to 50 ppm ethanol was up to 24.5, and the response time and recovery time were about 1 and 10 seconds, respectively. In addition, the fluctuation of the response was less than ±3% on remeasurement after 3 months. The enhanced ethanol sensing properties are attributed to the small size of the SnO₂ nanoparticles and the heterojunction of the core/shell structures of MWCNTs/SnO₂. Espinosa et al. demonstrated that the addition of a small quantity of oxygen-functionalized MWCNTs to metal oxides (SnO₂, WO₃ or TiO₂) can significantly improve the detection capability of metal oxides-based sensors at low operating temperature [70]. In particular, microsensors based on SnO₂/MWCNTs hybrid films operated at room temperature showed higher response towards NO₂ in the ppb range. TiO₂/MWCNTs sensors showed the lowest response to NO₂ and irresponsive to CO even at 150°C. The recovery time of the SnO₂/MWCNTs sensors was reduced from 45 minutes at room temperature down to 20 minutes at 150°C, while in the case of WO₃/MWCNTs sensors, the recovery time was reduced from 120 to 45 minutes. Furthermore, the response is fully reversible. A mechanism of response based on the development of two depletion layers, one at the surface of metal oxide grains and another at the interface of the n-metal oxide/p-MWCNT heterostructure, is postulated to be responsible for the improvement observed. Hieu et al. fabricated an SnO₂/MWCNTs composite-based NH₃ sensor by thin film microelectronic technique [71]. At room temperature, the optimal composite sensor exhibited much higher response and faster response recovery (less than 5 minutes) to NH₃ with concentration from 60 to 800 ppm, in comparison with the CNTs-based NH₃ sensor. The enhancement of the response to NH₃ of the composite sensors may result from the p-n heterojunction formed by CNTs and SnO₂ nanoparticles. The response of the MWCNTs/SnO₂ composite thin film gas sensor strongly depends on the preparation process of the sensitive film. The composite thin film with 15 wt% MWCNTs with diameter of 60–100 nm, the calcination temperature of 530°C under vacuum of 10⁻² Torr, and the film thickness of 400 nm are optimal conditions. The response of the sensor to NH₃ increases with increasing MWCNTs content and the composites using MWCNTs with the larger diameter show higher response because larger diameter MWCNTs would increase the number of gas molecules adsorbed on the

TABLE 3: Summary of sensing performance of metal functionalized CNT sensors. (Note: N/S = Not-stated.)

Metal	CNT type	Sensor configuration	Targeted analytes	Detection limit	Response time	Recovery time	Reference
Pd	S-SWCNT	FET	H ₂	<40 ppm	5–10 s (for half resistance change)	400 s	[49]
Pd	SWCNTs	Resistor	H ₂	1000 ppm	N/S	N/S	[50]
Pd	SWCNTs	Resistor	H ₂	100 ppm	10 min	20 min	[51]
Pd	SWCNTs	Resistor	H ₂	100 ppm	3–60 s (for 36.8% resistance change)	~5 min	[52]
Pd	SWCNTs	Resistor	H ₂	~10 ppm	<10 min	<30 s	[53]
Pd	ACNTs	Resistor	H ₂	100 ppm	<7 min	N/S	[54]
Pd	SWCNTs	Resistor	CH ₄	6 ppm	2–4 min	N/S	[55]
Pd	MWCNTs	Resistor	CH ₄	2%	~310 s	~176 s	[56]
Pt	MWCNTs	Resistor	H ₂	N/S	10 min	15 min	[57]
Pd	MWCNTs	Resistor	H ₂	N/S	7 min	7 min	[58]
Pt	MWCNTs	Resistor	H ₂ , NO ₂ , H ₂ O	N/S	~10 min	~14 min	[59]
Au	SWCNTs	Resistor	NH ₃ , NO ₂	<120 ppb NH ₃	150 s	200 s	[60]
Au, Pt	MWCNTs	Resistor	NO ₂ , NH ₃	100 ppb NO ₂ , 5 ppm NH ₃	N/S	N/S	[61]
Au, Ag	MWCNTs	Resistor	NO ₂	500 ppb NO ₂	~20 min	N/S	[62]
Pt, Pd, Sn, Rh	SWCNTs	FET	H ₂ , CH ₄ , CO, H ₂ S	N/S	~5 min	N/S	[63]
Pd, Au	SWCNTs	Resistor	NO ₂ , HCN, HCl, Cl ₂ , acetone, benzene	5 ppm	N/S	N/S	[64]

material. Increasing the annealing temperature may result in the improvement of the contact between SnO₂ nanoparticles and CNTs but the higher calcinated temperature may also result in burning of CNTs by residual oxygen or damaging of CNTs structure. An increase in thickness of the thin film composite sensors results in a decrease in the response due to the increase of the diffusion length of gases. Wang et al. reported a gas sensor based on SnO₂ doped with hydroxyl functionalized MWCNTs for detecting indoor formaldehyde [72]. The response of the MWCNTs-doped SnO₂ sensor was much higher than that of an undoped SnO₂ sensor. The lowest concentration of formaldehyde vapor detected by a 5 wt.% MWCNTs-doped SnO₂ sensor was 0.03 ppm. The response and recovery time of the sensor to 0.05 ppm formaldehyde vapor is about 100 seconds and 90 seconds at 250°C. The sensor response to formaldehyde is higher than to acetone, methanol, toluene, benzene and ammonia. High adsorption capacity of MWCNTs enhance the adsorption ability of the SnO₂ for formaldehyde molecules. Reducing molecules like formaldehyde act as temporary n-type dopants when they interact with CNTs, which leads to a decrease in resistance and hence to an increase in response of the MWCNTs doped SnO₂ sensor. The MWCNTs-doped SnO₂ material contains at least three kinds of interfaces, such as between SnO₂ grains, between MWCNTs, and between SnO₂ grains and CNTs (existence of a heterostructure). Bittencourt et al. demonstrated that WO₃ films impregnated with MWCNTs showed response to 500 ppb NO₂ under ambient conditions and 10 ppm NH₃ at 150°C, far below the typical operating temperature of WO₃ sensors [73]. Oxygen plasma functionalized MWCNTs were added to WO₃

by drop-coating deposition method. The adsorption at the surface of CNTs modifies the depletion layer at the n-WO₃/p-MWCNTs heterojunctions and this results in the modulation of the depletion layer at the surface of WO₃ grains. This change in the depletion layer at the n/p junction that induces change in the WO₃ matrix may explain the improvement in response shown by hybrid sensors.

The detection of acetone and NH₃ was found to be possible at ambient temperature with TiO₂/MWCNTs gas sensors fabricated by sol-gel method [74]. The TiO₂/MWCNTs composites obtained by Ti-isopropoxide route are reported as room temperature sensitive coatings. Sensing was highly reproducible in the composites, with fast adsorption/desorption cycles at room temperature. Composites based on as-received MWCNTs show an increase in films resistance during acetone and ammonia adsorption, while composites based on functionalized MWCNTs show longer acetone desorption time (300 seconds) and a decrease in resistance during ammonia sensing. Theoretical ab initio calculations predicted an inversion in the acetone → Ti_xO_y/CNT charge transfer direction as the size of the oxide cluster increases, explaining the inverse changes in resistance of the composites versus the components but have not been successful in explaining the differences observed in the composites during NH₃ adsorption. Detection of NH₃ might be also possible through the intertube modulation effect (i.e., MWCNT-TiO₂/NH₃-MWCNT junctions) and where titania is acting as a buffer layer to avoid MWCNTs dedoping. Llobet et al. fabricated resistive oxygen sensors based on TiO₂/MWCNTs hybrids by drop-coating method [75]. The hybrid layers based on TiO₂ and MWCNTs possess

TABLE 4: Summary of sensing performance of metal oxide functionalized CNT sensors. (Note: N/S = Not-stated.)

Metal oxide	CNT type	Sensor configuration	Targeted analytes	Detection limit	Response time	Recovery time	Reference
SnO ₂	SWCNTs	Resistor	NO ₂	N/S	9 min	1.5 min	[65]
SnO ₂	SWCNTs	Resistor	H ₂	300 ppm	2–5 s (200–250°C)	3–5 s (200–250°C)	[66]
SnO ₂	SWCNTs	Resistor	NH ₃	10 ppm	~100 s	~3.2 min	[67]
SnO ₂	MWCNTs	Resistor	LPG, C ₂ H ₅ OH	10 ppm	N/S	N/S	[68]
SnO ₂	MWCNTs	Resistor	C ₂ H ₅ OH	10 ppm	~1 s (300°C)	~10 s (300°C)	[69]
SnO ₂	MWCNTs	Resistor	NO ₂	100 ppb	N/S	20 min (150°C)	[70]
SnO ₂	MWCNTs	Resistor	NH ₃	60 ppm	<5 min	<5 min	[71]
SnO ₂	MWCNTs	Resistor	formaldehyde	0.03 ppm	100 s (250°C)	90 s (250°C)	[72]
WO ₃	MWCNTs	Resistor	NO ₂ , CO, NH ₃	500 ppb NO ₂ , 10 ppm NH ₃	N/S	N/S	[73]
TiO ₂	MWCNTs	Resistor	acetone, NH ₃	N/S	10–40 s (acetone)	10–300 s (acetone)	[74]
TiO ₂	CNTs	Resistor	O ₂	10 ppm	5–8 min (350–550°C)	~20 min (350°C)	[75]
SnO ₂ , TiO ₂	SWCNTs, MWCNTs	Resistor	C ₂ H ₅ OH	100 ppm	<10 s (210–400°C)	<10 s (210–400°C)	[76]

an unprecedented responsiveness toward oxygen (i.e., more than four times higher than that shown by optimized Nb-doped TiO₂ films). Furthermore, hybrid sensors containing MWCNTs respond at significantly lower operating temperature than their nonhybrid counterparts. These new hybrid sensors show a strong potential for monitoring traces of oxygen (i.e., <10 ppm) in a flow of CO₂. The heterostructure n-TiO₂/p-MWCNTs can be formed at the interface between titania and carbon nanotubes. Hybrid sensors are significantly more responsive to oxygen than pure or Nb-doped titania sensors because a slight change in the concentration of adsorbed oxygen at its surface can result in a significant change in the depletion layer at the n-TiO₂/p-MWCNT heterostructure. Duy et al. constructed SnO₂-TiO₂ and MWCNTs-included SnO₂-TiO₂ thin films by sol-gel spin coating [76]. The inclusion of MWCNTs at specific contents into the mixed oxides improved response of the sensor at low operating temperature (below 280°C). The response and recovery time of the sensors is less than 10 seconds at operating temperature of 210–400°C. The improvement of the gas sensor performance and the shift of operation temperature toward the lower temperature region can be attributed to the amplification effect of the p-n junctions in addition to the effect of the grain boundaries.

Gas-sensing performance of metal oxides functionalized CNT gas sensors is summarized in Table 4.

4. Gas Sensors Based on Heteroatom-Containing Nanotubes

Doping of SWCNTs with heteroatoms will change the electronic properties of the nanotubes, thus changing their

interaction with gas molecules and their sensing properties as well. Theoretical calculation predicted that SWCNTs doping with B, N, and so forth will enhance their sensing properties toward electron-rich or electron-scarce molecules. Pristine CNTs-based gas sensors are currently limited to sense gases such as NH₃, NO₂, SO₂, O₂, and NO. However, many highly toxic gases (such as CO and formaldehyde) cannot be detected using the pristine CNTs gas sensors. To improve gas-sensing performance, Peng et al. propose to use B or N doped SWCNTs, or composite B_xC_yN_z nanotubes as sensing element [77]. Using first-principle calculations, they demonstrated that these sensors can detect CO and water molecules, and more important, the response of these sensors can be controlled by adjusting the doping level of heteroatoms in a nanotube. Subsequently, Wang et al. investigated reactivities of the intrinsic and Al-doped SWCNTs with CO by density functional theory (DFT) calculations [78]. The Al-doped SWCNTs present high response to CO, compared with the intrinsic SWCNTs. Wang et al. [79] and Zhang et al. [80] investigated reactivities of B-doped SWCNTs with HCOH or HCN by using density functional theory calculations. Compared with the intrinsic SWCNTs, B-doped SWCNTs presents high response to HCOH or HCN. This is attributed to the strong chemical interaction between the electron-rich oxygen atom in HCOH or nitrogen atom in HCN and the electron-scarce boron atom of the doped SWCNTs. Bai and Zhou [81] investigated the adsorption of NH₃ and NO₂ in B- or N-doped SWCNTs by using density functional computations. The N-doping did not change NH₃ adsorption on SWCNTs but B-doped SWCNTs could be used for NH₃ sensing. Both B- and N-doping made NO₂ chemisorption feasible in SWCNTs but the binding of NO₂ with B was too strong, indicating an impractical recovery time as gas sensors.

5. Conclusion and Remark

Carbon nanotubes are active elements for sensing a broad variety of gases with high response because of their unique structure and electronic properties, and their rich configurations as well. Modification of carbon nanotubes with functional groups and metal nanoparticles or incorporation of carbon nanotubes with polymers and metal oxides will greatly enhance the selectivity of the carbon nanotubes-based sensors. CNTs-based gas sensors have proved to work well at room temperature, which reduces power consumption of the device and enables the safer detection of flammable gases. However, much effort has to be done before the practical application of CNTs-based gas sensors. Firstly, CNTs with defined structure and property need to be produced in large quantity at low cost. Secondly, the sensing properties, especially the selectivity and recovery, have to be improved. For practical application, gas sensors are required to be with high selectivity, low operating temperature, quick response and recovery. One common disadvantage of CNTs-based gas sensors is the potential interference from relative humidity at room temperature. Other main drawbacks are slow recovery and poor selectivity. There have been a variety of attempts such as heat treatment, ultraviolet light irradiation, increasing carrier gas flux, and modification of CNTs with functional groups or other additives to overcome the limitation. The instability of the CNTs in air at elevated temperature will limit CNTs-based gas sensors being operated at high temperature. CNTs-based gas sensors are sensitive to many gases or vapors such as NO₂, NH₃, H₂, CH₄, and Cl₂ at room temperature but the operating temperature of CNTs-based gas sensors for detecting O₂, C₂H₅OH, LPG, and formaldehyde is still relatively high. More efforts are needed on studying the long-term stability and reliability of the CNTs-based sensors, which has been less studied. Nevertheless, the discovery of carbon nanotubes, a group of outstanding nanomaterials, provides excellent candidates for gas sensors, especially for nanosensors which could be vital to their specific applications such as in space shuttles and satellites. Sensors based on single SWCNT FET, well-aligned CNTs structure for field emission devices, or electrochemical systems are the most promising devices for practical applications.

Acknowledgments

Financial support of the work by the Research Fund for the Doctoral Program of Higher Education (RFDP) under Grant 20070561008 and the Natural Science Foundation of China under Grant 20773041 is greatly acknowledged.

References

- [1] Y. Saito, G. Dresselhaus, and M. S. Dresselhaus, *Physical Properties of Carbon Nanotubes*, Imperial College Press, London, UK, 1998.
- [2] H. Dai, "Nanotube growth and characterization," in *Carbon Nanotubes*, M. S. Dresselhaus, G. Dresselhaus, and P. Avouris, Eds., Springer, Berlin, Germany, 2001.
- [3] S. Iijima, "Helical microtubules of graphitic carbon," *Nature*, vol. 354, no. 6348, pp. 56–58, 1991.
- [4] S. Iijima and T. Ichihashi, "Single-shell carbon nanotubes of 1-nm diameter," *Nature*, vol. 363, no. 6430, pp. 603–605, 1993.
- [5] J. J. Davis, K. S. Coleman, B. R. Azamian, C. B. Bagshaw, and M. L. H. Green, "Chemical and biochemical sensing with modified single walled carbon nanotubes," *Chemistry: A European Journal*, vol. 9, no. 16, pp. 3732–3739, 2003.
- [6] J. Zhao, A. Buldum, J. Han, and J. P. Lu, "Gas molecule adsorption in carbon nanotubes and nanotube bundles," *Nanotechnology*, vol. 13, no. 2, pp. 195–200, 2002.
- [7] J. Kong, N. R. Franklin, C. Zhou, et al., "Nanotube molecular wires as chemical sensors," *Science*, vol. 287, no. 5453, pp. 622–625, 2000.
- [8] J. Zhang, A. Boyd, A. Tselev, M. Paranjape, and P. Barbara, "Mechanism of NO₂ detection in carbon nanotube field effect transistor chemical sensors," *Applied Physics Letters*, vol. 88, no. 12, Article ID 123112, 3 pages, 2006.
- [9] T. Helbling, R. Pohle, L. Durrer, et al., "Sensing NO₂ with individual suspended single-walled carbon nanotubes," *Sensors and Actuators B*, vol. 132, no. 2, pp. 491–497, 2008.
- [10] S. Peng, K. Cho, P. Qi, and H. Dai, "Ab initio study of CNT NO₂ gas sensor," *Chemical Physics Letters*, vol. 387, no. 4–6, pp. 271–276, 2004.
- [11] J. P. Novak, E. S. Snow, E. J. Houser, D. Park, J. L. Stepnowski, and R. A. McGill, "Nerve agent detection using networks of single-walled carbon nanotubes," *Applied Physics Letters*, vol. 83, no. 19, pp. 4026–4028, 2003.
- [12] N. Peng, Q. Zhang, Y. C. Lee, O. K. Tan, and N. Marzari, "Gate modulation in carbon nanotube field effect transistors-based NH₃ gas sensors," *Sensors and Actuators B*, vol. 132, no. 1, pp. 191–195, 2008.
- [13] M. Lucci, A. Reale, A. Di Carlo, et al., "Optimization of a NO_x gas sensor based on single walled carbon nanotubes," *Sensors and Actuators B*, vol. 118, no. 1–2, pp. 226–231, 2006.
- [14] J. Li, Y. Lu, Q. Ye, M. Cinke, J. Han, and M. Meyyappan, "Carbon nanotube sensors for gas and organic vapor detection," *Nano Letters*, vol. 3, no. 7, pp. 929–933, 2003.
- [15] R. J. Chen, N. R. Franklin, J. Kong, et al., "Molecular physisorption from single-walled carbon nanotubes," *Applied Physics Letters*, vol. 79, no. 14, pp. 2258–2260, 2001.
- [16] N. H. Quang, M. Van Trinh, B.-H. Lee, and J.-S. Huh, "Effect of NH₃ gas on the electrical properties of single-walled carbon nanotube bundles," *Sensors and Actuators B*, vol. 113, no. 1, pp. 341–346, 2006.
- [17] H.-Q. Nguyen and J.-S. Huh, "Behavior of single-walled carbon nanotube-based gas sensors at various temperatures of treatment and operation," *Sensors and Actuators B*, vol. 117, no. 2, pp. 426–430, 2006.
- [18] O. K. Varghese, P. D. Kichambre, D. Gong, K. G. Ong, E. C. Dickey, and C. A. Grimes, "Gas sensing characteristics of multi-wall carbon nanotubes," *Sensors and Actuators B*, vol. 81, no. 1, pp. 32–41, 2001.
- [19] L. H. Nguyen, T. V. Phi, P. Q. Phan, H. N. Vu, C. Nguyen-Duc, and F. Fossard, "Synthesis of multi-walled carbon nanotubes for NH₃ gas detection," *Physica E*, vol. 37, no. 1–2, pp. 54–57, 2007.
- [20] S.-I. Moon, K.-K. Paek, Y.-H. Lee, et al., "Bias-heating recovery of MWCNT gas sensor," *Materials Letters*, vol. 62, no. 16, pp. 2422–2425, 2008.
- [21] J. Suehiro, G. Zhou, and M. Hara, "Detection of partial discharge in SF₆ gas using a carbon nanotube-based gas sensor," *Sensors and Actuators B*, vol. 105, no. 2, pp. 164–169, 2005.

- [22] G. Sun, S. Liu, K. Hua, X. Lv, L. Huang, and Y. Wang, "Electrochemical chlorine sensor with multi-walled carbon nanotubes as electrocatalysts," *Electrochemistry Communications*, vol. 9, no. 9, pp. 2436–2440, 2007.
- [23] J. M. Nugent, K. S. V. Santhanam, A. Rubio, and P. M. Ajayan, "Fast electron transfer kinetics on multiwalled carbon nanotube microbundle electrodes," *Nano Letters*, vol. 1, no. 2, pp. 87–91, 2001.
- [24] R. Ionescu, E. H. Espinosa, E. Sotter, et al., "Oxygen functionalisation of MWNT and their use as gas sensitive thick-film layers," *Sensors and Actuators B*, vol. 113, no. 1, pp. 36–46, 2006.
- [25] J. Suehiro, G. Zhou, H. Imakiire, W. Ding, and M. Hara, "Controlled fabrication of carbon nanotube NO₂ gas sensor using dielectrophoretic impedance measurement," *Sensors and Actuators B*, vol. 108, no. 1-2, pp. 398–403, 2005.
- [26] L. Valentini, C. Cantalini, I. Armentano, J. M. Kenny, L. Lozzi, and S. Santucci, "Highly sensitive and selective sensors based on carbon nanotubes thin films for molecular detection," *Diamond and Related Materials*, vol. 13, no. 4–8, pp. 1301–1305, 2004.
- [27] W.-S. Cho, S.-I. Moon, K.-K. Paek, Y.-H. Lee, J.-H. Park, and B.-K. Ju, "Patterned multiwall carbon nanotube films as materials of NO₂ gas sensors," *Sensors and Actuators B*, vol. 119, no. 1, pp. 180–185, 2006.
- [28] T. Ueda, M. M. H. Bhuiyan, H. Norimatsu, S. Katsuki, T. Ikegami, and F. Mitsugi, "Development of carbon nanotube-based gas sensors for NO_x gas detection working at low temperature," *Physica E*, vol. 40, no. 7, pp. 2272–2277, 2008.
- [29] N. D. Hoa, N. Van Quy, Y. Cho, and D. Kim, "An ammonia gas sensor based on non-catalytically synthesized carbon nanotubes on an anodic aluminum oxide template," *Sensors and Actuators B*, vol. 127, no. 2, pp. 447–454, 2007.
- [30] C. S. Huang, B. R. Huang, Y. H. Jang, M. S. Tsai, and C. Y. Yeh, "Three-terminal CNTs gas sensor for N₂ detection," *Diamond and Related Materials*, vol. 14, no. 11-12, pp. 1872–1875, 2005.
- [31] M. Lucci, P. Regoliosi, A. Reale, et al., "Gas sensing using single wall carbon nanotubes ordered with dielectrophoresis," *Sensors and Actuators B*, vol. 111-112, pp. 181–186, 2005.
- [32] H.-L. Hsu, J.-M. Jehng, Y. Sung, L.-C. Wang, and S.-R. Yang, "The synthesis, characterization of oxidized multi-walled carbon nanotubes, and application to surface acoustic wave quartz crystal gas sensor," *Materials Chemistry and Physics*, vol. 109, no. 1, pp. 148–155, 2008.
- [33] J. Mäklin, T. Mustonen, K. Kordás, S. Saukko, G. Tóth, and J. Vähäkangas, "Nitric oxide gas sensors with functionalized carbon nanotubes," *Physica Status Solidi B*, vol. 244, no. 11, pp. 4298–4302, 2007.
- [34] D. Fu, H. Lim, Y. Shi, et al., "Differentiation of gas molecules using flexible and all-carbon nanotube devices," *Journal of Physical Chemistry C*, vol. 112, no. 3, pp. 650–653, 2008.
- [35] T. H. Tran, J.-W. Lee, K. Lee, Y. D. Lee, and B.-K. Ju, "The gas sensing properties of single-walled carbon nanotubes deposited on an aminosilane monolayer," *Sensors and Actuators B*, vol. 129, no. 1, pp. 67–71, 2008.
- [36] P. Qi, O. Vermesh, M. Grecu, et al., "Toward large arrays of multiplex functionalized carbon nanotube sensors for highly sensitive and selective molecular detection," *Nano Letters*, vol. 3, no. 3, pp. 347–351, 2003.
- [37] E. Bekyarova, M. Davis, T. Burch, et al., "Chemically functionalized single-walled carbon nanotubes as ammonia sensors," *Journal of Physical Chemistry B*, vol. 108, no. 51, pp. 19717–19720, 2004.
- [38] T. Zhang, S. Mubeen, E. Bekyarova, et al., "Poly(m-aminobenzene sulfonic acid) functionalized single-walled carbon nanotubes based gas sensor," *Nanotechnology*, vol. 18, no. 16, Article ID 165504, 6 pages, 2007.
- [39] K. H. An, S. Y. Jeong, H. R. Hwang, and Y. H. Lee, "Enhanced sensitivity of a gas sensor incorporating single-walled carbon nanotube-polypyrrole nanocomposites," *Advanced Materials*, vol. 16, no. 12, pp. 1005–1009, 2004.
- [40] X. Liu, J. Ly, S. Han, et al., "Synthesis and electronic properties of individual single-walled carbon nanotube/polypyrrole composite nanocables," *Advanced Materials*, vol. 17, no. 22, pp. 2727–2732, 2005.
- [41] P. Santhosh, K. M. Manesh, A. Gopalan, and K.-P. Lee, "Novel amperometric carbon monoxide sensor based on multi-wall carbon nanotubes grafted with polydiphenylamine-Fabrication and performance," *Sensors and Actuators B*, vol. 125, no. 1, pp. 92–99, 2007.
- [42] J. K. Abraham, B. Philip, A. Witchurch, V. K. Varadan, and C. C. Reddy, "A compact wireless gas sensor using a carbon nanotube/PMMA thin film chemiresistor," *Smart Materials and Structures*, vol. 13, no. 5, pp. 1045–1049, 2004.
- [43] K. S. V. Santhanam, R. Sangoi, and L. Fuller, "A chemical sensor for chloromethanes using a nanocomposite of multi-walled carbon nanotubes with poly(3-methylthiophene)," *Sensors and Actuators B*, vol. 106, no. 2, pp. 766–771, 2005.
- [44] B. Zhang, R. W. Fu, M. Q. Zhang, X. M. Dong, P. L. Lan, and J. S. Qiu, "Preparation and characterization of gas-sensitive composites from multi-walled carbon nanotubes/polystyrene," *Sensors and Actuators B*, vol. 109, no. 2, pp. 323–328, 2005.
- [45] L. Niu, Y. Luo, and Z. Li, "A highly selective chemical gas sensor based on functionalization of multi-walled carbon nanotubes with poly(ethylene glycol)," *Sensors and Actuators B*, vol. 126, no. 2, pp. 361–367, 2007.
- [46] L. Valentini, V. Bavastrello, E. Stura, I. Armentano, C. Nicolini, and J. M. Kenny, "Sensors for inorganic vapor detection based on carbon nanotubes and poly(o-anisidine) nanocomposite material," *Chemical Physics Letters*, vol. 383, no. 5-6, pp. 617–622, 2004.
- [47] C. Wei, L. Dai, A. Roy, and T. B. Tolle, "Multifunctional chemical vapor sensors of aligned carbon nanotube and polymer composites," *Journal of the American Chemical Society*, vol. 128, no. 5, pp. 1412–1413, 2006.
- [48] A. Ruiz, J. Arbiol, A. Cirera, A. Cornet, and J. R. Morante, "Surface activation by Pt-nanoclusters on titania for gas sensing applications," *Materials Science and Engineering C*, vol. 19, no. 1-2, pp. 105–109, 2002.
- [49] J. Kong, M. G. Chapline, and H. J. Dai, "Functionalized carbon nanotubes for molecular hydrogen sensors," *Advanced Materials*, vol. 13, no. 18, pp. 1384–1386, 2001.
- [50] I. Sayago, E. Terrado, M. Aleixandre, et al., "Novel selective sensors based on carbon nanotube films for hydrogen detection," *Sensors and Actuators B*, vol. 122, no. 1, pp. 75–80, 2007.
- [51] S. Mubeen, T. Zhang, B. Yoo, M. A. Deshusses, and N. V. Myung, "Palladium nanoparticles decorated single-walled carbon nanotube hydrogen sensor," *Journal of Physical Chemistry C*, vol. 111, no. 17, pp. 6321–6327, 2007.
- [52] Y. Sun and H. H. Wang, "Electrodeposition of Pd nanoparticles on single-walled carbon nanotubes for flexible hydrogen sensors," *Applied Physics Letters*, vol. 90, no. 21, Article ID 213107, pp. 1–3, 2007.
- [53] J. Sippel-Oakley, H.-T. Wang, B. S. Kang, et al., "Carbon nanotube films for room temperature hydrogen sensing," *Nanotechnology*, vol. 16, no. 10, pp. 2218–2221, 2005.

- [54] D. Ding, Z. Chen, S. Rajaputra, and V. Singh, "Hydrogen sensors based on aligned carbon nanotubes in an anodic aluminum oxide template with palladium as a top electrode," *Sensors and Actuators B*, vol. 124, no. 1, pp. 12–17, 2007.
- [55] Y. Lu, J. Li, J. Han, et al., "Room temperature methane detection using palladium loaded single-walled carbon nanotube sensors," *Chemical Physics Letters*, vol. 391, no. 4–6, pp. 344–348, 2004.
- [56] Y. Li, H. Wang, Y. Chen, and M. Yang, "A multi-walled carbon nanotube/palladium nanocomposite prepared by a facile method for the detection of methane at room temperature," *Sensors and Actuators B*, vol. 132, no. 1, pp. 155–158, 2008.
- [57] M. K. Kumar and S. Ramaprabhu, "Nanostructured Pt functionalized multiwalled carbon nanotube based hydrogen sensor," *Journal of Physical Chemistry B*, vol. 110, no. 23, pp. 11291–11298, 2006.
- [58] M. K. Kumar and S. Ramaprabhu, "Palladium dispersed multiwalled carbon nanotube based hydrogen sensor for fuel cell applications," *International Journal of Hydrogen Energy*, vol. 32, no. 13, pp. 2518–2526, 2007.
- [59] M. K. Kumar, A. L. M. Reddy, and S. Ramaprabhu, "Exfoliated single-walled carbon nanotube-based hydrogen sensor," *Sensors and Actuators B*, vol. 130, no. 2, pp. 653–660, 2008.
- [60] G. V. Kamarchuk, I. G. Kolobov, A. V. Khotkevich, et al., "New chemical sensors based on point heterocontact between single wall carbon nanotubes and gold wires," *Sensors and Actuators B*, vol. 134, no. 2, pp. 1022–1026, 2008.
- [61] M. Penza, G. Cassano, R. Rossi, et al., "Enhancement of sensitivity in gas chemiresistors based on carbon nanotube surface functionalized with noble metal (Au, Pt) nanoclusters," *Applied Physics Letters*, vol. 90, no. 17, pp. 171231–171233, 2007.
- [62] E. H. Espinosa, R. Ionescu, C. Bittencourt, et al., "Metal-decorated multi-wall carbon nanotubes for low temperature gas sensing," *Thin Solid Films*, vol. 515, no. 23, pp. 8322–8327, 2007.
- [63] A. Star, V. Joshi, S. Skarupo, D. Thomas, and J.-C. P. Gabriel, "Gas sensor array based on metal-decorated carbon nanotubes," *Journal of Physical Chemistry B*, vol. 110, no. 42, pp. 21014–21020, 2006.
- [64] Y. Lu, C. Partridge, M. Meyyappan, and J. Li, "A carbon nanotube sensor array for sensitive gas discrimination using principal component analysis," *Journal of Electroanalytical Chemistry*, vol. 593, no. 1–2, pp. 105–110, 2006.
- [65] B.-Y. Wei, M.-C. Hsu, P.-G. Su, H.-M. Lin, R.-J. Wu, and H.-J. Lai, "A novel SnO₂ gas sensor doped with carbon nanotubes operating at room temperature," *Sensors and Actuators B*, vol. 101, no. 1–2, pp. 81–89, 2004.
- [66] J. Gong, J. Sun, and Q. Chen, "Micromachined sol-gel carbon nanotube/SnO₂ nanocomposite hydrogen sensor," *Sensors and Actuators B*, vol. 130, no. 2, pp. 829–835, 2008.
- [67] N. D. Hoa, N. V. Quy, Y. S. Cho, and D. Kim, "Nanocomposite of SWCNTs and SnO₂ fabricated by soldering process for ammonia gas sensor application," *Physical Status Solidi A*, vol. 204, no. 6, pp. 1820–1824, 2007.
- [68] Y.-L. Liu, H.-F. Yang, Y. Yang, Z.-M. Liu, G.-L. Shen, and R.-Q. Yu, "Gas sensing properties of tin dioxide coated onto multi-walled carbon nanotubes," *Thin Solid Films*, vol. 497, no. 1–2, pp. 355–360, 2006.
- [69] Y. Chen, C. Zhu, and T. Wang, "The enhanced ethanol sensing properties of multi-walled carbon nanotubes/SnO₂ core/shell nanostructures," *Nanotechnology*, vol. 17, no. 12, pp. 3012–3017, 2006.
- [70] E. H. Espinosa, R. Ionescu, B. Chambon, et al., "Hybrid metal oxide and multiwall carbon nanotube films for low temperature gas sensing," *Sensors and Actuators B*, vol. 127, no. 1, pp. 137–142, 2007.
- [71] N. Van Hieu, L.T. B. Thuy, and N. D. Chien, "Highly sensitive thin film v gas sensor operating at room temperature based on SnO₂/MWCNTs composite," *Sensors and Actuators B*, vol. 129, no. 2, pp. 888–895, 2008.
- [72] J. Wang, L. Liu, S.-Y. Cong, J.-Q. Qi, and B.-K. Xu, "An enrichment method to detect low concentration formaldehyde," *Sensors and Actuators B*, vol. 134, no. 2, pp. 1010–1015, 2008.
- [73] C. Bittencourt, A. Felten, E. H. Espinosa, et al., "WO₃ films modified with functionalised multi-wall carbon nanotubes: morphological, compositional and gas response studies," *Sensors and Actuators B*, vol. 115, no. 1, pp. 33–41, 2006.
- [74] M. Sánchez, R. Guirado, and M. E. Rincón, "Multiwalled carbon nanotubes embedded in sol-gel derived TiO₂ matrices and their use as room temperature gas sensors," *Journal of Materials Science: Materials in Electronics*, vol. 18, no. 11, pp. 1131–1136, 2007.
- [75] E. Llobet, E. H. Espinosa, E. Sotter, et al., "Carbon nanotube-TiO₂ hybrid films for detecting traces of O₂," *Nanotechnology*, vol. 19, no. 37, Article ID 375501, 11 pages, 2008.
- [76] N. Van Duy, N. Van Hieu, P. T. Huy, N. D. Chien, M. Thamilselvan, and J. Yi, "Mixed SnO₂/TiO₂ included with carbon nanotubes for gas-sensing application," *Physica E*, vol. 41, no. 2, pp. 258–263, 2008.
- [77] S. Peng and K. Cho, "Ab initio study of doped carbon nanotube sensors," *Nano Letters*, vol. 3, no. 4, pp. 513–517, 2003.
- [78] R. Wang, D. Zhang, W. Sun, Z. Han, and C. Liu, "A novel aluminum-doped carbon nanotubes sensor for carbon monoxide," *Journal of Molecular Structure*, vol. 806, no. 1–3, pp. 93–97, 2007.
- [79] R. Wang, D. Zhang, Y. Zhang, and C. Liu, "Boron-doped carbon nanotubes serving as a novel chemical sensor for formaldehyde," *Journal of Physical Chemistry B*, vol. 110, no. 37, pp. 18267–18271, 2006.
- [80] Y. Zhang, D. Zhang, and C. Liu, "Novel chemical sensor for cyanides: boron-doped carbon nanotubes," *Journal of Physical Chemistry B*, vol. 110, no. 10, pp. 4671–4674, 2006.
- [81] L. Bai and Z. Zhou, "Computational study of B- or N-doped single-walled carbon nanotubes as NH₃ and NO₂ sensors," *Carbon*, vol. 45, no. 10, pp. 2105–2110, 2007.

Review Article

A Review of Carbon Nanotubes-Based Gas Sensors

Yun Wang and John T. W. Yeow

Systems Design Engineering, University of Waterloo, 200 University Avenue West, Waterloo, Ontario, Canada N2L 3G1

Correspondence should be addressed to John T. W. Yeow, jyeow@engmail.uwaterloo.ca

Received 31 December 2008; Revised 7 April 2009; Accepted 15 May 2009

Recommended by Michele Penza

Gas sensors have attracted intensive research interest due to the demand of sensitive, fast response, and stable sensors for industry, environmental monitoring, biomedicine, and so forth. The development of nanotechnology has created huge potential to build highly sensitive, low cost, portable sensors with low power consumption. The extremely high surface-to-volume ratio and hollow structure of nanomaterials is ideal for the adsorption of gas molecules. Particularly, the advent of carbon nanotubes (CNTs) has fuelled the inventions of gas sensors that exploit CNTs' unique geometry, morphology, and material properties. Upon exposure to certain gases, the changes in CNTs' properties can be detected by various methods. Therefore, CNTs-based gas sensors and their mechanisms have been widely studied recently. In this paper, a broad but yet in-depth survey of current CNTs-based gas sensing technology is presented. Both experimental works and theoretical simulations are reviewed. The design, fabrication, and the sensing mechanisms of the CNTs-based gas sensors are discussed. The challenges and perspectives of the research are also addressed in this review.

Copyright © 2009 Y. Wang and J. T. W. Yeow. This is an open access article distributed under the Creative Commons Attribution License, which permits unrestricted use, distribution, and reproduction in any medium, provided the original work is properly cited.

1. Introduction

Gas sensors, or chemical sensors, are attracting tremendous interest because of their widespread applications in industry, environmental monitoring, space exploration, biomedicine, and pharmaceuticals. Gas sensors with high sensitivity and selectivity are required for leakage detections of explosive gases such as hydrogen, and for real-time detections of toxic or pathogenic gases in industries. There is also a strong demand for the ability to monitor and control our ambient environment, especially with the increasing concern of the globe warming. Researchers from the national aeronautics and space administration (NASA) are seeking the use of high-performance gas sensors for the identification of atmospheric components of various planets. In addition, nerve agent sensing for homeland security is also at the centre of public concern [1].

Generally, there are several basic criteria for good and efficient gas sensing systems: (i) high sensitivity and selectivity; (ii) fast response time and recovery time; (iii) low analyst consumption; (iv) low operating temperature and temperature independence; (v) stability in performances. Commonly used gas sensing materials include vapour-sensitive polymers, semiconductor metal oxides,

and other porous structured materials such as porous silicon [2–4]. Since the most common gas sensing principle is the adsorption and desorption of gas molecules on sensing materials, it is quite understandable that by increasing the contact interfaces between the analytes and sensing materials, the sensitivity can be significantly enhanced.

Recent development of nanotechnology has created huge potential to build highly sensitive, low cost, portable sensors with low power consumption. The extremely high surface-to-volume ratio and hollow structure of nanomaterials is ideal for gas molecules adsorption and storage. Therefore, gas sensors based on nanomaterials, such as carbon nanotubes (CNTs), nanowires, nanofibers, and nanoparticles, have been investigated widely.

Carbon nanotubes, since been firstly discovered by Iijima in 1991 [5], have drawn the most research interests because of their unique geometry, morphology, and properties. Their preparation, properties (such as electronic, mechanical, thermal, and optical properties), and applications on various fields are all studied intensely. Theoretical and simulation works have also been conducted to understand this nanoscaled material and related phenomenon [6].

Carbon nanotubes belong to the family of fullerene structures. There are two types of nanotubes: single-walled carbon nanotubes (SWCNTs) and multiwalled carbon nanotubes (MWCNTs). An SWCNT can be considered as a one-atom-thick layer of graphite rolled up into a seamless cylinder with a diameter of several nanometers, and length on the order of 1–100 microns [7]. MWCNTs consist of multiple layers of graphite wrapped up together to form a tube shape, sharing the same central axis. The structure of carbon nanotubes provides them with inherently unique electrical, physical, and chemical properties. Mechanically, CNTs are the strongest and stiffest fibers that are known currently due to the C–C bond. Thermally, CNTs have high thermal stability in both vacuum and air. In terms of electrical properties, CNTs can be either metallic or semiconducting, depending upon the tube diameter and the chirality (the direction in which the graphite sheet is rolled to form the tube) [8]. The chirality is usually represented by an integer pair (n, m) . Nanotubes with $n - m = 3j$ (j being a nonzero integer) are metallic while all the others are semiconducting. The dielectric property of nanotubes is highly anisotropic due to their nearly one-dimensional structures, which may enable nanotubes to carry high currents with negligible heating effect [9].

Upon exposure to certain gases, the change in the properties of CNTs or CNTs-based composites can be detected by various methods. As a result, CNTs-based gas sensing systems and the theoretical analyses of gas adsorption and collision effects on the nanotubes have been the subjects of intense research [10, 11]. In this paper, the current status of CNTs gas sensor-related technologies is reviewed. This paper is organized as follows: in Section 2 the synthesis techniques of CNTs and different fabrication methods of CNTs-based gas sensors will be introduced; Section 3 will be focussed on the simulation and theoretical works on the interaction between CNTs and the adsorbed gas molecules; in Section 4, CNTs gas sensors based on different sensing mechanisms will be summarized with their design and sensing behaviour; Section 5 will highlight the functionalization of CNTs and CNTs-based nanocomposites for gas sensing; the conclusion with the chance and challenges that the CNTs gas sensing technology is facing will be addressed in Section 6.

2. Fabrication of CNTs Gas Sensors

2.1. Growth of CNTs. Three main techniques to prepare CNTs are as follows: (i) arc-discharge technique; (ii) laser ablation technique; (iii) chemical vapour deposition (CVD) technique [12].

The carbon arc-discharge method is the first technique that was used to grow CNTs. The process is carried out in a vacuum chamber with two carbon electrodes as carbon source. Inert gas (typically helium) is supplied to increase the speed of carbon deposition. When high dc voltage is applied between the carbon anode and cathode, plasma of the inert gas is generated to evaporate the carbon atoms. The ejected carbon atoms are then deposited on the negative electrode to form CNTs. Both SWNTs and MWNTs can be grown by this method, while the growth of SWNTs

requires catalysts. It is the principal method to produce high-quality CNTs with nearly perfect structures. In the laser ablation technique, a carbon target is ablated by intense laser pulses in a furnace in the presence of an inert gas and a catalyst. CNTs are formed and collected on a cold substrate. Both the arc-discharge and laser-ablation methods require high growth temperature, which is about 3000–4000°C for the evaporation of carbon atoms from solid carbon source.

In a CVD system, a gas hydrocarbon source (usually methane, acetylene or ethylene) flows into the reaction chamber. The hydrocarbon molecules are broken into reactive species at the temperature range of 550–1000°C. The reactive species react in the presence of catalysts (usually metal particles such as Ni, Fe or Co) that are coated on the substrate, leading to the formation of CNTs. Compared with the first two techniques; CNTs can be synthesized at relatively low temperature using CVD method. Therefore, this technique is more efficient and allows scaleup growth of SWCNTs. By modification and calculated control of the growth parameters, vertically aligned MWCNTs growth can be achieved by CVD technique. This enhances CNTs electronic properties in different applications. High-quality SWCNTs can also be obtained by the optimization of the catalysts. However, one of the main disadvantages of CVD technique is the relatively high defect densities in MWCNTs, which can be attributed to the lack of sufficient thermal energy.

In all of these three growth methods, CNTs come with a number of impurities, which may have negative effects on CNTs' inherent properties. In order to make CNT-based devices more efficient and consistent, purification is an important process to obtain high-quality nanotubes. Generally, the most commonly observed impurities are carbonaceous impurities and metallic impurities. The carbonaceous components are the byproducts of the reaction process while the metallic impurities are residual catalysts. To eliminate the carbonaceous impurities, the main method is oxidation. Two approaches are developed: (i) gas phase purification, which involves high temperature and has low yield production; (ii) liquid phase purification, where nanotubes are washed in acidic solutions. Nitric acid, sulphuric acid, and their mixture are all commonly used for liquid purification [13]. Metallic impurities can be removed by heating the samples up to the evaporation temperature of the impurity. With the development and modification of different purification procedure, so far CNTs samples with a purity of up to 99.6% can be obtained [14]. The quality of as-grown CNTs and the purification can be inspected by microscopic techniques such as atomic force and scanning tunneling microscopy, or spectroscopic techniques such as Raman spectroscopy.

2.2. Fabrication of CNTs Gas Sensors. There are several methods to integrate CNTs to different gas sensor structures. Li et al. developed a resistive gas sensor by simply casting SWCNTs on interdigitated electrodes (IDEs) [14]. The electrodes were fabricated by photolithography and evaporation of Ti and Au (60 nm in thickness together) on silicon oxide. As-grown SWCNTs were purified with acid first and then by air

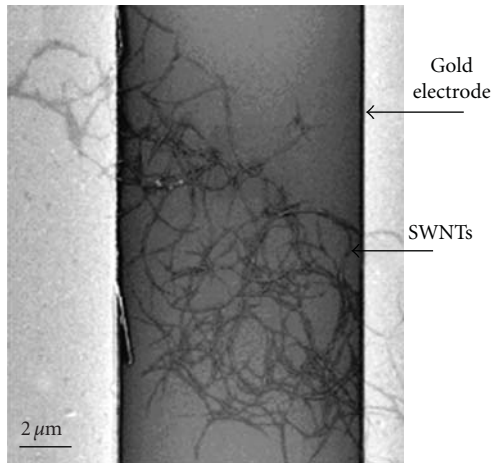


FIGURE 1: SEM image of SWCNTs across two gold electrodes [14].

oxidation before being integrated with the IDEs. As a result, the final SWCNTs had a relatively high purity up to 99.6%, and the impact of impurities on the sensor's characteristic was minimized. The purified nanotubes were then dispersed in dimethylformamide (DMF) and drop-deposited onto the electrode area. A network of nanotubes subsequently formed after the evaporation of DMF, as shown in Figure 1. Another simple method is screen-printing of CNTs onto patterned electrodes. Lee et al. [15] screen-printed CNTs paste mixed with MWNTs, terpineol, ethylcellulose, and glass frits onto electrode-coated glass as the gas sensing element for NO_2 detection. The organic binder can be removed by annealing in N_2 ambient.

Fabrication of CNTs sensors can also be achieved by dielectrophoresis (DEP) method. DEP is the electrokinetic motion of dielectrically polarized materials in nonuniform electric fields and has been used to manipulate CNTs for separation, orientation, and positioning of CNTs [16–22]. Suehiro et al. [23] demonstrated that the DEP fabrication could establish a good electrical connection between CNTs and the electrodes. During fabrication, the CNTs with high purity were suspended in ethanol and ultrasonicated for 60 minutes. The system to fabricate the CNTs-based gas sensor is schematically depicted in Figure 2. An interdigitated microelectrode was patterned on a glass substrate. The electrode had a castle-wall pattern in order to form high and low electric field regions periodically. The castle-wall electrode was surrounded by a silicon rubber spacer to form a sealed chamber in which CNTs suspension was continuously fed from a reservoir by a peristaltic pump. The DEP trapping of MWCNTs on the microelectrode was performed with an ac voltage. After a desired period of time, the DEP process was stopped and the ethanol was evaporated at room temperature. The DEP-fabricated CNTs gas sensors successfully detected various vapours such as NH_3 , NO_2 , SO_2 , and HF. With this technique, the amount of trapped CNTs can be controlled by monitoring electrical impedance of the sensor and various metal materials can be employed as the electrodes [24].

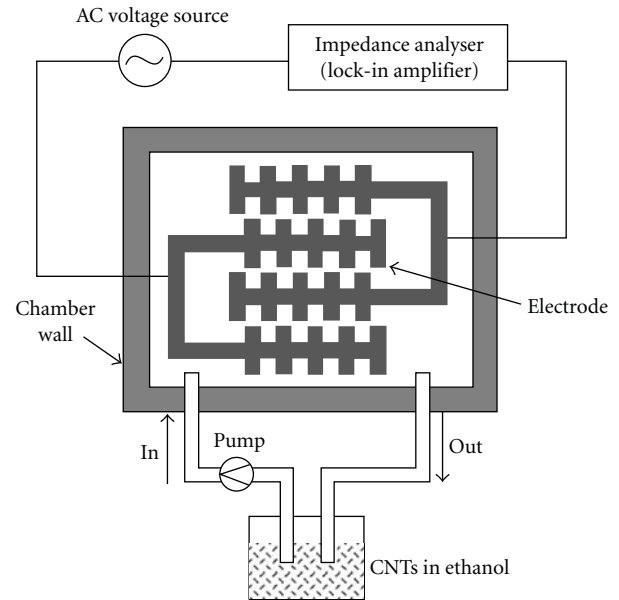


FIGURE 2: Schematic diagram of the experimental setup for MWCNT gas sensor fabrication on a microelectrode using DEP [23].

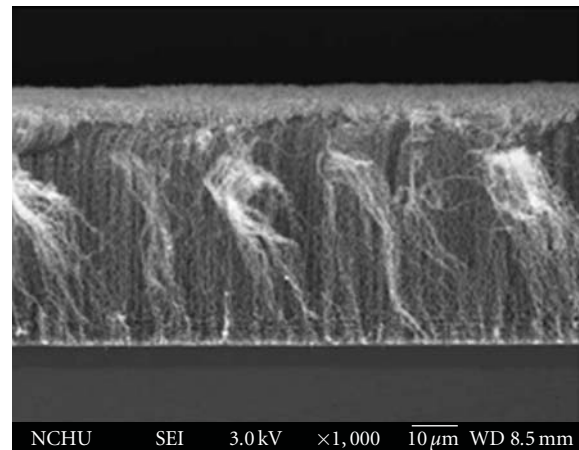


FIGURE 3: Cross-sectional SEM images of the vertically aligned CNTs mat [25].

To obtain well aligned CNTs for better sensor behaviour, directly growth of the CNTs mats on the sensor substrates is required. Huang et al. [25] fabricated a three terminal N_2 gas sensor with vertically aligned CNTs. The CNTs were grown by thermal CVD on (100) n-type silicon substrate at 700°C . A 30 nm thick Fe layer was sputtered on the substrate as catalyst and C_2H_2 was used as the carbon source. A preheating process was carried out before the growth of CNTs and the substrate was cooled down at room temperature in N_2 ambient. The as-grown CNTs mat is shown in Figure 3.

Jang et al. [26] fabricated an NH_3 gas sensor with laterally aligned MWNTs. N-type heavily doped Si wafer with SiO_2 layer on top was used as the substrate. The Nb electrodes

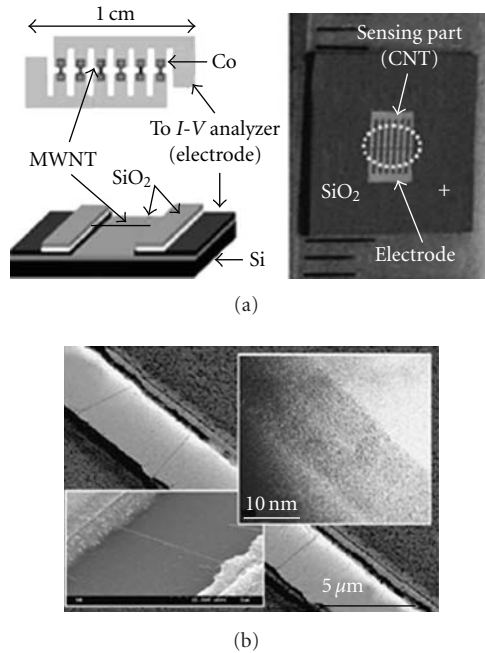


FIGURE 4: (a) Photograph of completed MWNTs based chemical sensor, (b) SEM image of aligned CNTs resting on SiO₂ surface after directed growth. The CNTs show clear alignment in the direction of the electric field. The insert shows TEM image of laterally grown CNTs [26].

were deposited and patterned on the substrate. The catalyst and oxide were then deposited and patterned by lift-off to be aligned to the electrodes, where top oxide layer is introduced as a barrier layer for vertical growth and exposure gas, covering the top of the Co catalytic layer. Aligned MWNTs across the gap between the electrodes were grown in thermal CVD system with electrical feed-through. Figure 4 shows the structure of the sensor and the laterally aligned CNTs connecting the electrodes.

Tabib-Azar and Xie [28] also successfully prepared self-aligned and self-welded MWNTs between prepatterned electrodes by low pressure CVD (LPCVD) for NH₃OH and HCl sensing. Ding et al. [29] achieved the growth of aligned CNTs in an anodic aluminum oxide (AAO) template for hydrogen sensor. With the development in the preparation techniques, controllable fabrication of CNTs-based gas sensors with improved performance can be achieved [30].

3. Theoretic and Simulation Studies of the Gas Adsorption on CNTs

3.1. Molecule Adsorption on SWNTs. The adsorption of various gas molecules on SWNTs is usually studied by first-principles calculations using density functional theory (DFT). The binding energy, tube-molecule distance, and charge transfers are generally investigated. Peng and Cho [31] studied the adsorption of NO₂ on to SWNTs by this method. Figure 5 shows one binding configuration for NO₂ gas molecule on the (10,0) SWNT with three units. NO₂

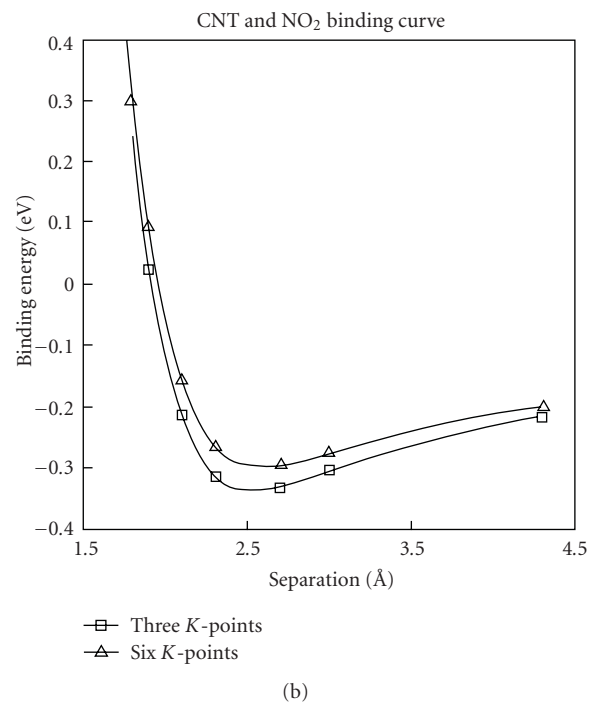
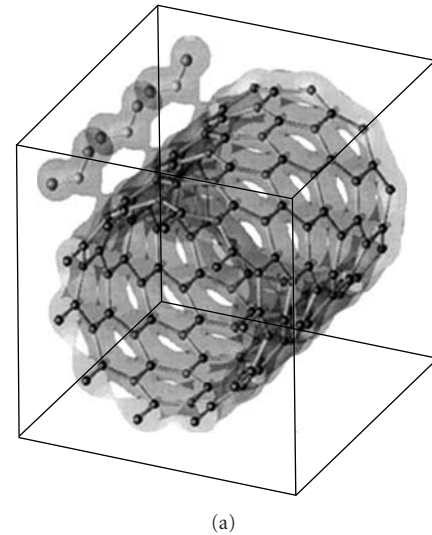


FIGURE 5: (a) Total valence electron charge density plot. The value of charge contour is 0.0015 (e/Å³) showing the binding charge between the SWNT (10,0) and the NO₂ molecule. Three units are shown in this figure. (b) Binding energy curve for NO₂ interacting with (10,0) SWNT as a function of distance from NO₂ to the nanotube. The solid line curve is a fitting with universal binding curve [31].

gas molecule of this configuration is found to bind with SWNT with adsorption energy of 0.3 eV, and it is also found that the molecule has high diffusion kinetics on nanotubes surfaces. Electron density analysis shows that charge transfer is induced from C atom to the NO₂ gas molecule leading to hole (or p-type) doping of semiconducting (10,0) nanotubes.

TABLE 1: Equilibrium tube-molecule distance (d), adsorption energy (E_a), and charge transfer (Q) of various molecules on (10,0), (17,0), and (5,5) individual SWNTs^a. The optimal adsorption sites are given in the table: T (top of a carbon atom), B (top of the centre of the C–C bond), C (top of the centre of carbon hexagon) [27]. ^(a)Tube-molecule distance d is defined as the nearest distance between atoms on the molecule and the nanotube for T site, or the distance between the centre of the gas molecule and the centre of the carbon hexagon (carbon-carbon bond) for the C (B) site. The adsorption energy $E_a(d)$ is defined as the total energy gained by molecule adsorption at equilibrium distance: $E_a(d) = E_{\text{tot}}(\text{tube} + \text{molecule}) - E_{\text{tot}}(\text{tube}) - E_{\text{tot}}(\text{molecule})$. Charge transfer (Q) denotes the total Mulliken charge number on the molecules, positive (Q) means charge transfer from molecule to tube.

	NO ₂	O ₂	H ₂ O	NH ₃	CH ₄	CO ₂	H ₂	N ₂	Ar
(10,0) SWNT									
d (Å)	1.93	2.32	2.69	2.99	3.17	3.20	2.81	3.23	3.32
E_a (meV)	797	509	143	149	190	97	113	164	57
Q (e)	-0.061	-0.128	0.035	0.031	0.027	0.016	0.014	0.008	0.01
Site	T	B	T	T	C	C	C	C	C
(5,5) SWNT									
d (Å)	2.16	2.46	2.68	2.99	3.33	3.54	3.19	3.23	3.58
E_a (meV)	427	306	128	162	122	109	84	123	82
Q (e)	-0.071	-0.142	-0.033	0.033	0.022	0.014	0.016	0.011	0.011
Site	T	B	T	T	C	C	C	C	C
(17,0) SWNT									
d (Å)	2.07	2.50	2.69	3.00	3.19	3.23	2.55	3.13	3.34
E_a (meV)	687	487	127	133	72	89	49	157	82
Q (e)	-0.089	-0.096	0.033	0.027	0.025	0.015	0.012	0.006	0.01
Site	T	B	T	T	C	C	C	C	C

Zhao et al. [27] studied the adsorption of various gas molecules (NO₂, O₂, NH₃, N₂, CO₂, CH₄, H₂O, H₂, Ar) on both single SWNT and SWNT bundles using first principles method. The self-consistent field (SCF) electronic structure calculations are performed based on density functional theory (DFT) with either localized basis (DMol) or plane-wave basis (CASTEP).

For individual SWNT, the equilibrium tube-molecule distance, adsorption energy, and charge transfer for various molecules on (10,0), (17,0) and (5,5) SWNTs were calculated, as shown in Table 1. The results show that most of the studied molecules (except for NO₂ and O₂) are charge donors with small charge transfer (0.01 ~ 0.035e) and weak binding (≤ 0.2 eV). These gas molecules can be identified as physisorption. For O₂ and NO₂, it shows that they both are charge acceptors with large charge transfer and adsorption energies. These results are consistent with reported experimental results [32, 33]. It also demonstrated that there is no clear dependence of adsorption on the tube size and chirality.

For SWCNTs bundle, there are four distinct sites for gas molecules to be adsorbed onto (shown in Figure 6): (i) the external surface of the bundle; (ii) the groove formed at the contact between adjacent tubes on the outside of the bundle; (iii) the interior pore of individual tubes; (iv) interstitial channel formed between three adjacent tubes within the bundle [34, 35]. The gas adsorption on these sites is decided by the binding energy of the gas molecule as well as the site availability. Some of these sites may not be available for certain gases because of the gas molecule dimension and the site diameter. The interior pore is only accessible when the SWCNT is uncapped or has defects on the tube

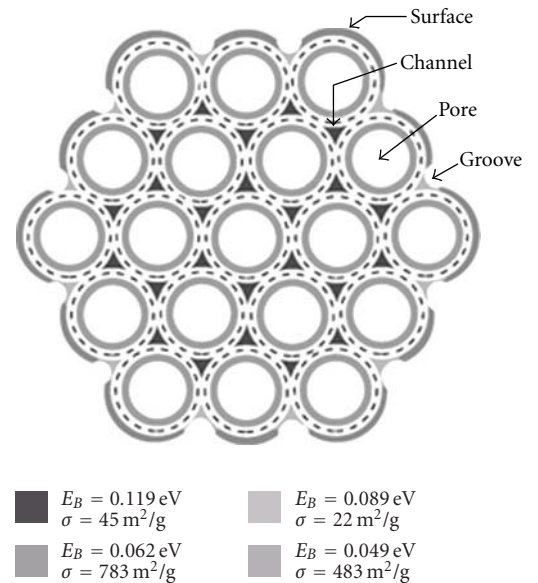


FIGURE 6: Schematic structure of a SWNT bundle showing the available sites for gas adsorption. Dashed line indicates the nuclear skeleton of the nanotubes. Binding energies (E_B) and specific surface area contributions (σ) for H₂ adsorption on these sites are indicated [34].

walls [36]. Williams and Eklund [34] calculated the binding energy (E_B) and specific surface area contributions (σ) for H₂ adsorption on these sites as shown in Figure 6. It shows that E_B (channels) $>$ E_B (grooves) $>$ E_B (pores) $>$ E_B (surface), while the pores and surface have much larger specific surface

TABLE 2: Equilibrium tube-molecule distance (d), adsorption energy (E_a) and charge transfer (Q) of the H_2 molecule on different adsorption sites in the (10, 10) SWNT bundle [27].

Site	d (Å)	E_a (meV)	Q (e)
Surface	3.01	94	0.014
Pore	2.83	111	0.012
Groove	3.33	114	0.026
Interstitial	3.33	174	0.035

area contributions. Zhao et al. [27] also calculated the tube-molecule distance, adsorption energy, and charge transfer of these sites for H_2 adsorption using first principles method, as shown in Table 2. These results are consistent with William's results obtained by empirical force field simulation.

3.2. Effects of Molecule Adsorption on Electronic Properties of CNTs. Generally, the electronic property of an SWNT is determined by the tube chirality and diameter [37]. However, it has been demonstrated experimentally that the electronic properties of SWNTs are very sensitive to their chemical environment, especially on oxygen exposure. Collins et al. [33] measured the electrical resistance, thermoelectric power (TEP), and local density of states of SWNTs by transport measurement and scanning tunneling spectroscopy. The results showed that these parameters can be reversibly "tuned" by exposure to very small concentrations of oxygen, as shown in Figure 7. Isolated semiconducting nanotubes can be converted into apparent metals through room-temperature exposure to oxygen. Sumanasekera et al. [38] also demonstrated experimentally that, by degassing the SWNTs mat in vacuum at 500 K, the TEP value decreased slowly from an initial value of $+54 \mu V/K$, changed sign, and then eventually approached a constant value of $-44 \mu V/K$, as shown in Figure 8. Nuclear magnetic resonance (NMR) study of SWNTs also proved that the spin-lattice relaxation rates of all nanotubes increased dramatically upon exposure to oxygen [39]. Jhi et al. studied the electronic and magnetic properties of oxidized CNTs theoretically using the ab initio pseudopotential total energy method [40]. The calculations showed consistent results with the experimental ones. These results demonstrated the potential for CNTs application as sensitive gas sensors. However, they also indicate that many reported electronic properties measured on as-prepared nanotubes should be assigned to oxygen-doped CNTs instead of intrinsic CNTs [33, 38].

Generally, the electronic property changes of CNTs upon exposure to gas molecules are attributed to the charge transfer between the molecules and the nanotubes (the molecules act as electron donors or acceptors). However, Sumanasekera et al. [38] demonstrated experimentally that both of the thermopower S and the resistance of the degassed SWNT mat R can be very sensitive to inert gases (N_2 and He, which can hardly have electron transfers with CNTs) for T (temperature) > 100 K, as shown in Figure 8. In the case of these gases, it is expected that the charge transfer between the molecules and the nanotubes is negligible. Without charge transfer, it is believed that the resistance changes are due

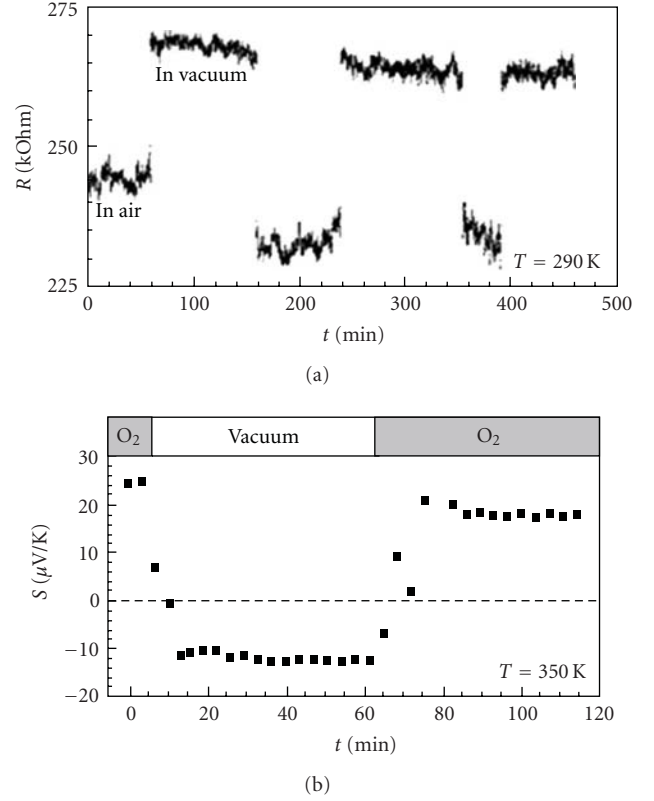


FIGURE 7: (a) Sensitivity of the electrical resistance R of SWNT films to gas exposure at 290 K; (b) sensitivity to environmental conditions of thermoelectric power S for SWNTs at 350 K. Both the magnitude and the sign can be altered by oxygen exposure. In vacuum, S is n-type, whereas in an oxygen environment, S is p-type, with a larger magnitude [33].

to the change in the electron and hole free carrier lifetimes (or, equivalently, the carrier mobility). These large changes in the carrier lifetime can be caused either by the increased carrier scattering from dynamic defect states associated with momentarily adsorbed gas or due to nonthermal, localized SWNT phonons generated by collisions of the gas molecules with the tube wall.

Based on these observations, it is summarized that the thermoelectric response of a bundle of SWNTs to variety of gases can be either caused by a charge-transfer-induced change of Fermi energy or by the additional scattering channel (identified with impurity sites associated with the adsorbed molecules) for conduction electrons in the tube wall. An equation was developed to understand this assumption [36]:

$$S = S_0 + (\rho_a/\rho_0)(S_a - S_0), \quad (1)$$

where S_0 and S_a are, respectively, the contributions to the thermopower from the host resistivity ρ_0 and the additional impurity resistivity ρ_a associated with the adsorbed gas. This equation is known as the Nordheim-Gorter (N-G) relation [41]. When applied to the thermoelectric transport in SWNTs bundles with adsorbed gas molecules, it can indicate

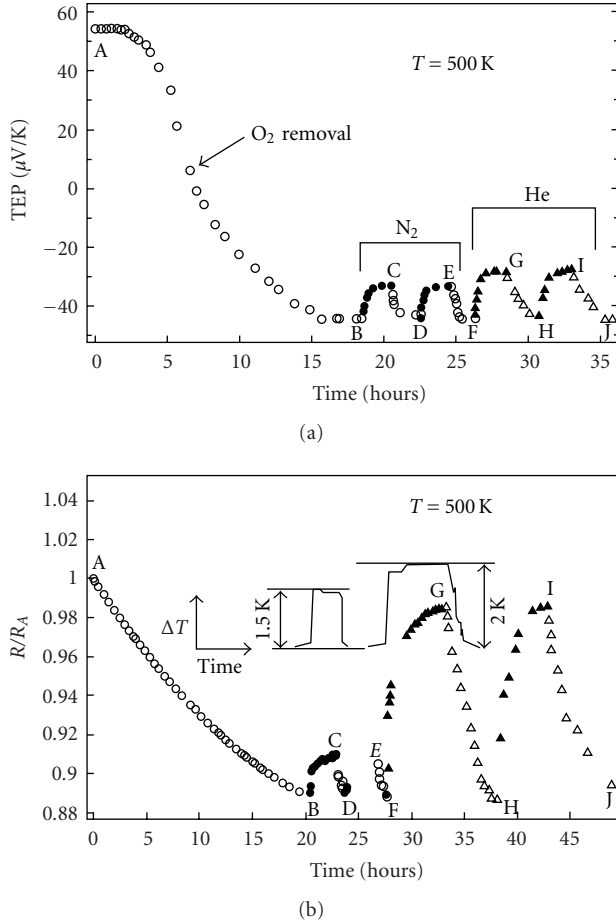


FIGURE 8: (a) Thermopower S versus time for a mat of SWNTs at $T = 500$ K initially saturated with air at ambient conditions. The sample is under dynamic vacuum when open symbols are used and dark symbols representing intervals when N_2 and He are present. N_2 is introduced at B and D; He is introduced at F and H. Vacuum pumping is applied at A, C, E, G, and I; (b) four probe resistance ratio of SWNT mat at 500 K versus time. Data normalized to sample resistance at A. Points A through I have the same meaning as described for (a). Shown in the inset is the time dependence of the temperature during the admission of each gas and subsequent pumping [38].

whether the gas molecules are physisorbed or chemisorbed, as shown in Figure 9.

The effects of other gases such as alcohol and water molecules on the electrical transport of SWNT bundles are also studied [42]. Strong effects on both the TEP and resistivity for methanol, ethanol, isopropanol, and butanol were observed. The N-G plots indicated that these molecules are all physisorbed to the tube wall. However, water vapour does not have any effect on the TEP but has a significant impact on the resistance, as shown in Figure 10.

3.3. Simulation Study for Functionalization of CNTs Gas Sensors. Theoretical and simulation research cannot only explain the observed experimental results with in-depth mechanism, but can also simulate the CNTs behaviours

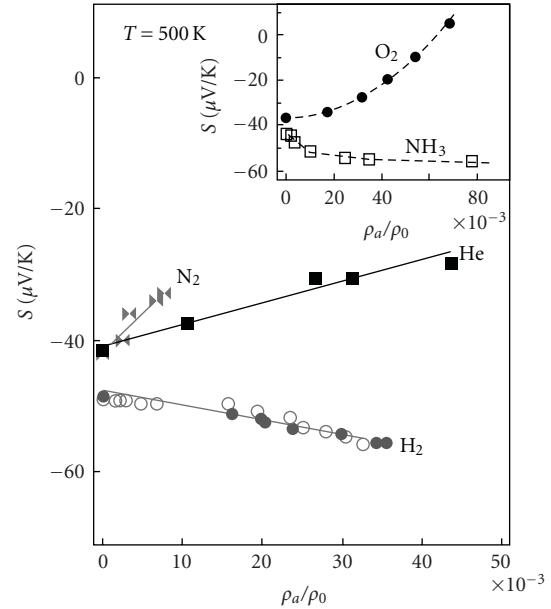


FIGURE 9: N-G plots (S versus ρ) showing the effect of gas adsorption on the electrical properties of the mat. A linear N-G plot indicates that the physisorption is taking place. The inset shows the N-G plots for O_2 (electron acceptor) and NH_3 (electron donor). The data in the inset strongly curved indicating chemisorption is taking place [36].

under certain assumptions of interest before carrying out the actual experiment.

It has been demonstrated that the electronic properties of semiconducting CNTs are very sensitive to certain gas exposure. However, the range of molecules that can be detected by CNTs sensors is limited to the molecules that have large binding energies and charge transfers with the nanotubes. Gas molecules such as toxic gases (CO), water, and bimolecular cannot be detected since they do not adsorb on the nanotubes surface. To overcome this challenge, Peng et al. [43] proposed the design of a new type of CNTs sensors with modified electronic and chemical properties by substitutional doping of impurity atoms (boron and nitrogen) into intrinsic SWNTs or by using composite $B_xC_yN_z$ nanotubes. To investigate the validation of the idea, the ab initio simulations are performed with the VASP using the density functional theory (DFT) and the local density approximation (LDA) with ultrasoft pseudopotential, plane-wave basis sets, and periodic boundary conditions.

The interaction of these boron- or nitrogen-doped CNTs with both carbon monoxide and water molecules was calculated. It demonstrated that, when an intrinsic CNT is doped with impurities through a replacement of carbon atoms, the local physical properties around the impurity atoms undergo a significant change, resulting in the change of the local chemical reactivity. The simulation results for water adsorption on both the intrinsic and modified CNTs are shown in Table 3. All the configurations studied are shown in Figure 11. It shows that CNTs with boron doping and intrinsic BC_2N type 2 nanotubes have better sensitivity

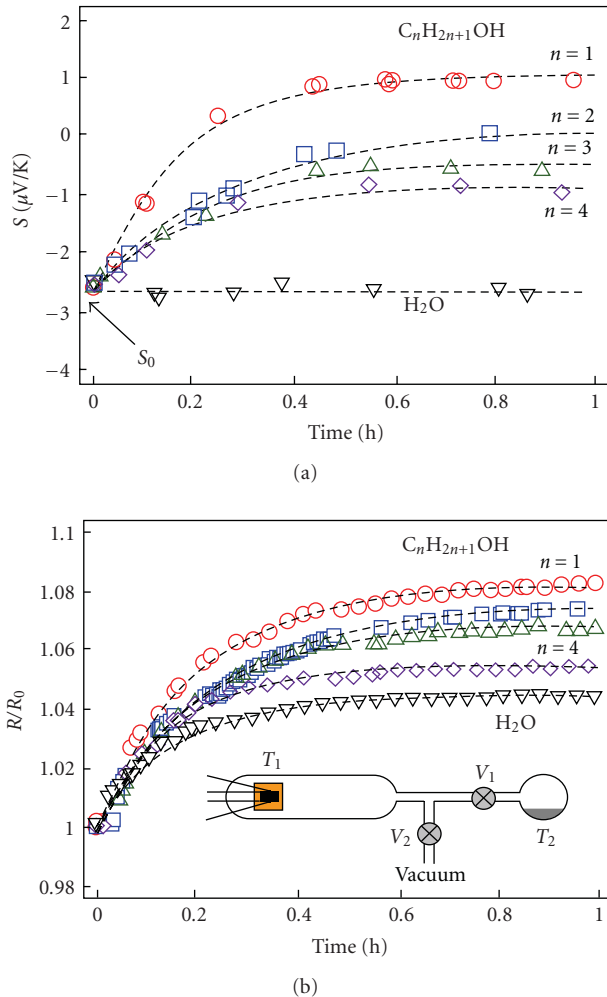


FIGURE 10: (a) The time dependence of the TEP response of a SWNT thin film to successive exposure to vapours of water and alcohol molecules ($\text{C}_n\text{H}_{2n+1}\text{OH}$; $n = 1-4$) at 40°C ; (b) the time dependence of the normalized four-probe resistance response of an SWNT thin film to successive exposure to vapours of water and alcohol molecules at 40°C [42].

to H_2O due to the strong interaction and a large electron charge transfer. The author also concluded that CO and H_2O molecules undergo chemical adsorption with the boron-doped CNTs, while physical adsorption with the nitrogen-doped CNTs-based on the value of the binding energy. Since the synthesis of B- or/and N-doped CNTs and $\text{B}_x\text{C}_y\text{N}_z$ nanotubes have already been proved feasible experimentally [44, 45], it is believed that CNTs base gas sensors with a wide range of detectable gas molecules can be achieved experimentally.

4. Design of CNTs Gas Sensors Based on Different Sensing Mechanism

4.1. Resistance Change. It has been demonstrated that CNTs electronic properties can be extremely sensitive to the exposed environment due to gas molecule adsorption. The

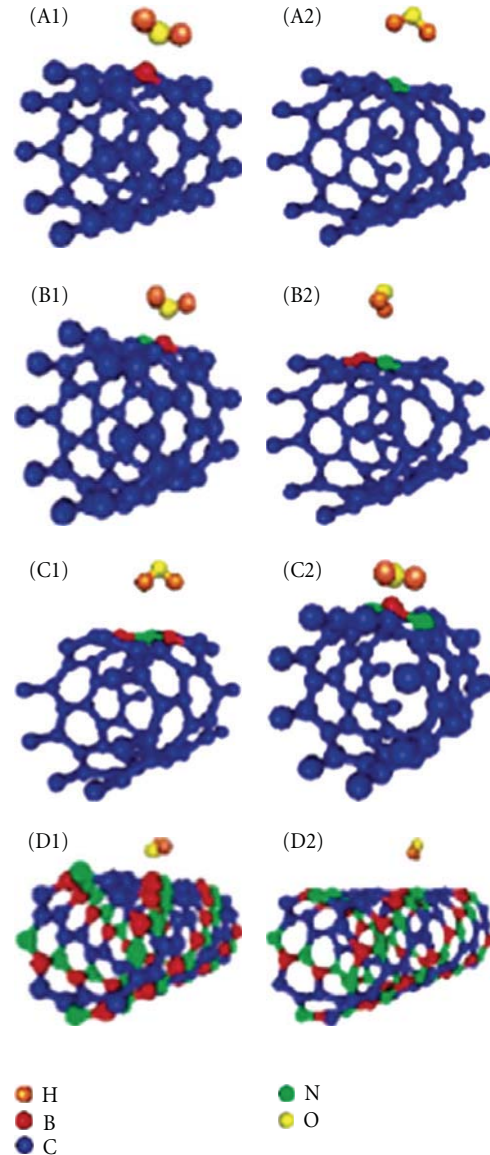


FIGURE 11: Configurations for water adsorption on modified CNTs. (A1) Semiconducting (8,0) CNT with one carbon atom replaced by a boron atom that binds to an H_2O molecule, where the boron atom is close to the oxygen atom. (A2) Semiconducting (8,0) CNT with one carbon atom replaced by one Nitrogen atom binds to an H_2O molecule, where the nitrogen atom is close to the oxygen atom. Semiconducting (8,0) CNT with one carbon atom replaced by a boron atom and another by a nitrogen atom that binds to an H_2O molecule, where the boron atom is close to the oxygen atom as in (B1), and the nitrogen atom is close to the oxygen atom as in (B2). (C1) Semiconducting (8,0) CNT with two carbon atoms replaced by two boron atoms and one by a nitrogen atom that binds to an H_2O molecule, where the nitrogen atom is close to the oxygen atom. (C2) Semiconducting (8,0) CNT with one carbon atom replaced by one boron atom and two others by two nitrogen atoms that bind to an H_2O molecule, where the boron atom is close to the oxygen atom. Semiconducting (8,0) BC_2N type 2 nanotube that binds to an H_2O molecule, where (D1) BN_2 group binds to an H_2O molecule with the boron atom close to the oxygen atom, and (D2) B_2N group binds to an H_2O molecule with the nitrogen atom close to the oxygen atom [43].

TABLE 3: Calculated data for adsorption of H₂O on the doped carbon nanotubes or B_xC_yN_z Nanotubes [43].

	E_g (eV) ^f	Configuration	E_b (eV)	D (Å)	ET (e) ^g
CNT	0.56	H ₂ O		no binding	
B-CNT ^a	0.44	B-H ₂ O ^h	-0.56	1.70	-0.12
N-CNT ^b	0.43	N-H ₂ O ⁱ	-0.23	3.12	-0.02
BN-CNT ^c	0.48	B-H ₂ O	-0.48	1.72	-0.20
		N-H ₂ O	-0.24	3.14	-0.02
B2N-CNT ^d	0.44	N-H ₂ O	-0.64	3.15	-0.28
BN2-CNT ^e	0.42	B-H ₂ O	-0.53	1.51	-0.08
BC ₂ N-type 2	0.93	B-H ₂ O	-0.48	1.72	-0.21
		N-H ₂ O	-0.18	3.14	-0.05

^a Intrinsic nanotube doped with boron atom in 2-unit cell.

^b Intrinsic nanotube doped with nitrogen atom in 2-unit cell.

^c Intrinsic nanotube doped with boron-nitrogen atom pair in 2-unit cell.

^d Intrinsic nanotube doped with boron-nitrogen-boron atom pair in 2-unit cell.

^e Intrinsic nanotubes doped with nitrogen-boron-nitrogen atom pair in 2-unit cell.

^f HOMOLUMO band gap.

^g Electron charge transfer from the nanotube to molecules.

^h H₂O molecule binds to the nanotube with the oxygen atom close to the boron atom.

ⁱ H₂O molecule binds to the nanotube with the oxygen atom close to the nitrogen atom.

thermopower, resistance, and density of states of single SWNT or SWNT bundles all showed significant change when exposed to certain gases, as discussed in Section 3. Since sensors based on resistance change as output are easy to build, test, and calibrated, resistance sensors are the most commonly used architecture in the design of CNTs gas sensors.

4.1.1. Semiconducting CNTs FET Gas Sensors. As addressed in a previous section, SWCNTs can be either semiconducting or metallic. If two metal contacts are connected to each end of an individual semiconducting SWNT (S-SWCNT), the metal/S-SWCNT/metal device exhibits p-type transistor characteristics. Therefore, the resistance response of CNTs to gas adsorption can be detected with field effect transistors (FETs) [46–50]. Kong et al. [46] built an S-SWCNT transistor with a single SWNT for chemical sensing. The device was fabricated by controlled CVD growth of individual SWCNTs on SiO₂/Si substrates with patterned catalyst islands. Polysilicon in the back side acted as gate of the transistor. Figure 12 shows the conductance versus time curves of the transistor upon exposure to NO₂ and NH₃ at room temperature. A sharp increase in conductance of the S-SWCNT FET by about three orders of magnitude was observed after introducing 200 ppm of NO₂ into the testing chamber (Figure 12(a)). The response time was about 2–10 seconds, and the sensitivity (the ratio between resistance after and before gas exposure) was about 100 to 1000. When the same sample was exposed to a 1% NH₃ flow after recovery, the conductance of the device decreased dramatically within 1 to 2 minute(s), and the sensitivity was about 10 to 100 (Figure 12(b)).

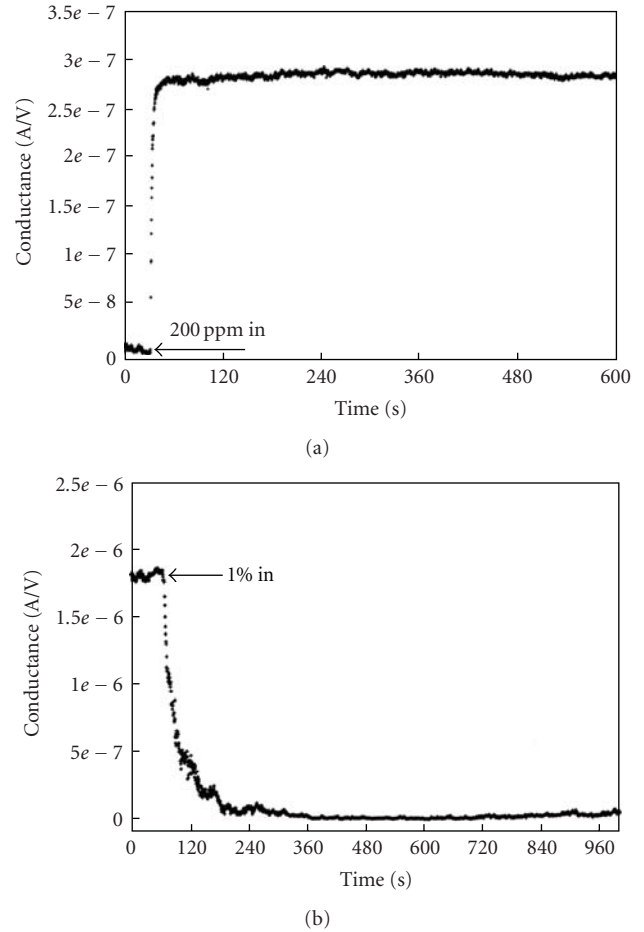


FIGURE 12: Conductance change of the FET sensor when exposed to (a) NO₂ and (b) NH₃ gases [46].

Someya et al. [47] characterized the influence of alcohols adsorption on the resistance of SWCNTs using the same transistor structure (see Figure 13). The measurements were carried out under flow of dry nitrogen with and without addition of alcoholic vapour. Figure 14 shows the drain current versus time curves of the device upon exposure to different saturated alcoholic vapour at room temperature (except for tertiary-butanol) with $V_g = -20$ V. For the vapour of methanol, tertiary-butanol, 1-propanol, 2-propanol, and ethanol, the response time was within 5–15 minutes and the current reduction were in the range of 50%–90%. Short recovery time (less than few seconds) and excellent repeatability can be obtained if the gate voltage is released briefly and then restored before the next cycle. No degradation of the sensor performance was observed over 1 hour operation. Moreover, the different response characteristic of the device to different alcoholic vapour also suggests its potential application on the identification of gas sources.

Compared with SWCNTs, the mechanism of MWCNTs' response to gas adsorption is more complicated due to the multilayer tube structure. However, they also show high sensitivity to specific gases experimentally [48, 49].

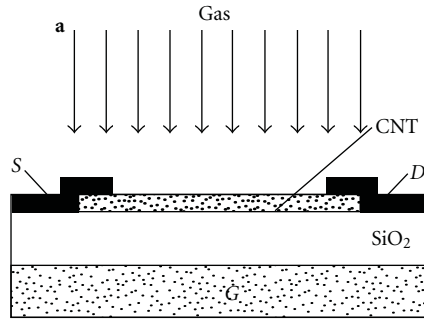


FIGURE 13: Scheme of the SWCNTs based FET sensor [47].

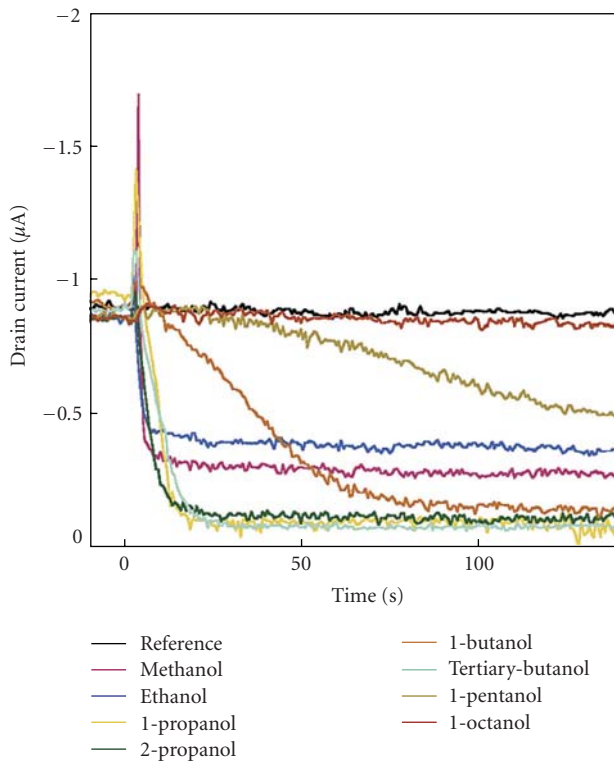
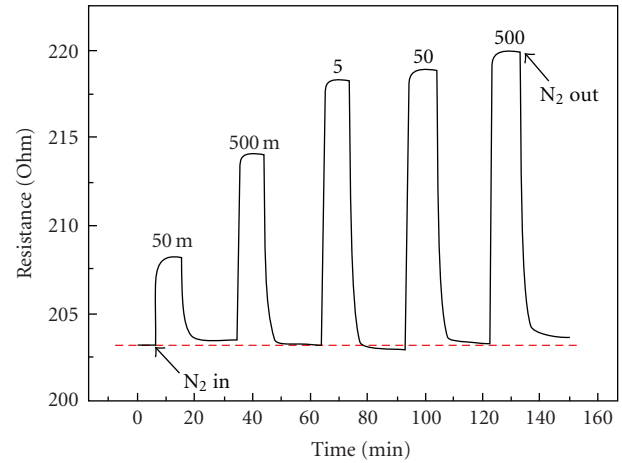
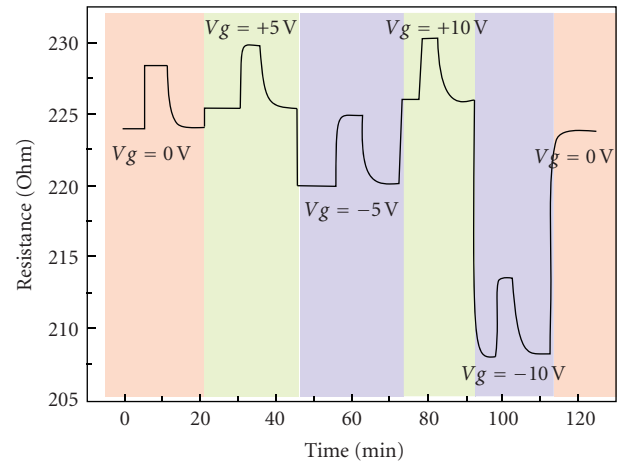


FIGURE 14: Drain currents a function of time upon exposure to saturated vapour of various kinds of alcohols: methanol, ethanol, 1-propanol, 2-propanol, 1-butanol, tertiary-butanol, 1-pentanol, and 1-octanol [47].

Huang et al. [25] synthesized vertically aligned MWNTs mat by thermal CVD and tested their resistance sensitivity to N_2 with the FET structure. The MWNTs showed p-type semiconducting property and the source and drain resistance increased when exposed to N_2 . Figure 15(a) shows the electrical resistance between source and drain at 10 V bias voltages without any gate voltage under various N_2 filling pressure from 50 mTorr to 500 Torr. The increasing resistance was explained by N_2 acting as an electron donor to CNTs and decreasing the concentration of conducting holes on CNTs. The sensor showed relative fast response and the resistance returned back to its initial value in vacuum, which indicated N_2 molecules were physisorbed



(a)



(b)

FIGURE 15: (a) The electrical resistance between source and drain at 10 V bias voltage without any gate voltage under various N_2 filling pressure from 50 mTorr to 500 Torr. (b) The electrical resistance of CNTs mat measured at a fixed 5 V source drain bias voltage while applying various gate voltages under a 5 Torr N_2 pumping and filling environment [25].

to the CNTs mat. The effect of the gate voltage on the sensor's behaviour was also studied. Figure 15(b) shows the electrical resistance of CNTs mat measured at a fixed 5 V source drain voltage and various gate voltages, under a 5 Torr N_2 pumping and filling environment. The initial electrical resistance increased when the positive gate voltage was applied and decreased with negative voltage. The reason was that electrons (holes) induced by positive (negative) gate voltage neutralized (added) some conducting holes in p-type CNTs, which caused the change of the free holes concentration and the electrical resistance of the CNTs mat. The recovery of the resistance to its initial value after a cycle of N_2 filling and pumping was observed during different positive and negative gate voltages. It was also demonstrated that the sensor sensitivity increased with the decrease of the gate voltage from positive to negative and the trend was more

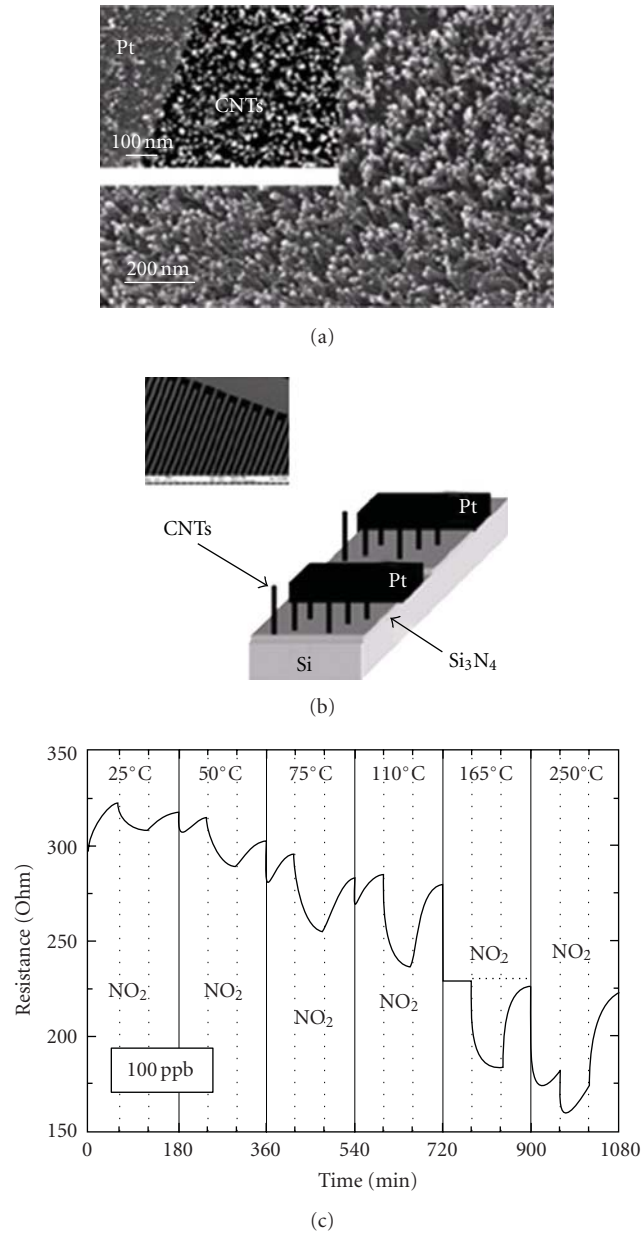


FIGURE 16: (a) SEM image of the as-grown structure of CNTs on Si/Si₃N₄; (b) schematic diagram of CNTs linking pre-patterned platinum contacts in resistor geometry; (c) dynamic gas responses of CNTs thin film at different operating temperatures in dry air and 100 ppb of NO₂ [52].

obvious under higher N₂ pressure. This was believed due to the increase of the gas-binding sites caused by negative gate voltage.

4.1.2. CNTs-Based Two Terminal Resistor Gas Sensors . The resistance change of CNTs under gas exposure can also be detected by two terminal resistors with dc voltage. Interdigitated electrodes are generally applied in these kind of sensors to provide larger sensing areas and sufficient contacts between the electrodes and the coated CNTs [51]. Valentini et al. [52] designed a CNT serpentine resistor for

the detection of various gases including NO₂, CO, NH₃, H₂O, and C₂H₅OH. The sensor was fabricated by photolithography defining Pt IDEs on Si₃N₄ substrate, and then CNTs films were grown on the substrate using radiofrequency plasma enhanced CVD (RF PECVD) with Ni as the catalyst. Figures 16(a) and 16(b) show the as-grown CNTs and a scheme of the sensor design. Figure 16(c) shows the dynamic response of the film resistance at different operating temperature from 25 to 250°C and different NO₂ concentration with dry air mixture. The sensor showed good sensitivity to NO₂ at room temperature. At 165°C, the sensor showed the best response as a tradeoff between the higher resistance variations and the fast and reproducible baseline recovery. The sensor's resistance response of other gases was also studied. In summary, NO₂ exposure drastically decreases the electrical resistance; NH₃, H₂O, C₆H₆ and ethanol exposure increases the electrical resistance; CO exposure does not affect the resistance; removing the gas exposure totally restores the initial resistance.

Li et al. developed a similar gas sensor by simply casting SWCNTs on IDEs [14]. The sensor is shown in Figure 17. Upon exposure to NO₂, the conductance change of the sensor showed a linear response to the gas concentration with a detection limit of less than 4 ppb. The recovery time was about 10 hours but can be intensively shortened by UV light treatment, as shown in Figure 17. The sensor's response to organic vapour such as benzene, acetone, and nitrotoluene was also measured.

Wong et al. [53] built a microelectronic gas sensor with CNTs in a thin-layered Pd/CNTs/n⁺-Si structure for hydrogen detection. The sensor was fabricated on an n-type silicon wafer, which acted as an ohmic supporting substrate. MWCNTs were grown selectively on the substrate via catalytic activation with microwave PECVD. Annealing of the CNTs layer was carried out to improve the adhesion with the silicon substrate. A thin layer of Pd was then sputtered on top of the CNTs layer as the gate electrode. The *I-V* characteristic of the device exhibit Schottky diode behaviour at room temperature with instantaneous current changes (reduction) when it was exposed to constant flow of hydrogen gas at room temperature, as shown in Figure 18(a). The reduction of the current in the presence of hydrogen was believed to be due to an increase in the barrier height between the Pd-CNTs interface after H₂ adsorption. The sensor was also detected at elevated temperature. Increasing current change was observed with increasing operating temperature. The sensor still showed Schottky diode behaviour at 80°C, while it changes to ohmic in both open air and H₂ environment at 170°C, as shown in Figure 18(b). This was explained by the change in the electrical properties of the CNTs at elevated temperature.

4.2. Carbon Nanotubes Enhanced Ionization Chamber for Gas Sensing. In the case of chemical gas sensors, it is difficult to detect gas molecules with low adsorption energy. Compared to these sensors, ionization gas sensor is based on the fingerprinting ionization characteristics of the detected gases. The ionization of detected gas is caused by the collisions of molecules with accelerated electrons. There is no adsorption

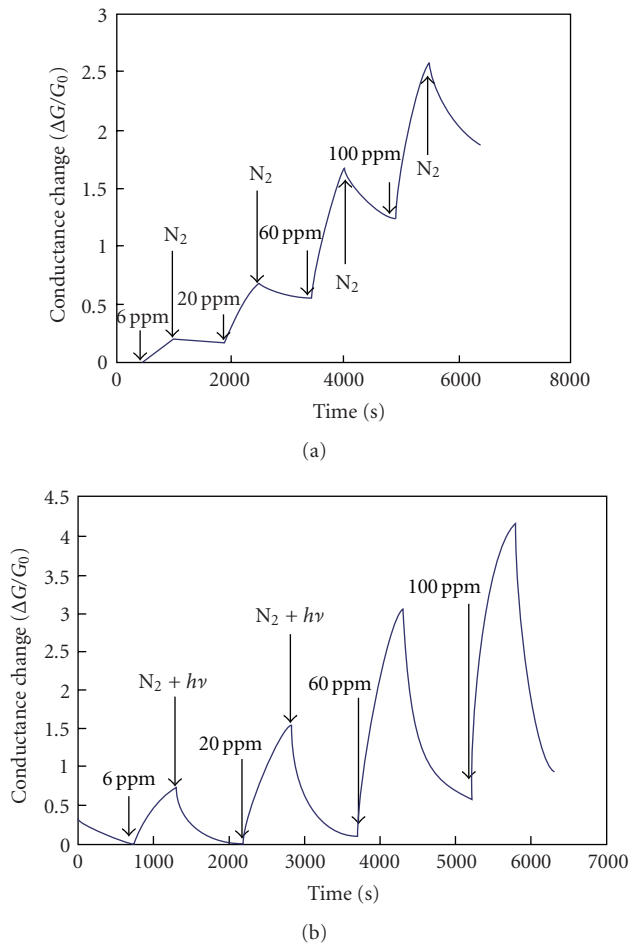


FIGURE 17: Representative sensor response NO_2 . Various concentrations of the sample gas and the pure gas injections are shown by arrows. The sample gas is NO_2 in a $400 \text{ cm}^3/\text{min}$ nitrogen flow at room temperature. Ultrapure nitrogen is used for dilution and purging. (a) Without UV light in the recovery. (b) With UV light for sensor recovery. The UV illumination and N_2 purging start simultaneously [14].

and chemical interaction between the device and interested molecules. Therefore, they are not limited to identify gases with low adsorption energy and poor charge transfer with the sensing materials. Sensing of inert gases or gas mixtures can easily be achieved by ionization chamber. However, the issues related to conventional ionization gas sensors are their bulky architectures, considerable high power consumption, and breakdown voltage, which is inefficient and risky in operation. CNTs, due to their extremely sharp tip structure, can induce a large field enhancement factor and thereby intensively increase the electric field around the tips to initiate corona discharge at very low voltage [54]. Therefore, the effect of gas adsorption on their field emission properties and CNTs enhanced ionization gas sensors have attracted a great amount of research interests [55–62].

A miniaturized gas ionization sensor with aligned MWNT film as anode was developed by Ashish Modi et al. in 2003 [55]. Figure 19 shows a diagram of the sensor

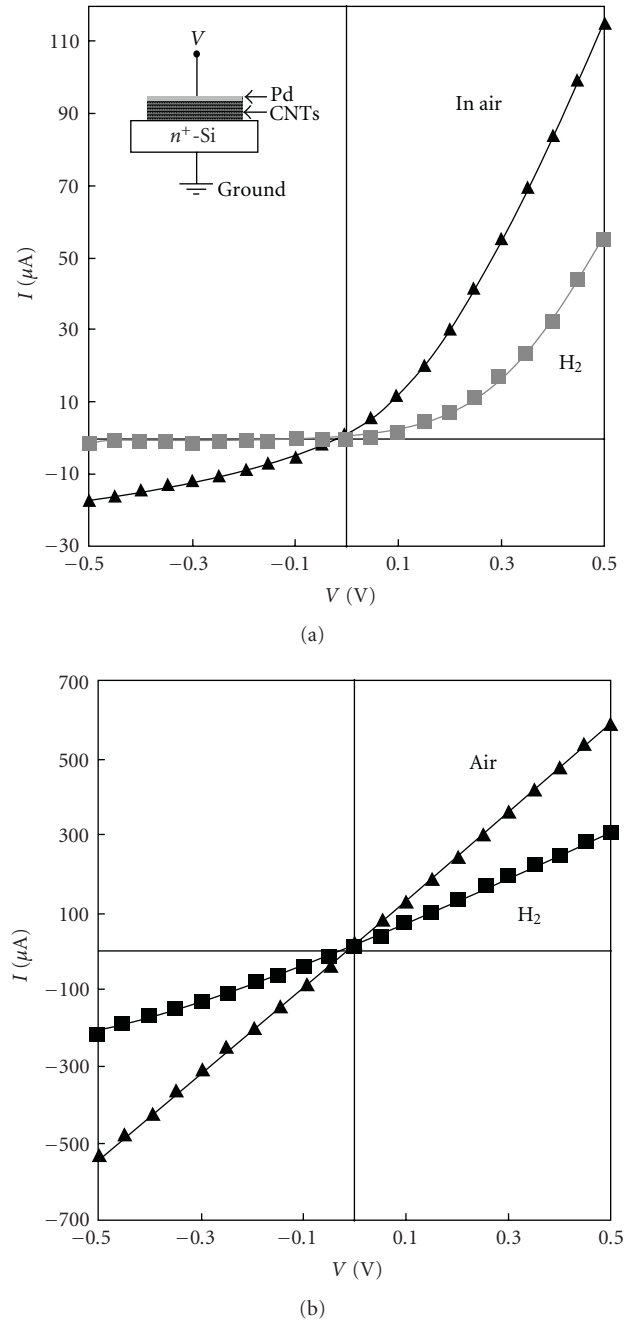


FIGURE 18: (a) Plot of measured current versus applied voltage (I - V) of the CNTs-based sensor in air and after exposure to constant flow of H_2 (concentration, 100%; flow rate, $10 \text{ mL}/\text{min}$) at room temperature. (b) Plot of measured current versus applied voltage (I - V) of the CNTs-based sensor in air and after exposure to constant flow of H_2 (concentration, 100%; flow rate, $10 \text{ mL}/\text{min}$) at 170°C [53].

structure. It consists of MWNT film anode, Al plate cathode and a $150 \mu\text{m}$ thick glass insulator between them. The vertically aligned MWNT film was prepared by CVD on SiO_2 substrate with tip diameter in the range of $25 \sim 30 \text{ nm}$ and $30 \mu\text{m}$ in length (Figure 19(c)). During operation, individual MWNTs create very high nonlinear electric fields

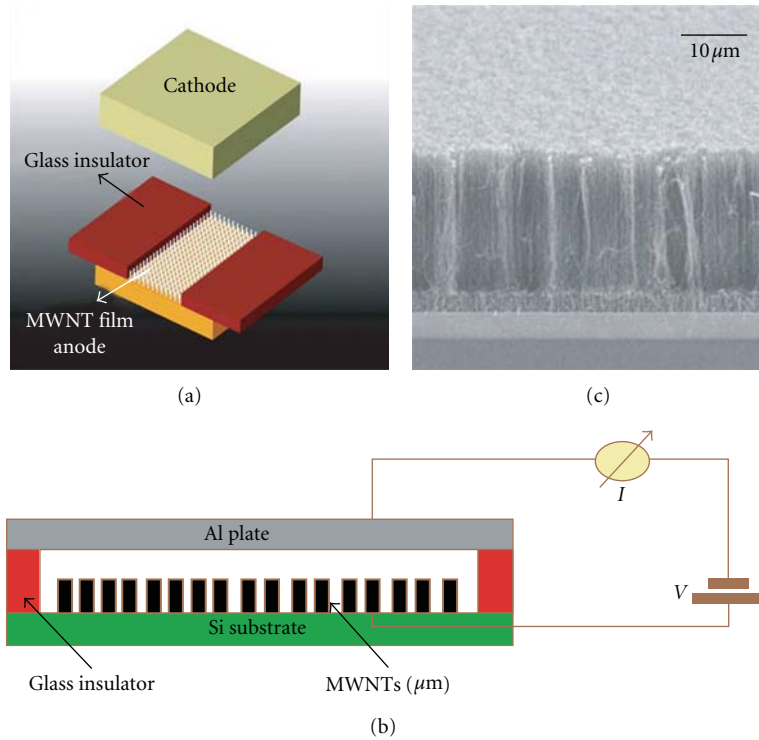


FIGURE 19: (a) Schematic diagram of the nanotube sensor device; (b) diagram of actual test set-up; (c) SEM micrograph of vertically aligned MWCNT film used as the anode [55].

near the tips [56, 57]. This results in the formation of a “corona” or conduction filament of high ionized gas that surrounds the MWNT tips, and thereby promotes the formation of a self-sustaining interelectrode discharge at very low voltage. Compared with ionization chamber with metal anode (without CNTs), the breakdown voltage of air was brought down dramatically from 960 V to 346 V. Different gases including NH_3 , CO_2 , N_2 , O_2 , He, Ar, and air were tested and showed distinct and precise breakdown voltage (Figure 20).

The precise breakdown voltage provides a “fingerprint” to each gas and indicates the potential for gas identification within a mixture of gases. The discharge current of each gas showed almost linear relationship with the gas concentration, but the breakdown voltage was rarely affected by the concentration (see Figure 21). This was explained by the fact that the discharge current is dominated by the number of molecules per unit volume and the breakdown voltage depends mainly on the intensity of electric field and the bonding energy of the gas molecules.

Nanotubes are good electron emitter due to their sharp tip curvature and low electron escaping work function. If CNT films are deposited as cathode of the device instead of anode, the breakdown process will be initiated by a negative corona. Field emission may occur under low pressure to enhance the ionization, and lower breakdown voltage can be obtained as a result. Kim [58, 59] designed an ionization chamber with CNTs as the emitters for the detection of gases with low adsorption energy. The fabrication process and structure of the sensor are shown in Figure 22. CNTs were

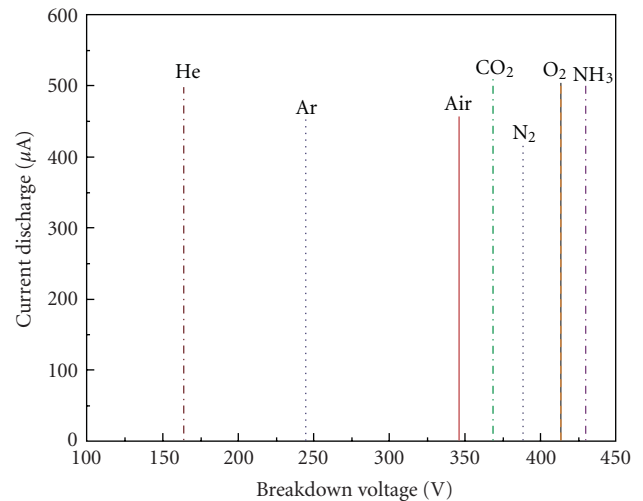
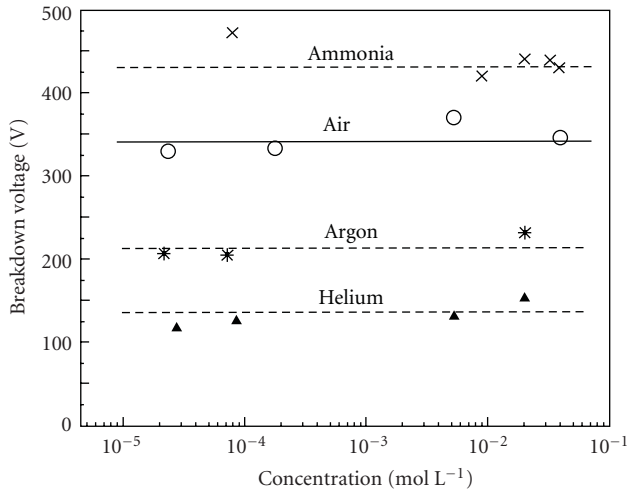
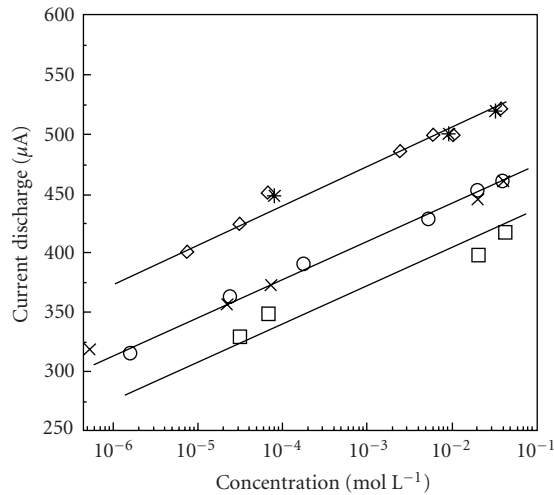


FIGURE 20: Current-voltage curves for electrical breakdown for NH_3 , CO_2 , N_2 , O_2 , He, Ar and air [55].

grown on n-type silicon substrate by CVD and served as the cathode. During operation, once electrons are emitted from the CNTs under certain voltage, they are accelerated towards the anode, collide with gas molecules, and induce ionization of the neutral molecules. Eventually it will lead to a current multiplication of breakdown. By Paschen’s law, the initial sparking breakdown voltage in an air gap is a function of the product of gas pressure and the electrodes distance.



(a)



(b)

FIGURE 21: Effect of gas concentration on the electrical breakdown. (a) Breakdown voltage as a function of concentration; breakdown voltages vary only slightly with gas concentration; (b) discharge current at breakdown as a function of gas concentration. The discharge current varies logarithmically with concentration [55].

Therefore, the initial breakdown voltages are measured as a function of the gas concentration. Figure 23 shows the dependence of the initial breakdown voltage on air concentration in the chamber. On contrary with Madi's results [55], the breakdown voltage decreases with increasing concentration and then increase again. The decreasing of breakdown voltage at first was explained by the dependency of the discharge current on the amount of neutral molecules, which can provide electron-ion pairs generated by collisions. When the concentration increases to a certain value, the ionization rate is predominantly determined by the length of the mean free path rather than the numbers of the molecules.

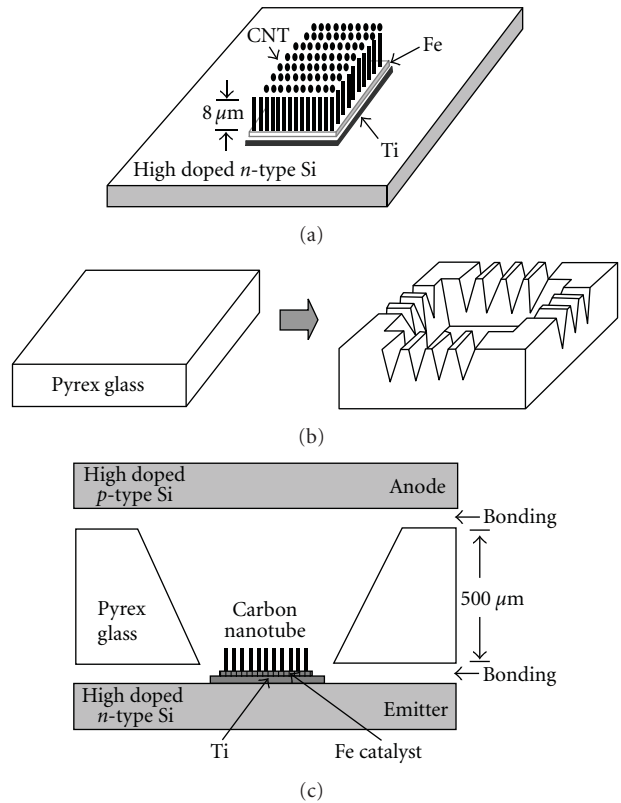


FIGURE 22: Fabrication process: (a) CNT electron emitters, (b) glass patterning by sand blast method, and (c) Si/glass anodic bonding [58].

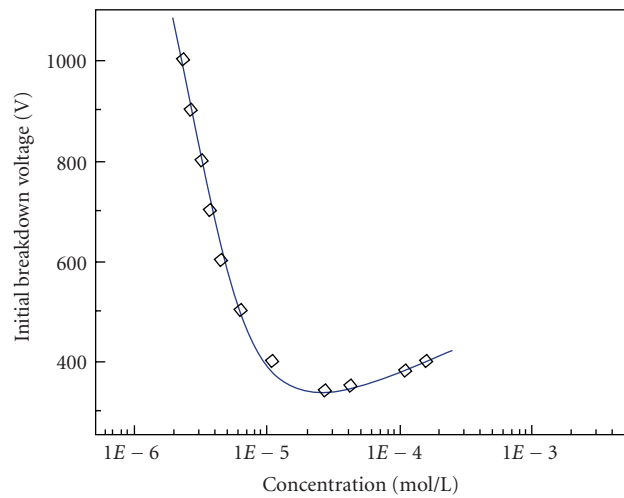


FIGURE 23: Dependence of initial breakdown voltage on air concentration [59].

With higher concentration, which means shorter mean free path, the ionization rate is reduced which results in higher breakdown value [59].

Another important factor that dominates the ionization characteristic is the distance between anode and cathode. According to Paschen's curve, a certain gap distance is

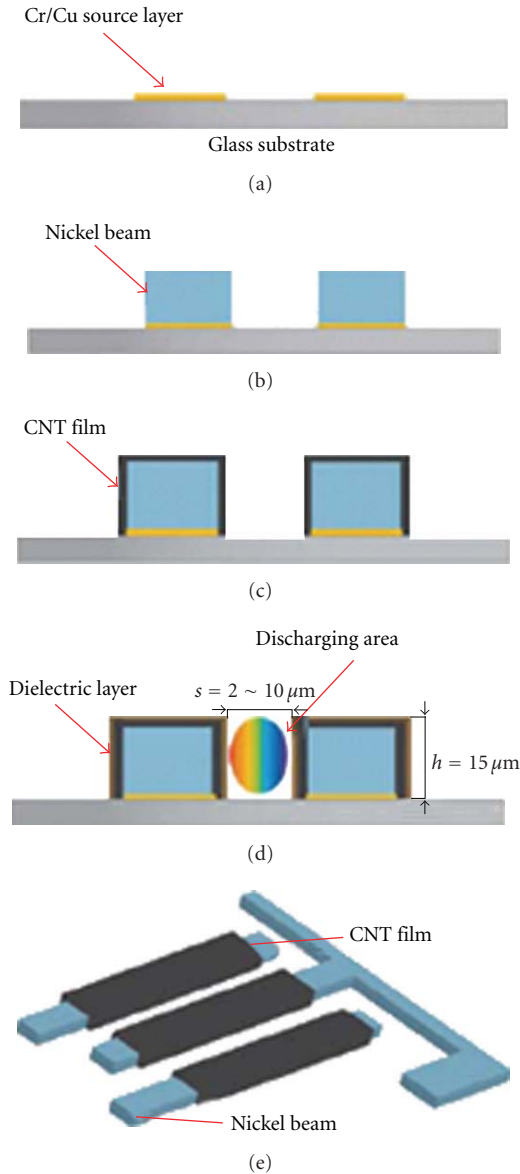
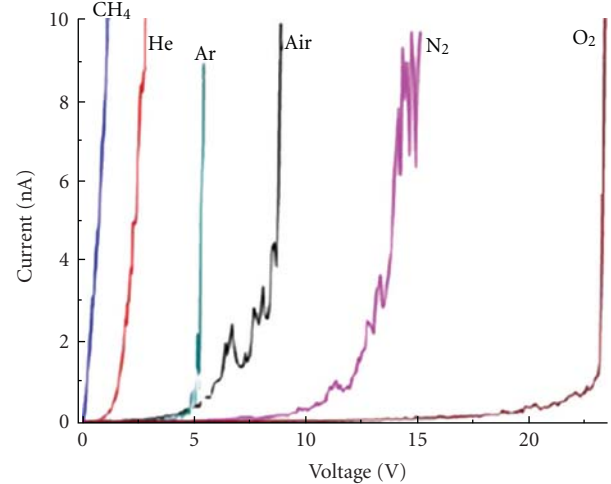


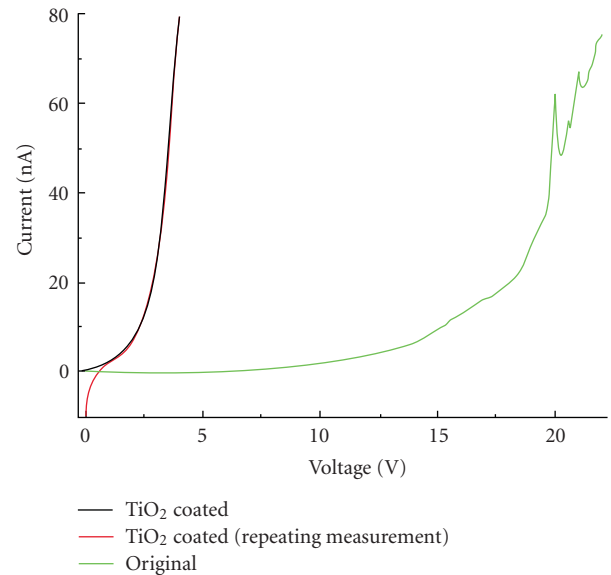
FIGURE 24: Fabrication process flow and schematic diagram of the sensor [60].

required for breakdown phenomenon to be induced, and the breakdown voltage decreases by bringing the electrodes closer. In the capacitor-architecture device, it is very difficult to control the electrode gap under $10 \mu\text{m}$ to gain a safe operation voltage. Hou et al. [54] introduced a novel hollow slot electrode system with CNT sidewalls and electrode spacing of $6\text{--}12 \mu\text{m}$ for gas ionization sensors, which dramatically decreased the threshold voltage to $5\text{--}40\text{ V}$.

Based on same idea and integrated dielectric barrier discharge (DBD) mechanism, Wu et al. [60] designed and fabricated a novel ionization gas sensor with short-gas spacing, CNTs and DBD coating to realize low power consumption and breakdown voltage. As shown in Figure 24, the IDE electrodes are deposited and patterned on glass substrate. CNTs are deposited by electrophoresis method and



(a)



(b)

FIGURE 25: (a) The discharge $I\text{-}V$ curves of 6 different gases. (b) The gas discharge $I\text{-}V$ curves of the same device before and after TiO_2 coated [60].

then a thin film of TiO_2 dielectric barrier was deposited by sputtering on top of CNTs serving as the DBD layer. The results show that the sensor can successfully distinguish different gases by the fingerprinting breakdown voltage, as shown in Figure 25(a). With the device of $8 \mu\text{m}$ spacing gap, the breakdown voltage for air is brought down dramatically to 5 V . It is also demonstrated that the DBD layer effectively lowers the breakdown voltage and improves the reproducibility of the device (Figure 25(b)). The low power consumption and breakdown voltage show a bright future of compact, battery powered, safe operation, and wide range of the applications of CNTs-based ionization gas sensors.

4.3. CNTs Based Gas Sensing Capacitor. Yeow and She [63] demonstrated the use of randomly aligned CNTs-based

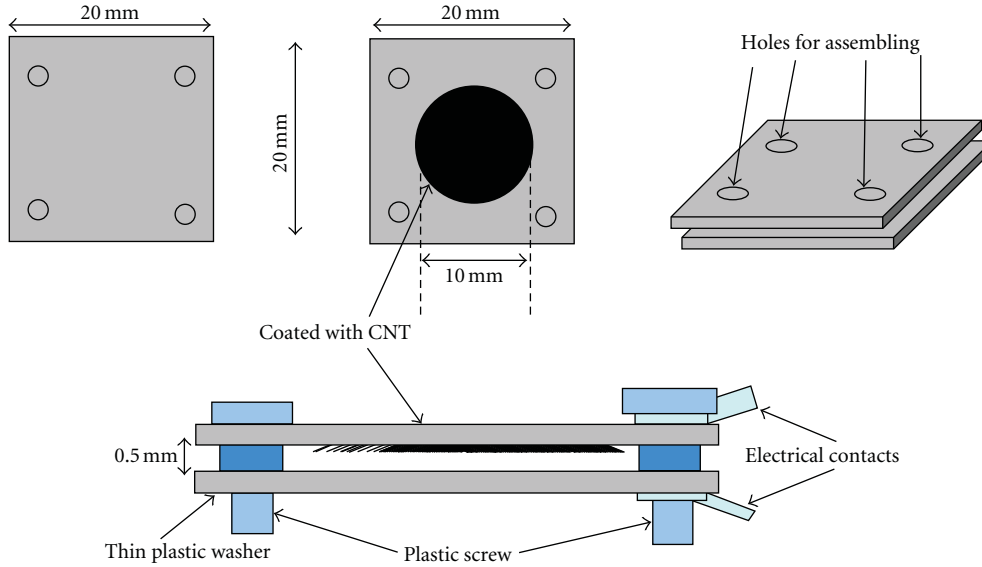


FIGURE 26: Parallel plate capacitive humidity sensor with MWNTs deposited on one plate [63].

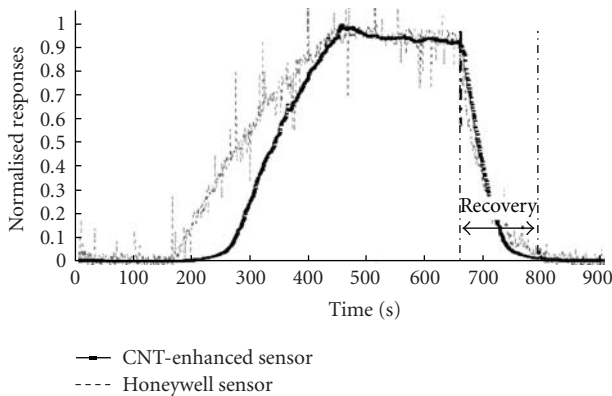


FIGURE 27: The normalized response of the nanotube and the Honeywell sensors [63].

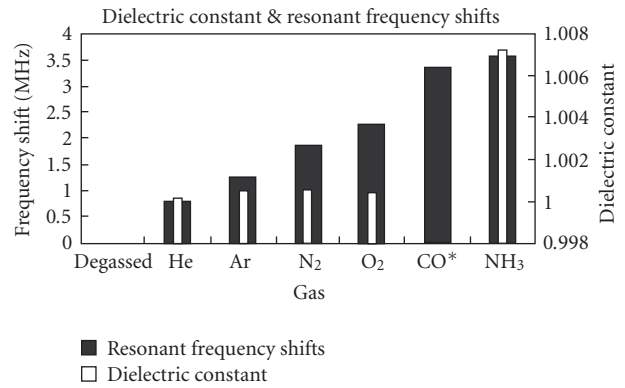


FIGURE 29: Resonant frequency shifts (solid bars) and dielectric constants (open bars) of various polar and nonpolar gases. At this point, room temperature value for dielectric constant of CO is not available in the literature [65].

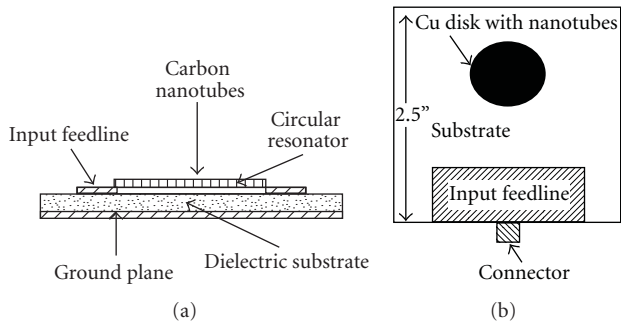


FIGURE 28: (a) Schematic of front view of the resonator circuit. (b) Top view of the resonator sample coated with nanotubes [65].

capacitor for humidity sensing. The structure of the parallel plate capacitor is shown in Figure 26. The sensor showed linear response to humidity change from 65% to 80% and

very fast response and recovery in this sensing range (as shown in Figure 27). It is believed that the increase of the capacitance under high relative humidity is caused by capillary condensation, which is induced by the nanopores and interstitial gaps in the random aligned CNTs structure.

Snow et al. [64] also developed a capacitor with SWNTs and highly doped Si substrate as the two plates. The sensor showed high sensitivity to a wide range of vapours. When excitation voltage is applied between the two plates, a large concentration of electric field is created at the tip of the nanotubes. This results in the polarization of the adsorbed molecules and the increase of the capacitance value.

4.4. Resonance Frequency Shifts. The change of the electrical property of CNTs upon exposure to gases can also be applied to resonator sensors. Chopra et al. [65, 66] fabricated a

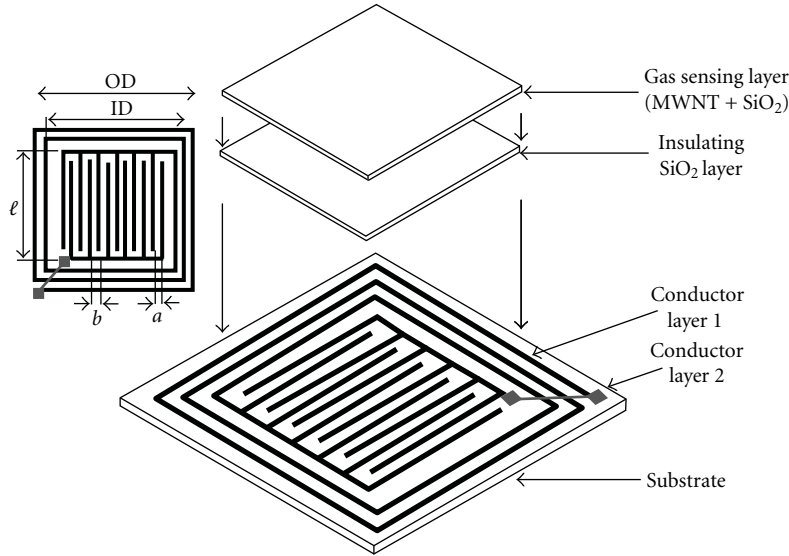


FIGURE 30: Schematic drawing of the MWNT gas sensor. A planar inductor interdigital capacitor pair is photolithographically defined upon a copper clad printed circuit board. The capacitor is first coated with a protective electrically insulating SiO_2 layer followed by a layer of gas responsive MWNT- SiO_2 composite [68].

circular disk resonator with SWNTs coated on top of the disk. The design of the sensor is shown in Figure 28. The input feedline also serves as the output port to an analyzer. According to

$$f_0 = \frac{1.841c}{2\pi a\sqrt{\epsilon_r}}, \quad (2)$$

where f_0 is the resonant frequency of the resonator, c is the speed of light in vacuum, a is the radius of the disk, and ϵ_r is the relative dielectric constant of the substrate, when the CNTs-based resonator is exposed to certain vapours, the change of the dielectric constant of the circular disk with CNTs on top results in the resonate frequency shift. Figure 29 shows the sensor's response to different gases. The sensor can detect a wide range of vapours including NH_3 , CO , N_2 , He , O_2 , and Ar with low concentrations. Since different gas caused different shift value of the resonate frequency, the sensor possess a good sensing selectivity.

CNTs-coated surface acoustic waves (SAWs) sensor also showed high sensitivity to volatile organic vapours [67]. Ong et al. [68] built a wireless, inductor-capacitor resonant-circuit (LC) gas sensor with MWNT- SiO_2 composite as the sensing layer. Figure 30 showed the sensor's structure. It consists of a printed LC resonant circuit that is first coated with a protective, electrically insulating SiO_2 layer, followed by a second layer of gas-responsive MWNT- SiO_2 mixture with the SiO_2 matrix acting to physically bind the MWNTs to the sensor. When the sensor is exposed to various gases, the relative permittivity ϵ_r' and the conductivity (proportional to ϵ_r'') of the MWNTs change, resulting in the change of the effective complex permittivity of the coating and hence the resonant frequency of the sensor. The frequency spectrum of the sensor is obtained by a sensor-monitoring loop antenna. It is found that the ϵ_r'' of the nanotubes shifted lower when exposed to CO_2 , NH_3 (which are reducing gases) and higher

when exposed to O_2 (which is oxidizing agent). This can be explained by the p-type nature of the MWNTs. The change of the nanotubes' permittivity ϵ_r' upon exposure to the gases was caused by the permittivity difference between the agents and the MWNTs. With this wireless, passive, remote query sensor platform, long term monitoring from within sealed containers and environment can be achieved.

5. Functionalized CNTs and CNTs-Based Composites for Gas Sensing

5.1. Functionalization of CNTs for Gas Sensing. Covalent sidewall functionalization opens new doors for the application of CNTs in many areas [69–71]. As discussed in Section 2, the electronic sensitivity of CNTs to various gases is highly limited by the binding energy and charge transfers of the molecules with the CNTs wall. It was proved theoretically that by doping CNTs with B- and/or N- and $\text{B}_x\text{C}_y\text{N}_z$ groups, their electronic properties can be very sensitive to a wide range of gas vapours [43].

Sin et al. [72] demonstrated the resistance response of chemically functionalized MWNTs (f-CNTs) to alcohol vapours with ultralow power consumption. For the fabrication of the sensor, purified MWNTs were sonicated in 3 : 1 concentrated sulfuric acid and nitric acid for different time intervals. By this method, the MWCNTs can be oxidized and COOH groups will be grafted along the sidewall and the tube ends of the MWCNTs as shown in Figure 31(a). It is believed that with the polar COOH groups attached onto the nanotubes surface, the sensors will give stronger responses towards the alcohol vapours as their absorption efficiency with these volatile organic molecules will be increased due to the dipole-dipole interactions (mainly hydrogen bonding) between the COOH and the polar organic molecules. Figure 31(b) shows a schematic diagram of how the ethanol

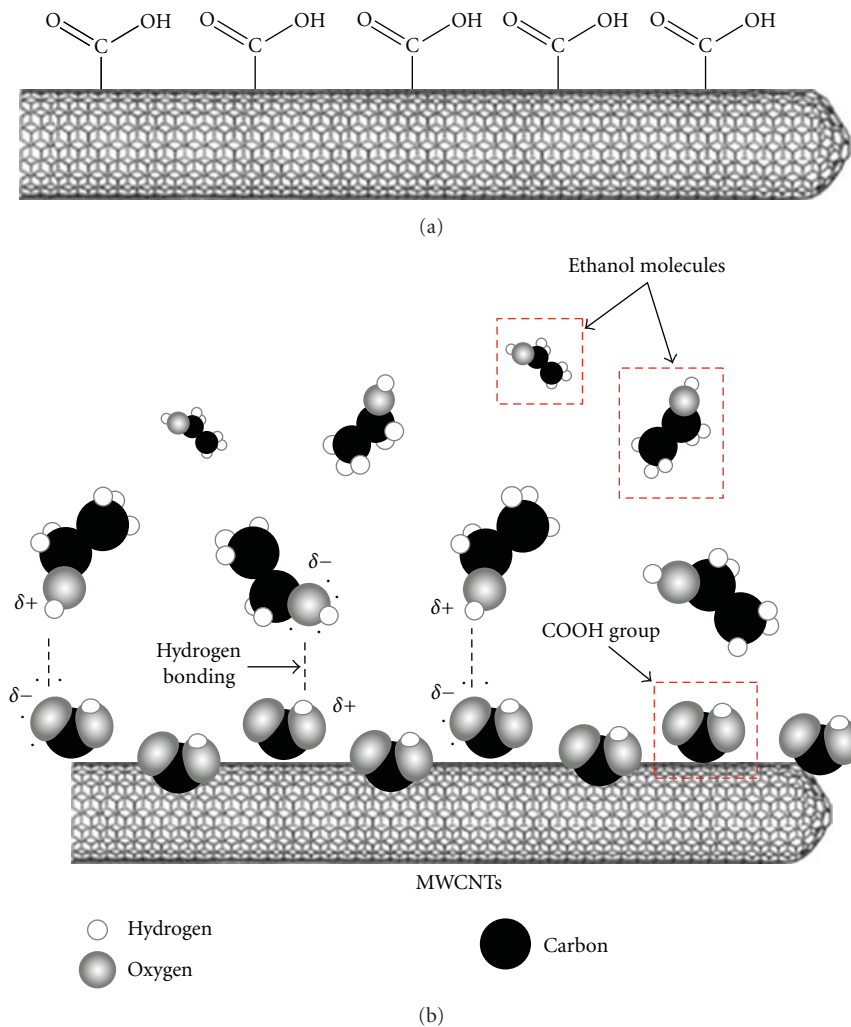


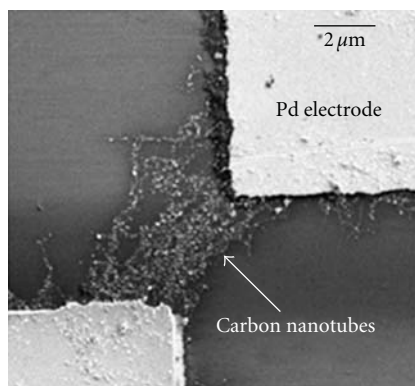
FIGURE 31: (a) Schematic diagram of the chemically functionalized carbon nanotubes, which have COOH groups attached along the sidewall of the MWCNTs. (b) The proposed mechanism for alcohol vapour detection using f-CNTs sensors. The COOH groups tend to form hydrogen bonding with the ethanol molecules at room temperature [72].

molecules interact with the COOH groups through hydrogen bonds. The f-CNTs were batch manipulated across Au microelectrodes by electrophoresis and their resistance change was measured for alcohol exposure. The sensor showed a linear response to alcohol vapour concentrations from 1 to 21 ppm and good selectivity to air flow, water vapour and alcohol vapour. Compared to bare CNTs, the functionalized CNTs increased the sensitivity from $\sim 0.9\%$ to 9.6% .

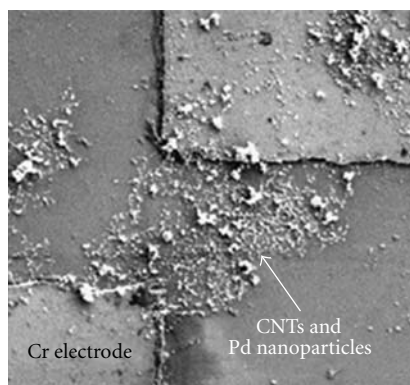
Hydrogen sensing is always an important topic in gas sensing research due to the safety concerns of handling hydrogen-based utilities. Although CNTs have been proved to be a good gas sensing material, pure CNTs show no response to H_2 due to the weak binding energy [73]. However, when functionalized with Pt or Pd, which act as a catalyst for the adsorption of H_2 , CNTs can be very sensitive to hydrogen [74, 75]. Take Pt as an example, hydrogen molecules dissociate into atomic hydrogen on Pt surfaces and form PtH_2 , which will lower the work function of Pt and cause the electron transfer from Pt to MWNTs [76–78].

There are several ways to functionalize CNTs with Pt or Pd. Krishna Kumar and Ramaprabhu [79] dispersed Pt nanoparticles into MWNTs by a series of chemical solution treatment. Suehiro demonstrated two effective methods [80]. For one method, SWCNTs were DEP-trapped onto a microelectrode made of Pd so that the CNT/Pd interface was formed at both ends of CNTs lying over the Pd electrode surface (shown in Figure 32(a)). The other type of CNT/Pd gas sensor was fabricated by simultaneously DEP-trapping SWCNTs and Pd nanoparticles onto a chromium (Cr) microelectrode (see Figure 32(b)). Both types of the CNT/Pd gas sensors could respond to hydrogen, while the CNT sensor without the Pd functionalization could not.

5.2. CNTs/Polymer Composites Gas Sensors. Organic polymers are one of the principal materials applied in gas sensing systems. Some conducting polymers can behave like semiconductors due to their heterocyclic compounds which display physicochemical characteristics. As a result,



(a)



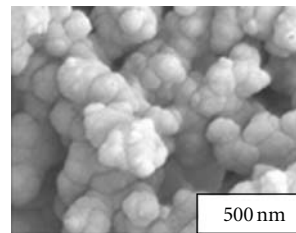
(b)

FIGURE 32: Scanning electron microscope (SEM) images of types A and B sensors trapped in castellated microelectrode gaps by positive DEP: (a) type A (CNTs trapped onto a Pd microelectrode); (b) type B (CNTs and Pd nanoparticles trapped onto a Cr microelectrode) [80].

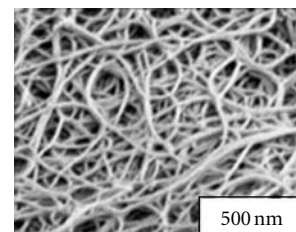
reversible changes in the sensing layer's conductivity can be detected upon polar chemicals' adsorption on the surfaces at room temperature [81]. This effect is believed to be caused by the charge transfer between gas molecules and the polymer or the polymer film's swelling [82]. This sensing response has intensively driven the motivation to develop high sensitive and selective gas/chemical sensors by tailoring the compounds of different organic polymers.

Non-conductive polymers can also be used as gas sensors. For some polymers, the bulk dissolution of gas into the film can cause changes of their physical properties [82]. Since most physical property changes are not readily detectable; researchers have tried to integrate polymers with other functional sensing elements to achieve easier detection process. For example, a recent experimental and theoretical study on the chemical sensing characteristic of polymer-coated resonators was reported by Avramov et al. [83] and Yantchev et al. [84].

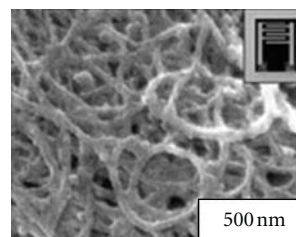
Another promising sensing material based on polymers is conducting particles-insulating matrix composition. The polymer acts as the insulating matrix while dispersed conducting particles provide the conducting path for sensing



(a)



(b)



(c)

FIGURE 33: FESEM images of (a) pure Ppy, (b) purified SWNT bundles, and (c) the SWNT/Ppy nanocomposite. Inset: optical microscope image of the electrodes [90].

[85]. Due to adsorption of interested analyt, there are volumetric changes of the matrix polymer. This can lead to a distinct change in percolation-type conductivity around a critical composition of the material, which is known as "percolation threshold". Generally, the percolation threshold is dependent on the shape of the conducting particle. Composite consisted of particles with higher aspect ratio shows lower threshold and higher sensitivity [86]. CNTs, with almost one-dimensional thread-like structure and good conductivity, are ideal as the dispersed particles in this conducting particles-insulating matrix composition for gas sensing systems. Therefore, CNTs/polymer composites have been intensively studied for gas sensors [87–89].

An et al. [90] prepared an SWNT/polypyrrole (Ppy) nanocomposite by a simple and straightforward in situ chemical polymerization of pyrrole and SWMTs mixture. The composite was then spin-casted onto prepatterned IDEs for resistance measurement. Figure 33 shows the SEM image of the Ppy, SWNTs, and SWNT/Ppy nanocomposite. The resistance responses of all three materials to NO₂ are shown in Figure 34. Although all of them showed degradation under long time exposure, the nanocomposite showed a better sensitivity than the pure materials, which was due to the enhanced conductivity of the material by dispersed CNTs.

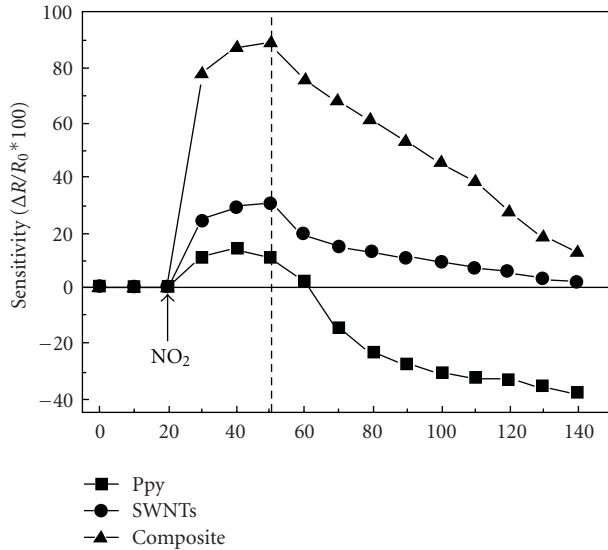


FIGURE 34: The change in sensitivity as a function of gas exposure time at an NO_2 concentration of 3000 ppm [90].

Cho et al. investigated the chemical sensing characteristic of SWCNT-Ethyl cellulose (EC) composite [85]. To get uniform dispersion of CNTs and stable composite, the material was prepared carefully with several steps. Poly (p-phenylenevinylene-co-2,5-dioctoxy-m-phenylenevinylene) (PmPV) was used as the dispersant of the nanotubes and chloroform was used as the media. The nanotubes sol was sonicated for 4 hours before mixed with EC, and then the mixture was sonicated for other 6 hours. The mixed sol were sprayed on interdigitated electrodes and annealed at 80°C for 24 hours to form the thin sensing film. The sensor's response to benzene and ethanol was measured separately as a function of gas concentration and SWCNTs' content in the composite. The change of resistance showed almost linear relationship with concentration. The maximum sensitivity was 9% for the film with 5 wt.% SWCNT contents when exposed to 5,000 ppm of benzene. The sensor's response to ethanol was less obvious and with some noise, however, it showed good linearity within the concerned range with short response and recovery time, as shown in Figure 35.

Based on the same idea, Philip et al. [91] developed composite thin film of polymethylmethacrylate (PMMA) with MWCNTs or oxidation-modified MWCNTs (f-CNTs) for gas sensing. The resistance changes of both the composites were evaluated upon exposure to different gases including dichloromethane, chloroform, acetone, and so forth. Both the CNT/PMMA and the f-CNT/PMMA composites showed increasing resistance upon exposure to these vapours at room temperature, as shown in Figure 36. This behaviour was explained on the basis of volume expansion and polar interaction of the CNT surface with vapour molecules. The f-CNT/PMMA showed significant improvement on the sensor's behaviour including the sensitivity and the response time and recovery, as shown in Figure 36. This can be

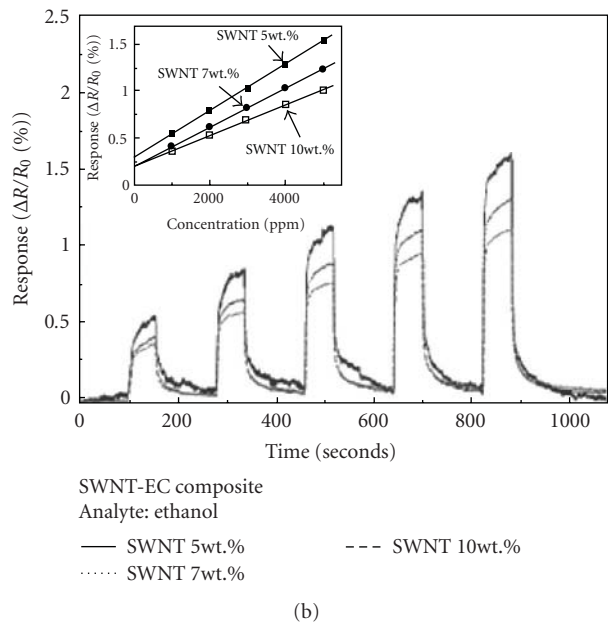
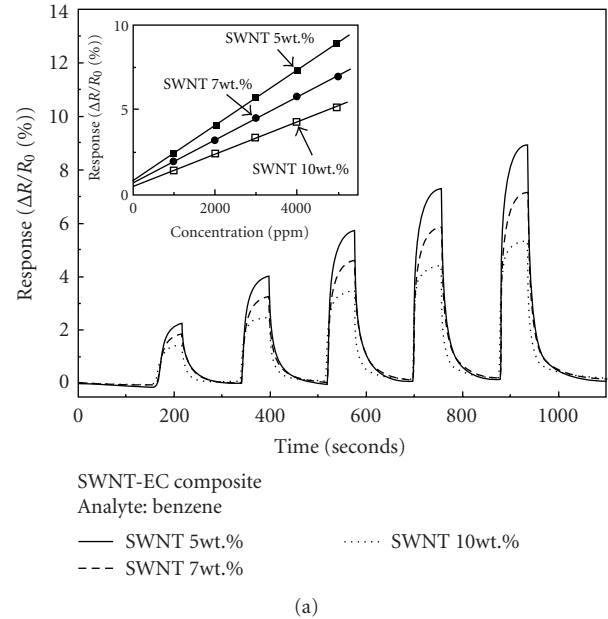


FIGURE 35: (a) The gas sensing properties of the SWNT-Polymer (EC) composites for benzene vapour. (b) The gas sensing properties of the SWNT-Polymer (EC) composites for ethanol vapour. The concentrations of the vapours ranged from 1000 ppm to 5000 ppm. The insets in the upper left corners show the linear relationship [85].

explained by the effects of oxidation on the electronic properties of CNTs that was discussed in a previous section.

In addition of CNT/polymer composite, the sensing characteristics of polymer-coated CNTs film to specific gases were also investigated. In general, CNTs do not have sensing response to all gases and vapours but only the ones with high adsorption energy or that can interact with them. Therefore, coating or doping of an enhance element on CNTs may broaden the application range. Based on the IDE SWCNTs resistance gas sensor that they developed,

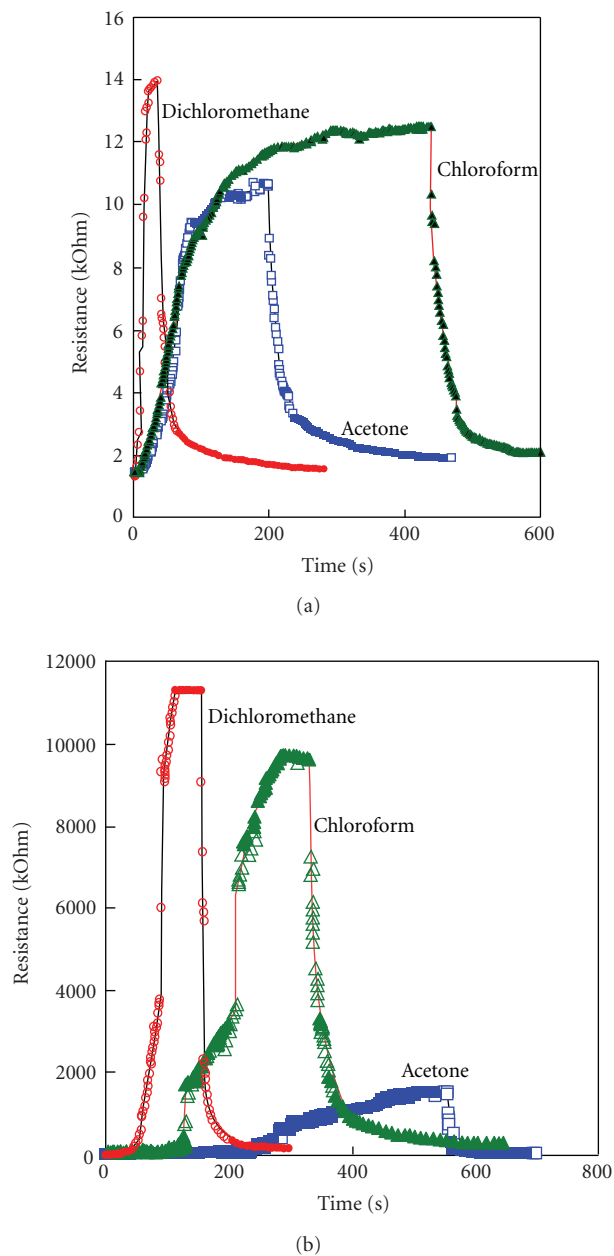


FIGURE 36: (a) Response of the CNT/PMMA composite to dichloromethane, chloroform, and acetone vapours; (b) Response of the f-CNT/PMMA composite to dichloromethane, chloroform and acetone vapours [91].

Li et al. studied the sensing character of the same structure but with polymer coatings on CNTs [92]. Chlorosulfonated polyethylene was dissolved in tetrahydrofuran (THF) solvent as a coating solution for Cl_2 sensing, and Hydroxypropyl cellulose was dissolved in chloroform as coating to detect HCl. The resistance of polymer coated SWCNT film changed upon exposure to Cl_2 and HCl while uncoated pure SWCNTs showed no sensing signal. The sensing response demonstrates a huge potential of using modified CNTs gas

sensing materials for a broad range of gases and chemical vapours.

6. Conclusions

With less than twenty years history, the progress and application in CNTs-related technology has been developed impressively fast due to their unique inherent morphologies and properties. CNTs-based sensors have demonstrated huge potential and found their application in various areas. Gas sensors based on both SWNTs and MWNTs have been developed. The nanotubes can be integrated with different sensor architectures by direct-growing, drop-deposition, printing, or DEP method. It has been proved both theoretically and experimentally that, the electrical resistance, thermoelectric power, and local density of states of SWNTs can be reversibly changed by exposure to certain vapours. This can be attributed to the charge transfer between the molecules and the nanotubes, or the change of the charge carriers lifetime in CNTs. Therefore, gas sensing FET or resistors that measure the resistance change of CNTs as the transducer is the most commonly used sensor structures. However, this limits the range of the gases that CNTs sensors can detect, especially for the sensing of inert agents. Compared with the resistance sensors, CNTs enhanced ionization chambers allow the detection of gas molecules with low adsorption energy, hence a wide range of vapours. With CNTs integrated, the breakdown voltage can be lowered significantly. Other promising methods to improve the sensing characteristics include the functionalization of CNTs and nanocomposites of CNTs with various polymers, which can broaden the sensing range or enhance the sensitivity. CNTs can also be integrated into resonators sensors. By measuring the change of the resonate frequency, wireless gas sensing can be achieved.

Although CNTs have demonstrated their great potential for gas sensing experimentally, there are still several challenges remained before the real-world application. Synthesis of pure and ideal CNTs is still challenging and costly. It is very difficult to grow defect-free nanotubes continuously to macroscopic length. The precise control over the growth or dispersion of CNTs on surfaces is another problem. Depending on the preparation technique and process, the property and behaviour of the sensors can vary significantly, which is very crucial to the stability of the CNTs-based devices. Therefore, the ability to synthesize of identical and reproducible CNTs with consistent properties is very important for the application of CNTs in all areas. Degradation of the devices has to be investigated more deeply before real-world application. Slow response and recovery is another challenge to be addressed for CNTs-based gas sensors, which is caused by the nature of gas adsorption and desorption process to the nanotubes. However, it was demonstrated that by integrating a microheater under the MWCNTs sensing layer or shortly exposure to UV light, the response time of the sensor can be improved [93, 94]. It is believed that, with the increase interests and development of related technologies, CNTs gas sensors have a promising future and will bring a huge change to the current industries and our everyday life.

References

- [1] J. Li, "Carbon nanotubes applications: chemical and physical sensors," in *Carbon Nanotubes: Science and Applications*, M. Meyyappan, Ed., CRC Press, Boca Raton, Fla, USA.
- [2] Z. M. Rittersma, "Recent achievements in miniaturised humidity sensors—a review of transduction techniques," *Sensors and Actuators A*, vol. 96, no. 2-3, pp. 196–210, 2002.
- [3] R. Fenner and E. Zdankiewicz, "Micromachined water vapor sensors: a review of sensing technologies," *IEEE Sensors Journal*, vol. 1, no. 4, pp. 309–317, 2001.
- [4] E. Traversa, "Ceramic sensors for humidity detection: the state-of-the-art and future developments," *Sensors and Actuators B*, vol. 23, no. 2-3, pp. 135–156, 1995.
- [5] S. Iijima, "Helical microtubules of graphitic carbon," *Nature*, vol. 354, no. 6348, pp. 56–58, 1991.
- [6] M. Meyyappan, *Carbon Nanotubes: Science and Applications*, CRC Press, Boca Raton, Fla, USA.
- [7] M. S. Dresselhaus, G. Dresselhaus, and P. C. Eklund, *Science of Fullerenes and Carbon Nanotubes*, Academic Press, New York, NY, USA, 1996.
- [8] R. Saito, M. Fujita, G. Dresselhaus, and M. S. Dresselhaus, "Electronic structure of chiral graphene tubules," *Applied Physics Letters*, vol. 60, no. 18, pp. 2204–2206, 1992.
- [9] M. Dresselhaus, G. Dresselhaus, and P. Avouris, *Carbon Nanotubes: Synthesis, Structure, Properties and Applications*, Springer, Berlin, Germany, 2001.
- [10] N. Sinha, J. Ma, and J. T. W. Yeow, "Carbon nanotube-based sensors," *Journal of Nanoscience and Nanotechnology*, vol. 6, no. 3, pp. 573–590, 2006.
- [11] J. Li and H. T. Ng, "Carbon nanotubes sensors," in *Encyclopedia of Nanoscience and Nanotechnology*, vol. 1, pp. 591–601, Marcel Dekker, New York, NY, USA, 2004.
- [12] H. Dai, "Nanotube growth and characterization," in *Carbon Nanotubes: Synthesis, Structure, Properties and Applications*, M. S. Dresselhaus and G. Dresselhaus, Eds., pp. 29–54, Springer, New York, NY, USA, 2000.
- [13] T. W. Ebbesen, "Production and purification of carbon nanotubes," in *Carbon Nanotubes: Preparation and Properties*, T. W. Ebbesen, Ed., pp. 139–162, CRC Press, Boca Raton, Fla, USA, 1997.
- [14] J. Li, Y. Lu, Q. Ye, et al., "Carbon nanotubes sensors for gas and organic vapour detection," *Nano Letters*, vol. 3, no. 7, pp. 929–933, 2003.
- [15] Y. D. Lee, W.-S. Cho, S.-I. Moon, et al., "Gas sensing properties of printed multiwalled carbon nanotubes using the field emission effect," *Chemical Physics Letters*, vol. 433, no. 1–3, pp. 105–109, 2006.
- [16] K. Yamamoto, S. Akita, and Y. Nakayama, "Orientation and purification of carbon nanotubes using ac electrophoresis," *Journal of Physics D*, vol. 31, no. 8, pp. L34–L36, 1998.
- [17] K. Bubke, H. Gnewuch, M. Hempstead, J. Hammer, and M. L. H. Green, "Optical anisotropy of dispersed carbon nanotubes induced by an electric field," *Applied Physics Letters*, vol. 71, no. 14, pp. 1906–1908, 1997.
- [18] T. Prasse, J.-Y. Cavaille, and W. Bauhofer, "Electric anisotropy of carbon nanofibre/epoxy resin composites due to electric field induced alignment," *Composites Science and Technology*, vol. 63, no. 13, pp. 1835–1841, 2003.
- [19] X. Q. Chen, T. Saito, H. Yamada, and K. Matsushige, "Aligning single-wall carbon nanotubes with an alternating-current electric field," *Applied Physics Letters*, vol. 78, no. 23, pp. 3714–3716, 2001.
- [20] X. Liu, J. L. Spencer, A. B. Kaiser, and W. M. Arnold, "Electric-field oriented carbon nanotubes in different dielectric solvents," *Current Applied Physics*, vol. 4, no. 2–4, pp. 125–128, 2004.
- [21] F. Wakaya, T. Nagai, and K. Gamo, "Position control of carbon nanotube using patterned electrode and electric field," *Microelectronic Engineering*, vol. 63, no. 1–3, pp. 27–31, 2002.
- [22] R. Krupke, F. Hennrich, H. B. Weber, et al., "Contacting single bundles of carbon nanotubes with alternating electric fields," *Applied Physics A*, vol. 76, no. 3, pp. 397–400, 2003.
- [23] J. Suehiro, G. Zhou, and M. Hara, "Fabrication of a carbon nanotube-based gas sensor using dielectrophoresis and its application for ammonia detection by impedance spectroscopy," *Journal of Physics D*, vol. 36, no. 21, pp. L109–L114, 2003.
- [24] J. Suehiro, H. Imakiire, S. Hidaka, et al., "Schottky-type response of carbon nanotube NO₂ gas sensor fabricated onto aluminum electrodes by dielectrophoresis," *Sensors and Actuators B*, vol. 114, no. 2, pp. 943–949, 2006.
- [25] C. S. Huang, B. R. Huang, Y. H. Jang, M. S. Tsai, and C. Y. Yeh, "Three-terminal CNTs gas sensor for N₂ detection," *Diamond and Related Materials*, vol. 14, no. 11-12, pp. 1872–1875, 2005.
- [26] Y.-T. Jang, S.-I. Moon, J.-H. Ahn, Y.-H. Lee, and B.-K. Ju, "A simple approach in fabricating chemical sensor using laterally grown multi-walled carbon nanotubes," *Sensors and Actuators B*, vol. 99, no. 1, pp. 118–122, 2004.
- [27] J. Zhao, A. Buldum, J. Han, and J. P. Lu, "Gas molecule adsorption in carbon nanotubes and nanotube bundles," *Nanotechnology*, vol. 13, no. 2, pp. 195–200, 2002.
- [28] M. Tabib-Azar and Y. Xie, "Sensitive NH₃OH and HCl gas sensors using self-aligned and self-welded multiwalled carbon nanotubes," *IEEE Sensors Journal*, vol. 7, no. 10, pp. 1435–1439, 2007.
- [29] D. Ding, Z. Chen, S. Rajaputra, and V. Singh, "Hydrogen sensors based on aligned carbon nanotubes in an anodic aluminum oxide template with palladium as a top electrode," *Sensors and Actuators B*, vol. 124, no. 1, pp. 12–17, 2007.
- [30] T. Ueda, S. Katsuki, and N. Heidari Abhari, "Effect of laser irradiation on carbon nanotube films for NO_x gas sensor," *Surface & Coatings Technology*, vol. 202, pp. 5325–5328, 2008.
- [31] S. Peng and K. Cho, "Chemical control of nanotube electronics," *Nanotechnology*, vol. 11, no. 2, pp. 57–60, 2000.
- [32] C. Cantalini, L. Valentini, L. Lozzi, I. Armentano, J. M. Kenny, and S. Santucci, "NO₂ gas sensitivity of carbon nanotubes obtained by plasma enhanced chemical vapor deposition," *Sensors and Actuators B*, vol. 93, no. 1–3, pp. 333–337, 2003.
- [33] P. G. Collins, K. Bradley, M. Ishigami, and A. Zettl, "Extreme oxygen sensitivity of electronic properties of carbon nanotubes," *Science*, vol. 287, no. 5459, pp. 1801–1804, 2000.
- [34] K. A. Williams and P. C. Eklund, "Monte Carlo simulations of H₂ physisorption in finite-diameter carbon nanotube ropes," *Chemical Physics Letters*, vol. 320, no. 3-4, pp. 352–358, 2000.
- [35] G. Stan and M. W. Cole, "Hydrogen adsorption in nanotubes," *Journal of Low Temperature Physics*, vol. 110, no. 1-2, pp. 539–544, 1998.
- [36] C. K. W. Adu, G. U. Sumanasekera, B. K. Pradhan, H. E. Romero, and P. C. Eklund, "Carbon nanotubes: a thermoelectric nano-nose," *Chemical Physics Letters*, vol. 337, no. 1–3, pp. 31–35, 2001.
- [37] J. Han, in *Carbon Nanotubes: Science and Application*, M. Meyyappan, Ed., CRC Press LLC, Boca Raton, Fla, USA, 2005.
- [38] G. U. Sumanasekera, C. K. W. Adu, S. Fang, and P. C. Eklund, "Effects of gas adsorption and collisions on electrical transport in single-walled carbon nanotubes," *Physical Review Letters*, vol. 85, no. 5, pp. 1096–1099, 2000.

- [39] X.-P. Tang, A. Kleinhammes, H. Shimoda, et al., "Electronic structures of single-walled carbon nanotubes determined by NMR," *Science*, vol. 288, no. 5465, pp. 492–494, 2000.
- [40] S.-H. Jhi, S. G. Louie, and M. L. Cohen, "Electronic properties of oxidized carbon nanotubes," *Physical Review Letters*, vol. 85, no. 8, pp. 1710–1713, 2000.
- [41] R. D. Barnard, *Thermoelectricity in Metals and Alloys*, John Wiley & Sons, New York, NY, USA, 1972.
- [42] H. E. Romero, G. U. Sumanasekera, S. Kishore, and P. C. Eklund, "Effects of adsorption of alcohol and water on the electrical transport of carbon nanotube bundles," *Journal of Physics: Condensed Matter*, vol. 16, no. 12, pp. 1939–1949, 2004.
- [43] S. Peng and K. Cho, "Ab initio study of doped carbon nanotube sensors," *Nano Letters*, vol. 3, no. 4, pp. 513–517, 2003.
- [44] Z. Weng-Sieh, K. Cherrey, N. G. Chopra, et al., "Synthesis of BxCyNz nanotubules," *Physical Review B*, vol. 51, no. 16, pp. 11229–11232, 1995.
- [45] W.-Q. Han, J. Cumings, X. Huang, K. Bradley, and A. Zettl, "Synthesis of aligned BxCyNz nanotubes by a substitution-reaction route," *Chemical Physics Letters*, vol. 346, no. 5–6, pp. 368–372, 2001.
- [46] J. Kong, N. R. Franklin, C. Zhou, et al., "Nanotube molecular wires as chemical sensors," *Science*, vol. 287, no. 5453, pp. 622–625, 2000.
- [47] T. Someya, J. Small, P. Kim, C. Nuckolls, and J. T. Yardley, "Alcohol vapor sensors based on single-walled carbon nanotube field effect transistors," *Nano Letters*, vol. 3, no. 7, pp. 877–881, 2003.
- [48] O. K. Varghese, P. D. Kichambre, D. Gong, K. G. Ong, E. C. Dickey, and C. A. Grimes, "Gas sensing characteristics of multi-wall carbon nanotubes," *Sensors and Actuators B*, vol. 81, no. 1, pp. 32–41, 2001.
- [49] J. Chung, K.-H. Lee, J. Lee, D. Troya, and G. C. Schatz, "Multi-walled carbon nanotubes experiencing electrical breakdown as gas sensors," *Nanotechnology*, vol. 15, no. 11, pp. 1596–1602, 2004.
- [50] J. Sippel-Oakley, H. T. Wang, B. S. Kang, et al., "Carbon nanotube films for room temperature hydrogen sensing," *Nanotechnology*, vol. 16, pp. 2218–2221, 2005.
- [51] T. Ueda, S. Katsuki, K. Takahashi, H. A. Narges, T. Ikegami, and F. Mitsugi, "Fabrication and characterization of carbon nanotube based high sensitive gas sensors operable at room temperature," *Diamond and Related Materials*, vol. 17, no. 7–10, pp. 1586–1589, 2008.
- [52] L. Valentini, C. Cantalini, I. Armentano, J. M. Kenny, L. Lozzi, and S. Santucci, "Highly sensitive and selective sensors based on carbon nanotubes thin films for molecular detection," *Diamond and Related Materials*, vol. 13, no. 4–8, pp. 1301–1305, 2004.
- [53] Y. M. Wong, W. P. Kang, J. L. Davidson, A. Wisitsora-At, and K. L. Soh, "A novel microelectronic gas sensor utilizing carbon nanotubes for hydrogen gas detection," *Sensors and Actuators B*, vol. 93, no. 1–3, pp. 327–332, 2003.
- [54] Z. Hou, D. Xu, and B. Cai, "Ionization gas sensing in a microelectrode system with carbon nanotubes," *Applied Physics Letters*, vol. 89, no. 21, Article ID 213502, 3 pages, 2006.
- [55] A. Modi, N. Koratkar, E. Lass, B. Wei, and P. M. Ajayan, "Miniaturized gas ionization sensors using carbon nanotubes," *Nature*, vol. 424, no. 6945, pp. 171–174, 2003.
- [56] W. A. De Heer, A. Chatelain, and D. Ugarte, "A carbon nanotube field-emission electron source," *Science*, vol. 270, no. 5239, pp. 1179–1180, 1995.
- [57] N. de Jonge, Y. Lamy, K. Schoots, and T. H. Oosterkamp, "High brightness electron beam from a multi-walled carbon nanotube," *Nature*, vol. 420, no. 6914, pp. 393–395, 2002.
- [58] S. J. Kim, "Gas sensors based on Paschen's law using carbon nanotubes as electron emitters," *Journal of Physics D*, vol. 39, no. 14, pp. 3026–3029, 2006.
- [59] S. Kim, "CNT sensors for detecting gases with low adsorption energy by ionization," *Sensors*, vol. 6, no. 5, pp. 503–513, 2006.
- [60] J. Wu, H. Liu, D. Xu, et al., in *Proceedings of the 3rd IEEE International Conference on Nano/Micro Engineering and Molecular System*, Sanya, China, January 2008.
- [61] A. Wadhawan, R. E. Stallcup II, K. F. Stephens II, J. M. Perez, and I. A. Akwani, "Effects of O₂, Ar, and H₂ gases on the field-emission properties of single-walled and multiwalled carbon nanotubes," *Applied Physics Letters*, vol. 79, no. 12, pp. 1867–1869, 2001.
- [62] Z. Yong, L. Junhua, and L. Xin, "The structure optimization of the carbon nanotube film cathode in the application of gas sensor," *Sensors and Actuators A*, vol. 128, pp. 278–289, 2006.
- [63] J. T. W. Yeow and J. P. M. She, "Carbon nanotube-enhanced capillary condensation for a capacitive humidity sensor," *Nanotechnology*, vol. 17, no. 21, pp. 5441–5448, 2006.
- [64] E. S. Snow, F. K. Perkins, E. J. Houser, S. C. Badescu, and T. L. Reinecke, "Chemical detection with a single-walled carbon nanotube capacitor," *Science*, vol. 307, no. 5717, pp. 1942–1945, 2005.
- [65] S. Chopra, A. Pham, J. Gaillard, A. Parker, and A. M. Rao, "Carbon-nanotube-based resonant-circuit sensor for ammonia," *Applied Physics Letters*, vol. 80, no. 24, pp. 4632–4636, 2002.
- [66] S. Chopra, K. McGuire, N. Gothard, A. M. Rao, and A. Pham, "Selective gas detection using a carbon nanotube sensor," *Applied Physics Letters*, vol. 83, no. 11, pp. 2280–2282, 2003.
- [67] M. Penza, F. Antolini, and M. Vittori Antisari, "Carbon nanotubes as SAW chemical sensors materials," *Sensors and Actuators B*, vol. 100, no. 1–2, pp. 47–59, 2004.
- [68] K. G. Ong, K. Zeng, and C. A. Grimes, "A wireless, passive carbon nanotube-based gas sensor," *IEEE Sensors Journal*, vol. 2, no. 2, pp. 82–88, 2002.
- [69] J. L. Bahr and J. M. Tour, "Covalent chemistry of single-wall carbon nanotubes," *Journal of Materials Chemistry*, vol. 12, no. 7, pp. 1952–1958, 2002.
- [70] A. Hirsch, "Functionalization of single-walled carbon nanotubes," *Angewandte Chemie International Edition*, vol. 41, no. 11, pp. 1853–1859, 2002.
- [71] S. Niyogi, M. A. Hamon, H. Hu, et al., "Chemistry of single-walled carbon nanotubes," *Accounts of Chemical Research*, vol. 35, no. 12, pp. 1105–1113, 2002.
- [72] M. L. Y. Sin, G. C. T. Chow, G. M. K. Wong, W. J. Li, P. H. W. Leong, and K. W. Wong, "Ultralow-power alcohol vapor sensors using chemically functionalized multiwalled carbon nanotubes," *IEEE Transactions on Nanotechnology*, vol. 6, no. 5, pp. 571–577, 2007.
- [73] S. Dag, Y. Ozturk, S. Ciraci, and T. Yildirim, "Adsorption and dissociation of hydrogen molecules on bare and functionalized carbon nanotubes," *Physical Review B*, vol. 72, no. 15, Article ID 155404, 8 pages, 2005.
- [74] I. Sayago, E. Terrado, E. Lafuente, et al., "Hydrogen sensors based on carbon nanotubes thin films," *Synthetic Metals*, vol. 148, no. 1, pp. 15–19, 2005.
- [75] J. Kong, M. G. Chapline, and H. Dai, "Functionalized carbon nanotubes for molecular hydrogen sensors," *Advanced Materials*, vol. 13, no. 18, pp. 1384–1386, 2001.

- [76] A. T. Gee, B. E. Hayden, C. Mormiche, and T. S. Nunney, "The role of steps in the dynamics of hydrogen dissociation on Pt(533)," *Journal of Chemical Physics*, vol. 112, no. 17, pp. 7660–7668, 2000.
- [77] R. A. Olsen, Ş. C. Bădescu, S. C. Ying, and E. J. Baerends, "Adsorption and diffusion on a stepped surface: atomic hydrogen on Pt(211)," *Journal of Chemical Physics*, vol. 120, no. 24, pp. 11852–11863, 2004.
- [78] A. Mandelis and C. Christofides, *Physics, Chemistry and Technology of Solid State Gas Sensor Devices*, John Wiley & Sons, New York, NY, USA, 1993.
- [79] M. Krishna Kumar and S. Ramaprabhu, "Nanostructured Pt functionalized multiwalled carbon nanotube based hydrogen sensor," *Journal of Physical Chemistry B*, vol. 110, no. 23, pp. 11291–11298, 2006.
- [80] J. Suehiro, S. Hidaka, S. Yamane, and K. Imasaka, "Fabrication of interfaces between carbon nanotubes and catalytic palladium using dielectrophoresis and its application to hydrogen gas sensor," *Sensors and Actuators B*, vol. 127, no. 2, pp. 505–511, 2007.
- [81] P. N. Bartlett, P. B. M. Archer, and S. K. Ling-Chung, "Conducting polymer gas sensors—part I: fabrication and characterization," *Sensors and Actuators*, vol. 19, no. 2, pp. 125–140, 1989.
- [82] M. C. Petty and R. Casalini, "Gas sensing for the 21st century: the case for organic thin films," *Engineering Science and Education Journal*, vol. 10, no. 3, pp. 99–105, 2001.
- [83] I. D. Avramov, S. Kurosawa, M. Rapp, P. Krawczak, and E. I. Radeva, "Investigations on plasma-polymer-coated SAW and STW resonators for chemical gas-sensing applications," *IEEE Transactions on Microwave Theory and Techniques*, vol. 49, no. 4, pp. 827–837, 2001.
- [84] V. M. Yantchev, V. L. Strashilov, M. Rapp, U. Stahl, and I. D. Avramov, "Theoretical and experimental mass-sensitivity analysis of polymer-coated SAW and STW resonators for gas sensing applications," *IEEE Sensors Journal*, vol. 2, no. 4, pp. 307–312, 2002.
- [85] S. M. Cho, Y. J. Kim, Y. S. Kim, Y. Yang, and S.-C. Ha, "The application of carbon nanotube—polymer composite as gas sensing materials," *Proceedings of IEEE Sensors*, vol. 2, pp. 701–704, 2004.
- [86] J. K. Abraham, B. Philip, A. Witchurch, V. K. Varadan, and C. Channa Reddy, "A compact wireless gas sensor using a carbon nanotube/PMMA thin film chemiresistor," *Smart Materials and Structures*, vol. 13, no. 5, pp. 1045–1049, 2004.
- [87] Y. Wanna, N. Srisukhumbowornchai, A. Tuantranont, A. Wisitorsaat, N. Thavarungkul, and P. Singjai, "The effect of carbon nanotube dispersion on CO gas sensing characteristics of polyaniline gas sensor," *Journal of Nanoscience and Nanotechnology*, vol. 6, no. 12, pp. 3893–3896, 2006.
- [88] L. Valentini, V. Bavastrello, E. Stura, I. Armentano, C. Nicolini, and J. M. Kenny, "Sensors for inorganic vapor detection based on carbon nanotubes and poly(*o*-anisidine) nanocomposite material," *Chemical Physics Letters*, vol. 383, no. 5-6, pp. 617–622, 2004.
- [89] M. Wienecke, M.-C. Bunesco, M. Pietrzak, K. Deistung, and P. Fedtke, "PTFE membrane electrodes with increased sensitivity for gas sensor applications," *Synthetic Metals*, vol. 138, no. 1-2, pp. 165–171, 2003.
- [90] K. H. An, S. Y. Jeong, H. R. Hwang, and Y. H. Lee, "Enhanced sensitivity of a gas sensor incorporating single-walled carbon nanotube-polyppyrrrole nanocomposites," *Advanced Materials*, vol. 16, no. 12, pp. 1005–1009, 2004.
- [91] B. Philip, J. K. Abraham, and A. Chandrasekhar, "Carbon nanotube/PMMA composite thin films for gas-sensing applications," *Smart Materials and Structures*, vol. 12, pp. 935–939, 2003.
- [92] J. Li, Y. Lu, and M. Meyyappan, "Nano chemical sensors with polymer-coated carbon nanotubes," *IEEE Sensors Journal*, vol. 6, no. 5, pp. 1047–1051, 2006.
- [93] T. Ueda, M. M. H. Bhuiyan, H. Norimatsu, S. Katsuki, T. Ikegami, and F. Mitsugi, "Development of carbon nanotube-based gas sensors for NO_x gas detection working at low temperature," *Physica E*, vol. 40, no. 7, pp. 2272–2277, 2008.
- [94] W.-S. Cho, S.-I. Moon, Y.-D. Lee, Y.-H. Lee, J.-H. Park, and B. K. Ju, "Multiwall carbon nanotube gas sensor fabricated using thermomechanical structure," *IEEE Electron Device Letters*, vol. 26, no. 7, pp. 498–500, 2005.

Review Article

Conductometric Gas Nanosensors

Girolamo Di Francia, Brigida Alfano, and Vera La Ferrara

*Italian Agency for New Technologies, Energy, and the Environment (ENEA), CR-Portici P.le E. Fermi 1,
80055 Napoli, Italy*

Correspondence should be addressed to Girolamo Di Francia, difrancia@portici.enea.it

Received 29 December 2008; Accepted 20 April 2009

Recommended by Giorgio Sberveglieri

This paper presents a review of the current research activities in the field of gas nanosensors. Nanomaterials are characterized by physical and chemical properties that differ from their macroscopic counterparts and, in particular, by an enhanced chemical reactivity even at room temperature. This effect has stimulated the development of chemical sensors based on several different nanomaterials. Here we focus most attention on carbon nanotubes, silicon and metal oxide nanoparticles and metal nanowires. After introducing a few general definitions a discussion on the fundamental properties of the nanostate used in the sensor field is presented and several nanosensors, based on the aforementioned nanomaterials, are discussed. Finally, some personal conclusions will be drawn.

Copyright © 2009 Girolamo Di Francia et al. This is an open access article distributed under the Creative Commons Attribution License, which permits unrestricted use, distribution, and reproduction in any medium, provided the original work is properly cited.

1. Introduction

Gopel first introduced the term “chemical nanosensor” in the early nineties. At that time, only a minor interest was reserved to nanotechnologies by the scientific community and the number of yearly papers regarding this topic was less 5% than the actual number. In its early formulation the term was meant to describe, in most cases, a chemical sensor characterized by the matching of solid state materials with suitable “key-lock” structures, often biostructures, capable of molecular recognition. In this frame, the natural choice for the solid state material was then a structure on the nanoscale [1, 2].

A chemical nanosensor can be defined as an electronic device, consisting of a transducer and a sensitive element that relies, for its operating mechanism, on at least one of the physical and chemical properties typical of the nanostate. Basically it operates as any other chemical sensor: a charge transfer occurs between molecules and a “sensitive” material, resulting in an electrical and/or optical signal that is related to the molecules type and number. However unlike macroscopic sensors, chemical nanosensors can take advantage of the merging of four different features typical of the nanostate: (1) the quantum confinement, (2) the surface-to-volume ratio, S/V , with a specific surface termination

and nanoparticle (NP) doping, (3) the NP morphology and aggregation, and (4) the nanomaterial agglomeration state (the word nanoparticle, NP, is here used to describe, in general, any kind of structure with at least one of its dimension in the nanorange. Sometimes expressions such as nanowire, nanodot, or nanotube will be used, when a more precise reference to the morphology is required). These properties improve the sensitive material behavior of room temperature (RT) operating devices and high sensitivities have been demonstrated. In fact, in the last 10 years almost 2000 papers referring to “chemical nanosensors” have been published and the field seems to be one of the most immediate and promising sectors for the application of nanotechnologies [3]. This rapid growth can be attributed largely to recent advances in nanotechnologies that enabled the synthesis and engineering of materials to realize devices that exhibit functionalities specifically originated by their nanostate [4].

Here we present a review of current research activities on gas nanosensors. The paper is divided into three sections. In the first section the operating mechanisms of chemical nanosensors will be discussed in terms of the four features outlined above. In the second section we review the current research activities in this field, discussing the performances of devices mainly based on carbon nanotubes, nanosilicon,

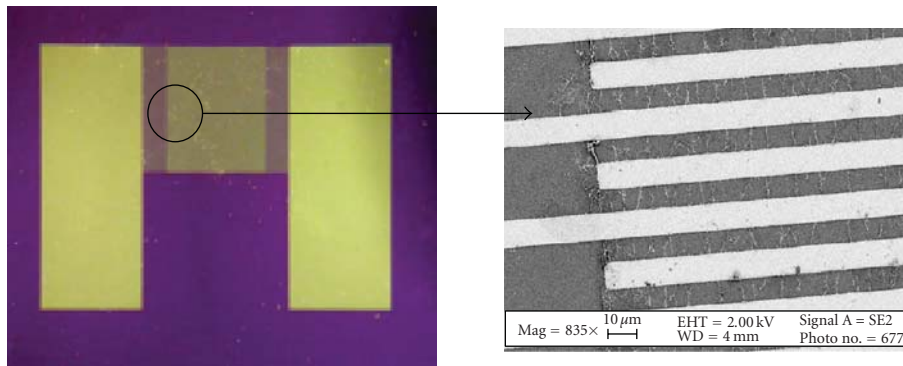


FIGURE 1: Optical and electronic images of a hydrogen nanosensor fabricated by the authors. An array of palladium nanowires is assembled, by means of ac dielectrophoresis, directly onto a silicon chip. Wires grow almost perpendicularly to interdigitated electrodes. The RT response of the devices depends on the size and morphology of the sensitive elements. Electric current changes can be reversible and greater than 140% in 4% H₂.

nanometal oxides, and nanometals, which account for more than 90% of the published papers. In the last section some conclusions are drawn, with a focus on device design and proposed sensing. For the sake of brevity we will not deal with polymer nanocomposite-based chemical sensors, except in a few cases. It should be noted that chemical nanosensors were reviewed, although with different approaches, in 2006 and 2007 by Huang and Choi, Jiménez-Cadena et al., and Riu et al. [5–7].

2. Properties of the Nanostate

There is not an exact understanding of the mechanisms for quantum confinement, surface-to-volume ratio, NP morphology, and aggregation/agglomeration states to control nanomaterial sensitivity. Nevertheless, there is clear evidence for nanostate-enhanced chemical reactivity [8]. In the following an account of the principal findings related to each of the four features is presented.

2.1. Quantum Confinement. In a metallic material, quantum confinement (QC) plays a key role in setting up and determining material properties when one dimension is comparable to the de Broglie wavelength which, for a typical metal such as copper, is a fraction of an nm. However, unless low temperatures and high magnetic fields are employed, scattering or incoherent phenomena prevent the observation of QC related effects, even in the nanorange. For a non-metallic material the comparative dimension is the Bohr exciton radius which falls, in many cases, in the range of 1 to 10 nm. Since the exciton binding energy increases for decreasing the confinement dimension, a nonmetallic nanomaterial can exhibit quantum effects even around room temperature, opening the way to fabrication of QC-based nanosensors. In this range, ionization potentials or chemical affinities, just to mention two of the quantities classically considered unscalable, are shown to depend on the size and are different from the atomic and the bulk extrema [9]. In other words nanoscale particles can be considered as “new,” size-dependent, solid state materials with their own chemical

functionalities. In this respect, for each element a new class of materials originates and new devices and systems can be engineered by virtue of their size.

A very interesting consequence, as far as sensors are concerned, is that these materials exhibit a different chemical activity than their bulk counterparts [10, 11]. For instance, Brus has shown that in a semiconductor nanocrystal the rate of charge transfer, k_q , is greatly enhanced and mainly determined by quantum confinement effects [12, 13]. More recently Di Francia et al. have modeled the interaction between a Silicon NP and a gaseous ensemble [14]. Neglecting diffusion effects, the model expresses the reaction rate constant, k_q , by the following classical relationship:

$$k_q = p * Z * \exp\left(-\frac{\Delta G^*}{K_B T}\right). \quad (1)$$

Here p is the probability of electron transfer in the activated complex and ΔG^* is the free energy required to form the activated complex from the separate reactants [15, 16]. For an adiabatic reaction $p \approx 1$, while in the nonadiabatic case $p < 1$. Z is the collision frequency, which has a linear dependence on the reactants cross-sections [17]. Z is expressed in Torr⁻¹s⁻¹ for reactions in the gas phase.

According to Marcus theory:

$$\Delta G^* = \frac{1}{4\lambda} (\lambda + \Delta G_0)^2, \quad (2)$$

where ΔG_0 is the standard free energy of the reaction and λ is defined as the “reorganization term” [16]. λ is a parameter related to the reorganization of the reactants electronic levels upon the electron transfer event and it is the sum of an inner and an outer term: $\lambda = \lambda_i + \lambda_o$ [16]. For gaseous reactions the last term is negligible and $\lambda = \lambda_i$ [18]. A similar expression holds both for adiabatic ($p \approx 1$) and nonadiabatic ($p < 1$) reactions, although with a suitable redefinition of the various terms [15]. In the latter case p must be treated quantum-mechanically and is a function of the reagent-product wavefunctions overlap. When quantum effects are exhibited, Z , p , and ΔG^* will depend, in general, on the

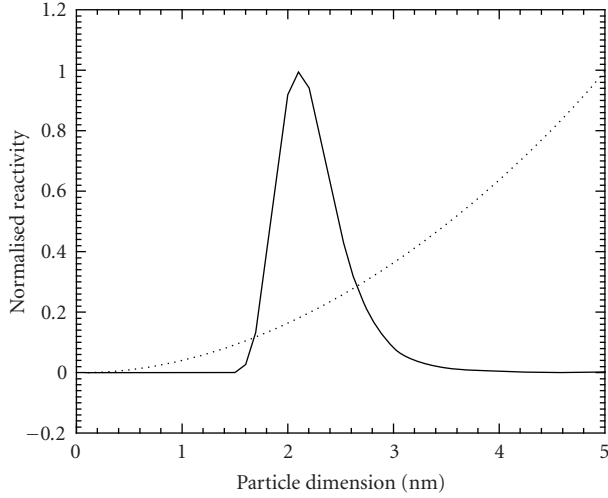


FIGURE 2: Plot of (3) where the resonant rate constant and the sole surface effect (dashed) are reported for the case of a silicon nanoparticle.

confinement energy E_c , that is, on the particle size d_p . For the case investigated the reaction rate constants for unpassivated and passivated nanoparticles are given, respectively, by

$$k_q = Z' * d_p^2 * \exp\left[-\frac{1}{4K_B T \lambda_v} (\lambda'_v - E_c(d_p))^2\right], \quad (3)$$

where $\lambda'_v = \lambda_v - (E_{O^*_2} - E_g)$, or

$$k_q = Z' * d_p^2 * \exp(-\gamma * d_p) \quad (4)$$

where γ is a scaling factor [14].

For both situations the model predicts the existence of a resonant energy (i.e., of a resonant dimension) that strongly enhances the NP-molecule charge transfer. In Figure 2 the effect is shown for the case of the interaction between a silicon NP and molecular oxygen. Two conclusions can be drawn from the model. First, since the characteristics of the electron transfer resonance are only determined by the specificity of the NP-molecule interaction, nanosensors relying on this effect could be highly selective and their response tuned towards a specific analyte by means of proper selection of the nanoparticle material and size. Second, “quantum” sensitivity will mainly depend on the ability to fabricate nanosensors operating on the highest number of singly operating NPs. This is probably the most difficult task to achieve since NP ensembles usually show physical properties that are very different from the individual components [19].

2.2. S/V Ratio and Surface Termination. According to (3) and (4), below and above the resonant region it is the surface that mainly determines the nanosensor performance. The surface-to-volume ratio, S/V, and the surface termination shape the specificity of the nanostate since surface and bulk states compete for control of the materials physical and chemical properties [20]. This effect is strongly dependent

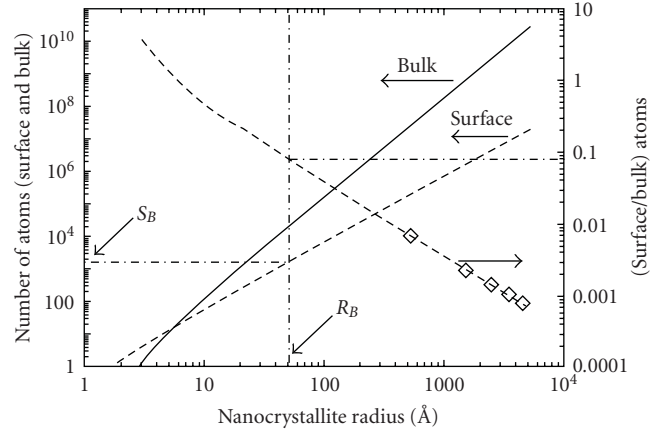


FIGURE 3: Number of surface and bulk atoms for a crystalline silicon spherical NP versus its bulk dimension. R_b is the Bohr exciton radius and S_b the corresponding number of NP surface atoms [22].

on the surface termination and becomes more evident the smaller the NP dimensions are, even if quantum effects are not intense [21]. In Figure 3 the number of surface and bulk atoms has been computed and reported for the case of a crystalline silicon spherical NP versus its bulk dimension. The right axis shows that for decreasing nanocrystalline radius, the S/V ratio rapidly increases reaching values around 10% for NP dimensions just below the silicon Bohr exciton radius [22]. As a result, the interaction cross-section decreases and surface states, which are more sensitive to external molecules, increasingly determine NP physical and chemical properties. The latter effect is more pronounced when defects, surface adsorbed species, or an NP doping are present [21, 23].

2.3. NP Morphology. For nanoparticles exhibiting the same S/V ratio, morphological differences may result in different chemical properties. For example convex surface structures have lower dissolution rates than concave ones [24]. Convex structures are also thermodynamically less stable, so that these particles can suffer preferential dissolution and have higher equilibrium solubility [25, 26]. In some cases their equilibrium solubility can even be above saturation concentrations, leading to precipitation and growth of aggregates. This thermodynamic instability can be particularly strong, resulting in forms of “natural attachment” with defect-free structures and homogeneous crystal orientation [27]. NP aggregates are the most common form for a nanomaterial with physical and chemical properties which are different from basic block, although strongly dependent on it [19]. They are very complex to model since they can be assimilated to macroscopic quantum confined structures. A possible way to overcome this problem is through the use of NP specific surface passivating treatments that, however, strongly deprive reactivity.

2.4. NP Agglomeration. NPs and NP aggregates very often tend to form agglomerates. This further complicates the

problem introducing a new route for physical and chemical property modification. Agglomerates could be considered, technologically speaking, as the “natural” NPs state, characterized, for instance, by nanowires (NWs), bundles, or nanodot pellets, which are generally difficult to control in terms of number of constituents, shape, morphology, and so forth. Nanodevices fabrication requires a standard platform for technological process manufacturing and this, in turn, necessitates well-defined technological treatments to remove agglomerates. This is a research area that is still in its infancy.

The unique physical and chemical properties that nanoscale materials exhibit stem from a competition/ merging of the above elements, whose relative weights are mainly determined by the way the materials are engineered. Top down approaches provide highly controllable processes (such as the lithographic process) and lead, in general, to the fabrication of few structures, even single quantum dots, whose physical properties can be finely predicted theoretically or to synthesize a much larger number of nanostructures, as in the case of the electrochemical etching, by means of self-adjusting mechanisms, still difficult to model. In both cases agglomeration is not exhibited, but aggregation directly determines the physical properties, at least in the latter case. “Bottom up” approaches, such as vacuum deposition or electrochemical growth, show similar features. Agglomeration, however, is usually observed in this case [28].

3. Nanosensors

In the following, an overview of the status of the current research activities in this field is delineated. Due to the large number of papers, we selected the works that, in our view, better describe the evolution of this field, mainly in the last few years.

3.1. Carbon Nanotubes. Tubes are potentially very interesting in the sensor field since they are characterized by high, theoretically infinite, S/V ratio. Kong et al. first reported on a dramatic decrease, or increase, of the electrical resistance, measured by means of scanning tunneling microscopy, in single-walled carbon nanotubes (SWCNT) exposed to NO_2 , or NH_3 , respectively, [29]. In the former case the increased electrical conductivity in NO_2 was attributed to a partial charge transfer from the SWCNT to NO_2 , resulting in an increase in the hole concentration. In the latter case, some not clearly defined intermediate species were suggested to have played a key role. SWCNTs have also been shown to exhibit an extreme oxygen sensitivity [30]. In this case, an increase in the electrical conductivity in an oxidizing environment has been reported and it was suggested that defects could play a major role in the mechanism. The same group had previously reported on some singularities appearing in the electrical conduction of SWCNTs and similarly attributed this to the presence of some kind of defect [31].

Following that finding, several CNT-based nanosensors began to be investigated. Li et al. proposed a simple resistive device, shown in Figure 4, fabricated by casting a solution

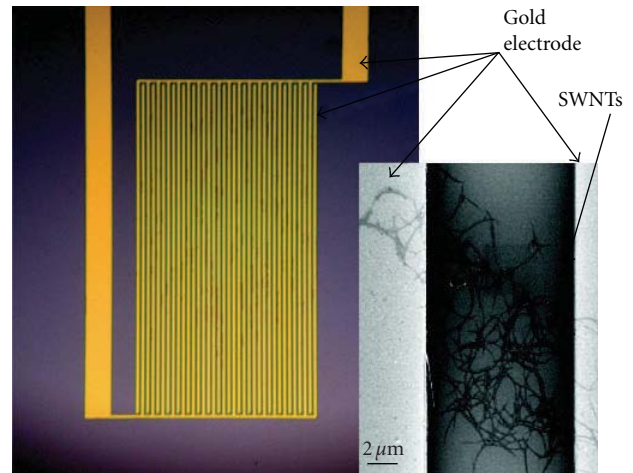


FIGURE 4: NO_2 and nitrotoluene nanosensor. Images show the interdigitated electrodes and the bundle of SWCNTs across the two gold electrodes working as the sensitive material. (Reprinted from [32], copyright 2003, with permission from the American Chemical Society.)

of purified SWCNT in dimethylformamide on a silicon substrate [32]. The device operated at room temperature and exhibited a very high sensitivity to NO_2 and nitrotoluene with 44 ppb and 262 ppb detection limits, respectively, in N_2 . It was speculated that the operating mechanism was related to charge transfer on individual nanowires, with additional hopping effects modulating the conductivity.

The following year, the same group reported on an SWCNT-based gas sensor, specifically designed for methane with an operating range in dry air between 6 and 100 ppm [33]. The device was fabricated by casting, using a suspension of purified SWCNT in deionized water (DIW) where sputtered Pd nanoparticles were dispersed. These weak complexes allowed methane adsorption along the NW walls, changing the conductivity by means of a charge transfer mechanism. This group also stressed, for the first time, the requirement of “sensor training”: the device was observed to improve its performances with use (mainly in terms of baseline stabilization). The adopted process reflects the temperature conditioning processes typical of semiconductor oxide-based chemical sensors.

Valentini et al. then proposed another interesting methane sensor based on CNTs and fabricated on a silicon wafer, with Pt interdigitated (IDE) contacts, a platinum heater and operating around 1000 ppm. The device switched from p-type to n-type upon exposure and the possible role of defects adsorbed atmospheric oxygen, acting as intermediate towards other external gas molecules, was suggested [34].

The feasibility of a simple and original fabrication process was demonstrated by Wongwiriyan et al., by selectively growing SWCNTs directly onto an alumina substrate, patterned with Pt IDE and coated with e-gun deposited Al and Fe clusters acting as catalysts. The device, shown in Figure 5, operates as an NO_2 SWCNT-based gas sensors with a detection limit down to 50 ppb [35].

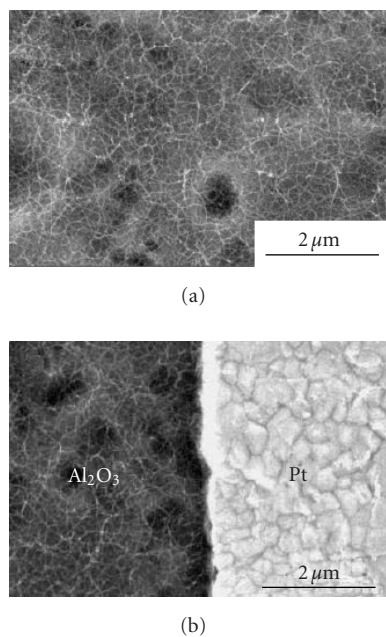


FIGURE 5: The original fabrication process demonstrated by Wongwiriyan et al. SEM images show as-grown SWCNT networks (a) on alumina substrate, and (b) at the boundary between an alumina layer and Pt electrode. (Reprinted with permission from [35]. Copyright JJAP 2005.)

Similar sensitivities towards NO_2 in dry air (up to 100 ppb) were claimed by Penza et al. This group fabricated a multiwalled carbon nanotube (MWCNT)-based gas sensor on an Alumina substrate. Fe was used as a catalyst for the growth. The enhanced sensitivity was obtained using Pt and Au as reaction catalysts and explained in terms of a spillover mechanism. NH_3 sensitivities up to 5 ppm were reported [36].

Several sensor devices based on a Field Effect Transistor (FET) architecture have also been proposed. An FET sensor has been fabricated using the Si/SiO₂ substrate as the gate and depositing Mo both as catalyst, for SWCNT growth and to form source/drain (S/D) contacts to the device. Arrays of CNTs were then deposited as bridges between S/D electrodes. The device, coated with Polyethylenimine or Nafion, exhibited detection limits of 100 ppt towards NO_2 and 10 ppm towards NH_3 . In both cases the electrical current decreased. Recovery was accomplished using UV illumination [37].

Similarly, an NO_x and NH_3 SWCNTs-based chemical sensor has been fabricated by means of dielectrophoretic process on an FET structure. It was found that NH_3 reduces the conductivity because of the charge transfer to the SWCNT, whereas NO_x induces an opposite effect [38].

In order to improve the sensitivity of SWCNT-based sensor, nanotube functionalization has been suggested. By means of an electrochemical process, SWCNTs have been, for instance, functionalized with polyaniline (PANI). The PANI-SWCNT composite behavior has been tested in NH_3 , exhibiting a detection limit of 50 ppb. The response time at

room temperature is of the order of minutes and the recovery time is a few hours [39].

Nguyen's group fabricated a gas sensor from an SWCNT powder by the screen-printing method followed by an annealing treatment. The sensor has been tested up to 5 ppm of NH_3 diluted in 500 sccm N_2 at room temperature. The sensitivity increased as the gas concentration increased but diminished when the NH_3 concentration reached 40 ppm. Sensor recovery was achieved by increasing the carrier flow or heating the device during the desorption step [40].

MWCNTs synthesized under ambient conditions and coated with SnO_2 were investigated as sensitive elements in a sensor that exhibited fast responses to liquefied petroleum gas (LPG) and ethanol ($\text{C}_2\text{H}_5\text{OH}$) with a recovery time of only a few seconds [41].

A thiol functionalized MWCNT-based chemical sensor was designed and developed for the detection of the first four fundamental aliphatic hydrocarbons: methanol (CH_3OH), ethanol ($\text{C}_2\text{H}_5\text{OH}$), propanol ($\text{C}_3\text{H}_7\text{OH}$), and butanol ($\text{C}_4\text{H}_9\text{OH}$). High degrees of selectivity and sensitivity up to a detection concentration of 1 ppm have been demonstrated. It was shown that in the presence of a chemical species, the surface of the nanotubes undergoes a change resulting in a shift of the resonant frequency peak [42].

Single-walled carbon nanohorns (SWNHs), produced by the gas-injected arc-in-water method, have been used by Suehiro et al. to fabricate a room temperature NO_2 and NH_3 nanosensors. Agglomerated SWNHs were deposited on a glass substrate between metal electrodes and manipulated under dielectrophoresis. It was found that conductance of the DEP-fabricated SWCNHs sensor increased or decreased upon exposure to ppm-levels of NO_2 or NH_3 , respectively, [43].

To detect NO_2 , Lee et al. deposited, by casting, a dispersion of as-grown SWCNT powder into dimethylformamide on a pair of interdigitated electrodes. A 350°C annealing was used to eliminate the DMF molecules adsorbed on the surface. The sensors were exposed to NO_2 concentrations in the range of 3 ppm to 10 ppm and the gas sensing property was assigned to a direct charge transfer from the physically adsorbed molecules to the individual p-type semiconducting SWCNTs [44].

In order to improve device selectivity, Suehiro et al. proposed a liquid-phase electrochemical reaction to realize a Pd-functionalized CNT hydrogen sensor. The CNTs were immersed in a palladium acetate solution together with a graphite rod. DC voltage was applied so that palladium acetate could be reduced and catalytic Pd could be electrodeposited on the CNT surface. The CNT sensor reversibly responded to hydrogen gas in air in the concentration range from 0.05% to 1% at room temperature [45].

Sin et al. realized alcohol sensors by depositing bundles of chemically functionalized multiwalled carbon nanotubes across Au electrodes on an SiO₂/Si substrate using an AC electrophoretic technique. The multiwalled carbon nanotubes were chemically functionalized with COOH groups by oxidation. It was found that the sensors were selective towards water vapors and alcohol vapors in air. The sensor response was linear for alcohol vapor concentrations from

1 ppm to 21 ppm with a detection limit of 0.9 ppm. The response time was around 1 second. Recovery was obtained by passing a current of 100 μA –200 μA for about 100–200 seconds through the sensing elements [46].

Finally, an interesting approach was proposed by Vieira et al., by combining single-walled carbon nanotubes and poly(3,3-dialkyl-quarterthiophene). The devices containing only nanotubes or pure polymer provided minimal response, whereas the nanocomposite material (1 wt.% of nanotubes in the polymer) exhibited excellent sensitivity and selectivity to hydrogen, ammonia, and acetone. Moreover they observed that even small amounts of gas doping (10 ppb) resulted in exponential changes in the overall conductivity profile of the nanocomposite sensor, thus anticipating an element of “gain” within the chemical sensor. The proposed mechanism takes into account an effect of modulation of the polymer electrical conductivity induced by the SWCNT interaction with the analyte [47].

In Table 1 an overview of the results, presented above, is shown. Sensors generally operate at RT. Responsivity is fairly high and recovery is often observed, although with long characteristic times. In most cases, some sort of conditioning process has been performed.

3.2. Crystalline Silicon. The physical properties of crystalline silicon are quite insensitive to the environment. Actually, this is one of its relevant characteristics as an electronic material. It is then quite surprising to observe that when reduced to the nanoscale, in a porous structure, crystalline silicon strongly reacts, even explosively, with various analytes [48, 49]. The silicon Bohr exciton radius is about 5 nm and when silicon is electrochemically engraved, a porous silicon (PS) structure with wall thicknesses in the range of 2 nm to 5 nm is formed [50]. The resulting nanocrystallites show novel properties, determined by the quantum confinement and by surface defects that play a key role in determining material physical properties, since the structure is characterized by a high S/V ratio that roughly increases with the inverse of the wall thickness [51, 52]. PS high chemical reactivity towards the environment has stimulated great interest in the sensor field. Properties such as its photoluminescence quenching and/or the electrical conductivity deep change, induced by molecules adsorbed onto its surface, are very interesting for gas sensor applications especially taking into account that they are observed at room temperature. Therefore, several PS-based sensor devices have been investigated, operating on both optical and electrical effects.

In Table 2 a summary of the chemical families detected with such devices is given.

Although very high sensitivities have often been reported, selectivity is rarely an issue [80, 81]. Actually, the instability of the native surface termination is the major barrier preventing wide applications of PS in the sensor field. In typical porous silicon formation the material surface, although mainly characterized by a stable Si–H coverage, is partially defected and prolonged exposure to air, in standard operating conditions, can deteriorate the passivation which is required for the material to be effectively used in sensor technology.

Several methods to overcome this problem have been investigated in order to overcome this problem. For instance, Massera et al. demonstrated that stabilizing its surface with a prolonged exposure to high NO_2 concentrations prior to use greatly improved the electrical performance of a PS NO_2 gas sensor [82]. Recently, Ali et al. investigated the effect of surface passivation in a hydrogen sensor based on Porous silicon [83]. Two types of samples were prepared, one with typical HF anodizing solution and the other with the addition of H_2O_2 . The device based on peroxide treated PS showed a better electrical (I–V) sensitivity, which was attributed to a more efficient surface passivation, confirmed by the Fourier transform infrared (FT-IR) measurements. Lewis et al. observed that a novel process for device metal coating using electronless deposition provided enhanced sensitivity and selectivity to NO_x , CO, and NH_3 [84]. Rahimi and Irajizad presented another method to improve the selectivity and sensitivity of a PS-based hydrogen gas sensor. By means of an electronless process, Pd nanoparticles were deposited onto a porous silicon surface. Hydrogen sensing occurs on the basis of a change in the Schottky barrier height at the silicon-palladium interface. Variations of the electrical resistance, at room temperature, in the presence of diluted hydrogen concentrations down to levels of only a few thousand ppm, were observed [85].

Mahmoudi et al. showed how sensitive and reversible detection of CO_2 and propane could be achieved by means of photoluminescence-quenching modified porous Si [86]. In this case, porous silicon coated with a hydrocarbon group (CH_x) was annealed at different temperatures, allowing the carbon to react with silicon and to produce SiC. An intense blue light is emitted from the thermally carbonized PS surface after annealing at 600°C. Good sensitivity for organic solvent detection was observed after thermal annealing of microcavity devices based on this technology [87].

A completely different approach to silicon-based nanosensors, although mainly investigated for biosensors, is to exploit the properties of silicon nanowires. Hahn and Lieber first reported on a very sensitive DNA sensor fabricated by modifying the surface of a silicon nanowire. In this case the effect of surface states on the silicon nanowire quantum properties observed at the nanoscale could play an effective role in the device sensitivity [88]. This effect is similar to the one reported by Di Francia et al. and observed on suitably functionalised porous silicon [89]. The effect of different environments on silicon nanowires has been also investigated, opening the way to silicon nanowire-based chemical sensors. For instance Zhou et al. first reported on a NH_3 and RH sensitive and reversible sensors based, as shown in Figure 6, on bundles of silicon nanowires [90]. Recent accounts on these approaches can be found in [91, 92].

3.3. Metal Oxides. Metal Oxides (MOX) possess a broad range of electronic, chemical, and physical properties that are often highly sensitive to changes in the chemical environment. In fact, most commercial solid state chemical sensors are based on appropriately structured and doped metal

TABLE 1: CNT-based nanosensor properties and performances. Sensors generally operate at RT. In several cases some sort of conditioning process is used for improving device characteristics. Recovery is obtained with quite empirical approaches.

Material	Chemical species detected (carrier)	Range	Recovery	Conditioning	notes	Ref.
SWCNT	NO ₂ (N ₂) Nitrotol. (N ₂)	10s to 100s ppb	Yes, slow, better with UV light	No		[32]
SWCNT (Pd charged)	CH ₄ (air)	10–100 ppm	Yes, slow, better with UV light	Yes	Operated at 40°C	[33]
CNT	CH ₄ (vacuum) O ₂ (vacuum)	0.01–12 mbar	No	No		[34]
SWCNT	NO ₂	50 ppb	Not Available (NA)	No	Carrier data NA	[35]
MWCNT	NO ₂ (dry air) NH ₃ (dry air)	100 ppb 5 ppm	Yes, slow	No	Operated at T > 150°C	[36]
SWCNT	NO ₂ ; NH ₃ in Ar diluted in air	100 ppt 100 ppm	Yes with UV light	No	Selectivity obtained with polymer coating	[37]
Commercial SWCNT	NH ₃ (N ₂) NO _x (N ₂)	30% in aqueous solution 13.5 ppm	Yes with electrostatic perturbation	Yes	Sensitivity depends on gate voltage. NH ₃ reduces the conductivity; NO _x induces an opposite effect	[38]
PANI-SWCNT network	NH ₃	50 ppb _v	Yes, with argon	Yes	At room temperature sensor response is completely reversible	[39]
SWCNT	NH ₃ (N ₂)	5 ppm	Yes, increasing the carrier flow or heating during the desorption	Yes	Annealing pretreatment increased the sensor sensitivity. Sensitivity diminished when NH ₃ concentration reached 40 ppm	[40]
MWCNT (SnO ₂ particles coated)	LPG C ₂ H ₅ OH in 50% RH	100–1000 ppm 10–200 ppm	Yes (few seconds)	Yes	Working temperature 325°C. Sensor response is linear with gas concentrations	[41]
MWCNT (thiol funct.)	CH ₃ OH C ₂ H ₅ OH C ₃ H ₇ OH C ₄ H ₉ OH (DI water)	1 ppm	NA	NA	Resonant freq. Shift. Freq. response is due to the binding between Thiol group and ionic hydrocarbon	[42]
SWCNT	NO ₂	3–10 ppm	No	NA	Dispersion of SWCNT powder into dimethylformamide	[44]
Commercial SWCNT	H ₂ (air)	0.05–1%	Yes	No	Pd-functionalized	[45]
Commercial SWCNT	alcohol	1–21 ppm	Yes	No	Recovery by current injection	[46]
Commercial SWCNT	NH ₃ and H ₂	0.01–1000 ppm	NA	NA	Composite with conducting polymers	[47]

oxides (mainly SnO₂ and ZnO) that have proved capable of detecting a variety of gases with high sensitivity, good stability and also for low production cost.

The fundamental sensing mechanism for most metal oxide-based gas sensors relies on the change in electrical conductivity due to charge transfer between surface complexes, such as O⁻, O₂⁻, H⁺, and OH⁻, and interacting molecules. Normally this process requires an activation energy so that classical MOX sensors only operate at high temperatures, generally above 200°C [93]. This means that

power consumption is a problem that is becoming more and more urgent in view of the new concepts of pervasive sensing, based on an increasing number of sensing units. Because of the enhanced chemical reactivity of nanomaterials at lower temperatures, it seemed “natural” to investigate if nano-MOX could exhibit equal, or improved, sensing behaviors than their classical macroanalogues, but for minor energy expense.

During recent years several MOX-based nanosensors have been investigated. In 2002 Law et al. fabricated

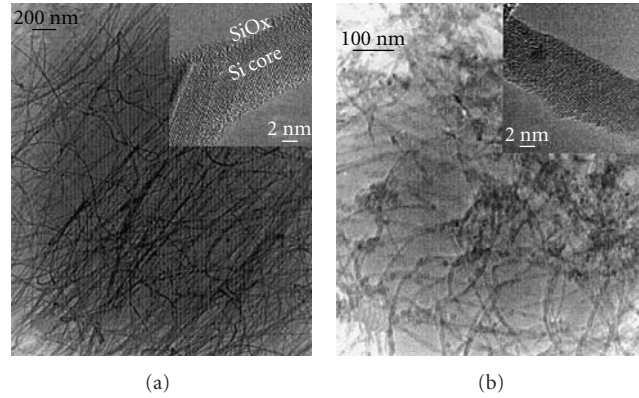


FIGURE 6: Silicon nanowire-based gas sensor. Transmission electron micrographs (TEM) of (a) nonetched and (b) HF-etched Si nanowires. The insets show the high-resolution TEM. (Reprinted from [90], copyright (2003) with permission from Elsevier.)

TABLE 2: Chemical families detected with porous silicon-based chemical sensors (adapted from [53]).

Chemical family	Electrical	Optical	Other	References
Alcohols	x	x	x	[54–62]
Ketons	x	x	x	[55, 61, 63]
Alkanes			x	[64–68]
Hal. Aliphatic	x			[63, 69, 70]
Ethers			x	[63]
Carboxylic acid	x	x	x	[63, 71]
Cicloaliphatic	x			[63]
Aromatic	x	x	x	[55, 61, 63, 72]
Halog. Aromatic.	x			[73]
Inorganic	x	x	x	[54–56, 68, 73–79]
Halogens		x		[49]

and tested the performance of individual SnO_2 single-crystal nanoribbons configured as four-probe conductometric chemical sensors. They found a detection limit for NO_2 of 3 ppm with response/recovery times of the order of seconds. The change in the electrical conductivity was observable even near RT and was modulated by molecular adsorption on surface states assisted by ultraviolet (UV) light with an energy near the SnO_2 bandgap [94].

Comini et al. deposited SnO_2 nanobelts on Platinum interdigitated electrodes and investigated their behavior in the range 300°C – 400°C . The device showed excellent sensitivity towards CO, ethanol, and NO_2 which could be detected down to only a few ppbs. While CO and ethanol adsorption resulted in an increase in the conductivity, NO_2 increased the nanobelts electrical resistivity [95]. Because of the macroscopic dimensions, the suggested operating mechanism was assumed similar to the classical, possibly improved by the higher S/V ratio [93].

Kolmakov et al. used nanoporous alumina as a template for synthesizing arrays of parallel Sn nanowires, which were converted to polycrystalline SnO_2 nanowires of controlled composition and size. Conductance measurements on the individual nanowires were carried out in inert, oxidizing,

and reducing environments in the temperature range 25°C – 300°C . Configured as a CO sensor, a detection limit of a hundreds of ppms in dry air at 300°C was measured with a sensor response time of 30 seconds. The effect was ascribed to the CO reacting with preadsorbed oxygen species to form carbon dioxide, reducing the steady-state surface oxygen concentration and donating electrons into the bulk, with a subsequent conductivity increase [96].

Neri et al. fabricated SnO_2 powders, annealed at 600°C , that showed good sensitivity to low concentrations of ethanol (50 ppm–200 ppm). A remarkable enhancement of the sensitivity towards $\text{C}_2\text{H}_5\text{OH}$, as well as response and recovery time, was observed by the addition of 1 wt% Pt. Pt enhances the adsorption and dissociation of molecular oxygen on semiconductor surfaces due to its peculiar catalytic properties. The surface species trap electrons from the metal oxide conduction band, increasing the resistance of the doped sample [97].

In Figure 7 a hydrogen sensor fabricated by Fields et al. from single SnO_2 nanobelts, synthesized via catalyst-free thermal evaporation is shown. The sensitivity and response time of the sensors without any catalyst on the surface to 2% hydrogen at temperatures between 25°C and 80°C were measured. A sensitivity higher than $0.3/(\%\text{H}_2)$, with a response time of about 220 seconds and power consumption of only 10 nW at room temperature, was demonstrated [98].

Chen et al. observed that SnO_2 – In_2O_3 nanocomposites exhibited high responsivity and selectivity towards CO and NO_x , with a sensitivity depending on the composition and calcination temperature of the composites and on the device operating temperature. Sensing performance was further improved through the introduction of a small amount of metals or other oxides as dopants and surface coatings [99].

Similarly, $\text{SnO}_2/\text{Fe}_2\text{O}_3$ nanocomposites have been used to realize an ethanol gas sensor (10 ppm–200 ppm), operating in the temperature range 150°C – 450°C . Different sensor performances could be obtained by balancing the $\text{SnO}_2/\text{Fe}_2\text{O}_3$ content. The gas sensing mechanism is, in both cases, similar; the adsorbed air oxygen reacts with the excess electrons in the nanocomposite to give chemisorbed oxygen anions that react with a reducing gas (e.g., CO) [100].

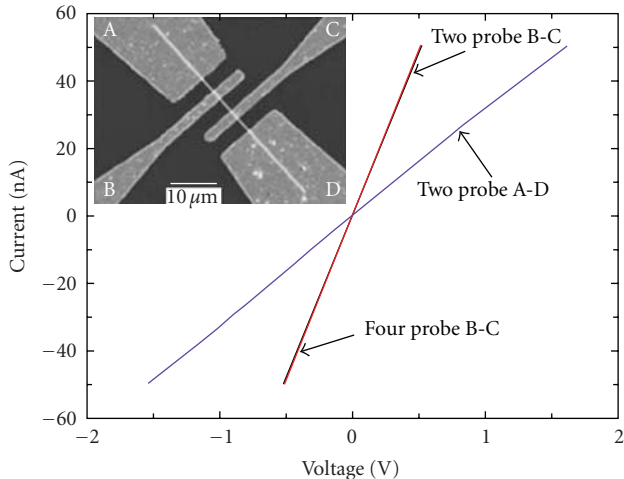


FIGURE 7: Hydrogen sensors based on single SnO_2 nanobelts synthesized via catalyst-free thermal evaporation. Scanning electron microscopy image of the device and its electrical behavior in 2 and 4 probe configurations. (Reprinted from [98], copyright 2006, with permission from American Institute of Physics.)

$\text{SnO}_2/\text{MoO}_3$ nanocomposites have shown a response to alcohols, $\text{C}_n\text{H}_{2n+n}\text{OH}$ ($n = 1-4$), and NH_3 , explained in terms of the acid-base scheme: Mo atoms at the SnO_2 surface change the surface acidity and, in turn, its reactivity towards alcohols and ammonia or amine groups [101].

A humidity detector was realized using a single SnO_2 nanowire as the sensing unit in a two-probe configuration. This sensor, shown in Figure 8, exhibited a fast and fairly high response to relative humidity (RH) in air. The proposed operating mechanism was based on a model where physisorbed water molecules, reacting with the Lewis acid site (Sn) and Lewis base site (O) on the SnO_2 surface to form $(\text{Sn}_{\text{Sn}}^+-\text{OH}^-)$ complexes, released electrons. As a result, the depletion layer becomes thinner and increases the surface conductivity of the SnO_2 nanowire [102].

A similar architecture, but in a 4-probe configuration, was also investigated by Mangkorntong and Thepnurat who reported on a single SnO_2 nanowire-based sensor, shown in Figure 9 with a good room temperature sensitivity towards ethanol (1000 ppm) [103].

Shen et al. distributed PdO particles randomly on the surface of SnO_2 nanowire testing sensors based on both undoped and Pd-doped SnO_2 nanowires. The devices showed a reversible response to H_2 at room temperature, with a response increasing for increasing Pd concentration [104]. Sensitivity improvement towards oxidizing and reducing gases in single, quasi-1D, chemiresistors (i.e., tin oxide nanowires or nanobelts) was similarly demonstrated by Kolmakov et al., after surface decoration with noble metal catalyst particles [105].

Recently, branched nanostructures have attracted great interest because they can provide means for improving parallel connectivity, enhancing device performance. For example, Wan et al. synthesized branched semiconducting

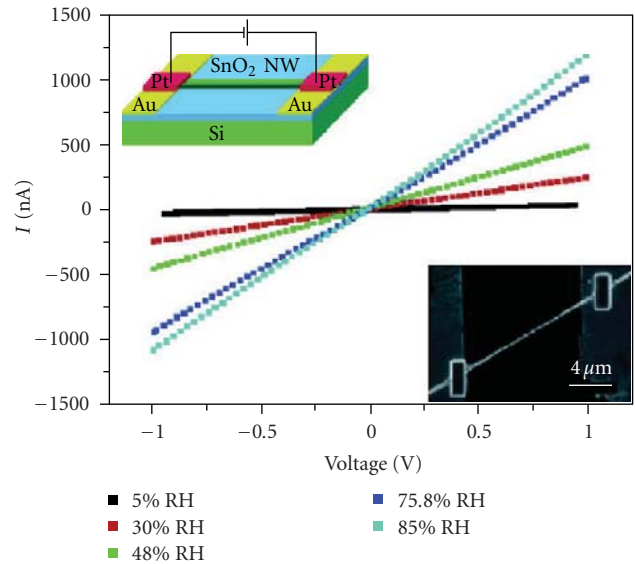


FIGURE 8: Humidity detector realized using a single SnO_2 nanowire as the sensing unit in a 2-probe configuration. SEM image of a single SnO_2 NW placed between two Au electrodes. Here the two Pt boxes have been deposited by Focused Ion Beam. (Reprinted from [102], copyright 2007, with permission from American Chemical Society.)

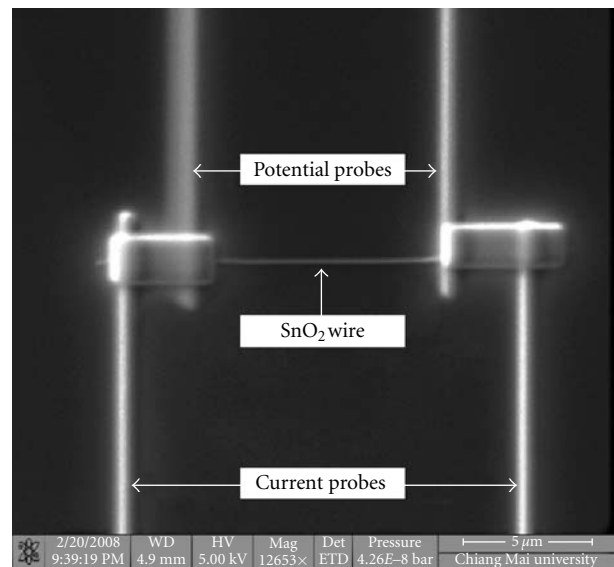


FIGURE 9: Ethanol nanosensor realized using a single SnO_2 nanowire as the sensing unit in a 4-probe configuration. (Reprinted from [103], copyright 2008, with permission from the authors.)

SnO_2 nanowires to realize a chemical nanosensor with excellent sensing characteristics for ethanol [106].

In 2004 Wang et al. fabricated individual ZnO nanowire transistors that exhibited high sensitivity to oxygen. The sensing properties of the chemical nanosensor, investigated using UV irradiation, were related to the trapping and releasing of carriers in the wires. Next year, the same research group fabricated sensors sensitive towards ethanol based on multipod-shaped, large surface area ZnO nanorods, having

more than four up to tens of needle-like nanorods united at a common junction. With such a technology, they realized a sensor, shown in Figure 10 capable to detect 10 ppm hydrogen at room temperature, with a rapid recovery [107–109].

In 2007, vertically aligned ZnO nanowire arrays were grown on a langasite substrate by Cheng et al. The gas sensor device showed good sensing properties for NO₂ [110].

Tang et al. realized a selective NH₃ gas sensor based on a Fe₂O₃–ZnO nanocomposite, operating at room temperature. The increased sensitivity and selectivity to NH₃ was attributed to the addition of Fe₂O₃ nanoparticles, which promotes the adsorption of NH₃ molecules on the oxide surface and accelerates the oxidizing process [111].

However, the standard technique to enhance sensitivity and selectivity is the use of Pt, Au, or Cu catalysts. Wongka et al., for example, impregnated zinc oxide nanowires with platinum and gold nanoparticles to realize an ethanol sensor operating up to a concentration of 100 ppm and at working temperature of 180°C–300°C. An enhancement of sensitivity and recovery time was observed for ethanol sensor based on zinc oxide nanowires impregnated with platinum, but no enhancement was observed for zinc oxide nanowire impregnated with gold nanoparticles [112].

Similarly, Comini et al. investigated zinc oxide nanowire networks using an evaporation/condensation technique with uniform copper addition. Cu increased the sensor response to acetone, ethanol, NO₂, and CO gases at 400°C [113]. Finally, transistors based on both single and multiple In₂O₃ nanowires operating at room temperature have been shown to detect NO₂ down to ppb levels. The nanowires conductance was observed to decrease with increasing gas concentration [114].

In Table 3 an overview of the above results for SnO₂ nanosensors is given. Sensor response is generally high and recovery rather fast, in spite of the often ambient temperature operating conditions. It should be noted that, as for the previous cases, some sort of conditioning process was often undertaken.

3.4. Metal Nanosensors. Most of the papers related to this topic discuss nanosensor devices based on nanowires. The reason being that metal nanowires have features such as strength, ductility, and chemical stability, that make them attractive candidates for device processing. Furthermore, when the diameter of these structures is in the nanorange, they could represent interesting transducers since the S/V ratio increases with the inverse of the wire diameter. However, the basic operating mechanism for this class of sensors is strictly related to innate metal characteristics. For example, H₂ nanosensors based on Pd nanowires work by virtue of a change in the Pd crystalline phase upon exposure to low concentrations of H₂ and/or by means of surface conversion into the more insulating PdH₂ after H₂ interaction [115–117].

Walter et al. realized different metal nanowires using the electrochemical step-edge decoration technique (ESED) and characterized them as chemical sensors. Depending essentially on the kinetics of the reduction reaction, two different

ways of preparing metal nanowires have been developed. For metal cations with a slow transfer rate, as Molybdenum or Cadmium, metal oxide wires (MoO_x and Cd(OH)₂, resp.) were electrodeposited from aqueous solutions. The resulting wires were converted into pure metal wires by reduction with H₂, or with H₂S, at high temperature. In contrast, from acidic solutions of palladium, gold, silver, and copper, no oxide formation is observed and nanowires are obtained as pure metals by electrodeposition [115]. Conductive gas sensors based on silver and palladium nanowires were fabricated. Ag nanowires, with diameters ranging from 150 nm to 950 nm and lengths up to 100 μm, upon exposure to ammonia vapor showed an increase in electrical resistance (up to 10 000%) that was fast (<5 seconds) and reversible. The same reversible behavior, although characterized by a slower response time (1 minute), was recorded in the presence of liquid amine vapor, while an irreversible resistance increase was found when they were exposed to hydrogen sulfide. Conversely, carbon monoxide, oxygen, hydrocarbons, argon, and water caused no change in resistance for exposures up to 10 seconds [118].

Arrays of palladium nanowires were investigated as H₂ sensors [115–117]. Macroscopic Pd-based hydrogen sensors suffer from two major drawbacks: response times that span from 0.5 second to several minutes, which is too slow to monitor gas in real-time conditions, and the fact that a number of gas molecules, such as methane, oxygen, and carbon monoxide adsorb onto the sensor surfaces and block the adsorption sites for hydrogen molecules. Pd nanowire hydrogen sensors offer solutions to the above problems. They have a large surface-to-volume ratio and are characterized by the presence of small (nanogaps) that the H₂ induced Pd swelling tends to close, as shown in Figure 11. The result is a response time that can be as fast as 20 milliseconds, when devices are characterized at high H₂ concentrations (>8%), and devices that seem to be less subject to poisoning by common contaminants. Hydrogen exposure produced a strong increase in the electrical current as investigated by Favier and coworkers [116, 117]. Nanowires consist of agglomerated Pd grains with “intergrain” nanogaps. When exposed to hydrogen, the gas diffuses into the lattice and reacts with the metal forming a metal hydride (PdH_x), resulting in a volumetric wire expansion with a partial or total closure of the gaps. A strong increase in the electrical conductivity can then be observed. Grain swelling is not completely reversible: after H₂ removal, the grains come back to the initial volume but not to the initial position.

Palladium mesowires and nanowires can be fabricated by electrodeposition from aqueous solutions of Pd²⁺ onto step edges naturally present on highly oriented pyrolytic graphite surfaces. Freshly deposited Pd nanowires are then detached from the graphite and transferred onto a glass substrate by means of cyanoacrylate.

Another technique, which simplifies the previous one by avoiding the use of a template, is to directly manufacture a Pd nanowire array onto a crystalline silicon substrate. The choice of a silicon substrate opens the way to the direct integration of this kind of sensor device in microelectronics. Pd nanowire arrays were actually assembled directly onto a

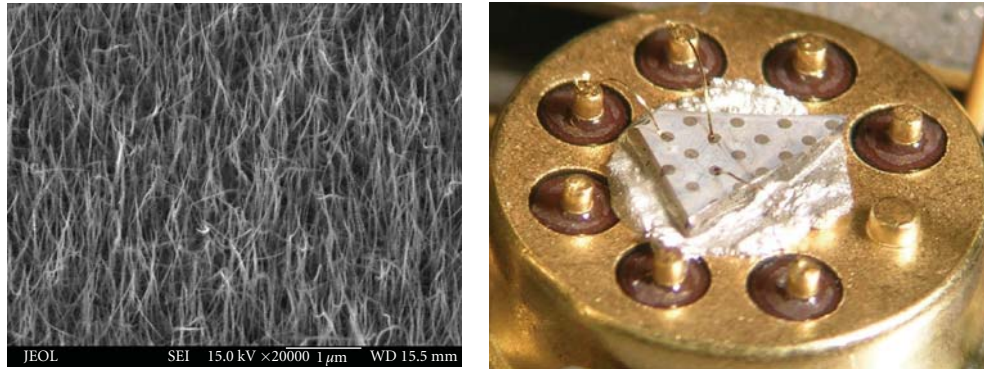


FIGURE 10: H₂ nanosensor based on ZnO nanorods. SEM of ZnO multiple nanorods (left), and photograph of the nanorods contacted by Al/Pt/Au electrodes (right). The ZnO chip has edge length ~5 mm in the left photo. (Reprinted from [109], copyright 2005, with permission from American Institute of Physics.)

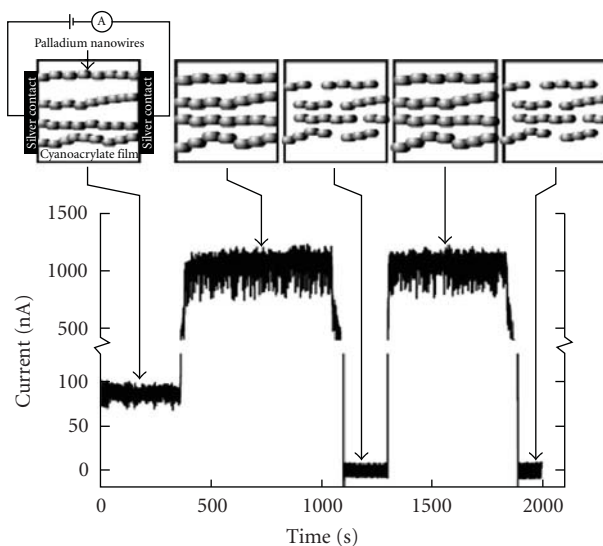


FIGURE 11: H₂ Pd nanowire hydrogen sensors are characterized by a strong response in less than 20 milliseconds. Shown at top is the mechanism proposed for sensor operation. (Reprinted from [116], copyright 2001, with permission from the American Association for the Advancement of Science.)

silicon chip, by means of AC dielectrophoresis using a metal salt solution as a feed material. It was showed that nanowire morphology affects the electrical conductivity when devices are exposed to up to 4% of hydrogen, in nitrogen carrier, at room temperature. It was found that thinner nanowires (less than 90 nm wide) responded faster than thicker ones, with up to 140% current changes in the presence of 4% H₂ [119, 120].

4. Discussion and Conclusions

In the above sections we reported on almost one hundred sensor devices based on different nanomaterials. It is worth noting, however, that none of these has yet emerged as commercially valuable. In this section, this point is discussed in order to understand the existence of possible technological

constraints intrinsically limiting the development of saleable gas nanosensors.

First of all, let us observe that gas nanosensor fabrication technology is far from being assessed for either the sensitive film and the transducer. In Table 4 gas nanosensors reviewed in this work have been classified according to their transduction mechanism. Although all the most common gas sensor architectures are considered, optical and electrically conductive devices (including FETs) are the most frequently investigated.

Nanosensor device processing requires at least two distinct steps: (1) sensitive nanomaterial production and selection, and (2) placing the sensitive nanomaterial on prepatterned electrodes, sometimes followed by an NP alignment procedure.

With respect to the first step, Table 5 presents an overview of the different fabrication processes used for the sensitive element for each gas nanosensors type. Although several processes, both “top-down” and “bottom-up” have actually been exploited to fabricate the sensitive material, it appears that chemical-based techniques, probably by virtue of their flexibility, are favoured.

At present it is the second step, that is the ability to connect the micro-(nano) world to the macro-one, creating functional heterostructures and interfaces between the nanomaterial and the electrodes, that seems to be the most critical one. This is probably true not only for nanosensors but for any nanodevice. Actually, most of the reported gas nanosensor transducers are fabricated using standard electronic processing techniques and only in a few cases have specific nanotools, such as the Focused Ion Beam, been employed (although mainly as nano-soldering equipment). However, any technological process on a nanomaterial needs to be set up in such a way as to prevent nanomaterial deterioration with manipulation and to preserve the properties of the nanostate.

In this respect several different approaches have been discussed, mainly following two different strategies: (1) the deposition of the nanomaterial in the form of a dispersion on a prepatterned substrate, and (2) the formation of contacting electrodes onto the deposition itself.

TABLE 3: A summary of SnO₂ based nanosensor properties and performances. Sensors generally show high responses and often work at RT. In several cases, some sort of conditioning process is adopted to improve device characteristics.

Material	Chemical species (carrier)	Range	Recovery	Conditioning	notes	Ref.
SnO ₂ nanoribbons	NO ₂ (synthetic air)	3 ppm	Yes, few seconds by UV irradiation	Yes	Reversible at RT. Photoinduced desorption of the analyte	[94]
SnO ₂ nanobelts	NO ₂ (synthetic air)	few ppb	Yes	Yes	Operating temperature is 400°C. CO and ethanol increase the conductivity, while NO ₂ decreases the conductivity, of the SnO ₂ nanobelts	[95]
SnO ₂ nanowires	CO (dry air)	few hd ppm	Yes	Yes	CO increases the conductivity with response times of ~30 s at 300°C	[96]
SnO ₂ nanopowders	C ₂ H ₅ OH (air)	50–200 ppm	Yes	Yes	Annealing at 600°C	[97]
Single SnO ₂ nanobelts	H ₂	2% H ₂	Yes	Yes	Operating temperatures between 25°C and 80°C. Resistance decreases with response time <220 s; power cons. <10 nW @ 25°C	[98]
SnO ₂ –In ₂ O ₃ nanocomposite oxides	CO (air) NO ₂ (air)	Sensitivity of 16.0 and 7.5 to CO and NO ₂ , respectively	NA	Yes	Nanocomposites calcined at 600°C. Sensitivity increases with gas concentration at 100°C–300°C	[99]
SnO ₂ /Fe ₂ O ₃ nanocomposites	CO ethanol H ₂ S NO ₂ (RH 30%)	CO (40–150 ppm), ethanol (10–200 ppm), H ₂ S (2–10 ppm) NO ₂ (50 ppb–10 ppm)	NA	Yes	Temperature range: 150°C–450°C. Increasing of Fe ₂ O ₃ content results in oxidation enhancement.	[100]
SnO ₂ /MoO ₃ nanostructure	C _n H _{2n+1} OH (n = 1–4); NH ₃ in air	1 µl alcohols (300°C); 500 ppm NH ₃ (350°C)	NA	Yes	Electric sensor response to the alcohols decreases with increasing MoO ₃ content	[101]
single SnO ₂ nanowire	RH	5%–85% RH	Yes	Yes	Pt boxes deposited by focused ion beam (FIB) improve electrode contact. R decreases with the increase of RH in air at 30°C	[102]

TABLE 4: Nanosensor architectures.

Sensor type	CNT	Nanosilicon	Nano-MOX	Nanometal	References
Optical	x	x	x		[51, 56–58, 60, 62, 64, 65, 67, 70–74, 76, 79, 86–89, 121, 122]
Conductive	x	x	x	x	[29, 30, 32–36, 39–47, 54, 59, 61, 63, 66, 68, 75–78, 80–85, 90, 91, 94–101, 103–106, 108, 109, 111–113, 115–120]
QMB	x				[121, 123]
MEMS	x		x		[124–126]
SAW	x		x		[110, 127, 128]
FET	x	x	x		[37, 38, 92, 102, 107, 114, 122, 129–133]

TABLE 5: The different nanomaterial fabrication processes used for gas nanosensor sensitive layer fabrication.

Sensitive layer processing technique	CNT	Nanosilicon	Nano-MOX	Nanometal	References
Commercial material	x		x		[33, 34, 38–40, 44–47, 121, 123, 127, 128, 131]
Electrochemical		x	x		[51, 54, 56–58, 60, 61, 63–67, 70–87, 89, 96, 133]
Chemical			x		[91, 97, 99–101, 110, 111, 126, 134]
Electro/dielectrophoresis				x	[115–120]
MBE			x		[109, 135]
Thermal evaporation			x		[94, 95, 98, 104, 107, 122, 130]
Pyrolysis	x				[41, 43]
Microwave			x		[42, 68]
CVD-VLS	x				[35, 88, 102, 124, 129, 132]
HiPco	x				[32]
Laser ablation	x		x		[30, 31, 114]

TABLE 6: Classification of the reviewed papers according to the different technological strategies followed for gas nanosensor device fabrication.

Gas nanosensor technological process	References
(1) Deposition of the nanomaterial in the form of a dispersion on a prepatterned substrate.	[32, 38–42, 45, 68, 82, 94, 95, 97, 100, 104, 107, 111, 118, 121–123, 127–132, 134]
(2) Nanomaterial, in the form of a dispersion, is deposited on the substrate and contacting electrodes are realized onto the nanomaterial.	[54, 61, 63, 75, 76, 78, 80, 81, 84, 85, 88, 91, 96, 98, 99, 102, 106, 109, 114, 126]
(3) “Growth in place”: the fabrication of the nanomaterial is performed exactly where the nanodevice architecture requires it, exploiting existing electrodes.	[35, 46, 110, 119, 120, 124, 133]
Others (mainly optical)	[51, 56–58, 60, 65–67, 70–74, 79, 87, 89]

In the former case, nanomaterial is prepared in the form of a dispersion which is then deposited by some suitable technique (spin-coating, printing, dip coating, etc.) onto a prepatterned transducer (generally fabricated using standard electronic techniques). A postannealing is often exploited to improve the contact characteristics. This approach nominally preserves the nanomaterial characteristics and allows, to some degree, its alignment when electrochemical techniques are adopted. However dispersions are very rarely characterized in terms of particle size, polydispersion index, solvent/solute interaction, and so forth so that the results reported suffer from poor reproducibility. Moreover, the quality of the contact nanomaterial/electrode is rarely investigated. Annealing treatments are quite regularly adopted, often on a purely empirical basis, both to free the dispersion

from its solvent and to improve the electric contact characteristics, but their effectiveness is not clear.

In the latter case the nanomaterial, in the form of a dispersion, is deposited on the substrate and contacting electrodes are deposited onto the nanomaterial itself using standard techniques (thermal or e-beam evaporation, sputtering, etc.) or even using silver paint. Again, a postannealing is often exploited to improve the contact characteristics. Devices based on single nanoparticles “captured” from random dispersions and contacted with this technique have been investigated.

It is worth noting that since the first approach does not require any further nanomaterial treatment, it is generally considered the most suitable to preserve nanomaterial physical properties.

Actually, a third approach exists, although discussed in an only limited number of papers. It is the so-called “growth in place” technique that allows fabrication of the nanomaterial exactly where the nanodevice architecture requires it, strongly simplifying the process and avoiding excessive handling of the nanomaterial [136, 137].

In Table 6 papers reviewed have been classified according to the different technological strategies followed for gas nanosensor fabrication.

Apart from a few notable exceptions, mainly observed in silicon-based nanosensors, none of the reported devices seem to operate by exploiting quantum effects; nanomaterial characteristic dimensions are still too far from the Bohr exciton radius for quantum properties to become apparent. In spite of this, different proposed nanosensors show enhanced reactivities towards a wide range of analytes and are characterized by fairly high sensitivities at an operating temperature which is very often near room temperature. This effect has been attributed to the combination of an improved S/V ratio and the presence of surface defects that strongly link the electrical conductance of the device to the nanomaterial environment.

Although in a few cases no recovery at all could be observed, in many devices the response and recovery times could be measured in the range from seconds to several tens

of minutes. This should not be surprising since the operating temperature is often the ambient temperature, but it is actually one of the most serious limitations to nanosensor applications. Procedures to improve response and recovery times have been suggested by various authors. Mechanical perturbations such as gas over- or underpressure, external heating, light illumination at various frequencies (from IR to UV), application of external electric fields, have been all exploited to improve device recovery and, in a few cases, also to enhance sensitivity. In most cases these treatments proved to be effective, but no theoretical background was proposed to account for their effect.

Selectivity is rarely an issue and it is at most pursued by using some kind of catalyst to accelerate a given reaction, mainly in the case of MOX nanosensors.

Finally, sensor conditioning (or training) is quite a common processing step. Since one of the main advantages of a nanosensor is its ability to operate at RT, conditioning cannot be performed by heating the sensor around the operating temperature, as happens in standard solid state chemical sensors with operating temperatures of hundreds of °C. Several processes have been proposed involving prolonged soaking in the target analyte with or without, light illumination or mild heating. The effect has been shown to always be positive, mainly on the sensor baseline.

In summary, the gas nanosensors so far investigated have several problems, the most important being: (1) lack of reliable and well-assessed fabrication processes, (2) very long response and recovery times, and (3) quite unstable baselines. These factors remain important technological issues that prevent, at present, the development of saleable gas sensors made from nanomaterials. On the other hand, no technological constraint seems to intrinsically limit the development of saleable gas nanosensors.

The results we have discussed in fact show that the enhanced chemical reactivity of the nanostate can be effectively used to fabricate devices working at room temperature. However, since the fabrication process is itself under investigation, the proposed devices are often not reproducible and characterized by parameters whose meaning is limited by poor statistics. Moreover, the fabrication process often requires unconventional and expensive equipment so that economic requirements could further limit commercial development. An effort should be made to define standards both in nanomaterial characterization and in fabrication techniques. In this respect, recent "growth in place" approaches seem to be a very useful technological platform for nanosensor fabrication since such approaches can prevent nanomaterial deterioration with manipulation and preserve the properties of the nanostate.

References

- [1] W. Gopel, "Nanostructured sensors for molecular recognition," *Philosophical Transactions of the Royal Society of London A*, vol. 353, p. 333, 1996.
- [2] W. Gopel, "Chemical sensing, molecular electronics and nanotechnology: Interface technologies down to the molecular scale," *Sensors and Actuators B*, vol. 4, p. 1, 1991.
- [3] Chemical AND nano* AND sensor*, 1998–2007, <http://apps.isiknowledge.com>.
- [4] Nanotechnology: Basic Information, <http://es.epa.gov/ncer/nano/questions/index.html>.
- [5] X.-J. Huang and Y.-K. Choi, "Chemical sensors based on nanostructured materials," *Sensors and Actuators B: Chemical*, vol. 122, p. 659, 2007.
- [6] G. Jiménez-Cadena, J. Riu, and F. X. Rius, "Gas sensors based on nanostructured materials," *Analyst*, vol. 132, no. 11, pp. 1083–1099, 2007.
- [7] J. Riu, A. Maroto, and F. X. Rius, "Nanosensors in environmental analysis," *Talanta*, vol. 69, no. 2, pp. 288–301, 2006.
- [8] A. P. Alivisatos, "Semiconductor clusters, nanocrystals, and quantum dots," *Science*, vol. 271, no. 5251, pp. 933–937, 1996.
- [9] L. E. Brus, "A simple model for the ionization potential, electron affinity, and aqueous redox potentials of small semiconductor crystallites," *The Journal of Chemical Physics*, vol. 79, no. 11, pp. 5566–5571, 1983.
- [10] M. Antonietti and C. Göltner, "Superstructures of functional colloids: chemistry on the nanometer scale," *Angewandte Chemie International Edition*, vol. 36, no. 9, pp. 910–928, 1997.
- [11] M. Antonietti, K. Landfester, and Y. Mastai, "The vision of "nanochemistry", or is there a promise for specific chemical reactions in nano-restricted environments?" *Israel Journal of Chemistry*, vol. 41, no. 1, pp. 1–5, 2001.
- [12] L. E. Brus, "Model for carrier dynamics and photoluminescence quenching in wet and dry porous silicon thin films," *Physical Review B*, vol. 15, no. 8, 1996.
- [13] L. E. Brus, "Electron-electron and electron-hole interactions in small semiconductor crystallites: the size dependence of the lowest excited electronic state," *The Journal of Chemical Physics*, vol. 80, no. 9, pp. 4403–4409, 1984.
- [14] G. Di Francia, L. Quercia, I. Rea, P. Maddalena, and S. Lettieri, "Nanostructure reactivity: confinement energy and charge transfer in porous silicon," *Sensors and Actuators B: chemical*, vol. 111–112, pp. 117–124, 2005.
- [15] N. Sutin, "The Kinetics of Inorganic Reactions in Solution," *Annual Review of Physical Chemistry*, vol. 17, p. 119, 1966.
- [16] R. A. Marcus, "Electron transfer reactions in chemistry. Theory and experiment," *Reviews of Modern Physics*, vol. 65, no. 3, pp. 599–610, 1993.
- [17] G. M. Brown and N. Sutin, "A comparison of the rates of electron exchange reactions of ammine complexes of ruthenium(II) and -(III) with the predictions of adiabatic, outer-sphere electron transfer models," *Journal of the American Chemical Society*, vol. 101, no. 4, pp. 883–892, 1979.
- [18] G. A. Zalesskaya, E. G. Sambor, and N. N. Bely, "Photoinduced gas-phase electron transfer reactions," *Journal of Fluorescence*, vol. 14, no. 2, pp. 173–180, 2004.
- [19] D. K. Ferry and R. Akis, "Nonlocal effects in semiconductor nanostructure transport," *Journal of Physics: Condensed Matter*, vol. 20, no. 45, Article ID 454201, 2008.
- [20] M. J. Sailor and E. J. Lee, "Surface chemistry of luminescent silicon nanocrystallites," *Advanced Materials*, vol. 9, no. 10, pp. 783–793, 1997.
- [21] N. Yamazoe, "New approaches for improving semiconductor gas sensors," *Sensors and Actuators B*, vol. 5, no. 1–4, pp. 7–19, 1991.
- [22] G. Di Francia, M. Della Noce, V. La Ferrara, L. Lancellotti, P. Morvillo, and L. Quercia, "Nanostructured porous silicon for gas sensor applications," *Materials Science and Technology*, vol. 18, no. 7, pp. 767–771, 2002.

- [23] Z. Zhou, R. A. Friesner, and L. Brus, "Electronic structure of 1 to 2 nm diameter silicon core/shell nanocrystals: surface chemistry, optical spectra, charge transfer, and doping," *Journal of the American Chemical Society*, vol. 125, no. 50, pp. 15599–15607, 2003.
- [24] R. Tang, C. A. Orme, and G. H. Nancollas, "Dissolution of crystallites: surface energetic control and size effects," *ChemPhysChem*, vol. 5, no. 5, pp. 688–696, 2004.
- [25] A. W. Adamson and A. P. Gast, *Physical Chemistry of Surfaces*, John Wiley & Sons, New York, NY, USA, 1997.
- [26] R. K. Iler, *The Chemistry of Silica: Solubility, Polymerization Colloid and Surface Properties and Biochemistry*, John Wiley & Sons, New York, NY, USA, 1979.
- [27] H. Zhu and R. S. Averback, "Sintering processes of two nanoparticles: a study by molecular dynamics," *Philosophical Magazine Letters*, vol. 73, p. 27, 1997.
- [28] B. K. Teo and X. H. Sun, "From top-down to bottom-up to hybrid nanotechnologies: road to nanodevices," *Journal of Cluster Science*, vol. 17, no. 4, pp. 529–540, 2006.
- [29] J. Kong, N. R. Franklin, C. Zhou, et al., "Nanotube Molecular Wires as Chemical Sensors," *Science*, vol. 287, p. 5453, 2000.
- [30] A. Zettl, "Extreme oxygen sensitivity of electronic properties of carbon nanotubes," *Science*, vol. 287, no. 5459, pp. 1801–1804, 2000.
- [31] P. G. Collins, A. Zettl, H. Bando, A. Thess, and R. E. Smalley, "Nanotube nanodevice," *Science*, vol. 278, no. 5335, pp. 100–103, 1997.
- [32] J. Li, Y. Lu, Q. Ye, M. Cinke, J. Han, and M. Meyyappan, "Carbon nanotube sensors for gas and organic vapor detection," *Nano Letters*, vol. 3, no. 7, pp. 929–933, 2003.
- [33] Y. Lu, J. Li, J. Han, H.-T. Ng, C. Binder, C. Partridge, and M. Meyyappan, "Room temperature methane detection using palladium loaded single-walled carbon nanotube sensors," *Chemical Physics Letters*, vol. 391, no. 4–6, pp. 344–348, 2004.
- [34] L. Valentini, I. Armentano, L. Lozzi, S. Santucci, and J. M. Kenny, "Interaction of methane with carbon nanotube thin films: role of defects and oxygen adsorption," *Materials Science and Engineering C*, vol. 24, no. 4, pp. 527–533, 2004.
- [35] W. Wongwiriyan, S.-I. Honda, H. Konishi, et al., "Direct growth of single-walled carbon nanotube networks on alumina substrate: a novel route to ultrasensitive gas sensor fabrication," *Japanese Journal of Applied Physics*, vol. 44, no. 11, pp. 8227–8230, 2005.
- [36] M. Penza, G. Cassano, R. Rossi, et al., "Effect of growth catalysts on gas sensitivity in carbon nanotube film based chemiresistive sensors," *Applied Physics Letters*, vol. 90, no. 10, Article ID 103101, 2007.
- [37] N. H. Vedala, Y. C. Choi, X. Y. Zhou, G. Kim, and W. B. Choi, in *Materials Research Society Symposium Proceedings*, vol. 858E, Materials Research Society, 2005, HH13.22.1.
- [38] M. Lucci, A. Reale, A. Di Carlo, S. Orlanducci, et al., "Optimization of a NO_x gas sensor based on single walled carbon nanotubes," *Sensors and actuators B: Chemical*, vol. 118, no. 1–2, pp. 226–231, 2006.
- [39] T. Zhang, M. B. Nix, B.-Y. Yoo, M. A. Deshusses, and N. V. Myung, "Electrochemically functionalized single-walled carbon nanotube gas sensor," *Electroanalysis*, vol. 18, no. 12, pp. 1153–1158, 2006.
- [40] H.-Q. Nguyen and J.-S. Huh, "Behavior of single-walled carbon nanotube-based gas sensors at various temperatures of treatment and operation," *Sensors and Actuators B*, vol. 117, no. 2, pp. 426–430, 2006.
- [41] Y.-L. Liu, H.-F. Yang, Y. Yang, Z.-M. Liu, G.-L. Shen, and R.-Q. Yu, "Gas sensing properties of tin dioxide coated onto multi-walled carbon nanotubes," *Thin Solid Films*, vol. 497, no. 1–2, pp. 355–360, 2006.
- [42] S. K. Padigi, R. K. K. Reddy, and S. Prasad, "Carbon nanotube based aliphatic hydrocarbon sensor," *Biosensors and Bioelectronics*, vol. 22, no. 6, pp. 829–837, 2007.
- [43] J. Suehiro, N. Sano, G. Zhou, H. Imakiire, K. Imasaka, and M. Hara, "Application of dielectrophoresis to fabrication of carbon nanohorn gas sensor," *Journal of Electrostatics*, vol. 64, no. 6, pp. 408–415, 2006.
- [44] K. Lee, J.-W. Lee, K.-Y. Dong, and B.-K. Ju, "Gas sensing properties of single-wall carbon nanotubes dispersed with dimethylformamide," *Sensors and Actuators B*, vol. 135, no. 1, pp. 214–218, 2008.
- [45] J. Suehiro, S.-I. Hidaka, S. Yamane, and K. Imasaka, "Fabrication of interfaces between carbon nanotubes and catalytic palladium using dielectrophoresis and its application to hydrogen gas sensor," *Sensors and Actuators B*, vol. 127, no. 2, pp. 505–511, 2007.
- [46] M. L. Y. Sin, G. C. T. Chow, G. M. K. Wong, W. J. Li, P. H. W. Leong, and K. W. Wong, "Ultralow-power alcohol vapor sensors using chemically functionalized multiwalled carbon nanotubes," *IEEE Transactions on Nanotechnology*, vol. 6, no. 5, pp. 571–577, 2007.
- [47] S. M. C. Vieira, P. Beecher, I. Haneef, et al., "Use of nanocomposites to increase electrical "gain" in chemical sensors," *Applied Physics Letters*, vol. 91, no. 20, Article ID 203111, 2007.
- [48] M. du Plessis, "Nanoporous silicon explosive devices," *Materials Science and Engineering B*, vol. 147, no. 2–3, pp. 226–229, 2008.
- [49] M. J. Sailor, in *Properties of Porous Silicon*, L. T. Canham, Ed., p. 364, INSPEC, London, UK, 1997.
- [50] A. Halimaoui, in *Properties of Porous Silicon*, L. T. Canham, Ed., p. 12, INSPEC, London, UK, 1997.
- [51] E. Gross, D. Kovalev, N. Künzner, et al., "Spectrally resolved electronic energy transfer from silicon nanocrystals to molecular oxygen mediated by direct electron exchange," *Physical Review B*, vol. 68, no. 11, Article ID 115405, 2003.
- [52] U. Gösele, "Nanocrystals: shedding new light on silicon," *Nature Nanotechnology*, vol. 3, no. 3, pp. 134–135, 2008.
- [53] G. Di Francia, V. La Ferrara, L. Lancellotti, and L. Quercia, "Porous silicon based gas sensor," *Recent Research Development in Electrochemistry*, vol. 3, p. 93, 2000.
- [54] A. Foucaran, F. Pascal-Delannoy, A. Giani, A. Sackda, P. Combette, and A. Boyer, "Porous silicon layers used for gas sensor applications," *Thin Solid Films*, vol. 297, no. 1–2, pp. 317–320, 1997.
- [55] A. E. Aliev, Sh. U. Yuldashev, P. K. Khabibullaev, M. H. Khan, and F. A. Khalid, "Studies on sensitivity of porous silicon surfaces to environmental gases," *Journal of Materials Engineering and Performance*, vol. 6, no. 2, pp. 161–164, 1997.
- [56] L. A. Balagurov, B. M. Leiferov, E. A. Petrova, A. F. Orlov, and E. M. Panasenko, "Influence of water and alcohols on photoluminescence of porous silicon," *Journal of Applied Physics*, vol. 9, p. 7143, 1996.
- [57] F. Yin, X. P. Li, Z. Z. Zhang, and X. R. Xiao, "Investigation on the surface reactivity of luminescent porous silicon," *Applied Surface Science*, vol. 119, no. 3–4, pp. 310–312, 1997.
- [58] W. J. Jin, G. L. Shen, and R. Q. Yu, "Organic solvent induced quenching of porous silicon photoluminescence," *Spectrochimica Acta Part A*, vol. 54, no. 10, pp. 1407–1414, 1998.

- [59] G. Di Francia, F. De Filippo, V. La Ferrara, et al., in *Proceedings of the 12th EC Solid State Transducers*, p. 544, Southampton, UK, September 1998.
- [60] M. S. Salem, M. J. Sailor, K. Fukami, T. Sakka, and Y. H. Ogata, "Sensitivity of porous silicon rugate filters for chemical vapor detection," *Journal of Applied Physics*, vol. 103, no. 8, Article ID 083516, 2008.
- [61] J. P. Clarkson, P. M. Fauchet, V. Rajalingam, and K. D. Hirschman, "Solvent detection and water monitoring with a macroporous silicon field-effect sensor," *IEEE Sensors Journal*, vol. 7, no. 3, pp. 329–335, 2007.
- [62] V. Vrkoslav, I. Jelínek, G. Broncová, V. Král, and J. Dian, "Polypyrrole-functionalized porous silicon for gas sensing applications," *Materials Science & Engineering C*, vol. 26, no. 5–7, pp. 1072–1076, 2006.
- [63] I. Schechter, M. Ben-Chorin, and A. Kux, "Gas sensing properties of porous silicon," *Analytical Chemistry*, vol. 67, no. 20, pp. 3727–3732, 1995.
- [64] G. Dolino, D. Bellet, and C. Faivre, "Adsorption strains in porous silicon," *Physical Review B*, vol. 54, no. 24, pp. 17919–17929, 1996.
- [65] D. R. Huanca, F. J. Ramirez-Fernandez, and W. J. Salcedo, "Porous silicon optical cavity structure applied to high sensitivity organic solvent sensor," *Microelectronics Journal*, vol. 39, no. 3–4, pp. 499–506, 2008.
- [66] M. Archer, M. Christophersen, and P. M. Fauchet, "Electrical porous silicon chemical sensor for detection of organic solvents," *Sensors and Actuators B*, vol. 106, pp. 347–357, 2005.
- [67] T. Holec, T. Chvojka, I. Jelínek, et al., "Determination of sensoric parameters of porous silicon in sensing of organic vapors," *Materials Science & Engineering C*, vol. 19, no. 1–2, pp. 251–254, 2002.
- [68] J. Cerdà, A. Cirera, A. Vilà, A. Cornet, and J. R. Morante, "Deposition on micromachined silicon substrates of gas sensitive layers obtained by a wet chemical route: a CO/CH₄ high performance sensor," *Thin Solid Films*, vol. 391, no. 2, pp. 265–269, 2001.
- [69] S. Jang, Y. Koh, J. Kim, and H. Sohn, "Detection of G-type nerve agent simulants based on a double reflection DBR porous silicon interferometer," *Journal of the Korean Physical Society*, vol. 52, no. 2, pp. 212–215, 2008.
- [70] L. De Stefano, L. Moretti, I. Rendina, and L. Rotiroti, "Pesticides detection in water and humic solutions using porous silicon technology," *Sensors and Actuators B*, vol. 111–112, pp. 522–525, 2005.
- [71] R. R. Chandler-Henderson, B. Sweryda-Krawiec, and J. L. Coffey, "Steric considerations in the amine-induced quenching of luminescent porous silicon," *Journal of Physical Chemistry*, vol. 99, no. 21, pp. 8851–8855, 1995.
- [72] E. Guillermain, V. Lysenko, R. Orobtschouk, et al., "Bragg surface wave device based on porous silicon and its application for sensing," *Applied Physics Letters*, vol. 90, no. 24, Article ID 241116, 2007.
- [73] R. B. Bjorklund, S. Zangoie, and H. Arwin, "Planar pore-filling-adsorption in porous silicon," *Advanced Materials*, vol. 9, no. 13, pp. 1067–1070, 1997.
- [74] J. Harper and M. J. Sailor, "Photoluminescence quenching and the photochemical oxidation of porous silicon by molecular oxygen," *Langmuir*, vol. 13, no. 17, pp. 4652–4658, 1997.
- [75] N. K. Ali, M. R. Hashim, and A. Abdul Aziz, "Effects of surface passivation in porous silicon as H₂ gas sensor," *Solid-State Electronics*, vol. 52, no. 7, pp. 1071–1074, 2008.
- [76] R. Prabakaran, L. Silva, E. Fortunato, R. Martins, and I. Ferreira, "Investigation of hydrocarbon coated porous silicon using PECVD technique to detect CO₂ gas," *Journal of Non-Crystalline Solids*, vol. 354, no. 19–25, pp. 2610–2614, 2008.
- [77] J. Tuura, M. Björkqvist, J. Salonen, and V.-P. Lehto, "Electrically isolated thermally carbonized porous silicon layer for humidity sensing purposes," *Sensors and Actuators B*, vol. 131, no. 2, pp. 627–632, 2008.
- [78] S. Khoshnevis, R. S. Dariani, M. E. Azim-Araghi, Z. Bayindir, and K. Robbie, "Observation of oxygen gas effect on porous silicon-based sensors," *Thin Solid Films*, vol. 515, no. 4, pp. 2650–2654, 2006.
- [79] P. Rivolo, P. Pirasteh, A. Chaillou, et al., "Oxidised porous silicon impregnated with Congo Red for chemical sensing applications," *Sensors and Actuators B*, vol. 100, no. 1–2, pp. 99–102, 2004.
- [80] L. Pancheri, C. J. Oton, Z. Gaburro, G. Soncini, and L. Pavesi, "Very sensitive porous silicon NO₂ sensor," *Sensors and Actuators B*, vol. 89, no. 3, pp. 237–239, 2003.
- [81] G. Di Francia, A. Castaldo, E. Massera, I. Nasti, L. Quercia, and I. Rea, "A very sensitive porous silicon based humidity sensor," *Sensors and Actuators B*, vol. 111–112, pp. 135–139, 2005.
- [82] E. Massera, I. Nasti, L. Quercia, I. Rea, and G. Di Francia, "Improvement of stability and recovery time in porous-silicon-based NO₂ sensor," *Sensors and Actuators B*, vol. 102, no. 2, pp. 195–197, 2004.
- [83] N. K. Ali, M. R. Hashim, and A. Abdul Aziz, "Effects of surface passivation in porous silicon as H₂ gas sensor," *Solid-State Electronics*, vol. 52, no. 7, pp. 1071–1074, 2008.
- [84] S. E. Lewis, J. R. Deboer, J. L. Gole, and P. J. Hesketh, "Sensitive, selective, and analytical improvements to a porous silicon gas sensor," *Sensors and Actuators B*, vol. 110, no. 1, pp. 54–65, 2005.
- [85] F. Rahimi and A. Irajizad, "Characterization of Pd nanoparticle dispersed over porous silicon as a hydrogen sensor," *Journal of Physics D*, vol. 40, no. 23, pp. 7201–7209, 2007.
- [86] Be. Mahmoudi, N. Gabouze, L. Guerbous, M. Haddadi, H. Cheraga, and K. Beldjilali, "Photoluminescence response of gas sensor based on CHx/porous silicon-effect of annealing treatment," *Materials Science and Engineering B*, vol. 138, no. 3, pp. 293–297, 2007.
- [87] D. R. Huanca, F. J. Ramirez-Fernandez, and W. J. Salcedo, "Porous silicon optical cavity structure applied to high sensitivity organic solvent sensor," *Microelectronics Journal*, vol. 39, no. 3–4, pp. 499–506, 2008.
- [88] J.-I. Hahm and C. M. Lieber, "Direct ultrasensitive electrical detection of DNA and DNA sequence variations using nanowire nanosensors," *Nano Letters*, vol. 4, no. 1, pp. 51–54, 2004.
- [89] G. Di Francia, V. La Ferrara, S. Manzo, and S. Chiavarini, "Towards a label-free optical porous silicon DNA sensor," *Biosensors and Bioelectronics*, vol. 21, no. 4, pp. 661–665, 2005.
- [90] X. T. Zhou, J. Q. Hu, C. P. Li, D. D. D. Ma, C. S. Lee, and S. T. Lee, "Silicon nanowires as chemical sensors," *Chemical Physics Letters*, vol. 369, no. 1–2, pp. 220–224, 2003.
- [91] J. Jie, W. Zhang, K. Peng, G. Yuan, C. S. Lee, and S.-T. Lee, "Surface-dominated transport properties of silicon nanowires," *Advanced Functional Materials*, vol. 18, no. 20, pp. 3251–3257, 2008.
- [92] F. Patolsky and C. M. Lieber, "Nanowire nanosensors," *Materials Today*, vol. 8, no. 4, pp. 20–28, 2005.

- [93] R. Sze, *Semiconductor Sensor*, John Wiley & Sons, New York, NY, USA, 1994.
- [94] M. Law, H. Kind, B. Messer, F. Kim, and P. Yang, "Photochemical sensing of NO₂ with SnO₂ nanoribbon nanosensors at room temperature," *Angewandte Chemie International Edition*, vol. 41, no. 13, pp. 2405–2408, 2002.
- [95] E. Comini, G. Faglia, G. Sberveglieri, Z. Pan, and Z. L. Wang, "Stable and highly sensitive gas sensors based on semiconducting oxide nanobelts," *Applied Physics Letters*, vol. 81, no. 10, p. 1869, 2002.
- [96] A. Kolmakov, Y. Zhang, G. Cheng, and M. Moskovits, "Detection of CO and O₂ using tin oxide nanowire sensors," *Advanced Materials*, vol. 15, no. 12, pp. 997–1000, 2003.
- [97] G. Neri, A. Bonavita, G. Micali, et al., "Ethanol sensors based on Pt-doped tin oxide nanopowders synthesised by gel-combustion," *Sensors and Actuators B*, vol. 117, no. 1, pp. 196–204, 2006.
- [98] L. L. Fields, J. P. Zheng, Y. Cheng, and P. Xiong, "Room-temperature low-power hydrogen sensor based on a single tin dioxide nanobelt," *Applied Physics Letters*, vol. 88, no. 26, Article ID 263102, 2006.
- [99] A. Chen, X. Huang, Z. Tong, S. Bai, R. Luo, and C. C. Liu, "Preparation, characterization and gas-sensing properties of SnO₂-In₂O₃ nanocomposite oxides," *Sensors and Actuators B*, vol. 115, no. 1, pp. 316–321, 2006.
- [100] M. Rumyantseva, V. Kovalenko, A. Gaskov, et al., "Nanocomposites SnO₂/Fe₂O₃: sensor and catalytic properties," *Sensors and Actuators B*, vol. 118, no. 1-2, pp. 208–214, 2006.
- [101] J. Arbiol, J. R. Morante, P. Bouvier, et al., "SnO₂/MoO₃-nanostructure and alcohol detection," *Sensors and Actuators B*, vol. 118, no. 1-2, pp. 156–162, 2006.
- [102] Q. Kuang, C. Lao, Z. L. Wang, Z. Xie, and L. Zheng, "High-sensitivity humidity sensor based on a single SnO₂ nanowire," *Journal of the American Chemical Society*, vol. 129, no. 19, pp. 6070–6071, 2007.
- [103] N. Mangkorntong and M. Thepnurat, "A single SnO₂ nanowire gas sensor," *Chiang Mai University Journal of Natural Sciences*, vol. 7, pp. 165–170, 2008.
- [104] Y. Shen, T. Yamazaki, Z. Liu, et al., "Microstructure and H₂ gas sensing properties of undoped and Pd-doped SnO₂ nanowires," *Sensors and Actuators B*, vol. 135, no. 2, pp. 524–529, 2009.
- [105] A. Kolmakov, X. Chen, and M. Moskovits, "Functionalizing nanowires with catalytic nanoparticles for gas sensing application," *Journal of Nanoscience and Nanotechnology*, vol. 8, no. 1, pp. 111–121, 2008.
- [106] Q. Wan, J. Huang, Z. Xie, T. Wang, E. N. Dattoli, and W. Lu, "Branched SnO₂ nanowires on metallic nanowire backbones for ethanol sensors application," *Applied Physics Letters*, vol. 92, no. 10, Article ID 102101, 2008.
- [107] Q. H. Li, Y. X. Liang, Q. Wan, and T. H. Wang, "Oxygen sensing characteristics of individual ZnO nanowire transistors," *Applied Physics Letters*, vol. 85, no. 26, pp. 6389–6391, 2004.
- [108] T. Gao and T. H. Wang, "Synthesis and properties of multipod-shaped ZnO nanorods for gas-sensor applications," *Applied Physics A*, vol. 80, no. 7, pp. 1451–1454, 2005.
- [109] H. T. Wang, B. S. Kang, F. Ren, et al., "Hydrogen-selective sensing at room temperature with ZnO nanorods," *Applied Physics Letters*, vol. 86, no. 24, Article ID 243503, 3 pages, 2005.
- [110] H. Cheng, L. Qin, and Q.-M. Wang, "PID-2 high temperature langasite BAW gas sensor based on ZnO nanowire arrays," in *Proceedings of IEEE Ultrasonics Symposium (IUS '07)*, pp. 1361–1364, New York, NY, USA, October 2007.
- [111] H. Tang, M. Yan, H. Zhang, et al., "A selective NH₃ gas sensor based on Fe₂O₃-ZnO nanocomposites at room temperature," *Sensors and Actuators B*, vol. 114, no. 2, pp. 910–915, 2006.
- [112] W. Wongka, S. Yata, A. Gardchareon, P. Mangkorntong, N. Mangkorntong, and S. Choopun, "Zinc oxide nanowires impregnated with platinum and gold nanoparticle for ethanol sensor," *Chiang Mai University Journal of Natural Sciences*, vol. 7, no. 1, pp. 185–190, 2008.
- [113] E. Comini, M. Ferroni, N. Poli, et al., "Doped ZnO nanowires: towards homojunctions," in *Proceedings of IEEE Sensors Conference*, pp. 835–838, Lecce, Italy, October 2008.
- [114] D. Zhang, Z. Liu, C. Li, et al., "Detection of NO₂ down to ppb levels using individual and multiple In₂O₃ nanowire devices," *Nano Letters*, vol. 4, no. 10, pp. 1919–1924, 2004.
- [115] E. C. Walter, K. Ng, M. P. Zach, R. M. Penner, and F. Favier, "Electronic devices from electrodeposited metal nanowires," *Microelectronic Engineering*, vol. 61-62, pp. 555–561, 2002.
- [116] F. Favier, E. C. Walter, M. P. Zach, T. Benter, and R. M. Penner, "Hydrogen sensors and switches from electrodeposited palladium mesowire arrays," *Science*, vol. 293, no. 5538, pp. 2227–2231, 2001.
- [117] E. C. Walter, F. Favier, and R. M. Penner, "Palladium mesowire arrays for fast hydrogen sensors and hydrogen-actuated switches," *Analytical Chemistry*, vol. 74, no. 7, pp. 1546–1553, 2002.
- [118] B. J. Murray, E. C. Walter, and R. M. Penner, "Amine vapor sensing with silver mesowires," *Nano Letters*, vol. 4, no. 4, pp. 665–670, 2004.
- [119] C. Cheng, R. K. Gonela, Q. Gu, and D. T. Haynie, "Self-assembly of metallic nanowires from aqueous solution," *Nano Letters*, vol. 5, no. 1, pp. 175–178, 2005.
- [120] V. La Ferrara, B. Alfano, E. Massera, and G. Di Francia, "Palladium nanowires assembly by dielectrophoresis investigated as hydrogen sensors," *IEEE Transactions on Nanotechnology*, vol. 7, no. 6, pp. 776–781, 2008.
- [121] M. Penza, G. Cassano, P. Aversa, et al., "Alcohol detection using carbon nanotubes acoustic and optical sensors," *Applied Physics Letters*, vol. 85, no. 12, pp. 2379–2381, 2004.
- [122] H.-K. Liao, E.-S. Yang, J.-C. Chou, W.-Y. Chung, T.-P. Sun, and S.-K. Hsiung, "Temperature and optical characteristics of tin oxide membrane gate ISFET," *IEEE Transactions on Electron Devices*, vol. 46, no. 12, pp. 2278–2281, 1999.
- [123] H.-W. Chen, R.-J. Wu, K.-H. Chan, Y.-L. Sun, and P.-G. Su, "The application of CNT/Nafion composite material to low humidity sensing measurement," *Sensors and Actuators B*, vol. 104, no. 1, pp. 80–84, 2005.
- [124] A. Jungen, C. Meder, M. Tonteling, C. Stampfer, R. Linderman, and C. Hierold, "A MEMS actuator for integrated carbon nanotube strain sensing," in *Proceedings of IEEE Sensors Conference*, pp. 1–4, Irvine, Calif, USA, October–November 2005.
- [125] S. Deshpande, A. Karakoti, G. Londe, H. J. Cho, and S. Seal, "Room temperature hydrogen detection using 1-D nanostructured tin oxide sensor," *Journal of Nanoscience and Nanotechnology*, vol. 7, no. 9, pp. 3354–3357, 2007.
- [126] P. Bhattacharyya, P. K. Basu, B. Mondal, and H. Saha, "A low power MEMS gas sensor based on nanocrystalline ZnO thin films for sensing methane," *Microelectronics Reliability*, vol. 48, no. 11-12, pp. 1772–1779, 2008.
- [127] M. Penza, M. A. Tagliente, P. Aversa, M. Re, and G. Cassano, "The effect of purification of single-walled carbon nanotube bundles on the alcohol sensitivity of nanocomposite Langmuir-Blodgett films for SAW sensing applications," *Nanotechnology*, vol. 18, no. 18, Article ID 185502, 2007.

- [128] S. Sivaramakrishnan, R. Rajamani, C. S. Smith, K. A. McGee, K. R. Mann, and N. Yamashita, "Carbon nanotube-coated surface acoustic wave sensor for carbon dioxide sensing," *Sensors and Actuators B*, vol. 132, no. 1, pp. 296–304, 2008.
- [129] A. A. Pesetski, J. E. Baumgardner, E. Folk, J. X. Przybysz, J. D. Adam, and H. Zhang, "Carbon nanotube field-effect transistor operation at microwave frequencies," *Applied Physics Letters*, vol. 88, no. 11, Article ID 113103, 2006.
- [130] M. S. Arnold, P. Avouris, Z. W. Pan, and Z. L. Wang, "Field-effect transistors based on single semiconducting oxide nanobelts," *Journal of Physical Chemistry B*, vol. 107, no. 3, pp. 659–663, 2003.
- [131] S. Dasgupta, S. Gottschalk, R. Kruk, and H. Hahn, "A nanoparticulate indium tin oxide field-effect transistor with solid electrolyte gating," *Nanotechnology*, vol. 19, no. 43, Article ID 435203, 2008.
- [132] C. S. Lao, Q. Kuang, Z. L. Wang, M.-C. Park, and Y. Deng, "Polymer functionalized piezoelectric-FET as humidity/chemical nanosensors," *Applied Physics Letters*, vol. 90, no. 26, Article ID 262107, 2007.
- [133] G. Barillaro, A. Diligenti, L. M. Strambini, E. Comini, and G. Faglia, "FET-like silicon sensor with a porous layer for NO₂ detection," in *Proceedings of IEEE Sensors Conference*, pp. 121–124, Irvine, Calif, USA, October–November 2005.
- [134] H. C. Wang, Y. Li, and M. J. Yang, "Fast response thin film SnO₂ gas sensors operating at room temperature," *Sensors and Actuators B*, vol. 119, no. 2, pp. 380–383, 2006.
- [135] M. Kroneld, S. Novikov, S. Saukko, P. Kuivalainen, P. Kostamo, and V. Lantto, "Gas sensing properties of SnO₂ thin films grown by MBE," *Sensors and Actuators B*, vol. 118, no. 1-2, pp. 110–114, 2006.
- [136] L. Rotkina, J.-F. Lin, and J. P. Bird, "Nonlinear current-voltage characteristics of Pt nanowires and nanowire transistors fabricated by electron-beam deposition," *Applied Physics Letters*, vol. 83, no. 21, pp. 4426–4428, 2003.
- [137] T.-Y. Choi, B. Kang, and D. Poulidakos, "Focused ion beam in thermal science and engineering," *Microscopy and Microanalysis*, vol. 13, supplement 2, pp. 1498–1499, 2007.

Review Article

Fabrication of TiO₂ Nanotube Thin Films and Their Gas Sensing Properties

Yongxiang Li, Xiaofeng Yu, and Qunbao Yang

State Key Laboratory of High Performance Ceramics and Superfine Microstructures, Shanghai Institute of Ceramics, Chinese Academy of Sciences, 1295 Dingxi Road, Shanghai 200050, China

Correspondence should be addressed to Yongxiang Li, yxli@mail.sic.ac.cn

Received 3 January 2009; Accepted 28 May 2009

Recommended by Giorgio Sberveglieri

The fabrication process and the growth mechanism of titanium/titania nanotubes prepared by anodization process is reviewed, and their applications in the fields of dye sensitized solar cells, photocatalysts, electrochromic devices, gas sensors, and biomaterials are presented. The anodization of Ti thin films on different substrates and the growth process of anodic titanium oxide are described using the current-time curves. Special attention is paid on the influences of the initial film smoothness on the resulted nanoporous morphologies. The “threshold barrier layer thickness model” is used to discuss the growth mechanism. As a case study for gas sensing, anodized highly ordered TiO₂ nanotube arrays and nanoporous thin films that show porous surface with an average diameter of 25 nm and interpore distance of 40 nm were prepared. Gas sensors based on such nanotube arrays and nanoporous thin films were fabricated, and their sensing properties were investigated. Excellent H₂ gas sensing properties were obtained for sensors prepared from these highly ordered TiO₂ nanotube arrays, which present stable response even at a low operating temperature of 90°C. Based on our experimental results, “H-induced O²⁻ desorption” mechanism was used for explaining the hydrogen gas sensing mechanism.

Copyright © 2009 Yongxiang Li et al. This is an open access article distributed under the Creative Commons Attribution License, which permits unrestricted use, distribution, and reproduction in any medium, provided the original work is properly cited.

1. Introduction

Nanoporous structures are of significant importance in a variety of nanostructured because they not only have the common properties that are widely seen in nanomaterials such as surface effect, size effect, and enhanced chemical and optical properties but can also be used as “nanotemplates” to fabricate other nanostructures such as nanodots, nanowires and, nanotubes, which further expand their potential applications. In recent years, in line with the increase in research on the development nanomaterials, the properties of a variety of novel functional devices have been largely explored based on the unique optical, mechanical, chemical, and electrical properties of nanomaterials.

It is undoubtedly agreed that anodic alumina oxide (AAO) is one of the most investigated nanostructures and has attracted lots of interests. With the development of AAO and its growth model and mechanism, the anodization process has been adopted to the other metals such as Ti, Ta, Nb, W, Hf, and Zr, and so forth (so called valve metals). Many

different nanostructures have been fabricated from those metals, and more applications as well as functionalities have been developed, and are still actively under investigations.

The applications of nanomaterials include photoluminescence [1–11], sensors [12–16], photo-catalysts [17], DSSCs [18–23], high-density vertical magnetic storage [24–30], field emission devices [31–37], rapid response electrochromic devices [38], and so forth. In this review paper, we focus on the recent progresses in the field of anodic titanium nanotube/nanoporous thin film fabrication and its applications in gas sensors.

2. Fabrication of Anodic Titanium Nanotubes

The preparations of TiO₂ nanotubes were reported through hydrothermal synthesis [39, 40] and templated sol-gel process [41]. However, the first report on nanoporous structure of anodized Ti metal can be traced to 1920s. In 1999, Zwilling et al. [42, 43] found that when chromium acid was used

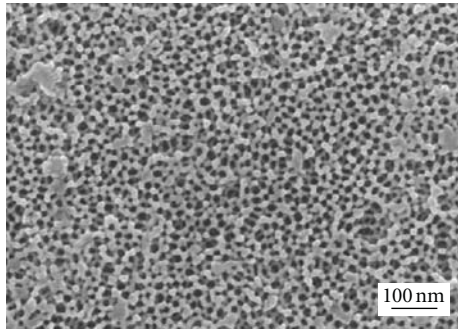


FIGURE 1: Typical SEM images of anodic titanium oxide (ATO) nanoporous thin film.

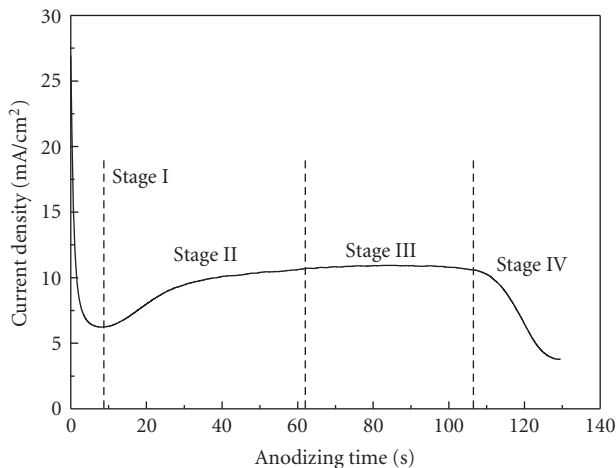


FIGURE 2: Current transient during the anodization process.

as the electrolyte to perform the anodization on titanium and its alloy (TA6V), a compact oxide film was obtained, while in an HF/chromium acidic electrolyte, a nanoporous structure was obtained instead. In 2001, Grimes and his team reported their systematic research on the nanotubular structures obtained by titanium anodization process. Such an anodization process has since attracted an increasing interest with the establishment of its growth model, crystal structure, and the other relating theories. Meanwhile, a series of functional devices were developed based on such nanostructures.

The development of anodic titanium nanostructures will be reviewed in this paper. Experimental results confirmed that the types of electrolytes as well as the anodizing potential, processing temperature, and reaction time are the key factors that affect the final nanostructures which all will be discussed in this paper. A comprehensive report on the gas sensing properties of such films will also be presented.

2.1. HF Acid-Based Anodization. HF acid is widely used as the electrolyte since it has the highest efficiency for the anodization of titanium, and the anodization parameters were studied and optimized. Gong et al. [44] reported that when 0.5 wt% HF was used, a nanoporous structure

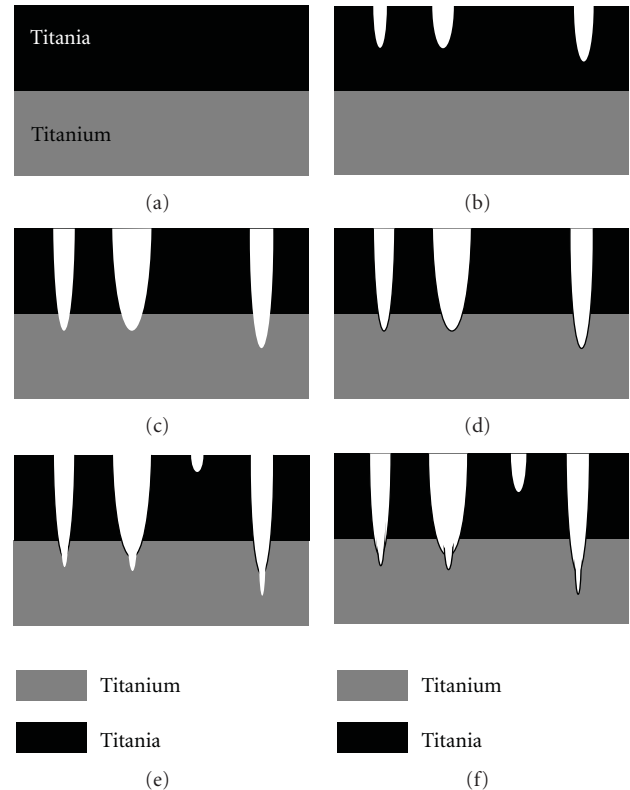


FIGURE 3: Schematic diagram of the passivation and repassivation effect during the anodization process.

was obtained at a relatively low anodizing potential (<3 V) while discrete nanotubular arrays were obtained when the potential >5 V. With increasing the anodizing potential to over 40 V, randomly distributed pores were observed because of the deterioration of the nanotube structure. Their research showed that the electrochemical window for the nanotube formation is in the range from 10 V to 40 V which strongly depended on and related to the concentration of the electrolyte and the applied potential. They also reported that the diameter, wall thickness, and length of the nanotubes increase with the increase of anodizing potentials.

More anodization experiments were performed in HF contained mixture electrolytes. Mor et al. [45–49] reported that when anodization was carried out in the oxalic acid/0.5 wt% HF (1 : 7 in volume ratio), the resulted nanotube did not show a significant difference in diameter and shape except for wall thickening. When anodized at 10 V, the inner diameters of the nanotubes were approximately 20 nm, and the wall thicknesses were ~15 nm. Further study showed that the wall thickness and the tube length are both a function of the anodizing temperature. With decreasing anodizing temperature, because of the low dissolution rate, the wall thickness increases and then causes a high filling between the interspace of neighboring nanotubes which ultimately connects the nanotubes and forms a nanoporous structure. This result proved that, during the anodization process, chemical dissolution and electrochemical etching are the two key processes.

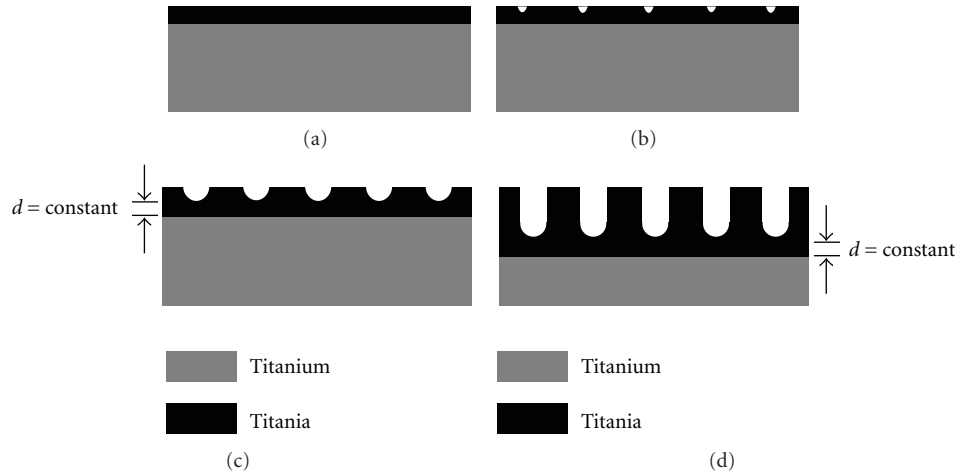


FIGURE 4: Schematic diagram of the dynamic balance during the anodization process.

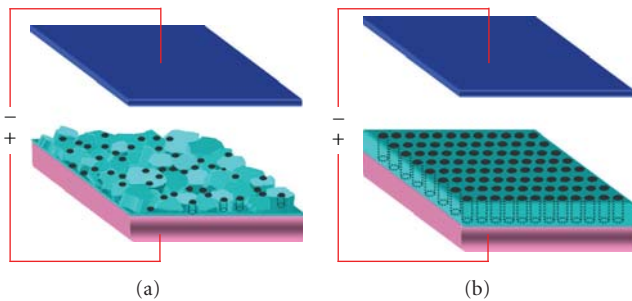


FIGURE 5: Schematic diagram of the relationship between the surface structure and the final morphology.

Beranek et al. [50] reported the anodization process in $\text{H}_2\text{SO}_4/\text{HF}$ electrolyte. In their report, the anodic current goes smoothly when anodization is performed in H_2SO_4 electrolyte. In HF-electrolyte, however, continuous oscillation occurs, and the scope is related to the concentration. They explained that there exists a competition between oxide formation and dissolution, and HF is the key factor, which causes the dissolution of oxide layer. Such a competition finally results in a length limitation when nanotubes are fabricated in HF contained electrolytes. The study of the relationship between the length of the nanotube and the “competition between oxide formation and dissolution” is very unique. They also observed an oscillation in the anodizing current, but they did not give a reasonable explanation for it.

2.2. Neutral Electrolyte-Based Anodization. As discussed above, Beranek’s discussion on the relationship between nanotube length limitation and growth mechanism is very interesting, and such a viewpoint was confirmed by Macak et al. [51, 52] and Bauer [53]. Macak pointed out that there exists a length limitation of several hundred nanometers when anodization is performed in HF-based electrolytes. The reason for such a limitation is the dissolution caused by

acidic electrolyte on the top of nanotubes. As a result, in order to obtain nanotubes with a higher aspect ratio (L/D), the dissolution rate at both top and bottom of the nanotube should be adjusted, which means that the formation rate of the nanotube at the bottom should be enhanced while the dissolution of the existed nanotube on the top should be restrained. They realized it by the application of a type of neutral electrolyte, and the nanotubes with extremely large aspect ratio were obtained. The neutral buffered electrolytes used in their experiments were $\text{NH}_4\text{F}/(\text{NH}_4)_2\text{SO}_4$ [51] and $\text{NaF}/\text{Na}_2\text{SO}_4$ [52]. By the application of neutral electrolyte, a low pH value was established at the bottom of the nanotube which enhanced the growth rate, while at the top and wall area of the nanotube, a relatively high pH value prevented the electrochemical dissolution. As a result, the “second generation” nanotube array with large aspect ratio was succeeded. The research which has been performed by Macak to adjust the pH value of the electrolyte at different parts of the nanotubes is of significant importance.

Anodic titanium nanotube arrays with a length of several micron meters were also reported by Grimes et al. [54, 55] when the anodization was performed in a KF (or NaF) electrolyte. According to their results, the pH value has a significant effect on the electrochemical dissolution during the anodization process. Such an effect is caused by the hydrolysis of titanium ions. Usually, longer nanotubes are formed when keeping the pH value of the electrolyte at a high level (< 7). At a given pH value, the length and diameter of the nanotube increase with increasing the anodization potential. However, at a given potential, the diameter is not affected by the pH value.

Cai et al. [54] reported that the extension of anodizing time does not increase the length of the nanotubes when anodization is performed in strong acidic electrolyte ($\text{pH} < 1$); in weak acidic electrolyte, however, the tube length increases with the increasing of anodizing time. According to their results, the nanotubes with large aspect ratio can be obtained in a pH range of 3–5. The nanotubes formed in an electrolyte with a low pH value is found to be short but

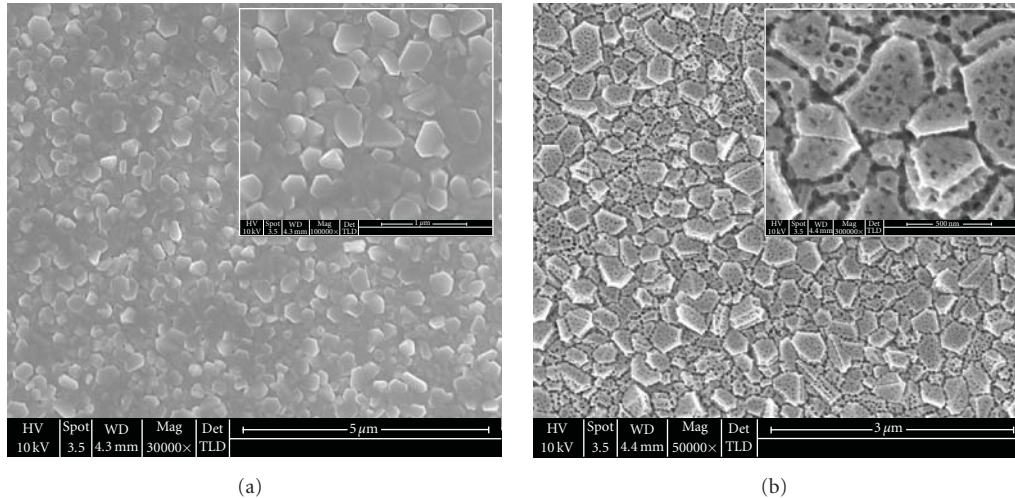


FIGURE 6: SEM images of (a) Ti thin film fabricated by RF-sputtering and (b) after anodization in a 0.5 wt% NH₄F/EG electrolyte.

very “clean”, while a high pH value may help to form longer nanotubes, severe coverage occurs at the open mouth of the nanotubes, and no nanotubular structure could be formed in alkaline electrolytes. The studies of the effect of pH value on nanostructure morphologies given by Cai and coworkers are systematic, they confirmed again that the competition between formation and dissolution of oxide layer is the key driving force of nanotube growth, and the major factor of the length of final tubes as well.

Macak et al. [56–58] and Richter et al. [59] noticed subtly in their results the regular strips on the outer wall of nanotubes and ascribed such strips to the current oscillations. They explained that when associating anodizing time with the tube length, the frequency of current oscillation exactly matches the distance between the neighboring strips. Based on this assumption, the pH value breaking is the primary cause of the current oscillation and final formation of the strips. Subsequently, they replaced the conventional electrolyte with a high-viscosity electrolyte to control the pH breaking, and the nanotubes with smooth walls were successfully prepared.

2.3. Organic Electrolyte-Based Anodization. With the development of Ti anodization techniques, a variety of electrolytes were investigated to evaluate their effects on the nanostructure morphologies. The electrolytes used are not within the limitation in conventional aqueous solutions but with multiple choices to organic solutions. Tsuchiya et al. [60] reported one type of titanium nanotube arrays with “coral reefs” morphology which is quite different from the previously reported nanostructures. Such nanotube arrays were fabricated at high anodizing potential in F-contained “water-free” acetic acid electrolyte. However, they did not give the explanation of the effect as why the using of acetic acid may result in such a nanostructure.

Ruan et al. [61] formed highly ordered nanotube arrays when performed the anodization in an HF-contained

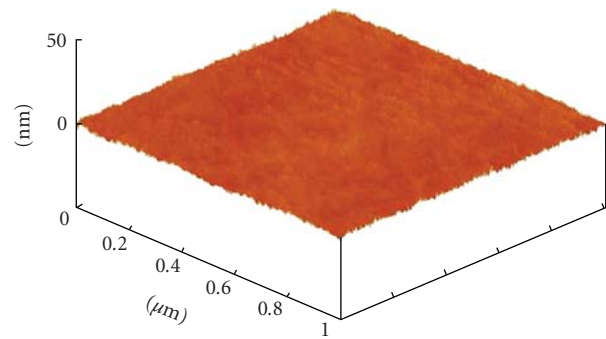


FIGURE 7: AFM image of Ti thin films fabricated by an FCVA process.

dimethylsulfoxide (DMSO)/ethanol mixture electrolyte. According to their report, the nanotubes obtained in such an electrolyte present an enhanced photoelectric response compared with that formed in conventional aqueous electrolytes. The excellent properties were ascribed to the unique morphologies. However, they did not point out the relationship between the electrolyte and the morphology.

3. Mechanism Model and Crystallization Process

The most widely acceptable growth mechanism of anodic titanium is originated from the growth mechanism of AAO [55]. The formation process of titanium nanotubes is similar to those of AAO including the following procedures: (1) formation of an oxide layer at Ti metal surface when reacting with O²⁻ and OH⁻ at the anode; after that, the anions diffuse into the oxide layer and continuously react with the metal beneath; (2) migration of Ti⁴⁺ from the oxide/metal interface to metal/electrolyte interface under the electric field; (3) dissolution at the oxide/electrolyte interface;

Ti-O bond becomes weak under the applied electric field which causes the dissolution; Ti^{4+} goes into the electrolyte while the free O^{2-} ions diffuse across the oxide layer and react with Ti metal at the oxide/metal interface; (4) since acidic electrolytes are most used for the Ti anodization, the chemical dissolution cannot be neglected. In the Ti anodization, nanotubular structures (discrete nanotubes) instead of nanoporous structure are commonly obtained compared with that in Al anodization process.

It is of significant importance to investigate the crystal structure of anodic titanium since it is closely related to its properties and applications. For instance, anatase titanium dioxide is widely used in DSSCs, while TiO_2 with rutile phase finds its applications in gas sensors as a dielectric layer.

The as-prepared anodic titanium is amorphous and crystallizes after annealing process. Varghese et al. [62] investigated the crystallization process of anodic titanium by anodizing titanium in HF electrolyte at 20 V with the following annealing in O_2 at different temperatures. According to their report, anodic titanium remains an amorphous structure when the annealing temperature is below $250^\circ C$, and anatase structure appears at the annealing temperature between 250 and $280^\circ C$. When the temperature is close to $430^\circ C$, rutile phase can be found according to the XRD results. Beyond $430^\circ C$, rutile phase becomes dominant, and at annealing temperature between 620 and $680^\circ C$, the anodic titanium transfers fully to rutile phase TiO_2 . Varghese et al. also investigated the grain size of the anatase TiO_2 as well as the rutile TiO_2 and found that initially the grain size of anatase phase increases with the temperature increasing. It followed by a decrease at $480\sim 580^\circ C$ and increases again after $580^\circ C$. As for the grain size of rutile phase, it continuously increases with the increasing of annealing temperature. There is 31% rutile phase structure at $430^\circ C$ and 75% at $480^\circ C$; it reaches 91% when annealing temperature is as high as $580^\circ C$.

When the anodization was performed in $H_3BO_3-HNO_3-HF$ electrolyte or in HNO_3-HF electrolyte followed by annealing in O_2 , very similar results were obtained compared with that in HF electrolyte. In KF (or NaF), the XRD results showed that the anodic titanium remains amorphous below the annealing temperature of $230^\circ C$, and not until $280^\circ C$ it starts to crystallize. The results are exactly the same with the experiments performed in HF aqueous solutions without any added acid. Therefore, one can draw a conclusion that neither the concentration of electrolyte nor the pH value has any effects on the crystallization temperature of titanium nanotubes.

It is worthy to mention that, according to Mor's studies on the anodization of titanium thin film sputtered on glass substrates, when there is discontinuous metal thin film remaining at the bottom of nanotubes, even at an annealing temperature of $500^\circ C$, no rutile phase is obtained. Such a result is in contrast with that when anodization was performed on Ti metal sheet/foil. However, when the nanotubes with thick, continuous metal film was annealed, both anatase and rutile were obtained at an annealing temperature of $480^\circ C$, which is similar to the XRD results when performing anodization on Ti sheet [54, 63, 64]. Based

on these results, Mor et al. gave their assumption that rutile phase only forms at the oxide/metal interface when Ti metal is thermal oxidized, while because of the confinement by the wall of the nanotubes, the increscent nuclear grain size prevents its transformation to rutile phase. This assumption was confirmed by selected area electron diffraction (SAED) when analyzing single nanotube which is annealed at $600^\circ C$; anatase instead of rutile phase was observed at the wall of the nanotube.

4. Applications of Anodic Titanium

4.1. Water Photolysis. Grimes and his coworkers [65–68] reported their research on the water photolysis by using anodic titanium nanotube arrays as the anode. By illuminating the nanotube arrays under UV light ($320\sim 400$ nm, 100 mW/cm²) and then investigating the relationship between $I-V$ curve and anodizing temperature, they found that the current density obtained from nanotubes anodized at 1.5 V, $5^\circ C$ is 3 times higher than that of anodized at $50^\circ C$ and, low temperature anodization always results in the increasing of the slope in $I-V$ curve. The highest quantum efficiency of 90% is obtained when the sample anodized at 10 V; $5^\circ C$ is illuminated under 337 nm UV light (2.7 mW/cm²).

4.2. Dye Sensitized Solar Cells (DSSCs). Mor et al. [69, 70] reported transmitted type of DSSCs based on highly ordered TiO_2 nanotube arrays. In their research, Ti thin film with a thickness of 400 nm was sputtered on an FTO glass substrate followed by an anodization process in 0.5% HF/acetic acid (7 : 1 in volume ratio) electrolyte at 10 V. The obtained nanotube arrays were annealed at $450^\circ C$ for 3 hours to be transformed to anatase phase. Before being used in DSSCs, the nanotubes were treated in 0.2 M $TiCl_4$ for 1 hour followed by annealing again at $450^\circ C$ for another 30 minutes. Dye adsorption was realized by dipping the sample into 0.3 mM N719 (Dyso) contained ethanol solution for 12 hours. A 25 nm Pt coated conductive glass was used as the counter electrode and a methoxypropionitrile (MPN) solution containing 0.5 M LiI, 0.05 M I_2 , 0.6 M N-methylbenzimidazole, 0.1 M guanidinium thiocyanate, 0.5 M tert-butylpyridine was used as the electrolyte. The effective area for the cell was 0.25 cm². At a given length of nanotubes (3.6 μm), the short circuit current (J_{sc}) could reach ~ 10.3 mA/cm², while an open circuit voltage (V_{oc}) of ~ 0.84 V was obtained under an illumination of AM-1.5 (100 mW/cm²). The filling factor (FF) was 0.54 with a photoconversion efficiency of 4.7%.

Mor et al. [69, 70] mentioned that the photoconversion efficiency increases with the increasing of the tube length and the results obtained in this case (when nanotubes with 3.6 μm length is used) can only be reached when a 10 μm thick conventional nanocrystalline TiO_2 is used. Such a high efficiency is obviously ascribed to the large surface area obtained by the nanotubular structure. But still there are some problems need to be solved in this type of devices. The first one is the dye adsorption efficiency. Since there only exists an open mouth for each nanotube, the remaining

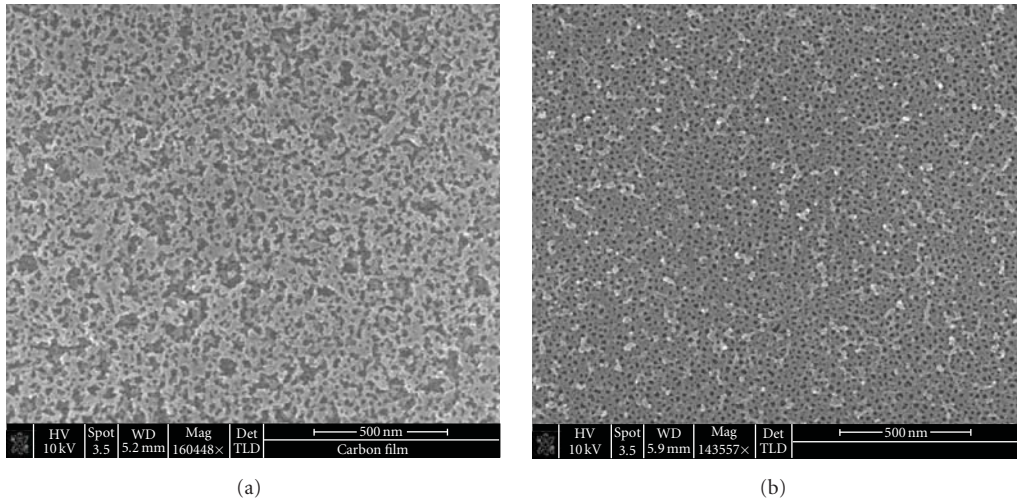


FIGURE 8: SEM images of nanoporous TiO₂ layer fabricated by the anodization of FCVA-deposited Ti thin film on a quartz substrate.

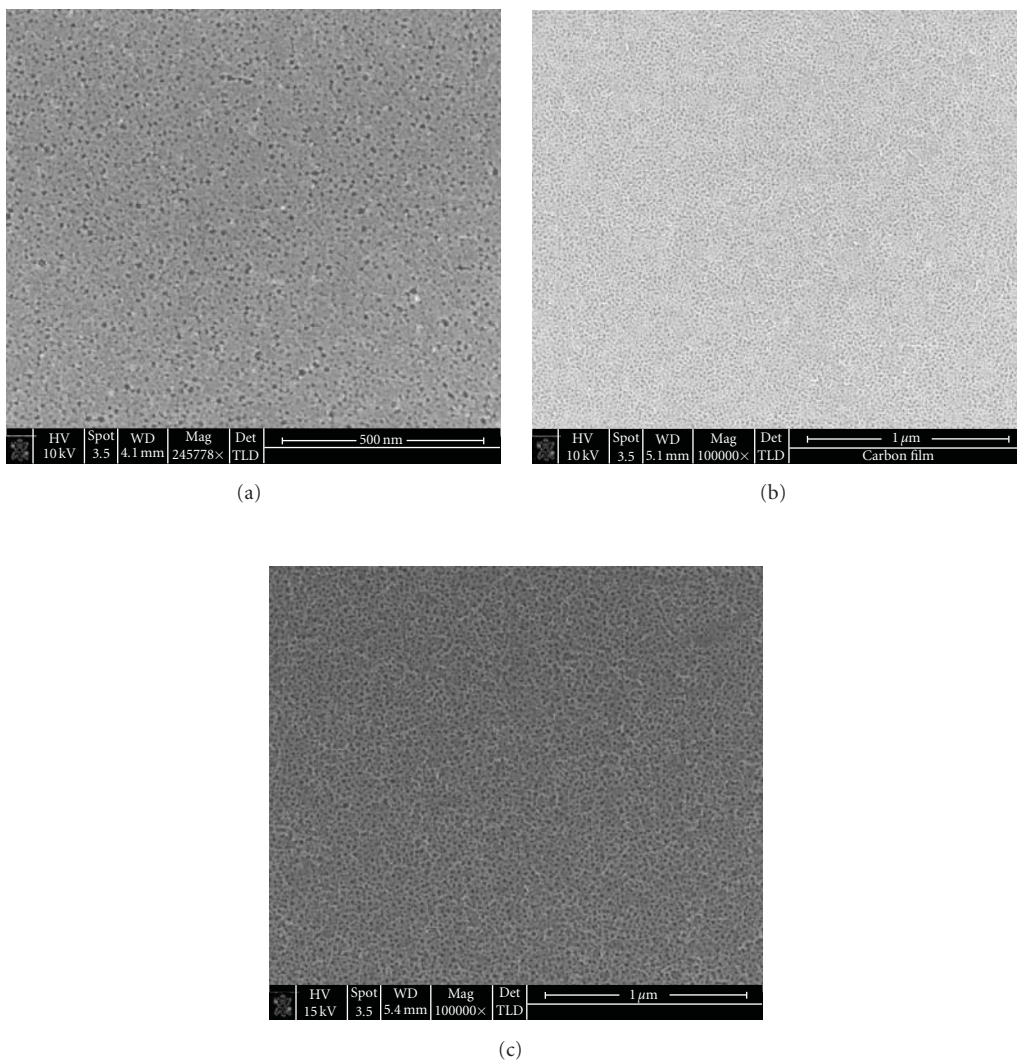


FIGURE 9: SEM images of nanoporous TiO₂ layer fabricated by the anodization of FCVA-deposited Ti thin film at different potentials: (a) 2 V, (b) 10 V, and (c) 20 V.

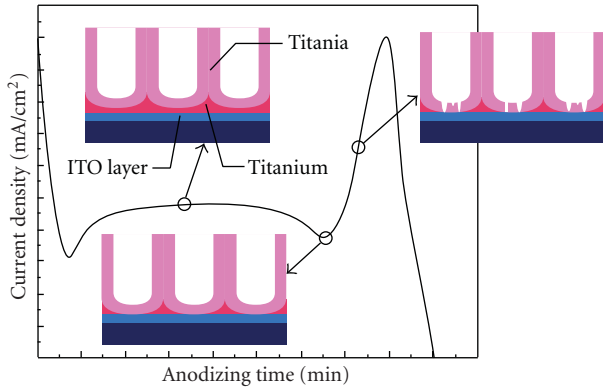


FIGURE 10: Schematic diagram of ITO-based Ti thin film during the anodization process.

atmosphere inside the nanotube prevents the fully filling of dye-contained solution into the nanotube which causes a very limited adsorption at only the open mouth part. The second is that the remaining oxide layer at the bottom of the nanotubes increases the resistance and decreases the FF of the device. The third problem is the repeated annealing process which results in an increase of FTO resistance.

Paulose et al. [71] reported another reflective type DSSCs based on titanium nanotube arrays anodized from Ti sheet. The anodization was performed in KF electrolyte at 25 V with a tube length of $6\ \mu\text{m}$ and a diameter and a wall thickness of 110 nm and 20 nm, respectively. The nanotubes were annealed at 580°C for 6 hours for crystallization. In this type of solar cell, a 1.3 nm Pt coated TCO glass was used as the counter electrode, and the other structure is exactly the same as the device prepared by Mor et al. [69, 70]. The effective area of this device was $0.4\ \text{cm}^2$. When illuminated at AM-1.5 ($100\ \text{mW}/\text{cm}^2$), J_{sc} of $15\ \text{mA}/\text{cm}^2$ and V_{oc} of $0.84\ \text{V}$ were obtained. The FF for such device was 0.43 with a total photoconversion efficiency of 5.44%. Paulose pointed out that the low FF was ascribed to the thick barrier layer at the bottom of the nanotubes. They also supposed that the stepwise potential decrease, which is widely used in the anodization of Al to reduce the thickness of barrier layer, could also be used in this case to improve the properties of this device.

4.3. Gas Sensors. As a functional semiconductor material, TiO_2 is widely used in the field of gas sensors. Nanostructural TiO_2 attracts an increasing interest due to its large surface area since the sensing process is mainly a surface process between the gas molecules and metal oxide surface.

Many investigations showed that highly ordered nanotube arrays have excellent response to hydrogen gas at room temperature [72–76]. According to these reports, there is no significant relationship between the sensitivity and the length of the nanotubes since the sensitivity only increases from 7 to 8.7 when the nanotube length increases from 380 nm to $1\ \mu\text{m}$. However, due to the large surface area of the nanotubular structure, the sensitivity of nanotube-based sensors is much higher than that of compact TiO_2 thin film

sensors. Further discussion on nanoporous TiO_2 -based gas sensors will be presented later in this paper.

4.4. Electrochromic Devices. Ghicov et al. [77] reported the electrochromic properties of titanium nanotubes fabricated by anodization in a $1\ \text{M}\ \text{H}_3\text{PO}_4 + 1\ \text{M}\ \text{NaOH} + 0.5\ \text{wt}\% \text{HF}$ electrolyte at 20 V. The prepared nanotube has a length of $1\ \mu\text{m}$, a diameter of 100 nm, and a wall thickness of 10 nm. The H^+ intercalation changes the energy band structure of TiO_2 which causes the color change. Since the efficiency of ion intercalation and deintercalation is closely related to the surface area, the large aspect ratio of titanium nanotubes provided a largely increased storage capability for H^+ . They concluded that the anodic titanium nanotube will find its applications in the field of display devices, hydrogen storage as well as supercapacitors.

4.5. Bioactive Materials. Yang et al. [78] and Oh et al. [79] reported the application of anodic titanium as a bioactive material. Their studies showed that phosphorite grows easily on the anodic titanium surface by immersing the samples into simulated body fluid (SBF), which means that anodization is one of the effective methods to prepare bioactive materials. Yang also reported that, with the incubation for 3 days, phosphorite only grows on samples anodized at high potentials (150 and/or 180 V) but not on that anodized at a low potential (90 V). They believed that the different surface morphologies obtained at different anodization potentials is the key factor for the phosphorite growth.

5. Fabrication of Nanoporous Anodic Titanium Thin Films

Since the applications of functional devices need some special requirements on the substrate, for example, optical devices need transparent substrates while surface acoustic wave (SAW) devices need piezoelectric substrates, more and more groups have focused their research interests on the fabrication of anodic films based on the anodization of titanium films on different substrates instead of titanium metal sheets/foils [49, 70, 72, 80–83]. Because the anodization is performed on titanium thin films, therefore, a variety of substrates can be chosen in the film deposition processes. As a result, the obtained anodic films with nanostructures can find wide potential applications in a variety of devices.

As we have discussed previously many technical problems need to be solved, and the growth mechanism of nanostructural anodic thin films needs to be investigated since thin films have different properties compared with the bulk materials. The limited thickness of thin films also needs to be considered during the anodization process. The investigation on the optimal thin film anodization parameters becomes highly important.

In this section, the study of nanoporous titanium thin films on different substrates including Si, ITO, and quartz will be presented based on the research outcome from the authors' research laboratory and their team. By investigating the I - V curves, anodizing potential, type of

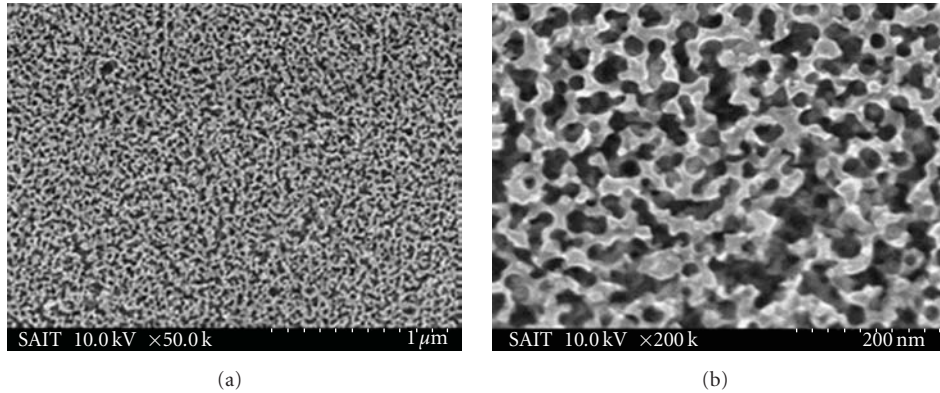


FIGURE 11: SEM image of nanoporous Ti on ITO substrate.

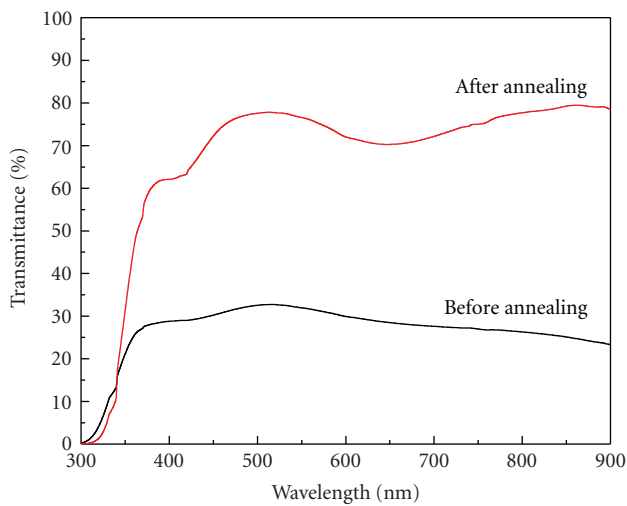


FIGURE 12: Transmittance spectra of ATO nanoporous thin films on ITO substrate before and after heat treatment.

electrolyte, initial morphology of Ti films as well as their crystal structures, a growth mechanism is developed for the nanoporous/nanotube anodic thin films formation.

5.1. Experimental Procedure

5.1.1. Ti Thin Film Deposition

RF Sputtering. Ti films were deposited on a chosen substrate by RF magnetic sputtering. The base chamber pressure was below 9.0×10^{-6} Torr. During the deposition process, the argon gas pressure was 1.0×10^{-2} Torr. The distance between the target and sample was 50 mm, and the sputtering power was 100 W. No substrate heating was performed. The desired film thickness was in a range from 300 nm to 500 nm.

Filtered Cathodic Vacuum Arc (FCVA) Deposition. The source featured a water-cooled rotating M60-threaded copper base, which accepted a 70 mm diameter cathode (99.99% purity Ti for these experiments). The cathode was struck

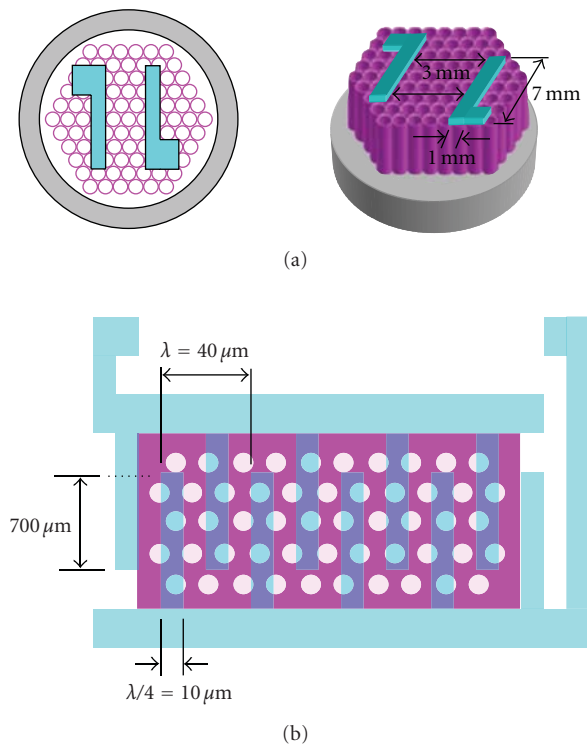


FIGURE 13: Schematic diagram of Anodic Titanium Oxide (ATO) nanotube-based gas sensors: (a) the first type and (b) the second type.

by a grounded mechanical striker to initiate the plasma. An arc current of 120 A (with an average arc power of 3 kW) was found to be sufficient to produce a stable plasma. For these experiments, a sample bias of -50 V was used. A magnetic filter was employed to prevent the deposition of macroparticles onto the sample, thereby minimizing surface roughness. The thickness of the film deposited in the process was approximately 300 nm.

5.1.2. Anodization. Before anodization, the specimen was degreased in acetone using an ultrasonic bath for several

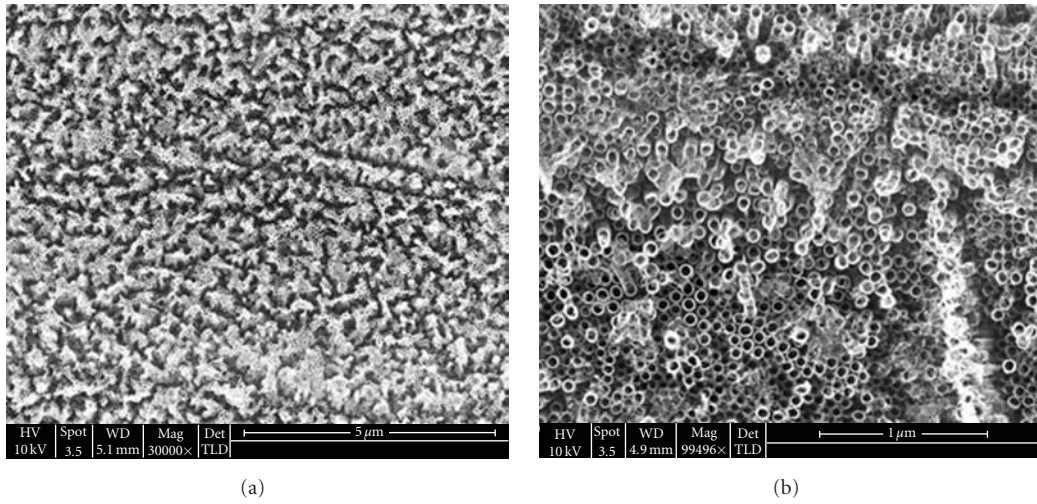


FIGURE 14: SEM images of the ATO nanotube arrays for gas sensor.

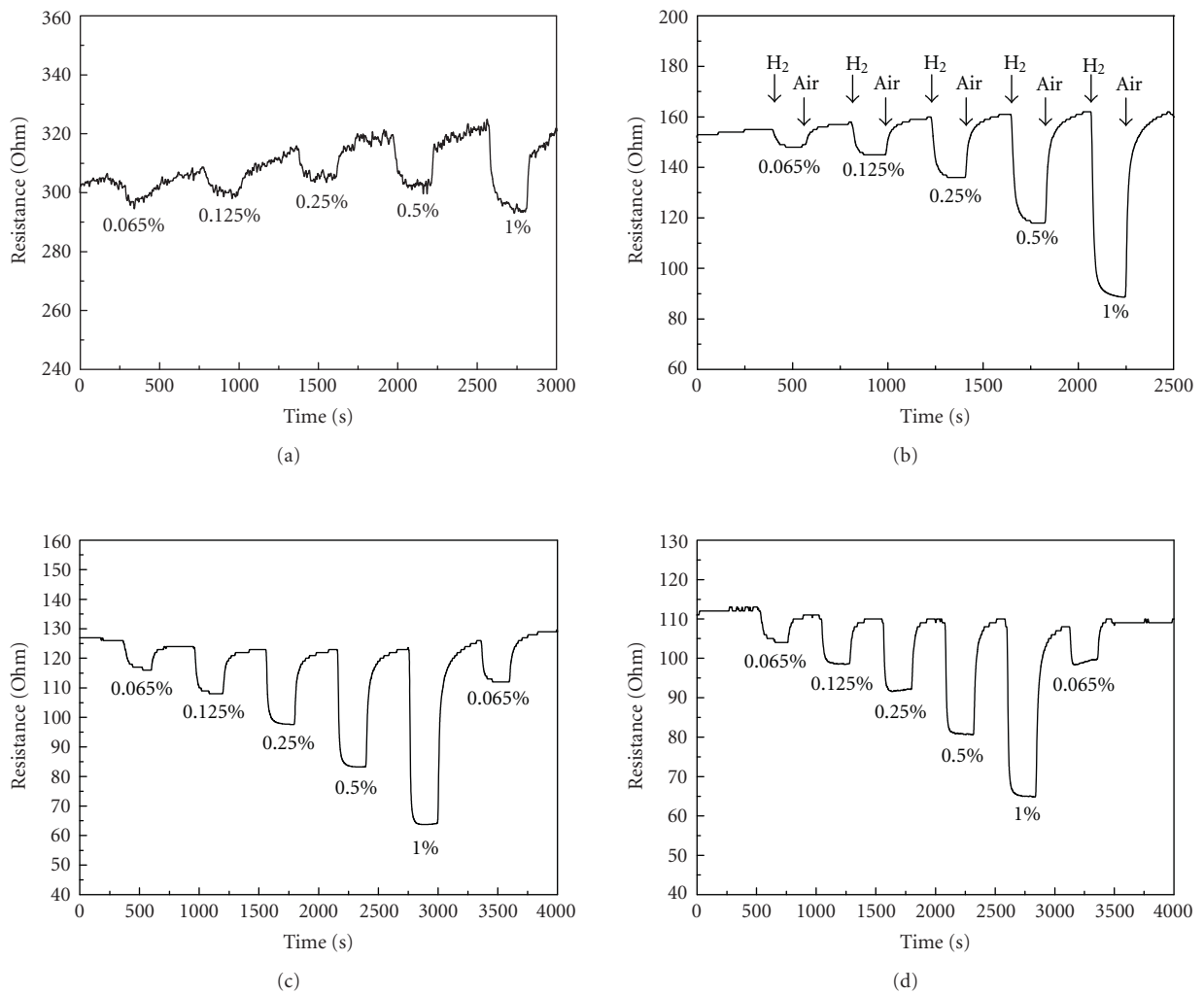


FIGURE 15: Dynamic response of ATO nanotube arrays-based gas sensor to H₂ at different working temperatures: (a) 90°C, (b) 160°C, (c) 190°C, and (d) 215°C.

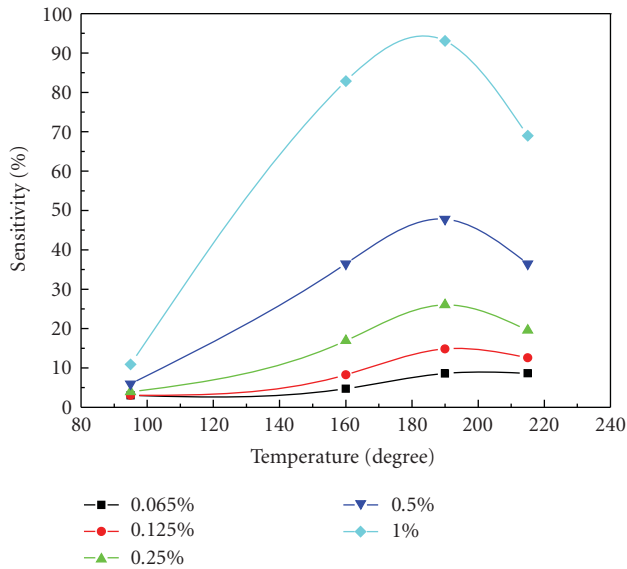


FIGURE 16: The relationship between sensitivity and working temperatures for the ATO nanotube arrays-based gas sensor.

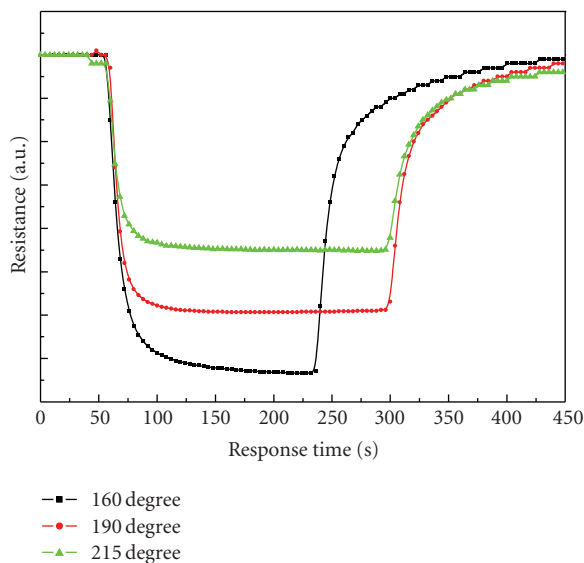


FIGURE 17: Response time for the ATO nanotube arrays-based gas sensor to H_2 (1%).

minutes and then rinsed in deionized water. No polishing process was adapted. The anodization was performed using a conventional two-electrode system. Silicon substrate with titanium film was attached to a silver rod that was used as the working electrode. A platinum sheet ($2 \times 1.5 \text{ cm}^2$) with a platinum wire was used as the counter-electrode. The distance between the working and counter-electrodes was kept at 3 cm. The anodization potential was applied using a potentiostat (Agilent E3645A) interfaced with a computer. The electrolyte was stirred using a magnetic flea during the anodization process.

5.1.3. Annealing. In order to investigate the crystallization, samples after anodization were annealed in a quartz tube furnace at different temperatures with the temperature ramp of $3^\circ\text{C}/\text{min}$. Either air or pure oxygen gas was used for annealing.

5.1.4. Characterization. The morphologies of microstructures were investigated using a field emission scanning electron microscope (SEM; JSM-6700F, JEOL Inc.). X-ray diffraction (XRD) analysis was performed using a Rigaku D/max 2550V diffractometer with $\text{Cu K}\alpha$ radiation at 45 kV and 100 mA. UV-Vis spectrum was obtained by a UV-Vis spectrometer (SHIMADZU-23101PC).

5.2. Results and Discussion

5.2.1. Nanoporous Anodic Titanium Film and Its Growth Model. Figure 1 shows the typical SEM image of nanoporous anodic titanium thin film after anodization. Anodization was performed on Ti film (300 nm) sputtered on a Si substrate in a 0.5 wt% aqueous HF electrolyte at 3 V. The temperature was kept at 3°C using an ice bath during the process to prevent the oxide formed from being dissolved in acidic solution. The porous surface shows connecting pores with the average diameter of 25 nm and interpore distance of 40 nm.

Figure 2 shows the typical current density transient recorded during anodization under a constant voltage when self-organized pores were obtained. The pore formation process in anodic titanium oxide is similar to that of PAA, which can be divided into four stages.

- (i) In the first stage, a compact oxide barrier layer is formed on the electrolyte-metal interface, which leads the current to decrease sharply due to the low conductivity of the metal oxide.
- (ii) In the second stage, some cracks and narrow slits appear on the surface due to field-enhanced dissolution of the oxide layer. Diffusion of the electrolyte into such cracks enhances the dissolution rate compared with other areas, which enlarges the cracks and connects the neighboring cracks. Meanwhile, this process enlarges the interface between electrolyte and oxide layer which decreases the resistance and increases the anodizing current. In this stage, initial tiny pores are nuclear in the cracks, and therefore such cracks are named as “easy path”.
- (iii) The current reaches a stable state in the third stage, which corresponds to the random formation of porous structure in the slits and cracks. These slits and cracks extend over the whole surface area. Such a process is a competition between the pore formation and dissolution of the oxide layer. The stable state of the current density transient indicates that the pore formation reaches equilibrium with the pore dissolution.
- (iv) In the fourth stage, when the dissolution rate is larger than the formation rate, the porous structure is consumed and current reduces.

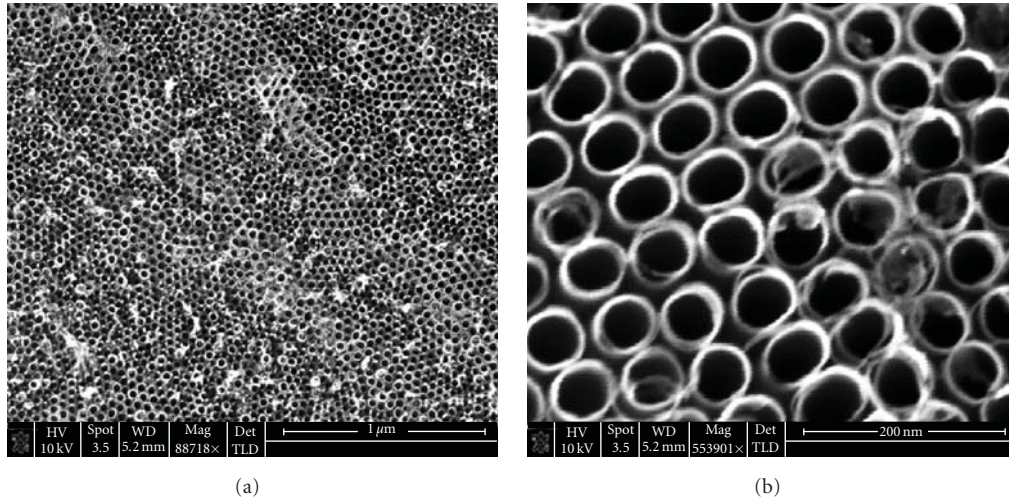


FIGURE 18: SEM images of the highly ordered ATO nanotubes for the gas sensor.

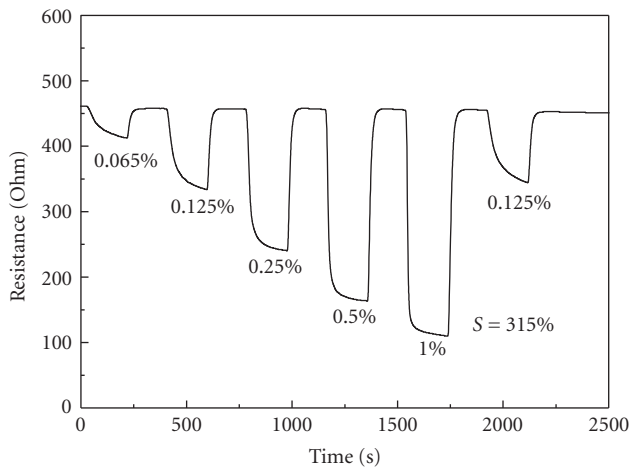


FIGURE 19: Dynamic response for the highly ordered ATO nanotube-based sensor to H₂.

5.2.2. Effect of Anodizing Conditions on the Morphologies

Anodizing Potential and Concentration of Electrolyte. We can assume that the formation of different surface structures is strongly correlated with the thickness of the compact oxide layer formed at the initial stage of the anodization process. There must be a threshold thickness above which the big corrosion pits form; when the thickness of the oxide layer is below the threshold, porous structure forms. According to the study of the anodic aluminum oxide nanoporous process, it is presumed that the compact titanium oxide layer formed at the initial of stage of the anodization process is in the range of 0.1–1 nm. The schematic diagrams of the formation processes for the two different structures are shown in Figures 3 and 4.

At a high anodizing potential, when the electric field is strong, a thick oxide layer forms due to large Ti ion dissolution and reprecipitation of hydroxide film. The oxide

layer is compact with a considerable thickness (Figure 3(a)). Such a thick compact oxide layer (referred to as a “barrier layer”) prevents the migration of OH[−] under the electric field from the electrolyte to the metal/oxide interface. At the same time, it prevents the migration of Ti⁴⁺ ions from the metal/oxide interface to the electrolyte. This barrier layer protects the metal thin film from being etched away. When anodization continues, the fluoride ions will attack the defect sites on the surface of the barrier layer which cause small notches (Figure 3(b)). Electrolytes pour into the notches and accelerate their growth until the metal/oxide interface is reached (Figure 4(c)). The exposure of metal substrate to electrolyte causes the current transient to increase due to the sudden departure of Ti⁴⁺ ions from the metal substrate to the electrolyte. Soon, the bottom of the pits is covered by an oxide layer (repassivated), and hence the current transient decreases (Figure 3(d)). In addition, localized breakdowns may occur at the bottom of the pits, and new notches can be generated; this is followed by repassivation (Figures 3(e) and 3(f)). That may explain the formation of corrosion pits and why it always occurs with the current oscillations. Because of the barrier layer, the anodization can last for a long time and, the current oscillation is kept undamped.

When porous structures are formed at a low potential, the barrier layer formed at the beginning of anodization is much thinner than that for a high potential (Figure 4(a)). Microslits appear on the surface of the oxide layer; this is followed by the growth of pores, as the electric field intensity at the pore bottom is much higher than that at the walls due to their different curvatures. Titanium is etched at a higher rate near the bottom, which allows the formation of pores in the direction normal to the surface. At the same time, owing to the remaining thin oxide layer, the OH[−] ions may migrate to the metal/oxide interface, followed by the formation of oxide. If the rates of oxide formation and dissolution at the bottom are equal, the thickness of the barrier layer is kept constant (Figures 4(b)–4(d)). The $j - t$ curve recorded in such a process (as shown in Figure 2) is quite smooth and

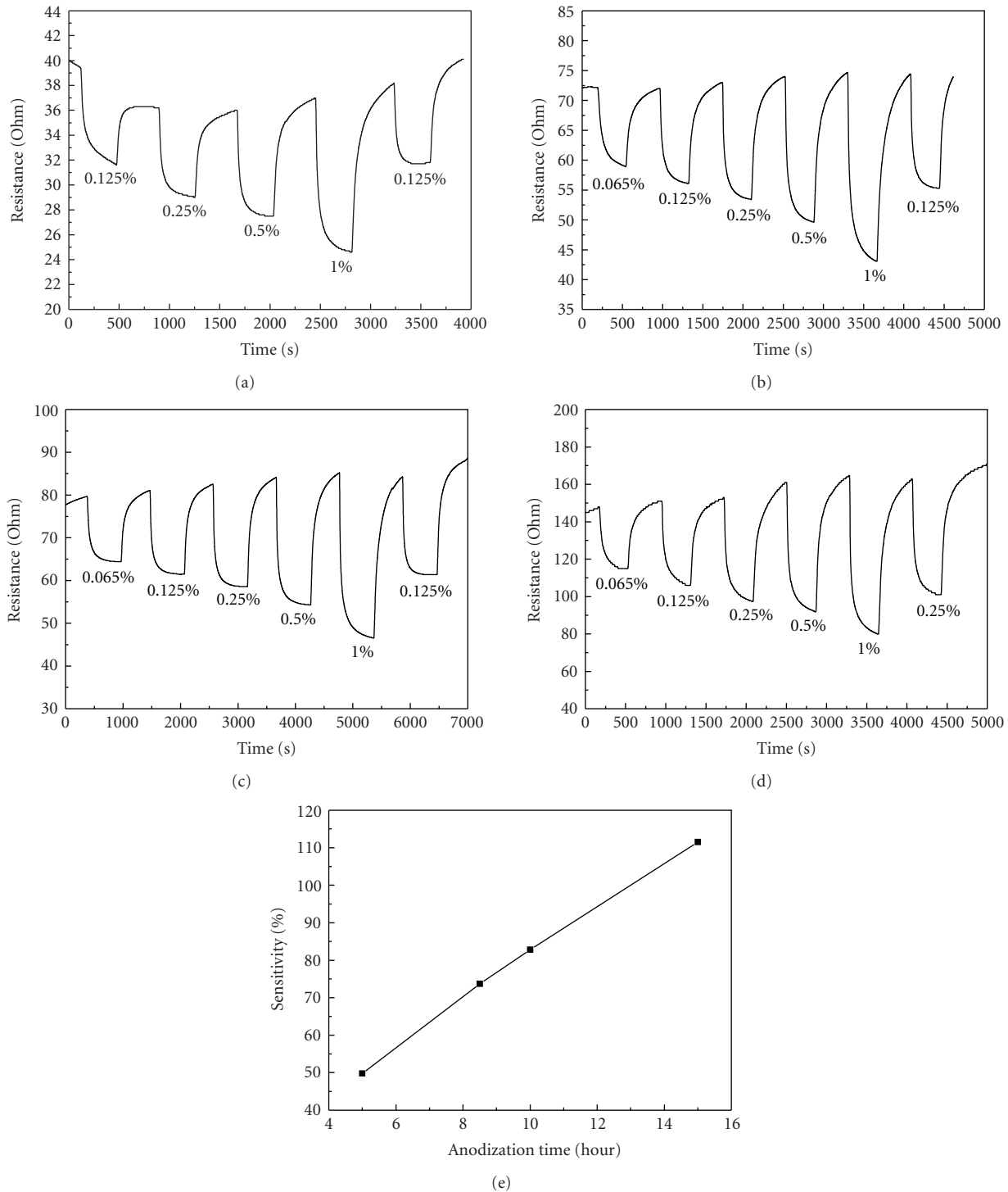


FIGURE 20: Dynamic response to H_2 of ATO nanotubes fabricated from different anodization time.

without oscillations which can be due to nondirect exposure of the metal substrate to the electrolyte.

The Film Smoothness. In the previous reports, acidic electrolytes were mainly utilized to obtain nanopores/nanotubes in the Ti thin films [72, 84–86] while the neutral electrolyte was widely used for the anodization of Ti foils [57–60]. This

phenomenon is ascribed to be due to the differences of initial surface morphologies. A schematic diagram is presented in Figure 5, which explains the influence of the electric-field on the formation of the nanopores onto smooth and granular surfaces. When the potential is applied to a smooth surface, homogeneous distribution of the electric field was formed between the two electrodes (working and counter

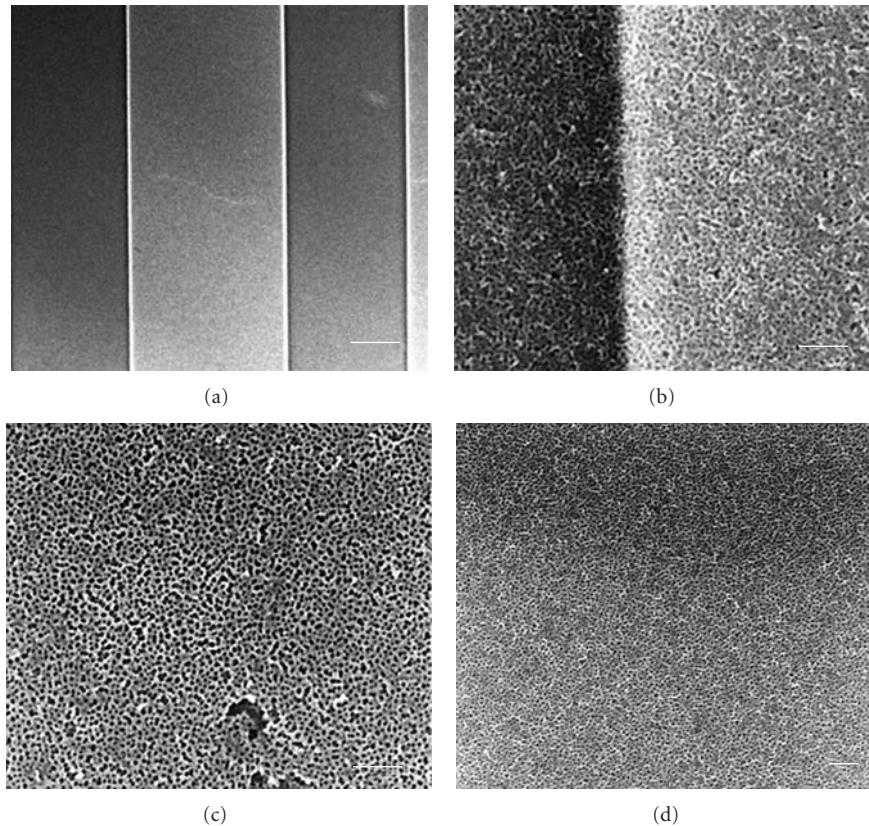


FIGURE 21: SEM image of nanoporous TiO_2 thin film on LiNbO_3 substrate. (a) SAW device, (b) the interface between Au electrode and LiNbO_3 substrate, (c) nanoporous thin film on LiNbO_3 substrate and, (d) nanoporous thin film on Au electrode.

electrode). Thereby, nanopores form homogeneously on the whole surface induced by the electric field. In the case of the granular surface, however, because of the large curvatures in the boundary of the connected grains, the electric field distribution is far from homogeneous which results in preferential nanopore growths in these parts, and randomly distributed nanopores are formed eventually.

Thereby the formation of uniform nanostructures always corresponds to the smoothness of the initial surface morphology. It is well known that in order to obtain highly ordered AAO nanoporous structures, a pretreatment by electropolishing process in an acidic electrolyte is required, which helps to reduce the time (named as “initial time”) cost for pore ordering in later anodization process. For titanium anodization, however, no effective prepolishing method has ever been used, neither mechanical nor electrochemical.

Figure 6 shows SEM images of the surface morphologies of Ti film deposited by RF sputtering before and after anodization in a neutral electrolyte (0.5 wt% NH_4F in EG solution). As can be seen in Figure 6(a), the film consists of randomly distributed grains. During the anodization process, this level of roughness generates inhomogeneous electric field distributions on the surface. As what we have discussed, pores are often quickly formed on surface sites with small radius of curvature, where a high electric field density occurs (i.e., between grains). As can be seen in

Figure 6(b) the morphology of the anodized surface is highly inhomogeneous.

In order to achieve a highly smooth Ti films, we used the Filtered Cathodic Vacuum Arc (FCVA) deposition technique. The SEM inspection of the FCVA-deposited Ti films revealed extremely low defect density and roughness. AFM was also used to confirm the low surface roughness of these Ti films prior to anodization. The RMS of the film with a thickness of 300 nm was found to be less than 0.5 nm over a $500 \times 500 \text{ nm}^2$ surface area.

The anodization was firstly performed on the Ti thin films prepared by FCVA on quartz substrates in a neutral aqueous electrolyte containing 0.5 wt% NH_4F and 1 M $(\text{NH}_4)_2\text{SO}_4$. This anodization process was initially performed at 3°C , as previous work showed that homogeneous nanopores were obtained at low temperatures [84, 86]. Figure 8(a) shows an SEM image of the sample after anodization at 3 V. The anodization was carried out in two steps. In the initial step a less ordered structure was formed. While with the continuation of the anodization process this layer dissolved, and a nanoporous structure was formed. However, the initial layer still covered most of the surface. Apparently, the neutral electrolyte and the low temperature caused a low dissolution rate in this process. In order to obtain a smooth surface a higher temperature anodization process was used. At roomtemperature (20°C) the anodization was performed

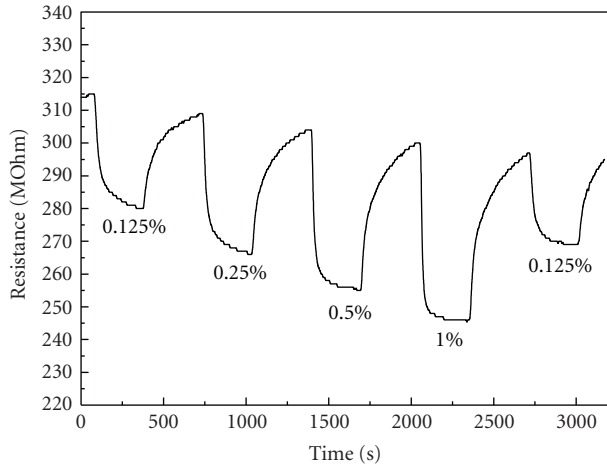


FIGURE 22: Dynamic response to H_2 of ATO nanoporous thin film-based gas sensors.

in the same electrolyte at 3 V, and the SEM image is shown in Figure 8(b). Ordered nanopores with a diameter in the range of 15–20 nm were clearly observed in the SEM image. Although anodized at room temperature, relatively thin Ti layers (<300 nm thickness) can be used as starting layers in this process as it produces regular pores without an extended activation etch.

Further anodization trials were conducted on Ti thin films deposited on quartz substrates by FCVA using 0.5 wt% NH_4F in ethylene glycol at room temperature (20°C). The SEM images of anodization performed at different potentials are shown in Figure 9. The sample shown in Figure 9(a) was anodized at 2 V for 1 hour resulting in the development of nanopores with diameters ranging from 5 nm to 8 nm. At 10 V, larger pores with diameters of approximately 12 nm–15 nm were obtained as shown in Figure 9(b). When anodization was performed at a potential of 20 V, the pores diameters were in the range from 15 nm to 20 nm (Figure 9(c)). It appears that at higher potentials the walls between pores are dissolved in many sites. These results reveal that the anodization on the FCVA-deposited Ti thin film can be performed in a potential range from 2 V to 15 V by using a neutral electrolyte at room temperature to obtain various pore diameters.

5.2.3. Transparent Conductive Substrates. Figure 10 shows a typical I - V curve recorded during the anodization process of titanium thin film on ITO glass. It can be seen that at the initial state, due to the formation of barrier layer and nucleation of nanopores, the anodic current experiences a decreasing process first, and then, followed by is increasing. When the pores grow steadily, anodic current keeps at a stable state. During this period, the nanopores reach the metal/ITO interface; because of the assumption of titanium metals, the anodic current grows to a minimum value again. However, after the exposure of ITO layer to the electrolyte, due to its dissolution, the current increases one more time until all the ITO is dissolved, and the current goes to zero.

Thereby in order to guarantee the growth of nanopores without damaging the ITO layer, current monitoring is very important to stop the anodization when there is a second current increasing which indicates the dissolution of ITO layer.

Figure 11 shows the SEM images of ITO-based titanium thin film after anodization. The titanium film with a thickness of 300 nm was sputtered on ITO glass substrate. The anodization was performed in 0.5 wt% HF + 1 M H_2SO_4 electrolyte at 5 V in an ice water bath ($\sim 3^\circ C$). As discussed above, the anodization was ceased when the 2nd current increasing is seen. The anodic film presents a nanoporous structure with an average pore diameter of 20 nm. It is also observed that the neighboring pores are not connected with each other which are ascribed to the dissolution due to the low pH value and high anodization potential.

Annealing at 400°C in O_2 for 3 hours proves not only improving the crystallization of the anodic thin film (from amorphous to anatase) but also increasing its transparency from less than 30% to 75% as well, as shown in Figure 12. The change of transparency also reflects the change of crystallization, and its high transparency provides the potential applications in the optoelectronic devices.

6. Gas Sensing of Anodic Titanium Thin Films

6.1. Fabrication and Characterization of Gas Sensors. Two types of gas sensors were assembled. One was based on nanotubular titanium oxide anodized from titanium metal/foil, and the other was nanoporous titanium oxide thin film on $LiNbO_3$ substrate with Au electrodes.

The structure of the first type of sensor is shown in Figure 13(a), which uses nanotubular titanium oxide as the main part with effective area of 3.14 cm² (sphere shape with diameter of 1 cm). Two parallel Pt lines with a width and a length of 1 mm, 7 mm, respectively, were sputtered as the electrodes. The thickness of each electrode is 100 nm. The distance of the two electrodes is kept as 4 mm.

The second type of sensor is shown in Figure 13(b). It is based on a 64° YX $LiNbO_3$ substrate with 160 gold finger-pair electrodes. The periodicity and aperture width of the Au finger-pair are 40 μm and 700 μm , respectively. The titanium thin film was sputtered on the substrate followed by anodization.

For the dynamic response characterization of the first type of sensors, the resistance was measured by KEITHLEY 2001 multimeter, while for the second type of sensors, the frequency of surface acoustic wave (SAW) was recorded. In each testing cycle, the test chamber was filled by synthetic air first followed by filling of test gas with a given concentration through a multiflow controller and lasted for a desiring period. Finally, synthetic air was used to fill the chamber again.

6.2. Gas Sensing Properties of Anodic Nanotube TiO_2 . Figure 14 shows the morphology of the titanium oxide nanotube arrays used as the first type of sensor. The anodization was performed in 0.5 wt% NH_4F -contained EG

electrolyte at 20 V for 12 hours followed by annealing in O₂ at 500°C for 6 hours. It is observed that a highly ordered nanotube arrays with average tube diameter of 50~70 nm were obtained after a “multistep” anodization process. The length of nanotubes is around 2~5 μm, that gives a high aspect ratio which is of significant importance in gas sensing applications.

Dynamic response of this type of sensor to H₂ with different concentrations is performed at 90, 160, 190, and 215°C (Figure 15). As an n-type semiconductor, when exposed in a reducing gas, the resistance of titanium oxide decreased. Therefore, the sensitivity of the sensor is defined as $S = (G_{\text{gas}} - G_{\text{air}})/G_{\text{air}}$, that is $S = (R_{\text{air}} - R_{\text{gas}})/R_{\text{gas}} \cdot G_{\text{air}}$, G_{gas} represents the conductivity of titanium oxide nanotubes in the testing gas atmosphere. At lower temperature (90°C), unstable response is observed as shown in Figure 15(a). With the increasing of working temperature, more stable response is obtained with good repeatability (Figures 15(b), 15(c) and 15(d)). The relation between the sensitivity and working temperature is shown in Figure 16, from which we can observe that the sensitivity increases with the increasing of H₂ concentration regardless of the working temperature. However, such curve shows a sensitivity maximum with the increasing of working temperature and decreasing again. In our experiment, the optimal operating temperature of the sensor is at 190°C.

Figure 17 shows the quick response time for the titanium oxide nanotube-based sensor. It is observed that for either response time or recovery time, less than 10 seconds is required to reach 50% resistance change. Taken into consideration of the tube wall thickness (7~15 nm), the intercalation and deintercalation of H₂ into the nanotubes are far much easier than in the thin films, which prolong the response and discovery times. Hence, the advantage of nanotubes for gas sensing is prominent.

Multistep anodization was performed to fabricate highly ordered TiO₂ nanotubes as shown in Figure 18. In this process, anodization was performed at a given condition followed by the removal of formed nanotubular structure in diluted HF solution and, then the sample was anodized again at the exactly same condition. The whole cycle was repeated one or two times until a much more ordered structure was obtained. H₂ sensor based on it was assembled and tested. The dynamic response is shown in Figure 19. We are pleased to find that when the sensor is working at 90°C, it presents extreme excellent stability compared with the previous normal nanotube-based sensor. Furthermore, the sensitivity (to 1.0% H₂) is as high as 315% while the sensitivity for the previous is only 11%. We ascribed such a high stability and sensitivity to the highly ordered nanostructure which enlarges the aspect ratio.

The change of sensitivity also occurs with the length of nanotubes, which can be manipulated by the anodizing time. Anodization was performed in same 0.5 wt% NH₄F electrolyte at 20 V for different anodization time, 5, 8.5, 10, and 15 hours, respectively. Dynamic responses to H₂ for nanotube-based sensors with different tube lengths are shown in Figures 20(a)–20(d), and the relation between sensitivity and anodizing time is shown in Figure 20(e). It

can be seen that with the increasing of tube length, the base resistance increases, 37, 74, 82.4, and 156 Ω, respectively. The sensitivity also increases linearly with the anodizing time. Thereby it is ascribed to the increasing length of nanotubes which enlarges the aspect ratio (surface to volume area).

6.3. Nanoporous TiO₂ Thin Film-Based Gas Sensors.

Figure 21 shows the morphologies of Ti thin film sputtered on LiNbO₃ substrate (with Au electrodes) after anodization. The anodization was performed in 0.5% (NH₄)F-contained EG electrolyte at 5 V. It can be observed that nanopores distribute homogeneously on the whole device surface, as shown in Figure 21(a). On the Au/ LiNbO₃ interface, because of the geometric step, the distribution of nanopores is less ordered, while on either LiNbO₃ substrate or Au electrode the distribution of nanopores is much better (Figures 21(c) and 21(d)). Before being used in gas sensors, the nanoporous thin film on substrate was annealed in O₂ at 400°C for 3 hours. The dynamic response of this type of sensor is shown in Figure 22, which presents a good sensitivity and stability.

7. Summaries

It was shown that due to their ordered and controllable structures, nanoporous/nanotubes semiconducting titanium oxide materials have great potential applications in various fields such as electronics, photoelectric conversion, photocatalysts and, low dimensional titanate-based perovskite ferroelectric materials and nanodevices.

In view of the above-mentioned aspects, we may come to the conclusion that the anodization technique is very effective and unique in fabricating nanostructural titanium. The anodization has been extended to the other metals such as W [87–91], Nb [92–95], Zr [96–99], Hf [100, 101], and Ni [102] and attracts more and more interests on fundamental studies and their various applications.

Generally speaking, as a newly developed method, there still remain lots of problems to be solved for the anodization of titanium. The growth mechanism of nanotubular TiO₂, for instance, has been mostly derived from the anodization of aluminum oxide which cannot be completely acceptable. If the semiconducting property of titanium oxide is taken into consideration, in contrast to the insulating aluminum oxide, the chances are that the growth mechanism needs to be modified. Furthermore, just as the development of AAO, now that the morphology of anodic titanium has been further controlled, more efforts should be exerted to find practical applications. As a semiconductor material, titanium oxide has already attracted lots of interests. Due to the unique advantages provided by nanostructures, anodic titanium will further find its applications in more newly developed functional devices [84–86, 103–105]. In order to meet the increasing requirements for the potential applications, the anodization technique needs to be optimized. For instance, when anodization is performed on a titanium sheet, the metal substrate remained has the short-circuit problem which limits its applications in the electrical devices, while the opacity limits the applications in optical devices. As

a result, the fabrication of nanostructural thin films based on different substrates (Si, glass and organic flexible ones) becomes significantly important.

In this paper, we reviewed the fabrication of titanium oxide nanotube arrays, nanoporous thin films as well as their growth model and applications. Our research results showed that highly ordered titanium oxide nanotube arrays-based gas sensor has excellent response to H₂. By using “multistep anodization process”, highly ordered nanotube arrays were obtained, and gas sensors based on such nanostructure presented a fast and stable response even at a low operating temperature of 90°C. Meanwhile, such sensors show very high sensitivity and present good dynamic response. In this paper, response to H₂ was presented as a case study.

Acknowledgment

This work was supported by the National Natural Science Foundation of China (NSFC, no. 50703047), China-Australia Special Scientific Research Fund, and Samsung Advanced Institute of Technology (SAIT), Republic of Korea.

References

- [1] J. H. Wu, X. L. Wu, N. Tang, Y. F. Mei, and X. M. Bao, “Strong ultraviolet and violet photoluminescence from Si-based anodic porous alumina films,” *Applied Physics A*, vol. 72, no. 6, pp. 735–737, 2001.
- [2] T. Gao, G. Meng, Y. Tian, S. Sun, X. Liu, and L. Zhang, “Photoluminescence of ZnO nanoparticles loaded into porous anodic alumina hosts,” *Journal of Physics: Condensed Matter*, vol. 14, no. 47, pp. 12651–12656, 2002.
- [3] R. Kudrawiec, J. Misiewicz, L. Bryja, I. S. Molchan, and N. V. Gaponenko, “Photoluminescence investigation of porous anodic alumina with spin-on europium-containing titania sol-gel films,” *Journal of Alloys and Compounds*, vol. 341, no. 1–2, pp. 211–213, 2002.
- [4] R. Kudrawiec, A. Podhorodecki, N. Mirowska, et al., “Photoluminescence investigation of europium-doped alumina, titania and indium sol-gel-derived films in porous anodic alumina,” *Materials Science and Engineering B*, vol. 105, no. 1–3, pp. 53–56, 2003.
- [5] N. V. Gaponenko, I. S. Molchan, G. E. Thompson, et al., “Photoluminescence of Eu-doped titania xerogel spin-on deposited on porous anodic alumina,” *Sensors and Actuators A*, vol. 99, no. 1–2, pp. 71–73, 2002.
- [6] A. E. Gridnev and V. V. Chernyshev, “Periodic oscillations of luminescence intensity at the formation of anodic oxides on aluminum in oxalic acid,” *Russian Journal of Electrochemistry*, vol. 40, no. 8, pp. 872–873, 2004.
- [7] Y. Yamamoto, N. Baba, and S. Tajima, “Colored materials and photoluminescence centers in anodic film on aluminum,” *Nature*, vol. 289, pp. 572–574, 1981.
- [8] H. A. Lopez and P. M. Fauchet, “1.54 μm electroluminescence from erbium-doped porous silicon composites for photonic applications,” *Physica Status Solidi A*, vol. 182, no. 1, pp. 413–418, 2000.
- [9] Y. Zhao, D. Yang, C. Zhou, Q. Yang, and D. Que, “Photoluminescence properties of the composite of porous alumina and poly (2,5-dibutoxy-1,4 phenylenevinylene),” *Journal of Luminescence*, vol. 105, no. 1, pp. 57–60, 2003.
- [10] R. Jia, Y. Shen, H. Luo, X. Chen, Z. Hu, and D. Xue, “Photoluminescence properties of morin and lysozyme molecules absorbed on anodic porous alumina membrane,” *Applied Surface Science*, vol. 233, no. 1–4, pp. 343–351, 2004.
- [11] Y. Du, W. L. Cai, C. M. Mo, J. Chen, L. D. Zhang, and X. G. Zhu, “Preparation and photoluminescence of alumina membranes with ordered pore arrays,” *Applied Physics Letters*, vol. 74, no. 20, pp. 2951–2953, 1999.
- [12] Z. Ling, S. Chen, J. Wang, and Y. Li, “Fabrication and properties of anodic alumina humidity sensor with through-hole structure,” *Chinese Science Bulletin*, vol. 53, no. 2, pp. 183–187, 2008.
- [13] N. D. Hoa, N. Van Quy, Y. Cho, and D. Kim, “An ammonia gas sensor based on non-catalytically synthesized carbon nanotubes on an anodic aluminum oxide template,” *Sensors and Actuators B*, vol. 127, no. 2, pp. 447–454, 2007.
- [14] D. Ding, Z. Chen, S. Rajaputra, and V. Singh, “Hydrogen sensors based on aligned carbon nanotubes in an anodic aluminum oxide template with palladium as a top electrode,” *Sensors and Actuators B*, vol. 124, no. 1, pp. 12–17, 2007.
- [15] G. Gorokh, A. Mozalev, D. Solovei, V. Khatko, E. Llobet, and X. Correig, “Anodic formation of low-aspect-ratio porous alumina films for metal-oxide sensor application,” *Electrochimica Acta*, vol. 52, no. 4, pp. 1771–1780, 2006.
- [16] T. Mukherjee, S. K. Hazra, and S. Basu, “Porous titania thin films grown by anodic oxidation for hydrogen sensors,” *Materials and Manufacturing Processes*, vol. 21, no. 3, pp. 247–251, 2006.
- [17] N. Negishi, T. Iyoda, K. Hashimoto, and A. Fujishima, “Preparation of transparent TiO₂ thin-film photocatalyst and its photocatalytic activity,” *Chemistry Letters*, pp. 841–842, 1995.
- [18] C. Lieber, “Nanowire-based photovoltaics build small powerful solar cells,” *Advanced Materials & Processes*, vol. 166, p. 24, 2008.
- [19] Y. Gao, M. Nagai, T.-C. Chang, and J.-J. Shyue, “Solution-derived ZnO nanowire array film as photoelectrode in dye-sensitized solar cells,” *Crystal Growth and Design*, vol. 7, no. 12, pp. 2467–2471, 2007.
- [20] E. Enache-Pommer, J. E. Boercker, and E. S. Aydil, “Electron transport and recombination in polycrystalline TiO₂ nanowire dye-sensitized solar cells,” *Applied Physics Letters*, vol. 91, no. 12, Article ID 123116, 2007.
- [21] C.-H. Ku and J.-J. Wu, “Electron transport properties in ZnO nanowire array/nanoparticle composite dye-sensitized solar cells,” *Applied Physics Letters*, vol. 91, no. 9, Article ID 093117, 2007.
- [22] J.-J. Wu, G.-R. Chen, H.-H. Yang, C.-H. Ku, and J.-Y. Lai, “Effects of dye adsorption on the electron transport properties in ZnO-nanowire dye-sensitized solar cells,” *Applied Physics Letters*, vol. 90, no. 21, 2007.
- [23] U. Bach, D. Lupo, P. Comte, et al., “Solid-state dye-sensitized mesoporous TiO₂ solar cells with high photon-to-electron conversion efficiencies,” *Nature*, vol. 395, no. 6702, pp. 583–585, 1998.
- [24] P. Zhou, D. Xue, H. Luo, and X. Chen, “Fabrication, structure, and magnetic properties of highly ordered prussian blue nanowire arrays,” *Nano Letters*, vol. 2, no. 8, pp. 845–847, 2002.
- [25] S. Yang, H. Zhu, D. Yu, Z. Jin, S. Tang, and Y. Du, “Preparation and magnetic property of Fe nanowire array,” *Journal of Magnetism and Magnetic Materials*, vol. 222, no. 1–2, pp. 97–100, 2000.

- [26] D. H. Qin, L. Cao, Q. Y. Sun, Y. Huang, and H. L. Li, "Fine magnetic properties obtained in FeCo alloy nanowire arrays," *Chemical Physics Letters*, vol. 358, no. 5-6, pp. 484-488, 2002.
- [27] Y. W. Wang, L. D. Zhang, G. W. Meng, X. S. Peng, Y. X. Jin, and J. Zhang, "Fabrication of ordered ferromagnetic-nonmagnetic alloy nanowire arrays and their magnetic property dependence on annealing temperature," *Journal of Physical Chemistry B*, vol. 106, no. 10, pp. 2502-2507, 2002.
- [28] X. Y. Zhang, G. H. Wen, Y. F. Chan, R. K. Zheng, X. X. Zhang, and N. Wang, "Fabrication and magnetic properties of ultrathin Fe nanowire arrays," *Applied Physics Letters*, vol. 83, no. 16, pp. 3341-3343, 2003.
- [29] C. W. Wang, Y. Peng, S. L. Pan, H. L. Zhang, and H. L. Li, "Mossbauer spectrum studies of magnetic anisotropy of alpha-Fe nanowire arrays in alumina template," *Acta Sinica Sinica*, vol. 48, pp. 2146-2150, 1999.
- [30] X. Y. Yuan, G. S. Wu, T. Xie, Y. Lin, and L. D. Zhang, "Self-assembly synthesis and magnetic studies of Co-P alloy nanowire arrays," *Nanotechnology*, vol. 15, no. 1, pp. 59-61, 2004.
- [31] H. Gao, C. Mu, F. Wang, et al., "Field emission of large-area and graphitized carbon nanotube array on anodic aluminum oxide template," *Journal of Applied Physics*, vol. 93, no. 9, pp. 5602-5605, 2003.
- [32] S.-H. Jeong and K.-H. Lee, "Fabrication of the aligned and patterned carbon nanotube field emitters using the anodic aluminum oxide nano-template on a Si wafer," *Synthetic Metals*, vol. 139, no. 2, pp. 385-390, 2003.
- [33] N. I. Tatarenko and A. M. Mozalev, "Geometry and element composition of a nanoscale field emission array formed by self-organization in porous anodic aluminum oxide," *Solid-State Electronics*, vol. 45, no. 6, pp. 1009-1016, 2001.
- [34] W. J. Yu, Y. S. Cho, G. S. Choi, and D. Kim, "Patterned carbon nanotube field emitter using the regular array of an anodic aluminium oxide template," *Nanotechnology*, vol. 16, no. 5, pp. S291-S295, 2005.
- [35] P.-L. Chen, J.-K. Chang, C.-T. Kuo, and F.-M. Pan, "Field emission of carbon nanotubes on anodic aluminum oxide template with controlled tube density," *Applied Physics Letters*, vol. 86, no. 12, Article ID 123111, pp. 1-3, 2005.
- [36] D. W. Kang and J. S. Suh, "Fabrication temperature effect of the field emission from closed and open tip carbon nanotube arrays fabricated on anodic aluminum oxide films," *Journal of Applied Physics*, vol. 96, no. 9, pp. 5234-5238, 2004.
- [37] S.-H. Jeong and K.-H. Lee, "Field emission properties of low-density carbon nanotubes prepared on anodic aluminum-oxide template," *Journal of the Korean Physical Society*, vol. 45, no. 2, pp. L252-L255, 2004.
- [38] S. I. Cho, W. J. Kwon, S.-J. Choi, et al., "Nanotube-based ultrafast electrochromic display," *Advanced Materials*, vol. 17, no. 2, pp. 171-175, 2005.
- [39] P. Hoyer, "Formation of a titanium dioxide nanotube array," *Langmuir*, vol. 12, no. 6, pp. 1411-1413, 1996.
- [40] T. Kasuga, M. Hiramatsu, A. Hoson, T. Sekino, and K. Niihara, "Formation of titanium oxide nanotube," *Langmuir*, vol. 14, no. 12, pp. 3160-3163, 1998.
- [41] M. Zhang, Y. Bando, and K. Wada, "Sol-gel template preparation of TiO₂ nanotubes and nanorods," *Journal of Materials Science Letters*, vol. 20, no. 2, pp. 167-170, 2001.
- [42] V. Zwillling, M. Aucouturier, and E. Darque-Ceretti, "Anodic oxidation of titanium and TA6V alloy in chromic media. An electrochemical approach," *Electrochimica Acta*, vol. 45, no. 6, pp. 921-929, 1999.
- [43] V. Zwillling, E. Darque-Ceretti, A. Boutry-Forveille, D. David, M. Y. Perrin, and M. Aucouturier, "Structure and physico-chemistry of anodic oxide films on titanium and TA6V alloy," *Surface and Interface Analysis*, vol. 27, no. 7, pp. 629-637, 1999.
- [44] D. Gong, C. A. Grimes, O. K. Varghese, et al., "Titanium oxide nanotube arrays prepared by anodic oxidation," *Journal of Materials Research*, vol. 16, no. 12, pp. 3331-3334, 2001.
- [45] G. K. Mor, O. K. Varghese, M. Paulose, N. Mukherjee, and C. A. Grimes, "Fabrication of tapered, conical-shaped titania nanotubes," *Journal of Materials Research*, vol. 18, no. 11, pp. 2588-2593, 2003.
- [46] C. Ruan, M. Paulose, O. K. Varghese, G. K. Mor, and C. A. Grimes, "Fabrication of highly ordered TiO₂ nanotube arrays using an organic electrolyte," *Journal of Physical Chemistry B*, vol. 109, no. 33, pp. 15754-15759, 2005.
- [47] G. K. Mor, M. A. Carvalho, O. K. Varghese, M. V. Pishko, and C. A. Grimes, "A room-temperature TiO₂-nanotube hydrogen sensor able to self-clean photoactively from environmental contamination," *Journal of Materials Research*, vol. 19, no. 2, pp. 628-634, 2004.
- [48] G. K. Mor, O. K. Varghese, M. Paulose, and C. A. Grimes, "A self-cleaning, room-temperature titania-nanotube hydrogen gas sensor," *Sensor Letters*, vol. 1, pp. 42-46, 2003.
- [49] G. K. Mor, K. Shankar, M. Paulose, O. K. Varghese, and C. A. Grimes, "Enhanced photocleavage of water using titania nanotube arrays," *Nano Letters*, vol. 5, no. 1, pp. 191-195, 2005.
- [50] R. Beranek, H. Hildebrand, and P. Schmuki, "Self-organized porous titanium oxide prepared in H₂SO₄/HF electrolytes," *Electrochemical and Solid-State Letters*, vol. 6, no. 3, pp. B12-B14, 2003.
- [51] J. M. Macak, H. Tsuchiya, and P. Schmuki, "High-aspect-ratio TiO₂ nanotubes by anodization of titanium," *Angewandte Chemie International Edition*, vol. 44, no. 14, pp. 2100-2102, 2005.
- [52] J. M. Macak, K. Sirotna, and P. Schmuki, "Self-organized porous titanium oxide prepared in Na₂SO₄/NaF electrolytes," *Electrochimica Acta*, vol. 50, no. 18, pp. 3679-3684, 2005.
- [53] S. Bauer, S. Kleber, and P. Schmuki, "TiO₂ nanotubes: tailoring the geometry in H₃PO₄/HF electrolytes," *Electrochemistry Communications*, vol. 8, no. 8, pp. 1321-1325, 2006.
- [54] Q. Cai, M. Paulose, O. K. Varghese, and C. A. Grimes, "The effect of electrolyte composition on the fabrication of self-organized titanium oxide nanotube arrays by anodic oxidation," *Journal of Materials Research*, vol. 20, no. 1, pp. 230-236, 2005.
- [55] G. K. Mor, O. K. Varghese, M. Paulose, K. Shankar, and C. A. Grimes, "A review on highly ordered, vertically oriented TiO₂ nanotube arrays: fabrication, material properties, and solar energy applications," *Solar Energy Materials and Solar Cells*, vol. 90, no. 14, pp. 2011-2075, 2006.
- [56] J. M. Macak and P. Schmuki, "Anodic growth of self-organized anodic TiO₂ nanotubes in viscous electrolytes," *Electrochimica Acta*, vol. 52, no. 3, pp. 1258-1264, 2006.
- [57] J. M. Macak, H. Tsuchiya, L. Taveira, S. Aldabergerova, and P. Schmuki, "Smooth anodic TiO₂ nanotubes," *Angewandte Chemie International Edition*, vol. 44, no. 45, pp. 7463-7465, 2005.
- [58] L. V. Taveira, J. M. Macak, H. Tsuchiya, L. F. P. Dick, and P. Schmuki, "Initiation and growth of self-organized TiO₂ nanotubes anodically formed in NH₄F/(NH₄)₂SO₄ electrolytes," *Journal of the Electrochemical Society*, vol. 152, no. 10, pp. B405-B410, 2005.

- [59] C. Richter, Z. Wu, E. Panaitescu, R. J. Willey, and L. Menon, "Ultra-high-aspect-ratio titania nanotubes," *Advanced Materials*, vol. 19, no. 7, pp. 946–948, 2007.
- [60] H. Tsuchiya, J. M. Macak, L. Taveira, et al., "Self-organized TiO₂ nanotubes prepared in ammonium fluoride containing acetic acid electrolytes," *Electrochemistry Communications*, vol. 7, no. 6, pp. 576–580, 2005.
- [61] C. Ruan, M. Paulose, O. K. Varghese, and C. A. Grimes, "Enhanced photoelectrochemical-response in highly ordered TiO₂ nanotube-arrays anodized in boric acid containing electrolyte," *Solar Energy Materials and Solar Cells*, vol. 90, no. 9, pp. 1283–1295, 2006.
- [62] O. K. Varghese, D. Gong, M. Paulose, C. A. Grimes, and E. C. Dickey, "Crystallization and high-temperature structural stability of titanium oxide nanotube arrays," *Journal of Materials Research*, vol. 18, no. 1, pp. 156–165, 2003.
- [63] K.-N. P. Kumar, K. Keizer, A. J. Burggraaf, T. Okubo, and H. Nagamoto, "Textural evolution and phase transformation in titania membranes: II supported membranes," *Journal of Materials Chemistry*, vol. 3, no. 11, pp. 1151–1159, 1993.
- [64] O. K. Varghese, M. Paulose, K. Shankar, G. K. Mor, and C. A. Grimes, "Water-photolysis properties of micron-length highly-ordered titania nanotube-arrays," *Journal of Nanoscience and Nanotechnology*, vol. 5, no. 7, pp. 1158–1165, 2005.
- [65] O. K. Varghese and C. A. Grimes, "Appropriate strategies for determining the photoconversion efficiency of water photoelectrolysis cells: a review with examples using titania nanotube array photoanodes," *Solar Energy Materials and Solar Cells*, vol. 92, no. 4, pp. 374–384, 2008.
- [66] G. K. Mor, H. E. Prakasam, O. K. Varghese, K. Shankar, and C. A. Grimes, "Vertically oriented Ti-Fe-O nanotube array films: toward a useful material architecture for solar spectrum water photoelectrolysis," *Nano Letters*, vol. 7, no. 8, pp. 2356–2364, 2007.
- [67] K. Shankar, G. K. Mor, H. E. Prakasam, et al., "Highly-ordered TiO₂ nanotube arrays up to 220 μm in length: use in water photoelectrolysis and dye-sensitized solar cells," *Nanotechnology*, vol. 18, no. 6, Article ID 065707, 11 pages, 2007.
- [68] M. Paulose, G. K. Mor, O. K. Varghese, K. Shankar, and C. A. Grimes, "Visible light photoelectrochemical and water-photoelectrolysis properties of titania nanotube arrays," *Journal of Photochemistry and Photobiology A*, vol. 178, no. 1, pp. 8–15, 2006.
- [69] G. K. Mor, K. Shankar, M. Paulose, O. K. Varghese, and C. A. Grimes, "Use of highly-ordered TiO₂ nanotube arrays in dye-sensitized solar cells," *Nano Letters*, vol. 6, no. 2, pp. 215–218, 2006.
- [70] G. K. Mor, O. K. Varghese, M. Paulose, and C. A. Grimes, "Transparent highly ordered TiO₂ nanotube arrays via anodization of titanium thin films," *Advanced Functional Materials*, vol. 15, no. 8, pp. 1291–1296, 2005.
- [71] M. Paulose, K. Shankar, O. K. Varghese, G. K. Mor, B. Hardin, and C. A. Grimes, "Backside illuminated dye-sensitized solar cells based on titania nanotube array electrodes," *Nanotechnology*, vol. 17, no. 5, pp. 1446–1448, 2006.
- [72] G. K. Mor, O. K. Varghese, M. Paulose, K. G. Ong, and C. A. Grimes, "Fabrication of hydrogen sensors with transparent titanium oxide nanotube-array thin films as sensing elements," *Thin Solid Films*, vol. 496, no. 1, pp. 42–48, 2006.
- [73] M. Paulose, O. K. Varghese, G. K. Mor, C. A. Grimes, and K. G. Ong, "Unprecedented ultra-high hydrogen gas sensitivity in undoped titania nanotubes," *Nanotechnology*, vol. 17, no. 2, pp. 398–402, 2006.
- [74] O. K. Varghese, D. Gong, M. Paulose, K. G. Ong, E. C. Dickey, and C. A. Grimes, "Extreme changes in the electrical resistance of titania nanotubes with hydrogen exposure," *Advanced Materials*, vol. 15, no. 7-8, pp. 624–627, 2003.
- [75] O. K. Varghese, D. Gong, M. Paulose, K. G. Ong, and C. A. Grimes, "Hydrogen sensing using titania nanotubes," *Sensors and Actuators B*, vol. 93, no. 1–3, pp. 338–344, 2003.
- [76] Y. Shimizu, N. Kuwano, T. Hyodo, and M. Egashira, "High H₂ sensing performance of anodically oxidized TiO₂ film contacted with Pd," *Sensors and Actuators B*, vol. 83, no. 1–3, pp. 195–201, 2002.
- [77] A. Ghicov, H. Tsuchiya, R. Hahn, J. M. Macak, A. G. Munoz, and P. Schmuki, "TiO₂ nanotubes: H⁺ insertion and strong electrochromic effects," *Electrochemistry Communications*, vol. 8, no. 4, pp. 528–532, 2006.
- [78] B. Yang, M. Uchida, H.-M. Kim, X. Zhang, and T. Kokubo, "Preparation of bioactive titanium metal via anodic oxidation treatment," *Biomaterials*, vol. 25, no. 6, pp. 1003–1010, 2004.
- [79] H.-J. Oh, J.-H. Lee, Y. Jeong, Y.-J. Kim, and C.-S. Chi, "Microstructural characterization of biomedical titanium oxide film fabricated by electrochemical method," *Surface and Coatings Technology*, vol. 198, no. 1–3, pp. 247–252, 2005.
- [80] S.-Z. Chu, S. Inoue, K. Wada, S. Hishita, and K. Kumshira, "Self-organized nanoporous anodic titania films and ordered titania nanodots/nanorods on glass," *Advanced Functional Materials*, vol. 15, no. 8, pp. 1343–1349, 2005.
- [81] X. Yu, Y. Li, W. Ge, Q. Yang, N. Zhu, and K. Kalantar-Zadeh, "Formation of nanoporous titanium oxide films on silicon substrates using an anodization process," *Nanotechnology*, vol. 17, no. 3, pp. 808–814, 2006.
- [82] Y. D. Premchand, T. Djenizian, F. Vacandio, and P. Knauth, "Fabrication of self-organized TiO₂ nanotubes from columnar titanium thin films sputtered on semiconductor surfaces," *Electrochemistry Communications*, vol. 8, no. 12, pp. 1840–1844, 2006.
- [83] J. M. Macak, H. Tsuchiya, S. Berger, S. Bauer, S. Fujimoto, and P. Schmuki, "On wafer TiO₂ nanotube-layer formation by anodization of Ti-films on Si," *Chemical Physics Letters*, vol. 428, no. 4–6, pp. 421–425, 2006.
- [84] K. S. Raja, M. Misra, and K. Paramguru, "Formation of self-ordered nano-tubular structure of anodic oxide layer on titanium," *Electrochimica Acta*, vol. 51, no. 1, pp. 154–165, 2005.
- [85] R. P. Vitiello, J. M. Macak, A. Ghicov, H. Tsuchiya, L. F. P. Dick, and P. Schmuki, "N-doping of anodic TiO₂ nanotubes using heat treatment in ammonia," *Electrochemistry Communications*, vol. 8, no. 4, pp. 544–548, 2006.
- [86] A. Ghicov, J. M. Macak, H. Tsuchiya, et al., "Ion implantation and annealing for an efficient N-doping of TiO₂ nanotubes," *Nano Letters*, vol. 6, no. 5, pp. 1080–1082, 2006.
- [87] N. Mukherjee, M. Paulose, O. K. Varghese, G. K. Mor, and C. A. Grimes, "Fabrication of nanoporous tungsten oxide by galvanostatic anodization," *Journal of Materials Research*, vol. 18, no. 10, pp. 2296–2299, 2003.
- [88] H. Tsuchiya, J. M. Macak, I. Sieber, et al., "Self-organized porous WO₃ formed in NaF electrolytes," *Electrochemistry Communications*, vol. 7, no. 3, pp. 295–298, 2005.
- [89] S. Berger, H. Tsuchiya, A. Ghicov, and P. Schmuki, "High photocurrent conversion efficiency in self-organized porous

- WO₃,” *Applied Physics Letters*, vol. 88, no. 20, Article ID 203119, 2006.
- [90] J. Choi, Y.-B. Park, and A. Scherer, “Fabrication of a tungsten master stamp using self-ordered porous alumina,” *Nanotechnology*, vol. 16, no. 9, pp. 1655–1659, 2005.
- [91] N. R. de Tacconi, C. R. Chenthamarakshan, G. Yogeewaran, et al., “Nanoporous TiO₂ and WO₃ films by anodization of titanium and tungsten substrates: influence of process variables on morphology and photoelectrochemical response,” *Journal of Physical Chemistry B*, vol. 110, no. 50, pp. 25347–25355, 2006.
- [92] I. Sieber, H. Hildebrand, A. Friedrich, and P. Schmuki, “Formation of self-organized niobium porous oxide on niobium,” *Electrochemistry Communications*, vol. 7, no. 1, pp. 97–100, 2005.
- [93] J. Choi, J. H. Lim, S. C. Lee, J. H. Chang, K. J. Kim, and M. A. Cho, “Porous niobium oxide films prepared by anodization in HF/H₃PO₄,” *Electrochimica Acta*, vol. 51, no. 25, pp. 5502–5507, 2006.
- [94] J. Choi, J. H. Lim, J. Lee, and K. J. Kim, “Porous niobium oxide films prepared by anodization-annealing-anodization,” *Nanotechnology*, vol. 18, no. 5, Article ID 055603, 6 pages, 2007.
- [95] K. Kovacs, G. Kiss, M. Stenzel, and H. Zillgen, “Anodic oxidation of niobium sheets and porous bodies heat-treatment of the Nb/Nb-oxide system,” *Journal of the Electrochemical Society*, vol. 150, no. 8, pp. B361–B366, 2003.
- [96] H. Tsuchiya, J. M. Macak, I. Sieber, and P. Schmuki, “Self-organized high-aspect-ratio nanoporous zirconium oxides prepared by electrochemical anodization,” *Small*, vol. 1, no. 7, pp. 722–725, 2005.
- [97] H. Tsuchiya and P. Schmuki, “Thick self-organized porous zirconium oxide formed in H₂SO₄/NH₄F electrolytes,” *Electrochemistry Communications*, vol. 6, no. 11, pp. 1131–1134, 2004.
- [98] K. Yasuda and P. Schmuki, “Electrochemical formation of self-organized zirconium titanate nanotube multilayers,” *Electrochemistry Communications*, vol. 9, no. 4, pp. 615–619, 2007.
- [99] K. Yasuda and P. Schmuki, “Control of morphology and composition of self-organized zirconium titanate nanotubes formed in (NH₄)₂SO₄/NH₄F electrolytes,” *Electrochimica Acta*, vol. 52, no. 12, pp. 4053–4061, 2007.
- [100] H. Tsuchiya and P. Schmuki, “Self-organized high aspect ratio porous hafnium oxide prepared by electrochemical anodization,” *Electrochemistry Communications*, vol. 7, no. 1, pp. 49–52, 2005.
- [101] T. Shobha, C. S. N. Sarma, K. S. Sastry, and C. H. Anjaneyulu, “Anodization of hafnium in phosphate baths: radio tracer studies,” *Bulletin of Electrochemistry*, vol. 17, no. 11, pp. 519–522, 2001.
- [102] S.-Z. Chu, K. Wada, S. Inoue, S.-I. Todoroki, Y. K. Takahashi, and K. Hono, “Fabrication and characteristics of ordered Ni nanostructures on glass by anodization and direct current electrodeposition,” *Chemistry of Materials*, vol. 14, no. 11, pp. 4595–4602, 2002.
- [103] J. M. Macak, H. Tsuchiya, A. Ghicov, and P. Schmuki, “Dye-sensitized anodic TiO₂ nanotubes,” *Electrochemistry Communications*, vol. 7, no. 11, pp. 1133–1137, 2005.
- [104] W.-J. Lee, M. Alhoshan, and W. H. Smyrl, “Titanium dioxide nanotube arrays fabricated by anodizing processes,” *Journal of the Electrochemical Society*, vol. 153, no. 11, pp. B499–B505, 2006.
- [105] K. Zhu, N. R. Neale, A. Miedaner, and A. J. Frank, “Enhanced charge-collection efficiencies and light scattering in dye-sensitized solar cells using oriented TiO₂ nanotubes arrays,” *Nano Letters*, vol. 7, no. 1, pp. 69–74, 2007.

Review Article

Porphyrin-Based Nanostructures for Sensing Applications

Donato Monti,¹ Sara Nardis,¹ Manuela Stefanelli,¹ Roberto Paolesse,¹ Corrado Di Natale,² and Arnaldo D'Amico²

¹ Dipartimento di Scienze e Tecnologie Chimiche, Università di Roma "Tor Vergata", Via della Ricerca Scientifica, 00133 Roma, Italy

² Dipartimento di Ingegneria Elettronica, Università di Roma "Tor Vergata", Via del Politecnico, 00133 Roma, Italy

Correspondence should be addressed to Roberto Paolesse, roberto.paolesse@uniroma2.it

Received 14 February 2009; Revised 28 April 2009; Accepted 29 May 2009

Recommended by Yongxiang Li

The construction of nanosized supramolecular hosts via self-assembly of molecular components is a fascinating field of research. Such intriguing class of architectures, beside their intrinsic intellectual stimuli, is of importance in many fields of chemistry and technology, such as material chemistry, catalysis, and sensor applications. Within this wide scenario, tailored solid films of porphyrin derivatives are structures of great potential for, among others, chemical sensor applications. The formation of *supramolecules* relays on noncovalent interactions (electrostatic, hydrogen bond, π - π , or coordinative interactions) driven by the chemical information stored on the assembling molecules, such as shape and functional groups. This allows, for example, the formation of large well-defined porphyrin aggregates in solution that can be spontaneously transferred onto a solid surface, so achieving a solid system with tailored features. These films have been used, covering the bridge between nanostructures and microsystems, for the construction of solid-state sensors for volatiles and metal ion recognition and detection. Moreover, the variation of peripheral substituents of porphyrins, such as, for example, chiral appended functionalities, can result in the formation of porphyrin aggregates featuring high supramolecular chirality. This would allow the achievement of porphyrin layers characterised by different chiroptical and molecular recognition properties.

Copyright © 2009 Donato Monti et al. This is an open access article distributed under the Creative Commons Attribution License, which permits unrestricted use, distribution, and reproduction in any medium, provided the original work is properly cited.

1. Introduction

In the last few years the prefix nano- has been probably one of the most popular and widely used buzzwords, not only in the scientific community, but also to generally indicate systems whose components have dimensions in the nanometric scale. This general interest is due to the great expectation for the potential impact that the development of such miniaturized systems can have on fundamental topics, such as, for example, energy, environment, or security.

Despite this large popularity, the exact meaning of nanoscience and nanotechnology is not universally defined, as usual for a discipline not completely mature, anyhow the most general definition is related to the development and manipulation of structures (objects or devices) in the size range lower than 100 nm [1].

Even if this definition is not completely satisfying, one topic is for sure critical for nanotechnology: the miniaturization of the systems of interest is the necessary

requirement to improve the performances of the related devices. The dramatic development of electronic devices is in fact directly related to the size reduction of their components.

Miniaturization has been usually obtained by reducing the dimension of bigger components using techniques such as photolithography; this method is called "*top-down approach*" and, although well developed, it reaches its limit at the open door of the nanotechnology domain [2].

To overcome these limitations, the natural solution is represented by the opposite approach, which has been called "*bottom-up approach*;" the devices are build up from their fundamental building blocks, atoms or molecules, by their rational assembling.

Since the report of the preparation of carbon nanotubes [3], we have witnessed the preparation of a wide range of different nanostructured inorganic materials, obtained by the fine control of the growth conditions of such materials [4].

In the case of organic compounds, which are constituted by molecules, the preparation of nanostructures is far less developed; while the synthesis of molecular systems is a well-developed discipline, driven by the formation of stable chemical bonds, nanostructures should derive from multiple, weak, and noncovalent interactions of different nature, such as electrostatic and van der Waals forces or hydrophobic effects, π - π stacking interactions, metal coordination, and hydrogen bonding.

However, the ability to assemble molecular units in more complex architectures has taken advantage of the supramolecular chemistry development, the so-called chemistry beyond the molecule [5, 6]. Capitalizing the plurality of weak interaction pathways, molecules can self assemble giving different nanostructure motifs, such as tubes, rods, and sheets [7].

Among the huge number of molecular systems suitable for such an approach, porphyrins represent one of the most promising examples, for different reasons. Their planar aromatic macrocycle is optimal for π - π stacking interactions and it is a versatile platform for peripheral decoration with groups that can offer additional interaction motifs [8]. The synthetic chemistry of porphyrins is well developed and it is possible to choose among a wide substituent library to prepare the macrocycle of choice for the particular application [9, 10]. All these features will not be sufficient to justify an interest in porphyrins, if we do not consider the richness of properties these macrocycles are endowed with [11]. Photophysical and coordination features are just an example of the potentialities of such a macrocycle. Nature offers a magnificent example of porphyrin usefulness, whereas with this basic molecular framework Nature is able to activate and/or transport molecular oxygen in animals and convert sunlight in plant photosynthetic systems [12].

All these properties can be transferred in nanostructured materials based on porphyrin derivatives, for the application in different fields, ranging from catalysis to pharmacology.

2. Porphyrin-Based Nanostructures

In the last few years the exploration of porphyrins, metalloporphyrins, and their assemblies afforded a large number of nanomaterials featuring various electronic and structural characteristics, like rods, rings, particles, sheets, wires, and tubes. We summarize below few examples of porphyrin nanostructures reported in the literature.

2.1. Porphyrin Nanoparticles. A first class of porphyrin aggregates is represented by the preparation of porphyrin nanoparticles, that is, colloidal suspension of porphyrin aggregates having dimension in the order of hundreds of nm [13]. The size dimension of the particles strongly depend on the porphyrin structure and on the preparative protocols, where it is usually used as a surfactant to stabilize the suspension, avoiding the collapse of the nanoparticles in larger aggregates.

The interest in these systems depends on the potential applications in different fields, such as catalysts, or drug delivery. The aim is to develop architectures that can offer

a higher stability than monomer in solution, preserving or even increasing the activity of the starting molecular unit. The easiness of preparation and the possibility to modulate the size and properties of such nanoparticles represent the promising characteristics of these structures.

Drain et al., for example, exploited the formation of porphyrin nanoparticles by adding water to a solution of the porphyrin in an organic solvent, containing a few percent of a surfactant, such as low molecular weight poly-ethylenglycol [14]. The method works for a wide range of porphyrin structures; the presence of a surfactant is essential to assure the suspension stability, otherwise the porphyrin particles rapidly coagulate and precipitate from the solution. Following the same approach Sandanayaka et al. have characterized structural and photophysical properties of 5,10,15,20-tetrakis(4-carboxyphenyl)porphyrin (Figure 1(a)) nanoparticles obtained using ethylene glycol and the solvent mixture technique [15].

A different approach was pursued by Bangal and Perepogu who recently prepared pure nanoparticles of 5,10,15,20-tetraphenylporphyrin or 5,10,15,20-tetra(pentafluorophenyl)porphyrin (Figures 1(b)-1(c)), without the addition of surfactants as nanoparticle stabilizers [16]. In this case the approach is called "reprecipitation method" and it takes advantage of a careful choice of solvent mixtures, where the first one should act as good and the second as poor solvent to induce the nanoparticles formation.

2.2. Porphyrin Nanosheets. Wang et al. reported the preparation of porphyrin nanosheets by the reprecipitation method, injecting an ethanol solution of an SnPyTriPP complex (Figure 1(d)) into deionized water [17]. The formation of 2D aggregates are strongly dependent on the preparation method, because changing the water temperature led to completely different aggregates.

Following a different approach, large nanosheets have been prepared by Milic et al., by promoting dynamic aggregation in columnar stacks of square planar porphyrin nonamers, formed by TPyP units coordinated by PdCl₂ bridging group through the peripheral N-py atoms [18].

2.3. Porphyrin Nanorods and Nanorings. 5,10,15,20-tetrakis(4-sulfonatophenyl)porphyrin (Figure 1(e)) self-assembles in acidic aqueous solution into rods that can span over μ m lengths. These rods show an intriguing photoconductivity properties, with a rapid turn on/off rate [19, 20].

Nanorods are also obtained from the aggregation of 5,10,15,20-tetrakis(4-carboxyphenyl)porphyrin in acidic aqueous solutions [21]. In this case the structural motif of the aggregate strongly depends on the acid exploited for the aggregation; nanorods were obtained in HNO₃ solutions, while HCl induced the formation of nanorings. Porphyrin nanorings have been also obtained by evaporation of the solvent through a surface dewetting process [22].

Supramolecular nanorods of 5,15-diaryl-substituted porphyrins have been prepared by sonication method from an acetonitrile/toluene solution, which represents a poor/good solvent mixture [23].

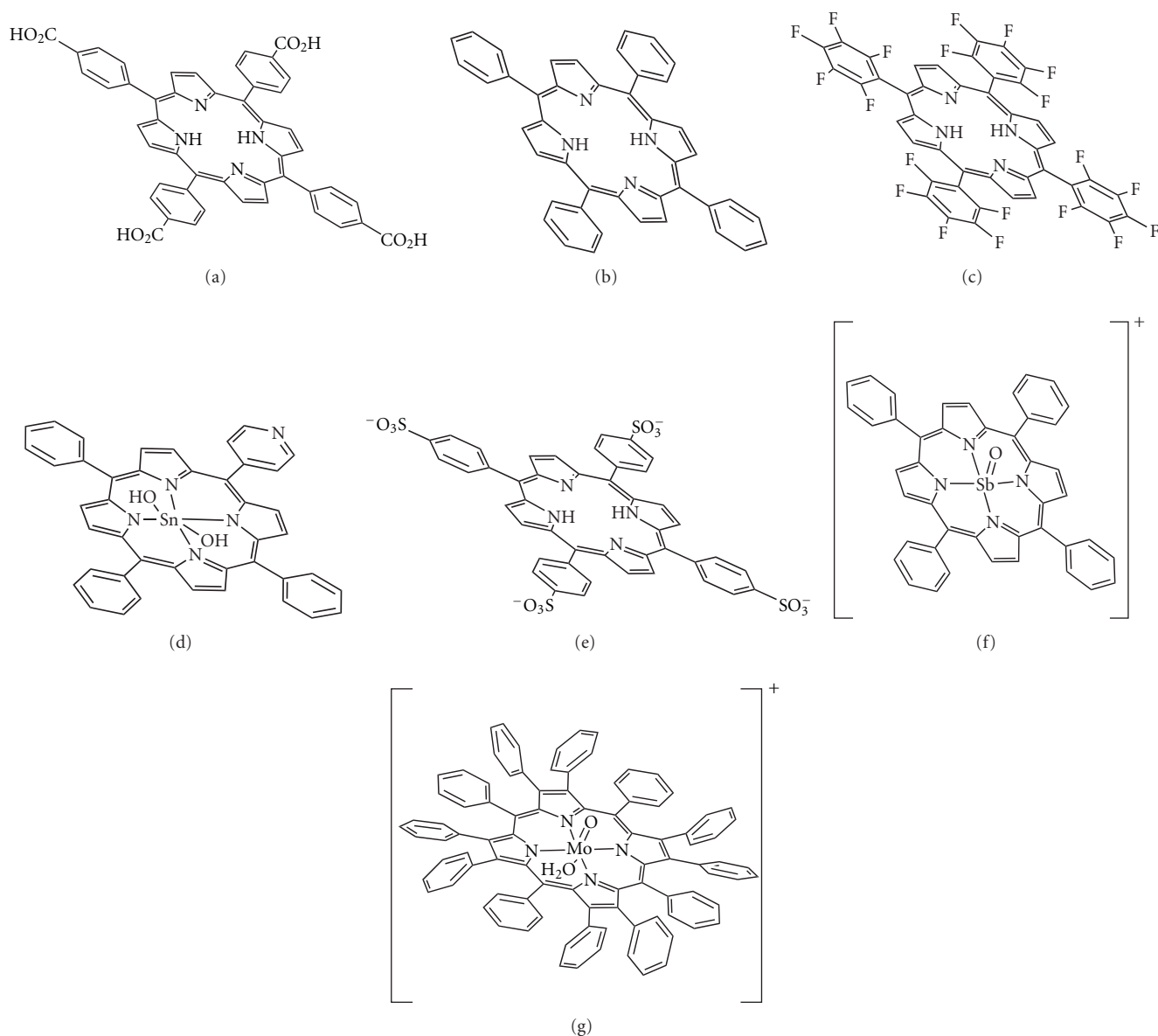


FIGURE 1: Molecular structures of (a) 5,10,15,20-tetrakis(4-carboxyphenyl)porphyrin; (b) 5,10,15,20-tetraphenylporphyrin; (c) 5,10,15,20-tetra(pentafluorophenyl)porphyrin; (d) 5-pyridyl-10,15,20-triphenylporphyrin Sn(IV) dihydroxide; (e) 5,10,15,20-tetrakis(4-sulfonatophenyl)porphyrin; (f) cationic 5,10,15,20-tetraphenylporphyrin oxoSb(V); (g) cationic dodecaphenylporphyrin oxoMo(V).

Fullerene-encapsulated hexagonal nanorods of 5,10,15,20-tetrakis(4-pyridyl)porphyrin Zn (ZnTPyP) have been prepared in DMF-acetonitrile solution with the aid of a surfactant and investigated to elucidate photoinduced electron transfer [24]. The nanostructure has a broad absorption spectrum, due to the supramolecular aggregation, and shows also a significant quenching of porphyrin fluorescence emission, in large part due to an efficient photoinduced electron transfer between ZnTPyP and fullerene. This behavior has been confirmed by comparison of the fluorescence of the empty ZnTPyP nanorods prepared without fullerene in the same conditions. Both the broad absorption spectrum and the presence of a photoinduced charge separation state [$C_{60}^{\bullet-}$ -ZnTPyP $^{\bullet+}$] give a significant enhancement of the

solar energy conversion, as demonstrated in a photoelectrochemical cell based on these nanorods as chromophores.

2.4. Porphyrin Nanowires. Dispersed nanowires can be obtained by assembly of amphiphilic Sn complex of porphyrin, whose lengths can be finely tuned using an amphiphilic polymer surfactant, Pluronic F127 [25]. The structural motif of the nanostructures ranges from nanowires to nanoplates by adjusting the synthetic protocol. The key factor is in this case the water solubility of the Sn porphyrin nanostructures; the growth of the amphiphilic aggregates makes these species more hydrophobic, with the consequent precipitation from the aqueous medium. The surfactant can increase the solubility interacting with

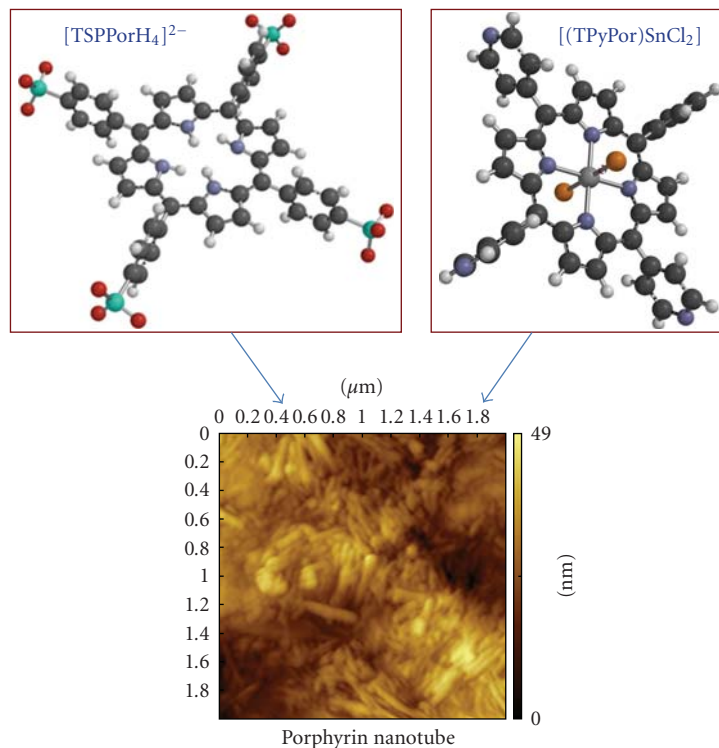


FIGURE 2: Molecular structures of the porphyrin moieties and AFM image of the deposited porphyrin nanotubes.

the growing aggregates, allowing the formation of larger nanostructures.

2.5. Porphyrin Nanotubes. Porphyrin nanotubes have been obtained by aggregation of oppositely charged porphyrin units as reported by Wang et al. [26]. The ionic self-assembly of two porphyrins bearing opposite ionic charge leads to the formation of J-aggregates, whose nonplanar shape induce the formation of nanotubular structures, reaching free floating aggregates having lengths of tens of nanometers.

Variation of the porphyrin structures may strongly influence the nanostructure obtained by ionic self-assembly. Nanofibers, for example, can be obtained in the assembling of an oxoantimony complex of tetraphenylporphyrin (Figure 1(f)) with tetrasulfonatophenylporphyrin [27].

Porphyrin nanotubes were also obtained by self-assembly of an Mo(V) complex of the dodecaphenylporphyrin, a fully substituted derivative having a saddle distorted macrocycle (Figure 1(g)) [28]. In this case the formation of the tubular structure takes advantage from the curved surface of the distorted porphyrin.

2.6. Miscellaneous of Porphyrin Aggregates. The first studies on the development of nanostructured porphyrin materials are related to the formation of the so-called “porphyrin sponges,” that is, nanoporous solids having cavities of molecular sizes [29]. These supramolecular networks were obtained by self-assembling driven by interactions of very weak nature and several molecules of solvates were necessary to stabilize the porphyrin assemblies. Robust

porphyrin-based organic zeolite analogs were prepared by self-assembling of TPyP metal complexes; these three-dimensional frameworks showed high thermal stability and a size-selective sorption mechanism towards guest species [30]. Following the same concept, H₂TCP macrocycle has also been used as building block for the preparation of porphyrin-based zeolite analogs. More robust frameworks were obtained from the self-assembling of resorcinol-substituted porphyrins; peripheral hydrogen bonds were exploited for the construction of supramolecular ordered solids, where the inner cavities can be exploited as selective molecular recognition sites. Kojima et al. studied the potentialities of bis- and tetraresorcinol substituted porphyrins as selective sensing layers using Quartz Crystal Microbalance technique [31].

Porphyrin nanochannels have been recently reported by Harada and Kojima [32], obtained by the self-assembly of the dodecaphenylporphyrin dihydrochloride salt during crystallization from CHCl₃/CH₃CN [33]. The saddle distortion of the macrocycle leads to the formation of porphyrin nanochannel where guest molecules can be included into the cavities. Porphyrin dication framework acts as electron deficient host where electron rich molecules, such as, for example, hydroquinone derivatives, are clathrate as guests.

We reported a facile and straightforward way to obtain porphyrin film with ordered morphology by spontaneous deposition of aggregates of amphiphilic tetraphenylporphyrin derivatives, possessing a cationic appended functionality [34]. The deposition of porphyrin aggregates is driven by hydrophobic effects, and, noteworthy, occurs spontaneously only in the case of the formation of ordered and

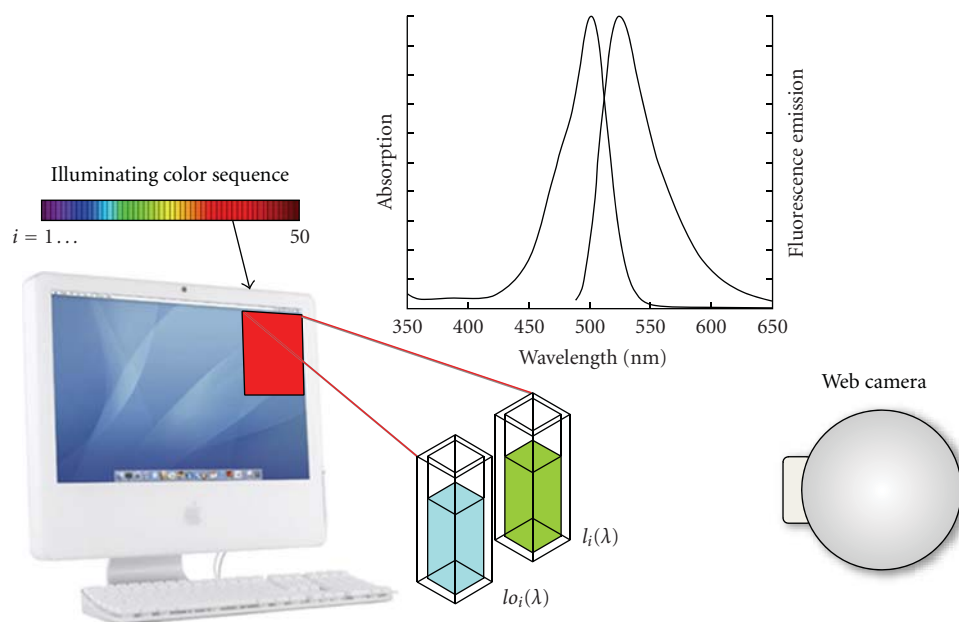


FIGURE 3: Sketch of the CSPT platform.

uniform aggregates. The occurrence of π -cation interaction should be taken into consideration for the achievement of these structures with ordered morphology. Deposition of the relative manganese or cobalt derivatives analogously occurs and the UV-visible spectral pattern of the films dramatically changes upon exposure to vapours of amines or olefins. The exploitation of these films for the construction of chemical sensors is reported in the following section.

3. Chemical Sensor Applications of Porphyrin Nanostructures

It is worth mentioning that while a great effort has been devoted to the preparation and characterization of porphyrin nanostructured materials, quite surprisingly only scant examples of practical applications have been reported focused in particular on catalysis or photovoltaic devices [7].

3.1. Porphyrin Nanotubes in CSPT Platform. Since chemical sensors could represent one of the most promising application fields for these porphyrin nanostructures, we have been interested in the exploitation of the porphyrin nanotubes, prepared by Wang's method [26], as sensing materials [35] (Figure 2). This geometrical motif is particularly appealing for sensor applications, because it can potentially show a dramatic increase in sensitivity/selectivity performances to respect the individual subunits. For example, the presence of the inner cavity can give rise to selective endohedral inclusion of different guests, or the interaction with analytes can alter the supramolecular arrangement of the molecular nanostructure; both these interaction pathways, alter the porphyrin J-aggregate optical properties.

Optical transduction is for this reason the mechanism of choice for such a nanostructure. The interaction mechanism

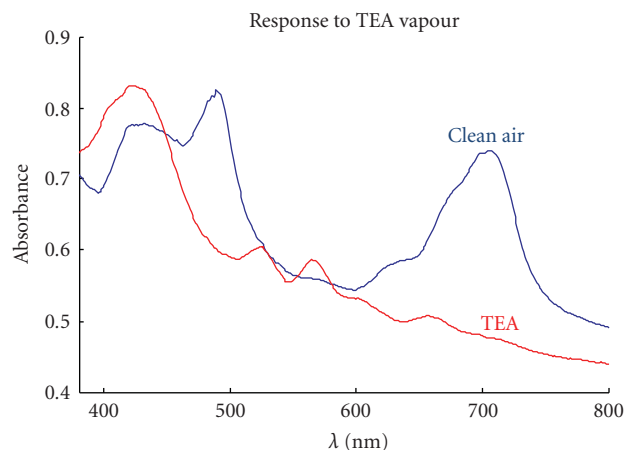


FIGURE 4: Nanotube optical spectra before and after the addition of 10^{-3} mol/L of triethylamine in solution.

of porphyrin nanotubes with analytes in aqueous solutions has been firstly investigated; subsequently, the development of solid state chemical sensors through their deposition in thin films has been attempted.

As sensing platform we decided to use the Computer Screen Photoassisted Technology (CPST); based on the combination of a computer screen, programmed to display millions of color combining wavelengths in the optical range, and a digital camera, decomposing the light into three broad channels, this technique is able to perform a spectroscopy measurement allowing a simultaneous evaluation of absorbance and fluorescence of samples (Figure 3) [36–38].

We first studied the modification of absorption spectra induced by the addition of different salts to solutions of both precursor porphyrins and formed nanotubes. We noted that

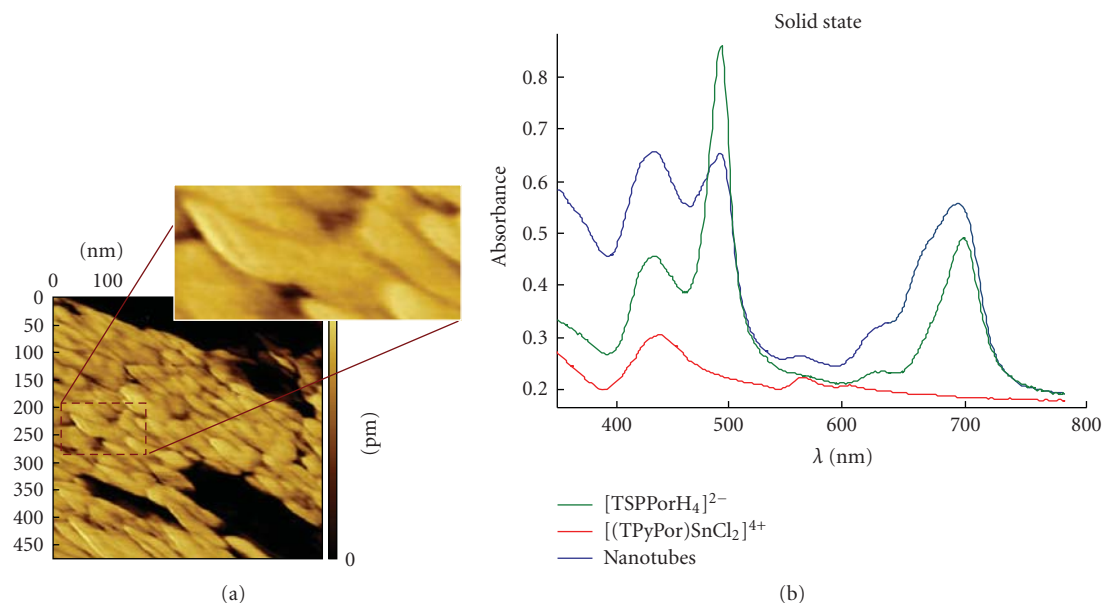


FIGURE 5: (a) AFM phase contrast image of a nanotube layer. In the inset a close-up view of a single structure is visible; (b) optical spectra of the porphyrin moieties and porphyrin nanotube in the solid state.

porphyrin nanotubes could offer additional features for ions detection, which cannot be possible in the case of isolated porphyrin moieties.

With these encouraging results, we have then studied the variations induced by the addition of organic compounds dissolved in solution, such as triethylamine (Figure 4), where it should be noted that other interaction mechanisms, such as acid-base or even coordination for the SnTPyPCL_2 moiety could be involved. Also in this case the porphyrin nanostructure was more sensitive than the subunits to the analyte addition.

This behavior prompted us to explore the possibility to utilize the chemical sensitivity of porphyrin nanotubes to detect compounds in gaseous phase. The subsequent step was devoted to the deposition of porphyrin nanotubes as solid layers to be used in the CSPT optical sensing platform. This is a critical step, because the forces involved are low energy interactions and consequently the resulting nanostructures are not rigid and they can be easily deformed when transferred in the solid film. Atomic force microscopy image of a layer of nanotubes directly deposited from the aqueous solution suggested the retention of the tubular structures, although their flattening cannot be excluded (Figure 5).

The direct deposition of nanotubes resulted in a film characterized by an excessive optical density that was not adequate to be measured with the CSPT. In order to overcome this problem nanotubes were dispersed in a polymeric matrix compatible with the formation process of the nanostructures. Polydimethylsiloxane (PDMS) was found compatible and the embedding of nanostructures inside the polymer took place as evidenced by optical spectra. Also in this case we cannot exclude a flattening of the porphyrin nanotubes into the polymeric matrix, but the retention of

the aggregate features in the resulting optical spectra allowed anyway their exploitation for sensing purpose. In order to study the sensing properties of nanotubes-polymer mixture PDMS was also requested not to interfere with the sensing process; as a matter of fact the chosen polymeric matrix showed a good permeability to the investigated compounds.

The response of sensing layer upon exposure of volatiles was measured by the differential absorbance, obtained subtracting the absorbance measured in pure nitrogen atmosphere as background.

As shown from CSPT signature, the sensing mechanism of the porphyrin nanotubes probably does not involve the inner cavity, with the analytes inducing a modulation of the interaction between porphyrins keeping the nanostructure in shape; nonetheless the differences between the changes of CSPT absorbance in presence of model volatiles suggest that a manifold of interactions is likely to take place (Figure 6).

The exploitation of the porphyrin aggregates is not limited to gases or volatiles detection, but these nanostructured assemblies can also be used in the solution.

3.2. Amphiphilic Porphyrin Aggregates. We have been involved in the development of chemical sensor based on amphiphilic porphyrin aggregates. We observed spontaneous deposition from an aqueous solution ($\text{H}_2\text{O}/\text{EtOH}$ 9 : 1; ν : ν) of the amphiphilic porphyrin derivative reported in Figure 7 on silanised glass surfaces; the solid film, resulting from a controlled J-type aggregation fashion, presents, beside a good mechanical stability, an appreciable fluorescence emission [39].

This property can be a crucial feature in the sensing of heavy and transition metal ions that typically quench the luminescence, often via deactivation to the triplet state by heavy metal atom effect. On the basis of these

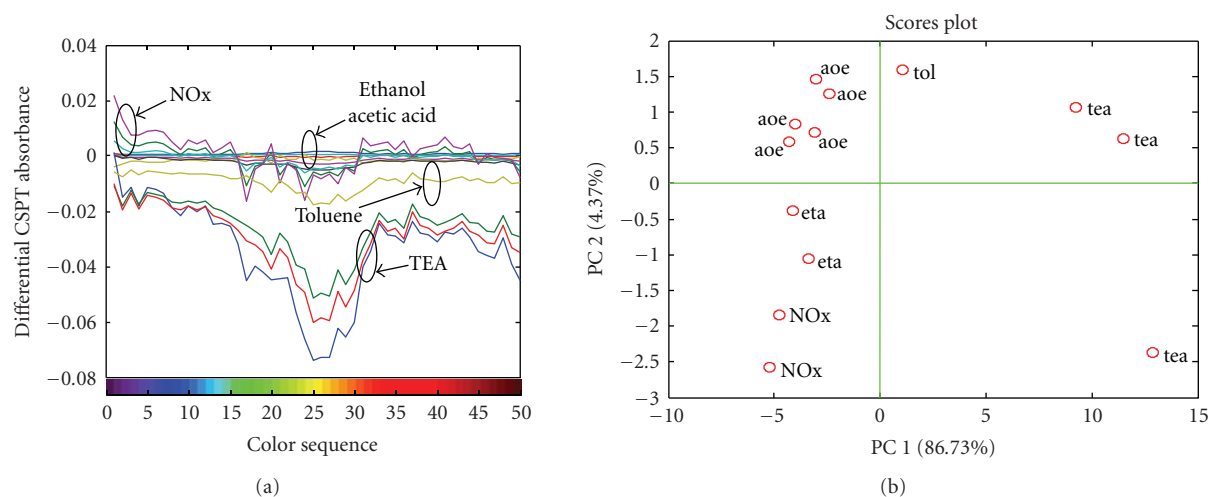


FIGURE 6: (a) Differential CSPT absorbances measured exposing the nanotube layers to the different vapors and gases. (b) Plot of the first two principal components calculated from the fingerprints shown in (a). Label data points indicate the compounds: tea: triethylamine, NOx, eta: ethanol, ace: acetic acid, and tol: toluene.

interesting results we investigated the potentialities of these simple systems for the construction of an efficient and specific luminescent solid-state chemosensor for the selective detection of Hg^{2+} ions in water.

We observed that the porphyrin emission was strongly quenched by simply dipping the porphyrin layered glass slides into diluted solutions of heavy metal salts, as reported in Figure 8: the efficient quenching of fluorescence emission of layered porphyrins by simple immersion into a solution of Hg^{2+} 1.0×10^{-5} M (Figure 8, trace d) is highlighted. Moreover the initial intensity could be restored, without loss of efficiency, washing the glass slides with a solution of *N,N,N',N'*-tetrakis(2-pyridilmethyl) ethylenediamine (TPEN).

A consistent quenching was also observed in the case of Hg^{2+} activity, as low as $1 \mu\text{M}$ concentration, pointing out the appreciable sensitivity of the investigated system. The concomitant examination of the UV-vis spectral pattern changes revealed the occurrence of a bathochromic shift of the porphyrin chromophores upon metal ion interaction, indicating the onset of coordinative interactions between the porphyrin core and the mercuric ion.

To test the reversibility and the stability of the system in operative conditions OFF/ON cycles (i.e., quenching with Hg^{2+} , restoring in a TPEN solution) were also performed. The results are graphically reported in Figure 9 and show that a cycle can be repeated several times, with no appreciable loss of sensitivity, or dissolution of the film. Moreover the authors extended this protocol to a flow-through device.

To study this issue, a porphyrin coated flow-through quartz cell was used and the fluorescence emission responses, upon passage of Hg^{2+} solutions, analyzed. Also in this case, a quenching of fluorescence was observed, when a solution of Hg^{2+} passed through the cell. The fluorescence change was found to be dependent on the ion concentration.

More interestingly a good selectivity of the porphyrin layer responses with respect to other transition and posttran-

sition metal ions, such as Cd^{2+} , Pb^{2+} , and Cu^{2+} was observed. Appreciable quenching of fluorescence, in fact, resulted only in the presence of more concentrated solution (mM range) of the corresponding ions, as shown in Figure 10.

Competition experiments revealed negligible interferences by the other metal cations. The spectroscopic changes featured in the presence of Hg^{2+} 1.0×10^{-5} M remained unaffected by further addition of Cd^{2+} , Cu^{2+} , and Pb^{2+} up to $100 \mu\text{M}$.

Conversely, a quenching effect could be observed upon addition of Hg^{2+} ($10 \mu\text{M}$) to a still emitting solution of the other cations ($\geq 100 \mu\text{M}$). The inspection of the UV-vis spectra upon addition of cations other than Hg^{2+} did not reveal evident perturbation of the porphyrin electronic states. The Soret band remained, in fact, virtually unchanged even at high concentration of added Cd, Cu, or Pb cations. This finding safely rules out, in these latter cases, the occurrence of metal coordination.

3.3. Towards Chiral Recognition. Following this approach, we surmised that the presence of a cationic chiral functionality on the porphyrin periphery would result in the achievement of solid-state systems expressing elements of supramolecular chirality. For this reason we synthesized a tetraphenylporphyrin bearing an (L)-prolinium moiety at one of the peripheral phenyl groups; this cationic chiral functionality steers the self-aggregation process toward the formation of large porphyrin aggregates featuring high supramolecular chirality, as evidenced by their CD spectra [40].

Prompted by these results we decided to perform some detailed spectroscopic studies (UV-Visible, CD, and RLS) on the heteroaggregation of amphiphilic chiral cationic porphyrin derivatives carried out in the presence of chiral aggregates of the anionic, that is, negatively charged chiral counterpart. The molecular structures of the porphyrin derivatives used in these studies are reported in Figures 7(b)-7(c) [40].

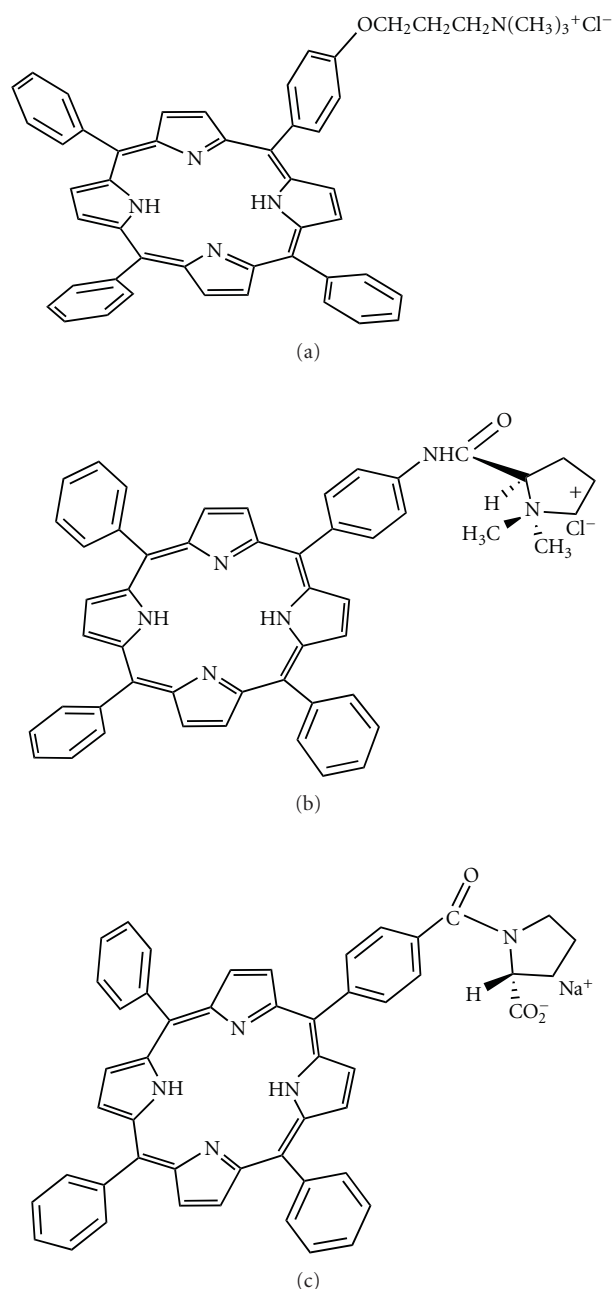


FIGURE 7: Molecular structures of (a) cationic amphiphilic porphyrin; (b) chiral cationic and anionic; (c) porphyrin counterparts.

Interesting features are evidenced by these binary systems. If the self-aggregation of the cationic moiety is carried out in the presence of preformed chiral aggregates of the anionic counterpart, the aggregation still occurs in a chiral fashion as witnessed by CD spectral changes upon heteroaggregation and more insight, a dramatic amplification of the resulting supramolecular aggregates, of about twenty-fold, is observed (Figure 11).

The ellipticity of the resulting heteroaggregates is higher compared to the one of the virtual sum “a + b” aggregates. This should indicate a strong template effect exerted by

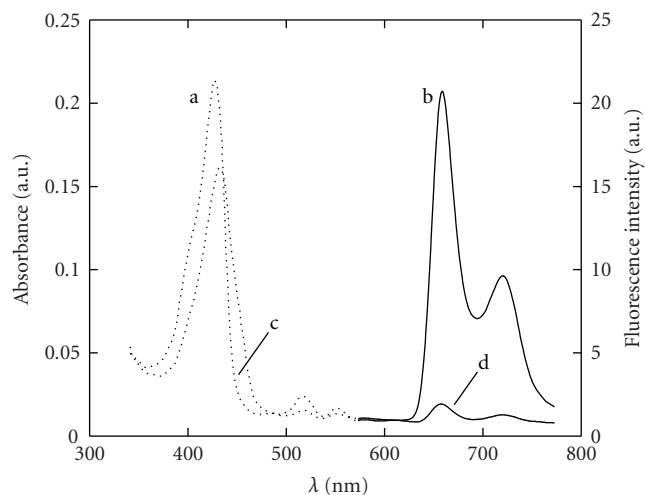


FIGURE 8: Absorption (dashed lines) and emission (solid lines, λ_{ex} 420 nm, λ_{em} 654, 720 nm) of porphyrin layers at different Hg^{2+} concentrations. (a) and (b) $[\text{Hg}^{2+}] = 0.0 \text{ M}$; (c) and (d) $[\text{Hg}^{2+}] = 1.0 \times 10^{-5} \text{ M}$.

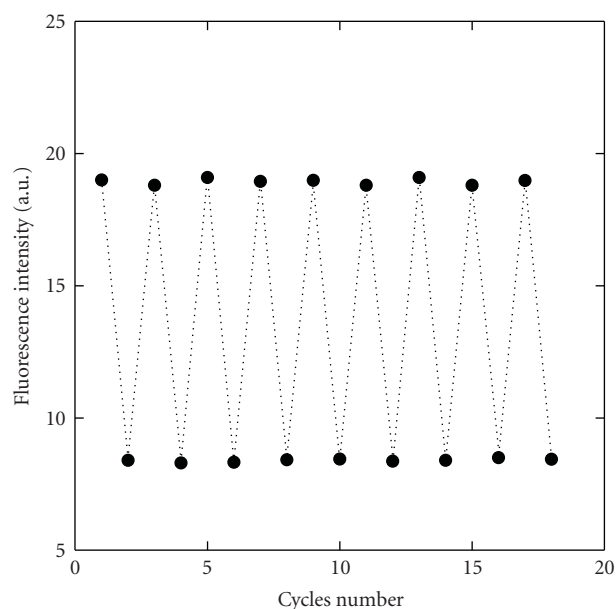


FIGURE 9: ON/OFF cycles of porphyrin layers in different aqueous solutions.

the presence of the anionic assemblies, reasonably onset by electrostatic forces.

The results obtained show that the electrostatic-templated aggregation induces a remarkable amplification of the chirality of the final porphyrin suprastructure. This can be of importance, *inter alia*, for the construction of complex hetero-porphyrin architectures in which the supramolecular chirality can be tuned ad hoc.

In summary, the results obtained in the case of the templated aggregation open interesting perspectives for the achievement of new porphyrin-based supramolecular

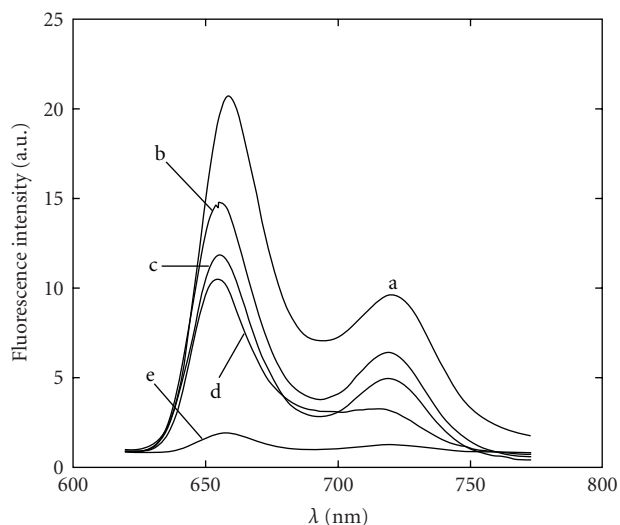
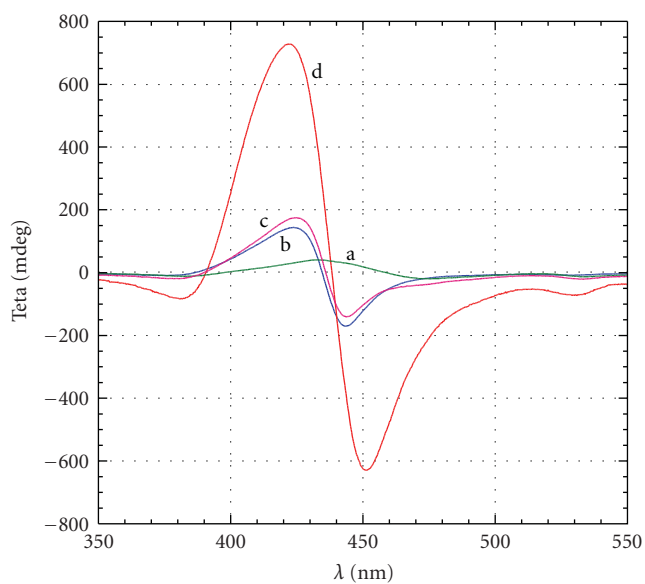


FIGURE 10: Fluorescence emission (λ_{ex} 420 nm) of porphyrin layers in different solutions. (a) H_2O , (b) Cd^{2+} (saturated solution), (c) Cu^{2+} (1.0×10^{-3} M), (d) Pb^{2+} (1.0×10^{-3} M) and (e) Hg^{2+} (1.0×10^{-5} M).



- a) PL(+) aggregates (7.5×10^{-6} M)
- b) PL(-) aggregates (1.5×10^{-5} M)
- c) Virtual "a + b" aggregates
- d) Templated aggregation

FIGURE 11: Amplification of CD signal (line d) for templated aggregation compared to both individual chiral aggregates (lines (a) and (b) and their virtual sum (line c).

species bearing attractive properties for the construction of stereoselective sensor systems, and the development of such a sensors is currently undergoing in our laboratories.

4. Conclusions

The synthetic versatility of porphyrins allows the preparation of molecular units capable of assembling in ordered supramolecular structures, characterized by different geometrical motifs. While porphyrin nanostructures have offered an elegant and rational approach to study the way to prepare supramolecular networks, trying to learn and mimic the lesson given by biological systems, the study of these systems is now reaching the exploitation in functional devices. Seminal applications of porphyrin nanostructures in sensor devices show their promising potentialities, where the supramolecular network can offer additional interaction pathways, exalting the selectivity/sensitivity performances, which cannot be offered by the single molecular unit. The possibility to prepare chiral porphyrin nanostructures opens the way to the deposition of layers suited for chiral discrimination; their successful exploitation in chemical sensors would have a tremendous impact in all the fields where chirality plays a fundamental role.

References

- [1] G. M. Whitesides, "Nanoscience, nanotechnology, and chemistry," *Small*, vol. 1, no. 2, pp. 172–179, 2005.
- [2] J. V. Barth, G. Costantini, and K. Kern, "Engineering atomic and molecular nanostructures at surfaces," *Nature*, vol. 437, no. 7059, pp. 671–679, 2005.
- [3] S. Iijima, "Helical microtubules of graphitic carbon," *Nature*, vol. 354, no. 6348, pp. 56–58, 1991.
- [4] S. V. N. T. Kuchibhatla, A. S. Karakoti, and S. Seal, "Hierarchical assembly of inorganic nanostructure building blocks to octahedral superstructures—a true template-free self-assembly," *Nanotechnology*, vol. 18, no. 7, Article ID 075303, 4 pages, 2007.
- [5] J. M. Lehn, in *Supramolecular Chemistry. Concepts and Perspectives*, VCH, Weinheim, Germany, 1995.
- [6] J.-M. Lehn, "Supramolecular chemistry—scope and perspectives: molecules, supermolecules, molecular devices (Nobel Lecture)," *Angewandte Chemie International Edition*, vol. 27, no. 1, pp. 89–112, 1988.
- [7] A. C. Grimsdale and K. Müllen, "The chemistry of organic materials," *Angewandte Chemie International Edition*, vol. 44, pp. 5592–5629, 2005.
- [8] T. S. Balaban, "Tailoring porphyrins and chlorins for self-assembly in biomimetic artificial antenna systems," *Accounts of Chemical Research*, vol. 38, no. 8, pp. 612–623, 2005.
- [9] K. M. Kadish, K. M. Smith, and R. Guilard, Eds., *The Porphyrin Handbook*, vol. 1, Academic Press, San Diego, Calif, USA, 2000.
- [10] S. Horn, K. Dahms, and M. O. Senge, "Synthetic transformations of porphyrins—advances 2004–2007," *Journal of Porphyrins and Phthalocyanines*, vol. 12, no. 10, pp. 1053–1077, 2008.
- [11] K. M. Kadish, K. M. Smith, and R. Guilard, Eds., *The Porphyrin Handbook*, vol. 6, Academic Press, San Diego, Calif, USA, 2000.
- [12] K. M. Kadish, K. M. Smith, and R. Guilard, Eds., *The Porphyrin Handbook*, vol. 4, Academic Press, San Diego, Calif, USA, 2000.

- [13] X. Gong, T. Milic, C. Xu, J. D. Batteas, and C. M. Drain, "Preparation and characterization of porphyrin nanoparticles," *Journal of the American Chemical Society*, vol. 124, no. 48, pp. 14290–14291, 2002.
- [14] C. M. Drain, G. Smeureanu, S. Patel, X. Gong, J. Garno, and J. Arijeloye, "Porphyrin nanoparticles as supramolecular systems," *New Journal of Chemistry*, vol. 30, no. 12, pp. 1834–1843, 2006.
- [15] A. S. D. Sandanayaka, Y. Araki, T. Wada, and T. Hasobe, "Structural and photophysical properties of self-assembled porphyrin nanoassemblies organized by ethylene glycol derivatives," *Journal of Physical Chemistry C*, vol. 112, no. 49, pp. 19209–19216, 2008.
- [16] A. K. Perepogu and P. R. Bangal, "Preparation and characterization of free-standing pure porphyrin nanoparticles," *Journal of Chemical Sciences*, vol. 120, no. 5, pp. 485–491, 2008.
- [17] Z. Wang, Z. Li, C. J. Medforth, and J. A. Shelnutt, "Self-assembly and self-metallization of porphyrin nanosheets," *Journal of the American Chemical Society*, vol. 129, no. 9, pp. 2440–2441, 2007.
- [18] T. N. Milic, N. Chi, D. G. Yablon, G. W. Flynn, J. D. Batteas, and C. M. Drain, "Controlled hierarchical self-assembly and deposition of nanoscale photonic materials," *Angewandte Chemie International Edition*, vol. 41, no. 12, pp. 2117–2119, 2002.
- [19] A. D. Schwab, D. E. Smith, C. S. Rich, E. R. Young, W. F. Smith, and J. C. de Paula, "Porphyrin nanorods," *Journal of Physical Chemistry B*, vol. 107, no. 41, pp. 11339–11345, 2003.
- [20] A. D. Schwab, D. E. Smith, B. Bond-Watts, et al., "Photoconductivity of self-assembled porphyrin nanorods," *Nano Letters*, vol. 4, no. 7, pp. 1261–1265, 2004.
- [21] S. C. Doan, S. Shanmugham, D. E. Aston, and J. L. McHale, "Counterion dependent dye aggregates: nanorods and nanorings of tetra(p-carboxyphenyl)porphyrin," *Journal of the American Chemical Society*, vol. 127, no. 16, pp. 5885–5892, 2005.
- [22] M. C. Lensen, K. Takazawa, J. A. A. W. Elemans, et al., "Aided self-assembly of porphyrin nanoaggregates into ring-shaped architectures," *Chemistry*, vol. 10, no. 4, pp. 831–839, 2004.
- [23] T. Hasobe, H. Oki, A. S. D. Sandanayaka, and H. Murata, "Sonication-assisted supramolecular nanorods of meso-diaryl-substituted porphyrins," *Chemical Communications*, no. 6, pp. 724–726, 2008.
- [24] T. Hasobe, A. S. D. Sandanayaka, T. Wada, and Y. Araki, "Fullerene-encapsulated porphyrin hexagonal nanorods. An anisotropic donor-acceptor composite for efficient photoinduced electron transfer and light energy conversion," *Chemical Communications*, no. 29, pp. 3372–3374, 2008.
- [25] S. J. Lee, J. T. Hupp, and S. T. Nguyen, "Growth of narrowly dispersed porphyrin nanowires and their hierarchical assembly into macroscopic columns," *Journal of the American Chemical Society*, vol. 130, no. 30, pp. 9632–9633, 2008.
- [26] Z. Wang, C. J. Medforth, and J. A. Shelnutt, "Porphyrin nanotubes by ionic self-assembly," *Journal of the American Chemical Society*, vol. 126, no. 49, pp. 15954–15955, 2004.
- [27] Z. Wang, K. J. Ho, C. J. Medforth, and J. A. Shelnutt, "Porphyrin nanofiber bundles from phase-transfer ionic self-assembly and their photocatalytic self-metallization," *Advanced Materials*, vol. 18, no. 19, pp. 2557–2560, 2006.
- [28] T. Kojima, R. Harada, T. Nakanishi, K. Kaneko, and S. Fukuzumi, "Porphyrin nanotubes based on self-assembly of Mo(V)-dodecaphenylporphyrin complexes and inclusion of Mo-oxo clusters: synthesis and characterization by X-ray crystallography and transmission electron microscopy," *Chemistry of Materials*, vol. 19, no. 1, pp. 51–58, 2007.
- [29] J.-H. Chou, M. E. Kosal, H. S. Nalwa, N. A. Rakow, and K. S. Suslick, "Applications of porphyrins and metalloporphyrins to materials chemistry," in *The Porphyrin Handbook*, K. M. Kadish, K. M. Smith, and R. Guilard, Eds., vol. 4, pp. 43–131, Academic Press, San Diego, Calif, USA, 2000.
- [30] K. Ariga, K. Endo, Y. Aoyama, and Y. Okahata, "QCM analyses on adsorption of gaseous guests to cast films of porphyrin-resorcinol derivatives," *Colloids and Surfaces A*, vol. 169, no. 1–3, pp. 177–186, 2000.
- [31] T. Kojima, T. Nakanishi, T. Honda, and S. Fukuzumi, "Photoinduced electron transfer in supramolecular assemblies involving saddle-distorted porphyrins and phthalocyanines," *Journal of Porphyrins and Phthalocyanines*, vol. 13, pp. 14–21, 2009.
- [32] R. Harada and T. Kojima, "A porphyrin nanochannel: formation of cationic channels by a protonated saddle-distorted porphyrin and its inclusion behavior," *Chemical Communications*, pp. 716–718, 2005.
- [33] D. Monti, M. Venanzi, M. Russo, et al., "Spontaneous deposition of amphiphilised porphyrin ordered film on glass," *New Journal of Chemistry*, vol. 28, pp. 1123–1128, 2004.
- [34] F. Dini, E. Martinelli, G. Pomarico, et al., "Chemical sensitivity of self-assembled porphyrin nano-aggregates," *Nanotechnology*, vol. 20, no. 5, Article ID 055502, 8 pages, 2009.
- [35] D. Filippini, S. P. S. Svensson, and I. Lundström, "Computer screen as a programmable light source for visible absorption characterization of (bio)chemical assays," *Chemical Communications*, vol. 9, no. 2, pp. 240–241, 2003.
- [36] D. Filippini, A. Alimelli, C. Di Natale, R. Paolesse, A. D'Amico, and I. Lundström, "Chemical senses of familiar devices," *Angewandte Chemie International Edition*, vol. 45, pp. 3800–3803, 2006.
- [37] E. Gatto, M. A. Malik, C. Di Natale, et al., "Polychromatic fingerprinting of excitation emission matrices," *Chemistry- A European Journal*, vol. 14, no. 20, pp. 6057–6060, 2008.
- [38] L. S. Dolci, E. Marzocchi, M. Montalti, et al., "Amphiphilic porphyrin film on glass as a simple and selective solid-state chemosensor for aqueous Hg^{2+} ," *Biosensors and Bioelectronics*, vol. 22, no. 3, pp. 399–404, 2006.
- [39] D. Monti, M. Venanzi, G. Mancini, C. Di Natale, and R. Paolesse, "Supramolecular chirality control by solvent changes. Solvodychromic effect on chiral porphyrin aggregation," *Chemical Communications*, no. 19, pp. 2471–2473, 2005.
- [40] D. Monti, M. Venanzi, M. Stefanelli, et al., "Chiral amplification of chiral porphyrin derivatives by templated heteroaggregation," *Journal of the American Chemical Society*, vol. 129, no. 21, pp. 6688–6689, 2007.

Review Article

Nanocrystalline Metal Oxides for Methane Sensors: Role of Noble Metals

S. Basu and P. K. Basu

*IC Design and Fabrication Centre, Department of Electronic and Telecommunication Engineering,
Jadavpur University, Kolkata 700032, India*

Correspondence should be addressed to S. Basu, sukumar.basu@yahoo.co.uk

Received 1 January 2009; Revised 7 July 2009; Accepted 23 July 2009

Recommended by Giorgio Sberveglieri

Methane is an important gas for domestic and industrial applications and its source is mainly coalmines. Since methane is extremely inflammable in the coalmine atmosphere, it is essential to develop a reliable and relatively inexpensive chemical gas sensor to detect this inflammable gas below its explosion amount in air. The metal oxides have been proved to be potential materials for the development of commercial gas sensors. The functional properties of the metal oxide-based gas sensors can be improved not only by tailoring the crystal size of metal oxides but also by incorporating the noble metal catalyst on nanocrystalline metal oxide matrix. It was observed that the surface modification of nanocrystalline metal oxide thin films by noble metal sensitizers and the use of a noble metal catalytic contact as electrode reduce the operating temperatures appreciably and improve the sensing properties. This review article concentrates on the nanocrystalline metal oxide methane sensors and the role of noble metals on the sensing properties.

Copyright © 2009 S. Basu and P. K. Basu. This is an open access article distributed under the Creative Commons Attribution License, which permits unrestricted use, distribution, and reproduction in any medium, provided the original work is properly cited.

1. Introduction

Over the past 20 years, a great deal of research efforts has been directed towards the development of portable gas sensing devices for practical applications ranging from toxic gas detection to manufacturing process monitoring. For coalmines most of the accident occurs due to the presence of explosive and toxic gases like methane and carbon monoxide in air. In underground coalmines there are many kinds of ignition sources, such as electricity and frictions. Currently, it is suspected that a large roof fall may also act as the ignition source. This fall will compress air adiabatically and produce air temperature, well above the degree necessary to initiate a gas and/or coal dust explosion. So it is essential to monitor continuously the concentration of hazardous gases like CH₄ and CO and alarm if the gas concentration level is above a certain safety limit. Continuous research and development activities are being pursued to explore a gas sensor for detection of low concentrations of methane in the coalmine atmosphere at substantially low temperature so

that the methane explosion is not further accelerated by the prevailing high temperature in the Mines [1, 2].

Semiconducting oxides are the fundamentals of smart devices as both the structure and morphology of these materials can be controlled precisely and so they are referred to as functional oxides. They have mainly two structural characteristics: cations with mixed valence states and anions with deficiencies. By varying either one or both of these characteristics, the electrical, optical, magnetic, and chemical properties can be tuned, giving the possibility of fabricating smart devices. The structures of functional oxides are very diverse and varied, and there are endless new phenomena and applications. Such unique characteristics make oxides one of the most diverse classes of materials, with properties covering almost all the aspects of materials science and in the areas of physics such as semiconductors, superconductivity, Ferro electricity, and magnetism.

Since the demonstration almost 50 years ago [3] that the adsorption of gas on the surface of a semiconductor can bring about a significant change in the electrical resistance

of the material, there has been a sustained and successful effort to make use of this change for the purposes of gas detection [4]. Sensing toxic and flammable gases is a subject of growing importance in both domestic and industrial environments. Metal oxides such as Ga_2O_3 , SnO_2 , WO_3 , TiO_2 , and ZnO [4–9] are stable physically and chemically and are widely investigated for gas and humidity detections. Sensing performance, especially response, is controlled by three independent factors: the receptor function, transducer function, and utility. Receptor function concerns the ability of the oxide surface to interact with the target gas. Chemical properties of the surface oxygen of the oxides are responsible for this interaction in an oxide-based device and this function can be largely modified. A considerable change in the response takes place when an additive (noble metal, acidic or basic oxide) is loaded on the oxide surface [8, 9]. Transducer function concerns the ability to convert the signal caused by chemical interaction of the oxide surface (work function change) into electrical signal. This function can be realized by the measure of the current through a system containing an innumerable number of grains and grain boundaries, to which a double-Schottky barrier model can be applied.

It has been observed by almost all researchers working with oxide semiconductors for gas sensing that the operation of such sensors with selectivity for a particular gas is extremely difficult, especially when the changes in the electrical properties are used as the sensor signal. Use of sensor arrays and artificial neural network can normally solve this problem. In fact today's chemical sensors are much more reliable with the implementation of ANN logic to improve the selectivity [10].

The objective of the present review is to discuss the role of noble catalyst metals to improve the functional properties of nanocrystalline oxide gas sensors for methane sensing.

2. Different Types of Semiconductor Metal Oxide Gas Sensors

Different structures of metal oxide gas sensors are innovated through research and development for the last few decades to improve the gas sensing performance. Some important structures are discussed in the following section.

2.1. Resistive Type Metal Oxide Gas Sensors. The first established and probably most well-known family of solid-state gas sensors comprises the resistive type metal oxide semiconductor sensors. This type of sensors are normally operated at temperature where the main contribution to variation of sensor signal originates from changes in the electronic conductivity due to charge transfer during chemisorptions and catalytic reactions at the surface and at grain boundaries. The advantage of this sort of sensors is the ease of fabrication and direct measurement capability. The resistance is measured between the two contacts taken from the top of the sensing (metal oxide) films deposited on a nonconducting substrates like glass [11], alumina [12], SiO_2 [13], and so forth.

2.2. Schottky Type Gas Sensors. The functional characteristics of sensors, for example, response magnitude and response time were improved over the resistive type sensors by adopting Schottky structures with catalytic metal electrode contacts as reported. Since most of the catalytic noble metals (Pd, Pt, Rh, etc.) make Schottky junctions with the semiconducting metal oxides and provide the catalytic effect as well as the collection of carriers, the metal layer serves as a gate for the diode. In presence of reducing gases, the hydrogen containing molecules suffers dissociative chemisorptions on metal electrode to produce atomic hydrogen. The atomic hydrogen diffuses into the metal/metal oxide junction and reduces the catalytic metal work function. The Schottky energy barrier changes due to the reduction of metal work function and this change can be measured by I-V, C-V, or any other electrical mode [14–16].

The double barrier Schottky junction in the metal-insulator-metal (MIM) configuration is another popular gas sensor device recently reported for hydrogen and methane sensing. Two different metals are deposited on either side of the oxide semiconductor to form back-to-back Schottky junctions. The advantage of such devices is that the total barrier is higher against the flow of free carriers. So, the current is appreciably low in air and the difference in current between the presence and absence of gas is quite high. Therefore, the response is high, and due to vertical transport of free carriers through the metal-semiconductor junctions the response time is also shorter compared to the planer sensor devices. The single Schottky barrier junction in MIM configuration is also superior to the planer devices in terms of response, response time, and recovery time. Basu and his research group reported hydrogen and methane sensing using ZnO MIM sensors [17, 18].

2.3. Metal Oxide Homo Junction Gas Sensors. Normally metal oxides are *n*-type semiconductors. There are few metal oxides that also exhibit *p*-type conductivity such as CuO and NiO [19–21]. Recently *p*-type conductivity was reported in ZnO [19–21]. Thus the fabrication of semiconducting metal oxide *p*-*n* homo junction could be materialized with ZnO . Hazra and Basu [20, 21] showed that *p*-*n* ZnO homo junction is sensitive to H_2 as there is a substantial shift in the forward bias I-V characteristics on exposure to the reducing gases.

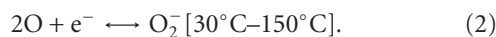
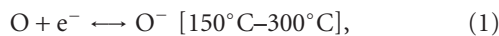
2.4. Metal Oxide Hetero Junction Gas Sensors. Change in the I-V characteristics (on exposure to the gaseous environment) of hetero junction made of two dissimilar metal oxides with different band gap has evolved another new kind of gas sensor structures. Amongst these, ZnO/CuO is relatively widely explored one [22, 23] for sensing CO. Hu et al. [24] showed that ZnO/CuO also has good response towards H_2S and alcohol. The NO_2 and CO_2 sensing properties of a hetero junction gas sensor formed between *n*-type ZnO and a *p*-type composite based on a mixture of $\text{BaTiO}_3/\text{CuO}/\text{La}_2\text{O}_3$ were evaluated by Ling et al. [25] It was found that the $\text{BaTiO}_3/\text{CuO}/\text{La}_2\text{O}_3$ sensors showed an increase in resistance when exposed to NO_2 . When exposed to CO_2

the BaTiO₃/CuO/La₂O₃ sensor showed a small decrease in resistance.

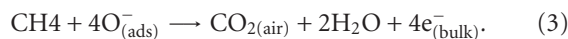
2.5. Mixed Metal Oxide Gas Sensors. Mixed oxides have recently emerged as promising candidates for gas detection [26–30]. It has been realized that such systems may benefit from the combination of the best sensing properties of the pure components. Formation of mixed oxides leads to the modification of the electronic structure of the system. This includes the changes in the bulk as well as in the surface properties. Bulk electronic structure, the band gap, Fermi level position, transport properties, and so forth are affected mostly in the case of compounds and solid solutions. Surface properties are expected to be influenced by new boundaries between grains of different chemical compositions. It is anticipated that all these phenomena will contribute advantageously to the gas sensing mechanism. The use of mixed oxides in gas detection (especially NO₂, H₂, CO) has been tried successfully *with* the following systems: SnO₂-TiO₂, SnO₂-WO₃, and TiO₂-WO₃ [30–36].

3. Methane Sensing Mechanism

It is well known that the performance of gas sensors can be improved by incorporation of noble metals on the oxide surface. SnO₂-based gas sensors in the form of thick film, porous pellets, or thin films, with Pt or Pd modifications, are widely applied for monitoring explosive and toxic gases in industry, urban and domestic life [37]. Such promoting effects are undoubtedly related to the catalytic activities of the noble metals for the oxidation of hydrocarbons. In case of planar type resistive gas sensors two metal contacts are taken from the metal oxide. A polycrystalline semiconductor has the structure with a large number of grains and grain boundaries. In contrast to the single crystalline materials, polycrystalline materials give rise to local potential barriers between the grains. The electrical properties of the surface of a thin film and the surface boundaries between the grains are affected by the adsorption and desorption of gaseous molecules. Oxygen ions can be found at the grain boundaries. At elevated temperature O₂ is chemisorbed by gaining [38, 39] one more electron from the surface. Due to this chemisorptions the resistivity of the material increases:



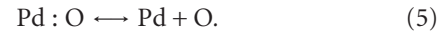
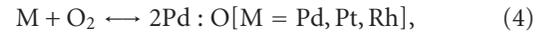
Methane molecules react with the chemisorbed oxygen at the grain boundaries. As a result negative charge carriers are added to the bulk and hence the resistance decreases:



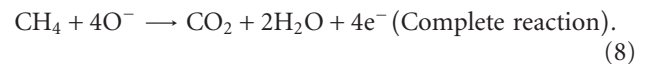
Therefore, by measuring the change in the conductivity of the semiconductor oxide thin films we can detect the reducing gases [40].

In case of Schottky type gas sensors, catalytic noble metals are taken as the electrode contacts to the oxides. At

an elevated temperature, the oxygen molecules are weakly bonded with the catalytic metal atoms (Pt, Pd-Ag, and Rh). The resulting complex subsequently dissociates and oxygen atoms are produced [41, 42]:



The oxygen atoms then undergo a spillover process and finally form negatively charged surface ions by gaining electrons from the oxide surface, yielding a high electrostatic potential in the junction [43]. The space charge region, being depleted of electrons, is more resistive than the bulk. The hydrogen or methane response mechanism of gas sensors with a noble metal/metal oxide Schottky junction is, so far, the best understood and is illustrated in Figure 1. The first step is the dissociative adsorption of hydrogen or hydrogen containing molecules (like CH₄) to produce H or CH₃ on the noble metal surface that reacts with adsorbed atomic oxygen to produce water. Further, the H or CH₃ spillover to metal oxide surface and reacts with chemisorbed ionic oxygen to produce water and free electrons that increases the current through the junction. If the device is operated at an elevated temperature ~ 100°C or above, which is normally the case, the water molecules formed will rapidly desorb from the surface:



The above diagrams clearly demonstrate the methane sensing mechanism of noble metal/metal oxide Schottky junctions. While Figure 1(b) shows a change in capacitance with voltage in presence of gas, the same change can be recorded from I-V characteristics of the Schottky Junction where current is modulated in presence of detecting gas and thus there is a shift in the I-V curves. The energy band diagram of a typical Schottky junction is shown in Figure 2 and it clearly indicates that there is shift in band bending in presence of the sensing gas. As a result, the barrier height is modified and in fact for reducing gases like methane there is decrease in barrier height (n-ZnO) thereby allowing more current through the junction and thus increasing the conductivity.

Further due to its high solubility in catalytic metal and its rapid diffusion through the metal, hydrogen reaches the catalytic metal/metal oxide interface and produces an interfacial dipole layer as shown in Figure 1(c). The electrically polarized potential at the catalytic metal/metal oxide interface lowers the work function of catalytic metal and thus reduces the barrier height which is shown in the Energy Band Diagram (Figure 2). The hydrogen at the interface acts as a shallow donor to metal oxide (e.g., ZnO) and thus the barrier height is further reduced. Also, the adsorbed hydrogen atoms passivate the interface states between noble metal and metal oxide sensors, preventing them from charging and pinning

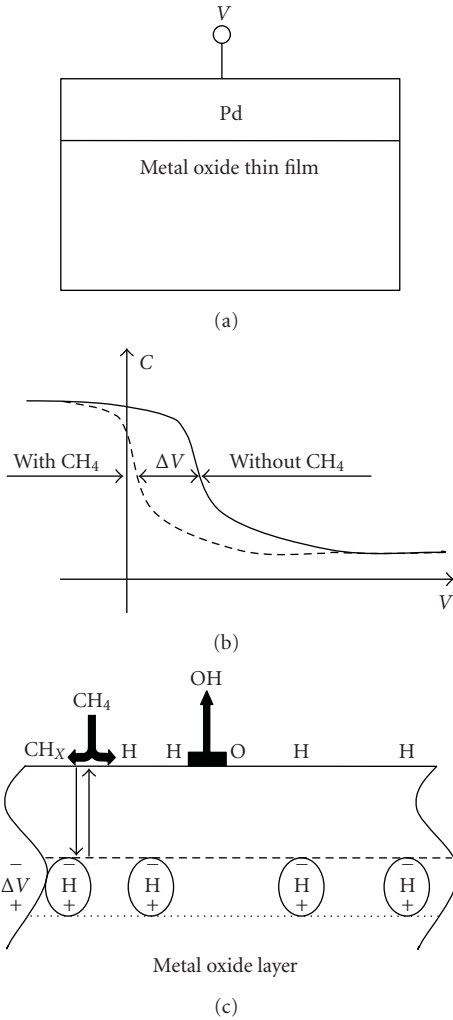


FIGURE 1: The schematic of hydrogen or methane sensing using catalytic metal on metal oxide film. (a) A typical noble metal/metal oxide Schottky junction. (b) When exposed to hydrogen or methane a voltage shift occurs in the capacitance—voltage characteristics. (c) Diffusion of hydrogen through the noble metal and formation of dipole layer across the noble metal/ metal oxide junction.

the fermi level. The passivated interface thus causes an improvement in the barrier height. Due to this lowering of barrier height, the current through the junction further increases in presence of the gas [5, 18, 44, 45], thereby yielding a high response.

4. Factors Related to the Improved Performance of a Gas Sensor

4.1. Grain Size Effect. Nano crystalline is a single phase or a multiphase of reduced size (1 nm to 100 nm) of at least one dimension. When the crystal size is decreasing, more and more surface is exposed. So fraction of atoms at the grain boundary increases and the grain boundaries contain a high density of defects like vacancies, dangling bonds, which can play an important role in the transport

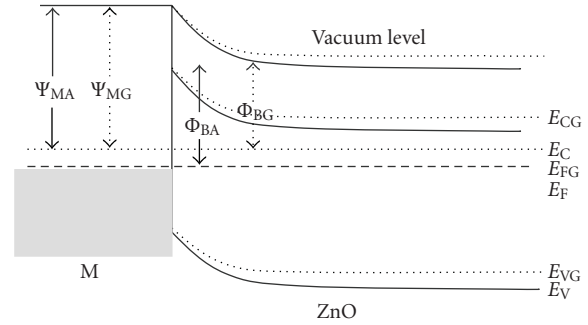


FIGURE 2: Band diagram of the Schottky Junction explaining the sensing mechanism. The barrier height reduces upon exposure to the reducing gas. Ψ_{MA} , Ψ_{MG} are the work function of M in air and in gas respectively. Φ_{BA} , Φ_{BG} are the barrier height of the junction in air and in gas, respectively. E_C , E_{CG} are the conduction band in air and in gas, respectively. E_V , E_{VG} are the valence band in air and in gas, respectively. E_F , E_{FG} are the fermi level in air and in gas, respectively. M is Pt, Pd, or Rh.

properties of electrons. Xu et al. [45] proposed a model to explain the dependence of depletion layer, due to adsorption of oxygen on the crystal size and to explain the high response of nanocrystalline metal oxide gas sensors. Later Rothschild and Komen [42] showed that the conductivity increases linearly with decreasing trapped charge densities and that the response to the gas-induced variations in the trapped charge density is proportional to $1/D$, where D is the average grain size. Figure 3 shows a schematic of few grains of nanocrystalline metal oxide thin films and the space charge region around the surface of each grain at the intergrain contacts. The space charge region, being depleted of electrons, is more resistive than the bulk. When the sensor is exposed to reducing gases, the electrons trapped by the oxygen adsorbate return to the oxide grains, leading to a decrease in the potential barrier height and thus the resistance drops. The crystallites in the gas sensing elements are connected to the neighboring crystallites either by grain boundary contacts or by necks. It was reported that [45] the higher response is obtained when grain size is much lower than twice the depletion width. The depletion region extends throughout the whole grains and the crystallites are almost fully depleted of electrons. As a result the conductivity decreases through the junction, and so the change of conductivity is very large in presence of reducing gases, thereby yielding a high response. Figure 3 demonstrates the three situations schematically.

Further, nanocrystalline metal oxides can reduce the operating temperature of the gas sensors. Zhang et al. [46] reported that the surface or interfacial tension decreases with decreasing particle size because of the increase in the potential energy of the bulk atoms of the particles. Smaller particles with increased molar free energy are more prone to adsorption per unit area of molecules or ions onto their surfaces in order to decrease the total free energy and to become more stable, and therefore, smaller particles have higher adsorption coefficient for gases. Thus, the adsorption

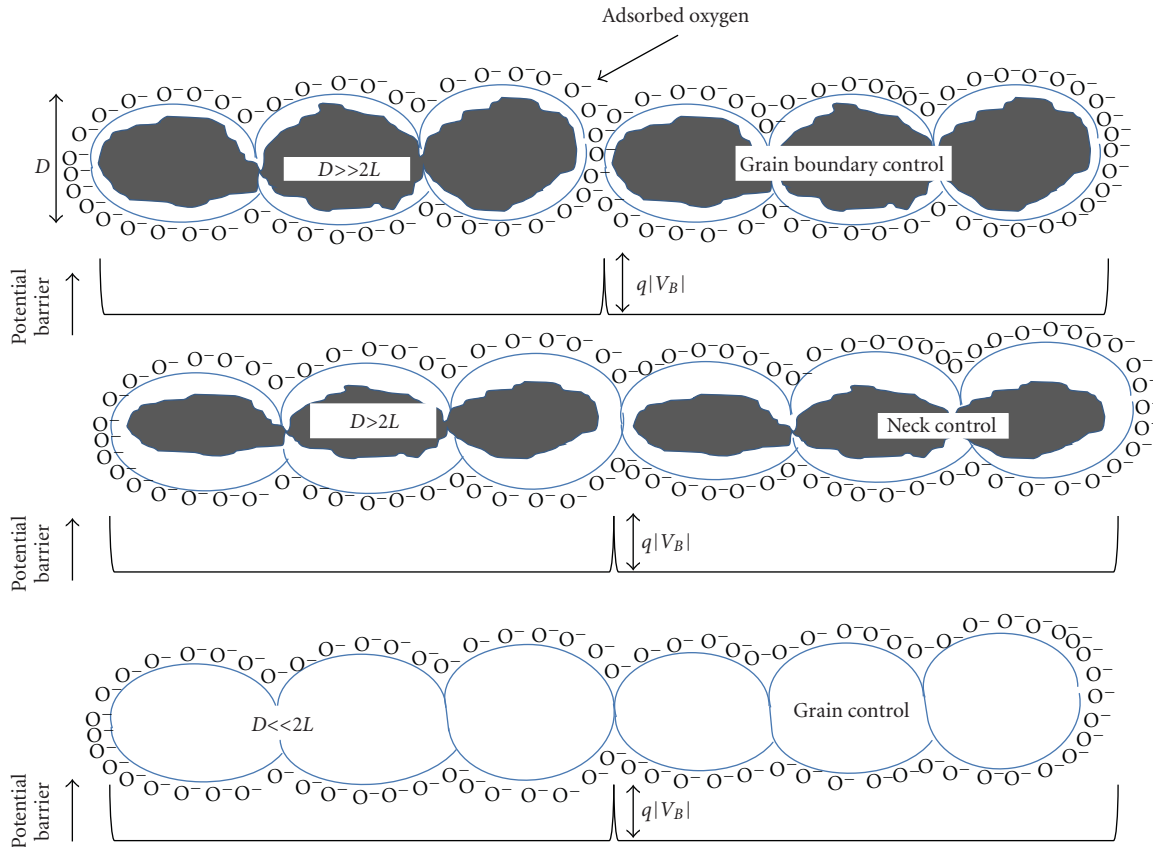


FIGURE 3: Schematic of few grains of nanocrystalline ZnO thin films and the space charge region around the surface of each grain at inter grain contacts.

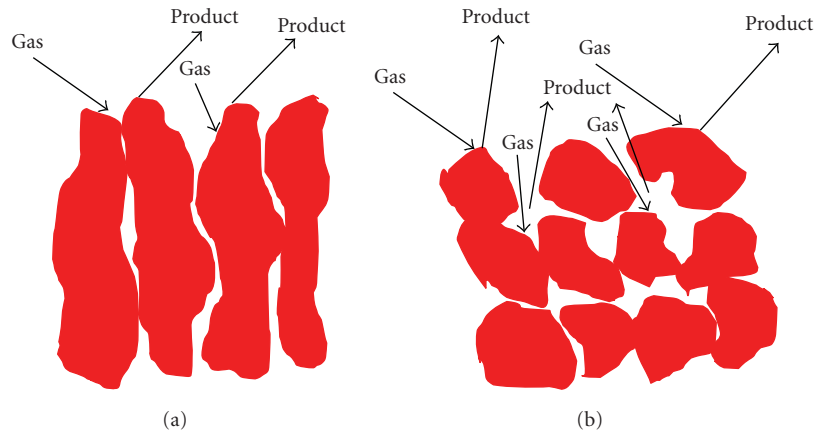


FIGURE 4: Schematic view of gas sensing reaction in (a) compact layer and (b) porous layer.

of oxygen or reducing gases takes place relatively easily onto the nano crystalline metal oxide surface.

4.2. Porosity and Thickness of the Metal Oxide Films. In compact metal oxide sensing layer, gases cannot penetrate into the layers and the gas sensing reaction is confined to the surface. In the porous layer, gases can access to the entire volume of the sensing layer and the gas sensing reaction can,

therefore, take place at the surface of the individual grains, at the grain boundaries, and at the interface between grains and electrodes as shown in Figure 4. Therefore, porous layer is more suitable for methane sensing as compared to compact layers which has been already reported [18, 47–50].

The thickness of the metal oxide thin films has a great role to play on the response of the sensors. To get high response of the metal oxide-based gas sensors the thickness

of the electron-depleted region, due to the chemisorptions of oxygen, should be as close as the thickness of the metal oxide thin films. Generally, it was reported that the response is profoundly higher than resistive type gas sensors made of thinner films [51, 52]. Babaei and Orvatinia [53] proposed a model to establish a mathematical relation between the steady-state response of the sensor and the thickness of the sensitive film used. It was shown that the response drops exponentially as the thickness of the sensitive film increases. On the other hand, some groups reported that for certain combinations of the structural parameters like porosity, cracks, and so forth, the gas response of the sensors could increase.

4.3. Incorporation of Noble Metals. The performance of gas sensing can be improved by incorporation of noble metals into the metal oxides. SnO₂-based gas sensors in the form of thick film, porous pellets or thin films with the inclusion of Pt or Pd are widely applied for monitoring the explosive and toxic gases in industry, in urban, and domestic life. In fact, the catalytic metals do not change the free energy of the reactions but lower the activation energy. The noble metals can be incorporated as (i) electrode contact on metal oxide and/or (ii) dispersed phase on the oxide surface.

4.3.1. Effect of Noble Metal Electrode Contact on Metal Oxide. There are quite a few reports of the applications of nanoporous noble metal thin films as the electrode contact onto the metal oxides [54, 55]. Lofdahl et al. [56] studied the role of noble metal gate morphology for sensing hydrogen and some hydrocarbons. The metal gates were made with different thickness gradients. It was observed that Pd shows higher response at the thicker part of the film whereas Pt gives more or less the same response for both the thinner, and thicker part of the film. However, both Pd and Pt metal contacts show poor stability with time after repeated gas exposure. The Pd blistering at the thicker part of the metal film was also reported [57] for repeated hydrogen or hydrocarbon exposure. The change of response at the thicker, thinner and blistered part of the Pd film can be explained by water forming reaction. According to this report thick compact Pd layer is suitable for improved gas sensing.

The reduction of methane on Pd is not so simple as that of hydrogen. Recently Su et al. [58] proposed a mechanism of CH₄ reduction on Pd surface. They worked on ZrO₂ supported by Pd thin films. At an elevated temperature Pd is oxidized and then PdO is reduced in presence of methane. Very rapid oxidation occurs as a consequence of electric field-driven transport of oxygen anions through the oxide film. Once the film thickness exceeds about 15 nm, oxidation occurs more slowly via diffusive transport of oxygen through the oxide film. The reducing gases diffuse to the metal-oxide boundary where reduction of the oxide occurs. After the reduction of PdO continuous diffusion of H through Pd to Pd/metal oxide junction takes place and a dipole layer is formed. Dissociative adsorption of methane followed by water formation occurs almost simultaneously due to reaction of hydrogen with the chemisorbed oxygen.

There are some drawbacks associated with the use of pure Pd metal due to blister formation because of the irreversible transition from the α phase of palladium to the β hydride phase at low H₂ and at 300 K [59]. To overcome these problems Pd is alloyed to a second metal (13%–30% Ag) for H₂ or hydrocarbon sensing. Pd-Ag alloy is also attractive for use in gas sensors because of a numbers of other properties [60] reported as follows.

- (1) The rate of hydride formation is very low for Pd-Ag alloy than for pure Pd.
- (2) The solubility of hydrogen is actually greater up to about 30% Ag and the diffusion of hydrogen is not hindered by the Ag atom.
- (3) Alloy at the higher Ag concentrations (up to 45%) was reported to have higher rates of hydrogen adsorption in the temperature range 30°C–100°C.
- (4) The OH formation barrier energy is higher in presence of Pd-Ag alloy.
- (5) The mechanical properties of polycrystalline Pd-Ag alloy are better than Pd.

4.3.2. Effect of Noble Metal Dispersion onto the Metal Oxide Surface. The gas response of the oxides is improved by surface modification by using platinum group metals like Pt, Pd, and Rh. These additives act as activators of the surface reactions. Generally, surface modification takes advantage of the following important options [61–63]:

- (i) choosing a modifier that exhibits a catalytic activity in the solid-gas interactions,
- (ii) changing the reactivity of the material by changing the modifier concentration,
- (iii) the oxide semiconductor can affect the configuration of d electrons of surface-localized transition metals and change the surface activity by choosing a suitable “cluster-matrix” pair.

The most promising catalytic approaches are based on the “collective” and “local” site concepts. The “collective” site approach along with chemisorptions theory proposed by Volkenshtein [64] provides an idea of how the adsorbate affects the overall band structure of the modified matrix. It correlates the catalytic activity of the modifier directly to the valence state of the dopants in the oxide matrix and their influence on the charge carrier concentration in the semiconductor. On the other hand, the “local” sites approach is dealing with the concept of a nonuniform surface, which deals with the interaction of a semiconductor oxide with the gas phase to form a surface complex.

After noble metal deposition it is necessary to have subsequent annealing in the temperature range 300°C–600°C that improves the homogeneity and thus stabilizes the gas sensing properties [65]. The dispersed noble metals actually activate the spillover process as shown in Figure 5. Catalyst particles should be finely dispersed on the metal oxide matrix so that they are available near all the intergranular contacts. In an open atmosphere the oxygen molecules

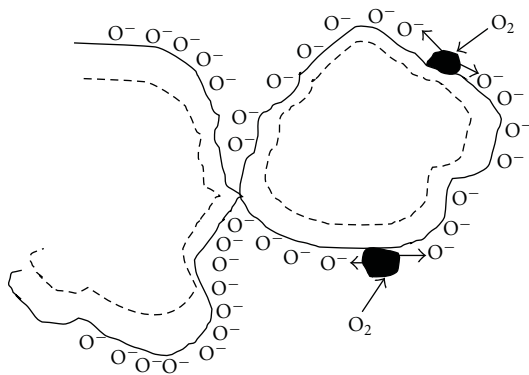


FIGURE 5: Oxygen spillover process in Pd modified ZnO thin films.

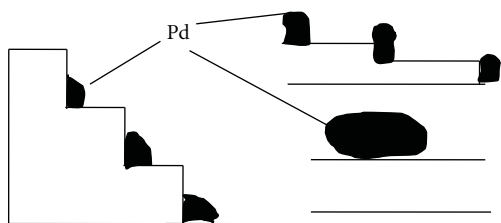


FIGURE 6: Nature of deposition of Pd modifier on the metal oxide matrix.

are first adsorbed on the catalyst and then spillover to the metal oxide matrix. At appropriate temperatures, the reducing gases are first adsorbed on to the surface of additive particles and then migrate to the oxide surface to react with surface oxygen species thereby increasing the surface conductivity. It was established that for attaining the optimal effect, surface cluster size should not exceed 1–5 nm [66], and the optimal distance between the clusters should be approximately equal to the oxygen surface diffusion length [67–69]. Recent experimental work has suggested that the noble metal clusters accumulate at the step edge of metal oxide (Figure 6). The functional parameters such as gas response, response time, recovery time, and selectivity have been dramatically improved through surface modification by noble metals. Further, the operating temperature can be shifted to lower value by introducing suitable noble metals.

5. Nanocrystalline Metal Oxide-Based Methane Sensors

Continuous research and development activities are being pursued to explore a gas sensor for detection of low concentrations of methane in the coalmine atmosphere at substantially low temperature so that the methane explosion is not further accelerated by the high sensing temperature. It has been realized that nanomaterials have great potential for the technological development almost in each area. The nanomaterials have some novel properties that attract for fundamental and technological research and development. The dots and wires in the nanoscale range develop

the unique electrical and optical properties of materials. Quantum confinement effect due to the change of size and shape of the nanoparticles can modify the energy bands of the semiconductors and insulators. There are great efforts towards the development of nanostructured ZnO and SnO₂, since the reactions at the grain boundaries and a complete depletion of the carriers in the grains can strongly modify the material transport properties of metal oxide. The materials are characteristically *n*-type semiconductors due to nonstoichiometry associated with oxygen vacancy and/or metal excess in the interstices, acting as donor states to provide conduction electrons. However, the overall surface resistance of such films is greatly influenced by the chemisorptions of oxygen from air as discussed above.

5.1. Nanocrystalline SnO₂. Tin oxide (SnO₂) is an *n*-type semiconductor with a wide band gap ($E_g = 3.6$ eV). Because of its excellent optical and electrical properties, SnO₂ is extensively used as a functional material for the optoelectronic devices, gas sensors, varistor, ion sensitive field effect transistors, and transparent conductive coatings for organic light emitting diodes [70–73]. R.f. sputtering [74], dc-magnetron sputtering [75], thermal evaporation [76, 77], ion beam deposition [78], spray pyrolysis [79], and Sol-gel [80] are the most studied methods for the preparation of SnO₂. Sberveglieri [81] presented a review of the techniques applied for SnO₂ films deposition and it was shown that most of the methods require high-temperature treatments in order to fabricate good-quality polycrystalline films. High temperature, however, damages the surface of the films and increases the interface thickness, which has negative effect on the optical properties, especially on the wave guiding. Pulsed laser deposition (PLD) technique was successfully applied for growing quality SnO₂ thin films [82, 83]. The film was produced by ablation of either Sn target in oxidizing oxygen atmosphere or SnO₂ target. PLD offered many advantages of reduced contamination due to the use of laser light, control of the composition of deposited structure, and in situ doping. It is a versatile and powerful tool for production of nanoparticles with desired size and composition, only by varying the deposition conditions.

Carotta et al. [84] systematically studied the responses of alkanes to SnO₂-based materials and a solid solution of Sn, Ti with particular emphasis to the dehydrogenation mechanisms of surface reaction of these gases and eventually to carbon oxides. The mechanism of interaction of the sensors versus alkanes has been modelled on the basis of previously reported studies on oxidation of alkanes via heterogeneous catalysis of metal-oxide materials [85–87]. Also the sensing properties of SnO₂- and TiO₂-based oxides versus alkanes were studied [88] under wet condition and in presence of ethanol. It was observed that the response versus alkanes is significantly high, when operating above 450°C. In general, the response of the sensors versus alkanes increases with the number of carbon atoms and with temperature [89, 90]. This behavior is explained through alkane oxidation via heterogeneous catalysis of metal-oxide materials [85–87]. O-species at surface (oxygen adsorbed on the sensor surface)

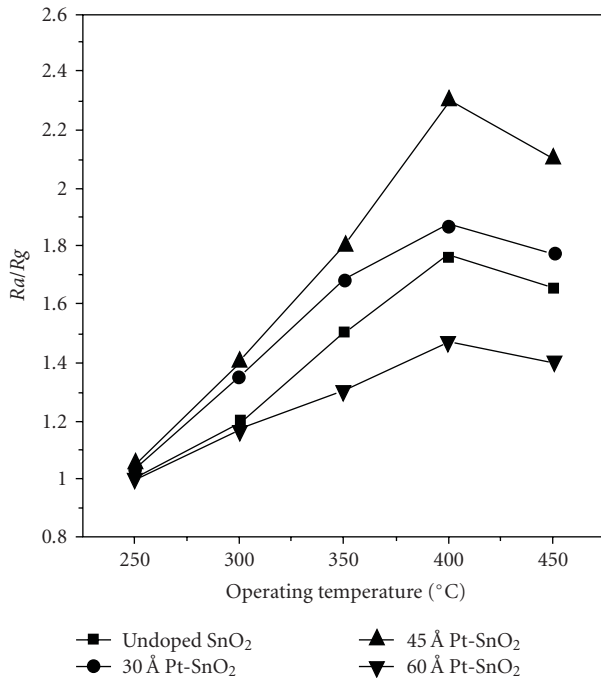


FIGURE 7: Response to 5000 ppm CH₄ as a function of operating temperature for undoped SnO₂ sensors with and without the Pt layers.

trap hydrogen and an alkyl radical is being created. The radical reacts to give a second homolytic C–H bond dissociation and to form an alkene and a second OH–bond on the surface. Finally, the whole process yields an alkene, which then gets oxidized to CO, CO₂, and other subproducts. The SnO₂ films were found suitable for this purpose at 650°C.

Recently Vaishampayan et al. [91], studied the response of the pristine SnO₂ and Pd: SnO₂ towards different reducing gases. The 1.5 mol% Pd doping showed an enhancement in response to 75% and 95% towards LPG at as low a temperature as 50°C and 100°C, respectively, quite promising compared to pristine SnO₂. Structural characterizations revealed that Pd doping reduces the crystallite size of SnO₂ and helps in forming distinct spherical nanospheres at a calcination temperature of 500°C. Thus the increase in LPG response can be correlated with the spherical morphology and decrease in the crystallite size (11 nm) of SnO₂ due to doping with Pd as compared with the pristine SnO₂ (26 nm) and the role of Pd as a catalyst.

Cabot et al. studied [92] a correlation between the catalytic activity and the sensor response of different modified SnO₂ samples to CH₄ as target gas. It was found that the catalytic oxidation of methane is more pronounced for Pd than Pt. Recently Das et al. [93] observed that nanosized (3.5–14.0 nm) tin dioxide powders can be prepared by sonication-assisted precipitation. Thick films prepared by using such powders showed very good methane response because the resistance of the films in air at an operating temperature of 350°C was much less than that of the films prepared by conventionally precipitated powder. Also such sonication-assisted precipitated powder needs a lower

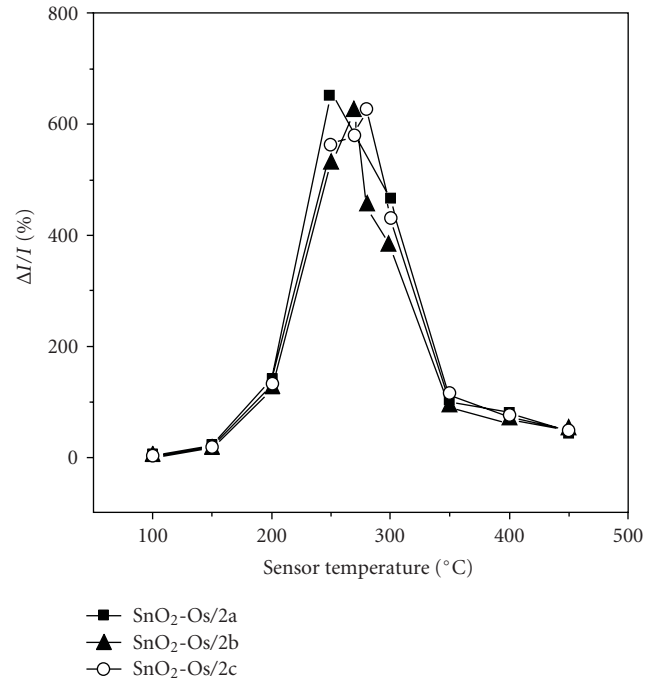


FIGURE 8: Response versus operating temperature for three Os-doped SnO₂ samples (2a, 2b, 2c are three SnO₂: Os samples doped with different Os concentrations).

amount of antimony doping for fabrication of real life gas sensors.

The undoped and 0.1 wt.% Ca-doped SnO₂ thin films were deposited by ion beam sputtering and were covered by 30–60 Å Pt layers that was annealed at 650°C. The methane sensors made of this film were tested in the temperature range 250–450°C. The best CH₄ response [94] was obtained at 400°C for a film with an optimal Pt thickness of 45 Å (Figure 7). Further it was found that the humidity dependence of CH₄ sensing up to 5000 ppm was relatively small because of the dense film structures.

Recently it was reported that Fe doped SnO₂ thick films also show response towards methane [95]. Quaranta et al. [96] studied the methane sensing properties of osmium-doped SnO₂ films that were prepared by Sol-gel technique using SnCl₄ and OsCl₃ precursors. The experimental data reported in this work show that Os doping improves the gas sensitive properties of the tin oxide thin films by enhancing the response to CH₄ and simultaneously by lowering the operating temperature that is shown in Figure 8. This is a promising work for producing a low-cost methane sensor. Probably, the role of Os is to act as a covalent site for catalyzing the oxidation of CH₄. Obviously, the reduction in the optimum operating temperature could lead to a cross-response effect, for example, response by CO. However, by using sensor in an array configuration, in which the interfering effects should not be a drawback, the problem of cross sensitivity may be solved. However, further studies are necessary to understand the true role of osmium in the catalytic property, reactivity, selectivity, and ageing effect in presence of interfering gases.

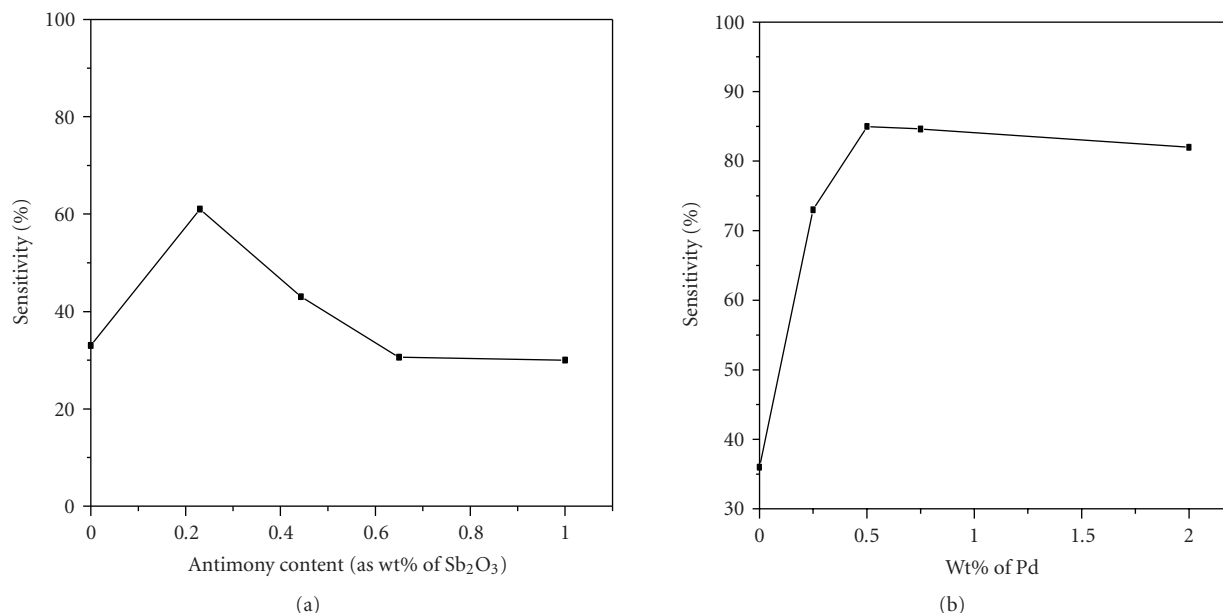


FIGURE 9: (a) Effect of antimony doping of tin dioxide on methane sensitivity and (b) effect of palladium concentration on methane sensitivity of tin dioxide.

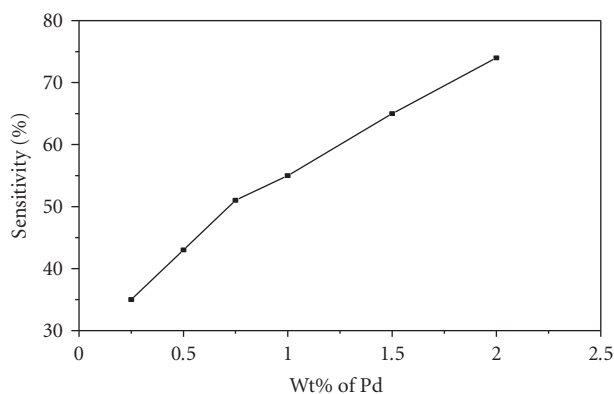


FIGURE 10: Effect of palladium concentration on methane sensitivity of antimony doped (0.5 wt.% as Sb₂O₃) tin dioxide coatings.

Chatterjee et al. [97] reported methane sensing characteristics of antimony-doped SnO₂ prepared by simultaneous precipitation of tin dioxide and antimony (0–1 wt.% as Sb₂O₃), tin dioxide and palladium (0–2 wt.% as Pd), tin dioxide with a fixed amount of antimony (0.5 wt.% as Sb₂O₃) and palladium (0–2 wt.% as Pd). Figures 9(a) and 9(b) demonstrate the dependence of methane sensitivity on antimony and palladium content in SnO₂ coating, respectively.

It was found that the antimony doping in small amounts gradually lowers the sensor resistance and there is an optimum antimony concentration (0.25%) where the response for methane is maximum (Figure 9(a))

The response of undoped tin dioxide for methane is maximum at 0.5 wt.% palladium (Figure 9(b)), but no such response saturation has been observed for palladium

concentration up to 2 wt.% for antimony doped tin dioxide samples (Figure 10).

Kim et al. [98] prepared SnO₂ from SnCl₄ by a precipitation method using an aqueous ammonia solution of SnCl₄. The response of this sensor to methane at 658 K was higher than that with supported Pd, Pt, Rh, or Ni catalyst. This sensor responded to methane in the range 500–10,000 ppm with sufficiently high response and response rates, though it also responded to many other gases. Such an excellent promoting effect of the supported Pd (Figure 11) catalyst is considered to originate from the high dispersion of Pd (or PdO) particles supported in addition to the high intrinsic activity of Pd for the catalytic oxidation of methane.

Urfels et al. [99] reported that Pt supported on high surface area tin (IV) oxide appears as a superior catalyst for the complete oxidation of traces of methane at low temperature, being even significantly more active than reference Pd/Al₂O₃ in the presence of large amounts of water in the feed. This is due to the fact that the inhibition of water on the catalytic activity is not as strong as for Pd/Al₂O₃. Pt/SnO₂ [100] is however more severely deactivated than Pd/Al₂O₃ upon steam ageing at 873 K and that would predict a shorter lifetime compared to Pd catalysts [12]. The presence of H₂S induces a strong and irreversible deactivation of Pt/SnO₂. The activity is hardly restored by treatment under oxidizing atmosphere below 773 K due to the stability of poisoning species.

Chakraborty et al. reported [101] a thick film methane sensor that was fabricated from nanosized tin dioxide powder containing antimony oxide and palladium. Thick film sensors, prepared with such powders, showed good methane response and nearly equivalent sensing properties of imported Figaro (Japan) sensors. Han et al. [102] worked on SnO₂ based-gas sensors and it was found that Fe₂O₃

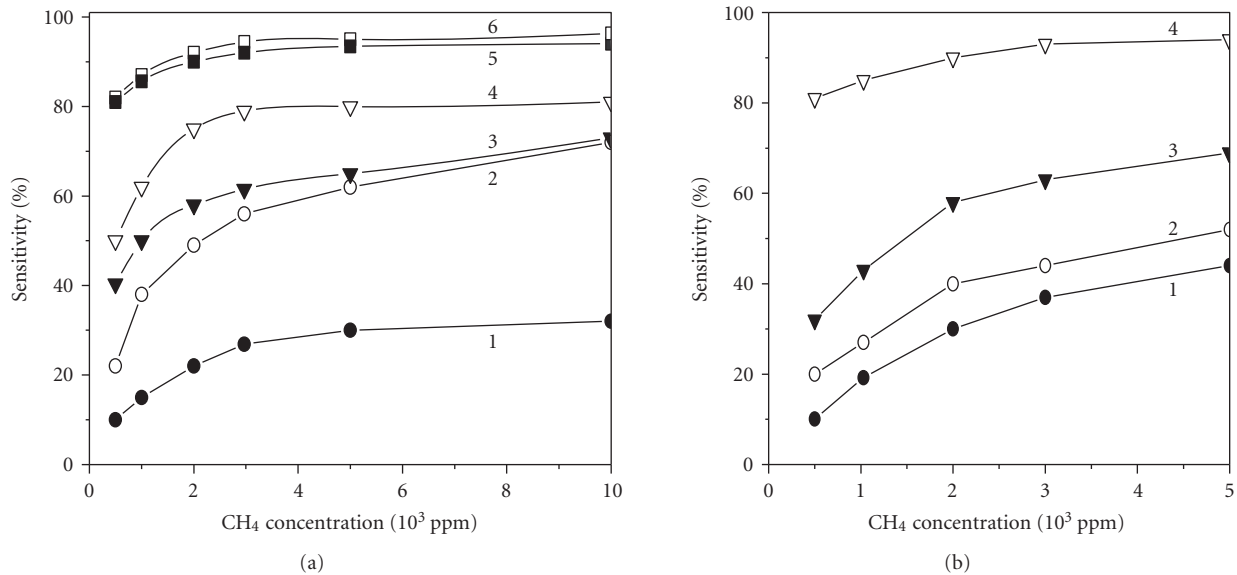


FIGURE 11: (a) The sensitivities of SnO₂-based sensors having various combinations of additives (Ca and Pt) and alumina supported metal catalysts (Pd and Pt) to methane at 658 K as a function of methane concentration. The additives (0.1 wt.%) were added to SnO₂ by a coprecipitation method, while the supported catalysts (5 wt.%) were mixed with SnO₂ powder. (1) SnO₂ (pure), (2) SnO₂ (Ca), (3) SnO₂ (Ca, Pt), (4) SnO₂ (pure) + Pt:alumina, (5) SnO₂ (pure) + Pd:alumina, and (6) SnO₂ (Ca,Pt) + Pd:alumina. (b) Influences of Pd loading methods on the methane sensitivities at 658 K (net Pd loading: 0.25 wt.%). (1) Impregnation from PdCl₂ solution. (2) Physical mixing of Pd black. (3) Rinsing method. (4) Physical mixing of Pd: alumina.

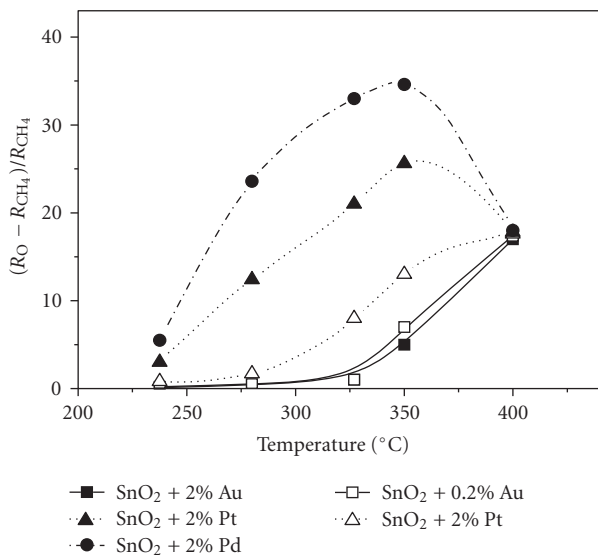


FIGURE 12: Sensor response to 1000 ppm CH₄ as a function of the operating temperature. Open symbols correspond to the SnO₂ materials with a nominal 0.2% additive concentration and black symbols correspond to those with 2% additive.

was a more effective additive than Pd or Pt. It showed high response and high selectivity for H₂, CH₄, and C₄H₁₀ and a little cross-sensitivity to ethanol and smoke. Malyshev and Pisyakov and his group [103] developed a production process of thick-film semiconductor gas sensors. The sensors

were proved to be highly efficient for detection of methane, hexane, hydrogen, carbon monoxide, ammonia, hydrogen sulphide, and ethanol. Saha et al. [104] studied the role of alumina on the methane response of the tin oxide thin films and a good response was observed. Above 350°C, in contrast to pure tin dioxide coatings, the methane response of iron doped tin dioxide coatings drastically decreased. The nanocomposites based on Sn, In, and Ti oxides were successfully derived by Chen et al. [105] with high response and selectivity for methane through optimizing the preparation parameters. Enhancement of gas-sensing properties of the semiconducting methane sensor could be attributed to the smaller crystallite size of SnO₂, the adsorption behavior and the chemical reaction of methane and O₂ on the composite surface, and to the introduction of the additives. The sensing behavior was directly related to the catalytic activity for methane oxidation.

5.2. Nanocrystalline ZnO. ZnO is a promising material for gas sensor. So far ZnO-based devices have attracted much attention as gas sensors because of their chemical response to different adsorbed gases, high chemical stability, amenability to doping, no toxicity, and low cost. ZnO gas sensors can be used not only for detecting the leakage of inflammable gases and toxic gases but also for controlling domestic gas boilers. Zinc oxide is a wide band gap semiconductor with many important properties, which make it commonly used in electronic and optoelectronic applications. Polycrystalline ZnO has been widely used in electronic industry. Pure ZnO is an intrinsic II-VI compound semiconductor with a band

gap of 3.2 eV at room temperature (30°C) and high exciton binding energy (60 meV). The nature of absorption shows that ZnO is a direct band gap semiconductor. The creation of native defects during preparation makes ZnO normally *n*-type [106–108]. The nonstoichiometry arises due to excess zinc interstitials or oxygen vacancies or both which make ZnO *n*-type semiconductor.

ZnO films can be prepared by many methods, such as thermal oxidation of Zn metallic films [109], sol gel process [110], sputtering [111], chemical vapor deposition [112], pulse laser deposition [113], evaporating method [114], and electrochemical process [115, 116].

For the last couple of years investigations on the development of a low-temperature methane detector using nanocrystalline ZnO-based chemical gas sensors with noble metals as the catalytic metal contacts have become quite important. The challenge is to attain the high response of low ppm testing gases, short response and recovery time, selectivity, and long-range stability. Nanocrystalline ZnO thin films demonstrate remarkable gas-sensing properties when the crystallite size becomes comparable to Debye length. Further, nanocrystalline and porous materials with controlled composition are of increasing interest in gas sensing because of their large surface to volume ratio that enhances the reaction probability between the adsorbed oxygen and methane gas.

Mitra and Mukhopadhyay [117] reported Methane (CH₄) response of zinc oxide (ZnO) thin film. The catalyst layer was formed on the surface of semiconducting ZnO following a wet chemical process from palladium chloride (PdCl₂) solution. A reasonable response of approximately 86%, fast response time of less than one minute, and a moderately fast recovery (approximately 3 minutes) are observed at 200°C. Although the operating temperature of 200°C is relatively on the lower side, the maximum response of 86% should be somewhat higher for application purpose.

Recently the methane sensing temperature between 210°C and 250°C is reported [118–120] depending upon whether the ZnO sensing film was grown electrochemically or by a sol-gel method, respectively. But these relatively high temperatures for detection of methane are still not suitable for applications in the coalmines.

The functional characteristics of the gas sensors, for example, response, response time, and recovery time were improved over the resistive Taguchi type sensors by adopting Schottky structures with catalytic metal contact. The vertical structure fabricated by growing metal oxides on the conducting surface and depositing a catalytic metal on the oxide improves the functional properties of the sensor devices because the electrons generated in the catalytic metal-oxide interface can be collected by the second electrode in the back with minimum carrier annihilation in the transport mechanism. Fonash [121] first studied the MIM configurations. The basic principle of the current conduction mechanism of an MIM sensor is that the electrons move from the upper metal electrode to the lower one through the active insulating layer vertically on the basis of back-to-back Schottky barrier junctions. In the MIM configuration

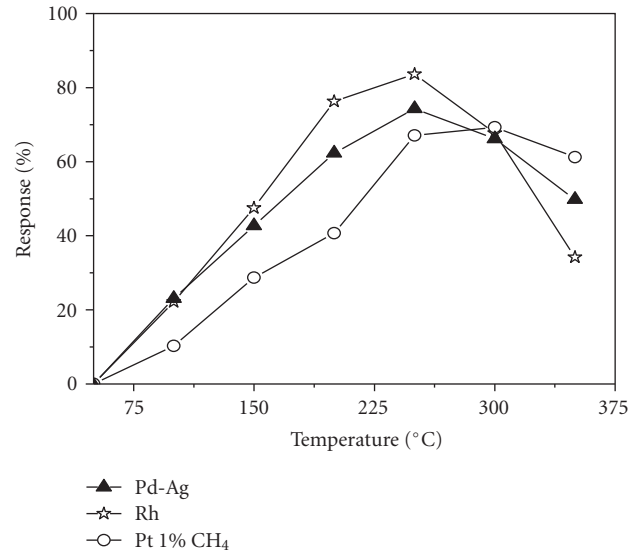


FIGURE 13: Response magnitude as a function of temperature for Pd-Ag, Rh, and Pt contacts.

since Zn contact to ZnO layer is ohmic by nature, only noble metal/ZnO junction acts as the barrier against electron flow. Room temperature hydrogen sensor using ZnO MIM structure was first reported by Dutta and Basu [122]. There are very few reports on Zinc oxide-based methane gas sensors with high response and faster response time and recovery time. So far the reported sensor structures on the oxide-based semiconductors and operating in the resistive mode at high temperatures showed longer response and recovery time [118–127].

Bhattacharyya et al. [120] studied the sol-gel grown ZnO-based gas sensors in the resistive mode. Pd-Ag and Rh contacts were found to produce a relatively lower optimum temperature of 250°C for sensing compared to 300°C for Pt contact. Further, Rh contact showed the higher response (83.6%) than Pd-Ag and Pt (Figure 13). It was further reported that the response and recovery time are shorter for Pd-Ag compared to Rh and Pt contacts, most probably due to the fact that solubility and diffusivity of hydrogen obtained from methane dissociation is higher for Pd-Ag compared to both Pt and Rh [128–131].

Basu et al. [126, 127] have studied electrochemically grown ZnO-based MIM Schottky gas sensors and the effect of different catalyst metals (Rh, Pt, and Pd-Ag) on methane sensing. The response versus temperature curves for different noble metal catalysts in pure nitrogen is shown in Figure 14 and it is observed that Rh gives higher response than Pd-Ag and Pt (Rh>Pd-Ag>Pt). In fact, the catalytic effect of Rh for dissociation of methane or hydrogen is stronger than Pd and Pt. In literature, it can be found that catalytic activity of Pd and Pt on methane or hydrogen is more or less the same [128–131]. But Figure 14 shows a higher response with Pd-Ag than Pt and thus contradicts the reported results. Figure 14(b) further shows that the response is somewhat reduced in synthetic air. It was reported that the oxygen is parallelly chemisorbed on the noble metal and there is a

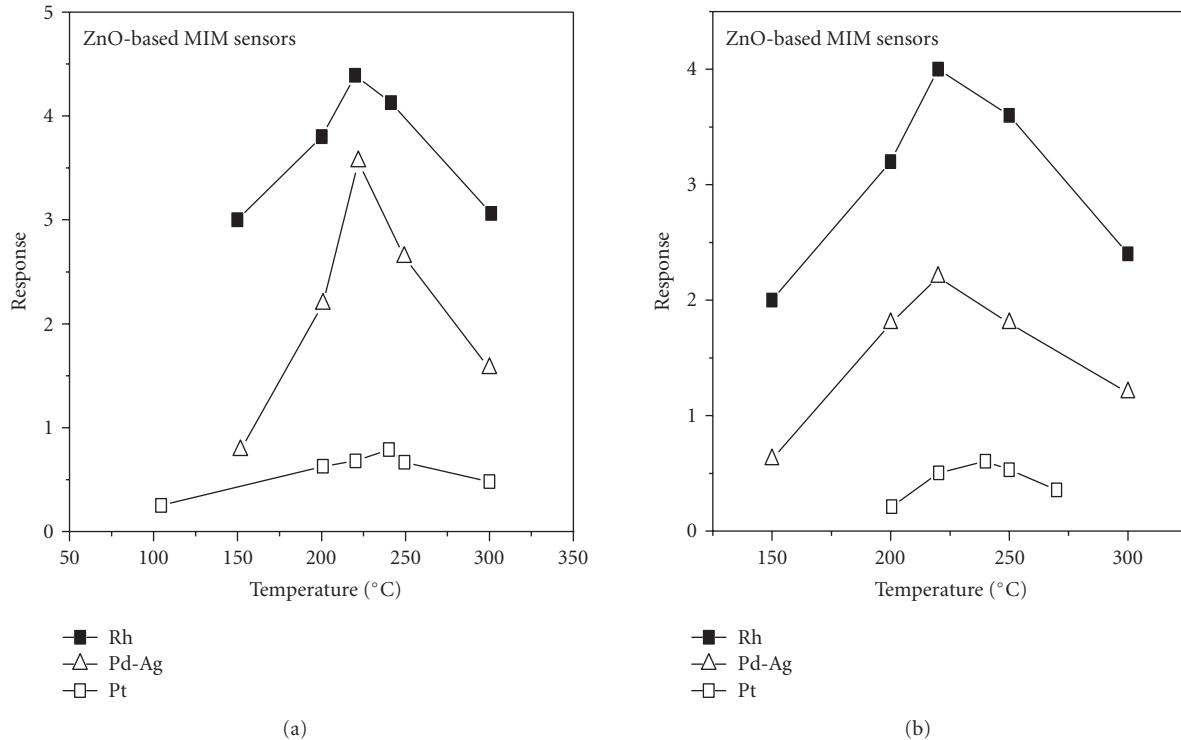


FIGURE 14: Response versus temperature curves of Pt/ZnO/ZnO, Pd-Ag (26%)/ZnO/Zn, and Rh/ZnO/Zn MIM sensors in the presence of 1% methane in (a) pure nitrogen and in (b) synthetic air.

competitive equilibrium between oxygen and hydrogen as the adsorbates on ZnO. As a result it may well be depicted that the adsorption sites for hydrogen are reduced and chemisorbed hydrogen reacts with oxygen instead of getting diffused into the noble metal/ZnO junction to produce H_2O molecules and thus reduce the current through the electrodes [126, 127]. Therefore, a lower response to hydrogen is obtained in synthetic air. The reactivity depends on the catalytic properties of the metal surface and differs between different metals. Since the OH formation energy barrier is much lower on Pt than Pd-Ag, most of the hydrogen produced by the dissociation of methane produces OH molecule for Pt contact. Then the water formation needs more than one step and thus the kinetics of sensing becomes slower.

Therefore, the devices using Pt as catalytic metal exhibit lower response and relatively longer response time than Pd-Ag for all the cases. The OH formation energy of Rh is higher than both Pd-Ag and Pt [128–131] and so Rh catalytic metal contact gives higher response than Pd-Ag and Pt. This corroborates the experimental results obtained by Bhattacharyya et al. [120].

Recently Bhattacharyya et al. [125] reported a ZnO-based resistive sensors with Au and Pd-Ag contact. The ZnO thin film was deposited by Sol-gel method. The crystal size of the films was in the range 45 nm–75 nm. The surface morphology studies revealed randomly oriented grains with hexagonal structure and a large number of

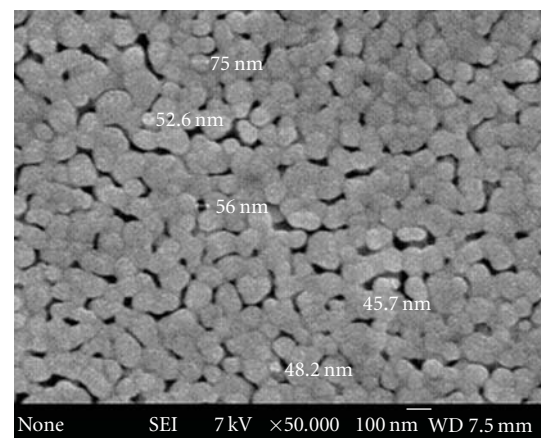


FIGURE 15: SEM images of the sol-gel grown nanocrystalline ZnO surface annealed at 600°C for 30 minutes.

pores of an average diameter 56 nm (Figure 15) that is very useful for methane gas sensing. It can be found that the operating temperature of sensing with Au contact was 350°C and it was reduced to 250°C (Figure 16) by using Pd-Ag catalytic contact with a response 74.3% and a response time ~16 seconds.

The same group reported a Pd-Ag/ZnO/Zn MIM methane sensor using sol-gel grown ZnO thin film, with

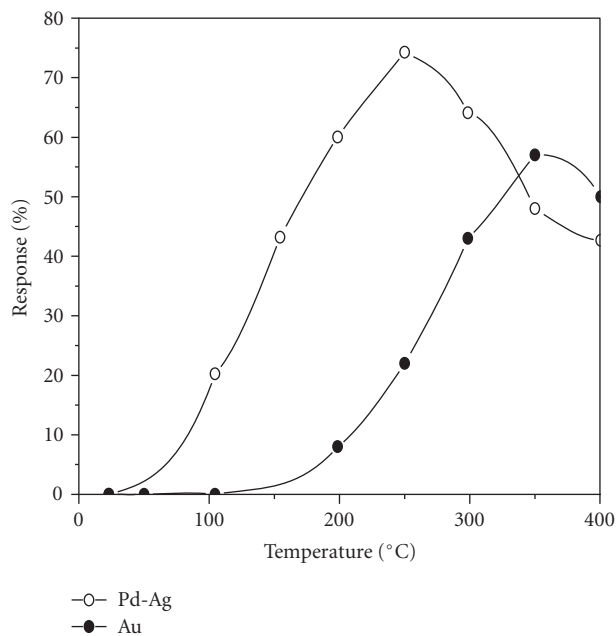


FIGURE 16: Response as a function of temperature.

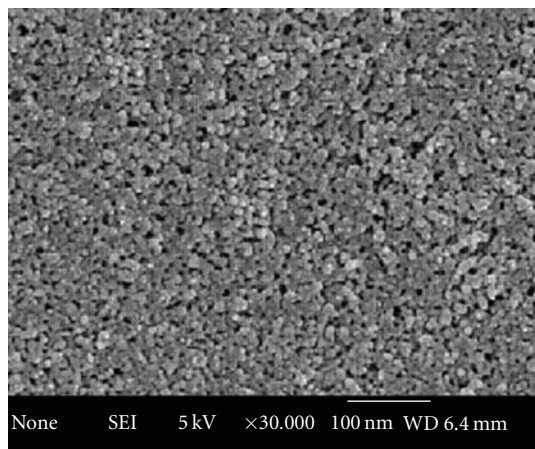


FIGURE 17: FESEM pictures of ZnO thin films grown electrochemically, with the magnification ($\times 30\,000$).

an operating temperature of 250°C and a response time ~ 11 seconds.

Basu [132] reduced the operating temperature of methane sensing to 100°C or less by using electrochemically grown nanocrystalline-nanoporous ZnO thin film and by modifying the oxide surface with Pd. Two different device configurations, for example, a planar structure and a metal-active insulator-metal (MIM) sandwich structure, both working on Schottky barrier mode were designed, fabricated, and tested for methane sensing. Pd-Ag alloy was used as the catalytic electrode ($0.2\ \mu\text{m}$) contact for both the planar and MIM configurations.

Figure 17 shows the FESEM picture of the electrochemically grown nanocrystalline ZnO thin film. The crystallite size obtained was below $10\ \text{nm}$ with a uniform distribution of the nanopores (size).

The variations of the response with operating temperature and with biasing voltage using 1% methane in nitrogen and in synthetic air were studied. The maximum response was obtained at 70°C and 100°C for the planar and the MIM sensor structures, respectively, with $3\ \text{V}$ forward bias for both (Figures 18 and 19).

The Pd-modified nanocrystalline ZnO (below $10\ \text{nm}$) enhances the oxygen spillover process on ZnO matrix, resulting in a large amount of chemisorbed oxygen that yields a high electrostatic potential across the Pd-Ag/ZnO Schottky interface.

The change of current in presence of methane is relatively higher for the planar structure that has two Schottky contacts with double barriers compared to the MIM structure with one Pd-Ag/ZnO junction. The performance was somewhat reduced in synthetic air for both the sensor structures due to a competitive equilibrium between oxygen (from air) and hydrogen as the adsorbates on ZnO. As a result the adsorption sites for hydrogen and thus the amount of hydrogen diffusing across the Pd-Ag/ZnO junction are reduced. The temperature for maximum response was reduced to 70°C for the planar and 100°C for the MIM structures for the Pd-modified ZnO nanocrystals. The possible reason for the response at substantially low temperature was mentioned as due to increased surface free energy of the nanocrystalline ZnO surface. Presence of dispersed Pd nano particles over ZnO surface further reduces the adsorption energy. As a result the sensors respond at considerably low temperature and with short time of response. It is worth mentioning here that imperfect structural orientation of the polycrystalline sensing layer (ZnO) also modulates the gas adsorption behavior and thus the sensing parameters.

Figure 20 demonstrates that the sensors using Pd modified ZnO thin films show temperature dependent selectivity for methane and hydrogen in presence of each other. For the planar sensors hydrogen response is maximum at 50°C where the response for methane is very low. At 70°C both hydrogen and methane respond almost to the same extent. On the other hand, MIM sensors show distinct selectivity for methane at 100°C where hydrogen response is almost zero.

Methane actually first dissociates to produce molecular hydrogen that subsequently decomposes catalytically to atomic hydrogen. The atomic hydrogen then takes part in gas sensing reaction. Therefore, the temperature for sensing methane is always higher than that of hydrogen.

The response time and recovery time were calculated from the transient response curves for different concentrations of methane and are shown in Table 1.

Table 1 shows that the response and recovery times of the MIM sensor are relatively shorter than the planar sensor. The possible interpretation has been given that the separation between two electrodes for the planar configuration is larger ($2\ \text{mm}$) than the MIM ($8\ \mu\text{m}$) configuration, resulting in the rapid current flow kinetics for the MIM configuration.

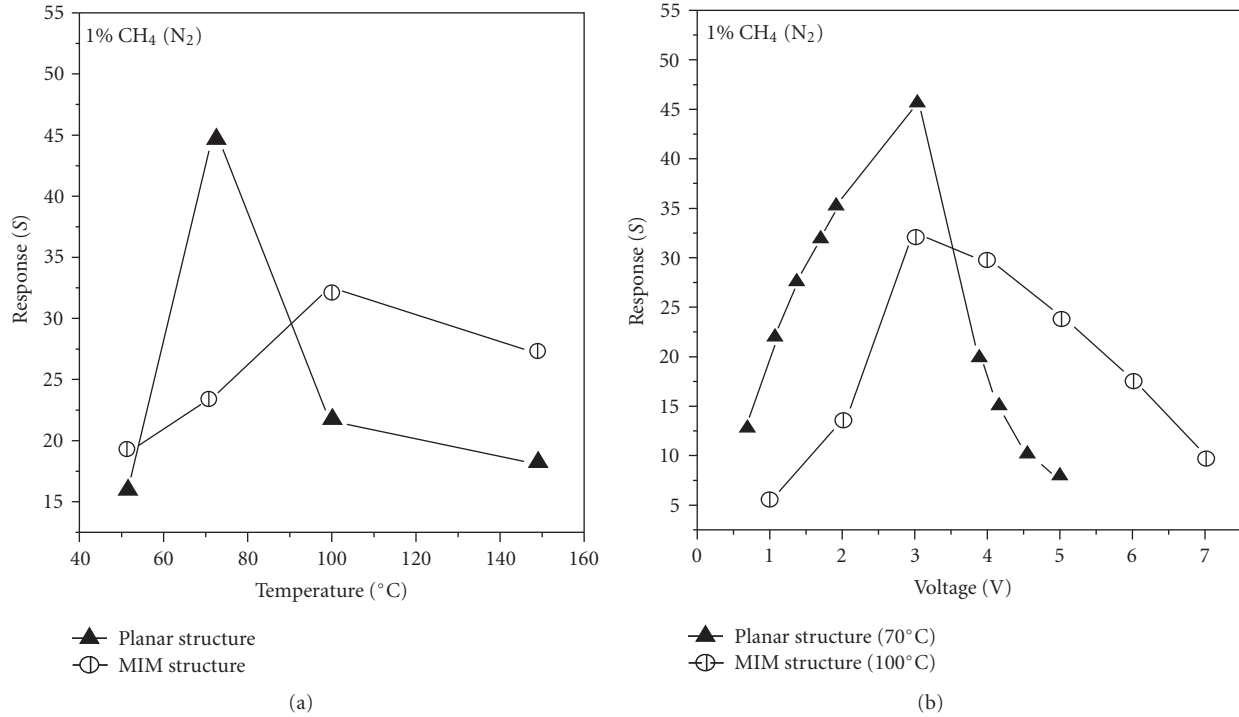


FIGURE 18: (a) Response versus temperature curves at 3 V and (b) response versus voltage curves, for planar and MIM sensor structures at 70°C and 100°C.

TABLE 1: The sensing results of the planar structures at 70°C and MIM structures at 100°C for different concentrations of methane using nitrogen and synthetic air as carrier gases.

% CH ₄	Response				Response time (s)				Recovery time (s)			
	Planar		MIM		Planar		MIM		Planar		MIM	
	Nitrogen	Synthetic air	Nitrogen	Synthetic air	Nitrogen	Synthetic air	Nitrogen	Synthetic air	Nitrogen	Synthetic air	Nitrogen	Synthetic air
0.01	21.2	9.2	18.2	6.5	16.2	19.2	10.2	13.2	33.2	34.2	18.7	20.3
0.05	25.4	14.6	22.3	11.4	13.3	17.4	6.7	9.3	30.3	32.8	17.2	19.2
0.1	39.3	18.3	23.2	16.8	11.1	16.4	6.03	8.2	27.5	29.6	16.8	17.3
0.5	42.2	21.6	25.2	17.2	8.4	15.2	4.02	6.9	25.7	27.4	16.1	17.1
1	47.5	25.7	32.2	20.4	4.6	12.6	2.69	4.2	22.7	23.4	16.0	16.2

The longer time of recovery was due to slower rate of desorption being interfered by the presence of air after the methane flow was cut off.

This investigation highlights the fact that the temperature of sensing methane at 100°C using Pd-Ag/Pd: ZnO/Zn MIM device configuration is suitable for practical applications as due to minimum interference from humidity.

There are very few reports on metal oxide-based methane gas sensors with high response and shorter response and recovery time. So far the reported sensor structures based on oxide semiconductors and operating in the resistive mode at high temperature showed relatively longer response (>10 seconds) and recovery (>40 seconds) time for methane sensing. In this investigation, particularly the

MIM sensor showed good response (~32), shorter response (~2.69 seconds), and recovery (~16 seconds) times as compared to the values reported by others [1–7, 91–105, 118–127, 133, 134].

Figure 21 presents the stability of both types of sensor structures. For 1% methane in nitrogen as carrier gas the study was continued for 33 days and showed a stable performance. In synthetic air the stability studied for about 9 hours was appreciably good.

5.3. Other Metal Oxide-Based Methane Gas Sensors. Apart from the ZnO-and SnO₂-based gas sensors, there are few metal oxides that give response towards the methane.

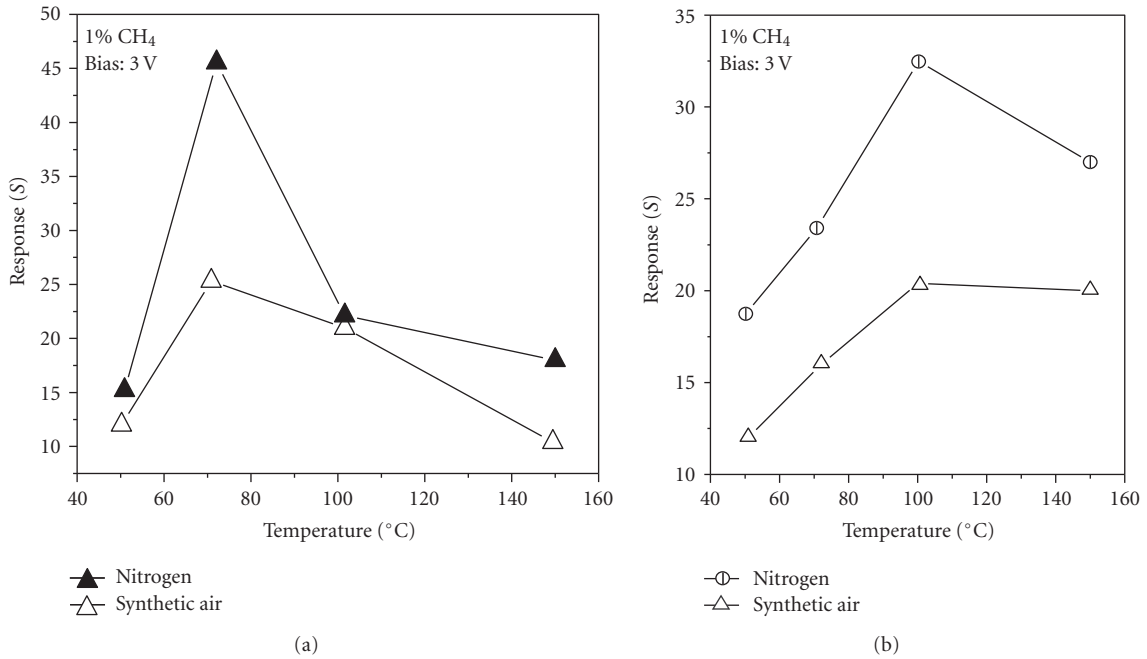


FIGURE 19: Response versus temperature curves of (a) the planar and (b) the MIM sensor structures at 3 V in the presence of 1% methane in pure nitrogen and in synthetic air.

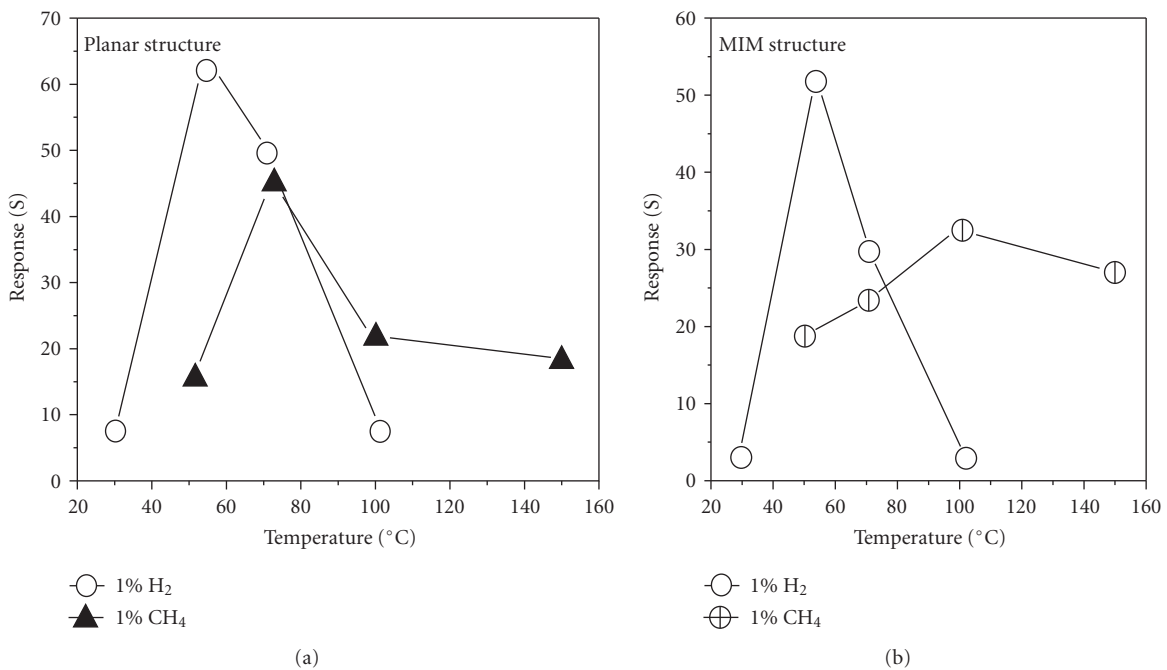


FIGURE 20: Response versus temperature plots of (a) the planar and (b) the MIM sensors in 1% H₂ and 1% CH₄ in pure N₂ environment.

Selective detection of methane in domestic environments using a catalyst sensor system based on Ga₂O₃ was reported by Flingelli et al. [133], and it was found that the use of catalytic gas filters consisting of porous Ga₂O₃ is very efficient to eliminate cross sensitivities to ethanol and organic

solvents. This technique yields selective sensors for indoor methane detection and this type of catalyst filter is very promising in term of robustness. Moreover, no expensive catalytic material like platinum is required. Recently, MoO₃-based CH₄ sensors were also reported [134]. However, the

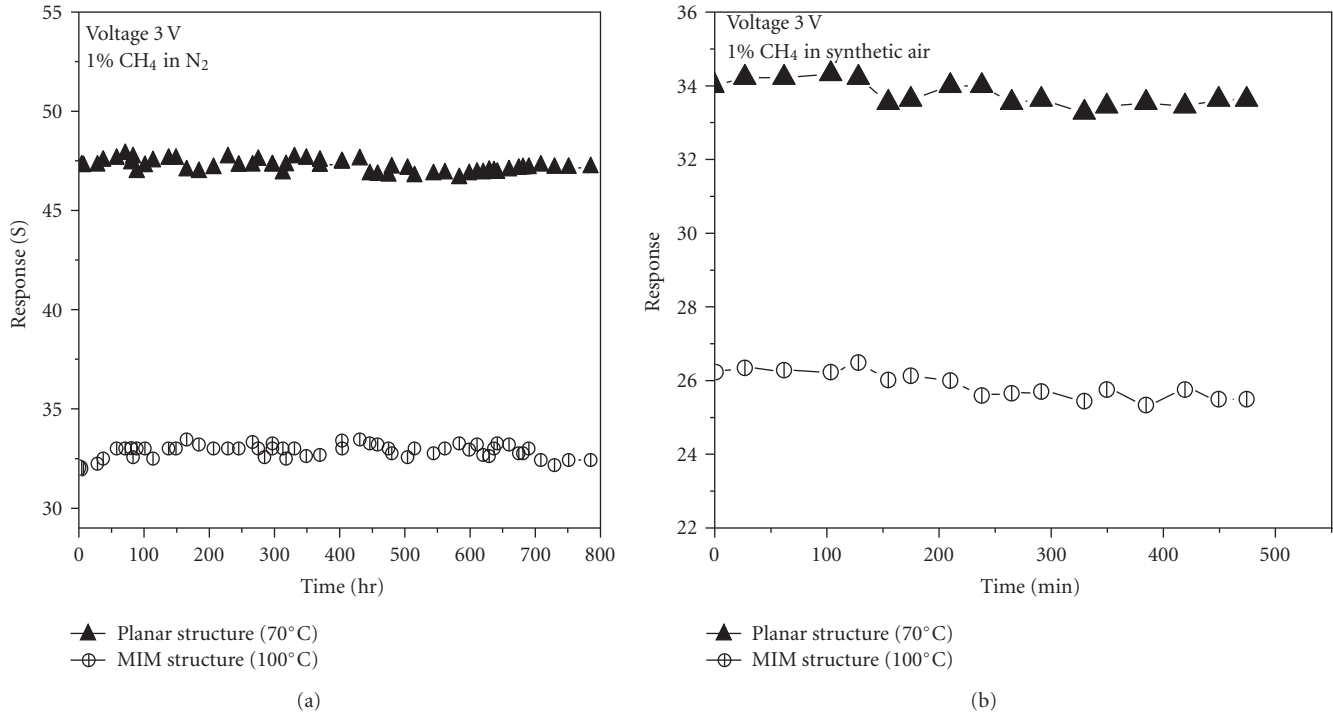


FIGURE 21: Stability study of both types of sensor structures using nitrogen as carrier gases.

sensor was operated at 500°C and the sensitivity for methane was quite poor.

6. Conclusion

This review article has focused on the recent achievement on the research and development of methane gas sensors using inexpensive metal oxides and the effect of noble metals, either as catalytic contact electrodes or as the sensitizing agents. Among them SnO₂ and ZnO sensors have been widely studied and have shown most promising results on gas response in terms of sensing temperature and voltage, sensitivity, time of response and stability. Nanocrystalline ZnO, after sensitization with Pd nanoparticles has shown the lowest temperature of methane sensing so far reported. Gas sensing mechanism has been briefly discussed from the point of view adsorption-desorption activation and the influence of noble metals.

Acknowledgments

The authors thankfully acknowledge the help and cooperation of Prof. H. Saha, Coordinator, and IC Design & Fabrication Centre, Department of Electronics & Telecommunication Engineering, Jadavpur University, Kolkata, for kindly providing the laboratory facilities. Thanks are also due to Dr. P. Bhattacharya, Ms. N. Saha, and Mr. S. K. Jana of the gas sensor group. P. K. Basu acknowledges CSIR, Government of India, for kindly providing a Senior Research Fellowship (SRF).

References

- [1] M. Fleischer and H. Meixner, "A selective CH₄ sensor using semiconducting Ga₂O₃ thin films based on temperature switching of multigas reactions," *Sensors and Actuators B*, vol. 25, no. 1–3, pp. 544–547, 1995.
- [2] J. Wöllenstein, M. Burgmair, G. Plescher, et al., "Cobalt oxide based gas sensors on silicon substrate for operation at low temperatures," *Sensors and Actuators B*, vol. 93, no. 1–3, pp. 442–448, 2003.
- [3] J. B. W. H. Brattain, "Surface properties of germanium," *Bell System Technical Journal*, vol. 32, 1952.
- [4] D. M. Wilson, S. Hoyt, J. Janata, K. Booksh, and L. Obando, "Chemical sensors for portable, handheld field instruments," *IEEE Sensors Journal*, vol. 1, no. 4, pp. 256–274, 2001.
- [5] J. Xu, Q. Pan, Y. Shun, and Z. Tian, "Grain size control and gas sensing properties of ZnO gas sensor," *Sensors and Actuators B*, vol. 66, no. 1, pp. 277–279, 2000.
- [6] A. Trinchi, S. Kaciulis, L. Pandolfi, et al., "Characterization of Ga₂O₃ based MRISiC hydrogen gas sensors," *Sensors and Actuators B*, vol. 103, no. 1–2, pp. 129–135, 2004.
- [7] X. Chen, W. Lu, W. Zhu, S. Y. Lim, and S. A. Akbar, "Structural and thermal analyses on phase evolution of sol-gel (Ba,Sr)TiO₃ thin films," *Surface and Coatings Technology*, vol. 167, no. 2–3, pp. 203–206, 2003.
- [8] E. Comini, M. Ferroni, V. Guidi, G. Faglia, G. Martinelli, and G. Sberveglieri, "Nanostructured mixed oxides compounds for gas sensing applications," *Sensors and Actuators B*, vol. 84, no. 1, pp. 26–32, 2002.
- [9] M. Rumyantseva, V. Kovalenko, A. Gaskov, et al., "Nanocomposites SnO₂/Fe₂O₃: sensor and catalytic properties," *Sensors and Actuators B*, vol. 118, no. 1–2, pp. 208–214, 2006.

- [10] T. Islam and H. Saha, "Hysteresis compensation of a porous silicon relative humidity sensor using ANN technique," *Sensors and Actuators B*, vol. 114, no. 1, pp. 334–343, 2006.
- [11] G. Kenanakis, D. Vernardou, E. Koudoumas, G. Kiriakidis, and N. Katsarakis, "Ozone sensing properties of ZnO nanostructures grown by the aqueous chemical growth technique," *Sensors and Actuators B*, vol. 124, no. 1, pp. 187–191, 2007.
- [12] A. Teleki, S. E. Pratsinis, K. Kalyanasundaram, and P. I. Gouma, "Sensing of organic vapors by flame-made TiO₂ nanoparticles," *Sensors and Actuators B*, vol. 119, no. 2, pp. 683–690, 2006.
- [13] J. Wöllenstein, M. Burgmair, G. Plescher, et al., "Cobalt oxide based gas sensors on silicon substrate for operation at low temperatures," *Sensors and Actuators B*, vol. 93, no. 1–3, pp. 442–448, 2003.
- [14] A. Trinch, W. Wlodarski, Y. X. Li, G. Feglia, and G. Sberveglieri, "Pt,Ga₂O₃/SiC MRSiC devices: a study of the hydrogen response," *Journal of Physics D*, vol. 38, p. 754, 2005.
- [15] L. Talazac, F. Barbarin, C. Varenne, L. Mazet, S. Pellier, and C. Soulier, "Gas sensing properties of pseudo-Schottky diodes on p-type indium phosphide substrates—application to O₃ and NO₂ monitoring in urban ambient air," *Sensors and Actuators B*, vol. 83, no. 1–3, pp. 149–159, 2002.
- [16] K.-W. Lin, H.-I. Chen, C.-T. Lu, et al., "A hydrogen sensing Pd/InGaP metal-semiconductor (MS) Schottky diode hydrogen sensor," *Semiconductor Science and Technology*, vol. 18, no. 7, pp. 615–619, 2003.
- [17] P. K. Basu, S. K. Jana, M. K. Mitra, H. Saha, and S. Basu, "Hydrogen gas sensors using anodically prepared and surface modified nanoporous ZnO thin films," *Sensor Letters*, vol. 6, no. 5, pp. 699–704, 2008.
- [18] P. K. Basu, P. Bhattacharyya, N. Saha, H. Saha, and S. Basu, "Methane sensing properties of platinum catalysed nano porous zinc oxide thin films derived by electrochemical anodization," *Sensor Letters*, vol. 6, no. 1, pp. 219–225, 2008.
- [19] M. Stamatakis, D. Tsamakidis, N. Brilis, I. Fasaki, A. Gian-noudakos, and M. Kompitsas, "Hydrogen gas sensors based on PLD grown NiO thin film structures," *Physica Status Solidi*, vol. 205, no. 8, pp. 2064–2068, 2008.
- [20] S. Basu and S. K. Hazra, "ZnO p-n homojunctions for hydrogen gas sensors at elevated temperature," *Asian Journal of Physics*, vol. 14, p. 65, 2005.
- [21] S. K. Hazra and S. Basu, "Hydrogen sensitivity of ZnO p-n homojunctions," *Sensors and Actuators B*, vol. 117, no. 1, pp. 177–182, 2006.
- [22] K.-K. Baek and H. L. Tuller, "Electronic characterization of ZnO/CuO heterojunctions," *Sensors and Actuators B*, vol. 13, no. 1–3, pp. 238–240, 1993.
- [23] Y. Ushio, M. Miyayama, and H. Yanagida, "Effects of interface states on gas-sensing properties of a CuO/ZnO thin-film heterojunction," *Sensors and Actuators B*, vol. 17, no. 3, pp. 221–226, 1994.
- [24] Y. Hu, X. Zhou, Q. Han, Q. Cao, and Y. Huang, "Sensing properties of CuO-ZnO heterojunction gas sensors," *Materials Science and Engineering B*, vol. 99, no. 1–3, pp. 41–43, 2003.
- [25] Z. Ling, C. Leach, and R. Freer, "Heterojunction gas sensors for environmental NO₂ and CO₂ monitoring," *Journal of the European Ceramic Society*, vol. 21, no. 10–11, pp. 1977–1980, 2001.
- [26] W.-Y. Chung, D.-D. Lee, and B.-K. Sohn, "Effects of added TiO₂ on the characteristics of SnO₂-based thick film gas sensors," *Thin Solid Films*, vol. 221, no. 1–2, pp. 304–310, 1992.
- [27] K. Zakrzewska, M. Radecka, and M. Rekas, "Effect of Nb, Cr, Sn additions on gas sensing properties of TiO₂ thin films," *Thin Solid Films*, vol. 310, no. 1–2, pp. 161–166, 1997.
- [28] M. Radecka, K. Zakrzewska, and M. Rekas, "SnO₂-TiO₂ solid solutions for gas sensors," *Sensors and Actuators B*, vol. 47, no. 1–3, pp. 194–204, 1998.
- [29] V. Dusastre and D. E. Williams, "Gas-sensitive resistor properties of the solid solution series Ti_x(Sn_{1–y}Sb_y)_{1–x}O₂ (0 < x < 1, y = 0, 0.01, 0.05)," *Journal of Materials Chemistry*, vol. 9, no. 2, pp. 445–450, 1999.
- [30] K. Zakrzewska, "Mixed oxides as gas sensors," *Thin Solid Films*, vol. 391, no. 2, pp. 229–238, 2001.
- [31] J. L. Solis and V. Lantto, "A study of gas-sensing properties of sputtered α-SnWO₄ thin films," *Sensors and Actuators B*, vol. 25, no. 1–3, pp. 591–595, 1995.
- [32] J. L. Solis and V. Lantto, "Gas-sensing properties of different α-SnWO₄-based thick films," *Physica Scripta T*, vol. 69, pp. 281–285, 1997.
- [33] P. Nelli, L. E. Depero, M. Ferroni, et al., "Sub-ppm NO₂ sensors based on nanosized thin films of titanium-tungsten oxides," *Sensors and Actuators B*, vol. 31, no. 1–2, pp. 89–92, 1996.
- [34] L. E. Depero, M. Ferroni, V. Guidi, et al., "Preparation and micro-structural characterization of nanosized thin film of TiO₂-WO₃ as a novel material with high sensitivity towards NO₂," *Sensors and Actuators B*, vol. 36, no. 1–3, pp. 381–383, 1996.
- [35] V. Guidi, M. C. Carotta, M. Ferroni, et al., "Preparation of nanosized titania thick and thin films as gas-sensors," *Sensors and Actuators B*, vol. 57, no. 1–3, pp. 197–200, 1999.
- [36] E. Comini, M. Ferroni, V. Guidi, G. Faglia, G. Martinelli, and G. Sberveglieri, "Nanostructured mixed oxides compounds for gas sensing applications," *Sensors and Actuators B*, vol. 84, no. 1, pp. 26–32, 2002.
- [37] P. Bhattacharyya, P. K. Basu, C. Lang, H. Saha, and S. Basu, "Noble metal catalytic contacts to sol-gel nanocrystalline zinc oxide thin films for sensing methane," *Sensors and Actuators B*, vol. 129, no. 2, pp. 551–557, 2008.
- [38] H.-W. Cheong and M.-J. Lee, "Sensing characteristics and surface reaction mechanism of alcohol sensors based on doped SnO₂," *Journal of Ceramic Processing Research*, vol. 7, no. 3, pp. 183–191, 2006.
- [39] L. Castañeda, "Effects of palladium coatings on oxygen sensors of titanium dioxide thin films," *Materials Science and Engineering B*, vol. 139, no. 2–3, pp. 149–154, 2007.
- [40] V. R. Shinde, T. P. Gujar, and C. D. Lokhande, "Enhanced response of porous ZnO nanobeads towards LPG: effect of Pd sensitization," *Sensors and Actuators B*, vol. 123, no. 2, pp. 701–706, 2007.
- [41] S. W. Hla, P. Lacovig, G. Comelli, A. Baraldi, M. Kiskinova, and R. Rosei, "Orientational anisotropy in oxygen dissociation on Rh(110)," *Physical Review B*, vol. 60, no. 11, pp. 7800–7803, 1999.
- [42] A. Rothschild and Y. Komem, "The effect of grain size on the sensitivity of nanocrystalline metal-oxide gas sensors," *Journal of Applied Physics*, vol. 95, no. 11, pp. 6374–6380, 2004.
- [43] S. L. Tait, Z. Dohnálek, C. T. Campbell, and B. D. Kay, "Methane adsorption and dissociation and oxygen adsorption and reaction with CO on Pd nanoparticles on MgO(1 0 0) and on Pd(1 1 1)," *Surface Science*, vol. 591, no. 1–3, pp. 90–107, 2005.

- [44] M. Ali, V. Cimalla, V. Lebedev, et al., "Pt/GaN Schottky diodes for hydrogen gas sensors," *Sensors and Actuators B*, vol. 113, no. 2, pp. 797–804, 2006.
- [45] C. Xu, J. Tamaki, N. Miura, and N. Yamazoe, "Relationship between gas sensitivity and microstructure of porous SnO₂," *Journal of The Electrochemical Society*, vol. 58, p. 1143, 1990.
- [46] H. Zhang, R. L. Penn, R. J. Hamers, and J. F. Banfield, "Enhanced adsorption of molecules on surfaces of nanocrystalline particles," *Journal of Physical Chemistry B*, vol. 103, no. 22, pp. 4656–4662, 1999.
- [47] C. Xu, J. Tamaki, N. Miura, and N. Yamazoe, "Grain size effects on gas sensitivity of porous SnO₂-based elements," *Sensors and Actuators B*, vol. 3, no. 2, pp. 147–155, 1991.
- [48] M. Tiemann, "Porous metal oxides as gas sensors," *Chemistry*, vol. 13, no. 30, pp. 8376–8388, 2007.
- [49] G. Sakai, N. S. Baik, N. Miura, and N. Yamazoe, "Gas sensing properties of tin oxide thin films fabricated from hydrothermally treated nanoparticles: dependence of CO and H₂ response on film thickness," *Sensors and Actuators B*, vol. 77, no. 1-2, pp. 116–121, 2001.
- [50] P. K. Basu, P. Bhattacharyya, N. Saha, H. Saha, and S. Basu, "The superior performance of the electrochemically grown ZnO thin films as methane sensor," *Sensors and Actuators B*, vol. 133, no. 2, pp. 357–363, 2008.
- [51] G. Korotcenkov, V. Brinzari, J. Schwank, M. DiBattista, and A. Vasiliev, "Peculiarities of SnO₂ thin film deposition by spray pyrolysis for gas sensor application," *Sensors and Actuators B*, vol. 77, no. 1-2, pp. 244–252, 2001.
- [52] G. Sakai, N. Matsunaga, K. Shimano, and N. Yamazoe, "Theory of gas-diffusion controlled sensitivity for thin film semiconductor gas sensor," *Sensors and Actuators B*, vol. 80, no. 2, pp. 125–131, 2001.
- [53] F. Hossein-Babaei and M. Orvatinia, "Analysis of thickness dependence of the sensitivity in thin film resistive gas sensors," *Sensors and Actuators B*, vol. 89, no. 3, pp. 256–261, 2003.
- [54] D. Ding, Z. Chen, and C. Lu, "Hydrogen sensing of nanoporous palladium films supported by anodic aluminum oxides," *Sensors and Actuators B*, vol. 120, no. 1, pp. 182–186, 2006.
- [55] I. Lundstrom, H. Sundgren, F. Winqvist, M. Eriksson, C. Krantz-Rulcker, and A. Lloyd-Spez, "Twenty-five years of field effect gas sensor research in Linkoping," *Sensors and Actuators B*, vol. 121, no. 1, pp. 247–262, 2007.
- [56] M. Lofdahl, C. Utaiwasin, A. Carlsson, I. Lundstrom, and M. Eriksson, "Gas response dependence on gate metal morphology of field-effect devices," *Sensors and Actuators B*, vol. 80, no. 3, pp. 183–192, 2001.
- [57] M. Armgarth and C. Nylander, "Blister formation in Pd gate MIS hydrogen sensors," *IEEE Electron Device Letters*, vol. 3, no. 12, pp. 384–386, 1982.
- [58] S. C. Su, J. N. Carstens, and A. T. Bell, "A study of the dynamics of Pd oxidation and PdO reduction by H₂ and CH₄," *Journal of Catalysis*, vol. 176, no. 1, pp. 125–135, 1998.
- [59] M. Wang and Y. Feng, "Palladium-silver thin film for hydrogen sensing," *Sensors and Actuators B*, vol. 123, no. 1, pp. 101–106, 2007.
- [60] R. C. Hughes, W. K. Schubert, T. E. Zipperian, J. L. Rodriguez, and T. A. Plut, "Thin film palladium and shiver alloys and layers for metal-insulator-semiconductor sensors," *Journal of Applied Physics*, vol. 62, p. 1074, 1987.
- [61] V. A. Drozdov, P. G. Tsyrlunikov, V. V. Popovskii, N. N. Bulgakov, E. M. Moroz, and T. G. Galeev, "Comparative study of the activity of Al-Pd and Al-Pt catalysts in deep oxidation of hydrocarbons," *Reaction Kinetics and Catalysis Letters*, vol. 27, no. 2, pp. 425–427, 1985.
- [62] B. L. Zhu, C. S. Xie, D. W. Zeng, W. L. Song, and A. M. Wang, "Investigation of gas sensitivity of Sb-doped ZnO nanoparticles," *Materials Chemistry and Physics*, vol. 89, no. 1, pp. 148–153, 2005.
- [63] M. N. Romyantseva, V. V. Kovalenko, A. M. Gas'kov, and T. Pagnier, "Metal-oxide based nanocomposites as materials for gas sensors," *Russian Journal of General Chemistry*, vol. 78, no. 5, pp. 1081–1092, 2008.
- [64] F. Volkenshtein, *Electronic Theory of Catalysis on Semiconductors*, Fizmatgiz, Moscow, Russia, 1960.
- [65] G. Korotcenkov, "Gas response control through structural and chemical modification of metal oxide films: state of the art and approaches," *Sensors and Actuators B*, vol. 107, no. 1, pp. 209–232, 2005.
- [66] J. F. McAleer, P. T. Moseley, J. O. W. Norris, D. E. Williams, and B. C. Tofield, "Tin dioxide gas sensors—part 2: the role of surface additives," *Journal of the Chemical Society, Faraday Transactions 1*, vol. 84, no. 2, pp. 441–457, 1988.
- [67] V. Brinzari, G. Korotcenkov, J. Schwank, and Y. Boris, "Chemisorption approach to kinetic analysis of SnO₂:Pd-based thin film gas sensors (TFGS)," *Journal of Optoelectronics and Advanced Materials*, vol. 4, no. 1, p. 147, 2002.
- [68] G. Korotcenkov, V. Brinzari, Y. Boris, M. Ivanov, J. Schwank, and J. Morante, "Influence of surface Pd doping on gas sensing characteristics of SnO₂ thin films deposited by spray pyrolysis," *Thin Solid Films*, vol. 436, no. 1, pp. 119–126, 2003.
- [69] V. R. Shinde, T. P. Gujar, and C. D. Lokhande, "Enhanced response of porous ZnO nanobeads towards LPG: effect of Pd sensitization," *Sensors and Actuators B*, vol. 123, no. 2, pp. 701–706, 2007.
- [70] W. Göpel and K. D. Schierbaum, "SnO₂ sensors: current status and future prospects," *Sensors and Actuators B*, vol. 26, no. 1–3, pp. 1–12, 1995.
- [71] M. J. Madou and S. R. Morrison, *Chemical Sensing with Solid-State Devices*, Academic Press, New York, NY, USA, 1989.
- [72] J.-H. Sung, Y.-S. Lee, J.-W. Lim, Y.-H. Hong, and D.-D. Lee, "Sensing characteristics of tin dioxide/gold sensor prepared by coprecipitation method," *Sensors and Actuators B*, vol. 66, no. 1, pp. 149–152, 2000.
- [73] K. L. Chopra, S. Major, and D. K. Pandya, "Transparent conductors—a status review," *Thin Solid Films*, vol. 102, no. 1, pp. 1–46, 1983.
- [74] T. W. Kim, D. U. Lee, J. H. Lee, D. C. Choo, M. Jung, and Y. S. Yoon, "Structural, electrical, and optical properties of SnO₂ nanocrystalline thin films grown on p-InSb (111) substrates," *Journal of Applied Physics*, vol. 90, no. 1, pp. 175–180, 2001.
- [75] G. G. Mandayo, E. Castano, F. J. Gracia, A. Cirera, A. Cornet, and J. R. Morante, "Strategies to enhance the carbon monoxide sensitivity of tin oxide thin films," *Sensors and Actuators B*, vol. 95, no. 1–3, pp. 90–96, 2003.
- [76] H. Ogawa, M. Nishikawa, and A. Abe, "Hall measurement studies and an electrical conduction model of tin oxide ultrafine particle films," *Journal of Applied Physics*, vol. 53, no. 6, pp. 4448–4455, 1982.
- [77] V. R. Katti, A. K. Debnath, K. P. Muthe, et al., "Mechanism of drifts in H₂S sensing properties of SnO₂:CuO composite thin

- film sensors prepared by thermal evaporation,” *Sensors and Actuators B*, vol. 96, no. 1-2, pp. 245–252, 2003.
- [78] B.-K. Min and S.-D. Choi, “SnO₂ thin film gas sensor fabricated by ion beam deposition,” *Sensors and Actuators B*, vol. 98, no. 2-3, pp. 239–246, 2004.
- [79] G. Korotcenkov, V. Brinzari, V. Golovanov, and Y. Blinov, “Kinetics of gas response to reducing gases of SnO₂ films, deposited by spray pyrolysis,” *Sensors and Actuators B*, vol. 98, no. 1, pp. 41–45, 2004.
- [80] S. Shukla, S. Patil, S. C. Kuiry, et al., “Synthesis and characterization of sol-gel derived nanocrystalline tin oxide thin film as hydrogen sensor,” *Sensors and Actuators B*, vol. 96, no. 1-2, pp. 343–353, 2003.
- [81] G. Sberveglieri, “Classical and novel techniques for the preparation of SnO₂ thin-film gas sensors,” *Sensors and Actuators B*, vol. 6, no. 1–3, pp. 239–247, 1992.
- [82] R. Dolbec, M. A. El Khakani, A. M. Serventi, and R. G. Saint-Jacques, “Influence of the nanostructural characteristics on the gas sensing properties of pulsed laser deposited tin oxide thin films,” *Sensors and Actuators B*, vol. 93, no. 1–3, pp. 566–571, 2003.
- [83] D. B. Chrisey and G. K. Hubler, Eds., *Pulsed Laser Deposition of Thin Films*, John Wiley & Sons, New York, NY, USA, 1994.
- [84] M. C. Carotta, V. Guidi, G. Martinelli, M. Nagliati, D. Puzovio, and D. Vecchi, “Sensing of volatile alkanes by metal-oxide semiconductors,” *Sensors and Actuators B*, vol. 130, no. 1, pp. 497–501, 2008.
- [85] H. H. Kung, “Oxidative dehydrogenation of light (C₂ to C₄) alkanes,” *Advanced Catalyst*, vol. 40, p. 1, 1994.
- [86] I.-C. Marcu, J.-M. M. Millet, and J.-M. Herrmann, “Semiconductive and redox properties of Ti and Zr pyrophosphate catalysts (TiP₂O₇ and ZrP₂O₇). Consequences for the oxidative dehydrogenation of *n*-butane,” *Catalysis Letters*, vol. 78, no. 1–4, pp. 273–279, 2002.
- [87] I.-C. Marcu, J.-M. M. Millet, and I. Săndulescu, “Oxidative dehydrogenation of isobutane over a titanium pyrophosphate catalyst,” *Journal of the Serbian Chemical Society*, vol. 70, no. 6, pp. 791–798, 2005.
- [88] M. C. Carotta, A. Cervi, A. Giberti, et al., “Ethanol interference in light alkane sensing by metal-oxide solid solutions,” *Sensors and Actuators B*, vol. 136, no. 2, pp. 405–409, 2009.
- [89] M. C. Carotta, A. Cervi, A. Giberti, et al., “Metal-oxide solid solutions for light alkane sensing,” *Sensors and Actuators B*, vol. 133, no. 2, pp. 516–520, 2008.
- [90] M. C. Carotta, V. Guidi, G. Martinelli, M. Nagliati, D. Puzovio, and D. Vecchi, “Sensing of volatile alkanes by metal-oxide semiconductors,” *Sensors and Actuators B*, vol. 130, no. 1, pp. 497–501, 2008.
- [91] M. V. Vaishampayan, R. G. Deshmukh, and I. S. Mulla, “Influence of Pd doping on morphology and LPG response of SnO₂,” *Sensors and Actuators B*, vol. 131, no. 2, pp. 665–672, 2008.
- [92] A. Cabot, A. Vilà, and J. R. Morante, “Analysis of the catalytic activity and electrical characteristics of different modified SnO₂ layers for gas sensors,” *Sensors and Actuators B*, vol. 84, no. 1, pp. 12–20, 2002.
- [93] N. Das, A. K. Halder, J. M. A. Sen, and H. S. Maiti, “Sonochemically prepared tin-dioxide based composition for methane sensor,” *Materials Letters*, vol. 60, no. 8, pp. 991–994, 2006.
- [94] B.-K. Min and S.-D. Choi, “Undoped and 0.1 wt.% Ca-doped Pt-catalyzed SnO₂ sensors for CH₄ detection,” *Sensors and Actuators B*, vol. 108, no. 1-2, pp. 119–124, 2005.
- [95] S. Bose, S. Chakraborty, B. K. Ghosh, D. Das, A. Sen, and H. S. Maiti, “Methane sensitivity of Fe-doped SnO₂ thick films,” *Sensors and Actuators B*, vol. 105, no. 2, pp. 346–350, 2005.
- [96] F. Quaranta, R. Rella, P. Siciliano, et al., “Novel gas sensor based on SnO₂/Os thin film for the detection of methane at low temperature,” *Sensors and Actuators B*, vol. 58, no. 1–3, pp. 350–355, 1999.
- [97] K. Chatterjee, S. Chatterjee, A. Banerjee, et al., “The effect of palladium incorporation on methane sensitivity of antimony doped tin dioxide,” *Materials Chemistry and Physics*, vol. 81, no. 1, pp. 33–38, 2003.
- [98] J. C. Kim, H. K. Jun, J.-S. Huh, and D. D. Lee, “Tin oxide-based methane gas sensor promoted by alumina-supported Pd catalyst,” *Sensors and Actuators B*, vol. 45, no. 3, pp. 271–277, 1997.
- [99] L. Urfels, P. Gelin, M. Primet, and E. Tena, “Complete oxidation of methane at low temperature over Pt catalysts supported on high surface area SnO₂,” *Topics in Catalysis*, vol. 30-31, pp. 427–432, 2004.
- [100] C. K. Kim, J. H. Lee, S. M. Choi, et al., “Pd- and Pt-SiC Schottky diodes for detection of H₂ and CH₄ at high temperature,” *Sensors and Actuators B*, vol. 77, no. 1-2, pp. 455–462, 2001.
- [101] S. Chakraborty, A. Sen, and H. S. Maiti, “Complex plane impedance plot as a figure of merit for tin dioxide-based methane sensors,” *Sensors and Actuators B*, vol. 119, no. 2, pp. 431–434, 2006.
- [102] K. R. Han, C.-S. Kim, K. T. Kang, H. J. Koo, D. Kang II, and J. He, “Development of SnO₂ based semiconductor gas sensor with Fe₂O₃ for detection of combustible gas,” *Journal of Electroceramics*, vol. 10, no. 1, pp. 69–73, 2003.
- [103] V. V. Malyshev and A. V. Pisyakov, “Dynamic properties and sensitivity of semiconductor metal-oxide thick-film sensors to various gases in air gaseous medium,” *Sensors and Actuators B*, vol. 96, no. 1-2, pp. 413–434, 2003.
- [104] M. Saha, A. Banerjee, A. K. Halder, J. Mondal, A. Sen, and H. S. Maiti, “Effect of alumina addition on methane sensitivity of tin dioxide thick films,” *Sensors and Actuators B*, vol. 79, no. 2-3, pp. 192–195, 2001.
- [105] A. Chen, S. Bai, B. Shi, Z. Liu, D. Li, and C. C. Liu, “Methane gas-sensing and catalytic oxidation activity of SnO₂-In₂O₃ nanocomposites incorporating TiO₂,” *Sensors and Actuators B*, vol. 135, no. 1, pp. 7–12, 2008.
- [106] X. L. Cheng, H. Zhao, L. H. Huo, S. Gao, and J. G. Zhao, “ZnO nanoparticulate thin film: preparation, characterization and gas-sensing property,” *Sensors and Actuators B*, vol. 102, no. 2, pp. 248–252, 2004.
- [107] M. Sucheá, S. Christoulakis, K. Moschovis, N. Katsarakis, and G. Kiriakidis, “ZnO transparent thin films for gas sensor applications,” *Thin Solid Films*, vol. 515, no. 2, pp. 551–554, 2006.
- [108] G. Eranna, B. C. Joshi, D. P. Runthala, and R. P. Gupta, “Oxide materials for development of integrated gas sensors—a comprehensive review,” *Critical Reviews in Solid State and Materials Sciences*, vol. 29, no. 3-4, pp. 111–188, 2004.
- [109] S. Cho, J. Ma, Y. Kim, Y. Sun, G. K. L. Wong, and J. B. Ketterson, “Photoluminescence and ultraviolet lasing of polycrystalline ZnO thin films prepared by the oxidation of the metallic Zn,” *Applied Physics Letters*, vol. 75, no. 18, pp. 2761–2763, 1999.
- [110] R. Bel Hadj Tahar, “Structural and electrical properties of aluminum-doped zinc oxide films prepared by sol-gel process,” *Journal of the European Ceramic Society*, vol. 25, no. 14, pp. 3301–3306, 2005.

- [111] A. Ashida, T. Nagata, and N. Fujimura, "Electro-optical effect in ZnO:Mn thin films prepared by Xe sputtering," *Journal of Applied Physics*, vol. 99, no. 1, Article ID 013509, 4 pages, 2006.
- [112] S. Muthukumar, C. R. Gorla, N. W. Emanetoglu, S. Liang, and Y. Lu, "Control of morphology and orientation of ZnO thin films grown on SiO₂/Si substrates," *Journal of Crystal Growth*, vol. 225, no. 2–4, pp. 197–201, 2001.
- [113] J. F. Muth, R. M. Kolbas, A. K. Sharma, S. Oktyabrsky, and J. Narayan, "Excitonic structure and absorption coefficient measurements of ZnO single crystal epitaxial films deposited by pulsed laser deposition," *Journal of Applied Physics*, vol. 85, no. 11, pp. 7884–7887, 1999.
- [114] M. Jin, J. Feng, Z. De-Heng, M. Hong-Lei, and L. Shu-Ying, "Optical and electronic properties of transparent conducting ZnO and ZnO:Al films prepared by evaporating method," *Thin Solid Films*, vol. 357, no. 2, pp. 98–101, 1999.
- [115] H. Yan, Y. Yang, Z. Fu, et al., "Fabrication of 2D and 3D ordered porous ZnO films using 3D opal templates by electrodeposition," *Electrochemistry Communications*, vol. 7, no. 11, pp. 1117–1121, 2005.
- [116] G. S. Wu, T. Xie, X. Y. Yuan, et al., "Controlled synthesis of ZnO nanowires or nanotubes via sol-gel template process," *Solid State Communications*, vol. 134, no. 7, pp. 485–489, 2005.
- [117] P. Mitra and A. K. Mukhopadhyay, "ZnO thin film as methane sensor," *Bulletin of the Polish Academy of Sciences: Technical Sciences*, vol. 55, no. 3, pp. 281–285, 2007.
- [118] P. Bhattacharyya, P. K. Basu, H. Saha, and S. Basu, "Fast response methane sensor based on Pd(Ag)/ZnO/Zn MIM structure," *Sensor Letters*, vol. 4, no. 4, pp. 371–376, 2006.
- [119] P. Bhattacharyya, P. K. Basu, H. Saha, and S. Basu, "Fast response methane sensor using nanocrystalline zinc oxide thin films derived by sol-gel method," *Sensors and Actuators B*, vol. 124, no. 1, pp. 62–67, 2007.
- [120] P. Bhattacharyya, P. K. Basu, C. Lang, H. Saha, and S. Basu, "Noble metal catalytic contacts to sol-gel nanocrystalline zinc oxide thin films for sensing methane," *Sensors and Actuators B*, vol. 129, no. 2, pp. 551–557, 2008.
- [121] S. J. Fonash, J.-A. Roger, and C. H. S. Dupuy, "Ac equivalent circuits for MIM structures," *Journal of Applied Physics*, vol. 45, no. 7, pp. 2907–2910, 1974.
- [122] S. Basu and A. Dutta, "Room-temperature hydrogen sensors based on ZnO," *Materials Chemistry and Physics*, vol. 47, no. 1, pp. 93–96, 1997.
- [123] M. Fleischer and H. Meixner, "A selective CH₄ sensor using semiconducting Ga₂O₃ thin films based on temperature switching of multigas reactions," *Sensors and Actuators B*, vol. 25, no. 1–3, pp. 544–547, 1995.
- [124] J. Wollenstein, M. Burgmair, G. Plescher, et al., "Cobalt oxide based gas sensors on silicon substrate for operation at low temperatures," *Sensors and Actuators B*, vol. 93, no. 1–3, pp. 442–448, 2003.
- [125] P. Bhattacharyya, P. K. Basu, H. Saha, and S. Basu, "Fast response methane sensor using nanocrystalline zinc oxide thin films derived by sol-gel method," *Sensors and Actuators B*, vol. 124, no. 1, pp. 62–67, 2007.
- [126] P. K. Basu, P. Bhattacharyya, N. Saha, H. Saha, and S. Basu, "The superior performance of the electrochemically grown ZnO thin films as methane sensor," *Sensors and Actuators B*, vol. 133, no. 2, pp. 357–363, 2008.
- [127] P. K. Basu, P. Bhattacharyya, N. Saha, H. Saha, and S. Basu, "Methane sensing properties of platinum catalysed nano porous zinc oxide thin films derived by electrochemical anodization," *Sensor Letters*, vol. 6, no. 1, pp. 219–225, 2008.
- [128] R. Löber and D. Hennig, "Interaction of hydrogen with transition metal fcc(111) surfaces," *Physical Review B*, vol. 55, no. 7, pp. 4761–4765, 1997.
- [129] E. P. J. Mallens, J. H. B. J. Hoebink, and G. B. Marin, "The reaction mechanism of the partial oxidation of methane to synthesis gas: a transient kinetic study over rhodium and a comparison with platinum," *Journal of Catalysis*, vol. 167, no. 1, pp. 43–56, 1997.
- [130] L. Opara, B. Klein, and H. Züchner, "Hydrogen-diffusion in Pd_{1-x}Ag_x (0 ≤ x ≤ 1)," *Journal of Alloys and Compounds*, vol. 253–254, pp. 378–380, 1997.
- [131] S. Eriksson, M. Nilsson, M. Boutonnet, and S. Järås, "Partial oxidation of methane over rhodium catalysts for power generation applications," *Catalysis Today*, vol. 100, no. 3–4, pp. 447–451, 2005.
- [132] P. K. Basu, S. K. Jana, H. Saha, and S. Basu, "Low temperature methane sensing by electrochemically grown and surface modified ZnO thin films," *Sensors and Actuators B*, vol. 135, no. 1, pp. 81–88, 2008.
- [133] G. K. Flingelli, M. M. Fleischer, and H. Meixner, "Selective detection of methane in domestic environments using a catalyst sensor system based on Ga₂O₃," *Sensors and Actuators B*, vol. 48, no. 1–3, pp. 258–262, 1998.
- [134] S. Barazzouk, R. P. Tandon, and S. Hotchandani, "MoO₃-based sensor for NO, NO₂ and CH₄ detection," *Sensors and Actuators B*, vol. 119, no. 2, pp. 691–694, 2006.

Research Article

Shrinkage Effects of the Conduction Zone in the Electrical Properties of Metal Oxide Nanocrystals: The Basis for Room Temperature Conductometric Gas Sensor

M. Manzanares,¹ T. Andreu,¹ J. D. Prades,^{1,2} J. Arbiol,^{1,3} F. Hernandez-Ramírez,^{2,4}
A. Cirera,¹ and J. R. Morante^{1,2}

¹ EME/XaRMAE/IN² UB, Departament d'Electrònica, Universitat de Barcelona, C/ Martí i Franquès, 1.08028 Barcelona, Spain

² IREC, Institut de Recerca en Energia de Catalunya, C/Josep Pla 2, B2, ground floor, 08019 Barcelona, Spain

³ TEM-MAT, Serveis Científicotècnics, Universitat de Barcelona, 08028 Barcelona, Spain

⁴ Electronic Nanosystems, SL.08028 Barcelona, Spain

Correspondence should be addressed to M. Manzanares, mmanzanares@el.ub.es

Received 23 January 2009; Accepted 21 May 2009

Recommended by Yongxiang Li

The influence of charge localized at the surface of minute metal oxide nanocrystals was studied in WO₃ and In₂O₃ nanostructures, which were obtained replicating mesoporous silica templates. Here, it is shown that the very high resistive states observed at room temperature and dark conditions were originated by the total shrinkage of the conductive zone in the inner part of these nanocrystals. On the contrary, at room temperature and under UV illumination, both photogenerated electron-hole pairs and empty surface states generated by photons diminished the negative charge accumulated at the surface, enlarging the conductive zone and, as a consequence, leading to a reduction of the electrical resistance. Under these conditions, empty surface states produced by UV light reacted with oxidizing gaseous molecules. The charge exchange associated to these reactions also affected the size of the inner conductive zone, and led to a new steady-state resistance. These chemical, physical and geometrical effects can be used for gas detection, and constitutes the basis for developing novel room temperature conductometric gas sensors responsive to oxidizing species.

Copyright © 2009 M. Manzanares et al. This is an open access article distributed under the Creative Commons Attribution License, which permits unrestricted use, distribution, and reproduction in any medium, provided the original work is properly cited.

1. Introduction

It is well known that the response of conductometric solid state gas sensors based on thin or thick films increases with the surface-to-volume ratio of the crystallites inside them. During the last decades, many efforts have been undertaken to reduce the grain size of these polycrystalline films to values below a few tens of nanometers. To achieve this goal, new wet chemical routes or modified physical deposition techniques have been used [1, 2]. In parallel to this scaling-down approach, the use of sensitive layers formed by bundles of nanowires has been proposed as well. However, the surface-to-volume ratio of the nanowires is not higher than the values reached with nanocrystals, and any significant improvement in the final performance of these prototypes was reported [3, 4].

It is noteworthy that the use of sensing films leads to other inherent restrictions such as gas diffusion in their inside, chemical sensing inhomogeneity, grain agglomeration and intergrain-boundary effects. Each one of them modifies the behavior of the prototypes and hampers the study of the grain size influence on the ideal sensor response expected in a scenario free of interfering effects [5–7].

The study of individual nanowires offers an excellent opportunity to avoid many of these interferences [8]. Furthermore, the direct influence of the nanowire radius on the sensor response has also been reported [9]. According to these results, response towards gases sharply increases with radii below 15 nm. In this situation, the conduction channel along the nanowire is close to total depletion and small variations in the charge trapped at the surface by gaseous molecules lead to huge effects on their electrical responses.

Typical sizes for depleted regions in metal oxides are close to 3–5 nm [10]. Therefore, nanowires thinner than 10 nm in diameter are considered excellent candidates to both study deep depletion effects and understand the complete shrinkage of the conductive zone. Unfortunately, there are still important technical drawbacks to manipulate and electrically contact individual ultrathin nanowires, hindering the fabrication of experimental prototypes.

In this paper, we report an alternative approach to study the shrinkage effects of the conductive zone in nanostructured metal oxides, overcoming the technical limitations associated with nanowires. This approach is based on the use of nanostructured In_2O_3 and WO_3 obtained as replicas of mesoporous templates [11, 12]. This method produces minute nanograins ordered in a network that facilitates gas diffusion through it, maintains the chemical sensing homogeneity, avoids grain agglomeration and diminishes grain boundary effects [13–15]. UV illumination is used to modulate their resistance several orders of magnitude, changing from an insulating to a semiconductor state useful for gas sensing applications even at room temperature. Likewise, surface functionalization is used to modify the density of active sites at the surface and, thus, to balance the influence of the surface and bulk effects on the overall response. This approach, that combines fully depleted nanomaterials with UV illumination and surface functionalization, opens the door to the development of room temperature conductometric gas sensors.

2. Experimental Setup

2.1. Synthesis Routes. As previously discussed, the use of templates is an attractive alternative to overcome the above-mentioned difficulties concerning the fabrication of the sensors and the interpretation of their response.

The soft-template methods, based on the use of surfactants, were initially discarded. Even though these methods reduce the dispersion of the particles, the fact that the template is removed before annealing produces agglomerated materials. In contrast, the template is removed in the hard-template methods afterwards, and this ensures a good control of the particle size since the template acts as a physical barrier to coalescence of the crystals during the calcination process.

The hard-template method also offers several additional advantages. Firstly, it allows obtaining a porous network distribution that depends on the nanotemplate structure, selected among a wide variety, such as MCM-41, SBA-15, KIT-6, and SBA-16. Second, the replication process using silica templates is easy to scale-up. This is an advantage compared with other hard-templates such as anodized aluminum oxides (AAOs) membranes. Third, mesoporous silica templates offer good thermal stability for the synthesis of metal oxides at relatively high temperatures [16].

Mesoporous silica was synthesized by using a nonionic triblock copolymer surfactant (EO20PO70EO20, Pluronic P123 from BASF) as a structure directing agent [17]. In this work, we have chosen the KIT-6 structure (three-dimensional cubic $Ia3d$) for the mesoporous silica template [18, 19]. KIT-6 was synthesized using the following proce-

cedure: 6 g of P123 were dissolved in 195 g H_2O , 30 g of HCl 37% and 6 g of 1-butanol. Then, 12.5 g of TEOS (tetraethyl orthosilicate) were added dropwise, and the mixture was stirred for 24 h at 36°C, followed by a hydrothermal treatment at 90°C. Finally, the mesoporous silica was filtered, washed, dried and calcinated at 550°C.

For obtaining mesoporous indium oxide or tungsten oxide, a two-impregnation process was performed. In a typical synthesis, 0.15 g of mesoporous silica (KIT-6) were firstly impregnated, respectively, with 1 mmol of $\text{In}(\text{NO}_3)_3 \cdot x\text{H}_2\text{O}$ ethanolic solution or with phosphotungstic acid (Alfa Aesar) which was used as a precursor for WO_3 . The mixture was stirred for 30 minutes, dried and calcinated at 350°C. The resulting powder was impregnated again with the precursor and calcinated at higher temperature than 600°C in order to obtain the metal oxide as a well-stabilized material. Finally, the silica template was removed by etching the material with a 2 M NaOH solution at 70°C for 24 hours or alternatively with HF. The solid was separated by centrifugation and cleaned several times with water and ethanol. In all cases, chemicals were of analytical grade and water used had been distilled twice and disionized with a Millipore Milli-Q system. XPS and EELS analyses revealed that all the silica was completely removed, at least, within the resolution limits of these techniques.

Some samples were functionalized with aminopropylphosphonate [20]. Since P–O–M bonds are more thermodynamically stable than Si–O–M bonds, phosphonate blocks the surface sites in the right direction. In addition to this, the reaction of metal oxides with phosphonate is easier even in the absence of hydroxyl groups.

2.2. Material Characterization. X-Ray Diffraction (XRD) analysis was performed on Siemens D500 and Bruker D4 X-ray Powder diffractometers, working with the Cu K_α radiation. Transmission Electron Microscopy (TEM) characterization was carried out using a Philips CM30 SuperTwin electron microscope operating at 300 keV and High Resolution TEM (HRTEM) was performed on a JEOL JEM 2010F electron microscope operating at 200 keV with a field emission gun. X-Ray Photoelectrons Spectroscopy (XPS) measurements were performed on a PHI equipment 5500 Multitechnique model, operating with Al K_α line at 1486.6 eV (0.9 eV of line width). Brunauer-Emmett-Teller (BET) analysis was performed using ASAP 2000 equipment (Micrometrics). For this purpose, samples were degassed at 150°C for 20 hours in a maximum vacuum of 266 Pa. Both porous replicas displayed high superficial specific area ($65 \pm 5 \text{ m}^2 \text{ g}^{-1}$) which was in range with the values obtained for the silica template ($62 \pm 5 \text{ m}^2 \text{ g}^{-1}$).

2.3. Sensors Fabrication and Measurement. Sensors were prepared by screen-printing of the as-synthesized powders and an organic solvent (1,2-propanediol) mixture onto alumina substrates. Platinum electrodes and a platinum heater had been previously printed at front and back sides of the substrates. Platinum heater allowed controlling the working temperature. Sensors were fired at 500°C for 30 minutes to evaporate the solvent and to ensure sample adherence to the

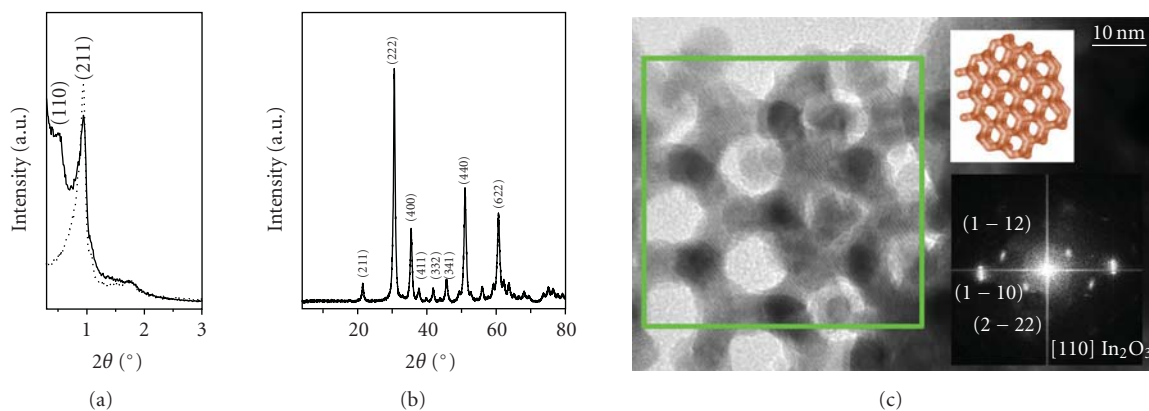


FIGURE 1: (a) Low angle X-ray diffractogram of mesoporous In_2O_3 . Dotted line corresponds to KIT-6 silica. The replica clearly shares the same large-scale mesoporous structure with the silica template. (b) Wide angle XRD of KIT-6 In_2O_3 . Main diffraction peaks of the cubic structure Ia-3 of In_2O_3 are clearly identified. (c) High-resolution Transmission Electron Microscopy and selected area diffraction pattern on the squared region of an In_2O_3 KIT-6 mesoporous replica. A sketch of the KIT-6 mesoporous structure is included for clarity (reprinted with permission from [14] Rossinyol, et al. *Adv. Funct. Mater.* 17, 1801–1806, 2007, Wiley-VCH Verlag GmbH & Co. KGaA (2007)).

alumina surface. Screen-printed powders were examined on a Field Emission Hitachi 4100 scanning electron microscope.

UV illumination was provided by different LED sources, from 365 nm to 310 nm, as well as a UV Xe lamp from Hamamatsu equipped with a high- and lowpass filter set. In both cases, the use of a controlled heater also allowed controlling the sensor temperature.

For the electrical characterization of the sensors, the gas-sensor devices were placed in a stainless steel test chamber where a controlled gaseous atmosphere was provided by means of mass flow controllers. DC electrical characterization of these devices was performed by applying an external bias and then recording the current by means of low-noise current amplifier in conjunction with a high sampling speed digital acquisition board. Most experiments were carried out also in a ProboStat cell located in a furnace or a similar item home made with 290 nm highpass windows. The temperature was precisely monitored and controlled by a thermocouple located next to the sample. The used gas flow ranged between 100 and 200 $\text{mL} \cdot \text{min}^{-1}$ without noticeable influence on the responses. Accurate gas compositions— NO_2 , CO , N_2 , O_2 , synthetic air (SA), humid air—were prepared using a gas mixer based on mass flow controllers (MFCs) controlled by computer. The sensor response was measured as the ratio of the resistance in presence and in absence of the target gas. The response was defined as $R_{\text{gas}}/R_{\text{air}}$ for oxidizing gases and $R_{\text{air}}/R_{\text{gas}}$ for reducing gases.

3. Results and Discussion

On the one hand, low-angle XRD patterns (Figure 1(a)) revealed that the template and the corresponding replica share the same mesoporous structure (KIT-6) and demonstrated that this was a general feature of the here-studied materials. On the other hand, wide-angle XRD patterns (Figure 1(b)) confirmed that the crystalline structure of the mesoporous In_2O_3 replicas was the cubic Ia-3 (JCPDS 6-0416) [13].

Figure 1(c) shows a high-resolution TEM image of an In_2O_3 replica of the KIT-6 mesoporous template that corresponds to a 3D gyroidal structure. It can be observed that the obtained material is crystalline and free of defects with branches around 7 nm in diameter. Specifically, the analysis of the selected area diffraction (SAED) patterns corroborated that In_2O_3 crystallizes in the cubic structure Ia-3. It is noteworthy that the analyzed region does not display any grain boundary. The material looks like a perfect single crystal trimmed according a mesoporous pattern. This porous network facilitates the diffusion of the gas across the nanostructured material.

In fact, no additional electron diffraction spots corresponding to other crystals are observed (inset in Figure 1(c)). Consequently, it can be asserted that these features are characteristic of the material at least at the scale of the analyzed region and represent the optimum scenario to study surface depletion effects caused by the charge trapped at the surface. This situation is similar to a bundle of ultrathin nanowires (less than 10 nm in radii) but presents an additional advantage: there are no contacts between grains (or nanowires) and, therefore, there is not any grain barrier effect. Similar structural features were observed in WO_3 [13].

Figure 2 shows the change in the resistance of nanostructured In_2O_3 when it is exposed to UV light. In dark conditions, the resistance values are in the gigaohm range (almost out of the scale of our measurement equipment). Under UV illumination (light density values of several W/cm^2 inside the chamber), the electrical resistance decreased several orders of magnitude. It is noteworthy these enormous variations in the resistance were only rapidly reverted after a thermal treatment. Similar results were obtained for WO_3 (Figure 3). For this material, UV illumination produced resistance changes of more than 8 orders of magnitude.

Often, grain boundary effects explain huge changes in the resistance of polycrystalline materials [21, 22]. However, the HRTEM and the electron diffraction analysis of our samples do not support this assumption. Therefore, it is necessary to

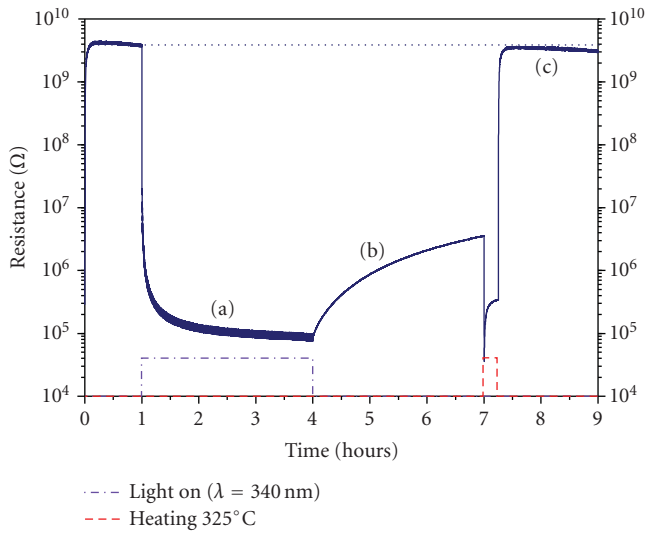


FIGURE 2: Resistance value variation at room temperature of an In_2O_3 nanostructured layer. Notice: (a) the resistance diminution in 4 orders of magnitude under illumination, (b) the PPC effect, and (c) the recovery of the initial value after heating for 15 minutes at 325°C .

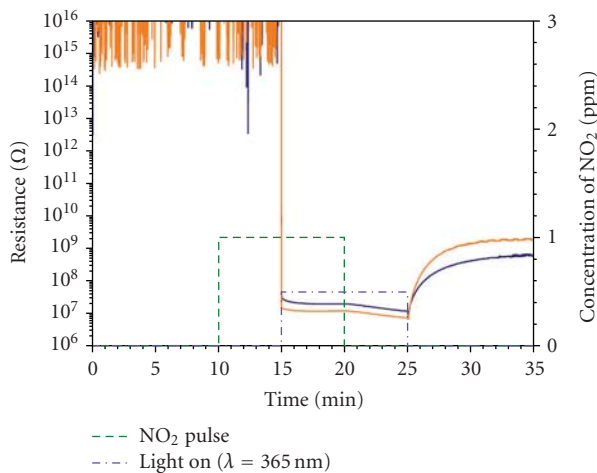


FIGURE 3: Resistance variation at room temperature for two similar samples of nanostructured WO_3 exposed to a sequence of UV light and NO_2 (1 ppm). The sample thickness ($300\mu\text{m}$) enlarges the response time. In dark conditions, no response was observed. The extremely high resistance cause spurious noise as resistance values approach to the limits of our equipment. After switching off the light, the PPC effect appears.

consider other explanations. Since the radii of the branches in the mesoporous network ($\sim 3.5\text{ nm}$) is comparable with the typical width of the surface depletion zone in metal oxides (3–5 nm) [10], it is plausible to assume an almost complete shrinkage of the conductive zone in the inner part of the material.

A detailed analysis of the transient behavior after switching on the light reveals two dynamics mechanisms. A fast one (below the second range) due to band-to-band electron-hole generation followed [23] by a slow one related to gas adsorption, desorption and diffusion processes [24].

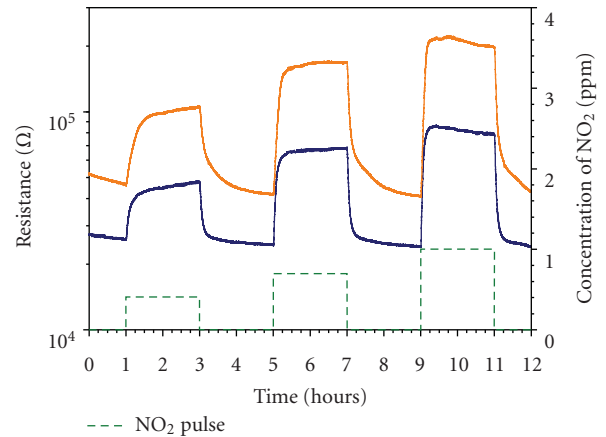


FIGURE 4: Resistance variation, at room temperature and under UV illumination ($\lambda = 365\text{ nm}$), of two similar samples of WO_3 (KIT-6 structure) exposed to a sequence of sub ppm NO_2 concentrations. Observe the baseline recovery.

Under UV illumination and at room temperature, these nanomaterials display a reversible response towards oxidizing gases which was not observed in dark conditions. According to previously reported models [25], UV illumination desorbs NO_2 molecules and oxygens from the metal oxide surface leading to partially reduced surfaces [26, 27]. In this situation, NO_2 molecules and oxygens in air compete for the same adsorption sites (which are light-induced surface oxygen vacancies, according to first principles calculations [28–30]). The higher efficiency of NO_2 molecules to refill the light-emptied sites explains the effective response. According to the depicted mechanism, the response to NO_2 at room temperature is determined by the balance between spontaneous adsorptions and light-induced desorptions. This mechanism also explains the recovery of the response under illumination.

Two different processes may explain the photoactivated desorption of oxidizing molecules [31]. On one hand, the built-in potential near the surface of metal oxide separates the photogenerated electron-hole pairs and accumulates positive charges at the outermost layer of the materials. These holes recombine with the electrons trapped by the oxidizing molecules, and this mechanism facilitates their desorption. On the other hand, UV light can photoionize the negative charges localized at the oxidizing adsorbate, causing their direct desorption.

After this continuous photodesorption processes, oxidizing gases find a reduced surface which is highly reactive, even at room temperature. Therefore, the oxidizing molecules will adsorb at a rate determined by the initial density of adsorption sites (intrinsic of the material and modified by other treatments like thermal treatments [32] or functionalization [20]), and the availability of empty sites (determined by the photon and gas densities [25]).

Still under UV illumination, the steady-state occupancy of the adsorption sites by NO_2 molecules determines the steady-state response of the sensor to this gas. The higher the occupancy, the more negative charge is trapped at

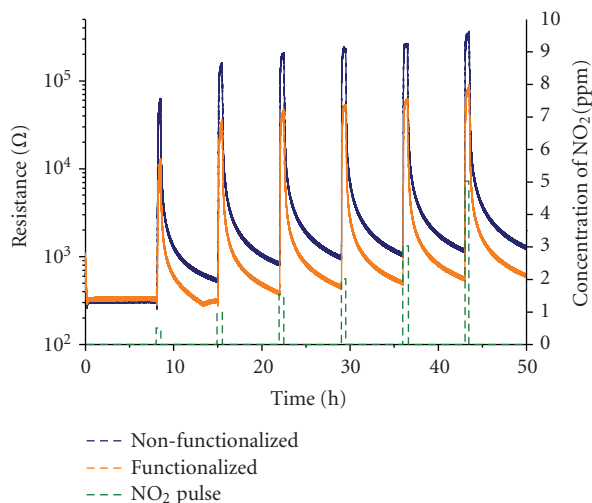


FIGURE 5: Resistance variation of a functionalized and a nonfunctionalized sensor under UV illumination ($\lambda = 340$ nm, room temperature) when exposed to different concentrations of NO_2 . Dotted lines are only a guide for the eye.

the surface of the mesoporous structure, the wider the depletion layer and the higher the resistance is. According to most of the models used to describe the equilibrium between molecules in a gas and the corresponding adsorbed species, the occupancy (or the coverage) is a monotonously growing function of the molecule concentration in the gas phase. Even in the most simplistic approximations, like the Langmuir isotherm [33], this dependence is not linear and the occupancy tends to 1 at higher concentrations. Therefore, at low NO_2 concentrations the resistance of the mesoporous network will be more sensitive to small variations of the NO_2 content in air. At higher concentrations, the response will saturate and the sensor will become less sensitive. This prediction is in good agreement with the behavior experimentally observed (Figure 5). A detailed model of these phenomena will be presented elsewhere [20]. It goes without saying that these saturation effects will take place at different concentrations depending on the size of the nanocrystals.

For completeness, functionalization agents were used to block a fraction of the sites available at the materials surface. Consequently, after the treatment, the density of adsorption sites was lower than before. According to the previous model, this treatment should lower the response towards NO_2 without modifying the resistance values in air and under illumination. Both predictions were corroborated experimentally (Figure 5, orange data set).

Finally, after switching off the light, the resistance does not recover the initial value (Figure 2). This new steady-state lasts for days and corresponds to the persistent photoconductivity effect (PPC), which was described elsewhere [31].

In the case of WO_3 , other models could partially explain the resistance reduction under UV illumination; such as the W^{6+} to W^{5+} valence change that explain the photoelectrochromic effects in this material [34]. However, the

fact that equivalent behaviors were observed in two different metal oxides supports the here-proposed description.

All in all demonstrates that UV illumination is an excellent tool to reduce the surface of metal oxides in a controlled manner to improve their response towards oxidizing gases. However, heat pulses are still necessary to reset the sensors conductivity, achieving a complete surface cleaning and thus, assuring the repeatability of the measurements.

4. Conclusions

Shrinkage effects of the conductive zone in nanostructured metal oxides were studied with mesoporous WO_3 and In_2O_3 . These single crystalline materials formed branched networks with radii in range of typical width of the depleted region in metal oxides. Conductometric measurements in dark conditions indicate that the conductive zone of these materials was (almost) completely depleted (especially in WO_3 samples).

Under illumination, both materials display significant response towards oxidizing gases even at room temperature. According to the depicted mechanism, illumination reduces the surface of metal oxides and facilitates a competitive behavior between the different oxidizing species in air. This mechanism is corroborated by the saturation observed in the response to high concentrations of target gases. These effects were also corroborated in functionalized materials.

In summary, it has been shown that illumination with photon energy above the band gap of the metal oxides is a powerful tool to control and regulate the occupation of the surface states. The here-presented results pave the way to the development of room temperature conductometric sensors of oxidizing gases based on a higher control of the surface states influence on the bulk conduction properties.

Acknowledgment

This work was partially supported by the Spanish Government (Projects MAGASENS (NAN2004-09380-C04-01) and N-MOSEN (MAT2007-66741-C02-01)); and the EU (Project NAWACS (NAN2006-28568-E)). JDP is indebted to the MEC for the FPU Grant.

References

- [1] C. N. Xu, J. Tamaki, N. Miura, and N. Yamazoe, "Correlation between gas sensitivity and crystalline size in porous SnO_2 -based sensors," *Chemistry Letters*, vol. 3, pp. 441–444, 1990.
- [2] H. Ogawa, M. Nishikawa, and A. Abe, "Hall measurement studies and an electrical conduction model of tin oxide ultrafine particle films," *Journal of Applied Physics*, vol. 53, no. 6, pp. 4448–4455, 1982.
- [3] J. Arbiol, A. Cirera, F. Peiró, et al., "Optimization of tin dioxide nanosticks faceting for the improvement of palladium nanocluster epitaxy," *Applied Physics Letters*, vol. 80, no. 2, pp. 329–331, 2002.
- [4] E. Comini, G. Faglia, G. Sberveglieri, Z. Pan, and Z. L. Wang, "Stable and highly sensitive gas sensors based on semiconducting oxide nanobelts," *Applied Physics Letters*, vol. 81, no. 10, pp. 1869–1871, 2002.

- [5] D. E. Williams and K. F. E. Pratt, "Classification of reactive sites on the surface of polycrystalline tin dioxide," *Journal of the Chemical Society Faraday Transactions*, vol. 94, no. 23, pp. 3493–3500, 1998.
- [6] R. W. J. Scott, S. M. Yang, N. Coombs, G. A. Ozin, and D. E. Williams, "Engineered sensitivity of structured tin dioxide chemical sensors: opaline architectures with controlled necking," *Advanced Functional Materials*, vol. 13, no. 3, pp. 225–231, 2003.
- [7] A. Cabot, A. Vilà, and J. R. Morante, "Analysis of the catalytic activity and electrical characteristics of different modified SnO₂ layers for gas sensors," *Sensors and Actuators B*, vol. 84, no. 1, pp. 12–20, 2002.
- [8] F. Hernández-Ramírez, A. Tarancon, O. Casals, et al., "Electrical properties of individual tin oxide nanowires contacted to platinum electrodes," *Physical Review B*, vol. 16, no. 8, Article ID 085429, 2007.
- [9] F. Hernández-Ramírez, A. Tarancón, O. Casals, J. Arbiol, A. Romano-Rodríguez, and J. R. Morante, "High response and stability in CO and humidity measures using a single SnO₂ nanowire," *Sensors and Actuators B*, vol. 121, no. 1, pp. 3–17, 2007.
- [10] C. Malagù, V. Guidi, M. Stefancich, M. C. Carotta, and G. Martinelli, "Model for Schottky barrier and surface states in nanostructured n-type semiconductors," *Journal of Applied Physics*, vol. 91, no. 2, pp. 808–814, 2002.
- [11] E. Rossinyol, J. Arbiol, F. Peiró, et al., "Nanostructured metal oxides synthesized by hard template method for gas sensing applications," *Sensors and Actuators B*, vol. 109, no. 1, pp. 57–63, 2005.
- [12] A. Cabot, J. Arbiol, E. Rossinyol, J. R. Morante, F. Chen, and M. Liu, "Synthesis of tin oxide nanostructures with controlled particle size using mesoporous frameworks," *Electrochemical and Solid-State Letters*, vol. 7, no. 5, pp. G93–G97, 2004.
- [13] A. Prim, E. Pellicer, E. Rossinyol, F. Peiró, A. Cornet, and J. R. Morante, "A novel mesoporous CaO-loaded In₂O₃ material for CO₂ sensing," *Advanced Functional Materials*, vol. 17, no. 15, pp. 2957–2963, 2007.
- [14] E. Rossinyol, A. Prim, E. Pellicer, et al., "Synthesis and characterization of chromium-doped mesoporous tungsten oxide for gas-sensing applications," *Advanced Functional Materials*, vol. 17, no. 11, pp. 1801–1806, 2007.
- [15] E. Rossinyol, E. Pellicer, A. Prim, et al., "Gadolinium doped ceria nanocrystals synthesized from mesoporous silica," *Journal of Nanoparticle Research*, vol. 10, no. 2, pp. 369–375, 2008.
- [16] L. Fernández-Romero, J. M. Montero-Moreno, E. Pellicer, et al., "Assessment of the thermal stability of anodic alumina membranes at high temperatures," *Materials Chemistry and Physics*, vol. 111, no. 2–3, pp. 542–547, 2008.
- [17] D. Zhao, Q. Huo, J. Feng, B. F. Chmelka, and G. D. Stucky, "Nonionic triblock and star diblock copolymer and oligomeric surfactant syntheses of highly ordered, hydrothermally stable, mesoporous silica structures," *Journal of the American Chemical Society*, vol. 120, no. 24, pp. 6024–6036, 1998.
- [18] D. Zhao, J. Feng, Q. Huo, et al., "Triblock copolymer syntheses of mesoporous silica with periodic 50 to 300 angstrom pores," *Science*, vol. 279, no. 5350, pp. 548–552, 1998.
- [19] F. Kleitz, S. H. Choi, and R. Ryoo, "Cubic Ia3d large mesoporous silica: synthesis and replication to platinum nanowires, carbon nanorods and carbon nanotubes," *Chemical Communications*, vol. 9, no. 17, pp. 2136–2137, 2003.
- [20] T. Andreu, M. Manzanares, H. Mutin, et al., "Phosphonate functionalization and shrinkage effects on the gas sensing properties using metal oxides mesoporous materials," submitted.
- [21] A. Diéguez, A. Vilà, A. Cabot, et al., "Influence on the gas sensor performances of the metal chemical states introduced by impregnation of calcinated SnO₂ sol-gel nanocrystals," *Sensors and Actuators B*, vol. 68, no. 1, pp. 94–99, 2000.
- [22] N. Barsan, D. Koziej, and U. Weimar, "Metal oxide-based gas sensor research: how to?" *Sensors and Actuators B*, vol. 121, no. 1, pp. 18–35, 2007.
- [23] J. D. Prades, R. Jimenez-Diaz, F. Hernández-Ramírez, et al., "Toward a systematic understanding of photodetectors based on individual metal oxide nanowires," *Journal of Physical Chemistry C*, vol. 112, no. 37, pp. 14639–14644, 2008.
- [24] F. Hernández-Ramírez, J. D. Prades, A. Tarancon, et al., "Insight into the role of oxygen diffusion in the sensing mechanisms of SnO₂ nanowires," *Advanced Functional Materials*, vol. 18, no. 19, pp. 2990–2994, 2008.
- [25] J. D. Prades, R. Jimenez-Diaz, F. Hernández-Ramírez, et al., "Equivalence between thermal and room temperature UV light-modulated responses of gas sensors based on individual SnO₂ nanowires," *Sensors and Actuators B*, vol. 140, no. 2, pp. 337–341, 2009.
- [26] J. D. Prades, R. Jimenez-Diaz, F. Hernández-Ramírez, et al., "On the role of the illumination conditions in the performance of room temperature gas sensors based on individual SnO₂ nanowires," submitted.
- [27] P. Camagni, G. Faglia, P. Galinetto, C. Perego, G. Samoggia, and G. Sberveglieri, "Photosensitivity activation of SnO₂ thin film gas sensors at room temperature," *Sensors and Actuators B*, vol. 31, no. 1–2, pp. 99–103, 1996.
- [28] J. D. Prades, A. Cirera, and J. R. Morante, "First-principles study of NO_x and SO₂ adsorption onto SnO₂ (110)," *Journal of the Electrochemical Society*, vol. 154, no. 8, pp. H675–H680, 2007.
- [29] J. D. Prades, A. Cirera, J. R. Morante, J. M. Pruneda, and P. Ordejón, "Ab initio study of NO_x compounds adsorption on SnO₂ surface," *Sensors and Actuators B*, vol. 126, no. 1, pp. 62–67, 2007.
- [30] M. Habgood and N. Harrison, "An ab initio study of oxygen adsorption on tin dioxide," *Surface Science*, vol. 602, no. 5, pp. 1072–1079, 2008.
- [31] J. D. Prades, F. Hernández-Ramírez, R. Jimenez-Diaz, et al., "The effects of electron-hole separation on the photoconductivity of individual metal oxide nanowires," *Nanotechnology*, vol. 19, no. 46, Article ID 465501, 2008.
- [32] J. D. Prades, J. Arbiol, A. Cirera, et al., "Defect study of SnO₂ nanostructures by cathodoluminescence analysis: application to nanowires," *Sensors and Actuators B*, vol. 126, no. 1, pp. 6–12, 2007.
- [33] M. C. Desjonquères and D. Spanjaard, *Concepts in Surface Physics*, Springer, Berlin, Germany, 2nd edition, 1996.
- [34] G. A. Niklasson and C. G. Granqvist, "Electrochromics for smart windows: thin films of tungsten oxide and nickel oxide, and devices based on these," *Journal of Materials Chemistry*, vol. 17, no. 2, pp. 127–156, 2007.

Research Article

Sb-SnO₂-Nanosized-Based Resistive Sensors for NO₂ Detection

T. Krishnakumar,¹ R. Jayaprakash,¹ N. Pinna,^{2,3} A. Donato,⁴ N. Donato,⁵
G. Micali,⁶ and G. Neri⁶

¹Nanotechnology Laboratory, Department of Physics, Sri Ramakrishna Mission Vidyalaya College of Arts and Science, Coimbatore, Tamilnadu-641 020, India

²Department of Chemistry, CICECO, University of Aveiro, 3810-193 Aveiro, Portugal

³World Class University (WCU) program of Chemical Convergence for Energy & Environment (C2E2), School of Chemical and Biological Engineering, College of Engineering, Seoul National University (SNU), Seoul 151-744, South Korea

⁴Department of Mechanics and Materials, University Mediterranea, 89100 Reggio Calabria, Italy

⁵Department of Matter Physics and Electronic Engineering, University of Messina, 98166 Messina, Italy

⁶Department of Industrial Chemistry and Materials Engineering, University of Messina, 98166 Messina, Italy

Correspondence should be addressed to G. Neri, neri@ingegneria.unime.it

Received 17 December 2008; Accepted 30 April 2009

Recommended by Giorgio Sberveglieri

A study over Sb-promoted tin oxide nanopowders for sensing applications is reported. SnO₂ nanopowders pure and promoted with 5 wt% of antimony were prepared by wet chemical methods and widely characterized by TEM, XRD, and XPS techniques. Thick film resistive sensors were fabricated by depositing the synthesized nanopowders by drop-coating on interdigitated alumina substrates. The sensing characteristics of the pure SnO₂ and Sb-promoted sensors for the monitoring of trace level of NO₂ were studied. The response of the sensors to water vapor was also investigated, revealing that Sb acts favorably eliminating the interference of humidity.

Copyright © 2009 T. Krishnakumar et al. This is an open access article distributed under the Creative Commons Attribution License, which permits unrestricted use, distribution, and reproduction in any medium, provided the original work is properly cited.

1. Introduction

Metal oxide semiconductors (MOs) in the form of highly porous films are widely used in resistive chemical sensors for the monitoring of gaseous species in several applications of technological interest [1]. Tin oxide (SnO₂) is the most used sensing material in commercially sensor devices for toxic gases detection [2]. It is well known that the sensing properties of SnO₂-based material depend on its chemical and physical characteristics, which are strongly dependent on the preparation conditions, dopant and grain size. This implies that the synthesis of the sensing material is a key step in the preparation of high-performance MOS gas sensors.

SnO₂ powders and films can be prepared by a variety of synthesis methods [3–8]. Furthermore, the electrical and sensing properties of the undoped tin oxide can be modulated by addition of proper amounts of suitable dopants. For example, promoting SnO₂ with antimony, the electrical properties can be enhanced in order to greatly reduce the resistivity of the sensing film [9, 10]. This is particularly advantageous specially at low temperature, because in this

temperature interval the electrical resistance of SnO₂ films is generally high and complicates the measurements with conventional instruments.

Grain size reduction is another of the main factors for enhancing the gas sensing properties of semiconducting oxides [11–13]. It is believed that improved sensing technologies can be configured and developed by taking advantage of recent advances in nanosized materials. They are currently receiving a great deal of attention due to their unique physical properties, which derive from their nanometer-scaled sizes. In such materials, for example, the surface-to-bulk ratio is much greater than coarse materials, so that the surface properties become paramount, which makes them particularly appealing in applications, such as gas sensors, where nanosized properties can be exploited. In this regards, pure and promoted SnO₂ nanocrystalline powders have attracted much attention because of their promising applications in practical sensor devices [14, 15].

Aim of this work is to develop a nitrogen dioxide (NO₂) sensor device based on SnO₂ nanopowders with particularly low cross-sensitivity to humidity. NO₂ is a major

TABLE 1: Main characteristics of the nanopowders synthesized and treated at different temperatures.

Code	Sb (wt%)	Treatment temperature (°C)	Crystalline structure	Mean grain size (nm)
SnO ₂	0	120	SnO, Tetragonal	26
		300	SnO ₂ , Cassiterite	29
		600	SnO ₂ , Cassiterite	31
Sb-SnO ₂	5	120	SnO	12
		300	SnO ₂ , Cassiterite	15
		600	SnO ₂ , Cassiterite	16

atmospheric pollutants causing acid rains and photochemical smog. Therefore, nowadays the more and more strict regulations on the emission of this toxic gas require fast and accurate detection of NO₂ at sub-ppm concentration. The development of semiconductor sensors for detecting NO₂ in air is then strongly demanding. Previous sensor devices based on tin oxide have been described in literature [16–18]. However, humidity effects on these sensors are relevant and can significantly affect performance and cause false alarms.

For this scope here we focused our attention on Sb-SnO₂ nanopowders, with aim to develop a sensor sensitive to nitrogen dioxide at low concentrations and with a humidity-independent character. Results of previous detailed characterizations by XRD, TEM, and XPS of the synthesized nanopowders [19, 20] were taken into account in order to correlate the microstructural properties with the sensing characteristics. Performances of the Sb-SnO₂ sensor were also compared with that of a reference sensor based on nanosized pure SnO₂ powders.

2. Experimental

2.1. Nanopowders Synthesis. Reference pure SnO₂ nanopowders were synthesized as follows. A 0.1 M solution of tin(II) chloride in deionized water was prepared. Then pH of the solution was maintained between 7 and 9 using liquid ammonia diluted with water. The resulting precipitate was washed with water until no chlorine ions are detected and further washed with ethanol to remove NH₄⁺ ions. The resulting precipitate was irradiated at a frequency of 2.45 GHz and power up to 1 kW in a microwave oven for 10 minutes.

The Sb-SnO₂ nanopowders were synthesized by a chemical precipitation technique. The appropriate amount of SbCl₃ in order to have a nominal 5 wt% in the Sb-SnO₂ powder was dissolved first in fuming HCl. The resulting clear solution was added dropwise into 0.1 mol SnCl₂·2H₂O (98%, Merck chemicals) of solution using water as solvent. The total solution was stirred for 30 minutes, and aqueous phase ammonia (25%) was added dropwise until the pH of the solution adjusted to 4. Within few seconds a white precipitate was obtained. It was washed with water and ethanol until no chlorine ions were detected and refluxed for 12 hours. The refluxed precipitate was filtered and dried at 120°C in air, and the residue was ground to fine powder in a mortar and pestle.

In order to characterize the thermal behavior of the as prepared SnO₂ and Sb-SnO₂ nanopowders, they were sintered at different temperatures (up to 600°C) in air for 5 hours at a rate of 5°C/minutes. Main characteristics of the nanopowders are reported in Table 1.

2.2. Nanopowders Characterization. XRD measurements were performed on a Bruker AXS D8 Advance instrument using the CuKα with wavelength of 1.541 Å. The average crystalline size of the nanoparticle was evaluated using the Scherrer formula

$$d = \frac{K\lambda}{\beta \cos \theta}, \quad (1)$$

where d is the mean crystalline size, K is a grain shape dependent constant (0.9), λ is the wavelength of the incident beam, θ is a Bragg reflection angle, and β is the full width half maximum. Transmission Electron Microscopy (TEM), Selected-Area Electron Diffraction (SAED), and Energy Dispersive Spectroscopy (EDS) were recorded on a Technai G20-stwin Higher Resolution Electron Microscope (HRTEM) using an accelerating voltage of 200 kV. The X-Ray Photoelectron Spectroscopy (XPS) analyses have been performed using the PHI ESCA system equipped with an Mg X-ray source ($h = 1253.6$ eV) with a hemispherical analyzer.

2.3. Sensing Tests. Sensors were made by depositing by drop coating films (1–10 μm thick) of the nanopowders dispersed in water on alumina substrates (6 × 3 mm²) with Pt interdigitated electrodes and a Pt heater located on the backside. A schematic picture of the sensor structure and a photo of one fabricated sensor device are reported in Figure 1. The sensors were then introduced in a stainless-steel test chamber for the sensing tests. The experimental bench for the electrical characterization of the sensors (Figure 2) allows to carry out measurements in controlled atmosphere. Gases coming from certified bottles can be further diluted in air at a given concentration by mass flow controllers. Electrical measurements were carried out in the temperature range from 50 to 250°C, with steps of 50°C, under a dry air total stream of 200 sccm, collecting the sensors resistance data in the four-point mode. A multimeter data acquisition unit Agilent 34970A was used for this purpose, while a dual-channel power supplier instrument Agilent E3632A was employed to bias the built-in heater of the sensor to perform measurements at superambient temperatures.

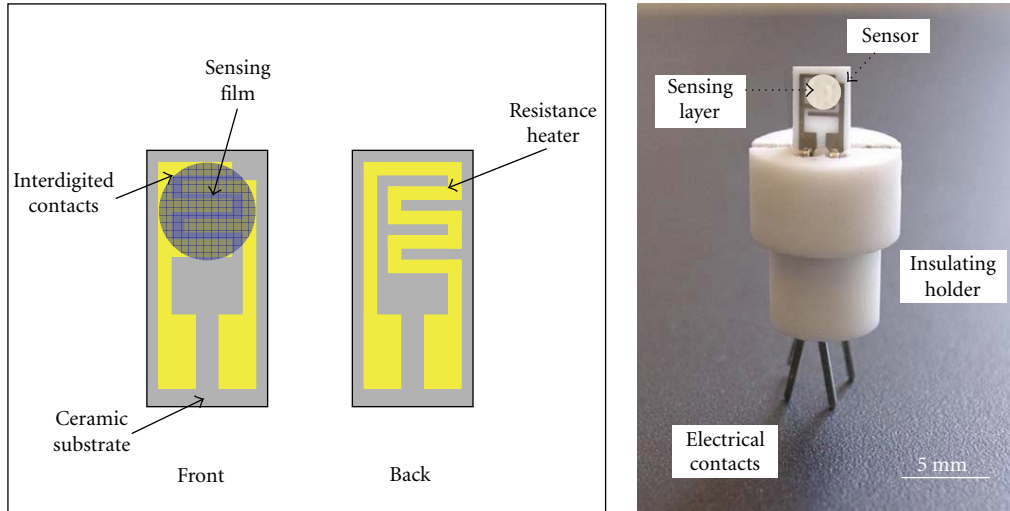


FIGURE 1: Schematic representation of the sensor architecture and photograph of the fabricated sensor device.

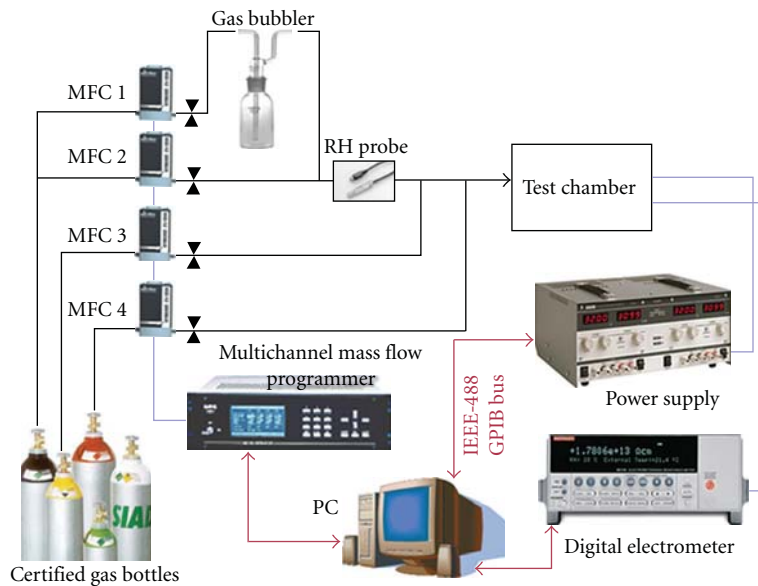


FIGURE 2: Experimental setup for gas sensors characterization.

The gas response, S , is defined as $S = R/R_0$ where R is the electrical resistance of the sensor at different NO_2 concentrations in dry air and R_0 the resistance in dry air.

Humidity tests were carried out in the range of 0%–100% RH. The different RH values were obtained by mixing dry and wet air (coming from a bubbler maintained at 20°C) into opportune volumetric ratios.

3. Results and Discussion

3.1. Microstructural Characterization. A detailed characterization of the nanopowders under study has been reported elsewhere [19, 20]. Here we recall briefly some data important for the present application. The analyses carried out on the “as prepared” materials showed that the main crystalline

phase is SnO . Increasing the calcination temperature, the microstructure evolved stably up to SnO_2 . The pure SnO_2 sample sintered at 600°C showed typical SnO_2 tetragonal Cassiterite reflections, with the calculated lattice parameters of tin oxide nanoparticles ($a = 0.483$ nm, $c = 0.325$ nm) in good agreement with the standard values ($a = 0.474$ nm, $c = 0.319$ nm). The average particle size, as estimated from XRD measurements, increases slightly with the treatment temperature (from 26 to 30 nm after calcination at 600°C).

Similar findings have been found on the Sb-promoted tin oxide nanopowders. On the sample sintered at 600°C, XRD analysis (Figure 3) indicated the existence of tetragonal Cassiterite type of Sb-substituted SnO_2 crystals, implying that all antimony ions came into the crystal lattice of bulk SnO_2 to substitute for tin ions. Calculation through the

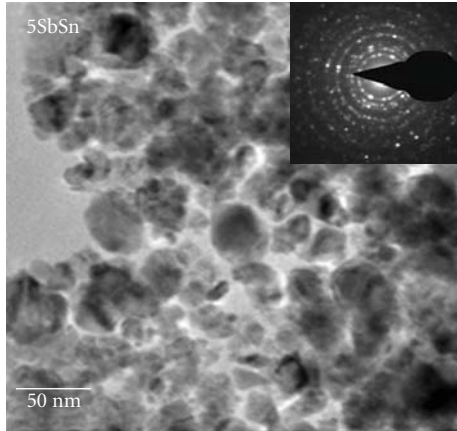


FIGURE 3: XRD characterization of the Sb-SnO₂ nanopowders treated at 600°C. Plane index related to SnO₂ Cassiterite is shown.

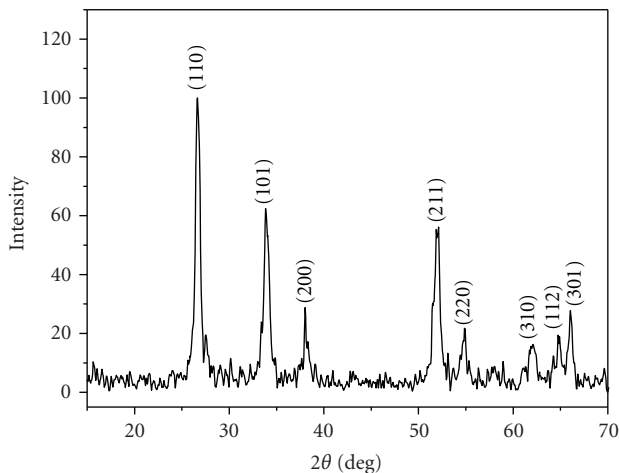


FIGURE 4: TEM characterization of the Sb-SnO₂ nanopowders treated at 600°C.

Scherrer formula indicated that the average particle size of 5 wt% antimony promoted tin oxide powder sintered at 600°C is in the range of 20 nm.

Typical morphology of the Sb-promoted tin oxide nanopowders treated at high temperature (600°C) is shown in the TEM micrograph in Figure 4. The corresponding SAED pattern is also reported in the insert. The particle size estimated from TEM measurements corresponds to the average size (20 nm) evaluated from XRD measurements, suggesting that they should be monocrystalline.

In order to investigate the stoichiometry of the 5 wt% Sb-SnO₂ nanopowders, a detailed XPS analysis has been carried out. At this concentration of antimony, the Sb⁵⁺ component was found to be dominant with only a small amount of Sb³⁺ content [20]. Due to the substitution of Sb⁵⁺ ion by replacing Sn⁴⁺ ion, the donor center was appeared very close to the conduction band of SnO₂; that is, donor level was merging with conduction band. This has reflected a decrease in the resistance of the sample.

From characterization data above reported and summarized in Table 1, it can be deduced that crystalline charac-

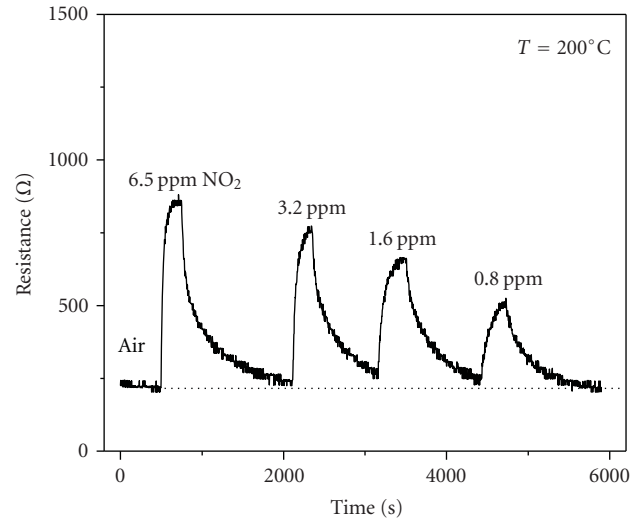


FIGURE 5: Transient response of the Sb-SnO₂ sensor operated at 200°C to different NO₂ concentrations.

teristics of SnO₂ were not affected by promoter addition. On the contrary, the grain size was largely dependent on the addition of Sb. Thus, the Sb-promoted powders have presented lower grain size with respect to the unpromoted one. This is in agreement with results reported by other authors [21]. Even if an absolute comparison cannot be made because the samples derive from different preparation methods, this behavior can be explained by the blocking effect of the Sb atoms on the grains growth.

3.2. NO₂ Sensing Tests. To perform sensing tests, sensor devices were fabricated depositing by drop coating the synthesized nanopowders on interdigitated alumina substrates, as described in the experimental section. The as synthesized SnO₂ and Sb-SnO₂ nanopowders resulted particularly suitable for deposition without the use of any further additive. After the sensing layer was deposited on the ceramic substrate, a high-temperature treatment was performed in order to stabilize the film microstructure.

Electrical measurements have shown, as expected, that the baseline resistance of Sb-promoted sensor in air is lower than measured for the pure SnO₂-based sensor. A low resistance of the sensing layer is a favorable factor implying a low noise in the measurement of the resistance and consequently a high signal/noise ratio. The low resistance of the Sb-SnO₂ film can be explained considering that SnO₂ is a metal oxide with *n*-type semiconducting behavior. In the presence of Sb⁵⁺, the SnO₂ conductivity increase can be due to the formation of holes.

Figure 5 shows a typical transient response to different NO₂ concentrations obtained with the Sb-SnO₂ sensor operated at 200°C. The sensing layer was in this case pretreated at 300°C. The responses are fast and reversible. The response time, τ_{res} , defined here as the time it takes for the resistance of the gas sensor to decrease to 90% of the minimum resistance when NO₂ is introduced into air, is fast ($\tau_{res} < 90$ seconds). The recovery time, τ_{rec} , the

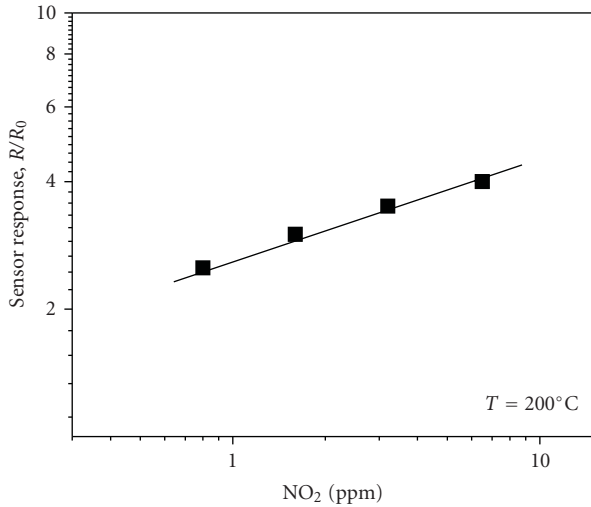


FIGURE 6: Response of the Sb-SnO₂ sensor as a function of the NO₂ concentration.

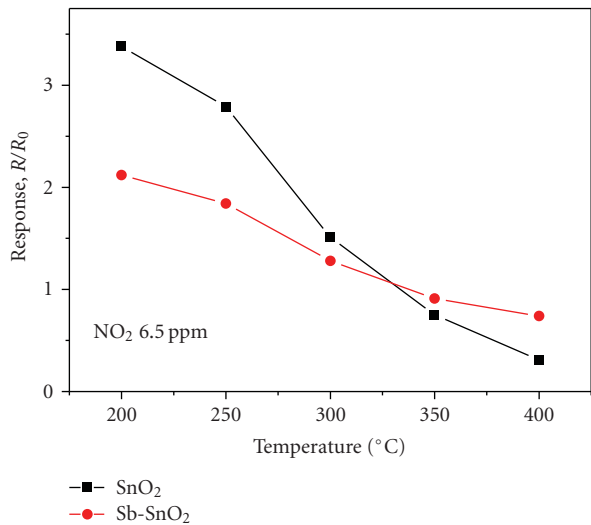


FIGURE 7: Response of the SnO₂ and Sb-SnO₂ sensors as a function of the operating temperature.

time required for 90% increment in resistance when NO₂ is turned off and air is reintroduced into the chamber, is instead longer. The response of the sensor correlate linearly with the concentration of the gas target (Figure 6). The good response to 0.8 ppm of NO₂ indicates the promising performance of the sensor for the detection of sub-ppm concentrations of nitrogen dioxide in air.

Tests carried out with sensing layer treated at higher temperatures have shown that the response slightly decreases. This can be attributed to a loss of surface area consequently to grain size increment. However, treatment temperature at least up to 400°C is necessary in order to stabilize the microstructure of the sensing layer, its grain size, and the adhesion to the substrate. Indeed, after thermal treatment, the adhesion of the sensing layer to the alumina substrate was found to be very tight and durable to stretch. Therefore,

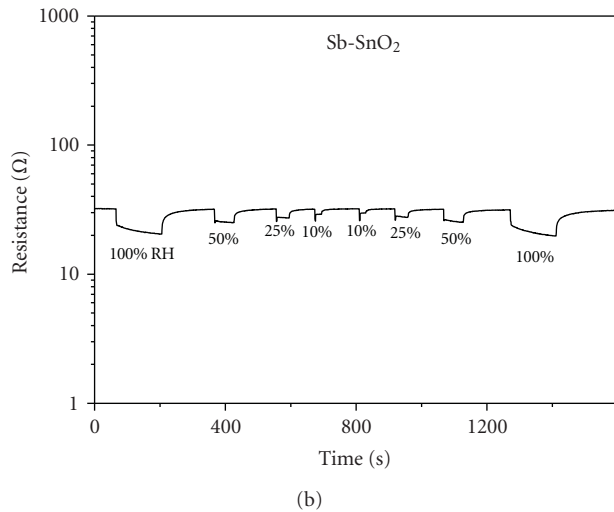
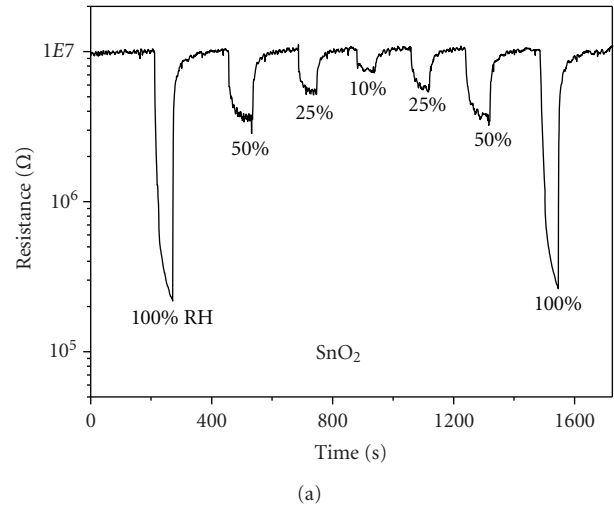


FIGURE 8: Dynamic response of the SnO₂ and Sb-SnO₂ sensors at the operating temperature of 200°C to step changes in relative humidity levels.

further sensing tests have been carried out with pretreatment temperature of 400°C.

Tests aimed to find the optimal operating temperature of the sensors for NO₂ monitoring are reported in Figure 7. The operative range investigated was between 200 and 400°C. The lower limit was related to the necessity to provide an adequate fast response/recovery time. At all operating temperatures, the pure SnO₂ sensor showed a larger response compared to Sb-promoted sensor. It was also observed that at operating temperature higher than 300°C the sensor response is lower than 1 (i.e., the resistance in nitrogen dioxide is lower than that registered in air). This can be explained on the basis of a transition from *n*- to *p*-type response, as observed for different metal oxide semiconductors exposed to various gases [22], leading in our case to an inverse response above 300°C. A more detailed investigation is however necessary in order to better understand the above observed behavior.

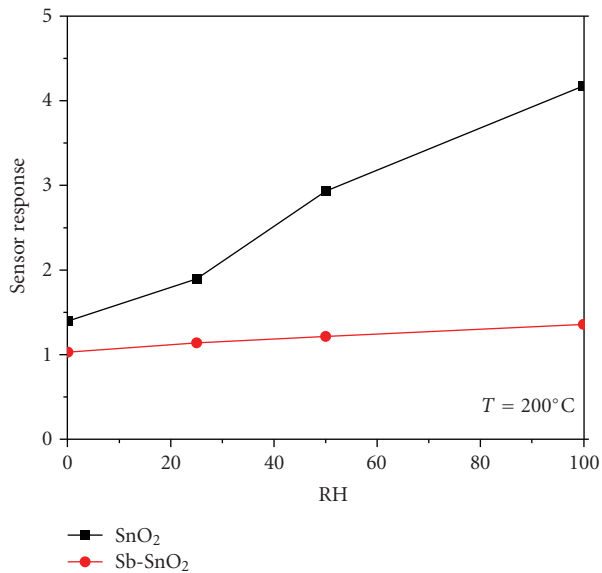


FIGURE 9: Magnitude of signal increases versus RH for both sensors investigated.

Taking into account all sensing characteristics (sensitivity, response/recovery time) and power consumption, the working temperature of 200°C provides the better opportunity for the sensor operation. Despite antimony addition worsens the response toward NO₂, it acts favorably eliminating the interference of humidity. In this regard, analyzing the response to different mixtures of NO₂ and RH, no influence of the water vapor on the NO₂ sensor response was observed.

3.3. Humidity Tests. It is well known that tin dioxide sensors are generally sensitive to humidity [23]. In order to understand the effects of water on the sensing characteristics of Sb-SnO₂ nanopowders, it is necessary to recall in brief the behavior of H₂O molecules adsorbed on the surface of metal oxide semiconductors. Water is a donor type molecule and giving one electron to the bulk becomes positively charged, and this leads to the formation of a negative space charge region; moreover, the adsorbed water molecules can dissociate into hydroxyl groups [24]. At low temperature this latter mechanism is slower than previous, but it gains importance increasing the temperature. In any case, humidity interferes with sensor operation because these mechanisms can lead to remarkable temporary or irreversible change in the sensor resistance with time (drift), complicating the detection of the gas target [25].

For accurate and reliable detection with our devices, it is then necessary to observe what effects relative humidity has upon the selective detection of NO₂ gas. Therefore, an experimentation with various RH concentrations was carried out to examine the effects of relative humidity on pure and Sb-promoted devices. Results collected in all ranges of temperature investigated have shown that the sensor resistance decreases as RH increases. As an example, the dynamic response of the sensors at the operating temperature of 200°C to step changes in relative humidity

levels is reported in Figure 8. The magnitude of signal increases with increasing RH, as reported in Figure 9 for both sensors investigated. It can be observed that the response to humidity is higher for the SnO₂-based sensor. This could be due to a different texture (in terms of surface area, pore size distribution, etc.) between the two sensing layers. Interestingly, this leads on the Sb-promoted device to a water response almost negligible. Therefore, it can be concluded that water vapor affects less the Sb-doped sensor, and this is advantageous because of the consequent stability of the sensor against ambient humidity fluctuations under practical working conditions for NO₂ monitoring.

4. Conclusions

SnO₂ nanopowders pure and promoted with 5 wt% of antimony were prepared by wet chemical methods and widely characterized by SEM, TEM, XRD, and XPS techniques.

The sensing characteristics of thick film resistive sensors fabricated by the pure SnO₂- and Sb-promoted sensors for the monitoring of trace level of NO₂ were studied. The attention was focused on the Sb-promoted tin oxide film, which has shown interesting properties as NO₂ sensor. Indeed, besides it resulted less sensitive to gas target with respect to the SnO₂ sensor, its sensing properties are not influenced by humidity. By optimizing the operating conditions, an NO₂ sensor with good sensitivity and negligible water influence has been developed.

References

- [1] N. Yamazoe, "Toward innovations of gas sensor technology," *Sensors and Actuators B*, vol. 108, no. 1-2, pp. 2-14, 2005.
- [2] K. Takahata, *Tin Dioxide Sensors—Development and Applications. Chemical Sensor Technology*, vol. 1, Elsevier, Amsterdam, The Netherlands, 1988.
- [3] N. S. Baik, G. Sakai, N. Miura, and N. Yamozoe, "Hydrothermally treated sol solution of tin oxide for thin-film gas sensor," *Sensors and Actuators B*, vol. 63, pp. 74-79, 2000.
- [4] Z. Han, N. Guo, F. Li, W. Zhang, H. Zhao, and Y. Qian, "Solvothermal preparation and morphological evolution of stannous oxide powders," *Materials Letters*, vol. 48, no. 2, pp. 99-103, 2001.
- [5] K. C. Song and J. H. Kim, "Synthesis of high surface area tin oxide powders via water-in-oil microemulsions," *Powder Technology*, vol. 107, no. 3, pp. 268-272, 2000.
- [6] C. H. Shek, J. K. L. Lai, and G. M. Lin, "Grain growth in nanocrystalline SnO₂ prepared by sol-gel route," *Nanostructured Materials*, vol. 11, no. 7, pp. 887-893, 1999.
- [7] D. Briand, M. Labeau, J. F. Currie, and G. Delabouglise, "Pd-doped SnO₂ thin films deposited by assisted ultrasonic spraying CVD for gas sensing: selectivity and effect of annealing," *Sensors and Actuators B*, vol. 48, no. 1-3, pp. 395-402, 1998.
- [8] N. Pinna and M. Niederberger, "Surfactant-free nonaqueous synthesis of metal oxide nanostructures," *Angewandte Chemie International Edition*, vol. 47, no. 29, pp. 5292-5304, 2008.
- [9] D. Zhang, Z. Deng, J. Zhang, and L. Chen, "Microstructure and electrical properties of antimony-doped tin oxide thin film deposited by sol-gel process," *Materials Chemistry and Physics*, vol. 98, no. 2-3, pp. 353-357, 2006.

- [10] S.-Y. Lee and B.-O. Park, "Structural, electrical and optical characteristics of SnO₂:Sb thin films by ultrasonic spray pyrolysis," *Thin Solid Films*, vol. 510, no. 1-2, pp. 154–158, 2006.
- [11] C. Xu, J. Tamaki, N. Miura, and N. Yamazoe, "Grain size effects on gas sensitivity of porous SnO₂-based elements," *Sensors and Actuators B*, vol. 3, no. 2, pp. 147–155, 1991.
- [12] S. G. Ansari, P. Boroojerdian, S. R. Sainkar, R. N. Karekar, R. C. Aiyer, and S. K. Kulkarni, "Grain size effects on H₂ gas sensitivity of thick film resistor using SnO₂ nanoparticles," *Thin Solid Films*, vol. 295, no. 1-2, pp. 271–276, 1997.
- [13] G. Korotcenkov, "Gas response control through structural and chemical modification of metal oxide films: state of the art and approaches," *Sensors and Actuators B*, vol. 107, no. 1, pp. 209–232, 2005.
- [14] N. Pinna, G. Neri, M. Antonietti, and M. Niederberger, "Non-aqueous synthesis of nanocrystalline semiconducting metal oxides for gas sensing," *Angewandte Chemie International Edition*, vol. 43, no. 33, pp. 4345–4349, 2004.
- [15] G. Neri, A. Bonavita, G. Rizzo, et al., "Towards enhanced performances in gas sensing: SnO₂ based nanocrystalline oxides application," *Sensors and Actuators B*, vol. 122, no. 2, pp. 564–571, 2007.
- [16] M. M. H. Bhuiyan, S. Katsuki, T. Ueda, and T. Ikegami, "Improvement in the sensitivity of SnO₂ thin film based NO_x gas sensor by loading with single-walled carbon nanotube prepared by pulsed laser deposition process," *Sensor Letters*, vol. 6, no. 4, pp. 635–640, 2008.
- [17] F. J. Gutierrez, L. Ares, J. I. Robla, et al., "NO_x tin dioxide sensors activities, as a function of doped materials and temperature," *Sensors and Actuators B*, vol. 16, no. 1–3, pp. 354–356, 1993.
- [18] G. Williams and G. S. V. Coles, "NO_x response of tin dioxide based gas sensors," *Sensors and Actuators B*, vol. 16, no. 1–3, pp. 349–353, 1993.
- [19] T. Krishnakumar, N. Pinna, K. P. Kumari, K. Perumal, and R. Jayaprakash, "Microwave-assisted synthesis and characterization of tin oxide nanoparticles," *Materials Letters*, vol. 62, no. 19, pp. 3437–3440, 2008.
- [20] T. Krishnakumar, R. Jayaprakash, N. Pinna, A. R. Phani, M. Passacantando, and S. Santucci, "Structural, optical and electrical characterization of antimony-substituted tin oxide nanoparticles," *Journal of Physics and Chemistry of Solids*, vol. 70, pp. 993–999, 2009.
- [21] E. C. P. E. Rodrigues and P. Olivi, "Preparation and characterization of Sb-doped SnO₂ films with controlled stoichiometry from polymeric precursors," *Journal of Physics and Chemistry of Solids*, vol. 64, no. 7, pp. 1105–1112, 2003.
- [22] T. Siciliano, A. Tepore, G. Micocci, A. Genga, M. Siciliano, and E. Filippo, "Transition from n- to p-type electrical conductivity induced by ethanol adsorption on α-tellurium dioxide nanowires," *Sensors and Actuators B*, vol. 138, no. 1, pp. 207–213, 2009.
- [23] M. Batzill and U. Diebold, "The surface and materials science of tin oxide," *Progress in Surface Science*, vol. 79, no. 2–4, pp. 47–154, 2005.
- [24] F. Réti, M. Fleischer, J. Gerblinger, et al., "Comparison of the water effect on the resistance of different semiconducting metal oxides," *Sensors and Actuators B*, vol. 26, no. 1–3, pp. 103–107, 1995.
- [25] N. Bărsan and R. Ionescu, "The mechanism of the interaction between CO and an SnO₂ surface: the role of water vapour," *Sensors and Actuators B*, vol. 12, no. 1, pp. 71–75, 1993.

Research Article

Highly Sensitive InO_x Ozone Sensing Films on Flexible Substrates

G. Kiriakidis,^{1,2} K. Moschovis,^{1,2} I. Kortidis,² and R. Skarvelakis²

¹ Physics Department, University of Crete, 71003 Heraklion, Crete, Greece

² IESL, Foundation for Research and Technology Hellas (FORTH), 71003 Heraklion, Crete, Greece

Correspondence should be addressed to G. Kiriakidis, kiriakid@iesl.forth.gr

Received 26 December 2008; Revised 16 March 2009; Accepted 1 May 2009

Recommended by Wojtek Wlodarski

InO_x thin films with a thickness of the order of 100 nm were grown by dc magnetron sputtering on glass, Si and flexible (PET) substrates. The electrical conductivity of InO_x thin films exhibited a change of two orders of magnitude during photoreduction with ultraviolet light and subsequent oxidation in ozone concentrations from 2370 to 15 ppb, at room temperature. Optical transparency of over 85% for all substrates was maintained. Film structural and ozone sensing properties were analyzed. Surface morphology investigations carried out by SEM for films on PET substrates showed extended surface cracking for bending angles beyond 40°. Optimization of growth conditions has led to films with extremely low detection levels for ozone down to 15 ppb at room temperature, demonstrating the wide prospective of utilizing these metal oxides as gas sensors on flexible substrates for a variety of automotive and air-conditioning applications.

Copyright © 2009 G. Kiriakidis et al. This is an open access article distributed under the Creative Commons Attribution License, which permits unrestricted use, distribution, and reproduction in any medium, provided the original work is properly cited.

1. Introduction

Metal oxides compose an interesting heterogeneous class of active materials with properties ranging from metallic and semiconducting to insulating, attracting research efforts from almost all fields of material science and physics. These materials find applications in micro/nanoelectronics, photovoltaics, light-emitting diodes, transparent thin film transistors, sensors and radio frequency identification systems (RFIDs) extending to superconductivity and magnetism.

A new thrust for the wider use of metal oxide based gas sensors is anticipated owing to the latest integration efforts on flexible substrates [1–4]. Successful application on flexible substrates may lead to simpler, faster and inexpensive fabrication techniques targeting novel roll-to-roll and printed processing applications with obvious advantages over conventional ceramic or silicon-based technologies.

Most of the recent efforts focus on the utilization of metal oxide sensing materials for the detection of volatile organic compounds (VOCs). Among these materials tin oxide (SnO_x) has been the favored and mostly studied gas sensing metal oxide over the last three decades. In all recent integration efforts the prime critical parameters for successful operation have been the heating element due to the high-temperature (>300°C) requirement for a typical

operation of the SnO_x-based gas sensors [4]. However, recent reports have emerged showing sensitivity levels in the low ppb (parts per billion) range at operating temperatures from around 100°C to Room Temperature (RT), based on Indium (In) and Zinc (Zn) oxide films grown by sputtering and spray pyrolysis [5–7]. Utilization of sensing ozone levels below the 75 ppb mark, as imposed lately by International bodies [8–10], is of paramount importance for health reasons, and efforts for low cost, disposable and reliable sensing elements particularly on flexible substrates will be proved very valuable for a variety of automotive and air-conditioning applications.

In the present work we report on the growth of InO_x thin films on amorphous, 0.25 mm thick, PET (polyethylene terephthalate) flexible substrates (HiFi Co) and corresponding films grown on glass (Corning 1737 F) and Si substrates by dc magnetron sputtering at RT, and on their sensing response characteristics.

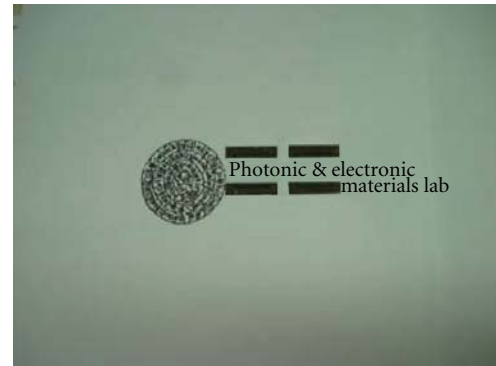
2. Experimental

Deposition of the InO_x thin films was done in a dc magnetron sputtering system (Alcatel 250) using a 99.999% pure In target. Detailed description of the deposition system may

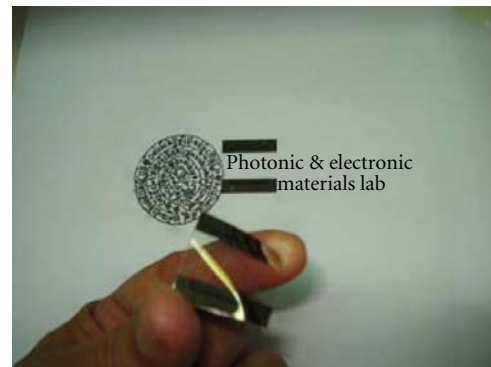
be found in refs [5, 11]. Films were grown with thicknesses in the range of 50 to 200 nm, at constant total pressure of 8×10^{-3} mbar, in a 100% oxygen plasma atmosphere at RT. Surface morphology was studied with Scanning Electron Microscopy (SEM). Electrical and sensing characterization (photoreduction/oxidation process) was performed in a home-designed system [12] at FORTH. During photoreduction the samples were directly irradiated in vacuum by a low power (4.5 mW/cm^2) UV light (254 nm) mercury pencil lamp at a distance of approximately 3 cm for 20 minutes till achieving a steady state. Our choice of a photoreduction process under vacuum rather than in ambient air was deliberate as we wanted to demonstrate sensitivity responses at ozone detection limits well below the concentration of Ozone in ambient air. It is well documented that the content of air in Ozone varies among other with altitude, season, temperature and humidity and takes values from 30 to 90 ppb [8–10]. These levels increase in the presence of UV and so detection of concentrations below these levels is impossible. Thus, by applying the photoreduction process at ambient air conditions one would be unable to fully photoreduce the film since at the same time on the film surface an oxidation process would be present due to (a) residual ozone in air, (b) ozone produced by the UV absorbed by the oxygen in air and (c) re-adsorption of atomic oxygen leaving the film surface after UV irradiation. The only experimentally correct procedure to fully reduce the film without competing oxidation processes and separate the photoreduction from subsequent oxidation with controlled oxidizing gas concentrations was to do the experiment under vacuum thus pumping away all residual and process produced gases during photoreduction, that is, having a gas free surface on which ultra low and accurately controlled gas mixtures could be introduced demonstrating the intrinsic sensing properties of the tested films. Subsequently, the chamber was back-filled with a controlled amount of Ozone flow (concentrations from 2370 to 15 ppb in synthetic air) as produced by an Ozone generator (Thermo 49i). The treatment lasted until a steady state of film maximum resistivity was reached, a process that span from 20 to 40 minutes after which no further changes in resistivity could be observed. The process of photoreduction and oxidation was repeated several times to establish repeatability. Sensing response was recorded in terms of the fractional resistance change [13] utilizing an electric field of 1 or 10 V cm^{-1} and monitoring the corresponding current with a pico-electrometer. Current-voltage (I-V) measurements were taken before each cycling to ensure the ohmic nature of the conducts.

3. Results and Discussion

The superior properties of InO_x over other metal oxides such as SnO_2 and ZnO in as far as ozone detection is concerned, have been elaborated in the past [14, 15]. These were attributed to the distinct surface structure of InO_x with the polar nature of a pure oxygen terminated sub-plane exhibiting a low binding energy for a number of oxygen atoms. This, in combination with the surface oxygen



(a)



(b)

FIGURE 1: (a) Transparent InO_x films on glass (left) and PET (right) substrate. (b) Flexibility of the film on PET.

deficiency on these films, leads to enhanced ozone sensitivity levels of the order of a few parts-per-billion (ppb) with fast response and recovery times.

Figures 1(a) and 1(b) demonstrates the high level of the InO_x film transparency both on the glass and 0.25 mm thick PET substrate. Optical transparency of more than 85%, detected by UV-VIS spectroscopy (not shown here) was maintained for either substrate while the optical band-gap (E_g) was 3.75 eV.

Film surface morphology analysis by SEM has shown smooth surfaces with a characteristic granular polycrystalline structure [5] for flat and bended films to angles up to 40° , beyond which extended cracks were developed as shown in Figure 2. A detailed investigation of the mechanical properties of these films as a function of bending angle and the study of the elastic to inelastic transition limits is currently under way. In the present, we report on the film sensing responses which were found to be independent of the applied substrate.

Figure 3 exhibits six circles of photoreduction-oxidation process for the InO_x films in three stages. During photoreduction (stage A), films reach 60% of their steady state conductivity within the first minute and a maximum value of $10^2 \text{ Ohm}^{-1} \text{ cm}^{-1}$ after five minutes of the UV light exposure in vacuum. The conductance rise when the film is illuminated with UV light is due both to the generation of free carriers within the film, and to photo-desorption of

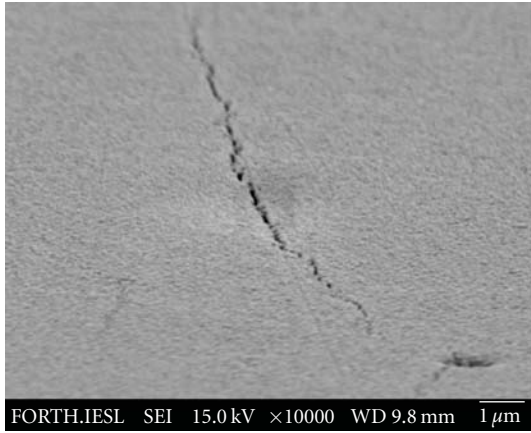


FIGURE 2: SEM image of the InO_x film on PET substrate under a bending angle of 40°.

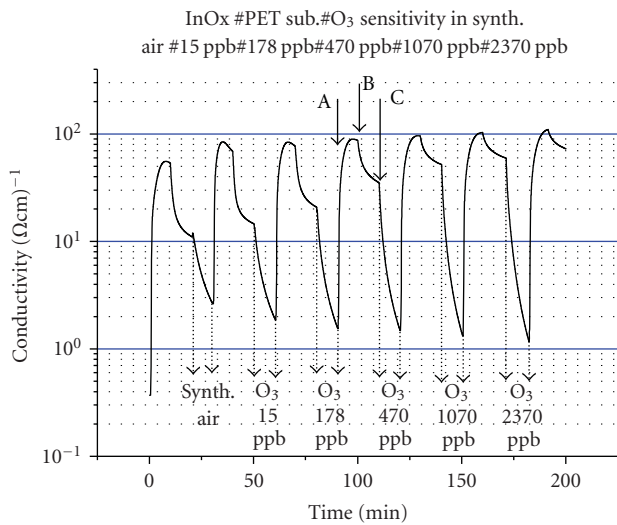


FIGURE 3: Photoreduction-oxidation process of the InO_x films.

surface species with a subsequent thinning of the electron depletion layer near the film surface. Consequently, the applied UV lamp was switched-off (stage B) and a reduction in conductivity of the order of 30% was recorded, probably due to an inherent oxidation process associated by absorption of residual oxygen in the chamber. During the following stage (C) the films were exposed to accurately controlled ozone concentrations in synthetic air (used as reference) ranging from 2370 to 15 ppb.

Figure 4 shows a normalized comparison of the exponential decays during the oxidation process at the above ozone concentrations. Although previous results utilizing SnO₂ [6] and aerosol spray pyrolysis of ZnO [7] have shown corresponding sensitivity levels for ozone of the order of 15 ppb too, to our knowledge, this is the first time that such extremely low sensing levels are reported for metal oxide thin films at room temperature (RT) on flexible substrates. The differences in the exponential decay is a measure, on the one hand, of the efficiency of these films to screen the various

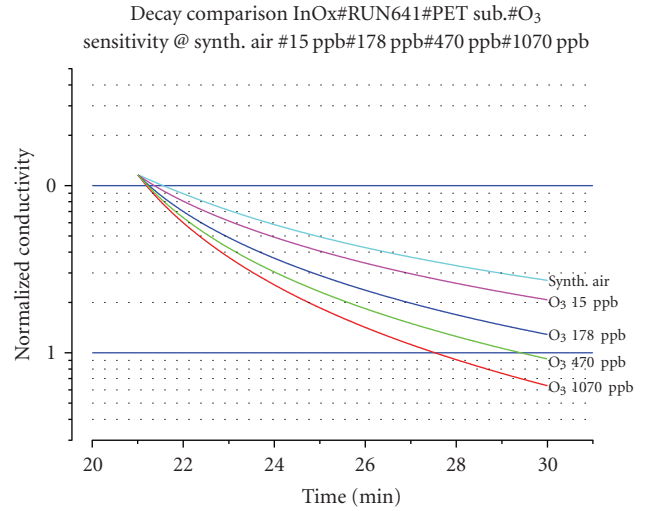


FIGURE 4: Normalized exponential decays from 1070 to 15 ppb ozone exposures.

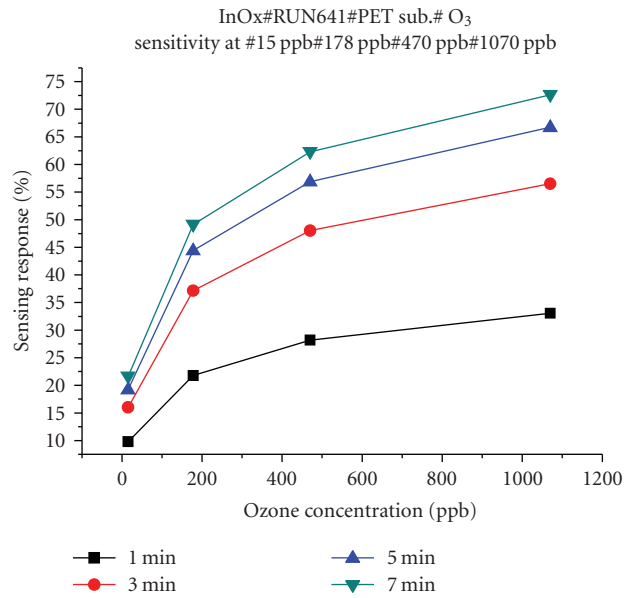


FIGURE 5: Sensing responses at ozone concentrations from 1070 to 15 ppb.

ozone concentrations down to the extremely low level of 15 ppb and on the other, to resolve these responses from the synthetic air, used as reference signal, within the first minute of analysis.

Indeed, Figure 5 depicts the recorded differences in the 7, 5, 3 and 1 minute of the oxidation decay process, demonstrating the capacitance to resolve extremely low ozone concentrations (15 ppb) while providing reliable readouts (10% sensing response) within the first minute of the exposure time.

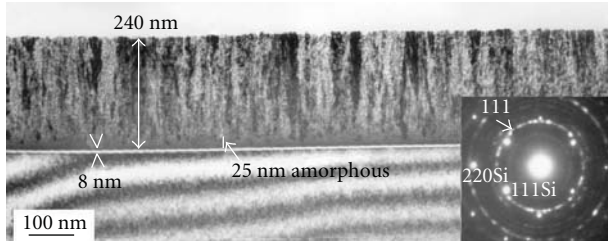


FIGURE 6: XTEM micrograph of the film structure on Si [001] orientation wafer. The thickness of the film is 240 nm with an initial 25 nm amorphous layer followed by a crystalline columnar structure. Between the substrate and the $\text{In}_2\text{O}_{3-x}$ film a very thin amorphous layer about 8 nm is observed.

It is widely accepted that surface effects and specific surface characteristics are related to processes such as catalytic activity or surface adsorption and are key for superior chemical sensor response. Films grown with the above conditions have gone through an extensive structural investigation. They have shown to exhibit a characteristic polycrystalline structure with a 20 nm mean width of columnar grains, as studied by combined cross-section TEM (XTEM) and Plane View TEM (PVTEM) supported by independent AFM. Detailed analysis on these films and an account of their structural characteristics have already been published recently elsewhere [16]. They revealed that the columnar morphology was an inherent property of the mode of growth independent of the chosen substrate. The films were amorphous in the early stage of growth (Figure 6) becoming crystalline after a critical thickness subject to the incubation time needed in order an amorphous material to generate nucleation centres at a given temperature.

Observations have also shown a correlation of critical surface parameters such as grain size, texturing, porosity and grain shape with the film sensing characteristics. AFM study of the film surfaces confirmed granular polycrystalline morphology. It was found that both the average lateral grain size and the surface roughness mainly increased with increasing the film thickness, a parameter that is directly controlled by the deposition temperature, and the growth total pressure.

It is generally accepted that film sensitivity correlates with surface parameters using the conduction model of metal oxide gas sensors approximation given by Barsan and Weimar [17]. The basic mechanism of gas detection is the interaction of the gaseous species with the surface of the semiconducting sensitive metal oxide layer. As a consequence of this surface interaction charge transfer takes place between the absorbed species and the semiconducting sensitive material [18]. According to this model, for small grains and narrow necks, when the mean free path of free charge carriers become comparable with the dimension of the grains, the surface influence on the mobility dominates over bulk phenomena. In the presence of the ionic species on the surface, after UV photoreduction, the electronic concentration in the surface states increases. The surface states concentration is correlated with the roughness and

grain size via surface-to-volume ratio. Thus, the basic mechanism of gas detection is the interaction of the gaseous species with the surface of the semiconducting sensitive metal oxide layer. However, since sensitivity is measured in terms of film conductivity which is directly effected by the size of the grain and thus the volume and type of scattering mechanisms that the free electrons are experiencing, it has been shown that films with grain size of the above order and grown under the reported growth conditions fulfill the above model criteria providing a convincing explanation for the reported enhanced gas sensitivities and thus the ultra low detection limits obtained.

The above film response characteristics combined with the room temperature growth and operation requirements, open-up the road for low-cost, highly sensitive gas sensing elements on flexible substrates challenging corresponding efforts based on carbon nano-tubes [19] while serving recent integration advances on flexible tag microlab gas sensor systems [3, 20].

4. Conclusions

InO_x thin films have been grown by DC magnetron sputtering on glass and PET substrates. High optical transparency for both substrates was maintained. Surface morphology investigations carried out by SEM for films on PET substrates showed extended surface cracking for bending angles beyond 40° . Films with columnar growth structure and nano size grains of the order of 20 nm used as gas sensing elements exhibited extremely low detection levels for ozone (15 ppb), at room temperature, demonstrating the wide prospective of utilizing these metal oxides as gas sensors on flexible substrates for a variety of applications.

Acknowledgments

This work was partially supported by the national funded project PENED 2003-03ED733.

References

- [1] A. Oprea, N. Bârsan, U. Weimar, J. Courbat, D. Briand, and N. F. de Rooij, "Integrated temperature, humidity and gas sensors on flexible substrates for low-power applications," in *Proceedings of the 6th IEEE Sensors Conference*, pp. 158–161, Atlanta, Ga, USA, October 2007.
- [2] X. Hao, J. Ma, D. Zhang, et al., "Transparent conducting antimony-doped tin oxide films deposited on flexible substrates by r.f. magnetron-sputtering," *Applied Physics A*, vol. 75, no. 3, pp. 397–399, 2002.
- [3] I. Sayhan, A. Helwig, T. Becker, et al., "Discontinuously operated metal oxide gas sensors for flexible tag microlab applications," *IEEE Sensors Journal*, vol. 8, no. 2, pp. 176–181, 2008.
- [4] D. Briand, S. Colin, J. Courbat, S. Raible, J. Kappler, and N. F. de Rooij, "Integration of MOX gas sensors on polyimide hotplates," *Sensors and Actuators B*, vol. 130, no. 1, pp. 430–435, 2008.
- [5] M. Suchea, N. Katsarakis, S. Christoulakis, S. Nikolopoulou, and G. Kiriakidis, "Low temperature indium oxide gas

- sensors,” *Sensors and Actuators B*, vol. 118, no. 1-2, pp. 135–141, 2006.
- [6] G. Kiriakidis, K. Moschovis, and S. B. Sadale, “Systems and set-ups for effective sensing response applications,” in *Sensors for Environment, Health and Security: Advanced Materials and Technologies*, M.-I. Baraton, Ed., vol. 24, pp. 159–178, Springer, New York, NY, USA, 2009.
- [7] S. J. Ippolito, S. Kandasamy, K. Kalantar-zadeh, et al., “Highly sensitive layered ZnO/LiNbO₃ SAW device with InO_x selective layer for NO₂ and H₂ gas sensing,” *Sensors and Actuators B*, vol. 111-112, pp. 207–212, 2005.
- [8] U.S. Food and Drug Administration, *Federal Register*, vol. 62, no. 74, pp. 18937–18964, 1997.
- [9] USA EPA NAAQS directory, March 2008.
- [10] Canada’s Clean Air Act and Canadian Environmental Protection Act (CEPA).
- [11] G. Kiriakidis, M. Bender, N. Katsarakis, et al., “Ozone sensing properties of polycrystalline indium oxide films at room temperature,” *Physica Status Solidi A*, vol. 185, no. 1, pp. 27–32, 2001.
- [12] C. Xirouchaki, G. Kiriakidis, T. F. Pedersen, and H. Fritzsche, “Photoreduction and oxidation of as-deposited microcrystalline indium oxide,” *Journal of Applied Physics*, vol. 79, no. 12, pp. 9349–9352, 1996.
- [13] M. F. Mabrook, C. Pearson, and M. C. Petty, “Inkjet-printed polypyrrole thin films for vapour sensing,” *Sensors and Actuators B*, vol. 115, no. 1, pp. 547–551, 2006.
- [14] G. Korotcenkov, I. Blinov, M. Ivanov, and J. R. Stetter, “Ozone sensors on the base of SnO₂ films deposited by spray pyrolysis,” *Sensors and Actuators B*, vol. 120, no. 2, pp. 679–686, 2007.
- [15] G. Kiriakidis, M. Sucheá, S. Christoulakis, and N. Katsarakis, “High performance gas sensing materials based on nanostructured metal oxide films,” *Reviews on Advanced Materials Science*, vol. 10, no. 3, pp. 215–223, 2005.
- [16] G. Kiriakidis, M. Sucheá, S. Christoulakis, K. Moschovis, T. Kitsopoulos, and J. Stoemenos, “Nano-structural and surface characteristics of non-stoichiometric In₂O_{3-x} thin films,” *International Journal of Nanotechnology*, vol. 6, no. 1-2, pp. 208–218, 2009, Guest Editors: A. G. Nassiopoulou and C. Fotakis.
- [17] N. Barsan and U. Weimar, “Conduction model of metal oxide gas sensors,” *Journal of Electroceramics*, vol. 7, no. 3, pp. 143–167, 2001.
- [18] S. Mishra, C. Ghanshyam, N. Ram, R. P. Bajpai, and R. K. Bedi, “Detection mechanism of metal oxide gas sensor under UV radiation,” *Sensors and Actuators B*, vol. 97, no. 2-3, pp. 387–390, 2004.
- [19] O. Kuzmych, B. L. Allen, and A. Star, “Carbon nanotube sensors for exhaled breath components,” *Nanotechnology*, vol. 18, no. 37, Article ID 375502, 7 pages, 2007.
- [20] E. Abad, B. Mazzolai, A. Juarros, et al., “Investigation of fabrication and encapsulation processes for a flexible tag microlab,” *Microsystem Technologies*, vol. 14, no. 4-5, pp. 527–534, 2008.

Research Article

Designing Zirconium Coated Polystyrene Colloids and Application

Diana Chira and Seong S. Seo

Department of Natural Sciences, Albany State University, 504 College Drive, Albany, GA 31705, USA

Correspondence should be addressed to Seong S. Seo, seong.seo@asurams.edu

Received 15 December 2008; Revised 20 March 2009; Accepted 29 March 2009

Recommended by Yongxiang Li

A simple technique has been developed to prepare core colloids that are modified using zirconium oxychloride, based on heating a solution of core colloid composites, consisting of poly (ethylenimine) (PEI) and zirconium oxychloride. The interaction of zirconium oxychloride with the polystyrene (PS) core colloids has been investigated using Fourier transform-infrared spectroscopy (FT-IR), energy dispersive X-ray spectroscopy (EDX), and scanning electron microscopy (SEM) data. FT-IR studies confirm the occurrence of amine groups present in PEI which are oxidized to carboxyl groups after the reaction. The EDX data and the SEM images confirm the presence of zirconium particles immobilized on the polystyrene surfaces. Demeton, a highly toxic nerve agent, was used due to its ability to easily bind through its organophosphate group illustrating a practical application of the PS-PEI-Zr particles. Attenuated Total Reflection (ATR) Spectroscopy was used to assess the interactions between the toxic nerve agent demeton-S and the PS-PEI-Zr particles. The results show that the presented technique for coating polystyrene core colloids with zirconium was successfully accomplished, and the newly formed particles easily bond with demeton agents through the P=O functional group.

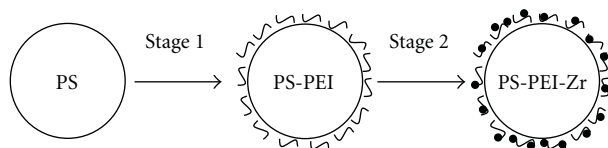
Copyright © 2009 D. Chira and S. S. Seo. This is an open access article distributed under the Creative Commons Attribution License, which permits unrestricted use, distribution, and reproduction in any medium, provided the original work is properly cited.

1. Introduction

Recently, numerous synthetic mechanisms have been employed for surface adsorption of metal nanoparticles (NPs) onto colloidal inorganic and organic spheres [1–6]. A particularly successful method of depositing the metal NPs on the surface of the colloids involves the use of an intermediate linker poly (ethylenimine), PEI, which can bind both transition metal ions, such as zirconium, and negatively charged colloids [7–10]. Additionally, the PEI serves as the reducing agent in the conversion of the metal ions to the metal NPs [11]. In such a scheme, the core component, usually polystyrene (PS) or silicon dioxide (SiO₂), serves as a supporting structure, and the outer NPs predominantly exhibit the properties that are attributed to the metal NP-core colloid composites. The advantages derived from these hybrid materials can be seen in their remarkable attributes which include enhanced conductivity, temperature stability, optical, and catalytic activity [12–14].

Over the years, there has been considerable interest surrounding the fabrication of core-shell spheres that consist of templated cores coated with shells that have different chemical compositions. These core-shell spheres often exhibit properties that are substantially different from those of the templated core (increased stability, higher surface area, different magnetic, and optical properties), making them attractive from both a scientific and technological standpoint [15–17]. Furthermore, the properties of core-shell particles can also be tailored in a controlled fashion by independently altering the composition, dimension, and structure of the core or shell. Application for such core-shell spheres is diverse, including biosensors [18], chemical sensors [19], and so forth.

Organophosphates (OPs) are well-known neurotoxins; they disrupt the cholinesterase enzyme that regulates acetylcholine [20–22], a neurotransmitter needed for proper nervous system function. Because of their high neurotoxicity, OP compounds have been exploited for use as pesticides and as nerve agents with application as chemical and biological



SCHEME 1: Procedure for coating PS colloids with metal.

warfare agents. As a result of the high toxicity of OPs, fast and effective detection of these toxic agents in the environment, public places, or workplaces and the monitoring of individual exposures to chemical warfare agents have become increasingly important for national security and health protection purposes [23–25]. Early detection and detection of low concentrations of OPs still remain an extremely difficult challenge. Such information may give an indication of terrorist activity, allowing proper procedures to be followed to mitigate potential danger. Analysis of OPs in environmental and biological samples is routinely carried out using analytical techniques, such as gas or liquid chromatography and mass spectrometry [26].

For OP detection, enzyme-biosensors of inhibition and noninhibition systems are mostly based on the immobilization of acetylcholinesterase (AChE) [27], tyrosinase enzyme (Tyr) [28], alkaline phosphatase (ALP) [29], or organophosphorus hydrolase (OHP) [30, 31] onto various electrodes. Due to their high sensitivity and selectivity toward OPs, these have been proposed for field screening of OP neurotoxins [32]. However, while these specific antibodies against OP pesticides have been recently developed for enzyme-linked immunoassay and immunosensors [33, 34], acetylcholinesterase is commercially available but OP hydrolase and antibodies against OPs are still only produced in laboratories, which limits wide applications of biosensors. Demeton is also used as pesticide, which on most metal oxides, in our case zirconium and adsorbs through the P=O functional group. IR spectroscopy in combination with Attenuated Total Reflection (ATR) spectroscopy is one of the most widely used techniques for surface infrared analysis. ATR-IR has been used for studying processes at surfaces or in films, such as adsorption [35–37] and diffusion [38–40].

The aim of this paper is to treat polystyrene colloids with zirconium oxychloride in order to create a hybrid material which may find utility as an organophosphate sensor. The composite colloids are obtained by coating PS with PEI followed by the addition of ZrO₂ (Figure 1). In this reaction scheme, PEI is relatively inert and thus does not have a significant effect, if any, on the ultimate formation of the NPs. The advantages of this method are simple operation, easy large scale production, and the generality for various core colloids. The zirconium acts as a selective probe targeting the phosphate group of the demeton which upon bonding shows a change in the ATR spectrum. Other inorganic ions have also found to have an affinity for P=O functional groups, such as Mg, thus paving the way for future research into different colloidal compositions for OP detection.

In this paper, we report a novel method for detecting OP chemical nerve agents by incorporating the enhanced properties of zirconium coated polystyrene core colloid composites with the strong affinity for chemical nerve agents. Polystyrene was utilized for the core component with the outer layer being comprised of zirconium NPs. We characterized the PS-PEI-Zr colloids by using SEM, EDX, and FT-IR spectroscopy. The prepared zirconium colloids were placed on the ATR ZnSe crystal forming a thin layer used for the detection of demeton-S.

2. Experimental Section

2.1. Materials. Poly (ethylenimine) (PEI), polystyrene (PS) colloids with an average size of 210 nm, sodium phosphate buffer, zirconium oxychloride, sodium citrate (C₆H₅O₇Na₃·2H₂O), absolute ethanol, ammonium hydroxide solution (NH₄OH, 25%), formaldehyde (HCHO, 37%), and Demeton-S were all obtained from Sigma-Aldrich.

2.2. Modification of Core Colloids with PEI (PS-PEI). 1 g of PS colloids was dispersed in 50 mL of phosphate buffer solution with a pH of 6.5 (solution A). 0.1 g of PEI was then dissolved in 5 mL of phosphate buffer to produce solution B (mass ratio of PEI to PS was 1 : 10). Solution B was stirred at room temperature (25°C) for 1 hour followed by three cycles of centrifugation (20 000 rpm) and washing with 10 mL of water.

2.3. Preparation of PS-PEI-Zr. PEI modified PS colloid solution was dispersed in 100 mL water, and 0.15 g of zirconium oxychloride was added and then heated for one hour at 100°C. After cooling to room temperature, the ammonia and sodium citrates were added into the dispersion solution. 12 mL of sodium citrate (1 M) was added to result in a 1 : 1 molar ratio of zirconium oxychloride to sodium citrate. Dropwise addition of NH₄OH (1 M) were used to bring the pH up to 10. Then, the HCHO diluted with ethanol was added. After completion, the solid was isolated by 3 cycles of centrifugation/washing.

2.4. Characterization. FTIR and ATR data were recorded with a *Perkin Elmer Spectrum BX FT-IR System*. The sample for the FTIR measurement was prepared by grinding a dry PS-PEI-Zr sample with KBr into fine powders which were then pressed at 20 000 psi into pellets. Scanning electron microscopy (SEM) was performed with a JSM-5900.

2.5. Demeton Adsorption on PS-PEI-Zr. 10 μL of the prepared PS-PEI-Zr colloids were placed on a Miracle Universal Plate composed of ZnSe crystal (PIKE Technologies, Single Reflection Horizontal ATR) and allowed to dry, forming a thin layer. 10 μL of 1 mM demeton-S solution were then added to the dry PS-PEI-Zr thin layer, and the ATR spectrum was obtained at a 4 cm⁻¹ resolution with a spectral range of 750–4000 cm⁻¹. Following this, an additional 10 μL of the

demeton-S solution were added to give a cumulative 20 μL , for which the ATR spectrum was obtained in each case.

3. Results and Discussion

In the present study, PEI-modified polystyrene colloids were used as the templates for the deposition of zirconium nanoparticles. Tian et al. [41, 42] have previously demonstrated that PEI acts as a reductant in the conversion of transition compounds into metallic particles. Moreover, through the use of TEM, XPS, and XRD they were able to identify the metallic particles whether it was Ag, Au, or another transition, and the exact oxidation state was thus obtained. In this study we use zirconium oxychloride which is reduced to metallic zirconium particles upon being adsorbed onto the PEI modified colloids. This chemistry is critical in the formation of the metal nanoparticles; otherwise, the PEI will simply be coated with a layer of oxychloride, changing the chemical properties we seek.

Following synthesis, the prepared composites were characterized by FT-IR spectroscopy, scanning electron microscopy (SEM), and EDX. Figure 1 shows SEM images of the prepared composites at different magnifications, showing the deposition of zirconium onto the core polystyrene colloids. A larger central PS core can be observed, and on the superficial surface, small protrusions of the Zr metal are visually attached which are shown by a porous network on the surface of the colloids as opposed to bare PS which shows a smooth consistent surface. Scanning electron microscopy images were obtained on a JSM-5900 which was operated at 30 kV. The SEM analysis was consistent and reproducible with a representative area shown in Figure 2. The synthesized PS-PEI-Zr composites were suspended in water, dispersed then on glass, and coated with approximately 10 nm of AuPd. The lighter edges is an edge effect, that is, secondary electrons can be collected from the top and bottom surfaces of the sphere edges, leading to an enhanced secondary electron signal. Figure 2 displays an EDX spectrum which quantitatively detects the constituent elements. The spectrum showed Zr LA1, Zr LB1, Zr LB3, Zr L1, Zr KA1, and Zr KB1 peaks, indicating the presence of the third layer of zirconium oxychloride on the polystyrene colloids. Other peaks detected in the EDX spectrum included Cl KA1, Cl KB1, and O KA1, exposing elements such as chlorine and oxygen, a result of the deposition of zirconium oxychloride on the polystyrene colloids.

In Figure 3, the IR spectra of PS, PS-PEI, and PS-PEI-Zr composites detect a peak at 2916 cm^{-1} which corresponds to the stretching vibration of C–H, also indicating the presence of PEI on the PS colloids. At around 1700 cm^{-1} , the presence of the C=O stretching of carboxyl is detected. Analyzing the PS-PEI curve, it is noticeable that the C=O bond is not present anymore due to the consummation of the carboxyl group of PS with PEI and Zr nanoparticles in the colloidal modifications. There are two more prominent peaks present at 1492 and 1452 cm^{-1} which are a result of the antisymmetric and symmetric stretching of O–C–O. These two are easily detectable in the PS curve, however,

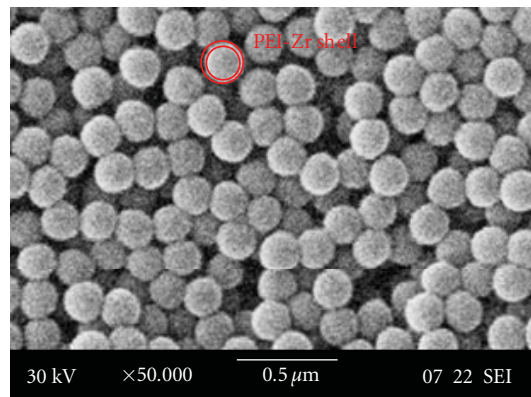


FIGURE 1: SEM image of PS-PEI-Zr spheres.

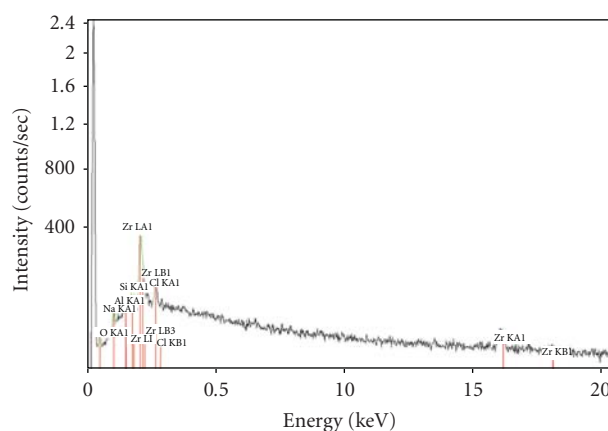


FIGURE 2: EDX of PS-PEI-Zr.

it diminishes in the PS-PEI curve and disappears almost completely in the PS-PEI-Zr curve. This is again due to the expenditure of the functional group in the formation of PS-PEI and PS-PEI-Zr colloids. The peak around 3500 cm^{-1} is characteristic of the N–H stretching vibration from the PEI, thus it is not present in the PS curve and does not considerably reduce in the PS-PEI-Zr curve. Analysis of the reaction mechanism occurring between PEI and Zr has previously been studied and reported by IR spectroscopy [43]. It was shown that two new IR bands involving interactions between Zr(IV) (Lewis Acid) and the nitrogen of the amine group (Lewis base) in PEI were present in the IR spectrum. A broad band in the 1580–1560 cm^{-1} region is observed both for aromatic amines (polyvinyl imidazole) and for aliphatic amines (polyethyleneimine), which can be easily assigned to the NH_2 asymmetric bending mode for the latter. A second band is observed in the 1450–1350 cm^{-1} range, depending on the nature of the amine group.

Figure 4 shows the ATR spectra for consecutive additions of 10 μL aliquots of a 0.06 M demeton solution to a thin layer of the PS-PEI-Zr colloids. Analysis of the ATR data and the relevant peaks shows that the binding of the PS-PEI-Zr colloids to demeton has been successfully achieved. All four peaks at 2350 cm^{-1} are designated peaks for the

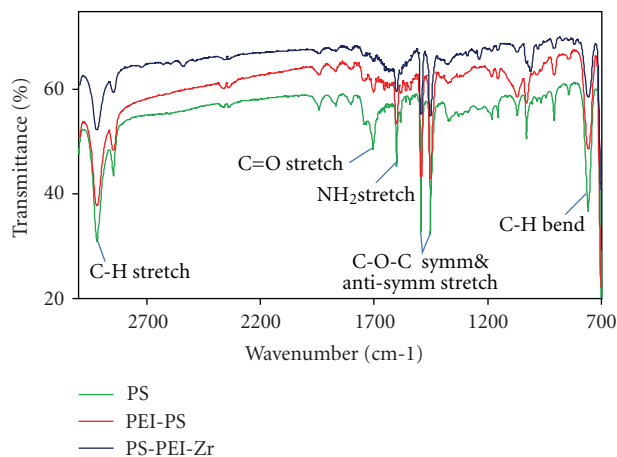


FIGURE 3: FT-IR spectra of PS, PS-PEI, and PS-PEI-Zr.

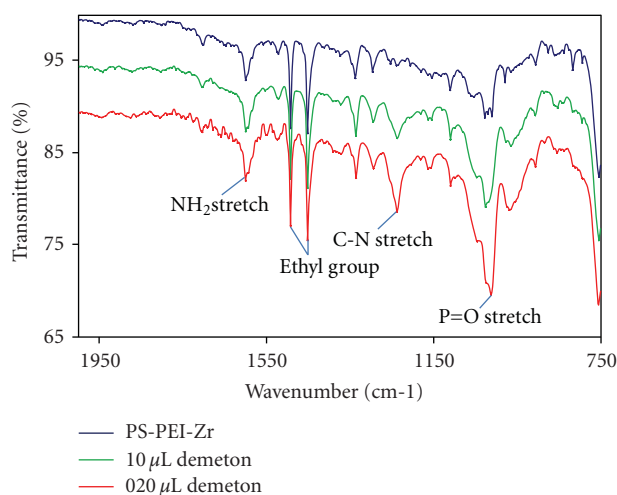


FIGURE 4: ATR spectrum PS-PEI-Zr with 10 and 20 μL of 0.06 M demeton.

presence of zirconium. Zirconium is not only present in the PS-PEI-Zr compound form, but also in its binding to demeton. At 1010 cm^{-1} there is a strong presence of P=O bond for PS-PEI-Zr bonded to $20\ \mu\text{L}$ of demeton; while there is a considerable reduction of those bonds with $10\ \mu\text{L}$ of demeton and even disappearance for the actual compound not bonded to the nerve agent. Zirconium is an ideal candidate for immobilization of molecules with oxygen groups as contained in phosphates [44]. Because of zirconium's affinity for phosphoric groups, by treating the PEI modified colloids with zirconium we are able to amplify the interaction of the colloids with demeton's P=O bond and thus see a significant change in the corresponding ATR spectrum. Thus, a similar sensor can be developed to sense other nerve agents with the organophosphate structure such as paraoxon. In contrast, if only PEI modified colloids were employed we would not expect to see a dramatic change in the ATR spectrum as there is no known specificity of PEI for the P=O group of demeton. The ethyl group is

distinguished at 1452 and 1492 cm^{-1} as a result of PS-PEI-Zr bonding with demeton, explaining why it is absent in the curve of PS-PEI-Zr without demeton. These peaks strongly increase in intensity with increasing amounts of demeton solution. As the concentration of demeton decreased, it was observed that no strong peak of demeton is noticeable due to the weak signal, leading to much more prominent peaks when 10 and $20\ \mu\text{L}$ of demeton are present. Based on the response of the PS-PEI-Zr nanocomposites to the experimental parameters of the concentration of demeton in 1 liter of solution, the minimum sensitivity limit of this platform for the detection of demeton is approximately 2.0 ± 0.2 PPB. This can be considered the effective dose which would result in a detectable change in the ATR spectrum. The above result allows us to propose a model for the development of chemical nerve agents through the use of ATR.

4. Conclusion

A simple method was developed to coat polystyrene colloids with zirconium particles. The zirconium nanoparticles were able to attach to polystyrene due to its modification with PEI, which increased the speed of the reaction and it had no appreciable effect on the formation of the core colloids. The detection of OPs has become important because many nerve agents and pesticides are organophosphates. The ability to detect small quantities and/or low concentrations of these compounds is critical. The strong bond formed between Zr and demeton allows for facile detection of the demeton peaks by using various characterization techniques. PS-PEI-Zr is simple to synthesize and utilize, and its use to detect OPs is useful for applications such as pesticide analysis. The developed method is an efficient strategy due to its simple operation, easy large-scale production, and generality for various core colloids.

Acknowledgments

This work was supported by grants from the National Institutes of Health, RIMI program, Grant P20 MD001085, and the Department of Defense, Grant W911NF-06-1-0433 whose supports are greatly appreciated.

References

- [1] F. Caruso, "Nanoengineering of particle surfaces," *Advanced Materials*, vol. 13, no. 1, pp. 11–22, 2001.
- [2] S. J. Oldenburg, R. D. Averitt, S. L. Westcott, and N. J. Halas, "Nanoengineering of optical resonances," *Chemical Physics Letters*, vol. 288, no. 2–4, pp. 243–247, 1998.
- [3] P. Schuetz and F. Caruso, "Semiconductor and metal nanoparticle formation on polymer spheres coated with weak polyelectrolyte multilayers," *Chemistry of Materials*, vol. 16, no. 16, pp. 3066–3073, 2004.
- [4] A. Dawson and P. V. Kamat, "Semiconductor-metal nanocomposites. Photoinduced fusion and photocatalysis of gold-capped TiO_2 (TiO_2/gold) nanoparticles," *Journal of Physical Chemistry B*, vol. 105, no. 5, pp. 960–966, 2001.

- [5] C. Pacholski, A. Kornowski, and H. Weller, "Site-specific photodeposition of silver on ZnO nanorods," *Angewandte Chemie International Edition*, vol. 43, no. 36, pp. 4774–4777, 2004.
- [6] M. Jakob and H. Levanon, "Charge distribution between UV-irradiated TiO₂ and gold nanoparticles: determination of shift in the fermi level," *Nano Letters*, vol. 3, no. 3, p. 353, 2003.
- [7] T. Ji, V. G. Lirtsman, Y. Avny, and D. Davidov, "Preparation, characterization, and application of Au-shell/polystyrene beads and Au-shell/magnetic beads," *Advanced Materials*, vol. 13, no. 16, pp. 1253–1256, 2001.
- [8] B. Sadtler and A. Wei, "Spherical ensembles of gold nanoparticles on silica: electrostatic and size effects," *Chemical Communications*, no. 15, pp. 1604–1605, 2002.
- [9] S.-E. Park, M.-Y. Park, P.-K. Han, and S.-W. Lee, "The effect of pH-adjusted gold colloids on the formation of gold clusters over APTMS-coated silica cores," *Bulletin of the Korean Chemical Society*, vol. 27, no. 9, pp. 1341–1345, 2006.
- [10] L. A. Belfiore and E. M. Indra, "Transition metal compatibilization of poly(vinylamine) and poly(ethylene imine)," *Journal of Polymer Science Part B*, vol. 38, no. 4, pp. 552–561, 2000.
- [11] X. Sun, S. Dong, and E. Wang, "One-step synthesis and characterization of polyelectrolyte-protected gold nanoparticles through a thermal process," *Polymer*, vol. 45, no. 7, pp. 2181–2184, 2004.
- [12] E. Prodan, C. Radloff, N. J. Halas, and P. Nordlander, "A hybridization model for the plasmon response of complex nanostructures," *Science*, vol. 302, no. 5644, pp. 419–422, 2003.
- [13] S. A. Kalele, A. A. Kundu, S. W. Gosavi, et al., "Rapid detection of *Escherichia coli* by using antibody-conjugated silver nanoshells," *Small*, vol. 2, no. 3, pp. 335–338, 2006.
- [14] S. W. Bishnoi, C. J. Rozell, C. S. Levin, et al., "All-optical nanoscale pH meter," *Nano Letters*, vol. 6, no. 8, pp. 1687–1692, 2006.
- [15] F. Caruso, "Nanoengineering of particle surfaces," *Advanced Materials*, vol. 13, no. 1, pp. 11–22, 2001.
- [16] U. Jeong, Y. Wang, M. Ibisate, and Y. Xia, "Some new developments in the synthesis, functionalization, and utilization of monodisperse colloidal spheres," *Advanced Functional Materials*, vol. 15, no. 12, pp. 1907–1921, 2005.
- [17] V. Salgueiriño-Maceira, M. A. Correa-Duarte, M. Spasova, L. M. Liz-Marzán, and M. Farle, "Composite silica spheres with magnetic and luminescent functionalities," *Advanced Functional Materials*, vol. 16, no. 4, pp. 509–514, 2006.
- [18] S. A. Kalele, S. S. Ashtaputre, N. Y. Hebalkar, et al., "Optical detection of antibody using silica-silver core-shell particles," *Chemical Physics Letters*, vol. 404, no. 1–3, pp. 136–141, 2005.
- [19] J. P. Walker and S. A. Asher, "Acetylcholinesterase-based organophosphate nerve agent sensing photonic crystal," *Analytical Chemistry*, vol. 77, no. 6, pp. 1596–1600, 2005.
- [20] T. L. Rosenberry, *Advances in Enzymology and Related Areas of Molecular Biology*, John Wiley & Sons, New York, NY, USA, 1975.
- [21] S. Zhang, H. Zhao, and R. John, "Development of a quantitative relationship between inhibition percentage and both incubation time and inhibitor concentration for inhibition biosensors-theoretical and practical considerations," *Biosensors and Bioelectronics*, vol. 16, no. 9–12, pp. 1119–1126, 2001.
- [22] S. Fennouh, V. Casimiri, and C. Burstein, "Increased paraoxon detection with solvents using acetylcholinesterase inactivation measured with a choline oxidase biosensor," *Biosensors and Bioelectronics*, vol. 12, no. 2, pp. 97–104, 1997.
- [23] J. Wang, "Microchip devices for detecting terrorist weapons," *Analytica Chimica Acta*, vol. 507, no. 1, pp. 3–10, 2004.
- [24] O. A. Sadik, W. H. Land Jr., and J. Wang, "Targeting chemical and biological warfare agents at the molecular level," *Electroanalysis*, vol. 15, no. 14, pp. 1149–1159, 2003.
- [25] Y. Lin, F. Lu, and J. Wang, "Disposable carbon nanotube modified screen-printed biosensor for amperometric detection of organophosphorus pesticides and nerve agents," *Electroanalysis*, vol. 16, no. 1-2, pp. 145–149, 2004.
- [26] J. Sherma, "Pesticides," *Analytical Chemistry*, vol. 65, no. 12, pp. 40R–54R, 1993.
- [27] B. Bucur, D. Fournier, A. Danet, and J.-L. Marty, "Biosensors based on highly sensitive acetylcholinesterases for enhanced carbamate insecticides detection," *Analytica Chimica Acta*, vol. 562, no. 1, pp. 115–121, 2006.
- [28] J. C. Vidal, S. Esteban, J. Gil, and J. R. Castillo, "A comparative study of immobilization methods of a tyrosinase enzyme on electrodes and their application to the detection of dichlorvos organophosphorus insecticide," *Talanta*, vol. 68, no. 3, pp. 791–799, 2006.
- [29] F. Mazzei, F. Botrè, S. Montilla, R. Pilloton, E. Podestà, and C. J. Botrè, "Alkaline phosphatase inhibition based electrochemical sensors for the detection of pesticides," *Journal of Electroanalytical Chemistry*, vol. 547, no. 1, pp. 95–100, 2004.
- [30] C. Karnati, H. Du, H.-F. Ji, et al., "Organophosphorus hydrolase multilayer modified microcantilevers for organophosphorus detection," *Biosensors and Bioelectronics*, vol. 22, no. 11, pp. 2636–2642, 2007.
- [31] P. Mulchandani, W. Chen, and A. Mulchandani, "Microbial biosensor for direct determination of nitrophenyl-substituted organophosphate nerve agents using genetically engineered *Moraxella* sp," *Analytica Chimica Acta*, vol. 568, no. 1-2, pp. 217–221, 2006.
- [32] D. De Souza, S. A. S. Machado, and R. C. Pires, "Multiple square wave voltammetry for analytical determination of paraquat in natural water, food, and beverages using microelectrodes," *Talanta*, vol. 69, no. 5, pp. 1200–1207, 2006.
- [33] V. A. Pedrosa, D. Miwa, S. A. S. Machado, and L. A. Avaca, "On the utilization of boron doped diamond electrode as a sensor for parathion and as an anode for electrochemical combustion of parathion," *Electroanalysis*, vol. 18, no. 16, pp. 1590–1597, 2007.
- [34] H. El Bakouri, J. M. Palacios-Santander, L. Cubillana-Aguilera, A. Ouassini, I. Naranjo-Rodríguez, and J. L. H.-H. de Cisneros, "Electrochemical analysis of endosulfan using a C18-modified carbon-paste electrode," *Chemosphere*, vol. 60, no. 11, pp. 1565–1571, 2005.
- [35] K. D. Dobson and A. J. McQuillan, "An infrared spectroscopic study of carbonate adsorption to zirconium dioxide sol-gel films from aqueous solutions," *Langmuir*, vol. 13, no. 13, pp. 3392–3396, 1997.
- [36] Y. Lu, L. Han, C. J. Brinker, T. M. Niemczyk, and G. P. Lopez, "Chemical sensors based on hydrophobic porous sol-gel films and ATR-FTIR spectroscopy," *Sensors and Actuators B*, vol. 36, no. 1–3, pp. 517–521, 1996.
- [37] B. J. Ninness, D. W. Bousfield, and C. P. Tripp, "In situ infrared technique for studying adsorption onto particulate silica surfaces from aqueous solutions," *Applied Spectroscopy*, vol. 55, no. 6, pp. 655–662, 2001.
- [38] M. G. Baschetti, E. Piccinini, T. A. Barbari, and G. C. Sarti, "Quantitative analysis of polymer dilation during sorption using FTIR-ATR spectroscopy," *Macromolecules*, vol. 36, no. 25, pp. 9574–9584, 2003.

- [39] R. Göbel, R. W. Seitz, S. A. Tomellini, R. Krska, and R. Kellner, "Infrared attenuated total reflection spectroscopic investigations of the diffusion behaviour of chlorinated hydrocarbons into polymer membranes," *Vibrational Spectroscopy*, vol. 8, no. 2, pp. 141–149, 1995.
- [40] U. Hellstern and V. Hoffmann, "Diffusion in ultrathin films studied by time resolved FTIR-ATR spectroscopy," *Journal of Molecular Structure*, vol. 349, pp. 329–332, 1995.
- [41] C. Tian, E. Wang, L. Gao, et al., "A precursor route for the preparation of metal-dielectric composite in large scale," *Chemistry Letters*, vol. 35, no. 7, pp. 812–813, 2006.
- [42] C. Tian, B. Mao, E. Wang, et al., "Simple strategy for preparation of core colloids modified with metal nanoparticles," *The Journal of Physical Chemistry C*, vol. 111, no. 9, pp. 3651–3657, 2007.
- [43] B. Chaufer, M. Rabiller-Baudry, A. Bouguen, J. P. Labbé, and A. Quémerais, "Spectroscopic characterization of zirconia coated by polymers with amine groups," *Langmuir*, vol. 16, no. 4, pp. 1852–1860, 2000.
- [44] M. Fang, D. M. Kaschak, A. C. Sutorik, and T. E. Mallouk, "A "mix and match" ionic-covalent strategy for self-assembly of inorganic multilayer films," *Journal of the American Chemical Society*, vol. 119, no. 50, pp. 12184–12191, 1997.

Research Article

A Simple Optical Model for the Swelling Evaluation in Polymer Nanocomposites

Anna De Girolamo Del Mauro,¹ Angelica Immacolata Grimaldi,² Vera La Ferrara,¹ Ettore Massera,¹ Maria Lucia Miglietta,¹ Tiziana Polichetti,¹ and Girolamo Di Francia¹

¹Department of Technological and New Materials, Nanomaterials and Devices Technologies Section (FIM MAT-NANO), Research Center ENEA Portici, Piazzale E. Fermi 1, 80055 Portici (NA), Italy

²Technological District on Polymeric and Composite Materials Engineering and Structures IMAST, Piazzale E. Fermi, I-80055 Portici (NA), Italy

Correspondence should be addressed to Tiziana Polichetti, tiziana.polichetti@portici.enea.it

Received 31 December 2008; Revised 24 April 2009; Accepted 30 May 2009

Recommended by Yongxiang Li

In the present study, we report on a simple optical method based on thin film interferometry for the swelling evaluation in polymer nanocomposite layers used for gas sensing applications. We show that white light interferometry can be profitably applied to characterize scattering materials such as polymer/carbon black nanocomposites. A properly adjusted experimental setup was implemented to monitor the swelling behavior of the sensitive films in real device operating conditions. In particular, the behavior of poly(2-hydroxyethyl methacrylate) (PHEMA) and of carbon black/PHEMA nanocomposite layers, used for volatile organic compounds (VOCs) detection, was investigated and measured under ethanol vapors exposure (max 1%). The method is very sensitive and the swelling in the range of only few nanometers can be measured. Interestingly, we have found that the nanocomposite undergoes a more pronounced swelling process with respect to pristine polymer. Ethanol diffusion coefficients in the nanocomposite were evaluated.

Copyright © 2009 Anna De Girolamo Del Mauro et al. This is an open access article distributed under the Creative Commons Attribution License, which permits unrestricted use, distribution, and reproduction in any medium, provided the original work is properly cited.

1. Introduction

Polymer films and their nanocomposites embedded in polymer matrix are well known to be sensitive to different analytes and are extensively used in sensing application where their different transduction properties (such as electrical, mechanical, and thermal properties) are exploited. The target set by the research in this area is the device response optimization in terms of sensitivity, selectivity, and stability [1]. Polymer nanocomposite-based chemical sensors work on the basis of a change of their electrical properties when they come into contact with a specific substance. Due to the solvent absorption, the volume of the polymer matrix increases (swelling) and, at the same time, the volumetric fraction of carbon particles decreases [2–5]. Therefore, the change in film volume results in a modification of the conduction paths throughout the film that is measured as a change in the electrical resistance.

Swelling measurement is thus very important to study the sensing layer operating mechanism and to optimize the sensor device performances.

Device optimization needs a comparison between electrical response and film expansion under volatile organic compounds (VOCs) exposure.

Optical methods, such as white light interferometry, are commonly used in commercial measuring system [6] to estimate transparent film thickness on reflective substrate. These method have the advantage to be non-contacting techniques. However, when applied to swelling evaluation, any optical method generally fails in two respects: (i) the swelling changes the distance between the optical probe and the sample; (ii) nanocomposites generally behave as strongly scattering material. Therefore, during analyte absorption, it may become very difficult to ascertain if the observed variation in the reflectance is due to the swelling or to the effect of the sample scattering. A method based on

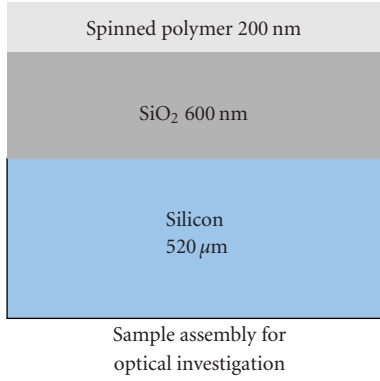


FIGURE 1: Section device scheme for optical investigation.

white light interferometry for the evaluation of the swelling of nonscattering materials, such as poly(2-hydroxyethyl methacrylate) (PHEMA), has been already proposed [3].

Here we show that white light interferometry can be profitably used for the swelling evaluation of scattering materials such as polymer/carbon black nanocomposites. Problems resulting from the change in the distance between the film and the optical probe have been overcome by a properly adjusted experimental setup as the relative change in film thickness during swelling is negligible with respect to the probe to sample distance.

Swelling of PHEMA/carbon black- (CB-) sensitive films in sensor devices operating in real conditions was evaluated.

2. Optical Model

Hereafter, the main assumptions and approximations of the proposed optical model are reported.

In Figure 1, a schematic picture of the polymer nanocomposite-based sensor investigated in this study is shown. The film thickness, together with the conductive filler content and the transducers geometry, determines the device impedance that must be considerably lower than the one of the substrate. From the optical point of view, the film thickness together with the carbon black content determines the optical absorbance and scattering and, in turn, affect the fringes contrast. As a consequence, the resulting tradeoff nanocomposite film thickness for our experimental setup ranges between 100 and 300 nm.

The system depicted in Figure 1 may be optically considered as composed by a nonabsorbing double layer onto an infinite thick substrate. In this frame, the SiO₂ layer has a double function: (i) electrical insulator; (ii) buffer layer to increase the optical path and thus the number of fringes in the interference spectra. In Table 1, the refractive indices and the extinction coefficients, in the visible range of PHEMA, SiO₂, CB, and ethanol are reported [7–9]. Bruggeman approximation [10] was used to evaluate refractive index for polymer composite.

Data show that the refractive indices of PHEMA and PHEMA/CB in the 400 nm–900 nm wavelength range differ by less than 1% and are very similar, in this range, to

TABLE 1: Refractive indices and extinction coefficients of the used materials; $\langle n \rangle$ is the weighted mean value for polymer nanocomposite.

Material	n	k	Weight (%)	Thickness (nm)	$\langle n \rangle$
SiO ₂	1.45	~0		600	
PHEMA	1.51	~0	98.5%	266	
CB	2	1	1.5%		
C ₂ H ₅ OH	1.33	~0	0.37%		
PHEMA/CB				866	1.520
PHEMA/CB/C ₂ H ₅ OH				866	1.524
SiO ₂ /PHEMA/CB/				866	1.488

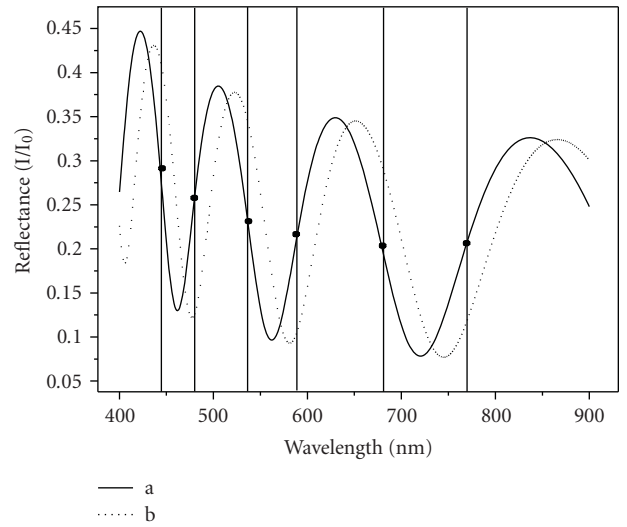


FIGURE 2: (a) reflectance spectrum of a 866 nm thick PHEMA layer; (b) fringe shift for a swelling of 30 nm. Black dots indicate inflection points.

the SiO₂ refractive index. Under such approximations, the double layer can be optically modeled as a single optical layer with an average refractive index, $\langle n \rangle$, that is the weighted mean between the SiO₂ and polymer layer refractive indices, according to the Bruggeman approximation [10].

Thus, the optical reflectance for the system depicted in Figure 1 is given, within a maximum 4% error, by

$$R = \frac{r_1^2 + r_2^2 + 2r_1r_2 \cos 2\theta}{1 + r_1^2r_2^2 + 2r_1r_2 \cos 2\theta}, \quad (1)$$

where, r_1 and r_2 are the reflectance between the first and second interface and between the second and the third interface given, respectively, by

$$r_1 = \frac{(n_0 - \langle n \rangle)}{(n_0 + \langle n \rangle)}, \quad r_2 = \frac{(\langle n \rangle - n_2)}{(\langle n \rangle + n_2)}, \quad (2)$$

and θ is the phase thickness of the coating

$$\theta = \frac{2\pi n_1 d_1}{\lambda}, \quad (3)$$

n_0 , $\langle n \rangle$ and n_2 are the air, the effective layer, and the substrate refractive indices, respectively. d_1 is the total thickness of the effective single layer.

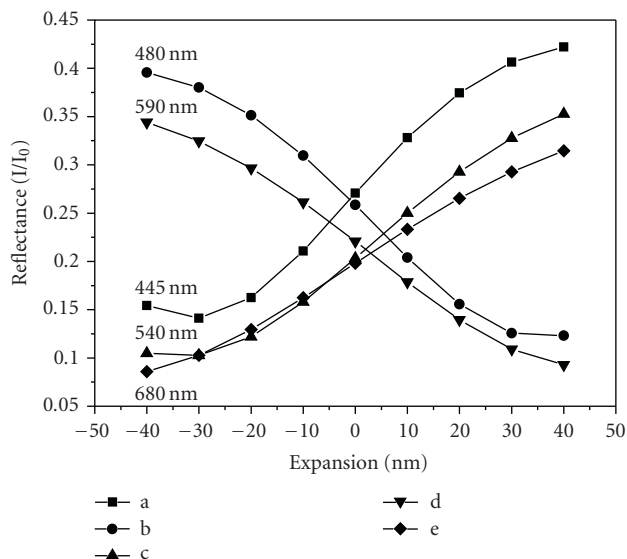


FIGURE 3: Simulated reflectance vs swelling for a 866 nm thick layer taken at the five inflection point wavelength: (a) negative inflection point (IP) at 445 nm; (b) positive IP at 480 nm; (c) negative IP at 540 nm; (d) positive IP at 590 nm

It is worth noting that for the PHEMA/CB (5%) composite (n) is the same as the layer with sole polymer within an error of less than 1%. The same is true for the nanocomposite upon absorption of up to 10000 ppm of ethanol, as shown in Table 1.

From the spectrum minima or maxima, both the layer thickness and the refractive index can be evaluated.

The model suggests that a variation in the single layer thickness (e.g., due to the swelling) will result in a modification of the optical reflectance spectra.

In Figure 2 the effect of 30 nm polymer swelling on the optical spectrum is shown. As expected, the film expansion produces a fringe shift. It can be noted that the curve slope near the inflection points quite rigidly translates. The resulting thickness variation may be particularly marked: at a fixed wavelength a less than 4% variation of the total thickness yield a reflectance variation larger than 50%.

This effect is more clearly visible in Figure 3 where the theoretical variation, at a fixed wavelength, of the reflectance intensity as a function of the layer expansion is reported. The model shows that if we fix the wavelength at an inflection point, a ± 15 nm thickness variation results in a $\pm 40\%$ linear reflectance change, so that extremely small swelling values can be evaluated.

3. Experimental

The PHEMA series of samples were prepared by dissolving the polymer (4 wt%) in hexafluor-2-propanol (HFIP), while the PHEMA/CB layers were obtained by dispersing carbon black Pearls 2000 (CABOT Corporation) (5.5 wt% with respect to polymer) in the PHEMA (1 wt%)/HFIP solution. The carbon black content is determined on a weight basis

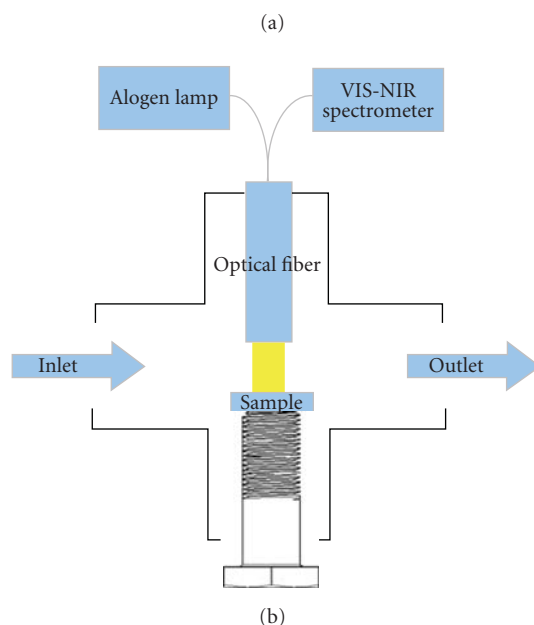
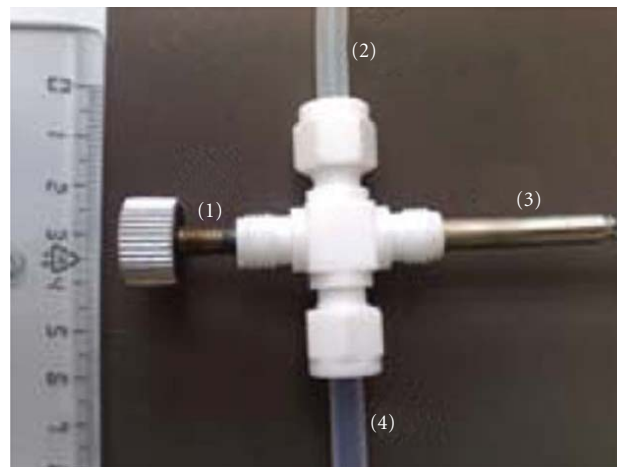


FIGURE 4: (a) photograph of the chamber for optical characterization in controlled environment: (1) sample holder, (2) gas inlet, (3) fiber optic holder, (4) gas outlet; (b) a scheme of the chamber for optical characterization.

of the components in the starting dispersion. Characterizations by means of Thermogravimetric Analysis (TGA) on PHEMA/CB nanocomposite film have shown that the weight ratio, polymer/filler, in the dispersion is preserved in the deposited film.

After sonication, the solutions were spin-coated on SiO_2 coated crystalline Si wafers. For this study, films with thickness between 100 nm and 300 nm have been deposited.

Preparation conditions and thickness values before exposing the samples to analyte are summarized in Table 2. Roughness and thickness were measured by means of a TENCOR profilometer. All these characterizations were carried out in ambient air.

Reflectance VIS spectrum fringes are acquired with S2000 Oceanoptics spectrometer. Thickness was evaluated using an Ocean Optics Nanocalc software [6].

TABLE 2: Summary of the preparation condition and of the thickness values before exposing to gas.

SAMPLE NAME	CB/PHEMA (wt%)	PHEMA/HFiP (wt%)	LAYER THICKNESS PROFILOMETER (nm)	LAYER THICKNESS INTERFEROMETER (nm)
PHEMA_a	0	4	200 ± 30	170 ± 5
PHEMA_b	0	4	250 ± 30	220 ± 5
PHEMA_c	0	4	100 ± 30	140 ± 5
PHEMA/CB_a	5.5	1	250 ± 70	250 ± 5
PHEMA/CB_b	5.5	1	300 ± 70	310 ± 5
PHEMA/CB_c	5.5	1	200 ± 70	200 ± 5

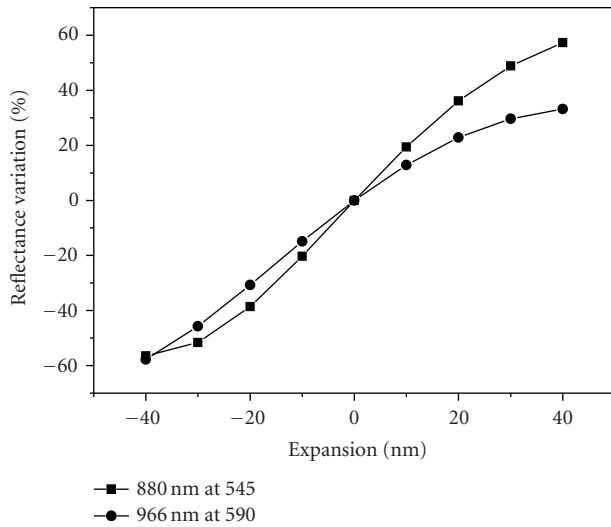


FIGURE 5: Simulated Reflectance variation of PHEMA_b (a) (880 nm thickness at 545 nm), and PHEMA/CB_a (b) (966 nm thickness at 590 nm).

The sensible layers were mounted in the test chamber and analyzed upon VOCs exposure. The experimental setup consists of a small chamber based on a modified multiple tube-fitting connector (Figures 4(a) and 4(b)).

Sample is placed on the top of an adjustable stage (Figure 4(a)-(1)). Fiber optic reflection probes are connected to a VIS-NIR light source through SMA connector and aligned with the sample (Figure 4(a)-(3)). The reflected light beam is collected by the fiber and directed to the spectrophotometer.

Measurements in controlled environment were performed using a Gas Sensor Characterization System better described elsewhere [11] connecting the optical chamber (Figure 4(a)-(2)) to the gas output of the electrical test chamber.

Ethanol at concentration of 3000 ppm and 12500 ppm in N_2 was used as testing analyte. The vapor was introduced in the test chamber by means of a bubbler system in controlled by mass flowmeters amounts. Gas mixture and concentration output (Figure 4(a)-(4)) were finally checked by a Thermo Antaris IGS FTIR gas analyzer.

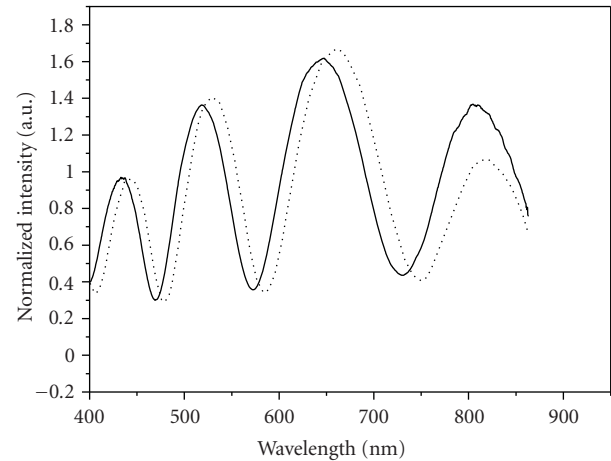


FIGURE 6: Reflected light intensity spectra of PHEMA_b sample under nitrogen (solid line) and exposed to 12500 ppm of ethanol vapors (dotted line).

4. Results and Discussion

As shown in Table 2, the optically evaluated thickness is, within the experimental error, equal to the value determined by the mechanical profilometer, confirming the validity of the employed model. Curiously, the agreement between optically and mechanically evaluated thickness seems to be even better for the nanocomposite rather than for the pure polymer.

The evaluation of the swelling is based on the experimental shift of the reflectance interference pattern at a fixed wavelength, chosen near the inflection point. As previously discussed, according to the model, a swelling of few tenths of nanometers is related to the optical reflectance variation at that wavelength.

In Figure 5, the simulated variations at a fixed wavelength as function of the swelling for the samples PHEMA_b and PHEMA/CB_a, calculated on the basis of (1), are reported. For a given reflectance, the corresponding layer expansion can then be readily evaluated.

Figure 6 shows the shift of interference fringes of PHEMA sample exposed to 12500 ppm of ethanol vapors, where a clearly observable effect of the volume change is detected. Using the outlined model a 19 nm swelling with a 10% confidence was calculated.

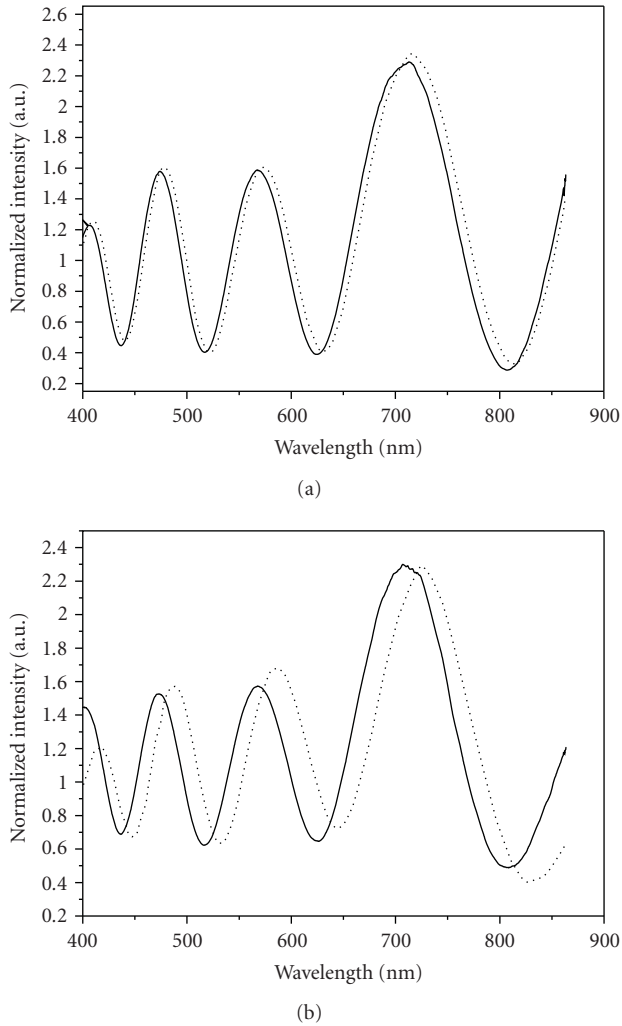


FIGURE 7: Reflected light intensity spectra of PHEMA/CB_a sample exposed to 3000 ppm (a) and to 12500 ppm (b) of ethanol vapors (dotted lines). Reflectance spectra of samples exposed to pure N₂ are shown for comparison (solid lines).

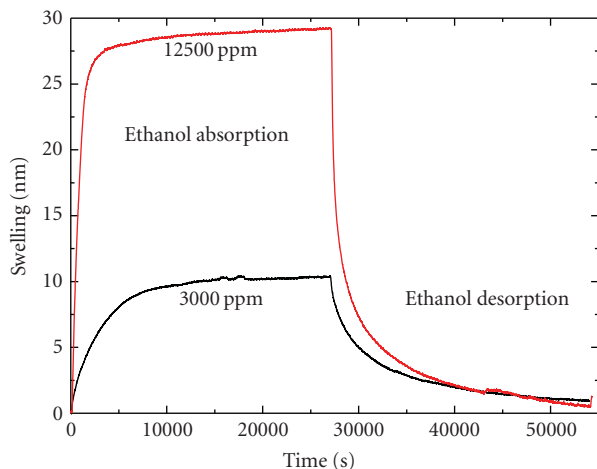


FIGURE 8: Swelling versus time for a PHEMA/CB_a film in 3000 ppm and 12500 ppm of ethanol vapors.

In Figures 7(a) and 7(b), the shifts of interference fringes of the PHEMA/CB_a sample exposed to 3000 ppm and 12500 ppm of ethanol vapors, respectively, are shown. The swelling evaluation gives a thickness variation of 10 nm for the sample exposed to 3000 ppm while an expansion of 31 nm is found when the same sample is exposed to 12500 ppm of ethanol. As expected, the amount of film expansion depends on the concentration of the analyte.

Nanocomposite layers exhibit a slightly larger swelling as compared to pure PHEMA layers. A similar result has been previously observed for nanostructured fluoropolymer (CF_x) and metal-CF_x composite films [12]. A possible active role of the metal filler has been suggested in that case, to account for this effect. In our case, preliminary investigations by means of Brunauer-Emmett-Teller (BET) measurements have highlighted the occurrence of a certain porosity in the nanocomposite with respect to the bare polymer. The enhanced specific surface could then account for the observed swelling.

In Figure 8 the swelling kinetics of PHEMA/CB_a sample recorded at 660 nm, at two different analyte concentrations, is reported. The swelling in presence of 12500 ppm is greater than the expansion related to 3000 ppm exposure. Data exhibit the typical $(t)^{1/2}$ law at least for the first 600 s. During this time interval a diffusive mechanism can be then assumed and, using the Fick equation, the diffusion coefficients can be estimated. For PHEMA exposed to 12500 ppm of ethanol the evaluated diffusion coefficient is equal to 1×10^{-14} cm²/s, while the diffusion coefficients for PHEMA/CB exposed to 3000 ppm and 12500 ppm of ethanol are 1×10^{-16} cm²/s and 0.5×10^{-14} cm²/s, respectively. Data for pure PHEMA are comparable with those reported by Goustouridis et al. [3].

5. Conclusions

In this work, we developed a simple optical method based on thin film white light interferometry to measure the swelling sensitivity of polymer and nanocomposite layers. The method allows to easily correlate polymer nanocomposite film expansion to light intensity variation at a fixed wavelength, as long as the swelling is small with respect to the whole layer thickness.

It was successfully applied to PHEMA and to nanocomposite carbon black/PHEMA layers which are a typical choice in chemical sensor technology. Interestingly, we have found that the nanocomposite undergoes a more pronounced swelling process with respect to pure polymers.

Acknowledgment

The authors gratefully acknowledge the Ministry of Universities and Research (MUR) for financial support as part of Public-Private Laboratory TRIPODE (Technologies and Research for the application of polymers in electronics devices).

References

- [1] M. A. Ryan, M. L. Homer, H. Zhou, K. Manatt, and A. Manfreda, "Toward a Second Generation Electronic Nose at JPL: Sensing Film Optimization Studies," Document Number: 2001-01-2308, Society of Automotive Engineers, July 2001.
- [2] S. Chatzandroulis, D. Goustouridis, and I. Raptis, "Characterization of polymer films for use in bimorph chemical sensors," *Journal of Physics: Conference Series*, vol. 10, no. 1, pp. 297–300, 2005.
- [3] D. Goustouridis, K. Manoli, S. Chatzandroulis, M. Sanopoulou, and I. Raptis, "Characterization of polymer layers for silicon micromachined bilayer chemical sensors using white light interferometry," *Sensors and Actuators B*, vol. 111–112, pp. 549–554, 2005.
- [4] A. Convertino, G. Leo, M. Tamborra, et al., "TiO₂ colloidal nanocrystals functionalization of PMMA: a tailoring of optical properties and chemical adsorption," *Sensors and Actuators B*, vol. 126, no. 1, pp. 138–143, 2007.
- [5] A. Carrillo, I. R. Martín-Domínguez, and A. Márquez-Lucero, "Modeling and experimental testing of the effect of solvent absorption on the electric properties of styrene butadiene rubber/carbon black chemical sensors," *Sensors and Actuators B*, vol. 113, no. 1, pp. 477–486, 2006.
- [6] <http://www.oceanoptics.com/products/nanocalc.asp>.
- [7] <http://www.texloc.com/closet/cl.refractiveindex.html>.
- [8] E. D. Palik, *The Handbook of Optical Constants of Solids*, Academic Press, New York, NY, USA, 1985.
- [9] <http://www.cabot-corp.com>.
- [10] D. A. G. Bruggeman, "Berechnung verschiedener physikalischer Konstanten von heterogenen Substanzen. I. Dielektrizitätskonstanten und Leitfähigkeiten der Mischkörper aus isotropen Substanzen," *Annals of Physics*, vol. 24, p. 636, 1935.
- [11] L. Quercia, F. Cerullo, V. La Ferrara, G. Di Francia, C. Baratto, and G. Faglia, "Fabrication and characterization of a sensing device based on porous silicon," *Physica Status Solidi A*, vol. 182, no. 1, pp. 473–477, 2000.
- [12] N. Cioffi, L. Torsi, I. Farella, et al., "The swelling of vapor-sensitive fluoropolymers modified with metal nanoparticles: interpretation of the material-vapor interaction mechanism," *Sensors and Actuators B*, vol. 100, no. 1–2, pp. 9–16, 2004.

Research Article

Schottky Junction Methane Sensors Using Electrochemically Grown Nanocrystalline-Nanoporous ZnO Thin Films

P. K. Basu,¹ N. Saha,¹ S. K. Jana,¹ H. Saha,¹ A. Lloyd Spetz,² and S. Basu¹

¹Department of Electronics & Telecommunication Engineering, IC. Design & Fabrication Centre, Jadavpur University, Kolkata 700032, India

²Department of Physics, Chemistry and Biology, Linköping University, SE-581 83 Linköping, Sweden

Correspondence should be addressed to S. Basu, sukumar_basu@yahoo.co.uk

Received 29 December 2008; Accepted 1 July 2009

Recommended by Giorgio Sberveglieri

Nanocrystalline-nanoporous ZnO thin films were prepared by an electrochemical anodization method, and the films were tested as methane sensors. It was found that Pd-Ag catalytic contacts showed better sensing performance compared to other noble metal contacts like Pt and Rh. The methane sensing temperature could be reduced to as low as 100°C by sensitizing nanocrystalline ZnO thin films with Pd, deposited by chemical method. The sensing mechanism has been discussed briefly.

Copyright © 2009 P. K. Basu et al. This is an open access article distributed under the Creative Commons Attribution License, which permits unrestricted use, distribution, and reproduction in any medium, provided the original work is properly cited.

1. Introduction

It is well known that gas sensing performance of sensors can be improved by incorporating noble catalyst metal into the nanocrystalline metal oxide-based matrix. A number of reports [1–3] have been published on nanocrystalline ZnO thin films to improve the methane sensing performance. The development of a low-temperature methane detector using nanocrystalline ZnO-based chemical gas sensors with noble metal catalytic contacts is an important proposition. The challenge is to attain lower detection limit, short response time, and long-term stability of the gas sensors. Nanocrystalline ZnO thin films demonstrate remarkable gas-sensing properties when the crystallite size becomes comparable to Debye length. Nanocrystalline and porous materials with controlled composition are of increasing interest in methane sensing because of their large surface to volume ratio that enhances the adsorption kinetics and the reaction between methane and adsorbed oxygen.

Recently it was [1–6] reported that methane-sensing temperature varies between 100°C and 250°C depending upon whether the ZnO thin film is grown electrochemically or by sol-gel method and upon the nature of the catalytic metals. But these relatively high temperatures for detection of methane are still not suitable for applications in the coalmines. In this work, nanocrystalline ZnO thin films were

prepared by electrochemical anodization of high-purity Zn (99.99%). While using Pt catalytic metal electrode methane sensing could be achieved at 240°C Pd-Ag (26%), and Rh electrodes could bring down the temperature to 210°C. But the temperature could be brought down to 100°C by incorporating Pd modification of the nanocrystalline ZnO thin film and by using Pd-Ag catalytic metal Schottky contact. In this communication, a comparative study between ZnO Schottky devices with different catalytic metal contacts and the effect of adding Pd to the nanoporous ZnO are presented.

2. Experimental

The noble metal/ZnO Schottky structure using nanocrystalline ZnO thin film, prepared by electrochemical anodization of Zn, was studied for gas sensing. A properly cleaned high-purity Zn foil of thickness 0.5 mm was taken as anode and platinum foil as cathode with 18 mm separation between the two electrodes and 0.3 M oxalic acid as electrolyte. A calomel electrode was taken as the reference. A 10 V potentiostatic power supply (Princeton Applied Research, Scanning Potentiostat-362, USA) was used during anodization. Sensitization of the grown ZnO films was performed by dipping into 0.01 M weak acidic aqueous solution of PdCl₂ for 2 seconds followed by baking at 110°C for 10

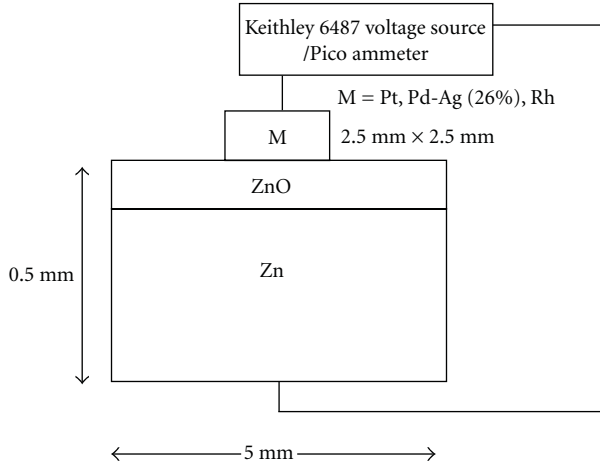


FIGURE 1: Schematic of the ZnO based Schottky sensor.

TABLE 1: The crystal size, pore size, and thickness of the anodized ZnO thin films.

Parameters	Anodized ZnO
Crystal size (nm)	2.40
Pore size (nm)	19–35
Thickness (μm)	8.20

minutes and annealing at 300°C in air for 30 minutes. Pt, Pd-Ag (26%) and Rh catalytic metals ($2.5\text{ mm} \times 2.5\text{ mm}$) of thickness $0.2\text{ }\mu\text{m}$ were deposited on ZnO films by e-beam evaporation using Al metal mask for Schottky contacts. The Zn substrate beneath the ZnO film was used as ohmic contact. Electrical connections were performed by using fine copper wire and silver paste. The schematic of the Schottky sensor structure is shown in Figure 1. In order to study the gas sensing properties high-purity methane, nitrogen, and synthetic air were used. For accurate control of the gas flow rate throughout the experiments, mass flow controller and mass flow meters (Digiflow, USA) were used. The current-voltage characteristics of the sensors were studied by a Keithley model 6487 Pico ammeters-voltage source.

3. Results and Discussions

The XRD and the FESEM (Field Effect Scanning Electron Microscopy) picture of the anodized ZnO thin films are shown in Figure 2. The average crystal size, the pore diameter, and the thickness are summarized in Table 1.

The V-I characteristics of the Schottky sensors were recorded at all the temperatures of measurements, and the magnitude of the response (S) was calculated from these data. The response (S) is defined as the ratio of the change of current in presence of methane in N_2 or air to the current in N_2 or air at constant voltage, both in the forward bias mode

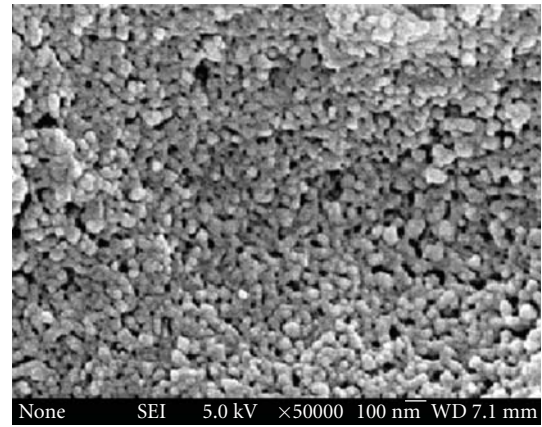
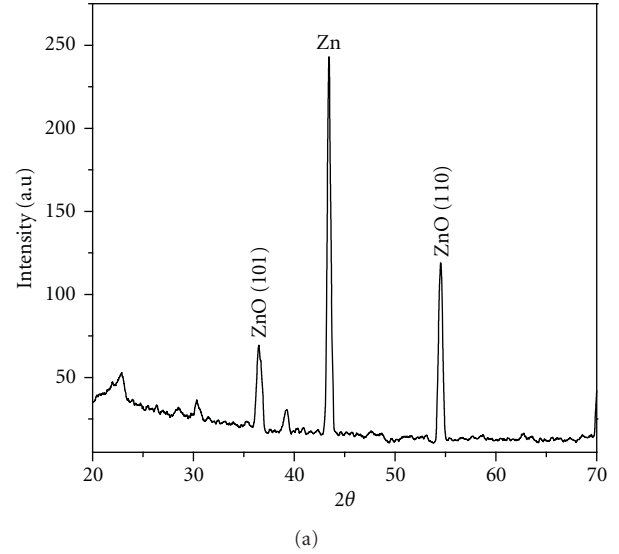


FIGURE 2: (a) XRD and (b) FESEM of ZnO thin films obtained by anodic oxidation of Zn in 0.3 M oxalic acid.

and expressed as

$$S = \left(\frac{I_g - I_a}{I_a} \right)_V, \quad (1)$$

where I_g is the current in presence of gas and I_a is the current in N_2 or air.

Figure 3(a) shows response versus temperature curves of the Schottky sensors with the unsensitized ZnO films using 1% CH_4 in pure N_2 . For Pt contact the maximum response was obtained at 240°C while for Pd-Ag and Rh contacts the maximum response was obtained at 210°C . For all three types of contacts the maximum response was obtained at 0.4 V bias, as shown in Figure 3(b). This may be significant for low power consumption of the sensor devices. Figure 4 shows the response versus temperature curves with 1% CH_4 in pure N_2 and in synthetic air, respectively. It is observed that the response of the sensors is higher in nitrogen compared to that in synthetic air.

In case of the Schottky gas sensors, catalytic noble metals were taken as electrode contacts. At an elevated temperature,

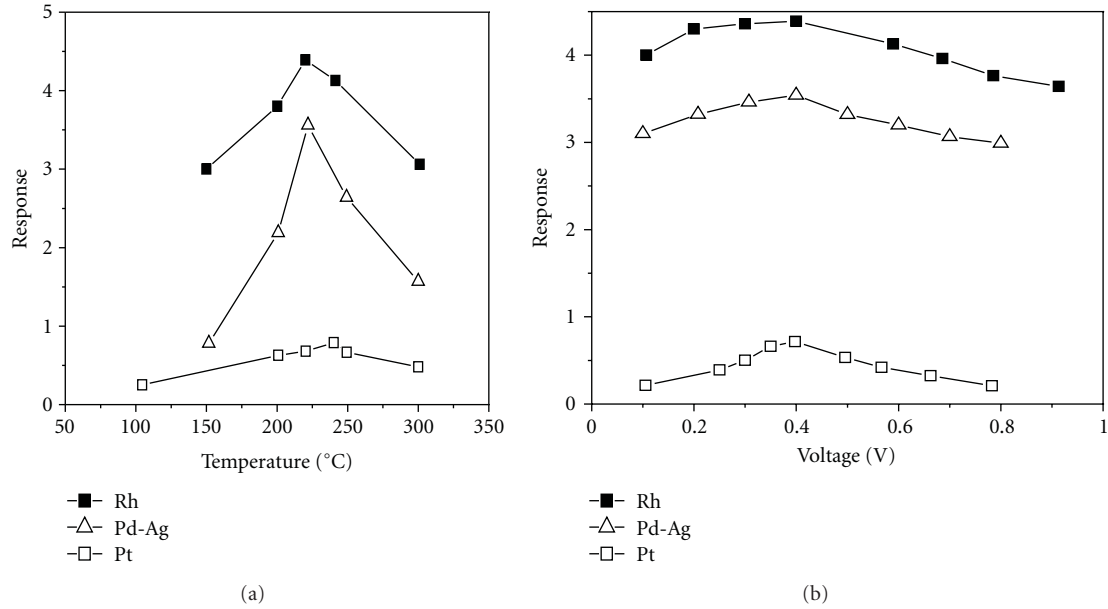


FIGURE 3: (a) Response versus temperature curves and (b) response versus voltage curves of the Schottky sensors using different catalytic contacts on ZnO thin films. It is observed that Rh gives maximum response. For Pt contact the maximum response was obtained at 240°C while for Pd-Ag and Rh contacts the maximum response was obtained at 210°C. For all three types of contacts the maximum response was obtained at 0.4 V bias.

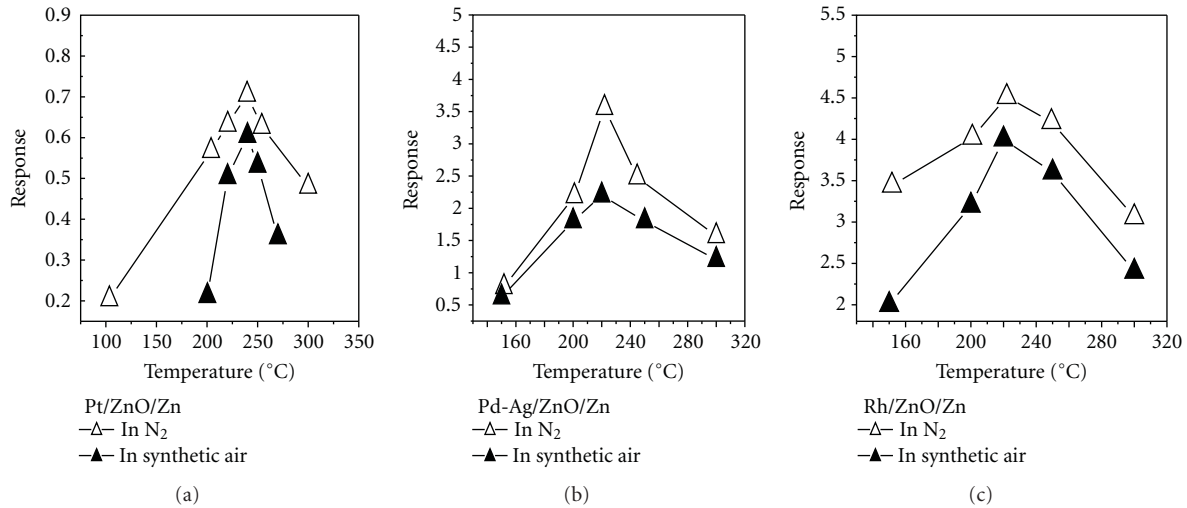
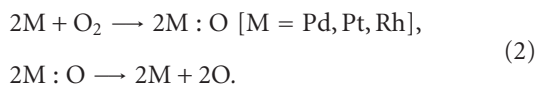


FIGURE 4: Response versus temperature curves of the (a) Pt/ZnO/Zn, (b) Pd-Ag (26%)/ZnO/Zn, and (c) Rh/ZnO/Zn Schottky sensors in presence of 1% methane in pure nitrogen and in synthetic air, respectively. The response of the sensors is higher in nitrogen than in synthetic air.

oxygen molecules are weakly bonded to the catalytic metal (Pt, Pd-Ag, and Rh) and are dissociated to oxygen atoms that are weakly adsorbed on the metal surface. The metal-oxygen complex subsequently dissociates



The oxygen atoms then undergo a spillover process and finally form negatively charged surface ions by gaining

electrons from the surface of ZnO, thereby yielding a high electrostatic potential in the junction [7–9]. The space charge region, being depleted of electrons, is more resistive than the bulk. The methane response mechanism with a noble metal/metal oxide Schottky junction is not so well understood and spectroscopic studies are needed in order to reveal the reaction pathways that may be different for different temperatures and even vary with the gas concentration. Here we present three possible mechanisms of gas sensors. The first is dissociative adsorption of CH₄ to produce H and

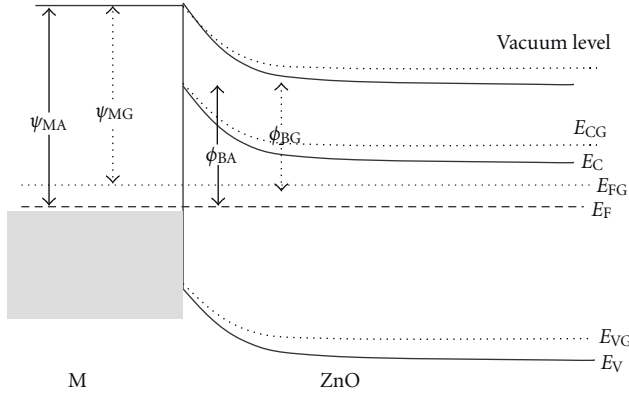
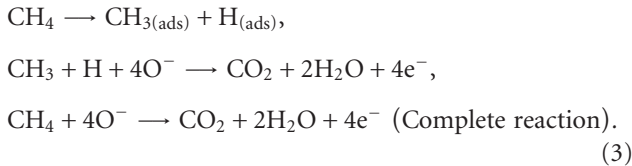


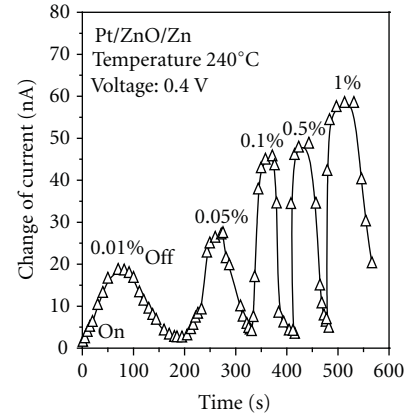
FIGURE 5: Band diagram of the Schottky Junction explaining the sensing mechanism. The barrier height reduces upon exposure to the reducing gas. ψ_{MA} , ψ_{MG} are the work function of M in air and in gas, respectively. ϕ_{BA} , ϕ_{BG} are the barrier height of the junction in air and in gas, respectively. E_C , E_{CG} are the conduction band in air and in gas, respectively. E_V , E_{VG} are the valence band in air and in gas, respectively. E_F , E_{FG} are the Fermi level in air and in gas, respectively, $M = \text{Pt, Pd, or Rh}$.

CH_x ($X = 3$) on the noble metal surface and reaction with adsorbed atomic oxygen to produce water. Furthermore, the H or CH_x spills over to the metal oxide and reacts with chemisorbed ionic oxygen to produce water and free electrons that increase the current through the junction. If the device is operated at a temperature of $\geq 100^\circ\text{C}$, which is normally the case for methane sensing, the water formed desorbs rapidly from the surface [10–12] (see reactions (3)):

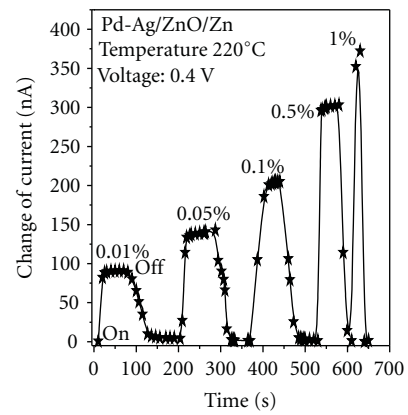


A second possibility is that due to high solubility and rapid diffusivity of hydrogen through catalytic metal, it reaches the catalytic metal/metal oxide interfaces and produces an interfacial dipole layer. The electrically polarized potential at the interface also lowers the work function of the noble metal and thus reduces the barrier height. Such sensing mechanism is summarized in Figure 5, where the reduction of the barrier height upon exposure to the reducing gas is shown. The adsorbed hydrogen atoms may, as a third possibility, passivate the interface states at the noble metal/metal oxide interface, preventing them from pinning the Fermi level. The passivated interface thus might cause a decrease in the barrier height. Due to this lowering of barrier height, the current through the junction increases [6, 13], yielding thereby a high response.

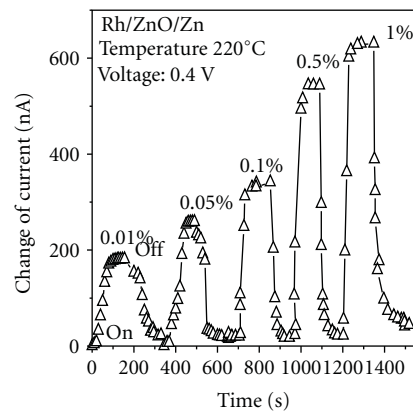
Palladium (Pd), Silver (Ag), Platinum (Pt), and Rhodium (Rh) are the most common metal catalysts that are used to improve the gas-sensing properties. Here Pt, Pd-Ag, and Rh catalysts were used for gas sensing applications. A Pd-Ag (26%) alloy metal contact was used instead of pure Pd. The reason is that the phase transition from α phase of pure



(a)



(b)



(c)

FIGURE 6: Transient response curves of (a) Pt/ZnO/Zn, (b) Pd-Ag (26%)/ZnO/Zn, (c) Rh/ZnO/Zn Schottky sensors at 0.4 V bias.

palladium to β phase hydride occurs at low H_2 concentration at 300 K and it is an irreversible process [14]. This will damage the sensor due to peeling-off of Pd. Moreover, the response time of more than 10 minutes for pure Pd contact sensors, as reported in the literature [15], is too long to allow real-time monitoring of flowing gas streams. To overcome these problems Pd was alloyed with 26% Ag for CH_4 sensing. Pd-Ag thin film is attractive for use [14]

TABLE 2: Response, response time, and recovery time of different noble metal contacts on ZnO thin film (calculated from Figure 6).

% of CH ₄	Response			Response time (s)			Recovery time (s)		
	Pt	Pd-Ag	Rh	Pt	Pd-Ag	Rh	Pt	Pd-Ag	Rh
0.01	0.18	0.99	1.22	52.2	22.3	130.2	58	48.3	148.3
0.05	0.29	1.38	1.82	40.2	19.7	52.2	42.3	46.2	120
0.1	0.62	2.21	2.48	27.9	16.4	42.8	30.1	38.1	89.2
0.5	0.68	3.11	3.87	20.3	12.1	38.2	26.2	20.2	80.2
1	0.71	3.81	4.39	18.8	8.8	30.2	22.8	16	78.4

TABLE 3: Response, response time, and recovery time of Pd-Ag/ZnO Schottky sensor with different concentrations of CH₄ in nitrogen using unmodified and Pd modified ZnO thin films at the corresponding optimum temperatures and voltages (calculated from Figures 6(b) and 9(a)).

% of CH ₄	Response		Response time (s)		Recovery time (s)	
	ZnO	Pd: ZnO	ZnO	Pd: ZnO	ZnO	Pd: ZnO
0.01	0.99	18.2	22.3	10.2	48.3	18.7
0.05	1.38	22.3	19.7	6.7	46.2	17.2
0.1	2.21	23.2	16.4	6.03	38.1	16.8
0.5	3.11	25.2	12.1	4.02	20.2	16.1
1	3.81	32.2	8.8	2.69	16	16.0

TABLE 4: Response, response time, and recovery time of Pd modified Pd-Ag/ZnO Schottky sensor with different concentrations of CH₄ in nitrogen and in synthetic air as the carrier gas (calculated from Figure 9).

% of CH ₄	Response		Response time (s)		Recovery time (s)	
	N ₂ as carrier gas	Synthetic air as carrier gas	N ₂ as carrier gas	Synthetic air as carrier gas	N ₂ as carrier gas	Synthetic air as carrier gas
0.01	18.2	6.8	10.2	13.8	18.7	20.0
0.05	22.3	11.0	6.7	9.9	17.2	19.7
0.1	23.2	17.0	6.03	8.7	16.8	17.7
0.5	25.2	17.8	4.02	7.2	16.1	17.0
1	32.2	24.8	2.69	4.6	16.0	15.9

because of the low rate of hydride formation, not much hindrance against hydrogen diffusivity, greater solubility of hydrogen, higher energy barrier due to OH formation and superior mechanical properties as compared to pure Pd. The alloy has quite high rate of hydrogen adsorption in the temperature range 30°C–100°C that is important for fast responding gas sensors.

It can be observed that Rh gives higher response than Pd-Ag and Pt (Rh > Pd-Ag > Pt) because the catalytic effect of dissociation of methane is higher than Pd and Pt [16]. Also the OH formation rate influences the size of the response as discussed below. In literature, it can also be found that the catalytic activity of Pd and Pt for methane dissociation is more or less the same [17]. But Figures 3 and 4 show a higher response of Pd-Ag alloy than Pt that implies that the catalytic activity of Pd-Ag is higher than that of pure Pd. In case of synthetic air that is shown in Figure 4 it can be noticed that the response is somewhat reduced. Since oxygen is already chemisorbed to a large extent on the noble metal surface the adsorption sites for methane is likely to be reduced. So dissociated hydrogen reacts with chemisorbed oxygen to produce H₂O molecules

instead of diffusing into the noble metal/ZnO junction, thereby yielding a weaker response. Since oxygen adsorption is most favorable on Pt it gives the most reduced performance in presence of synthetic air as compared to the other two metals, as shown in Figure 4. Similarly the OH formation energy of Rh is higher than Pd-Ag and Pt [18–21]. Thus this is another reason why the Rh catalytic metal contact gives higher response than Pd-Ag and Pt. The transient response of the sensors recorded in presence of different methane concentrations (0.01%, 0.05%, 0.1%, 0.5%, and 1%) and at 0.4 V bias is shown in Figure 6. From the transient response cycles the response and recovery time were calculated and are summarized in Table 2. The response time is defined here as the time to reach 67% of the saturation value of the current. After the gas pulse is cut off the time required to reduce the current to 67% is defined as the recovery time. It can be observed from Table 2 that the Pd-Ag contact shows shorter response time than Pt and Rh contacts, which may be due to the higher solubility and diffusivity of H in Pd-Ag compared to Rh and Pt and therefore H takes shorter time to reach the Pd-Ag/ZnO junction compared to that for Pt/ZnO and Rh/ZnO junctions, but it may also be because

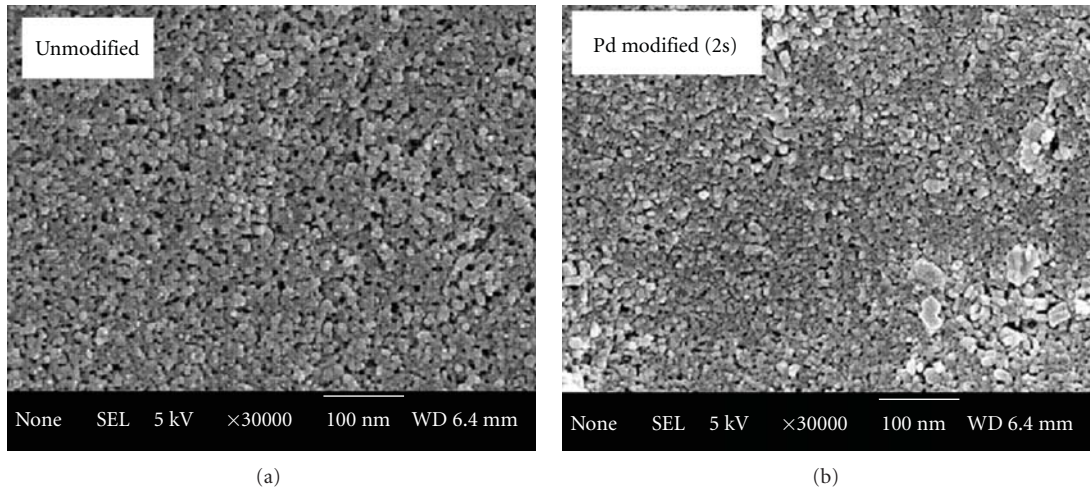


FIGURE 7: FESEM of (a) unmodified and (b) modified ZnO thin films. It is observed that there is little or no difference in the surface morphology after treatment with PdCl₂ solution [6].

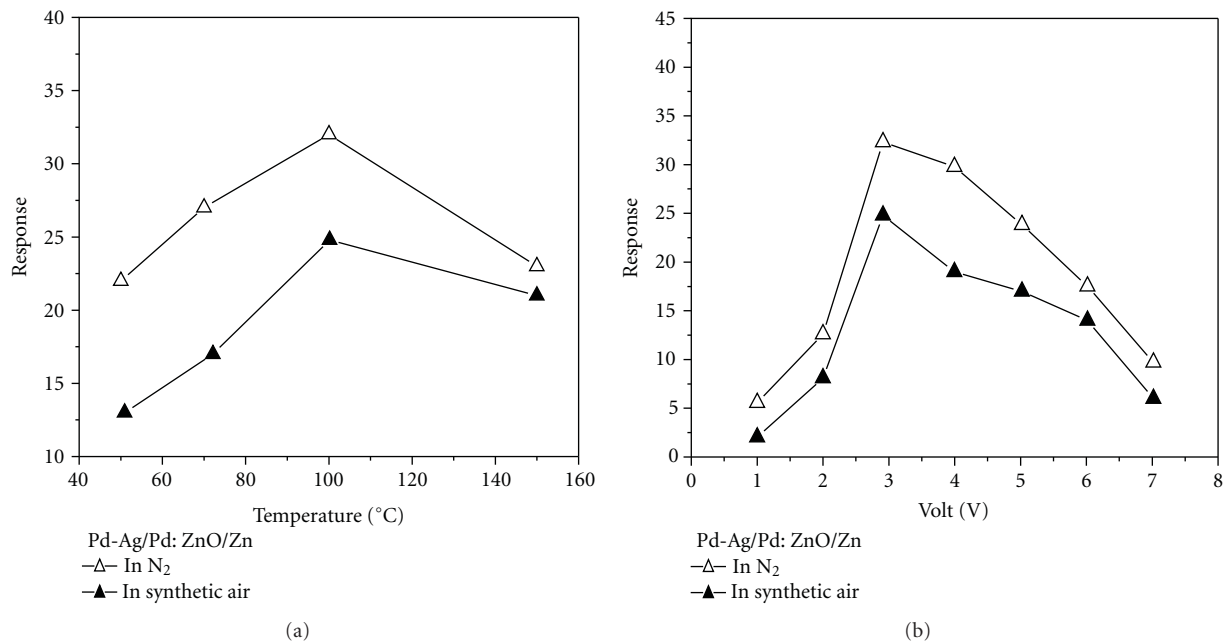


FIGURE 8: (a) Response versus temperature curves and (b) response versus voltage curves of the Pd modified Schottky sensor. It is observed that the response of the sensor is higher in nitrogen than in synthetic air and the maximum response is obtained at 100°C and at 3V.

of more favorable chemistry on the Pd-Ag surface. This is because the catalytic metal/ZnO is most likely highly porous due to a rather thin catalytic metal (200 nm) and a highly porous ZnO, which makes diffusion through the metal a noncritical parameter. It should also be noted in Table 2 that the recovery times for Pd-Ag and Pt are about the same. This is most likely because of the back reaction between hydrogen and oxygen for water formation, as well as carbon dioxide formation, on the catalytic metal surface both in the case of nitrogen and synthetic air. It is almost impossible to attain oxygen leakage free systems for measurements at atmospheric pressure in the laboratory. It can be inferred that Pd-Ag alloy is the most suitable catalytic metal amongst

the three for methane sensing using the Pd-Ag/ZnO Schottky junction.

There are very few reports on metal oxide based methane gas sensors with high response and fast response and recovery [6]. The reported sensor structures [1–5] on oxide based semiconductors operating in the resistive mode and at high temperatures showed longer response and recovery time. This is not suitable for low temperature applications, particularly in the mining environment. It may also incur higher power consumption and short battery lifetime.

To improve the sensing performance, the surface of ZnO thin films was chemically modified with Pd. From FESEM the surface morphology and the pore size were revealed for

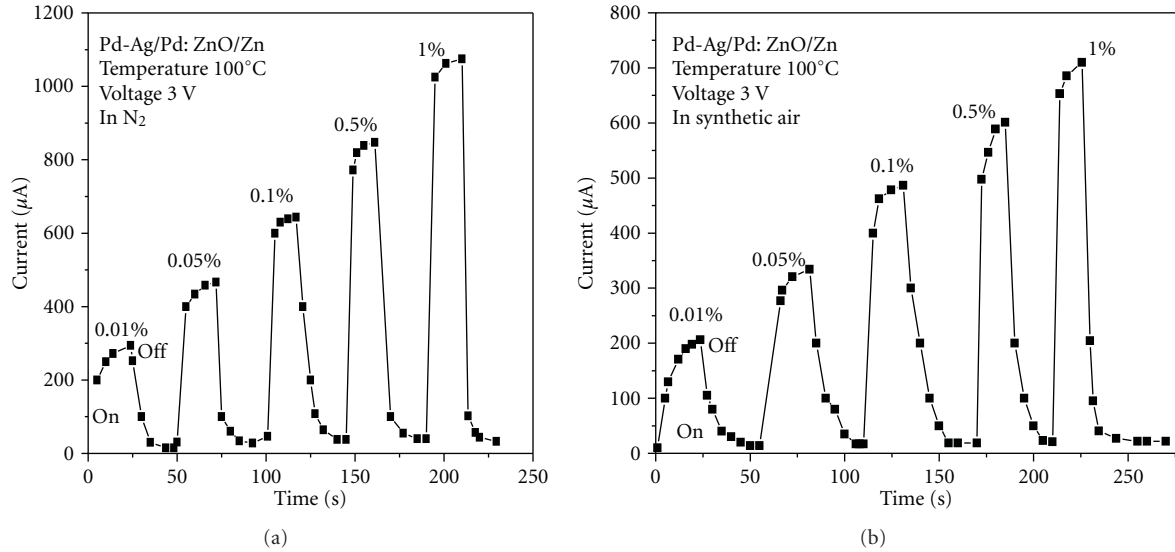


FIGURE 9: Transient response curves of the Pd modified Schottky sensor in 1% methane using (a) nitrogen and (b) synthetic air as the carrier gases at 100°C and at 3 V bias [6].

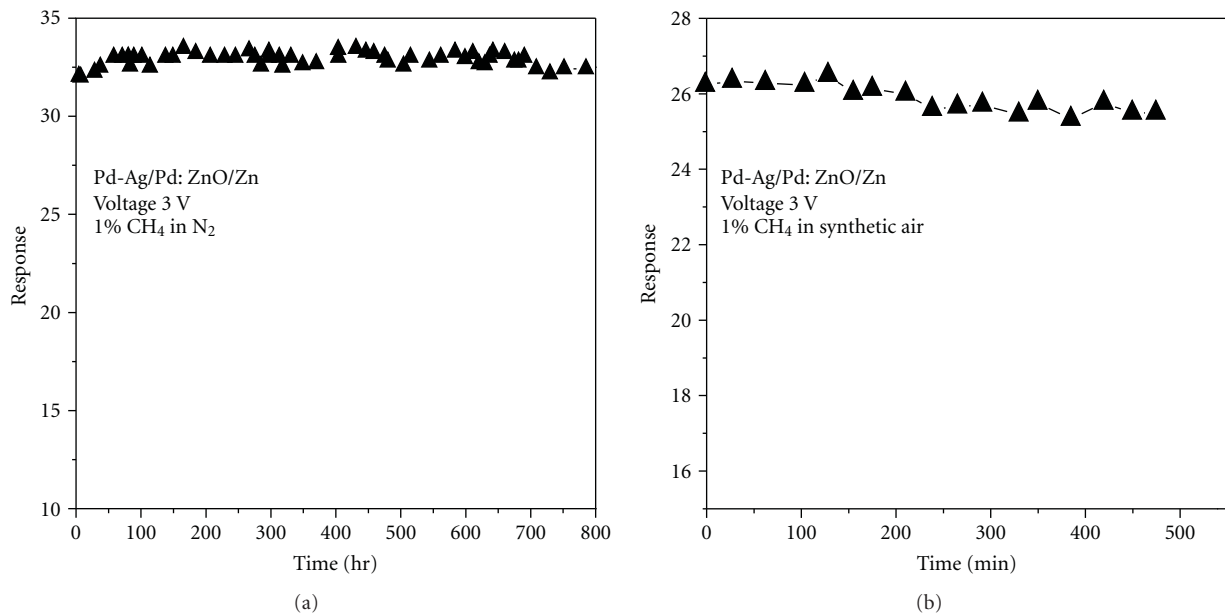


FIGURE 10: Stability study of the surface modified Schottky sensor structures using (a) nitrogen and (b) synthetic air as the carrier gases. It is observed that the sensor shows more or less stable performance in both the cases. However, the stability in synthetic air initially shows a little deterioration and then stabilizes.

both unmodified and modified ZnO surfaces (Figure 7). It was observed that there is little or no difference in the surface morphology after treatment with PdCl_2 solution [6]. The presence of Pd was confirmed by XPS studies. Table 3 shows the improvement of methane sensing parameters after Pd surface modification of ZnO thin film.

The variations of the response with operating temperature and with biasing voltage using 1% methane in nitrogen and in synthetic air are shown in Figure 8. It is observed from the figure that maximum response was obtained at 100°C

and at 3 V. It is further observed that the response is higher in pure nitrogen than in synthetic air.

For the nanocrystalline structure the adsorption energy [22, 23] is considerably lower, and the presence of dispersed Pd nanoparticles over ZnO surface further reduces it. As a result the sensors respond at considerably lower temperature. It is worth mentioning here that imperfect structural orientation of the polycrystalline sensing layer (ZnO) also modulates the gas adsorption behavior and thus the sensing parameters [24].

Figure 9 represents the transient response for different concentrations of methane at 100°C using nitrogen and synthetic air as carrier gases. The response time and recovery time with increasing methane concentrations as derived from the transient response curves are shown in Table 4.

It is apparent from the table that response time is shorter than recovery time that is true also for the cases in Tables 2 and 3. The Pd-Ag/ZnO surface seems to be favorable for the adsorption kinetics at the catalytic metal and Pd-Ag/ZnO interface, compare Tables 3 and 4, the same way the recovery time is longer than the response time for all cases in Tables 2–4. It is interesting to note that the recovery time in Table 4 is about the same in nitrogen and oxygen, which supports the earlier discussion that the back reaction is the same in nitrogen and oxygen atmosphere due to oxygen leakage into the system.

It should be noted that the sensing of methane at 100°C for Pd-Ag/ZnO might be suitable for practical applications due to the high response, speed of response, and recovery, because there is no accumulation of water molecules on the sensor surface at 100°C [12].

We tested the long-term stability of the Schottky sensor for 33 days in presence of 1% methane in nitrogen at 100°C, and the results are shown in Figure 10(a). It is evident from the figure that the sensors show more or less stable performance with a negligible variation of current over the above-mentioned period in a nitrogen atmosphere. We also tested the stability in synthetic air; see Figure 10(b) for 8 hours and a fairly good stability was obtained. The long-term stability in air needs to be further tested since this is the realistic atmosphere for a methane leak detector.

4. Conclusion

Our investigation confirms that methane can be detected at as low a temperature as 100°C using Pd-Ag alloy as the Schottky contact to nanocrystalline ZnO thin film, obtained by anodization of Zn and surface modified by using noble metal, for example, Pd. Nanocrystalline ZnO thin films, after Pd surface modification, showed improved sensing characteristics like large response, short response and recovery time. The stability of the sensor structure obtained in this study indicates that the sensor might be good for methane sensing in the coalmine environment.

Acknowledgment

One of the authors (P. K. Basu) gratefully acknowledges CSIR, Government of India, for a Senior Research Fellowship (SRF).

References

- [1] P. K. Basu, P. Bhattacharyya, N. Saha, H. Saha, and S. Basu, "The superior performance of the electrochemically grown ZnO thin films as methane sensor," *Sensors and Actuators B*, vol. 133, no. 2, pp. 357–363, 2008.
- [2] P. Bhattacharyya, P. K. Basu, H. Saha, and S. Basu, "Fast response methane sensor using nanocrystalline zinc oxide thin films derived by sol-gel method," *Sensors and Actuators B*, vol. 124, no. 1, pp. 62–67, 2007.
- [3] P. K. Basu, P. Bhattacharyya, N. Saha, H. Saha, and S. Basu, "Methane sensing properties of platinum catalysed nano porous zinc oxide thin films derived by electrochemical anodization," *Sensor Letters*, vol. 6, no. 1, pp. 219–225, 2008.
- [4] P. Bhattacharyya, P. K. Basu, C. Lang, H. Saha, and S. Basu, "Noble metal catalytic contacts to sol-gel nanocrystalline zinc oxide thin films for sensing methane," *Sensors and Actuators B*, vol. 129, no. 2, pp. 551–557, 2008.
- [5] P. Bhattacharyya, P. K. Basu, H. Saha, and S. Basu, "Fast response methane sensor based on Pd(Ag)/ZnO/Zn MIM structure," *Sensor Letters*, vol. 4, no. 4, pp. 371–376, 2006.
- [6] P. K. Basu, S. K. Jana, H. Saha, and S. Basu, "Low temperature methane sensing by electrochemically grown and surface modified ZnO thin films," *Sensors and Actuators B*, vol. 135, no. 1, pp. 81–88, 2008.
- [7] S. W. Hla, P. Lacovig, G. Comelli, A. Baraldi, M. Kiskinova, and R. Rosei, "Orientational anisotropy in oxygen dissociation on Rh(110)," *Physical Review B*, vol. 60, no. 11, pp. 7800–7803, 1999.
- [8] A. Rothschild and Y. Komem, "The effect of grain size on the sensitivity of nanocrystalline metal-oxide gas sensors," *Journal of Applied Physics*, vol. 95, no. 11, pp. 6374–6380, 2004.
- [9] S. L. Tait, Z. Dohnalek, C. T. Campbell, and B. D. Kay, "Methane adsorption and dissociation and oxygen adsorption and reaction with CO on Pd nanoparticles on MgO(1 0 0) and on Pd(1 1 1)," *Surface Science*, vol. 591, no. 1–3, pp. 90–107, 2005.
- [10] M.-S. Liao, C.-T. Au, and C.-F. Ng, "Methane dissociation on Ni, Pd, Pt and Cu metal (111) surfaces—a theoretical comparative study," *Chemical Physics Letters*, vol. 272, no. 5–6, pp. 445–452, 1997.
- [11] V. R. Shinde, T. P. Gujar, and C. D. Lokhande, "Enhanced response of porous ZnO nanobeads towards LPG: effect of Pd sensitization," *Sensors and Actuators B*, vol. 123, no. 2, pp. 701–706, 2007.
- [12] M. Lofdahl, C. Utaiwasin, A. Carlsson, I. Lundstrom, and M. Eriksson, "Gas response dependence on gate metal morphology of field-effect devices," *Sensors and Actuators B*, vol. 80, no. 3, pp. 183–192, 2001.
- [13] C. Xu, J. Tamaki, N. Miura, and N. Yamazoe, "Relationship between gas sensitivity and microstructure of porous SnO₂," *Journal of the Electrochemical Society*, vol. 58, p. 1143, 1990.
- [14] R. C. Hughes, W. K. Schubert, T. E. Zipperian, J. L. Rodriguez, and T. A. Plut, "Thin-film palladium and silver alloys and layers for metal-insulator-semiconductor sensors," *Journal of Applied Physics*, vol. 62, no. 3, pp. 1074–1083, 1987.
- [15] M. Wang and Y. Feng, "Palladium-silver thin film for hydrogen sensing," *Sensors and Actuators B*, vol. 123, no. 1, pp. 101–106, 2007.
- [16] S. Eriksson, M. Nilsson, M. Boutonnet, and S. Järås, "Partial oxidation of methane over rhodium catalysts for power generation applications," *Catalysis Today*, vol. 100, no. 3–4, pp. 447–451, 2005.
- [17] V. A. Drozdov, P. G. Tsyrlunikov, V. V. Popovskii, N. N. Bulgakov, E. M. Moroz, and T. G. Galeev, "Comparative study of the activity of Al-Pd and Al-Pt catalysts in deep oxidation of hydrocarbons," *Reaction Kinetics and Catalysis Letters*, vol. 27, no. 2, pp. 425–427, 1985.
- [18] R. Löber and D. Hennig, "Interaction of hydrogen with transition metal fcc(111) surfaces," *Physical Review B*, vol. 55, no. 7, pp. 4761–4765, 1997.

- [19] E. P. J. Mallens, J. H. B. J. Hoebink, and G. B. Marin, "The reaction mechanism of the partial oxidation of methane to synthesis gas: a transient kinetic study over rhodium and a comparison with platinum," *Journal of Catalysis*, vol. 167, no. 1, pp. 43–56, 1997.
- [20] L. Opara, B. Klein, and H. Zuchnerh, "Hydrogen-diffusion in $\text{Pd}_{1-x}\text{Ag}_x$ ($0 \leq x \leq 1$)," *Journal of Alloys and Compounds*, vol. 253-254, pp. 378–380, 1997.
- [21] I. Lundström, H. Sundgren, F. Winquist, M. Eriksson, C. Krantz-Rülcker, and A. Lloyd-Spetz, "Twenty-five years of field effect gas sensor research in Linköping," *Sensors and Actuators B*, vol. 121, no. 1, pp. 247–262, 2007.
- [22] S. Liu, K. Takahashi, K. Fuchigami, and K. Uematsu, "Hydrogen production by oxidative methanol reforming on Pd/ZnO: catalyst deactivation," *Applied Catalysis A*, vol. 299, no. 1-2, pp. 58–65, 2006.
- [23] H. Zhang, R. L. Penn, R. J. Hamers, and J. F. Banfield, "Enhanced adsorption of molecules on surfaces of nanocrystalline particles," *Journal of Physical Chemistry B*, vol. 103, no. 22, pp. 4656–4662, 1999.
- [24] V. Khranovskyy, J. Eriksson, A. Lloyd-Spetz, and R. Yakimova, "Oxygen absorption effect on the sensitivity and material stability of ZnO nanostructured films," in *Proceedings of IEEE Sensors*, pp. 874–877, Lecce, Italy, October 2008.

Review Article

On the Low-Temperature Response of Semiconductor Gas Sensors

A. Helwig,¹ G. Müller,¹ G. Sberveglieri,² and M. Eickhoff³

¹ EADS Innovation Works, Sensors, Electronics & Systems Integration, 81663 München, Germany

² CNR-INFM, SENSOR Laboratory, University of Brescia, 25133 Brescia, Italy

³ I. Physikalisches Institut, Justus Liebig Universität Gießen, 35392 Gießen, Germany

Correspondence should be addressed to A. Helwig, andreas.helwig@eads.net

Received 29 January 2009; Accepted 29 March 2009

Recommended by Yongxiang Li

The present paper compares three different kinds of semiconductor gas sensing materials: metal oxides (MOX), hydrogen-terminated diamond (HD), and hydrogenated amorphous silicon (a-Si:H). Whereas in MOX materials oxygen is the chemically reactive surface species, HD and a-Si:H are covalently bonded semiconductors with hydrogen-terminated surfaces. We demonstrate that these dissimilar semiconductor materials exhibit the same kind of low-temperature gas response. This low-temperature response-mechanism is mediated by a thin layer of adsorbed water with the semiconductor materials themselves acting as pH sensors. In this adsorbate-limited state the gas sensitivity is limited to molecular species that can easily dissolve in H₂O and subsequently undergo electrolytic dissociation. At higher temperatures, where a closed layer of adsorbed water can no longer exist, the gas response is limited by direct molecule-semiconductor interactions. In this latter mode of operation, MOX gas sensors respond to adsorbed gases according to their different oxidising or reducing properties. Hydrogenated amorphous silicon (a-Si:H), on the other hand, exhibits a significantly different cross sensitivity profile, revealing that gas-surface interactions may largely be restricted to analyte molecules with lone-pair and electron-deficient three-centre orbitals.

Copyright © 2009 A. Helwig et al. This is an open access article distributed under the Creative Commons Attribution License, which permits unrestricted use, distribution, and reproduction in any medium, provided the original work is properly cited.

1. Introduction

In recent years semiconductor gas sensors have found widespread commercial application in gas monitoring and alarm applications. To date most of these sensors employ metal oxide (MOX) semiconductors as gas sensitive materials [1–7]. Commercial MOX sensors mostly employ thick-film materials as sensing layers due to the fact that thick-film technologies are intrinsically low cost and that thick-film compositions can easily be controlled, allowing for the preparation of a wide range of MOX base materials and incorporation of numerous catalytic promoter impurities [3, 8]. In this way MOX gas sensors with different cross sensitivity profiles can be realised. Most recent advances in this field are three-sensor arrays deposited on a single ceramic heater chip. These three-sensor arrays are embedded in a single TO5 package and are marketed together with data acquisition boards and principal component analysis software [9].

In spite of this progress, MOX gas sensors have remained a subject of intense scientific interest, mainly because of two challenges: (i) the limited selectivity of MOX gas sensors

and (ii) their relatively large heating power consumption which makes MOX sensors and in particular MOX sensor arrays hard to employ in mobile applications and in bus-connected sensor networks. Whereas micromachined heater technologies have been investigated to decrease the heating power consumption of MOX gas sensor arrays [10–14], recent efforts have been focused on the preparation of MOX nanocrystals or nanowires [15–19]. Due to their very constrained geometry and good thermal insulation, self-heating effects in single nanowire sensors can be quite appreciable, thus opening up new ways towards ultralow power-heated MOX gas sensors [20]. Concerning progress in the fields of sensitivity, selectivity, and stability, nanowire technologies have considerably enhanced the sensitivity and the stability of MOX gas sensors but contributed relatively little towards a solution of the cross sensitivity problem.

A third line of research, which has attracted attention in the past few years, is the low-temperature sensitivity of MOX gas sensors. Work into this direction has shown that MOX gas sensors cannot only respond to gases at conventional operation temperatures of the order of several hundred centigrade but also at room temperature and slightly above

[21–26]. In this latter mode of operation UV photoactivation has also been shown to be effective [27–31]. Gases that could be detected under such conditions are NO_2 , NH_3 , H_2S , and a number of short-chain alcohols.

Although interesting from a phenomenological point of view, all these latter reports remain vague in providing a consistent explanation for these novel low-temperature sensing phenomena. The present paper intends to contribute to this discussion, summarising results from recent work on the low-temperature response of semiconductor gas sensors [32–35]. Comprehensive presentation of these data in a single review aims at developing a coherent picture of low-temperature gas sensing phenomena at semiconductor surfaces. As will be shown below, the essence of our findings is that semiconductor materials in general—and MOX materials in particular—tend to adsorb multiple layers of humidity from the ambient air, forming a closed liquid electrolyte layer on the surface. In this water adsorption-limited state, saturated semiconductor surfaces do not respond to changes in the ambient H_2O vapour pressure, and their response to reactive gases is limited to molecules that can easily dissolve in water and undergo electrolytic dissociation there. The active sensing layer in this case is the adsorbed water film, and the role of the underlying semiconductor materials is simply reduced towards serving as a pH sensor. In our previous work we have coined the term “dissociative gas sensing effect” for this kind of gas sensing mechanism.

In the following we develop this idea of a dissociative gas sensing effect by reviewing some relevant observations on MOX materials. We then provide the reader with the theoretical background for the analysis of low-temperature multilayer water adsorption phenomena. In the central part of this article we discuss gas sensing experiments that have been performed on hydrogen-terminated diamond (HD) surfaces. The reason for considering such a dissimilar semiconductor material is—that in contrast to the huge variety of MOX materials with their widely variable composition and morphology—HD is a well-characterised single-crystal material with a well-documented adsorbed liquid electrolyte layer on top [36, 37]. HD, therefore, has turned out to be an ideal model system for studying the dissociative gas sensing effect [33, 34]. As a third kind of semiconductor material, we have studied hydrogenated amorphous silicon (a-Si:H). The interest in this latter material stems from the fact that it can easily be incorporated into microsensor processes, exhibiting at the same time both a room-temperature dissociative gas sensing effect and an innovative kind of “coordinative gas response” that appears when the sensor operation temperature is raised above the water evaporation threshold [35]. In the final chapter we present a comprehensive model for the dissociative gas response, considering the partial steps of gas/liquid electrolyte and liquid electrolyte/semiconductor interactions.

2. Observations on Metal Oxide Gas Sensors

2.1. High-Temperature Response. As summarised in Figure 1, MOX gas sensors exhibit broad-range sensitivity to a wide

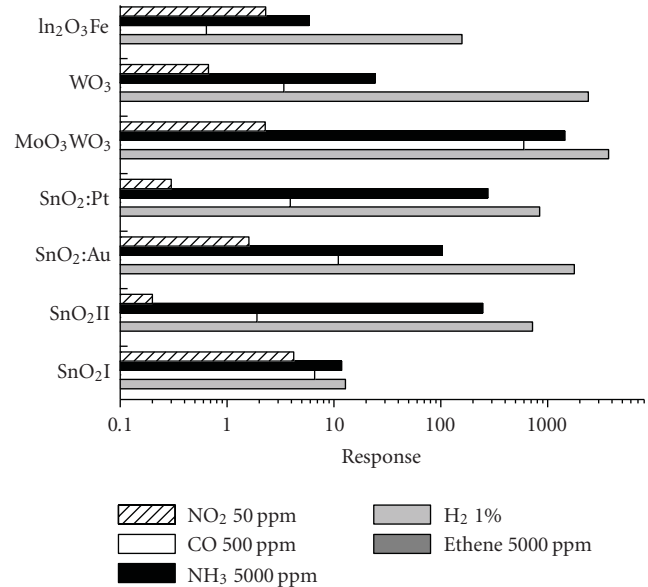


FIGURE 1: Gas sensitivity profiles of different MOX materials.

variety of analyte molecules. This broad-range sensitivity is due to the well-known combustive gas sensing effect in which adsorbed analyte molecules become oxidised by interactions with preadsorbed surface oxygen ions [2–4, 8]. In all cases a major sensitivity also occurs in the case of NO_2 which competes with O_2 in forming negative surface ion species.

A key observation on MOX gas sensors is that those chemical surface interactions that lead to a combustive gas response are thermally activated. This fact is evidenced in Figure 2, which shows the H_2 and the water vapour sensitivities of an $\text{SnO}_2\text{:Au}$ sensor [39] as a function of its operation temperature. As far as reducing analyte molecules are concerned, the shape of these sensitivity curves can be understood on the basis of two opposite trends: (i) a thermally activated surface combustion of the adsorbed analyte molecules which limits the response on the low-temperature side and (ii) a thermally activated and concentration-dependent desorption rate which limits the response at the high-temperature side [8, 38]. Figure 3 shows how the combination of both effects determines the temperature dependence of the gas response.

2.2. Low-Temperature Response. A significant new observation was that, in addition to this high-temperature gas sensitivity, MOX gas sensors also exhibit a small and slow and thus easily overlooked low-temperature response. There have been a number of reports, demonstrating sensitivity towards NO_2 , NH_3 , H_2S , and different alcohol vapours even at room temperature [21, 22, 31]. Some of these reports also demonstrate an enhancement of this low-temperature gas response upon irradiation with UV light [27–30]. A consistent explanation of the underlying sensing mechanism, however, is not given in these reports. More recently we have demonstrated that this low-temperature response exhibits a different cross sensitivity profile in comparison to the conventional combustive high-temperature response. This

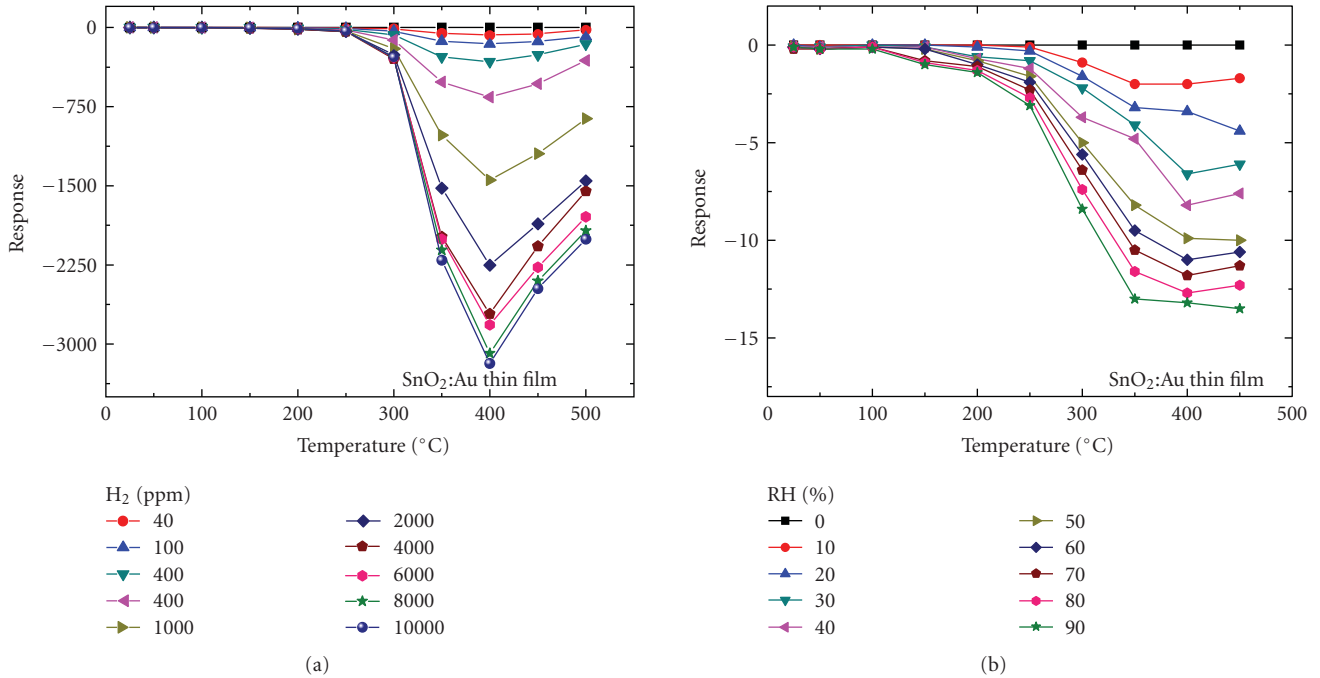


FIGURE 2: Surface temperature dependence of the sensitivity of a SnO₂:Au gas sensor: (a) towards H₂; (b) towards water vapour.

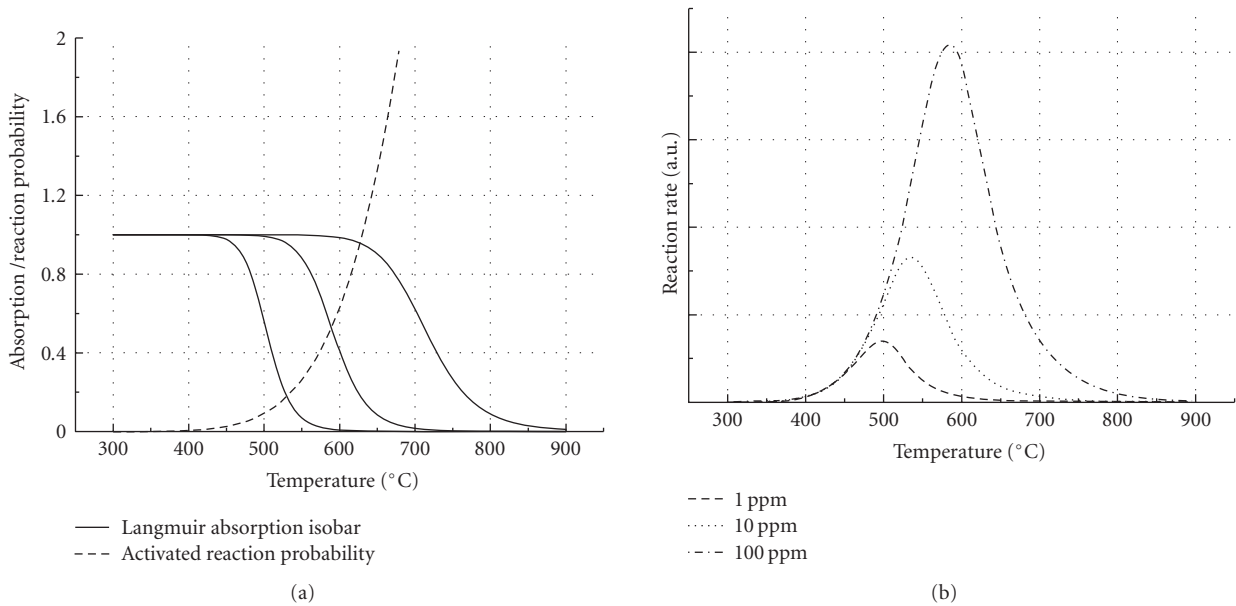


FIGURE 3: (a) Temperature dependence of the surface combustion and desorption rates of reducing analyte molecules; (b) cooperation of both effects in determining the temperature dependence of the MOX gas sensitivity [38].

fact is revealed from a comparison of Figures 4(a) and 4(b). Figure 4(a) moreover shows that the low-temperature cross sensitivity profile is virtually the same as that observed on hydrogen-terminated diamond (HD), that is, a completely dissimilar gas sensing material. Although due to the different kinds of charge carriers (p-type in the case of HD and n-type in case of MOX, see also Section 4.1) the actual sensor response points in opposite directions, the cross sensitivity

profile with regard to different analyte gases, however, is exactly the same. This latter observation paved the way for the idea that a completely new gas sensing mechanism might be involved at room temperature and slightly above [32–35].

Comparing the low- and the high-temperature gas sensing effects, it is evident that the low-temperature gas response is comparatively small and limited to a much smaller number of gases than the high-temperature one.

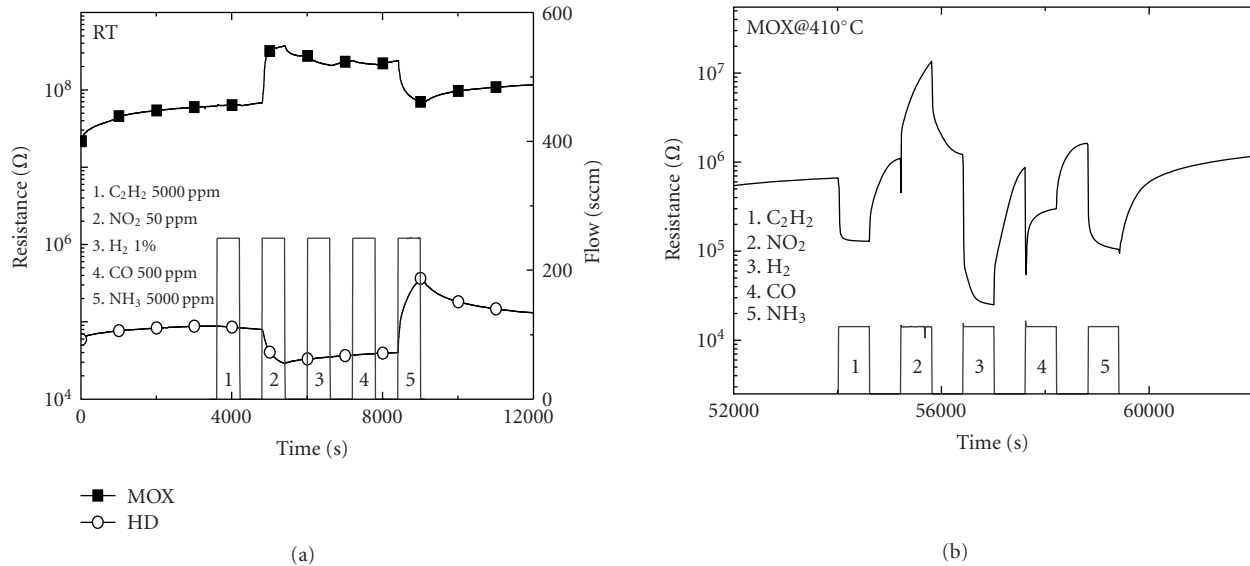


FIGURE 4: Low-temperature gas response of an $\text{SnO}_2\text{:Au}$ sensor to a number of reducing analyte gases: (a) as measured at room temperature, (b) as measured at the normally employed high sensor operation temperatures ($T_s = 400^\circ\text{C}$). The comparison in the left panel shows that $\text{SnO}_2\text{:Au}$ and HD show the same kind of cross sensitivity profiles despite of their very different semiconductor surface properties [32].

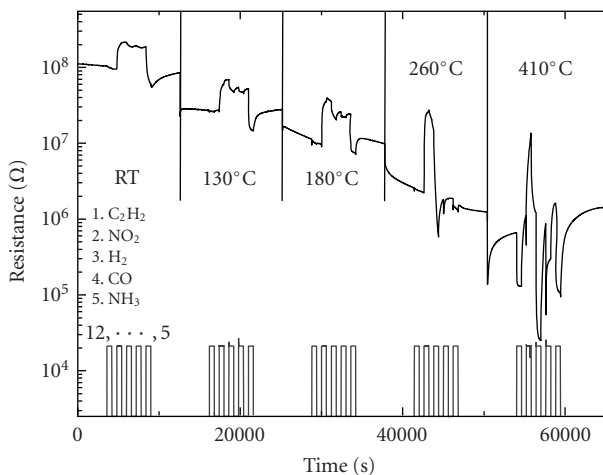


FIGURE 5: Transition from the low-temperature to the high-temperature gas response as the sensor operation temperature is increased from room temperature to about 400°C [32]. The data have been obtained on the same $\text{SnO}_2\text{:Au}$ gas sensor as in Figure 4.

Notable examples for a comparatively high low-temperature gas sensitivity are the responses towards NH_3 and NO_2 . A second relevant observation is that the response to both gases exhibits a huge asymmetry with regard to the response and recovery time constants: whereas response times are moderate, recovery times are extremely long.

Further clues to the nature of the low-temperature gas sensing effect can be obtained by observing changes in the gas response patterns when the operation temperature of the $\text{SnO}_2\text{:Au}$ gas sensors is increased, as displayed in Figure 5. These data demonstrate that the low-temperature gas response pattern starts to disappear at temperatures

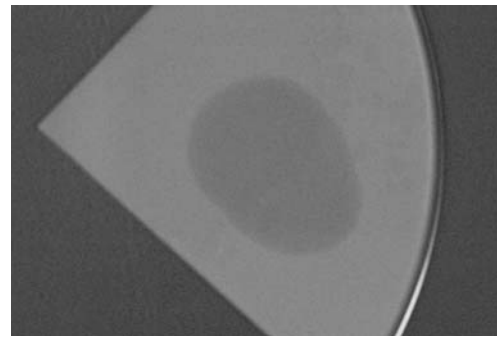


FIGURE 6: Result of a contact angle experiment as performed on a nanogranular SnO_2 film deposited on an oxidised silicon wafer [32].

around 200°C , and that it is replaced by the familiar broad-range high-temperature gas sensitivity which becomes dominant at temperatures around 400°C .

Comparing the low-temperature MOX and HD gas sensing effects and realising that both the p-type surface conductivity and the gas response of HD are due to a thin layer of adsorbed water on the diamond surface [36], a similar effect was suggested for MOX materials as well. Further evidence in favour of an adsorbed liquid electrolyte layer on MOX surfaces came from the observation that MOX surfaces are fairly hydrophilic. This latter fact is evidenced in Figure 6, showing that a drop of water suspended on a MOX surface spreads out rapidly, reducing the contact angle to almost zero.

Accepting the possibility that a closed liquid electrolyte layer might indeed exist at the MOX surface, the observed low-temperature cross sensitivity profiles can be explained as follows: the MOX surface and thus the semiconductor

band bending can only be affected once analyte molecules are dissolved in the surface water layer and dissociated there. Overall, this amounts to an indirect sensing mechanism which limits the role of the MOX layers towards that of a pH sensor [40]. Before we follow this idea further, we present some theoretical background that allows multilayer water adsorption phenomena on low-temperature solid surfaces to be analysed.

3. Multilayer Water Adsorption at Solid Surfaces

3.1. BET Isotherm. Multilayer adsorption of gases on solid surfaces is described by the BET isotherm. This isotherm was first introduced by Brunauer, Emmett, and Teller in 1938 [41]. The main assumptions leading to this isotherm are [42]

- (i) polymolecular adsorption of spherical particles;
- (ii) homogeneous surface with constant adsorption centre density;
- (iii) the heat of adsorption of the first adsorbed monomolecular layer drops to the heat of liquefaction for all following layers;
- (iv) all following polymolecular layers act like a liquid;
- (v) the number of adsorbate layers can reach infinity.

With these assumptions the relative surface coverage $\Theta(T, P)$ is obtained:

$$\Theta(P, T) = \left(\frac{P}{P_0(T) - P} \right) \cdot \left[\frac{c(T)}{1 + \left(\frac{P}{P_0(T)} \right) \cdot (c(T) - 1)} \right]. \quad (1)$$

In this equation P and P_0 represent the equilibrium and saturation vapour pressures of the adsorbate gas at the temperature T and $c(T)$ of the BET constant:

$$c(T) = \exp\left(\frac{\varepsilon_1 - \varepsilon_L}{k_B \cdot T}\right). \quad (2)$$

In this latter equation ε_1 and ε_L represent the heats of adsorption and liquefaction, respectively.

A particularly simple form of the BET isotherm is obtained in case the first layer is adsorbed as tightly as all the others. Then $c(T) = 1$ and the expression for the BET isotherm reduces to

$$\Theta(P, T) = \frac{P}{P_0(T) - P}. \quad (3)$$

For any vapour pressure P there exists a temperature T_{sat} at which the vapour pressure P in the air equals the saturation pressure $P_0(T_{\text{sat}})$. At all temperatures T lower than T_{sat} , the maximum vapour pressure $P(T)$ is limited by the saturation pressure at that temperature, that is, $P(T) = P_0(T)$. Equation (3) then predicts that under conditions of saturated water vapour, that is, at $T \leq T_{\text{sat}}$, a solid surface will adsorb infinitely many layers of water and thus form a closed layer of condensed water on the surface. For temperatures higher

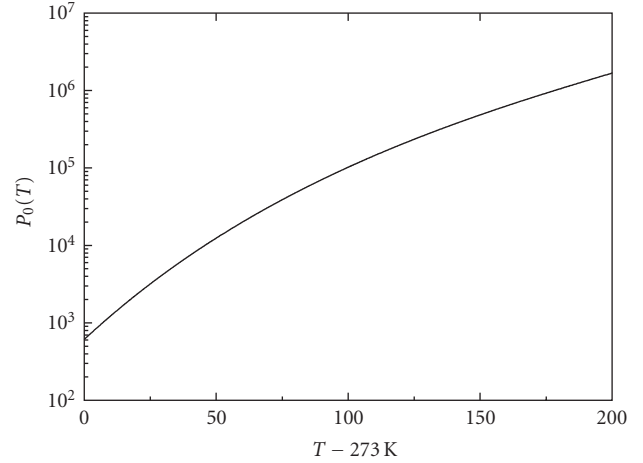


FIGURE 7: Saturation vapour pressure of water as a function of the temperature in the air.

than T_{sat} , the water vapour pressure in the air is supply-limited and lower than $P_0(T)$. In this limiting case, P is much smaller than $P_0(T)$, and the BET equation reduces to the familiar Langmuir isotherm [43]:

$$\Theta(P, T) = \frac{c(T) \cdot P}{c(T) \cdot P + P_0(T)}. \quad (4)$$

As $P_0(T)$ increases exponentially with temperature, the surface coverage $\Theta(T, P)$ in this temperature range drops exponentially as the temperature is increased beyond T_{sat} .

3.2. Water Adsorption at Solid Surfaces. Considering the main constituents of the ambient air (N_2 , O_2 , H_2O , and CO_2) as well as the range of analyte gases that have frequently been studied in gas sensing experiments, water vapour is outstanding insofar as it can occur in high concentrations (Figure 7) and at the same time exhibits a high boiling point (Figure 8(a)) and a concomitantly high heat of vaporisation (Figure 8(b)). Because of these properties, adsorbed water vapour can easily undergo multilayer adsorption leading to thin liquid electrolyte layers on solid surfaces, and it thus can completely alter the gas-surface interactions that may occur on a semiconductor surface.

In order to estimate the water coverage on a semiconductor surface using the BET equation, an estimate of the BET constant (2) is required. The value of this constant depends on two parameters: (i) the heat of liquefaction ε_L and (ii) the heat of adsorption ε_1 . The heat of liquefaction of water is known from literature ($\varepsilon_L = 0.424$ eV per molecule [45]). The heat of adsorption describes the adsorption energy of the first monolayer on the adsorbent surface. This latter value can vary strongly with the chemical composition and the morphology of the adsorbing solid. A first estimate for the heat of adsorption of water on MOX surfaces is 0.52 eV [44]. With $c(T)$ being known, the surface coverage of water on a MOX surface can now be obtained from (1).

Assuming that water vapour saturation in the air is reached at 30°C, it is revealed from Figure 9 that a MOX

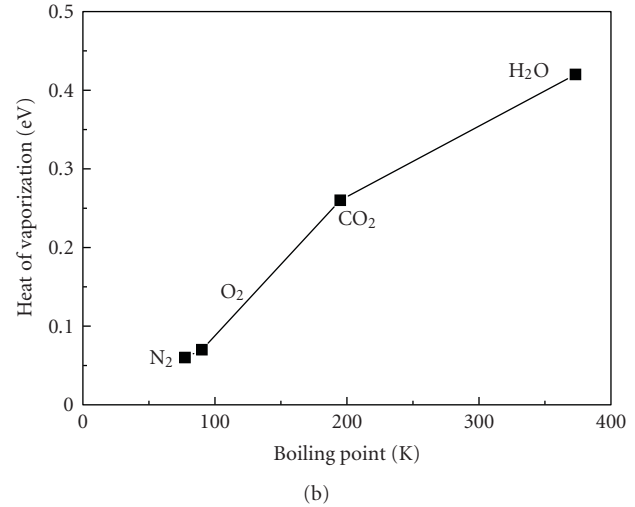
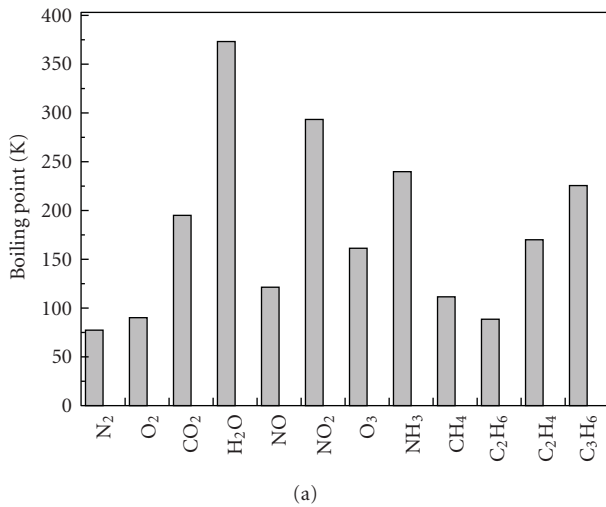


FIGURE 8: (a) Boiling points of the main air constituents and of a number of often studied analyte gas molecules; (b) heat of vaporisation of the main air constituents.

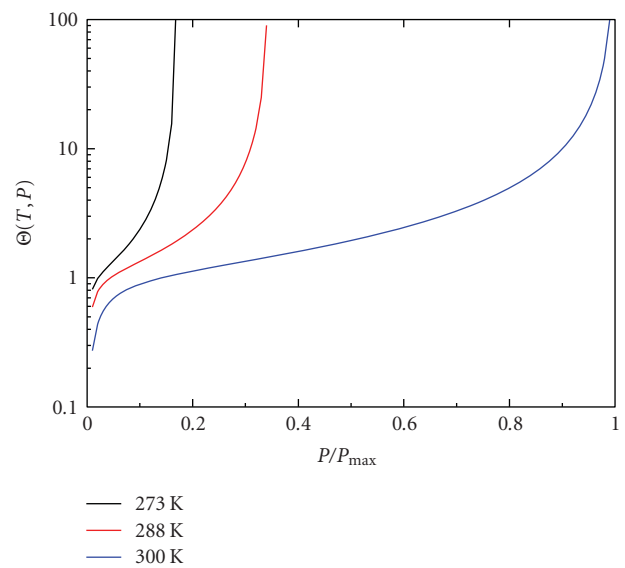
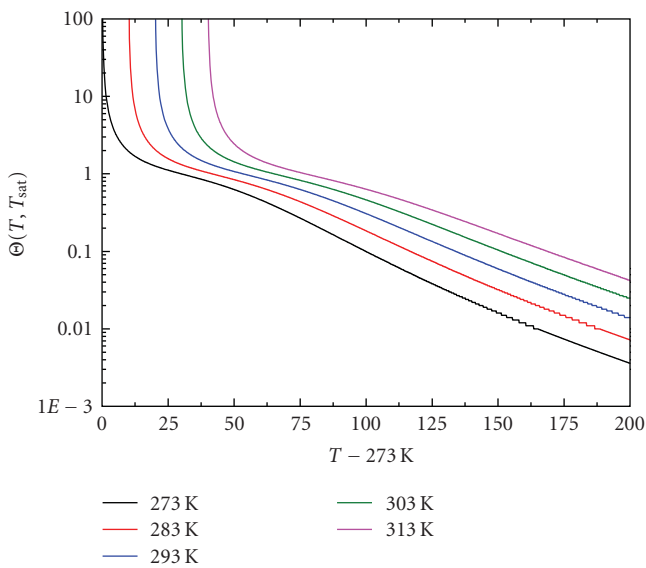


FIGURE 9: Surface coverage with water as a function of the MOX substrate temperature as evaluated from the BET isotherm. The heat of adsorption of the first monolayer was assumed to be $\epsilon_1 = 0.52$ eV [44].

FIGURE 10: Water coverage as a function of vapour pressure and substrate temperature (low-temperature region $T \leq T_{\text{sat}}$). $T_{\text{sat}} = 27^\circ\text{C}$ (300 K).

surface will always be covered by multiple layers of water as long as the substrate temperature remains at room temperature or below ($0 < T < 30^\circ\text{C}$). With a closed water film being present, oxygen surface adsorbates will not form. In case the substrate temperature is raised beyond the saturation temperature T_{sat} , the water surface coverage will rapidly drop into the range of a single monolayer as $T \sim 70^\circ\text{C}$ is approached. As a single monolayer of water is sufficient to prevent oxygen ionosorption, the normal combustible detection mechanism still will not work. First indications of a combustible response, however, might be expected when there is a tendency of the adsorbed water

to concentrate in patches with above-monolayer thicknesses. Raising the substrate temperature towards 150°C , the water coverage drops to about 0.1 monolayers which means that large patches of free semiconductor surface start to occur, providing adsorption sites for oxygen. In agreement with this expectation we have observed that MOX gas sensors start to respond to combustible gases as this temperature is exceeded (Figure 5) and that MOX layers start to respond to changes in the humidity concentration in the gas phase (Figure 2(b)).

Figures 10 and 11 refer to two situations in which the vapour pressure in the gas phase is varied from zero to the saturation vapour pressure considering that the air

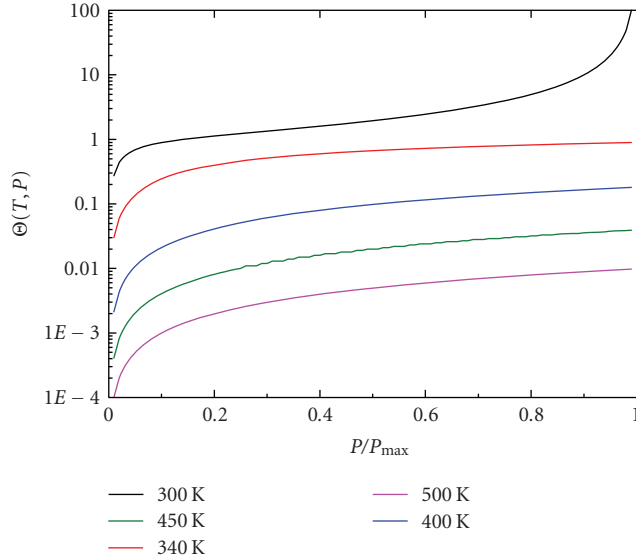


FIGURE 11: Water coverage as a function of vapour pressure and substrate temperature (high-temperature region $T \geq T_{\text{sat}}$). $T_{\text{sat}} = 27^\circ\text{C}$ (300 K).

temperature is 30°C . The first diagram reveals that, with the MOX substrate being kept at room temperature or below, multilayer water adsorption will take place also at water vapour pressures much lower than the saturation pressure level. A normal gas response, therefore, cannot be expected in this lower H_2O vapour pressure range as well. This situation changes, when the MOX substrates are heated to 150°C or more. In this latter case the surface water coverage varies over the entire H_2O pressure range and remains in the sub-monolayer range. In such situations oxygen ionosorption and a normal combustive gas response can occur, and, in addition, single H_2O molecules may directly adsorb on the MOX surface and thus give rise to a water-vapour-dependent response signal.

4. The Universality of the Low-Temperature Gas Response

The considerations in Sections 2 and 3 have indicated that a thin layer of condensed humidity might play an important role in determining the gas sensing properties of MOX gas sensors operated at or slightly above room temperature. In this paragraph we present the results of gas sensing experiments on alternative semiconductor materials which are known to carry condensed water layers on their surfaces under such moderate operation temperatures.

4.1. Hydrogen-Terminated Diamond (HD). Diamond with a bandgap of 5.5 eV is a bona-fide insulator in its undoped state. However, it has been shown that it can exhibit a pronounced p-type surface conductivity of up to $10^{-5}\ \Omega^{-1}$ per square when the surface is terminated with hydrogen [46, 47]. The best established model to explain this phenomenon is the transfer doping model of Maier et al. [36]. According

to these authors, a near-surface hole accumulation layer with carrier densities in the range of $10^{12}\text{-}10^{13}\ \text{cm}^{-2}$ forms via a transfer of diamond valence electrons to an adsorbed surface electrolyte layer. This effect, whose exact microscopic origin is still under debate, has already been employed for devices such as field effect transistors [48], single-hole transistors [49], or pH-sensors [50]. The interest in this present context is that similar devices also support gas sensing interactions that are strikingly similar to those found in room-temperature operated MOX gas sensors.

The investigated samples are shown in Figure 12. The left-hand side of this figure is a sketch of our present state of understanding of surface transfer doping in HD [36]. The essential information of this sketch is that a very thin surface p-type layer in the H-terminated diamond is formed when diamond valence electrons are transferred to H_3O^+ ions into the adsorbed liquid electrolyte layer. In the course of this transfer a fraction of the H_3O^+ ions is neutralised forming H_2O and O_2 molecules, the latter being emitted to the gas phase. In summary, a negative excess charge arises in the liquid electrolyte layer which is compensated by the surface hole accumulation layer in the diamond. Analyte gas molecules with the capability of dissolving and undergoing electrolytic dissociation can disturb this charge equilibrium and thus promote conductance changes, which have been monitored using the device structure presented in the right-hand part of Figure 12. In this device Ti/Au electrodes ($20\ \text{nm}/200\ \text{nm}$) were applied in a gap cell configuration to probe the surface conductivity of the diamond. The contact pad area was $1000\ \mu\text{m} \times 230\ \mu\text{m}$, and the spacing between the contacts was $1000\ \mu\text{m}$. Prior to the electrode deposition the diamond surface was processed in a way as to obtain an H-terminated surface in between the Ti/Au electrodes and an O-terminated surface in the periphery of the gap cell [33, 34].

Figures 13 and 14 present key results of the related gas sensing experiments.

Figure 13(a) can be regarded as a mirror image of the respective results for room-temperature operated MOX gas sensors (see also Figure 4(a)). Due to the fact that holes are the majority carriers in HD, we observe a resistivity decrease upon exposure to NO_2 and an increase upon exposure to NH_3 . The insensitivity towards C_2H_4 , H_2 , and CO , that is, towards a representative range of combustible gases, is demonstrated by the zero response towards C_2H_4 and the undisturbed long recovery from the NO_2 exposure during exposure to H_2 and CO . The long NO_2 recovery is terminated by the final exposure to NH_3 . As NH_3 was added in excess to the NO_2 , a conductivity effect of opposite sign is created and still persists a long time after the termination of the NH_3 -pulse. The other effect that is demonstrated in Figure 13(a) is that dilution of the hole gas by a partial conversion of H-termination to O-termination sites increases the gas sensitivity without altering the cross sensitivity profile. This latter effect was attributed to a catalytic effect of the O-termination sites in converting electronic into ionic charge and vice versa when charge carriers cross the semiconductor/liquid electrolyte interface [34, 37].

Figure 13(b) summarises the results of NO_2 and NH_3 gas sensing experiments in a plot of gas response versus

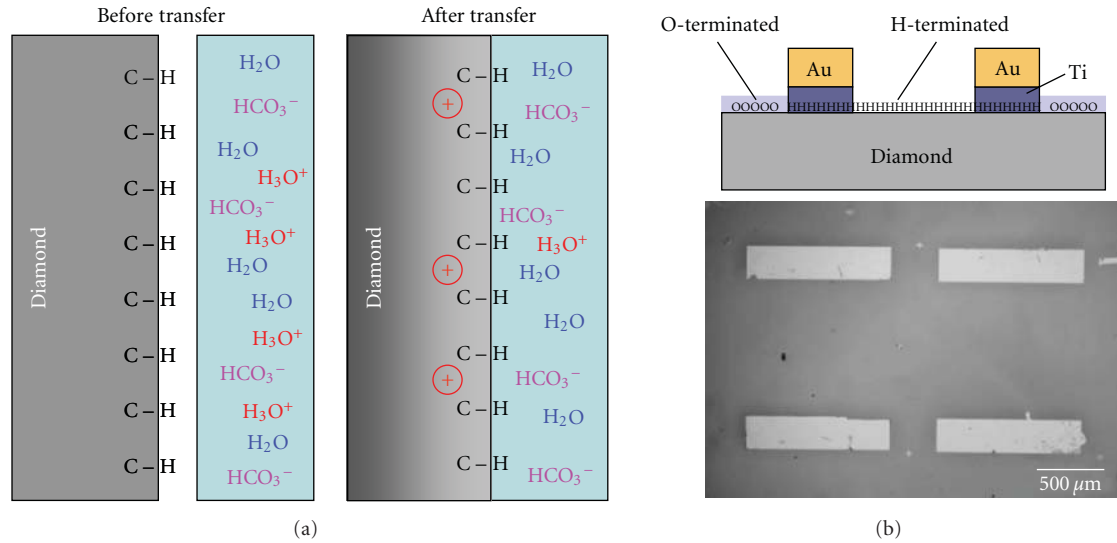


FIGURE 12: (a) Transfer of valence electrons from the diamond surface to an adsorbed liquid electrolyte layer according to Maier et al. [36]. The adsorbed water layer is assumed to be slightly acid due to the dissolution of atmospheric CO_2 ; (b) cross section through a hydrogen terminated diamond sensor (top) and onto a processed device (bottom).

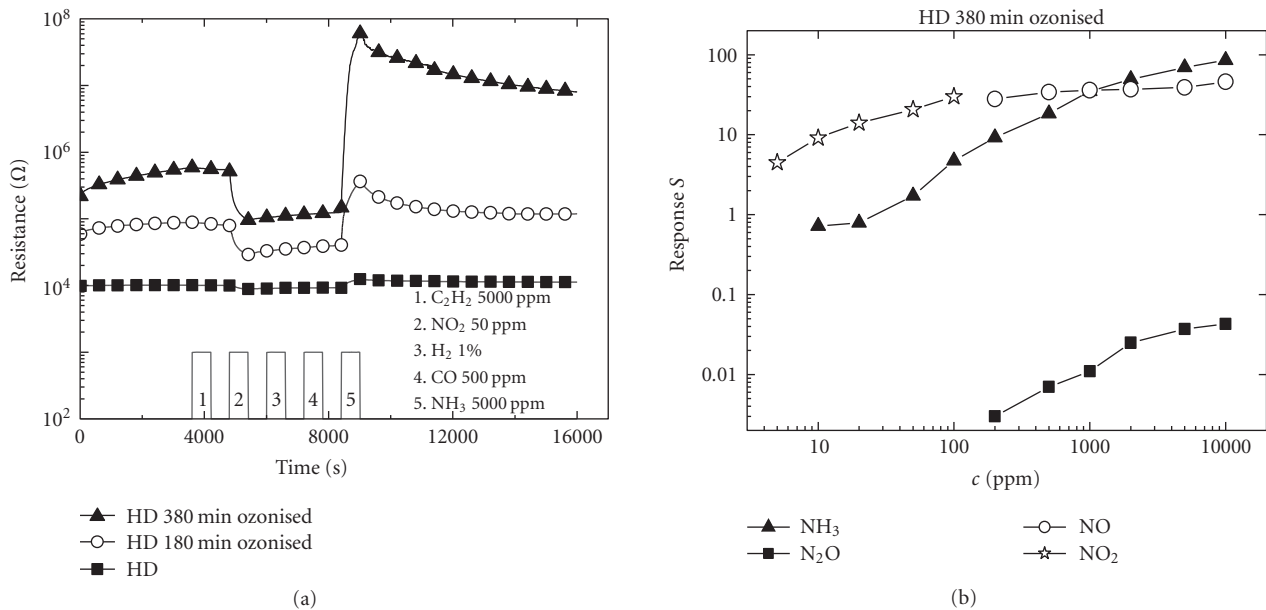


FIGURE 13: (a) Response of an HD sample, processed to exhibit different baseline resistances, towards a representative range of analyte gases; (b) concentration-dependent response of a hydrogen-terminated diamond sample towards different nitrogen bearing gases. NO and NO_2 exhibit an acidic (resistance decrease) and NH_3 and N_2O a basic (resistance increase) response. During these tests the HD sample was kept at room temperature.

concentration. In this plot we have also included data on a wider variety of gases that led to a gas response. In all cases these are nitrogen-bearing gases. In a previous publication [34] we have related the different levels of sensitivity to the individual gases to their different capabilities of dissolving there as acids or bases.

Figure 14, finally, shows that the HD sensors do not respond to changes in the H_2O vapour concentration in the

ambient air at all. We note here that room-temperature-operated MOX gas sensors exhibit a similar effect. A difference, however, arises when the adsorbed water layer is evaporated by increasing the sensor operation temperature: whereas in MOX gas sensors evaporation of the adsorbed humidity layer leads back to the usual combustive gas response, the surface transfer doping effect in the HD samples disappears. With the HD samples thus having

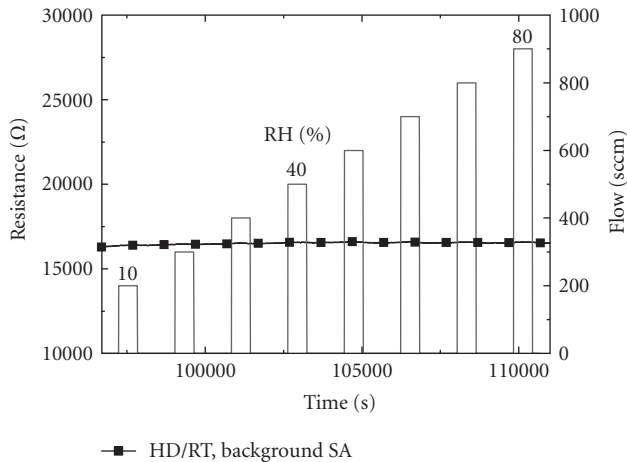


FIGURE 14: Response of an HD sample towards water vapour. During these tests the HD sample was kept at room temperature.

been returned to their intrinsic high-resistivity state, all gas sensitivity disappears as well until, eventually, the HD samples are rehydrated. All three semiconductor materials investigated here return to their dissociative sensing behaviour after a cycle of evaporation and readsorption of humidity at their surfaces [32–35].

The data in Figure 15 show a result of an actual test in a chemical laboratory in which an HD sensor was exposed to acid and base vapours emitted from a chemical laboratory workbench. These latter results clearly support the fact that HD sensors are able to sense acid and base vapours that dissolve in the electrolyte layer. During these experiments also the acids HCl, H_2O_2 , and CH_2O_2 were successfully detected.

4.2. Hydrogenated Amorphous Silicon (a-Si:H). A second semiconductor material, where the presence of adsorbed humidity layers has been confirmed, is hydrogenated amorphous silicon (a-Si:H). This material has found widespread commercial application in photovoltaic solar energy conversion and in large-area thin film electronic devices [51, 52]. In the course of these developments the basic material properties of a-Si:H have been intensively investigated [53, 54]. In this context it has been established that ambient humidity does give rise to adsorbed layers of water on a-Si:H surfaces [55–57]. Furthermore, it has been shown that NH_3 exposure of undoped a-Si:H films at room temperature can increase the conductance by several orders of magnitude [55]. In this early work it was argued by Tanielian and Fritzsche that misleading conclusions can be drawn about basic physical properties of a-Si:H films as long as there is uncertainty about the presence of surface adsorbates.

In the context of our present investigations we have reconsidered the phenomenon of the a-Si:H gas response, performing gas sensing tests under conditions which are more typical of gas sensor operation [35]. With regard to gas sensing tests performed at room temperature, our key results

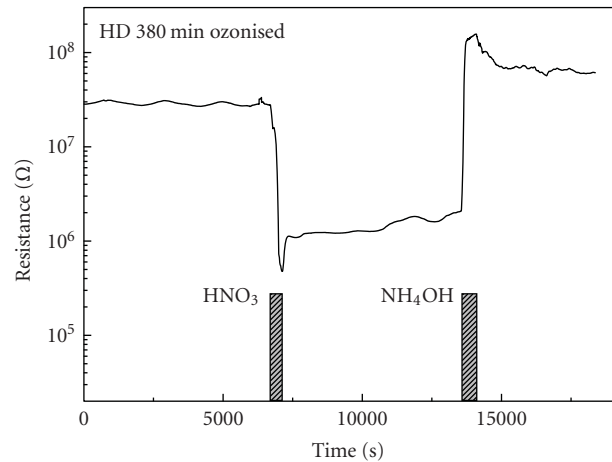


FIGURE 15: Response of an HD sample with a partially oxygenated surface towards acid and base vapours, generated in a clean-room environment.

are summarised in Figure 16. These data firstly show that—similar to the MOX and HD cases—a-Si:H films hardly respond to changes in the humidity content of the ambient air (Figure 16(a)). Secondly, we again observe pronounced and selective conductivity changes upon exposure towards NO_2 and NH_3 . Thirdly, very long recovery time constants are observed after the a-Si:H films had been exposed to NO_2 and particularly NH_3 . As already argued above, these results are consistent with the presence of an adsorbed liquid electrolyte layer at the a-Si:H surface. With regard to the MOX and HD cases, however, an important difference arises in that both NO_2 and NH_3 exposures lead to an increased conductance of the a-Si:H/electrolyte system. Considering the fact that undoped a-Si:H is almost intrinsic and therefore highly resistive at room temperature, it cannot be ruled out that the sensor resistance is dominated in this case by the adsorbed liquid electrolyte layer itself. In this case it is clear that opposite changes in the pH level of the surface electrolyte will always lead to a conductance increase of the a-Si:H/liquid electrolyte layer stack. An alternative explanation for this effect would be that pH changes in the surface electrolyte could either increase the small native n-type conductivity of the a-Si:H or turn its conduction from n-type to p-type. In both cases an increased conductivity would be expected upon exposure to acid-or base-forming gases.

In the a-Si:H case the firmest evidence for the existence of an adsorbed liquid electrolyte layer was obtained by operating the a-Si:H films at temperatures above the water evaporation threshold of about 150 to 200°C. Under these conditions the results of Figure 17 have been obtained. Here we see that—similar to the MOX case—a-Si:H films do start to respond to changes in the humidity content in the ambient air.

This latter result is interesting in two respects: firstly it adds evidence to the existence of a closed adsorbed humidity layer on the a-Si:H surface at room temperature and above, and secondly it shows that a-Si:H exhibits an intrinsic bulk conduction that is independent of the presence or absence

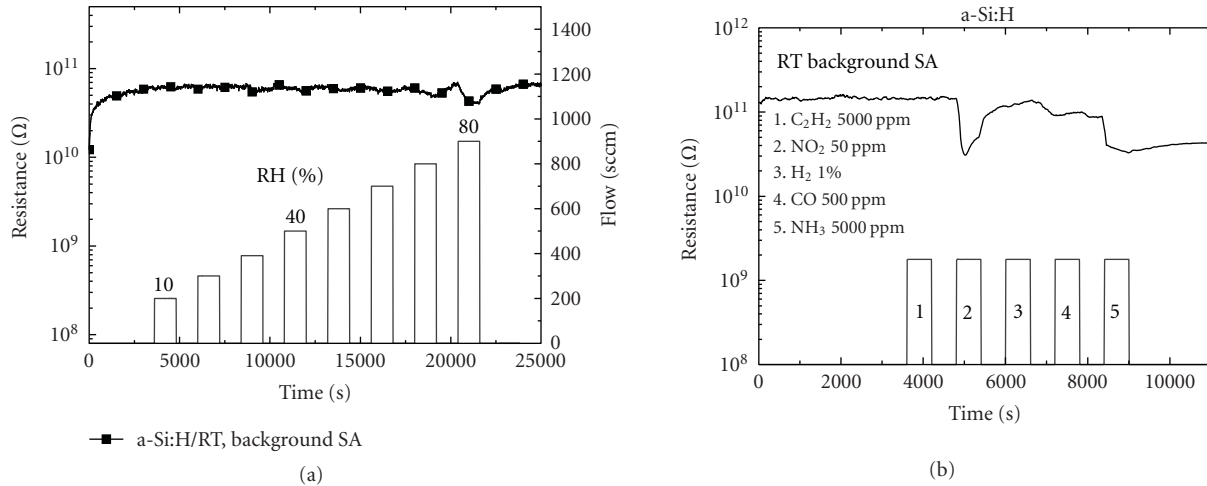


FIGURE 16: Resistivity response of an undoped a-Si:H film towards changes in the ambient humidity concentration (a) and towards a representative range of analyte gases (b). During these tests the a-Si:H film was kept at room temperature.

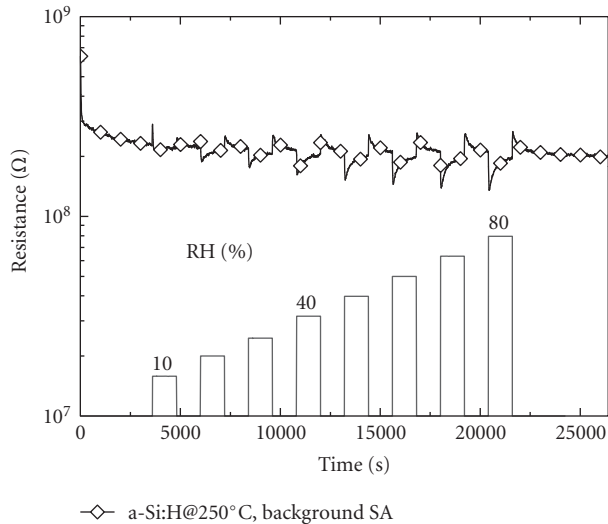


FIGURE 17: Response of an undoped a-Si:H film towards different concentrations of water vapour in the ambient air. Sensor operation temperature: 250°C.

of a surface electrolyte layer. Performing gas sensing tests at $T \sim 250^\circ\text{C}$, which is of the order of the deposition temperature of the a-Si:H films, gas response patterns can therefore be observed that are characteristic of H-terminated sensor surfaces. Such experiments could not be performed on H-terminated diamond as a finite level of p-type surface conductivity can only be observed when a surface adsorbate is present.

Operating a-Si:H films under adsorbate-free conditions, we still do observe a sensitivity towards NO_2 and NH_3 (Figure 18). With regard to water-free MOX surfaces, the surprising result is that the high-temperature a-Si:H gas sensitivity is far more selective than that of MOX materials. This latter fact is demonstrated in Figure 19, which shows that a-Si:H films do respond predominantly to nitrogen-

bearing gases. Gases which simply exhibit combustibility and which can easily be detected with heated MOX gas sensors such as H_2 and ethene lead to a response that is two orders of magnitude smaller than the NO_2 and NH_3 responses. This latter kind of selectivity has been explained in our previous publication [35] on account of the fact that a-Si:H films exhibit H-terminated surfaces that can easily interact with molecules which exhibit lone-pair orbitals like H_2O and NH_3 or electron-deficient three-centre orbitals like NO_2 . The proposed surface interactions of H_2O and NH_3 are illustrated in Figure 20.

5. Response and Recovery Time Constants

The results discussed so far have provided evidence that the room-temperature response of semiconductor gas sensors is mediated by a thin layer of condensed water. This limits the gas sensitivity to molecules which can easily dissolve and undergo electrolytic dissociation in water. A consequence of the electrolytic dissociation is that the resulting charged molecular fragments become hydrated, that is, they acquire a shell of oriented water molecules around them. This hydration effect severely reduces the reevaporation rate of the dissolved analytes back into the gas phase. Once a gas exposure pulse has been terminated, the back-reaction is therefore critically slowed down, and the sensor fails to return to baseline again. Considering potential applications of this low-temperature effect, it is therefore relevant to identify measures to decrease the recovery time constants. In the following we discuss some of these possibilities in the context of HD sensors.

5.1. Effect of Sensor Operation Temperature. A first and obvious measure is increasing the sensor operation temperature, keeping in mind the thermal stability of the surface electrolyte layer and of the H-termination of the diamond, which is the enabling factor for the surface transfer doping effect. Considering the stability of the H-termination, we note that

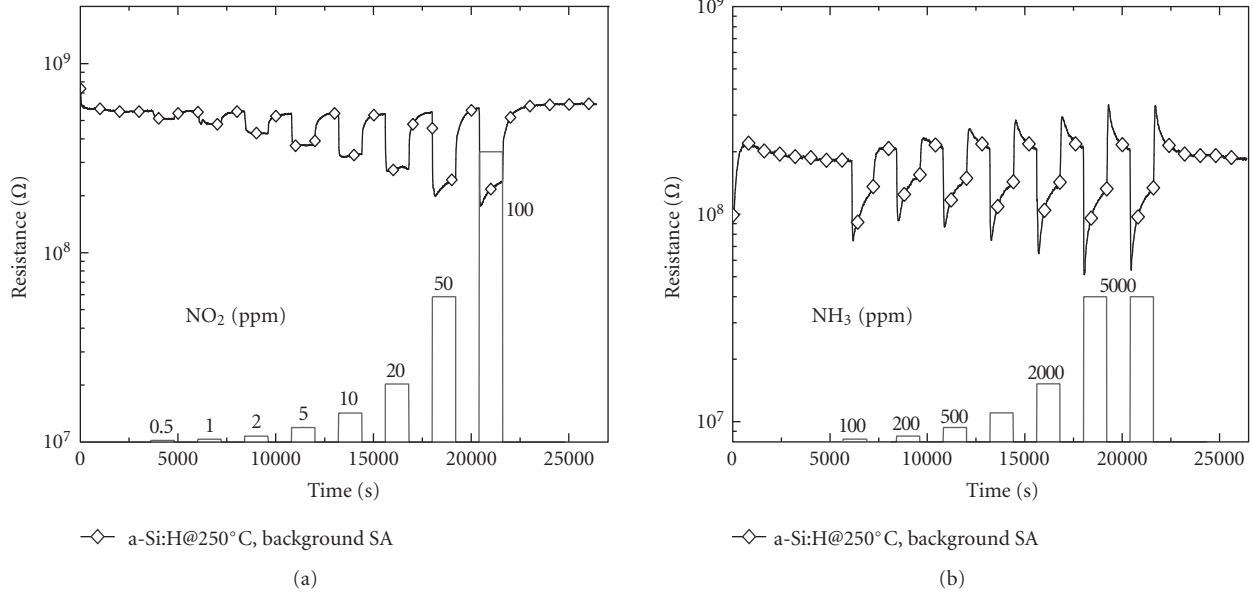


FIGURE 18: Response of an undoped a-Si:H film towards different concentrations of NO₂ (a) and NH₃(b). Sensor operation temperature: 250°C.

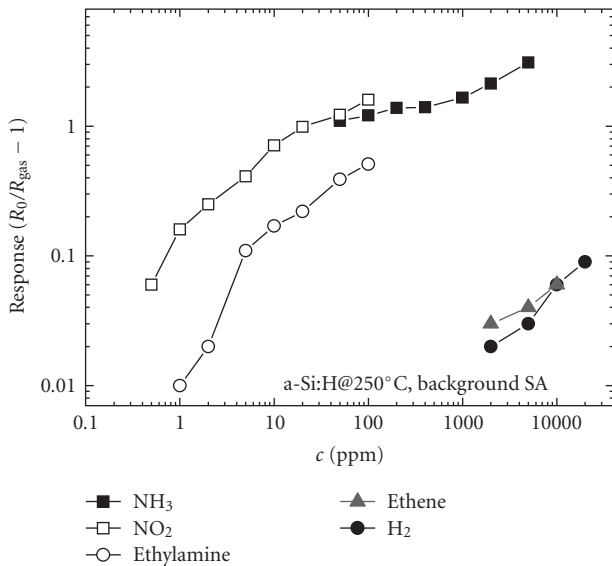


FIGURE 19: Response of an undoped a-Si:H film towards nitrogen- and nonnitrogen bearing gases. Sensor operation temperature: 250°C.

it is stable up to annealing temperatures in the order of 800°C in vacuum [58]. The adsorbed surface electrolyte, the second requirement for the formation of a hole accumulation layer, is less stable. Electrolyte desorption was already observed at temperatures above 150°C [34, 50]. Respecting these much more rigid temperature constraints, we have performed gas sensing tests up to surface temperatures of 140°C. Within the temperature interval from room temperature up to 140°C, we did not find any significant changes in the cross sensitivity behaviour. The main difference was that those gases that

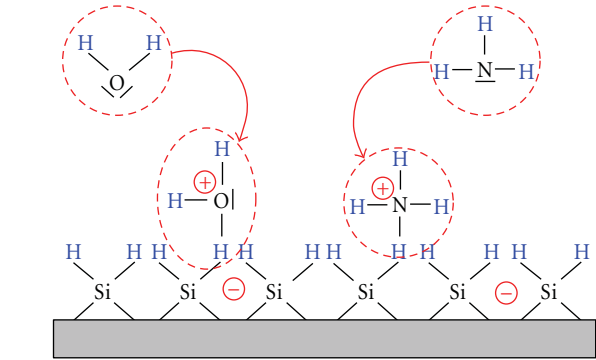


FIGURE 20: Proposed interaction of H₂O and NH₃ molecules on a water-free a-Si:H surface.

could be detected exhibited a faster response and recovery behaviour than at room temperature. This fact is illustrated in Figure 21, considering the special case of response to NH₃. These data show that both the response and recovery time constants decrease with increasing sensor operation temperature. As a second effect, we observe a reduction in the magnitude of the steady-state gas response. Compared to MOX materials, however, this temperature effect is quite small [59].

5.2. *Effect of UV Light Exposure.* The beneficial effect of UV light exposure on the response and recovery time is illustrated in Figure 22. Here, the transient response of an HD sample with a partially oxidised surface to two successive NH₃ pulses is shown. During the first gas pulse, light from a UV LED ($\lambda \sim 255$ nm) was used to irradiate the HD surface. Before the NH₃ exposure pulse the UV light decreased the baseline resistance of the sensor by roughly

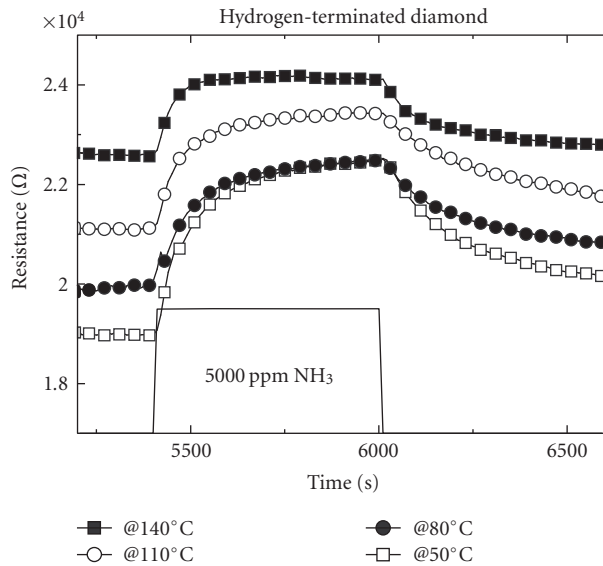


FIGURE 21: Response of a hydrogenated HD sample towards NH_3 gas pulses. In this experiment the HD sample was operated at successively higher temperature.

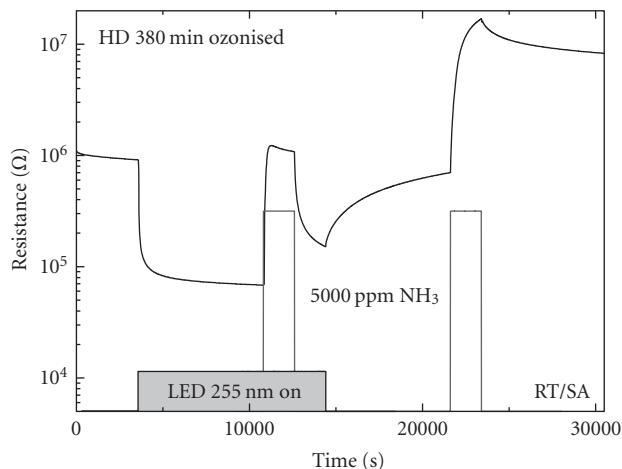


FIGURE 22: Response of an HD sample with a partially oxidised surface towards two NH_3 exposure pulses. During the first pulse the HD sample was illuminated with UV light.

one order of magnitude. Upon NH_3 exposure, a significantly shorter response time is observed as compared to the second exposure pulse, that was carried out in the dark. When the UV illumination was continued beyond the NH_3 exposure pulse, the UV light also lead to a decrease of the recovery time constant.

5.3. Effect of Ozone Exposure. The exposure to ozone further proved to be successful in the case of NH_3 detection. O_3 is heavily oxidising and can therefore be detected in ppb (10^{-9}) concentrations at heated MOX surfaces. In contrast, O_3 did not produce any gas response on room-temperature-operated HD gas sensors. However, as shown in Figure 23,

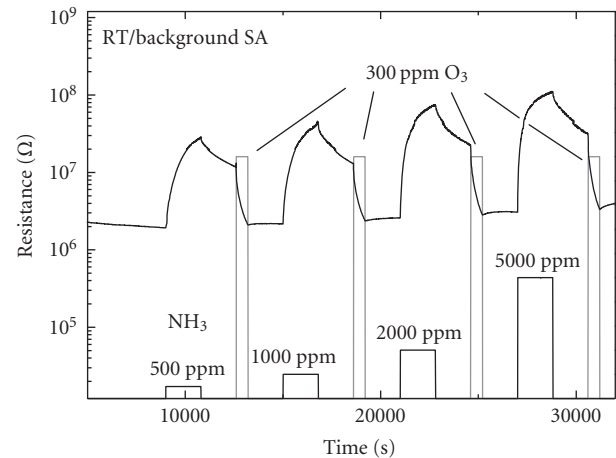


FIGURE 23: Response of an HD sample towards increasing NH_3 concentration steps. The short O_3 exposure pulses following each NH_3 exposure pulse demonstrate the O_3 -induced resetting of the sensor surface to baseline. During these tests the HD sample was kept at room temperature.

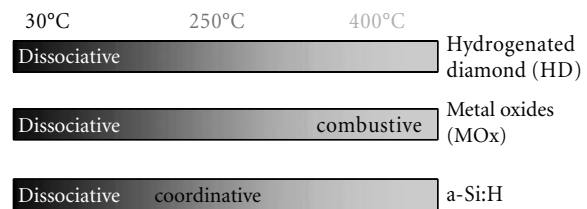


FIGURE 24: Semiconductor materials and temperature ranges which support the different kinds of sensing characteristics.

there was a huge effect when the O_3 was employed after an NH_3 exposure pulse.

A possible explanation for this latter effect is the well-known ozone oxidation reaction of NH_3 :



The resulting ammonia nitrate can disintegrate into NH_4^+ and NO_3^- ions again and thus produce opposing pH changes in the surface electrolyte, that is, re-establish neutrality again. As short-wavelength UV light can produce ozone, this latter reaction might also contribute to the UV acceleration effect.

6. Sensing Mechanisms

6.1. Semiconductors and Sensor Operation Temperature Ranges. In the previous sections we have presented the results of gas sensing tests on three different kinds of semiconductor materials: a first group of MOX materials where oxygen is the chemically reactive species at the sensor surface and a second group of materials, HD and a-Si:H, which both expose covalent, H-terminated C-H or Si-H bonds to the gas ambient. We have firstly shown that, irrespective of the chemical properties of the sensor surface, all kinds of semiconductor materials exhibit largely the

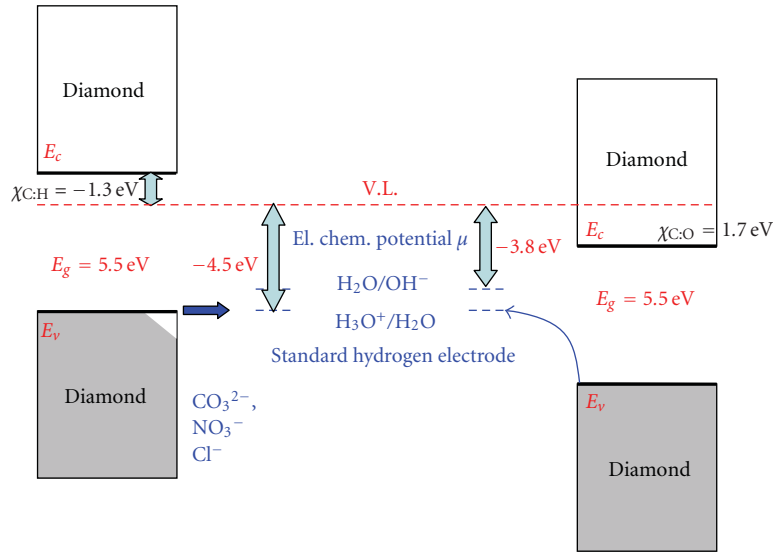


FIGURE 25: Position of the valence and conduction bands of H-terminated diamond (left) and O-terminated diamond (right) relative to the H_3O^+/H_2O and H_2O/OH^- redox levels in water (middle). The energetic match of the H_3O^+/H_2O redox level in water with the top of the valence band in H-terminated diamond facilitates the transfer of diamond valence electrons into the surface electrolyte and thus the formation of a p-type surface layer in undoped diamond.

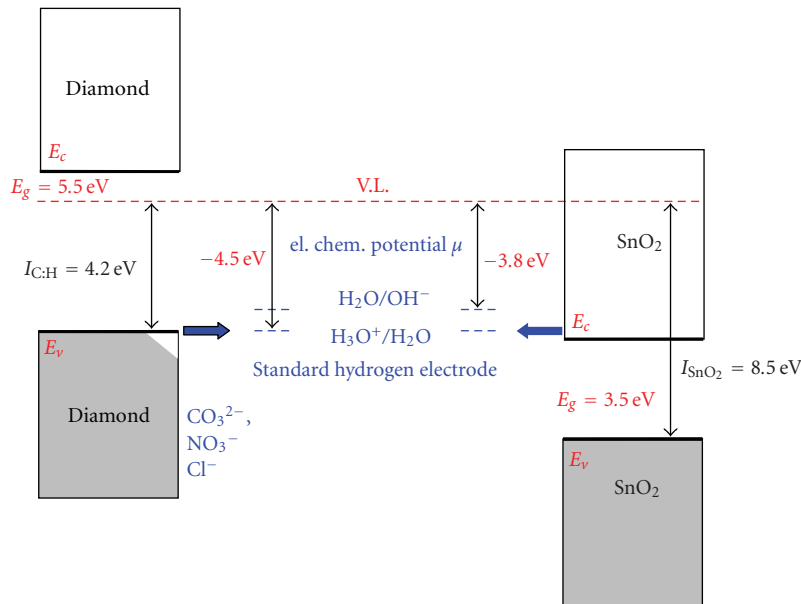


FIGURE 26: Energetic conditions at HD/liquid electrolyte and MOX/liquid electrolyte interfaces. V.L. denotes the vacuum level.

same kind of dissociative room-temperature gas response. Secondly, we have shown that at higher-temperatures, where closed adsorbed humidity layers can no longer exist, the different chemical composition of the sensor surfaces starts to matter giving rise to different kinds of sensor response. For clarity, this situation is visualised in Figure 24, defining once more the names that we have given to the different kinds of sensor response.

Among the sensing mechanisms mentioned, the combus- tive MOX effect has amply been considered and needs no

further discussion here [2, 8, 38, 60–63]. The coordinative effect, observed on water-free a-Si:H surfaces, is certainly a very innovative effect and of interest both from an application and a basic-science point of view. Clearly, however, with the very few data available at the moment, it is too early to arrive at definite conclusions yet. In the following we discuss the dissociative gas sensing effect in more detail, as it is universally observed at room temperature or slightly above on all three kinds of semiconductor materials investigated here. Trying to understand this latter effect is made possible

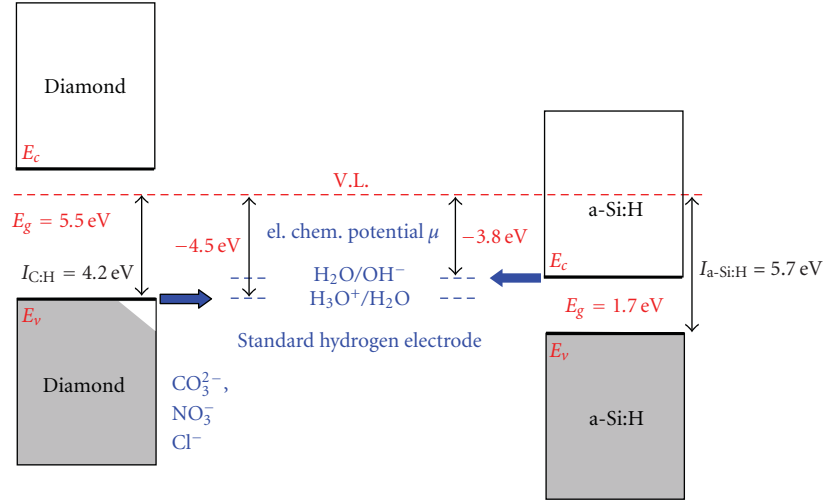
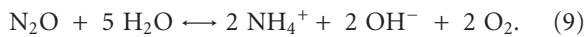
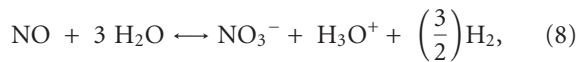
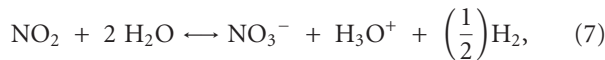
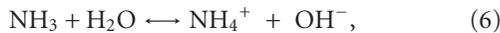


FIGURE 27: Energetic conditions at HD/liquid electrolyte and a-Si:H/liquid electrolyte interfaces. V.L. denotes the vacuum level.

by the following favourable situation: firstly there is a firm scientific basis that allows gas/liquid electrolyte interactions to be discussed and, secondly, there is a well-investigated model system where electronic interactions between an adsorbed liquid electrolyte layer and an underlying semiconductor substrate have been investigated. This model system is the HD/liquid electrolyte system. Trying to understand the universality of the low-temperature dissociative gas response, the common aspect of the gas/liquid electrolyte interaction needs to be considered, and then mechanisms need to be identified which explain how the gas-induced electrochemical changes in the surface electrolyte are communicated to the different semiconductor substrates.

6.2. Gas/Electrolyte Interactions. With a liquid electrolyte layer existing at the sensor surface, the first obvious step in the sensing mechanism is the penetration of the analyte gases into the liquid and absorption there. Considering those gases where we have detected a significant gas response in the liquid electrolyte/HD system, we have proposed that absorption in the liquid is followed by electrolytic dissociation and concomitant changes in the concentrations of H_3O^+ and OH^- ions, that is, ultimately changes in the pH value:



Considering these detection reactions, we have seen that these give rise to different levels of gas response. This fact is illustrated in Table 1.

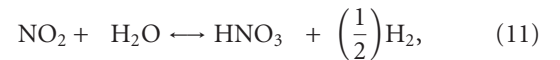
Attempting to relate the magnitude of the measured gas sensitivities to the physico-chemical properties of the

TABLE 1: Comparison of measured gas sensitivities to chemical data of the different analyte gases.

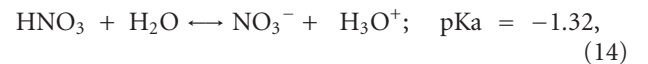
Analyte gas	$S_{\text{gas}} [c = 100 \text{ ppm}]$	Solubility	pK_a	pK_b
NO_2	30	hydrolyses (<2550 g/L)	-1.32	
NO	28	0.067 g/L	-1.32	
CO_2	n.a.	0.0005 g/L	3.3	
NH_3	5	541 g/L		4.79
N_2O	0.003	1.2 g/L		4.79

different analyte molecules, we have further proposed that the above reactions are overall results of two partial reactions.

(i) Absorption in the liquid:



(ii) Electrolytic dissociation inside the liquid:



The observed ordering of the gas sensitivities then arises from two causes: (i) decreasing ease of absorption due to the necessity of breaking up increasing numbers of H_2O molecules and of rearranging increasing numbers of covalent bonds to form HNO_3 or NH_3 , and (ii) poorer electrolytic dissociation of NH_3 relative to HNO_3 .

A final comment with regard to gas sensitivities relates to the absence of an observable CO_2 gas sensing effect. Within

our reasoning this latter insensitivity arises from the fact that CO_2 does not dissolve readily in water and that the corresponding acid H_2CO_3 is only a relatively weak one. It is therefore suggested that the sensor baseline resistance in ambient air is more likely to be determined by the trace levels of NO_2 (<1 ppm) than by the much more abundant CO_2 (~400 ppm).

6.3. Electrolyte/Semiconductor Interactions. With the absorbed gas concentrations having been converted into pH changes, the next question is how these changes are communicated to the underlying semiconductor substrate and converted into a conductance change there. To this end, one has to consider energy diagrams like the one shown in Figure 25. This latter diagram shows the relative arrangement of the diamond valence band maximum and the conduction band minimum as arranged on a common scale with the $\text{H}_2\text{O}/\text{OH}^-$ and $\text{H}_3\text{O}^+/\text{H}_2\text{O}$ redox levels in the adsorbed liquid electrolyte. As a common reference energy the vacuum level is drawn as a red dashed line all through this diagram.

Considering this diagram two important points need to be noted. Firstly, gas absorption in the liquid electrolyte leads to pH changes. pH changes in turn alter the number of positively charged H_3O^+ ions at the energy position of the $\text{H}_3\text{O}^+/\text{H}_2\text{O}$ and of OH^- ions at the $\text{H}_2\text{O}/\text{OH}^-$ redox couples, respectively. Secondly, provided these redox levels overlapped with filled or empty levels in the diamond valence or conduction bands, neutralisation reactions are enabled by shifting electronic charge across the semiconductor liquid electrolyte interface. Once such a charge transfer has taken place, the changed densities of conduction or valence band electrons give rise to a conductance change, that is, a sensor signal. Referring back to Figure 25, it is seen that there is such a favourable match in the case of the valence band maximum in H-terminated diamond and the $\text{H}_3\text{O}^+/\text{H}_2\text{O}$ redox level. Looking to the right-hand side of Figure 25, one can see that there is a completely unfavourable situation in the case of the liquid electrolyte/oxygenated diamond case. As a consequence, gas sensitivity is seen in the liquid electrolyte/HD system but not in the liquid electrolyte/OD one. The ultimate reason for this difference is the different direction of the C–H and C–O surface dipoles, leading to large differences in the related electron affinities [58, 64, 65].

Having considered the HD case, the question remains why there is also a dissociative gas sensing effect in the MOX and a-Si:H cases. This latter question is answered by the energy diagrams presented in Figures 26 and 27: in the first case there is a favorable match between the $\text{H}_3\text{O}^+/\text{H}_2\text{O}$ level and the bottom of the SnO_2 conduction band; in the second case between the $\text{H}_2\text{O}/\text{OH}^-$ level and the bottom of the a-Si:H conduction band. A full account of the pH sensitivity of MOX surfaces is provided in [40].

In concluding this chapter we note that all the above arguments apply to semiconductor/liquid electrolyte interfaces which are operated in a floating-gate manner as illustrated in Figure 12(b). In this configuration equilibration between the semiconductor and the liquid electrolyte needs to proceed via charge transfer processes across the semiconductor/liquid electrolyte interface. Charge exchange

processes across such interfaces are in general slow due to kinetic hindrances associated with the conversion of electronic to ionic charge and vice versa. Evidence for such hindrances comes from the observation of catalytic enhancement effects when H-termination sites at the HD/liquid electrolyte interface are replaced by OH-termination ones (Figure 13(a)). Another supporting evidence for such hindrances comes from observations on HD sensors operated as pH sensors in macroscopic volumes of liquid electrolyte using conventional electrochemical three-electrode configurations [66, 67].

7. Summary and Conclusions

In accordance with the BET isotherm, we found that, at surface temperatures below about 150°C , a thin layer of adsorbed humidity is likely to exist and to cover the surface of all studied semiconductor materials. Under these conditions a direct gas sensing interaction with the semiconductor surface cannot occur. In case an electronically favourable condition exists, that is, the redox level in the liquid electrolyte matching with either the conduction minimum or the valence band maximum in the semiconductor material, possible pH changes in the surface electrolyte can be communicated to the electronic system in the underlying semiconductor, and a conductometric gas response can be obtained.

This form of gas sensitivity is limited to gases, which are able to undergo electrolytic dissociation in water, and it is therefore called “dissociative gas response mechanism”. Gases that cannot undergo electrolytic dissociation remain largely undetected.

Heating MOX materials through the water evaporation threshold, a direct interaction of the analyte gas molecules with the surface oxygen ions is enabled. Under these conditions, the dissociative gas response vanishes and gives way to the widely known “combustive gas response mechanism”.

Heating hydrogen-terminated diamond (HD) specimens beyond the evaporation temperature of the surface electrolyte layer causes both the p-type conductivity in the diamond and the gas response to vanish. Both effects are related to the fact that HD does not support a bulk but rather a surface conductivity that is induced by a transfer of valence electrons to the adsorbed water layer. Direct gas-surface interactions with an H-terminated semiconductor surface, therefore, cannot be studied on HD surfaces. HD can be used as an innovative gas sensor material making use of the phenomenon of dissociative room-temperature gas response. Its gas sensing properties can be improved by using the observed effects of temperature, UV light exposure, ozone “cleaning” by oxidation, and catalytic enhancement via OH surface groups.

Hydrogenated amorphous silicon (a-Si:H) exhibits both an H-terminated surface and a bulk conductivity that is unrelated to the H-termination itself. Heating a-Si:H through the water evaporation threshold, a novel type of gas response can be observed that is far more selective than the combustive gas response at MOX surfaces. It is called “coordinative gas response mechanism”. Under heat-dried

conditions, a predominant response to nitrogen-bearing gases can be observed at a-Si:H surfaces. It involves both the surface bound H atoms of the a-Si:H films as well as the lone-pair electrons (NH₃) or three-centre bonds (NO₂) of nitrogen-containing analyte gas molecules.

References

- [1] W. Göpel and K. D. Schierbaum, "SnO₂ sensors: current status and future trends," *Sensors and Actuators B*, vol. 26, no. 1–3, pp. 1–12, 1995.
- [2] D. E. Williams, "Conduction and gas response of semiconductor gas sensors," in *Solid State Gas Sensors*, pp. 71–123, Adam Hilger, Bristol, UK, 1987.
- [3] K. Ihokura and J. Watson, *The Stannic Oxide Gas Sensor: Principles and Applications*, CRC Press, Boca Raton, Fla, USA, 1994.
- [4] S. R. Morrison, "Chemical sensors," *Semiconductor Sensors*, John Wiley & Sons, New York, NY, USA, 1994.
- [5] H. V. Shurmer, J. W. Gardner, and H. T. Chan, "The application of discrimination technique to alcohols and tobaccos using tin-oxide sensors," *Sensors and Actuators*, vol. 18, no. 3–4, pp. 361–371, 1989.
- [6] J. W. Gardner and P. N. Bartlett, "Electronic noses: principles and applications," *Measurement Science and Technology*, vol. 11, no. 7, p. 1087, 2000.
- [7] R. Menzel and J. Goschnick, "Gradient gas sensor microarrays for on-line process control—a new dynamic classification model for fast and reliable air quality assessment," *Sensors and Actuators B*, vol. 68, no. 1, pp. 115–122, 2000.
- [8] S. Ahlers, G. Müller, and Th. Doll, "Factors influencing the gas sensitivity of metal oxide materials," in *Encyclopedia of Sensors*, C. A. Grimes, E. C. Dickey, and M. V. Pisko, Eds., vol. 3, pp. 413–447, The Pennsylvania State University, University Park, Pa, USA, 2006.
- [9] <http://www.umweltsensortechnik.de>.
- [10] J. Spannhake, A. Helwig, O. Schulz, and G. Müller, "Micro-fabrication of gas sensors," in *Solid State Gas Sensing*, E. Comini, G. Faglia, and G. Sberveglieri, Eds., pp. 1–46, Springer Science, Business Media, LLC, Berlin, Germany, 2009.
- [11] G. Müller, A. Friedberger, P. Kreisl, S. Ahlers, O. Schulz, and T. Becker, "A MEMS toolkit for metal-oxide-based gas sensing systems," *Thin Solid Films*, vol. 436, no. 1, pp. 34–45, 2003.
- [12] G. Sberveglieri, W. Hellmich, and G. Müller, "Silicon hotplates for metal oxide gas sensor elements," *Microsystem Technologies*, vol. 3, no. 4, pp. 183–190, 1997.
- [13] A. Friedberger, P. Kreisl, E. Rose, et al., "Micromechanical fabrication of robust low-power metal oxide gas sensors," *Sensors and Actuators B*, vol. 93, no. 1–3, pp. 345–349, 2003.
- [14] J. Spannhake, O. Schulz, A. Helwig, A. Krenkow, G. Müller, and T. Doll, "High-temperature MEMS heater platforms: long-term performance of metal and semiconductor heater materials," *Sensors*, vol. 6, no. 4, pp. 405–419, 2006.
- [15] E. Comini, G. Faglia, G. Sberveglieri, Z. Pan, and Z. L. Wang, "Stable and highly sensitive gas sensors based on semiconducting oxide nanobelts," *Applied Physics Letters*, vol. 81, no. 10, p. 1869, 2002.
- [16] E. Comini, "Metal oxide nano-crystals for gas sensing," *Analytica Chimica Acta*, vol. 568, no. 1–2, pp. 28–40, 2006.
- [17] M. Epifani, L. Francioso, P. Siciliano, et al., "SnO₂ thin films from metalorganic precursors: synthesis, characterization, microelectronic processing and gas-sensing properties," *Sensors and Actuators B*, vol. 124, no. 1, pp. 217–226, 2007.
- [18] M. Epifani, A. Helwig, J. Arbiol, et al., "TiO₂ thin films from titanium butoxide: synthesis, Pt addition, structural stability, microelectronic processing and gas-sensing properties," *Sensors and Actuators B*, vol. 130, no. 2, pp. 599–608, 2008.
- [19] F. Hernandez-Ramirez, J. D. Prades, A. Tarancon, et al., "Portable microsensors based on individual SnO₂ nanowires," *Nanotechnology*, vol. 18, no. 49, Article ID 495501, 5 pages, 2007.
- [20] J. D. Prades, R. Jimenez-Diaz, F. Hernandez-Ramirez, et al., "Ultralow power consumption gas sensors based on self-heated individual nanowires," *Applied Physics Letters*, vol. 93, no. 12, Article ID 123110, 3 pages, 2008.
- [21] J. Zhao, L.-H. Huo, S. Gao, H. Zhao, and J.-G. Zhao, "Alcohols and acetone sensing properties of SnO₂ thin films deposited by dip coating," *Sensors and Actuators B*, vol. 115, no. 1, pp. 460–464, 2006.
- [22] H. C. Wang, Y. Li, and M. J. Yang, "Fast response thin film SnO₂ gas sensors operating at room temperature," *Sensors and Actuators B*, vol. 119, no. 2, pp. 380–383, 2006.
- [23] K. Anothainart, M. Burgmair, A. Karthigeyan, M. Zimmer, and I. Eisele, "Light enhanced NO₂ gas sensing with tin oxide at room temperature: conductance and work function measurements," *Sensors and Actuators B*, vol. 93, no. 1–3, pp. 580–584, 2003.
- [24] B.-Y. Wei, M.-C. Hsu, P.-G. Su, H.-M. Lin, R.-J. Wu, and H.-J. Lai, "A novel SnO₂ gas sensor doped with carbon nanotubes operating at room temperature," *Sensors and Actuators B*, vol. 101, no. 1–2, pp. 81–89, 2004.
- [25] C. Baratto, E. Comini, G. Faglia, G. Sberveglieri, M. Zha, and A. Zappettini, "Metal oxide nanocrystals for gas sensing," *Sensors and Actuators B*, vol. 109, no. 1, pp. 2–6, 2005.
- [26] M. Sucheai, N. Katsarakis, S. Christoulakis, S. Nikolopoulou, and G. Kiriakidis, "Low temperature indium oxide gas sensors," *Sensors and Actuators B*, vol. 118, no. 1–2, pp. 135–141, 2006.
- [27] E. Comini, A. Cristalli, G. Faglia, and G. Sberveglieri, "Light enhanced gas sensing properties of indium oxide and tin dioxide sensors," *Sensors and Actuators B*, vol. 65, no. 1, pp. 260–263, 2000.
- [28] E. Comini, G. Faglia, and G. Sberveglieri, "UV light activation of tin oxide thin films for NO₂ sensing at low temperatures," *Sensors and Actuators B*, vol. 78, no. 1–3, pp. 73–77, 2001.
- [29] T.-Y. Yang, H.-M. Lin, B.-Y. Wie, C.-Y. Wu, and C.-K. Lin, "UV enhancement of the gas sensing properties of nano-TiO₂," *Reviews on Advanced Materials Science*, vol. 4, no. 1, pp. 48–54, 2003.
- [30] S. Mishra, C. Ghanshyam, N. Ram, R. P. Bajpai, and R. K. Bedi, "Detection mechanism of metal oxide gas sensor under UV radiation," *Sensors and Actuators B*, vol. 97, no. 2–3, pp. 387–390, 2004.
- [31] T. Fu, "Sensing properties and mechanism of gas sensor for H₂S and NO₂ based on [Cu₅(bipyO₂)₆Cl₈]Cl₂," *Sensors and Actuators B*, vol. 123, no. 2, pp. 1113–1119, 2007.
- [32] A. Helwig, G. Müller, M. Eickhoff, and G. Sberveglieri, "Dissociative gas sensing at metal oxide surfaces," *IEEE Sensors Journal*, vol. 7, no. 12, pp. 1675–1679, 2007.
- [33] A. Helwig, G. Müller, O. Weidemann, A. Härtl, J. A. Garrido, and M. Eickhoff, "Gas sensing interactions at hydrogenated diamond surfaces," *IEEE Sensors Journal*, vol. 7, no. 9, pp. 1349–1353, 2007.
- [34] A. Helwig, G. Müller, J. A. Garrido, and M. Eickhoff, "Gas sensing properties of hydrogen-terminated diamond," *Sensors and Actuators B*, vol. 133, no. 1, pp. 156–165, 2008.

- [35] A. Helwig, G. Müller, G. Sberveglieri, and G. Faglia, "Gas sensing properties of hydrogenated amorphous silicon films," *IEEE Journal of Sensors*, vol. 7, no. 11, pp. 1506–1512, 2007.
- [36] F. Maier, M. Riedel, B. Mantel, J. Ristein, and L. Ley, "Origin of surface conductivity in diamond," *Physical Review Letters*, vol. 85, no. 16, pp. 3472–3475, 2000.
- [37] J. Ristein, M. Riedel, and L. Ley, "Electrochemical surface transfer doping the mechanism behind the surface conductivity of hydrogen-terminated diamond," *Journal of the Electrochemical Society*, vol. 151, no. 10, pp. E315–E321, 2004.
- [38] S. Ahlers, G. Müller, and T. Doll, "A rate equation approach to the gas sensitivity of thin film metal oxide materials," *Sensors and Actuators B*, vol. 107, no. 2, pp. 587–599, 2005.
- [39] G. Sberveglieri, "Recent developments in semiconducting thin-film gas sensors," *Sensors and Actuators B*, vol. 23, no. 2-3, pp. 103–109, 1995.
- [40] D. E. Yates, S. Levine, and T. W. Healy, "Site-binding model of the electrical double layer at the oxide/water interface," *Journal of the Chemical Society, Faraday Transactions 1*, vol. 70, pp. 1807–1818, 1974.
- [41] S. Brunauer, P. H. Emmett, and E. Teller, "Adsorption of gases in multimolecular layers," *Journal of the American Chemical Society*, vol. 60, no. 2, pp. 309–319, 1938.
- [42] H.-D. Dörfler, *Grenzflächen und kolloid-Disperse Systeme: Physik und Chemie*, Springer, Berlin, Germany, 2002.
- [43] I. Langmuir, "The constitution and fundamental properties of solids and liquids—part I: solids," *Journal of the American Chemical Society*, vol. 38, no. 11, pp. 2221–2295, 1916.
- [44] S. Qi, K. J. Hay, M. J. Rood, and M. P. Cal, "Equilibrium and heat of adsorption for water vapor and activated carbon," *Journal of Environmental Engineering*, vol. 126, no. 3, pp. 267–271, 2000.
- [45] F. Kohlrausch, *Praktische Physik 3, Tabellen und Diagramme*, W. G. Alberts ed., B. G. Teubner, Stuttgart, Germany, 23 edition, 1986.
- [46] M. I. Landstrass and K. V. Ravi, "Hydrogen passivation of electrically active defects in diamond," *Applied Physics Letters*, vol. 55, no. 14, pp. 1391–1393, 1989.
- [47] T. Maki, S. Shikama, M. Komori, Y. Sakaguchi, K. Sakuta, and T. Kobayashi, "Hydrogenating effect of single-crystal diamond surface," *Japanese Journal of Applied Physics*, vol. 31, no. 10A, pp. 1446–1449, 1992.
- [48] A. Hokazono and H. Kawarada, "Enhancement/depletion surface channel field effect transistors of diamond and their logic circuits," *Japanese Journal of Applied Physics*, vol. 36, no. 12A, pp. 7133–7139, 1997.
- [49] K. Hayashi, S. Yamanaka, H. Okushi, and K. Kajimura, "Study of the effect of hydrogen on transport properties in chemical vapor deposited diamond films by Hall measurements," *Applied Physics Letters*, vol. 68, no. 3, pp. 376–378, 1996.
- [50] J. A. Garrido, A. Härtl, S. Kuch, M. Stutzmann, O. A. Williams, and R. B. Jackmann, "pH sensors based on hydrogenated diamond surfaces," *Applied Physics Letters*, vol. 86, no. 7, Article ID 073504, 3 pages, 2005.
- [51] J. Kanicki, *Amorphous and Microcrystalline Semiconductor Devices*, Artech House, Boston, Mass, USA, 1992.
- [52] J. Pankove, Ed., *Semiconductors and Semimetals*, vol. 21D, Academic Press, New York, NY, USA, 1984.
- [53] W. Luft and Y. S. Tsuo, *Hydrogenated Amorphous Silicon Alloy Deposition Processes*, Marcel Dekker, New York, NY, USA, 1993.
- [54] F. J. Kampas and R. W. Griffith, "Hydrogen elimination during the glow-discharge deposition of a-Si:H alloys," *Applied Physics Letters*, vol. 39, no. 5, pp. 407–409, 1981.
- [55] M. Tanielian, H. Fritzsche, C. C. Tsai, and E. Symbalysty, "Effect of adsorbed gases on the conductance of amorphous films of semiconducting silicon-hydrogen alloys," *Applied Physics Letters*, vol. 33, no. 4, pp. 353–356, 1978.
- [56] M. Tanielian, M. Chatani, H. Fritzsche, V. Smid, and P. D. Persans, "Effect of adsorbates and insulating layers on the conductance of plasma deposited a-Si:H," *Journal of Non-Crystalline Solids*, vol. 35-36, no. 1, pp. 575–580, 1980.
- [57] M. Tanielian, "Adsorbate effects on the electrical conductance of a-Si:H," *Philosophical Magazine B*, vol. 45, no. 4, pp. 435–462, 1982.
- [58] J. B. Cui, J. Ristein, and L. Ley, "Dehydrogenation and the surface phase transition on diamond (111): kinetics and electronic structure," *Physical Review B*, vol. 59, no. 8, pp. 5847–5856, 1999.
- [59] A. Helwig, G. Müller, G. Sberveglieri, and G. Faglia, "Gas response times of nano-scale SnO₂ gas sensors as determined by the moving gas outlet technique," *Sensors and Actuators B*, vol. 126, no. 1, pp. 174–180, 2007.
- [60] H. Windischmann and P. Mark, "A model for the operation of a thin-film SnO_x conductance modulation carbon monoxide sensor," *Journal of the Electrochemical Society: Solid-State Science and Technology*, vol. 126, no. 4, pp. 627–633, 1979.
- [61] D. E. Williams, "Semiconducting oxides as gas-sensitive resistors," *Sensors and Actuators B*, vol. 57, no. 1–3, pp. 1–16, 1999.
- [62] N. Barsan and U. Weimar, "Conduction model of metal oxide gas sensors," *Journal of Electroceramics*, vol. 7, no. 3, pp. 143–167, 2001.
- [63] N. Barsan and U. Weimar, "Understanding the fundamental principles of metaloxide based gas sensors; the example of CO sensing with SnO₂ sensors in the presence of humidity," *Journal of Physics: Condensed Matter*, vol. 15, pp. R813–R839, 2003.
- [64] F. Maier, J. Ristein, and L. Ley, "Electron affinity of plasma-hydrogenated and chemically oxidized diamond (100) surfaces," *Physical Review B*, vol. 64, no. 16, Article ID 165411, 7 pages, 2001.
- [65] R. S. Gi, T. Mizumasa, Y. Akiba, Y. Hirose, T. Kurosu, and M. Iida, "Formation mechanism of p-type surface conductive layer on deposited diamond films," *Japanese Journal of Applied Physics*, vol. 34, no. 10, pp. 5550–5555, 1995.
- [66] J. A. Garrido, A. Härtl, M. Dankerl, et al., "The surface conductivity at the diamond/aqueous electrolyte interface," *Journal of the American Chemical Society*, vol. 130, no. 12, pp. 4177–4181, 2008.
- [67] M. Dankerl, A. Reitingner, M. Stutzmann, and J. A. Garrido, "Resolving the controversy on the pH sensitivity of diamond surfaces," *Physica Status Solidi. Rapid Research Letters*, vol. 2, no. 1, pp. 31–33, 2008.

Review Article

Quartz Crystal Microbalance as a Sensor to Characterize Macromolecular Assembly Dynamics

K. Kanazawa¹ and Nam-Joon Cho²

¹Department of Chemical Engineering, Stanford University, Stanford, CA 94305, USA

²Division of Gastroenterology, School of Medicine, Stanford University, Stanford, CA 94305, USA

Correspondence should be addressed to K. Kanazawa, procmon@msn.com

Received 22 December 2008; Accepted 10 April 2009

Recommended by Michele Penza

The quartz crystal microbalance sensor has a resonant frequency f and a quality factor Q which can be used to probe the properties of nanometer thick film loads. A recent review by Arnau (2008) has discussed many of the considerations necessary to accurately probe for these properties. To avoid needless duplication but to still provide an adequate background for the new user, we briefly outline the basic measurement methodologies and analytical techniques that were covered in the review. Details will be provided on some specific perspectives of the authors. For example, the special precautions necessary when dealing with soft films (polymeric and biological) under liquid are overviewed. To illustrate applications of the QCM technique, simple bilayer and vesicle behaviors are discussed, along with the structural transformation resulting from protein adsorption onto an intact vesicle adlayer. The amphipathic α -helical (AH) peptide interaction is given as a particular example. Lastly, we summarize a top-down approach to functionalize a surface with a cell membrane and to study its interaction with proteins.

Copyright © 2009 K. Kanazawa and N.-J. Cho. This is an open access article distributed under the Creative Commons Attribution License, which permits unrestricted use, distribution, and reproduction in any medium, provided the original work is properly cited.

1. Introduction

The transducer for the quartz crystal microbalance (QCM) sensor is often in the form of a piezoelectric circular disk. Many aspects of piezoelectric films used as sensors are discussed in some detail in a recent book [1]. The general form of the common AT-cut quartz resonator is illustrated below in Figure 1.

There are two electrodes on the crystal's opposing faces. Upon an excitation (mechanical or electrical), thickness shear acoustic waves can undergo constructive interference such that resonances occur at particular frequencies. These are discussed in the classical book by Lu and Czanderna [2], an excellent review article related to the QCM in electrochemistry by Buttry and Ward [3], and in an oft-quoted text by Bottom [4]. Two modes of operation are possible. The resonances can be observed either under steady-state conditions (such as under a steady applied radio frequency potential) or under transient conditions (such as a decay following an initial excitation). For both cases, it has been established that a very accurate equivalent circuit

describing the electrical behavior in the neighborhood of a resonance is given by the Butterworth Van Dyke (BVD) circuit as shown in Figure 2 and described by Cernosek et al. [5], and Muramatsu et al. [6].

The utility of the BVD circuit lies in the fact that the behavior of the resonator is generally probed using electrical signals. The physical behavior of the QCM is summarized in the elements of the BVD circuit. There are four elements. The branch on the left consists of a single element, the parallel capacitance C_P , which is simply the dielectric capacitance of the disc and can also reflect any external capacitances that occur when connecting the QCM to instrumentation. It does not reflect the motion of the disc and is a constant. The branch on the right is the so-called motional branch and consists of three components: the inductance L , a series capacitance C_S , and a series resistance R , which reflects the mechanical losses in the resonant system. These elements are sensitive to the disc's motion. The changes in these elements under loading of the quartz crystal by a liquid and/or a film are sensitive to the properties of the load. The series resonant frequency f_0 of L and C_S defines the resonant frequency and

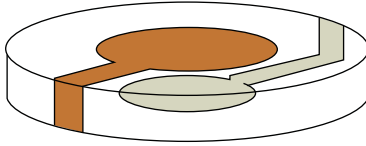


FIGURE 1: A piezoelectric disc forming the resonant transducer for the QCM.

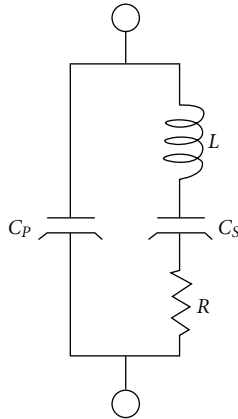


FIGURE 2: The butterworth van dyke electrical equivalent circuit near a resonance.

R characterizes the losses. Both of these are sensitive to the load properties as examined by Martin et al. [7], and Bandey et al. [8].

2. Measurement Methods

As mentioned earlier, it is possible to use both steady-state and transient methods to experimentally characterize the loaded resonator. We begin by discussing the steady-state methods: the oscillator system and the impedance analysis system.

The oscillator is an electronic amplifying circuit in which the transducer serves as an active element through which positive feedback is applied such that the system oscillates. When the parallel capacitance C_p can be neglected, and where the amplifier is nearly ideal, the circuit will oscillate at the zero-phase resonant frequency defined by the series resonance of L and C_s . But as illustrated in Figure 2, we see that C_p introduces an additional phase shift which can change the resonant frequency from its ideal value. A number of methods to correct for C_p have been previously discussed in detail [9]. The user needs only to recognize that this correction is necessary and to ensure that precautions are taken to remove the effect of C_p in their instrumentation. From the oscillator circuit, both the resonant frequency and the load loss are measured. This load loss can be related to the amount of feedback necessary to maintain oscillation or from the value of the current at resonance.

It is possible to excite the resonator not only at its fundamental frequency but at its odd harmonics [10]. The work, to be discussed later in this section, has shown that

the study of the harmonics can add valuable additional information about the film's properties. A particularly fine example of this work was recently done by Vogt et al. [11]. One of the primary values is to characterize the change in the resonant frequency under film load with the harmonic variation. If the resonant frequency change due to the film load is proportional to the harmonic number (1, 3, 5, 7, 9, etc.), this can be taken as some evidence that the film can be treated as a rigid film. This infers the applicability of the Sauerbrey relation [12] where the resonant frequency at a given resonance decreases linearly with increasing mass load. This simplification can be very useful in many cases as has been discussed, for example, by Rodahl et al. [13], and by Voinova et al. [14]. If this relation is not satisfied, it indicates that a more complex analysis of the mass loading and the viscous loss effects of the load must be considered.

In general, the oscillator circuits to date have not had the capability of measuring at multiple harmonic frequencies, although switching networks have been utilized to make this possible recently. Recently, a dual harmonic oscillator (DHO), which operates at the fundamental and the third harmonic has been developed [15] which was inspired by the studies showing such a possibility [16]. In the DHO, the crystal with its load is excited simultaneously at two harmonic frequencies, for example, the first and the third. The distorting influence of C_p has been removed, and both resonant frequencies and resistances at the two harmonic frequencies are measured. This simultaneous measurement of the same crystal (and therefore under identical conditions) is unique.

The second major steady-state method is that of impedance analysis. In this case, an rf voltage is applied across the crystal and is scanned over the region of the resonance of interest. Such methods are discussed, for example, by Kipling and Thompson [17], and by Lucklum et al. [18]. The QCM serves as a passive device under test. The ratio of the voltage to the current yields the electrical impedance of the device. Most applications of this scanning technique use the electrical admittance instead of the impedance. The admittance is simply the inverse of the impedance. The measurements taken are both the magnitude and phase of the admittance at each frequency or the real and imaginary parts of the admittance (the conductance and the susceptance). The use of the Butterworth Van Dyke circuit shown in Figure 2 is extremely useful in fitting the measurements. Typical conductance versus frequency and susceptance versus frequency curves are depicted in Figure 3. These curves were calculated using a one-dimensional model for lightly loaded resonator, and yield the conductance and susceptance in Siemens m^{-2} .

The conductance is a maximum, G_{max} , at the resonant frequency; the value of G_{max} yields the inverse of the resistance R . From B_{max} and B_{min} , the value of C_p can be determined.

The methodologies for obtaining these values are discussed in [17, 18]. As is so often the case, there are possible effects, which can distort the spectrum and result in inaccurate fittings. Two of the main sources of these effects are discussed in an article in this issue [19]. We can determine C_p from the

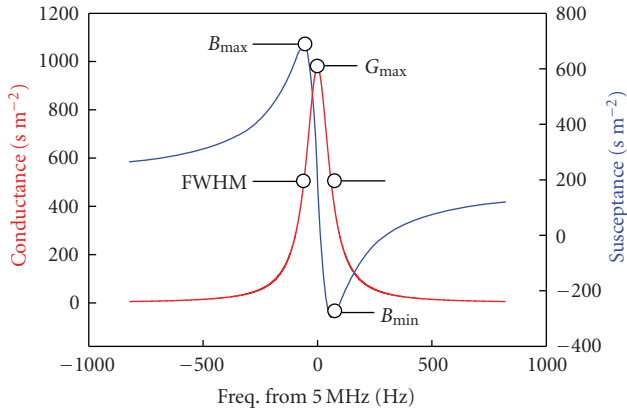


FIGURE 3: The conductance (red) and the susceptance (blue) versus the frequency from resonance are shown. Also, key points used for analysis are indicated.

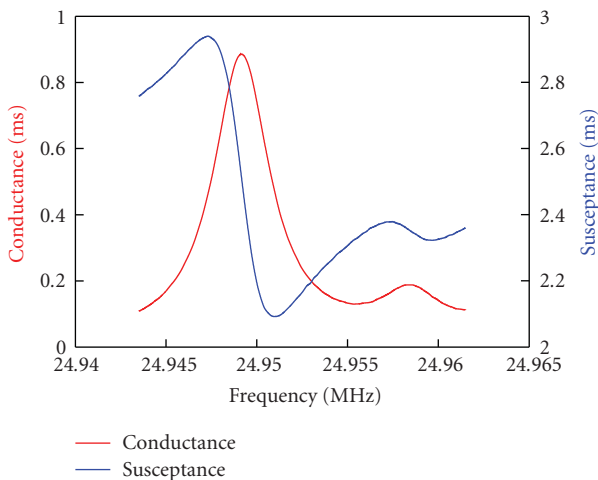


FIGURE 4: A spurious resonance (Spur) is shown lying above the main resonance of the 5th harmonic of a 5 MHz crystal. This is experimental data on a crystal in water with an area of $3.419 \times 10^{-5} \text{ m}^{-2}$. The conductance and susceptance are in milliSiemens.

spectrum above. In addition to the contribution of a shunt cabling to C_p , a shunt conductance can also be introduced via external cabling. This can be recognized and corrected. The effects of these shunting elements can be corrected for through the measurements. Finally, spurious resonances (spur) that lying a few kilohertz above the resonance can be excited and can distort the spectrum. We have also shown that this effect can be eliminated by specifically and quantitatively accounting for its effects. An example of the presence of a spur resonance is shown in Figure 4 as revealed by experimental data.

The main resonance is seen to occur at about 24.95 MHz but a spur is seen near 24.959 MHz. Its spectrum overlaps the main resonance spectrum, distorting it. This overlap can be removed by accounting for the spur using a separate resonance. The main resonance is then described accurately by a Lorentzian. From the fitting of the main resonance to the Lorentzian curve described by the Butterworth Van Dyke

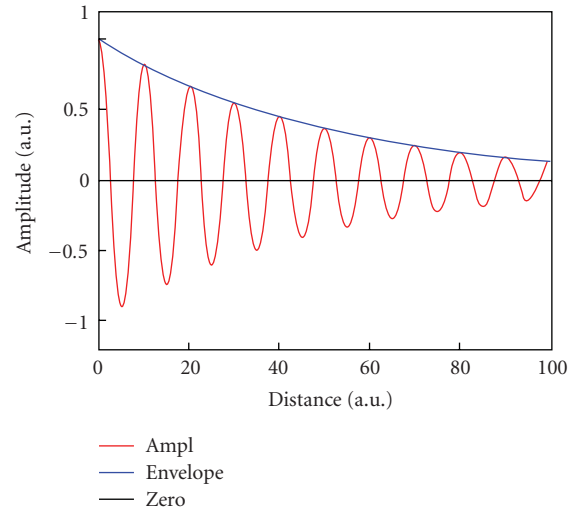


FIGURE 5: The current decay after excitation is suggested by the red curve.

circuit, the values of the elements of the circuit (L , C_s , R , and C_p) can be determined.

A very different approach was taken at Chalmers Institute of Technology where they used transient decay of a crystal to determine the properties of the loading film and liquid [20]. In a subsequent work, they focused on the transient current decay resulting from a short circuit analysis [13]. The frequency of the applied voltage is varied until reaching the frequency where the largest current is observed. The crystal is then shorted, leaving the current to decay. The cartoon in Figure 5 suggests the transient behavior of the current with time.

The red curve indicates the current decay after initial excitation. The period of the resonant frequency is given by the spacing between the peaks or by the alternate zero crossing of the current. The quality of the resonance is given by the decay time of the envelope, shown in the blue. The horizontal black line is the zero line shown for reference. The resonant frequency and the quality (Q) factor, or its inverse the dissipation D , can be measured for the resonator.

If the QCM is loaded with a lossy layer, then the envelope will decay more rapidly. The quality of the resonance can be related to the decay time. The details on how the films properties can be obtained from the resonant frequency and Q are given in [13]. In a commercialized system, it has been possible to collect data from a number of the odd resonances (1, 3, 5, and 7) and also (1, 3, 5, 7, 9, and 11).

3. Analytical Methods

In order to relate the changes in the behavior of the resonance to the properties of the load, it is necessary to employ a quantitative model. A number of these exist, and most of them are based on a one-dimensional analysis of the resonator and load as will be discussed in a later section. The model assumes a disc of infinite lateral extent, with the only dimensional variable being along the direction perpendicular

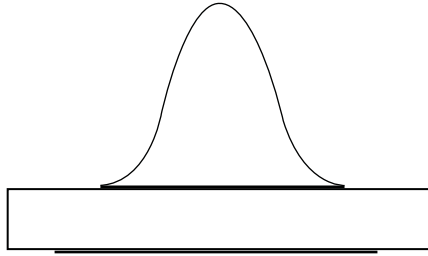


FIGURE 6: The distribution of the displacement amplitude is shown. The quartz and the electrodes are represented the rectangle and the dark lines, respectively.

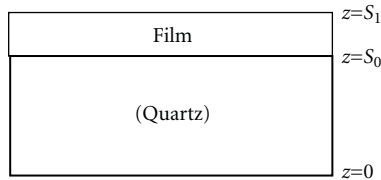


FIGURE 7: Mechanical representation of the quartz resonator loaded with a film.

to the disc. The actual behavior of the resonator is not one-dimensional however, but methods have been used to minimize this effect. This is briefly summarized in Figure 6.

The displacement of the device is not uniform over the surface [21, 22] and has a maximum at the center and decreases towards the electrode edges. In fact, this effect can be used for specific purposes such as rupture event scanning [23] or for binding perturbations studies [24]. For general cases, the one-dimensional models have been found to be quite adequate for the determination of load properties. The radial sensitivity function is mentioned here only to acquaint the user of that behavior. Its effect will be ignored in this presentation.

There are a large number of methods for analyzing the measurements such that the properties of the load on the QCM can be extracted. A number of different approaches have been taken. They include the purely mechanistic treatment where the acoustic resonances with the load in a purely mechanical manner, description in terms of mechanical-electrical analogs using the Butterworth Van Dyke circuit, transmission line analogs for the sensor, and a variety of simplifications based on linearizing the results from the more complex solutions. A full electromechanical analysis has been presented, which will be discussed in more detail at the end of the paper.

The initial analyses treated the acoustomechanical resonances of the slab of quartz. This view of the resonator can be summarized as in Figure 7.

Early studies treated the quartz and film as lossless. A steady-state sinusoidal acoustic shear vibration at a frequency f was assumed. The frequency f is a real quantity. Sauerbrey had in mind such a model when for thin elastic films he understood that the film mass could then be approximated as an additional quartz mass. This resulted in

a linear relation between the decrease in resonant frequency and the mass loading of the film with a proportionality constant dependent only on the quartz parameters. This has been of extreme value in the measurement of vapor deposited films in vacuum.

The linear behavior was valid for approximately 2% or less change in frequency. The range of quantitative relation between the resonant frequency and the mass loading can be extended in range if one accounts for the acoustic impedance of the film, which can be expressed in terms of the film density ρ and shear modulus μ

$$Z = \sqrt{\rho\mu}. \quad (1)$$

The multiple reflections at the surfaces at $S = 0$, $S = S_0$, and $S = S_1$ were summed and conditions for resonance determined [25]. This was put into a clean usable form by Lu and Lewis [26] and has proved very useful in extending the range of use of the QCM in a quantitative manner, although the simple linear functionality was lost. The curvature of the frequency-mass relation that was dependent on the material's property. However, the analysis was still restricted to lossless films.

Nomura and Minemura found that it was possible to use the QCM under liquid [27]. The liquid is viscous and introduces a loss into the system. In Figure 7, the liquid can be represented as an additional infinitely thick layer above the film. The relation between the frequency change and the liquid was found to be able to be described by the real part of a complex frequency as demonstrated in [28]. A complex frequency was necessary because of the existence of losses which precluded a steady-state solution under purely mechanical excitation. That is, a general time dependence of the type $e^{j\omega t}$ is assumed. If the angular frequency ω is complex, it can be seen that the real part gives a cycling sinusoid, while the imaginary part yields a time-decaying envelope. The general method used to solve for the resonance of such a layered system is to assign amplitude magnitudes to the acoustic waves traveling in the $+z$ direction and in the $-z$ direction. These acoustic waves are then required to satisfy the boundary conditions at the interfaces.

Prodded by the observation by Behling et al. [29], that the equations satisfying these boundary conditions can be separated into separate terms involving the mass and the viscoelastic properties of the load, it has been possible to obtain solutions using the complex frequency notion with the purely mechanical open circuit analysis to separate the mass loading from the viscoelastic parameters of the load. The separation into a mass dependent expression and a viscoelastic dependent expression permits some very useful simplifications under certain conditions. This description is not discussed further here, but is presently under preparation.

A variant of the mechanical model was used by the Chalmers group [30] to quantify the relation between the resonant frequency and the mass loading and viscoelasticity. They concentrated on the load, treating the quartz as a rigid body, as suggested in Figure 8.

By including the possibility of a steady-state external excitation such as by an externally applied voltage from a

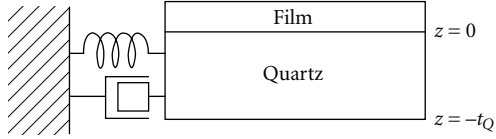


FIGURE 8: The configuration used where the quartz, shown by the open bottom rectangle, is treated as rigid and the effects of the load above it are summarized as changes in the spring constant and dashpot to the left of the quartz. Recall that the QCM under investigation is shorted. Therefore, the shunting impedances are shorted out and can be neglected.

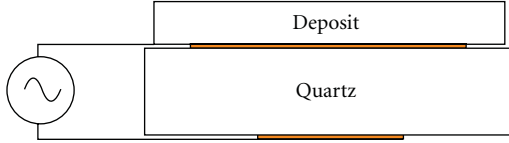


FIGURE 9: Electrodes at the bottom of the quartz and at the quartz-film interface allow the application of an rf voltage.

voltage source as suggested in Figure 9, it is possible to move to a complete solution under those conditions.

This ability to apply an external steady-state voltage made possible a number of different ways to analyze the resonator with a load. Again however, the acoustic waves in each media are assigned amplitudes and the boundary conditions at the interfaces need to be satisfied. In fact, if the model is analyzed using the physical parameters including the piezoelectric properties of the quartz, then it is possible to show that the electrical impedance can be represented by a transmission line equivalent circuit as shown in Figure 10 [31]. This equivalent circuit has been particularly useful to show further simplifications following simplifications. It is not possible to do a complete description of the transmission line approach here. It is hoped however, to show that the specific piezoelectric and dielectric properties of the quartz crystal are specifically taken into account in this analysis. More detailed treatments are to be found in [5, 18, 31]. The influences of the quartz piezoelectric constant and dielectric constant are shown in the specific elements representing the piezoelectric driving circuitry in the transmission line. A voltage driving source applies a voltage V to the circuit. The coupling to the quartz is represented by three elements, a capacitance C_0 , a reactive element jX , and a transformer with the turns ratio of $1 : N$:

$$C_0 = \frac{\epsilon_{22}A}{d_Q}, \quad (2a)$$

$$X = \frac{e_{26}^2}{\epsilon_{22}^2 \omega^2 Z_Q A} \sin(k_Q d_Q), \quad (2b)$$

$$N = \frac{\sqrt{A}}{(2e_{26}/\epsilon_{22} \omega Z_Q) \sin(d_Q/2)}. \quad (2c)$$

The variable A here is the effective area of the resonator, usually being the area of the smaller electrode. d_Q is the

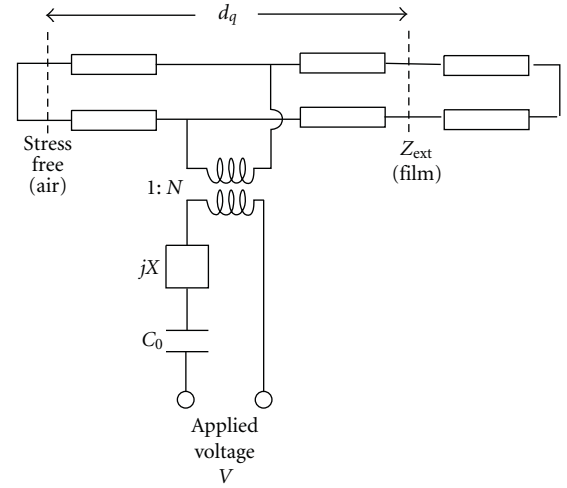


FIGURE 10: The representation of the transmission line equivalent circuit which serves as starting point for many useful simplifications. It includes the electric and piezoelectric properties of the quartz.

thickness of the resonator being about 3.3×10^{-4} m. ϵ_{22} is the dielectric constant of the quartz having the value of 3.982×10^{-11} fd/m. ω is the angular frequency. Z_Q is the acoustic impedance of the quartz which for loss less quartz is given by

$$Z_Q = \sqrt{\rho_Q \bar{c}_{66}}, \quad (2d)$$

where

$$\bar{c}_{66} = c_{66} + \frac{e_{26}^2}{\epsilon_{22}}. \quad (2e)$$

Here c_{66} is the appropriate mechanical shear modulus having the value of 2.901×10^{10} Pascals, e_{26} is the piezocoefficient having the value of -0.095 Coulombs m^{-2} . r_Q is of course the quartz density in $kgm m^{-3}$. k_Q is the propagation constant for the shear waves in the quartz and is given by the relation

$$k_Q = \omega \sqrt{\frac{\rho_Q}{\bar{c}_{66}}}. \quad (2f)$$

The section shown between the dashed lines represents the quartz and the right and left connections represent the interfaces of the quartz. We have portrayed the case where the crystal is loaded only on one face. The left face is left free so that the stress applied to that interface is zero. The electrical equivalent is a short circuit, as shown. On the right is the acoustic load provided by a film. The external surface of the film is assumed to be unloaded and is represented again by a short circuit. The various rectangular elements represent an electrical equivalent of the acoustic delay paths, giving rise to phase shifts across the elements. The general quartz elements do not change with load. Further simplifications of the analysis can be made under conditions where the resonance has a high Q factor.

Of many simplifications, one of the most useful ones was proposed by the Sandia group [10]. They have shown that the

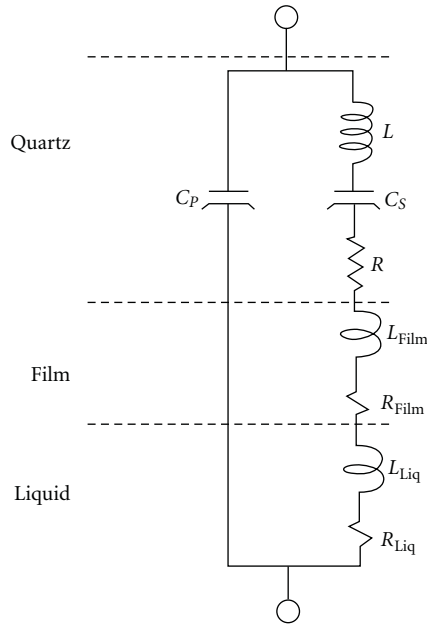


FIGURE 11: The Butterworth Van Dyke circuit can be modified, as shown, when the resonator is loaded with a film under a liquid.

transmission line can be reduced to a modified Butterworth Van Dyke circuit. Additional elements are added into the motional arm, as suggested in Figure 11. Here, the upper portion represents the unloaded quartz values. The portion below that represents the changes to the inductance and the resistance due to the mass loading of the film. Finally, the effects of the liquid are represented by the lower group of elements. For reasonably light film loadings, the film effects and the liquid effects can be treated as simple additive elements, as illustrated in Figure 11.

For the analysis of the transmission line model discussed above, the piezoelectric properties of the quartz were included. It is possible to take a complete solution for the resonator, including both the mechanical and electrical properties of the quartz as well as the loading of films and liquid without going to the transmission line equivalent. It is possible to solve for the behavior of the resonator under a variety of conditions. This approach is summarized in Figure 12 and described in [32].

At the top of the chart are indicated the parameters of the quartz, the film, and the liquid which are fed into a computational loop where the boundary conditions are satisfied. In order to satisfy these conditions, a quantity Q_4 is calculated in terms of some steady-state frequency f . Q_4 is defined as indicated by (3)

$$J = -j\omega\epsilon_{22}\frac{\Phi_0}{Q_4}. \quad (3)$$

The details for the calculation of Q_4 are given in the appendix. The constant Q_4 defines the relation between the current density J in amperes per sq meter and the voltage Φ_0 . From this relation, solutions under a variety of different conditions can be determined. It can be made specific to a

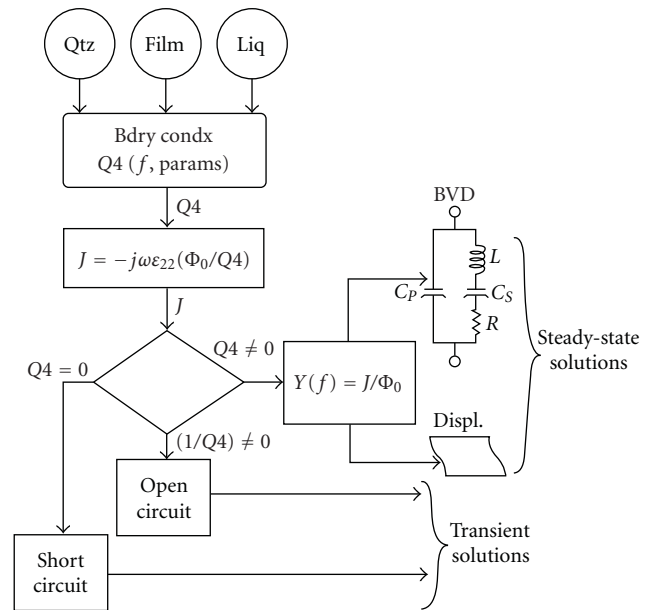


FIGURE 12: A flow diagram illustrating the complete electromechanical model.

crystal if desired by including a crystal area. In the case of the usual voltage source driven resonator, Φ_0 is a constant.

The utility of the Q_4 concept is that the solutions for a variety of experimental conditions can be obtained from this single quantity. One can obtain steady-state solutions under constant voltage or constant current conditions as well as transient solutions under open circuit or short circuit conditions, as explained further in the following.

Since the frequency variation of Q_4 is known, and then one can easily calculate the current density as a function of frequency under the condition of constant Φ_0 . The admittance as a function of frequency is then simply given by the ratio $J/(\Phi_0)$. On the other hand, if one wanted to calculate the admittance under conditions of constant current, then in a similar manner, Φ_0 can be calculated assuming a constant J . The admittance can be calculated again as the ratio of J to Φ_0 .

Both of these cases are steady-state solutions where Q_4 is nonzero. As suggested on the right hand side of the figure, one can use Q_4 to obtain the magnitudes of the acoustic displacements in the resonant structure as shown under "Displ" in the figure. Alternatively, one can calculate the admittance spectrum and fit it to Lorentzian BVD elements. These two possibilities are the outputs of the steady-state solutions.

In the case of the transient solutions, we first consider the short-circuit case. In that case, the applied voltage is zero. From (1), we can see that there is a trivial solution where J is zero. But there is another possibility of having a finite J with a zero applied voltage. This occurs when Q_4 is zero. To satisfy the conditions in this case, the frequency must be taken to be complex. And the real part yields the resonant frequency while the imaginary part yields the decay time, related to the dissipation. Similarly, we can consider the case where the

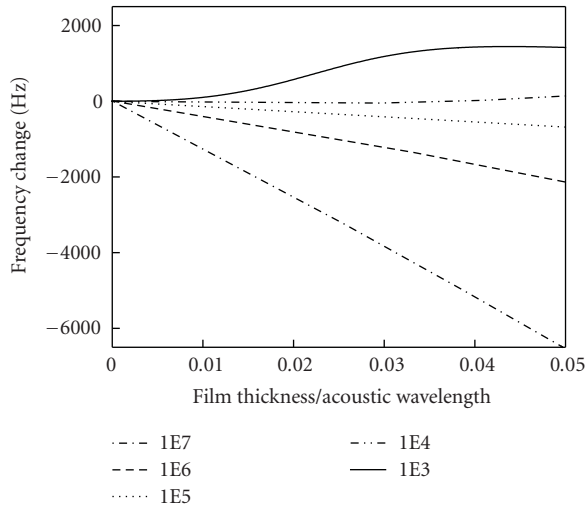


FIGURE 13: An example of the effect of the softness of a film under liquid on the frequency versus mass (thickness) relationship.

current is zero. Neglecting the trivial solution, we see that the voltage can be finite with a zero current if $1/Q_4$ is zero. Again the frequency is complex and has the same interpretations as in the case of the short circuit.

We see that this electromechanical treatment can yield the full set of steady-state and transient solutions.

4. Caveat

Recently the special behavior of the resonance under load for the case of a film under liquid, when the film is very soft, having shear moduli less than 1×10^3 Pa has been discussed [33]. It is mentioned here because the behavior is so counterintuitive that the user may feel that the experimental results should be discounted. The type of behavior that can be observed is that the frequency-mass relation is nonlinear, and is not proportional to the Sauerbrey relation even for the thinnest films. It is even possible that the frequency increases with load. This behavior has been traced to an induced resonance in the soft film caused by the need to satisfy the film-liquid boundary conditions. An example of this is given in Figure 13.

In this figure, we have plotted the acoustic thickness along the abscissa instead of the actual film thickness. This was done so that the comparisons among the films with varying shear moduli are clear. The acoustic thicknesses are dependent upon the parameters of the film and are here expressed as a fraction of the wavelength of the acoustic wave in the film. The point here is to show the variations in the frequency-thickness behavior. The case for the stiffest film (1×10^7 Pa) indicates Sauerbrey-type behavior. As the film softens with decreasing shear moduli, it is seen that slope of the curve decreases markedly and becomes almost flat for films of 1×10^4 Pa. At the softest film value shown here (1×10^3 Pa), the frequency can shift upward in a totally counterintuitive manner.

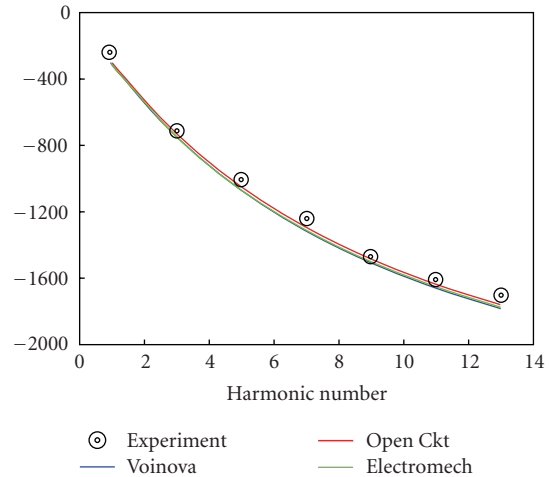


FIGURE 14: The behavior of the various models relative to the harmonic behavior of the resonances for a soft film of modulus 1.5×10^4 Pa is shown.

In order to compare the relative predictions of the various models, we plot in Figure 14 the results of the theoretical calculations using the three models: the Voigt-Voinova model, the open circuit model, and the full electromechanical treatment.

It is seen that the various models all yield virtually identical results. The models have been compared under other circumstances and they all yield virtually the same result. The user can use the model with which he is most comfortable with some assurance that it will yield results in agreement with other models.

To this point, we have tried to indicate the various QCM measurement methods and the various analytical methods. We have attempted to show the cautions which should be considered by the user. If considered, these cautions can lead to useful determinations of film properties with the QCM. In the remainder of this review, we shall highlight some of QCM applications related to biomimetic platforms and macromolecular interactions, primarily using the transient technique.

5. QCM-D as a Sensor Platform for Biomacromolecular Interaction Studies

With its ability to simultaneously detect mass and viscoelastic property changes, the quartz crystal microbalance with dissipation monitoring (QCM-D) is an ideal tool to study biological interactions [34–40]. Herein, we present four research topics that have had an impact in establishing QCM-D as a cutting-edge tool to study biomacromolecular interactions and provide a solid theoretical background to understand different modeling approaches. Lipid vesicles can interact with solid substrates in different ways depending on the surface properties [41]. First we introduce the fundamental sensor platform depending on surface-specific vesicle interactions. Then, we introduce an alpha helical

(AH) peptide derived from the hepatitis C virus (HCV), which interacts with an intact lipid vesicle platform to cause a structural transformation, resulting in a complete bilayer [35, 37]. We apply models to this system to examine how consideration of the adlayer's viscoelastic properties can improve data analysis [37]. In addition to these lipid-based platforms, other biological interactions such as protein adsorption can be studied with QCM-D [42]. We then illustrate the potential of the QCM-D technique in fundamental biological applications and compare it with more traditional biochemical assays by monitoring in situ AH peptide binding to lipid bilayers and cell membranes [34]. All of these studies have been conducted using crystals having a fundamental resonance frequency at 5 MHz.

5.1. Surface-Specific Vesicle Interactions. The early biomimetic systems focused on black lipid membranes [43], which were formed by painting a lipid bilayer across a gap in a solid surface. While many important studies came from this initial work, black lipid membranes' lack of robustness necessitated the development of improved systems. Characterization of black lipid membranes generally involves measuring the electrical resistance across the membrane by patch-clamping [44]. This characterization is nonspecific and many different lipid structures can indicate a strong electrical seal. Additionally, the lipid bilayer stability is very low because the structure is only supported at its edges and is essentially free-floating, making it more likely to rupture. Starting with Tamm and McConnell's work in 1985 [45, 46], solid-supported lipid bilayers (SLBs) became an alternative technique [47] with improved stability. The solid substrate to which the lipid bilayer is supported via hydrophilic interactions provides mechanical stability [41].

SLBs are a common model system to mimic biological membranes and are widely utilized as an experimental platform to study macromolecular interactions because their surface chemistry can be functionalized in a controlled fashion by changing the lipid composition or incorporating transmembrane proteins [47, 48]. These are only examples of the multitude of functionalization possibilities. A promising strategy is to use bottom-up processes driven by molecular self-assembly, principles such as the formation of SLBs from vesicle solutions as shown in Figure 15. There are several common methods that are available to researchers to make solid-supported lipid bilayers. The two most common techniques are vesicle fusion [47, 48] and the Langmuir-Blodgett (LB) or the Langmuir-Schaeffer (LS) transfer method [45]. After the pioneering work by Kasemo and coworkers [39, 41] using the quartz crystal microbalance-dissipation (QCM-D) technique to study vesicle interactions with solid surfaces, vesicle fusion became a very popular experimental technique to form SLBs due to the ability of QCM-D to characterize the entire process, including the quality of the formed bilayer in terms of viscoelasticity and acoustic mass. It was demonstrated that vesicles adsorb irreversibly on SiO₂, Si₃N₄, TiO₂, oxidized Pt, oxidized Au, and thiol-modified Au surfaces in a manner dependent on the surface's physical and chemical properties. Keller and

Kasemo [41] demonstrated for the first time that vesicles interact with different substrates to form three types of structures, namely, intact vesicle (Figures 15(b) and 15(d)), lipid bilayer (Figures 15(a) and 15(c)), and lipid monolayer, based on the surface properties.

The QCM-D technique provided new insight into the vesicle fusion process on silicon oxide to form SLBs by revealing a two-step mechanism as shown in Figure 15(c). For the first time, a constructed SLB could be characterized in terms of its viscoelastic and mass properties. In addition, a significant benefit over previous characterization techniques including atomic force microscopy (AFM) and fluorescence recovery after photobleaching (FRAP) is that the entire SLB formation process—specifically the vesicle fusion process—can be easily monitored. ΔF_{\max} indicates the critical vesicle concentration at which vesicle-vesicle and vesicle-surface interactions are optimized to induce vesicle rupture [39, 41]. Vesicle rupture creates bilayer islands with hydrophobic edges, which propagate further vesicle rupture until the lipid bilayer is complete and the edges are minimized. In terms of modeling, the SLBs thickness can be calculated by the Sauerbrey relationship [12] because the adsorbed layer is rigid as indicated by the relatively small dissipation changes shown in Figure 15(e). However, it should be noted that, at the critical vesicle concentration, the frequency and dissipation responses are overtone-dependent. Therefore, in order to better understand the structural transformation, it is necessary to use a viscoelastic model such as the Voigt-Voinova model [14], which extends the QCM solutions to include viscoelastic effects. These thickness calculations, presented in Figures 15(e) and 15(f) were consistent over the frequency overtones with a film having a frequency-independent viscosity.

Whereas the critical vesicle concentration of adsorbed vesicles necessary to induce vesicle rupture can be thought of as a partial coverage of the surface with intact vesicles, vesicle adsorption on other substrates such as TiO₂ and Au can form irreversible monolayers of intact vesicles, fully covering the surface as shown in Figures 15(d) and 15(f). Though these two systems are different in terms of surface coverage, the QCM-D frequency and dissipation responses are analytically similar. Both responses are overtone-dependent, necessitating the need for modeling that includes viscoelastic effects. In terms of forming an intact vesicle monolayer as a platform, there a number of parameters such as flow rate, vesicle size, and vesicle concentration that are critically important to platform reproducibility.

By using a viscoelastic model to calculate the adlayer thickness, it is possible to understand the degree of vesicle deformation. In Keller and Kasemo's work [41], they point out that adsorbed vesicles are no longer spherical but flatten out when adsorbed due to vesicle-surface and vesicle-vesicle interactions. They quantitatively analyzed this deformation process by calculating the theoretical frequency shift of an intact vesicle monolayer consisting of nondeformed vesicles (107 Hz) versus the experimental frequency shift (90 Hz) [41]. This work inspired researchers to revisit pathways to study vesicle fusion mechanisms and gave opportunities

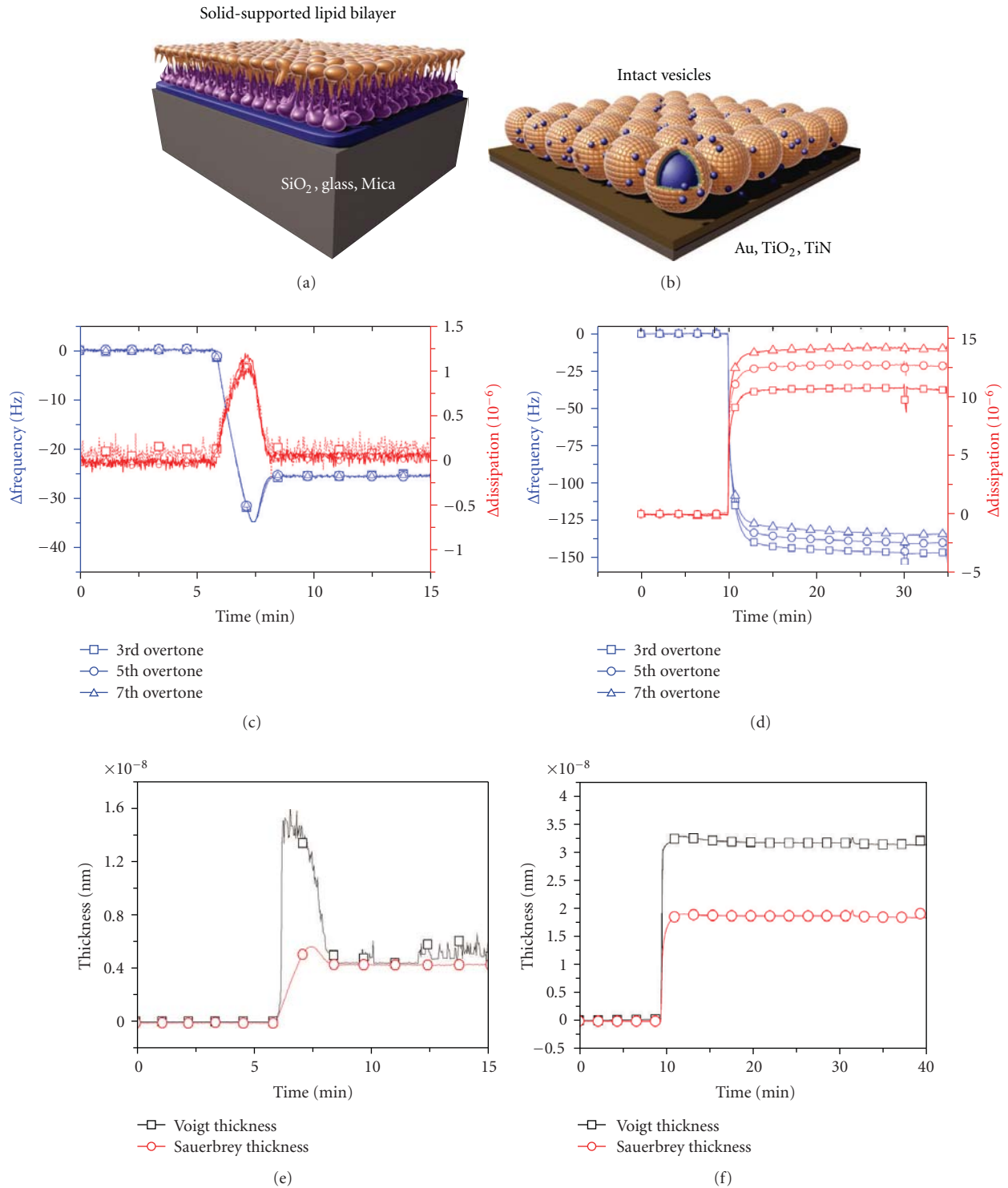


FIGURE 15: Surface specific vesicle adsorption kinetics on solid substrates. Illustration of (a) supported lipid bilayer on SiO₂ and (b) intact vesicles on gold. (c) The typical two-step kinetics of vesicle fusion from small unilamellar vesicles to form a bilayer on SiO₂. Note that the critical coverage occurred at 7.5 minutes. Three different overtones (3rd, 5th, and 7th) are also presented here for viscoelastic modeling. (d) The typical vesicle adsorption kinetics on a gold substrate are also presented. The huge mass uptake is caused by vesicle adsorption. Due to the viscoelastic nature of vesicles, the overtones do not merge. (e) Comparison of two different thickness calculation-based Sauerbrey and Voigt-based models to characterize the vesicle fusion process. Note the deviation at the critical coverage at 7.5 minutes due to the highly viscoelastic character of intact vesicles. (f) Comparison of two different thickness models by Sauerbrey and Voigt-based models for an adsorbed intact vesicle monolayer. Due to the viscoelastic nature of intact vesicles, the overtones do not merge. Since the adlayer's viscoelasticity causes high energy dissipation, the Sauerbrey model significantly underestimates the adlayer thickness compared with the Voigt-based model.

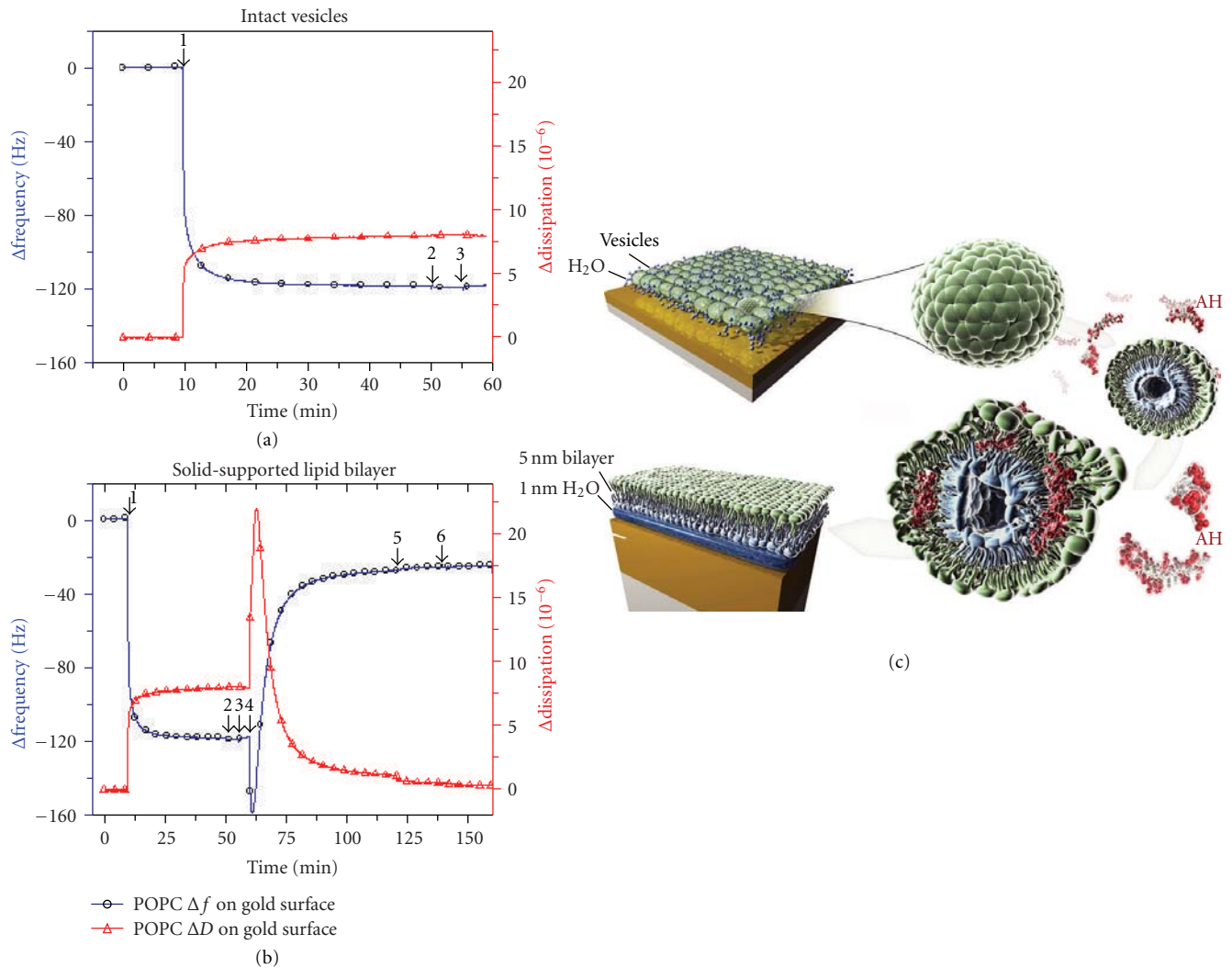


FIGURE 16: Structural transformation from intact vesicles to a lipid bilayer on a gold substrate mediated by an amphipathic α -helix peptide (AH) peptide. (a) Change in QCM resonant frequency and dissipation as a function of time for intact vesicles on oxidized gold. (b) Structural transformation from intact vesicles to a lipid bilayer $\Delta f(t)$ (blue curve) and $\Delta D(t)$ (red curve) show vesicle adsorption on oxidized gold. After 10 minutes (arrow 1) of stabilizing the frequency signal, a POPC vesicle solution (0.1 mg/mL, diameter = 59 nm \pm 0.2 nm) was injected into the liquid cell. After 50 and 55 minutes (arrows 2 and 3), the same buffer was used for two washes and the stability of the intact vesicle adlayer on the gold surface was observed. (b) At 60 minutes (arrow 4), an AH peptide solution was added (0.05 mg/mL) to the intact vesicle adlayer on the gold surface. After 120 and 140 minutes (arrows 5 and 6), the same buffer was used for two washes and the stability of the bilayer formed on the gold surface was observed. (c) Illustration of vesicle rupture and fusion processes to form a supported bilayer on a gold substrate. Reprint from [35].

to study in more detail interfacial science study between biomacromolecules and substrates.

5.2. Supported Bilayer Formed Peptide-Induced Vesicle Rupture. Given the aforementioned experimental work done by Keller and Kasemo [41], one of the limitations of forming the bilayer platform via vesicle fusion is the need to have specific surface interactions, for example, hydrophilic interactions, and properties, for example, polarizability. In order to overcome this energetic problem, a new method was recently introduced to form a bilayer on different substrates such as TiO₂ and Au, known to have insufficient surface

interactions and properties to rupture adsorbed vesicles, by introducing an amphipathic α -helical (AH) peptide as a vesicle destabilizing agent [35, 37]. This process resulted in the formation of planar bilayers on Au and TiO₂ surfaces, as seen in Figure 16.

By following the viscoelastic property and mass changes of this vesicle to bilayer transformation, we have successfully demonstrated that AH peptides destabilize and rupture the leaflets of intact lipid vesicles, allowing the ruptured vesicles to form planar bilayers [35, 37]. Regarding AH peptide's ability to destabilize vesicle structures, it is hypothesized that the peptide first creates instability on the vesicle surface by an electrostatic interaction. Based on similar biological systems

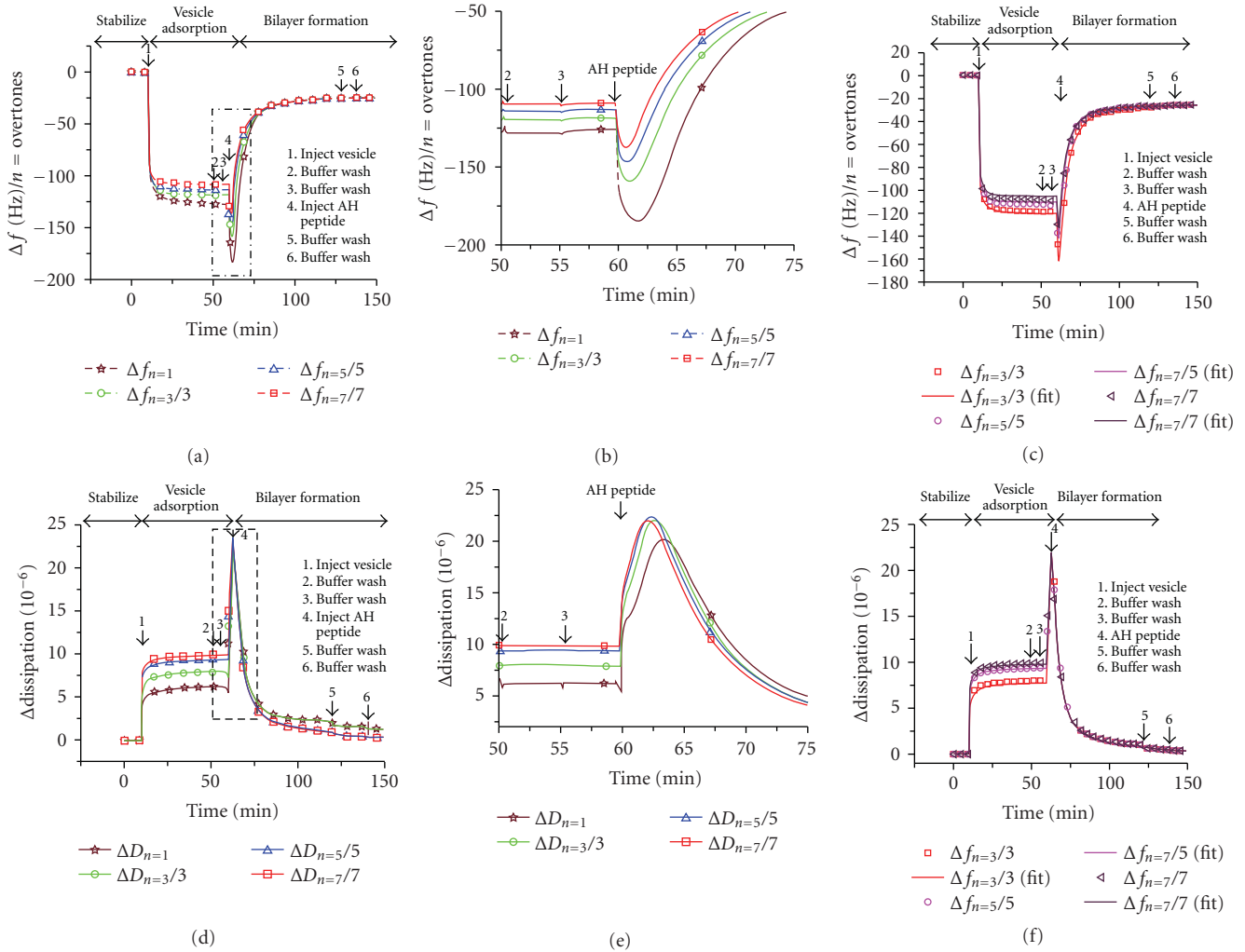


FIGURE 17: QCM-D signatures for structural transformation from intact vesicles to a supported bilayer induced by AH peptide. (a) QCM-D adsorption kinetics of the first four overtones ($\Delta f_n/n$ where $n = 1, 3, 5, 7$ vesicles in a Tris buffer solution (150 mM NaCl, pH 7.5) onto a gold surface. Vesicles are added after stabilizing the frequency signal for 10 minutes (see arrow 1). The film was then washed twice with the same buffer (see arrows 2 and 3). Upon addition of the AH peptide (see arrow 4), the vesicles rupture and form a bilayer on the gold surface. Two buffer washes were performed in order to ensure the stability of the film (see arrows 5 and 6). (b) Expanded view of (a). It is a detailed plot of AH peptide-induced vesicle rupture process from 50 to 75 minutes. The markers are also presented in order to distinguish the traces of the overtones (open star $\Delta f_n = 1$, open circle $\Delta f_n = 3$, open triangle $\Delta f_n = 5$, and open square $\Delta f_n = 7$, respectively). (c) Use of a Voigt-based model to fit Δf as shown in Figure 17(a) for the structural transformation from intact vesicles to a supported bilayer. The fit between the viscoelastic model (*Q-Tools* with density $\rho = 1100$ kg/m³) and the experimental data are presented. (d) Corresponding energy dissipation versus time plot demonstrates the viscoelastic nature of the film changes during the structural transformation from soft vesicle layer to a rigid bilayer. (e) Expanded view of (c) to capture energy dissipation change corresponding to vesicle-AH peptide interaction. (f) Corresponding ΔD fit using same model. Reprint from [37].

studied *in vivo*, it is likely that this leads to expansion of the vesicles, causing a frequency decrease, as well as the creation of microvilli (finger-like structures) on the outer leaflet of the vesicles [49, 50]. Vesicle expansion, resulting in a thicker, more viscoelastic film, and the formation of structures akin to microvilli on the vesicles' surfaces could explain the large increase in dissipation, which characterizes AH peptide's initial interaction with intact vesicles. Interestingly, AH peptide interaction with intact vesicles results in a final frequency shift relative to the initial state before vesicle adsorption of $25.5 \text{ Hz} \pm 0.5$, and the final dissipation value

is only 0.08×10^{-6} (Figure 16(b)), both values corresponding to a complete rigid bilayer formed by the conventional vesicle fusion process. Figure 16(c) illustrated the vesicle rupture and fusion processes to form a supported lipid bilayer. Using the Sauerbrey relationship the resultant film thickness is in good agreement with that of a lipid bilayer, indicating a transition of the soft vesicle layer to a thin and rigid bilayer film as a result of the AH peptide action. With this strategy to form lipid bilayers on substrates, which do not permit vesicle fusion, researchers can take advantage of the electrical properties of Au and the biocompatibility of TiO₂ to form

new biomimetic structures than can be used in various applications such as biosensor and lab-on-a-chip devices. This novel process to form bilayers on Au and TiO₂ shifts the focus on creating improved biomimetic systems away from materials-based problems.

Furthermore, in this model system as shown in Figure 16(b) is intriguing, since it demonstrated the “true” structural transformation from fully saturated single “intact vesicles” layer to lipid bilayer by foreign material, AH peptide. The structural properties can clearly be distinguished in situ by biochemical interactions between AH peptides and lipid molecules. After the “soft” intact vesicle layer is formed on the gold surface, the AH peptide only acts as “destabilizing agent” the layer of vesicles that opt to rupture due to interaction between vesicle-vesicle, and vesicle-surface (e.g., in this particular case, polarization of gold surface and hydrophilic interaction with TiO₂).

Unlike the classical vesicle rupture mechanism on an SiO₂ surface, this system made it possible to capture the structural transformation leading to the formation of a “rigid” bilayer on any solid substrate. To analyze this transformation, Cho et al. [37] first examined the validity of the Sauerbrey relation for both the “soft” and “rigid” layers by calculating adsorbed film thickness. While the Sauerbrey equation is still popular and simple to use for estimating film thickness, more accurate models have been derived to describe the effects of adding various types of foreign masses on a quartz crystal. In order to better understand the structural transformation from a “soft” to a “rigid” film, Cho et al. [37] compared the observed changes with calculations from the Voigt-Voinova model, which extends the QCM solutions beyond the Sauerbrey analogies to include viscoelastic effects. These changes were remarkably consistent over the harmonic frequencies with a film having a frequency independent viscosity. The mechanical loss tangent which is proportional to the ratio of the viscosity to the shear modulus is a parameter useful in characterizing a film as either solid-like or liquid-like. A comparison of the mechanical loss tangent as determined by the Voigt-Voinova fit using a frequency independent viscosity shows that the final “soft” vesicle layer had a $\tan \delta$ greater than unity, while that of the “rigid” bilayer had a $\tan \delta$ less than unity. This agrees with the notion that the “soft” layer is more liquid-like, while the “rigid” layer is solid-like.

5.3. Protein Adsorption. Numerous QCM-D studies have focused on small biomolecules such as proteins. These studies have included protein-protein and protein-surface interactions as well as conformational changes in protein films [51–60]. Here we describe a particular 2001 study by Höök et al. [42]. It is notable for characterizing the structural transformation of a mussel adhesive protein adsorbed onto a hydrophobic methyl-terminated surface. It is an ideal example to demonstrate the usefulness of simultaneous detection of mass and viscoelastic property changes to characterize a dynamic, multistep biological process. The adsorption kinetics of the protein and subsequent structural transformation induced by cross-linking are monitored in

terms of frequency and dissipation changes in order to understand the film properties.

As seen in Figure 18, the initial step involves adsorption of the protein onto a hydrophobic substrate. There is a large dissipation change ($D_1 = 15.8 \pm 0.2$) associated with the binding process, which indicates that the resulting protein film is highly viscoelastic. The normalized frequency and dissipation overtone deviations (25% for $n = 3$ and 34% for $n = 5$) are a result of the energy damping caused by the soft film properties. After adding a cross-linking agent, the dissipation decreases to nearly zero, indicating the formation of a nonviscoelastic film. By analyzing this change in dissipation upon cross-linking, it is clear that there is a structural transformation of the protein film on a macroscopic level because there is a significant change in the film’s physical properties.

In terms of modeling, this system is very similar to the AH peptide-induced vesicle rupture process because both involve the structural transformation of a non-Sauerbrey regime to a Sauerbrey regime. Initially, the protein film has a high bound water content and requires a viscoelastic model to accurately characterize this non-Sauerbrey regime. Following cross-linking, the protein film becomes rigid and the associated mass decrease is predicted to be caused by a decrease in bound water content, which is in agreement with the dissipation data. A lower bound solvent content characterizes more rigid films and therefore they satisfy all the conditions necessary to use the Sauerbrey relationship.

A very interesting aspect of this study is that the entire protein adsorption and cross-linking events were repeated in D₂O in order to check the validity of the fitting parameters that satisfy the Voigt model. This experimental step confirmed the validity of the Voigt model to describe the protein film in both the Sauerbrey and non-Sauerbrey regimes as well during the structural transformation.

5.4. Binding Dynamics of AH Peptide to Artificial Cell Membranes. As increasing advances in bionanotechnology are made, there is an increasing need to engineer biomembrane platforms, which use phospholipid bilayers to support, protect, and organize membrane proteins. New lipid-based platforms have enabled a wide array of new research on biological membranes by (a) controlling the parameters of the materials, such that optimal platforms are ensured for promoting the interaction with target molecules, (b) studying the total saturation of the acyl chains, and the interaction of the membrane lipids with the target since lipid phase behavior is influenced by the lipid composition, (c) evaluating the effect of changing temperature and pH conditions, which are known to alter the biophysical properties of lipids, and (d) adding accessory biologic factors, such as an insoluble detergent complex (raft) that can be utilized to enhance the interaction with the target. Most researchers apply a “bottom-up” strategy to achieve this goal by modifying phospholipid compositions and incorporation transmembrane protein into the bilayer system. Under normal conditions, transmembrane conformation and proper protein attachment to membrane are necessary

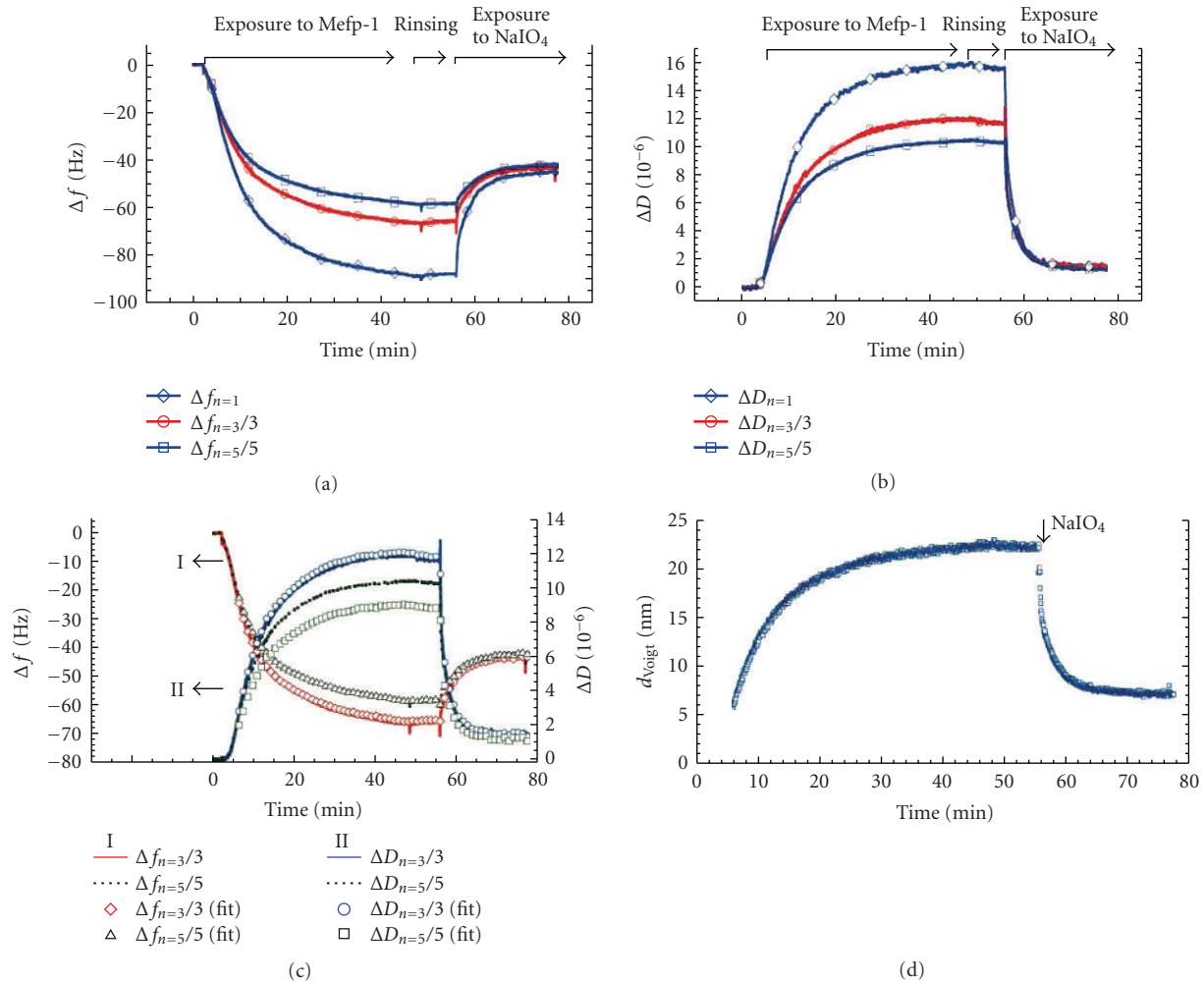


FIGURE 18: QCM-D response of overtones as a function of time for protein adsorption and subsequent cross-linking. (a) Exposure of the methyl-terminated surface to a buffer solution containing 25 mg/mL Mefp-1 in 0.1 M acetate buffer (0.75 M NaCl, pH 5.5), followed by exchange of the protein solution for a pure buffer solution. The cross-linking behavior of Mefp-1 was subsequently followed by addition of the same buffer solution containing 1 mM NaIO₄. (b) Corresponding dissipation as a function of time for experiment shown in (a). (c) The best fit between the viscoelastic model (obtained using Q-Soft software (Q-Sense AB)), and the experimental data shown in Figure 17(a). (d) Change in the effective thickness with respect to time obtained from the fit shown in (c). Reprint from [42].

via complex electrostatic interactions between proteins and phospholipids were necessary for proper functions. In here, as sensor system, we discussed the new “membrane on a chip” system employing “top-to-bottom” approach [47, 48], namely, utilizing cell derived the microsome to form functional membrane to study protein-protein interaction. As an model system, we presented the examples for monitoring the association of the NS5A AH peptide with a model lipid bilayer and cell-derived membranes. Furthermore, compare these results to conventional biochemical floatation assay to check the validity of new platform formed by “top-down” approach [34].

Conventional biological responses are often triggered by functional protein receptors. In order to capture this response, Cho et al. [34] made use of a novel “membrane-on-a-chip” system wherein the binding dynamics of a synthetic peptide corresponds to the NS5A AH to lipid bilayers

and cell-derived membrane by “top-down” approach that could be studied in real time using the quartz crystal microbalance with dissipation (QCM-D) method. Moreover, they found that significantly more peptide bound when cellular-derived membranes in which accompany with protein receptors. The direct evidence protein-peptide interaction was captured by eliminating protein receptors by prior treatment of the cellular membranes with trypsin. A control peptide, whose interaction with membranes involves trypsin-insensitive glycosaminoglycans, was not altered by the protease treatment. Similar results were obtained using standard biochemical membrane flotation assays of NS5A AH-containing proteins that support the validity of QCM-D platform used as bioassay. The aforementioned experimental results demonstrated the potential of QCM-D for studying these types of protein-membrane interactions as well as a broad range of problems involving membrane proteins

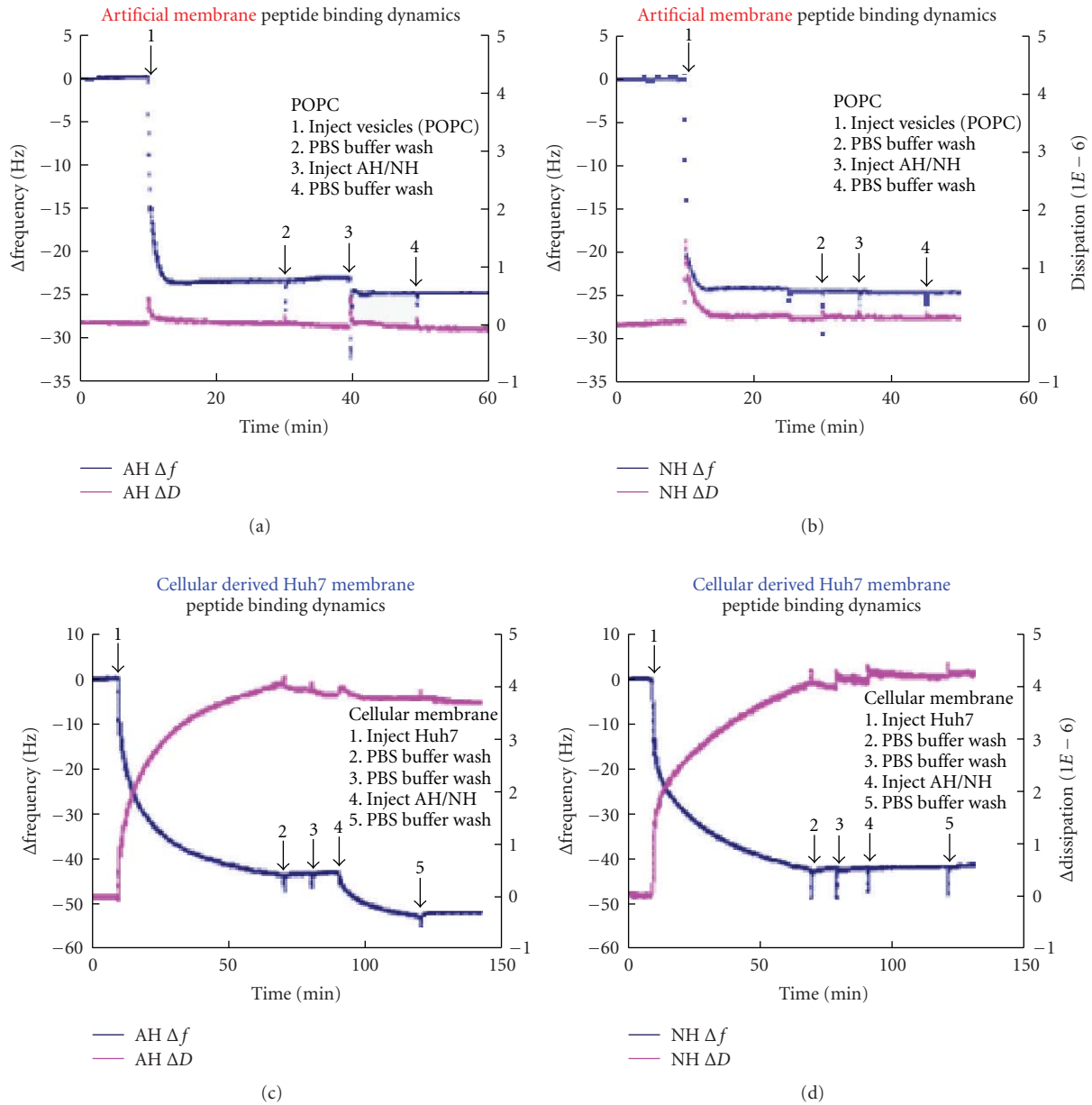


FIGURE 19: QCM-D analysis of AH peptide binding to a quartz crystal coated with POPC model lipid membrane and a cell-derived membrane. (a) AH peptide binding dynamics on a POPC model lipid bilayer. Frequency, $\Delta f(t)$, and dissipation, $\Delta D(t)$, changes detected by QCM-D as a function of time were recorded. (b) NH peptide binding dynamics to POPC model lipid bilayers. NH contains three mutations designed to disrupt the hydrophobic face of AH. (c) Binding of AH peptide to Huh7-derived microsome coated onto an SiO_2 quartz crystal substrate. The data show that the microsomes saturated at a higher mass than the model POPC membrane, presumably due to the presence of proteinaceous components. They also show by the dissipation value that those proteinaceous components are associated with higher viscoelastic energy dissipation, as expected. (d) No binding of NH peptide to Huh7-derived membranes adsorbed on an SiO_2 surface. Note that there are no changes in either the frequency or dissipation, which suggests that there is no binding to Huh7-derived membranes. Reprint from [34].

or lipids. Furthermore, using “top-down” approach with conventional bioseparation techniques will provide powerful tool to create functional platform to study interaction and biomacromolecular dynamics. The main advantage of the potential biosensor described in this study using QCM-D technique is that it is simple and quick to use and that it

shows the real-time kinetics of the interactions happening on the lipid bilayer derived from the cells that are comparable to the results obtained by traditional biochemical analysis. Standard biological assays can take days to complete experiments. However, using the unique “lab on a chip” approach of QCM-D can reduce assay time to hours.

6. Conclusions

It is hoped to have provided a view of the use of the quartz crystal microbalance as a sensor to probe various aspects of biomacromolecular assemblies. The importance of both the frequency change and dissipation change during the assembly process has been emphasized as well as the various means for exploring the source of these changes through modeling. The special information that can be gained using the QCM as one of the tools in the arsenal of detectors for macromolecular processes is illustrated by several examples. Among these are the study of surface specific interactions on lipid vesicles, the demonstration of a vesicle cell rupture caused by the adsorption of a peptide onto its surface, and the use of model fits to these processes. The importance of capturing both the frequency and dissipation data is demonstrated.

Appendix

We have gathered here the specific relations detailing the calculation of the quantity Q_4 . This has been made available to the reader who might be interested in doing the quantitative computations:

- e_{26} is the appropriate piezo constant for quartz having the value -0.095 C m^{-1}
- ϵ_{22} is the appropriate dielectric constant for the quartz with the value $3.982 \times 10^{-11} \text{ fd/m}$;
- c_{66} is the appropriate shear modulus for the quartz with the value $2.901 \times 10^{10} \text{ N m}^{-2}$
- d_Q is the quartz thickness in m,
- ρ_Q is the quartz density having the value of 2649 kgm m^{-3} ;
- \tilde{c}_{66} is the stiffened quartz shear modulus;
- k_Q is the acoustic wave propagation constant in the quartz;
- Q_1 is a collection of terms for the quartz;
- Q_2 is another set of terms for the quartz;
- ρ_L is the density of the liquid;
- η_L is the viscosity of the assumed Newtonian liquid;
- ρ_F is the density of the film on the quartz;
- μ_F is the shear modulus for the film in N m^{-2}
- k_F is the acoustic wave propagation constant in the film,
- η_F is the viscosity for the film in N sec m^{-2}

- k_L is the acoustic wave propagation constant in the liquid;
- T_1 is a collection of terms involving the film and the liquid;
- T_2 is a second collection of terms involving the film and the liquid;
- Q_3 is another collection of terms;

$$\tilde{c}_{66} = c_{66} + \frac{e_{26}^2}{\epsilon_{22}},$$

$$k_Q = \omega \sqrt{\frac{\rho_Q}{\tilde{c}_{66}}},$$

$$Q_1 = jk_Q \tilde{c}_{66} (1 - e^{-jk_Q d_Q}),$$

$$Q_2 = jk_Q \tilde{c}_{66} (1 - e^{jk_Q d_Q}),$$

$$\tilde{\mu}_F = \mu_F + j\omega\eta_F,$$

$$k_F = \omega \sqrt{\frac{\rho_F}{\tilde{\mu}_F}},$$

$$k_L = \omega \sqrt{\frac{\rho_L}{j\omega\eta_L}},$$

$$T_1 = 1 + \frac{jk_F \tilde{\mu}_F - \omega k_L \eta_L}{jk_F \tilde{\mu}_F + \omega k_L \eta_L} e^{j2k_F d_F},$$

$$T_2 = 1 - \frac{jk_F \tilde{\mu}_F - \omega k_L \eta_L}{jk_F \tilde{\mu}_F + \omega k_L \eta_L} e^{j2k_F d_F},$$

$$Q_3 = jk_F \tilde{\mu}_F \frac{T_2}{T_1}, \quad (\text{A.1})$$

We finally obtain the expression to be used for the quantity Q_4 ,

$$Q_4 = \left\{ \frac{e_{26}^2}{\epsilon_{22}} \times \frac{(1 - e^{-jk_Q d_Q}) + (1 - e^{jk_Q d_Q}) ((Q_1 - Q_3)/(Q_2 + Q_3))}{jk_Q \tilde{c}_{66} (e^{-jk_Q d_Q} - e^{jk_Q d_Q}) [(Q_1 - Q_3)/(Q_2 + Q_3)]} - d_Q \right\}. \quad (\text{A.2})$$

Acknowledgment

N.J. Cho is a recipient of an Americal Liver Foundation Postdoctoral Fellowship Award and a Stanford Dean's Fellowship.

References

- [1] A. Arnau Vives, *Piezoelectric Transducers and Applications*, vol. 26, Springer, Berlin, Germany, 2008, 125 illustration.
- [2] C. Lu and A. W. Czanderna, *Applications of Piezoelectric Quartz Crystal Microbalances*, Elsevier, New York, NY, USA, 1984.
- [3] D. A. Buttry and M. D. Ward, "Measurement of interfacial processes at electrode surfaces with the electrochemical quartz crystal microbalance," *Chemical Reviews*, vol. 92, no. 6, pp. 1355–1379, 1992.
- [4] V. E. Bottom, *Introduction to Quartz Crystal Unit Design*, Van Nostrand Reinhold, New York, NY, USA, 1982.
- [5] R. W. Cernosek, S. J. Martin, A. R. Hillman, and H. L. Bandey, "Comparison of lumped-element and transmission-line models for thickness-shear-mode quartz resonator sensors," *IEEE Transactions on Ultrasonics, Ferroelectrics, and Frequency Control*, vol. 45, no. 5, pp. 1399–1407, 1998.
- [6] H. Muramatsu, E. Tamiya, and I. Karube, "Computation of equivalent circuit parameters of quartz crystals in contact with liquids and study of liquid properties," *Analytical Chemistry*, vol. 60, no. 19, pp. 2142–2146, 1988.
- [7] S. J. Martin, V. E. Granstaff, and G. C. Frye, "Characterization of a quartz crystal microbalance with simultaneous mass and liquid loading," *Analytical Chemistry*, vol. 63, no. 20, pp. 2272–2281, 1991.
- [8] H. L. Bandey, A. R. Hillman, M. J. Brown, and S. J. Martin, "Viscoelastic characterization of electroactive polymer films at the electrode/solution interface," *Faraday Discussions*, vol. 107, pp. 105–121, 1997.
- [9] A. Arnau, "A review of interface electronic systems for AT-cut quartz crystal microbalance applications in liquids," *Sensors*, vol. 8, no. 1, pp. 370–411, 2008.
- [10] H. L. Bandey, S. J. Martin, R. W. Cernosek, and A. R. Hillman, "Modeling the responses of thickness-shear mode resonators under various loading conditions," *Analytical Chemistry*, vol. 71, no. 11, pp. 2205–2214, 1999.
- [11] B. D. Vogt, E. K. Lin, W.-I. Wu, and C. C. White, "Effect of film thickness on the validity of the sauerbrey equation for hydrated polyelectrolyte films," *Journal of Physical Chemistry B*, vol. 108, no. 34, pp. 12685–12690, 2004.
- [12] G. Sauerbrey, "Verwendung von Schwingquarzen zur Waegung duenner Schichten und zur Mikrowaegung," *Zeitschrift für Physik*, vol. 155, p. 206, 1959.
- [13] M. Rodahl, F. Hook, C. Fredriksson, et al., "Simultaneous frequency and dissipation factor QCM measurements of biomolecular adsorption and cell adhesion," *Faraday Discussions*, vol. 107, pp. 229–246, 1997.
- [14] M. V. Voinova, M. Jonson, and B. Kasemo, "Missing mass' effect in biosensor's QCM applications," *Biosensors and Bioelectronics*, vol. 17, no. 10, pp. 835–841, 2002.
- [15] M. Ferrari, V. Ferrari, and K. Kanazawa, "Dual-harmonic oscillator for quartz crystal resonator sensors," *Sensors and Actuators A*, vol. 145–146, no. 1–2, pp. 131–138, 2008.
- [16] J. R. Vig, "Dual-mode oscillators for clocks and sensors," in *Proceedings of the IEEE Ultrasonics Symposium (ULTSYM '99)*, vol. 2, pp. 859–868, Caesars Tahoe, Nev, USA, October 1999.
- [17] A. L. Kipling and M. Thompson, "Network analysis method applied to liquid-phase acoustic wave sensors," *Analytical Chemistry*, vol. 62, no. 14, pp. 1514–1519, 1990.
- [18] R. Lucklum, C. Behling, R. W. Cernosek, and S. J. Martin, "Determination of complex shear modulus with thickness shear mode resonators," *Journal of Physics D*, vol. 30, no. 3, pp. 346–356, 1997.
- [19] S. M. Yoon, N.-J. Cho, K. Kanazawa, and C. W. Frank, "Analyzing spur-distorted impedance spectra for the QCM," submitted to *Journal of Sensors*.
- [20] M. Rodahl, F. Hook, and B. Kasemo, "QCM operation in liquids: an explanation of measured variations in frequency and Q factor with liquid conductivity," *Analytical Chemistry*, vol. 68, no. 13, pp. 2219–2227, 1996.
- [21] P. J. Cumpson and M. P. Seah, "The quartz crystal microbalance; radial/polar dependence of mass sensitivity both on and off the electrodes," *Measurement Science & Technology*, vol. 1, no. 7, pp. 544–555, 1990.
- [22] L. Wimmer, S. Hertl, J. Hemetsberger, and E. Benes, "New method of measuring vibration amplitudes of quartz crystals," *Review of Scientific Instruments*, vol. 55, no. 4, pp. 605–609, 1984.
- [23] M. A. Cooper, "Biosensing using rupture event scanning (REVS)(TM)," *Measurement Science & Technology*, vol. 14, no. 11, pp. 1888–1893, 2003.
- [24] M. Edvardsson, M. Rodahl, and F. Hook, "Investigation of binding event perturbations caused by elevated QCM-D oscillation amplitude," *Analyst*, vol. 131, no. 7, pp. 822–828, 2006.
- [25] J. G. Miller and D. I. Bolef, "Acoustic wave analysis of the operation of quartz-crystal film-thickness monitors," *Journal of Applied Physics*, vol. 39, no. 12, pp. 5815–5816, 1968.
- [26] C.-S. Lu and O. Lewis, "Investigation of film-thickness determination by oscillating quartz resonators with large mass load," *Journal of Applied Physics*, vol. 43, no. 11, pp. 4385–4390, 1972.
- [27] T. Nomura and A. Minemura, "Behavior of a piezoelectric quartz crystal in an aqueous-solution and the application to the determination of minute amount of cyanide," *Nippon Kagaku Kaishi*, pp. 1621–1625, 1980.
- [28] A. Bund, A. Baba, S. Berg, et al., "Combining surface plasmon resonance and quartz crystal microbalance for the in situ investigation of the electropolymerization and doping/dedoping of poly(pyrrole)," *Journal of Physical Chemistry B*, vol. 107, no. 28, pp. 6743–6747, 2003.
- [29] C. Behling, R. Lucklum, and P. Hauptmann, "The non-gravimetric quartz crystal resonator response and its application for determination of polymer shear modulus," *Measurement Science & Technology*, vol. 9, no. 11, pp. 1886–1893, 1998.
- [30] M. Rodahl and B. Kasemo, "On the measurement of thin liquid overlayers with the quartz-crystal microbalance," *Sensors and Actuators A*, vol. 54, no. 1–3, pp. 448–456, 1996.
- [31] E. Benes, "Improved quartz crystal microbalance technique," *Journal of Applied Physics*, vol. 56, no. 3, pp. 608–626, 1984.
- [32] K. Kanazawa, "Steady state and transient QCM solutions at the metal | solution interface," *Journal of Electroanalytical Chemistry*, vol. 524–525, pp. 103–109, 2002.
- [33] K. Kanazawa, C. W. Frank, and J. Hardesty, "Resonances of soft films under liquid on the QCM," *ECS Transactions*, vol. 16, no. 11, pp. 419–429, 2008.
- [34] N.-J. Cho, K. H. Cheong, C. Lee, C. W. Frank, and J. S. Glenn, "Binding dynamics of hepatitis C virus' NS5A amphipathic peptide to cell and model membranes," *Journal of Virology*, vol. 81, no. 12, pp. 6682–6689, 2007.
- [35] N.-J. Cho, S.-J. Cho, K. H. Cheong, J. S. Glenn, and C. W. Frank, "Employing an amphipathic viral peptide to create a lipid bilayer on Au and TiO₂," *Journal of the American Chemical Society*, vol. 129, no. 33, pp. 10050–10051, 2007.
- [36] N.-J. Cho, J. N. D'Amour, J. Stalgren, W. Knoll, K. Kanazawa, and C. W. Frank, "Quartz resonator signatures under

- Newtonian liquid loading for initial instrument check," *Journal of Colloid and Interface Science*, vol. 315, no. 1, pp. 248–254, 2007.
- [37] N.-J. Cho, K. Kanazawa, J. S. Glenn, and C. W. Frank, "Employing two different quartz crystal microbalance models to study changes in viscoelastic behavior upon transformation of lipid vesicles to a bilayer on a gold surface," *Analytical Chemistry*, vol. 79, no. 18, pp. 7027–7035, 2007.
- [38] B. Kasemo, "Biological surface science," *Surface Science*, vol. 500, no. 1–3, pp. 656–677, 2002.
- [39] C. A. Keller, K. Glasmastar, V. P. Zhdanov, and B. Kasemo, "Formation of supported membranes from vesicles," *Physical Review Letters*, vol. 84, no. 23, pp. 5443–5446, 2000.
- [40] M. Rodahl, F. Hook, C. Fredriksson, et al., "Simultaneous frequency and dissipation factor QCM measurements of biomolecular adsorption and cell adhesion," *Faraday Discussions*, vol. 107, pp. 229–246, 1997.
- [41] C. A. Keller and B. Kasemo, "Surface specific kinetics of lipid vesicle adsorption measured with a quartz crystal microbalance," *Biophysical Journal*, vol. 75, no. 3, pp. 1397–1402, 1998.
- [42] F. Höök, B. Kasemo, T. Nylander, C. Fant, K. Sott, and H. Elwing, "Variations in coupled water, viscoelastic properties, and film thickness of a Mefp-1 protein film during adsorption and cross-linking: a quartz crystal microbalance with dissipation monitoring, ellipsometry, and surface plasmon resonance study," *Analytical Chemistry*, vol. 73, no. 24, pp. 5796–5804, 2001.
- [43] M. K. Jain, A. Strickholm, F. P. White, and E. H. Cordes, "Electronic conduction across a black lipid membrane," *Nature*, vol. 227, no. 5259, pp. 705–707, 1970.
- [44] W. A. Huemoeller and H. T. Tien, "A simple set-up for black lipid membrane experiments," *Journal of Chemical Education*, vol. 47, no. 6, pp. 469–470, 1970.
- [45] L. K. Tamm and H. M. McConnell, "Supported phospholipid bilayers," *Biophysical Journal*, vol. 47, no. 1, pp. 105–113, 1985.
- [46] H. M. McConnell, T. H. Watts, R. M. Weis, and A. A. Brain, "Supported planar membranes in studies of cell-cell recognition in the immune system," *Biochimica et Biophysica Acta*, vol. 864, no. 1, pp. 95–106, 1986.
- [47] E. Sackmann, "Supported membranes: scientific and practical applications," *Science*, vol. 271, no. 5245, pp. 43–48, 1996.
- [48] E. Sackmann and M. Tanaka, "Supported membranes on soft polymer cushions: fabrication, characterization and applications," *Trends in Biotechnology*, vol. 18, no. 2, pp. 58–64, 2000.
- [49] D. Gidalevitz, Y. Ishitsuka, A. S. Muresan, et al., "Interaction of antimicrobial peptide protegrin with biomembranes," *Proceedings of the National Academy of Sciences of the United States of America*, vol. 100, no. 11, pp. 6302–6307, 2003.
- [50] Y. Ishitsuka, D. Gidalevitz, A. J. Waring, R. I. Lehrer, and K. Y. Lee, "The selective interaction of protegrin-1 with a model cell membrane: the role of the lipid tail unsaturation," *Biophysical Journal*, vol. 84, p. 513a, 2003.
- [51] M. Andersson, A. Sellborn, C. Fant, C. Gretzer, and H. Elwing, "Acoustics of blood plasma on solid surfaces," *Journal of Biomaterials Science, Polymer Edition*, vol. 13, no. 8, pp. 907–917, 2002.
- [52] R. J. Barfoot, K. H. Sheikh, B. R. G. Johnson, et al., "Minimal F-actin cytoskeletal system for planar supported phospholipid bilayers," *Langmuir*, vol. 24, no. 13, pp. 6827–6836, 2008.
- [53] S. Belegriou, I. Mannelli, P. Lisboa, et al., "pH-dependent immobilization of proteins on surfaces functionalized by plasma-enhanced chemical vapor deposition of poly(acrylic acid)-and polyethylene oxide-like films," *Langmuir*, vol. 24, no. 14, pp. 7251–7261, 2008.
- [54] S. Boujday, A. Bantegnie, E. Briand, P.-G. Marnet, M. Salmain, and C.-M. Pradier, "In-depth investigation of protein adsorption on gold surfaces: correlating the structure and density to the efficiency of the sensing layer," *Journal of Physical Chemistry B*, vol. 112, no. 21, pp. 6708–6715, 2008.
- [55] H. Chen, X. Su, K. G. Neoh, and W.-S. Choe, "Context-dependent adsorption behavior of cyclic and linear peptides on metal oxide surfaces," *Langmuir*, vol. 25, no. 3, pp. 1588–1593, 2009.
- [56] C. Fant, H. Elwing, and F. Hook, "The influence of cross-linking on protein-protein interactions in a marine adhesive: the case of two byssus plaque proteins from the blue mussel," *Biomacromolecules*, vol. 3, no. 4, pp. 732–741, 2002.
- [57] R. Fogel, P. Mashazi, T. Nyokong, and J. Limson, "Critical assessment of the Quartz Crystal Microbalance with Dissipation as an analytical tool for biosensor development and fundamental studies: metallophthalocyanine-glucose oxidase biocomposite sensors," *Biosensors and Bioelectronics*, vol. 23, no. 1, pp. 95–101, 2007.
- [58] M. S. Lord, M. H. Stenzel, A. Simmons, and B. K. Milthorpe, "The effect of charged groups on protein interactions with poly(HEMA) hydrogels," *Biomaterials*, vol. 27, no. 4, pp. 567–575, 2006.
- [59] J. Malmstrom, H. Agheli, P. Kingshott, and D. S. Sutherland, "Viscoelastic modeling of highly hydrated laminin layers at homogeneous and nanostructured surfaces: quantification of protein layer properties using QCM-D and SPR," *Langmuir*, vol. 23, no. 19, pp. 9760–9768, 2007.
- [60] W. Y. X. Peh, E. Reimhult, H. F. Teh, J. S. Thomsen, and X. Su, "Understanding ligand binding effects on the conformation of estrogen receptor α -DNA complexes: a combinational quartz crystal microbalance with dissipation and surface plasmon resonance study," *Biophysical Journal*, vol. 92, no. 12, pp. 4415–4423, 2007.

Review Article

Integrated MEMS/NEMS Resonant Cantilevers for Ultrasensitive Biological Detection

Xinxin Li,¹ Haitao Yu,¹ Xiaohua Gan,¹ Xiaoyuan Xia,¹ Pengcheng Xu,¹ Jungang Li,¹ Min Liu,¹ and Yongxiang Li²

¹ State Key Lab of Transducer Technology, Shanghai Institute of Microsystem and Information Technology, Chinese Academy of Sciences, 865 Changning Road, Shanghai 200050, China

² State Key Lab of High Performance Ceramics and Superfine Microstructures, Shanghai Institute of Ceramics, Chinese Academy of Sciences, 1295 Dingxi Road, Shanghai 200050, China

Correspondence should be addressed to Xinxin Li, xxli@mail.sim.ac.cn

Received 6 January 2009; Accepted 14 April 2009

Recommended by Michele Penza

The paper reviews the recent researches implemented in Chinese Academy of Sciences, with achievements on integrated resonant microcantilever sensors. In the resonant cantilevers, the self-sensing elements and resonance exciting elements are both top-down integrated with silicon micromachining techniques. Quite a lot of effort is focused on optimization of the resonance mode and sensing structure for improvement of sensitivity. On the other hand, to enable the micro-cantilevers specifically sensitive to bio/chemical molecules, sensing materials are developed and modified on the cantilever surface with a self-assembled monolayer (SAM) based bottom-up construction and surface functionalization. To improve the selectivity of the sensors and depress environmental noise, multiple and localized surface modifications are developed. The achieved volume production capability and satisfactory detecting resolution to trace-level biological antigen of alpha-fetoprotein (AFP) give the micro-cantilever sensors a great promise for rapid and high-resoluble detection.

Copyright © 2009 Xinxin Li et al. This is an open access article distributed under the Creative Commons Attribution License, which permits unrestricted use, distribution, and reproduction in any medium, provided the original work is properly cited.

1. Introduction

For recognition and detection of individual cells and bio/chemical molecules, micromechanical cantilever sensors with picogram to femtogram mass-sensing resolution in air environment have been attracting intensive researches [1]. According to measurement scheme, sensing mechanism of the micromechanical cantilevers can be categorized into static and dynamic detecting methods. With the static detecting method, the target molecules are detected by measuring cantilever surface stress, which is induced by specific bio/chemical binding or interaction at the surface of the cantilever [2–6]. Differently, the dynamic detecting method employs the cantilever as a resonator. Induced by specific mass adsorbate, a shift in the resonant frequency is read out as the sensing signal [7–11].

The pioneer investigation by Thundat et al. demonstrated the mass-sensing capability of micromechanical resonant cantilevers [7]. With precise optical detection of atomic force microscopy (AFM), a single cell or virus has

been sensed in air environment [8, 9]. In ultrahigh vacuum, the resonant cantilevers even showed the mass resolution as high as attogram level [10]. However, these previously reported results were generally obtained in laboratories, with an off-sensor optical position sensing detection (PSD) of AFM mode used [11, 12]. For portable bio/chemical sensing applications, there is a recent trend to integrate the sensing and actuating elements into the cantilever for on-chip dynamic detection [6, 13, 14].

For static detection, the whole surface of one side of the cantilever is coated with a sensing layer, that is, affinity to the targeted analyte, while the other side is relatively passive. The specific reaction or combination between the analyte and the sensing layer can cause surface stress on the cantilever that gives rise to a bending of the cantilever [1, 4, 15, 16]. For a resonant cantilever, however, the sensing area would be better to be localized near the free end to enhance the mass loading signal and to depress cross-talk signal from spring-constant change.

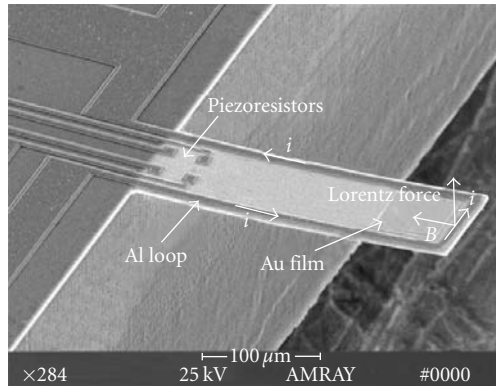


FIGURE 1: SEM image of the integrated resonant piezoresistive cantilever with the electromagnetic excitation schemes denoted.

For on-the-spot portable detection, microcantilevers integrated with on-chip read out are highly in demand. For example, piezoresistive read out based on measuring the bending stress of the cantilever is a suitable approach [17–19]. Using the piezoresistive cantilevers, chemical vapors have been detected with high sensitivity [20–22]. It is worth to point out that these previously developed piezoresistive microcantilevers, more often than not, comprised polysilicon piezoresistors in silicon nitride cantilever or doped single-crystalline silicon piezoresistors in silicon cantilever. For the former, the piezoresistive sensitivity of the polysilicon is lower compared to its single-crystalline counterpart [23]. For the latter, p-n junction isolation is generally used for the single-crystalline piezoresistors. Electronic noise relative to p-n junction current leakage is inevitable that more or less lowers the detecting resolution. For a static surface-stress sensing cantilever, the noise will directly degrade the detection resolution. For a resonant cantilever sensor, however, frequency shift is used to characterize the sensing signal and the noise in the piezoresistive output only indirectly influence the sensor performance. As long as the resonant amplitude of the cantilever is high enough, the piezoresistive output voltage can safely surpass the noise level and the frequency shift can be precisely read out.

Both resonant and static cantilever sensors have been developed in the State Key Lab of Transducer Technology located at Shanghai branch of Chinese Academy of Sciences. This review paper will mainly address the technical details and achievements about the resonant cantilevers and their biological sensing applications recently obtained in our lab.

2. Formation of the Integrated Resonant Cantilevers

Developed in the State Key Lab of Transducer Technology, the SEM image of an integrated silicon cantilever sensor is shown in Figure 1 for description of our design [24]. The piezoresistive sensing scheme and the electromagnetic excitation are utilized for the resonant cantilevers sensors. A small-bulk NdFeB magnet, purchased from Beijing Zhong Ke San Huan High-Tech Co., is mounted in the sensor

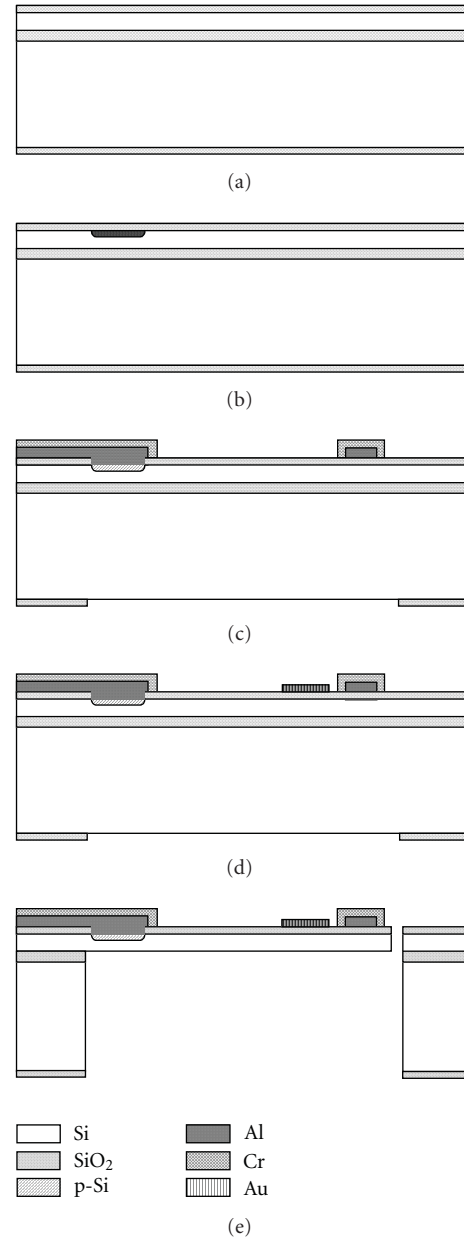


FIGURE 2: Fabrication processes of the integrated cantilever.

package to generate magnetic field of about 50 mT for Lorentz-force excitation. The magnet generated magnetic field is measured with a 3G-3-A Tesla-meter. When a *sine*-wave AC electric current is fed through the aluminum loop, the cantilever will vibrate under the Lorentz force. The driving force is located at the cantilever end, that is, the peak location of the 1st resonant mode. The piezoresistive wheatstone bridge for frequency signal read out is put near the cantilever root, where maximum vibration-induced stress is located.

Considering the surface area for mass adsorption and the configuration of the piezoresistors and the Lorentz-coil, identical dimension of $300 \times 100 \times 3 \mu\text{m}^3$ is designed. The calculated effective mass is 52.5 pg. The eigen-frequency for

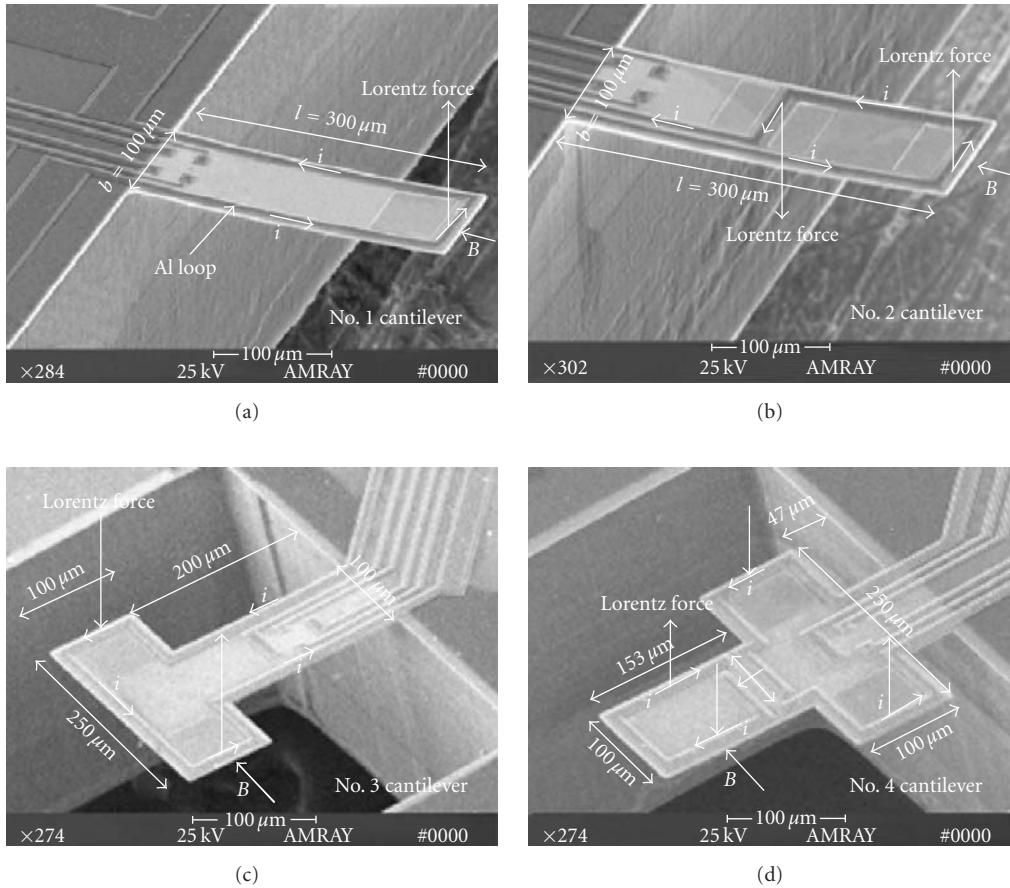


FIGURE 3: SEM images of the fabricated microcantilevers with the dimensions denoted. For the cantilevers from “a” to “d,” their resonance modes are the 1st flexure-mode, the 2nd flexure-mode, the 1st torsion-mode, and the 2nd torsion-mode, respectively.

the fundamental resonance mode is designed as 45.9 KHz. The sensitivity is calculated as 0.43 Hz/pg.

With the main process steps shown in Figure 2, the cantilever fabrication starts from (100) silicon on insulator (SOI) wafers, with 3.1 μm -thick 1–10 $\Omega \cdot \text{cm}$ n-type top-layer and 0.36 μm -thick buried oxide (BOX) layer [25]. (1) A 2000 \AA -thick SiO_2 layer is grown by dry oxidation. (2) By ion implantation, boron doping for the piezoresistor is implemented with 150 Ω targeted sheet-resistance. (3) Contact holes are opened and Al interconnection is processed. For protecting the Al from being damaged during the following cantilever gold-surface cleaning with $\text{H}_2\text{SO}_4 + \text{H}_2\text{O}_2$, an extra Cr layer is sputtered and patterned to cover the Al lines. (4) To immobilize a sensing film for specific molecular adsorption, 10 nm-thick Cr adhesion layer and 30 nm Au film are sequentially coated by using electron-beam evaporation. Then the Cr/Au sensing pads are formed at the cantilever-paddle terminals by lift-off process. (5) The $\langle 100 \rangle$ -oriented cantilever is shaped by front-side reactive ion etching (RIE) and backside deep RIE, respectively. The cantilever is released by removing the BOX-layer with HF. The SEM image of the fabricated cantilever is shown in Figure 1.

3. Resonance Mode Optimization of Dynamic Microcantilevers

Micromechanical resonant cantilever sensors are operated by detecting frequency shift, that is, directly induced by an additional mass. The detecting resolution of the resonant frequency, which determines the sensing resolution for mass adsorption, can be improved by enhancing the Q -factor value [26]. Most of practical resonant cantilever sensors need to be operated in atmosphere air where a large volume air is surrounding the cantilever. Therefore, air-drag energy loss is the main factor to limit the Q -factor of microscale resonant cantilever in air, and thus dominates the mass-sensing resolution. Resonance-mode optimization is found to be effective in improving the Q -value and mass sensing resolution. There have been individual reports on individual experimental findings of resonance-mode influenced sensing performance [27, 28]. Recently, we carried out a systematic study to reveal the effect of different orders of resonance modes of microcantilevers on Q -value and mass-sensing resolution [29].

We use theoretical analysis, finite-element simulation, and experimental measurement to investigate the air drag damping effect on Q -factor of the cantilevers in various

TABLE 1: Simulated results for a rectangular cantilevers resonating in different modes.

Mode	1st flexure	2nd flexure	1st torsion	2nd torsion
Resonant frequency (kHz)	52.3	328	293	924
Generalized mass (kg)	5.24e-11	5.23e-11	3.09e-11	2.58e-11
Damping coefficient C_d ($\mu\text{N}/\mu\text{m/s}$)	2.39e-8	2.37e-8	2.04e-8	1.80e-8
Damping ratio $\xi = C_d/2m\omega_0$	6.94e-4	1.09e-4	1.80e-4	6.01e-5
Quality factor $Q = 1/2\xi$	720	3587	2778	8319

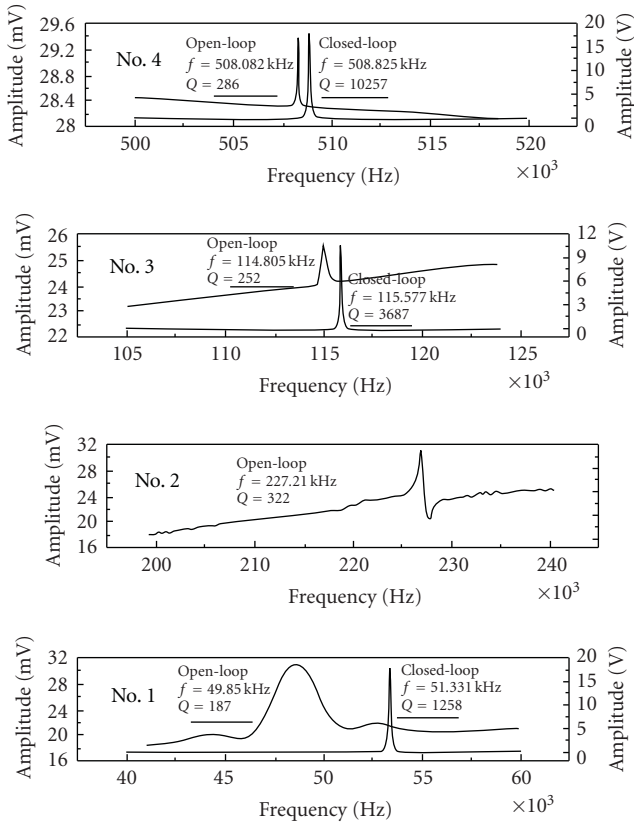


FIGURE 5: Measured amplitude-frequency responses for the 1st and 2nd flexural mode (no. 1 and 2), as well as, the 1st and 2nd torsion modes (no. 3 and 4) of cantilever sensors in the open-loop circuit (on the left side) and the closed-loop circuit (on the right side).

For further comparing the performance among the four types of microcantilever sensors, we implement a biotin-to-avidin specific binding experiment and frequency-shift test. Figure 6 shows the schematic process route for the immobilization of the biotin molecules and specific reaction with the avidin molecules. At first, biotin is anchored onto the Au sensing pads at the cantilever surface. The biotin is immobilized via a thiol-terminated self-assembled molecular layer (SAM). Then, the cantilever is immersed into 0.05 mM solution of Au-particle labeled streptavidin for 20 minutes to complete the biotin-avidin specific hybridization. The tested resonant frequency shift of the cantilevers versus specific biologic hybridization is shown in Figure 7. When

TABLE 2: Measured mass induced frequency shift, mass sensitivity, Allan variance (a standard parameter to evaluate resonant-frequency instability over a certain period of time) and sensing resolution for different modes of the cantilevers. The designed mass sensitivity, the calculated Allan variables based on measured frequency stability, and the finally obtained mass-sensing resolution based on the Allan variables analysis, are all listed for the corresponding cantilevers in corresponding resonant modes.

Cantilever type	No. 1	No. 2	No. 3	No. 4
Δf (Hz)	57.5	591.2	443	2330
Sensitivity (Hz/pg)	0.33	4.3	0.9	5.1
Allan variance	2.1e-6	3.3e-7	7.6e-7	1.8e-7
Mass resolution (fg)	313	29	23	9

the absorbed mass, Δm , is smaller enough compared with the mass of the cantilever, the mass sensing sensitivity can be expressed as

$$S = \frac{\Delta f}{\Delta m} = \frac{1}{2} \frac{f_0}{m_{\text{eff}}}, \quad (1)$$

where Δf is the frequency shift, f_0 is the initiated resonance frequency, and m_{eff} is the effective mass of the cantilever. By using the equation, we can calculate the mass sensitivity of the integrated microcantilever sensors. As shown in Table 2, among the four cantilever sensors, the 2nd torsion-mode cantilever-sensor behaves as the highest frequency change of 2330 Hz. Moreover, a better mass-sensing resolution is obtained for a higher mode cantilever and the 2nd torsion-mode exhibits the best resolution of about 9 fg, that is, almost the mass of a single vaccinia virus. In Table 2, Allan variance values for all the modes are also provided, which is a standard parameter to evaluate resonant-frequency instability over a certain period of time.

4. Trace-Level AFP Detection for Early-Stage Diagnosis of Hepatocellular Carcinoma

The torsion-mode resonant cantilever, which features higher Q -factor value compared to conventional bending resonant mode, is used for trace level biochemical detection. For improving the detection limit, the resonant silicon resonant cantilever with the torsional mode is optimally designed and fabricated. Our experiments have shown that the sensor behaves an ultrasensitive detection capability for alpha-fetoprotein (AFP) antigen [31], which is one of the most

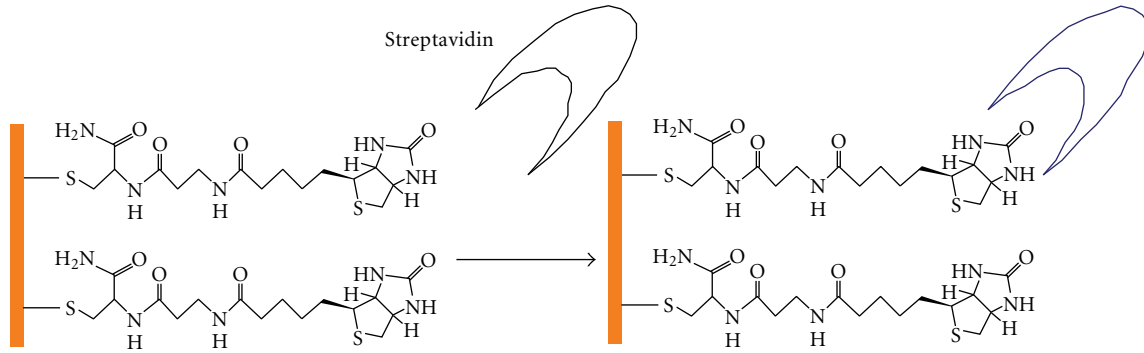


FIGURE 6: Schematic mechanism of the thiol-terminal biotin modified on the Au surface of the cantilever and the specific capture to gold-particle labeled streptavidin.

important tumor markers to indicate hepatocellular carcinoma (HCC) tumor spread and burden, cell differentiation, and aggressive potential [32]. It should be noticed that HCC is the fifth most common cancer worldwide and the third most common cause of cancer-related death, with about 500 000 new cases diagnosed in one year. For the purpose of early stage prognosis, an immunological sensor applied in detection of AFP would better feature the concentration detection limit of less than 10 ng/mL, that is, at ng/mL level [33]. Detailed technical treatments on the cantilever and the sensing experiments will be given in following subsections.

4.1. Immobilization of Self-Assembled Monolayer (SAM) Mediated mIg. To refresh the surface of the two Au sensing pads on the torsion-mode cantilever (see Figure 3(c)), the cantilever is pretreated in Piranha solution and then cleaned with deionized water. Together with the Au sensing pads, the cantilever is immersed in the SAM solution of 11-mercaptoundecanoic acid (MUA) at room temperature. Then the cantilever is sequentially rinsed by ethanol and deionized water. After dried by N_2 gas, the gold sensing surface has been modified by self-assembly of MUA. Before mIg immobilization, the cantilever is activated by DBPH [3,3-dithio-bis (propionic acid N-hydroxysuccinimide ester)] solution at room temperature. The cantilever is rinsed in ethanol and deionized water, then, dried by N_2 gas. Following these pretreatment steps, the cantilever is immersed into mIg solution for 1 hour. Then the cantilever is washed by the phosphate buffer solution of Phosphate Buffer Solution + Tween-20 (PBST) and deionized water. After linked to the Au surface, the mIg is suggested to be immediately used within a short period of time. When the mIg immobilized cantilever is restored under a low temperature of $-20^\circ C$, it can still be used for immunodetection within several days.

4.2. Cantilever Surface Silanization and Avidin Recognition by Specific Reaction with Biotin. A mass adsorption can decrease the resonant frequency of a microcantilever. It means that not only the specific analytes but also other contaminants nonspecifically attached to the cantilever surface can cause the frequency drop. Therefore, the specificity of the reaction

should be enhanced and nonspecific molecular adsorption should be effectively depressed. More importantly, in addition to the influence to mass weighing, the surface nonspecific adsorption can increase the spring constant by stiffening the microcantilever, thereby, inducing an increase in the resonant frequency [34]. We have found that the cantilever-stiffening cross-effect can severely counteract and weaken the specific mass induced frequency-shift signal. The measurement results of the biotin-avidin specific reaction in Figure 8(a) show that the stiffening cross-signal even surpasses the mass signal and the frequency reversely increases. To avoid the cross-effect induced by nonspecific adsorption, we modify the cantilever surface to resist nonspecific protein or other molecule adsorption. Herein polyethylene glycol (PEG) is used as an effective reagent to eliminate unspecific adsorption. Considering that the surface of the microcantilever is silicon (at backside) and silicon dioxide (at front side), PEG is grafted on the cantilever surface with the format of PEG-silane. The detailed processes are given in next paragraph.

After pretreated with H_2O_2/H_2SO_4 solution and sequentially cleaned by ethanol and deionized water, the cantilever is immersed into a biotin-SH solution for 12 hours. After rinsed in ethanol and deionized water, the SiO_2 front side and silicon back side of the cantilever (except for the gold surface at the end pad for specific sensing) are both silanized by PEG-silane solution and cleaned by deionized water. This PEG-silane surface modification is used to effectively depress nonspecific adsorption of protein on the cantilever that can cause cross-talk to the specific reaction signal. The PEG-silane surface modification processes are sketched in Figure 9. After the cantilever is coated with BSA solution and rinsed by PBST/deionized water, the resonant frequency of the sensor is measured by a network analyzer. Then the biotin monolayer on the gold surface reacts with an avidin-Au solution for 30 minutes.

After the cantilever is rinsed by PBST/deionized water and dried by nitrogen gas, the resonant frequency shift is tested. Plotted in Figure 8(b), the testing results show that, with the PEG precoating technique used, the cantilever significantly decrease its resonant frequency according to the adsorbed mass of avidin-Au. This indicates that PEG-silane

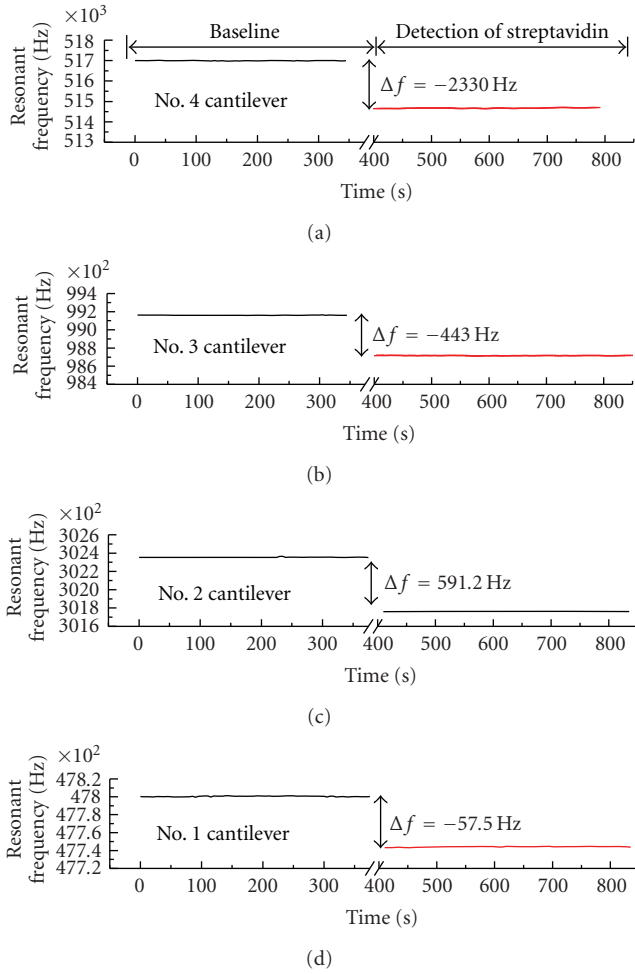


FIGURE 7: From bottom to top, the biotin-avidin specific hybridization induced frequency shifts are tested for the no. 1 cantilever in the 1st flexural mode, the no. 2 cantilever in the 2nd flexural mode, the no. 3 cantilever in the 1st torsional mode, and the no. 4 cantilever in the 2nd torsional mode, respectively.

can effectively resist nonspecific adsorption and improve the reliability of the sensor.

4.3. mIg Line Array Printing for Confirmation of AFP Specific Adsorption. To confirm that the antibody-antigen reaction has completed at the Au surface, monoclonal immunoglobulin (mIg) lines are arrayed on the patterned Au stripes of silicon chips. Since that there are discrete epitopes on the macromolecule outer surface, one macromolecular antigen can react with no less than two antibodies. Therefore, after the mIg captures one epitope of AFP, the other epitopes can be recognized by polyclonal immunoglobulins (pIg). Then the specifically adsorbed pIg is further reacted with the pIg Alkaline phosphatase-immunoglobulin (AP-Ig).

In this experiment, gold thin film stripes are electron-beam evaporated and patterned on a silicon chip whose surface was previously covered with SiO₂ by thermal oxidation. To validate the antibody-antigen specific reaction, the patterned Au stripes are firstly immobilized with mIg

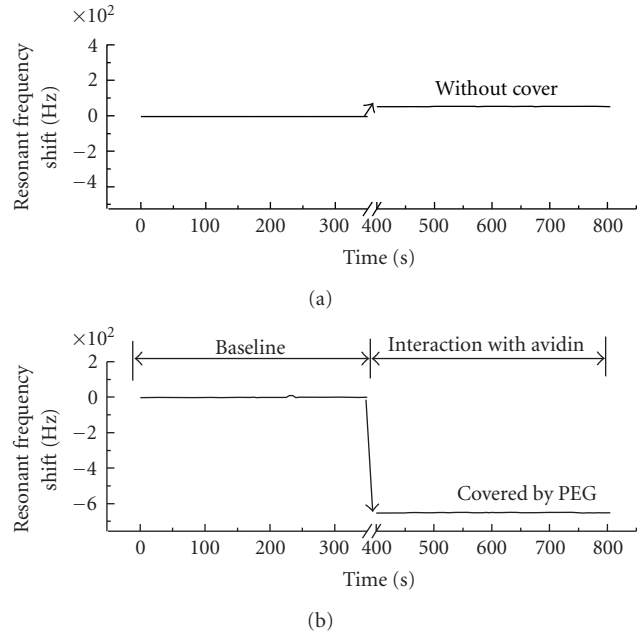


FIGURE 8: Comparison of the tested biotin-to-avidin reaction induced frequency shifts between the cantilever (a) without the PEG modification and (b) with the PEG-silane modification. By the PEG-silane modification method, the suppression of nonspecific adsorption effect on the detection performance is clearly indicated.

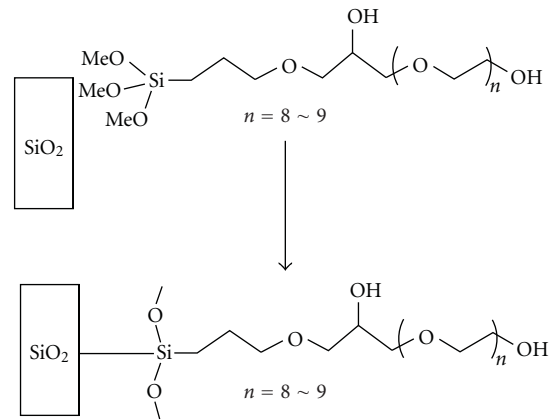


FIGURE 9: Cantilever-surface PEG-silane modification scheme for resisting against nonspecific protein adsorption.

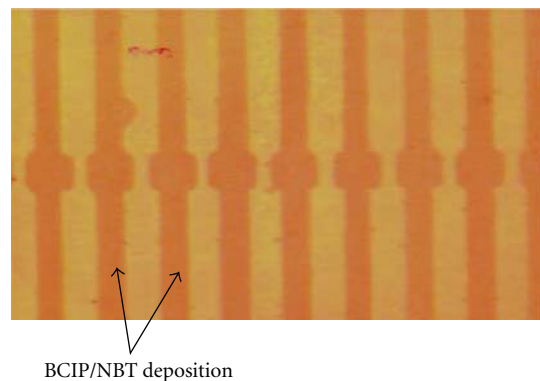


FIGURE 10: Microscope image of the BCIP/NBT deposition pattern.

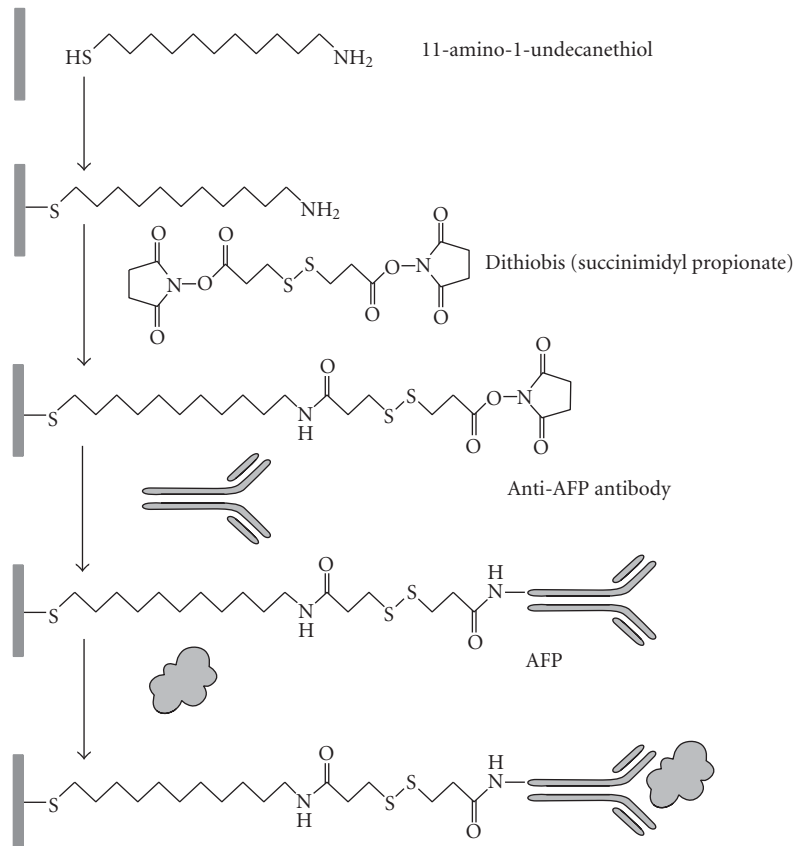


FIGURE 11: Serial immobilization processes of the anti-AFP antibody and the specific detection of AFP on the cantilever surface.

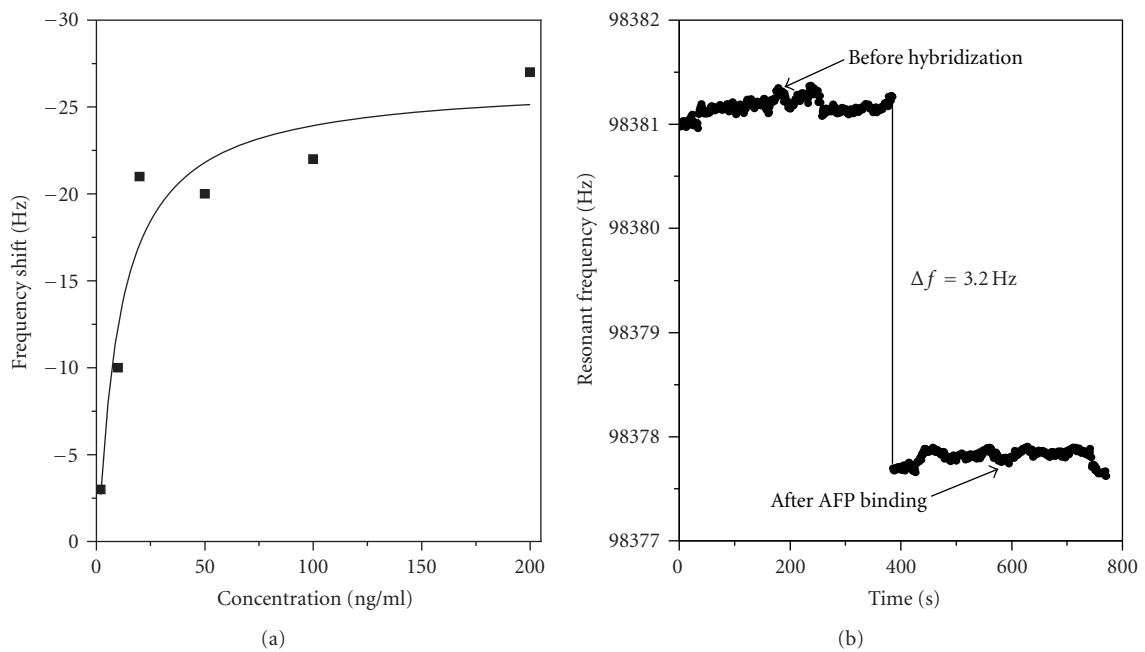


FIGURE 12: AFP testing results with the microcantilever sensor. (a) Sensor response signals in terms of various AFP concentrations. (b) Tested frequency shift for detection of ultralow AFP concentration of 2 ng/mL.

by using the processes described in previous subsection. Then the chip is immersed in bovine serum albumin (BSA) solution and, then, rinsed by PBST. After the Au stripes are coated by BSA, the chip is immersed in the AFP solution for 0.5–1 hour to complete the specific antigen-antibody reaction. Then, the chip is put in a pIg solution for 0.5 hour and washed again by PBST/deionized water. Then it is immersed in a pIg AP-Ig solution for 0.5 hour and washed by PBST/deionized water. Finally, the cantilever is put into the mixing solution of 5-bromo-4-chloro-3-indolyl-phosphate (BCIP) and Nitro-Blue-Tetrazolium (NBT) for 1 hour, and then, cleaned in deionized water and dried by nitrogen gas.

The Alkaline Phosphatase (AP) catalyses the complex of BCIP and NBT, resulting in that a colored deposition is formed on the surface for experimental observation under a microscope. The digital micrograph in Figure 10 shows that the deposition is only formed on the mIg lines, which indicates that the mIg does specifically capture AFP and the antibody-antigen reaction has occurred on the Au surface.

4.4. Recognition of AFP. The cantilever surface is cleaned and pretreated with H_2O_2/H_2SO_4 solution, then rinsed in ethanol/deionized water. After the SAM of MUA is formed on the Au end-pads of the cantilever, the cantilever surface is silanized by PEG-silane. The mIg is immobilized on top of the SAM of MUA. The steps of the mIg immobilization have been described above, thus, are not repeated again. Before measurement of the initial resonant-frequency, the cantilever is coated with BSA solution. Then the cantilever is used to recognize AFP. After the cantilever reacts with AFP of a certain concentration, it is washed by PBST and deionized water. After drying by nitrogen, the frequency shift of the cantilever is measured in lab air. The sequential processes of immobilization of mIg and the specific reaction with AFP are schematically demonstrated in Figure 11.

Prior to the reaction with AFP, the initial frequency of the microcantilevers is measured as the referential frequency. After the specific binding, AFP antigen is absorbed to the Au pads that have been previously immobilized with the anti-AFP antibody. Therefore, the mass addition of the microcantilever decreases the resonant frequency. Figure 12(a) shows the experimentally obtained frequency shifts in terms of various concentrations of AFP solution (i.e., 0 ng/mL, 2 ng/mL, 10 ng/mL, 20 ng/mL, 50 ng/mL, 100 ng/mL, and 200 ng/mL). The detectable concentration of AFP is better than the cut-off value of 15–20 ng/mL, which is widely accepted as one of the indicators of HCC. In the case of no AFP, there is no significant frequency shift. Since that the range of AFP levels for hepatitis patients with or without HCC normally overlaps, the normal referential range of AFP should be lower than 10 ng/mL. The frequency shift in Figure 12(b) indicates that the signal noise limited AFP detecting resolution can be better than 2 ng/mL Phosphate Buffer Solution (PBS) solution, the detection limit of the developed cantilever sensor can be considered at ng/mL level. Therefore, the microcantilevers have the ability to detect HCC at early stage, therefore has the potential to be applied in clinical assay.

5. Conclusions

Resonant microcantilever sensors have been intensively developed in Chinese Academy of Sciences in recent years. The optimization of resonance modes is studied for enhancing the detecting resolution to trace level targeted molecules. Both resonance exciting and signal pick-up elements are integrated in the cantilevers for low-cost portable applications. Multiple and localized self-assembly techniques are developed to enhance sensing specificity and depress cross-talk noise. Ultralow concentration biological detection has been successfully realized that shows great promise in future biomedical applications.

Acknowledgments

This research is supported by the NSFC Project under contract no. 60725414, the Chinese 973 Program (2006CB300405), and Chinese 863 Project (2006AA04Z365). Xinxin Li also appreciates the financial support of the NSFC Project (60721004).

References

- [1] N. V. Lavrik, M. J. Sepaniak, and P. G. Datskos, "Cantilever transducers as a platform for chemical and biology sensors," *Review of Scientific Instruments*, vol. 75, pp. 2229–2253, 2004.
- [2] J. R. Barnes, R. J. Stephenson, M. E. Welland, C. Gerber, and J. K. Gimzewski, "Photothermal spectroscopy with femtojoule sensitivity using a micromechanical device," *Nature*, vol. 372, no. 6501, pp. 79–81, 1994.
- [3] D. R. Baselt, G. U. Lee, K. M. Hansen, L. A. Chrisey, and R. J. Colton, "A high-sensitivity micromachined biosensor," *Proceedings of the IEEE*, vol. 85, no. 4, pp. 672–680, 1997.
- [4] J. Fritz, M. K. Baller, H. P. Lang, et al., "Translating biomolecular recognition into nanomechanics," *Science*, vol. 288, no. 5464, pp. 316–318, 2000.
- [5] T. Thundat, E. Finot, Z. Hu, R. H. Ritchie, G. Wu, and A. Majumdar, "Chemical sensing in Fourier space," *Applied Physics Letters*, vol. 77, no. 24, pp. 4061–4063, 2000.
- [6] A. Boisen, J. Thaysen, H. Jensenius, and O. Hansen, "Environmental sensors based on micromachined cantilevers with integrated read-out," *Ultramicroscopy*, vol. 82, no. 1–4, pp. 11–16, 2000.
- [7] T. Thundat, E. A. Wachter, S. L. Sharp, and R. J. Warmack, "Detection of mercury vapor using resonating microcantilevers," *Applied Physics Letters*, vol. 66, pp. 1695–1697, 1995.
- [8] B. Ilic, D. Czaplewski, M. Zalalutdinov, et al., "Single cell detection with micromechanical oscillators," *Journal of Vacuum Science and Technology B*, vol. 19, no. 6, pp. 2825–2828, 2001.
- [9] A. Gupta, D. Akin, and R. Bashir, "Single virus particle mass detection using microresonators with nanoscale thickness," *Applied Physics Letters*, vol. 84, no. 11, pp. 1976–1978, 2004.
- [10] T. Ono, X. Li, H. Miyashita, and M. Esashi, "Mass sensing of adsorbed molecules in sub-picogram sample with ultrathin silicon resonator," *Review of Scientific Instruments*, vol. 74, no. 3, pp. 1240–1243, 2003.
- [11] K. L. Ekinci, X. M. H. Huang, and M. L. Roukes, "Ultrasensitive nanoelectromechanical mass detection," *Applied Physics Letters*, vol. 84, no. 22, pp. 4469–4471, 2004.

- [12] Z. Djurić, "Mechanisms of noise sources in microelectromechanical systems," *Microelectronics Reliability*, vol. 40, no. 6, pp. 919–932, 1999.
- [13] C. Hagleitner, A. Hierlemann, D. Lange, et al., "Smart single-chip gas sensor microsystem," *Nature*, vol. 414, no. 6861, pp. 293–296, 2001.
- [14] E. Forsen, G. Abadal, S. Ghatnekar-Nilsson, et al., "Ultrasensitive mass sensor fully integrated with complementary metal-oxide-semiconductor circuitry," *Applied Physics Letters*, vol. 87, no. 4, Article ID 043507, 3 pages, 2005.
- [15] R. Berger, E. Delamarche, H. P. Lang, et al., "Surface stress in the self-assembly of alkanethiols on gold," *Science*, vol. 276, no. 5321, pp. 2021–2024, 1997.
- [16] T. Thundat, R. J. Warmack, G. Y. Chen, and D. P. Allison, "Thermal and ambient-induced deflections of scanning force microscope cantilevers," *Applied Physics Letters*, vol. 64, no. 21, pp. 2894–2896, 1994.
- [17] M. Tortonese, R. C. Barrett, and C. F. Quate, "Atomic resolution with an atomic force microscope using piezoresistive detection," *Applied Physics Letters*, vol. 62, no. 8, pp. 834–836, 1993.
- [18] J. Thaysen, A. Boisen, O. Hansen, and S. Bouwstra, "Atomic force microscopy probe with piezoresistive read-out and a highly symmetrical Wheatstone bridge arrangement," *Sensors and Actuators A*, vol. 83, no. 1, pp. 47–53, 2000.
- [19] P. A. Rasmussen, J. Thaysen, S. Bouwstra, and A. Boisen, "Modular design of AFM probe with sputtered silicon tip," *Sensors and Actuators A*, vol. 92, no. 1–3, pp. 96–101, 2001.
- [20] A. Kooser, R. L. Gunter, W. D. Delinger, T. L. Porter, and M. P. Eastman, "Gas sensing using embedded piezoresistive microcantilever sensors," *Sensors and Actuators B*, vol. 99, no. 2–3, pp. 474–479, 2004.
- [21] H. Jensenius, J. Thaysen, A. A. Rasmussen, L. H. Veje, O. Hansen, and A. Boisen, "A microcantilever-based alcohol vapor sensor-application and response model," *Applied Physics Letters*, vol. 76, no. 18, pp. 2615–2617, 2000.
- [22] L. A. Pinnaduwege, D. L. Hedden, A. Gehl, et al., "A sensitive, handheld vapor sensor based on microcantilevers," *Review of Scientific Instruments*, vol. 75, no. 11, pp. 4554–4557, 2004.
- [23] M. H. Bao, "Micro mechanical transducer," in *Handbook of Sensors and Actuators*, S. Middelhoek, Ed., Elsevier, Amsterdam, The Netherlands, 2000.
- [24] D. Jin, X. Li, H. Bao, et al., "Integrated cantilever sensors with a torsional resonance mode for ultrasensitive on-the-spot bio/chemical detection," *Applied Physics Letters*, vol. 90, no. 4, Article ID 041901, 2007.
- [25] D. Jin, X. Li, J. Liu, et al., "High-mode resonant piezoresistive cantilever sensors for tens-femtogram resolvable mass sensing in air," *Journal of Micromechanics and Microengineering*, vol. 16, no. 5, pp. 1017–1023, 2006.
- [26] T. R. Albrecht, P. Grütter, D. Horne, and D. Rugar, "Frequency modulation detection using high-Q cantilevers for enhanced force microscope sensitivity," *Journal of Applied Physics*, vol. 69, no. 2, pp. 668–673, 1991.
- [27] P. S. Waggoner and H. G. Craighead, "Micro- and nanomechanical sensors for environmental, chemical, and biological detection," *Lab on a Chip*, vol. 7, no. 10, pp. 1238–1255, 2007.
- [28] T. Kunstmann, A. Schlarb, M. Fendrich, D. Paulkowski, Th. Wagner, and R. Möller, "Combined normal and torsional mode in frequency-modulation atomic force microscopy for lateral dissipation measurement," *Applied Physics Letters*, vol. 88, no. 15, Article ID 153112, 2006.
- [29] X. Xia and X. Li, "Resonance-mode effect on microcantilever mass-sensing performance in air," *Review of Scientific Instruments*, vol. 79, no. 7, Article ID 074301, 2008.
- [30] X. Xia, Z. Zhang, and X. Li, "A Latin-cross-shaped integrated resonant cantilever with second torsion-mode resonance for ultra-resolvable bio-mass sensing," *Journal of Micromechanics and Microengineering*, vol. 18, no. 3, Article ID 035028, 2008.
- [31] Z. Zhang, H. Bao, H. Yu, and X. Li, "Ng/ml-level alpha-fetoprotein immunodetection with torsion-mode cantilever sensors for early-stage hepatocellular carcinoma diagnosis," in *Proceedings of the 14th International Conference on Solid-State Sensors, Actuators and Microsystems (TRANSDUCERS '07)*, pp. 1785–1788, Lyon, France, June 2007.
- [32] L. Zhou, J. Liu, and F. Luo, "Serum tumor markers for detection of hepatocellular carcinoma," *World Journal of Gastroenterology*, vol. 12, no. 8, pp. 1175–1181, 2006.
- [33] B. J. McMahon, L. Bulkow, A. Harpster, et al., "Screening for hepatocellular carcinoma in Alaska natives infected with chronic hepatitis B: a 16-year population-based study," *Hepatology*, vol. 32, no. 4, pp. 842–846, 2000.
- [34] G. Y. Chen, T. Thundat, E. A. Wachter, and R. J. Warmack, "Adsorption-induced surface stress and its effects on resonance frequency of microcantilevers," *Journal of Applied Physics*, vol. 77, no. 8, pp. 3618–3622, 1995.

Review Article

On Mass Loading and Dissipation Measured with Acoustic Wave Sensors: A Review

Marina V. Voinova

Department of Physics, University of Gothenburg, 412 96 Göteborg, Sweden

Correspondence should be addressed to Marina V. Voinova, marina.voinova@physics.gu.se

Received 31 December 2008; Accepted 18 April 2009

Recommended by Michele Penza

We summarize current trends in the analysis of physical properties (surface mass density, viscosity, elasticity, friction, and charge) of various thin films measured with a solid-state sensor oscillating in a gaseous or liquid environment. We cover three different types of mechanically oscillating sensors: the quartz crystal microbalance with dissipation (QCM-D) monitoring, surface acoustic wave (SAW), resonators and magnetoelastic sensors (MESs). The fourth class of novel acoustic wave (AW) mass sensors, namely thin-film bulk acoustic resonators (TFBARs) on vibrating membranes is discussed in brief. The paper contains a survey of theoretical results and practical applications of the sensors and includes a comprehensive bibliography.

Copyright © 2009 Marina V. Voinova. This is an open access article distributed under the Creative Commons Attribution License, which permits unrestricted use, distribution, and reproduction in any medium, provided the original work is properly cited.

1. Introduction

This paper introduces readers to microelectronic sensor devices based on surface acoustic waves (SAWs-sensors, Section 2) and on bulk acoustic waves (BAWs-sensors, QCM, Section 4, and thin-film bulk acoustic resonators (TFBARs, Section 5), addressing their physical principles, theory, and selected examples of practical applications. In the third section, we consider the magnetic analogue of SAW resonators, the so-called magnetoelastic sensors (MESs), ribbon-like oscillators that can be successfully used for remote query sensing of (bio)chemical or environmental changes. The fifth section with a brief discussion of a novel TFBAR technique concludes the first part of the paper. In the second part we provide selected examples of chemical and biological applications of the AW-based sensors and conclude with the outlook.

The mechanically oscillating sensors (or acoustic wave (AW) resonators) are commonly used for monitoring a negligible amount of surface mass. Also, AW devices enable researchers to measure other physical parameters such as thickness, viscosity, elasticity, and effects of roughness/sliding friction on thin films of different nature.

The main progress has been made in studying adsorbed molecular films, thin polymer films, and bioorganic layers on

surfaces. Successful characterization of biomolecular systems in their natural aqueous environment is the important objective of biosensing. The quartz crystal microbalance (QCM) and surface acoustic wave (SAW) sensors, which can operate in fluids, straightforwardly offer such a possibility. A polymer coated or biochemically modified sensor surface forms a “tolerant” biological interface which is available for further mounting of biomolecular complexes exposed to water solution. Biosensor systems based on functionalized QCM and SAW devices have become a suitable tool for in situ measurements in biofluids, in particular, for on-line detection of immunological reactions. The vast literature on SAW and QCM experiments and theory reveals a strong and continuous interest in this topic.

A special type of quartz resonator, the so-called electrochemical QCM (EQCM), is a sensor enabling detection of chemical parameters via electrical conductivity measurements both in the gaseous phase, vapours, and in various liquids. Typically EQCM is based on usage of electroconducting polymer arrays as a smart coating of the sensor surface.

Particular attention is focused now on biosensors and bioelectronics, biomedical and environmental applications of the AW sensors. A brief overview of the biology-related achievements is given in Section 6 (Chemical and Life Science Applications).

New developments are coming now due to the rise of governmental and public interest to the terrestrial ecology and extraterrestrial research. A great benefit of the quartz oscillators is that their operation is gravity independent so they can be successfully used in space exploration research [1–3]. “The most widely used complex measuring instrument in science is still the balance.” (NASA, <http://trs-new.jpl.nasa.gov/dspace/handle/2014/39937>.) QCM-based sensors are planned to be used [4] during The European ExoMars Rover Mission, which is prepared by ESA for a launch in 2009 and is devoted to the “search for life or traces of it, and of water, as a precondition for the existence of highly complex organisms.” (ESA MISSION, <http://www.esa.int/SPECIALS/ExoMars/SEM10VLPQ5F.0.html>.)

Another challenge is to use the quartz sensors for ecosystem observations and pollution control [5]. Terrestrial and marine applications of the QCM include coastal developments [6], aquatic microbial probes [7], studies of the ocean bio-foul [8], and safety and security [9].

For the convenience of reading, we organized the paper in the following way. Each chapter contains brief information about the basic principles, theory, and applications of the AW devices of a particular type. A special chapter on chemical and life science applications contains illustrations and basic principles of surface nanocomposite functionalization of AW sensors. The references are placed at the end of the paper. The list of companies that manufacture acoustic sensors of each type is appended after the list of references (see Appendix 6.4).

1.1. Physical Principles of Acoustic Wave (AW) Sensors. A biosensor device can be defined as an analytical microelectronic device either based on a combination of biomolecular sensor elements and a solid state transducer or applied to living organisms to monitor biological and biochemical processes in there [10]. Biocomponents conjugated with a solid state transducer provide a high selectivity to chemical analytes to such a hybrid device while the transducer element (e.g., metal electrode) can measure with a high precision and then convert the input chemical information into a digital electronic signal. In biosensors, common transducers are amperometric, potentiometric, and conductometric devices, optical sensors, thermal detectors, and acoustic sensors.

An acoustic biosensor is a type of a sensor device, where the transducer element is based on a solid slab of piezoelectric material that can generate acoustic waves in the sensor’s substrate. The most popular material for the acoustic sensor substrate is a quartz crystal cut in specific crystallographic directions (the so-called AT-cut and ST-cut quartz plates) so that the angle of the plate in the quartz crystal supports a shear deformation. We consider two different types of piezoelectric resonators, namely, bulk acoustic waves (BAWs) sensors based on a thickness shear vibration mode for AT-cut quartz and surface acoustic waves (SAWs) devices with a shear horizontal (SH) mode for ST-cut quartz and Rayleigh surface wave (RSAW) sensors.

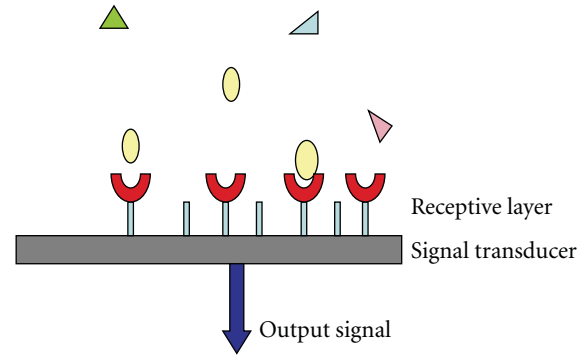


FIGURE 1: Principle of biosensor construction. Typically a biosensor device consists of a sensitive biomolecular layer (grafted polymers, supported membranes, bioreceptors, nucleic acids, enzymes or antibodies) immobilized onto the surface of solid substrate (transducer) that can measure the output signal (e.g., electrical catalytic current in enzyme-based biosensors, mass changes in acoustical piezoelectric resonators, etc.).

These devices are widely used now not only in a gas but also in liquid environments, in particular for biomolecular detection in biological fluids and immunosensor applications. In parallel with quartz resonators, we discuss two novel types of AW devices, namely, silicon-based resonators, (TFBARs) and magnetoelastic ribbon-based sensors (MESs) that recently received considerable attention for acoustic sensor technology.

The sensitivity of the acoustic sensor is proportional to the energy in the propagation path. In the bulk acoustic wave mode of propagation, the energy disperses from the oscillating surface of the transducer through the coating material. The ratio between the energy dissipated during one period of oscillation and the energy stored in the oscillating system determines the quality factor (Q-factor) of the resonator, an important characteristic of the device. In surface acoustic wave sensors, the energy is trapped near the oscillator surface, which increases the sensitivity of the device in measurements of the surface mass of thin films (see Section 2, in particular, Section 2.2).

2. Surface Acoustic Waves Sensors

2.1. Surface Acoustic Wave (SAW) Resonators: SH-SSW and RSAW. Primarily, surface acoustic wave (SAW) sensors have been designed and used for the detection of (toxic) chemical components in the gaseous phase. In the latest developments many research groups have used SAW-based devices for biological sensing in liquid environments as well.

The last two decades of intensive experimental efforts in the field of SAW-based biosensors include the design and fabrication of horizontally polarized shear waves- (SH SAW-) based devices, Love wave sensors, and Rayleigh-type surface acoustic wave sensors (RSAW), mass-sensitive devices operating in the high frequency range between 100 MHz and a few GHz. The usage of interdigital transducers (IDT) for the generation and detection of surface acoustic waves allows a

strong confinement of the acoustic energy to the surface of the piezoelectric slab regardless of its thickness [11]. Due to this confinement, the shift in acoustic wave velocity ΔV due to the surface mass change is very sensitive to the variations in viscosity, elasticity and electrical conductivity of the deposited layer. SAW-based sensors are widely used for detecting gases and volatile compounds. In liquids, after coating with layers of surface bound receptive layers (such as adsorbed antibodies or covalently bound hydrogel bound layers), these sensors can be used as biosensors by themselves or can be integrated with microfluidic systems [1, 12]. The interested readers can find further information on the latest technical developments in SAW biosensors in the excellent review by Lange et al. [13] and in the valuable product review article by Harris [9].

2.2. Love Wave Sensors. Surface waves on plane interfaces have amplitude which decays exponentially with the normal distance from the solid surface on which they propagate [14]. The so-called Love waves are of special interest for the SAW design. The related physical effect was originally discovered by Love. (A.E.H. Love. *Some Problems of Geodynamics* Cambridge University Press, Cambridge (1911).) He observed an effect caused by earthquake waves far from the epicenter due to the lower acoustic wave velocity of waves propagating along the stratified geological layers. Love wave device, a type of SH SAW sensors, is based on the finding that losses of acoustic energy to the bulk substrate can be drastically reduced by a resonating surface bound layer. Simultaneously, an acoustic bound layer resonance leads to a higher sensitivity of the sensor to surface mass. A Love-wave resonance is excited when the layer has optimal thickness and appropriate material parameters [11, 13]. polymethyl methacrylate (PMMA) coating was found a suitable wave-guiding material for these purposes. The first Love wave biosensor on PMMA-on-quartz-crystal was reported by Gizeli et al. [15]. PMMA served as a host matrix enabling a further mounting, for example, a coating with additional gold film, followed by thiol SAM- or a peptide layer deposition.

Two different types of biosensors based on Love wave devices are presented in [12, 16–18]; see also papers [11, 13] for a review.

2.3. SH SAW Sensors. The SH SAW sensors can be constructed on coated piezoelectric substrates like quartz, lithium niobate and lithium tantalate cut in a special way (e.g., Figure 2, shows the Y-cut X propagating lithium tantalate substrate. Two acoustic modes are excited by the electrodes in this crystalline direction). The phase velocity of surface shear waves, V , is lower than that of bulk shear waves, V_0 in the semi-infinite elastic half-space (i.e., the substrate). This difference in phase velocity can be monitored with high accuracy in SAW devices. Sensitive coating with polymer films results in the observation of resonant conditions in both modes as the layer thickness is increased. The shift in phase velocity $\Delta V = V - V_0$ and the damping coefficient Γ , simply the imaginary part of the SAW wave vector q , depend

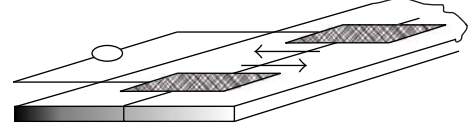


FIGURE 2: Sketch of the geometry of an SH SSW-based sensor.

on the surface mass and mechanical parameters of the layer coating the oscillator's surface.

From the analysis of the dispersion equation at no-slip boundary conditions between the coating thin layer and the resonator surface, one can find for the phase velocity shift and for the damping coefficient of the resonator the following expressions:

$$\begin{aligned} \frac{\Delta V}{V} &\approx 2 \left(\frac{\omega \rho_s}{V_0 \rho_0} \right)^2, \\ V_0 &= \sqrt{C_{44}/\rho_0} = \text{const}, \\ \Gamma &= \frac{q_0 \omega^3 \rho \eta}{\mu_0}. \end{aligned} \quad (1)$$

Here ρ_0 is the density of the crystal substrate, μ_0 is the elastic shear modulus of the substrate, ω is the oscillator frequency, $\rho_s \equiv \rho h$ is the surface mass of the thin coating film, and ρ , η , and h denote the film density, shear viscosity and thickness, respectively. In fact, the no-slip condition, for example, when the LB film is covalently bound to the substrate, corresponds to the Love wave polarization.

The coating film in biological applications can be a protein adsorbed layer, Langmuir-Blodgett film or supported lipid membrane. In the case of a double layer coating with different surface densities of the sublayers, (1) can be generalized to [19]

$$\frac{\Delta V}{V} \approx \frac{1}{2} \left(\frac{\omega \rho_s}{V_0 \rho_0} \right)^2 \left(1 + \frac{\rho_{s1}}{\rho_{s2}} \right)^2. \quad (2)$$

Here ρ_{s1}, ρ_{s2} values represent the surface density of the sublayers in the film. The result for the damping coefficient for the thin bilayer coating is given by the formula [19]

$$\Gamma = \Gamma_{\text{monolayer}} \left\{ 1 + \frac{\eta_{2s}}{\eta_{1s}} \left(1 + \frac{\eta_{1s} \rho_{1s}}{\eta_{2s} \rho_{2s}} \left(1 + \frac{\eta_{2s}}{\eta_{1s}} \right) \right) \right\}. \quad (3)$$

The surface mass and viscosity effects in biomolecular films can be measured also in other types of acoustic experiments, using the so-called bulk acoustic waves, or the BAW mode of propagation.

2.4. Rayleigh Surface Acoustic Wave (RSAW) Sensors. RSAW-based devices as it follows from their name are based on Rayleigh wave polarization. The analysis of the dispersion equation for the Rayleigh wave polarization in the limit of strong coupling between a surface bound layer and a solid substrate and when only mass loading is taken into account gives the following formula for the change ΔV of

the Rayleigh wave velocity V_R due to the presence of surface bound layer ρ_S :

$$\frac{\Delta V}{V_R} = k \frac{\rho_S}{\rho} \left(\frac{V_R}{c_t} \right)^2. \quad (4)$$

This result has been corrected for soft layers by accounting for the elastic moduli of the layer material (this correction for the Rayleigh polarization has been reported elsewhere [20]).

The first experimental realization of RSAW-based biosensors has been reported by Wohltjen and Dessy in 1979 [21]. The interested readers can find an account of later RSAW developments in gas sensing [22–24] and biosensors in [25] and in the extensive review by Lange et al. [13] (see also the outlook section, for microfluidic applications [26–29]).

3. Magnetoelastic Sensors (MESs)

Magnetoelastic ribbon-like oscillators are considered as the magnetic analogue of surface acoustic wave sensors [30–44]. Typically, they are made of amorphous

iron- or nickel-based “ribbons” (or thick films) such as Metglas (means metallic glass) (Allied Signal Corporation, Honeywell, <http://www51.honeywell.com/honeywell/>), a novel type of magnetostrictive materials (Figure 3). The big advantage of ferromagnetic magnetostrictive ribbons is the small size (5.0 cm \times 1.0 cm \times 30 μ m) of the strips and the low materials cost making this microsensor technology suitable for in situ measurements of chemical agents and contaminants in various media. In such magnetoelastic sensors (MESs) the longitudinal elastic standing waves are excited by an ac magnetic field at the mechanical resonance frequency when the conversion of the magnetic energy into elastic energy is at maximum [30].

Magnetoelastic thick film sensors also have the important advantage of enabling wireless operation and monitoring and are important new tools in sensing and biosensing [31–44].

The fundamental resonance frequency of a ribbon-like MES is given by

$$f_0 = \frac{1}{L} \sqrt{\frac{E}{\rho}}. \quad (5)$$

Here L is the ribbon length, E is the Young’s modulus, and ρ is the ribbon material density.

For a small mass gain attached to the one side of the oscillator, the resonance frequency change is equal to

$$\Delta f = f - f_0 = -f_0 \frac{\Delta m_S}{2M}. \quad (6)$$

Taking into account the elastic stress in the case of a uniform coating film, the ratio of the measured frequencies before and after the coating application is given by the formula [31]

$$\frac{f}{f_0} = \sqrt{\frac{M}{m_{\text{tot}}} + \left(1 - \frac{M}{m_{\text{tot}}}\right) \frac{E_f/\rho_f}{E/\rho}}, \quad (7)$$

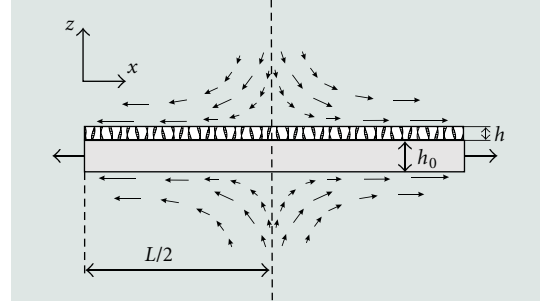


FIGURE 3: Sketch of a magnetoelastic sensor. A schematic (cross-sectional) illustration of longitudinal vibrations of a ribbon-like elastic plate coated with an organic layer and immersed into a bulk viscous liquid. The geometry of the system is shown directly on the figure body (picture is taken from [45]).

where the index “ f ” corresponds to the film parameters, M is the mass of the sensor, and m_{tot} is the total mass after coating.

Formula (7) enables us to deduce the film elasticity E_f from experimental data in gas or vacuum. In bulk liquid measurements, the change in resonance frequency of the magnetoelastic ribbon of density ρ and thickness d is proportional to the square root of the product of the density ρ_l and the shear viscosity η of the liquid [31, 32]:

$$\Delta f = -\frac{\sqrt{\pi f_0}}{2\pi \rho d} \sqrt{\eta \rho_l}. \quad (8)$$

The quality factor Q for low viscosity liquids is related to the damping and has the same form as the expression for the Q -factor for QCM resonators, namely

$$\frac{1}{Q} = \frac{1}{Q_0} + \frac{1}{\rho d \sqrt{\pi f_0}} \sqrt{\eta \rho_l}. \quad (9)$$

The expressions (8) and (9) give a correct result only in the case of an ideally smooth oscillator surface. The correction for the roughness which increases the viscous damping contribution has been published elsewhere [32]. Another correction factor is attributed to the effects of geometry that has been recently found in [45].

Among chemical and biomedical applications of wireless MES one can mention the remote query environmental monitoring [30, 33, 34, 42], bloodstream chemistry [38, 44], safety [39], bioaffinity detection [40], and many others.

Future developments in this field include in situ and in vivo experiments for example, gastric pH monitoring through the digestive tract [36] or measurements of enzymatic reactions in tissues and organs [37].

4. Bulk Acoustic Waves Resonators

4.1. *The Quartz Crystal Microbalance with Dissipation (QCM-D) Monitoring.* In addition to “genuine” surface waves, another type of shear waves can propagate in the plane of an overlayer-substrate interface. These are bulk acoustic waves (BAWs).

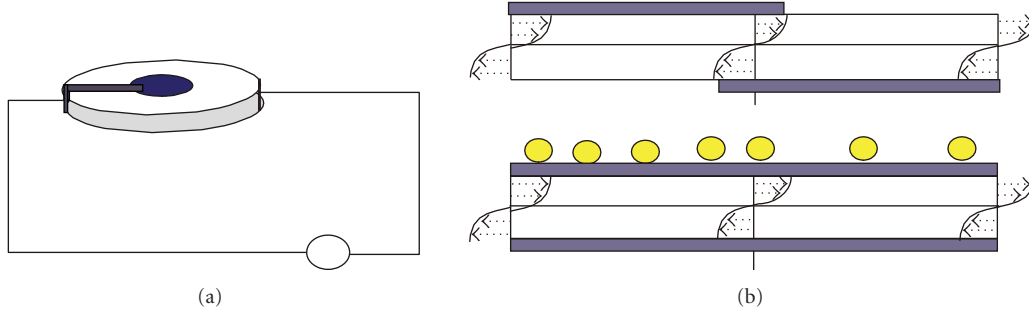


FIGURE 4: Sketch of a quartz crystal resonator: (a) schematic depiction of a quartz disk with deposited electrodes; (b) side view of the resonator; shear deformation produced by the electric field. This type of acoustic sensor operates in a BAW mode, when acoustic shear waves propagate in the direction normal to the quartz plane.

The acoustic BAW-based sensor shown in Figure 4 consists of a thin disk of AT-cut quartz crystal plate with metal (typically, gold) electrodes deposited on either side. When driven electrically to resonate, the crystal produces shear mechanical stress, acoustic shear waves which propagate out from the crystal faces. The fundamental frequency of the device in vacuum is given by formula

$$f_0 = \frac{1}{2h_0} \sqrt{\frac{\mu_0}{\rho_0}}, \quad (10)$$

where h_0 is the thickness of the quartz plate, ρ_0 is its density, and μ_0 is the shear elastic modulus of quartz (e.g., the fundamental resonance of a quartz oscillator is 5 MHz for a 0.33 mm crystal).

It has been found that the resonant frequency of such quartz plates decreases when its surface is coated with an overlayer constituting a mass load. The experimental fact that the changes of the surface mass are proportional to the shift of the crystal resonant frequency is the fundamental operational principle of quartz crystal microbalance (QCM).

Quartz crystal microbalance (QCM) is a thickness shear mode resonator which fundamental frequency is sensitive for even negligible changes in its surface mass ΔM (a microbalance principle of operation). For a small amount of mass deposited onto the QCM surface, the shift of resonance frequency is proportional to the surface mass ΔM of the deposit (Sauerbrey, 1959) [46]:

$$\frac{\Delta f}{f_0} \approx -\frac{\Delta M}{m_0}. \quad (11)$$

Equation (11), known as Sauerbrey's formula for the decrease of the resonance frequency, can only be used for thin films rigidly attached to the QCM surface.

When one face of the device is brought into contact with an aqueous solution, the shear waves are strongly absorbed within a few microns of the surface. The crystal detects changes in viscosity and density in this region by monitoring the change in its resonance frequency and damping due to the viscous dissipation in the overlayer. Experimentally, it is

convenient to obtain this viscous dissipation as the width of the resonant frequency or as the dissipation factor D [47–52]:

$$D = \frac{E_{\text{dissipated}}}{2\pi E_{\text{stored}}} = \frac{1}{\pi f \tau}. \quad (12)$$

Here, τ is the time constant for the decay of the vibration amplitude, the dissipation factor value is equal to the reciprocal quality factor Q .

When the rigid film is replaced by a Newtonian bulk liquid of shear viscosity η , the QCM resonant frequency shift is given by the following expression (Kanazawa and Gordon, 1985, [51]):

$$\Delta f \approx -\frac{1}{2\pi m_0} \sqrt{\frac{\rho \eta \omega}{2}}, \quad (13)$$

so the total response Δf for the system of a QCM rigid film-immersed-in-water is the sum of contributions from the film surface mass (11) and from the viscous contribution of water (13). However, a theoretical analysis shows that for nonrigid deposits this result is not valid. It was found that the viscous loss of energy in the overlayers causes the deviation from ideal behaviour and results in a nontrivial reduction in measured surface mass of the film, $M_s = M(1 - \alpha)$, where M is the “true” film mass and the viscous correction factor α depends on the mechanical properties of both the overlayer material and of the aqueous solution η , ρ . This reduction in resonance frequency has been predicted for the first time for the special case of viscous membrane bilayers [19]. Meanwhile, this result has been generalized for the case of arbitrary soft (viscoelastic) deposits [53]. For soft deposits, it was found that the reduction in liquid phase QCM measurements of surface mass M_s , comparing with the “true” mass M of the film is:

$$M_s = M \left\{ 1 - \frac{\eta_2 \rho_2 \omega}{\rho_1} \frac{G'}{G'^2 + G''^2} \right\}, \quad M = \rho_1 h_1. \quad (14)$$

Here G' is the storage modulus and G'' is the loss modulus of the soft (viscoelastic) overlayer, index “1” denotes the film properties, and index “2” corresponds to the liquid phase, respectively.

4.2. *Viscoelasticity of Polymeric Overlayers: Voight (Viscoelastic Solid) Model.* For the QCM-D characterization of macromolecular multilayer assemblies such as polymer “brush” films, adsorbed protein layers, or tethered supported membranes the mechanical properties of a viscoelastic material must be taken into account (for review, see, e.g., Johannmann’s paper [49]). A big family of polymeric coatings which conserve their shape and do not flow is well described by homogenous layers of Voight viscoelastic solids (a model element with parallel arrangement of a spring (for elasticity) and a dashpot (for viscous damping)). Even this relatively simple theoretical model has allowed us to demonstrate the most important consequences of adsorbate viscoelasticity [54] in terms of a deviation from the Sauerbrey relation relevant for a gas environment and ultrathin layers.

For the QCM operating in a gas phase or vacuum, it has been found that for the no-slip boundary conditions and in special case of thin soft overlayer:

$$\Delta f \approx -\frac{1}{2\pi\rho_0 h_0} h p \omega \left(1 + \frac{2h^2}{3\delta^2(1+\chi^2)} \right), \quad (15)$$

$$\Delta D \approx \frac{2h^3 \rho \omega}{3\pi f \rho_0 h_0} \frac{1}{\delta^2(1+\chi^2)},$$

$$\chi = \mu/\eta\omega, \quad (16)$$

$$\delta = \sqrt{\frac{2\eta}{\rho\omega}}.$$

In the case of a viscoelastic bilayer under a bulk layer of Newtonian liquid (index “B”), the calculated QCM response is given by the formulae:

$$\Delta f \approx -\frac{1}{2\pi f \rho_0 h_0} \left\{ \frac{\eta_B}{\delta_B} + \sum_{i=1,2} \left[h_i \rho_i \omega - 2h_i \left(\frac{\eta_B}{\delta_B} \right)^2 \frac{\eta_i \omega^2}{\mu_i^2 + \omega^2 \eta_i^2} \right] \right\}, \quad (17)$$

$$\Delta D \approx \frac{1}{\pi f \rho_0 h_0} \left\{ \frac{\eta_B}{\delta_B} + \sum_{i=1,2} \left[2h_i \left(\frac{\eta_B}{\delta_B} \right)^2 \frac{\mu_i \omega}{\mu_i^2 + \omega^2 \eta_i^2} \right] \right\}. \quad (18)$$

Formulae (15)–(18) the primary result of our early work [54]. The results of the theory can be applied for an analysis of QCM-D acoustic measurements of surface densities and/or shear viscosity and elasticity for thin polymeric coatings, adsorbed layer of proteins, or supported membranes after the transferring onto the solid substrate and in both the liquid and gaseous experimental conditions (Q-Sense). Also, the results are useful for understanding the shear response of biological bilayer membranes with a different composition of upper and lower monolayers corresponding to the observed compositional asymmetry of red blood cell membranes supported by an elastic substrate (protein network), bioaffinity measurements, immunological reactions, diatoms adhesion, and many others (see for review, [55–61]).

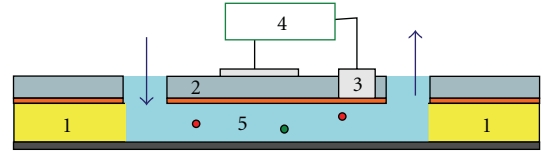


FIGURE 5: Sketch of the TFBAR structure in contact with liquid: 1-Si wafers, 2-AlN piezoelectric layer (aluminium nitride) piezoelectric layer, 3-Al electrodes, 4-analyzer, 5-liquid in a microfluidic system in contact with the resonator (for review, see [68]).

4.3. *QCM as a Mechanical Spectroscopy Tool.* The quartz crystal microbalance can naturally be considered as a mechanical spectroscopy tool which can monitor the viscoelastic material properties by probing samples performing small-amplitude oscillations at prescribed frequency ω [62]. Several groups have reported on the application of the QCM to the viscoelastic characterization of thin organic overlayers in a frequency range from a few Hz to about 100 MHz (for a review, see [49] and references therein). In particular, as a mechanical spectroscopy tool, the quartz crystal resonator can probe the storage and loss moduli of a thin soft polymeric sample such as adsorbed biomolecular layers, polymer cushions or liquid crystalline polymers in small amplitude oscillations where polymer materials exhibit linear viscoelasticity [62]. The experiments with thin films are of particular interest from the point of view of surface science since the viscoelastic moduli of a thin layer sample can sufficiently differ from the corresponding bulk magnitude.

5. Thin-Film Bulk Acoustic Resonators

Thin-film bulk acoustic resonators (TFBARs) are based on a vibrating small solid membrane that is fabricated onto a silicon substrate that can be functionalized with a sensing nanocomposite coating [63, 64] (Figure 5). TFBARs have attracted experimental attention since this novel technique is a high-Q-factor wireless system operating in the microwave region from 1 to 10 GHz [65–69]. This type of resonators meets the requirement for low-cost and small size sensors with the benefit of a high working frequency in comparison with similar SAW-based devices. The main progress in TFBARs has been triggered by FBAR filters applications for the telecom industry, particularly, in mobile phones [66–68].

Silicon-based TFBARs can be considered as a high-frequency version of the quartz crystal microbalance [64].

In gas measurements, the mass sensitivity S_m of the TFBAR oscillator increases with the square of the operating frequency:

$$S_m = -\frac{2f_0^2}{\rho_0 h_0^2}, \quad (19)$$

and the surface mass density Δm_s is proportional to the measured sensor signal Δf :

$$\Delta f = -S_m \Delta m_s. \quad (20)$$

Here f_0 is the resonant frequency of the TFBAR, ρ_0, h_0 are its density and thickness, respectively.

Depending on the structure, surface geometry, and composition of the sensing coatings, the mass sensitivity of the TFBAR systems can be sufficiently improved for nanocomposite layers embedded into a host polymer or another organic coating, for example, cadmium arachidate matrix with embedded SWCNTs arrays [64].

In vapour and liquid TFBARs measurements, the effects of viscosity must be taken into account [66]. Recently, fabrication and successful usage of TFBARs for biosensor applications have been reported in [68]. For the analysis of the experimental data of TFBARs in liquids, the theoretical models of Stockbridge [47] and Kanazawa and Gordon [51] have been used [66].

For correct interpretation of TFBARs measurements of viscoelastic and biological materials in liquid applications, formulae (14)–(18) can be of great help.

There are certain limitations of liquid and biological applications of TFBARs. Due to the higher operation frequency, TFBARs resonators are much thinner than QCMs and thus, more fragile. In general, the important engineering challenge is the optimization of the resonators' geometry from the view point of the sensitivity-to-noise ratio [66].

This TFBARs technique is a very promising method in view of biosensor purposes and, in particular, a combination of TFBAR devices in microfluidic arrays opens a new route towards lab-on-chip applications, microanalysis, and small size immunosensors.

6. Selected Examples of Applications of AW Sensors

6.1. Chemical and Life Science Applications of SAW-Based and BAW-Based Sensors. Biosensors based on acoustic resonators, like other bioanalytical methods such as immunoassays or enzyme assays, use biological compounds as the receptive overlayer that can distinguish between adsorbed analytes. Recent applications of thin layered films like self-assembled monolayers and supported bilayers (Figure 6(a)), Langmuir-Blodgett (LB) films (Figure 6(b)), protein monolayers (Figure 7) and multilayers of complex biomolecular architecture (Figure 8) as receptive layers in biosensors have stimulated detailed studies of the physical properties of such structures. Among novel promising nanomaterials for the surface functionalization of sensors one can list also stimuli-responsive polymer coatings, synthetic receptors, and carbon nanotubes. In particular, a thin-film bulk acoustic resonator functionalized with a nanocomposite LB layer of carbon nanotubes has been recently suggested as a fast response sensor for high-performance gas detection [63, 65].

With these model systems it is possible to construct multilayer amphiphilic films with controlled monolayer thickness and to create different coupling strengths between the adsorbed film and the chemically modified substrate. Specifically measurements of surface density and viscosity of these films are important both scientifically and, for example, with respect to their possible application in acoustical

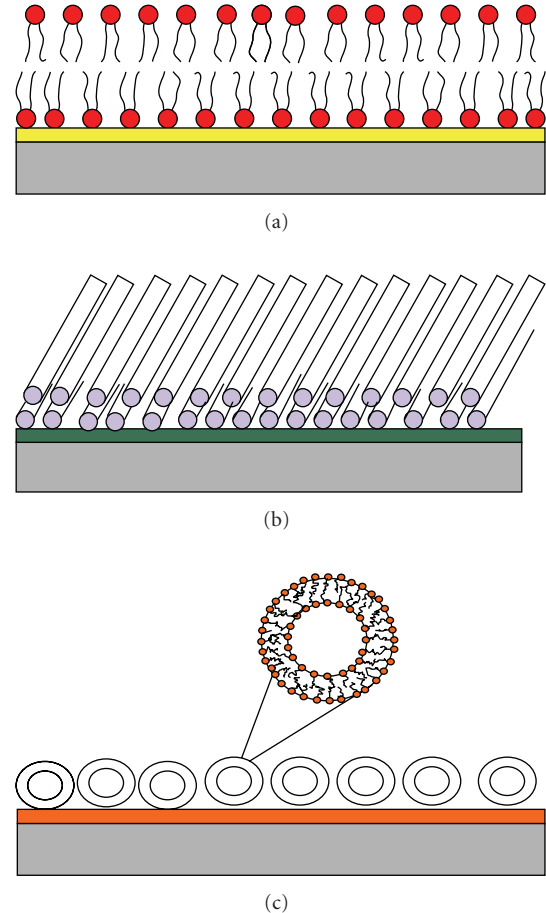


FIGURE 6: Sketch of supported membranes on the surface of an oscillating piezoelectric plate. (a) planar supported lipid bilayer : surface adjacent layer is anchored to the support;(b) Langmuir-Blodgett film made of rodlike liquid crystal molecules; (c) supported membrane made of lipid vesicles.

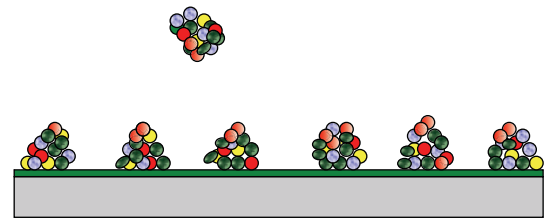


FIGURE 7: Protein layer adsorbed from a liquid phase onto a biochemically functionalized support.

biosensors, electronic nose and electronic tongue in which they can serve as sensitive elements.

This is also valid within the segregated (sublayer) structure model of adsorbed protein layers (Figure 7). The structure of the protein layer resembles a surfactant film composed of segregated head-and-tail regions. In this case, the relation between the upper and lower layer viscosities may vary in strong dependence of the phase state of protein and amphiphilic monolayer, respectively.

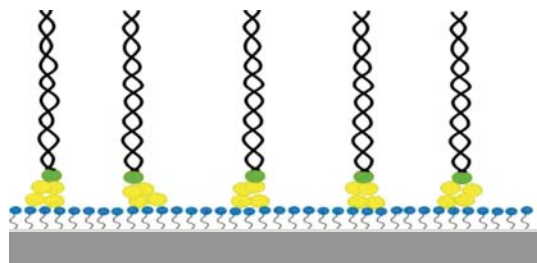


FIGURE 8: Multilayer architecture of biomolecular overlayer on the functionalized resonator surface. This QCM-based biosensor can be used, for example, for the detection of the DNA duplex formation and DNA-drug interactions. Binding of drugs increased energy dissipation (see for review [59]).

The dynamic (shear) viscosity of amphiphilic films is a key-importance rheological characteristic of a protein film or a fluid membrane, which is strongly dependent on temperature and phase state of the film, and on environmental conditions. Usually LB or SAM film acoustic sensors operate in vacuum or in a gaseous environment. In contrast, a lipid-water system or a protein layer adsorbed onto a solid surface in a fluid experiences “wet” conditions or a bulk aqueous medium at room temperature, which can change the viscosity of the film. In addition, the biomolecular layer adsorption process is extremely sensitive to the nature of the solid substrate in the sense that it can modify the overlayer structure schematically depicted in Figures 6(a) and 6(c). This is also valid within the segregated (sublayer) structure model of adsorbed protein layers (Figure 7). In this case, the relation between the upper and lower layer viscosities may vary in strong dependence of the phase state of protein and amphiphilic monolayer, respectively.

Amphiphilic bilayer films on supports can imitate the behavior of a bilayer lipid membrane. The constituent bilayer molecules are composed of hydrophilic groups attached to hydrophobic chains of different length. The phase diagrams of such amphiphilic molecules demonstrate a rich variety of properties and behavior depending on temperature and water content. Above the liquid crystalline-to-gel transition the hydrocarbon chains are approximately liquid and a bilayer membrane behaves like a two-dimensional fluid in the lateral plane due to the vanishing shear modulus of elasticity. Such a peculiar fluid is isotropic in its plane but it is anisotropic in the normal direction due to sub-layered head-and-tail structure [19]. Viscous properties of the layer can be characterized by different viscosity values, namely, the surface viscosity, and a “bulk” shear viscosity [70].

The surface viscosity of a fluid amphiphilic film is often considered to be a two-dimensional analogue of bulk viscosity and defined as the coefficient of proportionality between the tangential force per unit length and the gradient in the flow velocity of the liquid. These averaged surface characteristics can be measured, for example, by an interface shear rheometer at air-liquid interfaces or by using the oscillating barrier method in a LB trough. In contrast to

η , the “microscopic” shear viscosity may be defined as a contribution of fluid disordered chains. The “microviscosity” of the membrane core can be determined experimentally, for example, by a probe technique, and describe the local viscosity near the probe [71]. This “microviscosity” is often identified with the true membrane viscosity. However, this experimental technique could give rather different results with a strong dependence on the probe material and on the interaction between the probe and its local surroundings. Both of these viscosities may be changed after the deposition of an amphiphilic layer on the solid surface.

Both types of resonators (SAW and BAW) [19, 70] can be applied for the detection of phase transitions in biomolecular films adsorbed onto the surface of the sensor. These acoustic devices allow us to measure the acoustic response of the biofilm or supported lipid membrane in the lipid phase transition region where the viscosity of the membrane is subject to dramatic changes. For instance, during the liquid crystalline to gel transformation of a lipid membrane, the viscosity of the bilayer changes by more than 10 times, while the membrane density remains practically constant [70]. It is an interesting experimental fact that the two halves of a bilayer lipid membrane are so weakly coupled, that they can undergo a thermotropic phase transition independently. This must lead to changes in the SAW damping coefficient, while the corresponding SAW phase velocity shift due to the presence of the bilayer will be constant.

When the system is immersed in a water solution, anisotropy can arise from water trapping into the layer. This can result in a distinct overlayer viscosity in comparison with an air environment. This is especially important for protein adsorbed layers with nonuniform interfacial region structure and water distribution in the normal direction. These effects are also important for the lipid vesicles adsorption measured with QCM [72, 73].

In addition to its importance for biosensor applications, the study of the hydrodynamic modes of fluid amphiphilic films and adsorbed proteins are generally important for understanding the dynamics of lipid-water systems and the rheology of biological membranes. It is known, for instance, that living cell membranes, for example, in red blood cells experience shear stress in hydrodynamic flow through capillaries. As the lipid bilayer matrix of the membrane is a two-dimensional incompressible liquid adjacent to an elastic protein (spectrin-actin) network, the hydrodynamics of this layered structure are governed by the coupling of the fluid membrane to shear flows in an external bulk liquid. Recent efforts in measurements of hydrodynamic effects in QCM applications are reported in [74].

6.2. QCM in Electronic Nose Applications. Among artificial sensor systems, the array of electronic chemical sensors (electronic nose) working in gaseous environments and imitating the mammalian sense of smell remain, the primary instrumentation, although sensors operating in aqueous phase and having the same properties of electronic nose (the so-called electronic tongue) have been reported [74–82]. In many cases, the electronic tongue can be regarded as a wet

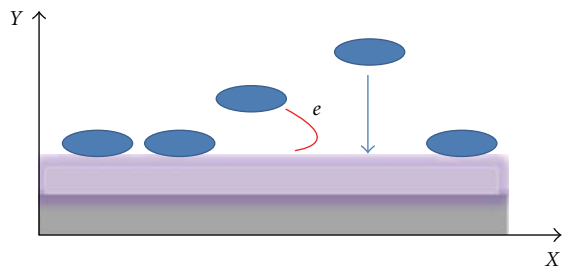


FIGURE 9: A sketch of the electrochemical detection of the redox enzyme reaction with charge transfer to the EQCM, a quartz crystal covered with a layer of electroconducting polymers on its surface and operating in a water solution with ions or buffer.

chemical counterpart of the electronic nose. Recently, the integration of the electronic nose, and the electronic tongue into a multisensor device has been proposed to improve the quality analysis of liquid samples and related volatile components. The simultaneous usage of these two types of sensors covered with the same sensing molecular compounds (metalloporphyrins) has been used by, for example, authors [75] to optimize the characteristics of the sensor.

A special type of quartz resonators, the so-called electrochemical QCM (EQCM), is a sensor enabling detection of chemical parameters via electrical conductivity measurements both in gaseous phase, vapours, and in various liquids. Typically the EQCM is based on usage of electroconducting polymer arrays as a smart coating for the sensor surface.

If the QCM device is used as a mass sensor in electronic tongue applications, the density and viscosity of the solution affect the resonance frequency of the oscillator. The classical result of Gordon and Kanazawa [51] is applicable here with a correction for a possible missing mass effect contribution [53]. The latter can be useful for interpreting QCM data in electronic tongue and biosensor applications since the correct estimation of the mass derived from the QCM response can be a crucial step towards using the microbalance as a sensor in complex biological liquids, where biomolecules or cells adsorbed from the solution make a soft layer on the receptive surface of the oscillator. In some situations, it is useful to combine the voltammetric electronic tongue (or EQCM) and QCM technique to relate the mass changes and charge transport problem in analytic chemistry applications and in situ electrochemical measurements [83]. For example, it has been reported elsewhere [76] that if a coating composed of redox active polymers, the QCM can monitor the mass changes which accompany the redox processes in polymer matrix. There the relationship between the charge, a measure of the total number of electrons produced or consumed in redox reactions, and mass transport has been derived from the combined QCM and voltammetry data.

Electronic noses based on the QCM device have been widely used as gas sensors to “smell” volatile organic compounds (VOCs) in food, olive oil, and wine industry applications as well as in health care and environmental monitoring, for security and safety purposes [77–83].

6.3. *The Problem of Sliding Friction for Viscoelastic Adlayers.* Successful applications of quartz resonators as a sensor element in electronic noses and electronic tongues (or EQCMs) bring up the fundamental question of how internal friction (effects of viscosity) and interfacial friction (slippage) can affect the QCM resonance frequency shift Δf and, hence, the mass sensitivity. In cases when the overlayer material exhibits a viscoelastic behaviour, both internal and interfacial friction may contribute to energy dissipation. Depending on the situation, the former or the latter type of friction may dominate. Recently, a dynamic “slip/no-slip” test that can be applied to QCM thin films spectroscopy has been suggested elsewhere [62]. The test is based on the theoretical finding that the peak in the viscous dissipation ΔD depends on the frequency while the peak value of the ΔD dissipation factor caused by sliding friction is frequency independent. It has been shown [62] that the combined action of these two mechanisms may cause a nonmonotonic variation of the shift in the dissipation factor ΔD of quartz oscillator when adlayer parameters are varied.

The effects of interfacial slippage must be taken into account when the condition of rigid attachment of the adlayer to the oscillator surface is violated. A finite amount of slippage can arise either from incommensurate densities [84] or weak coupling between the adlayer and the substrate and influence both the resonance frequency f and the oscillator dissipation ΔD (a comprehensive and extensive analysis of sliding friction can be found in the recent review by Krim [85] and in the book by Persson [84]).

For a quantitative characterization of slippage effects it is convenient to use the ratio of the inverse quality factor $\Delta(1/Q) \equiv \Delta D$ to the shift Δf of the QCM resonance frequency. This value has been introduced for the first time in the QCM community by Krim and Widom [86] as a “slip time”:

$$\tau = \frac{\Delta(Q^{-1})}{4\pi|\Delta f|}. \quad (21)$$

According to the results of Krim and Widom [86], a partial decoupling of the overlayer should occur when $2\pi f\tau \geq 0.5$. Such a relatively low decoupling threshold can lead to noticeable interfacial friction effects even in the case of molecularly thin films. In nanotribological QCM-experiments of Krim et al. [86, 87], the interfacial friction coefficient γ_f

$$\gamma_f = \frac{1}{\tau} \sim m_f \quad (22)$$

has been found to be proportional to the surface mass density $m_f = \rho_f h_f$ of the film. The authors [86] attributed the “slip time” τ as a relaxation time associated with film-momentum fluctuations. This result can also be viewed as the definition of the slip time as the characteristic time it takes for the film velocity to decrease by a factor of $1/e$. However, it has been shown [62] that for soft (viscoelastic) materials this result should be corrected because of additional viscous dissipation in the overlayers. In analogy with (21), in order to characterize the temporal QCM response when no-slip

boundary conditions apply, another characteristic value can be introduced:

$$\tau_0 = -\frac{\Delta(Q^{-1})}{4\pi\Delta\tilde{f}}. \quad (23)$$

Here $\Delta\tilde{f}$ is negative and tilde denotes no-slip conditions. Defined in this way, the characteristic time τ_0 can be attributed solely to the effects of internal friction (shear viscosity) on the damping of the QCM. One can find the coefficient of slippage, $\lambda \equiv 1/\gamma$, from the experimentally measured τ_S value as follows:

$$\lambda \approx \frac{\omega\tau_0 - \omega\tau_S}{2\pi\Delta\tilde{f}M}. \quad (24)$$

Simultaneous measurements of Δf and ΔD in QCM-D experiments at different frequencies open a way to estimate the coefficient of slippage, for example, by comparing the frequency behaviour of the dissipation factor at maximum [62] for various environmental parameters.

6.4. Future Outlook. Recent trends and the future outlook in the design, fabrication, and utilization of AW-based sensors span many different fields and interdisciplinary research. Sensor development stretches from nanoscale technology needs to terrestrial ecosystems (including the ecology of oceans and environment studies) and even extraterrestrial research. Surface acoustic wave- (SAW-) based devices are the most popular high frequency systems due to their extraordinary success in mobile and wireless communication, in electronics and the sensors industry [88, 89]. These SAW piezoelectric oscillators [90] as well as BAW devices such as quartz crystal microbalance have now got a varied number of applications ranging from high precision gravimetric measurements to biosensors. The selected examples are the usage of acoustic wave devices in the marine research [5, 6], coastal developments and biofoul control [7, 8], acoustic-counterflow microfluidics by surface acoustic waves [27–29], Life sciences and health care service [81, 83, 91, 92], safety, security, and Man-Portable Threat Warning Systems [9], further development of a microbalance system for dust and water vapour detection in the Mars atmosphere [1–3] and AW-sensors for astrobiology research [4].

There is a rapid progress in the material science of new polymeric coatings and dynamic macromolecular assemblies for biosensor purposes (see, e.g., the excellent reviews of Lehn [93] and Sanchez and coworkers [94]). The frontier chemical strategy for the innovative structures manufacturing is the combination of integrated synthesis and self-assembly or nanobuilding block techniques [71, 93–96], usage of hybrid Metal Organic Frameworks (MOFs) [94], and nanoclay-based compounds [97], new porous materials [95], and bioinspired structures functional coatings [98–100].

The combination of novel polymeric materials, synthetic or natural, with the advanced surface science nanotechnologies (a polymer pen lithography for the surface patterning is a selected current example [101]) will be a further step towards the design of “smart” biosensors of new generation.

Valuable information on recent trends in sensors technology the reader can find also in the International Frequency Sensor Association web portal [10].

Appendix

The List of (Selected) Companies Manufacturing AW Sensors

- (1) Q-sense (http://www.q-sense.com/diverse_use_of_qcm_d_demonstrated_in_latest_research-209.asp).
- (2) CENS (<http://research.cens.ucla.edu/>) UCLA's Center for Embedded Networked Sensing (CENS) with applications in the Terrestrial ecology.
- (3) Nanofilm (<http://www.nanofilm.de/>) (SAW biosensors).
- (4) E-QCM (<http://ichf.edu.pl/offers/instrum/quartz.htm>).
- (5) QCM (<http://www.elbotech.com/>).
- (6) QCM, EQCM of smaller size plus connection via Q-pod to PC via USB port to computerize data; also Combination of QCM sensor and INFICON Sigma Instruments products (<http://www.sig-inst.com/>).
- (7) EQCM company (http://www.meeck.pl/eqcm/en_m106.html).
- (8) DTI Defens Information Community (<http://www.dtic.mil/dtic/>).
- (9) Honeywell (<http://www51.honeywell.com/honeywell/>) (Allied Signal Corporation, production of Metglas).
- (10) Advalytix (<http://www.Advalytix.de/>) Microfluidic applications: SAW Technology can be used for pumping, dosing and mixing of reagents in low volumes.
- (11) Microsensor Systems Inc. (MSI), the world leader in Surface Acoustic Wave (SAW) based chemical sensing (<http://www.microsensorsystems.com/aboutus.html>) and (<http://www.microsensorsystems.com/>).
- (12) QCM100 and QCM200 (<http://www.thinksrs.com/>), Vacuum & Analytical Instruments.

Acknowledgments

The author would like to express special gratitude to Professor Mats Jonson, colleague and the coauthor of all her QCM publications, for his help and critical reading of the manuscript. Financial support from the Swedish SSF is gratefully acknowledged.

References

- [1] W. Gao, S. Osman, and J. Barengoltz, “Quantification of spore-forming bacteria carried by dust particles,” in *Proceedings of the 36th COSPAR Scientific Assembly*, Jet Propulsion Laboratory, National Aeronautics and Space Administration, Beijing, China, July 2006.

- [2] E. Palomba, L. Colangeli, P. Palumbo, A. Rotundi, J. M. Perrin, and E. Bussoletti, "Performance of micro-balances for dust flux measurement," *Advances in Space Research*, vol. 29, no. 8, pp. 1155–1158, 2002.
- [3] R. Battaglia, E. Palomba, P. Palumbo, L. Colangeli, and V. Della Corte, "Development of a micro-balance system for dust and water vapour detection in the Mars atmosphere," *Advances in Space Research*, vol. 33, no. 12, pp. 2258–2262, 2004.
- [4] E. Robens and D. Möhlmann, "Planning of gravimetric investigations on Mars," *Journal of Thermal Analysis and Calorimetry*, vol. 76, no. 2, pp. 671–675, 2004.
- [5] M. Berglin, J. Hedlund, C. Fant, and H. Elwing, "Use of surface-sensitive methods for the study of adsorption and cross-linking of marine bioadhesives," *Journal of Adhesion*, vol. 81, no. 7–8, pp. 805–822, 2005.
- [6] http://research.cens.ucla.edu/about/annual_reports/CENS-AnnualReport2008.pdf.
- [7] S.-R. Hong, S.-J. Choi, H. D. Jeong, and S. Hong, "Development of QCM biosensor to detect a marine derived pathogenic bacteria *Edwardsiella tarda* using a novel immobilisation method," *Biosensors and Bioelectronics*, vol. 24, no. 6, pp. 1635–1640, 2009.
- [8] P. J. Molino, O. M. Hodson, J. F. Quinn, and R. Wetherbee, "The quartz crystal microbalance: a new tool for the investigation of the bioadhesion of diatoms to surfaces of differing surface energies," *Langmuir*, vol. 24, no. 13, pp. 6731–6737, 2008.
- [9] C. M. Harris, "Product review: seeing SAW potential," *Analytical Chemistry*, vol. 75, no. 15, pp. 355A–358A, 2003.
- [10] "International Frequency Sensor Association (IFSA)," <http://www.sensorsportal.com>.
- [11] L. A. Francis, J.-M. Friedt, C. Bartic, and A. Campitelli, "A SU-8 liquid cell for surface acoustic wave biosensors," vol. 5455 of *Proceedings of SPIE*, pp. 353–363, 2004.
- [12] K. Länge, G. Blaess, A. Voigt, R. Götzen, and M. Rapp, "Integration of a surface acoustic wave biosensor in a microfluidic polymer chip," *Biosensors and Bioelectronics*, vol. 22, no. 2, pp. 227–232, 2006.
- [13] K. Länge, B. E. Rapp, and M. Rapp, "Surface acoustic wave biosensors: a review," *Analytical and Bioanalytical Chemistry*, vol. 391, no. 5, pp. 1509–1519, 2008.
- [14] H. Uberall, in *Physical Acoustics: Principles and Methods*, W. P. Mason and R. N. Thurston, Eds., Academic Press, New York, NY, USA, 1988.
- [15] E. Gizeli, N. J. Goddard, C. R. Lowe, and A. C. Stevenson, "A love plate biosensor utilising a polymer layer," *Sensors and Actuators B*, vol. 6, no. 1–3, pp. 131–137, 1992.
- [16] G. Kovacs and A. Venema, "Theoretical comparison of sensitivities of acoustic shear wave modes for (bio)chemical sensing in liquids," *Applied Physics Letters*, vol. 61, no. 6, pp. 639–641, 1992.
- [17] J. Du, G. L. Harding, J. A. Ogilvy, P. R. Dencher, and M. Lake, "A study of Love-wave acoustic sensors," *Sensors and Actuators A*, vol. 56, no. 3, pp. 211–219, 1996.
- [18] G. L. Harding, J. Du, P. R. Dencher, D. Barnett, and E. Howe, "Love wave acoustic immunosensor operating in liquid," *Sensors and Actuators A*, vol. 61, no. 1–3, pp. 279–286, 1997.
- [19] M. V. Voinova, M. Jonson, and B. Kasemo, "Dynamics of viscous amphiphilic films supported by elastic solid substrates," *Journal of Physics: Condensed Matter*, vol. 9, no. 37, pp. 7799–7808, 1997.
- [20] M. V. Voinova, A. M. Kosevich, and E. S. Syrkin, "Influence of Langmuir-Blodgett films on the characteristics of surface-waves in a crystal," *Acoustical Physics*, vol. 39, pp. 500–501, 1993.
- [21] H. Wohltjen and R. Dessy, "Surface acoustic wave probe for chemical analysis—I: introduction and instrument description," *Analytical Chemistry*, vol. 51, no. 9, pp. 1458–1464, 1979.
- [22] C. Zimmermann, D. Rebière, C. Déjous, J. Pistré, E. Chastaing, and R. Planade, "A love-wave gas sensor coated with functionalized polysiloxane for sensing organophosphorus compounds," *Sensors and Actuators B*, vol. 76, no. 1–3, pp. 86–94, 2001.
- [23] I. D. Avramov, A. Voigt, and M. Rapp, "Rayleigh SAW resonators using gold electrode structure for gas sensor applications in chemically reactive environments," *Electronics Letters*, vol. 41, no. 7, pp. 450–452, 2005.
- [24] I. D. Avramov, K. Länge, S. Rupp, B. Rapp, and M. Rapp, "Polymer coating behavior of rayleigh-SAW resonators with gold electrode structure for gas sensor applications," *IEEE Transactions on Ultrasonics, Ferroelectrics, and Frequency Control*, vol. 54, no. 1, pp. 157–166, 2007.
- [25] D. W. Branch and S. M. Brozik, "Low-level detection of a *Bacillus anthracis* simulant using Love-wave biosensors on 36° YX LiTaO₃," *Biosensors and Bioelectronics*, vol. 19, no. 8, pp. 849–859, 2004.
- [26] M. Cecchini, S. Girardo, D. Pisignano, R. Cingolani, and F. Beltram, "Acoustic-counterflow microfluidics by surface acoustic waves," *Applied Physics Letters*, vol. 92, no. 10, pp. 104103-1–104103-3, 2008.
- [27] J. W. Grate, S. J. Martin, and R. M. White, "Acoustic wavemicrosensors—part I," *Analytical Chemistry*, vol. 65, no. 21, pp. 940A–948A, 1993.
- [28] K. Sritharan, C. J. Strobl, M. F. Schneider, A. Wixforth, and Z. Guttenberg, "Acoustic mixing at low Reynold's numbers," *Applied Physics Letters*, vol. 88, no. 5, pp. 1–3, 2006.
- [29] A. Wixforth, "Acoustically driven programmable microfluidics for biological and chemical applications," *Journal of the Association for Laboratory Automation*, vol. 11, no. 6, pp. 399–405, 2006.
- [30] C. A. Grimes, K. G. Ong, K. Loiselle, et al., "Magnetoelastic sensors for remote query environmental monitoring," *Smart Materials and Structures*, vol. 8, no. 5, pp. 639–646, 1999.
- [31] S. Schmidt and C. A. Grimes, "Elastic modulus measurement of thin films coated onto magnetoelastic ribbons," *IEEE Transactions on Magnetics*, vol. 37, no. 4, part 1, pp. 2731–2733, 2001.
- [32] M. K. Jain and C. A. Grimes, "Effect of surface roughness on liquid property measurements using mechanically oscillating sensors," *Sensors and Actuators A*, vol. 100, no. 1, pp. 63–69, 2002.
- [33] M. Zourob, K. G. Ong, K. Zeng, F. Mouffouk, and C. A. Grimes, "A wireless magnetoelastic biosensor for the direct detection of organophosphorus pesticides," *Analyst*, vol. 132, no. 4, pp. 338–343, 2007.
- [34] C. Ruan, K. Zeng, O. K. Varghese, and C. A. Grimes, "Magnetoelastic immunosensors: amplified mass immunosorbent assay for detection of *Escherichia coli* O157:H7," *Analytical Chemistry*, vol. 75, no. 23, pp. 6494–6498, 2003.
- [35] D. Kouzoudis and C. A. Grimes, "Remote query fluid-flow velocity measurement using magnetoelastic thick-film sensors," *Journal of Applied Physics*, vol. 87, no. 9, pp. 6301–6303, 2000.

- [36] P. G. Stoyanov and C. A. Grimes, "Remote query magnetostrictive viscosity sensor," *Sensors and Actuators A*, vol. 80, no. 1, pp. 8–14, 2000.
- [37] S. Wu, X. Gao, Q. Cai, and C. A. Grimes, "A wireless magnetoelastic biosensor for convenient and sensitive detection of acid phosphatase," *Sensors and Actuators B*, vol. 123, no. 2, pp. 856–859, 2007.
- [38] L. G. Puckett, J. K. Lewis, A. Urbas, X. Cui, D. Gao, and L. G. Bachas, "Magnetoelastic transducers for monitoring coagulation, clot inhibition, and fibrinolysis," *Biosensors and Bioelectronics*, vol. 20, no. 9, pp. 1737–1743, 2005.
- [39] J. Wan, H. Shu, S. Huang, et al., "Phase-based magnetoelastic wireless biosensors for detecting *Bacillus anthracis* spores," *IEEE Sensors Journal*, vol. 7, no. 3, pp. 470–477, 2007.
- [40] C. Ruan, K. Zeng, O. K. Varghese, and C. A. Grimes, "A magnetoelastic bioaffinity-based sensor for avidin," *Biosensors and Bioelectronics*, vol. 19, no. 12, pp. 1695–1701, 2004.
- [41] Q. Y. Cai and C. A. Grimes, "A remote query magnetoelastic pH sensor," *Sensors and Actuators B*, vol. 71, no. 1-2, pp. 112–117, 2000.
- [42] R. Guntupalli, J. Hu, R. S. Lakshmanan, T. S. Huang, J. M. Barbaree, and B. A. Chin, "A magnetoelastic resonance biosensor immobilized with polyclonal antibody for the detection of *Salmonella typhimurium*," *Biosensors and Bioelectronics*, vol. 22, no. 7, pp. 1474–1479, 2007.
- [43] R. S. Lakshmanan, R. Guntupalli, S. Huang, et al., "Magnetoelastic material as a biosensor for the detection of salmonella typhimurium," in *Proceedings of the Symposium V: Materials, Devices, and Characterization for Smart Systems, MRS Fall Meeting*, Boston, Mass, USA, December 2008.
- [44] L. G. Puckett, G. Barrett, D. Kouzoudis, C. Grimes, and L. G. Bachas, "Monitoring blood coagulation with magnetoelastic sensors," *Biosensors and Bioelectronics*, vol. 18, no. 5-6, pp. 675–681, 2003.
- [45] M. V. Voinova and M. Jonson, "On theory of magnetoelastic sensors," unpublished.
- [46] G. Sauerbrey, "Use of quartz vibrator for weighing thin layers and as a micro-balance," *Zeitschrift fur Physik*, vol. 155, no. 2, pp. 206–222, 1959.
- [47] C. D. Stockbridge, "Effects of gas pressure on quartz-crystal microbalances," in *Vacuum Microbalance Techniques*, vol. 5, pp. 147–178, 1966.
- [48] M. Rodahl, F. Höök, C. Fredriksson, et al., "Simultaneous frequency and dissipation factor QCM measurements of biomolecular adsorption and cell adhesion," *Faraday Discussions*, vol. 107, pp. 229–246, 1997.
- [49] D. Johannsmann, "Studies of viscoelasticity with the QCM," in *Piezoelectric Sensors*, C. Steinem and A. Janshoff, Eds., pp. 49–110, Springer, New York, NY, USA, 1st edition, 2006.
- [50] L. Daikhin, E. Gileadi, G. Katz, V. Tsionsky, M. Urbakh, and D. Zagidulin, "Influence of roughness on the admittance of the quartz crystal microbalance immersed in liquids," *Analytical Chemistry*, vol. 74, no. 3, pp. 554–561, 2002.
- [51] K. K. Kanazawa and J. G. Gordon II, "Frequency of a quartz microbalance in contact with liquid," *Analytical Chemistry*, vol. 57, no. 8, pp. 1770–1771, 1985.
- [52] B. Zimmermann, R. Lucklum, P. Hauptmann, J. Rabe, and S. Büttgenbach, "Electrical characterisation of high-frequency thickness-shear-mode resonators by impedance analysis," *Sensors and Actuators B*, vol. 76, no. 1–3, pp. 47–57, 2001.
- [53] M. V. Voinova, M. Jonson, and B. Kasemo, "Missing mass' effect in biosensor's QCM applications," *Biosensors and Bioelectronics*, vol. 17, no. 10, pp. 835–841, 2002.
- [54] M. V. Voinova, M. Rodahl, M. Jonson, and B. Kasemo, "Viscoelastic acoustic response of layered polymer films at fluid-solid interfaces: continuum mechanics approach," *Physica Scripta*, vol. 59, no. 5, pp. 391–396, 1999.
- [55] J. Limson, O. O. Odunuga, H. Green, F. Höök, and G. L. Blatch, "The use of a quartz crystal microbalance with dissipation for the measurement of protein-protein interactions: a qualitative and quantitative analysis of the interactions between molecular chaperones," *South African Journal of Science*, vol. 100, no. 11-12, pp. 678–682, 2004.
- [56] D. Johannsmann, I. Reviakina, E. Rojas, and M. Gallego, *Analytical Chemistry*. In press.
- [57] M. Rodahl, F. Höök, A. Krozer, P. Brzezinski, and B. Kasemo, "Quartz crystal microbalance setup for frequency and Q-factor measurements in gaseous and liquid environments," *Review of Scientific Instruments*, vol. 66, no. 7, pp. 3924–3930, 1995.
- [58] M. Rodahl M, F. Höök, A. Kroze, and B. Kasemo, "Piezo-electric crystal microbalance Device," US patent no. US6006589, 1995.
- [59] F. Höök and B. Kasemo, "The QCM technique for biomacromolecular recognition: technical and theoretical aspects," O. S. Wolfbeis, Ed., *The Springer Series on Chemical Sensors and Biosensors*, 2006.
- [60] V. M. Mecea, "Is quartz crystal microbalance really a mass sensor?" *Sensors and Actuators A*, vol. 128, no. 2, pp. 270–277, 2006.
- [61] M. Gavutis, S. Lata, and J. Piehler, "Probing 2-dimensional protein-protein interactions on model membranes," *Nature Protocols*, vol. 1, no. 4, pp. 2091–2103, 2006.
- [62] M. V. Voinova, M. Jonson, and B. Kasemo, "On dissipation of quartz crystal microbalance as a mechanical spectroscopy tool," *Spectroscopy*, vol. 18, no. 4, pp. 537–544, 2004.
- [63] M. Penza, P. Aversa, G. Cassano, et al., "Thin-film bulk-acoustic-resonator gas sensor functionalized with a nanocomposite Langmuir-Blodgett layer of carbon nanotubes," *IEEE Transactions on Electron Devices*, vol. 55, no. 5, pp. 1237–1243, 2008.
- [64] M. Penza, M. A. Tagliente, P. Aversa, M. Re, and G. Cassano, "The effect of purification of single-walled carbon nanotube bundles on the alcohol sensitivity of nanocomposite Langmuir-Blodgett films for SAW sensing applications," *Nanotechnology*, vol. 18, no. 18, pp. 185502–185512, 2007.
- [65] M. Benetti, D. Cannatà, F. Di Pietrantonio, V. Foglietti, and E. Verona, "Microbalance chemical sensor based on thin-film bulk acoustic wave resonators," *Applied Physics Letters*, vol. 87, no. 17, Article ID 173504, 3 pages, 2005.
- [66] J. Bjurström, G. Wingqvist, V. Yantchev, and I. Katardjiev, "Temperature compensation of liquid FBAR sensors," *Journal of Micromechanics and Microengineering*, vol. 17, no. 3, pp. 651–658, 2007.
- [67] G. Wingqvist, J. Bjurström, L. Liljeholm, V. Yantchev, and I. Katardjiev, "Shear mode AlN thin film electro-acoustic resonant sensor operation in viscous media," *Sensors and Actuators B*, vol. 123, no. 1, pp. 466–473, 2007.
- [68] G. Wingqvist, J. Bjurström, A.-C. Hellgren, and I. Katardjiev, "Immunosensor utilizing a shear mode thin film bulk acoustic sensor," *Sensors and Actuators B*, vol. 127, no. 1, pp. 248–252, 2007.
- [69] K. M. Lakin and J. S. Wang, "Acoustic bulk wave composite resonators," *Applied Physics Letters*, vol. 38, no. 3, pp. 125–127, 1981.

- [70] M. V. Voinova and E. S. Syrkina, "Method for determining viscosity of liquid-crystalline Langmuir-Blodgett films," *Crystallography Reports*, vol. 43, no. 5, pp. 863–865, 1998.
- [71] A. M. Dopico, Ed., *Methods in Membrane Lipids*, Humana Press, 2007.
- [72] C. A. Keller and B. Kasemo, "Surface specific kinetics of lipid vesicle adsorption measured with a quartz crystal microbalance," *Biophysical Journal*, vol. 75, no. 3, pp. 1397–1402, 1998.
- [73] C. A. Keller, K. Glasmästar, V. P. Zhdanov, and B. Kasemo, "Formation of supported membranes from vesicles," *Physical Review Letters*, vol. 84, no. 23, pp. 5443–5446, 2000.
- [74] E. Tellechea, D. Johannsmann, N. F. Steinmetz, R. P. Richter, and I. Reviakine, "Model-independent analysis of QCM data on colloidal particle adsorption," *Langmuir*, vol. 25, no. 9, pp. 5177–5184, 2009.
- [75] J. W. Gardner and P. N. Bartlett, "Brief history of electronic noses," *Sensors and Actuators B*, vol. B18, no. 1–3, part 1, pp. 211–220, 1994.
- [76] C. S. S. R. Kumar, "Nanosystem characterization tools in the life sciences," in *Nanotechnologies for the Life Sciences*, vol. 3, p. 413, Wiley-VCH, New York, NY, USA, 2006.
- [77] J. W. Gardner and P. N. Bartlett, *Electronic Noses: Principles and Applications*, Oxford University Press, Oxford, UK, 1999.
- [78] E. R. Hirst, Y. J. Yuan, W. L. Xu, and J. E. Bronlund, "Bond-rupture immunosensors—a review," *Biosensors and Bioelectronics*, vol. 23, no. 12, pp. 1759–1768, 2008.
- [79] S. Rösler, R. Lucklum, R. Borngräber, J. Hartmann, and P. Hauptmann, "Sensor system for the detection of organic pollutants in water by thickness shear mode resonators," *Sensors and Actuators B*, vol. 48, no. 1–3, pp. 415–424, 1998.
- [80] T. Jacobs, G. Cama, M. Hartmann, et al., "Micro fluidic biosensor array for parallelized cell adhesion analysis during pathogenic infection," *IEEE Sensors*, pp. 1460–1463, 2008.
- [81] A. Mantini, C. Di Natale, A. Macagnano, R. Paolesse, A. Finazzi-Agrò, and A. D'Amico, "Biomedical application of an electronic nose," *Critical Reviews in Biomedical Engineering*, vol. 28, no. 3–4, pp. 481–485, 2000.
- [82] J. M. Beeley, C. Mills, P. A. Hammond, et al., "All-digital interface ASIC for a QCM-based electronic nose," *Sensors and Actuators B*, vol. 103, no. 1–2, pp. 31–36, 2004.
- [83] C. Di Natale, R. Paolesse, A. Macagnano, et al., "Electronic nose and electronic tongue integration for improved classification of clinical and food samples," *Sensors and Actuators B*, vol. 64, no. 1–3, pp. 15–21, 2000.
- [84] B. N. J. Persson, *Sliding Friction Sliding Friction: Physical Principles and Applications (NanoScience and Technology)*, Springer, New York, NY, USA, 2nd edition, 2000.
- [85] J. Krim, "QCM tribology studies of thin adsorbed films," *Nano Today*, vol. 2, no. 5, pp. 38–43, 2007.
- [86] J. Krim and A. Widom, "Damping of a crystal oscillator by an adsorbed monolayer and its relation to interfacial viscosity," *Physical Review B*, vol. 38, no. 17, pp. 12184–12189, 1988.
- [87] T. Coffey and J. Krim, "Quartz-crystal microbalance studies of the slippage of solid and liquid krypton monolayers on metal(111) and C₆₀ surfaces," *Physical Review B*, vol. 72, no. 23, Article ID 235414, 5 pages, 2005.
- [88] C. K. Campbell, "Applications of surface acoustic and shallow bulk acoustic wave devices," *Proceedings of the IEEE*, vol. 77, no. 10, pp. 1453–1484, 1989.
- [89] C. K. Campbell, *Surface Acoustic Wave Devices for Mobile and Wireless Communications*, Academic Press, Boston, Mass, USA, 1998.
- [90] J. W. Grate and G. C. Frye, "Acoustic wave sensors," *Sensors Update*, vol. 2, no. 1, pp. 37–83, 2001.
- [91] "Detection Method for Cancer Detection and Protein Investigation," Nanofilm Surface Analysis, <http://nanofilm.de>.
- [92] J. R. Heath and M. E. Davis, "Nanotechnology and cancer," *Annual Review of Medicine*, vol. 59, pp. 251–265, 2008.
- [93] J.-M. Lehn, "From supramolecular chemistry towards constitutional dynamic chemistry and adaptive chemistry," *Chemical Society Reviews*, vol. 36, no. 2, pp. 151–160, 2007.
- [94] C. Sanchez, B. Julián, P. Belleville, and M. Popall, "Applications of hybrid organic-inorganic nanocomposites," *Journal of Materials Chemistry*, vol. 15, no. 35–36, pp. 3559–3592, 2005.
- [95] C. Férey, C. Mellot-Draznieks, C. Serre, et al., "Chemistry: a chromium terephthalate-based solid with unusually large pore volumes and surface area," *Science*, vol. 309, no. 5743, pp. 2040–2042, 2005.
- [96] M. Barboiu, A. Cazacu, M. Michau, R. Caraballo, C. Arnal-Herault, and A. Pasc-Banu, "Functional organic-inorganic hybrid membranes," *Chemical Engineering and Processing: Process Intensification*, vol. 47, no. 7, pp. 1044–1052, 2008.
- [97] C. Mousty, "Sensors and biosensors based on clay-modified electrodes—new trends," *Applied Clay Science*, vol. 27, no. 3–4, pp. 159–177, 2004.
- [98] L. Zhai, F. C. Cebeci, R. E. Cohen, and M. F. Rubner, "Stable superhydrophobic coatings from polyelectrolyte multilayers," *Nano Letters*, vol. 4, no. 7, pp. 1349–1353, 2004.
- [99] C. Sanchez, H. Arribart, and M. M. G. Guille, "Biomimeticism and bioinspiration as tools for the design of innovative materials and systems," *Nature Materials*, vol. 4, no. 4, pp. 277–288, 2005.
- [100] C. Tamerler and M. Sarikaya, Eds., "Molecular biomimetics," *Materials Research Society*, vol. 33, no. 5, 2008.
- [101] F. Huo, Z. Zheng, G. Zheng, L. R. Giam, H. Zhang, and C. A. Mirkin, "Polymer pen lithography," *Science*, vol. 321, no. 5896, pp. 1658–1660, 2008.

Research Article

Analyzing Spur-Distorted Impedance Spectra for the QCM

Sae Moon Yoon,¹ Nam Joon Cho,² and Kay Kanazawa²

¹Electrical Engineering Department, Columbia University, 1300 S.W. Mudd, 500 West 120th Street, New York, NY 10027, USA

²Department of Chemical Engineering, Stanford University, Stanford, CA 94305, USA

Correspondence should be addressed to Kay Kanazawa, procmon@msn.com

Received 22 December 2008; Revised 17 March 2009; Accepted 26 April 2009

Recommended by Michele Penza

The quartz crystal microbalance (QCM) is a sensitive device for determining the properties of materials loading it. One of the fundamental means of making these measurements is the so-called impedance (or admittance) spectra method. The resonant properties of the piezoelectric QCM sensor are measured over a spectral range in the neighborhood of a resonance, both with load and without load. The changes in the spectrum upon loading can be compared to models that describe the changes based on the mass density, the shear modulus, and the viscosity of the load. This comparison can be made with confidence so long as the spectrum corresponds to the model assumption of a single main resonance. Often, there exists a spurious resonance lying above the main resonance which is not included in the models. This can change the shape of the spectrum in ways not included in the model analysis. We describe a method we have used that separates the spur resonance from the main resonance, permitting the parameters of the main resonance to be isolated from that of the spur. These corrected parameters of the main resonance can then be used with confidence in model analyses.

Copyright © 2009 Sae Moon Yoon et al. This is an open access article distributed under the Creative Commons Attribution License, which permits unrestricted use, distribution, and reproduction in any medium, provided the original work is properly cited.

1. Introduction

1.1. Basic Description. The quartz crystal microbalance (QCM) has become an important tool for monitoring in many types of nanolayer assemblies of organic and biological films. A nice overview for its use in biomolecular interactions is given by Cooper and Singleton [1]. The QCM sensor is a resonant piezoelectric device and is described in a recent book [2]. It can resonate at its fundamental frequency and also at its odd multiple harmonics as discussed in a review by Buttry and Ward [3]. It consists of a disk with electrodes on opposing faces. When a load is placed upon the quartz crystal, changes in its resonant behavior permit an evaluation of certain properties of the load. A variety of electronic methods can be used to determine these changes, with some of them nicely given by Arnau [4]. This has made it very valuable not only to determine the amount of material in the load, but additional load properties such as stiffness and viscosity as well. Fortunately, the resonance behavior has been shown to be accurately represented by a simple equivalent circuit permitting the use of sophisticated electronic techniques to determine changes in the resonant

properties. The full electrical equivalent for the QCM has been shown to be described by a so-called transmission line model [5] which can be simplified under conditions near a high Q resonance to the simple equivalent circuit as discussed by Cernosek, Martin, Hillman, and Bandey [6]. The equivalent circuit is called the Butterworth Van Dyke (BVD) circuit [7, 8] and is shown in Figure 1.

The elements of the right hand branch contain the motional information. The changes due to loading can be directly incorporated as changes in these elements. The changes due to loading can be incorporated simply as changes in the values of the three elements in the right hand branch. An alternate method is to preserve the values of three elements, taking them to be the value corresponding to the unloaded crystal. The changes can be incorporated as small additional elements and this allows one to focus on the changes.

1.2. Three Key Methods of Study. The three most common methods for studying the resonant behavior of the QCM are (A) using the sensor as the active element in an electronic oscillator, (B) examining the transient decay of the current

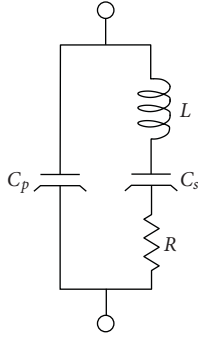


FIGURE 1: The Butterworth Van Dyke equivalent circuit.

after initial excitation of the sensor, and (C) recording the spectral behavior and its changes. The oscillator method is the most economical and is thus quite popular. From the measurement, it can determine the resonant frequency of the BVD circuit. More recently, it has become possible to also obtain the series resistance R . Generally, this is restricted to a single harmonic, although recently a dual harmonic oscillator has been described [9]. Two of the key properties of the resonance are its resonant frequency and the loss or energy dissipation. in the resonance. Using the oscillator approach, two of the properties of the circuit can be determined at a given harmonic, the resonant frequency f_N and the resistance R_N .

The transient decay method [10] excites the QCM at its resonant frequency, then shorts the crystal and records the time behavior of the decaying current. This has been designed such that the decay currents for the various harmonics can be sequentially recorded. From the current decay for each harmonic, it is possible to determine the resonant frequency and the decay time. The decay time is related to the dissipation. Again, two of the important properties at each harmonic resonance are determined, in this case the resonant frequency f_N and the dissipation D_N . These are discussed in more detail by Rodahl, et al. [11]. The ability to examine the behavior of multiple harmonics has been shown to be useful for interpreting the properties of the load. Although coming at an increased cost, it has shown itself to be extremely valuable in data analysis, particularly when studying viscoelastic loads.

Of primary interest in this paper is the study of the changes in the spectral behavior of the BVD circuit. This has come to be known as the “impedance” method and is used extensively. There have been a number of creative methods for determining the parameters of the load from spectral data, which demonstrates the versatility and flexibility of the impedance method. One, for example, is described by Berg et al. for the special case [12] in which an oscillating surface of quartz contacted an adjacent sphere. A somewhat different procedure was developed by Wang et al. [13] to use the admittance measurements to study gel swelling and deswelling. Another unusual application involves the use of impedance analysis for the measurement [14] of microliter volumes of liquid drops placed onto the crystals. The possibility of a scanning QCM was demonstrated by

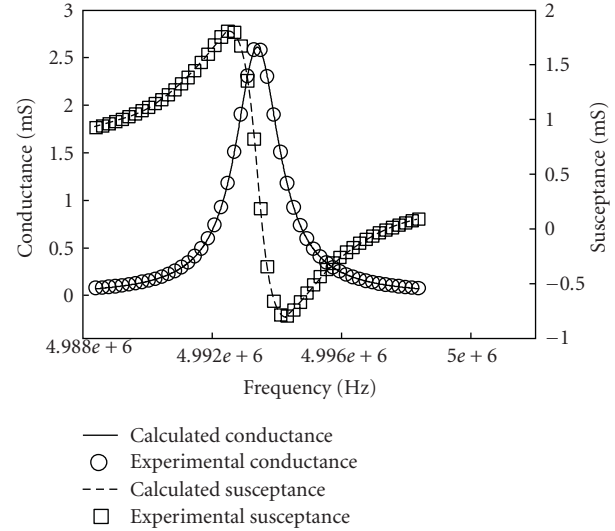


FIGURE 2: The experimental points for a 5 MHz fundamental crystal in water are illustrated by the circles (conductance) and squares (susceptance). The spectrum of the calculated 4 element BVD circuit is shown by the solid and dashed lines.

Oyama et al. [15], where scanning resolutions of 1 to 2 mm resolutions were found possible. There are many other nonstandard uses of QCM impedance analysis, which demonstrate that it is a very useful technique for many applications.

However, we focus here on the standard techniques and the possible degradations of the experimental data due to spurs. We consider the standard method to mean that the impedance being studied is that of a flat, AT-cut quartz disc with planar loads that can be modeled using a one-dimensional analysis. Electrically, the resonant behavior can be summarized in terms of the admittance of the BVD circuit, which is the ratio of the current to applied voltage. This is the inverse of the impedance. A common method is to show the real part of the admittance (the conductance G) or the imaginary part of the admittance (the susceptance B) as a function of the frequency. These are shown in Figure 2 with the units of G and B being the millisiemen (mS). The spectra for various harmonics can be recorded allowing for the study of multiple harmonics in this case as well. The ability to make a full determination of all three of the motional parameters in the BVD circuit drives much of the interest in this methodology.

The experimental data shows the behavior of a 5 MHz crystal in deionized 18 $\text{M}\Omega \cdot \text{cm}$ water. The calculated values were obtained by fitting the data to the BVD circuit. Although the fit is not perfect, it is very good and demonstrates the validity of the BVD representation. The resonant frequency is identified as the frequency of maximum conductance. The width of the peak is related to the loss, or dissipation of the resonance.

Another informative view of the admittance spectrum is a plot of the conductance along the abscissa and the susceptance along the ordinate, as shown in Figure 3.

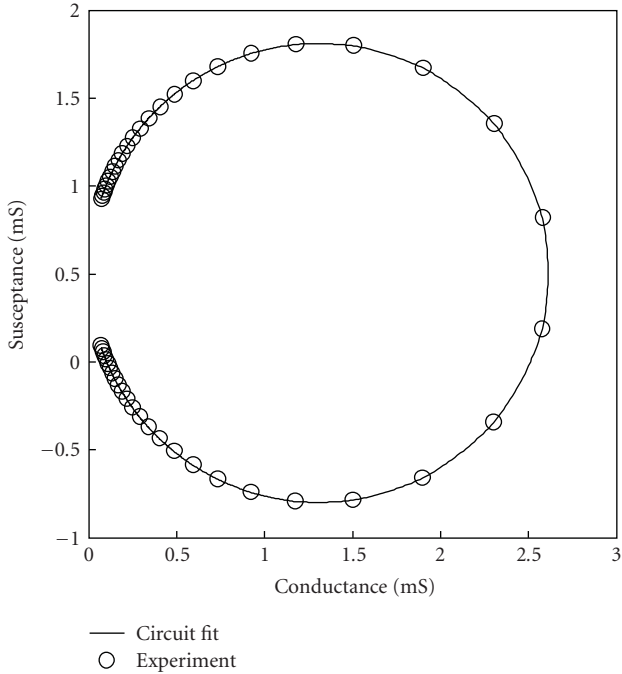


FIGURE 3: Admittance circle showing the circular form when the abscissa and ordinate scaling are identical.

If the same units are used on both axes, then it can be shown that the admittance plot is a circle. The diameter of the circle is the maximum conductance value. The circle center lies above the zero value of the ordinate and is due to the parallel capacitance C_p .

The agreement of the BVD description with experimental results shows that we can use these representations of the resonance to discuss the fitting procedure. There are sources that can distort these BVD diagrams and are discussed in the following section.

1.3. Deviations from the BVD. If a sufficiently large frequency span is taken for the spectrum, spurious resonances become visible. These are nicely described by Bottom in his classical text [15]. Taking the conductance data for several harmonics of the crystal in water, we observe, for example, as shown in Figure 4, the presence of an additional peak. The abscissa has been taken to be the index of the frequency plot. The frequency itself could not be used because it covers several harmonic ranges.

The additional resonance seen to the high frequency side of the main resonance is called a spurious resonance, or spur. The spur overlaps the main spectral peak giving rise to a distortion. We will show that the spur can be fully integrated into the fitting scheme to eliminate this source of distortion. The information in the susceptance data is better seen using the circular admittance plot.

The large admittance circles for the main resonances are visible. In addition, the smaller admittance circles for the spurs are also visible. The effects of the parallel capacitance,

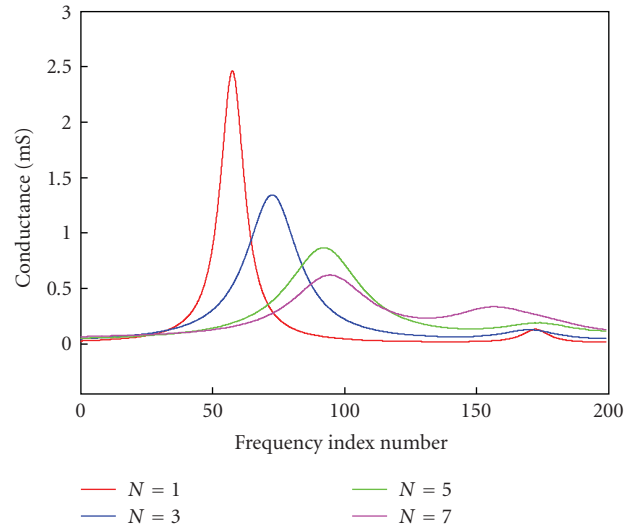


FIGURE 4: The conductance spectra are shown for several harmonics in the case of the quartz crystal having one face immersed in water.

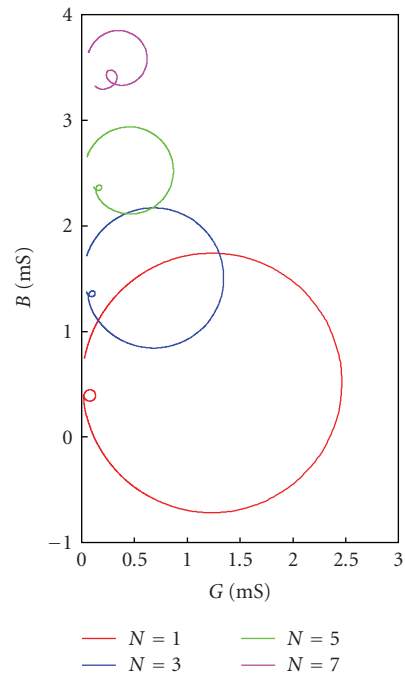


FIGURE 5: The circular admittance spectra over several harmonics.

C_p , are seen as the offset of the circles' centers along the ordinate. This vertical offset increases for increasing harmonic resulting from the increasing capacitive susceptance with increasing frequency. This capacitance reflects the dielectric capacitance of the quartz disk as well as the capacitance of wires and cables used to connect the crystal. The constancy of this capacitance is clearly seen if we subtract a susceptance value corresponding to 16 pf from each admittance circle. In that case, we then observe Figure 6.

In addition to the capacitance effect of C_p , we can also note that the admittance circles are not tangential to the

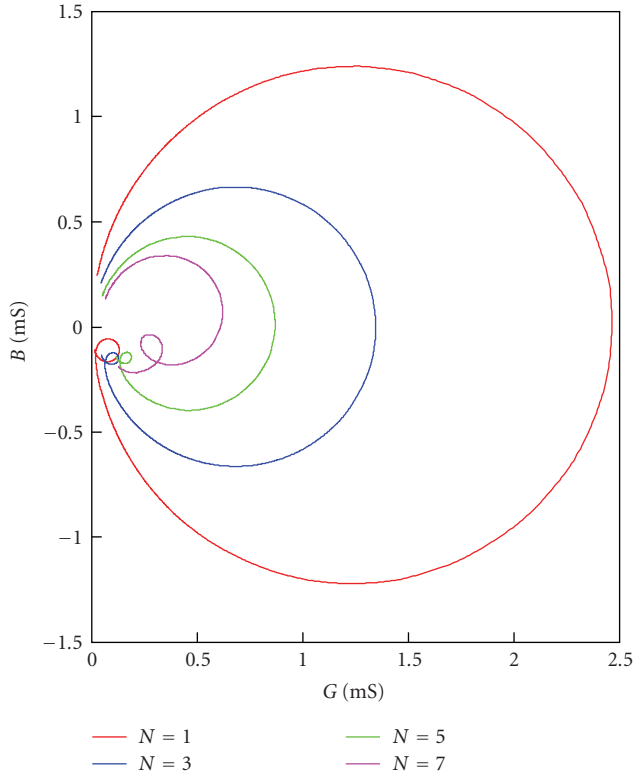


FIGURE 6: The admittance circles corrected for a constant 16 pf capacitance.

ordinate as would be expected from the simple BVD circuit. There is a horizontal offset that increases with increasing harmonic. This is not a large effect, but its effect can be described by the presence of a frequency dependent conductance in parallel with the BVD circuit. See, for example, the recognition and description of such a parallel path by Lucklum et al. [16].

These deviations are easily summarized in the circular admittance plots. The capacitance C_p gives rise to a vertical shift in the circle. The spurs are evident from the extra circle on the high frequency end, and a parallel conductive loading appears as a shift of the circle to the right.

2. Experimental Details

To obtain the experimental data used for fitting, we used quartz crystals obtained from Maxtek, Inc. The crystals had a diameter of 1 inch and were plano-plano 5 MHz AT cut crystals having asymmetrical electrodes. The thicknesses are in the range of $331 \mu\text{m}$. The smaller electrode defined the common areal region and had an areal value of $3.419 \times 10^{-5} \text{ m}^2$. The crystals were placed in the standard polyvinyl chloride holder was provided by Maxtek. The glass cell provided by Maxtek was used. The glass cell and the circular crystal holder are shown in Figures 7(a) and 7(b).

The PVC crystal holder shown in Figure 7(b) contained the crystal and was connected to the connector shown on the glass portion of the cell. O-rings sealed the crystal on both

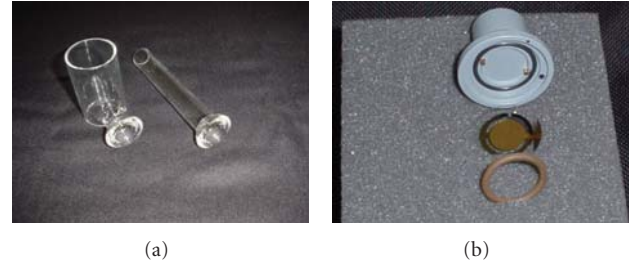


FIGURE 7: (a) Two types of glass cells are shown. The one on the left was used in this study. The PVC crystal holder is shown with the black O-ring. (b) The crystal is shown in front of the holder along with the sealing O-ring.

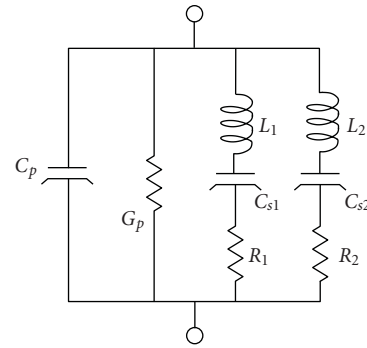


FIGURE 8: The equivalent circuit used at each harmonic.

sides. The holder was held to the cell by a spring clip. The circular crystal holder terminated in an SMB connector. To connect this unit to the Agilent 4291-A Impedance probe, it was necessary to use an approximate 1 foot length of SMB cable, and then an SMB to BNC adapter. The instrument used for capturing the spectra was the Agilent 4294 Precision Impedance Analyzer.

The crystal was cleaned by immersion in an ethanol solution and drying with a gentle stream of nitrogen. It was then placed in an oxygen plasma unit. Deionized water of $18 \text{ M}\Omega \cdot \text{cm}$ purity was used in the glass cell.

3. Fitting Procedure

The experimental data was treated in a fitting procedure designed to extract the values of the resonance properties. In the ideal case, the circuit shown in Figure 1 is appropriate. In such a case, the spectrum is described by a Lorentzian shape and a fit to this shape would be appropriate. For the high quality (low dissipation) circuits occurring with the QCM, the Lorentzian spectra exhibit a symmetry about the resonant frequency. As we have seen, spurs can distort the symmetry of the resonance. In addition we have also seen that the parallel capacitance C_p can displace the Lorentzian circles vertically and shunt conductances can displace them horizontally.

To incorporate the various aspects of the equivalent circuit, we use the circuit shown in Figure 8.

C_p is the parallel capacitance, including all of the connecting adapters and cables. G_p represents the effects due to a conductive shift of the circle to the right. The branch with the subscript 1 represents the motional aspects of the main resonance of the quartz crystal, while that with the subscript 2 represents the resonant spur. We can write the admittance in terms of the individual circuit elements shown above as

$$\begin{aligned} Y &= G + jB \\ &= G_p + j\omega C_p + \frac{1}{j\omega L_1 + (1/j\omega C_{S1}) + R_1} \\ &\quad + \frac{1}{j\omega L_2 + (1/j\omega C_{S2}) + R_2}. \end{aligned} \quad (1)$$

However, we have used an alternate expression for this same admittance in terms of parameters more convenient for the fitting procedure, and is shown below:

$$\begin{aligned} Y &= G_p + j\omega C_p + \frac{G1_{\max}}{1 + j(1/D1)((f/f_{10}) - (f_{10}/f))} \\ &\quad + \frac{G2_{\max}}{1 + j(1/D2)((f/f_{20}) - (f_{20}/f))}. \end{aligned} \quad (2)$$

The values used instead of L , C_s , and R are G_{\max} , D , and f_0 . $G1_{\max}$ is the maximum conductance of the main resonance, $D1$ is the dissipation of the main resonance peak and f_{10} is the resonant frequency of the main resonance. Dissipation is simply the inverse of the more familiar quality factor or Q of the circuit. It is treated in more detail by Rodahl et al. [10]. Relations connecting the parameters are as follows:

$$\begin{aligned} G1 &= \frac{1}{R1}, \\ f_{10} &= \frac{1}{2\pi\sqrt{(L1)(C_{S1})}}, \\ D1 &= \frac{R1}{2\pi f_{10}L1}. \end{aligned} \quad (3)$$

These connect the parameters describing the main resonance branch. There are a set of equivalent connecting equations for the spurious resonance branch. In order to fit the experimental spectra to (2), it is necessary to provide some "guess" values for these parameters. The experimental spectra are a record of the conductance and the susceptance over a range of frequencies. It is possible to obtain spectra with the number of frequencies in the range of 50, 100, 200, or 400 or more. We typically used the spectra consisting of 400 frequency values. We generated a subroutine with which we obtained starting guess values from the experimental spectra. The guess value of G_{\max} is obtained by recording the maximum value of G over a resonance. The frequency at which this occurs is taken as the guess value for the resonant frequency f_0 . To obtain a guess value for the dissipation is slightly more complex. We find the maximum value of the susceptance in the resonance region and take its frequency $f_{B\max}$. We calculate the frequency difference

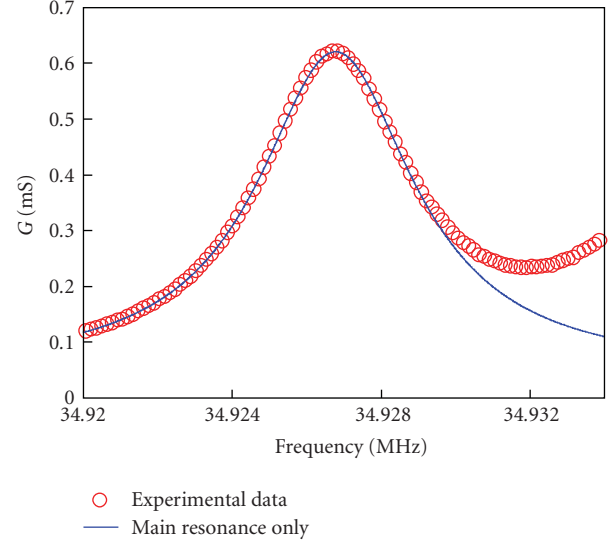


FIGURE 9: The calculated fit using only the main resonance (blue) with the experimental data shown in red circles.

$\Delta f = (f_0 - f_{B\max})$. Twice this value is taken as the full width at half maximum for the resonance. The guess value for the dissipation D is then taken to be $(2\Delta f/f_0)$. To fit a single main resonance (without spur), 5 guess values are required; C_p , G_p , $G1_{\max}$, f_{10} , and $D1$. For fitting to a main resonance with a spur, three additional guess values are required: $G2_{\max}$, f_{20} , and $D2$.

While there are many other possible ways to do the fitting, we chose to use the method called "genfit" in the Mathcad program. It is described in their literature as a least-squares nonlinear regression. For those more familiar with these methods, they also describe it as using a Levenberg-Marquardt approach to the minimization.

In beginning this experiment, we were not certain that the spur resonance could be included in the fit to a resonance. It was possible, for example, that the three-element equivalent circuit for the spur was too simplistic, or it was possible that the fitting procedure would not permit the inclusion of the large number of variables. We examined this possibility by an initial demonstration. For this demonstration, we have taken one case of the data for the seventh harmonic and compare the results of the fitting with and without spur inclusion.

In Figure 9, the main resonance of the conductance at the seventh harmonic is shown. The fits are made to the conductance data. When the spur effect is neglected, a careful look at the spectrum indicates that the experimental curve does not have the symmetrical shape expected for a single resonance. Even a possible shift in the position of the peak is suggested. We believe this to be the result of the overlap of the spurious resonance with the main resonance. We include the first spur of the seventh harmonic and obtain the following results.

Again, the fits were made using only the conductance data with the guess values being derived from the conductance spectrum as described earlier. The fit to the susceptance

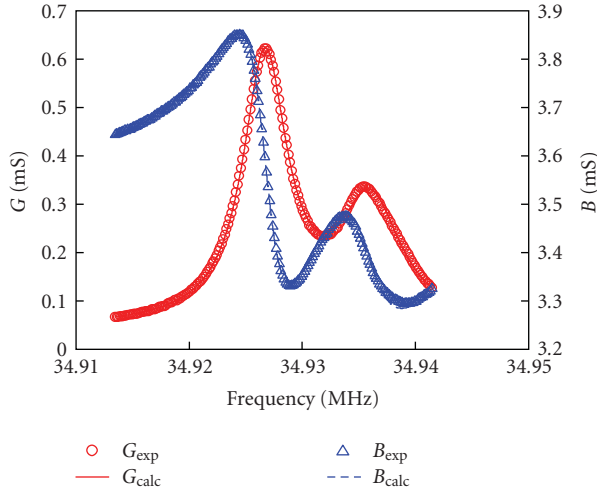


FIGURE 10: The seventh harmonic data are shown including the first spur. The experimental G and B values are shown by the red circles and the blue triangles, respectively. The calculated fits using the equivalent circuit of Figure 8 are shown by the solid red line and dashed blue line.

TABLE 1: Values of circuit parameters without correcting for spur (black) and with correcting for the spur (red).

N	Fmain MHz	Gmain mS	Dmain 10^{-6}
1	4.993348	2.45958	353.316
	4.993348	2.46127	352.953
3	14.970878	1.33199	188.701
	14.970874	1.33314	187.991
5	24.949092	0.844077	155.258
	24.949080	0.839339	153.141
7	34.936778	0.573590	145.474
	34.926700	0.549358	136.959

data is also extremely good. The quality of the fits provided confidence in the fitting procedure. By including the effects of the spur resonance, we feel that we can be more assured of the accuracy of the elements representing the main resonance. The accuracy of the representation for the main resonance is important since the changes due to the load are calculated from the one-dimensional electromechanical model which represents the single main resonance.

4. Results of the Fitting

This same procedure was used to fit the 1st, 3rd, and 5th harmonics as well. To show the changes incurred by including the spur, we have listed in Table 1 the values of the characteristics of the main resonance determined without the spur correction (black) and with the spur correction (red).

The differences do not appear to be large. However, we must remember that the changes induced by the additional

TABLE 2: Values of the BVD circuit at the various harmonics are given.

N	R Ω	L H	C_S fF
1	406.57	0.03668	27.70
	406.29	0.03369	27.69
3	750.76	0.04230	2.672
	750.11	0.04242	2.664
5	1184.7	0.04867	0.8359
	1191.4	0.04963	0.8200
7	1743.4	0.05461	0.3802
	1820.3	0.06056	0.3429

TABLE 3: Values calculated from the one-dimensional theory.

N	Res. Freq. Hz	Induct. H	C_S fF
1	4999210	0.03886	26.0833
3	15040717	0.03897	2.8736
5	25073036	0.03897	1.0338
7	35106021	0.03898	0.52733
9	45137744	0.03898	0.31898
11	55169313	0.03898	0.21352
13	65200803	0.03898	0.11259

TABLE 4: Values of C_p and G_p fitted to the data for the harmonics.

N	C_p (pf)	G_p (μS)	R_p ($K\Omega$)
1	16.134	4.0271	248.32
3	15.884	10.784	92.73
5	15.909	22.985	43.507
7	16.006	45.050	22.198

mass of the film and liquid are very small. So it is necessary to obtain a relatively high accuracy for these values. Using (3) it is possible to obtain direct relations between the values of f_0 , G_{\max} , and D with L , C_S , and R . These results are shown in Table 2 in the more familiar values of the BVD circuit elements.

An unexpected feature of these results is that the inductance appears to change with the harmonic. While not a major point of study here, we include the values calculated from the one-dimensional theory for comparison. The inductance was found to be almost constant, independent of harmonic. The calculated values are shown in Table 3.

We extended the values to the 13th harmonic to ensure the constancy of the inductance with harmonic number. The calculated changes are very small, which made the results of the measurements somewhat surprising. This is perhaps worthy of further study, but was not pursued here.

While we have not dwelled on the corrections for the parallel capacitance and the parallel conductance, these were also used in the fitting algorithm. For interest, these values are shown in Table 4.

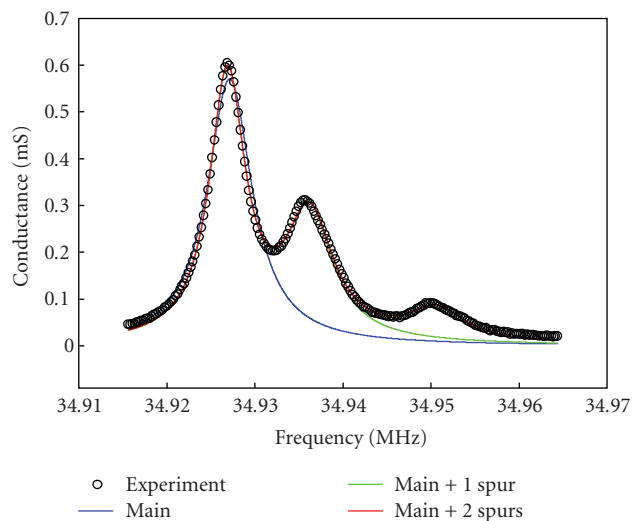


FIGURE 11: Fitting the conductance of the 7th harmonic containing two spurs.

As can be seen, the values for C_p are almost constant indicating again the invariance of the dielectric parameters with frequency. The conductance values are included only to indicate that the horizontal shift in the admittance circle can be accounted for. Because resistance is a more familiar variable than conductance, we have converted the conductance to resistance, shown in the last column. Except to remark on the monotonic behavior, we make no further comment on this variable.

The successes obtained in fitting the main resonance, spurs and parallel admittances were very satisfying. In the case of the 7th harmonic, a second spur was seen above the first spur. We extended the treatment discussed above to have an additional three elements branch to describe a second spur and attempted a fit to see whether the fitting routine was robust enough to include additional variables. The results are shown in Figure 11.

The agreements fitting to only the main resonance (blue), to the main and first spur (green) and to the main and both spurs (red) are very satisfying.

5. Conclusion

One major method for determining the physical parameters of loads placed on the quartz crystal microbalance is the admittance (or impedance) method. The recorded values caused by changes in the electrical measurements of the admittance spectrum are fit to a model. A major perturbation that can distort the measured electrical spectrum is the presence of spurious resonances. In addition, perturbations arising from the connection of the crystal transducer to the measurement apparatus can also distort the spectrum. We have shown a method by which these three effects can be quantitatively accounted for, increasing the confidence in the accuracy of the fit.

Acknowledgments

The authors wish to thank Stanford University's Center for Polymer Interfaces and Macromolecular Assemblies (CPIMA) for use of its facility. This work was completed through a CPIMA SURE program award to SMY.

References

- [1] M. A. Cooper and V. T. Singleton, "A survey of the 2001 to 2005 quartz crystal microbalance biosensor literature: applications of acoustic physics to the analysis of biomolecular interactions," *Journal of Molecular Recognition*, vol. 20, no. 3, pp. 154–184, 2007.
- [2] A. A. Vives, *Piezoelectric Transducers and Applications*, vol. 26, Springer, Berlin, Germany, 2008, 125 illustration.
- [3] D. A. Buttry and M. D. Ward, "Measurement of interfacial processes at electrode surfaces with the electrochemical quartz crystal microbalance," *Chemical Reviews*, vol. 92, no. 6, pp. 1355–1379, 1992.
- [4] A. Arnau, "A review of interface electronic systems for AT-cut quartz crystal microbalance applications in liquids," *Sensors*, vol. 8, no. 1, pp. 370–411, 2008.
- [5] E. Benes, "Improved quartz crystal microbalance technique," *Journal of Applied Physics*, vol. 56, no. 3, pp. 608–626, 1984.
- [6] R. W. Cernosek, S. J. Martin, A. R. Hillman, and H. L. Bandey, "Comparison of lumped-element and transmission-line models for thickness-shear-mode quartz resonator sensors," *IEEE Transactions on Ultrasonics, Ferroelectrics, and Frequency Control*, vol. 45, no. 5, pp. 1399–1407, 1998.
- [7] S. J. Martin, V. E. Granstaff, and G. C. Frye, "Characterization of a quartz crystal microbalance with simultaneous mass and liquid loading," *Analytical Chemistry*, vol. 63, no. 20, pp. 2272–2281, 1991.
- [8] H. Muramatsu, E. Tamiya, and I. Karube, "Computation of equivalent circuit parameters of quartz crystals in contact with liquids and study of liquid properties," *Analytical Chemistry*, vol. 60, no. 19, pp. 2142–2146, 1988.
- [9] M. Ferrari, V. Ferrari, and K. Kanazawa, "Dual-harmonic oscillator for quartz crystal resonator sensors," *Sensors and Actuators A*, vol. 145–146, no. 1–2, pp. 131–138, 2008.
- [10] M. Rodahl, F. Höök, A. Krozer, P. Brzezinski, and B. Kasemo, "Quartz crystal microbalance setup for frequency and Q-factor measurements in gaseous and liquid environments," *Review of Scientific Instruments*, vol. 66, no. 7, pp. 3924–3930, 1995.
- [11] M. Rodahl, F. Höök, and B. Kasemo, "QCM operation in liquids: an explanation of measured variations in frequency and Q factor with liquid conductivity," *Analytical Chemistry*, vol. 68, no. 13, pp. 2219–2227, 1996.
- [12] S. Berg, D. Johannsmann, and M. Ruths, "Frequency response of quartz crystal shear-resonator during an adhesive, elastic contact in a surface forces apparatus," *Journal of Applied Physics*, vol. 92, no. 11, pp. 6905–6910, 2002.
- [13] Z. Wang, D. Kuckling, and D. Johannsmann, "Temperature-induced swelling and de-swelling of thin poly(N-isopropylacrylamide) gels in water: combined acoustic and optical measurements," *Soft Materials*, vol. 1, pp. 353–374, 2003.
- [14] A. Saluja and D. S. Kalonia, "Measurement of fluid viscosity at microliter volumes using quartz impedance analysis," *AAPS PharmSciTech*, vol. 5, pp. 1–14, 2004.

- [15] N. Oyama, T. Tatsuma, S. Yamaguchi, and M. Tsukahara, "Scanning electrode quartz crystal analysis," *Analytical Chemistry*, vol. 69, no. 6, pp. 1023–1029, 1997.
- [16] R. Lucklum, G. Behling, R. W. Cernosek, and S. J. Martin, "Determination of complex shear modulus with thickness shear mode resonators," *Journal of Physics D*, vol. 30, no. 3, pp. 346–356, 1997.

Review Article

Nanostructure-Enhanced Surface Acoustic Waves Biosensor and Its Computational Modeling

Guigen Zhang^{1,2,3}

¹Department of Bioengineering, Clemson University, Clemson, SC 29634, USA

²Department of Electrical and Computer Engineering, Clemson University, Clemson, SC 29634, USA

³Institute for Biological Interfaces of Engineering, Clemson University, Clemson, SC 29634, USA

Correspondence should be addressed to Guigen Zhang, guigen@clemson.edu

Received 29 December 2008; Revised 1 May 2009; Accepted 23 June 2009

Recommended by Wojtek Wlodarski

Surface acoustic wave (SAW) devices are considered to be very promising in providing a high-performance sensing platform with wireless and remote operational capabilities. In this review, the basic principles of SAW devices and Love-mode SAW-based biosensors are discussed first to illustrate the need for surface enhancement for the active area of a SAW sensor. Then some of the recent efforts made to incorporate nanostructures into SAW sensors are summarized. After that, a computational approach to elucidate the underlying mechanism for the operations of a Love-mode SAW biosensor with nanostructured active surface is discussed. Finally, a modeling example for a Love-mode SAW sensor with skyscraper nanopillars added to in its active surface along with some selected results is presented.

Copyright © 2009 Guigen Zhang. This is an open access article distributed under the Creative Commons Attribution License, which permits unrestricted use, distribution, and reproduction in any medium, provided the original work is properly cited.

1. Introduction

Biosensors are analytical devices that combine a biologically sensitive element with a physical transducer to selectively and quantitatively discern specific compounds in a given biological environment [1]. Biosensors play a crucial role in safeguarding public health and protecting the environment. Due to the ever-increasing concerns over public health and environmental safety, improving the performance of biosensors becomes not just a technological issue but rather issues of life and death and quality of life. High performance biosensors are required to detect, specifically and sensitively, biological species that can cause harm to humans at a concentration range well below the harmful threshold level. Ideally, such biosensors should be built upon a wireless platform with which detections can be made through remote and wireless operations.

Surface acoustic wave (SAW) based biosensors have the potential to meet these requirements because their excitation and data communication can be achieved via a wireless means [2]. SAW-based sensors are microelectromechanical systems in which high frequency acoustic waves travel close to the surface of a piezoelectric substrate. Because of the

confinement of the acoustic energy near the surface within the range of one acoustic wavelength, SAW devices are highly sensitive for discerning any surface perturbation such as molecular absorption or adsorption and change of viscoelastic properties.

To use a SAW device as a sensor, very often a two-port delay-line configuration is used. In such a two-port delay-line SAW sensor, two sets of interdigitated transducers (IDTs) placed atop of a piezoelectric substrate are necessary for generating and receiving acoustic waves. The first set of IDTs is called the transmitter and the second set the receiver. The transmitter converts an alternating electrical signal into an acoustic wave which travels along the surface of the piezoelectric substrate, and the receiver converts the acoustic wave back to an electrical signal for detection and analysis. The area between the generator and receiver is often coated with a chemically sensitive surface for molecular absorption or adsorption. SAW sensors can be used to detect molecular absorption and adsorption events or changes in the viscoelastic properties of the sensitive surface by measuring the wave characteristics such as frequency shift and insertion loss.

SAW devices have been widely used as sensors for gaseous, chemical, and biological species detection [3–10].

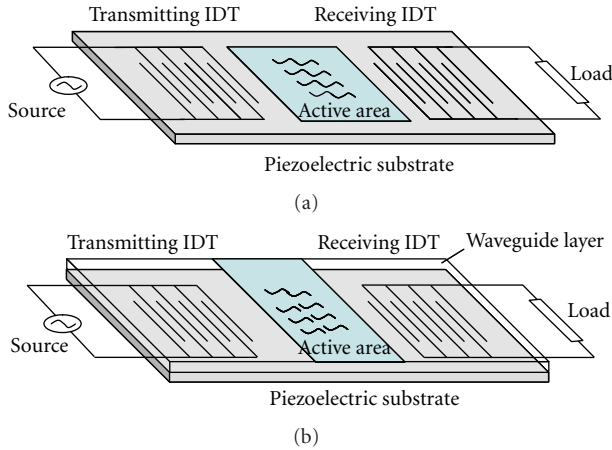


FIGURE 1: Schematic representations of a two-port delay-line SAW sensor (a) and a Love-mode SAW sensor (b).

The underlying principles for their operations and applications have been widely discussed and these discussions can be found in several books [2, 11–13]. Recently, the applications of SAW devices as biosensors were summarized by Länge et al. [14] and their applications as gas and vapor sensors were summarized by Ippolito et al. [15]. In light of this, the focus of this review will be on the use of nanostructures to enhance the detection performances of SAW sensors. We will begin by briefly laying out the basic operating principles of a SAW device and a Love-mode SAW sensor to present the need for surface enhancement in a Love-mode SAW sensor. We will then summarize some recent efforts in incorporating nanostructures into SAW biosensors. After that, we will discuss a computational approach to elucidate the underlying mechanism of Love-mode SAW biosensors incorporated with nanostructures. Finally, we will present a modeling example of a Love-mode SAW sensor incorporated with skyscraper nanopillars along with some selective results.

2. The Need for Enhancing the Active Area of a Love-Mode SAW Sensor

Acoustic waves are mechanical waves generated by the displacements of atoms in a solid piezoelectric material such as quartz, lithium niobate and lithium tantalite. When an alternating mechanical strain is applied to a piezoelectric substrate, the atoms of the piezoelectric material will be displaced from their original locations against the elastic forces that tend to restore them. This action results in a mechanical wave propagating close to the surface of the material [16].

In a common two-port delay-line configuration, a SAW sensor consists of two transducers placed on the surface of the piezoelectric substrate as illustrated in Figure 1(a). The left transducer (the transmitter) is for generating a mechanical wave and the right transducer (the receiver) is for picking up the wave. The transmitter is used to convert an alternating electrical excitation into acoustic wave in the

solid piezoelectric material. The generated acoustic wave travels along the surface of the piezoelectric material where the biological detection occurs. By a reverse process, the receiver converts the acoustic wave back to electrical signals. In such a two-port delay-line biosensor the dimensions of the IDTs determine the wavelength of the acoustic wave: $\lambda = 2(W_{el} + W_{sp})$ where W_{el} is the width of each individual electrode in the IDEs and W_{sp} the spacing between two adjacent individual electrodes. The frequency of operation is governed by $f_0 = v_0/\lambda$, where λ is the wavelength of the acoustic wave and v_0 is the travel velocity of the acoustic wave in the piezoelectric material [2, 11–13].

In order to achieve high sensitivity in SAW sensors, it is essential to confine a maximum amount of acoustic energy near the surface of the substrate and minimize wave scattering into the bulk of the substrate. To achieve this, Love-mode acoustic wave devices have been developed based on the physical effect discovered by Love [17]. In Love-mode SAW devices, a waveguide layer (see Figure 1(b)) made of a dielectric material is used to confine acoustic energy close to the surface of the devices. For high waveguide efficiency the coated material should have a wave velocity less than that of the base piezoelectric substrate material [13]. Dielectric materials such as silicon dioxide, parylene, polymethylmethacrylate, photoresists, novolac resin are good waveguide materials.

Aside from trapping a maximal amount of acoustic energy close to the active surface of a SAW sensor, increasing the area of the active surface can lead to an increased amount of molecular absorption or adsorption. To provide a large detection range and high detection sensitivity, it would be ideal to have a sufficiently large surface area for the active region such that a larger amount of molecular absorption or adsorption at the active region can be achieved. Based on a brief survey of the state of SAW sensor development and application, we proposed some strategies for enhancing the performances of SAW sensors by taking advantage of nanotechnology, especially adding nanostructures to the active area of SAW sensors in 2006 [18] based on the belief that nanostructures would increase the specific surface area due to their high surface to volume ratio. Indeed, nanostructures such as nanoparticles, nanotubes, nanofibers, nanorods, and nanopillars have been successfully employed for this purpose in the past several years.

3. Efforts in Applying Nanostructures to the Active Area of SAW Sensors

The nanostructures added to the active surface of SAW sensors can be categorized mainly into four groups: (1) dispersed nanoparticles and nanoparticle conjugates, (2) random nanofibers, nanobelts, and nanotubes, (3) standing nanostructures, and (4) porous nanostructures. In the following sections, we will discuss these efforts according to these categories.

3.1. Nanoparticles and Nanoparticle Conjugates. Levit et al. [19] used a SAW sensor to detect toluene vapors after coating the sensor with fluoroalkyl acrylate (FAA) polymeric

TABLE 1: Material constants for a XY-lithium-niobate piezoelectric substrate.

XY lithium niobate	
C_{11}	$20.3 \times 10^{10} \text{ N} \cdot \text{m}^{-2}$
C_{12}	$5.3 \times 10^{10} \text{ N} \cdot \text{m}^{-2}$
C_{13}	$7.5 \times 10^{10} \text{ N} \cdot \text{m}^{-2}$
C_{14}	$0.9 \times 10^{10} \text{ N} \cdot \text{m}^{-2}$
C_{33}	$24.5 \times 10^{10} \text{ N} \cdot \text{m}^{-2}$
C_{44}	$6.0 \times 10^{10} \text{ N} \cdot \text{m}^{-2}$
e_{15}	$3.7 \text{ C} \cdot \text{m}^{-2}$
e_{22}	$2.5 \text{ C} \cdot \text{m}^{-2}$
e_{31}	$0.2 \text{ C} \cdot \text{m}^{-2}$
e_{33}	$1.3 \text{ C} \cdot \text{m}^{-2}$
ϵ_{11}	44
ϵ_{33}	29
ρ	$4600 \text{ kg} \cdot \text{m}^{-3}$

nanoparticles (~ 100 nm diameter). The obtained sensitivity results were compared with those obtained with SAW sensors coated with the same polymer without nanoparticles. They found that a single layer coating consisting of packed polymer nanoparticles provided a surface area approximately three times greater than that of a film without nanoparticles. When exposed to toluene at a concentration of 3100 ppm, the SAW sensors coated with FAA containing nanoparticles exhibited three times greater frequency shift than SAW sensors coated with FAA without nanoparticles. Chiu and Gwo [20] showed a linear dependence of frequency shift upon surface mass density of colloidal Au nanoparticles (~ 10 nm diameter) using a dual delay-line Rayleigh SAW sensor (built on a LiNbO_3 128° YX substrate) in a dry environment. The linear relationships reveal that the higher the mass density of Au nanoparticles the higher the frequency shift is. Moreover, they also performed detection of oligonucleotides by conjugating the oligonucleotides with Au nanoparticles in reference with a control device having just Au nanoparticles using a Love-mode SAW device (built on a LiTaO_3 36° YX substrate) in an aqueous environment. They showed that frequency shift depends on the concentration of Au nanoparticles used to bind the oligonucleotides. Based on their results, they estimated an “atto gram mass standard” for the sensitivity of their nanoparticles enhanced SAW sensors. In another study, the same group applied a similar approach using Rayleigh SAW devices built on AlN substrates [21] to detect oligonucleotides conjugated with Au nanoparticles. They showed a clear change in insertion loss as well as in resonant frequency as the experimental procedure progresses from surface functionalization, noncomplimentary reactions, to after hybridization. Au colloidal nanoparticles have also been mixed with sol gel containing titania and spin-coated onto the active surface of SAW sensors fabricated on LiNbO_3 64° YX substrates [22] for hydrogen gas detection. Higher-frequency shifts were observed at 1% H_2 in a temperature range from 150 to 300°C for the SAW sensors coated with titania containing Au nanoparticles than their counterparts coated with only titania.

3.2. Random Nanofibers, Nanobelts, and Nanotubes. Of the techniques using random nanofibers to enhance the active surface of SAW sensors, conductive polymers such as polyaniline and polypyrrole are popular choices for the materials because they can be polymerized by an electrochemical means. Wu et al. [23] coated a layer of polyaniline nanofibers as the selective layer for relative humidity detection using a dual delay-line SAW system built on a LiNbO_3 128° YX substrate. The use of polyaniline nanofibers renders the SAW sensor responsive to humidity change in a close-to-linear relationship. Sadek et al. [24] used a polyaniline/ In_2O_3 nanofiber composite to improve the sensing performance of SAW sensors for H_2 , NO_2 , and CO detection. Good repeatability was obtained for H_2 and CO gases. For NO_2 , the repeatability was not as good due possibly to the poisoning of the sensitive composite by the NO_2 gas at high concentrations. In a recent study, Sadek et al. [25] used a polyaniline/ WO_3 nanofiber composite-based SAW devices built on a LiNbO_3 64° YX substrate with a ZnO waveguide layer for hydrogen gas detection at room temperature. The developed sensors showed good repeatability and a close-to-linear relationship (especially at high H_2 concentrations) between hydrogen concentration and frequency shift. In a similar approach, Atashbar et al. [26] applied polyaniline nanofibers on top of an AlN waveguide layer of a SAW sensor fabricated on a LiNbO_3 64° YX substrate for hydrogen detection at room temperature.

Polypyrrole is another conducting polymer often used. IL-Mashat et al. [27] developed a SAW gas sensor with polypyrrole nanofibers as the active sensing layer. They demonstrated sensitive responses of the sensors to H_2 and NO_2 . Aside from these conducting polymer nanofibers, ZnO nanobelts have also been used as the active layer in a SAW sensor [28]. In this study, Sadek et al. deposited a layer of ZnO nanobelts on the active surface of a SAW sensor and demonstrated sensitive responses of the sensor to gases at a high temperature: H_2 at 185°C and NO_2 at 160°C . Interesting enough, the dose-response calibration curve for H_2 exhibited almost a linear relationship while the curve for NO_2 was nonlinear.

Of all the nanofiber cases discussed earlier, the main purpose for using these nanostructures, including polyaniline nanofibers, polyaniline/oxide composites, polypyrrole nanofibers, and ZnO nanobelts, is to make the SAW sensors responsive to their intended targets such as humidity or various gases. However, the benefit of using these nanofibers or nanobelts is clearly visible from one common feature of these SAW sensors: they all showed rapid responses to their intended targets owing possibly to the high specific areas of these nanostructures. One critical issue associated with multitarget sensors, though, is their specificity: It is imperative that they be able to differentiate various different targets.

Penza et al. explored the coating of a layer of single-walled carbon nanotubes (SWCNTs) and multiwalled carbon nanotubes (MWCNTs) onto commercially available 433.92 MHz two-port SAW resonators for vapor detection [29–31]. In general, SWCNT produced more shift in wave frequency than did MWCNT. For SAW sensors coated with SWCNT, large frequency shifts for low concentrations of

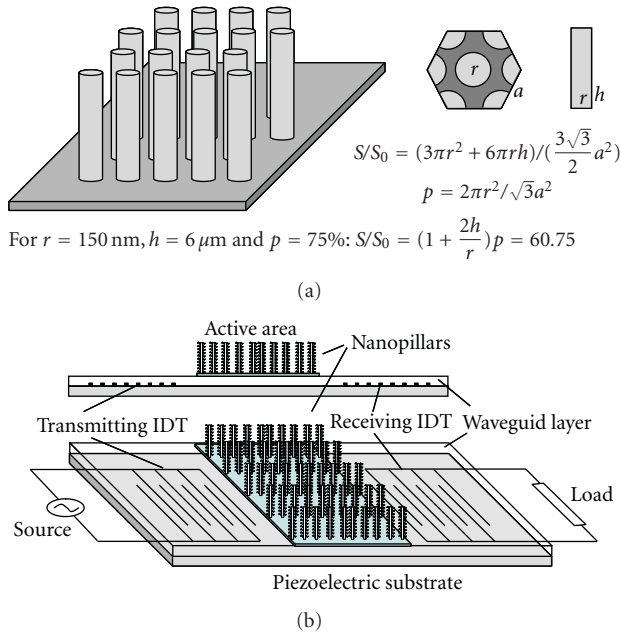


FIGURE 2: An illustration for the increase in surface area due to the cylindrical walls of the nanopillars (a), and a schematic representation of a two-port delay-line Love-mode SAW sensor with standing nanopillars added to the active area.

ethanol (720 KHz for 86 ppm) and ethylacetate (655 KHz for 178 ppm) were noted, and for sensors coated with MWCNT frequency shifts of 150 KHz, 160 KHz, 110 KHz for 86 ppm ethanol, 178 ppm ethylacetate and 93 ppm toluene in nitrogen, respectively, were observed. Recently, Penza et al. [32] applied a thin layer of SWCNT to the active area of a Love-mode SAW sensor built on LiTaO_3 36° YX substrate with a ZnO waveguide layer for various gases detection. They showed good linear relationship between the gas concentration and SAW phase change for the SAW sensors in response to NO_2 , NH_3 , and H_2 with detection sensitivity of 3.3×10^{-2} , 4.7×10^{-2} , and 1.8×10^{-2} °/ppm respectively. One unique aspect of this work is that the authors also measured the change in electrical conductance of the SWCNT layer in response to gas exposure and matched the changes in electrical conductance and in SAW frequency shift nicely together in time. Such a correlated approach to multiple species detection may provide a unique capability to differentiate among various target species, a much-needed feature for a sensor that is responsive to multiple molecular species.

3.3. Standing Nanostructures. In addition to these random nanofibers, nanobelts, and nanotubes, vertical standing nanostructures such as nanowires, nanorods, and nanopillars have also been incorporated into the active surface of SAW sensors. For example, Arsat et al. [33] incorporated standing polyaniline nanowires on top of a LiTaO_3 SAW device for hydrogen detection. By varying the thickness of the polyaniline nanowire film they found that a thicker film led to a faster detection response. Sadek et al. [34] deposited standing ZnO nanorods onto the active surface

of a SAW sensor fabricated on a LiNbO_3 64° YX substrate using a RF sputtering technique and used the SAW sensor for hydrogen detection. They demonstrated an optimum operating temperature range for the SAW sensor from 260 to 270°C with fairly good detection repeatability. Lately, more efforts were made to add ZnO nanorods to the active surface of SAW sensors. Wang et al. [35] fabricated a two-port SAW sensor incorporated with ZnO nanorods for UV detection. Huang et al. [36] from the same group pushed their effort one step further by adding Pt coated ZnO nanorods to a SAW sensor and used it for hydrogen detection.

Again as in those nanofiber and nanotube cases, the standing nanorods incorporated into the SAW sensors were mainly for rendering the SAW sensors responsive to their intended targets rather than for enhancing the sensing performances of the SAW sensors. A recent report shed some new light on this regard. Water and Chen [37] used a hydrothermal technique to add standing ZnO nanorods onto the active area of a Love-mode SAW sensor fabricated on a ST-cut Quartz substrate with an RF-sputtered ZnO waveguide layer. They reported an interesting finding that the detection sensitivity increases as the height of the nanorods increases when the ratio of nanorod height to wavelength is less or equal to 0.014; beyond this ratio the sensitivity decreases as the nanorod height increases until reaching zero when the ratio reaches 0.027.

3.4. Porous Nanostructures. Sato et al. [38] reported the use of a SAW device coated with nanoporous anodized alumina as a humidity sensor. They found that a SAW device coated with a $1.0 \mu\text{m}$ thick nanoporous alumina film yielded a much higher sensitivity when compared with a polyimide film coated SAW device. The transient response of the SAW device with nanoporous film was one order faster than that of the polyimide-coated SAW device. Hohkawa et al. [39] observed that SAW sensors incorporated with porous anodized alumina coated with platinum or cobalt were sensitive to ammonia. Varghese et al. [40] reported the detection of ammonia using nanoporous alumina with pore size of approximately 43 nm using a SAW sensor at room temperature. At a resonant frequency of 98.5 MHz a linear relationship was established between ammonia concentration and frequency shift. Moreover, these nanoporous alumina enhanced SAW sensors were capable of measuring both low and high concentrations of ammonia. This is a remarkable improvement when compared with ammonia SAW sensors based on L-glutamic acid hydrochloride [41] where the sensors saturated quickly.

Siegal et al. [42, 43] used nanoporous carbon (NPC) film coated SAW sensors to detect a range of gases such as carbon tetrachloride, benzene, and trichloroethylene and achieved sensitivity values of 1070, 698, and 662 ppm, respectively. These sensitivity values are significantly higher when compared with the responses of dendrimer polymer coated SAW devices. In the studies, they also compared the response of siloxane coated SAW devices against NPC film coated SAW devices in detecting toluene, methanol and acetone. The NPC coated SAW devices showed much higher

TABLE 2: Material constants for gold and PMMA.

	Gold	PMMA
E	79 GPa	3 GPa
ν	0.42	0.40
ρ	$19300 \text{ kg} \cdot \text{m}^{-3}$	$1100 \text{ kg} \cdot \text{m}^{-3}$

responses than their counterparts. The extrapolation of their reported data suggests that with NPC films of appropriate density ($<1.0 \text{ g} \cdot \text{cm}^{-3}$), acetone concentration of less than 1 ppb could be achieved.

4. A Computation Approach to Elucidating the Effect of Adding Skyscraper Nanopillars

Most of the nanostructures used in the approaches discussed earlier are generally coated or deposited onto the active surface. Because of the limited size of the active area, these approaches have their limitation in terms of how much the active surface area can be enhanced. As discussed previously [18], we believe that the use of vertically standing nanostructures holds great promise to providing a highly enhanced active surface area. This is because by building up in a “skyscraper” metaphor a much larger surface area increase can be achieved within a limited footprint area. As illustrated in Figure 2(a), in which a hexagonal array of vertically aligned nanopillars is constructed on a planar substrate, for a case with $r = 150 \text{ nm}$, $h = 6 \mu\text{m}$ and $p = 75\%$ for the nanopillars (note, $p \leq 91\%$), a surface area increase (S/S_0 , where S is the enhanced area and S_0 is the footprint area) of 61-fold is achieved. Therefore, adding 3D skyscraper nanopillars onto the active surface of a SAW sensor (see Figure 2(b)) will offer a significant increase in its overall active surface area. However, adding nanostructures to the active surface of a SAW sensor will change the surface morphology, which in turn would add scattering loss and affect profoundly the behavior of wave propagation. To elucidate this impact it is imperative that the effect of adding standing nanostructures on the wave propagation and detection sensitivity be investigated analytically.

Over the years, various analytical methods have been used to study the underlying mechanism for SAW propagation. Among these methods, the delta function model [44], equivalent network model [45], Green’s function model [46, 47], and coupling-of-mode method [48] are most notable. For instance, the Green’s function method was applied to determine material parameters such as elastic constants and density in a nanoscale TiN thin film [49]. Generally, these methods are able to address certain design issues associated with SAW devices, but they cannot predict the full-scale behavior of these SAW devices. In these models, the second-order effects such as backscattering, diffraction and mechanical loading have either been ignored or simplified, thus making it highly difficult to predict the behavior of the SAW devices for high-frequency applications where the second-order effects are significant.

Finite-element analysis (FEA) has been proven advantageous for both component level and systems level analyses of SAW devices. The frequency response characterization of SAW filters [50, 51], the electrical parameter characterization of SAW devices [52, 53], and the simulation of a SAW hydrogen sensor [54] have all been analyzed using FEA. We thus believe that FEA is well suited for investigating the effect of changing morphology of the sensitive surface on the propagation of SAW and the detection performance of a SAW sensor.

5. The Underlying Governing Equations for SAW Operation

The propagation of acoustic waves in a piezoelectric material is governed by the following coupled electromechanical constitutive equations:

$$\begin{aligned} T &= C_E \bullet S - e^t \bullet E, \\ d &= e \bullet S + \epsilon \bullet E, \end{aligned} \quad (1)$$

where T is the stress tensor, C_E the stiffness matrix, S the strain tensor, e the piezoelectric coupling tensor, E the electric field vector, d the electrical displacement, ϵ the dielectric matrix, and the superscript t represents the transpose of a matrix. These constitutive equations can be related to the applied electrical potential and the induced mechanical displacements by applying Newton’s law for mechanical movements and Gauss’s law for electrostatic movements. According to Newton’s second law of motion, the stress can be expressed as $\nabla \bullet T = \rho \ddot{u} - F$, where ρ is the density of the substrate material, \ddot{u} is the particle acceleration, and F is the mechanical force. Since there is no internal or external force acting on the substrate, this equation reduces to $\nabla \bullet T = \rho \ddot{u}$. Based on Gauss’s law, the electrical displacement can be expressed as $\nabla \bullet d = 0$ when the electrical charge density is zero. Moreover, in a linear material, the electrical displacement is directly proportional to the electric field $d = \epsilon E$. This equation can be further written as $d = -\epsilon \nabla \varphi$ after applying $E = -\nabla \varphi$, where φ is the electric potential. Moreover, the linear strain-displacement relationship can be written as $S = (\nabla u + \nabla \hat{u})/2 = \nabla_s u$.

With these relationships, the constitutive equation (1) can be expressed in terms of the applied potential (φ) and the induced mechanical displacement and acceleration (u and \ddot{u}) along with the material properties (C_E , e^t , and ϵ) as

$$\begin{aligned} \nabla \bullet [e^t \bullet \nabla \varphi] + \nabla \bullet [C_E \bullet \nabla_s u] - \rho \ddot{u} &= 0 \\ \nabla \bullet [e^t \bullet \nabla_s u] &= \nabla \bullet [\epsilon \bullet (\nabla \varphi)] \end{aligned} \quad (2)$$

For an anisotropic piezoelectric material like the XY-lithium-niobate substrate, the stiffness matrix (C_E), the piezoelectric

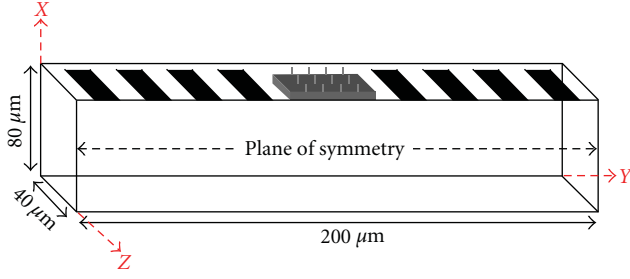


FIGURE 3: A computer model of a two-port delay-line SAW sensor with the active area incorporated with 12 evenly spaced standing nanopillars.

coupling matrix (e), and the dielectric matrix (ε) can be expressed as

$$C_E = \begin{pmatrix} C_{11} & C_{12} & C_{13} & C_{14} & 0 & 0 \\ C_{12} & C_{11} & C_{13} & -C_{14} & 0 & 0 \\ C_{13} & C_{13} & C_{33} & 0 & 0 & 0 \\ C_{14} & -C_{14} & 0 & C_{44} & 0 & 0 \\ 0 & 0 & 0 & 0 & C_{44} & C_{14} \\ 0 & 0 & 0 & 0 & C_{14} & \frac{(C_{11} - C_{12})}{2} \end{pmatrix}, \quad (3)$$

$$e = \begin{pmatrix} 0 & 0 & 0 & 0 & e_{15} & -e_{22} \\ -e_{22} & e_{22} & 0 & e_{15} & 0 & 0 \\ e_{31} & e_{31} & e_{33} & 0 & 0 & 0 \end{pmatrix},$$

$$\varepsilon = \begin{pmatrix} \varepsilon_{11} & 0 & 0 \\ 0 & \varepsilon_{22} & 0 \\ 0 & 0 & \varepsilon_{33} \end{pmatrix}.$$

For an isotropic material such as gold and polymethylmethacrylate (PMMA), the stiffness matrix can be calculated from its Young's modulus E and Poisson ratio ν as

$$C_E = \frac{E}{(1 + \nu)(1 - 2\nu)} \times \begin{pmatrix} 1 - \nu & \nu & \nu & 0 & 0 & 0 \\ \nu & 1 - \nu & \nu & 0 & 0 & 0 \\ \nu & \nu & 1 - \nu & 0 & 0 & 0 \\ 0 & 0 & 0 & \frac{(1 - 2\nu)}{2} & 0 & 0 \\ 0 & 0 & 0 & 0 & \frac{(1 - 2\nu)}{2} & 0 \\ 0 & 0 & 0 & 0 & 0 & \frac{(1 - 2\nu)}{2} \end{pmatrix}. \quad (4)$$

The piezoelectric coupling matrix of an isotropic material is zero and its dielectric matrix has a common constant value for the three elements along the principal diagonal line: $\varepsilon_{11} = \varepsilon_{22} = \varepsilon_{33} = \varepsilon$, $\varepsilon = 2.6$ for PMMA and $\varepsilon = 6.9$ for gold.

6. A Modeling Example and Some Selected Results

Recently, we developed a finite element based computational method to investigate the SAW propagation behavior in nanostructure enhanced SAW biosensors [55, 56]. A brief summary of the technical details of the modeling consideration is discussed here. A two-port delay-line SAW sensor having a flat sensitive surface with 12 nanopillars incorporated onto it is illustrated in Figure 3. Due to symmetry, only a half-structure model needs to be considered. For the SAW device, two sets of IDTs are placed $40 \mu\text{m}$ apart: the one on the left is for generating the SAW and the one on the right is for receiving the SAW. Each of the two IDTs has four electrode fingers arranged in two alternating pairs, with the width and the spacing of the electrodes both set at $10 \mu\text{m}$. The SAW sensor has a flat gold film with dimensions of $20 \mu\text{m} \times 20 \mu\text{m} \times 1 \mu\text{m}$ placed in between the two IDTs. To enhance the sensing performance using nanostructures, square gold nanopillars having a width of 100 nm and a height varying from 100 nm up to $1 \mu\text{m}$ are added to the flat gold film. For examining the detection performance of these SAW sensors, a thin film (100 nm) of PMMA is placed on top of the sensitive surface to simulate molecular adsorption.

For SAW generation, an impulse electrical signal (5) is applied to the electrode fingers of the generator IDTs. The generated wave travels to the right along the Y direction (note that the wave will actually travel in both directions and the left-traveling wave will be reflected back to the right after it reaches the left edge). After being interrogated by the PMMA film adsorbed on the sensitive surface, the acoustic wave is converted back to an electrical signal at the receiver IDTs. In the models, the following electrical boundary conditions are applied: zero charge/symmetry is applied to the top boundary surrounding the IDTs and to the symmetric plane, and ground condition is applied to all other boundaries. The impulse potential to the electrodes is applied in an alternating manner (i.e., V_{i+} at the first and third electrodes, and V_{i-} at the second and fourth electrodes):

$$V_{i+} = \begin{cases} +0.5V, & t \leq 1\text{ns}, \\ 0V, & t \geq 1\text{ns}, \end{cases} \quad V_{i-} = \begin{cases} -0.5V, & t \leq 1\text{ns}, \\ 0V, & t \geq 1\text{ns}. \end{cases} \quad (5)$$

The output voltage at the receiver IDTs is obtained in a similar alternating manner by measuring the differential potential between the first-third pair and the second-fourth pair of electrodes.

COMSOL Multiphysics (Burlington, MA) is used to find numerical solutions to the problem defined by the governing equation (2). The material constants listed in Tables 1 and 2 [50, 51] are used in the numerical analyses. In each case, signal attenuation due to PMMA adsorption at the sensitive surface is examined by quantifying the insertion loss (IL) characteristics using the following formula:

$$IL = -20 \times \log_{10} \left| \frac{V_{\text{output}}}{V_{\text{input}}} \right| \quad (6)$$

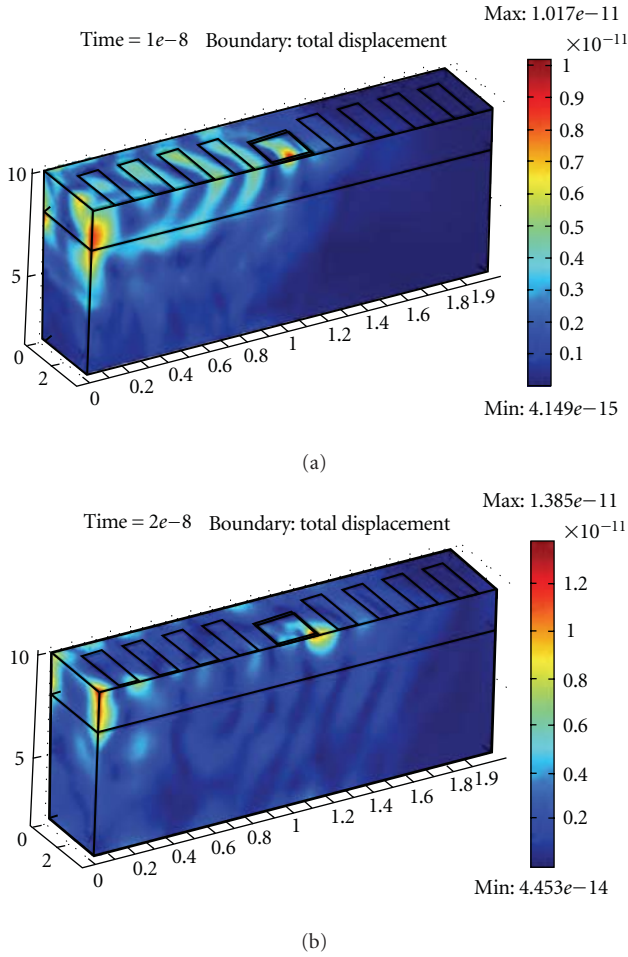


FIGURE 4: Snapshots of wave propagation from the SAW model captured at 10 ns (a) and at 20 ns (b) after the application of an impulse excitation.

Figure 4 shows two snap-shot images of wave propagation in the SAW sensor captured at 10 ns and 20 ns, respectively, after the impulse potential is applied. These images reveal that the generated wave has traveled a distance of approximately $39 \mu\text{m}$ away from the leading edge of the generator IDT in 10 ns, and after 20 ns the wave reached the other side of the substrate. Based on the travel distance, the velocity of the acoustic wave is estimated to be 3900 m/s, which is close to the reported value (ranging from 3700 to 3750 m/s) for an acoustic wave traveling in a XY-lithium-niobate piezoelectric material [57]. Figure 5(a) shows the obtained IL spectra for a flat control case (i.e., a SAW sensor with a flat gold sensitive surface) before and after the adsorption of a 100 nm thick PMMA film, and Figures 5(b) and 5(c) show the IL spectra for the SAW sensors with 9 and 12 nanopillars, respectively, before and after the adsorption of a PMMA film of the same thickness. From these IL spectra, the resonant frequency for the flat control case is calculated to be 98.5 MHz. Based on the design, this SAW sensor is expected to have a resonant frequency of $f = 97.5 \text{ MHz}$ which is reasonably close to the observed value. The slight difference observed here can be attributed to the interference

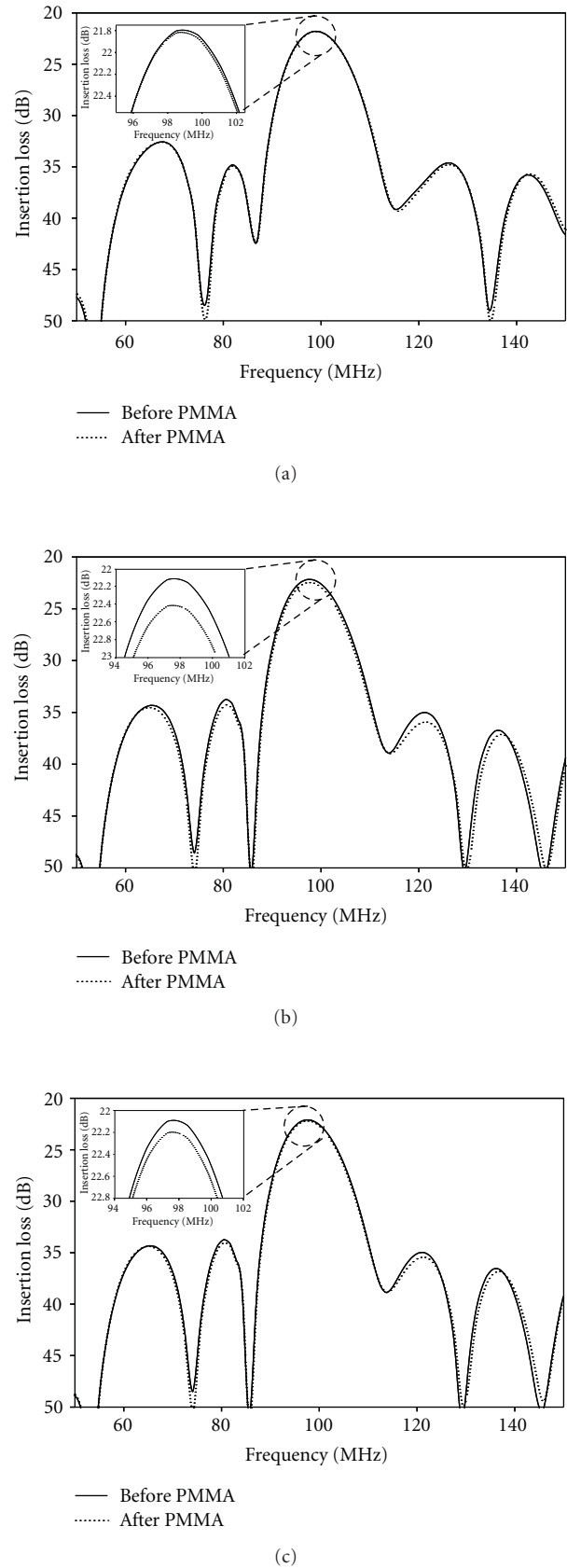


FIGURE 5: Insertion loss spectra for the flat control case (a), a nanocase with 9 nanopillars (b), and a nanocase with 12 nanopillars (c) with each insert showing a zoom-in view of the peak frequency.

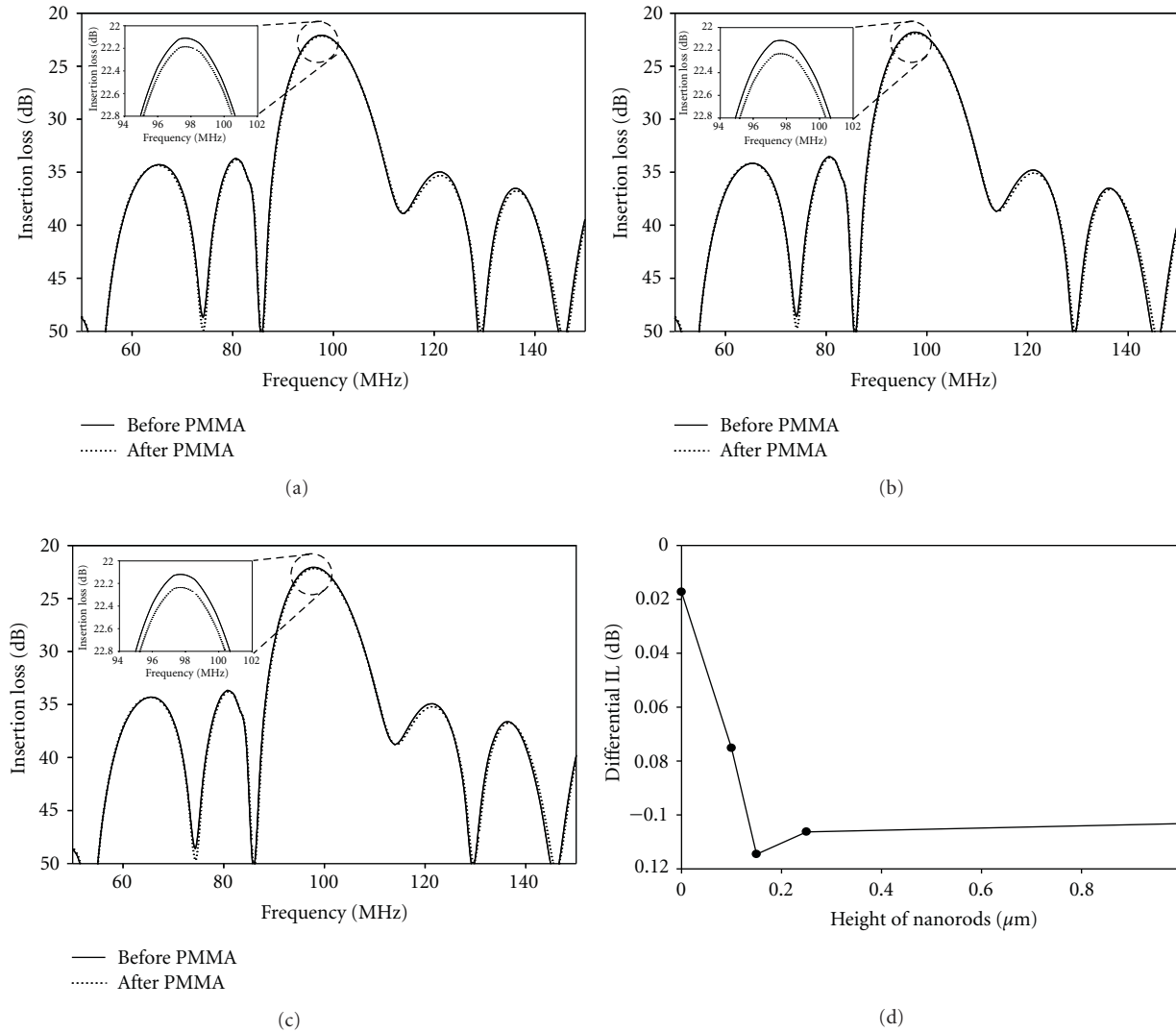


FIGURE 6: Insertion loss spectra for a SAW sensor with 9 nanopillars having a height of 100 nm (a), 150 nm (b), and 250 nm (c) before and after the adsorption of a 100 nm thick PMMA film with each insert showing a zoom-in view of the peak frequency. (d) Variation of the differential IL with the height of nanopillars.

of the reflected wave and the fact that only four individual electrodes are considered for the IDTs in the model whereas the theoretical value is predicted based on a much larger number of individual electrodes.

Higher IL is observed from simulation for a sensor with nanopillars than one without nanopillars. For instance, the peak IL for the SAW sensor with a flat sensitive surface is 21.802 dB, but the peak IL for the SAW sensors with 9 nanopillars and 12 nanopillars is 22.103 dB and 22.123 dB, respectively, before the adsorption of the PMMA film. After the adsorption of the PMMA film, the peak IL increases to 21.820 dB (flat), 22.206 dB (9-nanopillar), 22.421 dB (12-nanopillar) for the respective SAW sensors. By taking the ratio of the differential IL measurement to the actual mass of the adsorbed PMMA, the detection sensitivity of a SAW sensor is quantified. The actual mass of the adsorbed PMMA is calculated by multiplying the volume of the adsorbed

PMMA in each case by the density $\rho=1000 \text{ kg} \cdot \text{m}^{-3}$ of PMMA material. The detection sensitivity for the flat control case is calculated as 0.345 dB/ng while the detection sensitivity for the SAW sensors with 9 and 12 nanopillars are 1.94 dB/ng (5.62 times higher than the flat control case) and 5.85 dB/ng (16.96 times higher than the flat control case), respectively. Thus, the addition of vertically standing nanopillars to the flat sensitive surface is responsible for the increase in the total surface area for molecular adsorption, thus leading to increased detection sensitivity.

Figures 6(a)–6(c) show the IL spectra for a SAW sensor with 9 nanopillars having different pillar heights before and after the adsorption of the 100 nm thick PMMA film. The obtained peak IL measures 22.125 dB, 22.128 dB and 22.105 dB, respectively, when the nanopillars are 100 nm, 150 nm and 250 nm tall before the adsorption of the PMMA film. After the adsorption of the PMMA film, the peak

IL values increases to 22.200 dB, 22.243 dB, and 22.211 dB, respectively. Figure 6(d) shows the variation of the differential peak IL (due to the adsorption of the PMMA film) with the nanopillar height. With nanopillar heights being 100 nm, 150 nm, 250 nm, and 1 μm , a differential peak IL of 0.075 dB, 0.115 dB, 0.106 dB, and 0.103 dB is measured, respectively. The differential peak IL increases significantly when the height of nanopillars increases from zero to 150 nm, and beyond this height the differential peak IL decreases slightly as the height of nanopillars increases. This fact suggests that it may not be beneficial to have nanopillars taller than 150 nm. Moreover, this result is consistent with the observation made by Water and Chen [37] from their experimental work.

7. Summary

Love-mode SAW biosensors hold great promise to deliver high sensitivity and wireless and remote operational capabilities that are ideal for many biological applications. Although many parameters such as waveguide thickness, substrate material, and waveguide material have been explored in efforts to improve the performance of SAW-based biosensors, there is a technological disjunction that hinders the application of SAW sensors for highly demanding biological detection needs. To address this issue, one solution is to incorporate vertically aligned, optimally spaced and mechanically robust nanostructures into the active area of the SAW biosensors. Based on a computational modeling analysis, it is clear that adding standing nanopillars to the sensitive surface does provide the desired benefits: it provides increased surface area for increased molecular adsorption, thus leading to increased attenuation per unit thickness of molecular adsorption. In general, increasing the number and the height of nanopillars will increase the detection sensitivity of the SAW sensors, but such an increase due to nanopillar height will reach a limit.

Acknowledgments

I would like to thank my student Yeswanth L. Rao for his contribution to the modeling work summarized here that he had done during his doctoral study at the University of Georgia. I would also thank the financial supports from the National Science Foundation, the Faculty of Engineering at the University of Georgia, and the Institute for Biological Interfaces of Engineering at Clemson University.

References

- [1] G. Zhang, "Nanotechnology-based biosensors in drug delivery," in *Nanotechnology in Drug Delivery*, M. M. de Villiers, et al., Ed., vol. 163, chapter 6, Springer, New York, NY, USA, 2009.
- [2] C. K. Campbell, *Surface Acoustic Wave Devices: For Mobile and Wireless Communication*, Academic Press, San Diego, Calif, USA, 1998.
- [3] M. D. Ward and D. A. Buttry, "Insitu interfacial mass detection with piezoelectric transducers," *Science*, vol. 249, pp. 1000–1007, 1990.
- [4] E. Gizeli, N. J. Goddard, C. R. Lowe, and A. C. Stevenson, "A love plate biosensor utilising a polymer layer," *Sensors and Actuators B*, vol. 6, no. 1–3, pp. 131–137, 1992.
- [5] G. L. Harding, J. Du, P. R. Dencher, D. Barnett, and E. Howe, "Love wave acoustic immunosensor operating in liquid," *Sensors and Actuators A*, vol. 61, no. 1–3, pp. 279–286, 1997.
- [6] T. Wessa, M. Rapp, and H. J. Ache, "New immobilization method for SAW-biosensors: covalent attachment of antibodies via CNBr," *Biosensors and Bioelectronics*, vol. 14, no. 1, pp. 93–98, 1999.
- [7] M. J. Fernández, J. L. Fontecha, I. Sayago, et al., "Discrimination of volatile compounds through an electronic nose based on ZnO SAW sensors," *Sensors and Actuators B*, vol. 127, no. 1, pp. 277–283, 2007.
- [8] B.-S. Joo, J.-S. Huh, and D.-D. Lee, "Fabrication of polymer SAW sensor array to classify chemical warfare agents," *Sensors and Actuators B*, vol. 121, no. 1, pp. 47–53, 2007.
- [9] J. Andrä, A. Böhring, T. M. A. Gronewold, U. Schlecht, M. Perpeet, and T. Gutschmann, "Surface acoustic wave biosensor as a tool to study the interaction of antimicrobial peptides with phospholipid and lipopolysaccharide model membranes," *Langmuir*, vol. 24, no. 16, pp. 9148–9153, 2008.
- [10] G. Treitz, T. M. A. Gronewold, E. Quandt, and M. Zabe-Kühn, "Combination of a SAW-biosensor with MALDI mass spectrometric analysis," *Biosensors and Bioelectronics*, vol. 23, no. 10, pp. 1496–1502, 2008.
- [11] M. Thompson and D. C. Stone, *Surface Launched Acoustic Wave Sensors: Chemical Sensing and Thin-Film Characterization*, John Wiley & Sons, New York, NY, USA, 1997.
- [12] D. S. Ballantine, R. M. White, S. J. Martin, et al., *Acoustic Wave Sensors: Theory, Design, and Physio-Chemical Applications*, Academic Press, San Diego, Calif, USA, 1997.
- [13] J. W. Gardner, V. K. Varadan, and O. O. Awadelkarim, *Microsensors, MEMS, and Smart Devices*, John Wiley & Sons, New York, NY, USA, 2001.
- [14] K. Länge, B. E. Rapp, and M. Rapp, "Surface acoustic wave biosensors: a review," *Analytical and Bioanalytical Chemistry*, vol. 391, no. 5, pp. 1509–1519, 2008.
- [15] S. J. Ippolito, A. Trinchi, D. A. Powell, and W. Wlodarski, "Acoustic wave gas and vapor sensor in Solid State Sensing," E. Comini, et al., Ed., chapter 8, Springer, New York, NY, USA, 2009.
- [16] B. A. Auld, *Acoustic Fields and Waves in Solids II*, Kreiger, Malabar, Fla, USA, 1990.
- [17] A. E. H. Love, *Some Problems of Geodynamics*, Cambridge University Press, Cambridge, UK, 1911.
- [18] Y. L. Rao and G. Zhang, "Enhancing the sensitivity of SAW sensors with nanostructures," *Current Nanoscience*, vol. 2, no. 4, pp. 311–318, 2006.
- [19] N. Levit, D. Pestov, and G. Tepper, "High surface area polymer coatings for SAW-based chemical sensor applications," *Sensors and Actuators B*, vol. 82, no. 2-3, pp. 241–249, 2002.
- [20] C.-S. Chiu and S. Gwo, "Quantitative surface acoustic wave detection based on colloidal gold nanoparticles and their bioconjugates," *Analytical Chemistry*, vol. 80, no. 9, pp. 3318–3326, 2008.
- [21] C.-S. Chiu, H.-M. Lee, C.-T. Kuo, and S. Gwo, "Immobilization of DNA-Au nanoparticles on aminosilane-functionalized aluminum nitride epitaxial films for surface acoustic wave sensing," *Applied Physics Letters*, vol. 93, no. 16, Article ID 163106, 2008.

- [22] A. Z. Sadek, D. Buso, A. Martucci, P. Mulvaney, W. Wlodarski, and K. Kalantar-zadeh, "Titanium dioxide-based 64° YX LiNbO₃ surface acoustic wave hydrogen gas sensors," *Journal of Sensors*, vol. 2008, Article ID 254283, 5 pages, 2008.
- [23] T.-T. Wu, Y.-Y. Chen, and T.-H. Chou, "A high sensitivity nanomaterial based SAW humidity sensor," *Journal of Physics D*, vol. 41, no. 8, Article ID 085101, 2008.
- [24] A. Z. Sadek, W. Wlodarski, K. Shin, R. B. Kaner, and K. Kalantar-zadeh, "A layered surface acoustic wave gas sensor based on a polyaniline/In₂O₃ nanofibre composite," *Nanotechnology*, vol. 17, no. 17, pp. 4488–4492, 2006.
- [25] A. Z. Sadek, W. Wlodarski, K. Shin, R. B. Kaner, and K. Kalantar-zadeh, "A polyaniline/WO₃ nanofiber composite-based ZnO/64° YX LiNbO₃ SAW hydrogen gas sensor," *Synthetic Metals*, vol. 158, no. 1-2, pp. 29–32, 2008.
- [26] M. Z. Atashbar, A. Z. Sadek, W. Wlodarski, et al., "Layered SAW gas sensor based on CSA synthesized polyaniline nanofiber on AlN on 64° YX LiNbO₃ for H₂ sensing," *Sensors and Actuators B*, vol. 138, no. 1, pp. 85–89, 2009.
- [27] L. Al-Mashat, H. D. Tran, W. Wlodarski, R. B. Kaner, and K. Kalantar-zadeh, "Polypyrrole nanofiber surface acoustic wave gas sensors," *Sensors and Actuators B*, vol. 134, no. 2, pp. 826–831, 2008.
- [28] A. Z. Sadek, W. Wlodarski, K. Kalantar-zadeh, et al., "H₂ and NO₂ gas sensors with ZnO nanobelt layer on 36° LiTaO₃ and 64° LiNbO₃ SAW transducers," *Proceedings of IEEE Sensors*, vol. 2005, pp. 1343–1346, 2005.
- [29] M. Penza, F. Antolini, and M. V. Antisari, "Carbon nanotubes as SAW chemical sensors materials," *Sensors and Actuators B*, vol. 100, no. 1-2, pp. 47–59, 2004.
- [30] M. Penza, F. Antolini, and M. V. Antisari, "Carbon nanotubes-based surface acoustic waves oscillating sensors for vapor detection," *Thin Solid Films*, vol. 472, p. 246, 2005.
- [31] M. Penza, G. Cassano, P. Aversa, et al., "Carbon nanotubes-coated multi-transducing sensors for VOCs detection," *Sensors and Actuators B*, vol. 111-112, pp. 171–180, 2005.
- [32] M. Penza, P. Aversa, G. Cassano, W. Wlodarski, and K. Kalantar-zadeh, "Layered SAW gas sensor with single-walled carbon nanotube-based nanocomposite coating," *Sensors and Actuators B*, vol. 127, no. 1, pp. 168–178, 2007.
- [33] R. Arsat, X. F. Yu, Y. X. Li, W. Wlodarski, and K. Kalantar-zadeh, "Hydrogen gas sensor based on highly ordered polyaniline nanofibers," *Sensors and Actuators B*, vol. 137, no. 2, pp. 529–532, 2009.
- [34] A. Z. Sadek, W. Wlodarski, Y. X. Li, et al., "A ZnO nanorod based layered ZnO/64° YX LiNbO₃ SAW hydrogen gas sensor," *Thin Solid Films*, vol. 515, no. 24, pp. 8705–8708, 2007.
- [35] W.-S. Wang, T.-T. Wu, T.-H. Chou, and Y.-Y. Chen, "A ZnO nanorod-based SAW oscillator system for ultraviolet detection," *Nanotechnology*, vol. 20, no. 13, Article ID 135503, 2009.
- [36] F.-C. Huang, Y.-Y. Chen, and T.-T. Wu, "A room temperature surface acoustic wave hydrogen sensor with Pt coated ZnO nanorods," *Nanotechnology*, vol. 20, no. 6, Article ID 065501, 2009.
- [37] W. Water and S.-E. Chen, "Using ZnO nanorods to enhance sensitivity of liquid sensor," *Sensors and Actuators B*, vol. 136, no. 2, pp. 371–375, 2009.
- [38] M. Sato, T. Yamamoto, T. Meguro, and K. Yamanouchi, "Sensitivity of an anadically oxidized aluminium film on a surface acoustic wave sensor to humidity," *Sensors and Actuators: B*, vol. 20, no. 2-3, pp. 205–212, 1994.
- [39] K. Hohkawa, K. Komine, H. Suzuki, T. Eguchi, Y. Sato, and K. Koh, "Piezoelectric sensor using a porous alumina film covered with a catalytic material," in *Proceedings of IEEE Ultrasonics Symposium*, vol. 1, pp. 513–516, 1998.
- [40] O. K. Varghese, D. Gong, W. R. Dreschel, K. G. Ong, and C. A. Grimes, "Ammonia detection using nanoporous alumina resistive and surface acoustic wave sensors," *Sensors and Actuators B*, vol. 94, no. 1, pp. 27–35, 2003.
- [41] C.-Y. Shen, C.-P. Huang, and H.-C. Chuo, "The improved ammonia gas sensors constructed by L-glutamic acid hydrochloride on surface acoustic wave devices," *Sensors and Actuators B*, vol. 84, no. 2-3, pp. 231–236, 2002.
- [42] M. P. Siegal, D. L. Overmyer, R. J. Kottenstette, D. R. Tallant, and W. G. Yelton, "Nanoporous-carbon films for microsensor preconcentrators," *Applied Physics Letters*, vol. 80, no. 21, p. 3940, 2002.
- [43] M. P. Siegal, W. G. Yelton, D. L. Overmyer, and P. P. Provencio, "Nanoporous carbon films for gas microsensors," *Langmuir*, vol. 20, no. 4, pp. 1194–1198, 2004.
- [44] R. H. Tancrell and M. G. Holland, "Acoustic surface wave filters," *Proceedings of IEEE*, vol. 59, no. 3, p. 393, 1971.
- [45] W. R. Smith, H. M. Gerals, J. H. Collins, T. M. Reeder, and H. J. Shaw, "Analysis of interdigitated surface wave transducers by use of equivalent circuit model," *IEE Transactions of Microwave Theory & Techniques*, vol. 17, no. 11, p. 856, 1969.
- [46] F. Huang and E. G. S. Paige, "The scattering of surface acoustic waves by electrical effects in two-dimensional metal film structures," *IEEE Transactions on Ultrasonics, Ferroelectrics, and Frequency Control*, vol. 35, no. 6, pp. 723–735, 1988.
- [47] D. Qiao, W. Liu, and P. M. Smith, "General Green's functions for SAW device analysis," *IEEE Transactions on Ultrasonics, Ferroelectrics, and Frequency Control*, vol. 46, no. 5, pp. 1242–1253, 1999.
- [48] E. Akcakaya, "A new analysis of single phase unidirectional transducers," *IEEE Transactions on Ultrasonics, Ferroelectrics, and Frequency Control*, vol. 34, no. 1, pp. 45–52, 1987.
- [49] V. K. Tewary, "Green's-function method for modeling surface acoustic wave dispersion in anisotropic material systems and determination of material parameters," *Wave Motion*, vol. 40, no. 4, pp. 399–412, 2004.
- [50] G. Xu, "Direct finite-element analysis of the frequency response of a Y-Z lithium niobate SAW filter," *Smart Materials and Structures*, vol. 9, no. 6, pp. 973–980, 2000.
- [51] G. Xu and Q. Jiang, "A finite element analysis of second order effects on the frequency response of a SAW device," *Journal of Intelligent Material Systems and Structures*, vol. 12, no. 2, pp. 69–77, 2001.
- [52] S. J. Ippolito, K. Kalantar-zadeh, D. A. Powell, and W. Wlodarski, "A finite element approach for 3-dimensional simulation of layered acoustic wave transducers," in *Proceedings of IEEE Conference on Optoelectronic and Microelectronic Materials and Devices*, p. 541, 2001.
- [53] S. J. Ippolito, K. Kalantar-zadeh, D. A. Powell, and W. Wlodarski, "A 3-dimensional finite element approach for simulating acoustic wave propagation in layered SAW devices," in *Proceedings of IEEE Ultrasonics Symposium*, vol. 1, pp. 303–306, 2003.
- [54] M. Z. Atashbar, B. J. Bazuin, M. Simpeh, and S. Krishnamurthy, "3D FE simulation of H₂ SAW gas sensor," *Sensors and Actuators B*, vol. 111-112, pp. 213–218, 2005.
- [55] Y. L. Rao and G. Zhang, "3D modeling of a surface-acoustic-wave based sensor," in *Proceedings of COMSOL Conference*, p. 89, 2007.

- [56] Y. L. Rao, *Nanostructure-enhanced surface acoustic Love wave devices for biosensing application*, Ph.D. dissertation, The University of Georgia, Athens, Ga, USA, 2008.
- [57] B. Lin, G. Chen, X. R. Zhang, D. Zhang, and J. C. Chen, "Calculation of the SAW velocity change of proton exchanged LiNbO₃ crystal," in *Proceedings of the American Institute of Physics*, vol. 657, p. 1284, 2003.

Review Article

Receptor Function and Response of Semiconductor Gas Sensor

Noboru Yamazoe and Kengo Shimanoe

Faculty of Engineering Sciences, Kyushu University, 6-1 Kasuga-koen, Kasuga, Fukuoka 816-8580, Japan

Correspondence should be addressed to Kengo Shimanoe, simanoe@mm.kyushu-u.ac.jp

Received 27 March 2009; Revised 27 March 2009; Accepted 19 April 2009

Recommended by Michele Penza

Theoretical approaches to receptor function and response of semiconductor gas sensor are described, following the illustrations of some relevant key issues such as tunneling transport. Depletion in small semiconductor crystals is characterized by the occurrence of new type depletion (volume depletion) after conventional one (regional depletion), and inclusion of both types makes it possible to formulate the receptor function and response to oxygen (air base), oxidizing gas (nitrogen dioxide), and reducing gas (hydrogen). The equations derived theoretically using physical parameters of the semiconductor side and chemical parameters of the gases side appear to reproduce satisfactorily the sensing behavior to the aforementioned gases as well as the influence of changes in physical parameters such as grain size and donor density. Extension to the semiconductor crystals dispersed with surface electron-traps shows that the traps act as a sensitizer to promote sensor response.

Copyright © 2009 N. Yamazoe and K. Shimanoe. This is an open access article distributed under the Creative Commons Attribution License, which permits unrestricted use, distribution, and reproduction in any medium, provided the original work is properly cited.

1. Introduction

A semiconductor gas sensor (called device hereafter) possesses an electrical resistance made with a porous assembly of tiny crystals of an n-type metal oxide semiconductor, typically SnO₂, In₂O₃, or WO₃. The crystals are often loaded with a small amount of foreign substance (noble metals or their oxides) called a sensitizer. When operated at adequate temperature in air, the resistor changes its resistance sharply on contact with a small concentration of reducing gas or oxidizing gas, enabling us to know the concentration from the resistance change. For its inauguration with a report by Seiyama et al. [1] and a patent by Taguchi [2], this group of sensors has been subjected to a tremendous amount of R&D efforts world wide aiming at improvements of sensing performances and extensions to new applications. Thanks to these researches, the group not only has grown to provide important tools to detect and/or control gases in places in modern society but also has pioneered to founding a new technology field where the devices are called chemical sensors. Speaking more exactly, semiconductor gas sensors have been classified into two subtypes, that is, surface-sensitive type operating at temperatures below 500°C and bulk-sensitive one operating at high temperature (typically at

800°C) [3]. This article is concerned with those of the former type only.

Apart from such remarkable achievements in practical applications, basic understandings of this group of sensors have hardly been satisfactory, despite tremendous efforts of so many researchers as summarized in reviews [5–8]. This is partly because there are many complex factors which affect sensing properties. Not only the selection of a proper oxide semiconductor is important but also the methods and conditions for fabricating sensor devices exert profound influences on gas sensing properties through changes in donor density, crystallite size, contacting geometry between crystals, packing density (or porosity), packing thickness, and so on [7]. In addition, the sensing properties are often modified largely with loading with foreign substances such as sensitizers. Understandings of these phenomena indeed have required interdisciplinary knowledge among semiconductor physics, surface chemistry, solid-state chemistry, and so on. In order to facilitate the understandings, we have proposed to assume that the sensing properties are determined by three main factors, that is, receptor function, transducer function, and utility factor, as schematically shown in Figure 1 [4]. The first factor is concerned with how each constituent crystal responds to the surrounding atmosphere

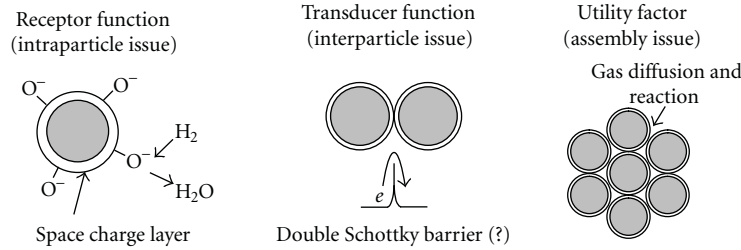


FIGURE 1: Three factors determining the response of semiconductor gas sensors [4].

containing oxygen and target gases (intraparticle issue). It is unanimous that oxygen is adsorbed on the crystals as negatively charged species, accompanied by the formation of a depletion layer inside the crystals. The target gases disturb the equilibrium through being adsorbed competitively or reacting with the adsorbed oxygen. The foreign substances like sensitizers dispersed on the crystals are assumed to affect these processes anyhow. The second factor is concerned with how the response of each particle is transformed into that of the whole device, and apparently this is related with the mechanism of electron transport between adjacent crystals (inter-particle issue). For a long time a double Schottky barrier model [9], which assumes migration transport of electrons over the barrier as shown, has been advocated for this process without critical check. The third one is concerned with the attenuation of the response due to the effect of diffusion and reaction of reactive target gases through the pores of the assembly of crystals (assembly issue) [10–12]. The above scheme has explained rather well qualitative nature of semiconductor gas sensors in several respects. However, it has failed to give quantitative understandings and, most importantly, to give new insights leading to innovations of this group of sensors. There should have been some serious defaults included in the scheme, particularly regarding the receptor and transducer functions.

Fortunately, we encountered an interesting finding several years ago that thin film devices fabricated from hydrothermally prepared colloidal suspensions of SnO_2 by a spin-coating technique showed temperature—almost independent resistances in air in the temperature range 150–400°C, as shown in Figure 2 [13]. Such thermal behavior of resistances is hardly consistent with the double Schottky barrier model mentioned above. Instead, tunneling transport of electrons across the contacts (or gaps) between adjacent crystals is strongly suggested. In addition, this transport mechanism has made much easier the theoretical modeling of receptor and transducer functions recently carried out [14–16], because the constituent crystals can now be treated independently from each other. As revealed during this process, depletion in small crystals easily goes beyond conventional one (regional depletion) to enter new type one (volume depletion). Obviously, it is a lack of such information that has delayed fundamental understandings of this group of sensors, for most of their valuable gas sensing properties show up in the stage of volume depletion or nearby.

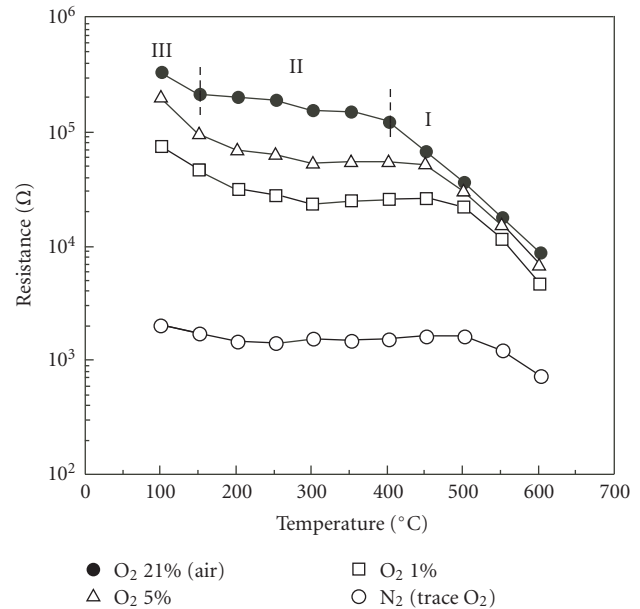


FIGURE 2: Resistance of device under selected partial pressures of oxygen as measured at various temperatures (spin-coated SnO_2 thin film) [13].

In this review, we try to describe our theoretical approaches to semiconductor gas sensors. After brief descriptions of some experimental facts theoretically important, how to formulate receptor function and response of large and small constituent crystals to oxygen, nitrogen dioxide, and hydrogen is described to sufficient details followed by the comparisons with some experimental data. Also included is a recent extension [17] carried out to understand the sensitizing effects exerted by electron-accepting substances.

2. Key Issues about SnO_2 Gas Sensors

2.1. Oxygen Adsorption on SnO_2 . The adsorption of oxygen on single-metal oxides was investigated by using a TPD technique by Iwamoto about 40 years ago [18]. He classified the transition of metal oxides into three groups depending on whether the amount of oxygen adsorbed and desorbed reversibly in the temperature range between room temperature and 500°C was large (Group A), small (B), or nondetectable (C). Group A consisted of p-type oxides, whereas some of n-type oxides such as SnO_2 , ZnO , and

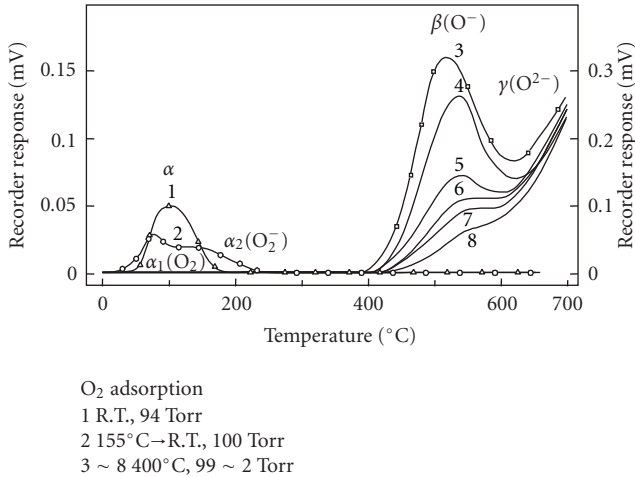


FIGURE 3: TPD chromatograms of oxygen desorbed from SnO₂ [19].

In₂O₃ belonged to B, and the others such as WO₃ and V₂O₅ belonged to C. It is suggestive that Group B consists of typical oxides used for semiconductor gas sensors.

Oxygen adsorption on SnO₂ was investigated in more detail by our group, also by using the TPD technique but for an extended temperature range up to 600°C. The results are shown in Figure 3 [19]. There are four types of oxygen, α_1 , α_2 , β , and γ , recognized to be desorbed from SnO₂ altogether. Of these, only the last two types, β (presumably O⁻) and γ (lattice oxygen O²⁻), are desorbed in the temperature range above 400°C after oxygen has been adsorbed during cooling from 600°C or at a fixed temperature of 400°C. On the other hand, after oxygen has been adsorbed in the lower temperature range (below 155°C), only α_1 (neutral molecular O₂) and α_2 (superoxide ion O₂⁻) are desorbed in the temperature range up to 250°C. Clearly these molecular adsorbates are formed only when the other dissociated species are absent. Also it is clear that at usual sensor operating temperatures (typically 300–400°C) β species prevails on the SnO₂ surface. The amount of adsorption of this species has been shown to be fairly small (less than 1% in surface coverage), suggesting that its adsorption is limited by the supply of electrons. Later, a report was published, which identified β to O²⁻ [20]. This identification cannot fit well to the theoretical analysis of response to oxygen, however. So it is assumed to be O⁻ in the following treatments.

2.2. Grain Size Effects. About twenty years ago, we explored experimental methods to prepare small grains (crystallites) of SnO₂. During this study, we found remarkable grain size effects [21]. As shown in Figure 4, the resistances under air (base) as well as under exposure to H₂ or CO in air, R_a and R_g , respectively, were found to increase sharply as the grain size (d_m) decreased beyond a critical value (d_c), while the sensor response to H₂ or CO, R_a/R_g , also increased, though more gradually, as d_m decreased. Intuitively we felt that the phenomena were associated with the completion

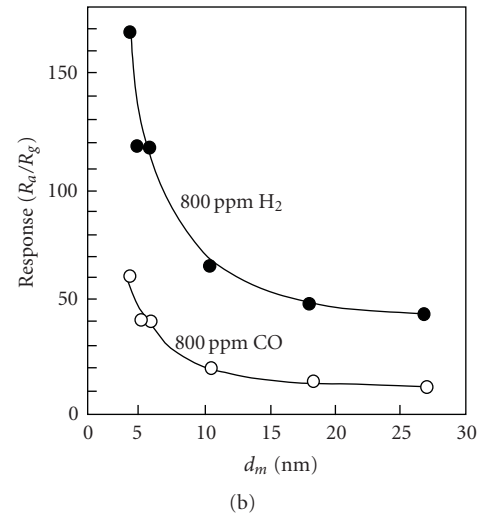
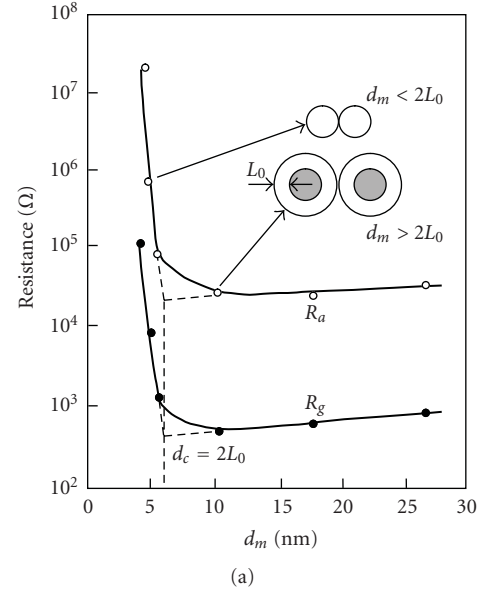
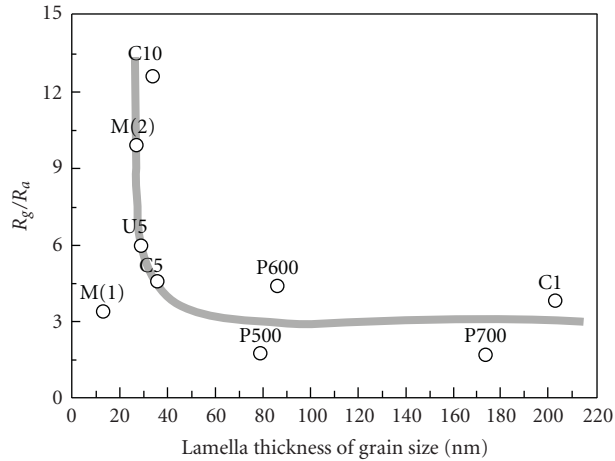


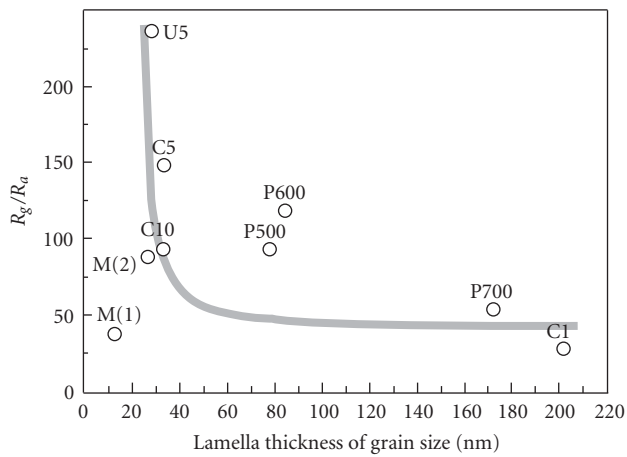
FIGURE 4: Grain size effects on resistance in air and sensor response to H₂ or CO in air observed with SnO₂ (brush-coated thick films) [21].

of depletion up to the whole region of constituent grains. Our interpretation (or assumption) was that d_c would be coincident with twice the thickness of depletion depth and that decreasing d_m beyond this point would be responsible for the sharp increases of R_a , R_g , and R_a/R_g for some reasons yet unknown. Later, similar size effects were also observed for the response of lamellar or granular WO₃-based devices to NO₂, as shown in Figure 5 [22].

Although such grain size effects seemingly appeared to match well to the double Schottky barrier model, their real meanings were left open for a long time. Some researchers tried to explain the grain size effects [23–26]. Among them, Rothschild and Komen pointed out that the size effects could be explained as reflecting changes in the surface area/volume ratio of the constituent SnO₂ grains [23, 24]. Such situation



(a)



(b)

FIGURE 5: Sensor response to 1 ppm NO_2 in air as correlated with granular size or lamellar thickness of constituent WO_3 crystals [22]. The symbols attached indicate the preparation methods used for respective WO_3 samples. See literature for details.

has turned out to appear typically in the stage of volume depletion in the present theory, as mentioned later.

2.3. Feasibility of Tunneling Transport. In sensor devices, constituent crystals are connected to adjacent ones either by contacts or by necks, the proportion of which depends on the methods and conditions of device fabrication. In case the device is fabricated through wet processes, the contact connections usually prevail, as seen in Figure 6 [13]. In such cases, it is easily understood that the device resistance is determined as a sum of the resistance of each contact. This idea has already been conceived in the double Schottky barrier model, which assumes that electrons migrate over the barrier at the contact. However, this model cannot be consistent with the temperature-almost-independent behavior shown in Figure 2, as already mentioned. From this consideration, we explored the possibility of tunneling transport of electrons [13]. The tunneling model used is

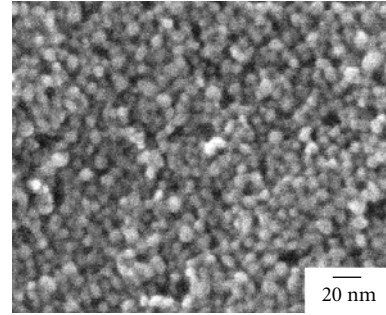


FIGURE 6: State of constituent grains as observed on SEM (spin-coated SnO_2 film) [13].

shown in Figure 7. The height of the wall to tunnel through is set to be equal to the electron affinity of the crystals, that is, the potential energy difference (V) between the vacuum level and the conduction band edge at the surface, while the thickness is set to the gap (L) between adjacent crystals. If V is known, tunneling probability (P) of an electron with energy E above conduction band edge can be estimated as a function of L by using a well-established equation. Reportedly, work function of SnO_2 is dispersed between 4.7 and 5.7 eV [27, 28], while donor levels are shallow from conduction band edge. Therefore, V takes a value of about 5.7 eV at the maximum. The tunneling probability thus estimated assuming $V = 6$ eV is shown in Figure 8. When the gap is zero (contact), P is unity naturally regardless of E . P decreases sharply with increasing L and decreasing E , but notably it still keeps a significant value (.01 or above) at $L = 0.1$ nm and $E = 0.03$ eV. Considering that thermal energy is 51.7 meV at 600 K, it is understood that electrons can tunnel through such a gap with a significant probability. What this means is that electrons, excited thermally, can be transported by tunneling not only through the directly contacting region ($L = 0$) but also through a small gap in its vicinity, as schematically shown in Figure 9. It follows that even in the case of point contact (contacting area zero) electrons can be transported by tunneling but this is not the case by migration. As shown in Figure 7, V is maintained at the same value in either of flat-band state (a) and bent-band state (b). Therefore, the tunneling probability is kept the same in both, only the number of electrons involved being decreased with a progress of band bending. In this way, the tunneling mechanism is confirmed to be feasible well to the electron transport between adjacent crystals. There is no reason to exclude it. Rather it can even eliminate difficulties encountered by the migration mechanism.

2.4. Models of Electron Transport between Grains. The mechanism of electron transport between neighboring crystals is directly related with the transducer function of sensors. There are probably three representative models, as schematically drawn in Figure 10. Spherical crystals (uniform in size), connected with neighbors through a contact or a neck, are assumed to be depleted of electrons in the outer region only. Double Schottky barrier model (a) is a

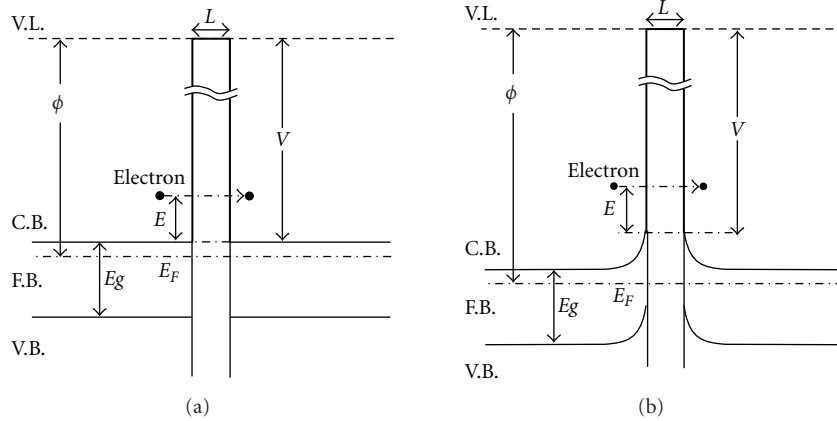


FIGURE 7: Model for electron tunneling across a gap between SnO₂ grains [13]. (a) Flat band condition, (b) Bent band condition. *V*: Wall height V.L.: Vacuum level, C.B.: Conduction band, F.B.: Forbidden band, V.B.: Valence band.

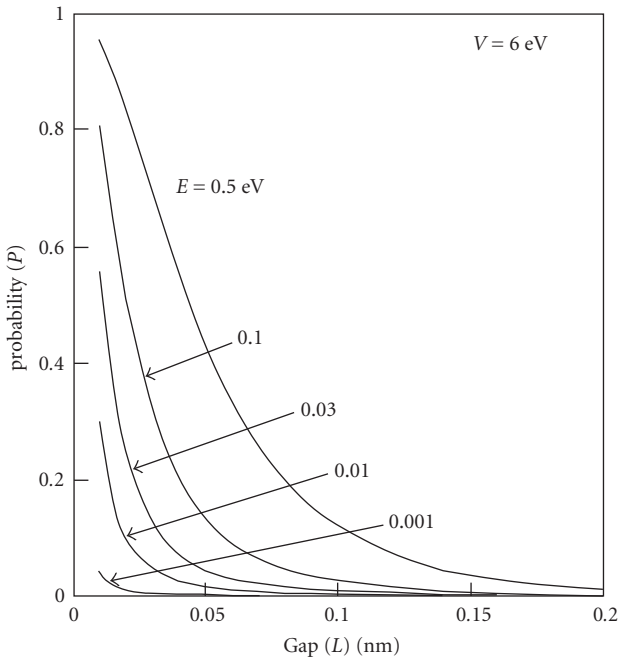


FIGURE 8: Tunneling probability calculated for various values of *E* as a function of gap width (*L*) [13].

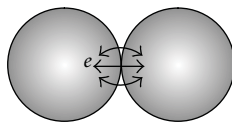


FIGURE 9: Schematic drawing of tunneling conduction across a gap between contacting spheres.

traditional one. It assumes that electrons are transported from nondepleted (core) region of one sphere to that of another by migration beyond a barrier in between. The barrier height not only determines the conductance of the contacting part but also gives rise to the activation energy of

conduction on changing temperature. Tunneling transport model (b) assumes that electrons located at the periphery of one sphere are transported to that of another by tunneling through a small gap (typically 0–0.1 nm) in between. The conductance is proportional to the density of electrons at the periphery, which is determined by the surface barrier height. On changing temperature, no activation energy is associated with the conductance provided that the barrier height is kept the same. Neck (or conduction channel) model (c) assumes that electrons migrate through a conduction channel which is formed by connecting the core regions of neighboring spheres. The channel width is narrowed at the neck parts so that the conductance is determined by the geometric relation between neck size and depletion depth. Of these models, (a) and (c), though looking likely at a glance, are not always free from various difficulties. Probably the most serious one appears after the depletion depth has reached the radius of spheres or necks. Such situation can happen easily when the size of spheres is reduced or gas adsorption is strengthened. Both models hardly seem to be applicable to such a situation. In our opinion, (b) seems to survive in various situations. Actually theoretical treatises in this article are based on this model.

It is remarked that important information concerning the transducer function is available from the Hall effects measurement. As generally accepted, conductance, σ , for an n-type semiconductor is given by the density, $[e]$, and mobility, μ , of charge carriers (electrons) as follows:

$$\sigma = -q[e]\mu. \tag{1}$$

Here q is the electric charge of proton. The values of $[e]$ and μ can be estimated independently from the Hall effects measurement. The measurements on semiconductor gas sensor devices have been carried out by Japanese experts [29, 30]. According to their results, σ and $[e]$ changed in parallel to each other with increasing concentration of reducing gases while μ was kept almost constant, as measured for sputtered SnO₂ thick film devices. This means that the change of $[e]$ is responsible exclusively for the change of σ , thus supporting the tunneling transport model (b) in Figure 10.

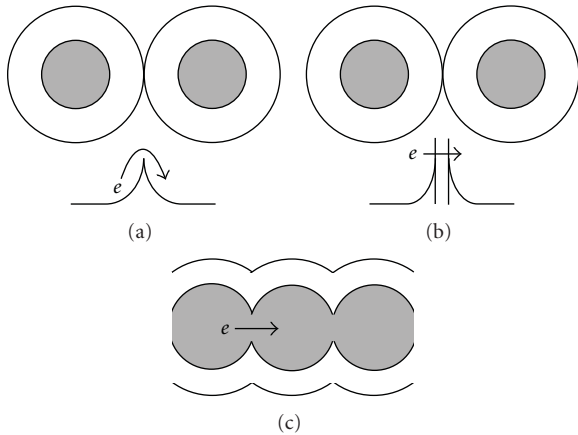


FIGURE 10: Models for electron transport between adjacent crystals.

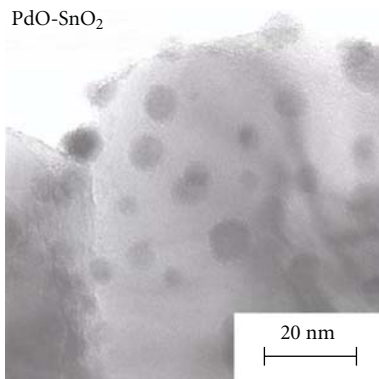


FIGURE 11: State of deposits of PdO on SnO₂ grain as observed on TEM [31].

An exceptional case has been reported with an SnO₂ device fabricated from tin metal by an evaporation and oxidation method [29]. In this case, both $[e]$ and μ increased with increasing concentration of target gas (ethanol), resulting in enhanced sensitivity of σ as compared with the sputtered devices. This difference in the behavior of μ probably arose from a change in the morphology of the constituent crystals. The authors explained such gas sensitivity of μ as resulting from very small crystals on the basis of a neck model like one shown as (c) in Figure 10, but it seems difficult to explain the gas sensitivity of $[e]$ based on this model. The tunneling transport model, on the other hand, seems to account for the sensitivity of both $[e]$ and μ better provided that dispersion in crystal size is admitted, though this is yet to be done.

2.5. Sensitization by Foreign Substances. As mentioned in Section 1, actual sensor devices are almost always loaded with small amounts of foreign substances so called sensitizers. Kinds of sensitizers used or confirmed are quite various, including noble metals (Pt and Au), noble metal oxides (PdO, Ag₂O, Rh₂O₃, etc.), base metal oxides (Fe₂O₃, Co₃O₄, etc.), alkaline or rare earth metal oxides (CaO, La₂O₃, etc.), and alkali metal oxide (Rb₂O). To make sensitization in effect, sensitizers should be dispersed well on the constituent

crystals of the sensor devices. As shown in Figure 11 [31], sensitizers are usually deposited as small particles adhering well to the underlying crystals. However, the roles of sensitizers (sensitization mechanisms) have not always been made clear. Beside the sensitization through modifying the acid-base property of the crystal surface which is vitally important in acid-base catalyzed reactions like the oxidation of alcohols, we have proposed two types of sensitization mechanisms, that is, chemical sensitization and electronic sensitization, operative for reducing gases [32]. The chemical sensitization is brought about from the catalytic actions of sensitizers like Pt. When target gas is resistant to oxidation like methane, for example, it is activated (or transformed) into more reactive intermediates like aldehydes before being exposed to the crystal surface. The electronic sensitization is in effect when the foreign substances draw electrons from the crystals, as easily witnessed from an increase in device resistance. Many of the sensitizers known are p-type oxides so that formation of p-n junctions between the tiny deposits of sensitizers and underlying SnO₂ (n-type) does not seem to be so unlikely. It has been shown that work function of SnO₂ is increased significantly by the loading with PdO (about 0.1 eV), Ag₂O (0.3 eV) and CuO (0.5 eV), as measured on XPS [33]. Here the figures in the parentheses are increments of work function in respective cases. In these cases, each sensitizer can undergo a redox change and, when it is reduced with the target gases, work function and device resistance have been confirmed to go back to their original values. It has been thus inferred that coupling of the formation of p-n junctions and the redox changes results in the sensitization. This mechanism, however, encounters difficulties in accounting for the sensitization exerted by the other sensitizers like Au, Fe₂O₃, Co₃O₄, and Rb₂O, which increase work function of SnO₂ more or less but are less facile or totally stable to redox changes. It seems that there are different mechanisms of electronic sensitization which cover the redox changes-free cases. Theoretical approaches to this issue are worth being carried out.

3. Theoretical Approach to Sensor Response to Oxygen

For a long time, the mechanism of gas sensing has been one of the most interested subjects in semiconductor gas sensors. Despite many efforts so far made, however, few have succeeded in revealing it from a fundamental point of view. As known well, chemisorption and catalysis of gas molecules on semiconductor surfaces were paid much attention in the age earlier than the inauguration of semiconductor gas sensors. An electronic theory was proposed to explain chemisorption and catalysis on semiconductors [34–36]. It explains well how the electron transfer between adsorbates and semiconductor results in the formation of a depletion, accumulation, or inversion layer in the subsurface of semiconductors. When applied for semiconductor gas sensors, it has been useful in understanding their behavior qualitatively. Unfortunately, however, no quantitative understandings have been available with it. There are several reasons for this, and the most serious one is, in our opinion, that the theory cannot deal

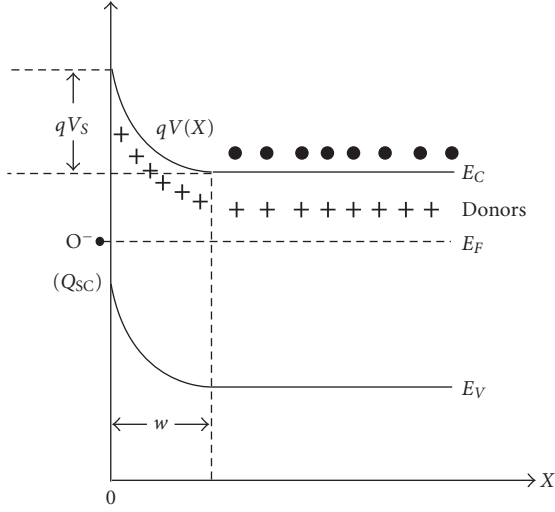


FIGURE 12: Schematic diagram of electrostatic equilibrium for large semiconductor crystals under exposure to oxygen. E_C : conduction band edge, E_V : valence band edge, E_F : Fermi level, Q_{sc} : surface charge density, w : depletion depth, qV : potential energy of electrons, qV_s : surface potential energy barrier [37].

correctly with so small semiconductor crystals as used in gas sensors. As easily understood, response to oxygen is a starting base of semiconductor gas sensors. The sensors are active in air, being alert to the access of target gases. In the beginning of this section, this theory is applied to the response to oxygen to demonstrate what comes out. Then a new theory is introduced to deal with small crystals, which is indispensable for understanding the response behavior of semiconductor gas sensors. In the following treatments, the semiconductor crystals taken into consideration are shaped in plate unless otherwise noted, because mathematical expressions for other shapes, sphere and column, become far more complex and tedious due to shape effect.

3.1. Conventional Theory of Depletion (Large Crystals).

Depletion of large semiconductor crystals can be treated with the conventional theory. Let us consider the adsorption of electron-accepting molecules (typically O_2) on the surface of a large n-type semiconductor crystal. This situation is well approximated by the adsorption on a plane of a large crystal cleaved in halves, as schematically drawn in Figure 12 [37]. As a result of electron transfer, a depletion layer is formed in the subsurface region, the layer thickness increasing with an increase in electron transfer. The electron transfer reaches equilibrium when Fermi level at the adsorbed species coincides with that in the semiconductor bulk.

The electrostatic equilibrium inside the crystal in such a case can be treated quantitatively under simplifying assumptions. Conventionally it is assumed that (1) donors are ionized completely, (2) there are no other electron-traps other than the adsorbates, and (3) all of conduction electrons up to a depth w are completely transferred to the surface (abrupt model). Since donors in SnO_2 are reportedly present at shallow levels (0.05–0.15 eV) below the conduction band

edge [38], the first assumption can be acceptable fairly well. The second one may be fit to an ionic semiconductor like SnO_2 better than to a nonionic semiconductor like silicon. The third one, though useful in simplifying mathematical treatments, cannot always be rationalized as mentioned later. However, abrupt model is used here always unless otherwise noted.

Under these assumptions, the density of surface charges, Q_{sc} , is nominally equal to $-qN_d w$, where q is electric charge of proton and N_d the density of donors of semiconductor:

$$Q_{sc} = -qN_d w = -qN_d L_D m. \quad (2)$$

Here m is reduced depletion depth defined by $m = w/L_D$. Under these conditions, electric potential, V , in the depletion region should satisfy the following Poisson's equation, where x is the depth from the surface and ϵ is the permittivity of semiconductor times the free space permittivity:

$$\frac{d^2 V}{dx^2} = -\frac{qN_d}{\epsilon}. \quad (3)$$

By introducing the boundary conditions that dV/dx as well as V are zero at $x = w$, (3) is solved to give the following depth profile of electric potential:

$$V(x) = -\left(\frac{qN_d}{2\epsilon}\right)(x-w)^2. \quad (4)$$

Potential energy of electrons, $qV(x)$, as well as the height of surface potential barrier, qV_s , are obtained from (4):

$$\begin{aligned} \frac{qV(x)}{kT} &= \left(\frac{q^2 N_d}{2\epsilon kT}\right)(x-w)^2 \\ &= \left(\frac{1}{2}\right)\left\{\frac{(x-w)}{L_D}\right\}^2, \end{aligned} \quad (5)$$

$$\begin{aligned} \frac{qV(X)}{kT} &= \left(\frac{1}{2}\right)(X-m)^2, \\ \frac{qV_s}{kT} &= \left(\frac{1}{2}\right)\left(\frac{w}{L_D}\right)^2 = \left(\frac{1}{2}\right)m^2. \end{aligned} \quad (6)$$

Here L_D is the Debye length of semiconductor given by $L_D = (q^2 N_d / kT)^{-1/2}$, and X is reduced distance defined by $X = x/L_D$. The density of electrons at the surface, $[e]_s$, is given from (6) as follows:

$$[e]_s = N_d \exp\left(\frac{-qV_s}{kT}\right) = N_d \exp\left(\frac{-m^2}{2}\right). \quad (7)$$

In this way, the surface density of adsorbates, $-Q_{sc}/q$, and electrons can be correlated uniquely through m once L_D and N_d are given.

3.2. Response of Large Crystals. It is assumed that oxygen is adsorbed as O^- exclusively on the semiconductor surface. Then the overall equation of oxygen adsorption and its equilibrium are expressed as follows:



$$(K_{O_2 P_{O_2}})^{1/2} [e]_s = [O^-]. \quad (8)$$

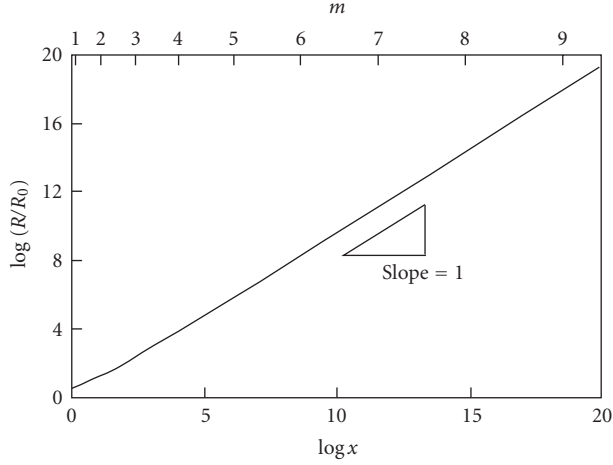


FIGURE 13: Correlation between R/R_0 and X on logarithmic scales [14]. $X = (K_{O_2}P_{O_2})^{1/2}/L_D$

K_{O_2} and P_{O_2} are the adsorption constant and the partial pressure of oxygen, respectively, and $[e]_S$ and $[O^-]$ are the surface densities of free electrons and O^- , respectively. Equation (8) indicates that $(K_{O_2}P_{O_2})^{1/2}$ determines the density ratio, $[O^-]/[e]_S$, not the respective quantities. These quantities are determined only after the chemical equilibrium is coupled with the electrostatic equilibrium just mentioned.

When O^- is solely responsible for the total charge density of the semiconductor as assumed,

$$[O^-] = \frac{-Q_{SC}}{q} = N_d L_D m. \quad (9)$$

By inserting (2) and (8) into (7), we obtain

$$(K_{O_2}P_{O_2})^{1/2} N_d \exp\left(\frac{-m^2}{2}\right) = N_d L_D m, \quad (10)$$

$$X = m \exp\left(\frac{m^2}{2}\right).$$

Here X is reduced adsorption strength of oxygen defined by $X = (K_{O_2}P_{O_2})^{1/2}/L_D$. Indication of (10) is that if X is given, m is determined uniquely. This in turn determines $[e]_S$ through (8). Thus we can correlate oxygen adsorption with the surface density of electrons.

In order to obtain the correlation with sensor resistance (R), we need to know the relation between R and $[e]_S$. The relation is simple if the tunneling transport model (Figure 10(b)) is assumed, as follows:

$$\frac{R}{R_0} = \frac{[e]_{S0}}{[e]_S} = \exp\left(\frac{m^2}{2}\right). \quad (11)$$

Here R_0 and $[e]_{S0}$ are the values of R and $[e]_S$ at the flat band state, respectively. The latter quantity coincides with N_d for the simplified mode used here. R and R_0 are influenced by many factors other than oxygen adsorption, such as packing of crystals and geometry of sensor device, but those influences can be canceled out effectively by normalizing R

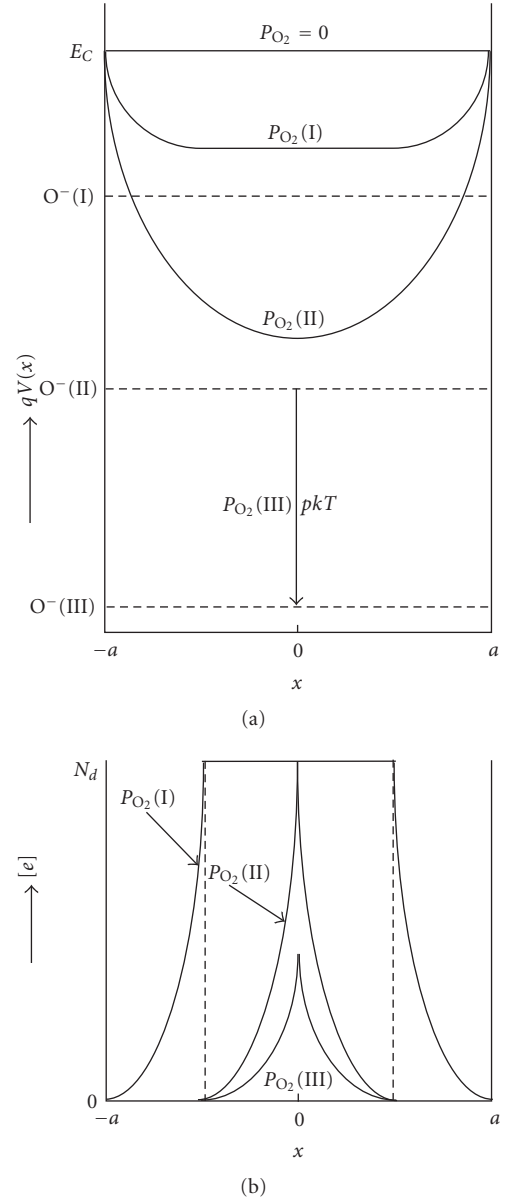


FIGURE 14: Schematic diagrams of electronic equilibrium for semiconductor plate (half thickness a) placed under various partial pressures of oxygen (P_{O_2}). (a) Depth profiles of potential energy. (b) Depth profiles of conduction electrons density assumed on abrupt model (broken lines) and modified model (full lines). See section 3.6 for modified model [15].

by R_0 . The correlation between R/R_0 and X thus obtained through (10) and (11) is shown on logarithmic scales in Figure 13 [14]. R/R_0 increases with increasing X and its slope becomes equal to unity in the middle region of X , explaining that the power law-type dependence of R on P_{O_2} with a power index of $1/2$ is actually observed. However, no important information else can be obtained from such a treatise. Similar conclusions have been obtained for the responses to NO_2 and H_2 [14]. This is because we have used conventional theory of depletion developed for large crystals, thus missing important information about the size and shape of crystals.

3.3. Two Types of Depletion in Small Crystals. Let us consider how depletion develops in a plate crystal of thickness $2a$ (a , half thickness), starting from the flat-band state, with increasing P_{O_2} in the ambient. The electrostatic equilibrium of this system is schematically drawn in Figure 14(a). When P_{O_2} is small, depletion takes place in the same way as previously seen in a large crystal, depletion depth increasing with increasing P_{O_2} . However, this way of depletion is finished at P_{O_2} (II) where depletion has extended to cover the whole region of the crystal. Obviously the value of P_{O_2} (II) decreases with decreasing half thickness (a). What would happen when P_{O_2} is further increased to P_{O_2} (III) in the figure? This is a main concern here. The above limit of depletion comes solely from the physics of the crystal. The chemistry of oxygen adsorption, on the other hand, does not care the physics. It requires (8) to hold at any stages, or, speaking more specifically, the ratio $[O^-]/[e]_s$ to increase linearly with increasing $X = (K_{O_2}P_{O_2})^{1/2}$. In order for the physics side (electrostatic equilibrium) to fulfill this requirement, the only available way is to allow Fermi level to shift down by a designated amount, $p kT$, whereas the band bending profile is kept unchanged. With this shift, not only the whole region from the surface adsorbates (O^-) to the bulk of the crystal can be placed at the same Fermi level but also the potential energy of electrons goes up to the level at which $[e]_s$ takes a value consistent with the chemical equilibrium condition (8). This way of establishing the electrostatic equilibrium is thus very different from one observed at lower P_{O_2} . It is noted that electron transfer from the bulk to the surface continues still in this stage, though it is only nominal when the abrupt model is used (Figure 14(b)). The electron transfer is made more apparent in case some electrons are left behind in the depletion layer (modified model) as illustrated in the same figure. In this case, the density of electrons inside the crystal decreases progressively as the Fermi level shift increases, showing that electrons are squeezed out from the whole crystal to be supplied to the surface. It is therefore convenient to distinguish the depletion in this stage from the conventional one in the initial stage up to P_{O_2} (II). We call them here volume depletion and regional depletion, respectively, while the border in between is called boundary depletion.

3.4. Response at Regional Depletion (Plate). As mentioned earlier, the occurrence of regional depletion followed by volume depletion is characteristic to small crystals. Receptor function and response of small plate crystals to oxygen in the stage of regional depletion are discussed here. The distribution of potential inside the plate is obtained by solving Poisson's equation, which is the same as (3) but has an origin located at a center of the plate with coordinate x being taken as a distance normal to the surface from origin (see Figure 14). In the stage of regional depletion, potential energy of electrons is expressed as shown below:

$$\begin{aligned} qV(x) &= \left(\frac{q^2 N_d}{2\epsilon} \right) \{x - (a - w)\}^2 & \text{for } |x| \geq a - w, \\ &= 0 & \text{for } |x| < a - w. \end{aligned} \quad (12)$$

These are rewritten in reduced form as

$$\begin{aligned} \frac{qV(X)}{kT} &= \left(\frac{1}{2} \right) \{X - (n - m)\}^2 & \text{for } |x| \geq n - m, \\ &= 0 & \text{for } |x| < n - m. \end{aligned} \quad (13)$$

Reduced quantities, X and m , are the same as defined before, and n is reduced size defined by $n = a/L_D$. These expressions are essentially the same as those derived for large crystals, though depletion in this case starts from both surfaces. Surface potential energy (barrier) is expressed by the same equation (7), while (9) holds also as assumed. As a result, either of (10) and (11) derived for large crystals can be used to correlate between R/R_0 and X also in this case. It is noted, however, that this can be valid only for plate crystals, which are free from the shape effect.

3.5. Response at Volume Depletion (Plate). Potential energy in the stage of boundary depletion is obtained by inserting $w = a$ in (12) or $m = n$ in (13) and that in volume depletion is larger by $p kT$ or p , as follows:

$$qV(x) = \left(\frac{q^2 N_d}{2\epsilon} \right) x^2 + p kT. \quad (14)$$

$$\frac{qV(X)}{kT} = \left(\frac{1}{2} \right) X^2 + p. \quad (15)$$

Here $p = 0$ indicates boundary depletion. The surface potential energy is obtained by inserting $X = n$ into (15):

$$\frac{qV_s}{kT} = \left(\frac{1}{2} \right) n^2 + p. \quad (16)$$

We can then express $[e]_s$ and R/R_0 by using n and p . $[O^-]$ is obtained from (9) if m is replaced by n . By inserting these quantities into the mass action law (8), we can correlate X with n and p . Thus we obtain a couple of equations:

$$\begin{aligned} X &= n \exp \left\{ \left(\frac{1}{2} \right) n^2 + p \right\}, \\ \frac{R}{R_0} &= \exp \left\{ \left(\frac{1}{2} \right) n^2 + p \right\}. \end{aligned} \quad (17)$$

These equations determine the correlation between R/R_0 and X . Unlike the case of regional depletion, however, R/R_0 is an explicit function of X , because we obtain from the couple of equations

$$\frac{R}{R_0} = \frac{X}{n} = \frac{(K_{O_2}P_{O_2})^{1/2}}{a}. \quad (18)$$

Normalized resistance is thus linear to $(K_{O_2}P_{O_2})^{1/2}$ and the reciprocal of a .

The correlations between R/R_0 and X in the stages of regional depletion and volume depletion are drawn for smaller selected values of n in Figure 15. In principle, regional depletion always precedes another on increasing X , but actually when n is small it is not visible well in the drawing on this scale, allowing volume depletion to prevail.

It is also clear that the slope of each correlation (sensitivity to oxygen) increases sharply with decreasing n and is inversely proportional to n or a in the stage of volume depletion. This indicates a size effect on the sensor response to oxygen. It is remarked that the derivative of R or normalized R with respect to the concentration (or partial pressure) of target gas in problem is usually defined as sensor sensitivity. In the case of oxygen adsorption, however, the sensitivity is better defined as the derivative of R/R_0 with respect to $P_{O_2}^{1/2}$, which is equal to $K_{O_2}^{1/2}/a$ in the stage of volume depletion.

3.6. *Effects of Shape and Size.* The same treatment can be extended to spherical crystals (radius a) and columnar crystals (columnar radius a). For this purpose, two things should be taken into account. First, Poisson's equation is transformed, for the convenience of solution, into one fitting to the symmetry of the crystal form. A polar spherical coordinates system and a columnar coordinates system are illustrated together with one-dimensional system so far used in Figure 16. In the respective systems, Poisson's equation is expressed as a function of a single variable as follows:

$$\begin{aligned} \frac{d^2V}{dx^2} &= \frac{-qN_d}{\varepsilon}, \quad (\text{Plate}), \\ \left(\frac{1}{r^2}\right) \frac{d}{dr} \left(r^2 \frac{dV}{dr} \right) &= \frac{-qN_d}{\varepsilon}, \quad (\text{Sphere}), \quad (19) \\ \left(\frac{1}{r}\right) \frac{d}{dr} \left(r \frac{dV}{dr} \right) &= \frac{-qN_d}{\varepsilon}, \quad (\text{Column}). \end{aligned}$$

Here r is radial displacement from the center of crystals. Each equation can be solved by using the same boundary conditions as used before to give a solution shown below:

$$\begin{aligned} V(x) &= -\left(\frac{qN_d}{2\varepsilon}\right) \{x - (a - w)\}^2, \quad (\text{Plate}), \\ V(r) &= -\frac{(qN_d/2\varepsilon) \{r - (a - w)\}^2 \{1 + 2(a - w)/r\}}{3}, \\ & \quad (\text{Sphere}), \\ V(r) &= -\left(\frac{qN_d}{4\varepsilon}\right) \left\{ r^2 - (a - w)^2 \left[1 + 2 \ln \left(\frac{r}{(a - w)} \right) \right] \right\}, \\ & \quad (\text{Column}). \end{aligned} \quad (20)$$

Second, the relations between total surface charge density (Q_{SC}) and depletion depth (w or m) should be altered to meet crystal symmetry:

$$\begin{aligned} \frac{Q_{SC}}{q} &= -N_d w = -N_d L_D m, \quad (\text{Plate}), \\ \frac{Q_{SC}}{q} &= \frac{-N_d \left\{ \int_{a-w}^a 4\pi r^2 dr \right\}}{(4\pi a^2)} \\ &= -\left(\frac{1}{3}\right) N_d L_D n \left\{ 1 - \left[\frac{(n - m)}{n} \right]^3 \right\}, \quad (\text{Sphere}), \end{aligned}$$

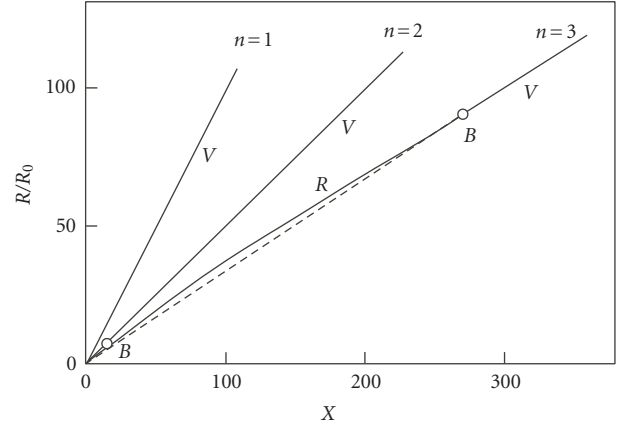


FIGURE 15: Correlations between R/R_0 and X for plate crystals with reduced thickness n [17].

$$\begin{aligned} \frac{Q_{SC}}{q} &= -N_d \frac{\left\{ \int_{a-w}^a 2\pi r dr \right\}}{(2\pi a)} \\ &= -\left(\frac{1}{2}\right) N_d L_D n \left\{ 1 - \left[\frac{(n - m)}{n} \right]^2 \right\}, \quad (\text{Column}). \end{aligned} \quad (21)$$

Here m and n are reduced depletion depth (w/L_D) and reduced size (a/L_D), respectively.

Based on the abrupt model, receptor function and sensor response to oxygen can be formulated for spherical and columnar crystals in the same way as done for plate crystals. The correlations between R/R_0 and X thus derived are summarized as follows.

Regional depletion. Plate:

$$\begin{aligned} X &= m \exp\left(\frac{m^2}{2}\right), \\ \frac{R}{R_0} &= \exp\left(\frac{m^2}{2}\right); \end{aligned} \quad (22)$$

Sphere:

$$\begin{aligned} X &= \left(\frac{n}{3}\right) \left\{ 1 - \left[\frac{(n - m)}{n} \right]^3 \right\} \\ & \quad \times \exp\left\{ \left(\frac{m^2}{6}\right) \left[1 + 2 \frac{(n - m)}{n} \right] \right\}, \quad (23) \\ \frac{R}{R_0} &= \exp\left(\frac{m^2}{6}\right) \left\{ \left[1 + 2 \frac{(n - m)}{n} \right] \right\}; \end{aligned}$$

Column:

$$X = \left(\frac{n}{2}\right) \left\{ 1 - \left[\frac{(n-m)}{n} \right]^2 \right\} \\ \times \exp \left\{ \left(\frac{1}{4} \right) \left[n^2 - (n-m)^2 \left[1 + 2 \ln \left(\frac{n}{(n-m)} \right) \right] \right] \right\}, \\ \frac{R}{R_0} = \exp \left\{ \left(\frac{1}{4} \right) \left[n^2 - (n-m)^2 \left[1 + 2 \ln \left(\frac{n}{(n-m)} \right) \right] \right] \right\}. \quad (24)$$

Volume depletion.

$$\frac{R}{R_0} = \left(\frac{S}{a} \right) (K_{O_2} P_{O_2})^{1/2}, \quad (25)$$

$S = 1$ (plate), 2 (column), or 3 (sphere).

S is the shape factor, which coincides with the surface area to volume ratio for each crystal shape. In the stage of volume depletion, sensitivity to oxygen decreases in the order, sphere $>$ column $>$ plate, due to the shape factor when a is the same.

It would be instructive to estimate roughly the values of L_D and n for SnO_2 crystals. Martinelli et al. have reported that the permittivity and the donor density of SnO_2 are 10^{-10} Fm^{-1} and $4.1 \times 10^{18} \text{ cm}^{-3}$, respectively, [39]. These values allow us to estimate $L_D = 2.8 \text{ nm}$ at 600 K . Actually, however, donor density values are scattered rather largely depending on reports and the highest one is $1.5 \times 10^{19} \text{ cm}^{-3}$ [27], which leads to $L_D = 1.4 \text{ nm}$. When we assume the former L_D value, SnO_2 grains of about 20 nm in diameter usually adapted in actual devices have $n = 3.6$. Then regional depletion in these grains is finished at the reduced depletion depth $m = n = 3.6$, which leads to $R/R_0 = 8.7$, $X = 10.4$, and $K_{O_2} P_{O_2} = 1.5 \times 10^3 \text{ nm}^2 \text{ atm}^{-1}$ according to (23). It follows that this value of R/R_0 is the maximum response to oxygen allowed by regional depletion, and therefore the maximum of conventional sensor response to reducing gases in air (R_a/R_g) as well. It is understood that larger responses in R/R_0 and R_a/R_g can never be acquired without the help of volume depletion.

3.7. Corrections for the Tailing of Electron Distribution. The abrupt model used above cannot always be rationalized, as mentioned. The assumption of complete transfer of electrons from the depletion region to the surface can be too drastic. It is likely that some electrons are left behind in the vicinity of the depletion frontier where potential energy of electrons remains modest, resulting in a tailing of electron distribution. For usual semiconductor devices, a distribution tail due to thermal fluctuations of electrons has been taken into consideration for correction [37]. However, this correction having aimed at applications for thick semiconductor devices hardly seems to be effective in gas sensors. It is worth remembering that the electron concentration at the surface, $[e]_S$, is estimated from V_S by assuming the Boltzmann distribution law. Then it would not be so unreasonable to assume that the same distribution law operates over the whole depletion region. If this assumption is admitted, the

amount of electrons transferred from the bulk to the surface, which contributes to $-Q_{SC}/q$, can be estimated exactly from the potential energy profiles as follows:

$$\frac{-Q_{SC}}{q} = N_d \int_{a-w}^a \left\{ 1 - \exp \left(-\frac{qV(x)}{kT} \right) \right\} dx, \quad (\text{Plate}),$$

$$\frac{-4\pi a^2 Q_{SC}}{q} = N_d \int_{a-w}^a \left\{ 1 - \exp \left(-\frac{qV(r)}{kT} \right) \right\} 4\pi r^2 dr, \quad (\text{Sphere}),$$

$$\frac{-2\pi a Q_{SC}}{q} = N_d \int_{a-w}^a \left\{ 1 - \exp \left(-\frac{qV(r)}{kT} \right) \right\} 2\pi r dr, \quad (\text{Column}). \quad (26)$$

Rearrangements result in

$$\frac{-Q_{SC}}{qN_d L_D} = m - \int_{n-m}^n \exp \left(-\frac{qV(x)}{kT} \right) dX, \quad (\text{Plate}), \quad (27)$$

$$\frac{-Q_{SC}}{qN_d L_D} = \left(\frac{n}{3} \right) \left\{ 1 - \left[\frac{(n-m)}{n} \right]^3 \right\} \\ - \left(\frac{1}{n^2} \right) \int_{n-m}^n R^2 \exp \left(-\frac{qV(R)}{kT} \right) dR, \quad (\text{Sphere}), \quad (28)$$

$$\frac{-Q_{SC}}{qN_d L_D} = \left(\frac{n}{2} \right) \left\{ 1 - \left[\frac{(n-m)}{n} \right]^2 \right\} \\ - \left(\frac{1}{n} \right) \int_{n-m}^n R \exp \left(-\frac{qV(R)}{kT} \right) dR, \quad (\text{Column}). \quad (29)$$

The second term in each equation represents the quantity to be corrected for the tailing effect. Once such a correction is available, the correlations between R/R_0 and X can be formulated in the same way as done before. The results are summarized below.

Regional depletion. Plate:

$$X = (m - A_P(m)) \exp \left(\frac{m^2}{2} \right), \\ \frac{R}{R_0} = \exp \left(\frac{m^2}{2} \right); \quad (30)$$

Sphere:

$$X = \left\{ \left(\frac{n}{3} \right) \left\{ 1 - \left[\frac{(n-m)}{n} \right]^3 \right\} - A_S(n, m) \right\} \\ \times \exp \left\{ \left(\frac{m^2}{6} \right) \left[1 + 2 \frac{(n-m)}{n} \right] \right\}, \quad (31) \\ \frac{R}{R_0} = \exp \left\{ \left(\frac{m^2}{6} \right) \left[1 + 2 \frac{(n-m)}{n} \right] \right\};$$

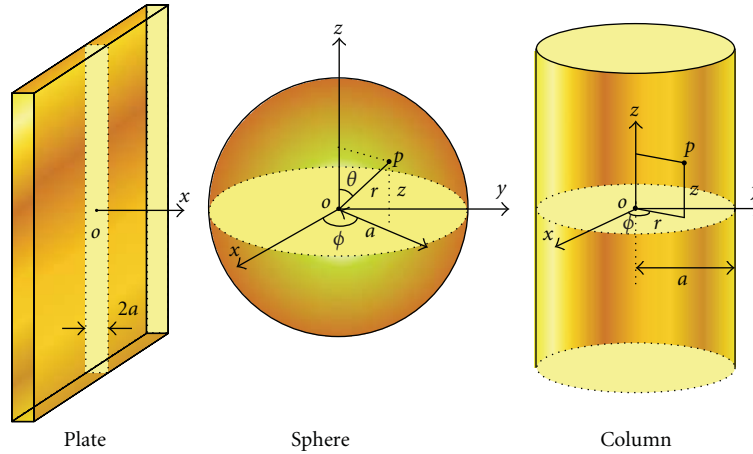


FIGURE 16: Coordinates systems adapted for plate, sphere, and column [15].

Column:

$$X = \left\{ \left(\frac{n}{2} \right) \left\{ 1 - \left[\frac{(n-m)}{n} \right]^2 \right\} - A_C(n, m) \right\} \\ \times \exp \left\{ \left(\frac{1}{4} \right) \left[n^2 - (n-m)^2 \left[1 + 2 \ln \left(\frac{n}{(n-m)} \right) \right] \right] \right\}, \\ \frac{R}{R_0} = \exp \left\{ \left(\frac{1}{4} \right) \left[n^2 - (n-m)^2 \left[1 + 2 \ln \left(\frac{n}{(n-m)} \right) \right] \right] \right\}. \quad (32)$$

$A(m)$ or $A(n, m)$ is the correction term appearing in (27) through (29), and suffices, P, S, and C standing for plate, sphere, and column.

Volum depletion. Plate:

$$\frac{R}{R_0} = \left(\frac{1}{n} \right) X + \left(\frac{1}{n} \right) A_P(n) \exp \left(\frac{n^2}{2} \right); \quad (33)$$

Sphere:

$$\frac{R}{R_0} = \left(\frac{3}{n} \right) X + \left(\frac{3}{n} \right) A_S(n) \exp \left(\frac{n^2}{6} \right); \quad (34)$$

Column:

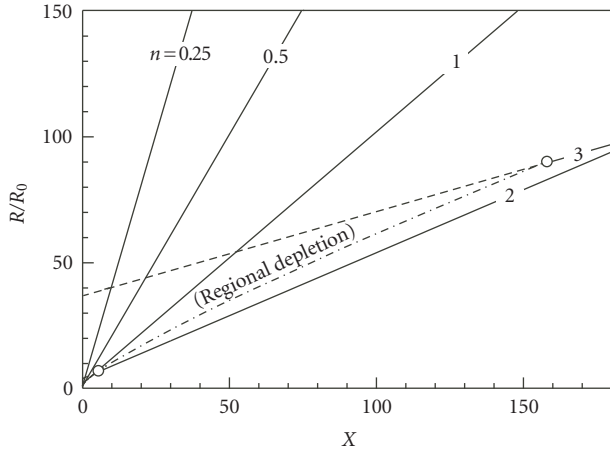
$$\frac{R}{R_0} = \left(\frac{2}{n} \right) X + \left(\frac{2}{n} \right) A_C(n) \exp \left(\frac{n^2}{4} \right). \quad (35)$$

$A(n)$ is the value of $A(m)$ or $A(n, m)$ at the boundary depletion ($m = n$). In each equation, the second term (intercept) is close to unity for smaller values of n but it increases rather sharply with increasing n in a range of larger n .

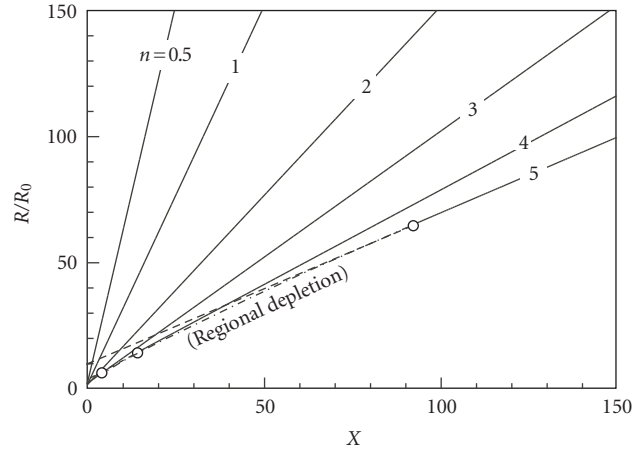
The correlations given by these equations are shown for the cases of planar and spherical crystals in (a) and (b) in Figure 17, respectively. Compared with Figure 15, the correlations for plate crystals (a) are more convex upward in the stage of regional depletion and this tendency becomes more conspicuous as n increases. Those for volume depletion, on

the other hand, are straight lines, which now have intercepts against ordinate. Such behavior of the correlations seems to fit better to actual observations. However, the assumption used for the correction needs to be checked thoroughly for verification.

3.8. Comparison with Experiments. Although the measurement of device resistance as a function of P_{O_2} is a very basic task, carrying out it satisfactorily has turned out to be surprisingly difficult. The resistance is sensitive to trace amounts of surface-active impurities, that is, contaminant reducing gases at ppm or sub-ppm levels in commercial tubes of oxygen or of oxygen diluted with nitrogen, and contaminant oxygen as well as contaminant reducing gases in high purity nitrogen. Since these tube gases are mixed together to control P_{O_2} , contaminants can be serious origins of disturbances. It is necessary to reduce contaminants as much as possible but complete reduction has been yet to achieve. With utmost precautions about contaminants, fairly reliable data acquisition is under way in our laboratory. For example, the data obtained with screen-printed thick films of SnO_2 of two different grain sizes (12 and 16 nm in diameter) at 300 and 350°C are shown in Figure 18. To check fitting between the data to the present theory, we need to know R_0 but it has been difficult to measure it precisely yet due to contaminant oxygen (about 100 ppm in volume) in nitrogen. Here the resistance in nitrogen, $R(\text{N}_2)$, is substituted for R_0 . The resistance data normalized by $R(\text{N}_2)$ are thus plotted as a function of square root of P_{O_2} in the figure. In spite of the ambiguity just mentioned, all the data at 300°C fall on a straight line fairly well in agreement with (25) or (34) derived for volume depletion. The data at 350°C, however, falls on a line which is convex upward in the beginning and then becomes linear, a feature characteristic to a change from regional depletion to volume depletion. From the slope of each straight line, full or partial, and grain size, we can deduce K_{O_2} using (25) or (34). The slopes for 12 nm and 16 nm grains are 157 and 118 $\text{nm atm}^{-1/2}$ at 300°C, respectively, both giving $K_{O_2} = 9.9 \times 10^4 \text{ nm}^2 \text{ atm}^{-1}$. The corresponding data at 350°C are



(a)



(b)

FIGURE 17: Correlations between R/R_0 and X for plate crystals (a) and spherical crystals (b) with reduced size n [15].

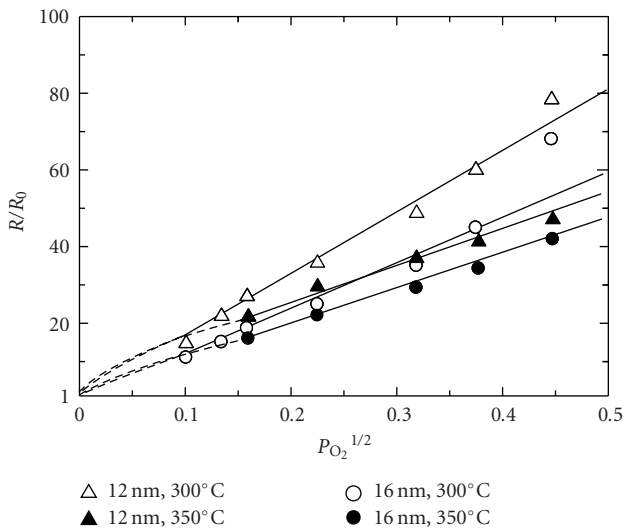


FIGURE 18: Normalized response to oxygen, $R/R(N_2)$, at two designated temperatures as correlated with $P_{O_2}^{1/2}$ for two screen-printed SnO_2 thick film devices different in grain size. $R(N_2)$; resistance in N_2 .

89 and 83 $\text{nm atm}^{-1/2}$, giving $K_{O_2} = 3.1$ and 4.9 in unit of $10^4 \text{ nm}^2 \text{ atm}^{-1}$, respectively. In principle, K_{O_2} is independent of grain sizes and this is in fact confirmed with these experimental data. These results are fairly satisfactory and seem to assure the soundness of the present theory.

Let us consider next the grain size effect on R_a already shown in Figure 4. The same data are plotted on logarithmic scales in Figure 19. When volume depletion is assumed to prevail in the whole grains size range tested, R_a/R_0 is inversely proportional to a according to (23) or (34), while it can be shown that R_0 is also inversely proportional to a if ideal packing of spheres is assumed. As a result, R_a should be essentially constant regardless of the variation of a . In fact, this is confirmed in the range of a above 3.5 nm (a_c). The

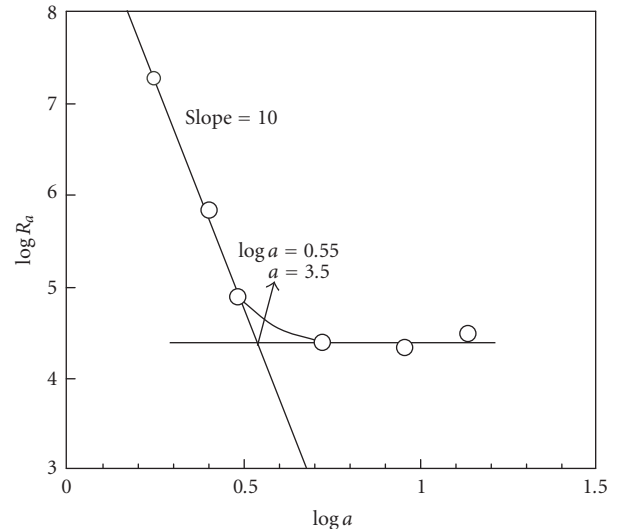


FIGURE 19: Grain size effect on R_a shown in Figure 4 as reproduced on the logarithmic scales [16].

sharp increase of R_a observed with decreasing a below a_c can be attributed to an increase in the number of grains without donors (insulating grains). This can happen when the grain size (diameter) is made smaller than an average separation between neighboring donors under the condition of a fixed donor density (N_d). From a_c , N_d is estimated to be $5.6 \times 10^{18} \text{ cm}^{-3}$, which is fairly close to reported values mentioned before. This in turn leads to $L_D = 2.4 \text{ nm}$ at 600 K. In this way, the grain size effect on base resistance is understood in a way largely different from what was imagined in the past.

4. Receptor Function and Response to NO_2

4.1. Modeling. NO_2 is selected here as a representative of oxidizing gases which are adsorbed as negatively charged ions

on the semiconductor surface. As generally accepted, it is assumed to undergo adsorption as follows:



The equilibrium of adsorption is written down:

$$K_{\text{NO}_2} P_{\text{NO}_2} [e]_S = [\text{NO}_2^-]. \quad (\text{36})$$

K_{NO_2} and P_{NO_2} are the adsorption constant and the partial pressure of NO_2 , respectively, and $[\text{NO}_2^-]$ is the surface density of NO_2^- . As noted, (R2) and (36) are quite similar to the corresponding equations for O_2 , (R1) and (8). This means that, in the absence of oxygen, receptor function and response to NO_2 can be treated in exactly the same way as done to oxygen so far. That is, if we define the reduced adsorptive strength of NO_2 as $Z = K_{\text{NO}_2} P_{\text{NO}_2} / L_D$, all of the correlations between R/R_0 and $X (= (K_{\text{O}_2} P_{\text{O}_2})^{1/2} / L_D)$ obtained to O_2 above can be transferred to the correlations to NO_2 by replacing X by Z .

In the coexistence of oxygen, we are placed in a different situation. Now both O_2 and NO_2 are adsorbed on the surface of crystals to compete for electrons. The mass action laws for O_2 and NO_2 , (8) and (36), should be satisfied simultaneously. That is,

$$[\text{O}^-] + [\text{NO}_2^-] = \{ (K_{\text{O}_2} P_{\text{O}_2})^{1/2} + K_{\text{NO}_2} P_{\text{NO}_2} \} [e]_S. \quad (\text{37})$$

This is a requirement from the chemistry side. In the physics side, it is required to have Fermi level kept the same at any sites among O^- , NO_2^- , and bulk of crystal in the band energy diagram, and nothing else is changed except that the total surface charge density is now contributed by the two kinds of adsorbates:

$$\frac{-Q_{\text{SC}}}{q} = [\text{O}^-] + [\text{NO}_2^-]. \quad (\text{38})$$

As a result, all the equations involving X so far derived to oxygen can survive if X is replaced by $X + Z$. That is, the response of plate crystals (half thickness a) is expressed as follows.

Regional depletion.

$$X + Z = m \exp\left(\frac{m^2}{2}\right), \quad (\text{39})$$

$$\frac{R}{R_0} = \exp\left(\frac{m^2}{2}\right).$$

Volume depletion.

$$\frac{R}{R_0} = \frac{(X + Z)}{n} = \frac{\{ (K_{\text{O}_2} P_{\text{O}_2})^{1/2} + K_{\text{NO}_2} P_{\text{NO}_2} \}}{a}. \quad (\text{40})$$

The meaning of (39) is the same as before; $X + Z$ determines m unequely and then does R/R_0 also unequely. Naturally, the correlations between R/R_0 and X shown in Figure 15 are in effect in this case, too, if the abscissa is redefined to be $X + Z$.

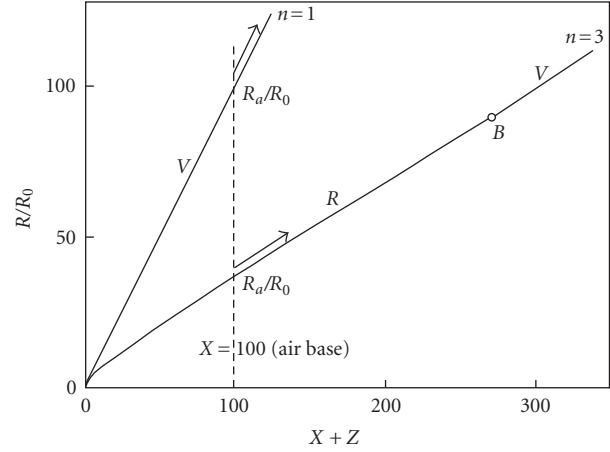


FIGURE 20: Correlations between R/R_0 and $X + Z$ derived for plate crystals [17].

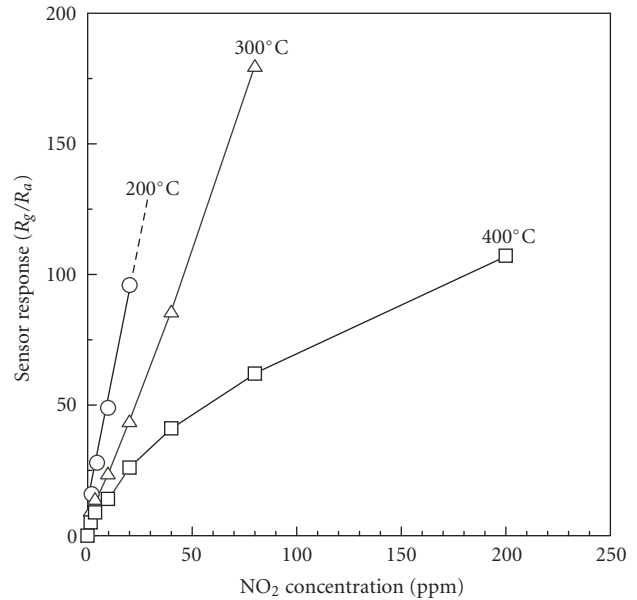


FIGURE 21: Sensor response to NO_2 at designated temperatures as correlated with NO_2 concentrations for granular WO_3 crystals prepared by pyrolysis [16].

Correlations in the stage of volume depletion can be derived for other shapes of crystals and are summarized as follows:

$$\frac{R}{R_0} = (X + Z) \left(\frac{S}{n}\right) = \{ (K_{\text{O}_2} P_{\text{O}_2})^{1/2} + K_{\text{NO}_2} P_{\text{NO}_2} \} \left(\frac{S}{a}\right),$$

$S = 1$ (plate), 2 (column), and 3 (sphere).

(41)

4.2. Response to NO_2 in Air. In the sensory measurement in air, P_{O_2} is fixed at P_{O_2} (air) and this determines the resistance level in air (air base), R_a/R_0 . Conventionally, sensor response has often been defined as the ratio of device resistance in gas (R_g) to that in air (R_a). The conventional response (R_g/R_a)

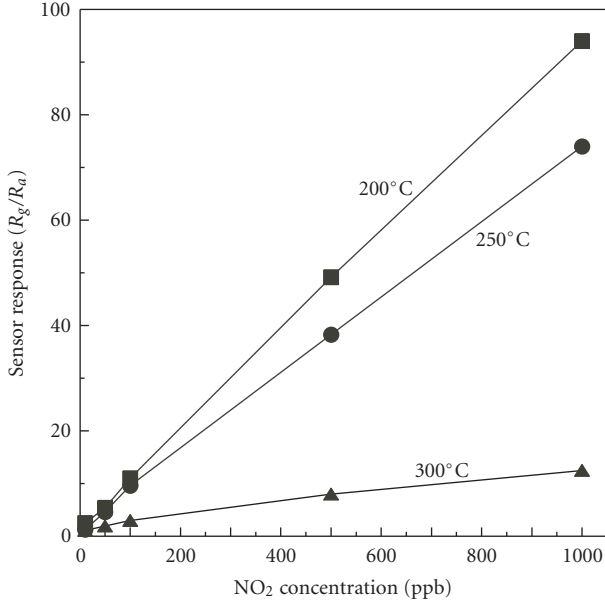


FIGURE 22: Sensor response to NO₂ at designated temperatures as correlated with NO₂ concentrations for lamellar WO₃ crystals prepared by wet process [16].

thus defined corresponds to the ratio of the response to $X + Z$ to that to X in the present treatment as follows:

$$\frac{R_g}{R_a} = \frac{(R_g/R_0)}{(R_a/R_0)}. \quad (42)$$

Let us consider the meaning of this using Figure 20, which depicts the correlations between R/R_0 and $X + Z$ for plates of two different thicknesses ($n = 1$ and 3). If X is assumed to take a value of 100, the air base (R_a/R_0) for $n = 1$ is already on a linear correlation line of volume depletion, and addition of Z simply increases the response along with the same line. From (40) or (41), we can derive

$$\frac{R_g}{R_a} = \left\{ \frac{K_{NO_2} P_{NO_2}}{(K_{O_2} P_{O_2})^{1/2}} \right\} + 1. \quad (43)$$

In this case the conventional response reflects the ratio of adsorptive strengths of the two components. In the case of thicker plates ($n = 3$), on the other hand, the air base point is still in the stage of regional depletion and, with an increase of Z , the response goes up toward volume depletion. The conventional response cannot be expressed in a simple equation like (43). The convex nature of the correlation lines tends to increase when the modified model is used (Figure 17), making the conventional response more nonlinear.

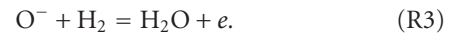
4.3. Comparison with Experiments. It has been shown that WO₃ is very sensitive to NO₂, though the sensitivity depends heavily on the methods of fabricating devices. Conventional sensor responses to NO₂ observed with two devices different in fabrication method are shown in Figures 21 and 22. For

the former device, WO₃ was prepared from ammonium paratungstate through pyrolysis at 600°C for 5 hours and the resulting crystals were granular (grain size not measured) [40]. The response is seen to be linear to P_{NO_2} in the tested range up to 80 ppm at 200 and 300°C but it changes to be apparently nonlinear at 400°C. On the basis of the present theory, the linear response at the lower temperatures reflects volume depletion, while that at the highest temperature does regional depletion. This change is easily understood from Figure 17(b) (after replacing X by $X + Z$) if we assume that Z is much larger than X , while K_{NO_2} decreases exponentially with increasing temperature.

In the case of Figure 22, WO₃ was prepared through a sol-gel process into shape of thin lamellae (ca 30 nm thick) [41]. The sensor response is seen to be linear at both temperatures of 200 and 250°C reflecting the involvement of volume depletion. It is as high as being able to detect NO₂ down to a level of 10 ppb at 200°C. Such high sensitivity comes from the smallness of lamellar size used, as understood from (40). From (40) and (42), the slope of each correlation, 9.4 or 7.4 in unit of 10^7 nm atm^{-1} , respectively, gives rise to $(K_{NO_2}/a)/(R_a/R_0)$. Thus we can estimate K_{NO_2} if R_a/R_0 is known. Unfortunately, this value is not known yet, but even when R_a/R_0 is assumed to take an ultimately small value of unity, K_{NO_2} can amount to a value as large as 1.4 or 1.1 in unit of 10^9 nm atm^{-1} , respectively. This confirms extremely strong nature of NO₂ adsorption.

5. Response to Hydrogen

5.1. Modeling. Hydrogen is selected here as a representative of reducing gases, which decreases the device resistance. It is unanimous that H₂ molecules react with O⁻ adsorbates on the semiconductor crystals. We assume that H₂ molecules collide directly with O⁻ ions (Eley-Rideal mechanism) and H₂O molecules formed are desorbed instantly from the surface:



This reaction consumes O⁻ ions, while they are resupplied from the gas phase through the reaction, (R1).

The rate of accumulation of [O⁻] is expressed by

$$\frac{d[O^-]}{dt} = k_1 P_{O_2} [e]_S - k_{-1} [O^-]^2 - k_3 P_{H_2} [O^-]. \quad (44)$$

Here t is time, k_1 and k_{-1} are the rate constants of forward and reverse reactions of (R1), respectively, k_3 is that of forward reaction of (R3), and P_{H_2} is the partial pressure of H₂. At steady state, $d[O^-]/dt = 0$, so that we obtain

$$(K_{O_2} P_{O_2})^{1/2} [e]_S = [O^-] \left\{ 1 + \left(\frac{c P_{H_2}}{[O^-]} \right) \right\}^{1/2}. \quad (45)$$

Here $K_{O_2} = k_1/k_{-1}$ (equilibrium adsorption constant) and $c = k_3/k_{-1}$. In the absence of H₂, this equation coincides with the mass action law of the oxygen adsorption equilibrium, (8). This means that the presence of H₂ modifies the value of [O⁻] simply according to (45). The electrostatic equilibrium

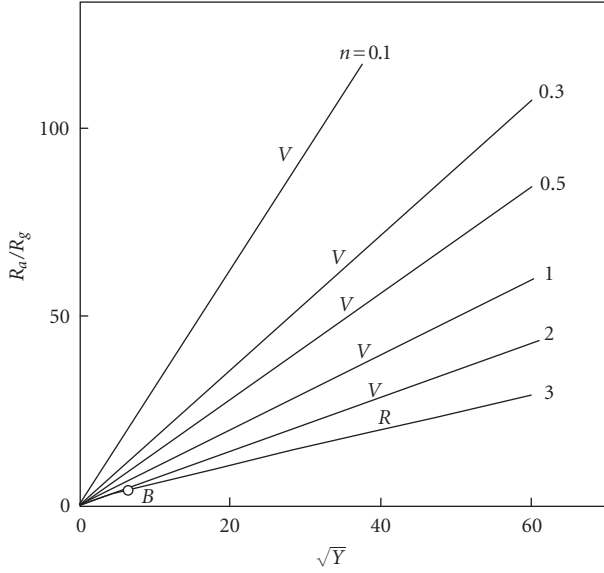


FIGURE 23: Theoretical sensor response to H_2 as correlated with $Y^{1/2}$ at $X = 1000$ [17].

of the crystal, on the other hand, does not see H_2 but $[O^-]$, requiring the depletion depth to change correspondingly. Thus the equations relating V_S and $[O^-]$ with m , n , and p in Section 3 can survive altogether in this new situation. Inserting those into (45) followed by rearrangement, we obtain an equation relating among $X(= (K_{O_2}P_{O_2})^{1/2}/L_D)$, $Y(= (c/L_D N_d)P_{H_2})$, and m , while R/R_0 is always derived from V_S . The sensor resistance measured to a mixture of H_2 and oxygen is expressed here as R_g in order to distinguish it from that measured to oxygen only. The sought correlations for plates can be summarized as follows.

Regional depletion.

$$X \exp\left(\frac{-m^2}{2}\right) = m \left\{ 1 + \left(\frac{1}{m}\right)Y \right\}^{1/2}, \quad (46)$$

$$\frac{R_g}{R_0} = \exp\left(\frac{m^2}{2}\right) \quad (\text{Plate}).$$

Volume depletion.

$$\frac{R_g}{R_0} = \frac{S(X/n)}{\{1 + (S/n)Y\}^{1/2}}, \quad (47)$$

$S = 1$ (plate), 2 (column), and 3 (sphere).

These equations show that under fixed X (or P_{O_2}), R_g/R_0 is an implicit or explicit function of Y . The equations in the stage of regional depletion for other shapes are excluded here for brevity.

5.2. *Response to H_2 in Air.* In usual sensor operation, P_{O_2} is fixed at that (0.21 atm) of the air. Sensor response is often

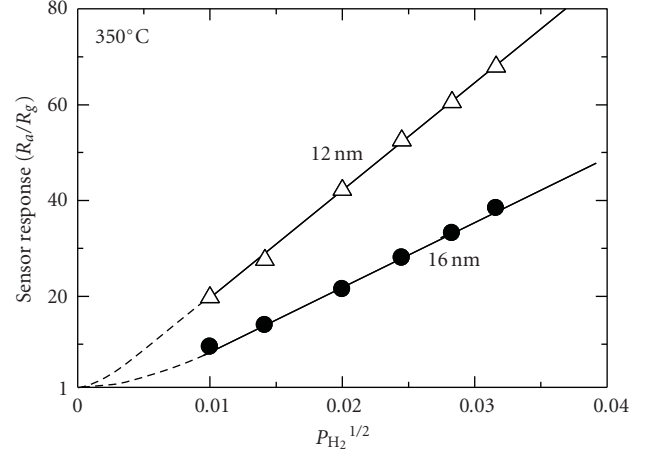


FIGURE 24: Observed sensor response to H_2 in air at 350°C as correlated with $P_{H_2}^{1/2}$ for SnO_2 devices different in grain size (screen-printed thick films).

defined as the ratio of the device resistance in air to that in the target gas (or normalized conductance), R_a/R_g . This corresponds to the response ratio in the present treatment as follows:

$$\frac{R_a}{R_g} = \frac{(R_a/R_0)}{(R_g/R_0)}. \quad (48)$$

Each term in the right-hand side can be estimated as a function of Y for fixed X by (46) or (47) so that the conventional sensor response can also be done. For example, Figure 23 shows the sensor response as a function of $Y^{1/2}$ for plate crystals, where n is selected between 0.1 and 3 and X is fixed at 1000. As easily understood, even when a large X is selected in order to secure deep stages of volume depletion in the absence of H_2 , the crystals are brought to regional depletion ultimately on increasing Y , and this tendency is enhanced with increasing n . Regional depletion is seen to begin at a relatively small value of $Y^{1/2}$ for $n = 3$. In the range of $Y^{1/2}$ where volume depletion prevails, (47) holds so that (48) is transformed into an explicit function of Y :

$$\frac{R_a}{R_g} = \left\{ 1 + \left(\frac{1}{n}\right)Y \right\}^{1/2} = \left\{ 1 + \left(\frac{c}{aN_d}\right)P_{H_2} \right\}^{1/2}. \quad (49)$$

When $(c/aN_d)P_{H_2}$ is far larger than unity,

$$\frac{R_a}{R_g} = \left\{ \frac{Y}{n} \right\}^{1/2} = \left\{ 1 + \left(\frac{c}{aN_d}\right)P_{H_2} \right\}^{1/2}. \quad (50)$$

This is why linear correlations appear in the range of volume depletion as shown. In the range of regional depletion, such linearity is not allowed, though detailed discussion is reserved here.

5.3. *Comparison with Experiments.* Sensor response (R_a/R_g) of two screen-coated SnO_2 thick film devices different in grain size (12 and 16 nm in diameter) to H_2 at 350°C is shown as a function of $P_{H_2}^{1/2}$ in Figure 24. The response

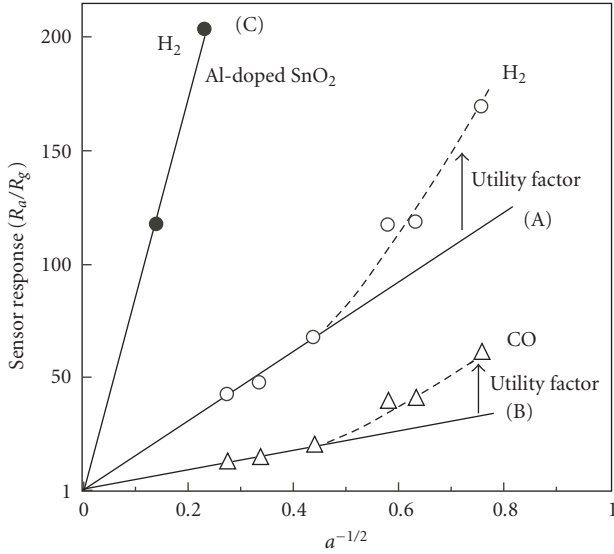


FIGURE 25: Grain size effect on sensor response shown in Figure 4 as reproduced in the relation between R_a/R_g and $a^{-1/2}$.

data of each device fall on a correlation line which is slightly concave upward initially and then becomes almost straight. This behavior is easily understood from (46)–(50). For example, (49) and (50) show that the linear relation is obtained when P_{H_2} is sufficiently large, and otherwise the concaved relation comes out. It is noted that the response as well as the slope of the correlation are larger with the smaller SnO_2 grains. This is also consistent with what is expected from the derived equations. It is reserved, however, that really quantitative analysis of the response behavior is not mature yet at present because of a lack of knowledge about many physicochemical constants needed. Probably we have to go up spirally repeating measurements and theoretical analyses.

Finally let us consider the grain size effects previously shown in Figure 4. The response data are reproduced in Figure 25, where the response is plotted against reciprocal of square root of a . Three data of the larger grains to either H_2 (A) or CO (B) fall on a straight line passing through origin in agreement with (50), while the remaining data on the smaller grains deviate upward probably through improvements of utility factor due to the appearance of insulating grains. The ratio of the slopes of straight lines, A/B , gives the ratio of the rate constants (k_2) of the oxidation reactions of H_2 and CO . The ratio is analyzed to be 14. Similar response data to H_2 (C) measured with Al-doped SnO_2 [42] are also included in the figure. The slope ratio, C/A , which is $1/29$ in this case, gives the ratio of donor density (N_d).

6. Influences of Electron-Traps Dispersed on the Crystals Surface (Plates)

6.1. Modeling of Receptor Function. Semiconductor gas sensors are usually sensitized by loading the constituent crystals with sensitizers, as mentioned before. Among a variety of sensitizers known, we consider here only those which draw electrons from the constituent crystals, increasing work

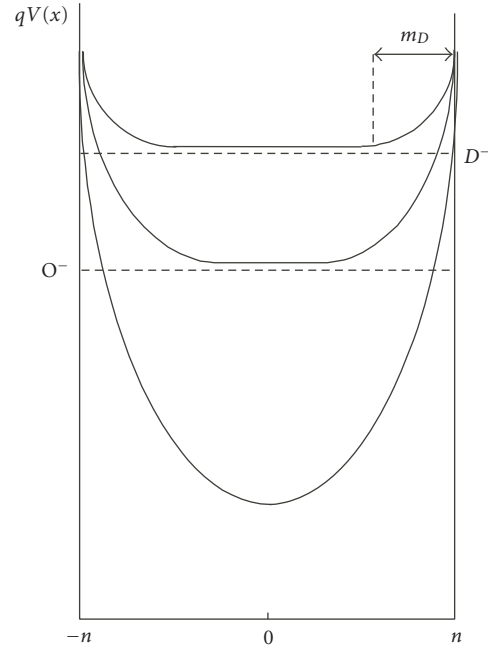


FIGURE 26: Diagram of electrostatic equilibrium drawn for small crystals loaded with surface electron-traps.

function of the crystals. Further, only the event of electron transfer between the sensitizers and the crystals is focused attention, excluding any other events such as redox changes of the sensitizers. It is assumed that the sensitizer in problem is deposited as tiny particles or clusters (denoted D), which form electron-trapping centers located in the forbidden band at the surface. Electrons would be transferred from the crystals to form ionized traps (D^-). Unlike the case of gas adsorption, however, the electrons once trapped do not return back to the crystals no matter how gas atmosphere changes, if the trapping level is deep enough. In the treatment of electrostatic equilibrium, D^- contributes to the total surface charge density (Q_s) together with ionized adsorbates, typically O^- and/or NO_2^- , as shown in Figure 26. For plate crystals placed in air, this is expressed as

$$Q_s = -q([D^-] + [\text{O}^-]) = -qmL_D N_d. \quad (51)$$

Here m is the reduced depletion depth in air. Obviously the presence of $[D^-]$ affects m depending on its magnitude. For ease of treatment, $[D^-]$ is expressed in terms of reduced depletion depth, m_D , it develops in the absence of oxygen. That is,

$$[D^-] = m_D L_D N_d. \quad (52)$$

Two cases are distinguished here depending on whether the electron transfer between the traps and the bulk of crystals is reversible (reversible traps) or not (irreversible traps).

In the case of reversible traps, trapped electrons participate in the electrostatic equilibrium of the crystals; $[D^-]$, $[\text{O}^-]$, and the bulk of each crystal are kept at the same Fermi level. By using (8) and (52), (51) is rewritten as

$$m_D L_D N_d + (K_{\text{O}_2} P_{\text{O}_2})^{1/2} [e]_s = mL_D N_d. \quad (53)$$

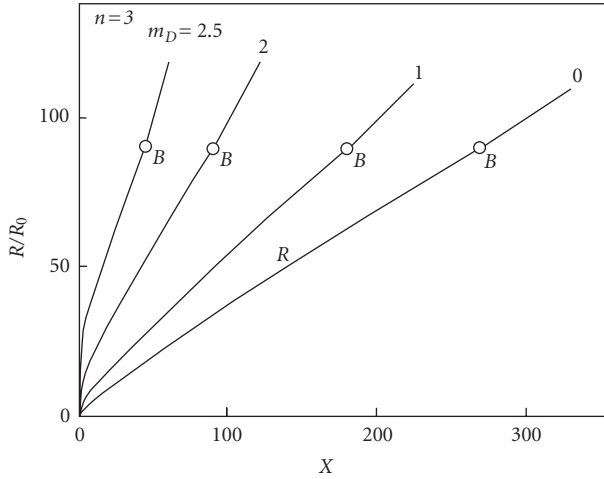


FIGURE 27: Correlations between R/R_0 and X for plate crystals dispersed with reversible electron-traps [17].

It is reminded that m and m_D are reduced depletion depths to $[D^-] + [O^-]$ and $[D^-]$, respectively. We know that $[e]_s$ as well as R/R_0 are expressed as a function of m , n , and p . The following equations result for correlating R/R_0 with X (abrupt model).

Regional depletion.

$$X \exp\left(\frac{-m^2}{2}\right) = m - m_D, \quad (54)$$

$$\frac{R}{R_0} = \exp\left(\frac{m^2}{2}\right).$$

Volume depletion.

$$\frac{R}{R_0} = \exp\left\{\left(\frac{n^2}{2}\right) + p\right\} = \frac{X}{(n - m_D)}. \quad (55)$$

The correlations derived for $m_D = 0, 1, 2$, and 2.5 , and $n = 3$ are shown in Figure 27. For given X , R/R_0 increases dramatically with increasing m_D . In the stage of volume depletion, R/R_0 of a trap-dispersed plate of reduced size n is the same as that exhibited by a clean plate of reduced size $n - m_D$. The response in the stage of regional depletion is seen to be also enhanced dramatically on increasing m_D .

In the case of irreversible traps, trapped electrons are assumed to stay at the traps permanently. It is suspected that such case may happen when the foreign deposits react with the surface of the constituent crystals. For example, the component cations of the deposits are dissolved into the lattice of underlying crystals at the surface or nearby. The dissolved cations may act as strong acceptors of electrons (irreversible traps). Anyway those trapped electrons amounting to depth m_D are kept off from the electrostatic equilibrium. As a result, oxygen adsorption cannot take place until P_{O_2} exceeds a

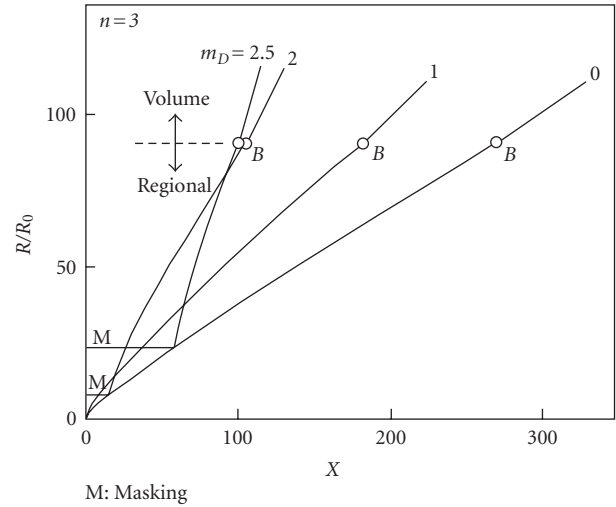


FIGURE 28: Correlations between R/R_0 and X for plate crystals dispersed with irreversible electron-traps [17].

critical point ($P_{O_2}(D)$) at which depletion depth reaches m_D in the absence of $[D^-]$. Equation (51) is rewritten as

$$[D^-] + \left\{ (K_{O_2} P_{O_2})^{1/2} - (K_{O_2} P_{O_2}(D))^{1/2} \right\} [e]_s = m L_D N_d. \quad (56)$$

The resulting correlating equations are summarized as follows:

Regional depletion.

$$(X - X_D) \exp\left(\frac{-m^2}{2}\right) = m - m_D, \quad (57)$$

$$\frac{R}{R_0} = \exp\left(\frac{m^2}{2}\right).$$

Volume depletion.

$$(X - X_D) \exp\left\{-\left(\frac{n^2}{2}\right) - p\right\} = n - m_D, \quad (58)$$

$$\frac{R}{R_0} = \exp\left\{\left(\frac{n^2}{2}\right) + p\right\} = (X - X_D)(n - m_D).$$

Here $X(D) = (K_{O_2} P_{O_2}(D))^{1/2} / L_D$. The correlations given by these equations are shown in Figure 28, where m_D and n are set to the same values as those used in Figure 27. It is seen that the response does not appear up to $X = X_D$ (masking) and then rise up steeply with a slope increasing with increasing m_D . The irreversible traps are thus effective also in enhancing the sensitivity to O_2 , though in a manner different from that with the reversible traps.

6.2. *Response to NO_2 or H_2 in Air.* In this section, response of electron-trap dispersed plates to NO_2 or H_2 in air is discussed

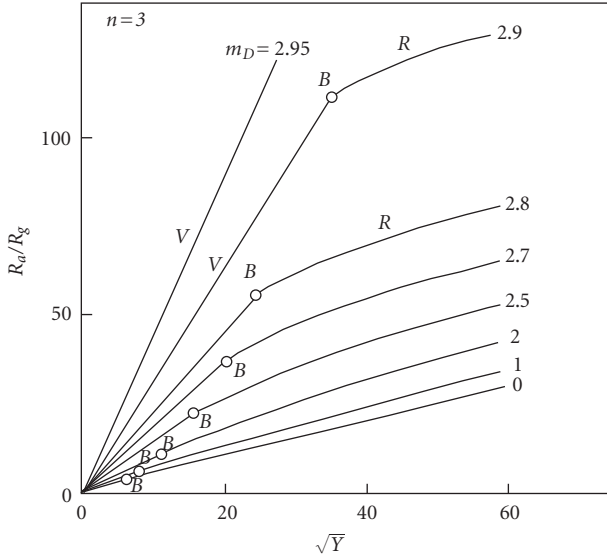


FIGURE 29: Correlations between R_a/R_g and $Y^{1/2}$ for plate crystals dispersed with reversible electron-traps [17].

briefly. Under exposure to NO_2 in air, total surface charge density is written as follows:

$$Q_s = -q([D^-] + [O^-] + [\text{NO}_2^-]) = -qmL_D N_d. \quad (59)$$

For either type of traps, reversible and irreversible, the sought correlations between R/R_0 and $X + Z$ are essentially the same as those obtained between R/R_0 and X if X is replaced by $X + Z$. At fixed X , the sensitivity of R/R_0 to Z increases sharply with increasing m_D .

The response to H_2 in air can be developed in the same way as done for clean plate crystals. $[O^-]$ is given by (45), while $[D^-]$ is kept constant. Using these equations, it is possible to derive the sought correlations for reversible traps as follows.

Regional depletion.

$$X \exp\left(\frac{-m^2}{2}\right) = (m - m_D) \left\{ 1 + \left[\frac{1}{(m - m_D)} \right] Y \right\}^{1/2}, \quad (60)$$

$$\frac{R_g}{R_0} = \exp\left(\frac{m^2}{2}\right).$$

Volume depletion.

$$\frac{R_g}{R_0} = \left\{ \frac{X}{(n - m_D)} \right\} \left\{ 1 + \left[\frac{1}{(n - m_D)} \right] Y \right\}^{1/2}, \quad (61)$$

$$\frac{R_a}{R_g} = \left\{ 1 + \left[\frac{1}{(n - m_D)} \right] Y \right\}^{1/2} \quad (62)$$

$$= \left\{ 1 + \left[\frac{1}{(n - m_D)} \right] \left[\frac{c}{L_D N_d} \right] P_{\text{H}_2} \right\}^{1/2}.$$

Equation (62) formulates conventional sensor response. The response is drastically promoted by increasing m_D ,

as illustrated in Figure 29, where correlations are sought between R_a/R_g and $Y^{1/2}$ with n and X being fixed at 3 and 1000, respectively. However, the manner of promotion of the response is considerably different from that of the thickness effect observed with clean plates (Figure 23).

In the case of irreversible traps, the correlations are given as follows.

Regional depletion.

$$(X - X_D) \exp\left(\frac{-m^2}{2}\right) = (m - m_D) \left\{ 1 + \left[\frac{1}{(m - m_D)} \right] Y \right\}^{1/2},$$

$$\frac{R_g}{R_0} = \exp\left(\frac{m^2}{2}\right). \quad (63)$$

Volume depletion.

$$\frac{R_g}{R_0} = \left\{ \frac{(X - X_D)}{(n - m_D)} \right\} \left\{ 1 + \left[\frac{1}{(n - m_D)} \right] Y \right\}^{-1/2}, \quad (64)$$

$$\frac{R_a}{R_g} = \left\{ 1 + \left[\frac{1}{(n - m_D)} \right] \left[\frac{c}{L_D N_d} \right] P_{\text{H}_2} \right\}^{1/2}. \quad (65)$$

Expression of conventional sensor response (65) is seen to be identical to (62). This is quite natural because it does not matter in the stage of volume depletion whether the traps are reversible or not.

7. Discussion

To those who have been engaged in semiconductor gas sensor researches like us, it is a long-time dream to acquire a theoretical background of sensor researches. For a long time, many people have exerted efforts to upgrade capabilities of sensors or to extend applications of sensors empirically from various standpoints of sensing materials, material preparation and processing, sensitizers and stabilizers, sensing body structure and fabrication, device structure, electrodes, signal processing, transients based sensing, and so forth. These efforts have contributed to ever continuing progresses of gas sensors. However, it has not always been easy to understand well the meaning of a new progress achieved in a particular category, to those working in different categories. Even it has happened that the finders themselves do not understand their remarkable findings well, failing to connect them to another progress. All these have arisen mainly from a lack of a theoretical background commonly possessed by gas sensor researchers.

The theoretical concept available to semiconductor gas sensors has so far been almost nothing more than the concept of semiconductor catalysis born a long time ago. It has been useful for qualitative interpretations of gas sensors but almost powerless for quantitative analyses. A main reason for this is that the concept has ignored the role or meaning of so small semiconductors as used in gas sensors. Behavior of small semiconductors is considerably different from that

of large ones and this difference provides gas sensors with profound merits. This is a truth unrevealed so far. We have shown in this article that gas response behavior of small semiconductors can be formulated by using well-established concepts and well-known parameters in physics and chemistry. The equations derived seem to work well on understanding the response behavior experimentally observed, though available data are still limited at present. No doubt the equations need to be checked more rigorously by experiments. Nevertheless we believe we are at a new starting point for theoretical approaches to semiconductor gas sensors. It is anticipated that such approaches will contribute much to strengthening and expanding the background of gas sensors. The treatments described in this article have focused attention to receptor function of semiconductors only, setting transducer function to work in a simple mode. Elaboration of the transducer function is one of the most important subjects of theoretical approaches.

8. Conclusions

Through the theoretical approaches to semiconductor gas sensors described here, the following conclusions can be drawn.

(1) Receptor function and response of small semiconductor crystals can be formulated in principle by using the chemical parameters of gases side, such as partial pressure, adsorption constant and rate constant, and the physical parameters of semiconductor side, such as shape and size, donor density, and Debye length.

(2) Theoretical equations account for well-response behavior to oxygen, nitrogen dioxide, and hydrogen, as well as the grain size effects involved, though the tested examples are limited in number.

(3) Electron-traps dispersed on the crystal surface influence strongly on receptor function and response to gases, thus exerting a kind of sensitization effect.

List of parameters and symbols frequently used

K_{O_2} and K_{NO_2} :	Equilibrium adsorption constants of O_2 and NO_2
P_{O_2} , P_{NO_2} and P_{H_2} :	Partial pressures of O_2 , NO_2 and H_2
$P_{O_2}(D)$:	P_{O_2} giving m_D in the absence of D
$[e]_s$:	Surface density of conduction electrons
$[O^-]$, $[NO_2^-]$ and $[D^-]$:	Surface densities of O^- , NO_2^- , and D^-
D and D^- :	Extrinsic electron-traps, neutral (D) and ionized (D^-)
Q_s :	Total surface charge density
q :	Electric charge of proton
N_d and ϵ :	Donor density and permittivity of oxide semiconductor
L_D :	Debye length
a and n :	Half thickness of plates and reduced thickness (a/L_D)

w and m :	Depletion depth and reduced depletion depth (w/L_D)
m_D :	Reduced depletion depth in vacuum due to extrinsic traps
x and X :	Displacement from origin and reduced displacement (x/L_D)
$V(x)$, $V(X)$, and V_s :	Potential energy of electrons at x , X and surface
p :	Fermi level shift
X :	$= (K_{O_2}P_{O_2})^{1/2}/L_D$
Y :	$= (c/L_D N_d)P_{H_2}$
Z :	$= K_{NO_2}P_{NO_2}/L_D$
$X(D)$:	$= (K_{O_2}P_{O_2}(D))^{1/2}/L_D$
c :	$= k_3/k_{-1}$
k_1 and k_{-1} :	Rate constants of oxygen adsorption and desorption (R1)
k_3 :	Rate constant of surface reaction (R3)
R and R_0 :	Resistances at P_{O_2} and flat band state
R_a and R_g :	Resistances in air and target gas

Acknowledgment

The authors are grateful to Mr. Koichi Suematsu for providing them with experimental data on sensor response to oxygen and hydrogen.

References

- [1] T. Seiyama, A. Kato, K. Fujiishi, and M. Nagatani, "A new detector for gaseous components using semiconductive thin films," *Analytical Chemistry*, vol. 34, no. 11, pp. 1502–1503, 1962.
- [2] N. Taguchi, "Published patent application in Japan," S37-47677, October 1962.
- [3] G. Heiland, "Homogeneous semiconducting gas sensors," *Sensors and Actuators*, vol. 2, pp. 343–361, 1982.
- [4] N. Yamazoe, "Toward innovations of gas sensor technology," *Sensors and Actuators B*, vol. 108, no. 1–2, pp. 2–14, 2005.
- [5] K. Ihokura and J. Watson, *The Stannic Oxide Gas Sensor: Principles and Applications*, CRC Press, Japan, 1994.
- [6] G. Korotcenkov, "The role of morphology and crystallographic structure of metal oxides in response of conductometric-type gas sensors," *Materials Science and Engineering R*, vol. 61, no. 1–6, pp. 1–39, 2008.
- [7] Y. Shimizu and M. Egashira, "Basic aspects and challenges of semiconductor gas sensors," *MRS Bulletin*, vol. 24, no. 6, pp. 18–24, 1999.
- [8] A. Gurlo, N. Barsan, and U. Weimar, *Gas Sensors Based on Semiconducting Metal Oxides, Metal Oxides: Chemistry and Applications*, Marcel Dekker, New York, NY, USA, 2004.
- [9] M. Madou and S. R. Morrison, *Chemical Sensing with Solid State Devices*, Academic Press, Boston, Mass, USA, 1989.
- [10] G. Sakai, N. Matsunaga, K. Shimano, and N. Yamazoe, "Theory of gas-diffusion controlled sensitivity for thin film semiconductor gas sensor," *Sensors and Actuators B*, vol. 80, no. 2, pp. 125–131, 2001.
- [11] N. Matsunaga, G. Sakai, K. Shimano, and N. Yamazoe, "Diffusion equation-based study of thin film semiconductor gas sensor-response transient," *Sensors and Actuators B*, vol. 83, no. 1–3, pp. 216–221, 2002.

- [12] N. Matsunaga, G. Sakai, K. Shimano, and N. Yamazoe, "Formulation of gas diffusion dynamics for thin film semiconductor gas sensor based on simple reaction-diffusion equation," *Sensors and Actuators B*, vol. 96, no. 1-2, pp. 226–233, 2003.
- [13] N. Yamazoe, K. Shimano, and C. Sawada, "Contribution of electron tunneling transport in semiconductor gas sensor," *Thin Solid Films*, vol. 515, no. 23, pp. 8302–8309, 2007.
- [14] N. Yamazoe and K. Shimano, "Theory of power laws for semiconductor gas sensors," *Sensors and Actuators B*, vol. 128, no. 2, pp. 566–573, 2008.
- [15] N. Yamazoe and K. Shimano, "Roles of shape and size of component crystals in semiconductor gas sensors—I: response to oxygen," *Journal of the Electrochemical Society*, vol. 155, no. 4, pp. J85–J92, 2008.
- [16] N. Yamazoe and K. Shimano, "Roles of shape and size of component crystals in semiconductor gas sensors—II: response to NO₂ and H₂," *Journal of the Electrochemical Society*, vol. 155, no. 4, pp. J93–J98, 2008.
- [17] N. Yamazoe and K. Shimano, "Receptor function of small semiconductor crystals with clean and electron-traps dispersed surfaces," *Thin Solid Films*. In press.
- [18] M. Iwamoto, Y. Yoda, N. Yamazoe, and T. Seiyama, "Study of metal oxide catalysts by temperature programmed desorption 4. Oxygen adsorption on various metal oxides," *Journal of Physical Chemistry*, vol. 82, no. 24, pp. 2564–2570, 1978.
- [19] N. Yamazoe, J. Fuchigami, M. Kishikawa, and T. Seiyama, "Interactions of tin oxide surface with O₂, H₂O and H₂," *Surface Science*, vol. 86, pp. 335–344, 1979.
- [20] Y. Mizokawa and S. Nakamura, "ESR and electric conductance studies of the fine-powdered SnO₂," *Japanese Journal of Applied Physics*, vol. 14, no. 6, pp. 779–788, 1975.
- [21] C. Xu, J. Tamaki, N. Miura, and N. Yamazoe, "Grain size effects on gas sensitivity of porous SnO₂-based elements," *Sensors and Actuators B*, vol. 3, no. 2, pp. 147–155, 1991.
- [22] Y.-G. Choi, G. Sakai, K. Shimano, N. Miura, and N. Yamazoe, "Wet process-prepared thick films of WO₃ for NO₂ sensing," *Sensors and Actuators B*, vol. 95, no. 1–3, pp. 258–265, 2003.
- [23] A. Rothschild and Y. Komem, "On the relationship between the grain size and gas-sensitivity of chemo-resistive metal-oxide gas sensors with nanosized grains," *Journal of Electroceramics*, vol. 13, no. 1–3, pp. 697–701, 2004.
- [24] A. Rothschild and Y. Komem, "The effect of grain size on the sensitivity of nanocrystalline metal-oxide gas sensors," *Journal of Applied Physics*, vol. 95, no. 11, pp. 6374–6380, 2004.
- [25] N. Barsan, "Conduction models in gas-sensing SnO₂ layers: grain-size effects and ambient atmosphere influence," *Sensors and Actuators B*, vol. 17, no. 3, pp. 241–246, 1994.
- [26] N. Barsan and U. Weimar, "Conduction model of metal oxide gas sensors," *Journal of Electroceramics*, vol. 7, no. 3, pp. 143–167, 2001.
- [27] M. Batzill and U. Diebold, "The surface and materials science of tin oxide," *Progress in Surface Science*, vol. 79, no. 2–4, pp. 47–154, 2005.
- [28] J. Ding, T. J. McAvoy, R. E. Cavicchi, and S. Semancik, "Surface state trapping models for SnO₂-based microhotplate sensors," *Sensors and Actuators B*, vol. 77, no. 3, pp. 597–613, 2001.
- [29] H. Ogawa, M. Nishikawa, and A. Abe, "Hall measurement studies and an electrical conduction model of tin oxide ultrafine particle films," *Journal of Applied Physics*, vol. 53, no. 6, pp. 4448–4455, 1982.
- [30] H. Ohnishi, "Current state and subjects of gas sensor technology in city gas industries," *Materials Integration*, vol. 21, no. 5, pp. 167–177, 2008.
- [31] S. Matsushima, J. Tamaki, N. Miura, and N. Yamazoe, "TEM observation of the dispersion state of Pd on SnO₂," *Chemistry Letters*, vol. 18, no. 9, pp. 1651–1654, 1989.
- [32] N. Yamazoe, "New approaches for improving semiconductor gas sensors," *Sensors and Actuators B*, vol. 5, no. 1–4, pp. 7–19, 1991.
- [33] S. Matsushima, Y. Teraoka, N. Miura, and N. Yamazoe, "Electronic interaction between metal additives and tin dioxide in tin dioxide-based gas sensors," *Japanese Journal of Applied Physics*, vol. 27, no. 10, pp. 1798–1802, 1988.
- [34] P. B. Weisz, "Effects of electronic charge transfer between adsorbate and solid on chemisorption and catalysis," *The Journal of Chemical Physics*, vol. 21, no. 9, pp. 1531–1538, 1951.
- [35] T. Wolkenstein, *The Electron Theory of Catalysis on Semiconductors*, Pergamon Press, Oxford, UK, 1963.
- [36] H. Eyring, D. Henderson, and W. Jost, Eds., *Physical Chemistry: An Advanced Treatise*, vol. 10, Academic Press, San Diego, Calif, USA, 1976.
- [37] S. M. Sze, *Semiconductor Devices: Physics and Technology*, John Wiley & Sons, New York, NY, USA, 1985.
- [38] J. Maier and W. Göpel, "Investigations of the bulk defect chemistry of polycrystalline Tin(IV) oxide," *Journal of Solid State Chemistry*, vol. 72, no. 2, pp. 293–302, 1988.
- [39] C. Malagù, V. Guidi, M. Stefancich, M. C. Carotta, and G. Martinelli, "Model for Schottky barrier and surface states in nanostructured *n*-type semiconductors," *Journal of Applied Physics*, vol. 91, no. 2, pp. 808–814, 2002.
- [40] M. Akiyama, H. Tamaki, N. Miura, and N. Yamazoe, "Tungsten oxide-based semiconductor sensor highly sensitive to NO and NO₂," *Chemistry Letters*, vol. 1991, pp. 1611–1614, 1991.
- [41] Y.-G. Choi, G. Sakai, K. Shimano, N. Miura, and N. Yamazoe, "Wet process-prepared thick films of WO₃ for NO₂ sensing," *Sensors and Actuators B*, vol. 95, no. 1–3, pp. 258–265, 2003.
- [42] C. Xu, J. Tamaki, N. Miura, and N. Yamazoe, "Grain size effects on gas sensitivity of porous SnO₂-based elements," *Sensors and Actuators B*, vol. 3, no. 2, pp. 147–155, 1991.

Review Article

Optimized Feature Extraction for Temperature-Modulated Gas Sensors

Alexander Vergara,^{1,2} Eugenio Martinelli,³ Eduard Llobet,²
Arnaldo D'Amico,³ and Corrado Di Natale³

¹*Institute for Nonlinear Science, University of California, San Diego, La Jolla, CA 92093-0402, USA*

²*MINOS, Universitat Rovira i Virgili, Avda. Països Catalans, 26, 43007 Tarragona, Spain*

³*Department of Electronic Engineering, University of Rome Tor Vergata, via del Politecnico 1, 00133 Roma, Italy*

Correspondence should be addressed to Corrado Di Natale, dinatale@uniroma2.it

Received 26 January 2009; Accepted 3 April 2009

Recommended by Michele Penza

One of the most serious limitations to the practical utilization of solid-state gas sensors is the drift of their signal. Even if drift is rooted in the chemical and physical processes occurring in the sensor, improved signal processing is generally considered as a methodology to increase sensors stability. Several studies evidenced the augmented stability of time variable signals elicited by the modulation of either the gas concentration or the operating temperature. Furthermore, when time-variable signals are used, the extraction of features can be accomplished in shorter time with respect to the time necessary to calculate the usual features defined in steady-state conditions. In this paper, we discuss the stability properties of distinct dynamic features using an array of metal oxide semiconductors gas sensors whose working temperature is modulated with optimized multisinusoidal signals. Experiments were aimed at measuring the dispersion of sensors features in repeated sequences of a limited number of experimental conditions. Results evidenced that the features extracted during the temperature modulation reduce the multidimensional data dispersion among repeated measurements. In particular, the Energy Signal Vector provided an almost constant classification rate along the time with respect to the temperature modulation.

Copyright © 2009 Alexander Vergara et al. This is an open access article distributed under the Creative Commons Attribution License, which permits unrestricted use, distribution, and reproduction in any medium, provided the original work is properly cited.

1. Introduction

In a seminal paper by Zaromb and Stetter [1] the possibility to approach the quantitative and the qualitative analysis of simple and complex gas mixtures with solid-state sensor arrays and intelligent signal processing algorithms was introduced. Since that, countless examples of this approach appeared in literature and, among the used sensors technologies, metal-oxide semiconductor gas sensors were largely investigated [2–5]. Even if these researches corroborated the initial hypothesis, the practical application of solid-state sensors is still limited in practice by nontolerable instability of sensors signals. This is manifested as a nonpredictable temporal variation of the sensor signal whose more evident consequence is the spread of sensors responses when the sensor undergoes the same gas exposure. Consequently, calibrated sensor response patterns become, even at short time

scale, obsolete providing false evaluations and requiring, as countermeasure, frequent calibrations. The instability of sensor signals derives from two main sources. The first is clearly found in the nature of the chemical and physical processes occurring in the sensor [6], such as ageing (e.g., the reorganization of the sensor surface) and poisoning (e.g., irreversible analyte binding). The second source of instability, often neglected, pertains to uncontrolled changes of the measurement conditions due for instance to fluctuations of the sample flow rate or the temperature of gas and sensors. In addition, other issues related to the experimental setup can induce either memory effects (such as systematic errors due to repeated measurement sequences) or short-term effects (system warm-up, thermal trends). These effects may also trigger the degradation of samples that in some cases can give rise to nonreproducible sensor responses that can be attributed to sensors drift. The sources of sensor instability

due to nonaccurate measurement procedure can hopefully be counteracted by careful experimental designs.

The removal of those effects of physical and chemical origins resulting in sensors instability is a complicated task that requires a deep knowledge of the physics and the chemistry involved in the sensing process and, even more complicated, in the control of those technological steps related to the sensor fabrication process. Nonetheless, disregarding the “physical” approach to sensor stability, several authors demonstrated that it is possible to improve the sensor performance by an intelligent selection of the sensor features [7], by an optimization of the sensor operating conditions [8], and by a clever design of signal processing algorithms [9].

Feature extraction is defined as the operation necessary to extract from the temporal evolution of the sensor signal a set of synthetic descriptors that can be used in computations aimed at identifying the gas components in a mixture and their concentration. Features are practically related to the measure of the sensor signal in two conditions defined by the absence and the presence of the sample. The signal measured in these two states can be combined in order to obtain different quantities. For instance, in case of chemically sensitive resistances the simplest features that can be defined are, $R_{\text{gas}} - R_{\text{ref}}$, and $(R_{\text{gas}} - R_{\text{ref}})/R_{\text{ref}}$ where R_{gas} and R_{ref} are the sensor resistance measured in presence of the sample and the reference atmosphere, respectively. It is known that even these simple quantities have different stability properties [10]. A methodology suggested to improve the sensor performance consists in the time modulation of the sensor signal obtained changing at least one of the sensor operating conditions. In case of metal-oxide semiconductor gas sensors, since the sensor properties are strongly dependant on the sensor temperature [11], the modulation of temperature is an easy method to obtain a time variable sensor signal. In these sensors temperature modulation is expected to alter the kinetics of both adsorption and reaction processes taking place at the sensor surface. Temperature modulation leads to the development of response patterns, which may be characteristic of the species being detected. In other words, by retrieving information from response dynamics, new response features are obtained that can confer more selectivity to metal oxide sensors. Indeed, several authors have developed this strategy and applied several techniques to extract features that are important for the discrimination or quantification of gases. Fast Fourier Transform (FFT) and Discrete Wavelet Transform (DWT) have been used as feature extraction tools in several studies [12–17]. Various researches shown that the features extracted from temperature modulated gas sensors are more stable with respect to sensors operated at fixed temperature [18–22]. An important set of parameters to be adjusted is defining the temperature modulation profile. In case of simple sinusoidal modulation some results evidenced the existence of optimal modulation frequencies whose application results in a general improvement of selectivity and stability [14, 15].

Concerning the expected efficiency of the methods based on optimized features extraction, signal processing, and operative conditions it is important to consider that it

is rather unlikely that these approaches can remove the degradation of physical and chemical properties of a sensor, but since the instability is also due to the fluctuations of the experimental conditions signal processing optimization can be considered as the search of features that are less sensitive to those quantities that fluctuate among repeated measurements.

In this paper, we illustrate the stability properties of a number of distinct features derived from systems theory, a discipline defining the instruments to study and represent complex time evolving systems.

In this study, the features are simultaneously extracted from a temperature-modulated array of metal-oxide semiconductor gas sensor. The stability is evaluated in a four-classes pattern recognition problem assuming that improved stability results in a better classification of the four classes. Sensors were operated in a discontinuous mode temperature modulation where they are normally kept nonpowered and the temperature modulation is applied only during the time interval when feature extraction is performed [23].

2. System Theory and Sensors Features Extraction

Elements of systems theory have been used in the past to model sensors behavior considering not only the steady state changes but also the dynamic evolution of signals. Attempts to model these behaviors using either time series or analytical approximation have been shown in the past [24–27], and the use of specific methods to extract only the dynamic information was also demonstrated [28, 29]. Nonetheless, only recently one of the central concepts for the analysis of dynamics systems, the phase space, has been taken into consideration. In order to define the phase space let us consider a system whose state is completely described by n scalar variables. Different states corresponds to different points in an n -dimension vector space defined by an orthonormal basis where each direction corresponds to one of the scalar variables. The main property of such space is the unique correspondence between points in the space and states of the system.

Practically, the information gained about a system, such as a sensor, is contained in the temporal evolution of the measured signal. Nonetheless, from the time dependence of this scalar quantity a number of novel variables can be generated. For instance, in mechanical systems, the observation of the position with the time gives place to variables such as velocity (first derivative) and acceleration (second derivative) from which the phase space is constructed.

As a consequence, a system, observed through a single scalar quantity for a period of time, is represented by a sequence of points in the phase space. Once suitably parameterized with the time, this sequence forms a trajectory containing all the captured information about the phenomena underlying the system evolution. The relation between the observed signals and the internal variables forming the phase space has been demonstrated by the embedding theorem of Takens [30]. According to this theorem, the

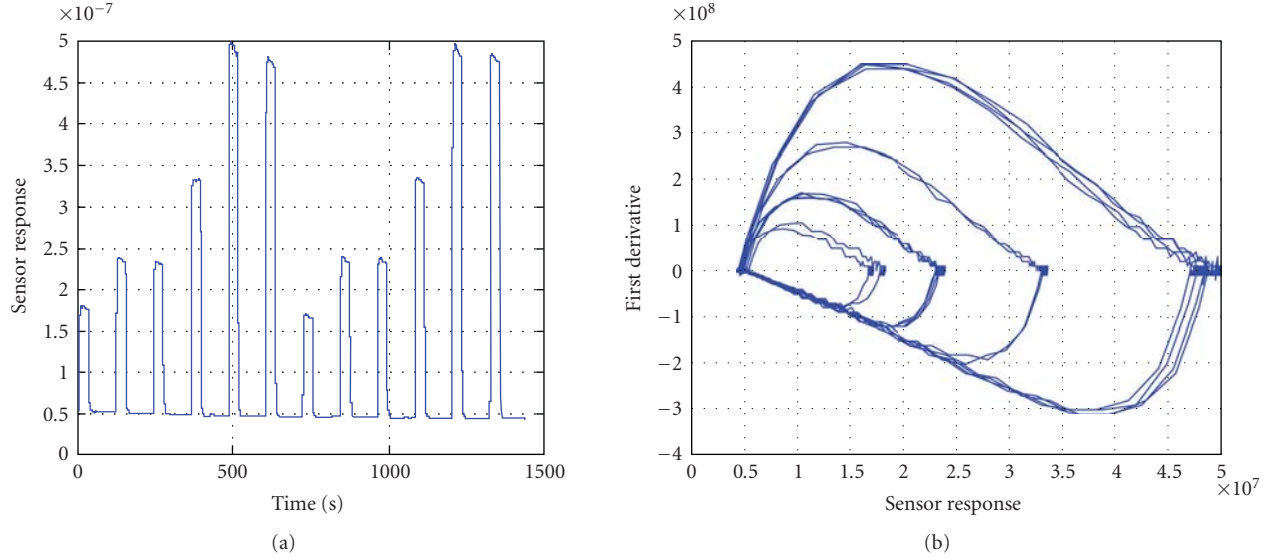


FIGURE 1: Responses of a SnO₂ gas sensor in presence of different gas concentrations; (a) the sensor response in the time domain; (b) phase space of SnO₂ sensor with $f(t)$ and $f'(t)$ as canonical variables.

variables of the phase space are given by a number of differentiable transformations of the observed signal such as a set of independent coordinates $x(t)$, $x(t + \tau_1)$, $x(t + \tau_2)$, \dots , $x(t + \tau_n)$. Each variable of this set represents the experimental time series at different time samples (after a specific time delay τ_n , a multiple of the sampling time step T_s). Any dynamic state of the system is therefore represented in a multidimensional phase space as $y(t) = [x(t), x(t + \tau_1), x(t + \tau_2), \dots, x(t + \tau_n)]$. The number of coordinates defining the phase space and the values of the time delays τ_n must be chosen suitably in order to obtain an optimal description of the phenomena. There are sufficient conditions to avoid false projection and ambiguities of the trajectories.

From a general point of view, a chemical sensor can be considered as a dynamic system whose response signal temporally evolves following, with its proper dynamics, the concentration of the analytes. The information is in the temporal evolution of a single scalar quantity (i.e., in the sensor signal) and from this time dependence, a number of new variables can be generated. The minimum set of variables able to describe the state and the evolution of the sensor comprises the response signal (i.e., the observed variable) and its first derivative. Therefore, a phase space can be defined by the orthonormal basis formed by the observed signal and its first derivative. The use of the phase space in the field of gas sensors was first introduced in 2003 [31]. In the Figure 1 the responses of SnO₂ sensor in presence of different gas concentrations and the relative trajectories spanned in the phase space are shown.

The description of the trajectory in the phase space give rise to novel features related to the underlying phenomena that can be used to build more accurate gas identification models. The area spanned by the trajectory when it undergoes a transformation (e.g., during the adsorption) is

a rather straightforward descriptor to quantify the process. In this quantity both the magnitude and the velocity of the sensor response are considered. However, the area is a descriptor that overlooks some characteristics of the trajectory evolution (i.e., the shape of the trajectory). This is the reason to include other descriptors, for example, the dynamic moments (DMs), that can describe also the morphology of the trajectories [32].

Among the possible quantities that can bring such notions, the following DMs are here discussed, all of them are defined as combination of the phase space variables:

$$DM2 = \frac{1}{n} \sum_{i=0}^n x_i y_i \quad (1)$$

$$DM3_{PB} = \frac{\sqrt{2}}{2n} \sum_{i=0}^n (x_i^2 y_i - x_i y_i^2) \quad (2)$$

$$DM3_{SB} = \frac{\sqrt{2}}{2n} \sum_{i=0}^n [2x_i^3 + 3(x_i^2 y_i - x_i y_i^2)] \quad (3)$$

$$DM3_X = \frac{1}{2n} \sum_{i=0}^n (x_i^3 - 3x_i y_i^2) \quad (4)$$

$$DM3_Y = \frac{1}{2n} \sum_{i=0}^n (x_i^3 - 3x_i^2 y_i) \quad (5)$$

where $x(t)|_{t_i+k}$ and $y(t)|_{t_i+k+\tau} = x(t+\tau)|_{t_i+k+\tau}$ are portions of the sensor signal ($t_i = 0, 1, 2, 3, \dots$; $k = 1, 2, 3$ and 5 s; $\tau = 1, 2$ and 3 s). Each DM describes a different morphological feature of the trajectory, so that the collective use of more than one moment is usually required for an exhaustive description of a phase space trajectory. The first gas sensor signal described by DMs was the quartz

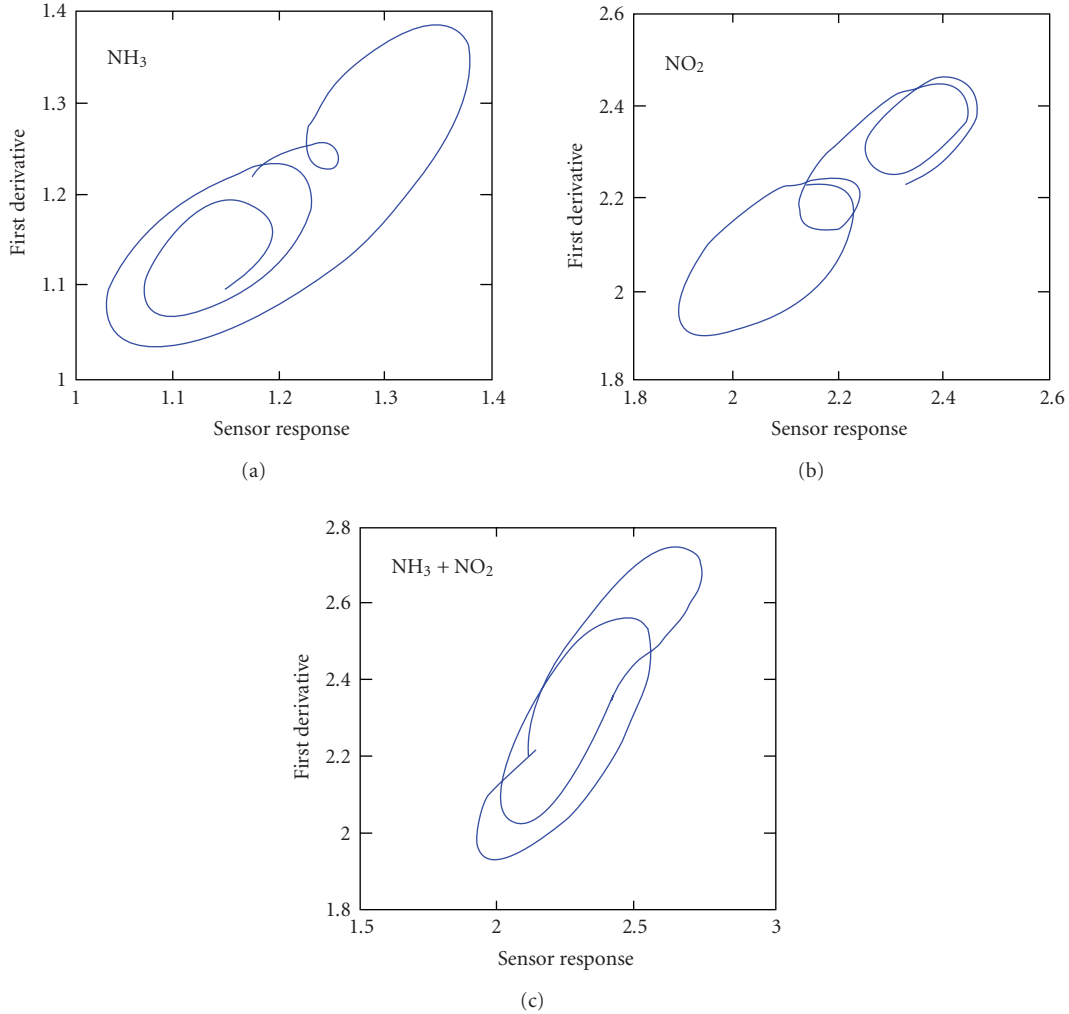


FIGURE 2: Example of the signal response of a tungsten oxide microhotplate sensor to ammonia (500 ppm), nitrogen dioxide (1 ppm) and ammonia + nitrogen dioxide (500 + 1 ppm) in the phase space domain. The first derivative of the sensor response for a time lag equal to 3 ms (y -axis) is plotted versus the sensor response (x -axis). Reproduced from [33] Elsevier Science, with permission.

microbalance [33], whereas in the example here illustrated they are applied to temperature modulated metal-oxide gas sensors. In Figure 2 typical trajectories in the phase space of a tungsten oxide gas sensor in the presence of the gases are shown. The exposure to different gases and mixtures results in evidently distinct trajectories. These differences are transformed in quantities by the application of the dynamic moment.

Phase space is an example of a principle of the classical signal theory applied to the study of the time evolution of a gas sensor signal. Following the suggestions of signal theory let us consider a gas sensor array as a mathematical object, where the observable signals of each sensor are part of a multidimensional array. When the sensors simultaneously interact with the same chemical compounds, the signals of the sensors becomes characterized by a certain degree of mutual correlation. The amount of correlation may change according to the quality and quantity of the gas species to which the array is exposed. One of the quantities that can

express the relationship between the sensors of an array is the mutual energy. Given two generic signals $x(t)$ and $y(t)$, the mutual energy in the interval (t_0, t_1) is given by the following definition:

$$\xi_{xy} = \int_{t_0}^{t_1} x(t)y(t)dt. \quad (6)$$

The value of the energy likely depends on the affinity between the gas species present and the sensor active layer. Hereafter, we call energy vector (EV) the following quantity:

$$EV = \left| \begin{array}{cccccccc} \xi_{1,1} & \xi_{1,2} & \dots & \xi_{1,k} & \xi_{2,1} & \xi_{2,2} & \dots & \xi_{2,k} & \dots & \xi_{k-1,k-1} \\ \dots & \xi_{k,k} & \dots \end{array} \right|, \quad (7)$$

where k is the number of sensors in the array, and the generic vector element ξ_{xy} is defined by (7). This method



FIGURE 3: Four-element micro-hotplate array mounted on a standard TO-8 support.

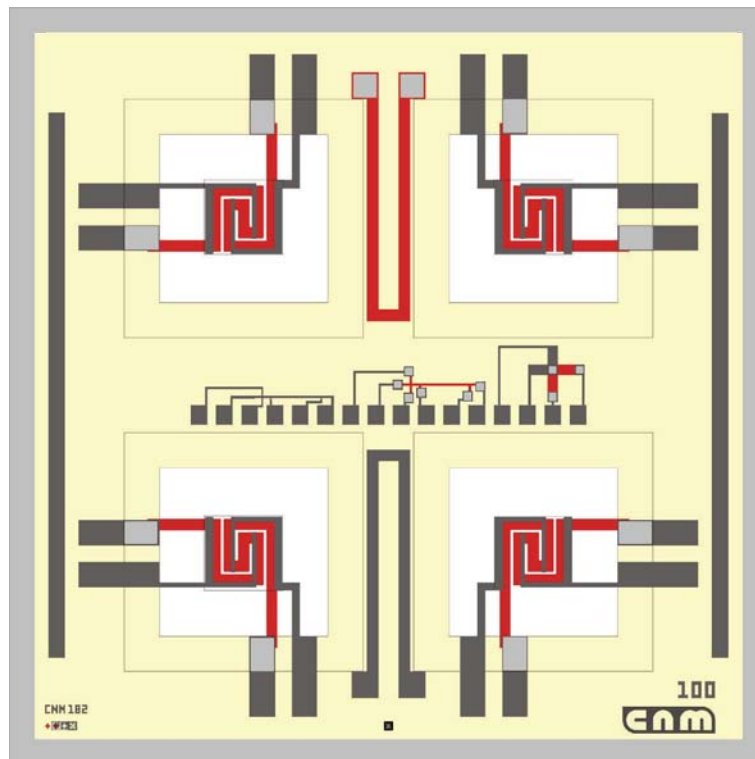


FIGURE 4: Chip layout where heating meanders and interdigitated electrodes can be identified.

was originally proposed by Martinelli [34] and later more extensively applied to gas sensors arrays by Vergara et al. [35].

3. Experimental

3.1. Sensor Fabrication. Sensing layers were deposited over an integrated four microhotplates fabricated using microsystems technology. Basically, each sensor was formed by a gas-sensitive layer, interdigitated electrodes, insulating layers and a poly-silicon heater, all stacked on a $0.2 \mu\text{m}$ thick Si_3N_4 membrane grown by low-pressure chemical vapor deposition (LPCVD). The micro hotplate was characterized by a temperature coefficient of resistivity (TCR) equal to 6.79×10^{-4} . Heaters resistance was also used to measure the actual temperature of the sensor membranes. The power

consumption was about 80 mW when working at 480°C and the thermal response of the coated membranes was measured to be near 20 milliseconds (thermal response was estimated to be about 10 milliseconds in bare devices). The technological fabrication steps of the substrates are reported elsewhere [36, 37]. Finally, the 4-element microhotplate array was packaged on a standard TO-8 package (see Figures 3 and 4). Each chip had 4 membranes, that can be functionalized with proper sensing layers, the size of which was $450 \times 450 \mu\text{m}^2$ and the electrode area was $50 \times 50 \mu\text{m}^2$.

The sensor array was formed by four thick-film metal oxide layers. The following materials were used: 1% Pt-doped and 1% Pd-doped tin oxide (Sensors A and B) and 1% Pt-doped and 1% Pd-doped tungsten oxide (Sensors C and D). These were deposited using a drop coating technique. A paste

was prepared dispersing the active material (SnO_2 or WO_3 nanopowders + 1% Pd or Pt) in glycerol. This process was repeated four times in order to obtain four different layers on the different membranes that integrated a micro-sensor array. The as-deposited films were dried in an oven at 180°C for 2 hours. Subsequently; they were annealed in situ at 480°C for 2 hours. The purpose of annealing was to ensure a good adherence of the active material to the sensor substrates and to burn out the organic vehicle (i.e., glycerol) used in the paste. The selection of these materials was based on previous experience for an analogous gas analysis application [38].

3.2. Experimental-Setup. An array composed of seven micro-hotplate gas-sensors was placed in a 20 mL volume air-tight test chamber to measure vapors of acetaldehyde, ethylene, ethanol and ammonia. This chamber was connected to a continuous flow system that allowed us to obtain, with high reproducibility, different concentrations of pollutant gases diluted in dry air. Mass flow controllers provided the dilution of test gases (at the desired concentrations) in dry air. The total gas flow was set to 200 mL/min and kept constant. The moisture level was kept to 10% of relative humidity (measured at $30^\circ\text{C} \pm 1^\circ\text{C}$) during all the experiments.

The signals of the micro-gas sensor array were measured when the operating temperature of sensors was modulated using an optimized multisinusoidal signal. The multisinusoidal signal was generated using a written-in-house MATLAB code. A set of six modulating frequencies (optimal frequencies selected in a systematic way) was employed to synthesize the temperature-modulating multisinusoidal signal. For the sake of simplicity, the same multisinusoidal signal was applied to the heating element of every sensor within the array. The frequencies composing this signal were 12.8 mHz, 25.6 mHz, 38.5 mHz, 92.9 mHz, 339.7 mHz and 682.7 mHz. The first three frequencies are known to be more important for gas identification, while the last three frequencies are helpful both for identifying and quantifying the gases considered [39]. The range of modulating frequencies is far below the cut-off frequency of the metal oxide coated membranes, which is the inverse of their thermal response (i.e., $(1/20)10^{-3}\text{s}^{-1} = 50\text{ Hz}$) [22].

3.3. Databases. The following compounds were tested: acetaldehyde (50 ppm), ethylene (50 ppm), ethanol (25 ppm), and ammonia (50 ppm). Five sessions of measurements were performed. Each session consisted in 12 replicas of each exposure, resulting in a total of 240 measures; samples sequence, in each session, was randomized. Among the measurement sessions, sensors were powered off. Each measurement took 312 seconds corresponding to the time of application of the multisinusoidal temperature modulation. The whole experiment was performed in four months. During the entire measurement process, before and after each measurement, both sensors and their heating elements were not powered. Finally, the sensors were powered when the analyte was already into the sensors cell.

The sampling rate of the sensor signals was set at 100 samples per second, which was far higher than the frequency

range applied to the temperature modulating signal. The peak to peak amplitude of the multisinusoidal current signal applied to the heater was equal to 2 mA. It corresponds to a sensor operating temperature range between 220°C and 450°C . Figure 5 shows a typical transient response from a Pd-doped SnO_2 gas sensor in the presence of 50 ppm of ammonia when the measurement time was set to 312 s.

3.4. Data Analysis. From the recorded signals the previously defined features called dynamic moments and energy vectors were calculated. For sake of comparison the following standard quantities were also calculated and considered in the analysis:

Steady state feature extraction $\Delta R/R_0$, where the ΔR is the shift of the resistance between the instant value of the measure and the initial baseline (R_0) according to this formula:

$$\frac{\Delta R(t_i)}{R_0} = \frac{\overline{R(t_i)} - R_0}{R_0} \quad (8)$$

$$\overline{R(t_i)} = \frac{1}{5} \sum_{j=1}^5 R(t_{i-j})$$

with $t_i = 0, 1, 2, 3, \dots$

- (i) The integral of the sensor signal $\text{INT}(x(t_i))_k = \int_{t_i}^{t_i+k} x(t) dt$ with k values considered in the data analysis are 1, 2, 3 and 5 ($t_i = 0, 1, 2, 3, \dots$).
- (ii) The Fast Fourier Transform (FFT) coefficients of the sensor signal calculated on the entire temperature modulation applied to the sensor [40];

In order to reduce the measurement time all the features, except FFT, have been calculated in the first 20 seconds of each measurement.

Partial Least Square Discriminant Analysis (PLS-DA) has been utilized as classifier to compare the performance of features. For validation purposes, the entire dataset was split in training and testing sub-dataset (144 and 96 measurements, resp.). The number of latent variables used for PLS-DA models [41] was optimized minimizing the generalization errors applying the Leave-One-Out Cross-validation (LOO-CV).

4. Results and Discussion

Collected data was analyzed in order to study the performance of the defined features in a shorter time with respect to the whole time during which the temperature modulations was applied. To this scope, only the first twenty seconds of the sensors response were considered. Since FFT requires the entire modulation period to be efficiently calculated it was not included in this analysis. Features were calculated every second in the first 20 s considering sensor signal lengths of 1 s, 2 s, 3 s, and 5 s.

The classification rates are summarized in Figure 6. The results obtained in validation and calculated considering a signal portion of 1 s are shown. All the features shown in

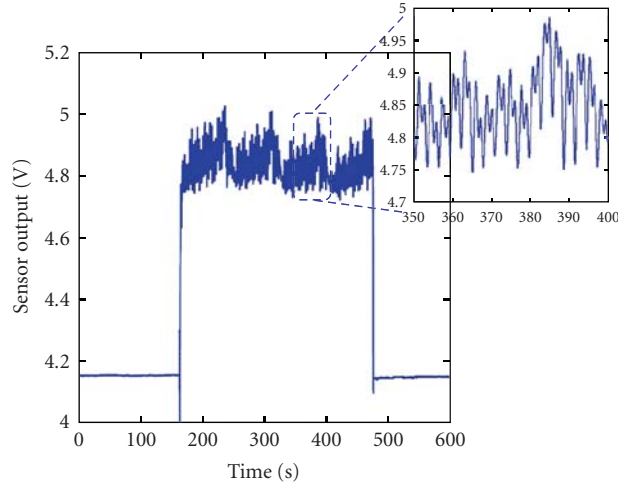


FIGURE 5: Typical time behavior of a gas sensor signal during the measurement phase.

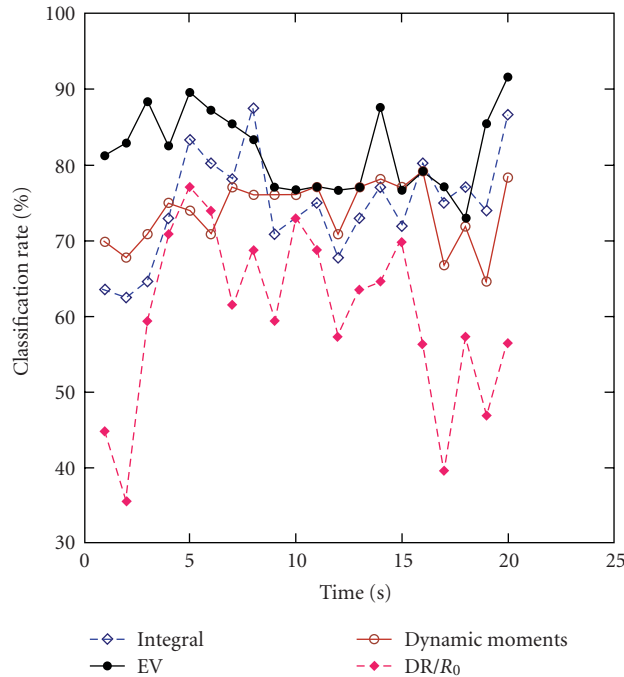


FIGURE 6: Classification rates in the validation phase using four features calculated with signals in the first twenty seconds of the temperature modulation. All features were calculated in a time window of 1 s.

Figure 6 achieved more than 93% of correct classification in training. Among these features, EV achieved the highest classification rate equal to 91%. Furthermore, EV provides discrimination rate higher than 80% in the first second of measurement the classification rate reaches 90% after 5 s. Common features, such as $\Delta R/R_0$, give the worst performance in almost all the twenty seconds. Finally, it is important to note that the classification rates of EV and DMs are quite constant over the entire measurement time. EV results are even promising for real applications, in particular considering that a short measurement time results in reduced

sensor power consumption. It is important to remark that the application of dynamic feature extraction contributes to a reduction of the measurement time as it was observed since several years ago applying a multiexponential fit to the signal of SnO₂ based gas sensors [42].

The performance of features such as EV, Integral and DMs are clearly dependent on the signal behavior and their results could change considering different time windows. This effect is shown in Figure 7 where a summary of the classification rate of the above features considering a time window of 2 s is shown using a box-whisker plot.

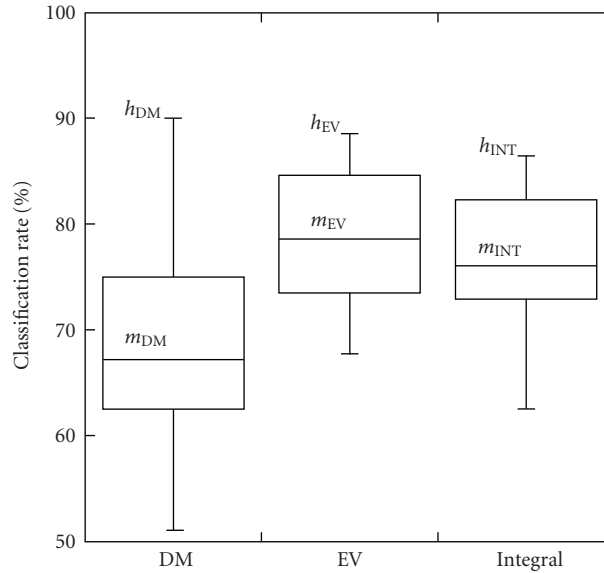


FIGURE 7: Box-plots of the classification rates in validation of Integral, Dynamic Moments and Energy Vector. Each features was calculated in a time window of 2 seconds.

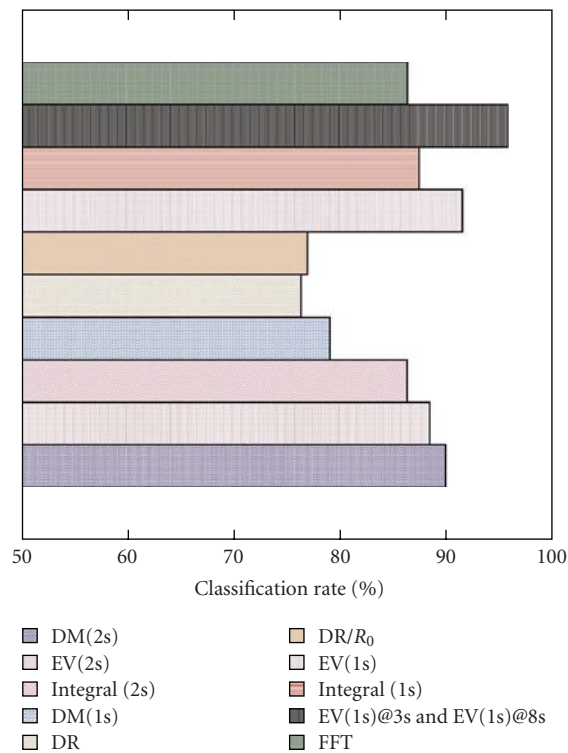


FIGURE 8: Comparison of the best classification rates in validation obtained by each considered feature.

DMs' have the highest classification rate (h_{DM} , about 90%), but this occurs only in a particular situation determined by a particular matching of the signal with the requirements of DM. The box-plot for these descriptors is characterized by a low mean value (m_{DM}) with respect to the h_{DM} confirming a large variability in the first 20 s. A different behavior is observed for EV, where the distribution of the

classification rate is less dispersed than that of DMs. Finally, the integral shows the same order of variability of the EV but, generally, a lower classification rate. A supplementary investigation has been done considering the performance of the features calculated using 3 s and 5 s of the sensors signal portion. In this case, the classification rate was lower than the previous cases.

A further improvement was obtained considering more EVs calculated at different times but using for each calculus a time lengths of 1 s. EVs were calculated at 3 s and 8 s. In this case the classification rate of validation reached 96% and almost 100% in training. In Figure 8 a summary of the best performance obtained in validation for each feature is shown.

The best result is obtained using a combination of two different EVs. This means that EVs did not provided totally overlapped information. These results are better appreciated considering that FFT, calculated with the whole experiment time of 312 s, provided the 86% of correct classifications.

Concerning the performance of DMs, results show that it is possible to increase the classification rate but only in a precise interval of the signal evolution and combining different DMs. This last detail reinforces the efficiency of the recognition power of EV that was almost independent from the temperature modulation applied and, on the other hand, the difficulties to determine an optimized configuration for DMs features.

EV promising results are fundamentally due to the combination in these features of the relations between couples of sensor signals putting in evidence the cross-correlation among sensors, and that this quantity is expected to be weakly sensitive to any instability source.

5. Conclusions

The stability of different kinds of features has been investigated utilizing an array of optimized multisinusoidal signal temperature modulated metal oxide gas sensors. For this measurement setup, results have evidenced that the dynamic features achieve better performance with respect to the standard feature extraction such as $\Delta R/R_0$, the integral or the FFT. The DMs have shown a good discrimination but the performances are strongly dependent by the considered portion of the signal evolution. Instead, the EV has shown an almost constant classification rate along the time with respect to the temperature modulation being also able to obtain more than 90% of correct classification rate in the first 5 s. This aspect is of fundamental importance for practical applications since this feature is able to accurately identify and classify different species using few seconds of the signal response independently from the position on the profile of the temperature modulation.

Moreover, further increment in sensing performance is obtained when more Evs, calculated at different time times are taken into account.

Finally conventional sensor arrays using the same type of construction technology have been thoroughly investigated and are widely utilized today in many critical applications. It remains as a standing question, however, how to maximize their performance and simultaneously minimize the time required for it. This is an important question, because sensors composing an array can convey different attributes of the process being monitored, and, when properly conditioned, can complement each other. In this frame, a more complex classification task and the utilization of quality/variety of

chemo-sensing technologies using this feature extraction procedure will require more deep investigations.

References

- [1] S. Zaromb and J. R. Stetter, "Theoretical basis for identification and measurement of air contaminants using an array of sensors having partly overlapping selectivities," *Sensors and Actuators*, vol. 6, no. 4, pp. 225–243, 1984.
- [2] K. D. Schierbaum, U. Weimar, and W. Göpel, "Multicomponent gas analysis: an analytical chemistry approach applied to modified SnO₂ sensors," *Sensors and Actuators B*, vol. 2, no. 1, pp. 71–78, 1990.
- [3] C. Di Natale, A. D'Amico, F. A. M. Davide, G. Faglia, P. Nelli, and G. Sberveglieri, "Performance evaluation of an SnO₂-based sensor array for the quantitative measurement of mixtures of H₂S and NO₂," *Sensors and Actuators B*, vol. 20, no. 2–3, pp. 217–224, 1994.
- [4] X. Wang, S. Yee, and P. Carey, "An integrated array of multiple thin-film metal oxide sensors for quantification of individual components in organic vapor mixtures," *Sensors and Actuators B*, vol. 13, no. 1–3, pp. 458–461, 1993.
- [5] J. W. Gardner, A. Pike, N. F. De Rooij, et al., "Integrated array sensor for detecting organic solvents," *Sensors and Actuators B*, vol. 26, no. 1–3, pp. 135–139, 1995.
- [6] N. Bârsan, R. Ionescu, and A. Vancu, "Calibration curve for SnO₂-based gas sensors," *Sensors and Actuators B*, vol. 19, no. 1–3, pp. 466–469, 1994.
- [7] D. M. Wilson, K. Dunman, T. Roppel, and R. Kalim, "Rank extraction in tin-oxide sensor arrays," *Sensors and Actuators B*, vol. 62, no. 3, pp. 199–210, 2000.
- [8] M. Roth, R. Hartinger, R. Faul, and H.-E. Endres, "Drift reduction of organic coated gas-sensors by temperature modulation," *Sensors and Actuators B*, vol. 36, no. 1–3, pp. 358–362, 1996.
- [9] M. Holmberg and T. Artursson, "Drift compensation, standards, calibration methods," in *Handbook of Machine Olfaction: Electronic Nose Technology*, T. C. Pearce, S. S. Schiffman, H. T. Nagle, and J. W. Gardner, Eds., pp. 325–346, Wiley-VCH, Weinheim, Germany, 2002.
- [10] S. W. Moore, J. W. Gardner, E. L. Hines, W. Göpel, and U. Weimar, "A modified multilayer perceptron model for gas mixture analysis," *Sensors and Actuators B*, vol. 16, no. 1–3, pp. 344–348, 1993.
- [11] M. J. Madou and S. R. Morrison, *Chemical Sensing with Solid-State Devices*, Academic Press, Boston, Mass, USA, 1989.
- [12] S. Nakata, H. Nakamura, and K. Yoshikawa, "New strategy for the development of a gas sensor based on the dynamic characteristics: principle and preliminary experiment," *Sensors and Actuators B*, vol. 8, no. 2, pp. 187–189, 1992.
- [13] R. E. Cavicchi, J. S. Suehle, K. G. Kreider, M. Gaitan, and P. Chaparala, "Fast temperature programmed sensing for micro-hotplate gas sensors," *IEEE Electron Device Letters*, vol. 16, no. 6, pp. 286–288, 1995.
- [14] A. Heilig, N. Bârsan, U. Weimar, M. Schweizer-Berberich, J. W. Gardner, and W. Göpel, "Gas identification by modulating temperatures of SnO₂-based thick film sensors," *Sensors and Actuators B*, vol. 43, no. 1–3, pp. 45–51, 1997.
- [15] R. E. Cavicchi, J. S. Suehle, K. G. Kreider, M. Gaitan, and P. Chaparala, "Optimized temperature-pulse sequences for the enhancement of chemically specific response patterns from micro-hotplate gas sensors," *Sensors and Actuators B*, vol. 33, no. 1–3, pp. 142–146, 1996.

- [16] E. Llobet, R. Ionescu, S. Al-Khalifa, et al., "Multicomponent gas mixture analysis using a single tin oxide sensor and dynamic pattern recognition," *IEEE Sensors Journal*, vol. 1, no. 3, pp. 207–213, 2001.
- [17] E. Llobet, J. Brezmes, R. Ionescu, et al., "Wavelet transform and fuzzy ARTMAP-based pattern recognition for fast gas identification using a micro-hotplate gas sensor," *Sensors and Actuators B*, vol. 83, no. 1–3, pp. 238–244, 2002.
- [18] W. M. Sears, K. Colbow, and F. Consadori, "Algorithms to improve the selectivity of thermally-cycled tin oxide gas sensors," *Sensors and Actuators*, vol. 19, no. 4, pp. 333–349, 1989.
- [19] S. Nakata, S. Akakabe, M. Nakasuji, and K. Yoshikawa, "Gas sensing based on a nonlinear response: discrimination between hydrocarbons and quantification of individual components in a gas mixture," *Analytical Chemistry*, vol. 68, no. 13, pp. 2067–2072, 1996.
- [20] S. Nakata, E. Ozaki, and N. Ojima, "Gas sensing based on the dynamic nonlinear responses of a semiconductor gas sensor: dependence on the range and frequency of a cyclic temperature change," *Analytica Chimica Acta*, vol. 361, no. 1–2, pp. 93–100, 1998.
- [21] R. Aigner, F. Auerbach, P. Huber, R. Müller, and G. Scheller, "Sinusoidal temperature modulation of the Si-Planar-Pellistor," *Sensors and Actuators B*, vol. 18, no. 1–3, pp. 143–147, 1994.
- [22] A. Vergara, E. Llobet, J. Brezmes, et al., "Optimised temperature modulation of metal oxide micro-hotplate gas sensors through multilevel pseudo random sequences," *Sensors and Actuators B*, vol. 111–112, pp. 271–280, 2005.
- [23] A. Vergara, J. L. Ramírez, and E. Llobet, "Reducing power consumption via a discontinuous operation of temperature-modulated micro-hotplate gas sensors: application to the logistics chain of fruit," *Sensors and Actuators B*, vol. 129, no. 1, pp. 311–318, 2008.
- [24] F. A. M. Davide, C. D. Natale, A. D'Amico, et al., "Structure identification of non-linear models for QMB polymer-coated sensors," *Sensors and Actuators B*, vol. 25, no. 1–3, pp. 830–842, 1995.
- [25] G. E. Searle, J. W. Gardner, M. J. Chappell, K. R. Godfrey, and M. J. Chapman, "System identification of electronic nose data from cyanobacteria experiments," *IEEE Sensors Journal*, vol. 2, no. 3, pp. 218–228, 2002.
- [26] D. M. Wilson and S. P. DeWeerth, "Odor discrimination using steady-state and transient characteristics of tin-oxide sensors," *Sensors and Actuators B*, vol. 28, no. 2, pp. 123–128, 1995.
- [27] M. Nakamura, I. Sugimoto, and H. Kuwano, "Application of plasma-polymer-film-coated sensors to gas identification using linear filters," *Sensors and Actuators B*, vol. 33, no. 1–3, pp. 122–127, 1996.
- [28] P. Accettola, M. Balsi, A. D'Amico, C. Di Natale, A. Macagnano, and F. Sortino, "Time-constant extracting filters for fast gas identification in electronic noses," *Electronics Letters*, vol. 38, no. 11, pp. 510–511, 2002.
- [29] J. Samitier, J. M. López-Villegas, S. Marco, et al., "A new method to analyse signal transients in chemical sensors," *Sensors and Actuators B*, vol. 18, no. 1–3, pp. 308–312, 1994.
- [30] F. Takens, "Detecting strange attractors in turbulence," in *Dynamical Systems and Turbulence*, D. Rand and L. S. Young, Eds., vol. 898 of *Lecture Notes in Mathematics*, pp. 366–381, Springer, Berlin, Germany, 1980.
- [31] E. Martinelli, C. Falconi, A. D'Amico, and C. Di Natale, "Feature extraction of chemical sensors in phase space," *Sensors and Actuators B*, vol. 95, no. 1–3, pp. 132–139, 2003.
- [32] A. Fichera, C. Losenno, and A. Pagano, "Clustering of chaotic dynamics of a lean gas-turbine combustor," *Applied Energy*, vol. 69, no. 2, pp. 101–117, 2001.
- [33] A. Vergara, E. Llobet, E. Martinelli, C. Di Natale, A. D'Amico, and X. Correig, "Feature extraction of metal oxide gas sensors using dynamic moments," *Sensors and Actuators B*, vol. 122, no. 1, pp. 219–226, 2007.
- [34] E. Martinelli, *Investigation on alternative approaches to chemical sensors data treatment*, Ph.D. thesis, University of Rome Tor Vergata, Rome, Italy, 2003.
- [35] A. Vergara, E. Martinelli, E. Llobet, F. Giannini, A. D'Amico, and C. Di Natale, "An alternative global feature extraction of temperature modulated micro-hotplate gas sensors array using an energy vector approach," *Sensors and Actuators B*, vol. 124, no. 2, pp. 352–359, 2007.
- [36] I. Gràcia, J. Santander, C. Cané, M. C. Horrillo, I. Sayago, and J. Gutierrez, "Results on the reliability of silicon micromachined structures for semiconductor gas sensors," *Sensors and Actuators B*, vol. 77, no. 1–2, pp. 409–415, 2001.
- [37] M. C. Horrillo, I. Sayago, L. Arés, et al., "Detection of low NO₂ concentrations with low power micromachined tin oxide gas sensors," *Sensors and Actuators B*, vol. 58, no. 1–3, pp. 325–329, 1999.
- [38] P. Ivanov, E. Llobet, A. Vergara, et al., "Towards a micro-system for monitoring ethylene in warehouses," *Sensors and Actuators B*, vol. 111–112, pp. 63–70, 2005.
- [39] A. Vergara, E. Llobet, J. Brezmes, et al., "Quantitative gas mixture analysis using temperature-modulated micro-hotplate gas sensors: selection and validation of the optimal modulating frequencies," *Sensors and Actuators B*, vol. 123, no. 2, pp. 1002–1016, 2007.
- [40] T. Eklöv, P. Mårtensson, and I. Lundström, "Enhanced selectivity of MOSFET gas sensors by systematical analysis of transient parameters," *Analytica Chimica Acta*, vol. 353, no. 2–3, pp. 291–300, 1997.
- [41] M. Barker and W. Rayens, "Partial least squares for discrimination," *Journal of Chemometrics*, vol. 17, no. 3, pp. 166–173, 2003.
- [42] C. Di Natale, S. Marco, F. Davide, and A. D'Amico, "Sensor-array calibration time reduction by dynamic modelling," *Sensors and Actuators B*, vol. 25, no. 1–3, pp. 578–583, 1995.

Review Article

YSZ-Based Oxygen Sensors and the Use of Nanomaterials: A Review from Classical Models to Current Trends

Carlos López-Gándara,^{1,2} Francisco M. Ramos,¹ and Albert Cirera²

¹F&E—Francisco Albero S.A., R&D Advanced Materials, Rafael Barradas 19, 08908 L'Hospitalet de Llobregat, Barcelona, Spain

²MIND/IN2UB, Electronics Department, Universitat de Barcelona, Martí i Franquès 1, 08028 Barcelona, Spain

Correspondence should be addressed to Albert Cirera, acirera@ub.edu

Received 1 January 2009; Revised 1 June 2009; Accepted 23 July 2009

Recommended by Giorgio Sberveglieri

This work reviews physicochemical models on the operation and the response of potentiometric oxygen gas sensors based on ion-conducting electrolytes. The aim for describing the electric response and some properties like response time, ionic conductivity, catalytic activity, or gas selectivity of these devices has led to the development of some models in the last decades. These models have provided information on relations between the response of the sensors, their design and fabrications process, and some morphological properties, like grain size of the electrolyte, diffusion on protective layers, or density of three-phase boundary points in the measuring electrodes. Current trends on improving catalysis, gas selectivity, and activation energy for ion conducting by using nanomaterials are described as well.

Copyright © 2009 Carlos López-Gándara et al. This is an open access article distributed under the Creative Commons Attribution License, which permits unrestricted use, distribution, and reproduction in any medium, provided the original work is properly cited.

1. Introduction

Chemical gas sensors have been widely developed in the last decades for different purposes. Oxygen sensors, which have been the most studied devices in this area, have been appropriate devices for combustion control in automotive applications [1, 2]. Also, most of the different electrochemical gas sensing devices have the same phenomenology and working principles, which are almost identical to the ones of typical oxygen sensors. Therefore, understanding the oxygen sensing mechanisms leads to a vast knowledge on many other similar gas sensing devices.

Oxygen sensing can be achieved by means of different working principles: among others, electrochemical, pumping gauge, or resistive oxygen sensors have been developed in the past. One of the most usual systems is the electrochemical oxygen sensor, based on ceramic ion-conducting electrolytes. Moreover, current trends in the development of these sensors, such as the implementation of nanomaterials to improve sensing characteristics or promoting gas selectivity in nonequilibrated gas mixtures, demand a precise knowledge on which parameters determine the sensors behavior. The complexity of these systems and the difficulty to establish all the processes involved in their normal operation mode has

lead to different physical and physicochemical models across the years.

This work is focused on reviewing models on ion-conducting potentiometric oxygen sensors. Their static and dynamic response is modeled. Some concerns on the electrolyte characteristics are presented, and models of the electrode properties are considered as well. A special emphasis is made on the use of nanomaterials in the electrodes and electrolytes. Selective sensing in these devices thanks to the mixed potential is also commented.

2. Background

2.1. Structure of the Sensor. Potentiometric sensing devices based on ion-conducting ceramics usually present the same basic structure (Figure 1):

Measured gas/Metal/Ion conductor/Metal/Reference gas. (1)

A ceramic ion-conducting electrolyte is covered by two catalytic active metals and is put in contact with two different atmospheres: the measuring one and a reference atmosphere whose composition is known (generally air).

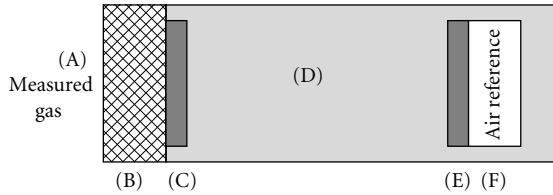


FIGURE 1: Schematic structure of a potentiometric planar oxygen sensor. (A) Measuring atmosphere. (B) Porous protective layer. This layer is optional as it prevents from electrode degradation and sometimes it improves the sensor response due to gas species diffusion. (C) Measuring electrode, catalytically active, generally made of platinum. (D) O_2^- ion-conductive ceramic electrolyte. The most used electrolyte is Y_2O_3 -doped ZrO_2 (YSZ). (E) Reference electrode, in contact with (F) Air reference atmosphere. Some sensors have been occasionally described without a reference atmosphere. Also, a heating element (a dissipative low resistance) is optionally put in front of this sensor structure to achieve stable, high enough temperatures.

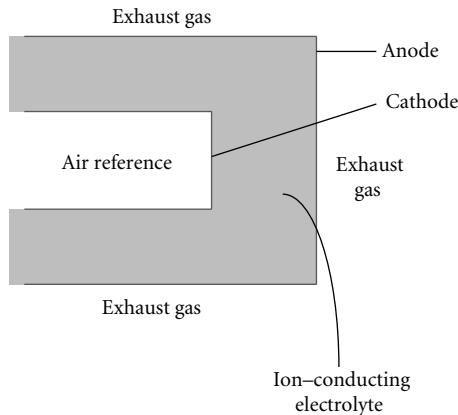


FIGURE 2: Schematic structure of a thimble-type potentiometric oxygen sensor.

In oxygen sensors, this structure consists in a O^{2-} conductor such as Y_2O_3 -doped ZrO_2 (YSZ) with platinum electrodes. Ion-conduction is thermally activated above 600–650 K in this ceramic. Gas sensors can optionally include a dissipative resistance near the sensing cell as a heating element to reach a stable, high temperature. This is usual in gas sensors for automotive applications, such as lambda sensors. Also, a protective layer is sometimes put over the measuring electrode to prevent from corrosion or to avoid changing the catalyst properties as ageing the sensor.

When initially developed, oxygen sensors were thimble-type (Figure 2). Since the 1980s, these sensors were also designed in planar-type (see Figures 1 and 3). Although the planar structure requires lower size, lower power consumption for the heating element, and lower fabrication costs and enables better stability in the measurements, the physical principles governing the behavior of the sensors are essentially the same in both thimble and planar types. As will be shown in Section 2.3, some planar sensors work with no air reference in one of their electrodes.

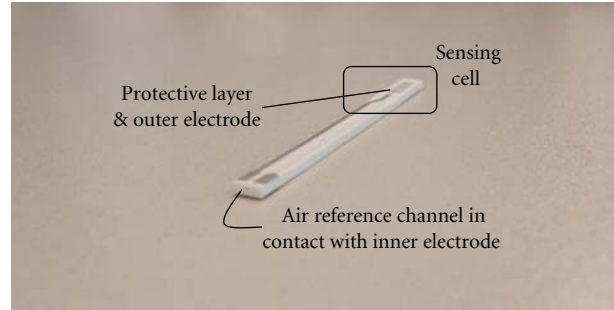


FIGURE 3: Image of a real commercial oxygen potentiometric sensor made of YSZ. The sensing cell consists in a Pt electrode exposed to the unknown gas, the ceramic electrolyte (YSZ), and another Pt electrode exposed to air via the reference channel, which is not in contact with the measured gas in the normal operation mode of the sensor. Also, a protective and diffusive layer is put over the measuring electrode. The layer is visually indistinguishable from the electrode.

The ceramic process for developing planar sensors requires techniques like tape casting, screen printing, piling up substrates, or ceramic sintering. Structural and electrochemical properties of the resulting devices are extremely dependent on the conditions these techniques have been carried out.

2.2. *Response of the Sensor.* When exposed to a certain gas mixture, an open circuit voltage V_{OC} can be measured between the working and reference electrodes:

$$V_{OC} = \frac{k_B T}{4e} \ln \frac{p_{O_2, REF}^*}{p_{O_2}^*}, \quad (2)$$

where k_B is Boltzmann's constant, T is the temperature, e the elementary charge, $p_{O_2, REF}^*$ is the oxygen's partial pressure in the reference gas (which corresponds to a 21% O_2 concentration in air), and $p_{O_2}^*$ is the oxygen's partial pressure in the measuring gas. The term $k_B T/4e$ is frequently referred as $RT/4F$, which is exactly the same. This is the well-known Nernst equation.

According to (2), the electric response of the sensors would be a logarithmic dependence on $p_{O_2}^*$, which does not seem a very sensitive response (see Figure 4 for a simple model of response to O_2 - N_2 mixtures), with output voltages of some mV in front of concentrations of about 1%–10% O_2 in N_2 . It can be seen that, at the typical temperatures of operation, the Nernst open circuit voltage would be near 1 volt if the relation $p_{O_2, REF}^*/p_{O_2}^*$ was very high, that is, when oxygen's partial pressure in the air reference was several orders of magnitude higher than the oxygen's partial pressure in the measured gas (e.g., less than ppm of O_2 in the measured gas). However, due to the presence of metal catalysts such as platinum in the electrodes, oxygen sensors may be sensitive to other gas species. For instance, reducing species such as CO and hydrocarbons, which may be present in the measured gas, can react with oxygen in the catalytically active Pt electrodes. Near the measuring electrodes, as the equilibrium concentration of oxygen may

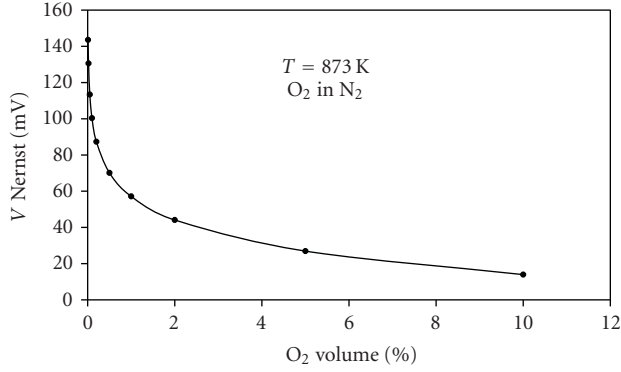


FIGURE 4: Modeled Nernstian response for an imaginary sensor with an air reference (21% O₂) according to (2), for oxygen concentrations in the range from 0.01% to 10% vol.

be extremely depleted after reacting with CO or HCs, the YSZ-based sensors can show high voltages (near 1V) when exposed to nonequilibrated mixtures containing reducing gases and oxygen. Platinum electrodes let O₂ molecules react with the reducing species, causing a deep local decrease of $p_{O_2}^*$ in their adsorption sites. Equation (2) is still valid, but only for the chemically equilibrated gas mixture near the Pt electrodes, and not for the O₂ concentration in the nonequilibrated bulk gas. Therefore, the introduction of nonequilibrated reducing species may result in a voltage drop near 1 volt, and oxygen sensors can subsequently work also as reducing gas sensors. In other words, potentiometric oxygen sensors based on O²⁻ conduction are paradoxically more sensitive to the presence of reducing species than to oxygen. The presented structure (1) works as lambda sensors in automotive applications for combustion control and exhaust gas sensing.

In combustion engines, the parameter λ is a signal on how close is the combustion of a mixture air/fuel to stoichiometric conditions [4]. λ is defined as

$$\lambda = \frac{(\text{volume of air/volume of fuel})(\text{actual})}{(\text{volume of air/volume of fuel})(\text{stoichiometric})}. \quad (3)$$

A stoichiometric mixture corresponds to $\lambda = 1$. Lean mixtures (excess of oxygen, air/fuel ratio higher than the stoichiometric air/fuel ratio) are characterized by $\lambda > 1$, whereas rich mixtures (lack of oxygen, air/fuel ratio lower than the stoichiometric air/fuel ratio) are characterized by $\lambda < 1$.

YSZ-based sensors can work as λ -sensors. Figure 5 shows a typical response for a lambda sensor exposed to several exhaust gases corresponding to different values of the parameter λ . In the lean region ($\lambda > 1$), O₂ concentration reaches 1%–3% in equilibrium. As said before, $V([O_2])$ is in the order of tens of mV with a logarithmic dependence, not very sensitive to $p_{O_2}^*$. In the rich region, the exhaust gas contains significant amounts of carbon monoxide and hydrocarbons, that is, reducing gases. This justifies the high open circuit voltage for $\lambda < 1$. Near $\lambda = 1$, there is an abrupt voltage drop due to the change from rich to lean conditions. In this region, the oxygen concentration in equilibrium changes

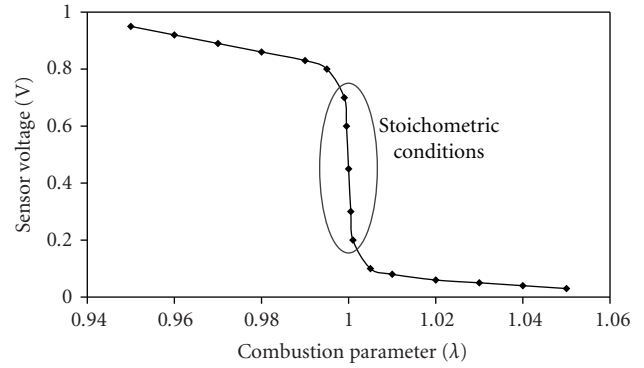


FIGURE 5: Typical response of a potentiometric oxygen sensor in terms of the combustion parameter λ .

in several orders of magnitude. Therefore, in practice, this kind of sensors works with a binary response, rich/lean. The determination of the rich/lean conditions is a useful information in combustion control.

Regarding other characteristics of the electric response, these sensors may offer excellent response times (no more than hundreds of milliseconds) in both oxidizing and reducing atmospheres. The response is dependent on temperature, not only due to thermal activation of ionic conduction and the T dependence in (2) but also because of the temperature influence on catalytic conversion in the electrodes. This causes a local $p_{O_2}^*$ dependence on the temperature near the metal electrodes.

Ceramics offer strong mechanical stability and thermal stress resistance. This helps to keep the behavior of the sensor not so dependent on ageing effects. However, structural phase transitions in some regions of the ionic conductor and a low degradation of the electrodes may appear through a long time of usage (above hundreds of hours of operation). This can affect the response, specially the response time.

2.3. Sensors without Air Reference. In the recent years, some planar oxygen sensors have been designed without air reference. Its structure consists in

$$\begin{array}{c} \text{Measured gas/Electrode 1/Ion conductor/} \\ \text{Electrode 2/Measured gas.} \end{array} \quad (4)$$

As said before, the physical principles governing the behavior of ion-conducting oxygen sensors are the same for both thimble and planar-type sensors, even in the case of no air reference in one of the electrodes. Equation (2) would be perfectly applicable to a sensing element with no air reference, that is, with both electrodes exposed to the same gas. However, as the two electrodes would detect the same oxygen partial pressure p^* , a zero voltage would be obtained:

$$V_{OC} = \frac{k_B T}{4e} \ln \frac{p^*}{p^*} = \frac{k_B T}{4e} \times 0 = 0 \text{ volts.} \quad (5)$$

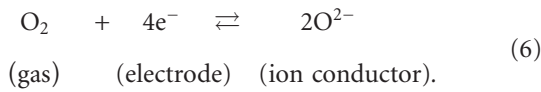
In order to provide nonzero potentiometric responses, commercial and experimental sensors with no air reference

usually incorporate a metal catalyst different from Pt or a metal oxide in one of the electrodes. This introduces different working functions in each electrode and provides an additional output voltage [6–10].

Using different materials in each electrode in sensors with or without air reference is a way to improve selectivity to oxygen or to other molecular species. Nanomaterials are currently a useful tool to improve selectivity, as will be shown in Section 4.2.

3. Steady-State Response of the Potentiometric Sensor

From a qualitative point of view, oxygen molecules in both measuring and reference electrodes are in local equilibrium with the nearest oxygen ions in the electrolyte, due the reaction



When the oxygen concentration in the measuring atmosphere is not the same as in the reference atmosphere, the electrochemical cell of the sensor is pushed to a nonequilibrium state, as two different O^{2-} local concentrations near the two respective electrodes are demanded to reach equilibrium (6) with oxygen molecules in contact to each electrode. The distribution of oxygen ions across the electrolyte is altered to reach equilibrium. As a consequence, a nonzero voltage must be detected between the electrodes due to this nonuniform charge distribution across the ion-conductor.

3.1. Derivation of the Nernst Voltage. The ideal Nernst open circuit voltage can be easily derived from elementary thermodynamics. The Gibbs free energy of a molecule, G , is

$$G = H - TS = H - k_B T \ln \Omega, \quad (7)$$

where H is the enthalpy, S is the entropy, and Ω is the number of states available to the molecule. This number of states must vary linearly with the volume of the system, which is inversely proportional to the oxygen partial pressure, p^* . Therefore, G can be rewritten as

$$G = H - k_B T \ln (\text{constant} \times p^*). \quad (8)$$

If the oxygen partial pressure in the measured and reference gases is different, their respective Gibbs free energies, G_M and G_R , will be also different. Thus, this difference in Gibbs energies between oxygen molecules in the two atmospheres must be

$$\begin{aligned} \Delta G &= G_M - G_R \\ &= \Delta H - k_B T [\ln (\text{constant} \times p_M^*) - \ln (\text{constant} \times p_R^*)] \\ &= \Delta H + k_B T \ln \frac{p_R^*}{p_M^*}, \end{aligned} \quad (9)$$

where p_R^* and p_M^* are the oxygen partial pressures in the reference and measured gases, respectively.

This energy difference must be equal the difference of electric energy ΔU . As four electrons are transferred in reaction (6), $\Delta U = -4e\Delta V$. Thus,

$$\Delta V = V_R - V_M = \frac{k_B T}{4e} \ln \frac{p_R^*}{p_M^*}, \quad (10)$$

where V_R and V_M are the electric potentials of the reference and measuring electrode, respectively.

The use of Gibbs energy in this derivation and other descriptions concerning the sensors behavior has been widely replaced by the use of the electrochemical potential [11, 12], $\tilde{\mu} = \mu + q \cdot V$, where μ is the chemical potential and V is the electric potential. Note that $\tilde{\mu}$ and μ have energy dimensions although they are called potentials by abuse of language.

3.2. Classical Models of the Potentiometric Response. As seen in the previous section, to derive the Nernst voltage it is assumed that there is only ionic conduction in the electrolyte and both electrodes are catalytically active. The resulting Nernst equation (2) shows no dependence on the electrodes and electrolyte characteristics; that is, the theoretical equilibrium voltage is the same whatever the physicochemical properties of the sensor are.

However, experiments have shown that the output voltage is dependent on the properties of the electrodes and the electrolyte, not only in the transient process but also in steady-state conditions. Nonideal behavior is easily observed under reducing atmospheres. Response differences between sensors led some authors to model their respective behavior in terms of their different properties. Also, Nernst equation is derived assuming that thermodynamical equilibrium is reached; that is, no faradic current across the sensor is detected. As a consequence, processes of adsorption, reduction, or desorption of different molecular species in the electrodes are not contemplated in Nernst equation as the sensor would provide then a rate-determined response instead of an equilibrium response.

The first models of the behavior of potentiometric oxygen sensors were developed for automotive applications and focused on the sensors response when exposed to engine air/fuel mixtures. These models took into account the interaction between different molecular species in the electrodes. They are considered to model the behavior of non-Nernstian sensors or mixed potential sensors.

Comparisons between ideal and experimental sensor voltage curves led Fleming [3] to the following considerations.

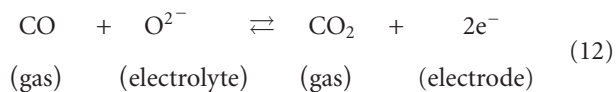
(i) CO is the main reducing gas which may adsorb onto Pt electrodes [13]. Therefore, CO is assumed to be the unique gas apart from O_2 to affect sensor voltage.

(ii) CO may deplete the local oxygen partial pressure near the measuring electrode via the reaction:



The resulting oxygen concentration in equilibrium after reaction (11) is responsible of the ideal equilibrium Nernst voltage in reducing mixtures.

(iii) However, CO may affect the sensor voltage by depleting directly the oxygen ions in the electrolyte near the measuring electrode:



(iv) The open circuit voltage results from the superposition of two Nernst voltages linked with the two previous reactions:

$$V_{\text{out}} = \alpha \times V_{\text{reaction O}_2} + \beta \times V_{\text{reaction CO}}. \quad (13)$$

(v) The equilibrium voltages $V_{\text{reaction O}_2}$ and $V_{\text{reaction CO}}$ can be calculated in terms of estimated equilibrium constants for reactions (6) and (12), respectively.

(vi) The parameters α and β depend on the fraction of adsorption sites occupied by O_2 and CO species in the platinum electrodes. They can be estimated in terms of heat adsorption for CO and O_2 on Pt and thermodynamical constants.

Thus, the output voltage in front of the engine air/fuel ratio is considered as a function of four parameters: the equilibrium constants for two chemical reactions and the fraction of CO and O_2 adsorbed molecules in platinum. Additionally, this model contemplated the possibility of different electron electrochemical potentials between the two electrodes. The steady-state high voltage in nonequilibrated reducing mixtures is explained with this ancient model even in actual planar Pt/YSZ/Pt potentiometric sensors. Fleming also provided a first model to understand why the step voltage from high to low values was not always so abrupt and did not appear at a same gas composition in all sensors [3].

Fleming's model was later improved by Anderson and Graves [14] to study the characteristics of the commented voltage step for a certain gas composition. They took into account the adsorption fraction for O_2 , CO, and also CO_2 and considered the existence of a gaseous boundary layer between the bulk gas region and the electrode/catalyst surface. They used the same equations as in Fleming's model for the steady-state adsorbed species but additionally assumed a transient mass transfer of O_2 , CO, and CO_2 between the bulk gas and the boundary layer and certain transient adsorption/desorption rates in the electrode. By solving numerically the system, steady-state oxygen concentrations in the electrode were found.

Anderson focused on calculations for estimating the sensor voltage when exposed to different O_2/CO mixtures. He took into account the effect of different surface reaction rate constants in the electrodes and found different theoretical voltage curves in terms of the reaction rate constant of the reaction



and its inverse reaction rate constant. In the case of lower reaction constants for oxygen combustion, that is, a higher inverse reaction rate than the reaction rate of (14), voltage curves did not show the step-like behavior shown in Figure 5.

Also, the calculated responses in sensors with identical reaction rate constants but different mass transfer rate constants were compared. It was shown that differences in the dynamic process (changes in mass transfer across the hypothetical boundary gas or in the reaction rate constants) may cause differences in the steady-state response and not only in the transient response. This is not reflected in Nernst equation as it only takes into account the equilibrium oxygen partial pressure in front of the electrodes, without considering the process which leads to this local oxygen partial pressure.

Up to now, the commented models did not take into account the possibility of implementing a protective, diffusive layer schematically similar to the one shown in Figure 1, although this last work contemplated a hypothetical diffusive gas boundary layer. Saji et al. [15] used YSZ sensors with a porous ceramic coating over the measuring electrode. A same sensor was exposed to different oxygen/combustion gas mixtures at different temperatures, and different voltage steps were found again depending on the combustion gas. In experiments with different gas mixtures, the voltage step appeared at a different combustion parameter. In fact, differences in the step voltage characteristics were observed in mixtures as similar as nonequilibrated $\text{H}_2\text{-O}_2\text{-N}_2$ and $\text{D}_2\text{-O}_2\text{-N}_2$. A different combustion voltage step for hydrogen and for deuterium suggested an influence of the molecular mass in the response.

These results and the observed differences in temperature led Saji to develop a more complete model of the sensors steady-state response. According to this model, the sensors response depends on three temperature-activated phenomena:

- (i) spontaneous equilibration of the initially nonequilibrated gas mixture,
- (ii) oxygen reactions in an electrode-electrolyte contact following (6),
- (iii) carbon monoxide reactions following (12).

At a high enough temperature (over 900 K), step voltages were observed at the stoichiometric oxygen/combustion gas mixtures. This measurements, along with evidences suggesting that gas phase reactions occur spontaneously in gas mixtures containing oxygen and combustible gas at high temperatures, with no need of a Pt catalyst, made Saji assume that the gas mixture was equilibrated in the measuring electrode and the voltage was in accordance with the predicted ideal Nernst voltage. In a middle temperature region (650–800 K), there was still no spontaneous reaction and the gas mixture entered the porous coating without chemical equilibration. As mass transport across a porous layer is governed by diffusion and each molecule has a different diffusion coefficient, steady-state concentrations across the ceramic coating were different for the different gas species (Figure 6). Assuming that the pore diameter is much less than the mean free path of the gas molecules (Knudsen diffusion), Saji found the following equation to calculate the

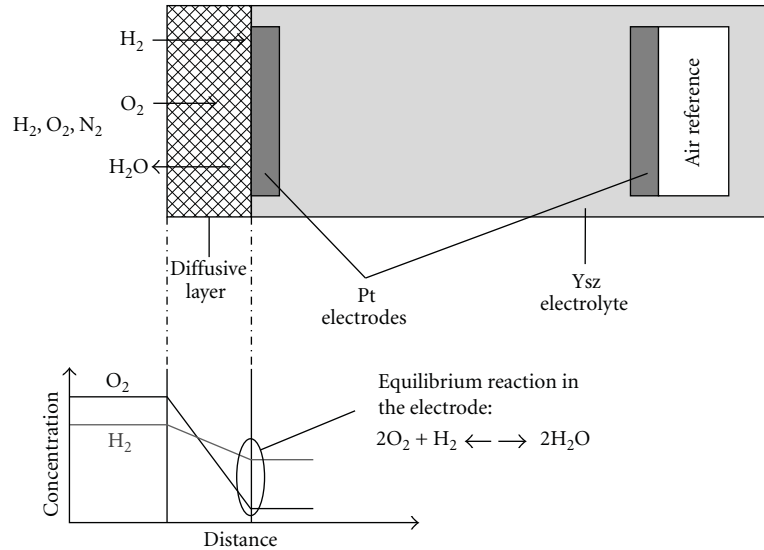


FIGURE 6: Representation of the diffusion of O_2 and H_2 across a porous layer covering one of the electrodes. According to Saji et al. [15], diffusion of the molecular species may lead to important differences between the bulk gas concentration and the measured concentration in the electrodes. This would justify differences in the step voltage in some gas mixtures.

gas mixture composition where the step voltage appeared:

$$\frac{\frac{\text{oxygen concentration}}{\text{combustion gas concentration}} \text{ (voltage step)}}{\frac{\text{oxygen concentration}}{\text{combustion gas concentration}} \text{ (stoichiometric)}} \quad (15)$$

$$= \sqrt{\frac{M_{O_2}}{M_{\text{combustible gas}}}},$$

where M_x is the molecular mass of the component x . This model was in agreement with experimental data and explained why the voltage step for deuterium was different from the one for molecular hydrogen. Last, in a low-temperature region (below 650 K but at a temperature high enough to provide ionic conduction), reactions (6) and (12) and Fleming's original considerations were applicable.

Several experimental measurements with potentiometric sensors [16–20] led Brailsford et al. to try to develop similar models for both transient and equilibrium sensor responses when exposed to mixtures containing O_2 , CO, CO_2 , H_2 , and H_2O [21, 22]. Apart from considering different adsorption rates and the same possible reactions in the measuring electrode as in previous models, an additional reaction of adsorbed CO with adsorbed H_2O (a “water-gas” reaction) in the electrode was modeled. By comparing the Brailsford model to a hypothetical water-CO reaction [20], the voltage curve was not well fitted, at least at medium temperatures (631 K). At high temperatures (837 K), no big differences were observed between models with and without this reaction. Works of Brailsford et al. were useful for understanding the effects of various physicochemical processes involved in the operation of electrochemical sensors. However, their modeled CO- H_2O interaction appeared to be not necessary.

Fleming's model [3] and the later modifications incorporated competing reactions at the adsorption sites (i.e., the three-phase boundary sites) in the electrodes, for instance, one for oxygen (6) and another one for carbon monoxide (12). What Fleming characterized with adsorption and desorption constants for different gas species was later extensively considered as mixed potential of the potentiometric sensors.

3.3. Three-Phase Boundary. Up to now, a few electrodes characteristics have been considered: the main classical models of the sensor response focused on the interacting gases and the rates of reaction, adsorption, and desorption for each molecule species in the electrodes. As seen, this provided useful information to understand the sensors performance and good agreements between experimental and calculated data was generally obtained. However, the sensor was considered as a black box, with almost no influence on the response in terms of the electrode morphology or the electrolyte characteristics.

Morphological and catalytic properties of the electrodes are important to obtain an appropriate response. Moreover, models of the behavior of electrodes are important for current trends on implementation of nanomaterials as catalysts in this kind of sensors and in solid oxide fuel cells as well.

The triple phase boundary (TPB) is an important concept for studying processes in the electrodes. TPB sites are the regions where the measured atmosphere, the metal catalyst, and the electrolyte coexist. Reactions in electrochemical systems involving ion-conduction can only appear in TPB sites or nearby zones if the sensing electrode is metallic. For instance, reaction (6) is assumed to occur only where O_2 molecules can reach a Pt/YSZ contact zone. Otherwise it is

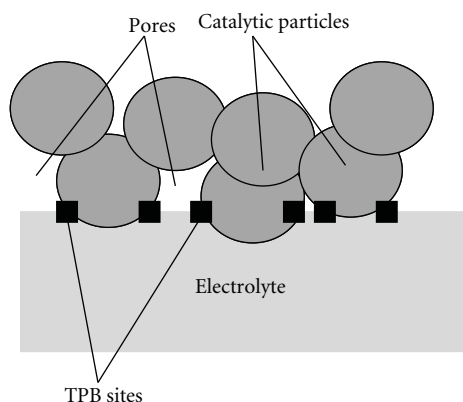


FIGURE 7: Scheme of the three-phase boundary sites in an interface electrode—electrolyte. Porous electrodes help increasing the density of three-phase boundary sites.

not possible to exchange electrons from the metal and change the amount of oxygen ions in the electrolyte.

Several works have confirmed the dependency of the electrode performance on the length of three-phase boundary sites [23–25], and different electrode configurations lead to different TPB lengths. We can define, regarding their TPB density, three types of suitable electrodes for potentiometric oxygen sensors: nonporous metallic electrodes, porous metallic electrodes, and cermet electrodes. Works on the three-phase boundary sites have been mainly focused on solid oxide fuel cells, but their results are perfectly applicable to electrochemical sensors.

Reactions in a nonporous pure metallic electrode are relatively difficult as the TPB sites are located exclusively in the contour of the electrode in contact with the electrolyte. Although gas molecules may adsorb in the entire surface of the electrode, most of them cannot react providing or extracting oxygen ions from the electrolyte as the contacts gas/catalyst/electrolyte are only in the contour of the electrode. This low density of TPB sites causes a current constriction as a high fraction of the contact area between metal and YSZ is inactive [26, 27]. Subsequently, the response time of sensors with this structure is slow. Hertz and Tuller [28] developed a model on the current constriction in TPB. Also, the response of the sensors may worsen due to ageing, as slight contaminations of the electrodes may affect a large fraction of three-phase boundary sites, given that most of them are allocated in a same region.

An improved configuration for electrodes in oxygen sensors is a porous metal electrode. Most of the commercial oxygen sensors incorporate porous Pt electrodes, as gas molecules can diffuse across the pores and the density of TPB sites increases [25, 29, 30]. Figure 7 shows a scheme of the structure of the interface porous Pt electrode/YSZ electrolyte. SEM images of the surface of porous Pt electrodes can be seen, for instance, in [29].

An electrode made of a ceramic/metal composite is known as a cermet electrode. These electrodes provide even more TPB sites. Using a porous Pt/YSZ composite instead of a metal phase over the YSZ electrolyte multiplies the

number of interfaces between the catalyst and the electrolyte [31]. TPB length is increased and problems with current constriction are avoided. Some authors have worked on the dynamics of TPB sites in these composites, as thermal and electrochemical history of the system may affect the TPB length [32–35]: for instance, high polarizations may modify the morphology of the electrode or block some fractions of the interfaces between Pt/YSZ with oxygen molecules or ions.

As an alternative to Pt/YSZ cermet electrodes, other cermet electrodes consisting in metal oxides mixed with a metal catalyst have been proposed in order to modify the mixed potential of the sensors and/or improve gas selectivity due to the promotion of one of the competing chemical reactions in the catalysts. For instance, selectivity to O_2 has been reported with NiO [36], CdO and SnO_2 for CO selectivity [37], ZnO for H_2 selectivity [38], $CdMn_2O_4$, $CdCr_2O_4$, and WO_3 , among others, for NO_x selectivity [39–42]. Nanomaterials have been applied to modify the mixed potentials and enhance gas selectivity, as it will be shown in the next section.

An interesting model of the transient and steady-state response of the potentiometric sensor including the classical views of the first models, mixed potentials, reaction rates, possible diffusion of molecular species, and TPB dynamics was developed by Zhuiykov [43, 44].

Zhuiykov considered a planar non-Nernstian potentiometric YSZ sensor with dissimilar electrodes: one made of porous platinum and the other one made of porous NiO deposited on a porous Pt film. The fact that Pt was porous improved the TPB sites density. No air reference was designed; that is, the two electrodes were exposed to the same atmosphere. The model studied the response to a $NO_2/O_2/H_2O$ mixture. The following phenomena were considered:

- (i) multicomponent diffusion of gaseous species through the porous electrodes; ordinary bulk diffusion as well as Knudsen and surface diffusion was modeled,
- (ii) adsorption, desorption, and partial dissociation of nitrogen dioxide within the solid oxide electrode,
- (iii) dissociation of water in the three-phase boundary sites,
- (iv) cathodic reaction of NO_2 in the three-phase boundary and in the electrode bulk of the solid oxide electrode,
- (v) electrochemical reaction of oxygen, following equation (6).

All the electrochemical reactions were assumed to occur at different kinetic rates in each electrode as their composition was different. This model offered a more detailed description of the main phenomena in this kind of potentiometric sensors. Also, some electrochemical stages were assumed to occur only in the TPB sites whereas some other phenomena were considered in the bulk electrodes and in the TPB sites as well. The competition of different rates for each electrochemical stage, together with time-dependent equations

for multicomponent gas diffusion phenomena, led Zhuiykov to get a transient and steady-state response of the sensor which was experimentally verified. Some phenomenological parameters which had been introduced in previous models [45, 46] were eliminated with this more detailed description. Moreover, this model could be extended to other non-Nernstian planar gas sensors with dissimilar electrodes.

Muroto et al. studied the dynamic behavior of the electrodes, with special emphasis on phenomena of activation and degradation of Pt/YSZ three-phase boundary sites and, generally, Pt/YSZ interfaces [47]. They proposed a scheme of the interface electrode-electrolyte and a representation of all the possible electrochemical driven changes (i.e., polarizing the sensor) and temperature effects. In particular, they found that low polarizations between the two sensor electrodes under certain controlled atmospheres might partially scratch some regions of the electrode, promoting electromigration of platinum and leading to the possible creation of new three-phase boundary sites. Thus, imposing an external polarization to the sensing devices could increase the density of TPB sites and subsequently improve the catalysis as well as lower the electrode impedance and response times. However, a too high polarization could damage the electrode due to cracking the platinum or promoting the formation of air bubbles between platinum and YSZ, lowering the effective density of TPB sites.

Ramamoorthy et al. [48] compared the response time of sensors with different metallic and metal oxide electrodes and tried to correlate to the charge transfer processes in the three-phase boundary sites. Although the total time of response was not only determined by the characteristic time of processes in electrodes, it was found that the fact that charge transfer reactions occur only in TPB sites in Pt electrodes leads to a current constriction phenomenon which is not observed in some complex metal oxide electrodes such as lanthanum strontium iron cobalt oxide (LSFCO). They made use of impedance spectroscopy in this work. Applications of this technique will be commented in next section.

3.4. Equivalent Electric Models and the Use of Impedance Spectroscopy. Characteristics and behavior of electrochemical sensors in terms of their equivalent electric models. In this field, impedance spectroscopy is a powerful tool to characterize electrically the oxygen sensors and fit their modeled electrical components.

Impedance spectroscopy is performed by means of a potentiostat who applies an external AC voltage to the sensor electrodes and detects a current in a wide range of frequencies. The corresponding impedance is calculated for each frequency. Imaginary versus real impedance is represented in terms of frequency. An alternative way to represent impedance spectra is using Bode diagrams.

In a first approximation, a typical electrochemical gas sensor can be electrically modeled as shown in Figure 8. As electrodes can exchange electrical charge following equation (6) and charges can be stored in the electrode structure or in the interface electrode-electrolyte [49], the two electrodes of the sensor are assumed to behave like a resistor in parallel to a capacitor. Ceramic electrolytes are usually

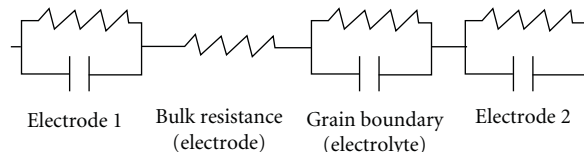


FIGURE 8: Minimum equivalent electric circuit of an oxygen sensor to fit to impedance spectra.

considered as a resistor in series with a parallel resistor-capacitor. As indicated in Figure 8, this represents the bulk (or intragranular) contributions and grain boundary (or intergranular) contributions.

More complex electrical models can be tried depending on the desired level of fitting accuracy or the needs of separating contributions from bulk, grain boundary, second phase, surface layer contributions, and so forth. For instance, a very low capacitor can be modeled in parallel to the resistance of the intragranular contributions, as bulk crystals are not perfect [50]. Also, capacitances in the electrodes and in the electrolyte can be replaced by constant phase elements. [48, 51–53]. Inductance contributions [54] or Warburg diffusion phenomena in electrodes [50, 55–57] can be implemented as well. Considerations on how to carry out impedance spectroscopies in ceramic materials and how to model and treat the measured data can be found at [58–61].

Meng and Shen [62] showed an example of an electrical model of an unconventional sensor with Pt-free electrodes: Ag/C and Ag-W₂/C electrodes. The electrolyte was modeled just with a single resistance as no capacitive effects were seen in the electrolyte in the range of the applied frequencies. Constant phase elements were introduced in the arcs corresponding to electrode contributions. Generally, it may be necessary to introduce constant phase elements in the electrodes instead of capacitors as they fit better impedance data when double layer capacitance effects (i.e., current constriction in the interface electrode-electrolyte) are present. With this model, the impedance spectra of the Ag-W₂/C would not be correctly fitted: it was necessary, in this case, to introduce a Warburg diffusion impedance due to mass transport phenomena in the electrode. Impedance data helped, in this case, to prove a faster kinetic process of oxygen reduction on the Ag-W₂C/C catalyst. Warburg diffusion is a representation of mass transport in the electrode instead of charge transport.

The influence of the electrode characteristics in the sensing response can be tested by impedance spectroscopy. As introduced before, Ramamoorthy et al. [48] compared three different electrodes for YSZ potentiometric oxygen sensors: platinum, lanthanum strontium iron cobalt oxide (LSFCO), and chromium oxide and correlated with the sensors response. It was found that the characteristic time of electrochemical reactions was controlled by resistance in Pt and chromia electrodes and by capacitance in LSFCO electrodes, but this was not the phenomenon who limited the response time of the sensor. These data suggested that the high response time in the sensors was due to surface diffusion of oxygen adsorbates, which was influenced by the electrode microstructure.

Regarding the sensor response, Frade et al. [63] observed that variations in the sensor response after polarizing the electrodes might be correlated by impedance spectroscopy. They also established relations between consequences of polarizing the sensor and the thickness and transport properties of the solid electrolyte.

Separating the different contributions in the electrolyte and the electrode is a key point when extracting information from impedance spectroscopy. First, the impedance of the two electrodes may be overwritten in the impedance spectra. Thus, it is relatively usual to design some test sensors with three electrodes in order to use an additional reference electrode. This helps separating the RC contributions for each electrode [64, 65]. Due to their differences in resistance and capacitance, it is relatively easy to separate electrode arcs from electrolyte arcs [26, 27, 58, 66], but problems arise for detecting bulk and grain boundary contributions in the electrolyte [67, 68]. Separating intragranular and intergranular contributions in the ceramic electrolyte may be useful to observe differences in the sintering process [69], to compare conductivities in YSZ with different yttria contents [70] or to analyze the effect on adding some MgO content to YSZ [68].

Some works have tried to establish general patterns for describing the factors determining the electrolyte conductivity [71]. However, high dispersion in conductivity measurements have been found in different works as a high number of parameters may affect the resistance of the electrolyte, not only the measurement conditions but also fabrication parameters, thermal history of the electrolyte, grain size, and so forth. A large discussion on the role of the grain boundaries in the total conductivity of ion-conducting ceramics was done by Guo and Waser [72]. They focused on models of space charge layers for describing grain-to-grain contacts.

4. Improving Potentiometric Oxygen Sensors: Current Trends on the Use of Nanomaterials

Research in nanomaterials has been carried out extensively in the recent years. The use of nanostructures shows usually similar advantages in different disciplines: miniaturization, material savings, lower energy consumption, and new physical and chemical properties due to scale effects.

Nanotechnology is an interesting research ambit in the field of electrochemical gas sensors. The use of nanomaterials has provided some improvements on the classical oxygen sensors, whose models of behavior have been presented in the previous sections. However, works on nanomaterials for oxygen sensing devices have been essentially for academic purposes and not yet commercially applied, as much research has to be done in the future. Moreover, research focuses on the development of solid oxide fuel cells, although these devices share most of their physicochemical properties with electrochemical sensors.

Göpel [73–75] commented on the possibility of hypothetical electrochemical nanosensors with the structure Pt/YSZ/Pt but appreciated several difficulties in its miniaturization. For instance, relatively large Pt clusters are required to form a spatially coherent net of an electron conducting

contact which allows the oxygen molecules to access the three-phase boundary, as large differences in the surface free energies between platinum and YSZ cause adhesion problems. Göpel suggested also that it would be hard to prepare epitaxial thin films with a structural control in the monolayer range.

More recently, Huang and Choi [76] commented some other problems and future challenges regarding the use of nanomaterials for gas sensing. For instance, mechanisms, such as pore diffusion or reactions of molecular oxygen, adsorbed oxygen or oxygen ions, and parameters like surface-to-volume ratios, have been intensely investigated in gas sensors, but further research is required to take account of these mechanisms coupled with particular nanostructures in the sensors. Selectivity could be improved with a more precise knowledge in this area.

Works with nanomaterials have focused on the improvements of the sensor characteristics. In the context of potentiometric ion-conducting oxygen sensors, we can divide the use of nanomaterials in these devices in three separate groups:

- (i) nanomaterials for lowering the electrode impedance, for instance, increasing the density of TPB sites, avoiding current constriction in the electrode/electrolyte contacts, or lowering the surface free energy between the electrode and the electrolyte,
- (ii) nanomaterials for improving gas selectivity for oxygen or other gas species by enhancing catalysis in the electrodes or by modifying the mixed potential of the electrodes, here, semiconducting oxides have been tried as an alternative to pure metal catalyst electrodes,
- (iii) nanomaterials for designing thin film electrolytes in order to lower the activation energy for ion-conduction and enabling lower operation temperatures.

4.1. Lowering the Electrode Impedance. As seen before, one of the most important elements in electrochemical oxygen sensors is the three-phase boundary. A high number of TPB sites ensures a good response time as it lowers the double layer capacitance. As the use of porous Pt, Pt-YSZ composites or other cermet composites is a good way to improve the TPB density, it seems obvious that particles with lower grain size and higher specific surface help enlarging the number of TPB sites.

Kimura and Goto [77] looked for an alternative to Pt in the electrodes and found that iridium may have similar or higher catalytic activity than Pt. They prepared Ir-YSZ nanocomposite electrodes by metalorganic chemical vapor deposition (MOCVD). The composite consisted in crystalline Ir and amorphous YSZ, with an average Ir particle size of 3 nm. Several composites were prepared with a controlled Ir composition from 3% to 71% vol. It could be seen that the electrical conductivity was up to 1000 times higher than that of Pt electrodes.

Later, the electrochemical performance of IrO₂/YSZ nanocomposite electrodes was investigated by Torres-Huerta et al. [78], with grain sizes between 15 and 30 nm. Although

this work was in the area of fuel cells, the observed properties are applicable to gas sensors. The modeled equivalent circuits after impedance spectra suggested that the polarization resistance was lower than in Pt conventional electrodes and Ir-YSZ electrodes [77], probably due to a higher density of triple phase boundary sites. Furthermore, the activation energy for the interfacial conductivity of the composites was in agreement with the energy of dissociation of oxygen molecules. By comparing to the activation energy for LSM or Pt electrodes [79], the authors suggested that the IrO₂-YSZ cermets might offer an efficient and competitive performance as electrode materials for YSZ electrolytes, although further analysis would be necessary.

An interesting improvement of the electrodes impedance was proposed by Wang et al. [80], also valid for fuel cells and electrochemical gas sensors. Based on quantum ab initio calculations, it was found that both the surface energy of a Pt_{0.7}Ni_{0.3} cluster and the energy change of the Pt-Ni alloy cluster upon ripening on YSZ were lower than pure Pt. Also, changes in microstructure properties after annealing nanoporous Pt and Pt-Ni thin films were compared. No changes were found in Pt-Ni nanoporous thin films, but a dramatic porosity reduction was observed in pure nanoporous platinum. Therefore, a lower electrode impedance, better thermal stability, and lower temperature of operation were expected.

The use of nanocomposites made of Pt mixed with carbon nanotubes has sometimes been suggested [81] to be applied in oxygen sensors. However, they have been implemented just in some hydrocarbon electrochemical sensors [82] or biosensors [83] have been designed with those nanocomposites.

4.2. Promoting Catalysis and Enhancing Gas Selectivity. Nanostructured materials are a useful tool to improve sensitivity and selectivity in potentiometric ion-conducting sensors as well as in sensors with other sensing principles. The use of nanoparticles as catalyst, for instance, may owe larger surface areas and, subsequently, higher catalytic activities than in bulk material catalysts. This should help maximizing the response. However, as said before, it is necessary to know the interactions between the gas being monitored and the nanostructures to get reliable and repetitive results.

In order to improve catalysis as well as electrode impedance in the electrocatalytic reduction of dissolved oxygen, Britto et al. [84] made use of carbon nanotube microelectrodes. Although their interest was improving the behavior of solid oxide fuel cells, results regarding the exchange current densities in the electrode are interesting when compared to graphite paste electrodes. It was found that an electrode made of carbon nanotubes showed an exchange current density of about 6 times the current density in electrodes made of graphite. However, an electrode made of carbon nanotubes with deposited palladium had an exchange current density of 10⁵ times the graphite paste electrode. This important change in the charge transfer together with the fact that reactions between oxygen and

hydrogen are usual in some measurements with oxygen sensors could help promoting oxygen selectivity as well as lowering the electrode impedance.

Later, Collins et al. [85] showed that carbon nanotubes are highly sensitive to the chemical environment in the case of single wall carbon nanotubes, electrical resistance, local density of states by direct exposition to air, different concentrations of dissolved oxygen, or very small amounts of adsorbed gases. The results of this work, therefore, showed that although selectivity and sensitivity to oxygen was excellent and this could have been a tool to improve the performances of oxygen sensors in the electrodes, the use of carbon nanotubes does not seem to be an easy tool to future developments in oxygen sensing with catalytic electrodes, as many properties are extremely dependent of the design process or some extrinsic conditions.

More recently, Cvelbar and Mozetič [86] studied an unconventional improvement on the catalysis by using a Nb₂O₅ nanowire array at the outer surface of an originally developed catalytic oxygen sensor. Thanks to the higher surface areas, a stronger catalysis than in a conventional catalyst was obtained. Also, oxygen atoms generated from dissociation of molecular oxygen were detected at densities of up to ten times lower than in conventional bulk catalysts. The results suggested that nanowire-based sensors could be used to detect small densities of gases (oxygen or other species) in environments where standard catalytic probes fail.

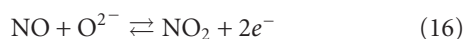
Not many works have focused on improvements in catalysis by means of nanomaterials in the electrodes for potentiometric oxygen sensors based on an ion-conducting electrolyte. However, electrodes of ion-conducting oxygen sensitive devices have been modified with nanostructured materials to promote selectivity to some gases in multicomponent gas mixtures with presence of oxygen. As will be shown, metal oxide nanoparticles have been useful to modify the mixed potential in the electrodes in non-Nernstian planar sensors.

As said before, the competition of reactions such as (6) for oxygen or (12) for carbon monoxide in metal catalysts had been already introduced in the classical models of the sensors response and suggested the concept of mixed potential. Modifying the mixed potential in an electrode can lead to a different sensor output voltage when exposed to certain gas mixtures. In fact, the combination of different electrochemical cells covered by different electrode materials can promote a net selective response to concrete molecular species. Some commercial sensors in automotive applications are based on this possibility.

Devices with some of these new electrodes suggest future development on new commercial selective gas sensors. For instance, Wu et al. [87] proposed the use of a porous CuO-ZnO nanocomposite over a Pt conventional paste. The structure CuO-ZnO/Pt/YSZ/Pt was studied as a selective CO sensing electrode. A high porosity was observed in the structure of the CuO-ZnO nanocomposite electrode. An output voltage of about 8 mV was detected for a 800 ppm CO concentration in air near 800 K. However the response equilibration time of the sensor was significantly slow, in the order of thirty minutes.

Li and Kale [88–91] studied electrodes made of tin-doped indium oxide (ITO) nanoparticles. Sensors with the structure ITO nanoparticles/YSZ/Pt exposed to air mixed with several CO concentrations near 900 K got higher sensitivities for CO and lower potentiometric response times than in previous works. This net response is non-Nernstian and was attributed to the mixed potential of electrodes made of ITO nanoparticles.

In an opposite direction, Plashnitsa et al. [92] studied a mixed potential sensor with almost no selectivity to carbon monoxide and other species such as hydrocarbons. By using gold nanoparticles coatings as sensing electrodes, sensitivity of 400 ppm CO in air was lowered to less than 10 mV at 870 K, whereas sensitivity to 400 ppm NO₂ was promoted to 60 mV. The obtained high sensitivity and high selectivity to NO₂ were attributed to the higher catalytic activity of the reaction



in the Au/YSZ interface than the catalytic activity of reaction (12), causing a modification of the respective mixed potentials. This work showed big differences between the behavior of electrodes with gold nanoparticles and gold bulk electrodes, as bulk Au electrodes had been described for mixed potential sensors for detection of CO [93–95] and hydrocarbons [92, 96, 97].

More nanocrystalline oxide solid electrolytes for mixed potential NO_x sensors can be found: there have been proposed structures based on nanostructured CuO-doped NiO electrodes [98], nano-structured perovskites such as LaFeO₃ [99], a more sensitive and stable version with LaFeO₃-doped Pt [100], or thin films of NiO electrodes [101, 102].

4.3. Nanomaterials in Electrolytes. High temperature of operation (around 850 K) in classical potentiometric ion-conducting sensors is one of their main limitations. The aim of getting higher conductivities and lowering this temperature has stimulated the research on alternatives to traditional YSZ bulk ceramics. Although increasing the Y₂O₃ doping in ZrO₂ can seem an easy way to enhance the ionic conductivity (due to the larger number of oxygen vacancies) of the ceramics, structural stability properties are affected. The main advantage of using bulk YSZ in oxygen sensors is that powders have high purity and uniform particle sizes, and this helps predicting the sensor properties as the grain size after sintering can be estimated. However, nanomaterials have provided some interesting improvements.

Several studies on synthesis of YSZ nanoparticles have been carried out, some of them with a relatively high dispersion in grain sizes [103–105]. By comparing conductivities and microstructure of single crystal, microcrystalline, and nanocrystalline YSZ, it was confirmed that the grain boundary resistance is the main contribution to the total resistance of nanocrystalline YSZ and other ceramic ion-conductors [106–109]. Kosacki et al. [110] studied and modeled the total electrical conductivity in nanocrystalline YSZ thin films with controlled grain sizes in the range of

1–400 nm and detected an enhancement of the activation energy for the ionic conductivity (0.93 eV in nanocrystalline YSZ in front of 1.23 eV in microcrystalline YSZ). They were also found a slight increase of undesired electronic conductivity at very low oxygen partial pressures (below 10⁻²⁰ atm).

Another experiment with YSZ thin films was prepared [111] by epitaxially growing nanocrystalline 10 mol% Y₂O₃-doped ZrO₂ over a MgO substrate, producing YSZ thin films of different thickness. Differences in conductivity and activation energies were studied. Equivalent circuits fitted to measurements from impedance spectroscopy, along with models of conductivity in two-phase materials [112], were applied to separate the YSZ/MgO surface/interface and YSZ lattice conductivities. As a result, and according to the applied two-phase materials model, a nanoscale effect with exceptionally high ionic conductivity below 60 nm thickness was interpreted, with ionic conductivities 1000 times higher than in bulk YSZ and an activation energy of 0.45 eV.

García-Sánchez et al. [113] worked on nanostructured YSZ thin films for solid oxide fuel cells, although the results are perfectly extensible to electrochemical sensors. An activation energy of 0.79 eV was achieved for ion-conduction through the grain boundaries, increasing the total conductivity of the material up to 0.033 S/cm at 923 K. Nanostructured YSZ was obtained via ultrasonic spray pyrolysis, and relevant changes in grain sizes were observed in terms of the deposition time and temperature.

Zhu and Fan [114] focused on the consequences of ceramic sintering temperature when using YSZ nanoparticles. It was found that 8 mol% YSZ nanopowders with an average grain size of 9 nm could be fully densified after 1300 K sintering for 24 hours, a temperature significantly lower than the usual 1650–1750 K for YSZ micrometric powder.

Nanostructured ion-conducting solid electrolytes have been claimed for possible oxygen sensing applications. Yadav and Hu [115] observed an order of magnitude enhancement in oxygen ion-conductivity in a Ag/YSZ/Ag cell exposed to two separate atmospheres containing oxygen and nitrogen. Conductivities of microstructured and nanostructured YSZ were extracted from impedance spectra and compared. Other patents have claimed similar nanostructured electrolytes for sensing devices [116–118], among other applications such as fuel cells or oxygen pumps.

Although it is not strictly a YSZ thin film for electrochemical gas sensors, it is interesting to comment the works of Dimitrov and Dushkin [119] on YSZ thin films with Pt nanoparticles for O₂ resistive detection as an alternative method for oxygen sensing with nanomaterials. Thin films of pure YSZ and films of YSZ with Pt nanoparticles were prepared by spray pyrolysis and by dip coating of a substrate as well. The electric resistance was measured in the samples when exposed to several oxygen and nitrogen cycles. Although the pure YSZ sample showed a higher sensitivity to oxygen at 1075 K, the Pt-YSZ sample had a faster response time and the response was relatively stable with time. A lower resistance in the case of the Pt-YSZ sample was attributed to the presence of the metal.

Later, junctions consisting in YSZ in contact to YSZ with embedded Pt nanoparticles were prepared, observed, and tested as electrochemical sensors [120, 121]. Different platinum loadings were compared, and Nernstian responses were found when exposed to 0.9% O₂ in N₂ for nanoparticle Pt loadings of 2.5% mol and 6.5% mol in YSZ.

5. Conclusions

Models of the behavior of YSZ-based potentiometric oxygen sensors have been reviewed. The classical models based on reaction rates and rates of adsorption of different gas species in the three-phase boundary sites are still useful to understand the general working principles of the sensors. Electric models fitted by impedance spectroscopy seem to be a powerful tool to extract information about phenomena in electrodes and electrolytes. The use of nanomaterials in these devices has shown promising improvements for modifying the mixed potentials to enhance gas selectivity, lowering the activation energies for ion-conduction, or avoiding current constriction in the electrode/electrolyte interfaces. However, they are still necessary more work to be done to implement the advantages of nanomaterials in commercial sensors, as problems with repeatability of measurements, dependence on experimental conditions, control of particle sizes, and spatially coherent nets of electron conducting contacts in the electrodes have to be solved.

References

- [1] E. Ivers-Tiff e, K. H. Hardtl, W. Menesklou, and J. Riegel, "Principles of solid state oxygen sensors for lean combustion gas control," *Electrochimica Acta*, vol. 47, no. 5, pp. 807–814, 2001.
- [2] R. Moos, "A brief overview on automotive exhaust gas sensors based on electroceramics," *International Journal of Applied Ceramic Technology*, vol. 2, no. 5, pp. 401–413, 2005.
- [3] W. J. Fleming, "Physical principles governing nonideal behavior of the zirconia oxygen sensor," *Journal of the Electrochemical Society*, vol. 124, pp. 21–28, 1977.
- [4] J. Brettschneider, "Berechnung des luftverhaltnisses lambda von luft-kraftstoff-gemischen und des einflusses von messfehlern auf lambda," *Bosch Technische Berichte*, vol. 6, pp. 177–186, 1979.
- [5] J. Riegel, H. Neumann, and H. M. Wiedenmann, "Exhaust gas sensors for automotive emission control," *Solid State Ionics*, vol. 152–153, pp. 783–800, 2002.
- [6] A. G. Mortimer and G. P. Reed, "Development of a robust electrochemical oxygen sensor," *Sensors and Actuators B*, vol. 24–25, no. 1–3, pp. 328–335, 1995.
- [7] A. K. M. S. Chowdhury, S. A. Akbar, S. Kapileshwar, and J. R. Schorr, "A rugged oxygen gas sensor with solid reference for high temperature applications," *Journal of the Electrochemical Society*, vol. 148, pp. G91–G94, 2001.
- [8] E. van Setten, T. M. Gur, D. H. A. Blank, J. C. Bravman, and M. R. Beasley, "Miniature Nernstian oxygen sensor for deposition and growth environments," *Review of Scientific Instruments*, vol. 73, no. 1, p. 156, 2002.
- [9] E. Di Bartolomeo, N. Kaabuuathong, M. L. Grilli, and E. Traversa, "Planar electrochemical sensors based on tape-cast YSZ layers and oxide electrodes," *Solid State Ionics*, vol. 171, no. 3–4, pp. 173–181, 2004.
- [10] H. Kaneko, T. Okamura, H. Taimatsu, Y. Matsuki, and H. Nishida, "Performance of a miniature zirconia oxygen sensor with a Pd-PdO internal reference," *Sensors and Actuators B*, pp. 331–334, 2005.
- [11] M. Kleitz and E. Siebert, "Electrode reactions in potentiometric gas sensor," in *Chemical Sensor Technology*, T. Seiyama, Ed., vol. 2, pp. 151–171, Kodansha, Tokyo and Elsevier, Amsterdam, The Netherlands, 1989.
- [12] M. Kleitz, E. Siebert, P. Fabry, and J. Fouletier, "Solid state electrochemical sensors," in *Sensors: A Comprehensive Survey*, T. Seiyama, Ed., vol. 2, pp. 341–428, VCH, Weinheim, Germany, 1991.
- [13] D. W. McKee, "Interaction of hydrogen and carbon monoxide on platinum group metals," *Journal of Catalysis*, vol. 8, no. 3, pp. 240–249, 1967.
- [14] J. E. Anderson and Y. B. Graves, "Steady-state characteristics of oxygen concentration cell sensors subjected to nonequilibrium gas mixtures," *Journal of the Electrochemical Society*, vol. 128, no. 2, pp. 294–300, 1981.
- [15] K. Saji, H. Kondo, T. Takeuchi, and I. Igarashi, "Voltage step characteristics of oxygen concentration cell sensors for nonequilibrium gas mixtures," *Journal of the Electrochemical Society*, vol. 135, pp. 1686–1691, 1988.
- [16] A. D. Brailsford and E. M. Logothetis, "A steady-state diffusion model for solid-state gas sensors," *Sensors and Actuators*, vol. 7, no. 1, pp. 39–67, 1985.
- [17] A. D. Brailsford, M. Yussouff, and E. M. Logothetis, "Theory of gas sensors," *Sensors and Actuators B*, vol. 13, no. 1–3, pp. 135–138, 1993.
- [18] A. D. Brailsford, M. Yussouff, E. M. Logothetis, and M. Shane, "Steady-state model of a zirconia oxygen sensor in a simple gas mixture," *Sensors and Actuators B*, vol. 24–25, no. 1–3, pp. 362–365, 1995.
- [19] A. D. Brailsford, M. Yussouff, and E. M. Logothetis, "Theory of gas sensors: response of an electrochemical sensor to multi-component gas mixtures," *Sensors and Actuators B*, vol. 34, no. 1–3, pp. 407–411, 1996.
- [20] A. D. Brailsford, M. Yussouff, and E. M. Logothetis, "Steady state model of electrochemical gas sensors with multiple reactions," *Sensors and Actuators B*, vol. 35–36, no. 1–3, pp. 392–397, 1996.
- [21] A. D. Brailsford, M. Yussouff, and E. M. Logothetis, "A first-principles model of the zirconia oxygen sensor," *Sensors and Actuators B*, vol. 44, no. 1–3, pp. 321–326, 1997.
- [22] J. T. Woestman, A. D. Brailsford, M. Shane, and E. M. Logothetis, "A model of the transient response of mass-transfer limited gas sensors," *Sensors and Actuators B*, vol. 45, no. 1, pp. 27–33, 1997.
- [23] H. Fukunaga, M. Ihara, K. Sakaki, and K. Yamada, "The relationship between overpotential and the three phase boundary length," *Solid State Ionics*, vol. 86–88, pp. 1179–1185, 1996.
- [24] M. Juhl, S. Primdahl, C. Manon, and M. Mogensen, "Performance/structure correlation for composite SOFC cathodes," *Journal of Power Sources*, vol. 61, no. 1–2, pp. 173–181, 1996.
- [25] S. P. Yoon, S. W. Nam, J. Han, T. H. Lim, S. A. Hong, and S. H. Hyun, "Effect of electrode microstructure on gas-phase diffusion in solid oxide fuel cells," *Solid State Ionics*, vol. 166, no. 1–2, pp. 1–11, 2004.
- [26] R. J. Aaberg, R. Tunold, and R. Odegard, "On the electrochemistry of metal-YSZ single contacts," *Solid State Ionics*, vol. 136–137, pp. 707–712, 2000.

- [27] S. Sridhar, V. Stancovski, and U. B. Pal, "Effect of oxygen-containing species on the impedance of the Pt/YSZ interface," *Solid State Ionics*, vol. 100, no. 1-2, pp. 17-22, 1997.
- [28] J. L. Hertz and H. L. Tuller, "Measurement and finite element modeling of triple phase boundary-related current constriction in YSZ," *Solid State Ionics*, vol. 178, no. 13-14, pp. 915-923, 2007.
- [29] S. P. Yoon, S. W. Nam, S. G. Kim, S. A. Hong, and S. H. Hyun, "Characteristics of cathodic polarization at Pt/YSZ interface without the effect of electrode microstructure," *Journal of Power Sources*, vol. 115, no. 1, pp. 27-34, 2003.
- [30] R. O'Hayre, D. Barnett, and F. B. Prinz, "The triple phase boundary: a mathematical model and experimental investigations for fuel cells," *Journal of the Electrochemical Society*, vol. 152, pp. 439-444, 2005.
- [31] L. Bultel, P. Vernoux, F. Gaillard, C. Roux, and E. Siebert, "Electrochemical and catalytic properties of porous Pt-YSZ composites," *Solid State Ionics*, vol. 176, no. 7-8, pp. 793-801, 2005.
- [32] T. Jacobsen, B. Zachau-Christiansen, L. Bay, and M. Juhl, "Hysteresis in the solid oxide fuel cell cathode reaction," *Electrochimica Acta*, vol. 46, no. 7, pp. 1019-1024, 2001.
- [33] T. Jacobsen and L. Bay, "Thermal memory effects at the Pt-YSZ interface," *Electrochimica Acta*, vol. 47, pp. 2177-2181, 2002.
- [34] A. Jaccoud, G. Foti, R. Wüthrich, H. Jotterand, and C. Comminellis, "Pt/YSZ microstructure and electrochemistry," *Topics in Catalysis*, vol. 44, no. 3, pp. 409-417, 2007.
- [35] J. Nielsen and T. Jacobsen, "Three-phase boundary dynamics at Pt/YSZ microelectrodes," *Solid State Ionics*, vol. 178, pp. 1001-1009, 2007.
- [36] E. L. Shoemaker, M. C. Vogt, F. J. Dudek, and T. Turner, "Gas microsensors using cyclic voltammetry with a cermet electrochemical cell," *Sensors and Actuators B*, vol. 42, no. 1, pp. 1-9, 1997.
- [37] N. Miura, T. Raisen, G. Lu, and N. Yamazoe, "Highly selective CO sensor using stabilized zirconia and a couple of oxide electrodes," *Sensors and Actuators B*, vol. 47, no. 1-3, pp. 84-91, 1998.
- [38] N. Miura, G. Lu, and N. Yamazoe, "Progress in mixed-potential type devices based on solid electrolyte for sensing redox gases," *Solid State Ionics*, vol. 136-137, pp. 533-542, 2000.
- [39] N. Miura, G. Lu, and N. Yamazoe, "High-temperature potentiometric/ampereometric NO_x sensors combining stabilized zirconia with mixed-metal oxide electrode," *Sensors and Actuators B*, vol. 52, no. 1-2, pp. 169-178, 1998.
- [40] S. Zhuiykov, T. Nakano, A. Kunimoto, and N. Miura, "Potentiometric NO_x sensor based on stabilized zirconia and NiCr₂O₄ sensing electrode operating at high temperatures," *Electrochemistry Communications*, vol. 3, no. 2, pp. 97-101, 2001.
- [41] N. Miura, S. Zhuiykov, T. Ono, M. Hasei, and N. Yamazoe, "Mixed potential type sensor using stabilized zirconia and ZnFe₂O₄ sensing electrode for NO_x detection at high temperature," *Sensors and Actuators B*, vol. 81, pp. 222-229, 2002.
- [42] N. F. Szabo and P. K. Dutta, "Strategies for total NO_x measurement with minimal CO interference utilizing a microporous zeolitic catalytic filter," *Sensors and Actuators B*, vol. 88, no. 2, pp. 168-177, 2003.
- [43] S. Zhuiykov, "Mathematical modelling of YSZ-based potentiometric gas sensors with oxide sensing electrodes—part I: model of interactions of measuring gas with sensor," *Sensors and Actuators B*, vol. 119, no. 2, pp. 456-465, 2006.
- [44] S. Zhuiykov, "Mathematical modelling of YSZ-based potentiometric gas sensors with oxide sensing electrodes—part II: complete and numerical models for analysis of sensor characteristics," *Sensors and Actuators B*, vol. 120, no. 2, pp. 645-656, 2007.
- [45] H. Näfe, "How to check the validity of Nernst's law in a potentiometric solid electrolyte galvanic cell," *Solid State Ionics*, vol. 113-115, pp. 205-217, 1998.
- [46] M. Er-Raki, M. Hasnaoui, A. Amahmid, and M. Bourich, "Soret driven thermosolutal convection in a shallow porous layer with a stress-free upper surface engineering computations," *International Journal of Computationally Aided Engineering*, vol. 22, no. 2, pp. 186-205, 2005.
- [47] E. Mutoro, S. Günther, B. Luerßen, I. Valov, and J. Janek, "Electrode activation and degradation: morphology changes of platinum electrodes on YSZ during electrochemical polarisation," *Solid State Ionics*, vol. 179, no. 33-34, pp. 1835-1848, 2008.
- [48] R. Ramamoorthy, S. A. Akbar, and P. K. Dutta, "Dependence of potentiometric oxygen sensing characteristics on the nature of electrodes," *Sensors and Actuators B*, vol. 113, no. 1, pp. 162-168, 2006.
- [49] A. Jaccoud, C. Falgairette, G. Fóti, and C. Comminellis, "Charge storage in the O₂(g), Pt/YSZ system," *Electrochimica Acta*, vol. 52, no. 28, pp. 7927-7935, 2007.
- [50] T. Wang, R. F. Novak, and R. E. Soltis, "A study of factors that influence zirconia/platinum interfacial impedance using equivalent circuit analysis," *Sensors and Actuators B*, vol. 77, no. 1-2, pp. 132-138, 2001.
- [51] G. Reinhardt, R. Mayer, and M. Rösch, "Sensing small molecules with amperometric sensors," *Solid State Ionics*, vol. 150, no. 1-2, pp. 79-92, 2002.
- [52] M. S. Ugorek, *A comparison of microstructure and electrical properties of 8 mol% yttria stabilized zirconia processed under conventional, microwave and fast-fire sintering techniques*, Ph.D. thesis, 2004.
- [53] L. Y. Woo, L. P. Martin, R. S. Glass, and R. J. Gorte, "Impedance characterization of a model Au/Yttria stabilized zirconia/au electrochemical cell in varying oxygen and NO_x concentrations," *Journal of the Electrochemical Society*, vol. 154, pp. J129-J135, 2007.
- [54] P. Costamagna, M. Panizza, G. Cerisola, and A. Barbucci, "Effect of composition on the performance of cermet electrodes. Experimental and theoretical approach," *Electrochimica Acta*, vol. 47, no. 7, pp. 1079-1089, 2002.
- [55] W. F. Zhang, P. Schmidt-Zhang, and U. Guth, "Electrochemical studies on cells M/YSZ/Pt (M=Pt, Pt-Ga₂O₃) in NO, O₂, N₂ gas mixtures," *Solid State Ionics*, vol. 169, pp. 121-128, 2004.
- [56] D. Eder and R. Kramer, "Impedance spectroscopy of reduced monoclinic zirconia," *Physical Chemistry Chemical Physics*, vol. 8, no. 38, pp. 4476-4483, 2006.
- [57] P. Ried, C. Lorenz, A. Brönstrup, et al., "Processing of YSZ screen printing pastes and the characterization of the electrolyte layers for anode supported SOFC," *Journal of the European Ceramic Society*, vol. 28, no. 9, pp. 1801-1808, 2008.
- [58] J. T. S. Irvine, D. C. Sinclair, and A. R. West, "Electroceramics: characterization by impedance spectroscopy," *Advanced Materials*, vol. 2, no. 3, pp. 132-138, 2004.
- [59] V. V. Kharton and F. M. B. Marques, "Interfacial effects in electrochemical cells for oxygen ionic conduction measurements: I. The e.m.f. method," *Solid State Ionics*, vol. 140, no. 3-4, pp. 381-394, 2001.

- [60] V. V. Kharton, F. M. B. Marques, E. V. Tsipis, et al., "Interfacial effects in electrochemical cells for oxygen ionic conduction measurements: III. Transference numbers vs. grain-boundary resistivity," *Solid State Ionics*, vol. 168, no. 1-2, pp. 137-151, 2004.
- [61] S. H. Jensen, A. Hauch, P. V. Hendriksen, M. Mogensen, N. Bonanos, and T. Jacobsen, "A method to separate process contributions in impedance spectra by variation of test conditions," *Journal of the Electrochemical Society*, vol. 154, pp. B1325-B1330, 2007.
- [62] H. Meng and P. K. Shen, "Novel Pt-free catalyst for oxygen electroreduction," *Electrochemistry Communications*, vol. 8, no. 4, pp. 588-594, 2006.
- [63] J. R. Frade, V. V. Kharton, A. L. Shaula, and F. M. B. Marques, "Interfacial effects in potentiometric oxygen sensors: the role of transport properties and thickness of solid electrolyte ceramics," *Sensor Letters*, vol. 6, no. 3, pp. 370-380, 2008.
- [64] G. Hsieh, T. O. Mason, and L. R. Pederson, "Experimental limitations in impedance spectroscopy—part I: simulation of reference electrode artifacts in three-point measurements," *Solid State Ionics*, vol. 91, no. 3-4, pp. 191-201, 1996.
- [65] G. Hsieh, T. O. Mason, and L. R. Pederson, "Experimental limitations in impedance spectroscopy—part II: electrode artifacts in three-point measurements on Pt/YSZ," *Solid State Ionics*, vol. 91, no. 3-4, pp. 203-212, 1996.
- [66] R. Radhakrishnan, A. V. Virkar, S. C. Singhal, G. C. Dunham, and O. A. Marina, "Design, fabrication and characterization of a miniaturized series-connected potentiometric oxygen sensor," *Sensors and Actuators B*, vol. 105, no. 2, pp. 312-321, 2005.
- [67] M. Zhou and A. Ahmad, "Synthesis, processing and characterization of calcia-stabilized zirconia solid electrolytes for oxygen sensing applications," *Materials Research Bulletin*, vol. 41, no. 4, pp. 690-696, 2006.
- [68] E. Caproni, F. M. S. Carvalho, and R. Muccillo, "Development of zirconia-magnesia/zirconia-yttria composite solid electrolytes," *Solid State Ionics*, vol. 179, no. 27-32, pp. 1652-1654, 2008.
- [69] N. Balakrishnan, T. Takeuchi, K. Nomura, H. Kageyama, and Y. Takeda, "Aging effect of 8 mol% YSZ ceramics with different microstructures," *Journal of the Electrochemical Society*, vol. 151, pp. 1286-1291, 2004.
- [70] M. Ghatee, M. H. Shariat, and J. T. S. Irvine, "Investigation of electrical and mechanical properties of 3YSZ/8YSZ composite electrolytes," *Solid State Ionics*, vol. 180, no. 1, pp. 57-62, 2009.
- [71] M. Mogensen, D. Lybye, N. Bonanos, P. V. Hendriksen, and F. W. Poulsen, "Factors controlling the oxide ion conductivity of fluorite and perovskite structured oxides," *Solid State Ionics*, vol. 174, no. 1-4, pp. 279-286, 2004.
- [72] X. Guo and R. Waser, "Electrical properties of the grain boundaries of oxygen ion conductors: acceptor-doped zirconia and ceria," *Progress in Materials Science*, vol. 51, no. 2, pp. 151-210, 2006.
- [73] W. Göpel, "Nanostructured sensors for molecular recognition," *Philosophical Transactions of the Royal Society A*, vol. 353, pp. 333-354, 1995.
- [74] W. Göpel, "Ultimate limits in the miniaturization of chemical sensors," *Sensors and Actuators A*, vol. 56, pp. 83-102, 1996.
- [75] W. Göpel, "Chemical analysis and sensorics with microstructured devices," *Mikrochimica Acta*, vol. 125, pp. 179-196, 1997.
- [76] X. Huang and D. Y. Choi, "Chemical sensors based on nanostructured materials," *Sensors and Actuators B*, vol. 122, pp. 659-671, 2007.
- [77] T. Kimura and T. Goto, "Ir-YSZ nano-composite electrodes for oxygen sensors," *Surface & Coatings Technology*, vol. 198, pp. 36-39, 2005.
- [78] A. M. Torres-Huerta, J. R. Vargas-García, and M. A. Domínguez-Crespo, "Preparation and characterization of IrO₂-YSZ nanocomposite electrodes by MOCVD," *Solid State Ionics*, vol. 178, no. 29-30, pp. 1608-1616, 2007.
- [79] A. Barbucci, R. Bozzo, G. Cerisola, and P. Costamagna, "Characterisation of SOFC composite cathodes using electrochemical impedance spectroscopy. Analysis of Pt/YSZ and LSM/YSZ electrodes," *Electrochimica Acta*, vol. 47, pp. 2183-2188, 2002.
- [80] X. Wang, H. Huang, T. Holme, X. Tian, and F. B. Prinz, "Thermal stabilities of nanoporous metallic electrodes at elevated temperatures," *Journal of Power Sources*, vol. 175, no. 1, pp. 75-81, 2008.
- [81] K. Gong, Y. Yan, M. Zhang, L. Su, S. Xiong, and L. Mao, "Electrochemistry and electroanalytical applications of carbon nanotubes: a review," *Analytical Sciences*, vol. 21, no. 12, pp. 1383-1393, 2005.
- [82] J. Wang, G. Chen, M. Wang, and M. P. Chatrathi, "Carbon-nanotube/copper composite electrodes for capillary electrophoresis microchip detection of carbohydrates," *Analyst*, vol. 129, no. 6, pp. 512-515, 2004.
- [83] S. Hrapovic, Y. Liu, K. B. Male, and J. H. T. Luong, "Electrochemical biosensing platforms using platinum nanoparticles and carbon nanotubes," *Analytical Chemistry*, vol. 76, no. 4, pp. 1083-1088, 2004.
- [84] P. J. Britto, K. S. V. Santhanam, A. Rubio, J. A. Alonso, and P. M. Ajayan, "Improved charge transfer at carbon nanotube electrodes," *Advanced Materials*, vol. 11, no. 2, pp. 154-157, 1999.
- [85] P. G. Collins, K. Bradley, M. Ishigami, and A. Zettl, "Extreme oxygen sensitivity of electronic properties of carbon nanotubes," *Science*, vol. 287, no. 5459, pp. 1801-1804, 2000.
- [86] U. Cvelbar and M. Mozetič, "Behaviour of oxygen atoms near the surface of nanostructured Nb₂O₅," *Journal of Applied Physics D*, vol. 40, no. 8, pp. 2300-2303, 2007.
- [87] N. Wu, M. Zhao, J. G. Zheng, et al., "Porous CuO-ZnO nanocomposite for sensing electrode of high-temperature CO solid-state electrochemical sensor," *Nanotechnology*, vol. 16, no. 12, pp. 2878-2881, 2005.
- [88] X. Li and G. M. Kale, "Novel nanosized ITO electrode for mixed potential gas sensors," *Electrochemistry Solid State Letters*, vol. 8, pp. 27-30, 2005.
- [89] X. Li and G. M. Kale, "Influence of thickness of ITO sensing electrode film on sensing performance of planar mixed potential CO sensor," *Sensors and Actuators B*, vol. 120, no. 1, pp. 150-155, 2006.
- [90] X. Li and G. M. Kale, "Planar mixed-potential CO sensor utilizing novel BLIO and ITO interface," *Electrochemistry Solid State Letters*, vol. 9, pp. 12-15, 2005.
- [91] X. Li and G. M. Kale, "Influence of sensing electrode and electrolyte on performance of potentiometric mixed-potential gas sensors," *Sensors and Actuators B*, vol. 123, no. 1, pp. 254-261, 2007.
- [92] V. V. Plashnitsa, P. Elumalai, and N. Miura, "Sensitive and selective zirconia-based NO₂ sensor using gold nanoparticle coatings as sensing electrodes," *Journal of the Electrochemical Society*, vol. 155, pp. 301-306, 2008.

- [93] J. Zosel, D. Tuchtenhagen, K. Ahlborn, and U. Gith, "Mixed potential gas sensor with short response time," *Sensors and Actuators B*, vol. 130, no. 1, pp. 326–329, 2008.
- [94] S. Thiemann, R. Hartung, H. Wulff, et al., "Modified Au/YSZ electrodes—preparation, characterization and electrode behaviour at higher temperatures," *Solid State Ionics*, vol. 86–88, pp. 873–876, 1996.
- [95] L. Chevallier, E. Di Bartolomeo, M. L. Grilli, et al., "Non-nernstian planar sensors based on YSZ with a Nb₂O₅ electrode," *Sensors and Actuators B*, vol. 129, no. 2, pp. 591–597, 2008.
- [96] T. Hibino, S. Wang, S. Kakimoto, and M. Sano, "Detection of propylene under oxidizing conditions using zirconia-based potentiometric sensor," *Sensors and Actuators B*, vol. 50, 1998.
- [97] J. Zosel, K. Ahlborn, R. Müller, D. Westphal, V. Vashook, and U. Gith, "Selectivity of HC-sensitive electrode materials for mixed potential gas sensors," *Solid State Ionics*, vol. 169, pp. 115–119, 2004.
- [98] V. V. Plashnitsa, T. Ueda, and N. Miura, "Improvement of NO₂ sensing performances by an additional second component to the nano-structured NiO sensing electrode of a YSZ-based mixed-potential-type sensor," *International Journal of Applied Ceramic Technology*, vol. 3, no. 2, pp. 127–133, 2007.
- [99] E. Di Bartolomeo, N. Kaabuuathong, A. D'Epifanio, et al., "Nano-structured perovskite oxide electrodes for planar electrochemical sensors using tape casted YSZ layers," *Journal of the European Ceramic Society*, vol. 24, no. 6, pp. 1187–1190, 2004.
- [100] J. W. Yoon, M. L. Grilli, E. D. Bartolomeo, et al., "The NO₂ response of solid electrolyte sensors made using nano-sized LaFeO₃ electrodes," *Sensors and Actuators B*, vol. 76, pp. 483–488, 2001.
- [101] V. V. Plashnitsa, T. Ueda, P. Elumalai, and N. Miura, "NO₂ sensing performances of planar sensor using stabilized zirconia and thin-NiO sensing electrode," *Sensors and Actuators B*, vol. 130, no. 1, pp. 231–239, 2008.
- [102] V. V. Plashnitsa, T. Ueda, P. Elumalai, T. Kawaguchi, and N. Miura, "Zirconia-based planar NO₂ sensor using ultrathin NiO or laminated NiO-Au sensing electrode," *Ionics*, vol. 14, no. 1, pp. 15–25, 2008.
- [103] S. C. Zhang, G. L. Messing, and M. Borden, "Synthesis of solid, spherical zirconia particles by spray pyrolysis," *Journal of the American Ceramic Society*, vol. 73, pp. 61–67, 1990.
- [104] Y. Q. Xie, "Preparation of ultrafine zirconia particles," *Journal of the American Ceramic Society*, vol. 82, pp. 768–770, 1999.
- [105] R. Jossen, R. Müller, S. E. Pratsinis, M. Watson, and M. K. Akhtar, "Morphology and composition of spray-flame-made yttria-stabilized zirconia nanoparticles," *Nanotechnology*, vol. 16, pp. 609–617, 2005.
- [106] I. Kosacki, B. Gorman, and H. U. Anderson, "Microstructure and electrical conductivity in nanocrystalline oxide thin films," in *Ionic and Mixed Conducting Ceramics*, T. A. Ramanarayanan, Ed., vol. 3, pp. 631–642, Electrochemical Society, Pennington, NJ, USA, 1998, PV 97-24.
- [107] Y. M. Chiang, E. B. Lavik, I. Kosacki, H. L. Tuller, and J. Y. Ying, "Defect and transport properties of nanocrystalline CeO_{2-x}," *Applied Physics Letters*, vol. 69, no. 2, pp. 185–187, 1996.
- [108] I. Kosacki and H. U. Anderson, "The transport properties of nanocrystalline SrCe_{0.95}Yb_{0.05}O₃ thin films," *Applied Physics Letters*, vol. 69, no. 27, pp. 4171–4173, 1996.
- [109] Y. M. Chiang, E. B. Lavik, I. Kosacki, H. L. Tuller, and J. Y. Ying, "Nonstoichiometry and electrical conductivity of nanocrystalline CeO_{2-x}," *Journal of Electroceramics*, vol. 1, no. 1, pp. 7–14, 1997.
- [110] I. Kosacki, T. Suzuki, V. Petrovsky, and H. U. Anderson, "Electrical conductivity of nanocrystalline ceria and zirconia thin films," *Solid State Ionics*, vol. 136-137, pp. 1225–1233, 2000.
- [111] I. Kosacki, C. M. Rouleau, P. F. Becher, J. Bentley, and D. H. Lowndes, "Nanoscale effects on the ionic conductivity in highly textured YSZ thin films," *Solid State Ionics*, vol. 176, no. 13-14, pp. 1319–1326, 2005.
- [112] A. F. Uvarov, "Estimation of composites conductivity using a general mixing rule," *Solid State Ionics*, vol. 136-137, pp. 1267–1272, 2000.
- [113] M. F. Garcia-Sánchez, J. Peña, A. Ortiz, et al., "Nanostructured YSZ thin films for solid oxide fuel cells deposited by ultrasonic spray pyrolysis," *Solid State Ionics*, vol. 179, no. 7-8, pp. 243–249, 2008.
- [114] Q. Zhu and B. Fan, "Low temperature sintering of 8YSZ electrolyte film for intermediate temperature solid oxide fuel cells," *Solid State Ionics*, vol. 176, no. 9-10, pp. 889–894, 2005.
- [115] T. Yadav and H. Hu, "Nanostructured solid electrolytes and devices," US patent no. 6387560, 1999.
- [116] T. Yadav and H. Hu, "Nanostructured powders and related nanotechnology," US patent no. 2004/0005485, 2004.
- [117] W. N. Lawless, "Ceramic fuel cell," US patent no. 6372375, 2002.
- [118] M. M. Seabaugh, S. L. Swartz, W. J. Dawson, and B. E. McCormick, "Ceramic electrolyte coating and methods," US patent no. 2005/0026017, 2005.
- [119] D. T. Dimitrov and C. D. Dushkin, "Oxygen detection using yttria-stabilized zirconia thin films doped with platinum," *Central European Journal of Chemistry*, vol. 3, no. 4, pp. 605–621, 2005.
- [120] D. T. Dimitrov, S. Y. Anastosova, and C. D. Dushkin, "Oxygen sensing junctions based on yttria-stabilized zirconia with platinum nanoparticles," *Review of Scientific Instruments*, vol. 77, Article ID 056108, 2006.
- [121] D. T. Dimitrov, C. D. Dushkin, N. L. Petrova, et al., "Oxygen detection using junctions based on thin films of yttria-stabilized zirconia doped with platinum nanoparticles and pure yttria-stabilized zirconia," *Sensors and Actuators A*, vol. 137, no. 1, pp. 86–95, 2007.

Research Article

Field-Assisted and Thermionic Contributions to Conductance in SnO₂ Thick-Films

C. Malagù,¹ M. C. Carotta,¹ G. Martinelli,¹ M. A. Ponce,² M. S. Castro,² and C. M. Aldao²

¹Department of Physics, University of Ferrara, Via Saragat 1/C, 44100 Ferrara, Italy

²Institute of Materials Science and Technology (INTEMA), National University of Mar del Plata, CONICET, Juan B. Justo 4302, B7608FDQ Mar del Plata, Argentina

Correspondence should be addressed to C. Malagù, malagu@fe.infn.it

Received 27 January 2009; Revised 27 May 2009; Accepted 23 June 2009

Recommended by Giorgio Sberveglieri

A deep analysis of conductance in nanostructured SnO₂ thick films has been performed. A model for field-assisted thermionic barrier crossing is being proposed to explain the film conductivity. The model has been applied to explain the behavior of resistance in vacuum of two sets of nanostructured thick-films with grains having two well-distinct characteristic radii ($R = 25$ nm and $R = 125$ nm). In the first case the grain radius is shorter than the depletion region width, a limit at which overlapping of barriers takes place, and in the second case it is longer. The behavior of resistance in the presence of dry air has been explained through the mechanism of barrier modulation through gas chemisorption.

Copyright © 2009 C. Malagù et al. This is an open access article distributed under the Creative Commons Attribution License, which permits unrestricted use, distribution, and reproduction in any medium, provided the original work is properly cited.

1. Introduction

In the last two decades, gas sensors based on SnO₂ thick films became the dominant solid state devices for the gas detection in domestic, commercial, and industrial alarms [1, 2]. It is widely accepted that, when oxygen chemisorbs, electrons transfer from the bulk to the surface of the grain modifying the barriers at the grain boundaries [3]. In particular, after oxygen chemisorption, the barrier height, V_s , and the depletion width, Λ , become larger and, as a consequence, the sample resistance increases. Different factors (such as type of defects, morphology, and additives) contribute to the electrical response of the gas sensor [4, 5].

The film resistivity (or conductivity) is broadly used to characterize a sensor, and the widely acknowledged phenomenological equation [2, 6, 7] is

$$\rho = \rho_o \text{Exp}\left(\frac{eV_s}{kT}\right), \quad (1)$$

where ρ_o is the bulk resistivity, k the Boltzmann constant, and T the absolute temperature.

In this work, the resistance of undoped SnO₂ thick-film gas sensors is analyzed as a function of temperature in vacuum and in dry air atmosphere. In order to explain

the results, thermionic and tunneling contributions to the electrical conduction have been considered.

2. Experimental

Commercial high-purity SnO₂ (Aldrich, medium particle size $0.4 \mu\text{m}$) was ground until a medium particle size of $0.1 \mu\text{m}$ (labeled powders P1). A calcination process carried out at 1100°C for 2 hours led to powders with larger particle size (labeled powders P2). Then, a paste was prepared with an organic binder (glycerol) and the powders P1 and P2. The used solid/organic binder ratio was 1/2. No dopants were added.

Thick, porous film samples were made by painting onto insulating alumina substrate on which electrodes with an interdigit shape have been deposited by sputtering. Finally, samples were thermally treated for 2 hours in air at 500°C . Samples were labeled S1 (small particle size) and S2 (large particle size). The thickness of the films was measured with a Surtronic 3+ (Taylor Hobson) profilometer with a diamond stylus (radius: $1 \mu\text{m}$). To image the tin oxide surfaces a JEOL JSM 6700F SEM was employed. The X-ray data were collected with a Siemens D-500 diffractometer using CuK α radiation.

Dynamical resistance curves were measured while changing the vacuum into air flux and, after having reached quasisaturation, changing the dry air flux back into vacuum (10^{-4} mmHg). In temperature cycling experiments, resistance was measured while raising and then decreasing the temperature from room temperature up to 420°C at a rate of $\sim 2^\circ\text{C}/\text{min}$ with the sample kept in air (40 mmHg).

3. Modelling

To model the resistance of the two sets of sensors, a field-assisted mechanism for barrier crossing is proposed (see [8]). We applied the WKB approximation to a double parabolic barrier of the following form:

$$V(r) = \begin{cases} \frac{V_s}{\Lambda^2}(r + \Lambda)^2, & -\Lambda \leq r \leq 0, \\ \frac{V_s}{\Lambda^2}(r - \Lambda)^2, & 0 \leq r \leq \Lambda. \end{cases} \quad (2)$$

The tunnelling and thermionic contributions to the current density, with respect to the flat band case, were calculated following the classical work of Crowell and Rideout for a single parabolic barrier [9]. The whole calculation resulted in a factor two in the exponent of the tunneling part of [9, equation (13)]. Thus, we found for the tunneling contribution, here called I_1 , and for the thermionic one, here called I_2 , respectively,

$$I_1 = \frac{eV_s}{kT} \int_0^1 \text{Exp} \left\{ -\frac{eV_s}{kT} \left[\alpha + \frac{2kTy(\alpha)}{E_{00}} \right] \right\} d\alpha, \quad (3)$$

$$I_2 = \text{Exp} \left(-\frac{eV_s}{kT} \right),$$

where

$$y(\alpha) = (1 - \alpha)^{0.5} - \alpha \text{Ln} \left[\frac{1 + (1 - \alpha)^{0.5}}{\alpha^{0.5}} \right], \quad (4)$$

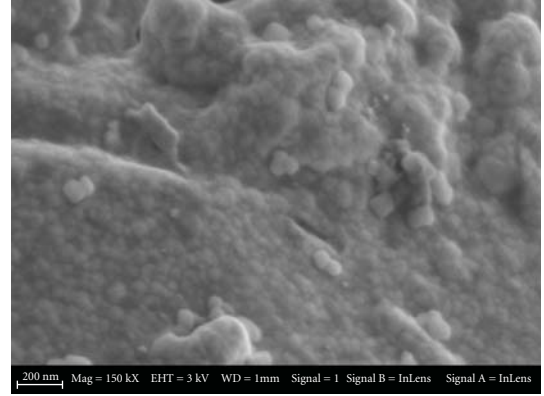
$$\alpha = \frac{E}{eV_s},$$

$$E_{00} = \frac{eh}{4\pi} \left(\frac{N_d}{m * \epsilon} \right)^{1/2},$$

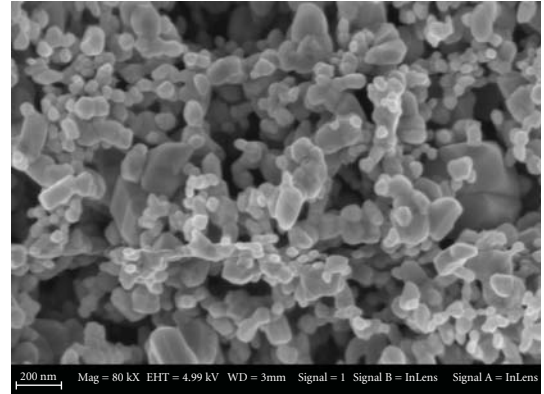
with E being the energy of an electron in the conduction band. From numerical solutions of (3) it turns out that the relative tunneling emission with respect to the thermionic one (I_1/I_2) is an increasing function of E_{00}/kT ratio. For a given material, E_{00} is fixed; thus the tunneling contribution is more effective at lower temperatures. Moreover the solution of (3) at a fixed temperature shows, as discussed in [8] (our factor two does not alter the trend), that the lower the barrier the more important the relative thermionic contribution with respect to the field assisted one. This phenomenon gives an explanation to the experimental evidence presented below.

4. Results and Discussion

In Figures 1(a) and 1(b), SEM micrographs of the samples S1 and S2 are shown. Both samples present homogeneous



(a)



(b)

FIGURE 1: (a) SEM micrograph for a sample labeled S1 ($R < \Lambda$). (b) SEM micrograph for a sample labeled S2 ($R > \Lambda$).

microstructures. From SEM micrographs a significant difference in the microstructures of S1 and S2 is observed. The samples showed the presence of agglomerates, but samples made with larger particle size (S2) showed a highly porous microstructure with the presence of some cracks (not shown in this figure). The average particle radius of samples labeled S1 was determined to be 25 nm, while for samples labeled S2 it was determined to be 125 nm. The mean thickness of the films determined by the profilometer was $100 \mu\text{m}$ for samples S1 and $440 \mu\text{m}$ for samples S2.

Since SEM imager for sample S1 is not clear enough to provide reliable grain size determination, we have performed X-Ray Diffraction (XRD) on this sample for comparison. From XRD, the film is found to be composed of SnO_2 with a high degree of crystalline. In Figure 2, the peak corresponding to the (211) plane is showed. The grain sizes of the samples were calculated following Scherrer's law [10]:

$$t = \frac{0,9 \cdot \lambda}{B \cdot \cos(\theta_B)}, \quad (5)$$

where t is the SnO_2 particle size; λ is the wavelength ($\text{Co} = 1.788 \text{ \AA}$); B is the angular width (in terms of $2\theta_B$) measured in radians that corresponds to the full width at half-maximum; θ_B is the value of the angle of the peak of the highest intensity. Through this equation, a particle size, t , of 41 nm

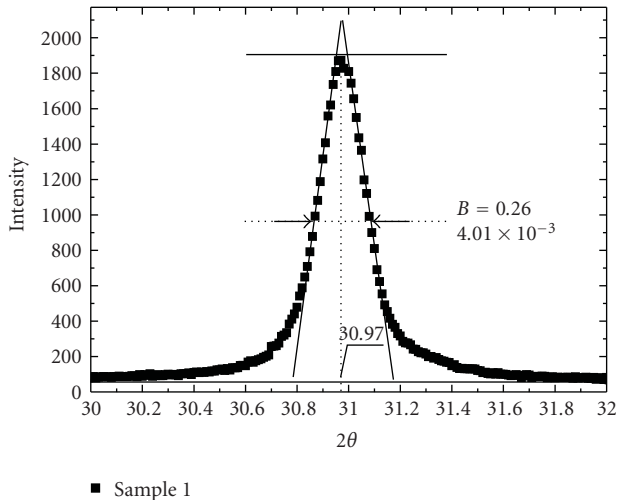


FIGURE 2: XRD of sample 1 to compare with SEM measurement.

was calculated for sample S1. This result is in agreement with that found using SEM.

Figure 3 shows the electrical response (resistance versus time) of the sample with smaller particle size after changing the vacuum (10^{-2} mmHg) into air flux ($t = 0$) and back into vacuum. In Figure 3, curve A—experiment carried out at 280°C —after a quick increasing due to air exposure, the electrical resistance is almost constant over a lapse of 700 seconds. On the other hand, at the temperature of 420°C (Figure 3, curve B) a diminution in the resistance after a quick increase is observed. Figure 4 shows electrical responses (resistance versus time) of the sample S2 after changing the vacuum into air flux ($t = 0$) and back into vacuum. Curve A shows an electrical response similar to those observed in sample S1 at the low temperature (Figure 3, curve A). When the temperature is increased at values close to 420°C , a slow decreasing in the resistance with exposure time was registered (Figure 4, curve B). This behavior is similar to that observed at the high temperature in sample S1 for the longest exposition times. However, due to the greater thickness in sample S2, a slower electrical response with respect to S1 in the studied temperature range is detected.

Resistance versus time curves can be understood by considering that intergranular potential barriers are responsible for the observed electrical response [11]. The rapid increase of the resistance, when samples are exposed to air, indicates that equilibrium at the surface is quickly reached. The interaction of oxygen with grain surfaces produces the transfer of electrons from the bulk to the surface. From this process, V_s and Λ become larger and, as a consequence, the sample resistance increases. The long term changes in the resistance observed after a quick initial change in the atmosphere can be explained in terms of oxygen in- and out-diffusion [12] that reflects in a slow change of the doping level, N_d .

Samples with larger particle size (S2) showed a relatively slower response than samples with smaller particle size (S1). This result could be explained by considering that samples

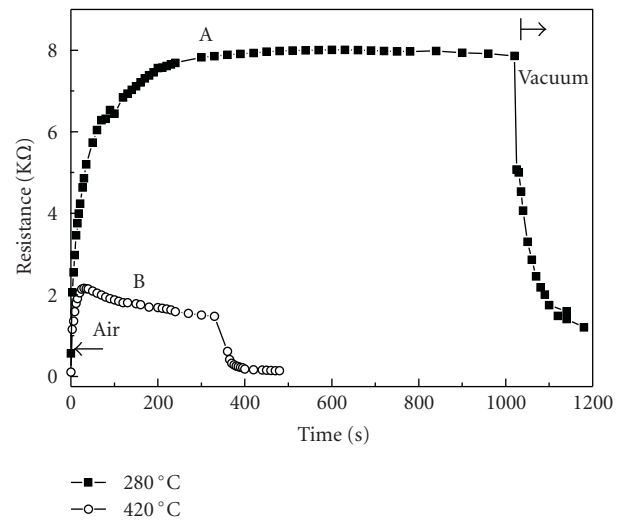


FIGURE 3: Dynamical response (resistance versus time) of S1 after changing the vacuum into air flux ($t = 0$) and back into vacuum. (a) $T = 280^\circ\text{C}$. (b) $T = 420^\circ\text{C}$.

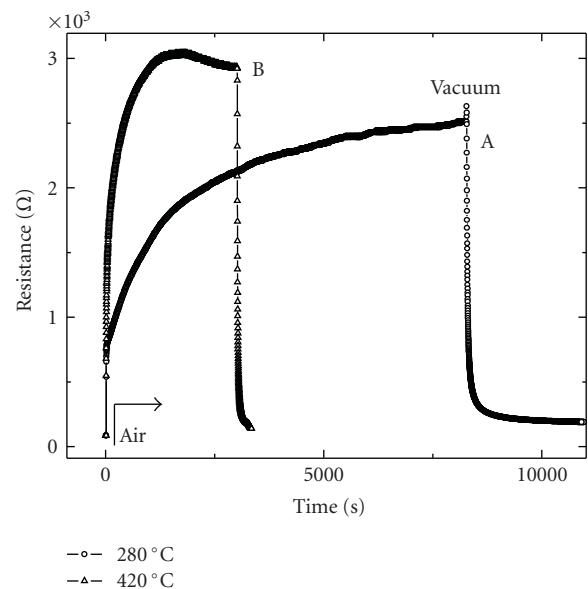


FIGURE 4: Dynamical response (resistance versus time) of S2 after changing the vacuum into air flux ($t = 0$) and back into vacuum. (a) $T = 280^\circ\text{C}$. (b) $T = 420^\circ\text{C}$.

S2 are thicker than S1. It has long been suggested that the response time of a semiconductor gas sensor could be related to the reactivity and diffusion of gas molecules inside gas sensing layers [13, 14].

Regarding the behaviour of resistance in vacuum a more subtle analysis is required. The values of resistance in vacuum for the samples S1 and S2 are reported in Table 1 at the temperatures of 280 and 420°C , respectively.

Samples S2 show a lower resistance than samples S1 at both temperatures due to the lower number of grains. But it is worth noticing that, whereas at the high temperature the value of the resistance is comparable to that of the smaller

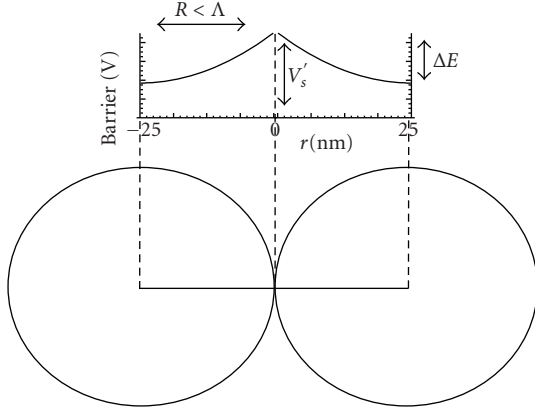


FIGURE 5: $R < \Lambda$, the potential is not zero at the centre of the grain. The potential barrier that electrons have to cross is $\Delta E < eV'_s$. V'_s is the distance between the conduction band at surface and the Fermi level; it holds $V'_s < V_s$ [13].

TABLE 1: Average resistance values in vacuum of samples S1 and S2 at the two operating temperatures.

	S1 ($R = 25$ nm)	S2 ($R = 125$ nm)
280°C	$R = 0.565$ k Ω	$R = 0.105$ k Ω
420°C	$R = 0.110$ k Ω	$R = 0.085$ k Ω

grained sample, at the low temperature the resistance of S1 is five times larger than that of S2. The case of grains with $R < \Lambda$ (S1) is sketched in Figure 5. In a previous work [15] we have demonstrated that the barrier height in vacuum, which we will call here V'_s , of SnO₂ grains with $R < \Lambda$ is expected to be about 10% lower than that of grains with $R > \Lambda$ because of the decrease of surface state density.

It must be observed that the density of electrons decreases exponentially with the distance of E_c from E_F in the same manner as the thermionic contribution increases due to the lower barrier. As explained in [8, equation (7)], if we call ΔE the barrier height and eV'_s the distance between E_c and E_F , then the Fermi level is $eV'_s - \Delta E$ below the bottom of the conduction band. The carrier density is then reduced by a factor $\text{Exp}[-(eV'_s - \Delta E)/kT]$. Consequently the total thermionic contribution to conductance is proportional to $\text{Exp}[-(eV'_s - \Delta E)/kT] \times \text{Exp}[-\Delta E/kT]$, where the first term is the change in carrier density and the second one is the probability of barrier crossing. This product gives exactly

$$\text{Exp}\left[\frac{-eV'_s}{kT}\right] = \text{Exp}\left[\frac{-E_c - E_F}{kT}\right]. \quad (6)$$

Therefore, if we do not invoke tunnelling, it is necessary for a semiconductor with lower distance between E_c and E_F to exhibit higher conductivity, which is contradicted by experimental evidence.

If the mechanism of barrier crossing were purely thermionic, the smaller grains would show less resistivity at every temperature, being the resistivity an exponential function of the barrier height; see (6). At the higher temperature, the number of electrical active grains, of the

samples S2, competes with its higher resistivity making the resistance of the two samples almost equal, $R(S1) = 1.3R(S2)$. Instead, at 280°C where the tunneling contribution (I_1) is dominant with respect to the thermionic (I_2) because at lower temperature $E_{00} \cong kT$, the effect of grain size is crucial. In the case of small grains, the actual barrier to be crossed, ΔE , is much lower than that of the larger grains, and, in the case of lower barrier, the relative tunneling contribution is reduced with respect to the thermionic one. In fact, at $R = 25$ nm the overlapping of potential barriers takes place, see Figure 5, and $\Delta E < V'_s < V_s$. Therefore a larger resistance for smaller grains is to be expected at the lower temperature. If instead the phenomenon were purely determined by thermionic emission, the barrier lowering of small grains could not produce different effects at different temperatures, the effect being only that of reducing the resistance of the small grains with respect to that of large ones. It would not then be possible to explain why $R(S1) = 5.4R(S2)$ at 280°C.

5. Conclusions

The resistance behavior of the two samples in oxygen has been explained in terms of barrier variations due to surface reactions. In the case of vacuum, to explain the greater resistance (Table 1) of small grains with respect to larger ones, in spite of the fact that the barrier of the latter is higher, it is necessary to invoke tunneling. It turns out that the relative tunneling contribution in the case of small grains is smaller because intergranular barriers are lower as a consequence of the lift of the potential at the centre of the grain.

Therefore, if the sensors are working at temperatures at which the tunneling crossing is dominant with respect to thermionic, it is possible that the decrease of the former contribution results in a very big increase in resistance for samples with a grain radius smaller than depletion width. This evidence could not be taken into account by bare thermionic emission.

Acknowledgment

This work has been possible thanks to the project of Scientific Cooperation between CNR (Italy) and CONICET (Argentina).

References

- [1] W. Göpel and K. D. Schierbaum, "SnO₂ sensors: current status and future prospects," *Sensors and Actuators B*, vol. 26, no. 1–3, pp. 1–12, 1995.
- [2] N. Barsan and U. Weimar, "Conduction model of metal oxide gas sensors," *Journal of Electroceramics*, vol. 7, no. 3, pp. 143–167, 2001.
- [3] G. Gaggiotti, A. Galdikas, S. Kaciulis, G. Mattogno, and A. Setkus, "Surface chemistry of tin oxide based gas sensors," *Journal of Applied Physics*, vol. 76, no. 8, pp. 4467–4471, 1994.
- [4] S. Capone, P. Siciliano, F. Quaranta, R. Rella, M. Epifani, and L. Vasanelli, "Moisture influence and geometry effect of Au and

- Pt electrodes on CO sensing response of SnO₂ microsensors based on sol-gel thin film,” *Sensors and Actuators B*, vol. 77, no. 1-2, pp. 503–511, 2001.
- [5] C. Xu, J. Tamaki, N. Miura, and N. Yamazoe, “Grain size effects on gas sensitivity of porous SnO₂-based elements,” *Sensors and Actuators B*, vol. 3, no. 2, pp. 147–155, 1991.
- [6] J. W. Orton and M. J. Powell, “The Hall effect in polycrystalline and powdered semiconductors,” *Reports on Progress in Physics*, vol. 43, no. 11, pp. 1263–1307, 1980.
- [7] P. Romppainen and V. Lantto, “The effect of microstructure on the height of potential energy barriers in porous tin dioxide gas sensors,” *Journal of Applied Physics*, vol. 63, no. 10, pp. 5159–5165, 1988.
- [8] C. Malagú, G. Martinelli, M. A. Ponce, and C. M. Aldao, “Unpinning of the Fermi level and tunneling in metal oxide semiconductors,” *Applied Physics Letters*, vol. 92, no. 16, Article ID 162104, 3 pages, 2008.
- [9] C. R. Crowell and V. L. Rideout, “Normalized thermionic-field (T-F) emission in metal-semiconductor (Schottky) barriers,” *Solid State Electronics*, vol. 12, no. 2, pp. 89–105, 1969.
- [10] B. D. Cullity, “Elements of X-Ray Diffraction,” Addison-Wesley, Reading, Mass, USA, 1978.
- [11] G. Blaustein, M. S. Castro, and C. M. Aldao, “Influence of frozen distributions of oxygen vacancies on tin oxide conductance,” *Sensors and Actuators B*, vol. 55, no. 1, pp. 33–37, 1999.
- [12] M. A. Ponce, C. Malagu, M. C. Carotta, G. Martinelli, and C. M. Aldao, “Gas indiffusion contribution to impedance in tin oxide thick films,” *Journal of Applied Physics*, vol. 104, no. 5, Article ID 054907, 5 pages, 2008.
- [13] G. Sakai, N. S. Baik, N. Miura, and N. Yamazoe, “Gas sensing properties of tin oxide thin films fabricated from hydrothermally treated nanoparticles: dependence of CO and H₂ response on film thickness,” *Sensors and Actuators B*, vol. 77, no. 1-2, pp. 116–121, 2001.
- [14] M. A. Ponce, C. M. Aldao, and M.S . Castro, “Influence of particle size on the conductance of SnO₂ thick films,” *Journal of the European Ceramic Society*, vol. 23, no. 12, pp. 2105–2111, 2003.
- [15] T. G. G. Maffei, G. T. Owen, C. Malagú, et al., “Direct evidence of the dependence of surface state density on the size of SnO₂ nanoparticles observed by scanning tunnelling spectroscopy,” *Surface Science*, vol. 550, no. 1–3, pp. 21–25, 2004.

Review Article

Nanotechnology: A Tool for Improved Performance on Electrochemical Screen-Printed (Bio)Sensors

Elena Jubete, Oscar A. Loaiza, Estibalitz Ochoteco, Jose A. Pomposo, Hans Grande, and Javier Rodríguez

New Materials Department, Sensors and Photonics Unit, Centre for Electrochemical Technologies (CIDETEC), Paseo Miramón 196, 20009 Donostia-San Sebastián, Spain

Correspondence should be addressed to Elena Jubete, ejubete@cidetec.es

Received 23 December 2008; Accepted 26 March 2009

Recommended by Wojtek Wlodarski

Screen-printing technology is a low-cost process, widely used in electronics production, especially in the fabrication of disposable electrodes for (bio)sensor applications. The pastes used for deposition of the successive layers are based on a polymeric binder with metallic dispersions or graphite, and can also contain functional materials such as cofactors, stabilizers and mediators. More recently metal nanoparticles, nanowires and carbon nanotubes have also been included either in these pastes or as a later stage on the working electrode. This review will summarize the use of nanomaterials to improve the electrochemical sensing capability of screen-printed sensors. It will cover mainly disposable sensors and biosensors for biomedical interest and toxicity monitoring, compiling recent examples where several types of metallic and carbon-based nanostructures are responsible for enhancing the performance of these devices.

Copyright © 2009 Elena Jubete et al. This is an open access article distributed under the Creative Commons Attribution License, which permits unrestricted use, distribution, and reproduction in any medium, provided the original work is properly cited.

1. Introducing Screen Printing Technology and the Applications of Nanomaterials in Screen Printed Electrodes (SPEs)

Screen printing technology is a low-cost thick film process that has been widely used in artistic applications and more recently in the production of electronic circuits and sensors. In the 80s the process was adapted to the production of amperometric biosensors [1–4], making their commercialization much easier. This was due to the multiple advantages that the technology offers including reduced expense, flexibility, process automation, reproducibility and wide selection of materials. A huge number of successful electrochemical devices have been built using this technique [5].

The process of screen printing is rapid and simple; it consists of squeezing an ink or paste through a patterned screen onto a substrate held on the reverse of the screen. Successive layers can be deposited by this procedure and repeat patterns can be designed onto the same screen to enhance production speed. The substrate needs to be an inert material, most commonly PVC [6], polycarbonate [7], polyester [8], or

ceramic [9], although nitrocellulose [10] and glass fibre [11] are also employed. Each layer is deposited through the corresponding mask providing a specific pattern. These masks are prepared by a photolithographic technique with photosensitive gels and nylon, polyester or, stainless steel meshes.

There are mainly two types of pastes that can be used in screen printed electrode (SPE) production: conductive or dielectric inks. The conductive inks give rise to the formation of conductive tracks on the electrodes. They are based on an organic binder where gold, silver, platinum or graphite are dispersed at high loads as conducting fillers. Recently water-based inks have also been employed [12–15]. Functional materials can also be part of the formulation such as cofactors, stabilizers and mediators, and more recently nanosized metals and carbon nanotubes. Dielectric inks are often based on polymers or ceramics and form the encapsulating layer of the sensor, delimiting the working area and electric contacts.

Regarding biosensors production via screen printing, the biological component (e.g., enzyme, antibody, nucleic acid) can be added in different ways, giving rise to different

preparation alternatives; the deposition by hand or the electrochemical entrapment after a multilayer deposition process is the most used alternatives. Another possibility is to introduce the biological material in a printing paste, printing it as a last layer on the electrode surface or as a one step deposition layer forming a biocomposite with the rest of the ingredients [16]. However, the incorporation of the biomolecules in screen printing pastes depends on their nature and is not always possible due to the paste drying conditions that can often bring the denaturalization of the biocomponent. Some of the most commonly used configurations for screen-printing enzymatic biosensors were reviewed by Albareda-Sirvent et al. [17]. More recently, arrays have been developed with multiple working electrodes on the same printed strip, for simultaneous electrochemical detection of different analytes including phenol/pesticides [18–20] or several target sequences of hybridization in genosensors, with up to 8 working electrodes on the same strip [21].

The design of new nanoscale materials has found a wide range of applications in the field of sensors, revolutionizing this field. They have also started to find their place in screen printed devices, bringing uncountable benefits. Among them, carbon nanotubes, nanowires and metallic nanoparticles have lately become favorite tools in the sensor area, since they can promote the electron transfer reactions of many molecules, lower the working potential of the sensor, increase the reaction rate, improve the sensibility, or in case of biosensors, contribute to a longer stability of the biocomponent. In genosensors and aptasensors the metallic nanoparticles can serve also as electroactive labels for electrochemical stripping techniques (e.g., stripping voltammetry, stripping potentiometric detection). Nanowires have also received considerable attention in nanoscale electronics and sensing devices [22–26], due to their high aspect ratios, capability of multisegmented synthesis, and surface modification compatibility. Recent research supports that nanowires can be applied in biofuelcells [27], adaptive sensors [28], and enzymes-based electrochemical sensors [29, 30]. They are also interesting tools for magnetic control of electrochemical reactivity or to adapt on demand (bio)electrocatalytic transformations as it was shown for ethanol/methanol [29] and glucose detection [27, 31].

The incorporation of nanomaterials in SPEs can be done following different alternative strategies. In most of the cases the addition of nanoparticles or nanotubes into screen printed inks, although possible [32], is not an easy task. In spite of not suffering from temperature stability problems in the same extent as enzymes or nucleic acids, they are insoluble in many solvents that constitute the matrix of screen printing pastes. For these reasons, other methods have been developed that are applied after the printing. These postprinting modifications include drop casting of the working electrode with nanotubes dispersed in DMF/water [33], Nafion [34], polyethylenimine [35], or DMSO [36], or electrodeposition of metallic particles [37]. More examples will be discussed in the following sections.

There are many good reviews concerning the preparation and application of nanomaterials in electrochemical sensors

[38–50]. However, there are scarce references on them to screen printed devices as electrodic material to support these nanomaterials. On the other hand, there are articles reviewing advances in SPE sensors [16, 51–57], but their content on applications of nanomaterials into these types of sensors is limited. In any case, there is no review, to the best of the authors' knowledge, dedicated exclusively to the application of nanotechnology to screen printed sensors. The following sections will be addressed to meet this need, covering examples of practical applications of screen printed sensors in the clinical and environmental field, explaining their basic principles and recent improvements with the use of nanotechnology.

2. SPE in Clinical Diagnosis

2.1. Glucose. Due to the prevalence of diabetes in the developed nations, 85% of the current market of biosensors is aimed to glucose monitoring, resulting in more than \$5 billion expense [58]. Disposable screen-printed biosensors are widely employed to address this need of frequent glucose monitoring in diabetics, and they are also used in food industry for quality control. They show a superior performance compared to reflectance devices since they give a rapid and accurate answer using disposable strips with no risk of instrument contamination. This shift toward electrochemical sensing has already been accounted for companies like Roche Diagnostics, Lifescan, Abott, and Bayer giving rise to more than 40 blood glucose meters on the market.

The majority of these devices are based on screen-printed carbon electrodes modified with the enzyme glucose oxidase (GOX), which oxidizes glucose to gluconic acid. In these systems, the presence of a mediator is needed to achieve direct electron exchange between the electrode and the redox centers of GOX, since these centers are situated in the interior of an insulating glucoprotein shell which prevents the direct process [59]. There are two major types of mediators: hydrogen peroxide oxidation mediating reagents and enzymatic glucose oxidation mediating reagents. The first type is employed in sensors where the oxygen participates actively in the oxidation of glucose catalyzed by glucose oxidase forming gluconic acid and H_2O_2 . Reduction or oxidation of H_2O_2 occurs at high potential in nonmediated electrodes. Therefore, mediators are employed in this type of glucose biosensors to lower such potentials. This is the case of prussian blue (PB) [60–64]). Instead of these mediators, metallized carbon can also be used in the working electrode as the dispersed metal particles have shown favorable catalytic activity to oxidation and reduction of H_2O_2 . The second type of mediators, the artificial mediating reagents, offers the advantage of not requiring oxygen in the system, which is the limiting reagent in the first type of systems and thereby lowering their sensitivities.

The use of nanotechnology has served to improve both types of systems. As mentioned previously, dispersed metal particles can be used to diminish the oxidation potential of H_2O_2 in glucose sensing without the need of mediators. If these particles are in the “nano” range, cannot only the potential be decreased but also the sensitivity enhanced. Shen

et al. [32] reached this effect very recently by adding iridium nanoparticles on a screen-printable homemade carbon ink based on hydroxyethyl cellulose, polyethylenimine and a commercial carbon material. They first made a study of feasibility applying this ink on the working electrode of a 3-electrode configuration. Over the printed working electrode the enzyme (GOX) was covalently attached via glutaraldehyde. They passed subsequently to successful mini disposable electrodes with a 3-electrode configuration, with a working diameter of 1 mm. These minielectrodes responded linearly to glucose between 0 to 15 mM and needed as little as 2 μ L Sample volume.

Zuo et al. [65] used a silver nanoparticles-doped silica sol-gel and polyvinyl alcohol hybrid film on a PB-modified screen-printed electrode to immobilize GOX. Although they did not avoid the use of the mediator for H₂O₂ detection (PB), they doubled the sensitivity of the sensor comparing with the biosensor without nanoparticles. The immobilized GOX remained with a 91% activity for 30 days in buffer.

The synthesis, characterization and immobilization of PB nanoparticles of 5 nm diameter have been reported [66] as mediators in Indium Tin Oxide (ITO) electrodes for the amperometric detection of H₂O₂. A similar strategy could be applied to SPE for the H₂O₂-based glucose detection.

Some other examples of nanomaterials for glucose sensing are applied to biosensors that do not require the formation of H₂O₂. Guan et al. [67] dispersed multiwalled carbon nanotubes (MWCNTs) within mineral oil following the procedure described by Rubianes and Rivas [68]. They mixed the MWCNT dispersion with an enzymatic solution of glucose GOX in citrate buffer and potassium ferrocyanide and deposited a drop of the mix over the working electrode of screen-printed electrodes. After the drop dried they tested these electrodes (several types varying the mixing time for enzyme/MWCNT) and compared them with the corresponding type without MWCNT. It was shown that the best response toward glucose was obtained in the systems where the MWCNTs were present and had been mixed with the enzymatic solution during 30 minutes before deposition. Longer mixing time would lead to axial electron transfer. A wider linear response range and higher sensitivity was reached when the MWCNTs were present.

Lu and Chen [69] drop-coated also the working electrode of their screen-printed strips with a solution containing magnetite nanoparticles (Fe₃O₄) with ferricyanide. In this case, the enzyme (GOX) was added in a later stage, after the nanoparticle-containing drop had dried. Sensitivity of 1.74 μ A mM⁻¹ was achieved. Rossi et al. [70] prepared and functionalized Fe₃O₄ nanoparticles with amino groups to link them covalently with GOX. The GOX-coated magnetite maintained the enzymatic activity for up to 3 months. Although they could have applied this modified enzyme in screen-printed sensors, they opted for quantifying the oxygen consumption from the transformation of glucose to gluconic acid catalyzed by this enzyme by measuring the increase of the steady state fluorescence intensity of Ru(phen)₃. This consumption of oxygen increased with the glucose concentration so glucose was able to be monitored without any surface of sensing material but directly in the

solution. In spite of being an elegant approach, a digital fluorescence imaging system was required, which is a more sophisticated piece of equipment than a small portable potentiostat.

Gao et al. [71, 72] built and patented a nanocomposite membrane to be screen printed into a carbon strip using an aqueous slurry ink of a diffusional polymeric mediator (polyvinyl ferrocene coacrylamide) on a PVPAC binder and alumina nanoparticles. The nanoparticulate membrane served not only as biosensing media but also for analyte regulating functions.

Wang et al. [27] reported the possibility of modulating the electrochemical reactivity toward glucose and methanol of a screen-printed working electrode using nickel nanowires. A screen-printed carbon strip served as the working electrode and was limited by a glass cylinder to form an electrochemical cell. An Ag/AgCl and platinum wire were used as reference and counter electrodes, respectively. The nanowires were previously grown by electrodeposition into nanopores of alumina membranes, then removed from the templates, washed and stored in a KOH solution until their use. After being magnetically separated from the storing solution, they were dispersed in a NaOH solution used as electrolyte and placed in the homemade electrochemical cell. The modulation of the magnetic field was performed by placing a small magnet under the working electrode surface. The magnetic properties of nickel and its catalytical action toward aliphatic alcohols and carbohydrates entitled this action, and an enhancement of the electrochemical signal was observed when the nickel nanowires were vertically oriented with a magnetic field. Similarly, when the nanowires were magnetically orientated in a horizontal position the enhancement was produced to a lesser extent. Moreover, such modulated redox transformation was observed multiple times, upon repetitive changes of surface orientation.

2.2. Cholesterol. The alarming increase of clinical disorders such as hypertension, heart related illnesses, cerebral thrombosis, arteriosclerosis, and coronary artery disease. due to abnormal levels of cholesterol in blood have stimulated the development of biosensors with the purpose of quantifying the levels of this compound. Besides, the quality control and nutritional labelling of foods in the food stuff industry is another application for the measurement of cholesterol [73, 74].

The biosensing element most commonly used in cholesterol biosensors is cholesterol oxidase (ChOx), which can be immobilized in the working electrode of screen-printed sensor, catalyzing the conversion of cholesterol in presence of oxygen and water into 4 cholestene-3 one and hydrogen peroxide. As in the case of glucose biosensing, amperometric measurements of hydrogen peroxide are often monitored, and here the high potential also causes interferential problems (ascorbic acid, uric acid and other easily oxidizable species); so mediators are also required. Some commonly used mediators in cholesterol sensing are cobalt phtalocianine [75], ferrocene derivatives [76] and phenothiazine derivatives [77]. Another possibility is also to add a mediator for cathodic determination of H₂O₂ such as prussian blue

(PB) [78], titanium dioxide [79] or metal hexacyanoferrate [80]. As in glucose sensing, there is also a possibility to avoid the route of H_2O_2 production; in this case peroxidase (POD) can be combined with ChOx with potassium ferrocyanide. The drawback of this last route can be that the air oxidation of ferrocyanide is taking place as a competitive reaction of the enzymatic oxidation since it can affect the system.

Several matrices have been employed to construct cholesterol sensors including glassy carbon or gold electrodes, graphite-Teflon, tungsten wire, ITO-coated glass and porous silicon. Advances implemented on these electrodes for cholesterol detection have been recently reviewed for Arya et al. [81], including the application of nanomaterials. However, there are only a few reports that focus on the development of disposable cholesterol biosensor. For example, in Arya's review only three out of one hundred cited references were based on screen-printed electrodes, two of them containing nanoparticles. This is an example of how the application of nanomaterials on screen-printed cholesterol sensors is a field that is yet starting.

A collaboration between Italian and Russian scientists has led to applications of gold nanoparticles [82] and very recently MWCNT [83] on screen-printed rhodium graphite electrodes for cholesterol detection. In both cases they did not use ChOx but opted for another enzyme, cytochrome P450scc, for its specific catalysis of cholesterol side chain. An interesting review on applications of this enzymatic family in biosensors can be found [84].

The same scientists had previously built a cholesterol sensor with this enzyme in SPE but without nanoparticles, by immobilisation of cytochrome P450scc biomolecule with glutaldehyde or agarose hydrogels over the rhodium-graphite working area [85]. This sensor needed the use of a mediator for electronic transfer: riboflavin. By drop coating the working area with gold nanoparticles suspended in chloroform, they converted the electrode into a nonmediated system, since the roughness of the surface was enough to penetrate the protein matrix, reaching a sensitivity for cholesterol of $0.13 \mu\text{A} \mu\text{M}^{-1}$. The addition of MWCNT to the electrode prior to the deposition of the electron transfer, P450scc enzyme, once the enzyme had been immobilized, would increase sensitivity more than 17 times with respect to bare electrodes, or 2.4 times with respect to the electrode containing gold nanoparticles. This catalytic effect is shown in Figure 1. Although the sensitivity to cholesterol was of the same order as using the gold nanoparticles, the linearity in the response improved significantly in the range of 10 to $80 \mu\text{M}$.

Li et al. [86] also proved the electron transfer improvement with MWCNT in an electrode containing ferrocyanide, POD, ChOx and cholesterol esterase. They performed clinical trials in blood of 31 patients with the biosensor showing fairly good correlation between this method and the results obtained by a clinical blood analyzer.

2.3. Hybridization Sensors. The detection of specific sequences of DNA is a booming field due to its applications for diagnosis of pathogenic and genetic diseases, forensic analysis, drug screening and environmental testing. Different

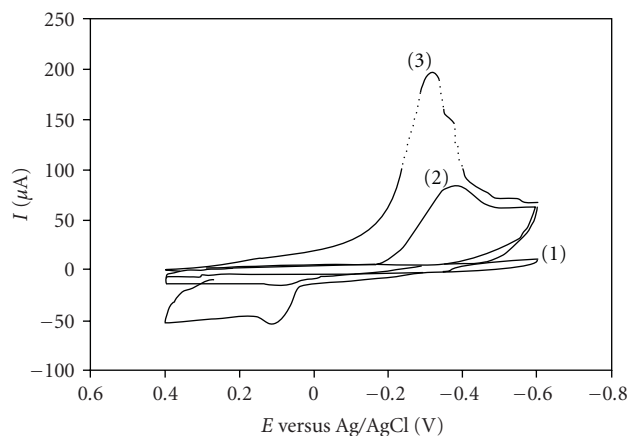


FIGURE 1: Cyclic voltammograms of screen-printed bare rhodium-graphite electrode for cholesterol detection (1), on electrodes modified with Au nanoparticles and P450scc (2), or with multi-walled carbon nanotubes and P450scc (3). Experiments were performed under aerobic conditions, 100 mM phosphate buffer, 50 mM KCl, pH 7.4, and the scan rate was 50 mV s^{-1} . With permission from [83].

strategies can be used for the detection of DNA in sensors, among them the most useful tools are the intrinsic electroactivity of nucleic acids [87], the use of DNA duplex intercalators [88], the labelling with enzymes [89], or the addition of electroactive markers [90].

Metallic nanoparticles (NPs) have emerged as appealing electroactive markers in electrochemical sensors, especially in stripping voltammetry. This technique is cheap, simple and fast in comparison with optical methods in which commercial DNA chips are based. Another advantage of the use of nanoparticles in DNA hybridization sensors is their multiplexing capability, being able to recognize different molecules in the same sample due to the distinct voltammetric waves produced by different electrochemical tracers [91]. Additionally, their life cycle is much longer than other markers, making their use even more attractive.

Although most of the work of application of metallic nanoparticles for DNA recognition events is performed in other types of electrodes (e.g., gold disks [92], glassy carbon electrodes [93], graphite-epoxy composite electrodes [94], pencil graphite electrode [95]) some examples have emerged regarding the use of SPE in combination with elements from nanotechnology and will be studied in the following paragraphs.

Wang et al. [96] developed a hybridization assay employing a combination of electrodes: a probe-modified gold surface and an SPE. The method was based on the electrostatic collection of silver cations along the DNA duplex, the reductive formation of silver nanoclusters along the DNA backbone, the dissolution of the silver aggregate with a nitric acid solution and the stripping voltammetry detection of the dissolved silver with the SPE. A scheme of the working protocol is shown in Figure 2.

DNA segments related with the BRCA breast-cancer gene were detected to concentrations as low as 200 ng/mL

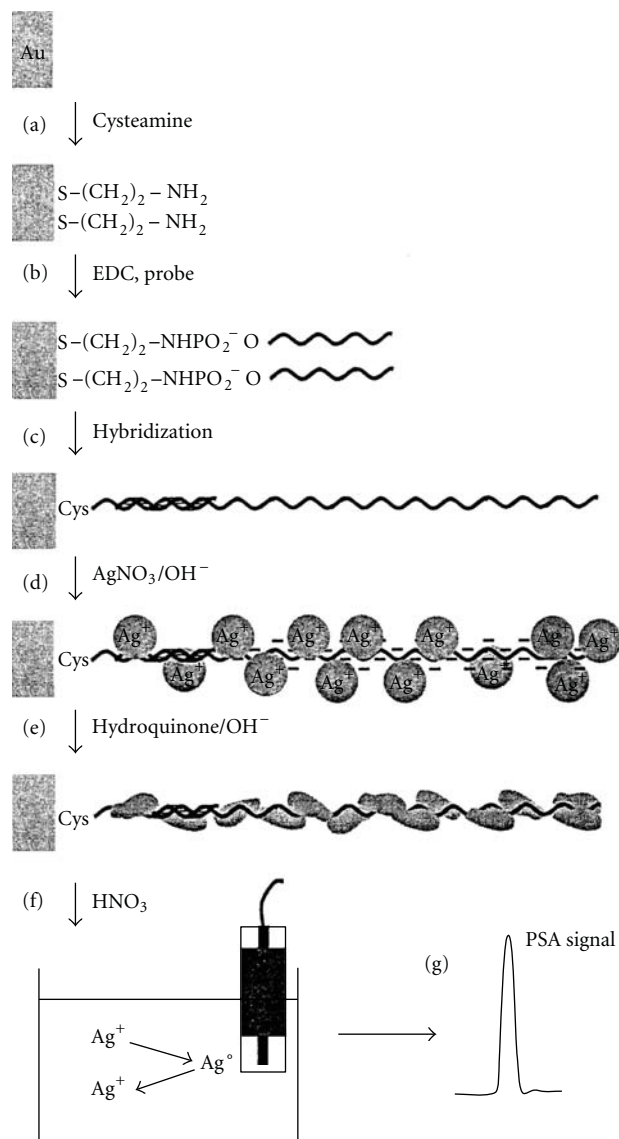


FIGURE 2: Immobilization and analytical protocol for DNA hybridization detection. (a) Formation of self-assembled cysteamine monolayer, (b) immobilization of ssDNA probe, (c) hybridization of complementary target, (d) "loading" of the silver ion to DNA, (e) hydroquinone-catalyzed reduction of silver ions to form silver aggregates on the DNA backbone, (f) dissolution of the silver aggregates in nitric acid (50%) and transfer to the detection cell, (g) stripping potentiometric detection with SPE. From [96] with the permission of Elsevier.

with an original strategy developed also by Wang et al. [97]. It was based on the use of magnetic particles as tools to perform DNA hybridization. The assay involved the hybridization of a target oligonucleotide to probe-coated magnetic beads, followed by binding of the streptavidin-coated gold nanoparticles to the capture target and catalytic silver precipitation on the gold-particle tags. The DNA-linked particle assembly was then magnetically collected onto a screen printing electrode surface with a permanent magnet positioned below. This way a direct contact between

the silver tag with the surface was managed and the solid-state electrochemical transduction was enabled. This silver aggregate did not form in the presence of only noncomplementary DNA. The described method did not require acidic solution or metal deposition of the silver, so the time needed for the assay was reduced. This technique of combined magnetism and metal detection is now used frequently for DNA hybridization detection not only for screen-printed sensors but also with other electrodic supports.

Suprun et al. [98] recently published the design of an SPE with gold nanoparticles (AuNPs) included in its surface as an electrochemical sensing platform of interactions from the protein thrombin and the thrombin binding aptamer. The nanostructured DNA aptasensor had the aptamer immobilized to the AuNP by avidin-biotin linkages. Detection of a binding between aptamer (APT) and thrombin was performed by introducing the aliquots of the targets and binding-buffer onto the electrodes. The difference between cathodic peak areas in the system SPE/AuNP/ APT/ thrombin and in the SPE/ AuNP/ APT/ buffer was measured in a stripping voltammetry with $E_{\text{ox}} = +1.2 \text{ V}$, and a calibration curve was built for different thrombin concentrations. The thrombin detection limit was 10^{-9} M .

The same detection limit (10^{-9} M) was also found for a thrombin biosensor designed by Kerman and Tamiya [99]. They developed an aptamer-based sandwich assay where the primary aptamer was immobilized on the surface of the SPE and the secondary aptamer on the AuNP. The electrochemical reduction current response of the Au nanoparticles was monitored to quantify detection of thrombin.

Gold nanoparticles and stripping voltammetry were employed by Authier et al. [95] for the quantitative detection of amplified human cytomegalovirus (HCMV) DNA. In this case it was only the oligonucleotide probe which was marked with gold nanoparticles. The detection was permitted after the release of the gold metal atoms anchored on the hybrids by oxidative metal dissolution, given rise to a response with anodic stripping voltammetry at a sandwich type screen printed microband electrode. With this technique it was possible to detect 5 pM-amplified HCMV DNA fragment.

2.4. Drugs Determination. New applications for SPE are emerging for determination of drugs in the pharmaceutical and biomedical fields. Recently Shih et al. [100] determined codeine, an effective analgesic and antitussive agent in pharmaceutical preparations. They developed a nontronite clay-modified screen-printed carbon electrode that detected codeine in urine by square wave stripping voltammetry. The codeine quantification was achieved by measuring the oxidation peak after background subtraction in voltammograms run between 0.6 and 1.3 V at a square wave frequency of 15 Hz and amplitude of 45 mV. Under these conditions they found linearity for codeine detection in the range of 2.5 to 45 μM .

Burgoa Calvo et al. [101] developed a silver nanoparticle-modified carbon SPE to detect lamotrigine (LTG), a new generation antiepileptic drug for treatment of patients with refractory partial seizures or without secondary generalization. They determined LTG by differential pulse adsorptive

stripping voltammetry with a detection limit of 3.7×10^{-7} M. The SPE used was modified with silver nanoparticles that had been electrodeposited from AgNO_3 in an acidic Britton-Robison solution by accumulating potential during a time under stirring. They studied different parameters of silver deposition to optimize the intensity of the reduction peak at -1.06 V needed for the LTG quantification. Good agreement was found between the level stated by the manufacturer of commercial capsules and the one measured by the biosensor.

Enzymatic amperometric sensors with gold nanoparticles have just been developed [102] for the determination of Phenobarbital, a first generation of anticonvulsant drug widely used to treat epilepsy. Different electrode preparation methods were evaluated to immobilize covalently the enzyme, cytochrome P450 2B4. The best results were obtained in gold SPE modified with electrodeposited gold nanoparticles and with the cytochrome attached covalently by Mercapto Propionic Acid/ N-hydroxysuccinimide with N-(3-dimethylamino)propyl)-N'-ethylcarbodiimide hydrochloride, or in carbon SPE functionalised with diazonium salt. The former covalent attachment in gold SPE without nanoparticles did not give any response to Phenobarbital. The same research group detected another antiepileptic drug, leveticeratum, by carbon screen-printed electrodes [103] but in this case without modification by nanoparticles, using peroxidase immobilization by pyrrole electropolymerization.

Martinez et al. [104] designed an MWCNT-modified SPE for Methimazole (MT) determination in pharmaceutical formulations. MT is used as a drug to manage hyperthyroidism associated with Grave's disease, but it has side effects as possible decrease of white blood cells in the blood. The designed sensor consisted of a rotating disk together with an MWCNT-modified graphite SPE (the working electrode was drop casted with a dispersion of the MWCNT in a mixture of methanol, water and Nafion). The rotating disk contained tyrosinase immobilized in its surface, which catalyzed the oxidation of catechol (C) to o-benzoquinone (BQ). The back electrochemical reduction of BQ was detected on MWCNT-modified graphite SPE at -150 mV versus Ag/AgCl/NaCl 3 M. Thus, when MT was added to the solution, this thiol-containing compound participate in Michael type addition reactions with BQ to form the corresponding thioquinone derivatives, decreasing the reduction current obtained proportionally to the increase of its concentration. This method made possible the determination of MT for concentrations from 0.074 to $63.5 \mu\text{M}$ with a reproducibility of 3.5%.

2.5. Ethanol Quantification. Quantification of ethanol is useful not only in clinical diagnostic analyses but also in fermentation and distillation processes. The amperometric biosensing response of ethanol can be based in two approaches: using alcohol oxidase (AOX) or alcohol dehydrogenase (ADH) as catalytic enzyme [52]. In the first case AOX is employed to catalyze the formation of aldehydes and H_2O_2 by oxidizing low molecular alcohols with O_2 . The electrochemical response would be given by the mediated oxidation of H_2O_2 , as in other biosensoric

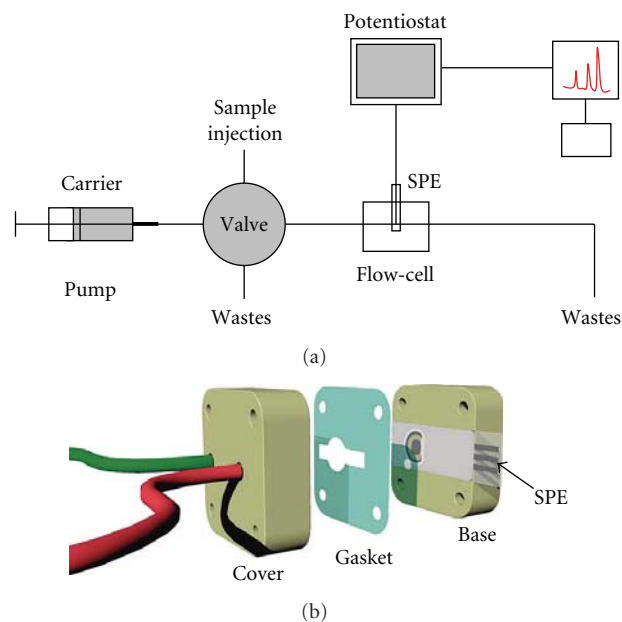
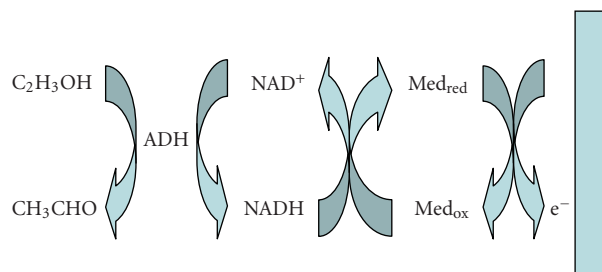


FIGURE 3: (a) Schematic diagram of the flow-injection sensing system. (b) 3D image of the electrochemical flow-cell containing the modified SPE. With permission from [106].



SCHEME 1: Detection of ethanol at the biosensor surface catalyzed by alcohol dehydrogenase (ADH).

detections (glucose, cholesterol). This is the case of the screen-printed sensor designed to determine ethanol in beer, built by Boujtita et al. [105], using cobalt phthalocyanine as mediator.

The second approach uses the action of the enzyme ADH catalyzing the oxidation of ethanol or other primary alcohols (excepting methanol) following Scheme 1. This mechanism was used by Liao et al. [107] to built an ethanol biosensor with ferricyanide-magnetite nanoparticles as mediator. They used the two-step immobilization method that Lu and Chen [69] had previously employed for glucose sensing. The method involved drop coating the carbon working electrode with a mix of Fe_3O_4 and ferricyanide, drying this layer at high temperature, and posterior addition of the enzyme in buffer (in this case ADH from baker's yeast (YADH) and NAD^+). The NAD^+ -YADH/Ferri- Fe_3O_4 based biosensor worked at 200 mV and showed excellent sensitivity for ethanol in buffer: $0.61 \mu\text{A mM}^{-1}$.

The use of nickel nanowires with SPE for ethanol/glucose detection was previously revised in the Section 2.1. Additionally, multi-segmented nickel-gold-nickel nanowires were recently employed in the detection of ethanol [29]. The principle of use was similar to the procedure reported for glucose/ethanol [27], but in this case the electrodic support to control magnetically the orientation of the nanowires was not a screen printed electrode but a glassy carbon disk.

3. SPE for Detection of Environmental Pollutants

3.1. Hybridization Sensors. The use of organophosphorus and carbamate pesticides in agriculture has risen exponentially in the last decade causing public concern regarding the environment and food safety. For this reason, many examples of screen-printed electrodes have been proposed for detection of pesticides to substitute other techniques such as HPLC that require trained personnel and can be time consuming and tedious. Most of the screen-printed biosensors are enzymatic systems based on cholinesterase (ChE) inhibition, alone or in combination with choline oxidase (CHO), or noninhibition systems based on organophosphorus hydrolase (OPH). However the applications of the later are quite limited since OPH is not a commercial enzyme. Few examples have also been reported using tyrosinase as biocomponent.

Andreescu and Marty [108] compiled in a good review the advances in cholinesterase biosensors, describing immobilization procedures, different designs and configurations including screen printing electrodes and practical applications. However, there is only one reference related to the use of nanomaterials on pesticide detection with SPE. The appearance of more work in this area will entitle us to complete that work.

Lin et al. [109] modified in 2003 the classical system of amperometric bienzymatic biosensor for pesticide detection that was used from the late 1980s (see Scheme 2) applying multiwalled carbon nanotubes covalently linked to the enzymes. The MWCNT were dispersed in DMF and dried over the carbon working area of the screenprinted electrode; they created carboxylic groups in their surface. Both enzymes were then immobilized by forming amide linkages with the MWCNT using 1-ethyl-3-(3-dimethylaminopropyl) carbodiimide (EDC) as coupling agent. Performing amperometric detections at 500 mV parathion was detected in buffer, without the use of mediators obtaining a linear calibration curve from 50 to 200 μM and a low detection limit of 0.05 μM .

Cai and Du [110] reported very recently the detection of Carbaryl using an MWCNT-based composite in screen-printed carbon electrodes. The nanotube containing composite was used to modify the other classic approach of pesticide detection: the monoenzymatic approach using cholinesterase to catalyze the hydrolysis of thiocholine (see Scheme 3). Since thiocholine is already electroactive, its oxidation is the reaction to be studied, without the need of a second enzyme. When pesticides are present they inhibit the

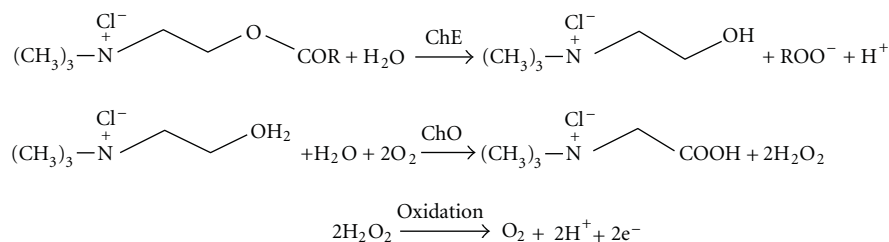
catalysis of thiocholine formation and a decrease in the signal is observed. Classically, this approach is used with mediators in the system (CoPh, PB) and the amperometric study of thiocholine oxidation can be performed at a low oxidation potential such as 100 mV. However, Cai and Du, avoided the use of mediators with the use of the MWCN-cross-linked cellulose acetate composite, with the cholinesterase covalently bounded to it. This was possible due to the catalytical activity of the nanotubes toward the oxidation of the enzymatically produced thiocholine. The percentage of inhibition of the thiocholine oxidation signal for different concentrations of Carbaryl was obtained by quantifying the peak current at the 535 mV oxidation peak that appeared in cyclic voltammetry before and after inhibition. The detection limit of this sensor for Carbaryl was 0.004 $\mu\text{g}/\text{mL}$ concentration (equivalent to a 10% decrease in signal).

A carbon nanotube-modified screen-printed sensor combined with a flow-injection system has been built very recently [106] for the assessment of salivary cholinesterase enzyme activity as an exposure biomarker of pesticides. The modification of the carbon screen-printed electrode was performed by drop casting of an aqueous dispersion of MWCNT, leaving it to dry naturally over the working electrode. A diagram of the flow injection system with the incorporated SPE is shown in Figure 3. A quick and noninvasive approach was reached to determine pesticide exposure by measuring the activity of cholinesterase in rat saliva via the electrochemical monitoring of oxidation of thiocholine production (see Figure 3). In this case the enzyme is not immobilized in the SPE but present in the saliva.

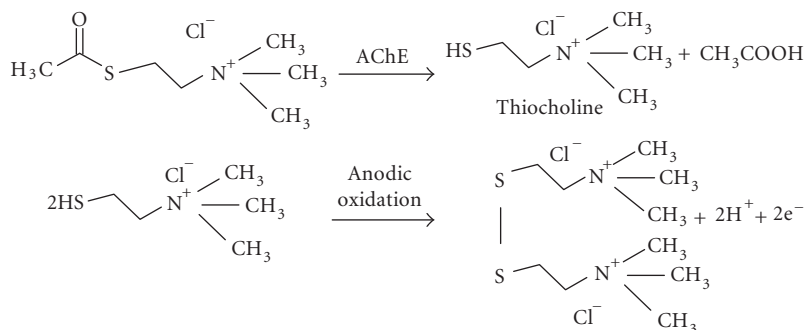
3.2. Metals. Although essential metals play an integral role in the life processes of living organisms being catalysts in biochemical reactions or essential nutrients, some other metals have no biological role (such as silver, aluminium, cadmium, gold, lead and mercury). High concentrations of most metals, regardless of being essential or nonessential are toxic for living cells [111]. Thus, there is a growing demand for rapid, inexpensive and reliable sensors for measurement of metals not only in the environment but also in biomedical and industrial samples. In this sense, SPE can be of great use for metal detection since it has been proved that they give comparable results to those obtained by more expensive, laboratory-based techniques [112].

In the past five years, research has been developed on the use of the enzyme urease as biorecognition element in screen-printed biosensors for the detection of metal ions [113–115]. However, no records have been found for urease inhibition-based SPE containing metallic- or carbon-based nanomaterials.

On the other hand, there are many other examples of screen-printed sensors without including any enzyme or biorecognition element (i.e., sensors, not biosensors) for metallic ion detection (see Figure 4) and some of them have seen improvements by the incorporation of nanomaterials. This section will focus on them. In most of the cases they are based on voltammetric stripping analysis, a technique that traditionally was undertaken by Hg electrodes and



SCHEME 2: First generation bi-enzymatic ChE/ChO amperometric biosensor [108]. With permission from Elsevier.



SCHEME 3: Approach used in monoenzymatic electrodes. In presence of pesticides the catalytic formation of thiocholine is partially inhibited and less electrochemical response is obtained for the oxidation of thiocholine.

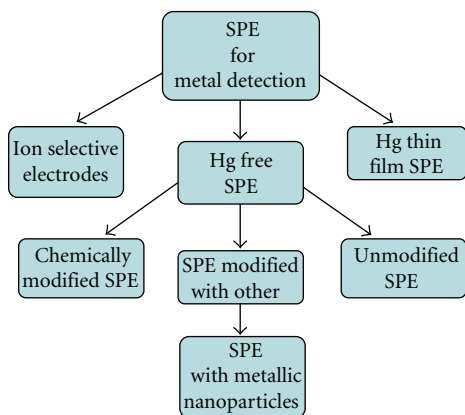


FIGURE 4: Different approaches for detection of metals with screen-printed electrodes.

that is one of the most sensitive alternatives for metal ion determination.

Domínguez-Renedo et al. [37] have recently published the detection of chromium (VI), a strong carcinogenic and toxic species, by means of an SPE modified by electrochemical deposition of metallic nanoparticles. Both gold and silver nanoparticle-modified electrodes were tested toward Cr (VI) by differential pulse voltammetry. For the electrode preparation, the silver deposition was similar to the procedure described by this group for lamotrigine detection [101] (see Section 2.4). For the electrodes that were modified

with gold nanoparticles, a solution of 0.5 M H_2SO_4 containing 0.1 mM of AuClO_4 was used for the electrochemical deposition of gold at the graphite working electrode, at a potential of 0.18 V during 200 seconds. While the best results in terms of sensibility (4×10^{-7} M) and reproducibility (%RSD = 3.2) were obtained by the gold nanomodified sensors, the silver-modified ones offered no interference in presence of any tested metallic ion (gold-modified sensors showed interference with Cu(II) in concentrations higher than 10^{-5} M).

The same preparation techniques for silver and gold nanoparticles in SPE were employed a year earlier to detect Sb (III) [116, 117]. In that case, the detection was performed using anodic stripping voltammetry. A sensitivity of 6.8×10^{-10} M was reached in the case of silver nanoparticles, while 9.4×10^{-10} M was measured in the case of gold nanoparticles. Common interferants in anodic stripping voltammetry (such as bismuth) did not affect the electrochemical response of these sensors.

Nanogold-modified SPEs were also employed to detect As(III) [118]. In this case the working electrode was previously treated with Triton X-100 solution. The gold-nanoparticles were obtained dissolving poly (L-lactide) in THF containing HAuCl_4 with posterior addition of NaBH_4 . The poly-L-lactide-established nanoparticles were then drop coated on the pretreated working electrode. Differential pulse anodic stripping voltammetry was also used here obtaining a linear calibration curve up to 4 ppb of As(III) with a detection limit ($S/N = 3$) of 0.09 ppb. Using the same types of electrodes, an indirect method to detect traces of

hydrogen sulphide was developed [119] by measuring the inhibited oxidation current of As(III). The detection limit for hydrogen sulphide was 0.04 μM .

3.3. Other Pollutants. Nitrites can contaminate water, foodstuff and environmental matrices by conversion into carcinogenic nitrosamines. Its quantitative determination is therefore of increasing interest. There is a large number of electrochemical sensors developed with this purpose [120–127], some of them including nanomaterials [122–130] but only one example [131] has been encountered using SPE and nanotechnology. The later work consisted of the immobilization of hemoglobin (Hb) into SPE containing colloidal gold nanoparticles incorporated into carbon ink. An unmediated sensor was thus created with sensitivity for nitrites of 0.1 μM . The colloidal gold nanoparticles decreased the background current, improved the conductivity, amplified the electrochemical signal, helped to retain the bioactivity and accelerated the electron transfer rate.

Hydrazine and its derivatives are potential reducing agents of environmental and toxicological significance. The application of SPE for the detection of this compound was performed already in 1995 for Wang and Pamidi [132]. They printed only the working electrode as a strip containing cobalt phthalocyanine or modified with mixed valent ruthenium and detected hydrazine spiked samples with concentrations of 10^{-5} M by amperometric and voltammetric measurements. No biomolecule was required. More recent work [133] includes the application of copper-palladium alloy nanoparticle plated screen-printed electrodes in a flow injection analysis system, reaching a linear detection range of 2–100 μM and a detection limit of 270 nM. The SPE, prepared under successive electrochemical deposition of Cu and Pd, showed and enhanced hydrazine electrocatalytic response at low detection potentials in neutral media.

4. Conclusions and Perspectives

This review has summarized recent applications of nanotechnology in thick film electrochemical sensors. Apart from a revision of the state of the art for this printing technique, the article has gathered different types of screen printing sensing devices by application topic. In every topic a brief introduction has been given to explain the mechanism of detection, followed by examples of nanotechnology applications, emphasizing on the preparation of the (bio)sensor and its response. The reported examples have shown situations where metallic nanoparticles and carbon nanotubes have been valuable for screen-printed sensors in different ways.

- (i) To substitute the use of other mediators, as it was demonstrated with MWCNT or iridium nanoparticles for H_2O_2 detection, substituting prussian blue in glucose sensors, or riboflavin in cholesterol sensors. The same was demonstrated with MWCNT in pesticide detection.
- (ii) As labels or electroactive markers for stripping voltammetry. Metallic nanoparticles were used to improve detection in SPE genosensors, to test drugs, or to detect metallic pollutants in SPE sensors.

- (iii) To retain the bioactivity of enzymes once they have been immobilized in the sensor, as it was the case of gold nanoparticles with hemoglobine in nitrite sensors.
- (iv) To eliminate interferences, as the Au and Ag nanoparticles in Sb sensors, where the interference of bismuth is not observed.
- (v) To improve the sensitivity of the devices. The increase in the surface area of the working electrode generally leads to more sensitive responses.

As summary, the coupling of electrochemical screen-printed sensors with nanoscale materials is being used as a tool for improved sensitivity, longer stability of the bioelement in biosensors and new detection possibilities. The application of nanomaterials in this type of electrochemical devices is still in progress and literature continues to grow and broaden. Although the use of nanotechnology in screen-printed sensors may not be the only key needed to solve some problems faced occasionally by these sensors (e.g., selectivity in some applications), it is certainly a step forward, and the implemented improvements are multiplying the future possibilities of these disposable sensor devices.

References

- [1] P. L. Baumbach, "Electrochemical sensor construction," UK patent no. 2073891, 1981.
- [2] M. Lambrechts, J. Suls, and W. Sansen, "A thick film glucose sensor," in *Proceedings of the 9th Annual Conference of the IEEE Engineering in Medicine and Biology Society (EMBS '87)*, pp. 789–799, Boston, Mass, USA, November 1987.
- [3] D. R. Matthews, R. R. Holman, E. Bown, et al., "Pen-sized digital 30-second blood glucose meter," *The Lancet*, vol. 1, no. 8536, pp. 778–779, 1987.
- [4] C. C. Liu, "Apparatus and method for sensing species, substances and substrates using oxidase," US Patent 4655880, 1987.
- [5] X.-E. Zhang, "Screen printing methods for biosensor production," in *Biosensors*, J. Cooper and T. Cass, Eds., pp. 41–58, Oxford University Press, Oxford, UK, 2nd edition, 2004.
- [6] S. Andreescu, L. Barthelmebs, and J.-L. Marty, "Immobilization of acetylcholinesterase on screen-printed electrodes: comparative study between three immobilization methods and applications to the detection of organophosphorus insecticides," *Analytica Chimica Acta*, vol. 464, no. 2, pp. 171–180, 2002.
- [7] S. Sánchez, M. Pumera, E. Cabruja, and E. Fàbregas, "Carbon nanotube/polysulfone composite screen-printed electrochemical enzyme biosensors," *Analyst*, vol. 132, no. 2, pp. 142–147, 2007.
- [8] F. Arduini, F. Ricci, C. S. Tuta, D. Moscone, A. Amine, and G. Palleschi, "Detection of carbamic and organophosphorous pesticides in water samples using a cholinesterase biosensor based on Prussian Blue-modified screen-printed electrode," *Analytica Chimica Acta*, vol. 580, no. 2, pp. 155–162, 2006.
- [9] H. Sántha, R. Dobay, and G. Harsányi, "Amperometric uric acid biosensors fabricated of various types of uricase enzymes," *IEEE Sensors Journal*, vol. 3, no. 3, pp. 282–287, 2003.

- [10] G. Cui, S. J. Kim, S. H. Choi, H. Nam, G. S. Cha, and K.-J. Paeng, "A disposable amperometric sensor screen printed on a nitrocellulose strip: a glucose biosensor employing lead oxide as an interference-removing agent," *Analytical Chemistry*, vol. 72, no. 8, pp. 1925–1929, 2000.
- [11] C. A. Galán-Vidal, J. Muñoz, C. Domínguez, and S. Alegret, "Glucose biosensor strip in a three electrode configuration based on composite and biocomposite materials applied by planar thick film technology," *Sensors and Actuators B*, vol. 52, no. 3, pp. 257–263, 1998.
- [12] F. J. Rawson, W. M. Purcell, J. Xu, et al., "A microband lactate biosensor fabricated using a water-based screen-printed carbon ink," *Talanta*, vol. 77, no. 3, pp. 1149–1154, 2009.
- [13] R. M. Pemberton, R. Pittson, N. Biddle, and J. P. Hart, "Fabrication of microband glucose biosensors using a screen-printing water-based carbon ink and their application in serum analysis," *Biosensors & Bioelectronics*, vol. 24, no. 5, pp. 1246–1252, 2009.
- [14] E. Crouch, D. C. Cowell, S. Hoskins, R. W. Pittson, and J. P. Hart, "Amperometric, screen-printed, glucose biosensor for analysis of human plasma samples using a biocomposite water-based carbon ink incorporating glucose oxidase," *Analytical Biochemistry*, vol. 347, no. 1, pp. 17–23, 2005.
- [15] E. Crouch, D. C. Cowell, S. Hoskins, R. W. Pittson, and J. P. Hart, "A novel, disposable, screen-printed amperometric biosensor for glucose in serum fabricated using a water-based carbon ink," *Biosensors & Bioelectronics*, vol. 21, no. 5, pp. 712–718, 2005.
- [16] M. Tudorache and C. Bala, "Biosensors based on screen-printing technology, and their applications in environmental and food analysis," *Analytical and Bioanalytical Chemistry*, vol. 388, no. 3, pp. 565–578, 2007.
- [17] M. Albareda-Sirvent, A. Merkoçi, and S. Alegret, "Configurations used in the design of screen-printed enzymatic biosensors. A review," *Sensors and Actuators B*, vol. 69, no. 1, pp. 153–163, 2000.
- [18] R. Solná, S. Sapelnikova, P. Skládal, et al., "Multienzyme electrochemical array sensor for determination of phenols and pesticides," *Talanta*, vol. 65, no. 2, pp. 349–357, 2005.
- [19] R. Solná, E. Dock, A. Christenson, et al., "Amperometric screen-printed biosensor arrays with co-immobilised oxidoreductases and cholinesterases," *Analytica Chimica Acta*, vol. 528, no. 1, pp. 9–19, 2005.
- [20] A. Crew, J. P. Hart, R. Wedge, J. L. Marty, and D. Fournier, "A screen-printed, amperometric, biosensor array for the detection of organophosphate pesticides based on inhibition of wild type, and mutant acetylcholinesterases, from *Drosophila melanogaster*," *Analytical Letters*, vol. 37, no. 8, pp. 1601–1610, 2004.
- [21] S. Laschi, I. Palchetti, G. Marrazza, and M. Mascini, "Development of disposable low density screen-printed electrode arrays for simultaneous electrochemical measurements of the hybridisation reaction," *Journal of Electroanalytical Chemistry*, vol. 593, no. 1–2, pp. 211–218, 2006.
- [22] I. Willner, R. Baron, and B. Willner, "Integrated nanoparticle-biomolecule systems for biosensing and bioelectronics," *Biosensors & Bioelectronics*, vol. 22, no. 9–10, pp. 1841–1852, 2007.
- [23] V. A. Pedrosa, X. Luo, J. Burdick, and J. Wang, "Nanofingers" based on binary gold-polypyrrole nanowires," *Small*, vol. 4, no. 6, pp. 738–741, 2008.
- [24] T. J. Morrow, M. Li, J. Kim, T. S. Mayer, and C. D. Keating, "Programmed assembly of DNA-coated nanowire devices," *Science*, vol. 323, no. 5912, p. 352, 2009.
- [25] B. He, T. J. Morrow, and C. D. Keating, "Nanowire sensors for multiplexed detection of biomolecules," *Current Opinion in Chemical Biology*, vol. 12, no. 5, pp. 522–528, 2008.
- [26] E. Piccin, R. Laocharoensuk, J. Burdick, E. Carrilho, and J. Wang, "Adaptive nanowires for switchable microchip devices," *Analytical Chemistry*, vol. 79, no. 12, pp. 4720–4723, 2007.
- [27] J. Wang, M. Scampicchio, R. Laocharoensuk, F. Valentini, O. González-García, and J. Burdick, "Magnetic tuning of the electrochemical reactivity through controlled surface orientation of catalytic nanowires," *Journal of the American Chemical Society*, vol. 128, no. 14, pp. 4562–4563, 2006.
- [28] R. Laocharoensuk, A. Bulbarello, S. B. Hocevar, S. Mannino, B. Ogorevc, and J. Wang, "On-demand protection of electrochemical sensors based on adaptive nanowires," *Journal of the American Chemical Society*, vol. 129, no. 25, pp. 7774–7775, 2007.
- [29] R. Laocharoensuk, A. Bulbarello, S. Mannino, and J. Wang, "Adaptive nanowire-nanotube bioelectronic system for on-demand bioelectrocatalytic transformations," *Chemical Communications*, no. 32, pp. 3362–3364, 2007.
- [30] U. Yogeswaran and S.-M. Chen, "A review on the electrochemical sensors and biosensors composed of nanowires as sensing material," *Sensors*, vol. 8, no. 1, pp. 290–313, 2008.
- [31] Ó. A. Loaiza, R. Laocharoensuk, J. Burdick, et al., "Adaptive orientation of multifunctional nanowires for magnetic control of bioelectrocatalytic processes," *Angewandte Chemie International Edition*, vol. 46, no. 9, pp. 1508–1511, 2007.
- [32] J. Shen, L. Dudik, and C.-C. Liu, "An iridium nanoparticles dispersed carbon based thick film electrochemical biosensor and its application for a single use, disposable glucose biosensor," *Sensors and Actuators B*, vol. 125, no. 1, pp. 106–113, 2007.
- [33] P. Fanjul-Bolado, P. Queipo, P. J. Lamas-Ardisana, and A. Costa-García, "Manufacture and evaluation of carbon nanotube modified screen-printed electrodes as electrochemical tools," *Talanta*, vol. 74, no. 3, pp. 427–433, 2007.
- [34] J. Wang, M. Musameh, and Y. Lin, "Solubilization of carbon nanotubes by Nafion toward the preparation of amperometric biosensors," *Journal of the American Chemical Society*, vol. 125, no. 9, pp. 2408–2409, 2003.
- [35] S. Laschi, E. Bulukin, I. Palchetti, C. Cristea, and M. Mascini, "Disposable electrodes modified with multi-wall carbon nanotubes for biosensor applications," *IRBM*, vol. 29, no. 2–3, pp. 202–207, 2008.
- [36] G. A. Rivas, M. D. Rubianes, M. C. Rodríguez, et al., "Carbon nanotubes for electrochemical biosensing," *Talanta*, vol. 74, no. 3, pp. 291–307, 2007.
- [37] O. Domínguez-Renedo, L. Ruiz-Espelt, N. García-Astorgano, and M. J. Arcos-Martínez, "Electrochemical determination of chromium(VI) using metallic nanoparticle-modified carbon screen-printed electrodes," *Talanta*, vol. 76, no. 4, pp. 854–858, 2008.
- [38] J. Wang, "Nanomaterial-based electrochemical biosensors," *Analyst*, vol. 130, no. 4, pp. 421–426, 2005.
- [39] G. B. Sergeev, "Nanoparticles in science and technology," in *Nanochemistry*, pp. 175–208, Elsevier, Amsterdam, The Netherlands, 2006.
- [40] C. M. Welch and R. G. Compton, "The use of nanoparticles in electroanalysis: a review," *Analytical and Bioanalytical Chemistry*, vol. 384, no. 3, pp. 601–619, 2006.

- [41] P. Alivisatos, "The use of nanocrystals in biological detection," *Nature Biotechnology*, vol. 22, no. 1, pp. 47–52, 2004.
- [42] E. Bakker, "Electrochemical sensors," *Analytical Chemistry*, vol. 76, no. 12, pp. 3285–3298, 2004.
- [43] A. Ambrosi, A. Merkoçi, and A. de la Escosura-Muñiz, "Electrochemical analysis with nanoparticle-based biosystems," *TrAC Trends in Analytical Chemistry*, vol. 27, no. 7, pp. 568–584, 2008.
- [44] A. Erdem, "Nanomaterial-based electrochemical DNA sensing strategies," *Talanta*, vol. 74, no. 3, pp. 318–325, 2007.
- [45] J. Wang, "Carbon-nanotube based electrochemical biosensors: a review," *Electroanalysis*, vol. 17, no. 1, pp. 7–14, 2005.
- [46] M. Pumera, S. Sánchez, I. Ichinose, and J. Tang, "Electrochemical nanobiosensors," *Sensors and Actuators B*, vol. 123, no. 2, pp. 1195–1205, 2007.
- [47] X.-J. Huang and Y.-K. Choi, "Chemical sensors based on nanostructured materials," *Sensors and Actuators B*, vol. 122, no. 2, pp. 659–671, 2007.
- [48] I. Willner, R. Baron, and B. Willner, "Integrated nanoparticle-biomolecule systems for biosensing and bioelectronics," *Biosensors & Bioelectronics*, vol. 22, no. 9-10, pp. 1841–1852, 2007.
- [49] Y. Yun, Z. Dong, V. Shanov, et al., "Nanotube electrodes and biosensors," *Nano Today*, vol. 2, no. 6, pp. 30–37, 2007.
- [50] V. Vamvakaki and N. A. Chaniotakis, "Carbon nanostructures as transducers in biosensors," *Sensors and Actuators B*, vol. 126, no. 1, pp. 193–197, 2007.
- [51] X.-E. Zhang, "Screen-printing methods for biosensor production," in *Biosensors*, J. Cooper and T. Cass, Eds., Practical Approach Series, pp. 41–58, Oxford University Press, Oxford, UK, 2004.
- [52] O. Domínguez-Renedo, M. A. Alonso-Lomillo, and M. J. Arcos-Martínez, "Recent developments in the field of screen-printed electrodes and their related applications," *Talanta*, vol. 73, no. 2, pp. 202–219, 2007.
- [53] J. P. Hart, A. Crew, E. Crouch, K. C. Honeychurch, and R. M. Pemberton, "Screen-printed electrochemical (bio)sensors in biomedical, environmental and industrial applications," in *Electrochemical Sensor Analysis*, S. Alegret and A. Merkoçi, Eds., vol. 49, pp. 497–557, Elsevier, Amsterdam, The Netherlands, 2007.
- [54] S. Laschi and M. Mascini, "Planar electrochemical sensors for biomedical applications," *Medical Engineering & Physics*, vol. 28, no. 10, pp. 934–943, 2006.
- [55] J. P. Hart, A. Crew, E. Crouch, K. C. Honeychurch, and R. M. Pemberton, "Some recent designs and developments of screen-printed carbon electrochemical sensors/biosensors for biomedical, environmental, and industrial analyses," *Analytical Letters*, vol. 37, no. 5, pp. 789–830, 2004.
- [56] A. Avramescu, S. Andreescu, T. Noguier, C. Bala, D. Andreescu, and J.-L. Marty, "Biosensors designed for environmental and food quality control based on screen-printed graphite electrodes with different configurations," *Analytical and Bioanalytical Chemistry*, vol. 374, no. 1, pp. 25–32, 2002.
- [57] V. B. Nascimento and L. Angnes, "Eletrodos fabricados por 'silk-screen'," *Química Nova*, vol. 21, no. 5, pp. 614–629, 1998.
- [58] J. D. Newman and A. P. F. Turner, "Home blood glucose biosensors: a commercial perspective," *Biosensors & Bioelectronics*, vol. 20, no. 12, pp. 2435–2453, 2005.
- [59] H. J. Hecht, H. M. Kalisz, J. Hendle, R. D. Schmid, and D. Schomburg, "Crystal structure of glucose oxidase from *Aspergillus niger* refined at 2.3 Å resolution," *Journal of Molecular Biology*, vol. 229, no. 1, pp. 153–172, 1993.
- [60] I. L. de Mattos, L. Gorton, and T. Ruzgas, "Sensor and biosensor based on Prussian Blue modified gold and platinum screen printed electrodes," *Biosensors & Bioelectronics*, vol. 18, no. 2-3, pp. 193–200, 2002.
- [61] K. Derwinska, K. Miecznikowski, R. Koncki, P. J. Kulesza, S. Glab, and M. A. Malik, "Application of Prussian Blue based composite film with functionalized organic polymer to construction of enzymatic glucose biosensor," *Electroanalysis*, vol. 15, no. 23-24, pp. 1843–1849, 2003.
- [62] W. Zhao, J.-J. Xu, C.-G. Shi, and H.-Y. Chen, "Multilayer membranes via layer-by-layer deposition of organic polymer protected Prussian Blue nanoparticles and glucose oxidase for glucose biosensing," *Langmuir*, vol. 21, no. 21, pp. 9630–9634, 2005.
- [63] T. Li, Z. Yao, and L. Ding, "Development of an amperometric biosensor based on glucose oxidase immobilized through silica sol-gel film onto Prussian Blue modified electrode," *Sensors and Actuators B*, vol. 101, no. 1-2, pp. 155–160, 2004.
- [64] A. Lupu, D. Compagnone, and G. Palleschi, "Screen-printed enzyme electrodes for the detection of marker analytes during winemaking," *Analytica Chimica Acta*, vol. 513, no. 1, pp. 67–72, 2004.
- [65] S. Zuo, Y. Teng, H. Yuan, and M. Lan, "Development of a novel silver nanoparticles-enhanced screen-printed amperometric glucose biosensor," *Analytical Letters*, vol. 41, no. 7, pp. 1158–1172, 2008.
- [66] P. A. Fiorito, V. R. Gonçalves, E. A. Ponzio, and S. I. Córdoba de Torresi, "Synthesis, characterization and immobilization of Prussian Blue nanoparticles. A potential tool for biosensing devices," *Chemical Communications*, no. 3, pp. 366–368, 2005.
- [67] W.-J. Guan, Y. Li, Y.-Q. Chen, X.-B. Zhang, and G.-Q. Hu, "Glucose biosensor based on multi-wall carbon nanotubes and screen printed carbon electrodes," *Biosensors & Bioelectronics*, vol. 21, no. 3, pp. 508–512, 2005.
- [68] M. D. Rubianes and G. A. Rivas, "Carbon nanotubes paste electrode," *Electrochemical Communications*, vol. 5, no. 8, pp. 689–694, 2003.
- [69] B.-W. Lu and W.-C. Chen, "A disposable glucose biosensor based on drop-coating of screen-printed carbon electrodes with magnetic nanoparticles," *Journal of Magnetism and Magnetic Materials*, vol. 304, no. 1, pp. e400–e402, 2006.
- [70] L. M. Rossi, A. D. Quach, and Z. Rosenzweig, "Glucose oxidase-magnetite nanoparticle bioconjugate for glucose sensing," *Analytical and Bioanalytical Chemistry*, vol. 380, no. 4, pp. 606–613, 2004.
- [71] Z. Gao, F. Xie, M. Shariff, M. Arshad, and J. Y. Ying, "A disposable glucose biosensor based on diffusional mediator dispersed in nanoparticulate membrane on screen-printed carbon electrode," *Sensors and Actuators B*, vol. 111-112, pp. 339–346, 2005.
- [72] Z. Gao, G. Xu, Y.-R. J. Ying, M. Shariff, M. Arshad, and F. Xie, "Biosensor," WO/2005/040404, 2005.
- [73] N. Bragagnolo and D. B. Rodriguez-Amaya, "Simultaneous determination of total lipid, cholesterol and fatty acids in meat and backfat of suckling and adult pigs," *Food Chemistry*, vol. 79, no. 2, pp. 255–260, 2002.
- [74] B.-S. Hwang, J.-T. Wang, and Y.-M. Choong, "A simplified method for the quantification of total cholesterol in lipids using gas chromatography," *Journal of Food Composition and Analysis*, vol. 16, no. 2, pp. 169–178, 2003.
- [75] M. A. T. Gilmartin and J. P. Hart, "Fabrication and characterization of a screen-printed, disposable, amperometric cholesterol biosensor," *Analyst*, vol. 119, no. 11, pp. 2331–2336, 1994.

- [76] L. Charpentier and N. El Murr, "Amperometric determination of cholesterol in serum with use of a renewable surface peroxidase electrode," *Analytica Chimica Acta*, vol. 318, no. 1, pp. 89–93, 1995.
- [77] T. Nakaminami, S. Kuwabata, and H. Yoneyama, "Electrochemical oxidation of cholesterol catalyzed by cholesterol oxidase with use of an artificial electron mediator," *Analytical Chemistry*, vol. 69, no. 13, pp. 2367–2372, 1997.
- [78] F. Ricci and G. Palleschi, "Sensor and biosensor preparation, optimisation and applications of Prussian Blue modified electrodes," *Biosensors & Bioelectronics*, vol. 21, no. 3, pp. 389–407, 2005.
- [79] S. Cosnier, A. Senillou, M. Grätzel, et al., "Glucose biosensor based on enzyme entrapment within polypyrrole films electrodeposited on mesoporous titanium dioxide," *Journal of Electroanalytical Chemistry*, vol. 469, no. 2, pp. 176–181, 1999.
- [80] J. Wang, X. Zhang, and M. Prakash, "Glucose microsensors based on carbon paste enzyme electrodes modified with cupric hexacyanoferrate," *Analytica Chimica Acta*, vol. 395, no. 1–2, pp. 11–16, 1999.
- [81] S. K. Arya, M. Datta, and B. D. Malhotra, "Recent advances in cholesterol biosensor," *Biosensors & Bioelectronics*, vol. 23, no. 7, pp. 1083–1100, 2008.
- [82] V. V. Shumyantseva, S. Carrara, V. Bavastrello, et al., "Direct electron transfer between cytochrome P450_{scc} and gold nanoparticles on screen-printed rhodium-graphite electrodes," *Biosensors & Bioelectronics*, vol. 21, no. 1, pp. 217–222, 2005.
- [83] S. Carrara, V. V. Shumyantseva, A. I. Archakov, and B. Samori, "Screen-printed electrodes based on carbon nanotubes and cytochrome P450_{scc} for highly sensitive cholesterol biosensors," *Biosensors & Bioelectronics*, vol. 24, no. 1, pp. 148–150, 2008.
- [84] N. Bistolas, U. Wollenberger, C. Jung, and F. W. Scheller, "Cytochrome P450 biosensors—a review," *Biosensors & Bioelectronics*, vol. 20, no. 12, pp. 2408–2423, 2005.
- [85] V. Shumyantseva, G. Deluca, T. Bulko, et al., "Cholesterol amperometric biosensor based on cytochrome P450_{scc}," *Biosensors & Bioelectronics*, vol. 19, no. 9, pp. 971–976, 2004.
- [86] G. Li, J. M. Liao, G. Q. Hu, N. Z. Ma, and P. J. Wu, "Study of carbon nanotube modified biosensor for monitoring total cholesterol in blood," *Biosensors & Bioelectronics*, vol. 20, no. 10, pp. 2140–2144, 2005.
- [87] F. Jelen, B. Yosypchuk, A. Kourilová, L. Novotný, and E. Paleček, "Label-free determination of picogram quantities of DNA by stripping voltammetry with solid copper amalgam or mercury electrodes in the presence of copper," *Analytical Chemistry*, vol. 74, no. 18, pp. 4788–4793, 2002.
- [88] P. Kara, K. Kerman, D. Ozkan, et al., "Electrochemical genosensor for the detection of interaction between methylene blue and DNA," *Electrochemistry Communications*, vol. 4, no. 9, pp. 705–709, 2002.
- [89] D. J. Caruana and A. Heller, "Enzyme-amplified amperometric detection of hybridization and of a single base pair mutation in an 18-base oligonucleotide on a 7- μ m-diameter microelectrode," *Journal of the American Chemical Society*, vol. 121, no. 4, pp. 769–774, 1999.
- [90] J. Wang, R. Polsky, A. Merkoçi, and K. L. Turner, "Electroactive beads" for ultrasensitive DNA detection," *Langmuir*, vol. 19, no. 4, pp. 989–991, 2003.
- [91] A. Merkoçi, "Electrochemical biosensing with nanoparticles," *FEBS Journal*, vol. 274, no. 2, pp. 310–316, 2007.
- [92] D. Du, J. Ding, Y. Tao, H. Li, and X. Chen, "CdTe nanocrystal-based electrochemical biosensor for the recognition of neutravidin by anodic stripping voltammetry at electrodeposited bismuth film," *Biosensors & Bioelectronics*, vol. 24, no. 4, pp. 869–874, 2008.
- [93] S. Niu, M. Zhao, L. Hu, and S. Zhang, "Carbon nanotube-enhanced DNA biosensor for DNA hybridization detection using rutin-Mn as electrochemical indicator," *Sensors and Actuators B*, vol. 135, no. 1, pp. 200–205, 2008.
- [94] M.T. Castañeda, A. Merkoçi, M. Pumera, and S. Alegret, "Electrochemical genosensors for biomedical applications based on gold nanoparticles," *Biosensors & Bioelectronics*, vol. 22, no. 9–10, pp. 1961–1967, 2007.
- [95] L. Authier, C. Grossiord, P. Brossier, and B. Limoges, "Gold nanoparticle-based quantitative electrochemical detection of amplified human cytomegalovirus DNA using disposable microband electrodes," *Analytical Chemistry*, vol. 73, no. 18, pp. 4450–4456, 2001.
- [96] J. Wang, O. Rincón, R. Polsky, and E. Dominguez, "Electrochemical detection of DNA hybridization based on DNA-templated assembly of silver cluster," *Electrochemistry Communications*, vol. 5, no. 1, pp. 83–86, 2003.
- [97] J. Wang, D. Xu, and R. Polsky, "Magnetically-induced solid-state electrochemical detection of DNA hybridization," *Journal of the American Chemical Society*, vol. 124, no. 16, pp. 4208–4209, 2002.
- [98] E. Suprun, V. Shumyantseva, T. Bulko, et al., "Au-nanoparticles as an electrochemical sensing platform for aptamer-thrombin interaction," *Biosensors & Bioelectronics*, vol. 24, no. 4, pp. 831–836, 2008.
- [99] K. Kerman and E. Tamiya, "Aptamer-functionalized Au nanoparticles for the electrochemical detection of thrombin," *Journal of Biomedical Nanotechnology*, vol. 4, no. 2, pp. 159–164, 2008.
- [100] W.-C. Shih, M.-C. Yang, and M. S. Lin, "Development of disposable lipid biosensor for the determination of total cholesterol," *Biosensors & Bioelectronics*, vol. 24, no. 6, pp. 1679–1684, 2009.
- [101] M. E. Burgoa Calvo, O. Domínguez-Renedo, and M. J. Arcos-Martínez, "Determination of lamotrigine by adsorptive stripping voltammetry using silver nanoparticle-modified carbon screen-printed electrodes," *Talanta*, vol. 74, no. 1, pp. 59–64, 2007.
- [102] M. A. Alonso-Lomillo, C. Yardimci, O. Domínguez-Renedo, and M. J. Arcos-Martínez, "CYP450 2B4 covalently attached to carbon and gold screen printed electrodes by diazonium salt and thiols monolayers," *Analytica Chimica Acta*, vol. 633, no. 1, pp. 51–56, 2009.
- [103] M. A. Alonso-Lomillo, O. Domínguez-Renedo, P. Matos, and M. J. Arcos-Martínez, "Electrochemical determination of levetiracetam by screen-printed based biosensors," *Bioelectrochemistry*, vol. 74, no. 2, pp. 306–309, 2009.
- [104] N. A. Martínez, G. A. Messina, F. A. Bertolino, E. Salinas, and J. Raba, "Screen-printed enzymatic biosensor modified with carbon nanotube for the methimazole determination in pharmaceuticals formulations," *Sensors and Actuators B*, vol. 133, no. 1, pp. 256–262, 2008.
- [105] M. Boujtita, J. P. Hart, and R. Pittson, "Development of a disposable ethanol biosensor based on a chemically modified screen-printed electrode coated with alcohol oxidase for the analysis of beer," *Biosensors & Bioelectronics*, vol. 15, no. 5–6, pp. 257–263, 2000.

- [106] J. Wang, C. Timchalk, and Y. Lin, "Carbon nanotube-based electrochemical sensor for assay of salivary cholinesterase enzyme activity: an exposure biomarker of organophosphate pesticides and nerve agents," *Environmental Science and Technology*, vol. 42, no. 7, pp. 2688–2693, 2008.
- [107] M.-H. Liao, J.-C. Guo, and W.-C. Chen, "A disposable amperometric ethanol biosensor based on screen-printed carbon electrodes mediated with ferricyanide-magnetic nanoparticle mixture," *Journal of Magnetism and Magnetic Materials*, vol. 304, no. 1, pp. e421–e423, 2006.
- [108] S. Andreescu and J.-L. Marty, "Twenty years research in cholinesterase biosensors: from basic research to practical applications," *Biomolecular Engineering*, vol. 23, no. 1, pp. 1–15, 2006.
- [109] Y. Lin, F. Lu, and J. Wang, "Disposable carbon nanotube modified screen-printed biosensor for amperometric detection of organophosphorus pesticides and nerve agents," *Electroanalysis*, vol. 16, no. 1-2, pp. 145–149, 2004.
- [110] J. Cai and D. Du, "A disposable sensor based on immobilization of acetylcholinesterase to multiwall carbon nanotube modified screen-printed electrode for determination of carbaryl," *Journal of Applied Electrochemistry*, vol. 38, no. 9, pp. 1217–1222, 2008.
- [111] I. Bontidean, A. Mortari, S. Leth, et al., "Biosensors for detection of mercury in contaminated soils," *Environmental Pollution*, vol. 131, no. 2, pp. 255–262, 2004.
- [112] K. C. Honeychurch and J. P. Hart, "Screen-printed electrochemical sensors for monitoring metal pollutants," *TrAC Trends in Analytical Chemistry*, vol. 22, no. 7-8, pp. 456–469, 2003.
- [113] D. Ogończyk, L. Tymecki, I. Wyżkiewicz, R. Koncki, and S. Głąb, "Screen-printed disposable urease-based biosensors for inhibitive detection of heavy metal ions," *Sensors and Actuators B*, vol. 106, no. 1, pp. 450–454, 2005.
- [114] B. B. Rodriguez, J. A. Bolbot, and I. E. Tothill, "Development of urease and glutamic dehydrogenase amperometric assay for heavy metals screening in polluted samples," *Biosensors & Bioelectronics*, vol. 19, no. 10, pp. 1157–1167, 2004.
- [115] B. B. Rodriguez, J. A. Bolbot, and I. E. Tothill, "Urease-glutamic dehydrogenase biosensor for screening heavy metals in water and soil samples," *Analytical and Bioanalytical Chemistry*, vol. 380, no. 2, pp. 284–292, 2004.
- [116] O. Domínguez-Renedo and M. J. Arcos-Martínez, "A novel method for the anodic stripping voltammetry determination of Sb(III) using silver nanoparticle-modified screen-printed electrodes," *Electrochemistry Communications*, vol. 9, no. 4, pp. 820–826, 2007.
- [117] O. Domínguez-Renedo and M. J. Arcos-Martínez, "Anodic stripping voltammetry of antimony using gold nanoparticle-modified carbon screen-printed electrodes," *Analytica Chimica Acta*, vol. 589, no. 2, pp. 255–260, 2007.
- [118] Y.-S. Song, G. Muthuraman, Y.-Z. Chen, C.-C. Lin, and J.-M. Zen, "Screen printed carbon electrode modified with poly(L-lactide) stabilized gold nanoparticles for sensitive as(III) detection," *Electroanalysis*, vol. 18, no. 18, pp. 1763–1770, 2006.
- [119] Y.-S. Song, G. Muthuraman, and J.-M. Zen, "Trace analysis of hydrogen sulfide by monitoring As(III) at a poly(L-lactide) stabilized gold nanoparticles modified electrode," *Electrochemistry Communications*, vol. 8, no. 8, pp. 1369–1374, 2006.
- [120] W. J. R. Santos, P. R. Lima, A. A. Tanaka, S. M. C. N. Tanaka, and L. T. Kubota, "Determination of nitrite in food samples by anodic voltammetry using a modified electrode," *Food Chemistry*, vol. 113, no. 4, pp. 1206–1211, 2009.
- [121] M. Sohail and S. B. Adeloju, "Electroimmobilization of nitrate reductase and nicotinamide adenine dinucleotide into polypyrrole films for potentiometric detection of nitrate," *Sensors and Actuators B*, vol. 133, no. 1, pp. 333–339, 2008.
- [122] M. G. Almeida, C. M. Silveira, and J. J. G. Moura, "Biosensing nitrite using the system nitrite reductase/Nafion/methyl viologen—a voltammetric study," *Biosensors & Bioelectronics*, vol. 22, no. 11, pp. 2485–2492, 2007.
- [123] H. Chen, C. Mousty, L. Chen, and S. Cosnier, "A new approach for nitrite determination based on a HRP/catalase biosensor," *Materials Science & Engineering C*, vol. 28, no. 5-6, pp. 726–730, 2008.
- [124] H. Chen, C. Mousty, S. Cosnier, C. Silveira, J. J. G. Moura, and M. G. Almeida, "Highly sensitive nitrite biosensor based on the electrical wiring of nitrite reductase by [ZnCr-AQS] LDH," *Electrochemistry Communications*, vol. 9, no. 9, pp. 2240–2245, 2007.
- [125] S. Cosnier, S. Da Silva, D. Shan, and K. Gorgy, "Electrochemical nitrate biosensor based on poly(pyrrole-viologen) film-nitrate reductase-clay composite," *Bioelectrochemistry*, vol. 74, no. 1, pp. 47–51, 2008.
- [126] W. Dhaoui, M. Bouzitoun, H. Zarrouk, H. B. Ouada, and A. Pron, "Electrochemical sensor for nitrite determination based on thin films of sulfamic acid doped polyaniline deposited on Si/SiO₂ structures in electrolyte/insulator/semiconductor (E.I.S.) configuration," *Synthetic Metals*, vol. 158, no. 17-18, pp. 722–726, 2008.
- [127] Z. Zhang, S. Xia, D. Leonard, et al., "A novel nitrite biosensor based on conductometric electrode modified with cytochrome *c* nitrite reductase composite membrane," *Biosensors & Bioelectronics*, vol. 24, no. 6, pp. 1574–1579, 2009.
- [128] Z. Dai, H. Bai, M. Hong, Y. Zhu, J. Bao, and J. Shen, "A novel nitrite biosensor based on the direct electron transfer of hemoglobin immobilized on CdS hollow nanospheres," *Biosensors & Bioelectronics*, vol. 23, no. 12, pp. 1869–1873, 2008.
- [129] X. Huang, Y. Li, Y. Chen, and L. Wang, "Electrochemical determination of nitrite and iodate by use of gold nanoparticles/poly(3-methylthiophene) composites coated glassy carbon electrode," *Sensors and Actuators B*, vol. 134, no. 2, pp. 780–786, 2008.
- [130] A. Salimi, R. Hallaj, H. Mamkhezri, and S. M. T. Hosaini, "Electrochemical properties and electrocatalytic activity of FAD immobilized onto cobalt oxide nanoparticles: application to nitrite detection," *Journal of Electroanalytical Chemistry*, vol. 619-620, no. 1-2, pp. 31–38, 2008.
- [131] X. Xu, S. Liu, B. Li, and H. Ju, "Disposable nitrite sensor based on hemoglobin-colloidal gold nanoparticle modified screen-printed electrode," *Analytical Letters*, vol. 36, no. 11, pp. 2427–2442, 2003.
- [132] J. Wang and P. V. A. Pamidi, "Disposable screen-printed electrodes for monitoring hydrazines," *Talanta*, vol. 42, no. 3, pp. 463–467, 1995.
- [133] C.-C. Yang, A. S. Kumar, M.-C. Kuo, S.-H. Chien, and J.-M. Zen, "Copper-palladium alloy nanoparticle plated electrodes for the electrocatalytic determination of hydrazine," *Analytica Chimica Acta*, vol. 554, no. 1-2, pp. 66–73, 2005.

Research Article

Sensitivity Improvement of an Impedimetric Immunosensor Using Functionalized Iron Oxide Nanoparticles

Imen Hafaid,^{1,2} Asma Gallouz,¹ Walid Mohamed Hassen,¹ Adnane Abdelghani,³ Zina Sassi,² Francois Bessueille,¹ and Nicole Jaffrezic-Renault¹

¹Laboratoire des Sciences Analytiques (UMR CNRS 5180), Université de Lyon, Batiment Raulin, Université de Claude Bernard, 43 boulevard du 11 Novembre 1918, 69622 Villeurbanne Cedex, France

²Laboratoire AMPERE (UMR CNRS 5180), INSA de Lyon, 69621 Villeurbanne, France

³Unité de Recherche de Physique des Semiconducteurs et Capteurs, IPEST, La Marsa 2070, Tunisia

Correspondence should be addressed to Imen Hafaid, imen.haf@yahoo.fr

Received 30 December 2008; Revised 18 May 2009; Accepted 8 July 2009

Recommended by Wojtek Wlodarski

This work has explored the development of impedimetric immunosensors based on magnetic iron nanoparticles (IrNP) functionalized with streptavidin to which a biotinylated FAB part of the antibody has been bound using a biotin-streptavidin interaction. SPR analysis shows a deviation on the measured (angle) during antigen-antibody recognition whereas label free detection using by EIS allows us to monitor variation of polarization resistance. Before detection, layers were analyzed by FTIR and AFM. Compared to immobilization of antibody on bare gold surface using aminodecanethiol SAM, antibody immobilization on nanoparticles permitted to reach lower detection limit: 500 pg/ml instead of 1 ng/ml to in the case of EIS and 300 ng/ml instead of 4.5 $\mu\text{g/ml}$ in the case of SPR. Thus, it permitted to improve the sensitivity: from 257.3 $\Omega \cdot \text{cm}^2 \cdot \mu\text{g}^{-1} \cdot \text{ml}$ to 1871 $\Omega \cdot \text{cm}^2 \cdot \mu\text{g}^{-1} \cdot \text{ml}$ in the case of EIS and from 0.003° $\mu\text{g}^{-1} \cdot \text{ml}$ to 0.094° $\mu\text{g}^{-1} \cdot \text{ml}$ in the case of SPR.

Copyright © 2009 Imen Hafaid et al. This is an open access article distributed under the Creative Commons Attribution License, which permits unrestricted use, distribution, and reproduction in any medium, provided the original work is properly cited.

1. Introduction

Immunosensors have arisen great interest with expectation of providing fast and highly sensitive immunological response. Immunosensors have widespread applications in clinical diagnostics, food safety and quality control, biological analysis, and environmental monitoring [1–5]. During the past years, the research in this field evolved quickly with the aim of improving the performance of the biosensors (specificity, stability, sensitivity, detection limit, etc.). In this approach, recent studies have been focused on the use of nanoparticles as tools to amplify the response signal from antibody—antigen interaction, which led to the improvement of the characteristics of the biosensor [6–8].

In the recent years, nanomaterials have been widely used in bioanalytical chemistry, bioseparations, and bioimaging for their unique and particular properties [9–12]. Iron oxide nanoparticles or magnetic beads are a kind of nanomaterial which might play an important role in the construction of electrochemical biosensors [13]. Firstly, iron

oxide nanoparticles have a very large surface area and good bio-compatibility. Most practically, they can be magnetic ally immobilized on Au substrates [14, 15]. Furthermore, these magnetic particles are especially designed for concentration, separation, purification, and identification of molecules and specific cells [16–18]. Besides, they are particularly suitable for integration in microfluidic devices.

A new approach allows to attach these magnetic particles by covalent binding on the substrate previously functionalized with self-assembled monolayer (SAM). The tailoring of the physical chemistry of surfaces has led to an increasing interest in using SAMs of thiol sulfur compounds as insulator [19–22]. The formed single molecular organized structures have numerous advantages, such as insulating nanostructures, free of defects, much more stable, especially in water and other solvents [23].

In this work, we report the development of an electrochemical Immunosensor based on iron oxide nanoparticles functionalized with the streptavidine. The Biotine tag anti-D-dimer reduced antibody was immobilized on the surface

of iron oxide nanoparticles linked to a previously functionalized gold electrode using 11-Amino-1-undecanethiol and glutaraldehyde as coupling agent.

For the purpose of developing this Immunosensors, surface plasmon resonance (SPR) and electrochemical impedance spectroscopy (EIS) techniques were selected. In first time, surface plasmon resonance (SPR) was used as optical characterization technique [24]. This technology has emerged as a powerful tool for *in situ* control of biomolecular interaction in real time [25]. SPR sensors are based on surface plasmon or electromagnetic wave propagating along a metal/dielectric interface. Since the wave vector of plasmon, k_{sp} , depends on the dielectric constants of both media, $k_{sp} = k_0 \sqrt{\epsilon_{metal} \epsilon_{sample} / (\epsilon_{metal} + \epsilon_{sample})}$ (where k_0 is the free space wave vector of the optical wave), it is extremely sensitive to properties of the dielectric medium which is in contact with the metal.

Surface plasmons are generally excited in the Kretschmann configuration by directing p-polarized light to a glass prism and reflecting from a gold film [26]. When the tangential x -component of the incident optical wave vector, k_x , is matched with k_{sp} , the pumping light energy is transferred to surface plasmons:

$$k_x = k_0 \cdot n_{glass} \cdot \sin \theta_{inc} = k_{sp}, \quad (1)$$

where n_{glass} is the refractive index of the prism and θ_{inc} is the angle of incidence.

Therefore, the information of biological binding (recognition) events on the gold film can be obtained by carefully monitoring the SPR coupling characteristics. In most SPR systems, the information of the biomolecular interactions is obtained from measurements of the angular or the spectral characteristics of light reflected under SPR.

In second time, electrochemical impedance spectroscopy (EIS) was used as transduction technique for the label free detection. This technique is an effective tool used on the one hand, for the qualitative and quantitative characterization of electrochemical processes occurring in the conducting polymer films [27, 28]. On the other hand, to probe the interfacial properties of modified electrode and often used for understanding chemical transformations and processes associated with the conductive supports and it can be used to probe antibody-antigen interaction in order to study the immunosensor responses [29–31].

While comparing with the development of an immunosensor-based on antibody coupled on a SAM, we attempt to show that the use of iron oxide nanoparticles allows to amplify the response signal and leads to the improvement of immunosensor characteristics.

2. Materials and Methods

2.1. Reagent. The magnetic coated streptavidin nanoparticles that display a diameter of 200 nm and an iron oxide content of about 70% (cf. Figure 1) were purchased from Ademtech SA. 11-Amino-1-undecanethiol (AUT) and Glutaraldehyde (GA) were obtained from Aldrich. Neutravidin

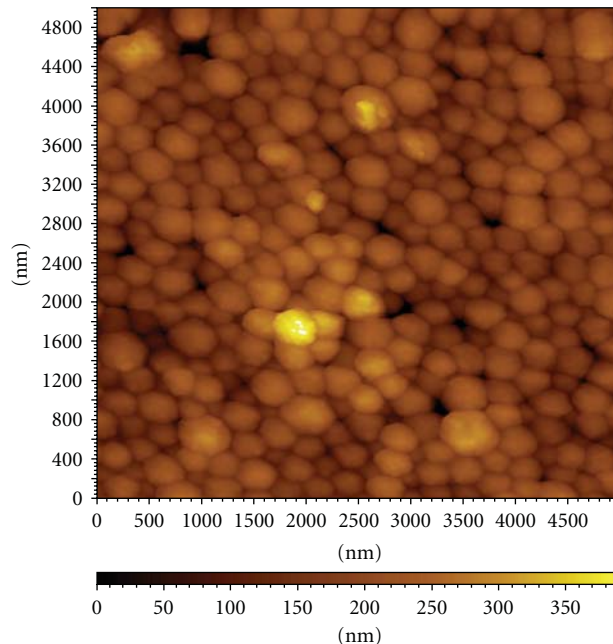


FIGURE 1: AFM images of the iron oxide nanoparticles.

(Neutv) was purchased from Pierce. The biot-tag anti-D-dimer reduced antibody (Fab fragment Biot-ScAc) and the antigen (peptide conjugated to BSA) were obtained from Wyeth Company (Aberdeen UK).

The buffer solution used for the electrochemical impedance experiments was Phosphate Buffer Saline (PBS) containing 137 mM NaCl, 2.7 mM KCl, 0.01 M K_2HPO_4 and 0.01 M KH_2PO_4 , pH 7. For the cyclic voltammetry experiments, the redox couple $Fe(CN)_6^{3-}/Fe(CN)_6^{4-}$ at a 5 mM concentration was used. All solutions were made up in ultrapure water (resistance $18.2 M\Omega cm^{-1}$) produced by a Millipore Milli-Q system.

2.2. Instrumentation

2.2.1. Surface Plasmon Resonance (SPR) Technique and Gold-Coated Substrates. Surface plasmon resonance spectrometer “Biosuplar 3” (<http://www.micro-systems.de/>) was developed at the Institute of Semiconductor Physics of the National Academy of Sciences of Ukraine (Kyiv). This optoelectronic device based on the phenomenon of surface plasmon resonance in the Kretschmann’s optical configuration was controlled by a computer via self-developed software. Gold film (45 nm) deposited through Cr adhesion layer (1–1.5 nm) onto a glass chip represented the sensor surface. An incident beam of p-polarized light from a semiconductor laser diode ($\lambda = 650$ nm) excited an oscillation of electronic plasma (i.e., surface plasmon) in this metallic film. A special prism capable of rotation on a computer-defined angle provided optimal conditions for the plasmon excitation. A plasmon resonance itself was registered as a drastic decrease of reflected light intensity.

In the present study, the SPR spectrometer flow cell ($V \sim 20 \mu\text{L}$) was connected to a Gilson Minipuls 3 pump.

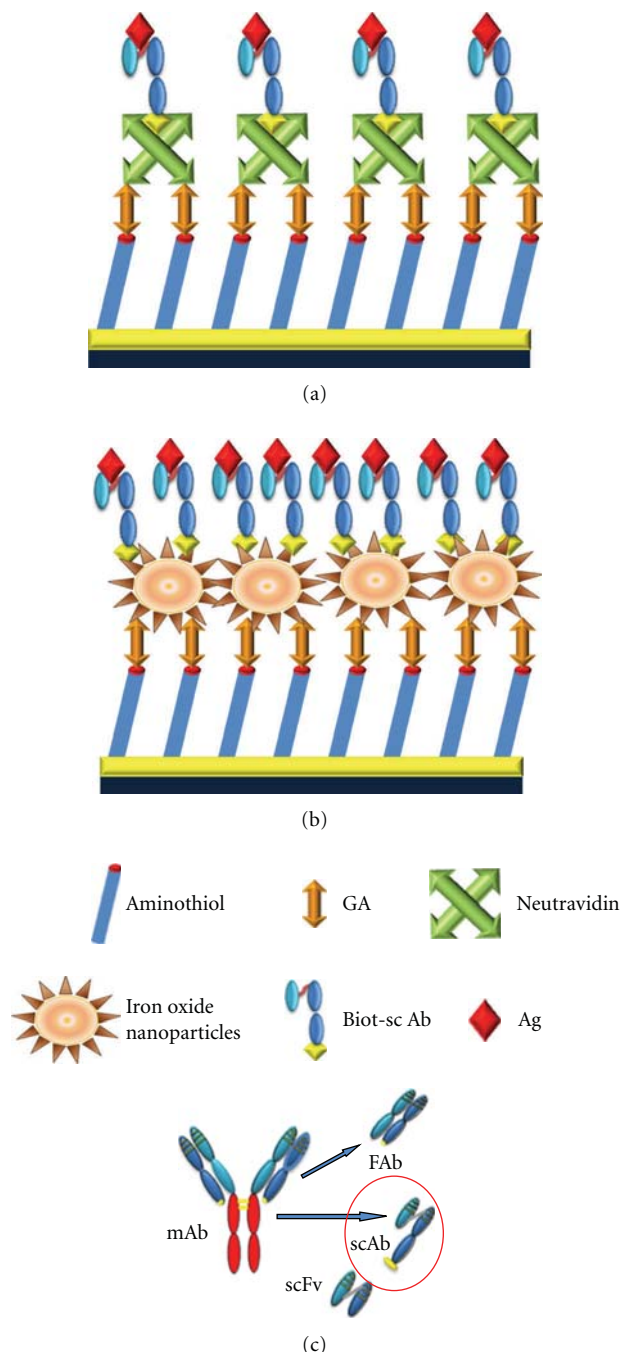
2.2.2. Impedance Spectroscopy. Cyclic Voltammetry and Electrochemical Impedance Spectroscopy (EIS) measurements were performed using a Voltlab 80 impedance analyzer. A conventional three electrode cell was used, including a saturated calomel electrode (SCE) as reference electrode, a platinum wire as counter electrode (0.54 cm^2), and a modified gold working electrode (0.19 cm^2). The impedance spectroscopy measurements were carried out in the frequency range from 0.05 Hz to 100 KHz at dc potential -400 mV , using a modulation voltage of 10 mV. Data simulation was made with the commercial software Zview (Scribner Associates, Charlottesville, VA). All electrochemical measurements were carried out at room temperature in PBS pH 7.4.

2.2.3. Atomic Force Microscopy. Atomic Force Microscopy (AFM) experiments were performed in air, using a Pico Plus molecular imaging microscope with a 300 nm scanning head. The images were registered in tapping mode using silicon pyramidal Si_3N_4 tips. The overage resonance frequency of the tips was 300 kHz in air. The image presented in this paper was acquired with 512 lines and were processed by means of a plane fit.

2.2.4. FTIR Spectroscopy. NICOLET 710 FT-IR spectrometer equipped with an MIR (Middle Infrared) source an MCT/A detector was used to obtain the FTIR spectra. All the spectra are collected during 128 scans for the reference and sample. Our strategy consisted of recording in reflexion mode the spectrum of the cleaned gold substrate and then of the gold substrate modified with the SAM. The spectrum of the cleaned electrode served as a reference. The difference between two spectra gave the spectrum of SAM.

2.2.5. Preparation of the Modified Electrode. Two systems were prepared, one based on the use of a thiol SAM (system 1) and the other based on the use of functionalized magnetic iron nanoparticles with the streptavidin (system 2).

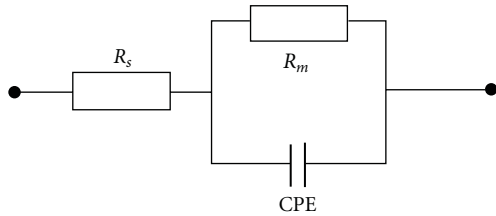
In the first step of the electrode modification, the 11-Amino-1-undecanethiol monolayer is chemisorbed on the gold electrode surface and exposed an array of amino groups towards the solution. In the second step, the electrode surface is activated with aldehyde groups and left the second carbonyl group of glutaraldehyde free on the top of the surface. Formation of bridge structures due to the reaction of both aldehyde groups of glutaraldehyde with the amino groups may be prevented by the application of a high concentration of the bifunctional reagent, that is, GA [32]. The last step, the amino group of neutravidin (Scheme 1(a): system 1) and of magnetic iron nanoparticles coated by streptavidin (Scheme 1(b): system 2) are covalently coupled with the aldehyde group of glutaraldehyde. The new membrane rich in binding sites of biotin allowed forming the high binding affinity with the biotin ligand attached on scAb antibody fragment. The Fab fragments were biotinylated in the hinge region, to ensure orientation of the fragment at the



SCHEME 1: (a) System 1: schematic representation of the fabrication process of the multilayer immunosensor based on SAM. (b) System 2: schematic representation of the fabrication process of the multilayer immunosensor based on iron oxide nanoparticles. (c) Fab fragment biotinylated antibody.

surface with the binding site facing a way from the surface. The system is shown schematically in Scheme 1(c).

Two types of gold electrodes are used as substrate for the bilayer fabrication. Evaporated gold ($\sim 300 \text{ nm}$ thickness) deposited on silicon using a titanium layer (30 nm thickness) used as substrate for the electrochemical experiments. These



SCHEME 2: Equivalent circuit model for complex impedance plot.

gold electrodes were provided by LAAS, CNRS Toulouse. Before modification, the gold surface was cleaned in an ultrasonic bath for 10 minutes in acetone, dried under a dry N_2 flow and then dipped for 1 minute into “piranha solution” comprising 7 : 3 (v/v) 98% H_2SO_4 /30% H_2O_2 . The gold substrate was then rinsed 2 to 3 times with ultra-pure water and dried under nitrogen flow. For the optical characterization the gold film (45 nm) deposited through Cr adhesion layer (1–1.5 nm) onto a glass chip was used. The gold surface was cleaned in the same way than the other ones, with a “piranha solution,” but for 15 seconds.

The aminothiols monolayer was prepared by soaking a clean gold electrode (Au) in 0.1 mM 11-Amino-1-undecanethiol (AUT) in ethanol solution for 24 hours at room temperature in darkness, washing the electrode thoroughly with ethanol to remove physically adsorbed 11-Amino-1-undecanethiol, immersing the electrode in PBS (pH 7.4) containing 5% (v/v) glutaraldehyde (GA) solution for 1 hour 30 minutes, and rinsing with PBS. Afterwards, for system 1, the electrode was immersed into 10^{-5} mM Neutravidin solution for 2 hours to achieve Schiff base reaction between the aldehyde group of glutaraldehyde and the amino group of Neutravidin. And for system 2, the electrode was immersed into 0.25 mg/ml magnetic coated streptavidin nanoparticles solution for 12 hours to form the Schiff base between the aldehyde group of glutaraldehyde and the amino group of streptavidin. Antibody scAb fragment with a *Biotin tag* (0.4 mg/ml) was immobilized on AUT/GA/Neut. films for 1 hour at room temperature, followed by thorough rinsing with PBS. Antigen at different concentrations was incubated on immobilized antibody for 30 minutes at room temperature. Scheme 1 shows the schematic steps for the formation of the bilayer and the antigen-antibody recognition for both systems.

3. Results and Discussion

3.1. Characterization of Self-Assembled Monolayer. The modified gold electrode with the self-assembled monolayer 11-Amino-1-undecanethiol was followed by several technique of characterizations.

3.1.1. Cyclic Voltammetry. Cyclic voltammetry is an effective and convenient method for probing the feature of the modified electrode surface. The step of the SAMs deposition was controlled by this technique. As is shown in Figure 2(a), the cyclic voltammogram defines the characteristics of a

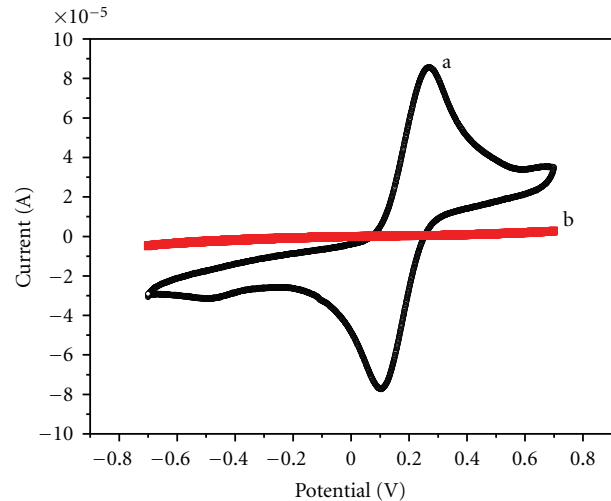


FIGURE 2: Cyclic voltammetric measurement with the presence of the 5 mM redox-probe $3[Fe(CN)_6]/K_4[Fe(CN)_6]$: (a) bare gold electrode; (b) SAM/Au-electrode. All experiments were performed in PBS 10 mM pH 7.4, scan rate 50 mV/s.

diffusion controlled redox process observed at the cleaned bare gold electrode. This reversible cyclic voltammogram indicates a clean gold surface. The formation of the SAM on the gold electrode (Figure 2(b)) resulted in an insulating surface in a sort of way and thus blocked the diffusion of ferro/ferricyanide towards the surface of electrode, therefore the blocking of the Faradaic current.

3.1.2. Impedance Measurement. Electrochemical Impedance Spectroscopy (EIS) is an effective tool for probing the feature surface-modified electrode while controlling its electrical properties [33, 34]. In a first time, this technique was used for the characterization of the impedance behavior of SAM modified gold electrode and for subsequent extraction of useful information from this. In Figure 3 Nyquist impedance plots for Au-electrode and SAM modified electrode at -400 mV dc potentials are presented, where $Re(z)$ is the real part and $Im(z)$ is the imaginary part of the complex impedance Z [35]. The membrane resistance values, R_m , were extracted from fitted data (Table 3) which are 8292 and $37120 \Omega cm^2$ for bare Au-electrode and mixed modified Au-electrode, respectively. The values of the fractional coverage area of the SAM monolayer (θ) can be calculated from the impedance diagrams using [36]

$$\theta = 1 - \frac{R_m}{R_m^*}, \quad (2)$$

where R_m and R_m^* are the values of the membrane resistance derived from the impedance diagram of the bare gold electrode and of the gold electrode SAM functionalized, respectively. In our system the coverage area was equal to 77%.

3.1.3. SPR Measurement. Optical characterization of the SAM layer was performed by SPR technique. Figure 4

TABLE 1: Optical parameters obtained by fitting the SPR curves for system 1 based on SAM.

Layer	Thickness (nm)	n	k	ϵ'	ϵ''
Bare gold	50.72	0.17	3.988	-15.87	1.355
Thiol	2.16	1.34	0	1.791	0
GA	0.1	1.45	0	2.10	0
Nev.	0.8	1.45	0	2.10	0
Ab	0.4	1.45	0	2.10	0

TABLE 2: Optical parameters obtained by fitting the SPR curves for system 2 based on iron oxide nanoparticles.

Layer	Thickness (nm)	n	k	ϵ'	ϵ''
Bare gold	50.72	0.17	3.89	-15.87	1.355
Thiol	2.16	1.34	0	1.791	0
GA	0.1	1.45	0	2.10	0
Iron oxide nanoparticles	301	0.28	2.98	-8.802	1.6688
Ab	1.2	1.45	0	2.10	0

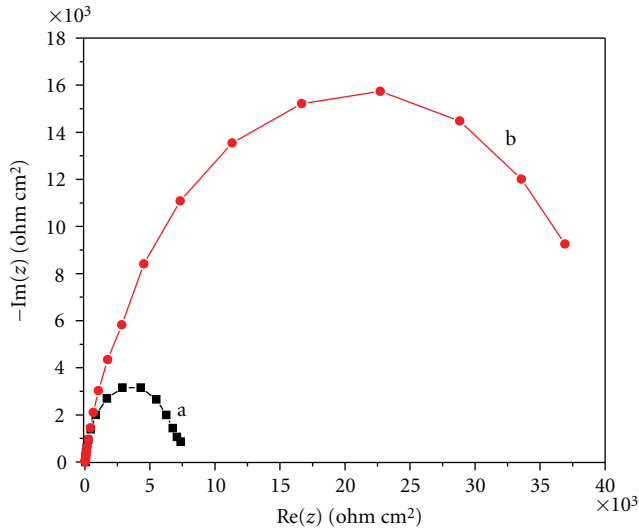


FIGURE 3: Nyquist diagram ($-\text{Im}(z)$ versus $\text{Re}(z)$) at -400 mV versus SCE in PBS solution 10 mM pH 7.4, obtained for the non-Faradic impedance measurement corresponding to (a) bare gold electrode and (b) self-assembled monolayer functionalized gold electrode.

presents the spectra of the reflected intensity versus incidence angle. These spectra show an incidence angle shift of 0.563° between the bare gold layer (Figure 4(a)) and the gold layer coated with SAM layer (Figure 4(b)). By fitting these spectra using the Winspall program, the thickness of each layer was calculated (see Table 1). The thickness of the gold around of 50.72 nm was checked by this fitting. Also, the thickness of the SAM layer was estimated to 2.16 nm. Furthermore, this fitting allows estimating the dielectric constant ϵ of each layer from [37]

$$\epsilon = \epsilon' + i\epsilon'', \quad (3)$$

with $\epsilon' = n^2 - k^2$, and: $\epsilon'' = 2 \cdot n \cdot k$.

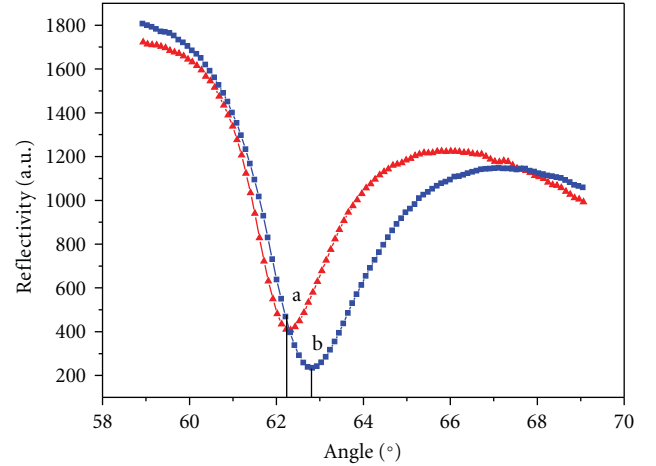


FIGURE 4: *In situ* SPR curves (reflected intensity (R) versus incidence angle (θ)) corresponding to: (a) bare gold electrode and (b) self-assembled monolayer functionalized gold electrode.

As k is the adsorbents index and n is the refraction index that were determined by fitting. Then the dielectric constant of the gold film was estimated to $\epsilon = -15.87 + i 1.355$. These values correspond to the wavelength of $\lambda = 650$ nm and they are comparable with literature [38].

3.2. Optical and Electrical Characterization of the Biofilm of System 1 (Based on SAM) and the Biofilm of System 2 (Based on Iron Oxide Nanoparticles)

3.2.1. SPR Measurement. A typical kinetics of step-by-step formation of the biofilm (system 1) is shown in Figure 5, that present the SPR angle sensorgrams. As the first step, we injected a glutaraldehyde solution (5%) into the sensor head containing a gold sensor surface functionalized by aminothiols (a signal from PBS served as the baseline). After 110 minutes and after rinsing by PBS buffer the incidence

TABLE 3: Fitting parameters obtained from the proposed equivalent circuit for the different layers of the immunosensor based on SAM.

Layer	R_s (Ωcm^2)	R_m (Ωcm^2)	CPE (Fcm^2)	α_{CPE}	χ^2
Bare gold	51.63	8292	1.8847E-5	0.96414	0.0011
Thiol	47.18	37120	4.0271E-6	0.9475	0.00058
GA	49.26	62535	3.2506E-6	0.94902	0.0011
Neutv.	43.22	48703	3.9494E-6	0.93945	0.0010
Ab	44.63	39869	4.1848E-6	0.93169	0.0010

TABLE 4: Fitting parameters obtained from the proposed equivalent circuit for the different layers of the immunosensor based on iron oxide nanoparticles.

Layer	R_s (Ωcm^2)	R_m (Ωcm^2)	CPE (Fcm^2)	α_{CPE}	χ^2
Bare gold	51.63	8292	1.8847E-5	0.96414	0.0011
Thiol	47.18	47280	4.4323E-6	0.95475	0.00023
Iron oxide nanoparticles	43.22	52673	3.0594E-6	0.92432	0.0011
Ab	44.63	74200	4.1848E-6	0.92349	0.0012

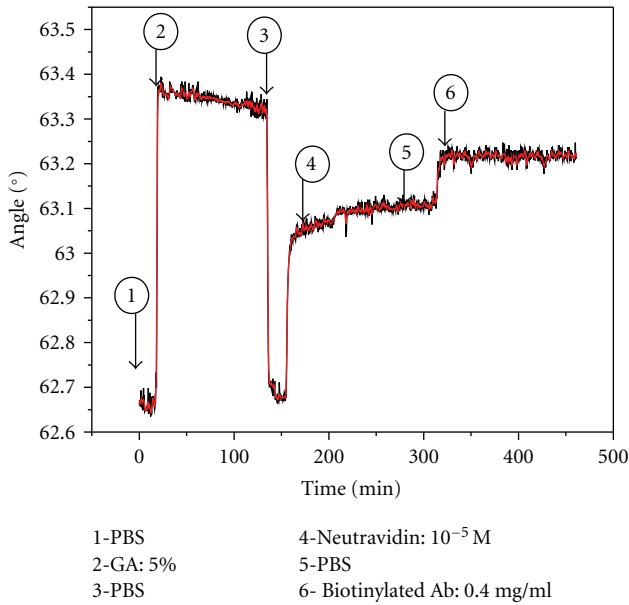
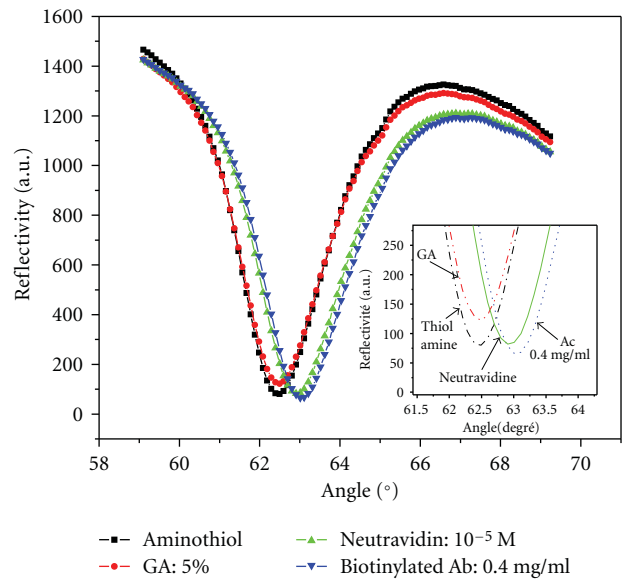


FIGURE 5: Building-up kinetics of the biofilm based on SAM. SPR responses for the step-by-step formation of multilayer. All measurements were performed in the flow cell, in PBS 10 mM pH 7.4.

angle was increased of 0.031° compared with the base line, indicating that a stable grafting of GA was achieved [29]. In the second step, neutravidin solution (10^{-5} M) was injected; this injection was accompanied by sharp changes in the signal until its saturation, suggesting that the neutravidin was indeed immobilized onto the GA activated surface. After 120 minutes of the injection, the SPR angle did not decrease during PBS flow, indicating that a stable immobilization of Neutravidin was achieved by covalent binding. An incidence angle shift of 0.465° was observed. Finely, Biotinylated Ab (0.4 mg/ml) was injected. An increase of 0.12° in incidence angle was observed after PBS flow, indicating an efficient binding reaction between biotinylated Ab and neutravidin

FIGURE 6: *In situ* SPR curves (reflected intensity (R) versus incidence angle (θ)) corresponding to the various layers grafted onto the gold electrode (system based on SAM): AUT, AUT-GA, AUT-GA-Neut., and AUT-GA- Neut.- Biot.ScAb.

(immobilization by biotin/avidin affinity) [39]. Using the incidence angle shift, the covering rate of antibody was determined according to

$$\Gamma_{\text{Ab}} = \frac{(\Delta\theta/K)}{(dn/dc)}, \quad (4)$$

where $\Delta\theta$, K , and dn/dc represent, respectively, variation of the incidence angle, conversion constant (5300 s of arc/nm) and refractive index increments (0.188 cm^3/g for the protein). For system 1, the covering rate of antibody reached 0.37 ng/mm^2 which corresponds to a surface density of antibody immobilized on the modified gold electrode of 148×10^9 Ab molecules/ mm^2 . With this surface density, the

TABLE 5: Comparison of analytical parameters of immunosensors based on SAM and immunosensor based on iron oxide nanoparticles.

	Analytical parameters	SAM system	IrNp System
Optical characterization	detection limit	4.5 $\mu\text{g/ml}$	300 ng/ml
	sensitivity	0.003 $^\circ \cdot \mu\text{g}^{-1} \cdot \text{ml}$	0.094 $^\circ \cdot \mu\text{g}^{-1} \cdot \text{ml}$
	Dynamic range	4.5 to 15 $\mu\text{g/ml}$	0.3 to 1 $\mu\text{g/ml}$
	The time response	45 minutes	30 minutes
	reproducibility	6.3%	5.7%
Electrical characterization	detection limit	1 ng ml^{-1}	500 pg ml^{-1}
	sensitivity	257.3 $\Omega \cdot \text{cm}^2 \cdot \mu\text{g}^{-1} \cdot \text{ml}$	1871 $\Omega \cdot \text{cm}^2 \cdot \mu\text{g}^{-1} \cdot \text{ml}$
	Dynamic range	1 to 50 ng ml^{-1}	0.5 to 50 ng ml^{-1}
	The time response	45 minutes	20 minutes
	reproducibility	8.7%	7.5%

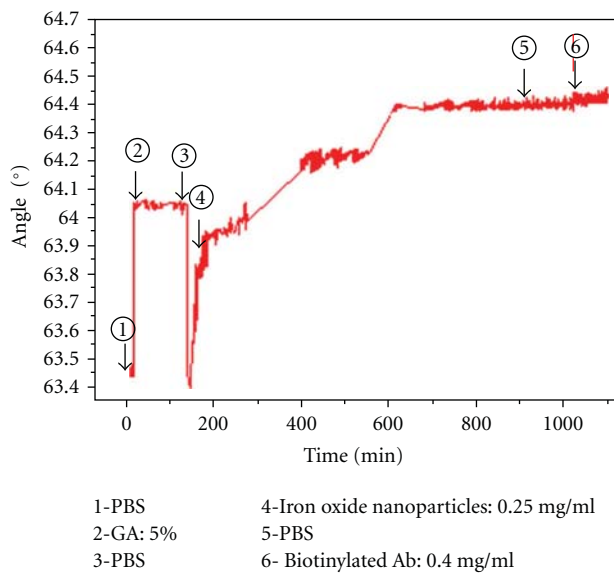
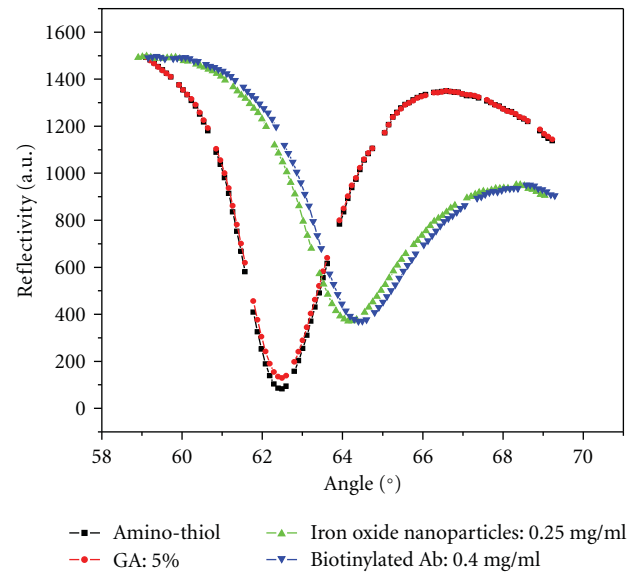


FIGURE 7: Building-up kinetics of the biofilm based on iron oxide nanoparticles. SPR responses to the step-by-step formation of multilayer. All measurements were performed in the flow cell in PBS 10 mM pH 7.4.

FIGURE 8: *In situ* SPR curves (reflected intensity (R) versus incidence angle (θ)) corresponding to the various layers grafted onto the gold electrode (system based on SAM): AUT, AUT-GA, AUT-GA-IrNP, and AUT-GA-IrNP. - Biot.ScAb.

average surface occupied by each Ab molecule of $6.73 \times 10^{-10} \text{ mm}^2$ was obtained.

For each step of grafting of the layers constituting the immunosensor membrane, the spectra presenting the reflected intensity versus incidence angle, after flowing PBS buffer, were recorded (see Figure 6). The thickness of each layer was calculated by fitting these spectra using the Winspall program. The refractive index used to fit the data for the protein layers was $n = 1.45$ [40]. This refractive index was assumed to be similar for all of the proteins and is commonly assumed for proteins studied by SPR. The fitting parameters are given in Table 1. Furthermore, this fitting allows estimating the dielectric constant ϵ . of each layer from (3).

In the same way, the building up of the membrane of immunosensor based on iron oxide nanoparticles was *in situ* controlled by SPR technique. Figure 7 shows the SPR angle sensorgrams. The results show that a stable immobilization

of GA was indicated by the increase of the incidence angle of 0.031° compared to the base line. The immobilization of GA was achieved by the covalent binding of the amino group of the modified gold electrode by reaction with aldehyde groups of glutaraldehyde. Afterwards, iron oxide nanoparticles solution (0.25 mg/ml) was injected on the new surface rich of aldehyde groups of glutaraldehyde. This injection was accompanied by sharp changes in the signal until its saturation, suggesting that the nanoparticles was indeed immobilized onto the GA activated surface. After 13 hours of the injection, the SPR angle did not decrease during the PBS flow, indicating that a stable immobilization of nanoparticles was achieved by covalent binding. An incidence angle shift of 1.681° was observed. Finally, Biotinylated Ab (0.4 mg/ml) immobilized by biotin/avidin affinity leading to an incidence angle shift of 0.266° .

For system 2, the covering rate of antibody reached $\Gamma_{\text{Ab}} = 0.95 \text{ mg/mm}^2$ which corresponds to a surface density

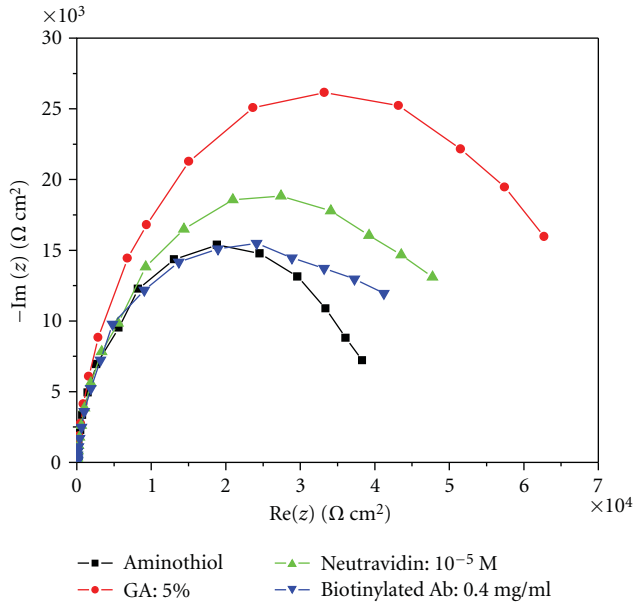


FIGURE 9: Nyquist diagram ($-\text{Im}(z)$ versus $\text{Re}(z)$) for the non-Faradic impedance measurements (at -400 mV versus SCE, in PBS solution 10 mM pH 7.4) corresponding to the various layers grafted onto the gold electrode (system based on SAM): AUT, AUT-GA, AUT-GA-Neut., and AUT-GA-Neut.- Biot.ScAb. Spectra were obtained between 0.05 Hz and 100 kHz. Amplitude of ac voltage: 10 mV.

of antibody immobilized on the modified gold electrode of 3.81×10^9 Ab molecules/ mm^2 which correspond to a doubled surface density compared to system 1.

For each step of grafting of the layers constituting the immunosensor membrane, the spectra presenting the reflected intensity versus incidence angle, after rinsing by PBS buffer, were recorded (see Figure 8). These spectra show the incidence angle shifts which correspond to each layer of the biofilm based on the iron oxide nanoparticles these results show again the construction of the biofilm layer by layer. Furthermore, the thickness of each layer was calculated by fitting these spectra using the Winspall program. The fitting parameters are given in Table 2. These results show that the average thickness of the nanoparticles layer is about 301 nm. Furthermore, AFM photograph of nanoparticles presented in Figure 1 shows their quasispherical shape. The distribution in size of the dried nanoparticles is the following one: the diameter range is between 160 nm to 500 nm with a mean diameter of 257 nm, and 28% of nanoparticles have a diameter of 240 nm. Therefore, the hydrodynamic diameter of the nanoparticles was determined using Malvern Nano-Zetasizer at 25°C . Magnetic nanoparticles were diluted at $1/200$ in a 1 mM NaCl solution pH 7 . The nanoparticles present a hydrodynamic diameter of 284 nm with a polydispersity coefficient of 0.1 and a zeta potential of -23.6 mV due to their streptavidin coating.

The comparison of the results of both systems proved that the use of the iron oxide nanoparticles increases the

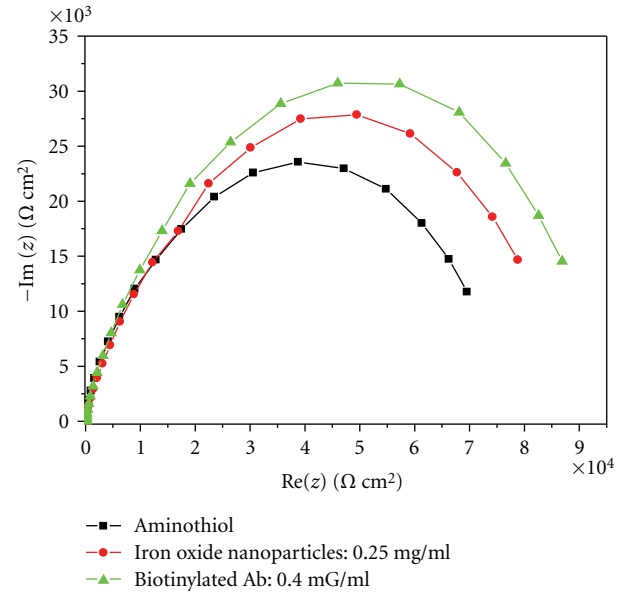


FIGURE 10: Nyquist diagram ($-\text{Im}(z)$ versus $\text{Re}(z)$) for the non-Faradic impedance measurements (at -400 mV versus SCE, in PBS solution 10 mM pH 7.4) corresponding to the various layers grafted onto the gold electrode (system based on iron oxide nanoparticles): AUT, AUT-GA- IrNP., and AUT-GA-IrNP-Biot.ScAb. Spectra were obtained between 0.05 Hz and 100 kHz. Amplitude of ac voltage: 10 mV.

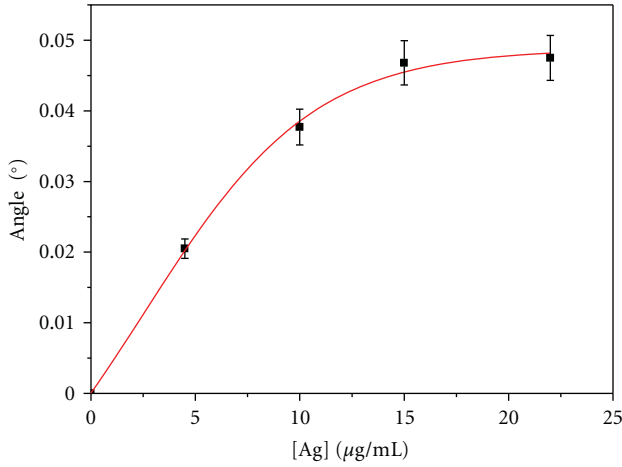
thickness of the layer of antibody from 0.4 to 1.2 nm, from where, the increase of the grafting density of antibody on the electrode.

3.2.2. Impedance Measurement. We used EIS to control the building up of the biofilm in PBS (10 mM, pH 7) at potential -400 mV. Figures 9 and 10 show the results of impedance spectroscopy measurements as Nyquist plots, for the assembly of the two biofilms on gold electrodes. All the electrical parameters values are presented in Table 3 and Table 4.

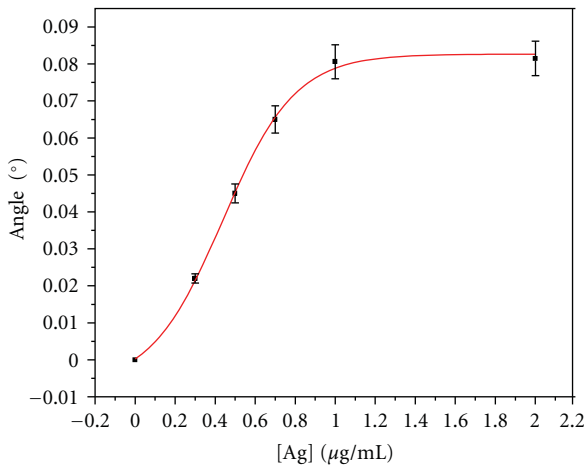
In the case of system 1 (based on SAM) (Figure 9), the fitting data (Table 3), the results show an increase of the membrane resistance R_m , of 37120 to 62535 Ωcm^2 , for GA film which reflected clearly the attachment of the GA film on the aminothioli functionalized electrode. Therefore, the capacitance element decreases, this is due to an increase in the thickness of the layer relating to

$$C_{\text{CPE}} = \frac{\epsilon_0 \epsilon_i A}{d_i}, \quad (5)$$

where ϵ_0 is the vacuum dielectric constant (8.85×10^{-14} F/ cm^2), ϵ_i is the dielectric constant of the layer i , A is the area of the surface, and d_i is the thickness of the layer. Afterwards, the decrease of R_m , during the grafting of neutravidin, further indicated the subsequent attachment of neutravidin on the modified electrode. Therefore, the



(a) Detection using system 1 based on SAM

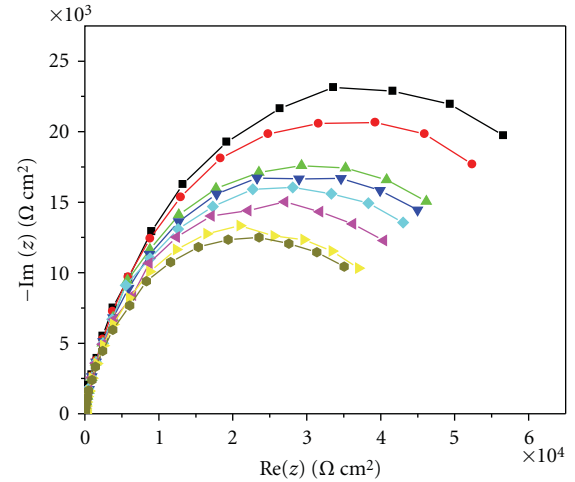


(b) Detection using system 2 based on iron oxide nanoparticles

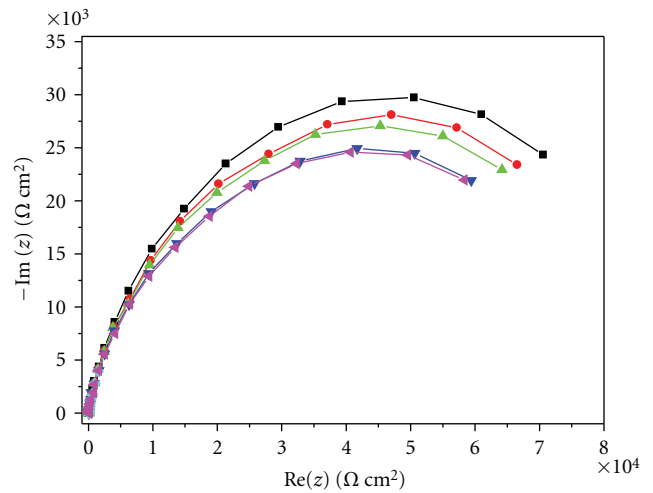
FIGURE 11: Optical calibration curves describing the variation of angle shift $\Delta\theta$ against antigen concentrations:

capacitance element increases, this is due to an increase in the dielectric constant, due to an increase in the conductivity that can be due to the grafting of a charged protein (neutravidin). Finally, the subsequent immobilization of scAb on the electrode was indicated by a decrease of R_m .

In the same measuring conditions, the building up of the biofilm of immunosensor based on iron oxide nanoparticles was controlled by EIS (Figure 10). From the fitting data (Table 4), The results show an increase of the membrane resistance R_m for IrNP film compared with SAM film, which reflected clearly the attachment of the IrNP film on modified electrode (no impedance measurements were performed when GA coupled SAM with IrNP). Therefore, the formation of an IrNP film will partially reduce the electron transfer of the modified electrode, so the conductivity of the whole IrNP layer decreases. Finally, the subsequent immobilization of scAb on the electrode was indicated by an increase of R_m .



(a) Detection using system 1 based on SAM



(b) Detection using system 2 based on iron oxide nanoparticles

FIGURE 12: Nyquist diagram ($-\text{Im}(z)$ versus $\text{Re}(z)$) at -400 mV versus SCE in PBS solution 10 mM $\text{pH } 7.4$, obtained for the non-Faradic impedance measurement on modified gold electrode with biotin tagged reduced antibody under various concentrations of antigen.

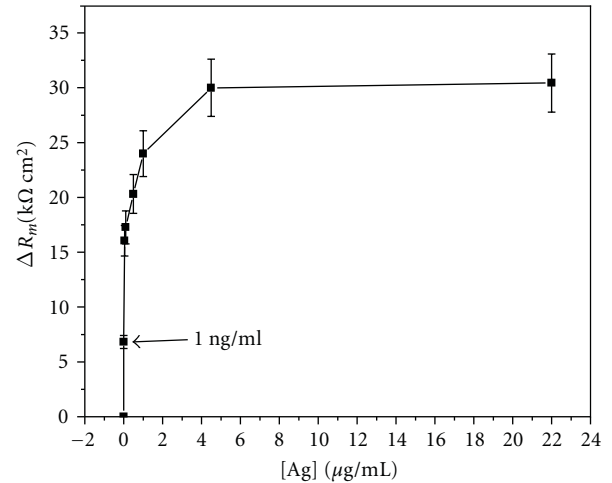
3.3. Electrical and Optical Detection via System 1 (Based on SAM) and via System 2 (Based on Iron Oxide Nanoparticles)

3.3.1. *Optical Detection.* In order to study the comparison of the two immunosensors responses, the optical calibration curves corresponding to the variation of incidence angle $\Delta\theta$ versus concentrations of specific antigen in PBS solution was

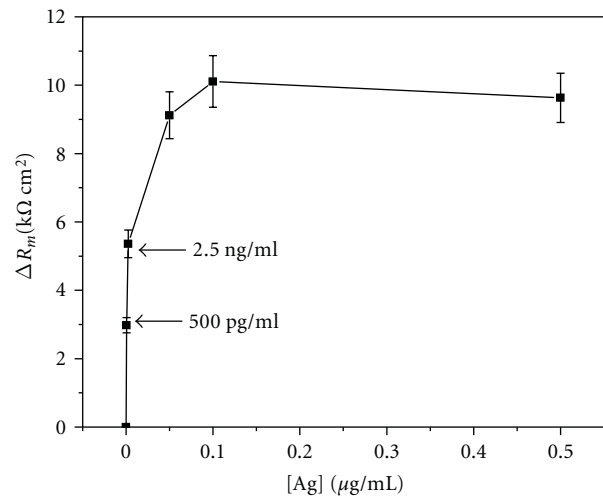
presented in Figure 11. Figure 11(a) presents the response of immunosensor developed with system 1. The immunosensor calibration curve with Ag concentrations presents a saturation part; however, the immunosensor response exhibits a linear relation between θ and the Ag concentrations ranging from 4.5 to 15 $\mu\text{g/ml}$ with a detection limit of 4.5 $\mu\text{g/ml}$, and an average response time of 45 minutes. The linear regression equation was $\theta = 0.003 [\text{Ag}] + 0.003$, with a correlation coefficient of 0.96. Figure 11(b) presents the response of immunosensor developed with system 2. The immunosensor calibration curve with Ag concentration presents a saturation part; however, the immunosensor response exhibits a linear relation between θ and the Ag concentration ranging from 0.3 to 1 $\mu\text{g/ml}$ with a detection limit of 300 ng/ml, and an average response time of 30 minutes. The linear regression equation was $\theta = 0.094 [\text{Ag}] + 0.002$, with a correlation coefficient of 0.98. Consequently, the results show a higher response in the case of the immunosensor based on iron oxide nanoparticles compared to immunosensor based on SAM.

3.3.2. Electrical Detection. Antigen—Antibody interactions were monitored by impedance spectroscopy in PBS solution (10 mM, pH 7) at -400 mV for system 1 and for system 2. Systematically, the electrodes modified with biotin-tagged antibody fragment were equilibrated with a range of concentrations of the specific antigen. The impedance spectra obtained after incubation with different concentrations of Antigen are shown in Figure 12. Immediately the impedance decreases clearly with the increase of [Ag], which indicates that a larger amount of Antigen was linked to the specific sites and the electron transfer decreases.

In order to study the comparison of both immunosensors responses, the electrical calibration curves corresponding to the variation of membrane resistance ΔR_m versus concentrations of specific antigen in PBS solution, was presented in Figure 13. Figure 13(a) presents the response of immunosensor developed with system 1. The immunosensor calibration curve with Ag concentration presents a saturation part; however, the immunosensor exhibits a linear relation between R_m and the Ag concentration ranging from 1 to 50 ng ml^{-1} with a detection limit of 1 ng ml^{-1} , and an average response time of 45 minutes. The linear regression equation in the range from 1 to 50 ng ml^{-1} was $R_m = 257.3 [\text{Ag}] + 3.248$, with a correlation coefficient of 0.83. Figure 13(b) presents the response of immunosensor developed with system 2. The immunosensor calibration curve with Ag concentration presents a saturation part; however, the immunosensor exhibits a linear relation between R_m and the Ag concentration ranging from 0.5 to 50 ng ml^{-1} with a detection limit of 500 pg ml^{-1} , and an average response time of 20 minutes. The linear regression equation in the range from 1 to 50 ng ml^{-1} was $R_m = 1871 [\text{Ag}] + 0.908$, with a correlation coefficient of 0.91. Consequently, comparing the characteristics of both Immunosensors, the results confirm that the using of the iron oxide nanoparticles improves immediately the characteristics of the immunosensor in terms of detection limit.



(a) Detection using system 1 based on SAM



(b) Detection using system 2 based on iron oxide nanoparticles

FIGURE 13: Electrical calibration curves describing the variation of membrane resistance ΔR_m against antigen concentrations.

4. Conclusion

In this study, we have developed an immunosensor based on functionalized iron oxide nanoparticles. By comparison with the development of an immunosensor based on SAM, we have demonstrated that the use of the functionalized iron oxide nanoparticles offers several advantages. The comparison of the results of both systems proved that the use of the iron oxide nanoparticles amplifies the response signal, so increases the thickness of the layer of antibody from 0.4 to 1.2 nm, from where, the increase of the grafting density of antibody on the electrode. In second time, we have demonstrated that by using electrochemical impedance spectroscopy combined with theoretical equivalent circuits models it is possible to determine the electrical properties. Furthermore, EIS allowed a thorough monitoring of the engineering of the bilayer membrane.

Table 5 shows the comparison of analytical parameters of immunosensors based on SAM and immunosensor based

on iron oxide nanoparticles from electrical and optical characterization. The comparison of characteristics of both immunosensors has showed that nanoparticles permitted to obtain the best characteristics. So, antibody immobilization on nanoparticles permitted to reach sensitivity and to reach lower detection limit: 500 pg/ml instead of 1 ng/ml to in the case of EIS and 300 ng/ml instead of 4.5 $\mu\text{g/ml}$ in the case of SPR. Thus, it permitted to improve the sensitivity from $257.3 \Omega \cdot \text{cm}^2 \cdot \mu\text{g}^{-1} \cdot \text{ml}$ to $1871 \Omega \cdot \text{cm}^2 \cdot \mu\text{g}^{-1} \cdot \text{ml}$ in the case of EIS and from $0.003^\circ \cdot \mu\text{g}^{-1} \cdot \text{ml}$ to $0.094^\circ \cdot \mu\text{g}^{-1} \cdot \text{ml}$ in the case of SPR.

References

- [1] S. Helali, A. Abdelghani, I. Hafaiedh, et al., "Functionalization of niobium electrodes for the construction of impedimetric biosensors," *Materials Science and Engineering C*, vol. 28, no. 5-6, pp. 826–830, 2008.
- [2] J. Ramón-Azcón, E. Valera, Á. Rodríguez, et al., "An impedimetric immunosensor based on interdigitated microelectrodes (ID μ E) for the determination of atrazine residues in food samples," *Biosensors & Bioelectronics*, vol. 23, no. 9, pp. 1367–1373, 2008.
- [3] I.-S. Park and N. Kim, "Development of a chemiluminescent immunosensor for chloramphenicol," *Analytica Chimica Acta*, vol. 578, no. 1, pp. 19–24, 2006.
- [4] M. Hnaïen, M. F. Diouani, S. Helali, et al., "Immobilization of specific antibody on SAM functionalized gold electrode for rabies virus detection by electrochemical impedance spectroscopy," *Biochemical Engineering Journal*, vol. 39, no. 3, pp. 443–449, 2008.
- [5] I. M. Ciumasu, P. M. Krämer, C. M. Weber, et al., "A new, versatile field immunosensor for environmental pollutants: development and proof of principle with TNT, diuron, and atrazine," *Biosensors & Bioelectronics*, vol. 21, no. 2, pp. 354–364, 2005.
- [6] B. Qu, X. Chu, G. Shen, and R. Yu, "A novel electrochemical immunosensor based on colabeled silica nanoparticles for determination of total prostate specific antigen in human serum," *Talanta*, vol. 76, no. 4, pp. 785–790, 2008.
- [7] M. Hnaïen, W. M. Hassen, A. Abdelghani, et al., "A conductometric immunosensor based on functionalized magnetite nanoparticles for E. coli detection," *Electrochemistry Communications*, vol. 10, no. 8, pp. 1152–1154, 2008.
- [8] Y. Y. Xu, C. Bian, Sh. Chen, and S. Xia, "A microelectronic technology based amperometric immunosensor for α -fetoprotein using mixed self-assembled monolayers and gold nanoparticles," *Analytica Chimica Acta*, vol. 561, no. 1-2, pp. 48–54, 2006.
- [9] A. C. Templeton, J. J. Pietron, R. W. Murray, and P. Mulvaney, "Solvent refractive index and core charge influences on the surface plasmon absorbance of alkanethiolate monolayer-protected gold clusters," *Journal of Physical Chemistry B*, vol. 104, no. 3, pp. 564–570, 2000.
- [10] C. Demaille, M. Brust, M. Tsionsky, and A. J. Bard, "Fabrication and characterization of self-assembled spherical gold ultramicroelectrodes," *Analytical Chemistry*, vol. 69, no. 13, pp. 2323–2328, 1997.
- [11] N. Chandrasekharan and P. V. Kamat, "Improving the photoelectrochemical performance of nanostructured TiO₂ films by adsorption of gold nanoparticles," *Journal of Physical Chemistry B*, vol. 104, no. 46, pp. 10851–10857, 2000.
- [12] G. Peto, G. L. Molnar, Z. Paszti, O. Geszti, A. Beck, and L. Gucci, "Electronic structure of gold nanoparticles deposited on SiO₂/Si(100)," *Materials Science and Engineering C*, vol. 19, no. 1-2, pp. 95–99, 2002.
- [13] N. Jaffrezic-Renault, C. Martelet, Y. Chevolot, and J.-P. Cloarec, "Biosensors and bio-bar code assays based on biofunctionalized magnetic microbeads," *Sensors*, vol. 7, no. 4, pp. 589–614, 2007.
- [14] W. M. Hassen, L. Angnes, A. Abdelghani, F. Bessueille, D. Leonard, and N. Jaffrezic-Renault, "Under flow impedimetric measurements using magnetic particles for label-free detection affinity target," *Materials Science and Engineering C*, vol. 28, no. 5-6, pp. 820–825, 2008.
- [15] W. M. Hassen, C. Chaix, A. Abdelghani, F. Bessueille, D. Leonard, and N. Jaffrezic-Renault, "An impedimetric DNA sensor based on functionalized magnetic nanoparticles for HIV and HBV detection," *Sensors and Actuators B*, vol. 134, no. 2, pp. 755–760, 2008.
- [16] Q. A. Pankhurst, J. Connolly, S. K. Jones, and J. Dobson, "Applications of magnetic nanoparticles in biomedicine," *Journal of Physics D*, vol. 36, pp. R167–R181, 2003.
- [17] M. A. M. Gijs, "Magnetic bead handling on-chip: new opportunities for analytical applications," *Microfluidics and Nanofluidics*, vol. 1, no. 1, pp. 22–40, 2004.
- [18] M. Shinkai, "Functional magnetic particles for medical application," *Journal of Bioscience and Bioengineering*, vol. 94, no. 6, pp. 606–613, 2002.
- [19] C. Berggren and G. Johansson, "Capacitance measurements of antibody-antigen interactions in a flow system," *Analytical Chemistry*, vol. 69, no. 18, pp. 3651–3657, 1997.
- [20] A. C. Howard, H. Z. Daniel, and O. Marc, "In vivo CH₃(CH₂)₁₁SAu SAM electrodes in the beating heart: in situ analytical studies relevant to pacemakers and interstitial biosensors," *Biosensors & Bioelectronics*, vol. 18, no. 1, pp. 11–21, 2003.
- [21] M. M. Vladimír, "New electroanalytical applications of self-assembled monolayers," *Trends in Analytical Chemistry*, vol. 21, no. 6-7, pp. 439–450, 2002.
- [22] S. Hleli, C. Martelet, A. Abdelghani, N. Burais, and N. Jaffrezic-Renault, "Atrazine analysis using an impedimetric immunosensor based on mixed biotinylated self-assembled monolayer," *Sensors and Actuators B*, vol. 113, no. 2, pp. 711–717, 2006.
- [23] M. M. Vladimír, R. Michael, and S. W. Otto, "Capacitive monitoring of protein immobilization and antigen-antibody reactions on monomolecular alkythiol films on gold electrodes," *Biosensors & Bioelectronics*, vol. 12, no. 9-10, pp. 977–989, 1997.
- [24] J. Melendez, R. Carr, D. U. Bartholomew, et al., "A commercial solution for surface plasmon sensing," *Sensors and Actuators B*, vol. 35, no. 1–3, pp. 212–216, 1996.
- [25] L. S. Jung, J. S. Shumaker-Parry, C. T. Campbell, S. S. Yee, and M. H. Gelb, "Quantification of tight binding to surface-immobilized phospholipid vesicles using surface plasmon resonance: binding constant of phospholipase A₂," *Journal of the American Chemical Society*, vol. 122, no. 17, pp. 4177–4184, 2000.
- [26] W.-C. Law, P. Markowicz, K.-T. Yong, et al., "Wide dynamic range phase-sensitive surface plasmon resonance biosensor based on measuring the modulation harmonics," *Biosensors & Bioelectronics*, vol. 23, no. 5, pp. 627–632, 2007.
- [27] A. Hallik, A. Alumaa, J. Tamm, et al., "Analysis of electrochemical impedance of polypyrrole," *Synthetic Metals*, vol. 156, no. 5-6, pp. 488–494, 2006.

- [28] C. Ehrenbeck, K. Jüttner, S. Ludwig, and G. Paasch, "The electrochemical impedance of a free-standing polypyrrole membrane," *Electrochimica Acta*, vol. 43, no. 19-20, pp. 2781–2789, 1998.
- [29] D. D. MacDonald, "Reflections on the history of electrochemical impedance spectroscopy," *Electrochimica Acta*, vol. 51, no. 8-9, pp. 1376–1388, 2006.
- [30] M. Wang, L. Wang, G. Wang, et al., "Application of impedance spectroscopy for monitoring colloid Au-enhanced antibody immobilization and antibody-antigen reactions," *Biosensors & Bioelectronics*, vol. 19, no. 6, pp. 575–582, 2004.
- [31] R. Pei, Z. Cheng, E. Wang, and X. Yang, "Amplification of antigen-antibody interactions based on biotin labeled protein-streptavidin network complex using impedance spectroscopy," *Biosensors & Bioelectronics*, vol. 16, no. 6, pp. 355–361, 2001.
- [32] R. K. Shervedani and S. A. Mozaffari, "Preparation and electrochemical characterization of a new nanosensor based on self-assembled monolayer of cysteamine functionalized with phosphate groups," *Surface & Coatings Technology*, vol. 198, no. 1–3, pp. 123–128, 2005.
- [33] X. Cui, D. Jiang, P. Diao, J. Li, R. Tong, and X. Wang, "Assessing the apparent effective thickness of alkanethiol self-assembled monolayers in different concentrations of $(\text{CN})_6/\text{Fe}(\text{CN})_6$ by ac impedance spectroscopy," *Journal of Electroanalytical Chemistry*, vol. 470, no. 1, pp. 9–13, 1999.
- [34] I. Navratilova and P. Skladal, "The immunosensors for measurement of 2,4-dichlorophenoxyacetic acid based on electrochemical impedance spectroscopy," *Bioelectrochemistry*, vol. 62, no. 1, pp. 11–18, 2004.
- [35] V. Freger and S. Bason, "Characterization of ion transport in thin films using electrochemical impedance spectroscopy. I. Principles and theory," *Journal of Membrane Science*, vol. 302, no. 1-2, pp. 1–9, 2007.
- [36] J. R. de Sousa, M. M. V. Parente, I. C. N. Diogenes, et al., "A correlation study between the conformation of the 1,4-dithiane SAM on gold and its performance to assess the heterogeneous electron-transfer reactions," *Journal of Electroanalytical Chemistry*, vol. 566, no. 2, pp. 443–449, 2004.
- [37] A. Ramanavičius, F. W. Herberg, S. Hutschenreiter, et al., "Biomedical application of surface plasmon resonance biosensors (review)," *Acta Medica Lituanica*, vol. 12, p. 1, 2005.
- [38] H. Raether, *Surface Plasmons*, Springer, New York, NY, USA, 1988.
- [39] J. Wong, A. Chilkoti, and V. T. Moy, "Direct force measurements of the streptavidin-biotin interaction," *Biomolecular Engineering*, vol. 16, no. 1–4, pp. 45–55, 1999.
- [40] W. Knoll, M. Liley, D. Piscevic, J. Spinke, and M. J. Tarlov, "Supramolecular architectures for the functionalization of solid surfaces," *Advances in Biophysics*, vol. 34, pp. 231–251, 1997.

Research Article

The Adsorption Properties of *Bacillus atrophaeus* Spores on Single-Wall Carbon Nanotubes

P. Cortes,¹ S. Deng,² and G. B. Smith³

¹Department of Mechanical & Aerospace Engineering, New Mexico State University, Las Cruces, NM 88003, USA

²Department of Chemical Engineering, New Mexico State University, Las Cruces, NM 88003, USA

³Department of Biology, New Mexico State University, Las Cruces, NM 88003, USA

Correspondence should be addressed to P. Cortes, pcortes@nmsu.edu

Received 21 September 2008; Accepted 19 March 2009

Recommended by Wojtek Wlodarski

An adsorption equilibrium and a kinetic study of *Bacillus atrophaeus* on Single-Wall Carbon Nanotubes (SWCNTs) were here performed to provide the basis for developing biosensor devices for detecting threatening micro-organisms in water supply systems. *B. atrophaeus* spores and carbon nanotubes were subjected to a batch adsorption process to document their equilibria and kinetics. Here, commercial nanotubes were either studied as received or were acid-purified before adsorption experiments. The *Bacillus* spores appear to show higher affinity towards the purified nanotubes than to the as-received nanomaterial. The effective diffusivity of the spores onto the purified nanotubes was found to be approximately 30 percent higher than onto the as-received nanotubes. It seems that the removal of amorphous carbon from the as-received nanotubes through a purification process yielded an intimate nanotubes-spore interaction as revealed by transmission electron microscopy. Freundlich model successfully correlated the adsorption equilibrium data for the nanotubes-spore interaction. Transmission electron micrographs showed extensive contact between the *Bacillus* and the purified nanotubes, but the association appeared less intimate between the spores and the as-received nanotubes.

Copyright © 2009 P. Cortes et al. This is an open access article distributed under the Creative Commons Attribution License, which permits unrestricted use, distribution, and reproduction in any medium, provided the original work is properly cited.

1. Introduction

Carbon nanotubes (CNTs) are one of the most promising materials in the areas of electronics, sensors, bio-manipulation, and medicine due to their unique mechanical, electrical, and chemical properties [1–4]. Indeed, a large amount of research on the area of sensors has positioned single-wall carbon nanotubes (SWCNTs) as one of the most capable structures for detecting diverse chemical and biological agents [5]. Recent studies have also shown the potential of carbon nanotubes as amperometric sensors for detecting analytes in solution without the requirement of any mediator due to their high electron transfer rates [6]. It has been shown that CNTs can act as a conducting channel for electrons towards redox active centers resulting in sensing materials for components such as cytochrome c, horseradish peroxidase, myoglobin, and glucose oxidase [7–10]. Li et al. [11] have studied the sensing properties of polymer-coated nanotubes for detecting hydrochloric acid (HCl) vapors.

They have shown that coated nanotubes are capable of sensing concentrations of HCl at levels as low as 2 ppm.

Detection of ammonia in water has been studied by Pantarotto et al. [12], and they have shown that the concentration can be measured based on the covered area of the CNTs by the ammonia. Current developments on nanotubes-based sensors performed by Nanosensors, Inc. [13] have shown that these nanomaterials can detect pathogenic microorganisms such as *E. coli* or *Salmonella* in food supplies. Studies carried out by Grüner [14] on sensors have shown that CNTs represent a real-time acquisition material with the potential of measuring intramolecular vibrations, anharmonic relaxations as well as conformational changes of the sensed media. Major challenges remain, however, in making devices that differentiate between adsorbed species in complex mixtures and provide rapid forward and reverse response. A recent work, based on the adsorption properties of different CNTs-bacterial systems, has shown that the adsorption kinetic is strongly dependant on the microorganism involved [15].

Here, it was reported that the adsorption of *S. aureus* upon as-received CNTs was considerably faster than that exhibited by *E. coli*. Evidently, the size of the microorganism influenced the rate of adsorption upon the carbonaceous material [15]. A research work carried out by Upadhyayula [16] on the adsorption equilibrium of *B. atrophaeus* upon commercial CNTs has also shown that the kinetics can be successfully predicted by the well-known Freundlich adsorption equation. These results are encouraging since predictive outcome on sensing signal may be simulated by established adsorption parameters. The study of *B. atrophaeus* (a nonpathogenic spore-forming bacterium) and CNTs system appears to be a good representation media of the interaction of nanotubes and lethal microorganisms such as *B. anthracis*. The rapid detection of microbial pathogens is of great interest due to the threats that they represent as a biological weapons [17]. We have shown that spores of Bacillus can survive in chlorinated tap water and can be recovered and identified on typical household water filters [18]. To date, the analytical detection methods of pathogenic contaminants on drinking water systems are complex and time consuming (between six hours to two days) [19]. Thus, the development of a pathogen detection device based on carbon nanotubes would represent a promising sensing platform.

In order to build an effective sensor device based on nanotubes, it is critical that these nanomaterials are free of their metal catalyst as well as of impurities such as amorphous carbon material. It has been shown that presence of amorphous carbon severely reduces the electrical properties of the nanostructures [20]. Additionally, elimination of amorphous carbon is a critical step for subsequent surface functionalization [21]. Indeed, by functionalizing their surface structures, specific chemical groups can be covalently attached to the nanotubes in order to address them into specific sensing applications. Undoubtedly, study of the physical attachment of biological organisms onto carbon nanotubes has to be initially performed in order to characterize their adsorption properties. The purpose of this research program is to study and compare the adsorption properties of *B. atrophaeus* onto as-received and purified SWCNTs for the development of a biothreat nanosensing devices.

2. Experimental Methodology

2.1. Absorbent Material. SWCNTs purchased from Carbolex, Inc. (Lexington, Ky, USA) were studied in this research program. These nanostructures were synthesized through an arc-discharge method yielding nanotubes with a diameter around 1.4 nm. A thermogravimetric analysis, performed in air by Carbolex, Inc. on these raw nanotubes, indicated that this material contained between 20 to 30 wt% of amorphous carbon. In this study, removal of amorphous carbon and impurities was performed by introducing 0.5 gram of carbon nanotubes into a 100 mL of a 2.6 M HNO₃ solution. The acid solution containing the nanotubes was placed in a shaker for 48 hours rotating at 150 r.p.m. at room temperature. Subsequently, the CNTs-acid solution was vacuum-filtered through a 5 μm pore size polycarbonate membrane, and the

filtrate washed with approximately 2 liters of deionized water. In this paper, both the as-received and the purified nanotubes were considered for the adsorption equilibrium and kinetics study.

2.2. Adsorbate Material. *B. atrophaeus* (formerly *B. subtilis* var. niger) was received from the U.S. Army Proving Grounds, Dugway, Utah, courtesy of Patricia Cox. Here, a stock culture was prepared following the purification method previously reported on *B. atrophaeus*-carbonaceous system [15]. The spores were stored in multiple capsules of 2 mL each at 4°C. These spores presented an elliptical shape with dimensions of 0.3 μm × 1 μm. The Schaeffer Fulton spore-staining method was also performed on the spores in order to identify the ratio between spores (nongrowing) and vegetative (growing) forms. Indeed, it is important to consider the amount of spores on each stage, since the adsorption and sensing mechanisms might be influenced by the spore/vegetative ratio. In this study, the ratio of spores to vegetative form was found to be around 2 : 1.

2.3. Adsorption Stage. Shaker experiments were performed to determine the kinetics and adsorption equilibrium of *B. atrophaeus* onto the as-received and the purified SWCNTs. Here, 0.1 gram of the as-received CNTs and 0.1 gram of the purified CNTs were added to different 250 mL flasks containing 99 mL of sterilized deionized water. Then, 1 mL of a spore solution of *B. atrophaeus* at a pre-established concentration was added to each flask at 1.3×10^4 , 4×10^5 , and 6×10^6 CFU/mL. (CFU: Colony Forming Unit). The flasks were then placed in a mechanical shaker at 200 r.p.m. at room temperature. Two milliliters of each CNTs/spore system were sampled at regular intervals and filtered through a 2 μm polycarbonate filter paper (Millipore, Mass, USA). The filtrates (containing unattached cells) of the CNTs/spore samples were inoculated on Tryptic Soy Agar (TSA) plates and incubated at 37°C for 24 hours, and the number of colonies grown on the plates was counted. The absorbed amount of spores onto the CNTs was calculated by a mass balance of the total spores in the solution before and after adsorption. The final concentration of the solution and the maximum adsorbed amount give the respective adsorption equilibrium concentration and adsorption capacity for the spores. The kinetic and equilibrium study performed in this research program was carried out on duplicates based on three different initial spore concentrations.

2.4. Microscopic Analysis. Optical analysis using a Hitachi S-3200 SEM and a Hitachi H 7650 TEM was performed on the as-received and purified CNTs to characterize their morphology. Microscopic observations of the CNTs/spore systems after the batch experiment were also carried out to elucidate their interaction.

3. Results and Observations

3.1. Microscopic Analysis. Initial evidence of the as-received material under the SEM showed bundles of aggregated

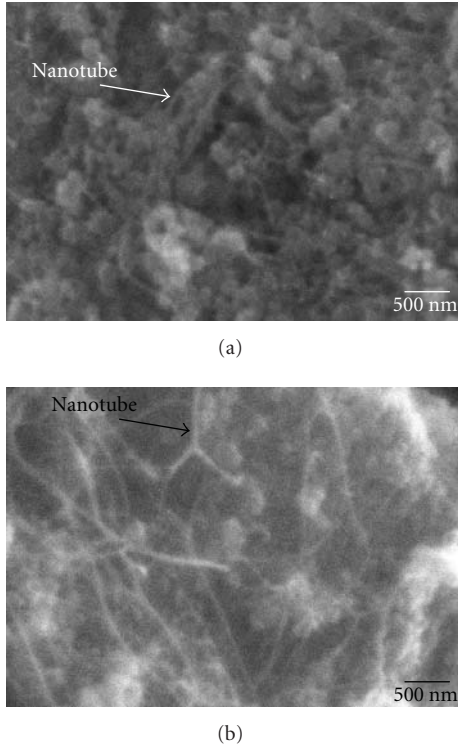


FIGURE 1: Scanning electron microscope micrograph of the SWCNTs (a) as-received and (b) purified.

nanotubes with a continuous entangled appearance (see Figure 1(a)). The presence of these continuous fibers agrees with previous studies carried out by Liu et al. on SWCNTs [22], where it has been shown that it is difficult to identify the end and beginning of an SWCNT. In contrast, Figure 1(b) shows an SEM micrograph of the SWCNTs after being subjected to an acid purification. From the figure, it can be observed that the chemical treatment disentangles the nanotubes as well as removes impurities such as amorphous carbon. Figure 2 shows TEM micrographs of the as-received and purified SWCNTs. This figure supports the findings observed on the SEM analysis, where it can be seen that a considerable amount of amorphous material has been removed after the nanotubes have been chemically treated.

3.2. Adsorption kinetics and Equilibrium. For the adsorption kinetic studies, samples were taken at different time intervals from the spores-CNTs batch experiments and were filtered. The variation of adsorbed spores onto the CNTs was established by counting the cells in the filtrate (representing the non-adsorbed spores) and subtracting them from the initial concentration.

Adsorption curves of the *B. atrophaeus*/as-received CNTs and the *B. atrophaeus*/purified CNTs for the three different initial spore concentrations here studied are shown in Figure 3. Here, the average fractional adsorption uptake (M_t/M_{\max}) is plotted against time (t); where M_t and M_{\max} are the adsorbed amounts per unit mass of adsorbent at a specific time and at infinity time, respectively. In this

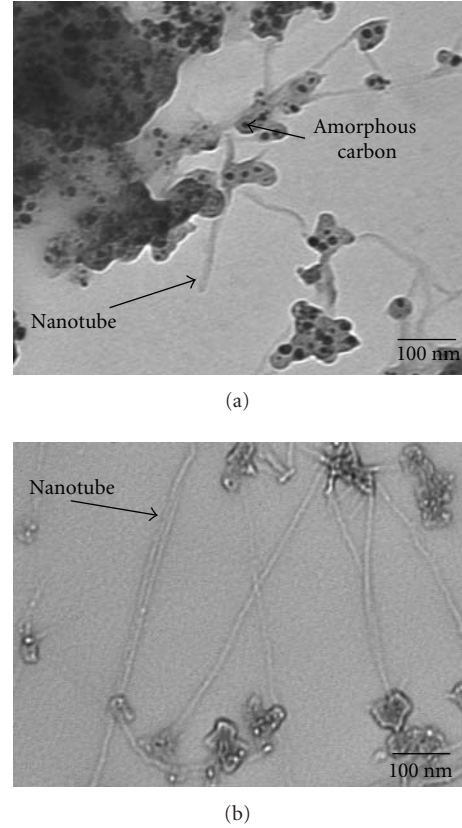


FIGURE 2: Transmission electron microscope micrograph of the SWCNTs: (a) as-received and (b) chemically treated.

study, M_{\max} was calculated from the last point of the kinetics study in the batch experiment. Figure 3 shows that the purified nanotubes yielded a higher adsorption uptake than that displayed by the as-received nanotubes. This is probably due to the fact that less amorphous carbon is present in the acid-purified nanotubes and, therefore, a more efficient adsorption process takes place on these purified CNTs. Indeed, it is interesting to note that in 1 minute of batch experiment, the treated nanotubes already adsorbed more than 80% of the spores. Figure 3 also shows that the maximum uptake increases at shorter times by decreasing the initial concentration of the absorbate material.

The effective diffusivity De of the spores onto the CNTs can be estimated using the following equation based on macropore diffusion process if the fractional uptake is greater than 70% [15]:

$$1 - \frac{M_t}{M_{\infty}} \approx \frac{6}{\pi^2} \exp\left(-\frac{\pi^2 De t}{r^2}\right), \quad (1)$$

where r is the absorbent particle radius, and t is the time. Indeed, it has been suggested in a previous study that the CNTs act as web during the bacteria nanotubes adsorption process [15]. Here, r is considered as the distance between carbon nanotubes aggregates, which is about $100 \mu\text{m}$ [16]. Hence, the diffusivity rate and the effective diffusivity (De) can be obtained from the slope of $\ln[(1 - M_t/M_{\infty})]$ against

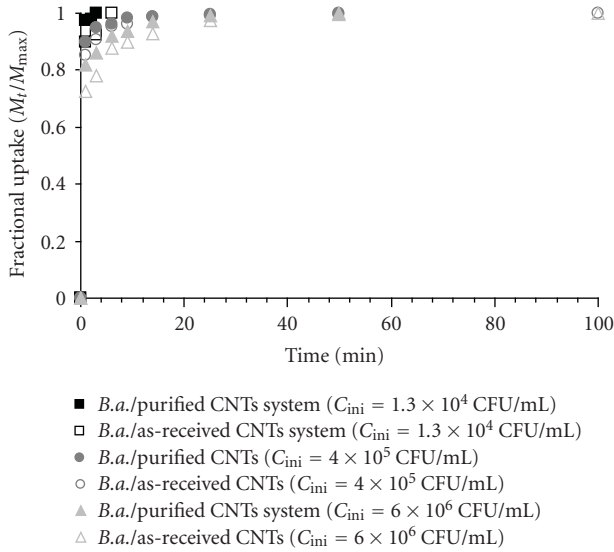


FIGURE 3: Adsorption uptake curves of *B. atrophaeus* on “as-received” and purified single-wall carbon nanotubes at room temperature.

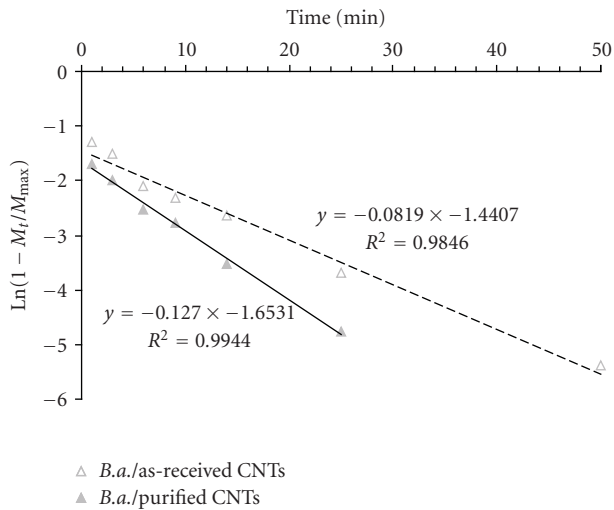


FIGURE 4: Correlation of adsorption kinetics data using a macro-pore diffusion model for the *B. atrophaeus* spores/nanotubes complex based on a spore initial concentration of 6×10^6 CFU/mL.

time (t); where the slope is given by $(-\pi^2 De/r^2)$ and the intercept by $\ln(6/\pi^2)$. Figure 4 shows the kinetic correlation for the *B. atrophaeus* and the two systems of CNTs here studied for the batch experiment based on the initial concentration of spores of 6×10^6 CFU/mL. From Figure 4, it can be observed that the effective diffusion rate of the spores onto the purified CNTs is more than 1.5 times greater than its as-received counterpart; this effect is probably due to the more intimate contact between the treated nanotubes and the spores. A conjecture that appears to agree with the TEM analysis.

Similar adsorption uptake curves were obtained with the other two concentrations of the absorbate here studied.

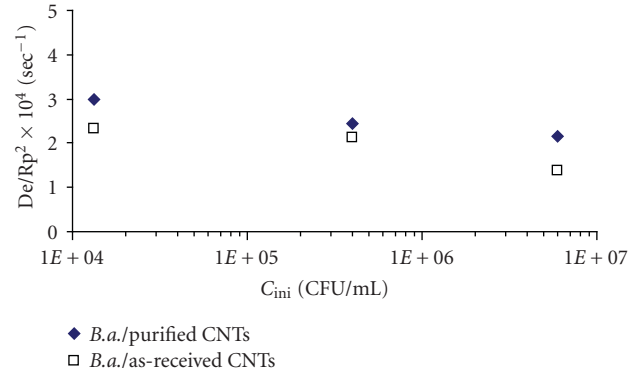


FIGURE 5: Diffusion time constant of the spores on as-received and purified nanotubes for different initial absorbate concentrations.

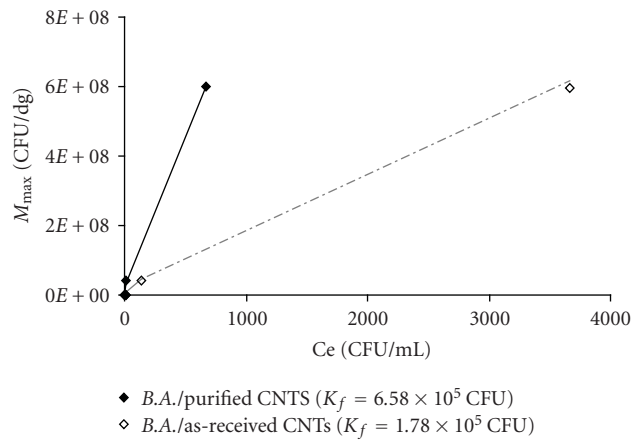


FIGURE 6: Adsorption equilibrium response of *B. atrophaeus* onto SWCNTs at room temperature. The solid lines represent the fitting of the Freundlich isotherm model to the experimental data.

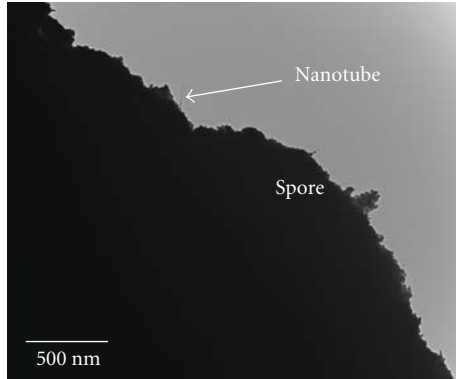
Indeed, by plotting the diffusivity rate of the three sets of experiments based on the initial spore concentration (see Figure 5), it can be observed that the diffusivity rate of spores onto the purified nanotubes is higher than that shown onto the as-received nanotubes. The effective diffusivity was then determined from the data presented on Figure 5. Table 1 shows the effective diffusivity of the samples here studied. As expected, the effective diffusivity for the *B. atrophaeus*/purified nanotubes is higher than that shown by the *B. atrophaeus*/as-received nanotube system. These results are again encouraging since they suggest that nanotubes with higher percent of purity may be used to develop a faster detection platform.

The maximum adsorbed amount of absorbate material (M_{max}) upon the nanotubes and its corresponding concentration in the supernatant (C_e) are plotted on Figure 6. Freundlich adsorption isothermal equation was used to fit the component adsorption data for the two systems-based CNTs here studied. The Freundlich isothermal is given by

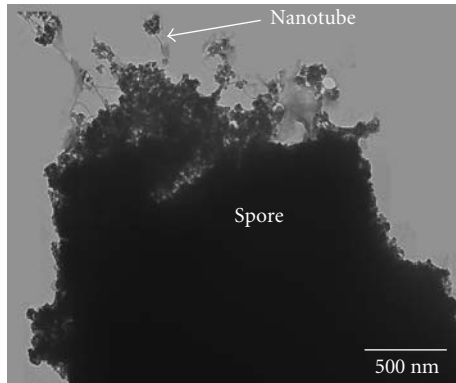
$$M_{max} = k_f C_e^{1/n}, \quad (2)$$

TABLE 1: Effective diffusivity of the *B.atrophaeus* spores onto purified and as-received SWCNTs for the three initial absorbate concentrations here studied.

Sample	Initial spore conc. (C_{ini})	Effective diffusivity D_e (cm^2/s)
<i>B. atrophaeus</i> /purified CNTs	1.33×10^4	3×10^{-10}
<i>B. atrophaeus</i> /as-received CNTs	1.33×10^4	2.33×10^{-10}
<i>B. atrophaeus</i> /purified CNTs	4×10^5	2.44×10^{-10}
<i>B. atrophaeus</i> /as-received CNTs	4×10^5	2.12×10^{-10}
<i>B. atrophaeus</i> /purified CNTs	6×10^6	2.14×10^{-10}
<i>B. atrophaeus</i> /as-received CNTs	6×10^6	1.38×10^{-10}



(a)



(b)

FIGURE 7: TEM picture of an isolated spores/untreated nanotubes complex following the shaker-batch interaction experiment. (a) After 1 minute. (b) After 50 minutes.

where k_f is the Freundlich adsorption coefficient, and n is the adsorption intensity parameter. Figure 6 shows a good fit between the isotherm and the experimental data (yielding r^2 higher than 0.98 for both systems). From the figure, the adsorption coefficient of the *B. atrophaeus*/purified CNTs is more than 3 times higher than the *B. atrophaeus*/as-received CNTs system. This again suggests that the removal of amorphous carbon increases the affinity of the nanotubes towards the spores.

3.3. *TEM Analysis.* Optical analysis of the bacillus-nanotubes systems following the batch experiments was carried out on a TEM to elucidate their interfacial interaction.

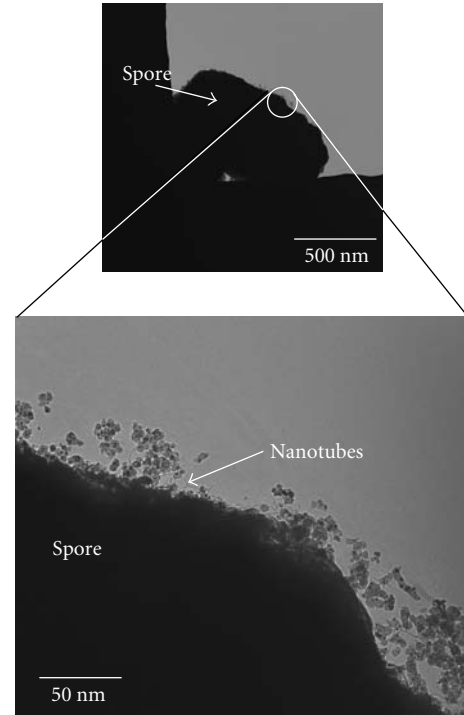


FIGURE 8: TEM picture of an isolated spores/purified nanotubes complex following a 1 minute shaking-batch interaction process.

Indeed, the sampled aliquots had to be diluted in order to be observed on the TEM. Typical micrographs of the CNTs-spores system are shown in Figure 7, where a strong interaction between both components can be observed. The figure shows the as-received nanotubes/bacillus complex after 1 and 50 minutes of shaking in the batch experiment. From the figure, it is observed that the interfacial contact increases at longer times, since more nanotube-spore material appears to be in contact after 50 minutes of shaking-batch interaction. Similar behavior was observed with the spore-purified CNTs system. Figure 8 shows the contact of the bacillus with the purified nanotubes after 1 minute in the shaker-batch experiment, and the amount of material interacting in this purified system appears to be higher than that shown with the as-received material. The micrograph shown in Figure 8 supports the kinetic data obtained in the present research work regarding the contention that there is stronger affinity

between spores and purified nanotubes compared to as-received nanotubes.

4. Conclusions

An adsorption equilibrium and a kinetic study of *B. atrophaeus* on SWCNTs have been here performed. The carbon nanotubes used in this study were investigated in its as-received condition as well as after being subjected to a chemical acid treatment. Evidence here presented demonstrates that the adsorption rate of spores onto purified nanotubes is faster than that shown onto untreated carbon nanotubes. Indeed, results have shown that the effective diffusivity of spores upon the nanotubes follows the same trend displayed by the adsorption rate. The Freundlich isotherm equation seems to fit well with the experimental data; here, the Freundlich adsorption coefficient of the *B. atrophaeus* on purified nanotubes was more than 3 times higher than that shown by its as-received counterpart. It has also been shown that the removal of amorphous carbon through the purification process evidently allows a more intimate interaction between the nanotubes and the spores. Optical analysis following spores-nanotubes interaction on a shaker-batch experiment supports the experimental data obtained during the kinetic process. Here, TEM micrographs showed higher interaction between the purified nanotubes and the spores than that exhibited between spores and the untreated nanotubes. This research work demonstrates the promising potential of building relatively short outcome biosensor devices based on diffusion parameters of microorganisms onto SWCNTs.

References

- [1] A. Javey, J. Guo, Q. Wang, M. Lundstrom, and H. Dai, "Ballistic carbon nanotube field-effect transistors," *Nature*, vol. 424, no. 6949, pp. 654–657, 2003.
- [2] P. P. Joshi, S. A. Merchant, Y. Wang, and D. W. Schmidtke, "Amperometric biosensors based on redox polymer-carbon nanotube-enzyme composites," *Analytical Chemistry*, vol. 77, no. 10, pp. 3183–3188, 2005.
- [3] B. I. Yakobson and R. E. Smalley, "Fullerene nanotubes: C_{1,000,000} and beyond," *American Scientist*, vol. 85, no. 4, pp. 324–337, 1997.
- [4] R. S. Ruoff, D. Qian, and W. K. Liu, "Mechanical properties of carbon nanotubes: theoretical predictions and experimental measurements," *Comptes Rendus Physique*, vol. 4, no. 9, pp. 993–1008, 2003.
- [5] E. Greenbaum, M. Rodriguez, and S. A. Sanders, "Biosensors for detection of chemical warfare agents," in *Dekker Encyclopedia of Nanoscience and Nanotechnology*, pp. 375–388, Marcel Dekker, New York, NY, USA, 2004.
- [6] Y. Lin, W. Yantasee, F. Lu, et al., "Biosensors based on carbon nanotubes," in *Dekker Encyclopedia of Nanoscience and Nanotechnology*, pp. 361–373, Marcel Dekker, New York, NY, USA, 2004.
- [7] J. Wang, M. Li, Z. Shi, N. Li, and Z. Gu, "Direct electrochemistry of cytochrome c at a glassy carbon electrode modified with single-wall carbon nanotubes," *Analytical Chemistry*, vol. 74, no. 9, pp. 1993–1997, 2002.
- [8] X. Yu, D. Chattopadhyay, I. Galeska, F. Papadimitrakopoulos, and J. F. Rusling, "Peroxidase activity of enzymes bound to the ends of single-wall carbon nanotube forest electrodes," *Electrochemistry Communications*, vol. 5, no. 5, pp. 408–411, 2003.
- [9] S. G. Wang, Q. Zhang, R. Wang, et al., "Multi-walled carbon nanotubes for the immobilization of enzyme in glucose biosensors," *Electrochemistry Communications*, vol. 5, no. 9, pp. 800–803, 2003.
- [10] G.-C. Zhao, L. Zhang, X.-W. Wei, and Z.-S. Yang, "Myoglobin on multi-walled carbon nanotubes modified electrode: direct electrochemistry and electrocatalysis," *Electrochemistry Communications*, vol. 5, no. 9, pp. 825–829, 2003.
- [11] J. Li, Y. Lu, and M. Meyyappan, "Nano chemical sensors with polymer-coated carbon nanotubes," *IEEE Sensors Journal*, vol. 6, no. 5, pp. 1047–1051, 2006.
- [12] D. Pantarotto, C. D. Partidos, R. Graff, et al., "Synthesis, structural characterization, and immunological properties of carbon nanotubes functionalized with peptides," *Journal of the American Chemical Society*, vol. 125, no. 20, pp. 6160–6164, 2003.
- [13] <http://www.nanosensorsinc.net>.
- [14] G. Grüner, "Carbon nanotube transistors for biosensing applications," *Analytical and Bioanalytical Chemistry*, vol. 384, no. 2, pp. 322–335, 2006.
- [15] S. Deng, V. K. K. Upadhyayula, G. B. Smith, and M. C. Mitchell, "Adsorption equilibrium and kinetics of microorganisms on single-wall carbon nanotubes," *IEEE Sensors Journal*, vol. 8, no. 6, pp. 954–962, 2008.
- [16] V. K. K. Upadhyayula, *Adsorption equilibrium and kinetics of microorganisms on single-wall carbon nanotubes*, Ph.D. thesis, New Mexico State University, Las Cruces, NM, USA, 2007.
- [17] J. B. Nuzzo, "The biological threat to U.S. water supplies: toward a national water security policy," *Biosecurity and Bioterrorism: Biodefense Strategy, Practice, and Science*, vol. 4, no. 2, pp. 147–159, 2006.
- [18] J. L. Sedillo, A. Quintana, K. Souza, K. H. Oshima, and G. B. Smith, "The development of point-of-use water filters as sampling devices in bioforensics: extent of microbial sorption and elution," *Journal of Environmental Monitoring*, vol. 10, no. 6, pp. 718–723, 2008.
- [19] A. Vaseashta and J. Irudayaraj, "Nanostructured and nanoscale devices and sensors," *Journal of Optoelectronics and Advanced Materials*, vol. 7, no. 1, pp. 35–42, 2005.
- [20] P. Cortés, K. Lozano, E. V. Barrera, and J. Bonilla-Rios, "Effects of nanofiber treatments on the properties of vapor-grown carbon fiber reinforced polymer composites," *Journal of Applied Polymer Science*, vol. 89, no. 9, pp. 2527–2534, 2003.
- [21] P. Cortés, T. Zhu, and R. Guzman, submitted to *Science and Technology of Advanced Materials*.
- [22] J. Liu, A. G. Rinzler, H. Dai, et al., "Fullerene pipes," *Science*, vol. 280, no. 5367, pp. 1253–1256, 1998.

Research Article

Electrochemical Sensing System Utilizing Simazine-Imprinted Polymer Receptor for the Detection of Simazine in Tap Water

Yusuke Fuchiwaki,¹ Naoki Sasaki,² and Izumi Kubo²

¹Health Technology Research Center, National Institute of Advanced Industrial Science and Technology (AIST), Midorigaoka 1-8-31, Ikeda, Osaka 563-8577, Japan

²Department of Bioengineering, Faculty of Engineering, Soka University, 1-236 Tangi-cho, Hachioji, Tokyo 192-8677, Japan

Correspondence should be addressed to Yusuke Fuchiwaki, yu-fuchiwaki@aist.go.jp

Received 30 December 2008; Accepted 21 May 2009

Recommended by Yongxiang Li

A simazine sensing system, composed of column packed with a molecularly imprinted polymer (Sim-MIP) and an electrochemical analyzer, was scaled down in order to easily determine the concentration of simazine, an environmentally restricted chemical, in tap water. In order to enhance the detection limit, the ratio of the eluent (dilution rate) in the electrolyte was optimized to 10%. A new in-house built column size with $\varnothing = 1.5$ mm was prepared, and 3 mg of Sim-MIP particles was packed in the column. During the sensing process, 90% of the simazine loaded to the column was collected by elution. The reductive current of simazine was determined up to 1–10 μ M. Solid phase extraction through the Sim-MIP column enabled simazine to be selectively detected from a mixed aqueous solution containing structural analogues in the range of 10–40 nM. Whether the concentration of simazine in tap water had reached environmentally restricted levels (10–40 nM) was determined within 1 hour using this system.

Copyright © 2009 Yusuke Fuchiwaki et al. This is an open access article distributed under the Creative Commons Attribution License, which permits unrestricted use, distribution, and reproduction in any medium, provided the original work is properly cited.

1. Introduction

Recently, triazine herbicides have been widely used to effectively increase the quantity of agricultural produce. Triazine herbicides are therefore distributed in the soil or irrigation water and may be spread to adjacent areas by wind, stream runoff, or evaporation. These herbicides are persistent in the natural environment and are therefore restricted to certain concentration levels for safety reasons [1].

Among the triazine herbicides, simazine has been commonly used around suburban areas, such as golf courses and dry riverbeds. However, simazine is suspected of being an endocrine disrupting chemical. According to the water-purity standards of the World Health Organization (WHO), tap water that is contaminated with 10 nM (2 ppb) of simazine is considered to be harmful. However, it is difficult to remove such trace amounts of simazine from tap water using common water purification systems.

In addition, there are few reports of simazine monitoring systems, despite numerous reports of sensors for atrazine, which belongs to the group of s-triazine herbicides that

includes simazine [2–7]. Therefore, a monitoring method that can be used to trace concentrations of simazine in untreated water is required.

In order to detect simazine, focus was made on molecularly imprinted polymers (MIPs) as a recognition element and a selective binder to simazine. We investigated the preparation of an imprinted polymer for simazine (Sim-MIP) from methacrylic acid (MAA) and ethylene glycol dimethacrylate (EDMA) as a sensor receptor for the construction of a simazine sensing system [8]. The electrochemical reduction of simazine by voltammetry was reported using a dropping mercury electrode [9]. We proposed a novel sensing system for simazine based on determination of its electrochemical coupling with Sim-MIP, which functions as a recognition element. The prepared Sim-MIP is more selectively bound to simazine under aqueous and acidic conditions through a hydrogen bond with the carboxyl group of MAA, compared with other triazines, such as atrazine and propazine. The sensing system was constructed from Sim-MIP particles packed in a column for the selective collection (solid phase extraction) of simazine and an

electrochemical analyzer, in which an amalgamated gold electrode was used as the working electrode in place of a dropping mercury electrode [10]. Use of the amalgamated electrode with electrochemical analyzing system provided a linear relationship between the concentration of simazine and the reductive current of simazine in the range of 10–30 μM . For the detection of 10 μM of simazine, 10 mL of a 100 nmol simazine solution was applied to the Sim-MIP packed column and eluted to a volume of 10 mL. The simazine in the eluent was then determined in a commonly used electrochemical vial, in which the electrodes were placed. Simazine at a level of 10 nM (WHO water-purity standard) could be detected with this system. The distinctive feature of the Sim-MIP solid-phase column is that a simazine concentration as low as 10 nM could be extracted. Therefore, for the detection of 10 nM simazine, a large volume (10 L) of 100 nmol simazine sample solution was applied to the column and eluted to a volume of 10 mL and then electrochemically analyzed. The results indicated that the column concentrated the simazine significantly; however, it took more than 10 hours to apply the entire sample solution to the column at a flow rate of 5 mL/min. Moreover, the obtained response showed low stability, because the large volume of sample solution was continued to be loaded onto the column. Although the performance showed that the system was applicable to a low concentration of simazine, it took an excessive amount of time, and also stable extraction was not easily achieved. Therefore, improvement of the sensing system is necessary to analyze the legally restricted concentration of tap water samples.

To establish a more efficient system for the evaluation of practical concentrations of simazine in the environment, the sensing system was improved to detect environmentally restricted concentrations of simazine in tap water within a short time frame. In order to reduce the time, the electrochemical cell setup and the Sim-MIP packed column were optimized. Basically, reduction of the volume of sample solution loaded to the column is required, which takes most of the time for the sensing process. Considering this, the system was scaled down by constructing an in-house built disposable column to realize a practical monitoring system. The optimum sensing system enabled simazine at environmentally restricted concentrations in tap water to be easily monitored within a time frame of 1 hour.

2. Experimental

2.1. Reagents. 6-Chloro-*N,N*-diethyl-1,3,5-triazine-2,4-diamine (simazine) and propazine were purchased from Wako Pure Chemicals (Osaka, Japan) as standard chemicals, and atrazine was purchased from Kanto Chemicals (Tokyo Japan). The structures of these herbicides are shown in Figure 1(a). Dimethylformamide (DMF), MAA, and EDMA were distilled prior to use in order to remove stabilizers (Figure 1(b)). Aqueous solutions of the triazine herbicides were prepared using water purified to 18.3 M Ω with a Milli-Q SP system (Millipore). All other chemicals were of laboratory grade and used without further purification.

Stock solutions of the herbicides were prepared at 2.0 mM by dissolving an appropriate amount of the triazine herbicide in methanol. Sample solutions were prepared by dilution of the stock solutions with 0.1 M KCl.

2.2. Preparation of MIP. The MIP for simazine was prepared using a previously reported procedure [8]. Simazine (1.34 mmol), MAA (9.99 mmol), EDMA (26.88 mmol), and azoisobutyronitrile (0.61 mmol) were mixed and dissolved in DMF (30 mL). After the solution was purged with dry nitrogen gas for 10 minutes, it was polymerized using UV light irradiation at 4°C for 5 hours. The obtained polymer was crushed in a mortar and sieved to between 30 and 60 μm diameter size. To remove the template (simazine), the polymer was washed three times in methanol/acetic acid (7:3 v/v).

2.3. Electrochemical Determination. In order to scale down the system, the electrochemical measurements were performed using a computer-controlled electrochemical analyzer (ALS 1200, Tokyo, Japan) and a three-electrode electrochemical cell setup in a glass vial that required only 1 mL of analyte solution. By reducing the volume of the electrochemical measurement solution from 10 to 1 mL, the initial sample solution used to load the column can be reduced. An amalgamated electrode as a working electrode was prepared on a gold electrode ($\varnothing = 1.6$ mm, BAS-Au) according to the recommended procedure given in the BAS Co. technique guide [11]. An Ag/AgCl (3 M NaCl) reference electrode and a auxiliary platinum wire electrode (BAS, Tokyo) were used.

All cyclic voltammetry electrochemical measurements were carried out in a glass vial containing a deoxygenated electrolyte (0.1 M KCl, pH 3.0) at room temperature. Simazine exhibited a reductive current at -1.08 V during the measurement at the scan rate of 0.1 V s^{-1} . The cathodic current difference at -1.08 V, with and without simazine, was recognized as the reductive current of simazine.

2.4. Sim-MIP Packed Column and Solid Phase Extraction (SPE). In our previous study, a commercially available column (I.D. = 3 mm, Eylea) was used, in which 20 mg of dried Sim-MIP particles were packed (Figure 1(c)) [10]. In this study, a small in-house built column (I.D. = 1.5 mm; Figure 1(d)) was prepared as an inexpensive setup to reduce the volume of the sample solution and to allow more stable and simpler extraction of simazine than the previous sensor setup. 3 mg of Sim-MIP particles were packed in the column. The procedure for sample application to the column was performed according to our previous report, as shown in Figure 1(e) [10]. In the first step, the sample solution was loaded and adsorbed onto the column packed with Sim-MIP. Dichloromethane was used to wash impurities from the Sim-MIP column resulting from sample solutions containing impurities, such as atrazine and/or propazine, as well as simazine. After removal of the impurities, methanol was loaded onto the column as the eluent to break the hydrogen bond between simazine and MAA. The eluent

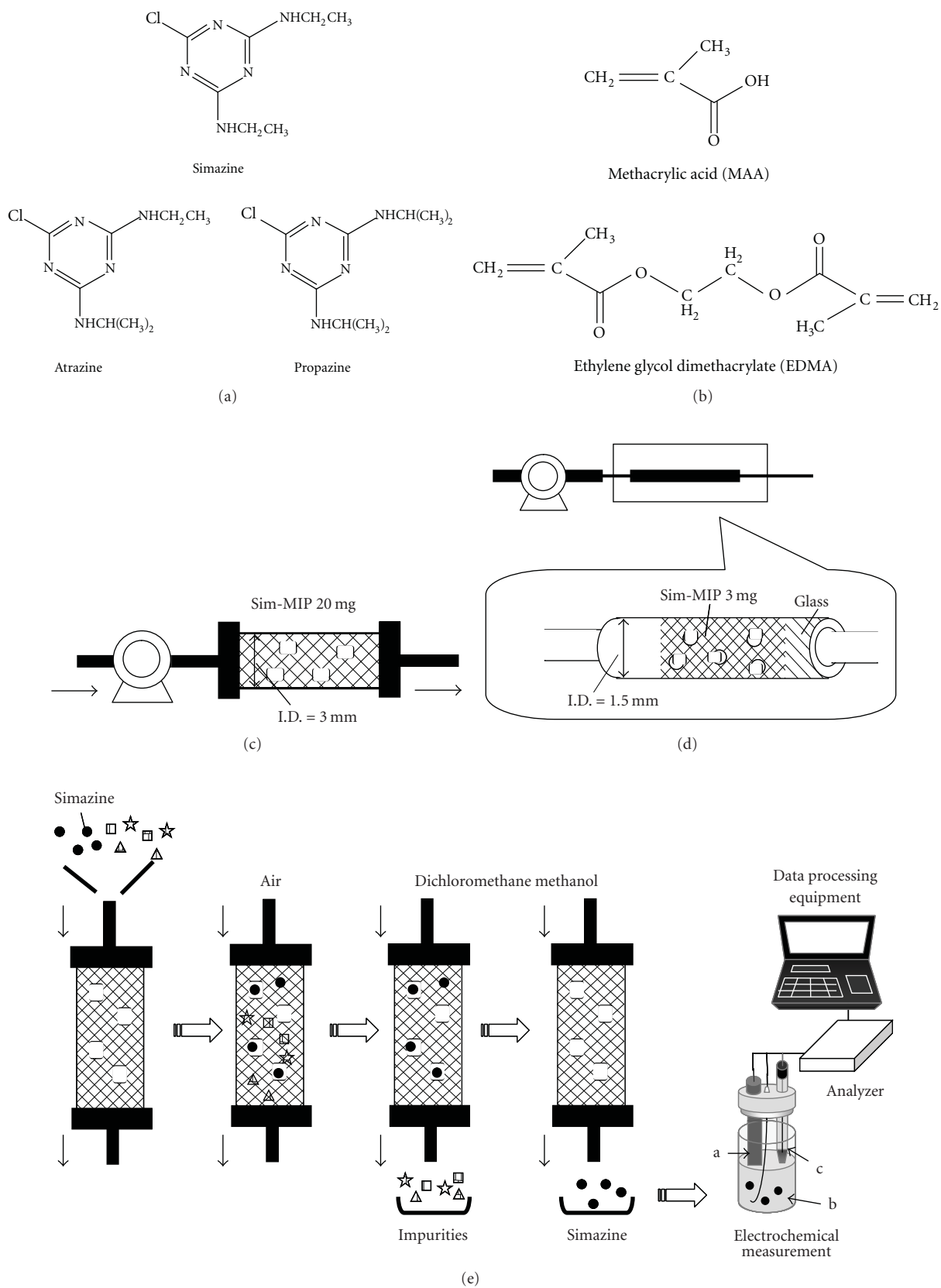


FIGURE 1: Schematic diagram of electrochemical sensing system for simazine. (a) Triazine compounds, (b) structural formula of MAA as functional monomer and EDMA cross-linking monomer, (c) the column packed with 20 mg of Sim-MIP, (d) the column packed with 3 mg of Sim-MIP, and (e) electrochemical sensing system combining the Sim-MIP packed column with electrochemical analyzing setup, a: an amalgamated electrode, (b) a vial containing 1 mL of solution, and (c) Ag/AgCl reference electrode.

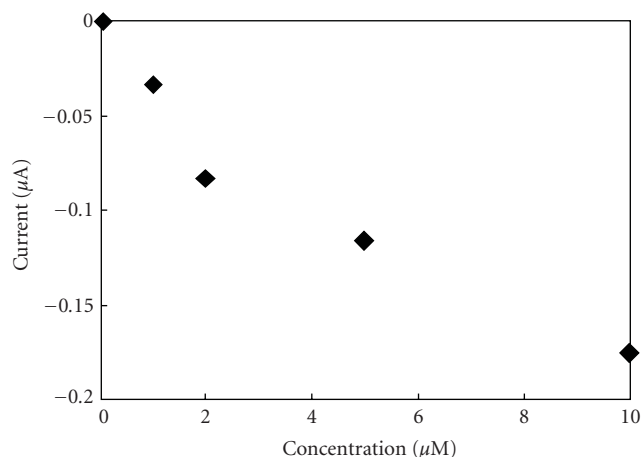


FIGURE 2: Calibration plot of simazine. One mL of the simazine solution containing 10% methanol was measured by cyclic voltammetry versus the scan rate of 0.1 V/sec. Reductive current of the cathodic peak was plotted against the concentration.

was mixed with electrolyte (0.1 M KCl, pH 3.0) at given ratios (1%–30%) and the sample in the electrolyte was then electrochemically measured by cyclic voltammetry. The flow rate of the loading solutions was 2.0 mL/min.

3. Results and Discussion

3.1. Electrochemical Measurement of Simazine on Amalgamated Gold Electrode. In our previous study, the highest reductive current of simazine was obtained for a pH 3.0 KCl solution as the electrolyte [8]. Simazine is electrochemically reduced through protonation, which precedes the electron-transfer reaction [9]. The electrochemical reaction of simazine has to be performed in acidic media. However, the reductive current of simazine is hardly detectable at a pH lower than 2.0; therefore, 0.1 M KCl (pH 3.0) was used as the electrolyte in the experiment.

The electrochemical detection of simazine was then performed after elution, in which simazine was eluted by methanol and mixed with the electrolyte. To reduce the detection time, reduction of the volume of simazine solution loaded onto the column is required; however, this would also result in reduction of the amount of simazine available for the electrochemical measurement. Therefore, optimum conditions for the sensitive electrochemical determination of simazine must be determined for this sensing process. For this purpose, the smaller volume of electrolyte is better, because simazine in the eluent would not be diluted. In other words, the dilution rate should be as low as possible.

Therefore, dilution of the eluent (methanol) by the electrolyte was examined at 1%, 10%, 20%, and 30%. The reductive current and peak potential of simazine (10 μM) at various dilutions were compared. The reductive current difference with and without simazine was also compared. The peak current of simazine was the highest at 10% methanol in the electrolyte, while there was no significant difference between the peak current at 1% and 10% dilution.

Each peak potential was -1.02 V at 1% methanol and -1.08 V at 10%. Higuera et al. reported that the peak current of simazine increased with the decrease in the peak potential in the range from -1.0 to -1.1 V due to changing proton concentration [9]. The results obtained are consistent with their study; therefore, the electrochemical measurement of simazine was performed at 10% methanol. For ratios higher than 10%, the reductive current of simazine decreased and was not observed at 30%. The peak potential shifted in the negative direction and overlapped the reductive potential of the proton itself, at around -1.2 V, and the electrochemical reduction of simazine and the proton compete at a higher concentration of methanol.

Based on this result, for the electrochemical determination, one hundred μL of the eluent was mixed with 900 μL of electrolyte solution to determine the concentration of simazine in 1 mL of the measurement solution. In addition, at volumes less than 1 mL of solution, the simazine did not reduce for stable electrochemical determination because of the change in dilution. Basically, it is difficult to completely maintain the diluted concentration of a mixed solution composed of methanol with the electrolyte at every measurement, because methanol is a volatile solvent. Moreover, simazine is a poorly water-soluble compound, so that precipitation would occur, even for a slight decrease in the methanol ratio of the mixed solution for a highly concentrated simazine solution. Thus, it was determined that for the electrochemical determination of simazine in a mixed measurement solution, 100 μL of methanol with 900 μL of electrolyte would be the optimum condition. As a result, the reductive peak current was dependent on the concentration of simazine up to 10 μM , and the electrochemical detection limit of simazine was 1 μM , as shown in Figure 2.

3.2. Improvement of the Sim-MIP Packed Column. The environmental standard for the simazine concentration in water is legally restricted to 19.8 nM (4 ppb) by the U.S. Environmental Protection Agency, 9.9 nM (2 ppb) by the World Health Organization, and 14.9 nM (3 ppb) in Japan. In our previous study, a sensing system was constructed by packing 20 mg of Sim-MIP particles in a commercially available column, which was coupled to an electrochemical analyzing system including an amalgamated gold electrode, and this system could detect the environmental restricted concentration of simazine [10]. In this system, a 100 nmol simazine sample solution (10 nM \times 10 L) was loaded on the Sim-MIP packed column and eluted using 1 mL methanol; however, a large volume of the simazine solution (10 L) must be loaded to collect 100 nmol of the simazine, requiring more than 10 h. This is not a suitable amount of time to detect a trace concentration of simazine. 1 μM of simazine in 1 mL (containing 1 nmol of simazine) was shown to be the limit of detection for the electrochemical system. To reduce the column loading time, we have proposed scaling down of the system, and the volume was reduced to 10% of that used in the previous study. However, the detection limit of the amalgamated gold electrode is 1 μM , which is higher than the environmental limit for simazine (10 nM)

TABLE 1: Improvement of the Column and Collected Simazine.

System	Column		Loaded simazine in sample			Eluent	Measurement		
	I. D. (mm)	Packed MIP (mg)	Concentration (nM)	Volume (mL)	Quantity (nmol)	Volume (mL)	Collected quantity (nmol)	Volume (mL)	Recovery (%)
1	3.0	20	10	1000	10	1.0	9.650	10	96.5
2	3.0	20	10	100	1	0.1	N.D.	1	N.D.
3	1.5	3	10	100	1	0.1	0.904	1	90.4

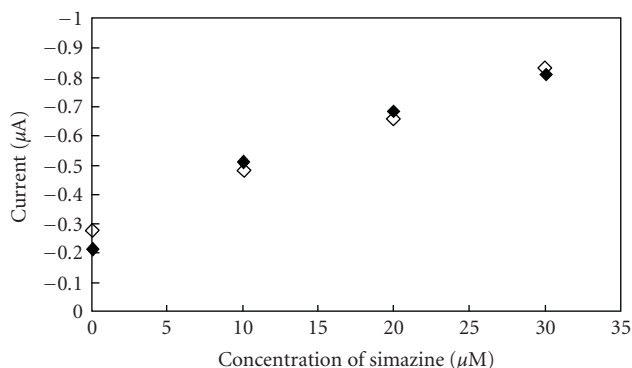


FIGURE 3: Calibration plot of simazine solution both with (◆) and without impurities (◇).

in tap water. Therefore, from such a trace concentration of simazine, 100 nmol has to be collected in the fabricated sensing system.

The examined column conditions are listed in Table 1. The recovered simazine in the eluent was determined by measurement of the UV light absorbance of simazine ($\lambda_{\max} = 220$ nm). When 1000 mL of the sample solution (10 nM) was loaded on a column packed with 20 mg of Sim-MIP, the recovery was 96.5%; however, in the case of 100 mL of sample loaded on the column, simazine was not detected in the eluent (0.10 mL). We consider that the volume of eluent may be insufficient for the size of the column. In order to take enough time to elute simazine with a small volume of eluent, the inner diameter of the column was reduced to half of the previous column, and was packed with 3 mg of Sim-MIP. When 100 mL of the sample was loaded on this column, the recovery in the eluent was 90%, so that it can be used as a small volume (1 mL) for electrochemical detection (Figure 1(e)b). When 100 mL of the sample was loaded on the column and eluted by 100 μ L of methanol, elution was completed within 1 h at a flow rate of 2 mL/min, as shown for system 3 in Table 1. Based on the calibration curve obtained, using this system, a linear relationship was observed in the concentration range of 10–40 nM. The sensitivity and reduction of the measurement time were improved by utilizing a small 3 mg Sim-MIP packed tube column, which was cheaper than that previously used (Figure 1(c)).

3.3. Selective Detection Of Simazine. With the use of an amalgamated gold electrode, triazine compounds such as atrazine and propazine exhibit similar CV profiles and

cathodic peaks similar to simazine. In our previous study, we examined the interference of atrazine and propazine in the determination of simazine, and the washing process using dichloromethane was so effective in removing the nonspecific adsorption of these compounds, and simazine was selectively detected, even from a sample solution also containing atrazine and propazine [10]. If compounds other than triazine herbicides are present in the tap water, these compounds would not be electrochemically detected in the negative potential area of the simazine cathodic peak, because water soluble and hydrophilic compounds are not adsorbed on the hydrophobic polymer of the Sim-MIP column.

In order to examine the effect of other triazine compounds, calibration plots of simazine with and without impurities such as atrazine (10 μ M) and propazine (10 μ M) were compared.

The sample solutions were eluted through the Sim-MIP packed column using the extraction procedure shown in Figure 1(e). The reductive current of the sample solution, both with and without impurities, showed a linear concentration dependence, and the slope was $-0.0204 \mu\text{A}/\mu\text{M}$ and $-0.0200 \mu\text{A}/\mu\text{M}$, respectively, and the calibration plots were almost the same in the examined range of simazine concentration (Figure 3). Therefore, when using this procedure, the presence of other triazine compounds has no effect on the measurement sensitivity.

3.4. Simazine Detection in Tap Water. Sample solutions of tap water spiked with 10, 20, or 40 nM of simazine were examined, and the concentrations were determined as 8.75, 22.5, and 43.5 nM, respectively. The simazine concentration found in tap water was almost the same as that expected, suggesting that there was no significant influence from unknown impurities in the tap water. Thus, it was shown that the electrochemical sensing system proposed in this study is applicable for the simple detection of environmentally restricted concentrations of simazine (10–40 nM) in tap water within a period of 1 hour.

4. Conclusion

A new electrochemical sensing system was fabricated using an in-house built column packed with 3 mg of Sim-MIP, coupled with an electrochemical analyzing system with an amalgamated gold electrode and a cell setup requiring 1 mL of analyte solution. 100 mL of a trace concentration of simazine solution was applied to the column, and simazine

was eluted by 100 μ L of methanol. One volume of eluent was mixed with nine volumes of electrolyte (0.1 M KCl, pH 3.0) for the electrochemical determination. The fabricated sensing system could specifically detect simazine in the range of 10–40 nM, even though there were other triazine compounds present. The environmental restricted concentration of simazine (10–40 nM) in tap water was determined within 1 hour. This sensing system provides a portable and low-cost method for the practical application of simazine sensing.

Acknowledgments

This work was supported by the Grant-in-aid from the Ministry of Education, Culture, Sports and Technology and the Open research project from Soka University and from Health Technology Research Center, National Institute of Advanced Industrial Science and Technology (AIST).

References

- [1] Q. Zhou, W. Wang, J. Xiao, et al., "Comparison of the enrichment efficiency of multiwalled carbon nanotubes, C18 silica, and activated carbon as the adsorbents for the solid phase extraction of atrazine and simazine in water samples," *Microchimica Acta*, vol. 152, no. 3–4, pp. 215–224, 2006.
- [2] J. Kniewald, M. Jakominic, A. Tomljenovic, et al., "Disorders of male rat reproductive tract under the influence of atrazine," *Journal of Applied Toxicology*, vol. 20, no. 1, pp. 61–68, 2000.
- [3] S. A. Piletsky, E. V. Piletskaya, A. V. Elgersma, et al., "Atrazine sensing by molecularly imprinted membranes," *Biosensors and Bioelectronics*, vol. 10, no. 9–10, pp. 959–964, 1995.
- [4] T. A. Sergeyeva, S. A. Piletsky, A. A. Brovko, et al., "Conductometric sensor for atrazine detection based on molecularly imprinted polymer membranes," *Analyst*, vol. 124, no. 3, pp. 331–334, 1999.
- [5] R. Shoji, T. Takeuchi, and I. Kubo, "Atrazine sensor based on molecularly imprinted polymer-modified gold electrode," *Analytical Chemistry*, vol. 75, no. 18, pp. 4882–4886, 2003.
- [6] C. Luo, M. Liu, Y. Mo, J. Qu, and Y. Feng, "Thickness-shear mode acoustic sensor for atrazine using molecularly imprinted polymer as recognition element," *Analytica Chimica Acta*, vol. 428, no. 1, pp. 143–148, 2001.
- [7] I. Kubo, R. Shoji, Y. Fuchiwaki, and H. Suzuki, "Atrazine sensing chip based on molecularly imprinted polymer layer," *Electrochemistry*, vol. 76, no. 8, pp. 541–544, 2008.
- [8] Y. Fuchiwaki, A. Shimizu, and I. Kubo, "6-chloro-*N,N*-diethyl-1,3,5-triazine-2,4-diamine (CAT) sensor based on biomimetic recognition utilizing a molecularly imprinted artificial receptor," *Analytical Sciences*, vol. 23, no. 1, pp. 49–53, 2007.
- [9] M. J. Higuera, M. R. Montoya, R. M. Galvín, and J. M. Rodríguez Mellado, "Contribution to the study of the electroreduction of 2-chloro-4,6-di(ethylamino)-1,3,5-triazine (simazine) on mercury electrodes," *Journal of Electroanalytical Chemistry*, vol. 474, no. 2, pp. 174–181, 1999.
- [10] Y. Fuchiwaki, N. Sasaki, and I. Kubo, "Development of an electrochemical sensing system for 6-chloro-*N,N*-diethyl-1,3,5-triazine-2,4-diamine (CAT) utilizing an amalgamated gold electrode and artificial sensor receptor," *Electrochemistry*, vol. 75, no. 9, pp. 709–714, 2007.
- [11] Technique guide of BAS corporation, <http://www.isesd.cv.ic.ac.uk>.

Research Article

A Novel Biosensor to Detect MicroRNAs Rapidly

Jie-Ying Liao,^{1,2} James Q. Yin,¹ and Jia-Chang Yue¹

¹ National Laboratory of Biomacromolecules, Institute of Biophysics, Chinese Academy of Sciences, Beijing 100101, China

² Center for Infection and Immunity, Institute of Biophysics, Graduate School of the Chinese Academy of Sciences (CAS), Beijing 100080, China

Correspondence should be addressed to James Q. Yin, jqwyin@ibp.ac.cn and Jia-Chang Yue, yuejc@sun5.ibp.ac.cn

Received 6 January 2009; Revised 13 May 2009; Accepted 9 July 2009

Recommended by Wojtek Wlodarski

δ -free F_0F_1 -ATPase within chromatophore was constructed as a novel biosensor to detect miRNA targets. Specific miRNA probes were linked to each rotary β subunits of F_0F_1 -ATPase. Detection of miRNAs was based on the proton flux change induced by light-driven rotation of δ -free F_0F_1 -ATPase. The hybridization reaction was indicated by changes in the fluorescent intensity of pH-sensitive CdTe quantum dots. Our results showed that the assay was attomole sensitivities (1.2×10^{-18} mol) to target miRNAs and capable of distinguishing among miRNA family members. Moreover, the method could be used to monitor real-time hybridization without any complicated fabrication before hybridization. Thus, the rotary biosensor is not only sensitive and specific to detect miRNA target but also easy to perform. The δ -free F_0F_1 -ATPase-based rotary biosensor may be a promising tool for the basic research and clinical application of miRNAs.

Copyright © 2009 Jie-Ying Liao et al. This is an open access article distributed under the Creative Commons Attribution License, which permits unrestricted use, distribution, and reproduction in any medium, provided the original work is properly cited.

1. Introduction

MicroRNAs (miRNAs) are small noncoding RNA molecules 20–22 nucleotides (nt) in length, which function to regulate gene expression. Recent studies have found that some miRNAs have altered expression in cancer cells, and specific alterations in miRNA expression may be an important biomarker for toxins which have serious effects on human health [1–4]. The effective detection is crucial for better understanding the roles of miRNAs in cancer cells, the response of cells to stress, and the process of cellular growth, proliferation, and metabolism. Therefore, many different methodologies have been used to profile miRNA expression, including Northern blotting with radio-labeled probes [5, 6], oligonucleotide microarrays [7, 8], and quantitative PCR-based amplification of precursor or mature miRNAs [9, 10]. However, the normal detection approaches require many steps such as enrichment, reverse transcription, amplification, labeling, and clean-up [11]. Most of these methods are time consuming due to overnight hybridization reaction and complicated fabrication. The most popular approaches to hybridization analysis such as Northern blotting and microarrays take a long time for hybridization of probes and their target molecules because of the static hybridization kinetics on a solid phase. To solve

this problem, microfluidics technology has been used to stir the hybridization solution to increase the rate of diffusion for rapid identification [12, 13]. For instance, the hybridization time of Surface Acoustic Wave (SAW) microagitation chips can be reduced and signal intensities increased more than 6 fold [14]. Thus, methods for rapid measuring the expression profiles of miRNAs will considerably accelerate the field in addition to the sensitivity and specificity.

Recent advances in nanotechnology have enabled the biosensor design and production of a variety of nanodevices for biological purpose. It is well known that F_0F_1 -ATPase is a complex of two parts, F_0 ($a_1b_2c_n$) and F_1 ($\alpha_3\beta_3r_1\delta_1\epsilon_1$). It is connected by a central stalk composed of γ and ϵ subunits and a peripheral stalk made of the δ and b subunits. The proton translocation through F_0 drives rotation of the c -ring oligomer together with $r\epsilon$ complex, forcing conformational changes in F_1 , which result in ATP synthesis from ADP and Pi [15, 16]. It is also known that the δ -subunit plays a switch role between the F_0 and F_1 in the ATP synthesis [17]. The δ -free F_0F_1 -ATPase is constructed with a_3 , b_3 , ϵ , and γ as well as c_n subunits as rotator and a , b_2 as stator. Based on this, Su et al. constructed a nanomotor by using δ -free F_0F_1 -ATPase within chromatophores [18].

Here, we developed a rapid method to detect miRNAs using the rotary nanoscale biosensor based on δ -free F_0F_1 -ATPase. The miRNA probe system, which was linked to the rotary β subunit of F_0F_1 -ATPase, was used to detect their target miRNAs. CdTe quantum dots- (QDs-) labeled chromatophores were responding to change of proton concentration of outside surface. In our experiments, miRNA probes linked to β subunit act as a rotary propeller. By this procedure, it is possible to monitor a real-time hybridization between the immobilized miRNA probes and the stirred target miRNAs. In addition, the procedure does not require enrichment, reverse transcription, amplification, and hybridization before detection. In this study, the method is sensitive to attomole of *mir-145* (1.2×10^{-18} mol) and is capable of discriminating a single base difference among *let-7* family members.

2. Materials and Methods

2.1. Materials. The water-soluble and pH-sensitive CdTe quantum dots (QDs) were gifts from Professor Tang Fangqiong (Technical Institute of Physics and Chemistry, Chinese Academy of Sciences, China). In this study, we used the QDs with maximum emission wavelength at 535 nm. ATP and streptavidin were purchased from Sigma-Aldrich (USA). Biotin-(AC5)2Sulfo-OSu was purchased from Dojindo (Japan). Lipidbiotin was purchased from Avanti. The δ -free ATPase within chromatophores was prepared as the previous study [18, 19]. The β -subunit of F_0F_1 -ATPase was expressed and purified as described previously [20]. The antibody was prepared according to the procedure [21]. *Mir-145* probe sequence is 5'-GGGGAU-UCCUGGAAACUGC-3'. The other probe sequences follow as *let-7a* (5'-AACTATAACAATCTACTACCTTATCCT-3'), *let-7a* (5'-UGAGGUAGUAGGUUGUAUAGUU-3'), *let-7b* (5'-UGAGGUAGUAGGUUGUGUGGUU-3'), *let-7c* (5'-UGAGGUAGUAGGUUGUAUGGUU-3'), and *let-7d* (5'-AGAGGUAGUAGGUUGCAUAGU-3'), respectively. Total RNA was extracted from MCF-7 human breast cancer cells by using TRIZOL reagent (Invitrogen) according to the manufacturer's instructions. All other analytically purified reagents are of analytical grade.

2.2. Cell Culture. The MCF-7 human breast cancer cell was kindly provided by Professor Jianwen Chen. Cells were maintained in Dulbecco's modified Eagle's medium (Sigma) supplemented with 10% fetal bovine serum (PAA) at 37°C in a humidified 5% CO₂ incubator.

2.3. Biosensor Assembly and miRNA Detection. The surface of chromatophores was labeled by QDs according to [22]. Briefly, the chromatophores (100 μ L) were resuspended in buffer A (50 mM tricine-NaOH, 5 mM MgCl₂, 10 mM KCl, pH 6.5) and incubated for 3 hours at room temperature with 100 μ L CdTe QDs ($1 \times 10^{15}/\mu$ L, dissolved in water). Free QDs were washed away by centrifuging at 13 000 rpm for 30 minutes at 4°C in three times. The precipitate (QD-labeled chromatophores) was re-suspended in 100 μ L of 50 mM tricine buffer (pH 6.5). Meanwhile, 2 μ L of 2 μ M biotin was

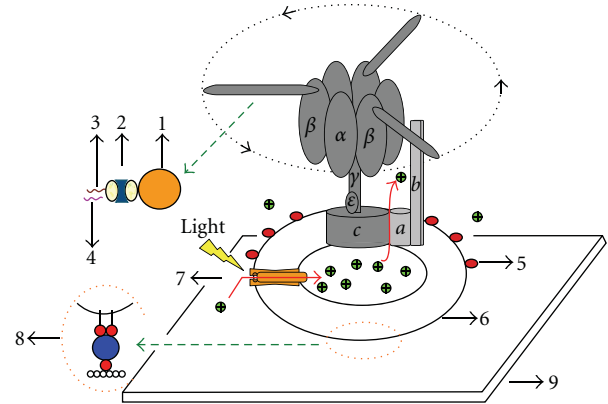


FIGURE 1: Schematic diagram of the biosensor based on F_0F_1 -ATPase within chromatophore. 1, 2, 3, 4, 5, 6, 7, 8, and 9 represent the antibody against β subunit, the linking system composed of [biotin-AC5-sulfo-OSu]-streptavidin-[biotin-AC5-sulfo-OSu], miRNA probe, target miRNA, 535 nm QDs, chromatophore, bacteriorhodopsins (BRs), the linking system of lipidbiotin-streptavidin-[biotin-AC5-sulfo-OSu]-Polylysine, and the glass surface, respectively.

added in 20 μ L β subunit antibody at room temperature for 30 minutes, followed by adding 2 μ L of 2 μ M streptavidin at room temperature for 30 minutes. The streptavidin-biotin-labeled β -subunit antibody was incubated with 5 μ L QDs-labeled chromatophores fixed on the glass slips at 37°C for 1 hour. Redundant free biotin-streptavidin-labeled β -subunit antibody was rinsed with 50 mM TSM buffer (50 mM Tricine-NaOH pH 7.0, 0.25 M sucrose, and 4 mM MgCl₂). Then 100 μ L 10 μ M miRNA probe labeled with biotin was added and incubated at room temperature for 30 minutes. Free probes were washed out by 50 mM TSM buffer. The δ -free F_0F_1 -ATPase with chromatophore was immobilized onto the glass surface through the biotin-streptavidin-biotin attachment. MiRNA probe system was hybridized with miRNA target in 100 μ L formamide hybridization solution at 37°C. Before the detection, the sample was exposed under the cooled light source with a 570 nm filter for one hour to initiate the rotation of the F_0F_1 -ATPase. During illumination, the buffer containing 2 mM NaN₃ and 2 mM ATP was infused into the chamber to inhibit the hydrolysis activity of the F_0F_1 -ATPase and hold force between the β_3 and γ to tightly band them together [18, 19, 23]. The hybridized reaction was recorded by our detection platform (BPCL) (see Supplementary Materials available online at doi: 10.1155/2009/671896). Fluorescence was excited at 471 nm and emitted at 535 nm.

2.4. Data Analysis. The data were presented as means \pm standard deviation of the mean. All experimental data were from average of at least 4–6 independent tests.

3. Results

3.1. Rotary Biosensor Design. Figure 1 showed the scheme of a novel rotary biosensor based on F_0F_1 -ATPase within

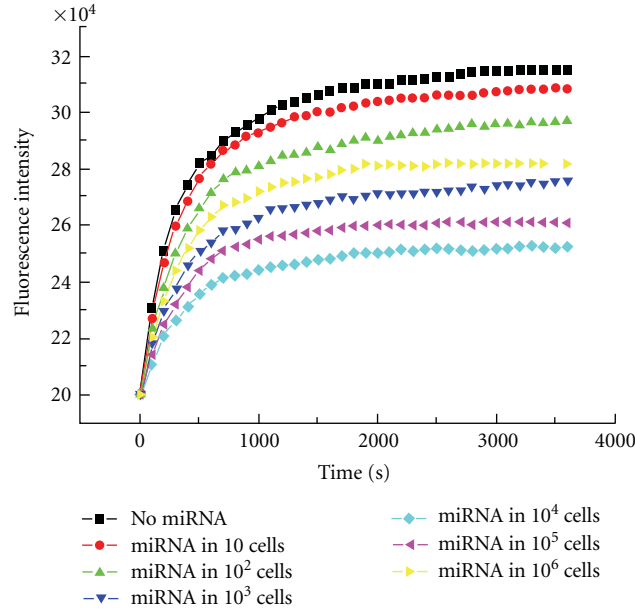
a chromatophore. Chromatophores were immobilized to glass surface by lipidbiotin-streptavidin-biotin-Polylysine system [18]. Each β subunit of F_0F_1 -ATPase was linked with a miRNA probe, which was used to detect target miRNA. Thus, three target miRNAs can bind specifically to a single F_0F_1 -ATPase. After illumination, the chromatophores can maintain the proton electrochemical gradient across the plasma membrane for a long time (see Supplementary Materials). The light-driven rotation of F_0F_1 -ATPase I resulted that the protons are pumped out of chromatophores and the proton concentration around chromatophores increased [15, 16], which leads to an enhancement of fluorescent intensity of CdTe quantum dots (QDs). The pH-sensitive QDs labeled on the outer surface of chromatophores are used as a proton sensor to detect proton flux [22]. Based on this, the changes of fluorescent intensity can indicate the alteration of H^+ concentration ($[H^+]$). When target miRNAs bind to the capture probes, the rotation of δ -free F_0F_1 -ATPase slows down, which leads to a decrease in fluorescent intensity. In the course of detecting target miRNAs, miRNA probes linked to β subunits function as a rotary propeller to stir the sample solution, which results in dynamic hybridization reaction. The rotation of δ -free F_0F_1 -ATPase-based biosensors enables one to monitor hybridization reactions in real time. In our experiment, the hybridization reaction is detected by recording the changes of fluorescence intensity. Using this method, the results can be obtained in 500 seconds.

3.2. Sensitivity and Detection Rang of miRNA Assay with Dynamic Hybridization Reaction. To determine the sensitivity of the method with dynamic hybridization property, we used miRNA (*mir-145*) probes to capture their target miRNAs in a complex RNA background and the change of fluorescence intensity was detected. The low limit of detection for the assays was found to be 1.2×10^{-18} mol (0.72×10^6 molecules) (see Supplementary Materials). Figure 2(a) showed the fluorescence intensity changes of biosensors with the different amounts of loads at 37°C , respectively. The no miRNA loading as control shows the low limit of detection. Serial 10-fold dilution of total RNA extracted from MCF-7 cells was used to analyze the detection range of the biosensors. The rate of fluorescence changes in 500 seconds were approximately 563.94 ± 9.68 U/s, 554.08 ± 9.95 U/s, 531.73 ± 10.97 U/s, 517.06 ± 4.19 U/s, 501.29 ± 10.05 U/s, 487.66 ± 6.95 U/s and 471.27 ± 5.94 U/s for biosensor hybridized with miRNA probe, miRNA from 10^1 cells, 10^2 cells, 10^3 cells, 10^4 cells, 10^5 cells and 10^6 cells, respectively. Using this novel rotary biosensor, we were able to detect not only amounts of relatively abundant miRNAs but also low level miRNAs because we observed a broad range of miRNAs expression levels from 1.2×10^{-18} mol (0.72×10^6 molecules) to 1.2×10^{-13} mol (0.72×10^{11} molecules). Compared to changes in fluorescence intensity of miR-145 from 10^6 cells, more miRNAs did not lead to the further changes because of the quantitative limitation of chromatophores. Increase of quantity of chromatophores can obtain a broader detection range. As shown in Figure 2(b), the rate of fluorescence changes in 500s of the different molecules is linear, and the detection range is about

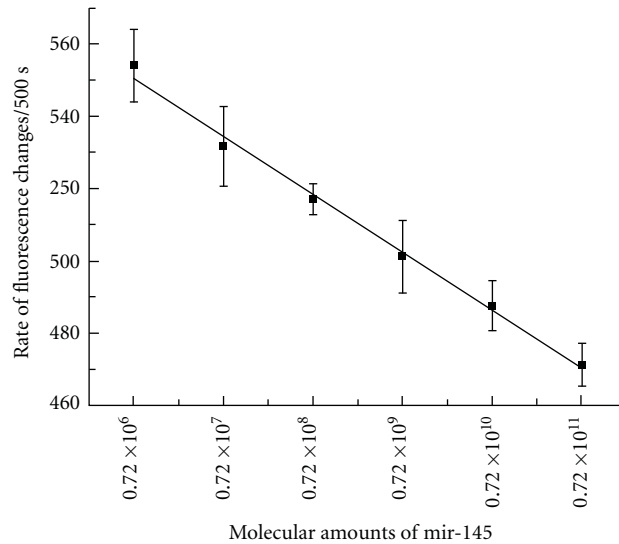
5 orders of magnitude, which implies that this method can be used to quantify miRNAs with a wide range.

3.3. Specificity of miRNA Assay with Dynamic Hybridization Reaction. Figure 3 showed the Specificity of miRNA assay with dynamic hybridization reaction by the four *let-7* family members. It is well known that Most human miRNAs differ by three or more nucleotide bases, but function as the different roles in cancer cells and the process of cellular growth, proliferation, and metabolism. In the *let-7* family, the members differ by only one or two nucleotide base. To determine whether our miRNA assay is capable of discrimination among family members under the condition of dynamic hybridization, we attempted to use *let-7a* probes to capture *let-7a*, *let-7b*, *let-7c*, or *let-7d* miRNA targets in 1 pM. The fluorescence intensity changes of *let-7a* binding to the *let-7a* probes (the rate of fluorescence change in 500 seconds: 471.36 ± 10.17 U/s) was relatively slight compared with that of the biosensor only loaded with miRNA probe (the rate of fluorescence change in 500 seconds: 559.96 ± 7.05 U/s), which indicated a specific binding to *let-7* miRNA target (Figure 3). In contrast, the fluorescence intensity changes of *let-7b*, *let-7c*, and *let-7d* binding to the *let-7a* probes (the rate of fluorescence change in 500 seconds: 553.14 ± 10.07 U/s, 549.42 ± 9.97 U/s and 552.99 ± 8.94 U/s) were more dramatic than that of *let-7a* binding to the *let-7a* probes and were similar to that of biosensor only loaded with miRNA probe. These results suggest that the rotary biosensor can be used to discriminate among the four *let-7* family members.

3.4. Comparative Analysis of Dynamic and Static Hybridization Reaction. The normal hybridization procedure fails to move solution volumes, and so this static hybridization reaction requires incubation over night. To demonstrate utility of the static hybridization, Figure 4 shows that the fluorescence intensity changes of biosensors were hybridized with miRNA target in $100 \mu\text{L}$ formamide hybridization solution at 37°C for 1 hour, 6 hours, and 12 hours, respectively. Before the detection, the sample in the buffer containing 2 mM NaN_3 and 2 mM ATP was exposed to the cooled light source with a 570 nm filter for 1 hour to initiate the rotation of the F_0F_1 -ATPase. Then, the results of static hybridization were recorded by our detection platform. Compared to the control only loaded with miRNA probe (565.89 ± 5.19 U/s), no significant binding signal was observed when hybridized with miRNA target for 1 hour (555.57 ± 8.15 U/s). These data suggested that the static hybridization was strongly correlated with the incubation time, which is consistent with previous study. The biosensor with dynamic hybridization (469.87 ± 8.01 U/s) can capture more target miRNAs than the biosensor with static hybridization for 6 hours (511.47 ± 10.01 U/s). But, upon static hybridization for 12 hours (451.90 ± 7.61 U/s), the rate of fluorescence changes was just slighter than that in dynamic hybridization (469.87 ± 8.01 U/s). The activity of δ -free F_0F_1 -ATPase did not change because of the overnight hybridization reaction (data not shown). In comparison with



(a)



(b)

FIGURE 2: Detection range of the miRNA biosensor assay with dynamic hybridization. (a) Total RNA extracted from MCF-7 cells was serially 10-fold diluted. Different amounts of miR-145 could be detected by the biosensor loaded without or with target miRNAs derived from 10 cells, 10^2 cells, 10^3 cells, 10^4 cells, 10^5 cells, and 10^6 cells reaction at 37°C , respectively. (b) Correlation between the rate of fluorescence changes and molecular amounts of miRNAs. The mean value was calculated from three independent detection experiments. Error bars show variations among the experiments as the standard deviation of the mean.

the static hybridization, the dynamic hybridization using the rotation of miRNA probe system will greatly reduce the time to detect target miRNAs.

4. Discussion

Here we present a novel method for the rapid detection of target miRNA. The miRNA probe system linked to rotary β subunit of δ -free F_0F_1 -ATPase was used to detect target miRNA. The change of proton flux was recorded through the

changes of fluorescence intensity of QDs, which can monitor real-time hybridization state [22]. In this study, the biosensor has function as a rapid, sensitive, and specific tool to detect miRNAs.

The recent miRNAs detection method has called for the rapidity of the hybridization reactions and real-time detection. In the normal hybridization reaction, the vicinity of the corresponding probe spot will take long time to finish, especially in case of low concentrated miRNA molecules. In our experiments, the rotation of F_0F_1 -ATPase-induced fluid

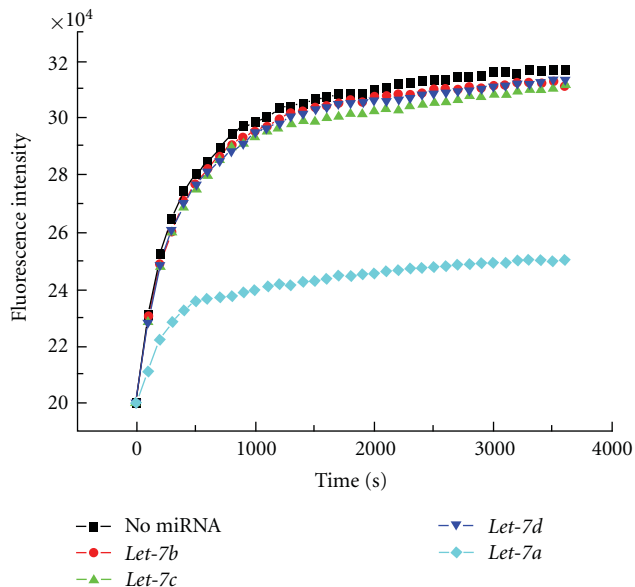


FIGURE 3: The miRNA biosensor with dynamic hybridization can be used to specifically detect the target miRNAs. The *let-7a* probes were used to capture their target miRNAs. The biosensor was only hybridized without any miRNAs or with incompletely complementary target *let-7b*, *let-7c*, *let-7d* or complete complementary target *let-7a* at 37°C, respectively.

movement of nanoliter volumes could increase in collision between the probe and the target, thereby accelerating the hybridization kinetics [24, 25]. The efficiency of biosensor with dynamic hybridization efficiency was more than that of static hybridization for 6 hours (Figure 4). Meanwhile, the rotation of δ -free F_0F_1 -ATPase makes it possible to monitor the real-time hybridization, which can yields data during the hybridization reaction. Furthermore, there is no need to reverse transcription and amplification before hybridization, thereby reducing the overall time of the detection.

The detection sensitivity was based on two lines of evidence. First, dynamic hybridization reaction might improve assay sensitivity. Peytavi et al. demonstrated that the microfluidic system increased the hybridization signal by 10-fold compared with a static hybridization system [13]. Other groups have demonstrated that inducing a microagitation in the fluid layer on a microarray can reach the signal amplification by 6-fold [14, 26]. Our method was sensitive enough to detect the amounts of miRNAs in 10 MCF-7 cells. Especially, *mir-145* is considered act as tumor suppressor genes or oncogenes and down-regulated in MCF-7 breast cancer cell line. Second, QDs have unique optical properties and exceptional photostability according to the previous study [27, 28]. In our experiments, more than two hundred QDs were attached on one chromatophore, which can enhance sensitivity in the process of miRNA detection (see Supplementary Material).

In terms of specificity, our method is capable of discrimination of a single base change in the target miRNAs even under particularly permissive binding condition. In

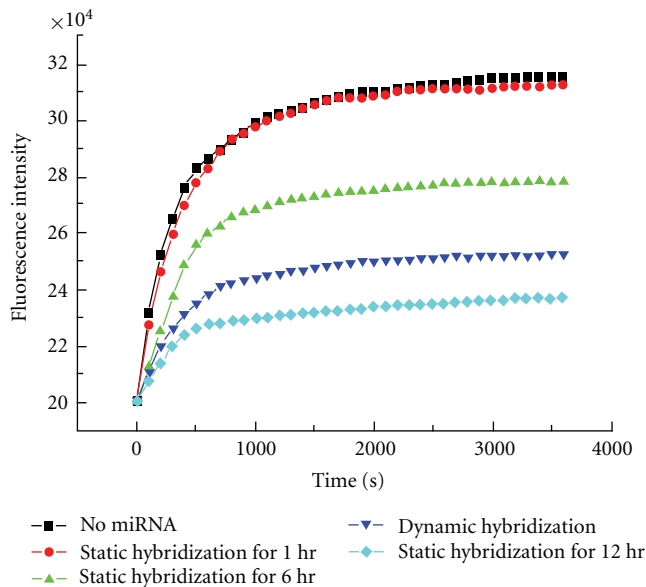


FIGURE 4: The dynamic hybridization resulted in a decrease in hybridization time. In the static hybridization, the biosensor was hybridized without or with miRNAs extracted from MCF-7 cells in the hybridization solution at 37°C for 1 hour, 6 hours, and 12 hours before detection, respectively. For the dynamic detection, the hybridization of biosensor and target miRNAs was monitored in real time without the preincubation with target miRNAs.

the experiments, we observed good discrimination among *let-7a*, *let-7b*, *let-7c*, and *let-7d* using *let-7a*-specific probes (Figure 3). During the hybridization reaction, the rotation of δ -free F_0F_1 -ATPase might decrease the binding of unspecific miRNAs. The results showed that rotary miRNA probe system tend to bind the target miRNA complementary completely to the probe sequence.

In conclusion, our results demonstrated that δ -free F_0F_1 -ATPase-based rotary biosensor is a promising research tool that can be applied to large-scale miRNAs detection combined with the lab-on-a-chip technology.

Acknowledgments

This work was supported by Grants from Basic Research Program of China National Natural Science of China (973-2007CB935901), Instrument Program of Chinese Academy of Sciences (07CZ203100), and National Natural Science Foundation of China (20873176).

References

- [1] M. Z. Michael, S. M. O'Connor, N. G. van Holst Pellekaan, G. P. Young, and R. J. James, "Reduced Accumulation of Specific MicroRNAs in Colorectal Neoplasia," *Molecular Cancer Research*, vol. 1, no. 12, pp. 882–891, 2003.
- [2] G. A. Calin, C.-G. Liu, C. Sevignani, et al., "MicroRNA profiling reveals distinct signatures in B cell chronic lymphocytic leukemias," *Proceedings of the National Academy of Sciences of the United States of America*, vol. 101, no. 32, pp. 11755–11760, 2004.

- [3] L. He, J. M. Thomson, M. T. Hemann, et al., "A microRNA polycistron as a potential human oncogene," *Nature*, vol. 435, no. 7043, pp. 828–833, 2005.
- [4] S. M. Johnson, H. Grosshans, J. Shingara, et al., "RAS is regulated by the let-7 microRNA family," *Cell*, vol. 120, no. 5, pp. 635–647, 2005.
- [5] J. Jiang, E. J. Lee, Y. Gusev, and T. D. Schmittgen, "Real-time expression profiling of microRNA precursors in human cancer cell lines," *Nucleic Acids Research*, vol. 33, no. 17, pp. 5394–5403, 2005.
- [6] A. M. Krichevsky, K. S. King, C. P. Donahue, K. Khrapko, and K. S. Kosik, "A microRNA array reveals extensive regulation of microRNAs during brain development," *RNA*, vol. 9, no. 10, pp. 1274–1281, 2003.
- [7] T. D. Schmittgen, J. Jiang, Q. Liu, and L. Yang, "A high-throughput method to monitor the expression of microRNA precursors," *Nucleic Acids Research*, vol. 32, no. 4, p. e43, 2004.
- [8] L. F. Sempere, S. Freemantle, I. Pitha-Rowe, E. Moss, E. Dmitrovsky, and V. Ambros, "Expression profiling of mammalian microRNAs uncovers a subset of brain-expressed microRNAs with possible roles in murine and human neuronal differentiation," *Genome Biology*, vol. 5, no. 3, p. R13, 2004.
- [9] M. Sioud and Ø. Røsoek, "Profiling microRNA expression using sensitive cDNA probes and filter arrays," *BioTechniques*, vol. 37, no. 4, pp. 574–580, 2004.
- [10] A. Válóczy, C. Hornyik, N. Varga, J. Burgyán, S. Kauppinen, and Z. Havelda, "Sensitive and specific detection of microRNAs by northern blot analysis using LNA-modified oligonucleotide probes," *Nucleic Acids Research*, vol. 32, no. 22, p. e175, 2004.
- [11] P. T. Nelson, D. A. Baldwin, L. M. Scarce, J. C. Oberholtzer, J. W. Tobias, and Z. Mourelatos, "Microarray-based, high-throughput gene expression profiling of microRNAs," *Nature Methods*, vol. 1, no. 2, pp. 155–161, 2004.
- [12] J. A. Benn, J. Hu, B. J. Hogan, R. C. Fry, L. D. Samson, and T. Thorsen, "Comparative modeling and analysis of microfluidic and conventional DNA microarrays," *Analytical Biochemistry*, vol. 348, no. 2, pp. 284–293, 2006.
- [13] R. Peytavi, F. R. Raymond, D. Gagné, et al., "Microfluidic device for rapid (< 15 min) automated microarray hybridization," *Clinical Chemistry*, vol. 51, no. 10, pp. 1836–1844, 2005.
- [14] A. Toegl, R. Kirchner, C. Gauer, and A. Wixforth, "Enhancing results of microarray hybridizations through microagitation," *Journal of Biomolecular Techniques*, vol. 14, no. 3, pp. 197–204, 2003.
- [15] P. D. Boyer, "The ATP synthase—a splendid molecular machine," *Annual Review of Biochemistry*, vol. 66, pp. 717–749, 1997.
- [16] J. Weber and A. E. Senior, "ATP synthesis driven by proton transport in F_0F_1 -ATP synthase," *FEBS Letters*, vol. 545, no. 1, pp. 61–70, 2003.
- [17] Y. B. Cui, Y. H. Zhang, J. C. Yue, and P. D. Jiang, "Direct observation of the clockwise light-driven rotation of F_0F_1 -ATP synthase complex," *Chinese Science Bulletin*, vol. 13, no. 49, pp. 1342–1347, 2004.
- [18] T. Su, Y. Cui, X. Zhang, et al., "Constructing a novel Nanodevice powered by δ -free F_0F_1 -ATPase," *Biochemical and Biophysical Research Communications*, vol. 350, no. 4, pp. 1013–1018, 2006.
- [19] Z. Yinghao, W. Jun, C. Yuanbo, Y. Jiachang, and F. Xiaohong, "Rotary torque produced by proton motive force in F_0F_1 motor," *Biochemical and Biophysical Research Communications*, vol. 331, no. 1, pp. 370–374, 2005.
- [20] X. Liu, Y. Zhang, J. Yue, P. Jiang, and Z. Zhang, " F_0F_1 -ATPase as biosensor to detect single virus," *Biochemical and Biophysical Research Communications*, vol. 342, no. 4, pp. 1319–1322, 2006.
- [21] W. C. Hanly, J. E. Artwohl, and B. T. Bennett, "Review of Polyclonal Antibody Production Procedures in Mammals and Poultry," *Institute of Laboratory Animal Research*, vol. 37, pp. 93–118, 1995.
- [22] Z. Yun, D. Zhengtao, Y. Jiachang, T. Fangqiong, and W. Qun, "Using cadmium telluride quantum dots as a proton flux sensor and applying to detect H9 avian influenza virus," *Analytical Biochemistry*, vol. 364, no. 2, pp. 122–127, 2007.
- [23] E. Muneyuki, M. Makino, H. Kamata, Y. Kagawa, M. Yoshida, and H. Hiata, "Inhibitory effect of NaN_3 on the F_0F_1 ATPase of submitochondrial particles as related to nucleotide binding," *Biochimica et Biophysica Acta*, vol. 1144, no. 1, pp. 62–68, 1993.
- [24] D. Axelrod and M. D. Wang, "Reduction-of-dimensionality kinetics at reaction-limited cell surface receptors," *Biophysical Journal*, vol. 66, no. 3, pp. 588–600, 1994.
- [25] M. K. McQuain, K. Seale, J. Peek, et al., "Chaotic mixer improves microarray hybridization," *Analytical Biochemistry*, vol. 325, no. 2, pp. 215–226, 2004.
- [26] I. Nindl, A. Toegl, W. Sterry, and E. Stockfleth, "High sensitivity and reproducibility of immunohistochemistry with microagitation," *Archives of Dermatological Research*, vol. 296, no. 6, pp. 278–281, 2004.
- [27] X. Wu, H. Liu, J. Liu, et al., "Immunofluorescent labeling of cancer marker Her2 and other cellular targets with semiconductor quantum dots," *Nature Biotechnology*, vol. 21, no. 1, pp. 41–46, 2003.
- [28] W. C. W. Chan and S. Nie, "Quantum dot bioconjugates for ultrasensitive nonisotopic detection," *Science*, vol. 281, no. 5385, pp. 2016–2018, 1998.

Research Article

Ozone Sensor for Application in Medium Voltage Switchboard

Letizia De Maria and Giuseppe Rizzi

Transmission and Distribution Department, ERSE, via Rubattino 54, 20134 Milan, Italy

Correspondence should be addressed to Letizia De Maria, demaria@erse-web.it

Received 30 December 2008; Revised 30 April 2009; Accepted 6 May 2009

Recommended by Yongxiang Li

The application of a new spectroscopic type fiber sensor for ozone detection in electrical components of Medium Voltage (MV) network is evaluated. The sensor layout is based on the use of an optical retroreflector, to improve the detection sensitivity, and it was especially designed for detecting in situ rapid changes of ozone concentration. Preliminary tests were performed in a typical MV switchboard. Artificial defects simulated predischarge phenomena arising during real operating conditions. Results are discussed by a comparison with data simultaneously acquired with a standard partial discharge system.

Copyright © 2009 L. De Maria and G. Rizzi. This is an open access article distributed under the Creative Commons Attribution License, which permits unrestricted use, distribution, and reproduction in any medium, provided the original work is properly cited.

1. Introduction

The reliability of electrical equipment in Medium Voltage (MV) substations is a prerequisite to guarantee the continuity of the service in an MV distribution network. Failure statistics of different electrical components of substations indicate the MV substation as one of the major causes of outages [1]. In particular, the MV switchboard very often suffers of flashover. The most effective technique to provide an early warning of failure in these electrical apparatus is to detect corona or surface predischarges phenomena. Since these phenomena, on long term, can give rise to breakdown and consequently lead to out-of-services it is important both to detect their inception and to follow their evolution by monitoring their induced effects, such as light emission, generation of acoustic noise, and ozone production [2]. However in general these signals are relatively low, and the high level of electrical interference exacerbates the problem of the infield measurement.

On the other hand until now high costs of traditional sensing devices heavily limited applications of any diagnostic system for assessing conditions of these low-cost electrical components.

Recently the feasibility of an innovative combined system has been investigated [3]. In this work, the system was assembled using high sensitivity and cheap sensors; these sensors are either commercially available or ad hoc developed prototypes. Fibre-optic-based sensors were chosen, having

the advantages to be not invasive, not affected by unwanted electrical disturbances, chemically inert and also quite cheap. An optical microphone and a fluorescent fibre-optic sensor were used to detect respectively the sound pressure and the light generated by predischarges inside the MV switchboard.

Further goal of this Research Project was a fibre-optic sensor development to detect the ozone produced by predischarge. Its integration into the assembled diagnostic prototype takes aim at detecting simultaneously three different predischarge effects for avoiding occurrence of false alarms.

The ozone sensor chosen by the authors [4] is based on a novel open path optical layout. This optical scheme guarantees a high sensitivity and, at the same time, the survival in the harsh environment of MV switchboard.

In the previous work the validation of the sensor was performed through calibration measurements on a gas flow cell, with different ozone concentrations and in a laboratory mock-up used to simulate a corona discharge simulator.

In this paper for the first time this sensor was mounted directly inside a real MV switchboard for assessing its capability to detect ozone produced by predischarge phenomena close to phase cable terminations.

2. Sensor Description

The developed sensor is based on the differential optical absorption of UV light by ozone, which strongly absorbs

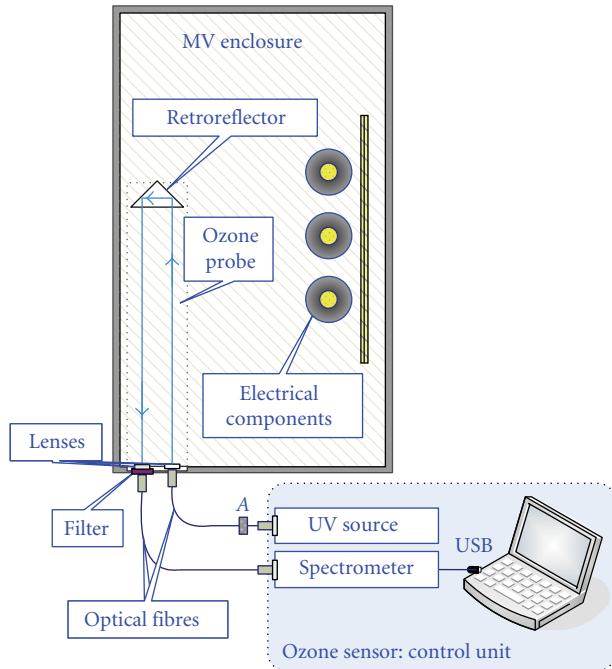


FIGURE 1: Optical scheme of the ozone sensor. The probe (on the left in the figure) mounted inside the MV switchboard is connected to the remote control unit by means of optical fibres.

in a wide spectral band between 200 nm and 375 nm; on the contrary it shows a negligible absorption in the region between 377.5 nm and 450 nm [5].

The ozone concentration C is evaluated from the intensity $I(\lambda)$ of wavelength λ measured by a spectrometer, by means of the Lambert-Beer law [6] $I(\lambda)/I_0(\lambda) = \exp(-\epsilon Cl)$, where l is the path length of the region containing the ozone, $I_0(\lambda)$ is the incident intensity and ϵ is the absorption coefficient. Through this law, the sensitivity to ozone concentration depends on the path length l . In the following C is expressed in ppm.

This spectroscopic technique is intrinsically suitable for the implementation of a whole optical fibre-based sensor to be located close to critical electrical components.

Up to now some efforts were already devoted to implement a fibre optic-based solution to assess the applicability of this spectroscopic technique for ozone detection in the industrial environment. O’Keeffe et al. [7] developed a small size probe, based on a PTFE, 5 cm long cell coupled to launching and collecting optical fibres, located on the opposite sides of the cell, to measure concentration of ozone higher than 25 ppm. The purpose of the present Project is the development of an optical fibre sensor able to detect the presence of a lower ozone concentration and to follow its evolution in time inside the MV switchboard. The novel fibre-optic layout schematically shown in Figure 1, has been implemented to fulfil this requirement.

The sensing probe (on the left in Figure 1) consists of a fixed length (40 cm) cylindrical enclosure, designed in ozone compatible material (PTFE). Longitudinal sides of this cylinder are open to allow the passage of the ozone.

A UV fused-silica retro reflector (a circular corner cube with 7 cm clear aperture) is tightly mounted on one end of this enclosure. The introduction of this retro reflector is for doubling the path length of the sensing probe, and for increasing therefore the sensitivity of the sensor to lower ozone concentration.

On the opposite side of this enclosure, two optical fibres are connected to collimating lenses. A UV filter (wavelength peak = 300 nm, FHWD = 140 nm) is positioned in front of the collecting lens, to remove spectral contributions of the UV source out of the two main ozone absorbing (at 254 nm) and not absorbing (at 375 nm) regions. UV solarisation resistant fibres (300 cm long, 400 micron diameter) are used as launching and collecting fibres, for preventing the degradation of fibres to UV exposure.

The launching fibre is coupled to the UV light source (a deuterium tungsten lamp). The collecting fibre is connected to a compact spectrometer, with fixed grating (spectral range 195–950 nm and resolution 0.25 nm). A variable attenuator (A) is mounted between the lamp and the launching fibre to avoid the saturation of the spectrometer.

The initial optical alignment of the back-reflected beam is performed by adjusting three screws on the top of this flange; these are blocked when the optics are aligned.

The spectrometer is USB-connected to the PC notebook and controlled by means of a proprietary software interface developed using Labview.

This interface was conceived as a polyfunctional interface for a smart management of the whole prototype assembled for the diagnostic of predischage phenomena. As this prototype consists of three different types of sensors (acoustic and optical sensors for detecting, resp., the sound and the light emission of the predischage and, presently, the ozone sensor), this interface allows an easily setting of configuration parameters, of measure start and of display and saving functions of the three sensors. Moreover, it is possible to display simultaneously the time behavior of signals coming out from each sensor, correlated to the same event of predischage. This combined analysis allows an efficient and more reliable diagnosis of initial failure of electrical components.

An example of the developed “ozone interface” is displayed in Figure 2. In this figure, a typical acquired spectrum of the UV filtered beam is shown (down in the figure). Settings of monitored wavelengths are shown on the right. The time trace of the transmitted intensity at 254 nm in presence of different ozone concentration is visible on the top.

The program acquires simultaneously also the transmitted intensity at the not absorbing wavelength. In this way any intensity losses within the sensor not correlated with ozone variations can be controlled in real time.

3. Sensor Calibration

Performances of the ozone sensor were validated in laboratory in presence of different ozone concentrations [4]. The lateral sides of the sensing probe were sealed to form a flow chamber. It was equipped with two gas accesses, located,

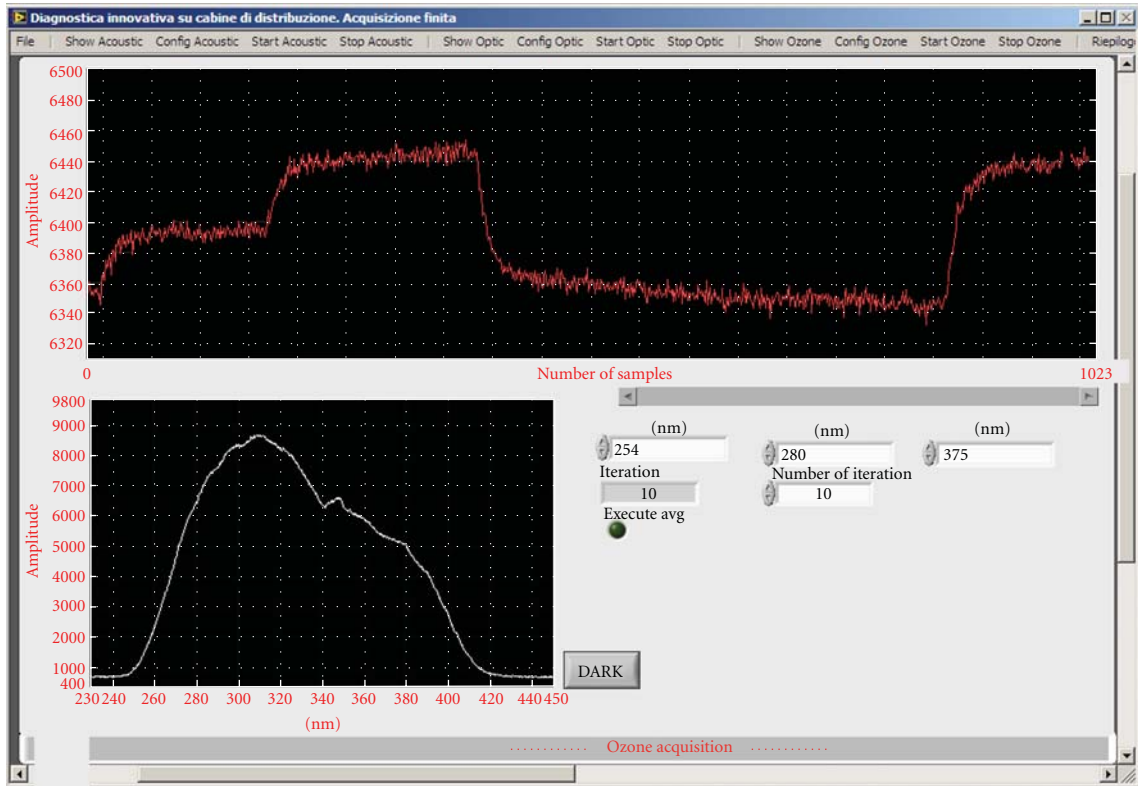


FIGURE 2: Control Panel of the ozone sensor, displaying the acquired spectrum (lower) and the time trace (upper) of the intensity at 254 nm monitored with change of ozone concentration.

respectively, close to the retro reflector and close to the output collecting lens to keep a uniform gas path with a constant flow rate (1 litre/min).

To test the response time and the linearity of the sensor two devices were used as reference ozone generators. A multi gas calibrator (mod. Series 100 EnviroNics manufactured) was used for generating calibrated ozone concentrations up to 2 ppm \pm 0.01 ppm; secondly an alternative laboratory system, used for determining the efficiency of NO/NO₂ catalytic converters (Gas Phase Titration method), was applied for producing calibrated higher ozone concentrations (range: 2–10 ppm) [8]. During all tests, spectra were averaged over 10 acquisitions and the acquisition time was 2.5 seconds long.

With the multigas calibrator, the ozone concentration was increased with maximum step of 0.5 ppm from 0 to 2 ppm; three series of measures were repeated for each concentration value. For each step, 5 minutes duration, time traces of intensities of both absorbing and not absorbing bands were recorded.

The linearity of the sensor was evaluated as $\text{Log}_{10}(I_0/I)$ versus the calibrated ozone concentration C (ppm), where I is the transmitted intensity at 254 nm measured for each step of concentration over stationary conditions.

Figure 3 shows an example of the sensor linearity in the range 0–2 ppm; the mean value and the standard deviation over three repetitions are shown.

The sensitivity of the sensor is equal to 0.01; that is, $\Delta C = 1$ ppm corresponds to $I/I_0 = 0.97$, corresponding to 200

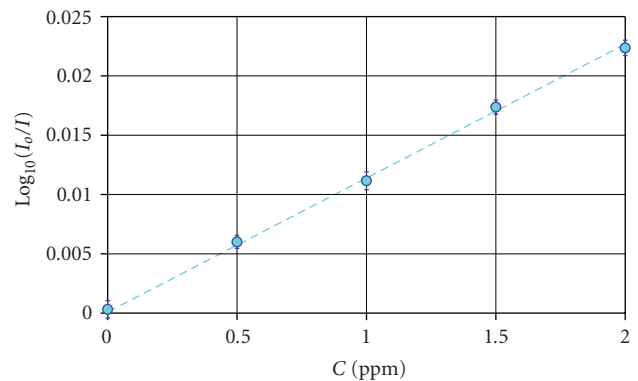


FIGURE 3: Linearity of the assembled ozone sensor; C (ppm) is the calibrated ozone concentration (provided by the Multigas calibrator).

counts. The repeatability is equal to $2\sigma/(\sqrt{3\bar{x}}) = 0.08$ ppm, where σ is the standard deviation of the mean, \bar{x} , with a coverage factor of 2. The concentration resolution is lower than 0.15 ppm.

The same sensitivity has been obtained with the other set-up in the range 2–10 ppm [4], but with a worst resolution.

During all tests, a very fast response time (seconds) to changes of the concentration in the flow chamber has been evidenced; this confirms that the sensor is suitable to follow

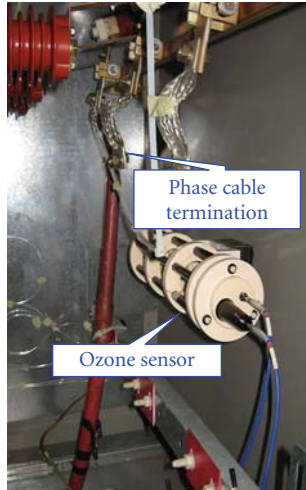


FIGURE 4: Experimental layout.

quick changes of ozone concentrations along the measuring path.

4. Experimental Details

To assess the feasibility of the new sensor in detecting ozone concentration under a real operating condition, a typical MV switchboard configuration was reproduced in the laboratory. Normalized components exploited in Italian distribution network (12/20 kV) were used. Inside, two different artificial defects were introduced once at a time to simulate predischarge activity. A wire (300 mm long and 1 mm diameter) was used to generate a corona phenomenon. A strip of electrical semiconducting tape (70 mm long and 15 mm wide) was attached to the phase cable termination to simulate a surface predischarge.

A standard Partial Discharge (PD) electrical system was used to monitor the predischarge activity [9]. This method provides the value of the predischarge amplitude in terms of apparent charge (picoCoulomb, pC).

For each type of defect, a series of tests were carried out by increasing the voltage applied to cable termination from 0 kV to the predischarge inception level (U_i), detected by the PD system, and then progressively up to 25 kV.

The ozone probe was installed inside the MV switchboard and connected to the control unit located outside of the MV enclosure, as schematically shown in Figure 1. The probe was located on a lateral wall of the enclosure as shown in Figure 4.

To check the presence of ozone concentration in the MV switchboard, a commercial ozone sensor with a typical acquisition times of one minute, was also located inside the metallic case.

5. Results and Discussion

Figure 5 shows an example of the ozone trend (red points) measured by the optical sensor versus time during three consecutive voltage applied ramps. The ozone level was

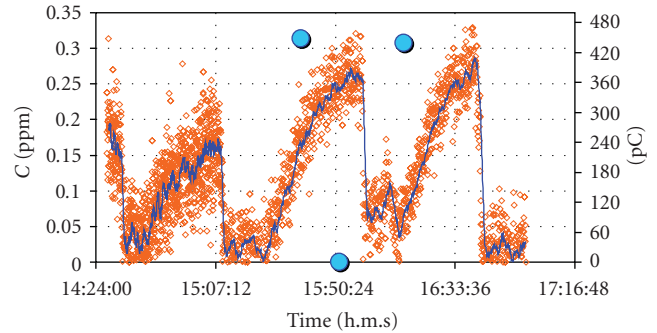


FIGURE 5: Ozone sensor response versus time measured in presence of the corona defect. The right vertical axis reports predischarge amplitudes (pC) by the standard PD electrical method.

evaluated by means of the calibration curve shown in Figure 3. Data shown in Figure 5 refer to ozone values measured inside the MV enclosure in presence of a corona defect. The acquisitions were 2.5 seconds long. The solid line (blue line) represents the average over 20 points. The vertical axis on the left shows predischarge amplitude values (in pC) measured by the standard PD system (blue dots in figure).

As shown in Figure 5, similar trends were obtained with the corona defect over three measure repetitions. This behavior is in good agreement with data registered by the PD system; it was confirmed that the corona phenomenon was quite stable. A slight delay in detecting both the corona inception and extinction was observed, even if a time of tenth seconds was confirmed. The ozone levels measured by the optical sensor were between 0.2 and 0.3 ppm (on plateau); these values were in good agreement with the average value measured by the commercial ozone system (0.23 ppm). As shown in Figure 5 the sensor started to detect ozone presence over three repetitions, when the amplitude of the corona predischarge was equal to 400 pC. This value was measured by the PD system at a voltage level equal to $1.25 U_i$. This is the minimum applied voltage necessary to record an ozone activity by means of this optical sensor. This value was compared with detectable threshold values of both the optical microphone and the fluorescent fiber-based sensor of the diagnostic prototype, respectively, equal to $1.15 U_i$ and to $1.1 U_i$. As evidenced, the sensitivity of the ozone sensor is slightly lower than sensitivities of optical and acoustic sensors. A lower sensitivity was obtained in presence of surface predischarges. The sensor began to appreciate the presence of ozone (0.15–0.2 ppm) only when the predischarge activity was higher than 1500 pC (equal to $2.5 U_i$). The amplitude of the surface predischarge, measured by the PD system at inception was about 600 pC. This is probably due to the high instability of this of phenomenon. To improve the sensitivity to both predischarges inception an optimization of the path length will be performed.

6. Conclusion

This paper was aimed at giving a contribution to the ongoing development of a combined diagnostic system for detection of predischarges in electrical components of MV distribution

network. In particular the application for the first time of a new fibre-optic sensor for detecting ozone variation induced by predischARGE in a MV switchboard, was evaluated. A novel layout of the spectroscopic type sensor, based on the use of an optical retroreflector, was adopted to improve its sensitivity. Optical fibres were used to connect the sensing probe, installed into the MV enclosure, to the remote control unit located outside.

Main advantages of this whole optical configuration are its installation inside the MV compartment without affecting service performances of electrical components; Moreover, any mutual interference between the optical sensor and the ozone produced by predischarges is avoided, since the sensor is based on a spectroscopic technique. As a consequence a long life in service is expected.

Main features of this sensor are linear response from 0.1 to 10 ppm and a concentration resolution lower than 0.15 ppm.

The validation of this sensor in a typical MV switchboard configuration either with a "corona defect" or with a semiconducting strip (surface predischARGE) has evidenced the sensor feasibility to follow predischARGE activities and to provide a correct measure of the ozone concentration produced. The minimum detectable threshold of the ozone signal in presence of a corona phenomenon was $1.3 U_i$, slightly higher than these of acoustic and optical sensors, and higher ($2.5 U_i$) with surface predischARGE.

Further developments will be sought to improve both the sensitivity and the speed of the sensor response, in presence of surface predischARGE phenomena.

Acknowledgments

This work has been financed by the Research Fund for the Italian Electrical System under the Contract Agreement between CESI RICERCA and the Ministry of Economic Development - General Directorate for Energy and Mining Resources stipulated on June 21, 2007 in compliance with the Decree no.73 of June 18, 2007. The authors also gratefully acknowledge Mr. R. Marini and Mr. P. Serragli for their technical support and Dr. L. Fialdini for helpful discussion.

References

- [1] X. Zhang, E. Gockenbach, and H. Borsi, "Life asset management of the electrical components in medium-voltage networks," in *Proceedings of the IEEE Russia Power Tech (PowerTech '05)*, pp. 1–7, St. Petersburg, Russia, June 2005.
- [2] G. Rizzi, M. Manzo, and C. Sidoti, "Condition assessment of power cables in the enel distribution network, considerations after 2 years trial," in *Proceedings of the 18th International Conference on Electricity Distribution (CIRED '05)*, vol. 1, pp. 71–76, Turin, June 2005, paper no. 361.
- [3] L. De Maria, G. Rizzi, J. Borghetto, R. Passaglia, U. Perini, and P. Serragli, "A new approach to integrity assessment of electrical components of the medium voltage for distribution network," in *Proceedings of the 19th International Conference on Electricity Distribution (CIRED '07)*, Vienna, Austria, May 2007, paper no. 0516.
- [4] L. De Maria, G. Rizzi, P. Serragli, R. Marini, and L. Fialdini, "Optical sensor for ozone detection in Medium Voltage Switchboard," in *Proceedings of the IEEE Sensors Conference*, pp. 1297–1300, Lecce, Italy, October 2008.
- [5] E. C. Inn, Y. Tanaka, and R. Nicole, "Absorption coefficient of ozone in the ultraviolet and visible regions," *Journal of the Optical Society of America*, vol. 43, no. 10, pp. 870–873, 1953.
- [6] H. Tanimoto, H. Mukai, S. Hashimoto, and J. E. Norris, "Intercomparison of ultraviolet photometry and gas-phase titration techniques for ozone reference standards at ambient levels," *Journal of Geophysical Research D*, vol. 111, no. 16, Article ID 16313, 2006.
- [7] S. O'Keefe, G. Dooly, C. Fitzpatrick, and E. Lewis, "Optical fibre sensor for the measurement of ozone," *Journal of Physics*, vol. 15, no. 1, pp. 213–218, 2005.
- [8] H. Tanimoto, H. Mukai, S. Hashimoto, and J. E. Norris, "Intercomparison of ultraviolet photometry and gas-phase titration techniques for ozone reference standards at ambient levels," *Journal of Geophysical Research*, vol. 111, Article ID 16313, 2006.
- [9] International Standard CEI IEC60270, "High Voltage test techniques Partial discharge measurements," 2000.